

ENGINEERING MECHANICS 2014

20th INTERNATIONAL CONFERENCE

MAY 12 - 15, 2014, SVRATKA, CZECH REPUBLIC



BOOK OF FULL TEXTS

Editor: Vladimír Fuis

**Institute of Solid Mechanics, Mechatronics and Biomechanics,
Faculty of Mechanical Engineering, Brno University of Technology**

**Institute of Thermomechanics,
Academy of Sciences of the Czech Republic, v.v.i. – branch Brno**

Association for Engineering Mechanics

**Institute of Theoretical and Applied Mechanics,
Academy of Sciences of the Czech Republic, v.v.i.**

ŽDAS, a.s., Žďár nad Sázavou

Czech Society for Mechanics

IFTToMM Member Committee of Czech Republic

Text may be copied and used freely, but credit should be given to this Proceedings.

Copyright © 2014 Brno University of Technology

Institute of Solid Mechanics, Mechatronics and Biomechanics

1st edition, 2014

ISBN 978-80-214-4871-1

ISSN 1805-8248

The Conference is hosted by the hotel ŽĎAS at Svatka.

All the papers were reviewed by members of the international scientific committee.

SCIENTIFIC COMMITTEE

Chairman:

Assoc. Prof. Vladimír Fuis, PhD. Brno University of Technology & IT AS CR, Brno, CZ

Members:

Prof. dr. Pavol Bauer Delft University of Technology, NL
Prof. Ján Benčat, PhD. University of Žilina, SK
Dr. Ouadie Bennouna ESIGELEC, FR
Prof. Jiří Burša, PhD. Brno University of Technology, CZ
Prof. Miloš Drdáčký, DSc. ITAM AS CR, Prague, CZ
Prof. Paola Forte University of Pisa, IT
Assoc. Prof. Karel Frydryšek, PhD. Technical University of Ostrava, CZ
Prof. Ardeshir Guran, PhD. Institute of Structronics, Ottawa, CA
Jaromír Horáček, DSc. IT AS CR, Prague, CZ
Assoc. Prof. L. Ilieva-Mitutsova, PhD. Bulgarian Academy of Sciences, Sofia, BG
Prof. Miroslav Jícha, PhD. Brno University of Technology, CZ
Prof. Milan Jirásek, DSc. Czech Technical University in Prague, CZ
Assoc. Prof. Jiří Kala, PhD. Brno University of Technology, CZ
Prof. Zdeněk Kala, PhD. Brno University of Technology, CZ
Prof. Zbyněk Keršner, PhD. Brno University of Technology, CZ
Prof. Alena Kohoutková, PhD. Czech Technical University in Prague, CZ
Prof. Anne-Maria Laukkanen, PhD. University of Tampere, FI
Prof. Dušan Maga, PhD. Czech Technical University in Prague, CZ
Prof. František Maršík, DSc. IT AS CR, Prague, CZ
Prof. Arkadiusz Mężyk Silesian University of Technology, Gliwice, PL
Prof. dr. Damijan Miljavec University of Ljubljana, Ljubljana, SI
Jiří Minster, DSc. ITAM AS CR, Prague, CZ
Jiří Náprstek, DSc. ITAM AS CR, Prague, CZ
Prof. Bořek Patzák, PhD. Czech Technical University in Prague, CZ
Prof. Michail Pavlenko Moscow State Mining University, RU
Prof. Dr. Paolo Pennacchi Politecnico di Milano, Milan, IT
Prof. Kazimierz Peszynski, PhD. Univ. of Technol. and Life Science, Bydgoszcz, PL
Prof. Jindřich Petruška, PhD. Brno University of Technology, CZ
Jiří Plešek, PhD. IT AS CR, Prague, CZ
Prof. Jaromír Příhoda, PhD. IT AS CR, Prague, CZ
Ladislav Půst, DSc. IT AS CR, Prague, CZ
Prof. Ján Sládek, DSc. ICA, SAS, Bratislava, SK

Prof. Vladimír Sládek, DSc.	ICA, SAS, Bratislava, SK
Prof. Pavel Šafařík, PhD.	IT AS CR, Prague, CZ
Prof. Michal Šejnoha, DSc.	Czech Technical University in Prague, CZ
Prof. Alexander Tesár, DSc.	ICA, SAS, Bratislava, SK
Prof. Václav Tesař, PhD.	IT AS CR, Prague, CZ
Prof. Tomasz Topoliński	Univ. of Technol. and Life Science, Bydgoszcz, PL
Prof. Pavel Vlasák, DSc.	Institute of Hydrodynamics AS CR, Prague, CZ
Prof. Yuri Sergeevich Voribiev	NAS of Ukraine, Kharkov, UA
Prof. Jaroslav Zapoměl, DSc.	IT AS CR, Ostrava, CZ
Prof. Vladimír Zeman, DSc.	University of West Bohemis in Pilsen, CZ
Prof. Anatoly P. Zinkovskii, DSc.	National Academy of Sciences, Kiev, UA
Prof. Rudolf Žitný, PhD.	Czech Technical University in Prague, CZ
Prof. Milan Žmíndák, PhD.	University of Žilina, SK

HONOURARY COMMITTEE

Miroslav Šabart, MSc.	Managing Director of ŽĎAS Inc.
František Mládek	Mayor of Svratka

List of sections:

KEY	Keynote Lectures
BIO	Biomechanics
DYN	Dynamics
FLU	Fluid Mechanics
FRA	Fracture Mechanics
HIS	Historical Structures
KIN	Kinematics
MCT	Mechatronics
REL	Reliability
SOL	Mechanics of Solids
TER	Termomechanics

Main Headings

Table of Contents (by the first Author's Name)	6
Table of Contents (by Sections)	17
Keynote Lectures	30
Papers	44
Authors Index	756

Table of Contents

KEYNOTE LECTURES

Burša J., Bansod Y.D.: <i>DESIGN AND APPLICATIONS OF PRESTRESSED TENSEGRITY STRUCTURE</i>	30
Hartl M., Křupka I., Omasta M., Šperka P.: <i>RECENT ADVANCES AND PROBLEMS IN LUBRICATED HERTZIAN CONTACTS</i>	34
Rudolf P., Štefan D., Pochylý F.: <i>DYNAMICS OF SWIRLING FLOWS IN INDUSTRIAL APPLICATIONS</i>	38

PAPERS

Andryszczyk M., Wirwicki M., Topoliński T.: <i>BIOMATERIALS USED FOR THE PRODUCTION OF STENTS - HOPES AND LIMITATIONS - REVIEW ARTICLE</i>	44
Ansari R.I., Sahir M.H.: <i>PERFORMANCE EVALUATION OF HYDROVAC GRAVITY POWER GENERATION SYSTEM</i>	48
Aromiński A.: <i>AUTOMOTIVE PIEZOELECTRIC SENSORS FOR SIMPLIFIED KNOCK DETERMINATION</i>	52
Astrouski I., Raudensky M.: <i>PLASTIC HEAT EXCHANGER USING TWISTED HOLLOW FIBERS</i>	56
Baláž I., Koleková Y.: <i>INTERACTION BETWEEN BENDING MOMENT AND SHEAR FORCE IN STEEL PLATED STRUCTURAL ELEMENTS</i>	60
Bednarik M., Holzer R., Laho M., Dunčko M.: <i>STONE FOR RESTORATION AND DECORATION PURPOSES IN WESTERN SLOVAKIA</i>	64
Bednář L., Miczan M., Tajč L., Hoznedl M.: <i>EXPERIMENTAL VALIDATION OF THE AERODYNAMIC FORCE ACTING ON A CONE OF A BALANCED CONTROL VALVE</i>	68
Belka M., Jedelsky J., Boiron O., Bailly L., Bertrand E., Zaremba M., Maly M., Lizal F.: <i>MEASUREMENT OF AIRFLOW IN TRACHEA USING PARTICLE IMAGE VELOCIMETRY AND LASER-DOPPLER ANEMOMETRY</i>	72
Benčat J.: <i>INDUSTRIAL MACHINERY DYNAMIC EFFECTS ON PRODUCTION PROCESS AND HALL STRUCTURES</i>	76
Beňovský P., Rusche H., Ridzoň F., Popovac M., Reichl Ch., Fleckl T.: <i>DROPWISE CONDENSATION MODELING</i>	80
Beroun S., Brabec P., Dittrich A., Mikulanin L.: <i>TEMPERATURE FIELD OF SPARK PLUG IN THE SI ENGINE</i>	84
Beroun S., Brabec P., Dittrich A., Nguyen T.T.: <i>INJECTOR OF LIQUID LPG</i>	88

Blanchard R., Morin C., Vella A., Sant Z., Hellmich Ch.: <i>INTRA-VOXEL MICRO-ELASTO-PLASTICITY FOR CT-BASED PATIENT-SPECIFIC FRACTURE RISK ASSESSMENT OF VERTEBRAE</i>	92
Blasiak S., Takosoglu J.E., Laski P.A.: <i>THE FLOW RATE OPTIMIZATION OF DIRECTIONAL PNEUMATIC CONTROL VALVE</i>	96
Bošanský M., Patzák B.: <i>ON PARALLELIZATION OF STIFFNES MATRIX ASSEMBLY</i>	100
Březina T., Březina L., Marek J., Hadaš Z., Vetiška J.: <i>SIMULATION ASSESSMENT OF SUPPRESSION OF MACHINE TOOL VIBRATIONS</i>	104
Bublík O., Jonášová A., Vimmr J.: <i>APPLICATION OF THE LATTICE BOLTZMAN METHOD FOR THE MODELLING OF PULSATILE FLOW IN IDEALISED BYPASS GEOMETRIES</i>	108
Bulejko P., Svěrák T.: <i>MECHANICAL AND FILTERING PROPERTIES OF NON-SINTERED POROUS SOLIDS FOR FILTRATION APPLICATIONS</i>	112
Cech V., Jedlicka L., Jevicky J.: <i>SOME PROBLEMS WITH THE ESTIMATION OF PROJECTILE TRAJECTORY PERTURBATIONS</i>	116
Čadek M., Marvalová B., Petříková I., Samal S.: <i>DETERMINATION OF MATERIAL PARAMETERS OF RUBBER AND RUBBER COMPOSITES BY BIAXIAL LOADING</i>	120
Čečrdle J.: <i>INFLUENCE OF PROPELLER BLADE FORCE SPANWISE DISTRIBUTION ON WHIRL FLUTTER CHARACTERISTICS</i>	124
Dolanský J.: <i>SIMULATION OF MOTION OF MULTIPLE PARTICLES IN A CLOSED CONDUIT USING THE LBM BASED APPROACH</i>	128
Doškár M., Novák J.: <i>REDUCING PERIODICITY IN MICROSTRUCTURE RECONSTRUCTION OF HETEROGENEOUS MATERIALS</i>	132
Dowkontt S., Ostapski W., Tułodziecki M.: <i>ANALYSIS OF SUBWAY WAGON ROLLER BEARING AXLE BOX STRESSES WITH MEDIUM OPERATION LOAD</i>	136
Duda S., Gembalczyk G., Lawniczek R., Trawinski T.: <i>COMPARISON OF DYNAMIC INTERACTIONS IN THE DRIVE SYSTEM OF ELECTRIC LOCOMOTIVE EU07 BEFORE AND AFTER THE MODERNIZATION DRIVE UNIT</i>	140
Duda S., Gembalczyk G., Lawniczek R.: <i>SIMULATION AND EXPERIMENTAL STUDIES ON THE CONTROL SYSTEM FOR MECHATRONIC REHABILITATION DEVICE WITH KEEP-UP MOVEMENT</i>	144
Dyk Š., Zeman V., Byrtus M.: <i>KINEMATICALLY EXCITED NON-LINEAR VIBRATION OF A BEAM ON ELASTIC SUPPORTS WITH CLEARANCES</i>	148
Dzikowska W., Żórawski D., Peszyński K.: <i>MODELLING AND INITIAL TESTS OF THE DYNAMIC PROPERTIES OF VIBROINSULATION MATS</i>	152

Écsi L., Jančo R., Élesztős P.: <i>AN IMPROVED THERMAL-STRUCTURAL FINITE ELEMENT MODEL FOR MANUFACTURING PROCESSES WITH HEAT GENERATION</i>	156
Eliáš J.: <i>DEM SIMULATION OF BALLAST OEDOMETRIC TEST</i>	160
Farrugia M., Grech N., Chircop M., Azzopardi J.P.: <i>SIMULATION AND IMPLEMENTATION OF TURBOCHARGING A 600CC ENGINE FOR FORMULA SAE</i>	164
Fenech G., Farrugia M.: <i>EXPERIMENTAL ANALYSIS OF A FIXED-SPEED AND A VARIABLE-SPEED AIR CONDITIONING SYSTEM</i>	168
Filipský J., Štorch V.: <i>COMPARISON OF PROPELLER ANALYSIS METHODS AND EXPERIMENTAL DATA</i>	172
Foglar M., Kovář M.: <i>BLAST PERFORMANCE OF FRC SPECIMENS WITH STEEL FIBERS OF LOW DUCTILITY</i>	176
Frydryšek K., Pleva L., Pompach M., Učeň O., Fojtík F., Kubín T., Theisz G., Žilka L., Poruba Z.: <i>EXTERNAL AND INTERNAL FIXATORS FOR TREATMENT OF COMPLICATED FRACTURES IN TRAUMATOLOGY AND ORTHOPAEDICS</i>	180
Fuis V.: <i>SHAPE DEVIATIONS ANALYSIS OF THE ALIGNED BARS</i>	184
Gajewski M., Jemiolo S.: <i>PROPOSITION OF CONSTITUTIVE MODEL FOR FIBRE-REINFORCED HYPERELASTIC MATERIALS</i>	188
Gołębiowska I., Sakiewicz W.: <i>BASE ISOLATION SYSTEMS IN BUILDING STRUCTURES</i>	192
Göringer J., Foglar M.: <i>CONCRETE DETERIORATION DUE TO AGGRESSIVE ENVIRONMENT AND CYCLIC LOADING – THEORETICAL STUDY</i>	196
Hać M., Ostapski W.: <i>INFLUENCE OF REDUCER DISK BALANCE ON FLEXURAL VIBRATION OF PROPELLER SHAFT</i>	200
Hadas Z., Vetiska J.: <i>ENERGY HARVESTING ANALYSIS OF BODY MOTION AS ENERGY SOURCE FOR BIOMEDICAL DEVICES</i>	204
Hájek R., Foglar M.: <i>EXPERIMENTAL EVALUATION OF THE EFFECTS OF A CONCRETE BARRIER TO PRESSURE WAVE PROPAGATION</i>	208
Hájek R., Foglar M.: <i>NUMERICAL MODELLING OF INTERACTION BETWEEN PRESSURE WAVE AND RIGID BARRIER</i>	212
Havlík J., Dlouhý T.: <i>EXPERIMENTAL VERIFICATION OF THEORETICAL MODELS TO CALCULATE THE HEAT TRANSFER COEFFICIENT IN THE SHELL-AND-TUBE HEAT EXCHANGER</i>	216
Holušová T., Seitl S., Fernández-Canteli A.: <i>MODIFIED COMPACT TENSION TEST: THE INFLUENCE OF THE STEEL BARS POSITION</i>	220

Horáček J., Bula V., Radolf V., Vampola T., Dušková M.: <i>MEASUREMENT OF VIBRATION, FLOW AND ACOUSTIC CHARACTERISTICS OF A HUMAN LARYNX REPLICA</i>	224
Hric V., Halama J., Fürst J.: <i>NUMERICAL SOLUTION OF INVISCID TRANSONIC FLOW IN A CHANNEL WITH COMPLEX EQUATION OF STATE</i>	228
Hrstka M., Profant T., Klusák J., Ševeček O., Kotoul M.: <i>A STABILITY CRITERION OF AN ORTHOTROPIC BI-MATERIAL NOTCH BASED ON THE STRAIN ENERGY DENSITY</i>	232
Hřibová V., Komínek J., Astrouski I., Raudenský M., Tseng A.A.: <i>HEAT TRANSFER SIMULATION OF HEAT EXCHANGERS MADE BY POLYMERIC HOLLOW FIBERS</i>	236
Hyhlík T.: <i>DEVELOPMENT OF MATHEMATICAL MODEL OF RAIN ZONE</i>	240
Chládek Š., Zolotarev I.: <i>IDENTIFICATION OF THE AEROELASTIC PROFILE BASED ON OPTICAL MEASUREMENT</i>	244
Chleboun J., Mikeš K.: <i>PARAMETER IDENTIFICATION IN INITIAL VALUE PROBLEMS FOR NONLINEAR ORDINARY DIFFERENTIAL EQUATIONS</i>	248
Iván L., Popovič M.: <i>OPTIMISATION IN THE EXPLICIT ANALYSIS OF THE ROAD BARRIERS</i>	252
Ivančo V., Orečný M., Huňady R.: <i>SIMULATION OF DROP TESTS OF THE CASK FOR RADIOACTIVE WASTE</i>	256
Janíček P.: <i>STRESS-STRAIN ANALYSIS OF CERAMIC HEADS IN THE DESTRUCTION DEVICE</i>	260
Janouchová E., Kučerová A., Sýkora J.: <i>EFFICIENT BAYESIAN PARAMETER IDENTIFICATION</i>	264
Joch L., Krautschneider R.: <i>STUDY OF EXTERNAL COOLING OF STEAM GENERATOR PGV-1000M COLLECTORS POCKET WELD № 111 FOR SUPPRESSING OF STRESS CORROSION CRACKING</i>	268
Jonášová A., Bublík O., Rohan E., Vimmr J.: <i>SIMULATION OF CONTRAST MEDIUM PROPAGATION BASED ON 1D AND 3D PORTAL HEMODYNAMICS</i>	272
Kabeláč J., Rossier S.: <i>REDUCTION FOR HIGH-RISE BUILDINGS SEISMIC ANALYSIS</i>	276
Kala Z., Valeš J.: <i>LATERAL-TORSIONAL BUCKLING OF I-SECTION BEAMS WITH INITIAL RANDOM IMPERFECTIONS</i>	280
Kalina M.: <i>COMPUTER NUMERICAL SOLUTION OF VON MISES PLANAR TRUSS BY THE POTENTIAL ENERGY</i>	284
Kazakevičiūtė-Makovska R.: <i>BIOLOGICAL SOFT TISSUES: MECHANICAL CHARACTERIZATION, DATA ANALYSIS AND MODELS' EVALUATION</i>	288

Kiš R., Malcho M., Janovcová M.: <i>CFD ANALYSIS OF FLOWS IN A HIGH-PRESSURE NATURAL GAS PIPELINES WITH DIFFERENT SHAPES OF ORIFICE PLATES</i>	292
Knobloch J., Holub M., Kolouch M.: <i>LASER TRACKER MEASUREMENT FOR PREDICTION OF WORKPIECE GEOMETRIC ACCURACY</i>	296
Kolařík F., Patzák B.: <i>IMPLEMENTATION OF STABILIZED FORMULATION FOR LEVEL SET EQUATION</i>	300
Koleková Y., Baláž I.: <i>INTERACTION BETWEEN BENDING MOMENT AND SHEAR FORCE IN ALUMINIUM PLATED STRUCTURAL ELEMENTS</i>	304
Kostecká M., Kolísko J., Bittner T., Huňka P., Mandlík T.: <i>THE INFLUENCE OF FROST RESISTANCE ON UHPC PLATES WITH DIFFERENT TYPES OF TEXTILES ARMATURES</i>	308
Koteš P., Vičan J.: <i>CORROSION OF REINFORCEMENT VERSUS RELIABILITY OF RC GIRDERS</i>	312
Koudelka T., Kruis J., Lepš M., Nosek J.: <i>FITTING MODEL PARAMETERS OF PRESTRESSED CONCRETE BRIDGE: COMPUTATIONAL ASPECTS</i>	316
Kovářová K., Ševčík R.: <i>METHODS OF A BUILDING STONE INTERNAL STRUCTURE STUDY</i>	320
Králík V., Němeček J., Jíra A., Fíla T., Zlámal P.: <i>ENERGY ABSORPTION OF CELLULAR FOAMS IN HIGH STRAIN RATE COMPRESSION TEST</i>	324
Kratochvíl O., Křižan J.: <i>ANALYSIS OF DYNAMIC RESPONSE OF FOOTBRIDGE VEVEŘÍ ON PEDESTRIAN LOAD</i>	328
Krčmář M., Materna A.: <i>ASSESSMENT OF THE CONSTITUTIVE PROPERTIES OF REACTOR STEEL USING AN INVERSE ANALYSIS ON THE SMALL PUNCH TEST</i>	332
Krejsa J., Vechet S., Chen K.: <i>MULTIPLE INDOOR ROBOT LOCALIZATION USING INFRARED BEACONS</i>	336
Kubíková T., Witter K., Liška V., Tonar Z.: <i>MORPHOMETRY AND RECONSTRUCTION OF HEPATIC LOBULES IN PIG BASED ON SERIAL HISTOLOGICAL SECTIONS</i>	340
Kučera P., Píštěk V.: <i>A COMPUTATIONAL MODEL OF POWERTRAIN COMPONENTS IN SIMULINK</i>	344
Kučerová A., Sýkora J., Zeman J.: <i>STOCHASTIC MODELLING OF HETEROGENEOUS MATERIALS BASED ON IMAGE ANALYSIS</i>	348
Květoň J., Eliáš J.: <i>PERFORMANCE COMPARISON OF LOCALIZATION LIMITERS</i>	352
Kyncl M., Pelant J.: <i>NUMERICAL SIMULATION OF THE TURBULENT COMPRESSIBLE GAS FLOW IN THE VANELESS MACHINES</i>	356

Laski P.A., Takosoglu J.E., Blasiak S.: <i>A DELTA TYPE CLOSED KINEMATICS CHAIN WITH PNEUMATIC MUSCLE ACTUATOR MANIPULATOR</i>	360
Lazarová E., Krúpa V., Ivaničová L., Kruľáková M.: <i>INVESTIGATION OF PROCESS DYNAMICS OF TBM EXCAVATION</i>	364
Lošák P.: <i>IDENTIFICATION OF VIBRATION CAUSES BASED ON SPECTROGRAMS DURING THE STRAIGHTENING PROCESS</i>	368
Machacek J., Charvat M.: <i>STUDY ON SHEAR CONNECTION BETWEEN BRIDGE STEEL TRUSS AND CONCRETE SLAB</i>	372
Majer Z., Náhlík L.: <i>NUMERICAL ESTIMATION OF MICRO CRACK PATHS IN POLYMER PARTICULATE COMPOSITE</i>	376
Makovička D., Makovička D.: <i>IMPACT OF MISSILE ON CONCRETE OR SOIL OBSTACLE</i>	380
Malíková L.: <i>PLASTIC ZONE EXTENT IN A CCT SPECIMEN DETERMINED FROM THE CRACK-TIP STRESS FIELD APPROXIMATED BY MEANS OF THE WILLIAMS EXPANSION</i>	384
Marcián P., Borák L., Narra N., Skalka P., Kaiser J., Wolff J.: <i>AN ALGORITHM FOR COMPUTATIONAL SIMULATION OF MANDIBLE BONE MODELING AND REMODELING AROUND DENTAL IMPLANTS</i>	388
Máša B., Náhlík L., Hutař P.: <i>ON AN ESTIMATION OF THE EXPONENT OF THE STRESS SINGULARITY: THREE DIMENSIONAL PROBLEMS AND EFFECT OF RESIDUAL STRESSES ON A CRACK ARRESTED ON THE INTERFACE</i>	392
Mikula J., Ševčík M., Hutař P., Náhlík L.: <i>FRACTURE MECHANICS ASSESSMENT OF CRACKED WELDED POLYOLEFIN PIPES</i>	396
Milewski G.: <i>COMPARATIVE ANALYSIS OF BURZYŃSKI-TORRE STRENGTH HYPOTHESIS FOR DENTINE AND ENAMEL</i>	400
Mlkvik M., Zaremba M., Jedelský J., Wigley G.: <i>INVESTIGATION OF THE SPRAY GENERATED BY A Y-JET ATOMIZER</i>	404
Myšáková E., Lepš M.: <i>COMPARISON OF METHODS FOR CONSTRAINED DESIGN OF COMPUTER EXPERIMENTS</i>	408
Náhlík L., Štegnerová K., Hutař P.: <i>ESTIMATION OF CRITICAL STRESS VALUES FOR CRACK INITIATION FROM SHARP V-NOTCHES</i>	412
Náprstek J., Fischer C.: <i>POST-CRITICAL MULTI-MODAL VIBRATION OF A CONTINUOUS INVERSE PENDULUM TYPE SYSTEM</i>	416
Náprstek J., Pospíšil S.: <i>AEROELASTIC DIVERGENCE MODELED BY MEANS OF THE STOCHASTIC RESONANCE</i>	420
Návrat T., Florian Z., Kočíš J., Vosynek P.: <i>BIOMECHANICAL TESTING OF SPINAL SEGMENT FIXED BY ARCOFIX SYSTEM</i>	424

Nekvasil R., Lošák P., Lukáč P.: <i>ANALYSIS OF DAMAGED CONNECTION PIPING</i>	428
Nevrlý J., Němec Z., Jurík M.: <i>EFFECTIVENESS OF KINETIC ENERGY RECOVERY EXPLORED BY MEANS OF EXPERIMENTAL STAND</i>	432
Nhan P.T., Samal S.M., Petrikova I., Marvalová B.: <i>CORRELATION BETWEEN ENHANCED MECHANICAL STRENGTH AND MICROSTRUCTURE RELIABILITY OF GEO-COMPOSITE</i>	436
Novotný J., Matěcha J., Pohan P.: <i>PASSIVE ELEMENTS FOR PRECISE DIRECTION AND MANAGEMENT OF AIR IN DATA RACKS</i>	440
Novotný P., Maršálek O., Zubík M., Drápal L.: <i>ANALYSIS OF SLIDE BEARING COMPUTATIONAL MODELS CONSIDERING ELASTIC DEFORMATIONS AND ROUGH SURFACES</i>	444
Nowicki K., Kolber P., Perczyński D., Wawrzyniak S.: <i>REVITALISATION OF INDUSTRIAL ROBOT CONTROL SYSTEMS</i>	448
Nowicki K., Perczyński D., Kolber P., Peszyński K.: <i>SIMULATION TESTS OF IRB6 ROBOT</i>	452
Nowogońska B.: <i>MODEL OF THE RELIABILITY PREDICTION OF MASONRY WALLS</i>	456
Ondra V., Lošák P.: <i>COMPARISON OF MODAL PARAMETER ESTIMATION TECHNIQUES FOR EXPERIMENTAL MODAL ANALYSIS</i>	460
Ostaszewski M., Siemieniako F.: <i>KINEMATIC MODEL OF MECHANICAL DESIGN FOR SUPPORT HUMAN LOWER LIMB</i>	464
Panáček T., Klapka M., Němec Z.: <i>OPTIMIZATION OF VALVE MANIFOLD TIMING SEQUENCE USING DIFFERENTIAL EVOLUTION ALGORITHM</i>	468
Parham E.: <i>THERMODYNAMICS PROPERTIES OF COPPER HALIDE ALLOY (CuBr_{0.5}Cl_{0.5})</i>	472
Pásek M., Šimurda J., Christé G.: <i>SENSITIVITY OF ACTION POTENTIAL TO CHANGES OF INWARD RECTIFIER POTASSIUM CURRENT IK1 IS DIFFERENT IN RECENT MODELS OF HUMAN VENTRICULAR CARDIOMYOCYTES</i>	476
Pavlenko M.V.: <i>PRINCIPLES OF VIBRATION IMPACT ON CRACKED METHANE-BEARING COAL SEAM</i>	480
Pečínka L., Švrček M.: <i>ACOUSTIC FREQUENCIES OF COOLANT IN PRIMARY CIRCUIT OF NPP TEMELIN AND POSSIBILITY OF RESONANCES WITH FUEL ASSEMBLY TVSA-T</i>	484
Perczyński D., Kolber P., Wawrzyniak S.: <i>MINIMISING OF THE OPERATION COSTS OF POWER TRANSFORMERS</i>	488
Podolka L.: <i>SOLVING ANCHORAGE AREA PRESTRESSED AND NONPRESTRESSED COMPOSITES</i>	492

Pokorný P., Náhlík L., Hutař P.: <i>THE EFFECT OF THRESHOLD VALUE ON THE RESIDUAL FATIGUE LIFETIME OF RAILWAY AXLES</i>	496
Polach P., Hajžman M.: <i>UTILIZING OF A WEIGHT-FIBRE-PULLEY-DRIVE MECHANICAL SYSTEM FOR THE INVESTIGATION OF A FIBRE BEHAVIOUR</i>	500
Popov G., Vaysfeld N., Zozulevich B.: <i>THE EXACT SOLUTION OF ELASTICITY MIXED PLAIN BOUNDARY VALUE PROBLEM IN A RECTANGULAR DOMAIN</i>	504
Pospíšilová A., Lepš M.: <i>ADAPTIVE UPDATE OF SURROGATE MODELS FOR RELIABILITY-BASED DESIGN OPTIMIZATION: A REVIEW</i>	508
Prášilová E., Florian Z., Marcián P.: <i>FINITE ELEMENT ANALYSIS OF COMPRESSION OF LUMBAR SPINE WITH DYNAMIC IMPLANT</i>	512
Přinosil M., Kabele P.: <i>SINGLE CRACK BEHAVIOR OF FIBER REINFORCED LIME-BASED MORTAR</i>	516
Půst L., Pešek L.: <i>VIBRATIONS OF BLADES BUNCHES</i>	520
Pustulka A.: <i>METHODS OF DETECTING THE UNDESIRABLE OBJECTS ON BELT CONVEYORS</i>	524
Radolf V., Horáček J., Bula V., Laukkanen A.M.: <i>AIR-PRESSURE CHARACTERISTICS AND VISUALIZATION OF BUBBLING EFFECT IN WATER RESISTANCE THERAPY</i>	528
Rohan E., Lukeš V., Novotný Z.: <i>MODELING AND OPTIMIZATION OF SHAPES AND INTERFACES IN VIBROACOUSTIC</i>	532
Řeháček S., Vacek V., Kolísko J., Huňka P., Čítek D., Brodňan M.: <i>STRUCTURAL TECHNICAL INSPECTION AND PROJECT PREPARATION FOR RECONSTRUCTION OF REINFORCED CONCRETE RAILWAY VIADUCT IN KRNSKO</i>	536
Řehák K., Skallerud B.: <i>STRAIN ANALYSIS OF BONE HEALING</i>	540
Řídký R., Buchar J., Rolc S., Drdlová M., Krátký J.: <i>NUMERICAL EXPLICIT ANALYSIS OF ABSORBING MATERIALS USED IN MULTILAYER MINE PROTECTION</i>	544
Řídký V., Šidlof P.: <i>PARALLEL NUMERICAL COMPUTATION OF DISTRIBUTION OF PRESSURE PAST AN OSCILLATING AIRFOIL NACA0015</i>	548
Sant Z., Vella A., Blanchard R., Hellmich Ch.: <i>MICROMECHANICS APPLIED TO MACRO-MODEL OF A SPINAL SEGMENT</i>	552
Shirneshan A.: <i>BSFC PREDICTION OF A DIESEL ENGINE FUELLED WITH BIODIESEL BY RSM</i>	556
Schrötter M., Hagara M., Lengvarský P.: <i>EXPERIMENTAL MODAL ANALYSIS OF WASHING MACHINE PULLEY</i>	560

Skalka P., Sobotka J.: ANALYSIS OF DYNAMIC LOADING OF BAR STRAIGHTENING MACHINE COMPONENTS	564
Sobotka J.: FREE VIBRATION ANALYSIS OF TIMOSHENKO BEAM WITH DISCONTINUITIES USING DISTRIBUTIONS	568
Sokol K.: INFLUENCE OF THE BENDING RIGIDITY FACTOR ON VIBRATION AND INSTABILITY OF A COLUMN WITH INTERNAL CRACK	572
Sokolski P.: ON POSSIBILITIES OF DIAGNOSING OF CATERPILLAR UNDERCARRIAGES IN LARGE-SIZE WORKING MACHINES	576
Solař J.: CALCULATING THE AIR FLOW VELOCITY IN AIR CAVITIES IN WALLS.....	580
Soltys R., Tomko M.: INFLUENCE OF AIRFLOW-RIVULET INTERACTION ON CIRCULAR CYLINDER IN UNIFORM FLOW.....	584
Stodulka J., Sobieczky H.: THEORETICAL AND NUMERICAL SOLUTION OF A NEAR SONIC FLOW CONSIDERING THE OFF-DESIGN CONDITIONS.....	588
Stránský J.: COMBINATION OF FEM AND DEM WITH APPLICATION TO RAILWAY BALLAST-SLEEPER INTERACTION	592
Stratil L., Šiška F., Hadraba H., Dlouhý I.: APPLICATION OF SIMPLIFIED MECHANICAL MODEL FOR DESCRIPTION OF SPECIMEN SIZE EFFECT ON RESISTANCE AGAINST STABLE TEARING.....	596
Strecker Z., Roupec J., Kubík M., Friedel D.: EXPERIMENTAL EVALUATION OF MR DAMPER TIME RESPONSE ON MODIFIED GROUNDHOOK ALGORITHM EFFICIENCY.....	600
Stryszewska T., Kaňka S.: AN APPLICATION OF ULTRASOUNDS TO ASSESSMENT OF HARMFUL SALTS ACCUMULATION IN THE BODY OF TRADITIONAL CERAMICS.....	604
Strzelecki P., Sempruch J.: HYBRID METHOD FOR DETERMINING FATIGUE CHARACTERISTIC IN HIGH CYCLE LIFE	608
Stříž B., Vyšanská M.: EVALUATION OF THE AREAL TEXTILE THINNING.....	612
Svojanovský T., Trtík L.: RHIZARTHROSIS AND ITS TREATMENT, STRESS AND DEFORMATION ANALYSIS OF THE TOTAL JOINT REPLACEMENT	616
Sýkora J.: NUMERICAL MODEL FOR HISTORICAL MORTARS EXPOSED TO FREEZING TEMPERATURES	620
Sykora M., Holický M., Lenner R., Manas P.: HUMAN SAFETY CRITERIA FOR EXISTING BRIDGES CONSIDERING EMERGENCY AND CRISIS SITUATIONS.....	624
Šána V., Polák M.: MATHEMATICAL DESCRIPTION OF BEHAVIOUR OF A HUMAN BODY DURING WALKING – STANCE PHASE	628

Šebek F., Kubík P., Petruška J.: <i>LOCALIZATION PROBLEM OF COUPLED DUCTILE FAILURE MODELS COMPARED TO UNCOUPLED ONES</i>	632
Šín P., Sergejev F., Štubňa I.: <i>FRACTURE TOUGHNESS OF KAOLIN FIRED AT DIFFERENT TEMPERATURES</i>	636
Švancara P., Horáček J., Martínek T., Švec J.G.: <i>NUMERICAL SIMULATION OF VIDEOKYMOGRAPHIC IMAGES FROM THE RESULTS OF THE FINITE ELEMENT MODEL</i>	640
Takosoglu J.E., Laski P.A., Blasiak S.: <i>INNOVATIVE MODULAR PNEUMATIC VALVE TERMINAL WITH SELF-DIAGNOSIS, CONTROL AND NETWORK COMMUNICATIONS</i>	644
Tej P., Vacek V., Kolísko J., Čech J., Lo Monte F.: <i>COMPUTER NONLINEAR ANALYSIS OF THE INFLUENCE OF MATERIAL CHARACTERISTICS ON THE RESPONSE OF A BASEMENT STRUCTURE LOADED BY GROUND WATER BUOYANCY</i>	648
Tesár A.: <i>AEROELASTICITY OF SLENDER FACADE SHEETS</i>	652
Tesař V., Hykl J.: <i>ATOMISER WITH EXCITATION BY A FLUIDIC OSCILLATOR</i>	656
Toman J., Szabo I., Singule V.: <i>ROBUST CONTROL ALGORITHM FOR PMSM MOTOR WITH HALL POSITION SENSORS</i>	660
Tomaszewski T., Sempruch J.: <i>PRACTICAL IMPLEMENTATION OF SELECTED MEAN STRESS MODELS FOR RESULTS OF FATIGUE TESTS REALIZED FOR MINI SPECIMEN</i>	664
Turjanicová J., Rohan E.: <i>HOMOGENIZATION OF THE ELECTRO-OSMOSIS PHENOMENA IN THE CORTICAL BONE POROUS STRUCTURE</i>	668
Urbanová S., Vorel J., Šejnoha M.: <i>THE INFLUENCE OF DIFFERENT IMPLEMENTATION OF PERIODIC BOUNDARY CONDITIONS INTO FEM SOFTWARE</i>	672
Uzny S.: <i>BIFURCATION LOAD OF A COLUMN COMPOSED OF PIPE AND ROD WITH TWO-PARAMETRIC ELASTIC ELEMENT</i>	676
Vampola T., Horáček J.: <i>NUMERICAL SIMULATION OF VIDEO-KYMOGRAPHIC RECORDS OF THE VOCAL FOLDS VIBRATION</i>	680
Vlasak P., Chara Z., Konfršt J., Krupička J.: <i>CONCENTRATION DISTRIBUTION OF COARSE-GRAINED PARTICLE-WATER MIXTURE IN HORIZONTAL PIPE</i>	684
Vlček V., Kozánek J., Zolotarev I.: <i>FLUTTER AT A LOW VELOCITY</i>	688
Vondál J., Steen M., Tummers M.J.: <i>TRACKING OF IMPINGING JET FLAME</i>	692
Vorel J., Boshoff W.P.: <i>NUMERICAL INVESTIGATION OF SHEAR BEHAVIOR SHCC STRUCTURAL ELEMENTS</i>	696

Wawrzyniak S., Peszyński K.: <i>MODELING AND SIMULATION OF THE RECUPERATIVE HEAT EXCHANGER</i>	700
Wieczorek B.: <i>THEORETICAL ALGORITHM TO ASSESS THE VALUES OF THE BREAKING LOAD OF THE BARS SITUATED IN THE SUPPORTING ZONE OF THE SLAB-COLUMN CONNECTION</i>	704
Wieczorek B.: <i>NUMERICAL MODELLING OF THE DESTRUCTION OF THE REINFORCEMENT BARS IN THE SUPPORTING ZONE OF THE COLUMN</i>	708
Wieczorek M.: <i>NUMERICAL ANALYSIS OF THE DEFORMATION OF THE CORNER PART OF THE SLAB-COLUMN STRUCTURES</i>	712
Wieczorek M.: <i>NUMERICAL ANALYSIS OF NARROW SINGLE-SPAN, GRAVITATIONALLY LOADED CONCRETE SLABS REINFORCED STEEL WITH A MEAN DUCTILITY</i>	716
Winczek J., Ziobrowski P.: <i>ON THE STRAIN-HARDENING PARAMETERS OF S355J2H STEEL CONSIDERING THE INFLUENCE OF TEMPERATURE</i>	720
Wirwicki M., Topoliński T., Andryszczyk M.: <i>ZIRCONIUM DIOXIDE – STATIC TEST ON GLUED CONNECTIONS</i>	724
Wydrych J., Borsuk G., Dobrowolski B.: <i>A NUMERICAL ANALYSIS OF THE FLOW THROUGH THE ELBOW IN THE BOILER PULVERIZED COAL SYSTEM</i>	728
Zachwieja J.: <i>DYNAMIC FIELD BALANCING OF SENSITIVE ROTOR</i>	732
Żak M., Słowiński J., Pezowicz C.: <i>MECHANICAL BEHAVIOR OF THE LAMELLAE ANNULUS FIBROSUS IN FINITE ELEMENT MODEL</i>	736
Zelenka J., Michálek T., Kohout M.: <i>COMPARATIVE SIMULATIONS OF GUIDING BEHAVIOUR OF AN ELECTRIC LOCOMOTIVE</i>	740
Zeman V., Hlaváč Z.: <i>SEISMIC RESPONSE OF NUCLEAR FUEL ASSEMBLY COMPONENTS</i>	744
Żórawski D., Dzikowska W., Peszyński K.: <i>MODELLING OF THE VIBRATING DRYER DRIVE SYSTEM</i>	748
Zrůbek L., Kučerová A., Novák J.: <i>PREDICTION OF ESHELBY'S INCLUSION PROBLEM SOLUTION USING ARTIFICIAL NEURAL NETWORK</i>	752

Table of Contents (by Sections)

KEY - KEYNOTE LECTURES

Burša J., Bansod Y.D.: <i>DESIGN AND APPLICATIONS OF PRESTRESSED TENSEGRITY STRUCTURE</i>	30
Hartl M., Křupka I., Omasta M., Šperka P.: <i>RECENT ADVANCES AND PROBLEMS IN LUBRICATED HERTZIAN CONTACTS</i>	34
Rudolf P., Štefan D., Pochylý F.: <i>DYNAMICS OF SWIRLING FLOWS IN INDUSTRIAL APPLICATIONS</i>	38

BIO - BIOMECHANICS

Andryszczyk M., Wirwicki M., Topoliński T.: <i>BIOMATERIALS USED FOR THE PRODUCTION OF STENTS - HOPES AND LIMITATIONS - REVIEW ARTICLE</i>	44
Blanchard R., Morin C., Vella A., Sant Z., Hellmich Ch.: <i>INTRA-VOXEL MICRO-ELASTO-PLASTICITY FOR CT-BASED PATIENT-SPECIFIC FRACTURE RISK ASSESSMENT OF VERTEBRAE</i>	92
Frydryšek K., Pleva L., Pompach M., Učeň O., Fojtík F., Kubín T., Theisz G., Žilka L., Poruba Z.: <i>EXTERNAL AND INTERNAL FIXATORS FOR TREATMENT OF COMPLICATED FRACTURES IN TRAUMATOLOGY AND ORTHOPAEDICS</i>	180
Horáček J., Bula V., Radolf V., Vampola T., Dušková M.: <i>MEASUREMENT OF VIBRATION, FLOW AND ACOUSTIC CHARACTERISTICS OF A HUMAN LARYNX REPLICA</i>	224
Janíček P.: <i>STRESS-STRAIN ANALYSIS OF CERAMIC HEADS IN THE DESTRUCTION DEVICE</i>	260
Jonášová A., Bublík O., Rohan E., Vimmr J.: <i>SIMULATION OF CONTRAST MEDIUM PROPAGATION BASED ON 1D AND 3D PORTAL HEMODYNAMICS</i>	272
Kazakevičiūtė-Makovska R.: <i>BIOLOGICAL SOFT TISSUES: MECHANICAL CHARACTERIZATION, DATA ANALYSIS AND MODELS' EVALUATION</i>	288
Kubíková T., Witter K., Liška V., Tonar Z.: <i>MORPHOMETRY AND RECONSTRUCTION OF HEPATIC LOBULES IN PIG BASED ON SERIAL HISTOLOGICAL SECTIONS</i>	340
Marcián P., Borák L., Narra N., Skalka P., Kaiser J., Wolff J.: <i>AN ALGORITHM FOR COMPUTATIONAL SIMULATION OF MANDIBLE BONE MODELING AND REMODELING AROUND DENTAL IMPLANTS</i>	388

Milewski G.: <i>COMPARATIVE ANALYSIS OF BURZYŃSKI-TORRE STRENGTH HYPOTHESIS FOR DENTINE AND ENAMEL</i>	400
Návrat T., Florian Z., Kočíš J., Vosynek P.: <i>BIOMECHANICAL TESTING OF SPINAL SEGMENT FIXED BY ARCOFIX SYSTEM</i>	424
Pásek M., Šimurda J., Christé G.: <i>SENSITIVITY OF ACTION POTENTIAL TO CHANGES OF INWARD RECTIFIER POTASSIUM CURRENT IK1 IS DIFFERENT IN RECENT MODELS OF HUMAN VENTRICULAR CARDIOMYOCYTES</i>	476
Prášilová E., Florian Z., Marcián P.: <i>FINITE ELEMENT ANALYSIS OF COMPRESSION OF LUMBAR SPINE WITH DYNAMIC IMPLANT</i>	512
Radolf V., Horáček J., Bula V., Laukkanen A.M.: <i>AIR-PRESSURE CHARACTERISTICS AND VISUALIZATION OF BUBBLING EFFECT IN WATER RESISTANCE THERAPY</i>	528
Řehák K., Skallerud B.: <i>STRAIN ANALYSIS OF BONE HEALING</i>	540
Sant Z., Vella A., Blanchard R., Hellmich Ch.: <i>MICROMECHANICS APPLIED TO MACRO-MODEL OF A SPINAL SEGMENT</i>	552
Svojanovský T., Trtík L.: <i>RHIZARTHROSIS AND ITS TREATMENT, STRESS AND DEFORMATION ANALYSIS OF THE TOTAL JOINT REPLACEMENT</i>	616
Švancara P., Horáček J., Martínek T., Švec J.G.: <i>NUMERICAL SIMULATION OF VIDEOKYMOGRAPHIC IMAGES FROM THE RESULTS OF THE FINITE ELEMENT MODEL</i>	640
Turjanicová J., Rohan E.: <i>HOMOGENIZATION OF THE ELECTRO-OSMOSIS PHENOMENA IN THE CORTICAL BONE POROUS STRUCTURE</i>	668
Vampola T., Horáček J.: <i>NUMERICAL SIMULATION OF VIDEO-KYMOGRAPHIC RECORDS OF THE VOCAL FOLDS VIBRATION</i>	680
Wirwicki M., Topoliński T., Andryszczyk M.: <i>ZIRCONIUM DIOXIDE – STATIC TEST ON GLUED CONNECTIONS</i>	724
Žak M., Słowiński J., Pezowicz C.: <i>MECHANICAL BEHAVIOR OF THE LAMELLAE ANNULUS FIBROSUS IN FINITE ELEMENT MODEL</i>	736

DYN - DYNAMICS

Benčat J.: <i>INDUSTRIAL MACHINERY DYNAMIC EFFECTS ON PRODUCTION PROCESS AND HALL STRUCTURES</i>	76
Cech V., Jedlicka L., Jevicky J.: <i>SOME PROBLEMS WITH THE ESTIMATION OF PROJECTILE TRAJECTORY PERTURBATIONS</i>	116

Čečrdle J.: <i>INFLUENCE OF PROPELLER BLADE FORCE SPANWISE DISTRIBUTION ON WHIRL FLUTTER CHARACTERISTICS</i>	124
Dyk Š., Zeman V., Byrtus M.: <i>KINEMATICALLY EXCITED NON-LINEAR VIBRATION OF A BEAM ON ELASTIC SUPPORTS WITH CLEARANCES</i>	148
Eliáš J.: <i>DEM SIMULATION OF BALLAST OEDOMETRIC TEST</i>	160
Gołębiowska I., Sakiewicz W.: <i>BASE ISOLATION SYSTEMS IN BUILDING STRUCTURES</i>	192
Hać M., Ostapski W.: <i>INFLUENCE OF REDUCER DISK BALANCE ON FLEXURAL VIBRATION OF PROPELLER SHAFT</i>	200
Chládek Š., Zolotarev I.: <i>IDENTIFICATION OF THE AEROELASTIC PROFILE BASED ON OPTICAL MEASUREMENT</i>	244
Iván L., Popovič M.: <i>OPTIMISATION IN THE EXPLICIT ANALYSIS OF THE ROAD BARRIERS</i>	252
Kabeláč J., Rossier S.: <i>REDUCTION FOR HIGH-RISE BUILDINGS SEISMIC ANALYSIS</i>	276
Kratochvíl O., Križan J.: <i>ANALYSIS OF DYNAMIC RESPONSE OF FOOTBRIDGE VEVEŘÍ ON PEDESTRIAN LOAD</i>	328
Kučera P., Pištěk V.: <i>A COMPUTATIONAL MODEL OF POWERTRAIN COMPONENTS IN SIMULINK</i>	344
Lošák P.: <i>IDENTIFICATION OF VIBRATION CAUSES BASED ON SPECTROGRAMS DURING THE STRAIGHTENING PROCESS</i>	368
Makovička D., Makovička D.: <i>IMPACT OF MISSILE ON CONCRETE OR SOIL OBSTACLE</i>	380
Náprstek J., Fischer C.: <i>POST-CRITICAL MULTI-MODAL VIBRATION OF A CONTINUOUS INVERSE PENDULUM TYPE SYSTEM</i>	416
Náprstek J., Pospíšil S.: <i>AEROELASTIC DIVERGENCE MODELED BY MEANS OF THE STOCHASTIC RESONANCE</i>	420
Ondra V., Lošák P.: <i>COMPARISON OF MODAL PARAMETER ESTIMATION TECHNIQUES FOR EXPERIMENTAL MODAL ANALYSIS</i>	460
Pečínka L., Švrček M.: <i>ACOUSTIC FREQUENCIES OF COOLANT IN PRIMARY CIRCUIT OF NPP TEMELIN AND POSSIBILITY OF RESONANCES WITH FUEL ASSEMBLY TVSA-T</i>	484
Polach P., Hajžman M.: <i>UTILIZING OF A WEIGHT-FIBRE-PULLEY-DRIVE MECHANICAL SYSTEM FOR THE INVESTIGATION OF A FIBRE BEHAVIOUR</i>	500
Půst L., Pešek L.: <i>VIBRATIONS OF BLADES BUNCHES</i>	520

Rohan E., Lukeš V., Novotný Z.: <i>MODELING AND OPTIMIZATION OF SHAPES AND INTERFACES IN VIBROACOUSTIC</i>	532
Řídký R., Buchar J., Rolc S., Drdlová M., Krátký J.: <i>NUMERICAL EXPLICIT ANALYSIS OF ABSORBING MATERIALS USED IN MULTILAYER MINE PROTECTION</i>	544
Schrötter M., Hagara M., Lengvarský P.: <i>EXPERIMENTAL MODAL ANALYSIS OF WASHING MACHINE PULLEY</i>	560
Sobotka J.: <i>FREE VIBRATION ANALYSIS OF TIMOSHENKO BEAM WITH DISCONTINUITIES USING DISTRIBUTIONS</i>	568
Strecker Z., Roupec J., Kubík M., Friedel D.: <i>EXPERIMENTAL EVALUATION OF MR DAMPER TIME RESPONSE ON MODIFIED GROUNDHOOK ALGORITHM EFFICIENCY</i>	600
Šána V., Polák M.: <i>MATHEMATICAL DESCRIPTION OF BEHAVIOUR OF A HUMAN BODY DURING WALKING – STANCE PHASE</i>	628
Tesár A.: <i>AEROELASTICITY OF SLENDER FACADE SHEETS</i>	652
Vlček V., Kozánek J., Zolotarev I.: <i>FLUTTER AT A LOW VELOCITY</i>	688
Zelenka J., Michálek T., Kohout M.: <i>COMPARATIVE SIMULATIONS OF GUIDING BEHAVIOUR OF AN ELECTRIC LOCOMOTIVE</i>	740
Zeman V., Hlaváč Z.: <i>SEISMIC RESPONSE OF NUCLEAR FUEL ASSEMBLY COMPONENTS</i>	744

FLU - FLUID MECHANICS

Ansari R.I., Sahir M.H.: <i>PERFORMANCE EVALUATION OF HYDROVAC GRAVITY POWER GENERATION SYSTEM</i>	48
Bednář L., Miczan M., Tajč L., Hoznedl M.: <i>EXPERIMENTAL VALIDATION OF THE AERODYNAMIC FORCE ACTING ON A CONE OF A BALANCED CONTROL VALVE</i>	68
Belka M., Jedelsky J., Boiron O., Bailly L., Bertrand E., Zaremba M., Maly M., Lizal F.: <i>MEASUREMENT OF AIRFLOW IN TRACHEA USING PARTICLE IMAGE VELOCIMETRY AND LASER-DOPPLER ANEMOMETRY</i>	72
Beňovský P., Rusche H., Ridzoň F., Popovac M., Reichl Ch., Fleckl T.: <i>DROPSWISE CONDENSATION MODELING</i>	80
Blasiak S., Takosoglu J.E., Laski P.A.: <i>THE FLOW RATE OPTIMIZATION OF DIRECTIONAL PNEUMATIC CONTROL VALVE</i>	96

Bublík O., Jonášová A., Vimmr J.: <i>APPLICATION OF THE LATTICE BOLTZMAN METHOD FOR THE MODELLING OF PULSATILE FLOW IN IDEALISED BYPASS GEOMETRIES</i>	108
Dolanský J.: <i>SIMULATION OF MOTION OF MULTIPLE PARTICLES IN A CLOSED CONDUIT USING THE LBM BASED APPROACH</i>	128
Filipský J., Štorch V.: <i>COMPARISON OF PROPELLER ANALYSIS METHODS AND EXPERIMENTAL DATA</i>	172
Hájek R., Foglar M.: <i>EXPERIMENTAL EVALUATION OF THE EFFECTS OF A CONCRETE BARRIER TO PRESSURE WAVE PROPAGATION</i>	208
Hájek R., Foglar M.: <i>NUMERICAL MODELLING OF INTERACTION BETWEEN PRESSURE WAVE AND RIGID BARRIER</i>	212
Hric V., Halama J., Fürst J.: <i>NUMERICAL SOLUTION OF INVISCID TRANSONIC FLOW IN A CHANNEL WITH COMPLEX EQUATION OF STATE</i>	228
Kiš R., Malcho M., Janovcová M.: <i>CFD ANALYSIS OF FLOWS IN A HIGH-PRESSURE NATURAL GAS PIPELINES WITH DIFFERENT SHAPES OF ORIFICE PLATES</i>	292
Kolařík F., Patzák B.: <i>IMPLEMENTATION OF STABILIZED FORMULATION FOR LEVEL SET EQUATION</i>	300
Kyncl M., Pelant J.: <i>NUMERICAL SIMULATION OF THE TURBULENT COMPRESSIBLE GAS FLOW IN THE VANELESS MACHINES</i>	356
Mlkvik M., Zaremba M., Jedelský J., Wigley G.: <i>INVESTIGATION OF THE SPRAY GENERATED BY A Y-JET ATOMIZER</i>	404
Novotný P., Maršálek O., Zubík M., Drápal L.: <i>ANALYSIS OF SLIDE BEARING COMPUTATIONAL MODELS CONSIDERING ELASTIC DEFORMATIONS AND ROUGH SURFACES</i>	444
Řidký V., Šidlof P.: <i>PARALLEL NUMERICAL COMPUTATION OF DISTRIBUTION OF PRESSURE PAST AN OSCILLATING AIRFOIL NACA0015</i>	548
Shirneshan A.: <i>BSFC PREDICTION OF A DIESEL ENGINE FUELLED WITH BIODIESEL BY RSM</i>	556
Soltys R., Tomko M.: <i>INFLUENCE OF AIRFLOW-RIVULET INTERACTION ON CIRCULAR CYLINDER IN UNIFORM FLOW</i>	584
Stodulka J., Sobieczky H.: <i>THEORETICAL AND NUMERICAL SOLUTION OF A NEAR SONIC FLOW CONSIDERING THE OFF-DESIGN CONDITIONS</i>	588
Tesař V., Hykl J.: <i>ATOMISER WITH EXCITATION BY A FLUIDIC OSCILLATOR</i>	656
Vlasak P., Chara Z., Konfršt J., Krupička J.: <i>CONCENTRATION DISTRIBUTION OF COARSE-GRAINED PARTICLE-WATER MIXTURE IN HORIZONTAL PIPE</i>	684
Vondál J., Steen M., Tummers M.J.: <i>TRACKING OF IMPINGING JET FLAME</i>	692

Wydrych J., Borsuk G., Dobrowolski B.: *A NUMERICAL ANALYSIS OF THE FLOW THROUGH THE ELBOW IN THE BOILER PULVERIZED COAL SYSTEM.....* **728**

FRA - FRACTURE MECHANICS

Foglar M., Kovář M.: *BLAST PERFORMANCE OF FRC SPECIMENS WITH STEEL FIBERS OF LOW DUCTILITY* **176**

Holušová T., Seitl S., Fernández-Canteli A.: *MODIFIED COMPACT TENSION TEST: THE INFLUENCE OF THE STEEL BARS POSITION* **220**

Hrstka M., Profant T., Klusák J., Ševeček O., Kotoul M.: *A STABILITY CRITERION OF AN ORTHOTROPIC BI-MATERIAL NOTCH BASED ON THE STRAIN ENERGY DENSITY* **232**

Květoň J., Eliáš J.: *PERFORMANCE COMPARISON OF LOCALIZATION LIMITERS* **352**

Majer Z., Náhlík L.: *NUMERICAL ESTIMATION OF MICRO CRACK PATHS IN POLYMER PARTICULATE COMPOSITE* **376**

Malíková L.: *PLASTIC ZONE EXTENT IN A CCT SPECIMEN DETERMINED FROM THE CRACK-TIP STRESS FIELD APPROXIMATED BY MEANS OF THE WILLIAMS EXPANSION.....* **384**

Máša B., Náhlík L., Hutař P.: *ON AN ESTIMATION OF THE EXPONENT OF THE STRESS SINGULARITY: THREE DIMENSIONAL PROBLEMS AND EFFECT OF RESIDUAL STRESSES ON A CRACK ARRESTED ON THE INTERFACE.....* **392**

Mikula J., Ševčík M., Hutař P., Náhlík L.: *FRACTURE MECHANICS ASSESSMENT OF CRACKED WELDED POLYOLEFIN PIPES.....* **396**

Náhlík L., Štegnerová K., Hutař P.: *ESTIMATION OF CRITICAL STRESS VALUES FOR CRACK INITIATION FROM SHARP V-NOTCHES* **412**

Pavlenko M.V.: *PRINCIPLES OF VIBRATION IMPACT ON CRACKED METHANE-BEARING COAL SEAM* **480**

Podolka L.: *SOLVING ANCHORAGE AREA PRESTRESSED AND NONPRESTRESSED COMPOSITES.....* **492**

Pokorný P., Náhlík L., Hutař P.: *THE EFFECT OF THRESHOLD VALUE ON THE RESIDUAL FATIGUE LIFETIME OF RAILWAY AXLES.....* **496**

Stratil L., Šiška F., Hadraba H., Dlouhý I.: *APPLICATION OF SIMPLIFIED MECHANICAL MODEL FOR DESCRIPTION OF SPECIMEN SIZE EFFECT ON RESISTANCE AGAINST STABLE TEARING.....* **596**

Strzelecki P., Sempruch J.: *HYBRID METHOD FOR DETERMINING FATIGUE CHARACTERISTIC IN HIGH CYCLE LIFE* **608**

Šebek F., Kubík P., Petruška J.: *LOCALIZATION PROBLEM OF COUPLED DUCTILE FAILURE MODELS COMPARED TO UNCOUPLED ONES.....* **632**

Šín P., Sergejev F., Štubňa I.: <i>FRACTURE TOUGHNESS OF KAOLIN FIRED AT DIFFERENT TEMPERATURES</i>	636
Tomaszewski T., Sempruch J.: <i>PRACTICAL IMPLEMENTATION OF SELECTED MEAN STRESS MODELS FOR RESULTS OF FATIGUE TESTS REALIZED FOR MINI SPECIMEN</i>	664
Vorel J., Boshoff W.P.: <i>NUMERICAL INVESTIGATION OF SHEAR BEHAVIOR SHCC STRUCTURAL ELEMENTS</i>	696

HIS - HISTORICAL STRUCTURES

Bednarik M., Holzer R., Laho M., Dunčko M.: <i>STONE FOR RESTORATION AND DECORATION PURPOSES IN WESTERN SLOVAKIA</i>	64
Kovářová K., Ševčík R.: <i>METHODS OF A BUILDING STONE INTERNAL STRUCTURE STUDY</i>	320
Řeháček S., Vacek V., Kolísko J., Huňka P., Čítek D., Brodňan M.: <i>STRUCTURAL TECHNICAL INSPECTION AND PROJECT PREPARATION FOR RECONSTRUCTION OF REINFORCED CONCRETE RAILWAY VIADUCT IN KRNSKO</i>	536
Stryzewska T., Kaňka S.: <i>AN APPLICATION OF ULTRASOUNDS TO ASSESSMENT OF HARMFUL SALTS ACCUMULATION IN THE BODY OF TRADITIONAL CERAMICS</i>	604
Sýkora J.: <i>NUMERICAL MODEL FOR HISTORICAL MORTARS EXPOSED TO FREEZING TEMPERATURES</i>	620

KIN - KINEMATICS

Ostaszewski M., Siemieniako F.: <i>KINEMATIC MODEL OF MECHANICAL DESIGN FOR SUPPORT HUMAN LOWER LIMB</i>	464
---	------------

MCT - MECHATRONICS

Aromiński A.: <i>AUTOMOTIVE PIEZOELECTRIC SENSORS FOR SIMPLIFIED KNOCK DETERMINATION</i>	52
Březina T., Březina L., Marek J., Hadaš Z., Vetiška J.: <i>SIMULATION ASSESSMENT OF SUPPRESSION OF MACHINE TOOL VIBRATIONS</i>	104
Duda S., Gembalczyk G., Lawniczek R., Trawinski T.: <i>COMPARISON OF DYNAMIC INTERACTIONS IN THE DRIVE SYSTEM OF ELECTRIC LOCOMOTIVE EU07 BEFORE AND AFTER THE MODERNIZATION DRIVE UNIT</i>	140

Duda S., Gembalczyk G., Lawniczek R.: <i>SIMULATION AND EXPERIMENTAL STUDIES ON THE CONTROL SYSTEM FOR MECHATRONIC REHABILITATION DEVICE WITH KEEP-UP MOVEMENT</i>	144
Dzikowska W., Żórawski D., Peszyński K.: <i>MODELLING AND INITIAL TESTS OF THE DYNAMIC PROPERTIES OF VIBROINSULATION MATS</i>	152
Hadas Z., Vetiska J.: <i>ENERGY HARVESTING ANALYSIS OF BODY MOTION AS ENERGY SOURCE FOR BIOMEDICAL DEVICES</i>	204
Knobloch J., Holub M., Kolouch M.: <i>LASER TRACKER MEASUREMENT FOR PREDICTION OF WORKPIECE GEOMETRIC ACCURACY</i>	296
Krejsa J., Vechet S., Chen K.: <i>MULTIPLE INDOOR ROBOT LOCALIZATION USING INFRARED BEACONS</i>	336
Laski P.A., Takosoglu J.E., Blasiak S.: <i>A DELTA TYPE CLOSED KINEMATICS CHAIN WITH PNEUMATIC MUSCLE ACTUATOR MANIPULATOR</i>	360
Nevrlý J., Němec Z., Jurík M.: <i>EFFECTIVENESS OF KINETIC ENERGY RECOVERY EXPLORED BY MEANS OF EXPERIMENTAL STAND</i>	432
Nowicki K., Kolber P., Perczyński D., Wawrzyniak S.: <i>REVITALISATION OF INDUSTRIAL ROBOT CONTROL SYSTEMS</i>	448
Nowicki K., Perczyński D., Kolber P., Peszyński K.: <i>SIMULATION TESTS OF IRB6 ROBOT</i>	452
Panáček T., Klapka M., Němec Z.: <i>OPTIMIZATION OF VALVE MANIFOLD TIMING SEQUENCE USING DIFFERENTIAL EVOLUTION ALGORITHM</i>	468
Perczyński D., Kolber P., Wawrzyniak S.: <i>MINIMISING OF THE OPERATION COSTS OF POWER TRANSFORMERS</i>	488
Takosoglu J.E., Laski P.A., Blasiak S.: <i>INNOVATIVE MODULAR PNEUMATIC VALVE TERMINAL WITH SELF-DIAGNOSIS, CONTROL AND NETWORK COMMUNICATIONS</i>	644
Toman J., Szabo I., Singule V.: <i>ROBUST CONTROL ALGORITHM FOR PMSM MOTOR WITH HALL POSITION SENSORS</i>	660
Wawrzyniak S., Peszyński K.: <i>MODELING AND SIMULATION OF THE RECUPERATIVE HEAT EXCHANGER</i>	700
Żórawski D., Dzikowska W., Peszyński K.: <i>MODELLING OF THE VIBRATING DRYER DRIVE SYSTEM</i>	748

REL - RELIABILITY

Dowkontt S., Ostapski W., Tułodziecki M.: <i>ANALYSIS OF SUBWAY WAGON ROLLER BEARING AXLE BOX STRESSES WITH MEDIUM OPERATION LOAD</i>	136
--	------------

Janouchová E., Kučerová A., Sýkora J.: <i>EFFICIENT BAYESIAN PARAMETER IDENTIFICATION</i>	264
Kala Z., Valeš J.: <i>LATERAL-TORSIONAL BUCKLING OF I-SECTION BEAMS WITH INITIAL RANDOM IMPERFECTIONS</i>	280
Koteš P., Vičan J.: <i>CORROSION OF REINFORCEMENT VERSUS RELIABILITY OF RC GIRDERS</i>	312
Nhan P.T., Samal S.M., Petrikova I., Marvalová B.: <i>CORRELATION BETWEEN ENHANCED MECHANICAL STRENGTH AND MICROSTRUCTURE RELIABILITY OF GEO-COMPOSITE</i>	436
Nowogońska B.: <i>MODEL OF THE RELIABILITY PREDICTION OF MASONRY WALLS</i>	456
Pospíšilová A., Lepš M.: <i>ADAPTIVE UPDATE OF SURROGATE MODELS FOR RELIABILITY-BASED DESIGN OPTIMIZATION: A REVIEW</i>	508
Pustulka A.: <i>METHODS OF DETECTING THE UNDESIRABLE OBJECTS ON BELT CONVEYORS</i>	524
Sokolski P.: <i>ON POSSIBILITIES OF DIAGNOSING OF CATERPILLAR UNDERCARRIAGES IN LARGE-SIZE WORKING MACHINES</i>	576
Sykora M., Holický M., Lenner R., Manas P.: <i>HUMAN SAFETY CRITERIA FOR EXISTING BRIDGES CONSIDERING EMERGENCY AND CRISIS SITUATIONS</i>	624
Tej P., Vacek V., Kolísko J., Čech J., Lo Monte F.: <i>COMPUTER NONLINEAR ANALYSIS OF THE INFLUENCE OF MATERIAL CHARACTERISTICS ON THE RESPONSE OF A BASEMENT STRUCTURE LOADED BY GROUND WATER BUOYANCY</i>	648
Wieczorek B.: <i>THEORETICAL ALGORITHM TO ASSESS THE VALUES OF THE BREAKING LOAD OF THE BARS SITUATED IN THE SUPPORTING ZONE OF THE SLAB-COLUMN CONNECTION</i>	704
Wieczorek B.: <i>NUMERICAL MODELLING OF THE DESTRUCTION OF THE REINFORCEMENT BARS IN THE SUPPORTING ZONE OF THE COLUMN</i>	708
Wieczorek M.: <i>NUMERICAL ANALYSIS OF THE DEFORMATION OF THE CORNER PART OF THE SLAB-COLUMN STRUCTURES</i>	712
Wieczorek M.: <i>NUMERICAL ANALYSIS OF NARROW SINGLE-SPAN, GRAVITATIONALLY LOADED CONCRETE SLABS REINFORCED STEEL WITH A MEAN DUCTILITY</i>	716

SOL - MECHANICS OF SOLIDS|

Baláž I., Koleková Y.: <i>INTERACTION BETWEEN BENDING MOMENT AND SHEAR FORCE IN STEEL PLATED STRUCTURAL ELEMENTS</i>	60
Bošanský M., Patzák B.: <i>ON PARALLELIZATION OF STIFFNES MATRIX ASSEMBLY</i>	100
Bulejko P., Svěrák T.: <i>MECHANICAL AND FILTERING PROPERTIES OF NON-SINTERED POROUS SOLIDS FOR FILTRATION APPLICATIONS</i>	112
Čadek M., Marvalová B., Petříková I., Samal S.: <i>DETERMINATION OF MATERIAL PARAMETERS OF RUBBER AND RUBBER COMPOSITES BY BIAXIAL LOADING</i>	120
Doškář M., Novák J.: <i>REDUCING PERIODICITY IN MICROSTRUCTURE RECONSTRUCTION OF HETEROGENEOUS MATERIALS</i>	132
Fuis V.: <i>SHAPE DEVIATIONS ANALYSIS OF THE ALIGNED BARS</i>	184
Gajewski M., Jemiolo S.: <i>PROPOSITION OF CONSTITUTIVE MODEL FOR FIBRE-REINFORCED HYPERELASTIC MATERIALS</i>	188
Göringer J., Foglar M.: <i>CONCRETE DETERIORATION DUE TO AGGRESSIVE ENVIRONMENT AND CYCLIC LOADING – THEORETICAL STUDY</i>	196
Chleboun J., Mikeš K.: <i>PARAMETER IDENTIFICATION IN INITIAL VALUE PROBLEMS FOR NONLINEAR ORDINARY DIFFERENTIAL EQUATIONS</i>	248
Ivančo V., Orečný M., Huňady R.: <i>SIMULATION OF DROP TESTS OF THE CASK FOR RADIOACTIVE WASTE</i>	256
Kalina M.: <i>COMPUTER NUMERICAL SOLUTION OF VON MISES PLANAR TRUSS BY THE POTENTIAL ENERGY</i>	284
Koleková Y., Baláž I.: <i>INTERACTION BETWEEN BENDING MOMENT AND SHEAR FORCE IN ALUMINIUM PLATED STRUCTURAL ELEMENTS</i>	304
Kostecká M., Kolísko J., Bittner T., Huňka P., Mandlík T.: <i>THE INFLUENCE OF FROST RESISTANCE ON UHPC PLATES WITH DIFFERENT TYPES OF TEXTILES ARMATURES</i>	308
Koudelka T., Kruis J., Lepš M., Nosek J.: <i>FITTING MODEL PARAMETERS OF PRESTRESSED CONCRETE BRIDGE: COMPUTATIONAL ASPECTS</i>	316
Králík V., Němeček J., Jíra A., Fíla T., Zlámal P.: <i>ENERGY ABSORPTION OF CELLULAR FOAMS IN HIGH STRAIN RATE COMPRESSION TEST</i>	324
Krčmář M., Materna A.: <i>ASSESSMENT OF THE CONSTITUTIVE PROPERTIES OF REACTOR STEEL USING AN INVERSE ANALYSIS ON THE SMALL PUNCH TEST</i>	332
Kučerová A., Sýkora J., Zeman J.: <i>STOCHASTIC MODELLING OF HETEROGENEOUS MATERIALS BASED ON IMAGE ANALYSIS</i>	348

Lazarová E., Krúpa V., Ivaničová L., Kruřáková M.: <i>INVESTIGATION OF PROCESS DYNAMICS OF TBM EXCAVATION</i>	364
Machacek J., Charvat M.: <i>STUDY ON SHEAR CONNECTION BETWEEN BRIDGE STEEL TRUSS AND CONCRETE SLAB</i>	372
Myřáková E., Lepř M.: <i>COMPARISON OF METHODS FOR CONSTRAINED DESIGN OF COMPUTER EXPERIMENTS</i>	408
Nekvasil R., Lořák P., Lukáč P.: <i>ANALYSIS OF DAMAGED CONNECTION PIPING</i>	428
Popov G., Vaysfeld N., Zozulevich B.: <i>THE EXACT SOLUTION OF ELASTICITY MIXED PLAIN BOUNDARY VALUE PROBLEM IN A RECTANGULAR DOMAIN</i>	504
Přinosil M., Kabele P.: <i>SINGLE CRACK BEHAVIOR OF FIBER REINFORCED LIME-BASED MORTAR</i>	516
Skalka P., Sobotka J.: <i>ANALYSIS OF DYNAMIC LOADING OF BAR STRAIGHTENING MACHINE COMPONENTS</i>	564
Sokól K.: <i>INFLUENCE OF THE BENDING RIGIDITY FACTOR ON VIBRATION AND INSTABILITY OF A COLUMN WITH INTERNAL CRACK</i>	572
Stránský J.: <i>COMBINATION OF FEM AND DEM WITH APPLICATION TO RAILWAY BALLAST-SLEEPER INTERACTION</i>	592
Stříž B., Vyřanská M.: <i>EVALUATION OF THE AREAL TEXTILE THINNING</i>	612
Urbanová S., Vorel J., řejnoha M.: <i>THE INFLUENCE OF DIFFERENT IMPLEMENTATION OF PERIODIC BOUNDARY CONDITIONS INTO FEM SOFTWARE</i>	672
Uzny S.: <i>BIFURCATION LOAD OF A COLUMN COMPOSED OF PIPE AND ROD WITH TWO-PARAMETRIC ELASTIC ELEMENT</i>	676
Zachwieja J.: <i>DYNAMIC FIELD BALANCING OF SENSITIVE ROTOR</i>	732
Zřúbek L., Kučerová A., Novák J.: <i>PREDICTION OF ESHELBY'S INCLUSION PROBLEM SOLUTION USING ARTIFICIAL NEURAL NETWORK</i>	752

TER - TERMOMECHANICS

Astrouski I., Raudensky M.: <i>PLASTIC HEAT EXCHANGER USING TWISTED HOLLOW FIBERS</i>	56
Beroun S., Brabec P., Dittrich A., Mikulanin L.: <i>TEMPERATURE FIELD OF SPARK PLUG IN THE SI ENGINE</i>	84
Beroun S., Brabec P., Dittrich A., Nguyen T.T.: <i>INJECTOR OF LIQUID LPG</i>	88

Écsi L., Jančo R., Élesztős P.: <i>AN IMPROVED THERMAL-STRUCTURAL FINITE ELEMENT MODEL FOR MANUFACTURING PROCESSES WITH HEAT GENERATION</i>	156
Farrugia M., Grech N., Chircop M., Azzopardi J.P.: <i>SIMULATION AND IMPLEMENTATION OF TURBOCHARGING A 600CC ENGINE FOR FORMULA SAE</i>	164
Fenech G., Farrugia M.: <i>EXPERIMENTAL ANALYSIS OF A FIXED-SPEED AND A VARIABLE-SPEED AIR CONDITIONING SYSTEM</i>	168
Havlík J., Dlouhý T.: <i>EXPERIMENTAL VERIFICATION OF THEORETICAL MODELS TO CALCULATE THE HEAT TRANSFER COEFFICIENT IN THE SHELL-AND-TUBE HEAT EXCHANGER</i>	216
Hřibová V., Komínek J., Astrouski I., Raudenský M., Tseng A.A.: <i>HEAT TRANSFER SIMULATION OF HEAT EXCHANGERS MADE BY POLYMERIC HOLLOW FIBERS</i>	236
Hyhlík T.: <i>DEVELOPMENT OF MATHEMATICAL MODEL OF RAIN ZONE</i>	240
Joch L., Krautschneider R.: <i>STUDY OF EXTERNAL COOLING OF STEAM GENERATOR PGV-1000M COLLECTORS POCKET WELD № 111 FOR SUPPRESSING OF STRESS CORROSION CRACKING</i>	268
Novotný J., Matěcha J., Pohan P.: <i>PASSIVE ELEMENTS FOR PRECISE DIRECTION AND MANAGEMENT OF AIR IN DATA RACKS</i>	440
Parham E.: <i>THERMODYNAMICS PROPERTIES OF COPPER HALIDE ALLOY (CuBr_{0.5}Cl_{0.5})</i>	472
Solař J.: <i>CALCULATING THE AIR FLOW VELOCITY IN AIR CAVITIES IN WALLS</i>	580
Winczek J., Ziobrowski P.: <i>ON THE STRAIN-HARDENING PARAMETERS OF S355J2H STEEL CONSIDERING THE INFLUENCE OF TEMPERATURE</i>	720

KEYNOTE LECTURES

DESIGN AND APPLICATIONS OF PRESTRESSED TENSEGRITY STRUCTURES

J. Burša, Y. D. Bansod*

Abstract: *The tensegrity framework consists of both compression members (struts) and tensile members (cables) in a specific topology stabilized by induced prestress. Tensegrity plays a vital role in technological advancement of mankind in many fields ranging from architecture to biology. In this paper we have reviewed topological classification of elementary cells of tensegrity structures including rhombic, circuit and Z type configurations. Further, different types of tensegrities created on the basis of these configurations are studied and analyzed, for instance Tensegrity prism, Diamond tensegrity, and Zig-zag tensegrity. Then we focus on special features, classification and construction of high frequency tensegrity spheres. They have a wide range of applications in the construction of tough large scale domes or in the field of cellular mechanics. The design approach of double layer high frequency tensegrities is outlined with help of a six frequency octahedral tensegrity network where inner and outer layers of tendons are inter-connected by struts and tendons. The construction of complicated single and double bonding spherical tensegrity systems using a repetitive pattern of locked kiss tensegrity is reviewed. Form-finding procedure to design a new tensegrity structure or improve the existing one by achieving the desired topology and level of prestress is discussed at the end. Types of tensegrities, their configurations and topologies studied in this paper can be helpful for their recognition and, consequently, bring their broader application in different technical fields.*

Keywords: Tensegrity, Struts, Cables, Prestress, Configuration.

1. Introduction

Fuller (1961) coined the term “tensegrity” by combining two words “Tensional + Integrity”; it means that integrity of a structure consisting of tension and compression components relies on the tension members. A brief definition of tensegrity structures could be ‘A tensegrity system is established when a set of discontinuous compressive components interacts with a set of continuous tensile components to define a stable volume in space’. They don’t need any support to keep their shape and are self-equilibrated prestressed structures (Fuller, 1975). Theory of tensegrity structures is well known in statuary, architecture or civil engineering while in other engineering branches the potential of these structures is not yet fully explored. This paper summarizes the up to date knowledge on tensegrity structures and presents some of their applications in various technical fields, especially in computational modelling.

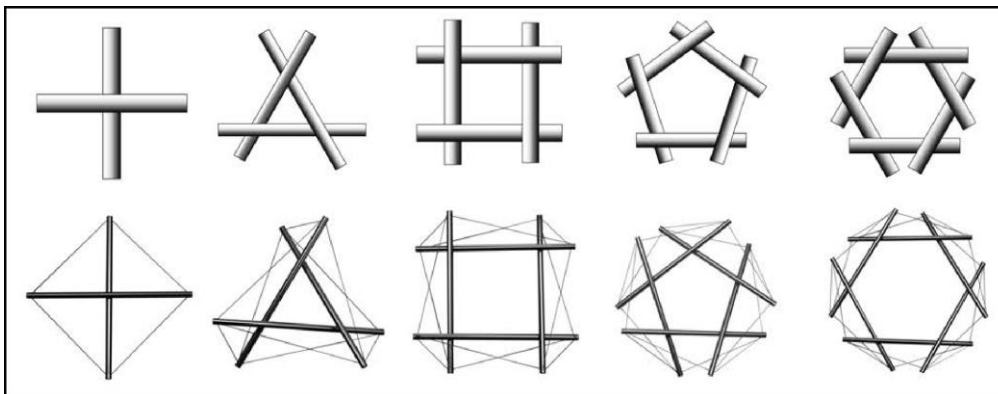


Fig. 1: Primary weave cells and equivalent basic 2D tensegrity modules (from Snelson (2012)).

* Prof. Jiri Bursa, PhD.; Yogesh Deepak Bansod M.Sc.: Institute of Solid Bodies, Mechatronics and Biomechanics, Faculty of Mechanical Engineering, Brno University of Technology, Technicka 2, 616 69, Brno; CZ, bursa@fme.vutbr.cz

2. Simplest and Diamond Tensegrities

Tensegrities differ from more usual strut-frames (lattice works, truss frames) by existence of cables bearing tension only. Therefore they can be designed as equivalents of statically indeterminate strut frames; prestress induced by pretension in cables ensures shape and integrity of the structure under load. The simplest 2D tensegrities are presented in Fig. 1. Fig. 2 presents creation of simple 3D tensegrities, while Fig. 3 shows how they can be enlarged into more complex multilayer structures.

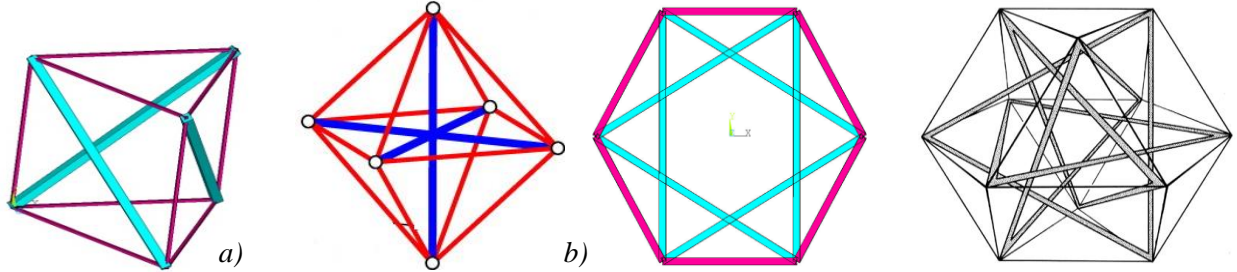


Fig. 2: a) Rhombic configuration; b) 2D and 3D tensegrity with circuit compression members.

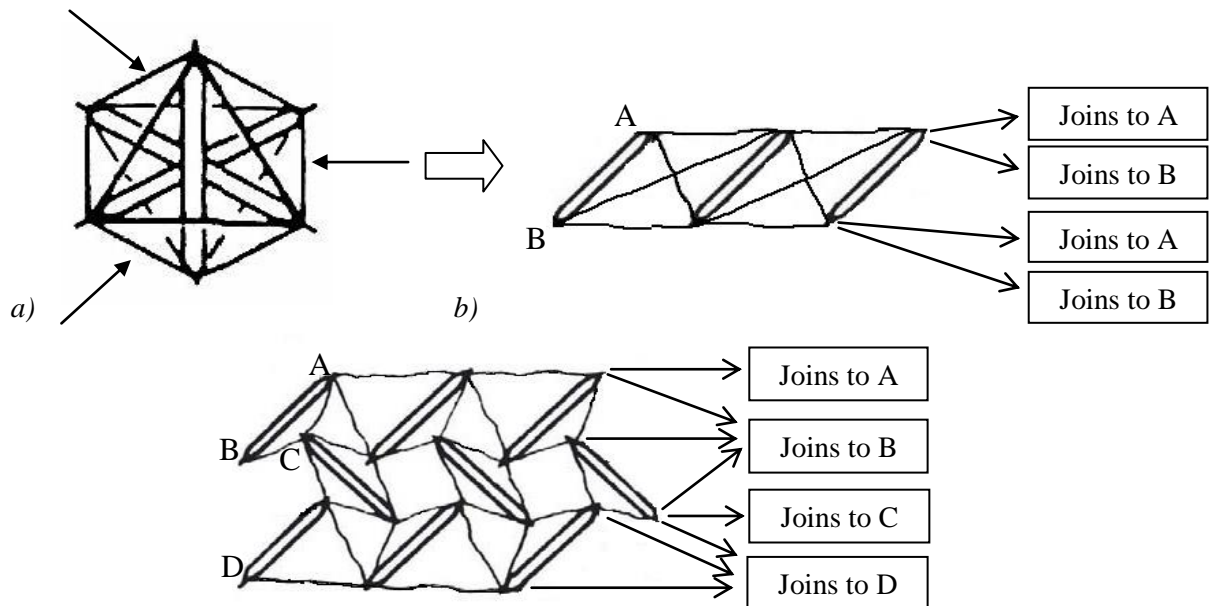


Fig. 3: Creation of more complex tensegrity structures from the octahedron.

3. High Frequency Spheres

Another principle of how to create more complex sphere-like tensegrities is based on principal (Platonic) polyhedrons (see Fig. 4). Triangular faces of these polyhedrons can be subdivided into smaller triangles (see Fig. 5) to create high frequency spheres with their shape closer to a sphere and with shorter elements more resistive to buckling.



Fig. 4: Principal (Platonic) polyhedrons.

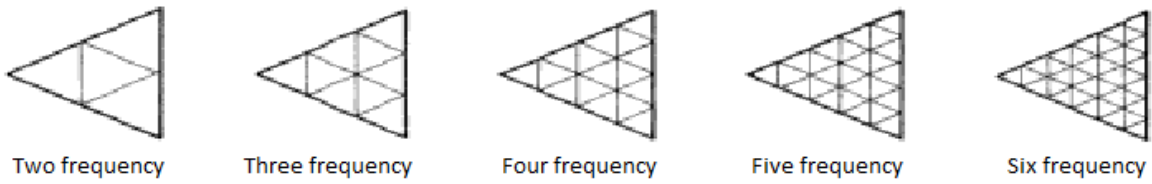


Fig. 5: Subdivisions of a triangular face applied in creation of high frequency spheres.

For higher frequencies the individual triangles can be created of basic triangular tensegrity units created on the basis of octahedron tensegrity. This unit consists of three struts with some of the vertexes shifted centrally from the strut end (see Fig. 6). A sphere-like tensegrity structure can then be created by repeating these basic units over the surface of a chosen geometrical body (see Fig. 7).

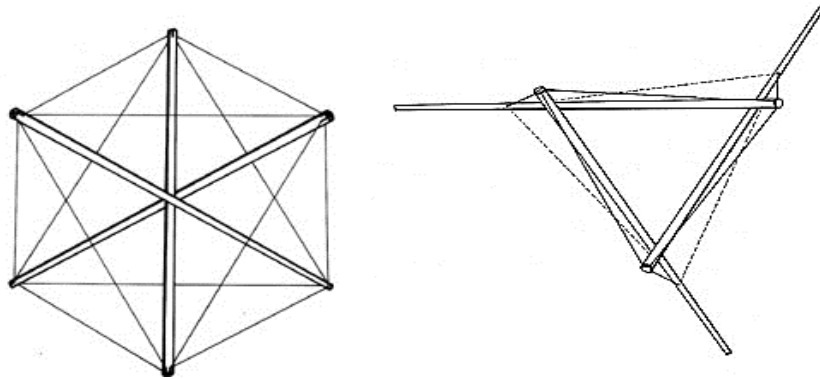


Fig. 6: Creation of a basic tensegrity unit from an octahedron by flattening it and removing some cables.

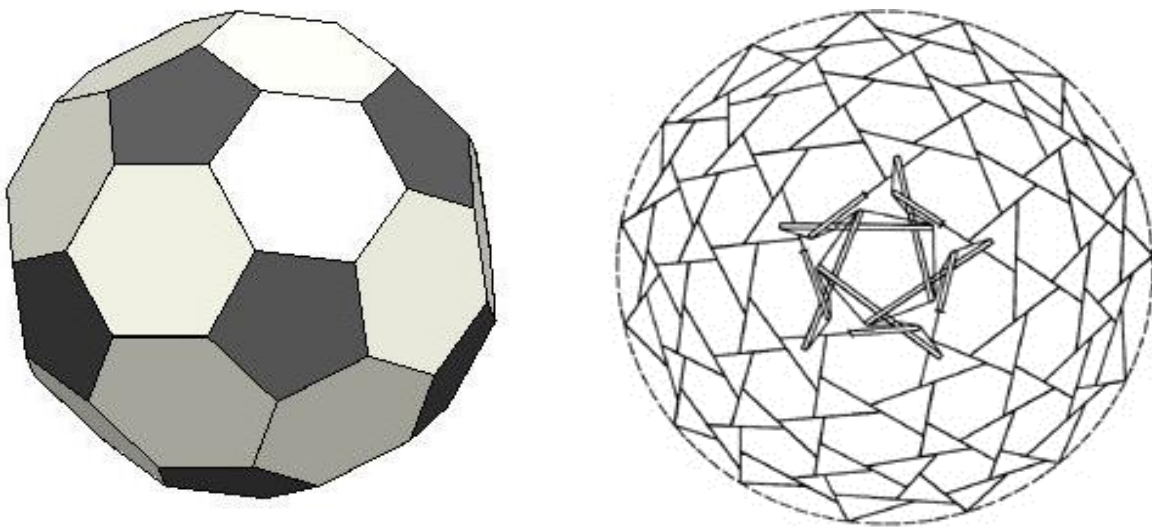


Fig. 7: Creation of a complex sphere-like structure from basic tensegrity units.

4. Examples Based on Form-Finding Technique

As shown above, the shape of the structure may vary rather substantially with respect to dimensions of the elements, positioning of vertexes, pretension of cables etc. The procedure of achieving a certain configuration of the structure is called form-finding. It is a method of how to design and generate a stable geometrical configuration of a tensegrity structure (when using mathematical modelling) inspired by specific geometrical forms under given conditions of pre-stress, such that it will remain stable and maintain its shape under a certain range of external loads and impacts.

Examples of complex tensegrity structures are presented, applied in the field of modelling of mechanical properties of living cells (Fig. 8). In many animal cells, the most important mechanical component of the

cell is cytoskeleton, a typical discrete structure created by submembrane actin stress fibres, intermediate filaments surrounding the nucleus and attached to membrane receptors, and microtubules oriented in radial directions and connecting centrosome (an organelle very close to nucleus) with membrane receptors. Realistic modelling of these structures during mechanical tests of cells is decisive for understanding the influence of mechanical stimuli on biochemical responses of the cell.

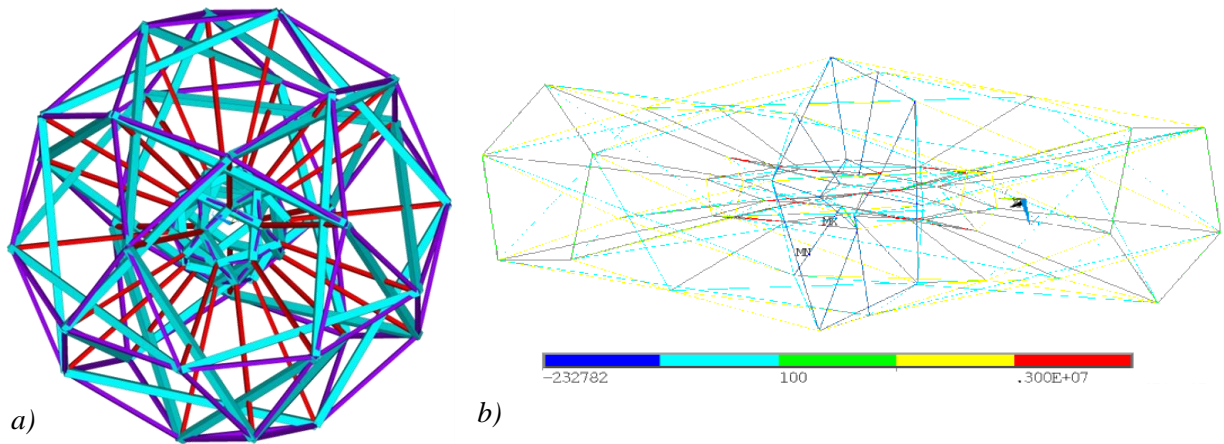


Fig. 8: a) Tensegrity based computational model of intracellular structure with 210 members; b) The same tensegrity model in simulated tension test of a cell (from Bursa et al. (2012)).

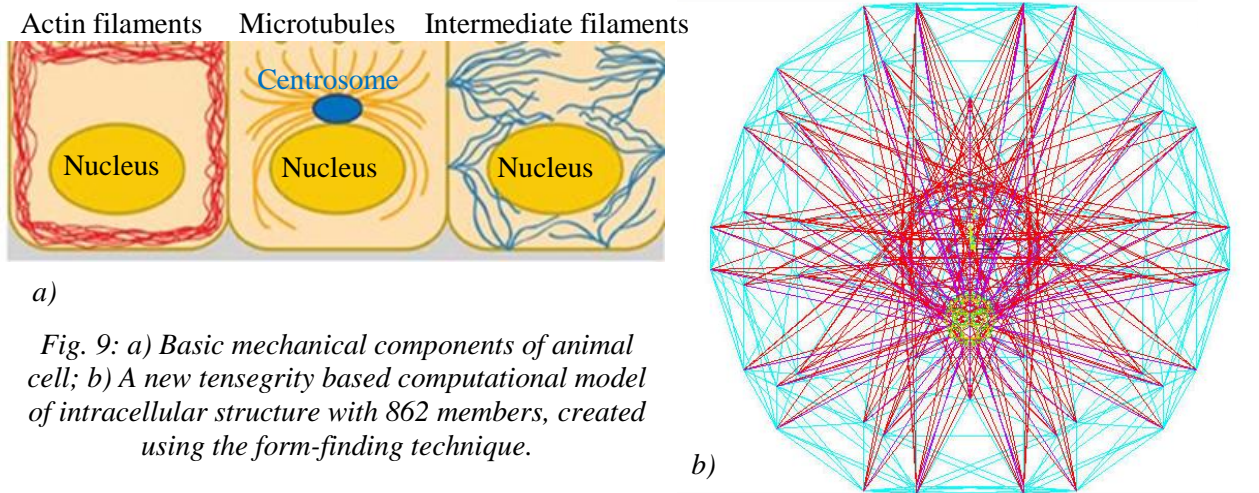


Fig. 9: a) Basic mechanical components of animal cell; b) A new tensegrity based computational model of intracellular structure with 862 members, created using the form-finding technique.

Acknowledgement

This work was supported by Czech Science Foundation project No. 13-16304S and faculty project No. FSI-S-14-2344.

References

- Fuller, R. B. (1961) Tensegrity, Portfolio and Art News Annual, 144 (4), pp. 112-127.
- Fuller, R. B. (1975) Synergetics: Explorations in the geometry of thinking, in collaboration with E. J. Applewhite, Macmillan Publishing Co. Inc., New York.
- Snelson, K. (2012) The art of tensegrity, International Journal of Space Structures, 27, pp. 71-80.
- Bursa, J., Lebis, R., Holata, J. (2012) Tensegrity finite element models of mechanical tests of individual cells, Technology and Health Care, 20 (2), pp. 135-150.

RECENT ADVANCES AND PROBLEMS IN LUBRICATED HERTZIAN CONTACTS

M. Hartl^{*}, I. Křupka^{*}, M. Omasta^{*}, P. Šperka^{*}

Abstract: *This review paper provides an introduction to the issue of lubricated Hertzian contacts and related elastohydrodynamic regime of lubrication. It deals with recent advances in such contacts in more detail. Emphasis is placed on the effects of surface topography involving real roughness and artificial features. These problems are discussed on the basis of experiments carried out at Institute of Machine and Industrial Design, Faculty of Mechanical Engineering, Brno University of Technology.*

Keywords: Elastohydrodynamic Lubrication, Optical Interferometry, Roughness.

1. Introduction

Improved understanding of contact mechanics of critical components is required in the design process of modern high efficiency mechanical systems. When such contacts have to transfer high load under relative movement, lubrication is necessary to ensure low energy consumption and long durability. Many machine elements (gears; rolling element bearings; cam/follower systems etc.) have contacting surfaces that do not conform to each other and thus concentrated contact occurs. The contact area is very small and the resulting pressure is very high.

From the point of view of machine design it is essential to know the values of stresses acting in such contacts. With assumption of dry elastostatic contact, these stresses can be calculated from analytical formulae, based on theory developed by Hertz in 1881. For a general point contact (with different principal relative radii of curvature in orthogonal planes) this theory predicts an elliptical contact area and a semi-ellipsoid contact pressure distribution. When a movement of the surfaces occurs, rolling and sliding is presented in the contact. In general, rolling results in increase in contact area and modification of contact stress distribution. However, the most critical influence on subsurface stress is due to sliding.

Lubrication is an effective way how to reduce friction and subsurface shear stress, separate surfaces and remove wear in rolling/sliding contacts. This case of lubricated Hertzian contacts is called elastohydrodynamic lubrication (EHL). EHL is a mode of fluid-film lubrication in which hydrodynamic action is significantly enhanced by surface elastic deformation. The lubricant is exposed to high pressures (up to 3 GPa) and shear rates (up to 10^8 s^{-1}) whereas lubricant film thickness is in submicron scale. Under these conditions, change of lubricant viscosity with pressure plays an important role. The lubricant behaviour fundamentally affects pressure distribution and lubricant film shape.

The EHL film thickness and shape has been the main area of interest since 1960s when milestone isothermal EHL theory was proposed (Dowson et al., 1962) and confirmed experimentally not long after that (Gohar and Cameron, 1963). Classical EHL theory predicts typical horse-shoe shaped film thickness profile and exit pressure spike, as shown in Fig. 1. Up to the present, considerable effort has been devoted to describe various phenomena which occur in EHL. In this effort an experiment play an important role because it allows confirming new theories, or on other hand, it may shed new light on this problem.

One of the most powerful experimental approaches in EHL is ball-on-disc tribometer coupled with optical interferometry method, which allow to determine film thickness distribution in contact between steel ball and transparent (mainly glass) disc (Spikes, 1999; Hartl et al., 2001). Typical EHL interferogram is shown in Fig. 1.

^{*} Prof. Ing. Martin Hartl, PhD., Prof. Ing. Ivan Křupka, PhD., Ing. Milan Omasta, PhD., Ing. Petr Šperka, PhD.: Faculty of Mechanical Engineering, Brno University of Technology; Technická 2896/2; 616 69, Brno; CZ, hartl@fme.vutbr.cz

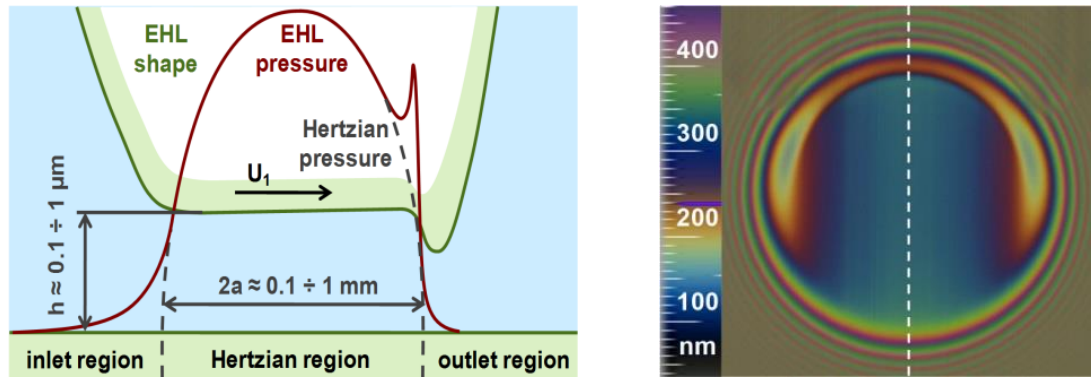


Fig. 1: EHL film thickness and pressure profile in rolling direction and EHL interferogram.

2. Surface Topography

2.1. Real roughness

In engineering practice no surface is ideally smooth. As the ratio of mean film thickness to surface roughness height is decreasing the roughness starts to substantially affect contact pressure distribution. When the film is broken down it results in further increase in the pressure as well as friction and wear caused by the direct surface interaction. Coherent effective lubricant film can be hardly formed under these operational conditions, so that, the knowledge of surface roughness influence on fluid film is essential. The initial studies of the roughness influence on the film thickness used a stochastic approach. Primarily the effects of roughness orientations on global film thickness variations were studied. During the last decades more interest has been focused on deterministic studies that can reflect local changes. One of the most important result have been development of an amplitude attenuation theory which provides analytical expressions that estimate how the amplitude of a given harmonic surface feature changes inside EHD contact. The behaviour can be completely described by a single curve known as an amplitude attenuation (reduction) curve, defined as the deformed to initial amplitude ratio. This theory says that roughness components with small wavelengths are deformed inside the contact much more than these with high wavelengths (Lubrecht and Venner, 1999). Recently, this theory was validated based on FFT analyses of real roughness measurements (Sperka et al., 2010; Sperka et al., 2012a). The scheme of this validation is shown in Fig. 2.

2.2. Artificial features

For a better understanding of the behavior of roughness in EHL contact, experimental works have been mostly oriented on the artificially produced asperities like ridges (negative) and bumps (positive). Someone can assume that passing of positive roughness features thru the contact should have strong impact on film thickness, while the effect of negative roughness features should be much less significant because this feature cannot interact with opposite surface. However, recent experiments show that the reality is the exact opposite, as shown in Fig. 3. Even a very high bump is nearly totally pushed into the surface thanks to high local pressure and a piezoviscosity of lubricant. However when equivalent surface ridge passes thru the contact, lubricant leaks from the surface feature due to low pressure and breakdown

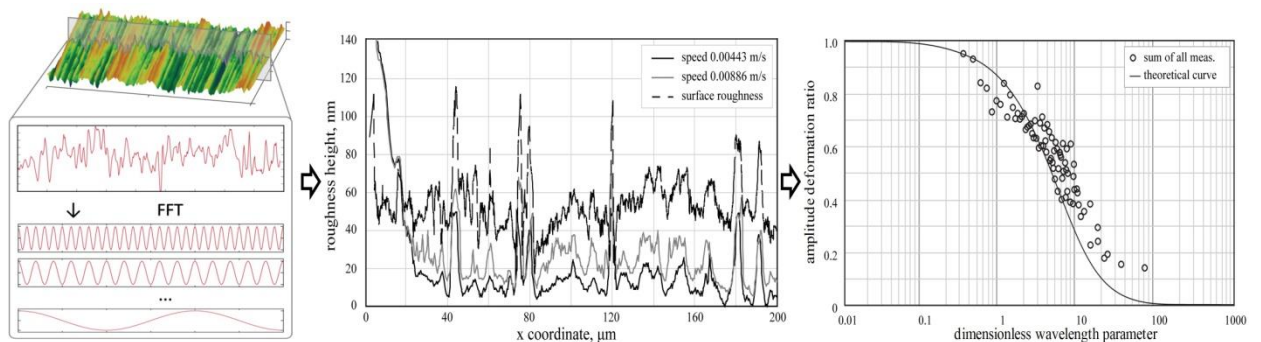


Fig. 2: Scheme of analysis of real roughness deformation (Sperka et al., 2010).

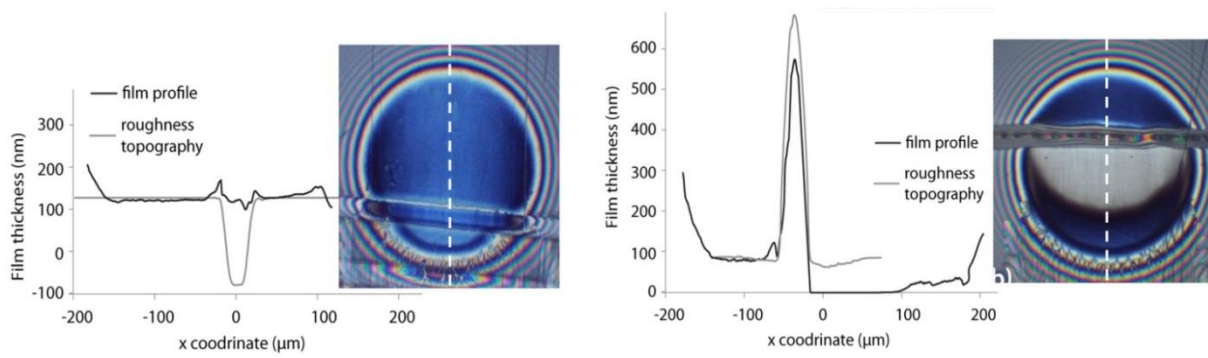


Fig. 3: Surface bump and ridge passing thru the EHL contact and its effect on film thickness.

of lubricant layer occurs (Kaneta et al., 1992; Sperka et al., 2012b). These results show that roughness effects on film thickness and roughness deformation cannot be neglected in prediction of lubrication regime. Other kind of surface topography consists in the artificial microtextured surfaces. Design of mechanical seals or piston rings involve lubricated contacts formed between conformal surfaces having artificially produced microfeatures of controlled size, shape, and density on sliding surfaces. In such a case of conformal sliding contact, microfeatures can be considered as lubricant reservoirs and can trap debris particles to diminish friction and wear.

Fig. 4 shows experimental results with an array of microdents prepared by mechanical indentation. They suggested that the microtexturing might help to improve the efficiency of lubrication films within highly loaded contacts once shallow microdents are used (Krupka et al., 2010). This effect may be beneficial mainly under transient conditions, especially when speed and load changes rapidly, as is the case of cam/tappet contact (Krupka et al., 2011). However, the presence of microdents within highly loaded contacts results not only in significant changes in lubricant film thickness but also in pressure distribution. Highly localized pressure peaks in the vicinity of microfeatures increase subsurface stresses. So, the effect of surface texturing on rolling contact fatigue was studied (Vrbka et al., 2010). It has been found that the application of surface texturing is not necessarily accompanied with the reduction of RCF life.

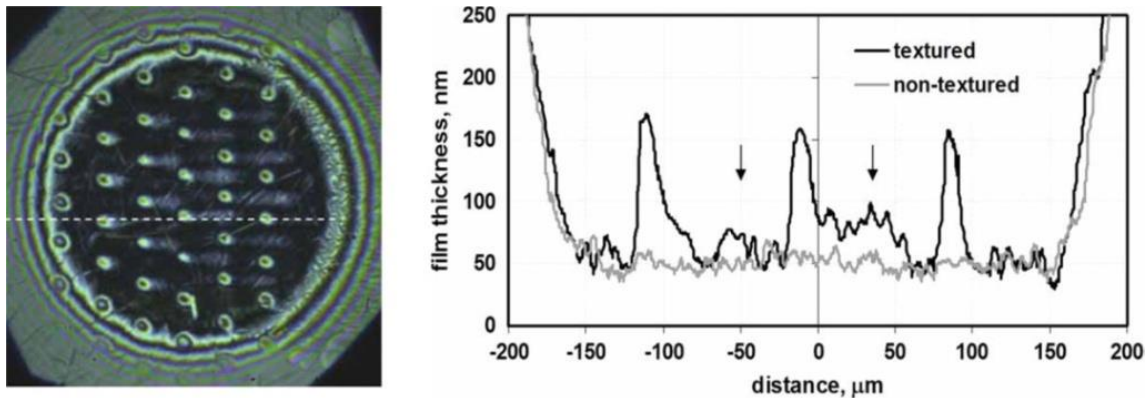


Fig. 4: Effect of surface texturing using microdents on film thickness (Krupka et al., 2010).

3. Specific In-Contact Film Shape

In smooth contacts classical EHL theory predicts flat plateau in central (in-contact) zone of EHL contact. However during last years some experimental and numerical studies showed that various film shape features may be formed in the in-contact zone, mainly under rolling-sliding conditions. Very common phenomenon is a dimple phenomenon (Kaneta et al., 1996). This effect is characterised by local increase in film thickness in the central part of the contact and occurs under the specific sliding conditions, as shown in Fig. 5. Several types of models have been proposed to explain the dimple phenomena. The most accepted is model of temperature–viscosity wedge action consisting in unequal temperature and thus viscosity distribution across the film thickness. Moreover, recently it has been found that among others also an angle between sliding and rolling velocity has a strong influence on in-contact film shape (Omasta et al., 2013). This phenomenon is due to the different heat flow through the contact.

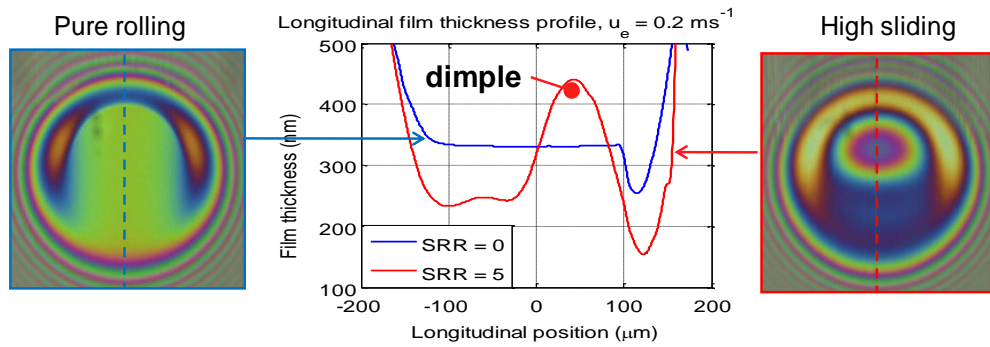


Fig. 5: Interferogram and film thickness profile for pure rolling and high sliding conditions.

4. Conclusions

Lubricated Hertzian contacts and hence EHL regime is of great importance in many mechanical components. An understanding of processes that take place in the contacts is crucial to make things work better. Recent findings obtained using optical interferometry brings new challenges and allow extending the present EHL theory.

Acknowledgement

This work is an output of research and scientific activities of NETME Centre, regional R&D centre built with the financial support from the Operational Programme Research and Development for Innovations within the project NETME Centre (New Technologies for Mechanical Engineering), Reg. No. CZ.1.05/2.1.00/01.0002 and, in the follow-up sustainability stage, supported through NETME CENTRE PLUS (LO1202) by financial means from the Ministry of Education, Youth and Sports under the „National Sustainability Programme I“.

References

- Dowson, D., Higginson, G. R., Whitaker, A.V. (1962) Elasto-hydrodynamic Lubrication: A Survey of Isothermal Solutions. *Journal Mechanical Engineering Science*, 4, pp. 121-162.
- Gohar, R., Cameron, A. (1963) Optical Measurement of Oil Film Thickness under Elasto-hydrodynamic Lubrication. *Nature*, 200, pp. 458-459.
- Hartl, M., I. Krupka, R. Poliscuk, M. Liska, et al. (2001) Thin film colorimetric interferometry. *Tribology Transactions*, 44(2), 270-276.
- Kaneta, M., Sakai, T., Nishikawa, H. (1992) Optical interferometric observations of the effects of a bump on point contact EHL. *Journal of Tribology-Transactions of the ASME*, 114(4), pp. 779-784.
- Kaneta, M., Nishikawa, H., Kanada, T., Matsuda, K. (1996) Abnormal Phenomena Appearing in EHL Contacts. *J. Tribol.*, 118, pp. 886-893.
- Krupka, I., Hartl, M., Svoboda, P. (2010) Effects of surface topography on lubrication film formation within elasto-hydrodynamic and mixed lubricated non-conformal contacts. *Proc of IMechE-Part J*, 224(J8), pp. 713-722.
- Krupka, I., M. Hartl, M. Zimmerman, P. Houska, et al. (2011) Effect of surface texturing on elasto-hydrodynamically lubricated contact under transient speed conditions. *Tribology International*, 44(10), pp. 1144-1150.
- Lubrecht, A. A., Venner, C.H. (1999) Elasto-hydrodynamic lubrication of rough surfaces. *Proc of IMechE—Part J: J Eng Trib*, 213(J5), pp. 397-404.
- Omasta, M., Křupka, I., Hartl, M. (2013) Effect of surface velocity directions on elasto-hydrodynamic film shape. *Tribology Transactions*, 56(2), pp. 301-309.
- Sperka, P., Krupka, I., Hartl, M. (2010) Experimental study of real roughness attenuation in concentrated contacts. *Tribology International*, 43(10), pp. 1893-1901.
- Sperka, P., Krupka, I., Hartl, M. (2012a) Experimental study of real roughness attenuation in rolling/sliding concentrated contacts. *Tribology International*, 46(1), pp. 14-21.
- Sperka, P., Krupka, I., Hartl, M. (2012b) The Behavior of Surface Roughness in EHL Contacts Under Small Slide to Roll Ratios. *Tribology Letters*, 47(3), pp. 357-366.
- Spikes, H.,A. (1999) Thin films in elasto-hydrodynamic lubrication: the contribution of experiment. *Proc Instn Mech Engrs, Part J*, 213, pp. 335-352.
- Vrbka, M., Samanek, O., Sperka, P. et al. (2010) Effect of surface texturing on rolling contact fatigue within mixed lubricated non-conformal rolling/sliding contacts. *Tribology International*, 43(8), pp. 1457-1465.

DYNAMICS OF SWIRLING FLOWS IN INDUSTRIAL APPLICATIONS

P. Rudolf*, D. Štefan*, F. Pochylý*

Abstract: Many industrial devices positively utilize the action of centrifugal forces induced by highly swirling flows (e.g. hydrocyclones, swirl burners). On the other hand swirling flow causes significant problems in operation of turbines or aircraft. Presented paper is going to review the current state of knowledge about swirling flows (stability of swirling flows, vortex breakdown phenomenon, helical precessing vortex core) and outline possible approaches leading to better understanding of these phenomena. Inevitably it is a mixture of analytical techniques, computational simulations and advanced experiments. It also proves efficient to employ some of the methods for spatio-temporal description of dynamical systems like proper orthogonal decomposition (POD).

Keywords: Swirling flow, Stability, Vortex rope, Proper orthogonal decomposition.

1. Introduction

Strongly swirling flows are quite common in lots of industrial applications. Resulting centrifugal forces are exploited in many devices especially in chemical and processing industries, furnaces and combustion chambers, HVAC, etc. The reason is that centrifugal forces are much more effective than only the action of gravity. Positive effect of swirl is utilized for solid particles separation and classification (cyclones, hydrocyclones), flame stabilization (swirl burners), cooling/heating of air (vortex tubes), in fluidic devices (swirl valves), measurement devices (vortex flowmeters). Most of these devices are mechanically very simple, very often with no moving parts. The only two problems, which are connected with their operation are:

- increased hydraulic losses,
- limit on the operation is imposed by stability of the swirling flow.

Whereas the first issue is not very severe and devices achieving same function with different design or using different principle would have similar energy consumption or much higher manufacturing costs, the latter issue poses a serious problem, because it restricts further intensification of the swirling apparatus processes. The limit point is so called vortex breakdown.

Swirling flows are also typical in turbomachinery, where vortical structures are tackled as undesirable features. Highly swirling flow leaves the runner of hydraulic, steam or combustion turbines. The rear diffuser of these machines is an appropriate place, where vortex breakdown occurs resulting in precessing helical vortex, which induces pressure pulsations, vibrations and noise. Instability of swirling flow also appears on wing tips, where it leads to stream disturbances, which limit air traffic.

Rather common are instabilities of the vortex breakdown type also in nature. The best known example is tornado or waterspout.

2. Swirling Flows and Coherent Structures

Swirling flows are very susceptible to instabilities. Instability of particular interest in industrial applications is vortex breakdown. This phenomenon is characterized by axial velocity decrease along the axis of the swirl, eventually internal stagnation point or even backflow, and by formation of bubble, which later transforms, with increased swirl intensity, into helical vortical tube. Precessing helical core

* Assoc. Prof. Pavel Rudolf, PhD., David Štefan, Prof. František Pochylý, PhD.: V. Kaplan Department of Fluid Engineering, Brno University of Technology, Technická 2896/2; 616 69, Brno; CZ, rudolf@fme.vutbr.cz, david.steffan@gmail.com, pochylly@fme.vutbr.cz

satisfies definition of the coherent structure, i.e. flow structure, which persists for a relatively long time or the flow structure which remains after subtracting the noise from the flow field.

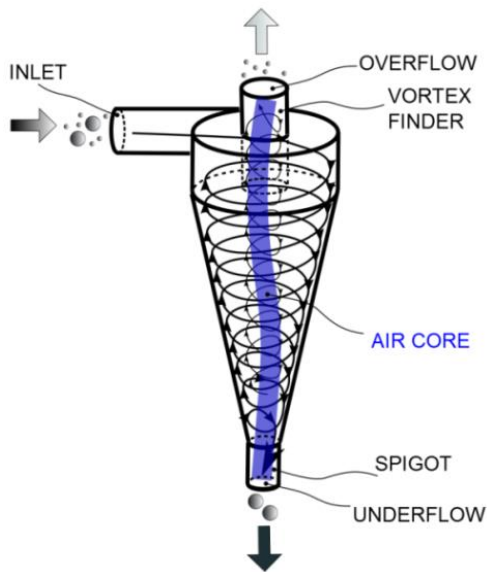


Fig. 1: Hydrocyclone (Rudolf, 2013).

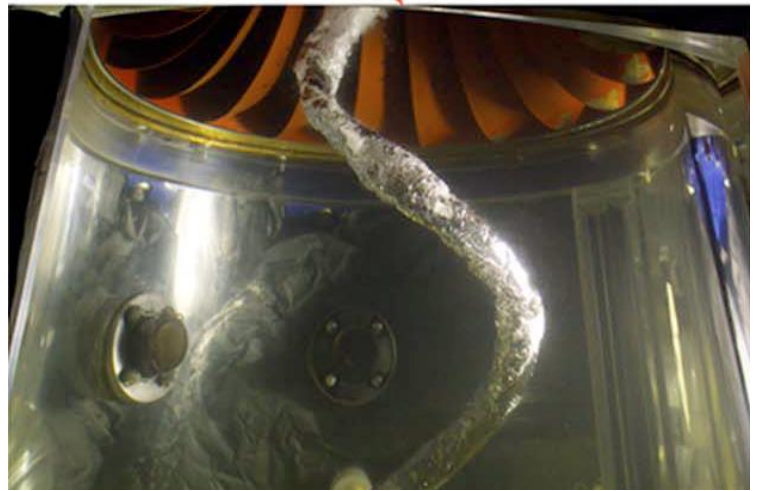


Fig. 2: Vortex rope in hydraulic turbine draft tube (Ciocan et al, 2007).

While vortex breakdown bubble can only be observed for low Reynolds numbers and relatively low swirl numbers (see Figs. 3, 4), the helical precessing core (see Fig. 2) forms a very compact vortical structure, which is associated with high Reynolds numbers and broad range of swirl numbers Sr .

$$Sr = \frac{1}{R} \frac{\iint_S v_{ax} v_t r dr}{v_{ax}^2} \quad (1)$$

Helical precessing core starts to appear for higher swirl rates in the aft of the vortex breakdown bubble. Further increase of swirl leads to disappearance of the bubble and helical precessing vortex core dominates the flow. It was hydraulic machinery, where this helical vortical structure, known also as vortex rope, was experimentally observed and studied for the first time. Characteristic frequency of the vortex rope rotation is 20-30% of the runner speed. Therefore it is a typical source of low frequency pressure pulsations in hydraulic turbines.

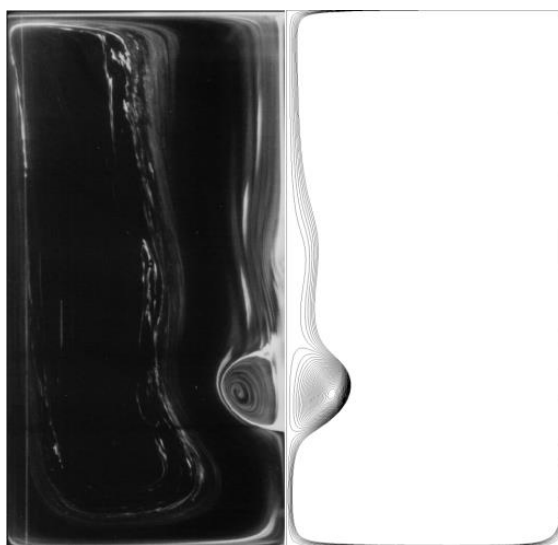


Fig. 3: Bubble vortex breakdown in cylinder with rotating top lid (laminar flow), exp.: left side (Escudier, 1984) comp.: right side (Rudolf, 2008).

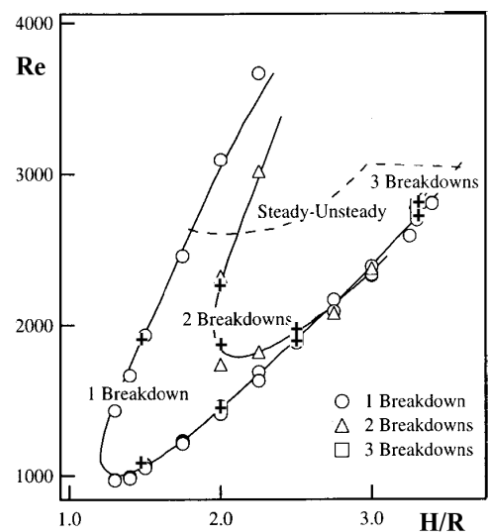


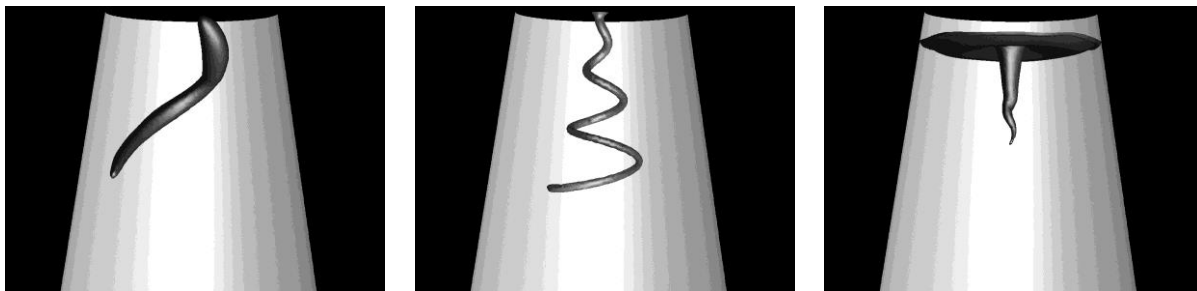
Fig. 4: VB map for cylinder with rotating lid, (Escudier, 1984), crosses: CFD simulation (Rudolf, 2008).

3. Stability of Swirling Flow

Theoretical analysis of the swirling flow stability is dating back to sixties, but systematic analysis of the vortex breakdown, including its spiral form, was initiated by Gupta et al (1984). Investigation carried out with Euler equations for inviscid flow by Pochylý et al (2009a) and Pochylý et al (2009b) revealed that the swirling flow is extremely sensitive to boundary conditions. Conclusion is that proper distribution of not only velocity components at the domain inlet, but especially their derivatives is decisive for the inception of the unstable behavior.

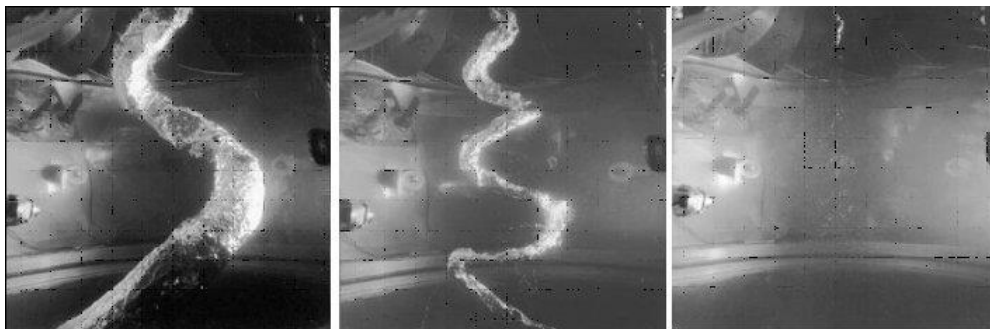
4. Computational Modeling of Swirling Flow

Development of computational methods in fluid mechanics enabled new possibilities in study of the swirling flows. While laminar flow computations are managed without difficulties, turbulent flows still pose problem due to the uncertainty in turbulence model choice. It was noted by Skoták and Rudolf (2001) that Reynolds stress model offers the minimum complexity level for correct capturing of the vortex rope in the hydraulic turbine draft tube. Yet higher level of detail, but at substantially higher computational costs, is offered by large eddy simulations and different crossovers between RANS and LES approaches (e.g. detached eddy simulation). However it still remains serious problem and obtaining reliable vortex breakdown map in turbulent regime for broad range of swirl numbers is not feasible. Computational complexity can be further increased by presence of vapour phase in case of cavitating vortex rope or by combination of phases (water - air - solid particles) in case of hydrocyclone (Rudolf, 2013).



a) 70% of BEP discharge b) 90% of BEP discharge c) 100% of BEP discharge

Fig. 5: Vortex rope visualized by contour of constant pressure (CFD simulation) (Rudolf, 2009).



a) 70% of BEP discharge b) 90% of BEP discharge c) 100% of BEP discharge

Fig. 6: Vortex ropes experimentally visualized by cavitation (Jacob, 1993).

5. Decomposition of Swirling Flows

Promising results in analysis of swirling flows are offered by application of proper orthogonal decomposition (POD). This technique was introduced by Lumley in 1967 (cited in Berkooz et al, 1993) for the spatio-temporal description of coherent structures in turbulent flow. Rudolf and Jízdny (2011) successfully applied POD for swirling flow in hydraulic turbine draft tubes. POD enables to decompose the flowfield into a set of spatial eigenmodes, which can be viewed as basic cornerstones of the flow.

Next step is development of low order dynamical model, which enables to model the spatio-temporal behavior of the swirling flow with only the most dominant eigenmodes.

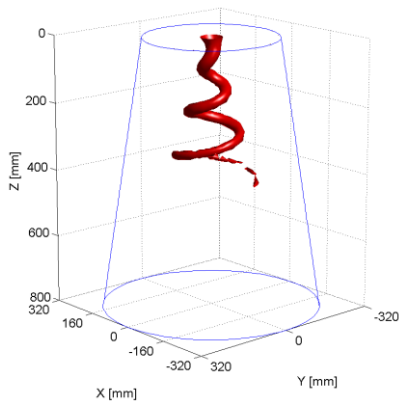


Fig. 7: Instantaneous snapshot of the vortex rope.

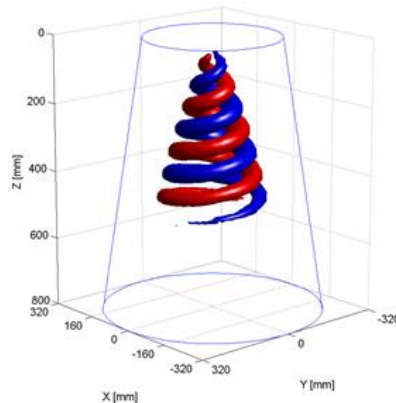


Fig. 8: First eigenmode of the pressure field.

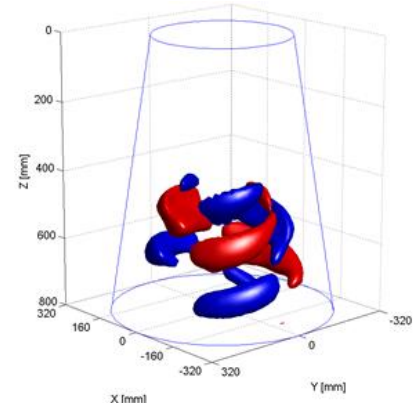


Fig. 9: Fifth eigenmode of the pressure field.

6. Conclusions

Present extended abstract provides a very rough overview of the swirling flows in industrial applications and methods for their analysis. Importance of swirling flow in technology, where it plays both positive and negative roles, is stressed and need for better analytical description is underlined. While computational and experimental methods offer much more complex view than in past, we still lack the fundamental understanding of the instability process leading to vortex breakdown.

Acknowledgement

This work is an output of research and scientific activities of NETME Centre, regional R&D centre built with the financial support from the Operational Programme Research and Development for Innovations within the project NETME Centre (New Technologies for Mechanical Engineering), Reg. No. CZ.1.05/2.1.00/01.0002 and, in the follow-up sustainability stage, supported through NETME CENTRE PLUS (LO1202) by financial means from the Ministry of Education, Youth and Sports under the „National Sustainability Programme I“.

References

- Berkooz, G., Holmes, P., Lumley, J. L. (1993) The proper orthogonal decomposition in analysis of turbulent flows, *Annual Review of Fluid Mechanics*, 23, pp. 539-579.
- Ciocan, G. D., Iliescu, M.S., Vu, T. C., Nenneman, B., Avellan, F. (2007) Experimental study and numerical simulation of the FLINDT draft tube rotating vortex, *Journal of Fluids Eng.*, 129, pp. 146-158.
- Escudier, M. (1984) Observations of the flow produced in a cylindrical container by a rotating endwall, *Experiments in Fluids*, 2, pp. 189-196.
- Gupta, A. K., Lilley, D. G., Syred, N. (1984) *Swirl flows*, Abacus Press.
- Jacob, T. (1993) Evaluation on a scale model and prediction of the stability of operation of Francis turbines, PhD Thesis, EPFL No 1146, Lausanne.
- Pochylý, F., Rudolf, P., Habán, V., Čermák, L. (2009a) A note on influence of velocity field on stability of the flow in axisymmetric domain with focus on origin of the cavitating vortex rope, In: *Proc. 3rd IAHR Int. Meeting of the WG on Cavitation and Dynamic Problems in Hydraulic Machinery and Systems - part II*, pp. 625-631.
- Pochylý, F., Čermák, L., Rudolf, P., Habán, V., Koutník, J. (2009b) Assessment of the steady swirling flow stability using amplitude- frequency characteristic. In: *Proc. 3rd IAHR Int. Meeting of the WG on Cavitation and Dynamic Problems in Hydraulic Machinery and Systems - part I*, pp. 25-34.
- Rudolf, P. (2013) Simulation of multiphase flow in hydrocyclone. *EPJ Web of Conf.*, 45, 1101.
- Rudolf, P., Skoták, A. (2001) Unsteady flow in the draft tube with elbow – Part B Numerical investigation. In: *10th Int. IAHR WG Meeting*, Trondheim.
- Rudolf, P. (2009) Connection between inlet velocity field and diffuser flow instability, *Applied and Computational Mechanics*, 3, No. 1, pp. 177-184.

PAPERS

BIOMATERIALS USED FOR THE PRODUCTION OF STENTS - HOPES AND LIMITATIONS - REVIEW ARTICLE

M. Andryszczyk^{*}, M. Wirwicki^{**}, T. Topoliński^{***}

Abstract: *Diseases of the cardiovascular system are on a high position in the statistics of deaths in our century. Nowadays in Poland, ischemic heart disease affects almost a million people and about 90 000 of them die every year. One of the most commonly used treatment methods is the coronary angioplasty with stent placement. There are many types of stents available, but we still need to look for new technologies and materials to provide better mechanical properties, physicochemical and biomedical stents.*

Keywords: Enter Stents, Biomaterials, Cardiology, Atherosclerosis.

1. Introduction

The term "ischemic heart disease" describes a pathophysiologically and clinically diversified state of functional or permanent damage of the heart muscle (Ziołkowski et al., 2009).

Population research has proven the steadily increasing prevalence of coronary heart disease. In Poland it is on average 620 cases per 100 000 for men and 220 cases per 100,000 for women. Rate of incidence depends on the place of the residence (lower in rural areas and higher in cities) and increases rapidly with age regardless of gender, especially after the age of 45. Currently we can notice a rise in the incidence of this disease among people between 20 and 30 years of age (Karasek, 2008; Jakubowska-Najnięgieł, 2008; Ziołkowski et al., 2009).

Taking into account the risk factors division made by Polish Cardiac Society (based on the guidelines of European Society of Cardiology), the most important and modifiable ischemic heart disease risk factors are considered to be: lifestyle, cigarette smoking, diet rich in an animal fat, physiological and biochemical factors, high cholesterol level (especially LDL), elevated triglycerides, hyperglycemia or diabetes and increased levels of homocysteine.

The age over 45 years for men and over 55 for women, premenopause and other arteries disease caused by atherosclerosis should be considered as non-modifiable and independent of the patient risk factors (Murray, 2006).

2. Coronary Atherosclerosis

The most common reason (90%) of ischemic heart disease is the atherosclerosis of the coronary arteries. Over the years, the aging process was considered responsible for coronary atherosclerosis. The new view on the pathomechanism of this disease was given not until the research from the mid of XIX century. The latest tests have shown, that atherosclerotic lesions are the result of a long process of inflammation, appearing in the vascular wall in response to inflammatory agents, hypoxia, free radicals or shear forces, damaging epithelial cells (Snarska, 2003).

* M.Sc Marek Andryszczyk: Institute of Mechanics and Machine Design, University of Technology and Life Sciences, Ks. Kordeckiego 20; 85-225, Bydgoszcz; Poland, marek.andryszczyk@utp.edu.pl

** M.Sc.Eng. Mateusz Wirwicki: Institute of Mechanics and Machine Design, University of Technology and Life Sciences, Ks. Kordeckiego 20; 85-225, Bydgoszcz; Poland, wirwicki@utp.edu.pl

*** Prof. Tomasz Topoliński: Institute of Mechanics and Machinery Construction, University of Technology and Life Sciences, Ks. Kordeckiego 20; 85-225, Bydgoszcz; Poland, topol@utp.edu.pl

The formation of atherosclerotic plaque in the coronary arteries begins with the permeation of the lipoprotein excess through endothelial layer. There they are caught by the immune cells (monocytes) and put into precinct of collagen fibers, forming the early fatty infiltration. Then the smooth muscle cell migrate from the central portion to the internal part of the vessel - Fig. 1 (Szwed, 2002).

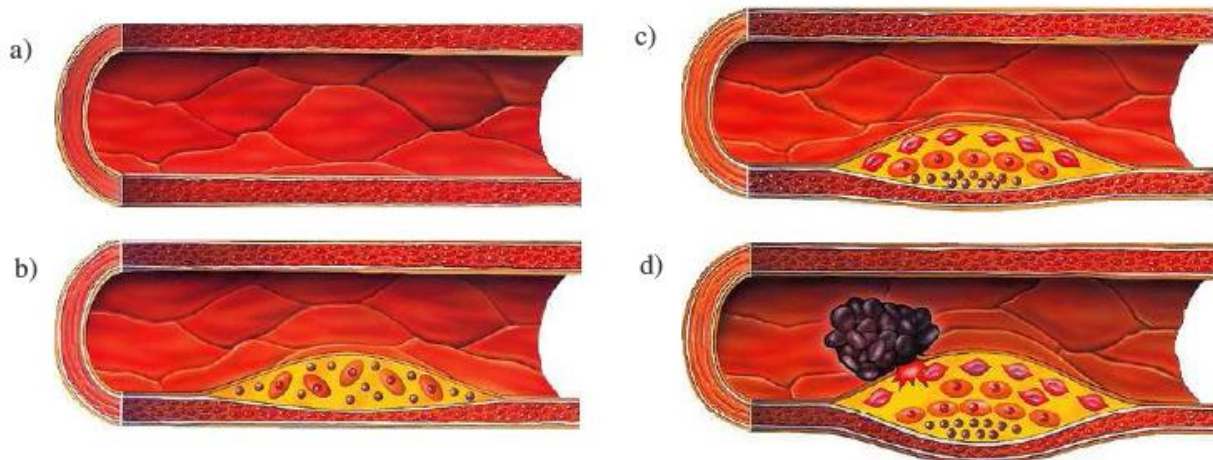


Fig. 1: The next phases of the formation atherosclerotic lesions in the coronary arteries: a) healthy artery; b) early fatty infiltration; c) atherosclerotic plaque; d) atherosclerotic plaque and thrombus (Marciniak, 2006).

2.1. Coronary stents

One of the most common treatment methods of coronary heart disease is percutaneous transluminal coronary angioplasty (PTCA). This is the procedure of expanding the atheromatously changed section of coronary artery, using a balloon catheter introduced in the place of constriction. Classical angioplasty is supplemented with other techniques, using various instruments, most often with the intravascular stents implantation, which perpetuate the effect of the coronary artery extension (Szkutnik, 2010).

Stents are a kind of metal, elastic scaffolding with a spatial, cylindrical construction and millimeter dimensions. They are implanted in a place of critically narrowed coronary artery section in order to support its walls and prevent from the narrowing of the vessel lumen.

2.2. Properties characterizing the implants

To avoid complications after the stent implantation and to improve its effectiveness, the metal stents construction should have the following properties (Patrick, 2001):

- flexibility, that makes it possible to carry the stent trough the bends of the coronary vessels and to implant it in a place of constriction;
- ease of movement in the catheter and arteries;
- low stent profile on the balloon;
- low thrombogenicity, that protects from thrombosis and disease relapses;
- tissue neutrality;
- good extensibility that facilitates the expansion mechanism;
- resistance to external forces, that reduces the vessel wall stretching and smooth muscle cells formation;
- small total stent surface;
- good rheological properties;
- good stent coverage of the vessel wall.

2.3. Material used in stent construction

The stents are made of biomaterial, which when introduced into the circulatory system may not result in dysfunctions of the body (damage to protein structure and blood morphotic elements, blocking the action of enzymes, changes in the composition of the electrolyte). At the same time they should not initiate

toxic, mutagenic or immunological reactions (Williams, 1986). Nowadays, there are many types of stents available on the market. They are made of different types of materials. The most popular include:

- austenitic steel AISI 316L (most of stents)
- nitinol (Radius™ , Cardiocoil™, HARTSTM, Paragon™),
- alloys of platinum with iridium (Angiostent™),
- tantalum (Wiktor®, Cordis™ , Strecker™),
- cobalt (Magic Wallstent™),
- gold (NIROYAL™),
- polymers (phosphorylcholine - DyvYsio™ stent, PTFE - Jostent®),
- alloys of cobalt (Driver™, Vision™),
- titanium (TTS)(Patrick W. Serruys., et al. 2001).

In the production of coronary stents the most commonly used material is an austenitic acid resistant steel (AISI 316L). The austenitic acid resistant steels are a group of materials, that the earliest were adapted to implantation in human body. It was inextricably linked with modernizing of chemical and phase composition.

Steels used for implants are of the highest quality and have the strictly defined composition. The main alloy elements in the steels of this type are chromium, nickel and molybdenum. Any other additions can cause the movement of boundaries of particular phases.

In the steels intended for stents the ratio of Cr-Ni-Mo should be about 18% - 15% - 2.5%. As a result of the nickel concentration increase, the resistance to stress corrosion of steel rises. Moreover, high energy of nickel chloride formation impede the penetration of chloride ions into the oxide passive layer. The molybdenum boosts the resistance to pitting corrosion, as well as chromium and helps to form the oxide layer on the surface.

A very important aspect for this type of steel is the kind of purity and inclusions. Type of inclusions, their shape, number and layout can have a great impact on the anisotropy of mechanical properties of the material, visualized more when the implant is miniaturized (Patrick, 2001).

2.4. Implants resistant to restenosis

Implantation of the metal stent can initiate a cascade reaction between blood components and the stent surface. This process is dangerous because it can cause blood clotting on the implant surface, which leads to recurrence of restenosis. Stents covered with the appropriate anticoagulants and materials lowering thrombogenicity, or those made of non-metallic materials, are used to prevent from such situations (Gabryel, 2009).

The most popular at present are polymer materials, which have good blood biotolerance and which are athrombogenic.

The number of species of non-biodegradable synthetic polymer used for the protective coating of stent surface is high, and the most popular are: polyurethane, silicone, polyethylene terephthalate, phosphorylcholine (Gabryel, 2009).

The use of biodegradable stents, made of natural polymers (such as polylactic acids, polyglycolide, a polysaccharide) can be regarded as a significant achievement. Because of its diverse structure and properties some of these materials are biodegradable. The research results show that using this type of solution is a very effective way to prevent from blood clotting process as well as from restenosis.

Concurrently with research on polymers began to use other biomaterials. The idea of using coatings of gold was aimed to improve the visibility of the stent in the screen. Reasons for choosing these coatings included the fact, that they limit the risk of blood clotting and reduce the implant's toxicity. The results showed, however, that they also can suffer from corrosion in body fluids' environment and do not prevent from restenosis (Edelman, 2001; Stefanini, 2011).

New promising test results were achieved after covering the coronary stents with amorphous silicon carbide. Preliminary results show, that this material has a good corrosion resistance in the body fluids' environment, and that the coatings effectively reduce platelet activation (Atar, 2009; Dahm, 2009).

Application of drug-eluting stents can be considered as a very important step. The atherogenic and anti-inflammatory substances are put into the polymer coatings structure. Then, when the implant is introduced, they are released gradually into the blood and vessel tissue. The medicines used in the surface layers of stents can be classified by their impact on the arteries wall and the coronary circulation system. The most commonly used are the medicines from the groups of drugs: anti-proliferative, immunosuppressive, inhibiting cell migration, stimulating the healing process and improving endothelial function and inhibiting clotting (Alfonso, 2013; Garg, 2013; Mulukutla, 2013).

On the market there are many types of stents made of various kinds of biomaterials and covered or not with drugs. Despite this fact, many research into new technologies, that provide better mechanical and physicochemical properties of stents are still carried out.

References

- Alfonso, F. (2013) New Drug-Eluting Stents: Polymer-Free, Biodegradable Polymers or Bioabsorbable Scaffolds?, *Rev Esp Cardiol*, 66, 423-426.
- Atar, E. (2009) Infrapopliteal Stenting with Silicon Carbide-Coated Stents in Critical Limb Ischemia: A 12 Month Follow-up Study, *Isr Med Assoc J*, 11, 611-614.
- Dahm, J. B., et al. (2009) Clinical Investigation into the Observation That Silicon Carbide Coating on Cobalt Chromium Stents Leads to Early Differentiating Functional Endothelial Layer, Increased Safety and Des-Like Recurrent Stenosis Rates: Results of the Pro-Heal Registry (Pro-Kinetic Enhancing Rapid in-Stent Endothelialisation), *EuroIntervention*, 4, 502-508.
- Edelman, E. R., et al. (2001) Gold-Coated Nitinol Stents in Porcine Coronary Arteries, *Circulation*, 103, 429-434.
- Gabryel, J., et al. (2009) Inflammatory mechanisms and restenosis after coronary stent implantation Metal and releasing drugs, *Postępy w Kardiologii Interwencyjnej*, 5, 5, (in Polish).
- Garg, S., Bourantas, C., Serruys, P. W. (2013) New Concepts in the Design of Drug-Eluting Coronary Stents, *Nat Rev Cardiol*, 10, 248-260.
- Karasek, D., Kubica, A., Sinkiewicz, W., Błażejowski, J., Bujak, R. (2008) Epidemic of Heart Failure - health and social problem of aging populations Polish and Europe, *Folia Cardiologica Excerpta*, 3, 242-248, (in Polish).
- Marciniak, J. (2006) Stents in Minimally Invasive Surgery, *Wydawnictwo Politechniki Śląskiej*, (in Polish).
- Maria Jakubowska-Najnięgiel, Piątkowski, R. (2008) Epidemiology of Heart Failure, *Terapia*, 9, 4-5, (in Polish).
- Mulukutla, S. R., et al. (2013) Benefit of Long-Term Dual Anti-Platelet Therapy in Patients Treated with Drug-Eluting Stents: From the NHLBI Dynamic Registry, *Am J Cardiol*, 111, 486-492.
- Murray, C. J., Kulkarni, S. C., Ezzati, M. (2006) Understanding the Coronary Heart Disease Versus Total Cardiovascular Mortality Paradox: A Method to Enhance the Comparability of Cardiovascular Death Statistics in the United States, *Circulation*, 113, 2071-2081.
- Patrick, W. S., Benno, J. R. (2001) *Handbook of Coronary Stents*; Fourth Edition, CRC Press.
- Snarska, B. (2003) Ischemic Heart Disease in the population of the Lodz Region, *Polski Przegląd Kardiologiczny*, 5, 437-442, (in Polish).
- Stefanini, G. G., et al. (2011) Long-Term Clinical Outcomes of Biodegradable Polymer Biolimus-Eluting Stents Versus Durable Polymer Sirolimus-Eluting Stents in Patients with Coronary Artery Disease (Leaders): 4 Year Follow-up of a Randomised Non-Inferiority Trial, *Lancet*, 378, 1940-1948.
- Szkutnik, M., Białkowski, J., Fiszer, R. (2010) Expanding aortic coarctation balloon angioplasty Using And / Or stent implantation - own experience, *Postępy w Kardiologii Interwencyjnej*, 1, 5, (in Polish).
- Szwed, A. (2002) Pathogenesis of Atherosclerosis and Coronary Events prevalence, *Postępy nauk medycznych*, 1, 2, (in Polish).
- Williams, D. F. (1986) *Definitions in Biomaterials: Proceedings of a Consensus Conference of the European Society for Biomaterials*, Elsevier.
- Ziołkowski, M., Kubica, A., Sinkiewicz, W., Maciejewski, J. (2009) Reducing Mortality from ischemic heart disease in Poland - Success Therapy Is healthy lifestyle, *Folia Cardiologica Excerpta*, 4, 265-272, (in Polish).

PERFORMANCE EVALUATION OF HYDROVAC GRAVITY POWER GENERATION SYSTEM

R. I. Ansari^{*}, M. H. Sahir^{**}

Abstract: A unique and novel design of hydro power generation system is presented in this paper. Series of experiments were performed to determine whether power can be produced by utilizing the effect of gravitational pull, atmospheric pressure and the force of suction by allowing a certain quantity of water in a specific shaped tank to fall freely under gravity on a turbine runner to establish automatic suction due to partial vacuum created in the storage tank and weight off set. After carrying out a mathematical modeling, a physical model, was constructed to study various hydraulic effect. The actual model consisted of overhead water tank 8.5 meter high, 60000 liters capacity fitted with a Francis type turbine and an alternator. Penstock pipe of 300 mm diameter size was used to take water from overhead tank to the turbine. Two auxiliary pumps were used to prime the overhead water tank. The tank was provided with 20 suction tubes of 63.3 millimeter diameter size. This power plant was designed to generate 28.6 KW of hydro power on the principal of energy transformation utilizing force of gravity, atmospheric pressure and vacuum. Being the new concept the results obtained exhibited that experimental model required certain improvements to make it feasible with maximum efficiency which are discussed under heading of recommendations. The design concept presented in this paper is an original work in this field.

Keywords: Hydrovac, Gravity, Vacuum, Suction tubes, OHTRWTSWT.

1. Introduction

Hydro power is the most long-established renewable energy technology. The first water wheels used in irrigation were developed in the far-east over two-thousand years ago. Persian wheel was the first ever hydraulic machine used for this purpose (Rosita Fitch, 2012). Towards the middle of the 19th Century the first water turbines were developed and later it continued till 21st century saw the world's largest hydro power plant- Three Gorges. Keeping in view the various laws of fluid mechanics and natural phenomena (Khurmi, 1970), it was thought that instead of constructing large reservoirs for hydropower, whether combination of universe-lasting gravitational force, atmospheric pressure and vacuum can be utilized effectively to design such a compact system which could produce hydro power or it can yield saving in energy in pumping devices? Hydrovac gravitational power generation is a new concept, utilizing the combined effect of gravitational force, atmospheric pressure and partial vacuum created in a water storage tank.

Evidence was found for similar work in US when a patent was filed for energy producing through a power plant specifically designed and structured for use in association with a natural reservoir of water such as the sea, ocean, lake, river, etc. (Thompson, 1987). An evidence of similar work was also found on the website <http://www.info@gravitypower.com> accessed on June 2003, which claimed that a study was undertaken in May 1998 on Gravity Power System by National Engineering Lab (NEL) Glasgow Scotland. Siphon type power plants which work on negative pressure are in use in China for last many decades (HRC, 2009).

2. Atmospheric Pressure and Vacuum

Standard atmospheric pressure can lift a column of water in a closed pipe up to height of 10.3 meter (at sea level) if the closed top end of tube is under vacuum (Fig. 1a).

^{*} R. I. Ansari, Faculty of Mechanical Engineering Department, National University of Sciences & Technology, Islamabad Pakistan, ansaripower2000@hotmail.com

^{**} Prof. M. H. Sahir, Department of Mechanical Engineering, UET Taxila, Pakistan

A certain quantity of water when stored in a tank at a head (h) is capable of producing power due to its potential energy. This water will tend to flow down through a nozzle, under the action of gravity and inertia and an instantaneous vacuum will be created at the top of air tight closed tank. This will evolve to establish an automatic suction through a primed suction tube. In this way a considerable amount of energy can be saved in pumping devices and also power can be generated (Fig. 1b).

3. Description

The basic mechanism is illustrated in Fig. 1c. A certain mass (m) of water is stored in an air tight overhead tank. When water will be flowing out of the delivery line (penstock) under gravity, theoretically the vacuum or negative pressure will be created on the top portion of this tank and two different situations can be encountered here:

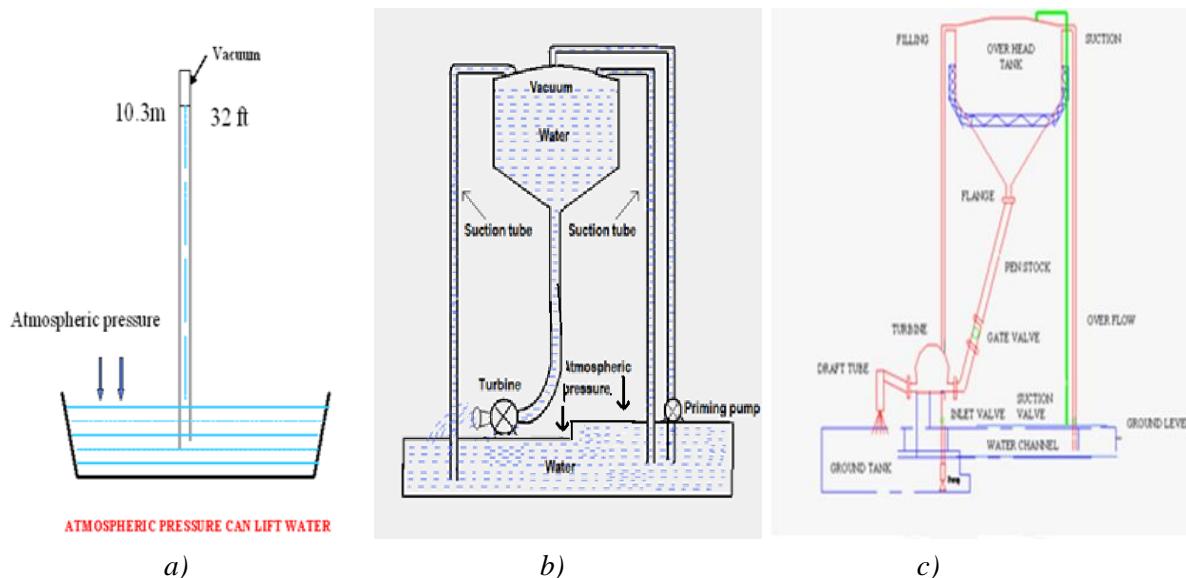


Fig. 1: Hydrovac Gravity Power System uses atmospheric pressure and vacuum to lift water.

Under one situation, the “water will not flow at all”. Once the vacuum on the top portion of tank is created and valves of the suction pipes are closed, “the system may be vacuum locked”, and this flow will not be established till the time air or some other fluid is injected in the tank. This situation can be observed in water bowzers and oil tankers where air has to be injected inside through vent plugs for smooth discharge at outlet.

Under other situation, when main outlet valve of penstock is open, water from gravity tank will flow out through turbine under free or forced flow condition and if the valves of already primed suction pipes are also open, negative pressure or vacuum on the top portion of tank will be created. If intensity of this negative pressure is sufficient enough to suck the water through already primed suction pipes and if the outlet flow pressure of water is greater than the atmospheric pressure, water will start flowing from gravity tank and will be sucked back into gravity tank through suction pipes submerged in water. Pressure of water at outlet can be managed to be greater than the atmospheric pressure if a specially designed gravity tank with minimum surface friction is used (Fig. 2). Intensity of negative pressure will depend upon a few critical values like tank height, tank diameter, type of bends & internal friction of suction tubes, rate of discharge from main tank and nozzle diameter. This way water can be lifted up to a specific height without consuming power or utilizing minimum power as compared to conventional water lifting system.

4. Methods

Two concrete water tanks of capacity 44,000 liters in round shape suction tank (RWT), 1.52 m deep just below the main overhead steel tank (OHT) and 60,000 liters in square shape discharge tank (SWT), 1.15 m deep respectively were constructed on two meter deep reinforced concrete raft foundation (Haruyuki, 2004). An overhead steel tank (OHT) of 60,000 liters capacity was manufactured for storage of water at 8.5 meter height (as it is a lower limit for atmospheric pressure to support a water column in Islamabad,

being 10.3 meter at sea level). Overhead tank was mounted on a hexagonal steel structure bolted on a 2 meter deep concrete raft foundation (Poulos, 2005), (Fig. 2).

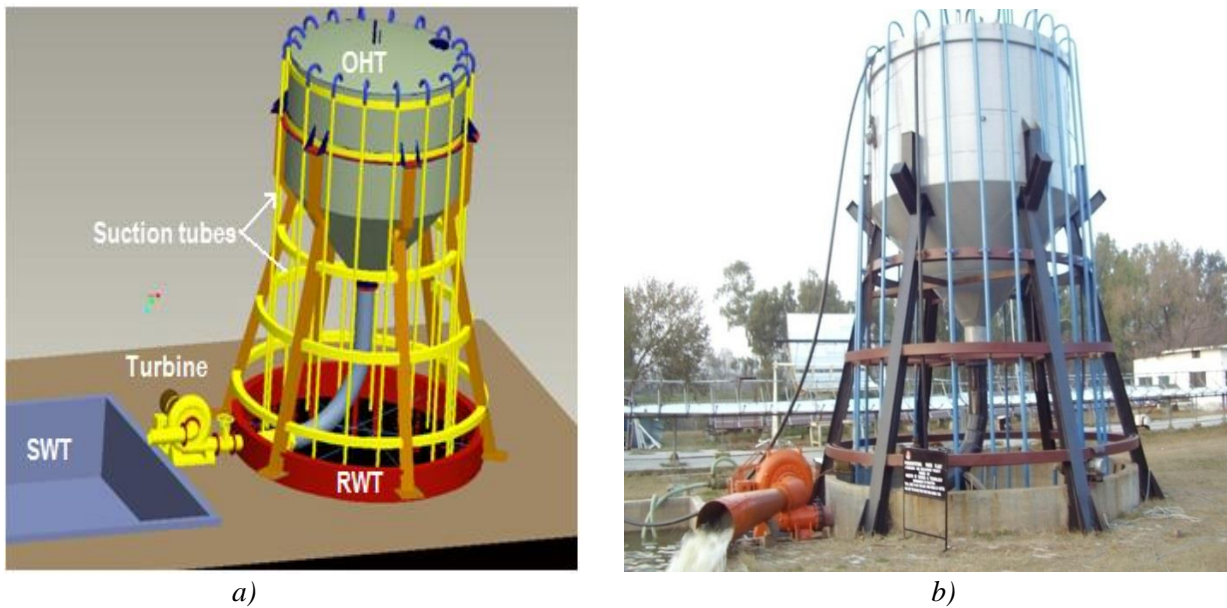


Fig. 2: Computer aided design and testing of working model.

A 300 mm diameter intake Francis type turbine was fitted on a Penstock. The diameter of the runner was 300 mm which was designed to give 50 kW at a head of 40 meters, (Fig. 2b).

4.1. Suction tubes

Twenty x 63.3 mm diameter mild steel suction pipes were fitted over the top cover of main overhead tank. These suction pipes were submerged in the lower round water tank. The purpose of these suction tubes was to suck the water from round shaped ground level reservoir (RWT) under siphon action (shown in Fig. 2).

5. Results and Discussions

Priming of the system: System was primed and a separate open end air vent tube was installed having an open end at height of 1.5 meter above the roof level of main tank which indicated the priming of the system. Total volume of the overhead tank and penstock was 69000 liters. The total time for priming the Overhead tank (OHT) and Round water tank (RWT) with one centrifugal pump of 2 kilowatt power was recorded as 108 minutes.

Measurement of rate of discharge through turbine: Actual discharge from turbine was measured by calculating the actual volume of water coming out from turbine in a unit time (Fig. 3).

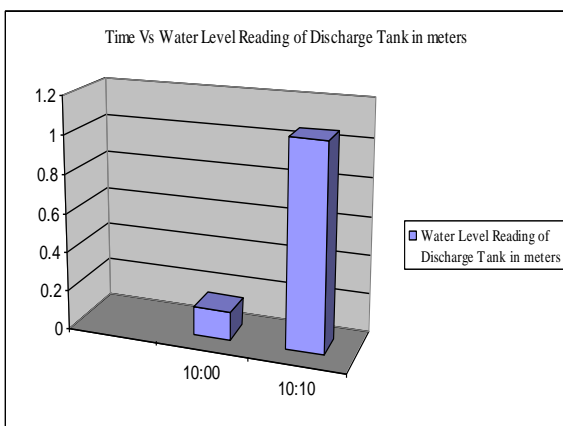


Fig. 3: Time verses water level reading.

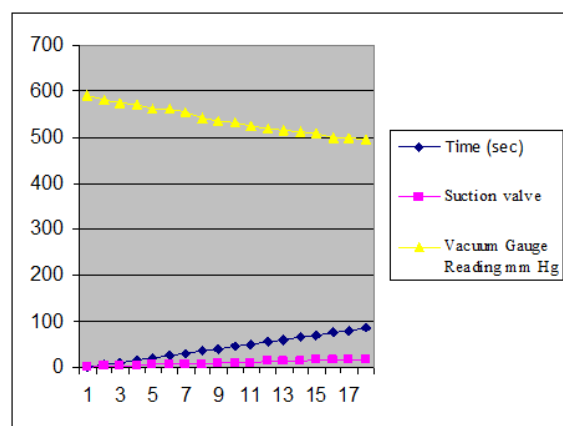


Fig. 4: Vacuum vs Suction valves.

Effect of opening suction valves: System was primed and Turbine valve was opened and system was taken to maximum limit of negative pressure (595 tor), then each suction valve was opened one after the other. Effect of opening 1 to 18 suction valves shown gradual decrease in the reading of negative pressure. Decrease in negative pressure may be due to minor leakage in the system or the phenomena of formation of vapours under intense negative pressure in the main overhead tank. Actual maximum power produced by the system was observed as 7.2 kW with voltage rating of 240 volts AC and current rating of 30 amperes for 45 minutes under controlled flow conditions.

6. Conclusion

Further research is required, which should be integrated with investigations including computational fluid dynamics (CFD) analysis based on friction less material of piping like HDPE, raised water level in base tank and air vent at throat of penstock and evaluation of various types of turbines with different performance characteristics.

7. Recommendations

Following are the recommendations:

- Francis turbine with 225 mm intake diameter may give positive results. It may be the most suitable option for present study.
- HDPE pipe and HDPE valves may be the best option to minimize friction losses.
- Trial with an additional 10 kW size motor may be used as starter to enhance the negative pressure (from 595 mm Hg to 610 mm Hg) in the main tank which can be disengaged after the suction is established.
- A sand filled float may be induced in the round water tank (RWT), which will increase the water level in the base tank and ultimately will increase the pressure at the base of suction tubes.
- Water level at the base tank can be increased by increasing the height of walls of RWT which will result in reduction of suction head.
- The water coming out from the draft tube can be reversed into the RWT if the suction is established.
- Air vent pipe at the throat of penstock will enhance the discharge pressure at turbine which may result in increase of vacuum inside the main tank.

Acknowledgement

Hydrovac Gravity Power system received its early sponsorship from High Precision Engineering a medium size entrepreneur near Islamabad for a proof-of-concept test unit and later sponsored by Ministry of Science and Technology, Government of Pakistan.

References

- The History of the Noria (2013) www.machinerylubrication.com/Read/1294/noria-history.
- Khurmi, R.S. (1987) *Hydraulics, Fluid mechanics and Hydraulic Machines*, pp. 2, 13, 116-123, 153, 270-77.
- United States Patent# 4698516 (1987) <http://www.freepatentsonline.com/4698516.html> admitted by Thompson.
- Gravity Power System <http://www.info@gravitypower.com>.
- Small Hydro Power- A text book specially designed for training workshops in TCDC program, HRC China.
- Haruyuki, Y., Wei, Li (2004) A new raft foundation system with shallow soil improvement, Hiroshima Univ., Higashihiroshima, Hiroshima, Japan.
- Poulos, H. G. (2005) Piled Raft Design Process For A High – Rise Structure, Department of Civil Engineering, University of Sydney, Australia.

AUTOMOTIVE PIEZOELECTRIC SENSORS FOR SIMPLIFIED KNOCK DETERMINATION

A. Aromiński*

Abstract: *A phenomenon of engine knocking is observed when a portion of the air-fuel mixture inside combustion chamber self ignites. Analyzing vibration signal from the flat response piezoelectric sensor located on cylinder block is one of the most popular method that provides sufficient accuracy in knocking determination. Knock sensors used in almost all modern gasoline engines can deliver a signal that is correctly interpreted by an engine control unit (ECU). This is possible due to the research and experience of manufacturers. This paper briefly presents a preliminary concept of using simple, relatively inexpensive automotive piezoelectric knock sensors to determine knock combustion phenomenon in prototype internal combustion engine. Initial "flat response" sensors tests without external amplification devices were conducted. Future research is expected to determine the actual range of using cars sensors for serious measurements.*

Keywords: Knock detection, Piezoelectric sensors, Internal combustion engine.

1. Introduction

Engine knocking is a phenomenon in which a portion of the air-fuel mixture inside combustion chamber self ignites. During that process, significant pressure increases and instabilities can be observed. Due to pressure waves, the cylinder block is likely to vibrate, usually in the 3-10 kHz frequency range (Bernhardt et al., 1988). The characteristic sound known as "knocking" or "pinging" can be observed. Optimal engine efficiency can be obtained near the threshold point of knocking, yet excessive knocking can decrease fuel economy, power output, and even lead to engine failure. It is therefore critical to determine whenever knocking occurs or false signals from various engine mechanical systems were acquired (Kiencke & Nielsen, 2005; Teichmann et al., 2012).

Analyzing the signal from the flat response piezoelectric sensor located on cylinder block seems to be the most popular solution that provides sufficient accuracy. Engine sensitivity to the appearance of knocking varies as a function of engine load and speed (Taylor, 1985). Knock sensors used in almost all gasoline engines can deliver a signal that is correctly interpreted by an engine control unit (ECU). This is possible due to the research and experience of manufacturers. Though a designer building a new prototype engine is at the beginning of a long road, the designer must determine the method of establishing bench measurements to be risk-free for the engine itself. This paper addresses some preliminary concepts of using typical sensors to determine knock phenomenon while not using an engine's ECU. It is not a vibration measuring method; instead, it is a simplified and relatively inexpensive solution to make bench tests safer for a prototype engine without incurring excess expenses.

Almost the same situation appears while testing changes in ignition systems, while testing electronic spark advance circuits, and while developing new fuel mixtures (Orliński, 2013). It is not possible to determine fuel anti-knock features while using original closed-loop ignition system of type found in production cars.

2. Components Description

At the beginning of test, two different models of "flat response" piezoelectric sensors from one manufacturer (NTK) were obtained. There was a significant time interval (more than 6 years) between

* Andrzej Aromiński, MSc.: IPBM Warsaw University of Technology, Narbutta 84, 02-524 Warsaw, Poland,
andrzej.arominski@simr.pw.edu.pl

production dates of the sensors. Both sensors were mounted on a steel plate and appropriate tightening torque was applied.

A precise data acquisition system with a sampling rate of 100 kS/s per channel and hi-input impedance greater than 10 M Ω was implemented. A professional actuator for further detailed testing of frequency response was selected.

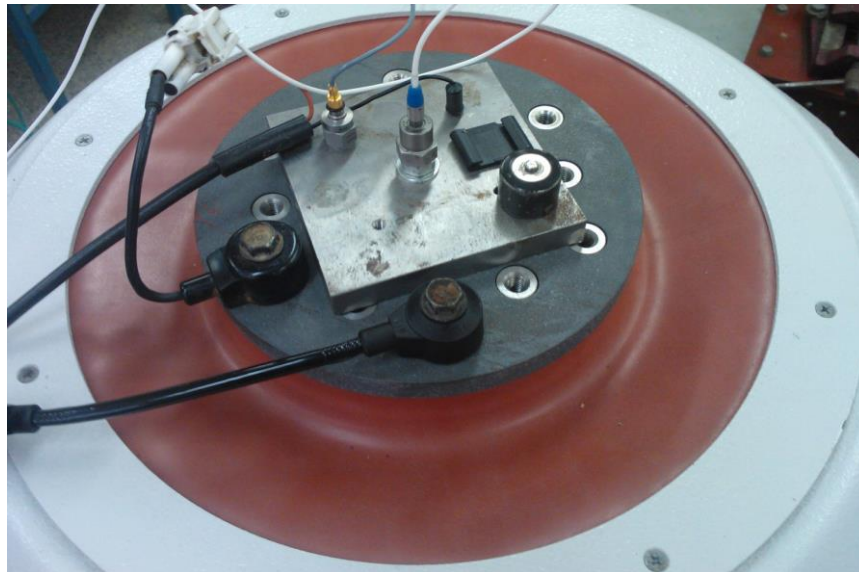


Fig. 1: Piezoelectric sensors mounted on actuator.

3. Measurements

Initial tests were conducted without any external amplifiers. Only excessive voltage protection was applied to the data acquisition system. As stated above, production date and sensor models were different but initial testing revealed that the piezoelectric element utilized in both was likely to be the same. Minor differences could be related to the unequal sensor distance from excitation force source, manufacturing tolerance, etc.

Fig. 2 represents voltage versus time response to impulse excitation; no signal conditioning algorithms were applied. Amplitudes up to 3 V were observed.

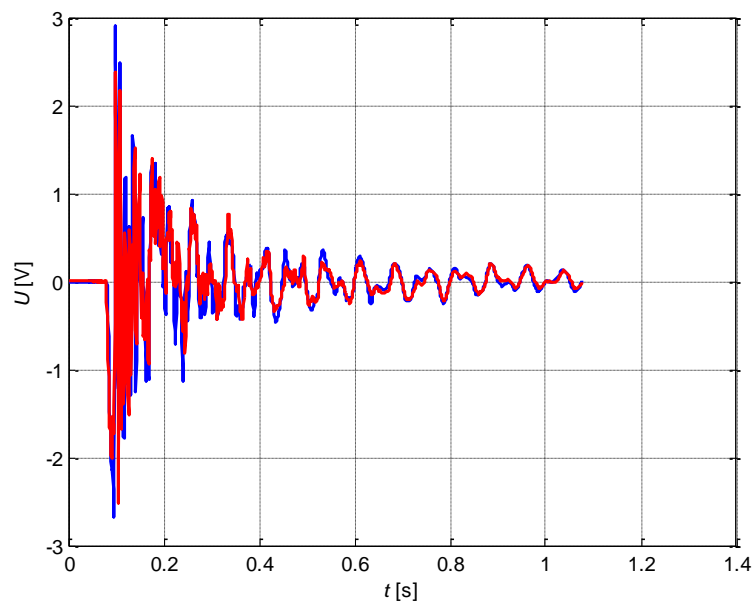


Fig. 2: Voltage over time diagram. Impulse response, no amplification.

A Fast Fourier Transform algorithm was used to determine voltage amplitude at desired frequency range.

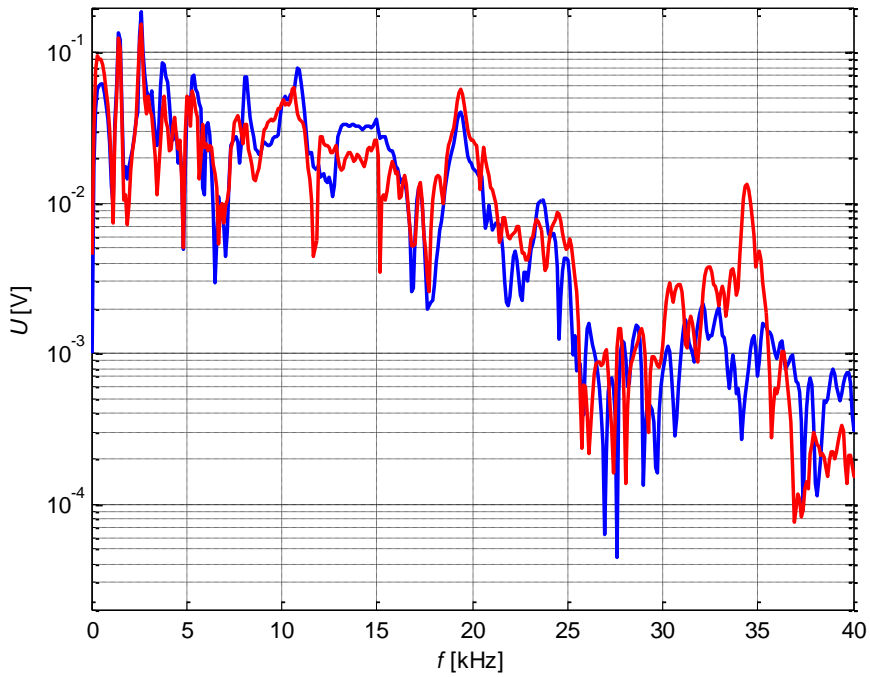


Fig. 3: FFT, semilogarytmic scale, frequency range 0-40 kHz.

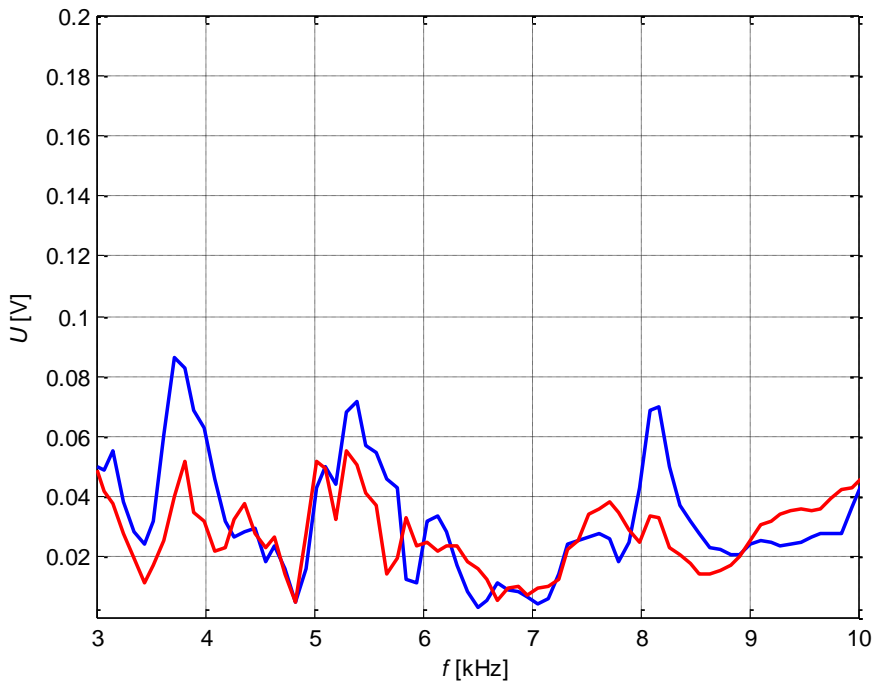


Fig. 4: FFT, linear scale, frequency range 3-10 kHz.

4. Conclusions

Conducted tests have shown that from the point of view of the knock phenomenon, voltage signal amplitude in a function of frequency is relatively small.

In the case of laboratory measurements, such a situation is acceptable. However, in the case of measurements conducted with a real engine, signal noise associated with the proximity of the ignition

system components can significantly exceed the amplitude of the input signal. Moreover, the resolution of 10-bit combined with +/- 5V range of A/D converters commonly used in the aftermarket automotive industry is insufficient for accurate analysis of a unamplified vibration signal.

Several other measurement methods based on operational amplifiers in various configurations (non-inverting voltage amplifier, charge amplifier) were examined as a preface to investigating further phenomenon. Utilizing automotive sensors that are used in cars is an inexpensive and comfortable solution; however, utilizing such sensors as scientific measurement tools can at best lead to misunderstandings.

Future research is expected to determine the actual range of using cars sensors for serious measurements.

References

- Bernhardt, M., Dobrzyński, S., Loth, E. (1988) Automotive engines. WkiŁ, Warsaw (in Polish).
- Kiencke, U., Nielsen, L. (2005) Automotive Control Systems, Springer.
- Orliński, P. (2013) Selected aspects of combustion process of biodiesel fuels. Wyd. Instytut Naukowo-Wydawniczy "SPATIUM", Radom (in Polish).
- Teichmann, R., Wimmer, A., Schwarz, C., Winklhofer, E. (2012) Combustion Engines Development pp. 39-117, Springer.
- Taylor, C. (1985) Internal Combustion Engine in Theory and Practice: Vol. 2 - 2nd Edition, The MIT Press.

PLASTIC HEAT EXCHANGER USING TWISTED HOLLOW FIBERS

I. Astrouski*, M. Raudensky*

Abstract: *Metallic heat exchangers have a number of well-known disadvantages, such as heavy weight and cost and low resistance to corrosion. Polymeric hollow fiber heat exchangers were proposed about a decade ago as an alternative for low temperature applications. A large-scale heat exchanger was prepared using hollow fibers with a special, “curly” shape. The heat exchanger’s thermal performance was studied using hot (40-90°C) ethyleneglycol-water brine flowing inside of the fibers and cool air (20-30°C) flowing across the fibers. Experiments showed that the heat exchanger can achieve a significant heat transfer rate and have high values of overall heat-transfer coefficients (60-230 Wm⁻²K⁻¹). Moreover, obtained results showed that the classical theory is not suitable to estimate outer convection and that special approach should be used.*

Keywords: Hollow fiber, Plastic heat exchanger, Overall heat transfer coefficient.

1. Introduction

Polymers have many advantages, such as having smooth surface, resistance to corrosion and low weight. They are non-toxic; easy to shape, form and machine; and can be blended with different fillers to obtain additional properties (Han & Chung, 2011). According to Malik & Bullard (2005), most commercially available polymer heat exchangers are used in corrosive environments or in low temperature applications. Many different fields of plastic heat exchanger applications (desalination, heat recovery, cooling and cryogenics, humidification, solar energy, microelectronics and the computer industry) were noted by Zaheed & Jachuck (2004). Using thin-wall polymeric hollow fibers as heat exchanger tubes was first proposed by Zarkadas & Sirkar (2004). Heat transfer of PHFHEs for desalination applications was studied (Song et. al., 2010). It was shown that such devices have overall heat transfer coefficients up to 2100 W m⁻²K⁻¹ and compactness (conductance per volume) up to 3.5·10⁶ W m⁻³K⁻¹.

Air heat transfer coefficients (HTC) are low and fins are usually used to increase the air-side heat transfer area in metal heat exchangers. However, polymer thermal conductivity is low so such polymer fins are ineffective and the primary heat transfer area of should be large enough. Hollow fibers are tubes of small diameter which can be closely packed within a small volume. According to Song, the packing density (heat transfer area to volume ratio) of hollow fibers can be as much as 3060 m²/m³. However, this means that many fibers need to be connected, uniformly distributed and supplied with fluid. Poor fiber distribution causes a so-called bypassing of liquid and decreases heat transfer. Using twisted fiber bundles is a simple method for distributing the fibers and preparing large-scale hollow fiber heat exchangers.

2. Theory

According to Zarkadas & Sirkar (2004), heat transfer inside a hollow fiber can be considered a conventional convection problem. It should be noted that only laminar-flow solutions are considered because PHFHEs normal operation are going in a laminar regime. Zarkadas & Sirkar (2005) proposed a relationship to calculate the mean Nusselt number of a thermal developing region based on limiting inside Nusselt number and incremental heat transfer number:

$$Nu_{T3} = \frac{\left(\frac{49}{11}\right) + Nu_w}{1 + \left(\frac{59}{220}\right) Nu_w} + \left\{ 0.0499 - \frac{0.06487}{[1 + \exp(0.45895 \cdot Nu_w + 2.46887)]} \cdot (4Gz/\pi) \right\} \quad (1)$$

* Ing. Ilya Astrouski, prof. Ing. Miroslav Raudensky, CSc.: Brno University of Technology, Faculty of Mechanical Engineering, Heat Transfer and Fluid Flow Laboratory, Technická 2896/2; 616 69, Brno; CZ, astrouski@lptap.fme.vutbr.cz

The geometrical configuration of twisted fiber bundles is difficult to describe because it is chaotic. Nonetheless, two approaches can be tested to estimate outer heat transfer. The Churchill & Bernstein (1977) relation can be used to calculate a Nusselt number across separate cylinders for a wide range of Reynolds and Peclet numbers ($10^2 < Re < 10^7$, $Pe > 0.2$):

$$Nu_d = 0.3 + \frac{0.62Re^{1/2}Pr^{1/3}}{[1+(0.4/Pr)^{2/3}]^{1/4}} \left[1 + \left(\frac{Re}{282,000} \right)^{5/8} \right]^{4/5} \quad (2)$$

The heat-transfer characteristics of an in-line bank of tubes can be estimated as proposed by Grimson (1937):

$$Nu = C \cdot Re^m \cdot Pr^{1/3} \quad (3)$$

The values of the constant C and the exponent m depend on the geometric parameters used to describe the tube-bundle arrangement ($C = 0.317$ and $m = 0.608$ values were used). Reynolds numbers were calculated based on the mean velocity occurring in the frontal cross section.

3. Experimental Study

Fig. 1 shows a hollow fiber bundle (a) and heat exchanger consisting of 4 bundles (b). Its parameters are as follows: the fiber amount is 1880 mm, length is 650 mm, outer/inside diameter is 0.7/0.6 mm, overall heat transfer area based on outer fiber surface is 2.7 m^2 and the frontal air flow area is 0.087 m^2 . Thermal performance tests were performed in a certified calorimeter room designed for testing automotive radiators. 50% by volume aqueous ethylene glycol (EG) solution was used as a hot medium circulated inside of the PHFHE and air was used as the cooling media. The inlet and exit temperatures and volume flow rates of the two streams were measured with calibrated equipment and observed in real time (frequency of 1 Hz). Temperatures of air were measured with sets of PT 100 temperature sensors placed in a regular pattern upstream (8 sensors) and downstream (19 sensors) of the heat exchanger. This gave the adequate approximation of air temperature fields to estimate mean temperatures. The inlet temperature of EG was 60°C and air inlet temperature was 20°C in 12 tests and 90°C and 30°C in other 9 tests.

Data reduction was performed as proposed by Zarkadas & Sirkar (2004). The effective mean temperature difference averaged over the total heat exchange area was determined by using the logarithmic mean temperature difference (LMTD) and appropriate LMTD correction factor F . The correction factor was calculated as suggested by Jeter (2006). Air-flow was considered as completely mixed and the flow inside the tubes was considered as completely unmixed. Additionally, we used the iterative procedure proposed by Zarkadas & Sirkar (2004) to determine simultaneously both the tube- and air-side heat-transfer coefficients based on our experimental data. In all calculations, liquids properties were evaluated at the average temperature between the inlet and outlet. The wall thermal conductivity needed for the calculations was taken to be equal to $0.18 \text{ W m}^{-1}\text{K}^{-1}$ for isotactic polypropylene (Mark, 1999).

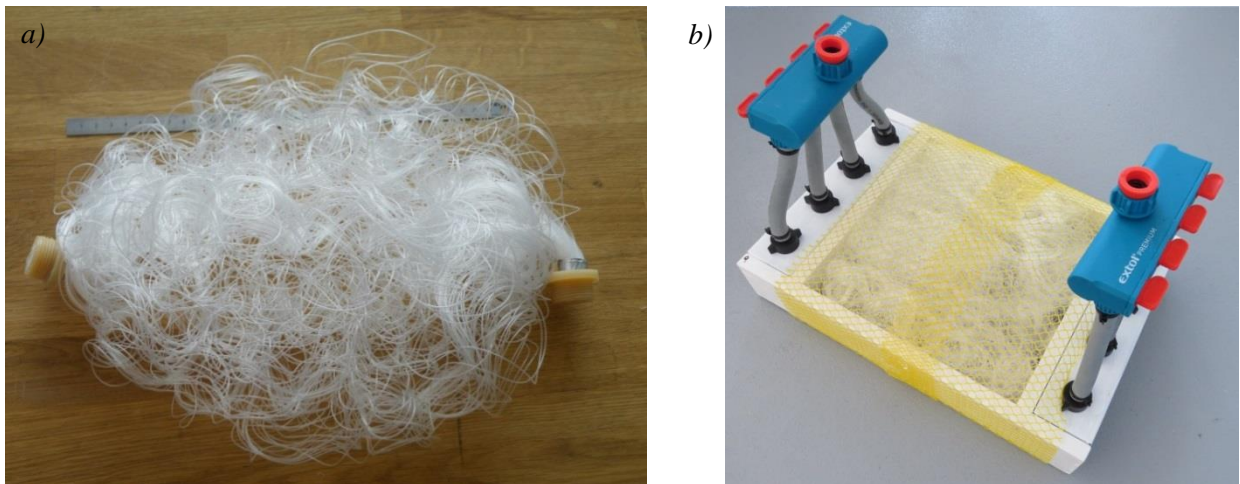


Fig. 1: a) Hollow fiber heat exchange bundle; b) Heat exchanger based on 4 bundles.

4. Results and Discussion

Tab. 1 gives the range of results obtained for the 21 heat-transfer tests performed with PHFHEs. It presents the tube- and air-side Reynolds numbers, the heat-transfer rates, the overall HTC based on the outside fiber area, the heat exchanger effectiveness, and the number of transfer units (NTU). Tab. 2 shows that the heat-transfer rate of this device can reach high values of up to 21.6 kW (the device is about 30x30x10 cm in size and several hundred grams in weight). Obtained overall HTCs (up to 230 W m⁻² K⁻¹) are reasonably high compared to finned-tube metal heat exchangers. In the literature (Holman, 2010), design values of 25-55 W m⁻² K⁻¹ are quoted for liquid-gas applications of finned-tube heat exchangers. These values include a total dirt factor which needs to be incorporated in the coefficients quoted in Tab. 1. However, the incorporation of the same fouling factor for polymer surfaces is questionable because limited experimental data about polymeric hollow fiber fouling is available. However, based on extremely high values of overall HTC it can be stated that PHFHEs have high thermal performance. Values of the thermal effectiveness and the NTU are high enough, up to 0.9 and 2.54, respectively. However, some experimental runs showed low NTU and effectiveness because the thermal effectiveness and NTU are functions of the relative heat capacity rates of both streams, overall HTC and heat transfer area. It can be concluded that the accomplishment of high NTUs and efficiency is primarily a problem of proper rating.

Tab. 2 shows the range of tube- and air-side coefficients and the percent contribution of each resistance to the total resistance. It is evident that the tube-side coefficients are very high and air-side coefficients are significantly lower. The results shown reveal that tube-side resistance would be the smallest of the three and that little improvement in the overall heat-transfer performance should be anticipated by increasing the tube-side Re number. The contribution of wall thermal resistance is also low despite the low thermal conductivity of polypropylene. These results agree with the calculated data from Astrouski and Raudensky (2012).

Results of 12 experimental runs (60 °C inlet temperature of EG) were used to create a plot of overall HTC versus tube- and air Reynolds numbers (see Fig. 2a). It was shown that HTC have small dependence on tube Reynolds numbers, which is in agreement with Equation 1. The same tendency was found for 9 tests with 90°C inlet temperature of EG. Therefore, PHFHEs can be operated with low tube-side velocities in order to achieve a combination of high thermal performance and low pressure drop provided by low inside velocity. On the other hand, HTC has a strong dependency on the air Reynolds number (see Fig. 2a) because air-side thermal resistance is dominant.

At this point, our experimental results will be examined against the theory presented earlier in the paper. Fig. 2b shows a graph of outer (air-side) HTC versus air Reynolds number. A high discrepancy exists between the experimental data and the theoretical prediction by both the Churchill & Bernstein (1977) and Grimson (1937) models. Both of these models overestimate heat HTC twice or more. This can be explained by the following facts: fiber orientation significantly differs from strict geometrical cross-flow (fibers are twisted and directed in various directions), some fibers are in touch between each other (this decreases effective heat transfer area), and fiber distribution is not uniform enough, so bypassing effects are significant. It can be concluded that a special approach should be developed to define fiber distribution and orientation and predict HTC based on these data.

Tab. 1: Thermal performance of heat exchanger from twisted hollow fibers.

number of runs	Re _t	Re _{air}	Q (kW)	U _o (W m ⁻² K ⁻¹)	ε	NTU
21	33-407	43-692	2.97-21.6	58-230	0.35-0.90	0.50-2.54

Tab. 2: Tube- and Air-Side Heat-Transfer Coefficients.

h _t (W m ⁻² K ⁻¹)	h _o (W m ⁻² K ⁻¹)	R _t /R _{ov} (%)	R _w /R _{ov} (%)	R _o /R _{ov} (%)
2983-3077	58-230	2-7	2-10	84-96

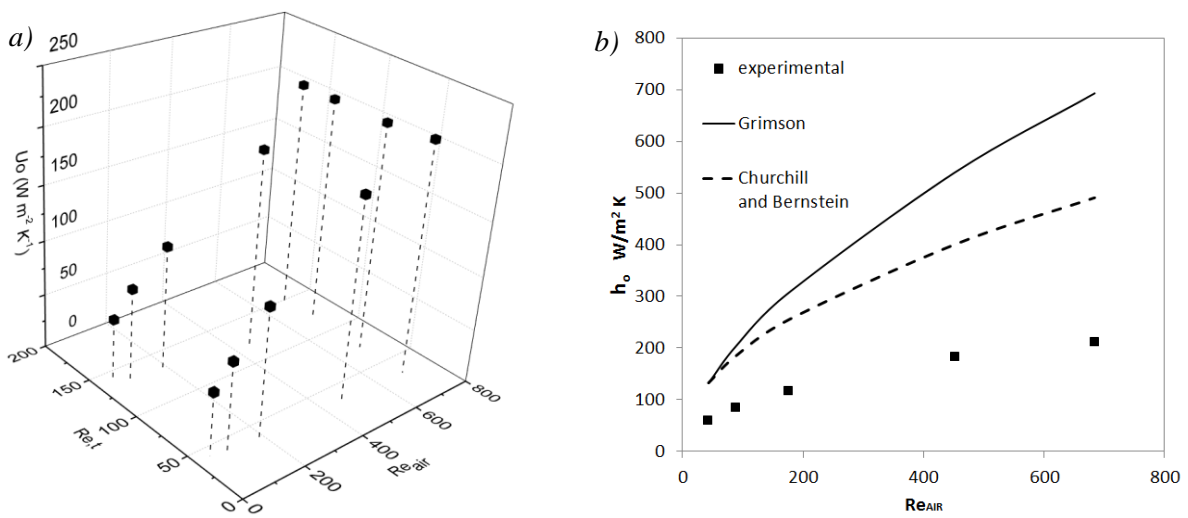


Fig. 2: a) Overall HTC vs tube- and air Reynolds numbers; b) Outer HTC vs air Reynolds number.

5. Conclusions

It was proven that the use of twisted hollow fibers to create large-scale gas-to-liquid heat exchangers can be successful. Experimental data showed that such device can achieve substantial values of heat transfer up to 21.6 kW) and have high values of overall HTC (up to $230 Wm^{-2}K^{-1}$). It was shown that air-side thermal resistance is dominant in all cases and defines heat transfer. On the other hand, it was shown that heat transfer across fiber bundles strongly depends on effects which are not described enough by existing theory. This issue requires further study which will include both: introduction of parameters describing fiber bundle geometry and experimentation establishing dependence of heat transfer on these parameters.

Acknowledgement

The present work has been supported by the European Regional Development Fund within the framework of the research project NETME Centre, CZ. 1.05/2.1.00/01.0002, under the Operational Programme Research and Development for Innovation.

References

- Astrouski, I., Raudensky, M. (2012) The study of polymeric hollow fiber heat exchangers, Proc. of the 18th Inter. Conf. Engineering mechanics, Svratka, pp. 47-57
- Churchill, S. W., & Bernstein, M. (1977) A Correlating Equation for Forced Convection from Gases and Liquids to a Circular Cylinder in Crossflow, J. Heat Transfer, vol. 99, pp. 300-306.
- Grimson, E. D. (1937) Correlation and Utilization of New Data on Flow Resistance and Heat Transfer for Cross Flow of Gases over Tube Banks," Trans. ASME, vol. 59, pp. 583-94.
- Han, S. & Chung, D.D.L. (2011) Increasing the through-thickness thermal conductivity of carbon fiber polymer-matrix composite by curing pressure increase and filler incorporation. Comp. Sci. and Tech., pp. 1944-1952.
- Holman, J. P. (2010) Heat Transfer, McGraw-Hill Book Company.
- Jeter, S. M. (2006) Effectiveness and LMTD Correction Factor of the Cross Flow Exchanger: a Simplified and Unified Treatment, ASEE Southeast Section Conference.
- Malik, T. & Bullard, C. W. (2005) Suitability of Polymer Heat Exchangers for Air Conditioning Applications, Air Conditioning and Refrigeration Center, University of Illinois.
- Mark, J. E. (1999) Polymer Data Handbook; Oxford University Press: New York.
- Song, L., Li, B., Zarkadas, D., Christian, S., Sirkar, K. K. (2010) Polymeric Hollow-Fiber Heat Exchangers for Thermal Desalination Processes. Ind. Eng. Chem. Res., 49 (23), pp. 11961-11977.
- Zaheed, L. & Jachuck, R. J. J. (2004) Review of polymer compact heat exchangers, with special emphasis on a polymer film unit. Appl. Therm. Eng. 24, pp. 2323-2358.
- Zarkadas, D. M.; Sirkar, K. K. (2004) Polymeric hollow fiber heat exchangers: An alternative for lower temperature applications. Ind. Eng. Chem. Res., 43, 8093-8106.
- Zarkadas, D. M.; Sirkar, K. K. (2005) Incremental heat transfer number for laminar flow in circular tubes with the boundary condition of the third kind and simple design formula for shell and tube laminar flow heat exchangers with constant external resistance. Int. J. Transp. Phenom., 7 (4), 297-306.

INTERACTION BETWEEN BENDING MOMENT AND SHEAR FORCE IN STEEL PLATED STRUCTURAL ELEMENTS

I. Baláž*, Y. Koleková**

Abstract: *Resistance of steel plated structural elements under interaction between bending moment and shear force according to EN 1993 compared with former national Slovak standard STN 73 1401: 1998 (Czech standard ČSN 73 1401: 1998). Parametrical study. Comparison of different interaction formulae.*

Keywords: Resistance, Local buckling, Interaction, Bending moment, Shear force, Steel structure.

1. Introduction

Design requirements of stiffened and un-stiffened steel plates which are subject to in-plane forces are given in Eurocode EN 1993-1-5 and EN 1993-1-1. Interaction between the bending moment and the shear force are treated:

a) in EN 1993-1-1, clause 6.2.8, related to the resistance of the cross-section. Where the shear force is present allowance should be made for its effect on the moment resistance. Where the shear force is less than half the plastic shear resistance its effect on the moment resistance may be neglected except where shear buckling reduces the section resistance, see EN 1993-1-5. Otherwise the reduced moment resistance should be taken as the design resistance of the cross-section, calculated using a reduced yield strength

$$(1 - \rho)f_y \quad (1)$$

for the shear area A_v , where the reduction factor reads

$$\rho = \left(\frac{2V_{Ed}}{V_{pl,Rd}} - 1 \right)^2, \quad V_{pl,Rd} = \frac{A_v(f_y / \sqrt{3})}{\gamma_{M0}} \quad (2a, b)$$

For welded I or H sections A_v may be taken as follows $A_v = A_w = h_w t_w$ (area of the cross-section web).

f_y is yield strength,

γ_{M0} partial factor for resistance of cross-sections whatever the class is,

V_{Ed} design shear force,

$V_{pl,Rd}$ plastic design shear resistance.

b) in EN 1993-1-1, clause 6.2.10, related to interaction between bending moment, shear and axial force. Influence of the axial force is not taken into account in this paper.

Where the shear and the axial forces are present, allowance should be made for the effect of both shear force and the axial force on the resistance of the moment. Provided that the design value of the shear force V_{Ed} does not exceed 50% of the shear resistance $V_{pl,Rd}$ no reduction of the resistances defined for the bending moment and the axial force in 6.2.9 is needed, except where the shear buckling reduces the section resistance, see clause 7.1 in EN 1993-1-5. Where V_{Ed} exceeds 50% of $V_{pl,Rd}$ the design

* Prof. Ing. Ivan Baláž, PhD.: Department of Metal and Timber Structures, Faculty of Civil Engineering, Slovak University of Technology, Radlinského 11; 813 68, Bratislava; Slovakia, ivan.balaz@stuba.sk

** Assoc. Prof. Ing. Yvona Koleková, PhD.: Department of Structural Mechanics, Faculty of Civil Engineering, Slovak University of Technology, Radlinského 11; 813 68, Bratislava; Slovakia, yvona.kolekova@stuba.sk

resistance of the cross-section to combinations of the bending moment and the axial force should be reduced using a reduced yield strength according to formula (1) for the shear area A_v , where the reduction factor is defined by formula (2a).

NOTE: Instead of reducing the yield strength f_{yw} also the plate thickness t_w of the relevant part of the cross section may be reduced.

c) in EN 1993-1-5, clause 7.1, related to plated structural components subject to in-plane loads.

Provided that $V_{Ed} / V_{b,Rd}$ does not exceed 0.5, the design resistance to bending moment and axial force need not be reduced to allow for the shear force. If $V_{Ed}/V_{b,Rd}$ is more than 0.5 the combined effects of bending and shear in the web of an I or box girder should satisfy:

$$\frac{M_{Ed}}{M_{pl,Rd}} + \left(1 - \frac{M_{f,Rd}}{M_{pl,Rd}}\right) \left(2 \frac{V_{Ed}}{V_{bw,Rd}} - 1\right)^2 \leq 1,0 \quad \text{for } \frac{M_{Ed}}{M_{pl,Rd}} \geq \frac{M_{f,Rd}}{M_{pl,Rd}} \quad (3)$$

where:

$M_{f,Rd}$ is the design plastic moment of resistance of the section consisting of the effective area of the flanges;

$M_{pl,Rd}$ the design plastic resistance of the cross section consisting of the effective area of the flanges and the fully effective web irrespective of its section class.

In addition the following requirements should be met

$$\frac{M_{Ed}}{f_y W_{eff}} \leq 1,0, \quad \frac{V_{Ed}}{V_{b,Rd}} \leq 1,0 \quad (4a, b)$$

$$\gamma_{M0}$$

where

$$V_{b,Rd} = V_{bw,Rd} + V_{bf,Rd} \leq \frac{\eta f_{yw} h_w t}{\sqrt{3} \gamma_{M1}} \quad (5)$$

Contributions of the web and flanges to the total buckling shear resistance are as follows

$$V_{bw,Rd} = \frac{\chi_w f_{yw} h_w t}{\sqrt{3} \gamma_{M1}}, \quad V_{bf,Rd} = \frac{b_f t_f^2 f_{yf}}{c \gamma_{M1}} \left[1 - \left(\frac{M_{Ed}}{M_{f,Rd}}\right)^2\right] \quad (6a, b)$$

Contribution of the flanges is usually negligible. All relevant quantities used in above formulae are defined in Eurocodes EN 1993-1-5 and EN 1993-1-1.

2. Parametrical Study and Comparison of Various Procedures

Graphical interpretation of Eurocode resistance formulae compared with former national STN 731401: 1998 (ČSN 731401: 1998) ones is shown in Fig. 1. Relative resistances valid for the web of the welded I-section calculated in the following numerical example for European and national standard are indicated in the diagram by symbols and their “coordinates”.

Formula (3) may be rewritten in the following form

$$\frac{V_{Ed}}{V_{bw,Rd}} = \frac{1}{2} \left[\sqrt{\frac{1 - \frac{M_{Ed}}{M_{pl,Rd}}}{1 - \frac{M_{f,Rd}}{M_{pl,Rd}}} + 1} \right] \quad (7)$$

Numerical example.

Graph in Fig. 1 is valid for:

material: $E = 210\text{GPa}$, $\nu = 0.3$, $f_y = 355\text{MPa}$, $\gamma_{M0} = 1.0$, $\gamma_{M1} = 1.0$,

welded I-section (class 4):

$h = 1550\text{mm}$, flange (class 1): $b = 300\text{mm}$, $t_f = 25\text{mm}$, web (class 4): $h_w = 1500\text{mm}$, $t_w = 10\text{mm}$, fill et weld: $a_w = 5\text{mm}$.

Ratio of bending moment resistances of the flanges and the gross I-section $M_{f,Rd} / M_{pl,Rd} = 0.67$.

For simply supported girder loaded in the midspan by the transverse force F_{Ed} , with a transverse stiffener under F_{Ed} , we obtain for girder geometry $L = 5h_w$ the following values of the resistances F_{Rd} :

a) according to EN 1993-1-5: $F_{Rd,EN} = 2955\text{ kN}$ from formula (3 or 8),

$M_{Ed,EN} / M_{pl,Rd} = 0.732$, $V_{Ed,EN} / V_{bw,Rd,EN} = 0.953$, relate to formula (8),

$M_{eff,Rd,EN} / M_{pl,Rd} = 0.799$, relates to formula (4a).

From formulae (4a) and (4b) we obtain $F_{Rd,EN} = 3227.8\text{ kN}$ and $F_{Rd,EN} = 3101.8\text{ kN}$, respectively.

b) according to STN 73 1401: $F_{Rd,STN} = 2765\text{ kN}$,

$M_{Ed,STN} / M_{pl,Rd} = 0.685$, $V_{Ed,STN} / V_{bw,Rd,EN} = 0.891$,

$M_{eff,Rd,STN} / M_{pl,Rd} = 0.812$, $V_{ba,Rd,STN} / V_{bw,Rd,EN} = 0.913$,

relate to formulae given in STN 73 1401 (not given in this paper).

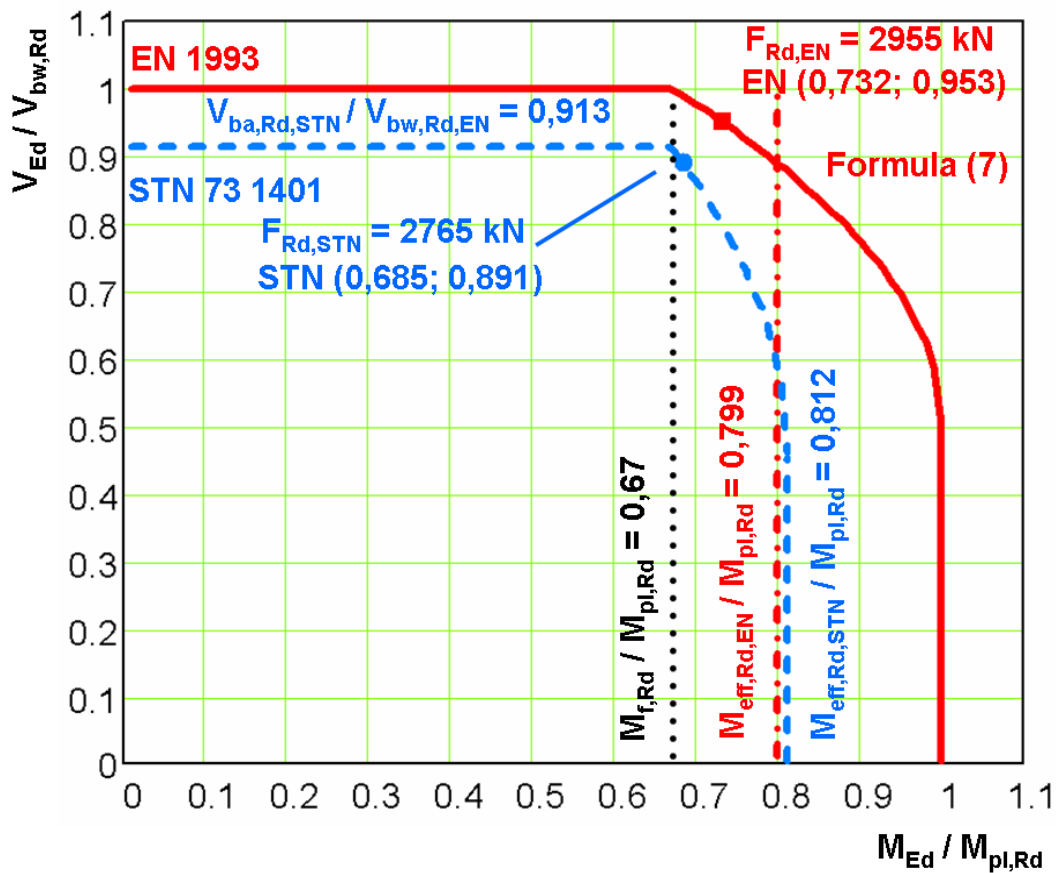


Fig. 1: Comparison of relative resistances calculated according to EN 1993-1-5 and STN 73 1401. Values of relative resistances of the web of the welded steel I-section (300 mm x 25 mm + 1500 mm x 10 mm + 300 mm x 25 mm, S355) loaded by combination of bending moment M_{Ed} and shear force V_{Ed} are indicated by “coordinates” of symbols \bullet and \blacksquare . Influence of M_{Ed} and V_{Ed} is characterised by the relationships $M_{Ed} = F_{Ed} L / 4$, $V_{Ed} = F_{Ed} / 2$, $L = 5 h_w$, $M_{Ed} / V_{Ed} = 2,5 h_w = 3.75\text{ m}$.

3. Conclusion

Local buckling of metal structural elements is important topic in agenda of working groups preparing new generation of Eurocodes, which will be available in 2019. Problems of web girder resistance to transverse forces were outlined in Baláž, Koleková (2013a, b) and Koleková & Baláž (2013a, b).

In this paper problems of steel plated structural elements under combination of the bending moment and the shear force are analysed. Twin paper (Koleková & Baláž, 2014) is focused on the same problem but for aluminium structures. Comparison of results of these two papers enable to improve both Eurocodes EN 1993 for steel and EN 1999 for aluminium structures and to prepare their harmonization.

Differences between EN and STN procedures:

- a) difference in the shear resistance definition;
- b) STN interaction formula is valid only for class 4 cross-sections. STN interaction formulae for classes 1, 2 and 3 cross-sections have different form. See clause 6.6.7 and Annex D in STN 73 1401;
- c) EN interaction formula is simpler;
- d) EN 1993 gives greater resistances comparing with STN 731401: 1998 (ČSN 731401: 1998).

Generally the following is valid:

- a) for the greater web slendernesses and for the steels with greater strengths the shear resistance is decisive. For such cases EN resistance may be greater up to 17 %;
- b) for opposite cases the bending moment resistance is decisive and difference in the resistances calculated according to EN and STN is negligible.

In above numerical example, which is part of the large parametrical study, the web slenderness is 150, steel grade S355 and the ratio of resistances $F_{Rd,EN} / F_{Rd,STN} = 2955 \text{ kN} / 2765 \text{ kN} = 1.069$. The difference in resistances is 6.9 %.

Acknowledgement

Project No. 1/0748/13 was supported by the Slovak Grant Agency VEGA.

References

- Baláž, I., Koleková, Y. (2013a) Elastic critical buckling stress of the web girder subjected to transverse force. In: Proc. of abstracts 19th International Conf. Engineering Mechanics, Svratka, Czech Republic, paper No. 126, pp. 17-18.
- Baláž, I., Koleková, Y. (2013b) Elastic critical buckling stress of the web girder subjected to transverse force. In: CD Proc. 19th International Conf. Engineering Mechanics, Svratka, Czech Republic, paper No. 126, pp. 11-16.
- Koleková, Y., Baláž, I. (2013a) Web girder resistance to transverse forces. In: Proc. of abstracts of 19th International Conf. Engineering Mechanics, Svratka, Czech Republic, paper No. 127, pp. 81-82.
- Koleková, Y., Baláž, I. (2013b) Web girder resistance to transverse forces. In: CD Proc. 19th International Conf. Engineering Mechanics, Svratka, Czech Republic, paper No. 127, pp. 290-299.
- Koleková, Y., Baláž, I. (2014) Interaction between bending moment and shear force in aluminium plated structural elements. In: Proc. 20th Int. Conf. Engineering Mechanics, Svratka, Czech Republic, pp. 304-307.
- EN 1993-1-1 (2005) and Corrigendum AC (2009) Eurocode 3 - Design of steel structures. Part 1-1: General rules and rules for buildings.
- EN 1993-1-5 (2006) and Corrigendum AC (2009) Eurocode 3 - Design of steel structures. Part 1-5: Plated structural elements.
- EN 1999-1-1 (2007) and Amendment A1 (2009) and Amendment A2 (2013) Eurocode 9 - Design of aluminium structures. Part 1-1: General structural rules.
- STN 73 1401 (1998) Designing steel structures, (in Czech).
- ČSN 73 1401 (1988) Design of Steel Structures, (in Czech).

STONE FOR RESTORATION AND DECORATION PURPOSES IN WESTERN SLOVAKIA

M. Bednarik^{*}, R. Holzer^{**}, M. Laho^{***}, M. Dunčko^{****}

Abstract: *The contribution is focused on assessing of important physical and mechanical properties of rocks quarried in Brezovské Karpaty Mts. with the aim of their utilization as decorative and prospective building stone for restorations. Carbonate sandstones and conglomerates of Upper Cretaceous and carbonate sandstone of Neogene sedimentary strata in Chtelnica - Trianova and Chtelnica - Malé Skalky were taken into consideration. Those quarries appeared to be suitable for excavation of an appropriate material for statuary and monumental purposes and for restoration work, as well. Samples for assessment of rock properties were taken from abandoned and quarry in operation. Tested specimens for laboratory tests in a form of cubes and cylinders were prepared from monoliths and drilled cores taken from the depth up to 1 m. For determination of rock quality following tests were taken as most relevant: densities, porosity, water absorption and strength properties estimated according to valid technical standards. Based on physical and mechanical properties of rocks assessed on a number of tested samples from two mining sites in Slovakia and one comparable site in Austria, quality assurance of the rock utilization as a decoration/restoration material is presented.*

Keywords: Decoration and restoration stone, Physical and mechanical properties of rock, Chtelnica-Trianova, Chtelnica-Malé Skalky.

1. Introduction

Scarcity of stone for restoration works in Slovakia is due to the intense tectonic history of Slovak Carpathians generally known. Therefore the aim of the investigation was to look for sound stone for decoration and restoration purposes, regarding its properties, durability and appearance. It was the author's effort to verify in the Western part of Slovakia (vicinity of Bratislava, Trnava, Skalica and others) the excavation possibility. Excavating of decoration stone and the stone masonry in Brezovské Karpaty Mts. with various stone treatments has a long history. The quarrying was concentrated in villages Dobrá Voda and Chtelnica-Trianova (livery company). Here, the founded quarries served huge blocks of easily workable sandstone or conglomerate used in many historical buildings, sculptures, grave stones, paving, etc. The stone was used in the city of Trnava - gothic portal, baptistery, paving, stairs, pavements, pylons, statue socles, etc. in interior and exterior of several churches. In Bratislava the stone from Trianova was used for stairs in the Erdödy palace, for the pavement in the Mindszenty atelier, in the gothic house portal in Biela Street, in well casing in the court of Bratislava castle, etc. The historical utilization of the material from Chtelnica-Malé Skalky is not known yet.

2. Geological Setting

The investigated sites have a very different litho-stratigraphical evolution. Investigated sedimentary rocks of the Upper Cretaceous built the transgressive overlap of Triassic dolomites and limestones of the s.c.

* Assoc. Prof. Martin Bednarik, PhD.: Dept. of Engineering Geology, Comenius University in Bratislava, Faculty of Natural Sciences, Mlynská dolina; 842 15, Bratislava; Slovakia, mbednarik@fns.uniba.sk

** Assoc. Prof. Rudolf Holzer, PhD.: Dept. of Engineering Geology, Comenius University in Bratislava, Faculty of Natural Sciences, Mlynská dolina; 842 15, Bratislava; Slovakia, rholzer7@gmail.com

*** RNDr. Marek Laho, PhD.: Dept. of Engineering Geology, Comenius University in Bratislava, Faculty of Natural Sciences, Mlynská dolina; 842 15, Bratislava; Slovakia, laho@fns.uniba.sk

**** Mgr. Martin Dunčko.: Dept. of Engineering Geology, Comenius University in Bratislava, Faculty of Natural Sciences, Mlynská dolina; 842 15, Bratislava; Slovakia, duncko@fns.uniba.sk

Brezovská group of Brezovské Karpaty Mts. Sandstones and conglomerates (Coniacian) within the quarry Trianova and Dobrá Voda represent a solid, thick bedded (1 to 2 m) structure. These greyish coloured, fine and middle grained sandstones and conglomerates with carbonate clasts possess a very variable grain composition, which varies vertically and laterally. The total thickness of the strata is 50 to 150 m. The mining site in Dobrá Voda was abandoned in 70-ties of the last century due to the important hydrogeological structure (karst water reservoir).

The quarry Malé Skalky is a part of Neogene filling of Dobrá Voda tectonic depression. Neogene sediments (Burdigalian) of Dobrá Voda evolution rest disconformly on subsided Mesozoic rock blocks. The rock formation is built up by Jablonica light greyish or beige-creamy carbonate (locally polymict) conglomerates and carbonate sandstones, very variable in grain composition. The rocks are purely built up by carbonate clasts connected with carbonate cement. Conglomerates are very variable in the grain size and alternate with sandstones vertically, even laterally. The thickness of the strata is from 40 to 80 m.

3. Field Investigation

In the site Trianova one rock block (monolith) was taken for the preparation of laboratory samples in the size of 50 x 50 x 50 mm. In the site Malé Skalky were taken cylindrical rock cores with the diameter of 50 and 35 mm using the portable electric drilling device, and one monolith for preparing of samples in the size of 50 x 50 x 50 mm, as well. Four boreholes were drilled into the depth of 1 m in horizontal direction into quarry wall (Fig. 1).



Fig. 1: Samples taking using portable core drilling machine (Holzer, 2013).

4. Physical and Mechanical Rock Properties

Regarding the quality/toughness/durability of rocks for their utilization as decoration or restoration stone following properties are considered as most important: specific and bulk density (STN EN 1936), water absorption (STN EN 13755), porosity (STN EN 1936), uniaxial strength of a dry sample (STN EN 1926), uniaxial strength of after sample saturation and uniaxial strength after the 25 cycles of freezing and thawing. Thereafter the durability index coefficients were calculated: coefficient of softening k_1 (σ_2/σ_1 , non-dimensional) and coefficient of freezing k_2 (σ_3/σ_1 , non-dimensional) reflecting their resistance against weathering (STN EN 12371). Beside it our concentration was devoted to the appearance, structure and colour of the stone. In tables (Tab. 1 and Tab. 2) results of the laboratory assessment of properties of conglomerates and sandstones from quarries Trianova and Malé Skalky are presented. In tables (Tab. 1 and Tab. 2) results of the laboratory assessment of properties of conglomerates and sandstones from quarries Trianova and Malé Skalky are presented.

In general, the older clastic Upper Cretaceous conglomerates and sandstones from Trianova possess considerably better properties than the younger Neogene sandstones from Malé Skalky. Analyzing the assessed data (Tab. 1) it is possible to conclude following: the tested conglomerate/sandstone from Trianova reached lower values of porosity and water saturation than the sandstone from Malé Skalky. On

the other side the differences in specific and bulk density are lesser expressive. Due to the relatively high porosity (STN 72 1800) the sandstone from Malé Skalky belongs to the group of porous sandstones. They exceed the minimum values of volume density and water saturation, whereby they are suitable as a natural stone for stonecutting purposes.

Tab. 1: Average physical rock properties.

Site Lithological type	Sample taking	Bulk density ρ_a (g.cm ⁻³)	Specific density ρ_s (g.cm ⁻³)	Porosity n (%)	Water absorption N (%)
Chtelnica-Trianova fine grained conglomerate	monolith	2.473	2.759	10.366	1.59
Chtelnica-Malé Skalky carbonate sandstone	monolith	2.183	2.761	20.926	7.753
Chtelnica-Malé Skalky carbonate sandstone	drilling core	2.257	2.746	17.66	5.65
		2.448	2.762	11.99	3.9
		2.464	2.787	11.6	3.6

Comparing values of uniaxial strength (Tab. 2), the resulting statement is that the conglomerate/sandstone from the site Trianova reaches higher hardness than the sandstone from the site Malé Skalky. The values of k_1 are very different. It is remarkable that the values from Trianova show lower resistance against water in the comparison to values k_1 from Malé Skalky (with the exception of the first sample the stone shows a very good resistance against the effects of water). The value k_2 from Trianova shows very good resistance of rock against freezing which is similar to the second borehole Malé Skalky. The lower k_2 from Malé Skalky are probably due to low number of testing samples. From the most of properties indicators results that the investigated rocks regarding STN 72 1800 is suitable for the utilization as a restoration/decoration stone.

Tab. 2: Average mechanical rock properties.

Site Lithological type	Sample taking	Sample size	Samples Nb. dry/saturated/ frozen	σ_{c1} (MPa)	σ_{c2} (MPa)	σ_{c3} (MPa)	k_1	k_2
Chtelnica-Trianova fine grained conglomerate	monolith	cube 50x50x50 mm	3/3/3	84.75	58.68	68.56	0.692	0.809
Chtelnica-Malé Skalky carbonate sandstone	monolith	cube 50x50x50 mm	5/5/5	20.6	18.8	15.28	0.912	0.742
Chtelnica-Malé Skalky carbonate sandstone	drilling core	cylinder $\varnothing=50$ mm, h=50 mm	4/3/3	33.43	21.17	20.82	0.65	0.622
		cylinder $\varnothing=50$ mm, h=50 mm	4/4/7	39.66	34.88	34.09	0.879	0.862
		cylinder $\varnothing=35$ mm, h=35 mm	3/3/2	39.55	39.05	19.17	0.987	0.483

5. Conclusions

Evaluating and comparing results of stone properties (own research and archive backgrounds) of investigated sites and the considered excavation, it is possible regarding the Slovak technical standard 72 1800 to set following statement:

- Qualitatively most proper stone for restorations provides the quarry Trianova with its Upper Cretaceous sandstones and conglomerates (Fig. 2).
- Stone from Malé Skalky shows otherwise „lower“ values of required properties (than Trianova) but despite of it, it is in properties very well comparable with the stone from the „Römersteinbruch“ in St. Margarethen (Austria). Some disadvantage of the site Malé Skalky is the variability of frequent alternation of conglomerates and sandstones. This will require a proper selection of blocks during the excavation process and exact definition of the utilization purpose (decoration, restoration) of individual lithological types.
- Stone from the quarry Malé Skalky is sufficiently comparable with the stone from St. Margarethen. Comparing the laboratory results has „our“ stone in many aspects even better – more favourable parameters.



Fig. 2: Monument of Holy family, quarry Trianova (Holzer, 2013).

References

- STN EN 1936 (2007) Natural stone test methods. Determination of real density and apparent density, and of total and open porosity, *SÚTN*, Bratislava, 12 p.
- STN EN 13755 (2008) Natural stone test methods - Determination of water absorption at atmospheric pressure. *SÚTN*, Bratislava, 12 p.
- STN EN 1926 (2007) Natural stone test methods. Determination of uniaxial compressive strength. *SÚTN*, Bratislava, 20 p.
- STN EN 12371 (2010) Natural stone test methods. Determination of frost resistance. *SÚTN*, Bratislava, 16 p.
- STN 72 1800 (1987) Natural building stone for stonecutting purposes. Technical requirements. *SÚTN*, Bratislava, 16 p.

EXPERIMENTAL VALIDATION OF THE AERODYNAMIC FORCE ACTING ON A CONE OF A BALANCED CONTROL VALVE

L. Bednář^{*}, M. Miczan^{**}, L. Tajč^{***}, M. Hoznedl^{****}

Abstract: This is the description of an experiment focused on the determination of the aerodynamic force acting on a cone of a balanced control valve. The force determined from the pressures is compared with the force acquired from the strain gauge measurement. Two variants of the operating characteristics of a turbine are considered. A force conversion measured on a model to the forces acting on a real design of a valve is stated.

Keywords: Turbine, Valve, Aerodynamic Force.

1. Introduction

The force required to separate a cone of a control valve off a saddle is proportional to the pressure difference on a cone and a contact surface. The valve stem, apart from the aerodynamic force, is also affected by own weight of movable parts of a valve, by the force from a pressure spring and by the friction force from sealing elements. There is a certain type series of actuators. If operating parameters of a turbine require valves with the power parameters exceeding the capacity of an actuator, it is necessary to implement a higher number of unbalanced valves or to use a balanced control valve.

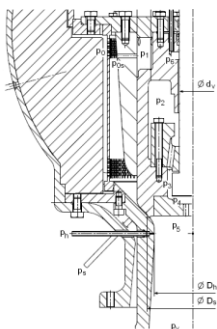


Fig. 1: Scheme of a control valve.

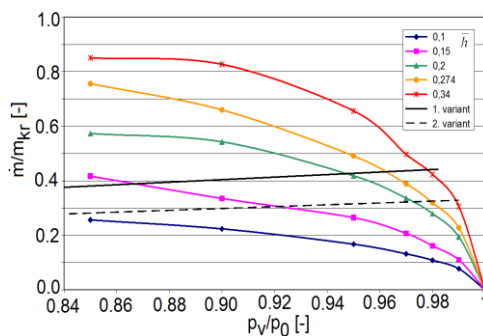


Fig. 2: Flow characteristics of a valve without the screen.

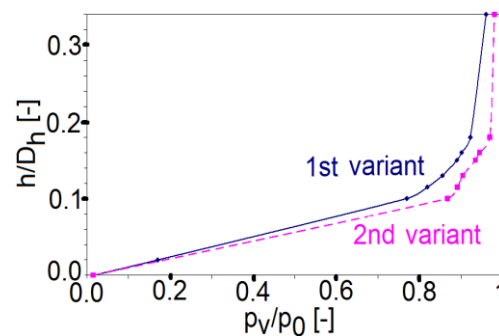


Fig. 3: Operating characteristics of a turbine.

A balanced valve comprises an inner bypass valve enabling to decrease the contact pressure acting on a cone and facilitating a cone to be separated off a saddle. A steam flow to the bypass valve is enabled through a ring slit, which reduces the pressure in the space under the slit. The aim is to ensure the chambers under the bypass cone, when the stem being separated off a saddle, to be emptied faster than the chambers out of this area. In order to be able to validate a design variant of a valve, a model in scale 1:1 was created.

2. A Model of a Balanced Valve

A design of a balanced valve is shown in the Fig. 1. Through the apertures in a guiding sleeve the steam also flows to the inner space to a bypass valve. There is the pressure p_1 above the part of a cone. After

* Ing. Lukáš Bednář, DOOSAN ŠKODA POWER s. r. o. Tylova 1/57, 301 28 Plzeň, CZ, lukas.bednar@doosan.com

** Ing. Martin Miczán, DOOSAN ŠKODA POWER s. r. o. Tylova 1/57, 301 28 Plzeň, CZ, martin.miczan@doosan.com

*** Ing. Ladislav Tajč, CSc., DOOSAN ŠKODA POWER s. r. o. Tylova 1/57, 301 28 Plzeň, CZ, ladislav.tajc@doosan.com

**** Ing. Michal Hoznedl, Ph.D., DOOSAN ŠKODA POWER s.r.o. Tylova 1/57, 301 28 Plzeň, CZ, michal.hoznedl@doosan.com

flowing through the slit the pressure is reduced to the value p_2 . In the vicinity of the bypass valve the pressures p_3 and p_4 are set up. The pressure p_5 acts on the bottom of a large cone. The output pressure in the diffuser is shown as p_v . All above said pressures, with the exception of the pressure p_5 , may be directly measured on a model of a valve. Apart from the above said pressures, there is also a tendency to record the pressures in the diffuser throat p_h and on the wall of a saddle p_s . In case of a higher elevation of a large cone an input slit opens and the pressures p_1 and p_2 become equal. However, at the same time the steam supply to a cone of a bypass valve closes. Then it is also reasonable to measure the pressure p_6 . In such a case the pressures p_3, p_4 and p_6 should be similar to the pressure p_5 . On a model of a valve by using strain gauges the contact force of a cone to the stem as well as the aerodynamic force acting on the stem is measured. A valve is connected to the suction of an aerodynamic tunnel. By changing the speed of the compressor the required pressure at the outlet from a valve is set up. The pressure ratio is fluctuating in the range $p_v / p_0 = 0.3 \div 1$. The input pressure is similar to the barometric pressure. However, the input pressure is much higher on the piece of work. In order to determine the total mass flow of a valve, a diaphragm being a part of an aerodynamic tunnel is used.

3. Findings from the Experiments

For a certain type and geometry of a valve there is a general flow characteristics shown in the Fig. 2, which is universal for the various media (the air and steam) as well as for the different dimensions of a valve. Only an entire geometric similarity is required. The results were confirmed by the calculations (Hajšman, 2011) as well as by the experiments. A general flow characteristics shows the dependence of a proportional mass flow $q = \dot{m}/\dot{m}_{kr}$ on the pressure ratio $\varepsilon_v = p_v/p_0$ (a note: \dot{m}_{kr} is a theoretical critical mass flow considered for the diffuser throat behind a valve, p_v is the pressure behind a valve and p_0 is the input pressure). Given values belong to constant $\bar{h}_p = h/D_h$, which is a real elevation of a large cone related to a diameter of the diffuser throat D_h .

A steam turbine creates one unit with a control valve. According to the required performance of the turbine, on the valve using the elevation of a stem a certain mass flow and the pressure ratio is set up. By this the pressure before the turbine itself is set up too. In the Fig. 2 there are also shown two variants of an operating characteristics of the turbine. The first variant ensures a higher mass flow, but the lower pressure before the turbine. However, in the valve itself the higher contact force of a large cone is applied on the stem. The other variant shows at full valve opening a higher proportional pressure p_v/p_0 , thus a lower loss in the turbine. However, the contact force on the movable parts of a valve is lower. There is a unified product series of valves due to which it is always necessary to decide whether it is better to choose bigger dimensions of a valve with the higher output pressure or smaller dimensions of a valve with the bigger contact force and bigger losses. In the Fig. 3 there is shown an elevation of a cone of a valve $\bar{h}_p = f(\varepsilon_v)$ for a considered operating characteristics of the turbine. In the conditions close to the certain operation of the turbine a small change of the pressure ratio corresponds to a big change of setting a large cone. A wide range of the change of the turbine performance (it concerns particularly starting and approaching the performance) occurs at the small range of the cone elevation.

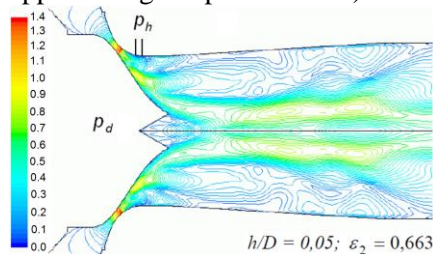


Fig. 4: Valve with a shaped cone.

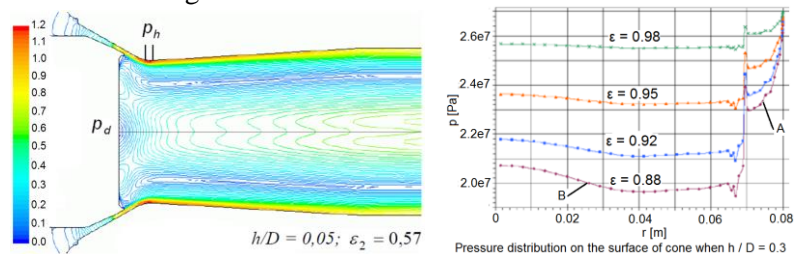


Fig. 5: Valve with cone with flat bottom.

A big emphasis is placed on the operational reliability of the valves. A correct function must be guaranteed also in case the gravitational forces act against the aerodynamic force acting on a cone of the valve. A step change of the position of a cone against a stem may cause the change in a flow area and due to this a step change of the turbine performance. Therefore, the contact force from the pressures on the surface of a cone is required to be in all modes of a turbine reasonably higher than a relevant gravitational force is. The gravitational force is permanent, but the aerodynamic force depends on the turbine operation. A minimum contact aerodynamic force occurs under the nominal operation conditions of the turbine. A contact aerodynamic force may be influenced by an appropriate shaping of the cone bottom and by

controlled distribution of the pressure on its surface (Matas et al, 2010; Hajšman et al, 2011; Jirka, 2007). A shaped cone shows the highest contact force. This is shown by the Fig. 4. If an expanding steam adheres to the surface of a cone, the pressure decreases on its surface and due to this the contact force gets higher. A drawback of this shaping is the existence of a ring Laval nozzle. Under the above-critical pressure conditions continuing under the low elevation of a cone, the unsteady flow, with the occurrence of shock waves accompanied by intense vibrations, arises. Even the destruction of pipelines may occur. The better reliability is shown by cone with flat bottom, which is shown by the Fig. 5. Cone with flat bottom enables to stabilize the flow conditions under the cone, however, there is a lower contact force. The lowest pressure is not on the cone bottom, but in the place of the wall of the diffuser throat.

A certain instability may occur within the transition from the subsonic to transonic field of flowing. It is related to the occurrence of shock waves and to a possible separation of the flow off the surface of a cone Fig 6 shows how the force acting on the cone with the flat bottom in a balanced valve being designed according to the Fig. 1, under the permanent elevation $\bar{h} = 0.115$ and a fluent change of the pressure ratio $\varepsilon_v = p_v / p_0$ changes. The friction forces between a guide sleeve and a cone appear to act on a cone too. A cone loading is, therefore, organized so that the loading force could increase gradually. Evaluation of dependencies was carried out only from one branch of the loading characteristics. The effect of shock waves after the occurrence of the transonic flow on a cone with the flat bottom is transferred. The influence of vibrations of an aerodynamic tunnel as well as possible resonance between own frequencies of the suspension of a valve with the frequencies from the compressor speed and the gear box of a sucking system of an aerodynamic tunnel shows up.

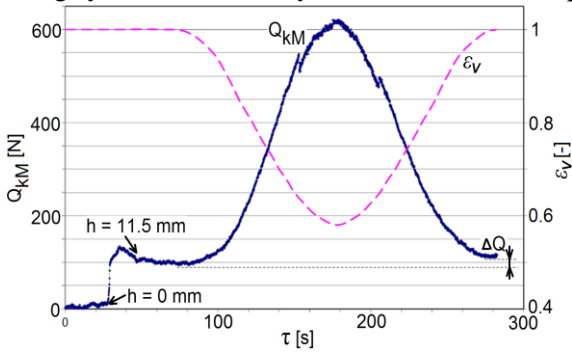


Fig. 6: Force on a cone with the flat bottom.

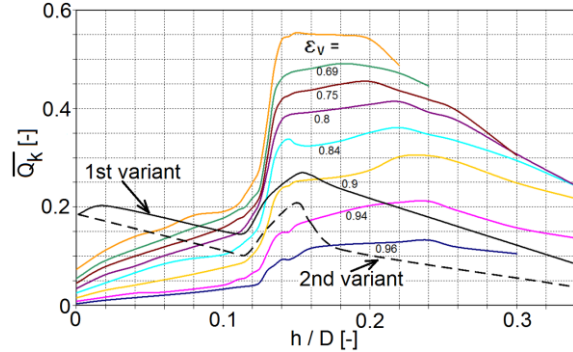


Fig. 7: General force characteristics of a valve.

The dimensionless force acting on a cone is the function of the relative elevation and the pressure ratio.

$$\bar{Q}_k(\varepsilon_v, \bar{h}) = \frac{Q_k}{p_0 S_s} \quad (1)$$

whereas $Q_k = f(h, p_0, p_v, S_s)$ is a real force acting on a cone, p_0 is the input pressure, p_v is the output pressure, h is an elevation and S_s is an area of a saddle.

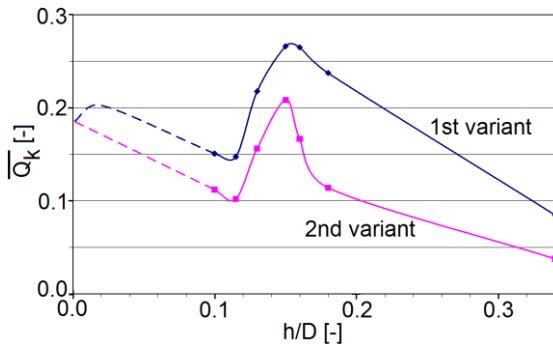


Fig. 8: Operational force characteristics.

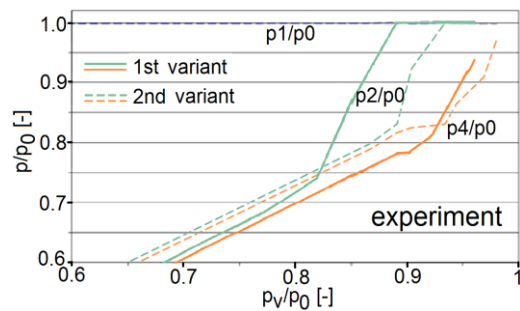


Fig. 9: Pressure ratios in inner chambers of a balanced valve.

In order to be able to determine the contact force of a cone for a particular operational variant of a valve and its dimensions, it is required to specify a general dimensionless force characteristic, which is for a certain valve specified in the Fig. 7. The operating characteristics for both chosen variants of the turbine operation are described in the Fig. 8. The transition from an area when a valve works as balanced one to the area of an unbalanced valve is highly evident. The pressure distribution in inner parts of a valve is shown in the Fig. 9.

The distribution of the pressure ratios shows three characteristic parts. An initial phase of the valve opening is influenced by shortening the length of the slit, which is finished by its entire opening. The pressure p_2 is gradually equalizing with the pressure p_1 . The other pressures are similar to the pressure p_2 . Under the further movement of a cone the inflow of the steam to the bypass valve begins to close down. The pressures p_3 up to p_6 are getting to be equal. After the entire closing of the flow, the pressures p_3 up to p_6 are practically the same. In the first variant the bigger differences of the pressures p_1 and p_4 occur, which proves the higher contact force. In the other variant the difference of the pressures acting on a cone decreases.

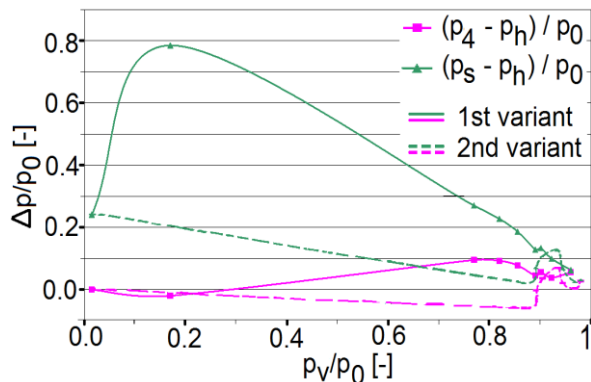


Fig. 10: Pressure differences around a saddle and the diffuser throat of a valve.

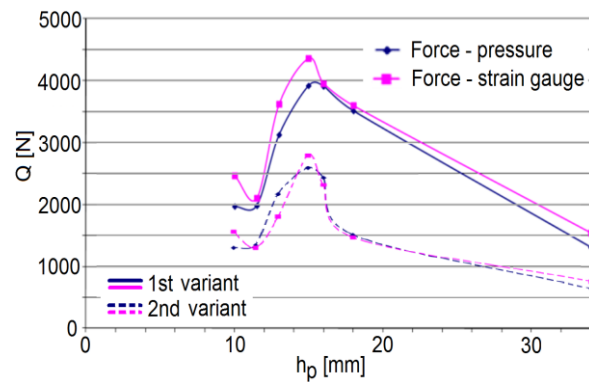


Fig. 11: Contact forces acting on a cone of a balanced valve.

The experiment does not allow to measure directly the pressure p_5 acting on the bottom of a cone. However, from the carried out calculations (Hajšman, 2011) it is known to be comparable with the pressure p_4 , which is measured. On the model of a valve the pressure loss on the perforated wall is recorded as well as the pressures in the diffuser throat and in the part of a saddle. Their changes depending on the operation pressure ratio p_v / p_0 are shown for both variants in Fig. 10. The pressure in the place of a throat is the lowest when the pressure bypasses without being separated off the wall. The pressure in the diffuser throat p_k may be measured easily. By using the diagrams in the Fig. 10 the pressure on the bottom of a cone as well as in other modifications of valves may be estimated. The result of the comparison of the measured and calculated contact forces on a cone from recorded pressures is shown in the Fig. 11. The comparison was carried out for input parameters of the steam considered for the regulation of the turbine performance installed in a laboratory, which is $p_0 = 14$ bar. Experimentally determined data are converted into these parameters. The forces calculated from the measured pressures acting on the certain area of a valve are considered. This determined contact force corresponds to the contact force directly measured by strain gauges.

4. Conclusions

- A tested valve fulfils the requirements for the decrease of the contact force at the start of a turbine.
- By choice of a valve from a unified production series the pressure loss on a valve as well as the size of a contact force on a cone may be influenced.
- In transition from the subsonic to transsonic area a valve is sufficiently stable.
- The forces determined from the pressures correspond directly to the measured forces.

References

Hajšman, M. (2011) Calculation of the flow characteristics of valves with different inlet diameter seat. Diploma Thesis WBU of Plzen, (in Czech).

Matas, R., Bednář, L. & Tajč, L. (2010) Numerical Simulations and Experiments as Modern Tools for Research of Control Valves for Steam Turbines; In: Proc. Experimental Fluid Mechanics 2010; Technical University of Liberec; pp. 398-409; ISBN: 978-80-7372-670-6.

Hajšman, M., Kovandová, D. & Matas, R. (2011) Some Aspects of Numerical Simulation of Control Valve for Steam Turbines, In: Proc. Experimental Fluid Mechanics 2011; Technical University of Liberec; pp. 642-653; ISBN: 978-80-7372-784-0.

Jirka, L. (2007) Computational studies of steam flow control valve. Diploma Thesis WBU of Plzen, (in Czech).

MEASUREMENT OF AIRFLOW IN TRACHEA USING PARTICLE IMAGE VELOCIMETRY AND LASER-DOPPLER ANEMOMETRY

M. Belka^{*}, J. Jedelsky^{**}, O. Boiron^{***}, L. Bailly^{****}, E. Bertrand^{*****},
M. Zaremba^{*****}, M. Maly^{*****}, F. Lizal^{*****}

Abstract: *A lot of attention has been given to the study of airflow in human respiratory airways recently, because airflow characteristics greatly influence transport and deposition of the particles in human lungs. In this paper the aerodynamics occurring in upper part of human trachea is investigated. Laser optical measurements were performed in a semirealistic model of the upper airways, from mouth to 4th generation of branching. The model was attached downstream to a generator of oscillating flow, which was set to sinusoidal flow for resting conditions with mean Reynolds number $Re = 1414$. Flow characteristics were measured using laser optical methods, in particular Particle Image Velocimetry and Laser-Doppler Anemometry. We found that the flow in trachea was biased to the front wall due to the laryngeal jet. The flow became turbulent during high velocity phases of the sinusoidal flow and generated turbulence intensity was observed up to 20 %. These data can help to understand the complicated flow in trachea and its implications in particle deposition studies.*

Keywords: Particle image velocimetry, Laser-Doppler anemometry, Model of human lungs, Flow measurement, Laryngeal jet.

1. Introduction

Transport of particles in human lungs is greatly influenced by the patterns of the airflow, such as turbulence levels and vortices. Therefore investigation of airflow characteristics in human respiratory airways has attracted much attention in recent decades. Results of these studies play key role in toxicology or drug delivery. During inspiration the air flows through mouth to pharynx, where it turns rapidly and enters larynx through epiglottis.

The complex laryngeal anatomy heavily affects the air flow entering the trachea and creates a jet (Corcoran and Chigier, 2000). This so-called laryngeal jet forms eddies, reverse and turbulent flows, which leads to increased deposition in trachea region. Some researchers observed that the jet biased the flow towards the posterior wall of the trachea (Lin et al., 2007), however others found biased flow to the anterior wall (Zhang & Kleinstreuer, 2004). The behaviour of the jet varies depending on the geometry used (Kleinstreuer & Zhang, 2010).

Non-intrusive laser optical methods are efficient tools for analysis of airflow characteristics. Major drawback of these methods is the fact that the measurement area has to be optically accessible. Therefore, most of previous studies have used simplified models of the human lungs made of glass or silicone (Kim & Chung, 2009; Grosse et al., 2007). In addition the air was substituted by working fluid with the same refractive index as the model walls.

In this paper the experimental investigation of tracheal flows was carried out through a semirealistic upper airways model using both two-dimensional Particle Image Velocimetry (2D2C PIV) and one-dimensional Laser-Doppler Anemometry (1C LDA). By combination of these methods spatially and

* Ing. Miloslav Belka: Brno University of Technology, Technicka 2896/2; 616 69, Brno; CZ, belka@fme.vutbr.cz

** Assoc. Prof. Jan Jedelsky, PhD: Brno University of Technology, Technicka 2; 616 69, Brno; CZ, jedelsky@fme.vutbr.cz

*** Aix Marseille Université, CNRS, IRPHE UMR 7342, F-13384, Marseille, France; olivier.boiron@centrale-marseille.fr

**** Aix Marseille Université, CNRS, Centrale Marseille, IRPHE UMR 7342, F-13384, Marseille, France

***** Brno University of Technology, Technicka 2896/2; 616 69, Brno; CZ

temporally resolved data of the flow were acquired. Air was used as working gas for preservation of real conditions.

2. Methods

2.1. Particle Image Velocimetry

Particle Image Velocimetry (PIV) was employed to acquire 2D-velocity flow fields in the simplified model of human upper airways displayed in Fig. 1b. The airways are modelled by thin-walled glass tubes, which facilitate measurement in various positions. The model includes respiratory airways from oral cavity to the 4th generation of branching. Branch volumes, lengths and branching angles are preserved in comparison to human anatomy.

The experimental setup is displayed in Fig. 1a. The model (2) was attached to a generator of oscillating flow (1) comprising four pistons, two for inspiration and two for expiration phase, which were driven through cylinders by an electromotor (3). The electromotor was controlled by a computer (4) enabling simulation of different shapes of motion with proper amplitude and frequency. Sinusoidal cyclic flow for resting conditions (tidal volume of 0.5 l and period of 4 s) was chosen in this case. The flow was seeded with micrometric particles from incense sticks. Smoke inlets (5) were situated on both sides of the model to obtain homogenous distribution of particles during simulation of both inspiration and expiration.

Single camera PIV system was used to collect the data. A dual-head pulsed Nd:YAG laser (New Wave Gemini, 120 mJ per pulse, 532 nm) with laser beam collimator optics produced 0.5 mm thick light sheet (6). The light was brought to the investigated position in trachea through an articulated arm placed in posterior position. Images of the flow were captured by a TSI power View 4Mp CCD camera (7) equipped with a 60 mm focal lens and a circular polarizing filter. The camera axis was aligned perpendicularly to the light sheet, thus sagittal view of the trachea was acquired. The PIV system was triggered by TSI 610035 synchroniser. The measurements were carried out at five instants during the breathing cycle (phase 45°, 90°, 180°, 270° and 360°). A set of 50 images was obtained for each phase for phase averaging. The images were processed using Insight 3G software. Cross-correlation was performed to determine the displacement of the particles within a 50 % overlapping interrogation window 32×32 pixels in size, giving a spatial resolution of 19,7 µm/pixel.

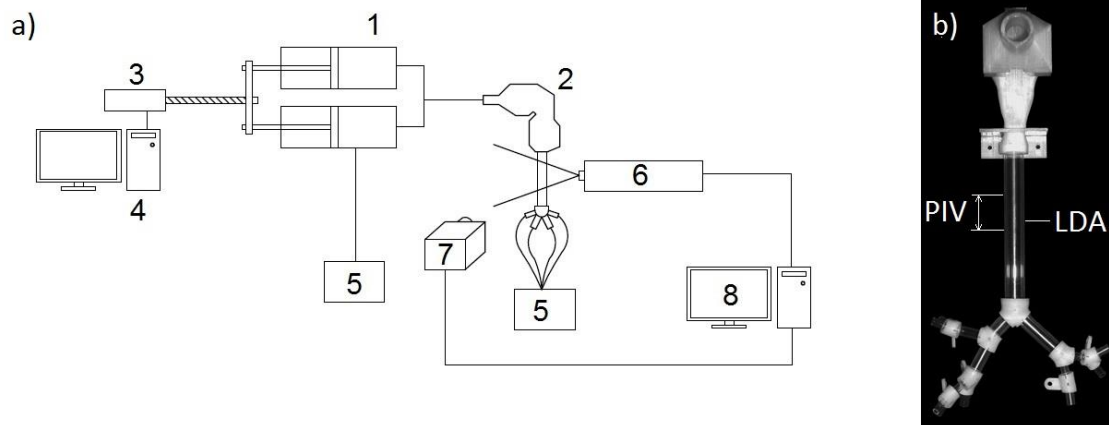


Fig. 1: a) Experimental setup; b) Model of human upper airways.

2.2. Laser-Doppler Anemometry

Point wise time-resolved measurement of flow velocity of particle-laden air in multiple points of the optically transparent model was provided under the cyclic breathing regimes using laser-Doppler anemometry (LDA). Dantec Dynamics Flow explorer 9065x0341 used BSA Flow software for measurement and analysis of the results. One pair of the crossing laser beams with wave length of 660 nm (power output: shifted beam 28 mW, un-shifted beam 33 mW) was used. The LDA worked in backscatter mode with the focal length of both the transmitter and receiver of 300 mm. Aerosol particles of di-2-ethylhexyl sebacate (DEHS) with 3 µm in diameter were produced by condensation monodisperse aerosol generator (CMAG TSI 3475), mixed in a static mixer with air and resulting dilute dispersed two-phase mixture was led to the lung model. The measurements were done in several points of one cross-section.

The LDA measured 1-component velocity and arrival time of individual aerosol particles. The velocity component normal to the corresponding cross-section of the tube in the airway model was traced. Temporally actual values of fluctuating velocity v' , were found by processing the velocity data samples in short time bins. Length of time window for the processing was set to a value significantly lower than the mean velocity change during the inspected time window (± 15 ms in this case). Minimum number of particles in each time bin was set to 9. Dividing v' by spatially and temporally mean velocity in the point gives the axial turbulence intensity (TI). The plots (Fig. 3) are constructed as a result of several overlapped breathing cycles.

3. Results

PIV provides spatially resolved results of velocity fields. Measurements were executed in a region from 7 to 10 cm above the first bifurcation (Fig. 1b). Velocity field for different phases of sinusoidal flow and actual velocity profiles are displayed in Fig. 2. As mentioned earlier, the flow in trachea is influenced by laryngeal jet during inspiration. Under our kinematic conditions, the jet-flow was impinged to the anterior side of trachea. Fig. 2 illustrates higher velocities in the anterior side mainly for the 90° phase.

The velocity profile was rather parabolic for the phase 45° , thus the flow was laminar at this moment of the sinusoidal cycle. As the velocity and Reynolds number increased, the velocity profiles became flat, which indicated turbulent flow for the phases 90° and 270° . In addition, oscillatory flow character could have partly contributed to the flat profiles (Womersley number $\alpha = 2.7$). Velocities during phases 180° and 360° were very low, as anticipated at the points of flow reversal.

As can be seen from the figures, the obtained data were not sufficiently good for PIV evaluation near the walls of the trachea. These blank regions were mainly created by reflections of the light. Moreover the amount of tracer particles was considerably smaller around the walls during high velocity phases.

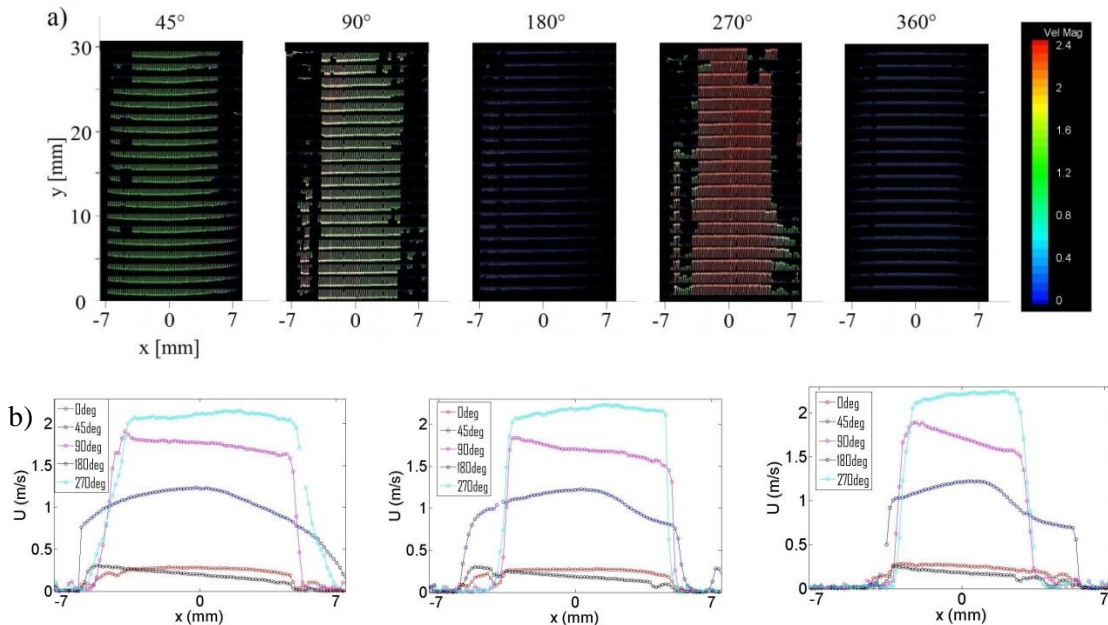


Fig. 2: a) Velocity fields for different phases of sinusoidal flow; b) Velocity profiles in several cross-sections ($y = 5; 15; 25$ mm).

Illustrative results of the LDA measurements in two positions of the cross-section C (8 cm above the first bifurcation, Fig. 1b) are shown in Fig. 3. Time-resolved axial velocities of individual aerosol particles as well as averaged velocity profiles and TI for one full cycle are displayed. The mean velocity course generally resemble the sinusoidal character of the breathing cycle, but some fluctuations with time scale of tens of milliseconds are visible on the velocity and namely on the TI profiles. These large scale velocity fluctuations and jumps placed namely close to the velocity reversals suggest for vortical structures that attend the flow.

The inspiratory flow ($0 < t \leq 2$ s) is influenced by the laryngeal jet and, however the turbulence is already partially decayed due to long distance, it is still turbulent even for the resting conditions with mean Reynolds number $Re = 1404$. TI varies significantly during the flow. Inspiratory flow is influenced by the

laryngeal jet (Lin et al., 2007), which generates turbulence with magnitude up to 20 % in both the points. It agrees with findings of others (Zhang and Kleinstreuer, 2004). Expiratory turbulence results from mixing of the streams from daughter branches. Its maximum is about 15 % for the centreline position and about 18 % for the R point. The expiratory part of the cycle for R point is more distorted from the sinusoidal shape.

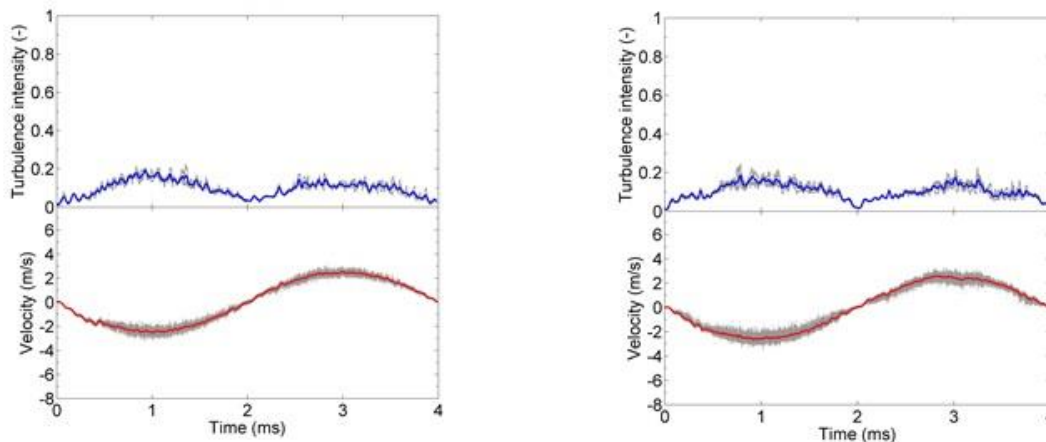


Fig. 3: Particle velocity during breathing cycle in cross-section 8 cm above the first bifurcation, in trachea centreline (left) and in position R (right), 4 overlapped cycles (right).

4. Conclusions

The spatially resolved velocity fields were obtained using PIV. The velocity profiles are asymmetrical during inspiration with higher velocities closer to the anterior side of the trachea. The observed velocity profiles were parabolic at low velocity phases, but they became flat at high velocity peaks indicating a transition from laminar to turbulent flow during the sinusoidal cycle. Moreover the effect of oscillation frequency was considerably low as expressed by Womersley number $\alpha = 2.7$.

This fact corresponds with the LDA results. The flow, as suggested by the TI plots, is relatively turbulent even for the resting conditions with mean Reynolds number $Re = 1404$. The time-resolved velocity curves acquired using LDA show small irregularities namely during the velocity reversals. These fluctuations and jumps are supposed to be caused by vortical structures that attend the flow.

The future work is planned to improve the quality of the PIV results and to mutually compare the methods.

Acknowledgement

Authors acknowledge financial support from the project № 105/11/1339 funded by the Czech Science Foundation and joint Czech – French project MOBILITY № 7AMB13FR047 (Flow and transport of medical aerosols in the human airways) funded by the Ministry of Education, Youth and Sports of the Czech Republic. The conception of the respiratory flow generator used for PIV measurements has been financially supported by the project ANR OXHELEASE (ANR-11-TECS-006).

References

- Corcoran, T. E. and Chigier, N. (2000) Characterization of the laryngeal jet using phase Doppler interferometry. *Journal of Aerosol Medicine-Deposition Clearance and Effects in the Lung* 13:125-137.
- Lin, C. L., Tawhai, M. H., McLennan, G., Hoffman, E. A. (2007) Characteristics of the turbulent laryngeal jet and its effect on airflow in the human intra-thoracic airways. *Respiratory Physiology & Neurobiology* 157:295-309.
- Zhang, Z. and Kleinstreuer, C. (2004) Airflow structures and nano-particle deposition in a human upper airway model. *Journal of Computational Physics* 198:178-210.
- Kleinstreuer, C., Zhang, Z. (2010) Airflow and Particle Transport in the Human Respiratory System. *Annual Review of Fluid Mechanics* 42:301-334.
- Kim, S. K., Chung, S. K. (2009) Investigation on the Respiratory Airflow in Human Airway by PIV. *Journal of Visualization* 12:259-266.
- Grosse, S., Schroder, W., Klaas, M., Klockner, A. and Roggenkamp, J. (2007) Time resolved analysis of steady and oscillating flow in the upper human airways. *Experiments in Fluids* 42:955-970.

INDUSTRIAL MACHINERY DYNAMIC EFFECTS ON PRODUCTION PROCESS AND HALL STRUCTURES

J. Benčat*

Abstract: *In this paper a dynamic characterization and vibration analysis has been used for the detection and identification of the machine processing condition and the effect of the production machinery vibration on building complex structures and production process. For sensitive process machines and structures dynamic response due to production machinery calculation procedures was applied using experimental input data via spectral analysis.*

Keywords: Machine vibration, Ground vibrations, Experimental tests, Vibration monitoring.

1. Introduction

In production hall all machines vibrate and, as the state of the machines worsen their vibration level increase and this causes increasing of the structure vibration level, too. An ideal indicator on this state, especially dynamic behavior is obtained via measuring and by supervising the vibration level produced by a machine (Karabay, 2007). While the increase in machine vibration allows us to detect the defects, the analysis of the machine vibration characteristics makes it possible to identify their reasons and to make a suggestion to eliminate them (Chandiranai & Pothala, 2006; Chen & Tsao, 2006). The analysis in frequency domain is generally carried out when the machine vibratory level is considered to be higher than the acceptable threshold (Newmark, 2011). This kind of vibrations if excessive can damage to nearby buildings and structures and also can negative affect the process in industrial production halls (Risbood, Dixit & Sahasrabudhe 2003; Tounsi & Otho, 1999).

2. Industrial Machinery Vibrations

The industrial production machinery process may cause undesirable vibrations transmitted from machine foundations via ground to production hall structures as well as nearby buildings and environment. The ground vibrations due to man activities recorded at a distance from machine foundations are analyzed assuming them to be a random and statistically stationary functions of the time. This kind of vibrations if excessive can damage to nearby buildings and structures (Dowding, 1996). Vibration which usually also has a negative impact on security and stability of the structures, facilities performance and people should be controlled by experimental analysis and the results compared (spectral picks limit, vibration levels, etc.) with relevant standards prescription values and criteria (Slovak Standard STN EN 1998 – 1/NA/Z1, 2010; Slovak Standard STN 73 0032, 2005). The case study regarding to the analysis of vibrations caused by unfavorable production machinery effects on hall structures and production process in *Justur a.s. St. Turá* industrial plant (Benčat, 2011) is describes in the paper.

2.1. Assessment of building vibration due to industrial activities

The assessment of building vibration due to industrial activities caused by production machines is a problem that can be solved through the application of research (Chiou & Liang, 1998; Lalwani, Mehta & Jain, 2008; Qi, He, Li, Zi, & Chen, 2008). This research consists mainly of defining the relationship between intensity vibrations in the ground (the vibration energy quantity) and the distance from the vibration source (Rizzo & Shippy, 2003). The intensity vibrations can appear in different physical quantities, such as the displacement, velocity and acceleration amplitudes, vibration frequency, ground

* Prof. Ján Benčat, PhD.: Research Centre, University of Žilina, Univerzitná 1; 010 26, Žilina; Slovakia, jan.bencat@gmail.com

motion intensity and energy etc. There are accessible several standards in the field of measurement of vibration regarding the building vibration limits in the European Union, USA, Australia, ISO codes and others. In Slovakia in the field of measuring and assessing of building vibrations due to ground motion the most commonly used standard is Slovak Standard STN EN 1998 – 1/NA/Z1 based on EC8 and Slovak Standard STN 73 0032, (in Slovak).

2.2. Machine effects on building structure and production process experimental analysis

This paper section shortly described study of the unfavorable production machinery effects on industrial building complex structures and also on vibration-sensitive production process in industrial plant of the *Justur a.s. St. Tura* (company). The complex of industrial processing buildings is fully described in (Benčat, 2011). The most sensitive part of the industrial processing buildings is the building **M1** fixed for special medical articles production, which is tailored to accurate technological processes. This building is joined with the adjacent processing building **M2** by partition wall. The vibrations caused by production traditional tool machinery effects in building M2 unfavorable affected the sensitive operations processing (CNC lathe MORI SEIKI SL–204) in adjacent building M1 even they have unfavorable effects on M1 structure with vibration velocities amplitude $v_{max} > 6.0$ mm/s. **To determine harmful machine vibration sources and to regulate their working regime**, it was need to *perform experimental measurements and monitoring of the machines – related vibrations and compare to the low-vibration fabrication machines criteria or relevant Standards*.

Experimental procedure and devices. The industrial processing buildings dynamic response (M1) due to traditional tool machinery in building M2 were measured in relevant structure points by accelerometers BK – 8306. The output signals from the accelerometers were preamplified and recorded on portable PC equipped with A/D converters of the software packages NI and DISYS, (Fig. 1). The experimental analysis has been carried out in the Laboratory of the Department of Structural Mechanics, CEF, University of Žilina (Benčat, 2011). The machines and structure vibrations frequencies were obtained using spectral analysis of the recorded response dynamic components, which are considered as ergodic and stationary. Spectral analysis (power spectra, PSD) was performed via National Instrument software package NI LabVIEW.

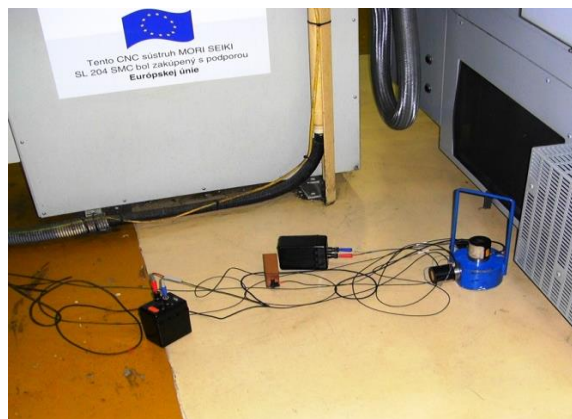


Fig. 1: Set of accelerometers with amplifiers and measuring PC in acquisition configuration to measure floor and mounts vibrations of the CNC lathe MORI SEIKI SL–204 (BK4).

The building structure dynamic response (BSDR) and the machines dynamic response (MDS) assessment procedure. The main purpose of the dynamic tests in the building M1 was to determine the structure vibrations level and machines vibrations level (in common processing regime and in out of operation regime) due to machinery effects working in building M2 and to compare to the limiting value recommended by machines producer (CNC lathe MORI SEIKI SL–204) prescription vibration level or standard level. In this case machine producer prescription was not available. To reach dynamic analysis target (BSDR, MDS) it was reason to carry out 2 series of experimental measurements and 14 days continual monitoring of the dynamic response of the CNC and M1 building structure at selected representative points (Benčat, 2011). During the first series of tests and 14 days monitoring in the both halls (M1, M2) there were performed normal machines production progress of work and during those processes there were measured in selected points vibration level amplitude values v_{max} (mm/s) and $max v_{rms}$ (mm/s) with results summarized in Fig. 2.

As the measured vibration level values for the structure fundament (BK3) and the most sensitive production equipment CNC lathe Mori Seiki, SL – 204 (BK5) had higher values than the standard upper limits of the vibration level (machine producer prescription vibration level was not available) it was necessary to perform the machines working regime adjusting in the hall M2 to obtain the required allowable vibration velocity.

After the machines working regime adjusting in hall M2 there were performed the second series of the tests in the same points and procedures as during the first series of the tests. The summarized measured vibration velocity values with their upper standard limits are plotted in Fig. 2. As an example of the machines induced vibrations analysis results in frequency domain (PSD) and time domain (velocities amplitude time history – $v(t)$) of the structure fundament (BK3) and the most sensitive production equipment CNC lathe Mori Seiky, SL – 204 (BK5) are plotted on Fig. 3.

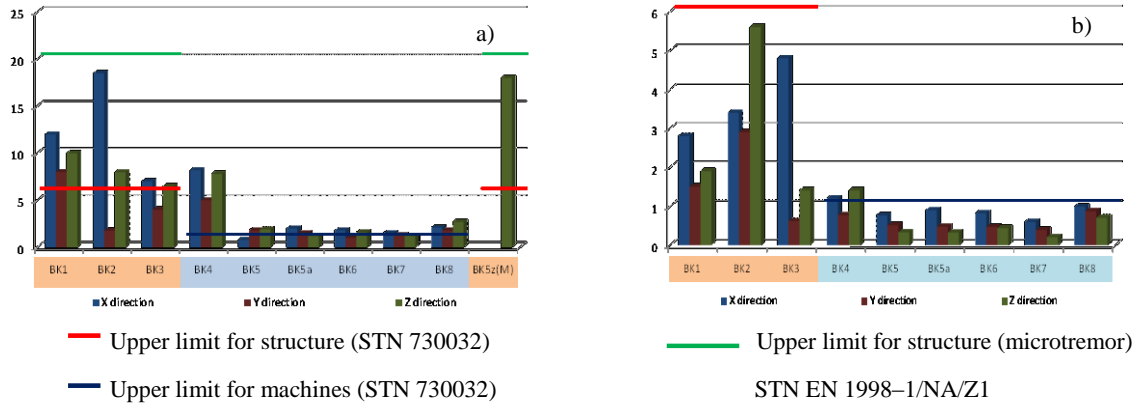


Fig. 2: Amplitude of extreme velocities values v_{max} (mm/s) of the tests: a) 1st series and monitoring; b) 2nd series.

The comparison of the measured vibration velocities extreme levels (after adjusted machine regime) and standard limits suggests fulfilling standards required criteria $v_{max} < 20$ mm/s, (STN, 2010) and $v_{max} < 6.0$ mm/s, (STN, 2005) for hall M1 structure where measured value was $v_{max} = 5.8$ mm/s and also for sensitive production equipment was fulfilled required standard criterion $v_{max} < 1.0$ mm/s, (STN, 2005) where measured value on the machine lathe Mori Seiki frame was $v_{max} = 0.76$ mm/s. According to the results of the structure spectral analysis the structure basic natural frequencies have values $f(n) < 10$ Hz (Benčat, 2011), it means there were no resonance effects because the exciting machines frequencies are over the 15 Hz, see also Fig. 3.

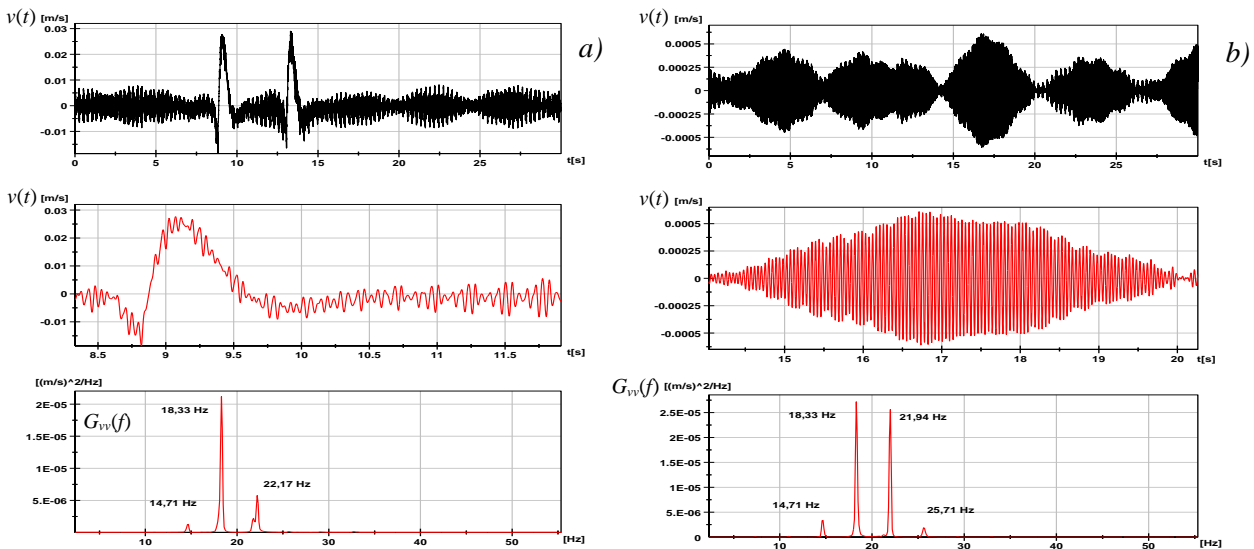


Fig. 3: Time histories $v(t)$ and PSD $G_{vv}(f)$ during: a) Monitoring (BK3); b) 2nd series of tests (BK5).

3. Conclusions

This paper presents an overview of the analysis of vibrations caused by unfavorable production machinery effects on building structures and production process, too. The results of the theoretical and experimental investigation of vibrations caused by production machinery dynamic effects in hall M2 on the M1 hall structures were analyzed mainly from aspects of the safety of the building structure and the influence of vibrations on production process conditions in production buildings M1 of the industrial plants *Justur a.s. St. Turá*.

Based on the results presented in the paper the following conclusions can be drawn:

- i) Since the most sensitive production equipment CNC lathe Mori Seiki in hall M1, during production process had inadmissible vibration level it was necessary to perform in the hall M2 machines working regime adjusting to obtain the required allowable vibration velocity for failure free production process. The machines regime adjusting in adjacent hall M2 caused reducing vibration level of the sensitive production equipment in hall M1 about 52%. The comparison of the measured vibration velocities level and standard limits suggests fulfilling required criteria for sensitive production equipment.
- ii) The relevant calculated data values following from experimental spectral and amplitude analysis of the production hall M1 structure dynamic response (spectral picks limit, vibration levels, etc.) were compared with relevant standards prescription values and criteria. From these comparisons it follows that all standards prescription values and criteria regarding building structure after machines regime adjusting in hall M2 were fulfilled, too.

Acknowledgement

The research is supported by European regional development fund and Slovak state budget by the project Research Centre of University of Žilina, ITMS 26220220183. We should also like to acknowledge support by the research project VEGA, Nr.G1/0169/12 granted by Scientific Grant Agency of the Slovak Republic Ministry of Education.

References

- Benčat, J. et al. (2011) Assessment of the structure and precision production machine dynamic response in Justur a.s. St. Turá, Report PC 22/SvF/10, University of Žilina, (in Slovak).
- Chandiranai, N.K. & Pothala, T. (2006) Dynamics of 2–dof regenerative chatter during turning, *Journal of Sound and Vibration* 290, pp. 448-464.
- Chen, C.K. & Tsao, Y.M. (2006). A stability analysis of regenerative chatter in turning process without using tailstock, *Int. J. Adv. Manuf. Technol.* 29 (7–8), pp. 648-654.
- Chiou, R.Y. & Liang, S.Y. (1998) Chatter stability of a slender cutting tool in turning with tool wear effect, *Int. J. Mach. Tools Manuf.* 38, pp. 315-327.
- Dowding, C. H. (1996) *Construction vibrations*, New York: Prentice–Hall, Upper Saddle River.
- Karabay, S. (2007) Design criteria for electro–mechanical transducers and arrangement for measurement cutting forces acting on dynamometers, *Mat. & Des.* 28, pp. 496-506.
- Lalwani, D. I., Mehta, N. K. & Jain, P. K. (2008) Experimental investigations of cutting parameters influence on cutting forces and surface roughness in finish hard turning of MND250 steel, *J. Mat. Proc. Tech.* 206, pp. 167-179.
- Newmark, M. S. et al. (2011) *Monitoring Construction Vibrations at Sensitive Facilities*, Acentech Incorporated, Cambridge, Massachusetts.
- Qi, K., He, Z., Li, Z., Zi, Y. & Chen, X. (2008) Vibration based operational modal analysis of rotor systems, *Measurement* 41, pp. 810-816.
- Risbood, K.A., Dixit, U.S. & Sahasrabudhe, A. D. (2003) Prediction of surface roughness and dimensional deviation by measuring cutting forces and vibrations in turning process, *J. Mat. Proc. Tech.* 132, pp. 203-214.
- Rizzo, F.J. & Shippy, D. J. (2003) An application of the correspondence principle of linear viscoelasticity theory, *SIAM, Journal on Applied Mathematics*, 21(2):321-330X.
- Slovak National Annex to Eurocode 8 (2010) *Design of structures for earthquake resistance. Part 1: General rules, seismic actions and rules for buildings*, STN EN 1998–1/NA/Z1. SUTN, Bratislava, (in Slovak).
- Slovak Standard (2005) *Calculation of buildings structures loaded by dynamic effect of machines*. STN 73 0032, SUTN, Bratislava, (in Slovak).
- Tounsi, N. & Otho, A. (1999) Identification of machine – tool – workpiece system dynamics, *Int. J. Mach. Tools Manuf.*, 1 367-1 384.

DROPWISE CONDENSATION MODELING

P. Beňovský*, H. Rusche**, F. Ridzoň***, M. Popovac*, Ch. Reichl*, T. Fleckl*

Abstract: *The present paper describes an approach to the numerical modeling of the condensation on the cooled surfaces of the air driven heat pump heat exchangers. The approach is based upon the classical nucleation theory and on a continuous growth law which are the necessary inputs for the simplified population balance equation solved by the quadrature method of moments. An example result is presented where one of the models' parameters: the driving force, is varied. The influence of the driving force on the condensate rates of a simple condensing heat exchanger is shown.*

Keywords: Condensation, Droplet nucleation, Growth, CFD, QMOM.

1. Introduction

To date different methods have been developed to calculate the amount of the precipitating condensate on a cooled surface. These methods (VDI, 2002) are based usually upon the Nusselt theory, Nusselt (1916). The main advantage of the calculations using the Nusselt theory is, that it gives a relatively fast indication of the performance of a condensing heat exchanger at steady state and usually nominal load. The drawback of the method, however, is that it is 1-D model with certain model assumptions like presumed geometry, steady flow, negligible vapor velocity, etc. Therefore, if one is interested in the transient behavior of the flow or wants to take into account the full geometrical features of the modeled domain, the Nusselt theory based calculation may not be appropriate anymore. Moreover, reviewed literature Song et al. (2009) and the experiments conducted at AIT, Pauschenwein et al. (2010) indicate that the initial stage of the condensation begins by the nucleation of the initial droplets and subsequent growth, all of which happens in the dropwise regime. Therefore, we have decided to adopt a different approach, namely to develop a numerical model coupled with a CFD code based upon sound physical modeling. For its implementation we have chosen the open source CFD library OpenFOAM® due to the code transparency and performance.

2. Methods and Results

In order to get a more detailed insight into the condensation kinetics during its initial stages we developed a numerical model containing both initial phases of droplet nucleation and growth. The choice to investigate the initial stages of the condensation is not arbitrary – the places where the condensation starts may indicate spots of enhanced heat transfer, change of the surface quality or similar effects. Further, if we think of a situation where yet another phase transition – droplet freezing – takes place, then these spots may very well be the ones where frosting leads to either narrowing of the flow pathway between the fins, decreasing of the heat transfer coefficient or both.

2.1. Description of the nucleation model

The nucleation is a process where the condensing species builds clusters of molecules from the available monomers in the system (Vehkamäki, 2006), e.g. water molecules in humid air condensing on a cold plate. There exists a discrete value of the droplet critical radius r^*

* Peter Beňovský, Mirza Popovac, Christoph Reichl, Thomas Fleckl: Austrian Institute of Technology, Giefinggasse 2, 1210 Vienna, Austria, peter.benovsky@ait.ac.at

** Dr. Henrik Rusche: Wikki GmbH, Göggestraße 24, 38118 Braunschweig, Germany, h.rusche@wikki-gmbh.de

*** Assoc. Prof. František Ridzoň, PhD.: Institute of Thermal Power Engineering, Faculty of Mechanical Engineering Slovak University of Technology, Nám. slobody 17, 812 31 Bratislava; Slovakia, frantisek.ridzon@stuba.sk

$$r^* = \frac{2\sigma m}{\rho RT \ln S}. \quad (1)$$

In Eq. (1) utilized symbols stand for: σ surface tension [N/m], m molar mass of water [kg.mol⁻¹], ρ density [kg/m³], R universal gas constant [J/mol.K], T temperature [K], S saturation ratio [-]

To form a droplet of this critical size (a droplet which is stable and will not evaporate), enough formation free energy needs to be available. The calculation of the formation free energy can be done according to the classical theory of Becker & Döring (1935) or its more recent updates, which address the inherent inconsistency of the theory (Girshick & Chiu, 1990), and attempt to improve the accuracy of the theory (Reiss et al., 1997). The expression for the formation free energy ΔG_{BD}^* during homogeneous nucleation according to Becker & Döring is then

$$\Delta G_{BD}^* = \frac{16\pi}{3} \frac{v_m^2 \sigma^3}{(kT \ln S)^2}. \quad (2)$$

Here v_m is the molecular volume [m³/mol], and k the Boltzmann constant [J/K].

Finally, the nucleation rate J is calculated

$$J_{BD} = \sqrt{\frac{2\sigma}{\pi m}} v_m \left(\frac{p_v}{kT} \right)^2 e^{-\frac{\Delta G_{BD}^*}{kT}}. \quad (3)$$

Where p_v is the vapour pressure [Pa].

The expressions for the improved nucleation rates (Reiss, Kegel & Katz, 1997) and (Girshick & Chiu, 1990) use the Becker & Döring nucleation rate Eq. (3), which is multiplied by the respective factors proposed by the authors. It is important to note that the expressions listed above hold for homogeneous nucleation, while heterogeneous nucleation prevails in the engineering practice. To amend this discrepancy, the formation free energy (Eq. (2)), is multiplied by a geometric factor. Furthermore, the volumetric nucleation rate has to be transformed into an areal one. To achieve this, one can use the monolayer approach which assumes, that the surface is completely wetted with a monolayer of water molecules. The final expressions for the heterogeneous nucleation can be found in literature Vehkamäki (2006). Nevertheless, the Eqs. (2) and (3) are always present in some form.

2.2. Description of the growth model

The growth of condensing droplets can proceed by two different mechanisms: the continuous growth of the droplets driven through diffusion processes and the coalescence of the droplets, the latter being a discontinuous change of the size. Because we are looking at the initial stage of the droplet formation, we will limit our focus to the continuous droplet growth. In literature different growth law formulations can be found e.g.: Heidenreich & Ebert (1995); Krischer & Grigull (1971); Vemuri & Kim (2006). For brevity only the growth equation formulated by Krischer & Grigull (1971) is reported

$$G(r) = \frac{\ln(1 + 1.75Bi)}{1.75Bi} \frac{\alpha_{Kin} \Delta T}{\rho \Delta h}. \quad (4)$$

Here Bi is the Biot number [-], α_{Kin} kinetic heat transfer coefficient [W/m².K], ΔT wall to bulk temperature difference [K], Δh latent heat [J/kg.K]

2.3. Mathematical model

Two physical models describing the nucleation and continuous growth were discussed in the previous paragraphs. The nucleation and the growth are essentially a variation of one droplet parameter out of many – the size. Thus, an equation is needed to track the variation of the number density of droplets with a certain quality (size) in physical space, time and the internal coordinate space. Such criteria are met by the population balance equation (PBE), Ramkrishna (2000). Restricting our attention to the nucleation and continuous growth of the non-moving droplets the PBE reads as

$$\frac{\partial n(r, x, t)}{\partial t} + \frac{\partial}{\partial r}(G(r)n(r, x, t)) = H(r, x, t). \quad (5)$$

In the equation $n(r, x_i, t)$ is the number density function which can change in the physical time and space (x_i, t) as well as in the internal coordinate space (r) . The right hand side of the equation $H(r, x_i, t)$ accounts for the discontinuous events: nucleation, droplet coalescence and breakage. There are several ways to solve the equation. Our choice was the quadrature method of moments (QMOM) McGraw (1997). For the application of QMOM it is necessary to transform Eq. (5) into a moment equation. The k^{th} order moment μ_k of a number density function is defined by

$$\mu_k = \int_0^\infty n(r, x, t) r^k dr. \quad (6)$$

The transformed PBE for the k^{th} order moment reads

$$\frac{d\mu_k}{dt} = J\delta(r - r^*) r^{*k} + k \cdot \sum_{i=0}^N \mu_{k-1} G(r_i). \quad (7)$$

Which is a set of ordinary differential equations (ODE) for the moments. These depend on the previously defined functions of the nucleation rate J (Eq. (3)), critical radius r^* (Eq. (1)), growth law $G(r)$ (Eq. (4)) and δ stands for the Dirac delta function. The mentioned models were implemented into an OpenFOAM® solver for the turbulent heat transfer. For the evaluation of the performance of the numerical apparatus several simulations of the flow over a cooled plate were done. The representative results are shown on Fig. 1.

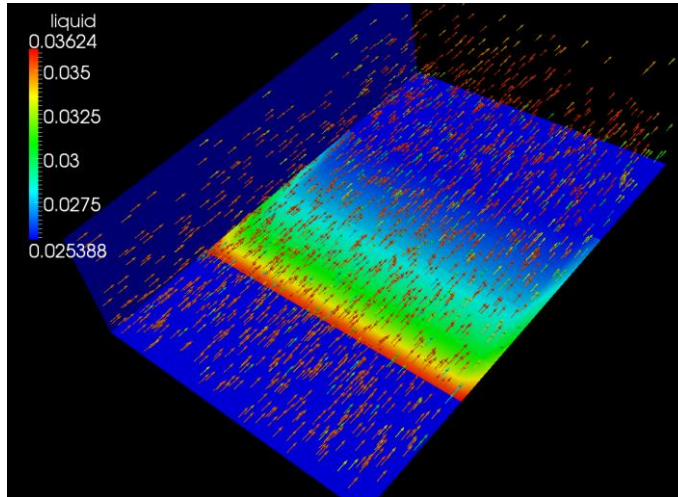


Fig. 1: Cooled wall in a rectangular channel (Condensing flow).

On Fig. 2 results of five simulations are reported. The domain is a simple rectangular channel. Humid warm air of 46°C enters the inlet and passes a cooled wall losing humidity due to the nucleation and the continuous droplet growth.

3. Conclusions

A method for the calculation of the condensation rates using the classical nucleation theory and population balance equation was briefly introduced. The methods' benefit is that it uses fewer empirical correlations than the conventional methods, and allows for physical modeling of the condensation process based on first principles. The comparison with the experimental results (not reported here) reveals that the features of the process are truly represented. For instance the curves on Fig. 2 have the same ordering, which means that the influence of the driving force ΔT is represented correctly. This paper set out to sketch an approach to the numerical modeling of the condensation within air heat exchangers. We can state that the presented procedure captures the initial stage of the condensation and the first part of our work is thus completed. The next phase will include the validation and rigorous testing of the model. Furthermore, the inclusion of the coalescence term in the PBE, model deployment in a two – phase solver, Rusche (2002), or the implementation of a second droplet internal coordinate: the droplet temperature (Marchisio & Fox, 2013) will be incorporated.

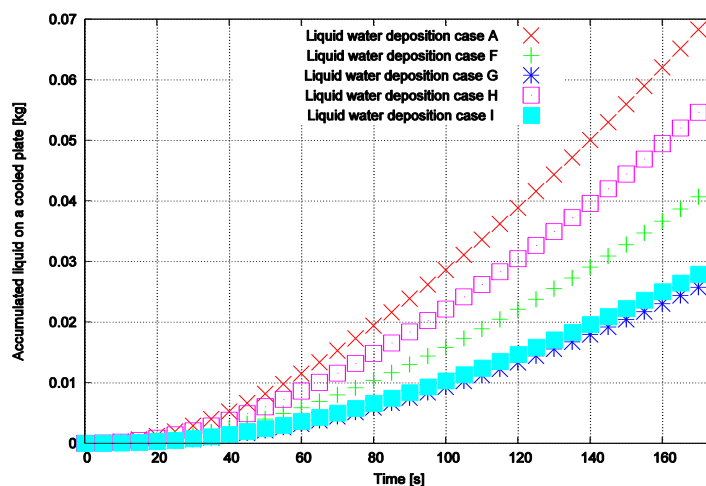


Fig. 2: Condensation rates: Case A, F, G flowrate = 375 m³/h cooled plate temperature A: 14⁰C, F: 17.5⁰C, G: 21.5⁰C. Case H, I flowrate 310 m³/h cooled plate temperature H: 17.5⁰C, I: 21.5⁰C.

Acknowledgement

The authors gratefully acknowledge the funding provided by Klima- und Energiefonds for the project 829964 in the framework of the “NEUE ENERGIE 2020” programme.

References

- Becker, R. & Döring, W. (1935) Kinetische Behandlung der Keimbildung in übersättigten Dämpfen. *Ann. Phys.*, 416, pp. 719-752.
- Girshick, S. L. & Chiu, C.-P. (1990) Kinetic nucleation theory: A new expression for the rate of homogeneous nucleation from an ideal supersaturated vapor. *J. Chem. Phys.*, 93, pp. 1273.
- Heidenreich, S. & Ebert, F. (1995) Condensational droplet growth as a preconditioning technique for the separation of submicron particles from gases. *Chemical Engineering and Processing: Process Intensification*, 34, pp. 235-244.
- Krischer, S. & Grigull, U. (1971) Mikroskopische Untersuchung der Tropfenkondensation. *Wärme - und Stoffübertragung*, 4, pp. 48-59.
- Marchisio, D. L. & Fox, R. O. (2013) *Computational Models for Polydisperse Particulate and Multiphase Systems*. Cambridge Books Online.
- McGraw, R. (1997) Description of Aerosol Dynamics by the Quadrature Method of Moments. *Aerosol Science and Technology*, 27, pp. 255-265.
- Nusselt, W. (1916) Die Oberflächenkondensation des Wasserdampfes. *VDI-Z.*, 60, pp. 541-546 and 569-575.
- OpenFOAM (2013). The open source CFD toolbox: <http://www.openfoam.com>.
- Pauschenwein, G. J.; Reichl, C.; Windholz, B.; Moretti, I. & Monsberger, M. (2010) CFD simulations for solar collectors including condensation and ice accretion., *Eurosun 2010*.
- Ramkrishna, D. (2000) *Population balances: Theory and applications to particulate systems in engineering*. Access Online via Elsevier.
- Reiss, H.; Kegel, W. K. & Katz, J. L. (1997) Resolution of the Problems of Replacement Free Energy, 1/S, and Internal Consistency in Nucleation Theory by Consideration of the Length Scale for Mixing Entropy. *Phys. Rev. Lett.*, 78, pp. 4506-4509.
- Rusche, H. (2002). *Computational fluid dynamics of dispersed two-phase flows at high phase fractions*, PhD Thesis, Imperial College, London.
- Song, T.; Lan, Z.; Ma, X. & Bai, T. (2009) Molecular clustering physical model of steam condensation and the experimental study on the initial droplet size distribution. *International Journal of Thermal Sciences*, 48, pp. 2228-2236.
- Vehkamäki, H. (2006) *Classical Nucleation Theory in Multicomponent Systems*. Springer, Berlin Heidelberg.
- Vemuri, S. & Kim, K. (2006) An experimental and theoretical study on the concept of dropwise condensation. *International Journal of Heat and Mass Transfer*, 49, pp. 649-657.
- VDI-Wärmeatlas (2002) *Berechnungsblätter für den Wärmeübergang*. Springer-Verlag, Berlin Heidelberg New York.

TEMPERATURE FIELD OF SPARK PLUG IN THE SI ENGINE

S. Beroun^{*}, P. Brabec^{**}, A. Dittrich^{***}, L. Mikulanin^{****}

Abstract: Spark plug is one of the most thermal loaded component in the cylinder of the SI (spark ignition) engine. The most exposed parts of the spark plug are the lowest part of the housing, centre and ground electrodes, which are inside of combustion chamber. The article shows the calculating field of temperature on spark plug and explains direct measuring of temperatures at spark plug housing. Process of calculating field of temperature on the spark plug through calibrated model was made for confirming efficiency of spark plugs housing design modifications of and the development of spark plug with integrated ignition chamber.

Keywords: Spark Plug, Thermal Stress, Heat Flow, Thermal Field.

1. Introduction

The all walls of combustion space in the cylinder engine are affected by heat transfer from cylinder charge. The temperature field in the material of wall from the surfaces in the cylinder determines next to the heat flow (which has a decisive influence and in different locations of engine cylinder is different) and heat conduction in the wall material and the heat transfer from the outer side wall to another heat transfer environment (coolant, the other walls material, ...).

Mechanism of heat transfer into the walls of combustion chamber depends on several factors which influence appears from essential of molecular-kinetic gas theory or their variability in the procedure of power cycle of SI engine. Heat flow into to walls of combustion chamber in the engine (cylinder, piston, cylinder head etc.) is defined by Newton's equation:

$$\dot{Q}_S = \alpha_p \cdot S \cdot (T_p - T_s), \quad (1)$$

where α_p is heat transfer coefficient, S is heat transfer surface, T_p is temperature of cylinder charge and T_s is temperature of the surface. The knowledge of heat transfer coefficient is very essential request for heat flow calculation. Heat transfer coefficient depends on lot of factors but most on the actual condition of cylinder charge (pressure, temperature, velocity of the fluid). The research tasks (theoretical, experimental) focused on solving of functional dependence of design and work conditions of heat transfer coefficient in cylinder of the engine are still actual and results into more accurate calculations.

One of the most uses the equation for calculation of heat transfer coefficient in cylinder of the engine is empiric Eichelberger's equation (year 1939). Equation for SI units:

$$\alpha_p = 2,485 \cdot \sqrt[3]{Z \cdot n} \cdot \sqrt{p \cdot T}. \quad (2)$$

α_p [W m⁻² K⁻¹], piston stroke Z [m], n engine revolutions [min⁻¹], p [MPa] a T [K] are immediate pressure and immediate temperature of cylinder charge. In the 1960s Woschni published the results of research work about heat transfer coefficient defined by characteristic numbers (Woschni, 1967). Calculation was based on description of heat transfer inside of tube with turbulent flow. Research works on the combustion engines in late 1990s (modern measuring and computational technique) allowed to get new knowledge which led to more accurate results of empiric equations for heat transfer coefficient and was

* Prof. Ing. Stanislav Beroun, CSc.: Technical University of Liberec, Studentská 2; 461 17, Liberec; CZ, stanislav.beroun@tul.cz

** Ing. Pavel Brabec, Ph.D.: Technical University of Liberec, Studentská 2; 461 17, Liberec; CZ, pavel.brabec@tul.cz

*** Ing. Aleš Dittrich: Technical University of Liberec, Studentská 2; 461 17, Liberec; CZ, ales.dittrich@tul.cz

**** Ing. Lukáš Mikulanin: Technical University of Liberec, Studentská 2; 461 17, Liberec; CZ, lukas.mikulanin@seznam.cz

more closer to values in the real engine. Newest empiric equation for heat transfer coefficient defined by Bargende (1990) is based on detailed explanation of condition in close proximity of walls (based on so-called wall function describes thermal boundary layer and different evaluations in cases of unburned mixture and burned gases). All equations referred above contains some differences (for each one different) of functional dependence of heat transfer coefficient in the engine depends on pressure and temperature of cylinder charge. Comparison of functional dependence of α_p according to various equations is on Fig. 1. Significant differences in values of heat transfer coefficient according to various equations are in the area of burning (particularly at Bargende's equation which includes the consequence of burned gas).

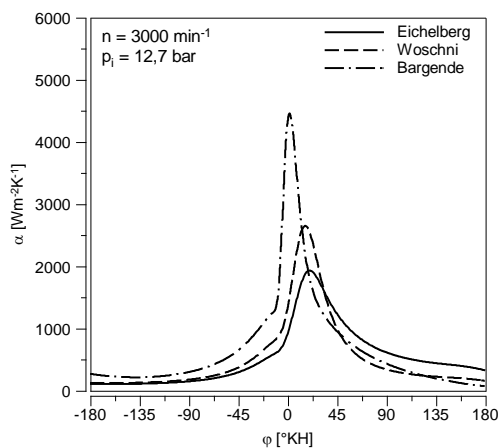


Fig. 1: Function of heat transfer coefficient calculated by various equations for vehicle atmospheric combustion engine.

2. Computational Model

Individual parts of computational model were based on description of thermal-mechanical process in cylinder of the engine. The basic is made by function dependence of gas pressure and temperature during operating cycle in cylinder of the engine for specific rating of the engine. Calculating of gas pressure and temperature was made in simple software which is long term used at workplace of authors. Result of calculating gas pressure and temperature is shown at Fig. 2.

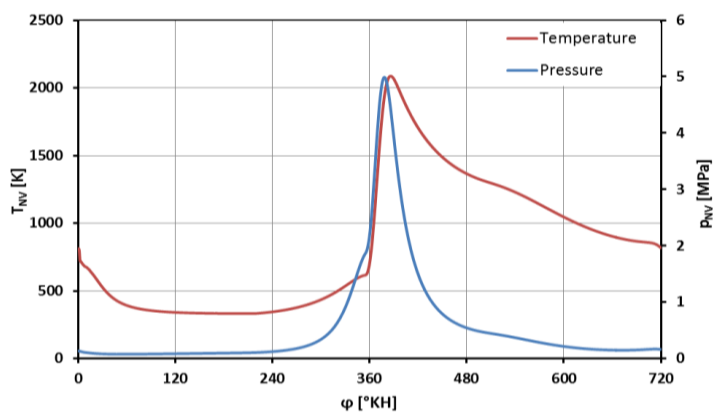
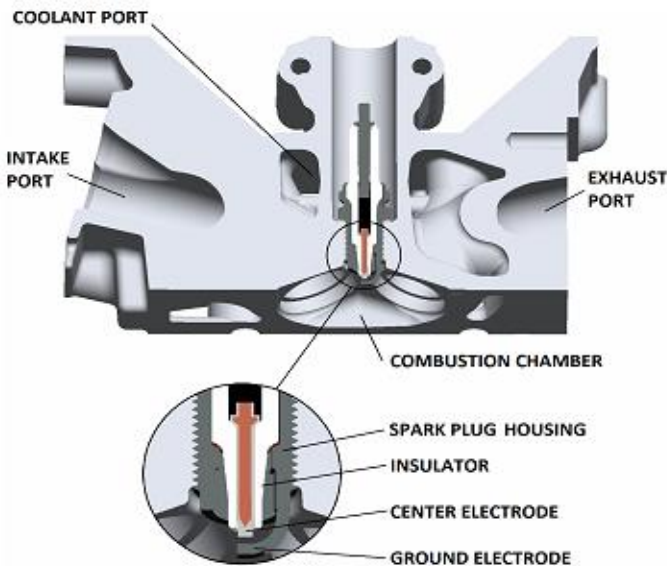


Fig. 2: Function of gas pressure and temperature in cylinder of the engine: computational model is verified by measured pressure cycle in cylinder (high pressure indication).

According to calculated function of gas pressure and temperature in cylinder of the engine have been calculated heat transfer coefficient according of Eichelberg equation. In the next step were computed dimensions of heat transfer surfaces which affect to thermal field of spark plug (cylinder head, lowest part of spark plugs housing, insulator, and center and ground electrode). Also was calculated heat flow into surfaces, for specific rating of the engine, referred above (heat flow for cylinder head and intake exhaust or cooling ports was made by same way).

Field of temperature was modelled by software Pro/ENGINEER Wildfire 4.0 in unit for finite elements method analysis called Pro/MECHANICA. Models of cylinder head and all parts of spark plug were created due to drawing documentation. Model respects the material aspect and attributes of each used part. On the all heat transfer surfaces of cylinder head and spark plug was used boundary condition of heat load named "HEAT LAOD". Heat flow values for heat transfer surfaces of cylinder head and spark plug was computed for $n = 5000 \text{ min}^{-1}$ a 100% engine load (Chiodi & Bargende, 2001).



Mesh of elements was generated by "AutoGEM" generator, in lowest part of spark plugs housing was used thickening of mesh for higher result precision (for mesh was used elements "tetra" with maximum size of element 1 mm for lowest part of housing should be presented as follows).

Fig. 3: Surfaces for boundary conditions.

Computed result of field of temperature in required spots was compared with result of direct measuring of temperatures on the housing of spark plug. Computational model was calibrated with correcting coefficient K (reference to Eichelberg equation), which changes values of heat flow into cylinder head and spark plug, to gain acceptable accordance with measured results.

3. Measuring Temperature of Spark Plugs Housing

In the spark plugs housing were drilled 2 holes of diameter 0.45 mm and depth until 0.45 mm from bottom of housing to put jacketed micro thermocouple ($\varnothing 0.25 \text{ mm}$). One measured spot is above a welded ground electrode and the other one is on the opposite side of the housing. Third measured spot is at seat surface on outer spark plugs gasket. The scheme of measuring spark plug housing and results measured at engines speed characteristic shown at Fig. 4.

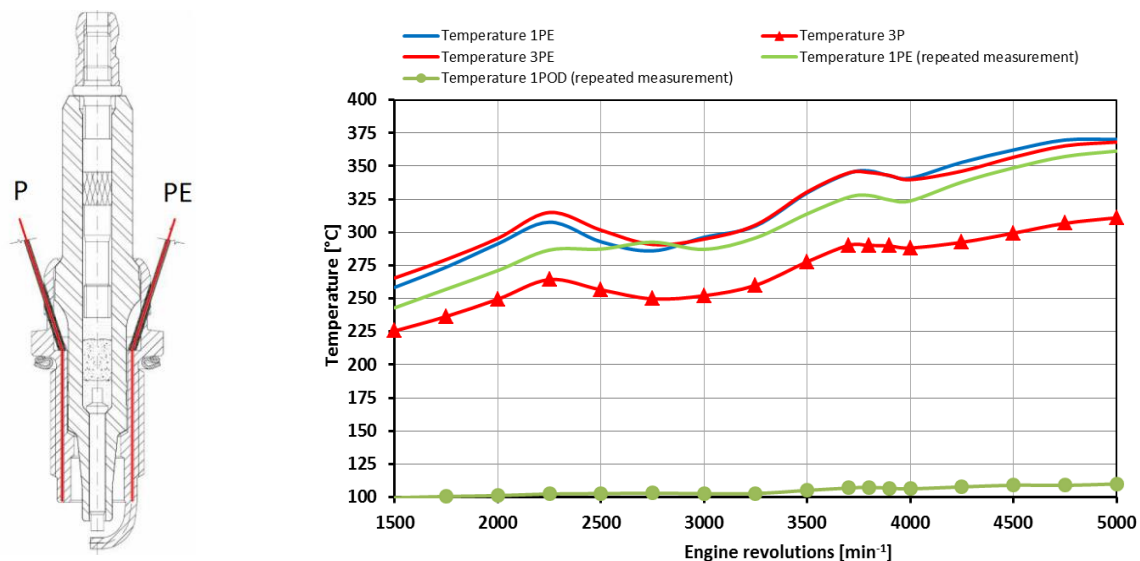


Fig. 4: Measuring spark plug with micro thermocouple inside of housing and results of measurement. For calibration were used measured temperatures at $n = 5000 \text{ rpm}$ and 100% engine load.

Note: Drilling of very small and depth holes into spark plugs housing was made by company SHD Zahrádky. Assembly of spark plug was made with cooperation of company BRISK Tábor. Assembly of micro thermocouple into holes with diameter 0.45 mm is made by using of thin walled pipes.

4. Calculating Field of Temperature for Spark Plug

Field of temperature on spark plug after calibration is shown at Fig. 5. To gain acceptable accordance with measured results in required spots was used correcting coefficient $K = 1.4$.

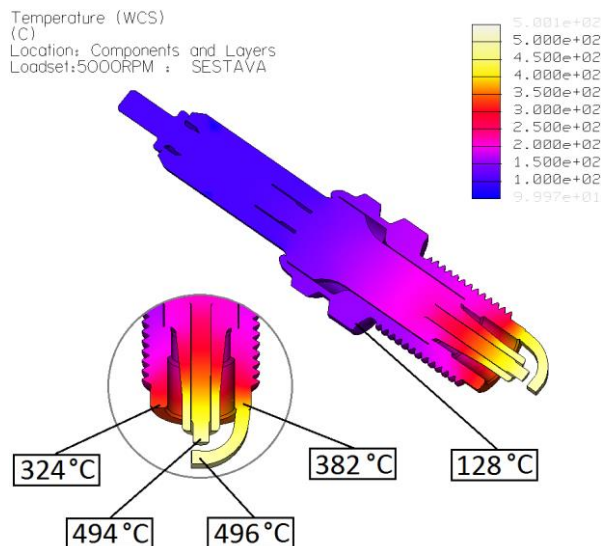


Fig. 5: Result of computed modelling of spark plugs temperature field.

Beside of knowledge of temperatures at lowest part of spark plug housing is very significant fact, that quite simple computational model is able to provide reliable results of temperatures at lowest part of spark plugs housing. The experiences from calculating of model or technically difficult measurement of temperatures of spark plug housing are very valuable for development of spark plug with integrated ignition chamber.

5. Conclusions

The results performed research works show the ability to solve the complicated problems by acceptable combination theoretic, computational and experimental procedures, which are found on reasonable simplification. Experimental program on spark plug with integrated ignition chamber cellule includes all procedures, which have been checked on classical spark plug.

All experimental works they are realized on a vehicle SI engine in Laboratory of driving units at Institute for nonmaterial, advanced technology and innovation on Technical University of Liberec. The results of research works contain first of all the criteria for complex evaluation (energy, power, emission and operation parameters) of the engine using the mixtures ignition by the spark plug with integrated ignition chamber. The investigation of the thermal load of new spark plug design (with ignition chamber, integrated to the housing of spark plug) has responsible position in this research works from standpoint of the functional reliability and durability of new spark plug design.

Acknowledgement

This research has been realized using the support of Technological Agency, Czech Republic, programme Centres of Competence, Project # TE01020020 Josef Božek Competence Centre for Automotive Industry.

References

Woschni, W. (1967) Untersuchen zum Wärmeübergang in Verbrennungsmotor, in: Proc. International Combustion Engines Conference Bucharest.

Chiodi, M. & Bargende, M. (2001) Improvement of Engine Heat-Transfer Calculation in the Three-Dimensional Simulation Using a Phenomenological Heat-Transfer Model, SAE, 2001-01-3601.

INJECTOR OF LIQUID LPG

S. Beroun^{*}, P. Brabec^{**}, A. Dittrich^{***}, T. T. Nguyen^{****}

Abstract: The formation of the mixture by injecting liquid LPG into the intake manifold of vehicle SI engine (conception MPI) is a perspective variant for alternative fuel system for operating the engine on LPG. This paper summarizes the results of theoretical and experimental research aimed at solving problems for injecting liquid LPG and presents a new design of the end part of the injector of liquid LPG.

Keywords: Alternative fuel LPG injector, Icing of injector, Computational and experimental research, New design of the icingless liquid LPG injector.

1. Introduction

The LPG injector is assembled from the electromagnetic valve (EV) and the end part (EP) with the channel for LPG leading to the outlet nozzle (ON) – see scheme at Fig. 1 (schema contains modifications LPG injectors for experimental research). After injection of LPG from the EV the LPG pressure extremely drops in the channel, the intensive evaporation of the LPG in the channel changes of liquid state to gaseous state and before outlet nozzle there is the damp steam of LPG with the very low temperature (temperature of damp steam of LPG at discharge by outlet nozzle is reduced to below -30 °C). The geometric parameters of the channel (the volume of the channel before outlet nozzle V_{BON}) and the outlet nozzle (the area of the outlet nozzle S_{ON}) have the very important influence both on the state of LPG and its physical quantities in the channel and the spray duration of the LPG to the manifold air.

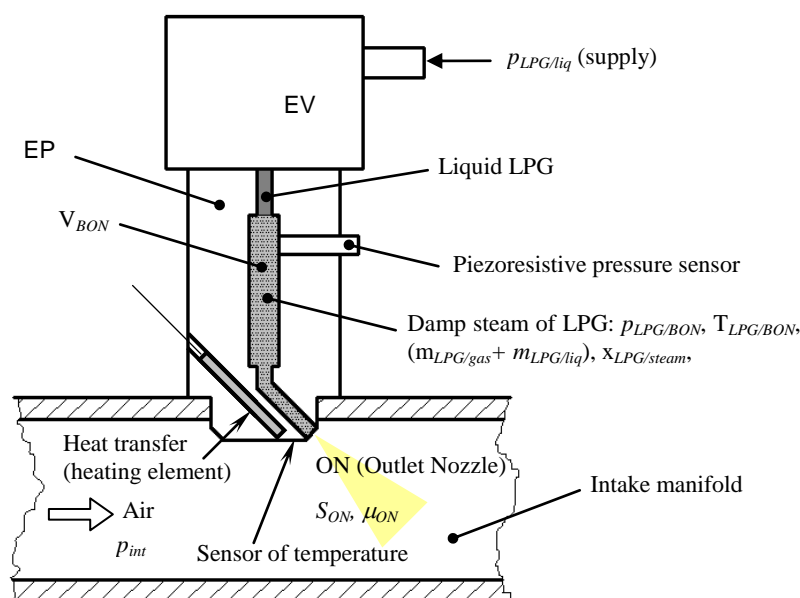


Fig. 1: The scheme of the injector for the liquid LPG injection.

^{*} Prof. Ing. Stanislav Beroun, CSc.: Technical University of Liberec, Studentská 2; 461 17, Liberec; CZ, stanislav.beroun@tul.cz

^{**} Ing. Pavel Brabec, PhD.: Technical University of Liberec, Studentská 2; 461 17, Liberec; CZ, pavel.brabec@tul.cz

^{***} Ing. Aleš Dittrich: Technical University of Liberec, Studentská 2; 461 17, Liberec; CZ, ales.dittrich@tul.cz

^{****} Ing. Thanh Tuan Nguyen, PhD.: Technical University of Liberec, Studentská 2; 461 17, Liberec; CZ, tuanpraha@gmail.com

By the effect of very low temperature of the LPG spray raises the icing from the humidity of the atmospheric air on the external surface of the outlet nozzle. The icing fractures off from the outside of the outlet nozzle is the risk for the trouble-free engine running (misfire chance) (Mareš et al., 2007). Trouble-free operation of the spark-ignition engine with liquid injection LPG therefore must be secured in such a structural solution to the end part of the injector of liquid LPG into the intake manifold to prevent freezing of the discharge nozzle of the injector. The design of the end part of LPG injector must be arranged against the icing forming.

The authors of this paper accomplish the original theoretical studies about the liquid LPG injection to the manifold air: the results of this research works are contained in (Beroun et al., 2013) and (Nguyen, 2013). Illustration from theoretical studies of processes in a channel in the EP is in Fig. 2.

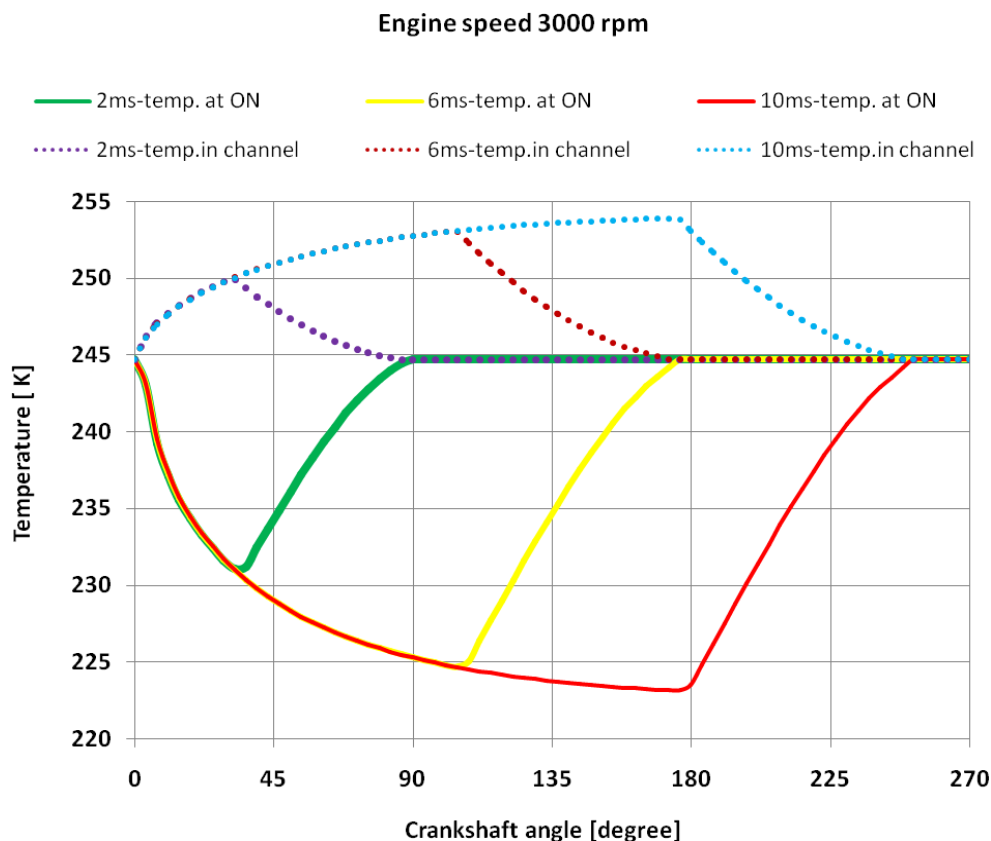


Fig. 2: The courses of the calculated temperature of LPG in the channel EP and outlet nozzle ON. The temperature of the damp steam of LPG in the channel is very low at the beginning of the injection of LPG into the empty channel, temperature damp steam of LPG in the channel increases with the increasing pressure of LPG in the channel, and the temperature of the damp steam of LPG in the channel again decreases during emptying the channel. Very low temperature damp steam of LPG in the outlet nozzle is intended expansion of damp steam of LPG (discharge takes place mostly critical speed).

2. Experimental Research of Liquid LPG Injector

In the end part of the liquid LPG injector was installed heating element and into the channel of end part of the injector liquid LPG was placed a pressure sensor. In the vicinity of the outlet nozzle is mounted the thermocouple on a wall. Liquid LPG injector was mounted in the intake manifold model and measurement was performed in all operating modes (motor speed-frequency injection, injection dose-opening time EV). Experimental works were carried out with the assembly of the fuel system (pressure tank for LPG with pump, injection pressure regulator and LPG solenoid valve) from company Vialle and the own (special) control unit for controlling the EV. Measurements were performed under laboratory conditions ($t_a \cong 20\text{ }^\circ\text{C}$). A selection of experimental results with a commentary is in Fig. 3. The programme of the measuring was performed both without the heating (marking „normal“) and with the heating of the end part of injector (with the intensity control of the heating to reach the temperature on the external surface of the outlet nozzle to $5\text{ }^\circ\text{C}$ – marking „reg.5C“).

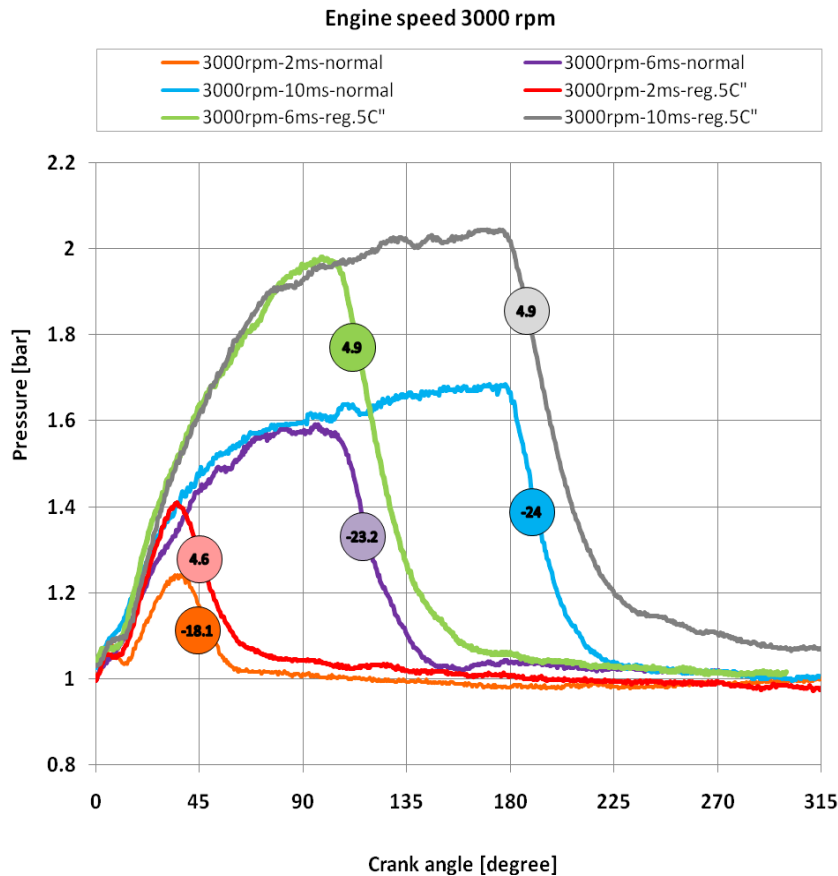


Fig. 3: Pressure courses in the channel of the EP of the injector there are significantly influenced by the temperature in the EP of the injector (the numbers in the circle are the measured temperature near the outlet nozzle). The heating of the end part of the injector increases both the temperature and the pressure LPG in the channel. The extension of time for spray duration of LPG into the intake manifold was due to an increasing the value of the steam quality "x" (coefficient of the steam saturation) and thus decreases the mass flow of LPG through an outlet nozzle into the intake manifold. Pressure course (especially evident in the region around zero) might be affected by cold temperature while the pressure sensor was exposed to very low temperature over a long period of time (temperature drift).

The experimental results showed that for elimination of the risk of "icing" is sufficient heat output for warming EP about 20 - 25 W. Measurements also showed that the heat input into the channel of end part of the injector extends the time of a flow of damp steam of LPG from the channel and is therefore ineffective - if the heating of end part of the injector is only in the region of outlet nozzle, required heating power will be then reduced to about 10 - 15 W. These findings led to the proposal of a new structural configuration of end part of the injector.

3. Construction of the End Part of the Liquid LPG Injector with Heating of Nozzle

The new design of the end part of the injector for the liquid LPG is designed so that the heat flow of heating had been directed to part of the outlet nozzle. This arrangement significantly reduces the required heating capacity to ensure the injection of liquid LPG without icing. Heating of the outlet nozzle is secured to either the flow of liquid from the engine cooling system or electrical heating. Both variants are structurally resolved, variant of heating the flow of liquid from the engine cooling system is already prepared as a specimen to verify on the engine (see Fig. 4). For the variant with electric heating is looking for a suitable heating element.

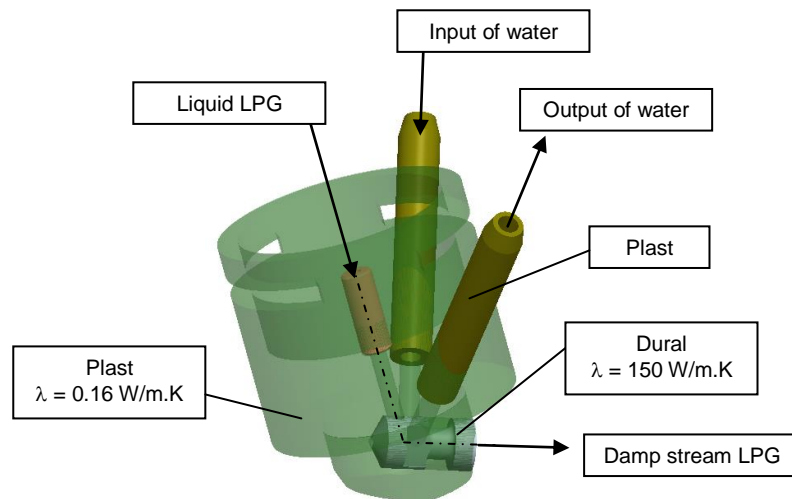


Fig. 4: The new design of the end part of the injector for the liquid LPG - heating of the outlet nozzle is secured by the flow of liquid from the engine cooling system.

4. Conclusions

The reliable solution for the troublefree variant of the liquid LPG injector for alternative fuel system for operating the engine on liquid LPG is the heating of the wall near the outflow nozzle: either by flow of the coolant from the cooling system of the engine, or using of the local electric heating. The research works show, that the sufficient heating power for heat flow of heating, which had been directed to the wall near the outflow nozzle, is for prevent of icing about 10 – 15 W (the solution is founded on the different values of the material heat conductivity for the end parts of injector). Fig. 4 shows the concept of such variant of LPG liquid injector with the heating using flow of coolant.

Acknowledgement

This research has been realized using the support of Technological Agency, Czech Republic, programme Centres of Competence, Project # TE01020020 Josef Božek Competence Centre for Automotive Industry

References

- Beroun, S., Brabec, P., Dittrich, A. , Dráb, O. & Nguyen Thanh, T. (2013) Computational Modeling of the liquid LPG Injection into the suction Manifold of an SI Vehicle Engine, in: Proc. 4th International Conference on Mechanical and Aerospace Engineering, Moscow, ISSN 1660-9336, pp. 355-359. Journal of Applied Mechanics and Materials, 390, pp. 355-359. ISSN 1660-9336 (<http://www.scientific.net/AMM.390.355>).
- Nguyen Thanh, T. (2013) Injection of liquid LPG into the intake manifold of the engine, Doctoral Thesis, Technical University of Liberec.
- Mareš, J., Beroun, S., Blažek, J. & Holubec, R. (2007) Automotive SI Engine with the Injection of the liquid LPG into the Inlet Manifold. Journal of KONES, Vol. 14, No. 3, ISSN 1231-4005.
- Cengel, Y. A., Boles, M. A. (2008) Thermodynamics, in: Proc. 6th edition. McGraw - Hill Comp., New York, ISBN 978-0-07-352921-9.
- Kim, H., Im, J. K., Lee, J. H., Park, J. N. (2007) An Apparatus for Preventing Icing of Injector for LPG Vehicle [patent]. KR 100757123. 10.9.2007.

INTRA-VOXEL MICRO-ELASTO-PLASTICITY FOR CT-BASED PATIENT-SPECIFIC FRACTURE RISK ASSESSMENT OF VERTEBRAE

R. Blanchard^{*}, C. Morin^{**}, A. Vella^{***}, Z. Sant^{****}, Ch. Hellmich^{*****}

Abstract: *Following previous studies employing X-ray physics and continuum micromechanics in order to retrieve voxel-specific elastic properties from Computed Tomographs (CT) (Hellmich et al., 2008), we here present an updated and improved approach applied to in-vivo images of vertebrae of a young patient. This approach concerns both elasticity and strength, and therefore promises considerable impact on patient-individual, image-based fracture risk assessment. This is done for the described voxel-specific heterogeneous case, as well as for vascular porosities averaged over the trabecular core. Homogeneous simulations obviously underestimate the fracture risk in the presently studies case.*

Keywords: Continuum micromechanics, Finite Element model, Spine, Bone strength.

1. Introduction

We here present a novel approach for a patient-specific failure risk assessment from in-vivo CT (Computer Tomography) images. This approach is directly based on the fundamentals of X-ray physics and those of applied micromechanics. Extending the methodology for relating CT data to voxel-specific elasticity in bone (Hellmich et al., 2008; Blanchard et al., 2013) and in biomedical materials for transplants (Scheiner et al., 2009, Dejaco et al., 2012), we here convert information from an in-vivo CT scan of a young patient into voxel-specific bone strength properties by means of a multiscale continuum micromechanics strength model (Fritsch et al., 2009). These properties are then mapped onto a Finite Element mesh, which allows for assessing the effect of material inhomogeneity of bone on the overall structural behavior of the organ. In this context, it is of particular importance to reproduce the morphology of the vertebral body in patient-specific applications, particularly in cases of certain spine pathologies such as scoliosis, where the heterogeneity in bone density within the organ is very important. Therefore, the consideration of patient-specific and spatial heterogeneity within the bone is crucial for medical application.

2. Methods

A CT scan of a motion segment of a 15-years-old male patient, consisting of two lumbar vertebral bodies L3 and L4 was obtained from Mater Dei Hospital, Malta. The HiSpeed Dual medical CT scanner from General Electrics in helical mode was employed with the following parameters: source voltage: 140 kV, source current: 110 μ A, exposure time: 1000 ms, image pixel size: 0.324 mm, slice spacing: 1.25 mm. The resulting DICOM images were then processed by means of a drawing software in order to capture the geometry of the structure and transported into a Finite Element analysis commercial software. The model has been already utilized in the work published by one of the co-author (Sant et al., 2012). For our purpose, the lumbar vertebral body L3 was isolated from the segment. In these CT images, capturing not

* Romane Blanchard: Vienna University of Technology, Institute for Mechanics of Materials and Structures, Karlsplatz 13/202, A-1040, Vienna, Austria, romane.blanchard@tuwien.ac.at

** Claire Morin: Ecole Nationale Supérieure des Mines, CIS-EMSE, CNRS:UMR 5307, LGF, F-42023, Saint-Etienne, France, claire.morin@emse.fr

*** Alain Vella: Mechanical Engineering Department, University of Malta, Tal Qroqq; MSD2080, Msida; Malta, (Imperial College London, Great Britain), carmel.v86@gmail.com

**** Dr. Ing. Zdenka Sant: Mechanical Engineering Department, University of Malta, Tal Qroqq; MSD2080, Msida; Malta, zdenka.sant@um.edu.mt

***** Prof. Christian Hellmich: Vienna University of Technology, Institute for Mechanics of Materials and Structures, Karlsplatz 13/202, A-1040, Vienna, Austria, christian.hellmich@tuwien.ac.at

only the bone structure of a vertebral body, but also the surrounding soft tissue, the X-ray attenuation information is stored in terms of 8-bit grey values, increasing with intensifying attenuation. In order to separate soft and hard tissues, we perform a statistical analysis of the voxel-specific attenuation information leading to the histogram depicted in Fig. 1a.

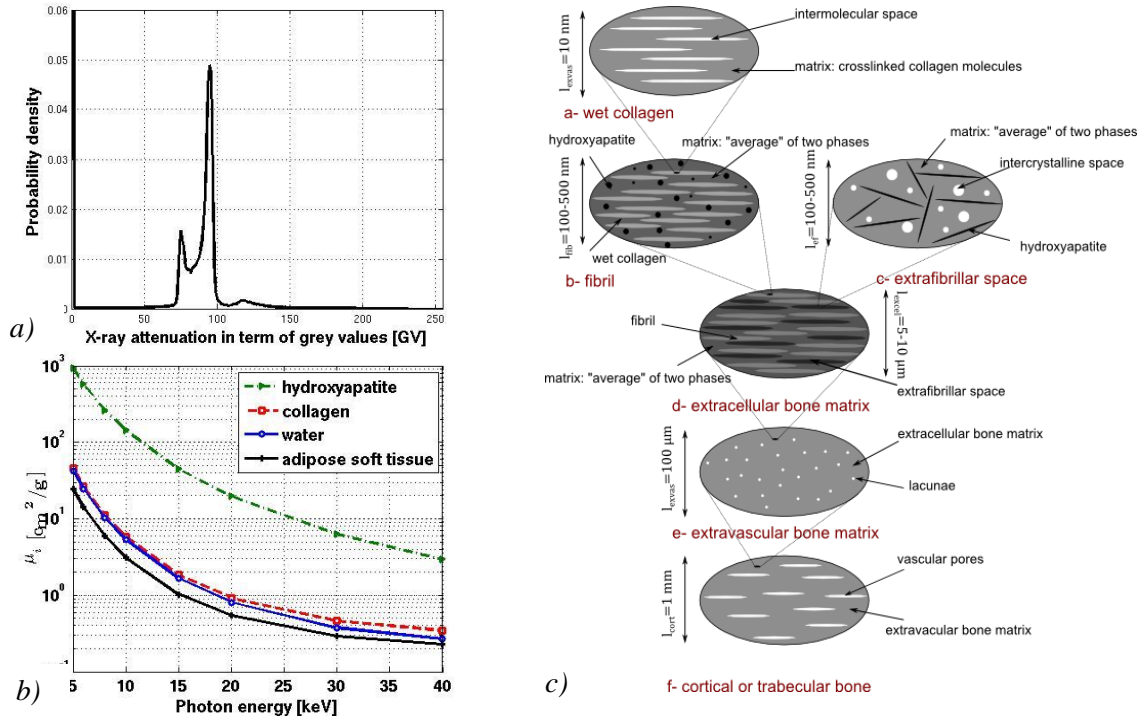


Fig. 1: a) Frequency distribution plot of the attenuation information in terms of grey values of the vertebral body L3; b) X-ray attenuation coefficients of the elementary constituents of bone tissue, as function of the photon energy; c) Multiscale micromechanical representation of bone material, similar to Fritsch et al. (2009).

As a first step, we translate the attenuation information in terms of grey values contained in each of the 0.324 mm - sized voxels building up the computed tomograph, into voxel-specific vascular porosity values. Therefore, we consider the linear relation between grey values and X-ray energy-dependent attenuation coefficients, involving three unknowns (two linearity constants and the X-ray energy). The latter are obtained from three known attenuation-energy relationships related to three characteristic points found in the grey value histogram: (i) the left-most peak in this histogram relates to fatty physiological fluid, at $GV_{\text{adipose}} = 70$, (ii) the central peak relates to soft tissues as found in the inner organs around the spine, at $GV_{\text{soft}} = 90$, and (iii) the densest voxel in the image relates to compact bone with quasi-zero vascular porosity, at $GV = 255$. The energy-dependent attenuation coefficient of fat is documented in the NIST-database (NIST, n.d.). The latter also gives access to the energy-dependent attenuation coefficients of collagen and water, and their volume ratio in soft tissue [which can be gained from their mass densities and that of soft tissue (Mast, 2000)]. The volume ratio, in turn, in conjunction with the average rule for attenuation coefficients, gives access to the attenuation coefficient of soft tissue.

Also the attenuation coefficient of compact bone is retrieved from averaging the attenuation coefficients of collagen, water, and hydroxyapatite, according to their volume fractions in vertebral extracellular bone matrix. The latter follows from the mass density of extracellular bone matrix in vertebrae (Malandrino et al., 2012), and the averaging of collagen, water, and hydroxyapatite mass densities according to the composition rules evidenced in Vuong and Hellmich (2011).

At the extravascular level, the average rule is written for an RVE of extravascular bone tissue composed of extracellular bone matrix and water-filled lacunar porosity, see Fig. 1c. The attenuation coefficient for extravascular bone matrix enters the average rule for an RVE of macroscopic bone made of extravascular bone matrix and the water-filled vascular porosity; see Fig. 1c. Knowing the attenuation coefficient at each and every grey value, we compute the grey-value-specific porosity.

The vascular porosity values, obtained in this way, enter a continuum micromechanics model for bone (Morin and Hellmich, 2013), which thereupon delivers voxel-specific elastic properties. The tissue mass densities can then be related to the Young's modulus, to the Poisson's ratio, and to the transverse shear modulus.

The latter are mapped onto a 3D Finite Element mesh developed from the same patient data (Sant et al., 2012), consisting of solid elements representing the trabecular bone material, and of shell elements representing cortical bone material. In order to investigate the effect of introducing material heterogeneity into the Finite Element simulation, we build two models: one so-called homogeneous model, with trabecular tissue having homogeneous material properties, namely the elastic properties of the average grey value present in the organ, and one model, so-called heterogeneous model, with element-specific elastic properties. In the latter case, the voxel-specific density is associated to the finite elements by a barycentric-based in-house algorithm. A distributed unit load of 1 MPa is applied onto the upper surface of the third lumbar vertebral body, corresponding anatomically to the upper endplate. The corresponding stress and strain distributions are computed throughout the organ.

These stress states are fed into a six-scale strength up-scaling model for bone, namely an algorithmically stabilized and physically improved version of (Fritsch et al., 2009), as to compute the element-specific proportionality factors by which the actual stresses are multiplied to reach the material yield or failure.

3. Results

The voxel-specific intertrabecular porosity and the elasticity reflect the very inhomogeneous nature of the investigated vertebra, see Fig. 2: The left side of the organ is less porous, and hence, denser and stiffer than the right side of the organ.

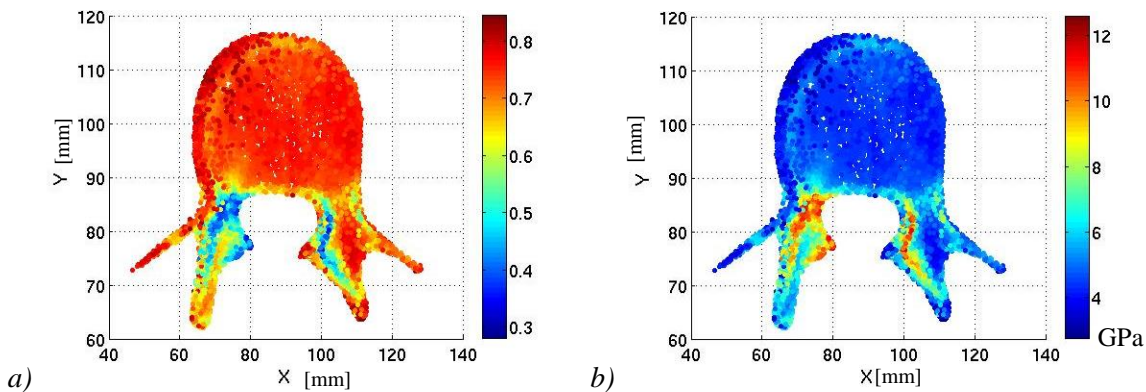


Fig. 2: Porosity and stiffness maps in a cross section of the Finite Element model, oriented orthogonal to the superior-inferior direction: a) Vascular porosity and b) Axial Young's modulus.

The factors by which the element-specific stresses, resulting from the 1 MPa pressure loading on the organ, needed to be proportionally magnified to reach the yield point of this element are shown in Fig. 3; which also allows for the comparison of the homogeneous and heterogeneous cases. These factors are directly quantifying fracture risk, on the rigorous basis of engineering mechanics; even for load cases of different magnitude, such e.g. 2 MPa pressure. For the latter case, the yield factors of Fig. 3 needed to be multiplied by $\frac{1}{2}$.

The analysis of the results shows that the first plastification (related to the minimum yield factor) occurs inside the cortical shell in both models, in only two finite elements located near the cranial endplate; this is consistent with the location of high risk of initial failure observed by Eswaran (2007). The second observation is that most of the plastification occurs inside the trabecular core, which is consistent with the observation of microcracks in the trabecular core (Fyrhie and Schaffler, 1994).

As regards the difference between homogeneous and heterogeneous models, the use of a homogeneous model induces an overestimation of the elastic properties and an underestimation of the yield in the organ (see Fig. 3), as well as it neglects the patient-specific heterogeneity of the bony organ created by bone remodelling induced by everyday loads on the spine.

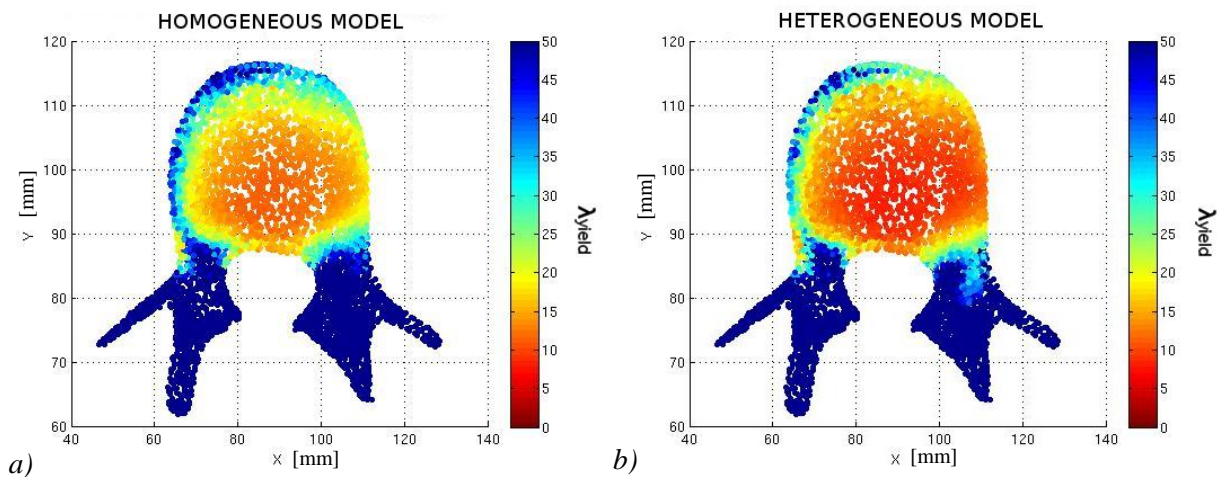


Fig. 3: Maps of the dimensionless yield factor related to 1 MPa pressure loading, shown across a cross section through the vertebral body, for: a) Homogeneous; b) Heterogeneous Finite Element model, undergoing a unit pressure loading.

Acknowledgement

Vertebra modelling was supported by the European Union Seventh Programme (FP7-ICT-2009-6) under the grant agreement number 269909, MySPINE; multiscale strength predictions became possible through the European Research Council (ERC), through the Project MICROBONE, grant number 257023, and the cooperation between Malta and Vienna is an outgrowth of COST Action MP1005, NAMABIO.

References

- Blanchard, R., Dejaco, A., Bongaers, E. & Hellmich C. (2013) Intravoxel bone micromechanics for microCT-based Finite Element simulations. *Journal of Biomechanics*, 46(15), pp. 2710-2721.
- Crawley, E., Evans, W. & Owen, G.M. (1988) A theoretical analysis of the accuracy of single-energy CT bone measurements, *Physics in Medicine and Biology*. 33(10), pp. 1113-1127.
- Dejaco, A., Komlev, V., Jaroszewicz, J., Swieszkowski, W. & Hellmich C. (2012) MicroCT-based multiscale elasticity of double-porous (pre-cracked) hydroxyapatite granules for regenerative medicine. *Journal of Biomechanics*, 45(6), pp. 1068-1075.
- Eswaran, S.K., Gupta, A., Keaveny, T.M. (2007) Locations of bone tissue at high risk of initial failure during compressive loading of the human vertebral body. *Bone*, 41(4), pp. 733-739.
- Fritsch, A., Hellmich, C., Dormieux, L. (2009) Ductile sliding between mineral crystals followed by rupture of collagen crosslinks: experimentally supported micromechanical explanation of bone strength. *Journal of Theoretical Biology*, 260, pp. 230–252.
- Fyhrie, D.P. and Schaffler M.B. (1994) Failure mechanisms in human vertebral cancellous bone. *Bone*, 15(1), pp. 105-109.
- Hellmich, C., Kober, C. & Erdmann, B. (2008) Micromechanics-based conversion of CT-data into anisotropic elasticity tensors, applied to FE simulations of a mandible. *Annals of Biomedical Engineering*, 36(1), pp. 108-122.
- Malandrino, A., Fritsch, A., Lahayne, O., Kropik, K., Redl, H., Noailly, J., Lacroix, D., & Hellmich, C. (2012) Anisotropic tissue elasticity in human lumbar vertebra, by means of coupled ultrasound-micromechanics approach. *Materials Letters*, 78, pp. 154-158.
- Mast, T.D. (2000) Empirical relationships between acoustic parameters in human soft tissues. *Acoustic Research Letters Online*. 1(2), pp. 37-42.
- Morin, C. & Hellmich, C. A multiscale poromicromechanical approach to wave propagation and attenuation in bone. *Ultrasonics*. In Press, <http://dx.doi.org/10.1016/j.ultras.2013.12.005>.
- NIST database www.nist.gov/pml/data/xraycoef
- Sant, Z., Cauchi, M. & Spiteri, M. (2012) Analysis of stress-strain distribution within a spinal segment. *Journal of Mechanics of Materials and Structures*, 7(3), pp. 255-263.
- Scheiner, S., Sinibaldi R., Pichler B., Komlev, V., Renghini, C., Vitale-Brovarone, C., Rustichelli, F. & Hellmich C. (2009) Micromechanics of bone tissue engineering scaffolds, based on resolution error-cleared computer tomography. *Biomaterials*, 30, pp. 2411-2419.
- Vuong, J. & Hellmich, C. (2011) Bone fibrillogenesis and mineralization: Quantitative analysis and implications for tissue elasticity. *Journal of Theoretical Biology*, 287, pp. 115-130.

OPTIMIZING THE FLOW RATE IN A PNEUMATIC DIRECTIONAL CONTROL VALVE

S. Blasiak^{*}, J. E. Takosoglu^{**}, P. A. Laski^{***}

Abstract: *The aim of the study was to optimize the flow of compressed air through a pneumatic directional control valve by optimizing the valve design. The 3D model of the valve was constructed in a CAD SolidWorks program. The assumptions concerning the performance included low friction, a small pressure loss, and accordingly high flow parameters, i.e. sonic conductance and critical pressure ratio. Ansys CFX, a computational fluid dynamics program, was used to simulate and optimize the flow of compressed air through the valve, and examine the basic flow characteristics. By optimizing the fluid flow at an early design stage, it will be possible to produce directional control valves with improved flow parameters.*

Keywords: Poppet valve, Control valve, Turbulent flow, CFD simulation, Numerical analysis.

1. Introduction

This work discusses a method for optimizing the flow of compressed air through a directional control valve, using the example of a poppet valve. Pneumatic directional control valves allow compressed air to flow into different paths by opening and closing ports to different pneumatic circuits. Developing a new valve or modifying an existing one is a demanding task; it requires great experience and knowledge on the character of the fluid flowing along the valve ways (Takosoglu et al., 2009). Modifications to the design need to be verified via testing. It is also vital to determine the flow parameters, i.e. the critical pressure ratio and sonic conductance, in accordance with the appropriate standard. Design modifications made to individual valves prior to their production would be extremely costly and time-consuming. If suitable software is employed to analyze the fluid flow and determine the flow characteristics, the design modification time will be shortened and the costs reduced. Simulations can be used to rigorously analyze the flow of compressed air through a valve, with the findings being applicable to the entire group of directional control valves. To perform a full verification, the simulation results need to be compared with the experimental data.

2. Solid Model of the Valve

The principle of operation of the 3/2 valve is illustrated in Fig. 1. In the initial position of the pilot piston (Fig. 1a), the fluid flows between ways 1 and 2, while way 3 is cut-off. After the plunger is moved to the opposite position (Fig. 1b), the fluid passes between ways 2 and 3, with way 1 being cut-off.

The solid model of the poppet valve is presented in Fig. 2. 3/2 directional control valves are the most common valves used in pneumatic drive and control systems.

3. Mathematical Model of the Flow

The flow analysis, conducted with a computational fluid dynamics (CFD) program, involved transforming differential transport equations to obtain detailed information about the phenomena

* Sławomir Blasiak, PhD.: Department of Mechanical Engineering and Metrology, Faculty of Mechatronics and Machine Design, Aleja Tysiąclecia Państwa Polskiego 7; 25-314 Kielce; Poland, sblasiak@tu.kielce.pl

** Jakub E. Takosoglu, PhD.: Department of Mechatronic Devices, Faculty of Mechatronics and Machine Design, Aleja Tysiąclecia Państwa Polskiego 7; 25-314 Kielce; Poland, qba@tu.kielce.pl

*** Paweł A. Łaski, PhD.: Department of Automation and Robotics, Faculty of Mechatronics and Machine Design, Aleja Tysiąclecia Państwa Polskiego 7; 25-314 Kielce; Poland, pawell@tu.kielce.pl

occurring in pneumatic control devices. The calculation process uses the laws of motion; the mathematical model of the directional control valve is developed in the form of equations describing the flow physics (Takosoglu et al., 2012). The turbulent flow of a viscous fluid is described with Reynolds equations (2)-(4), which, together with continuity equation (1) form a complete system of relationships able to determine the pressure and the flow rate area.

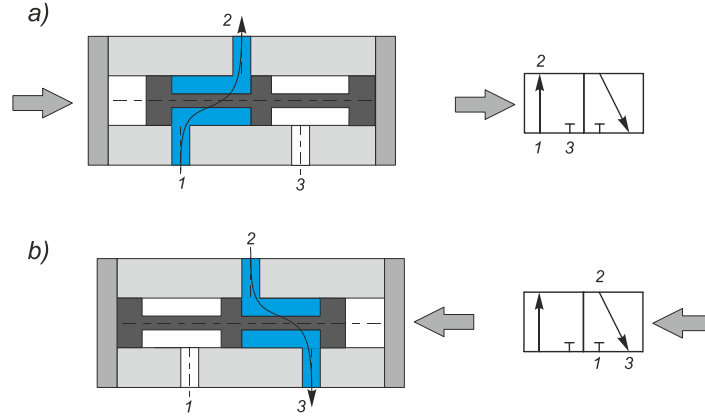


Fig. 1: Diagram of the 3/2 valve.

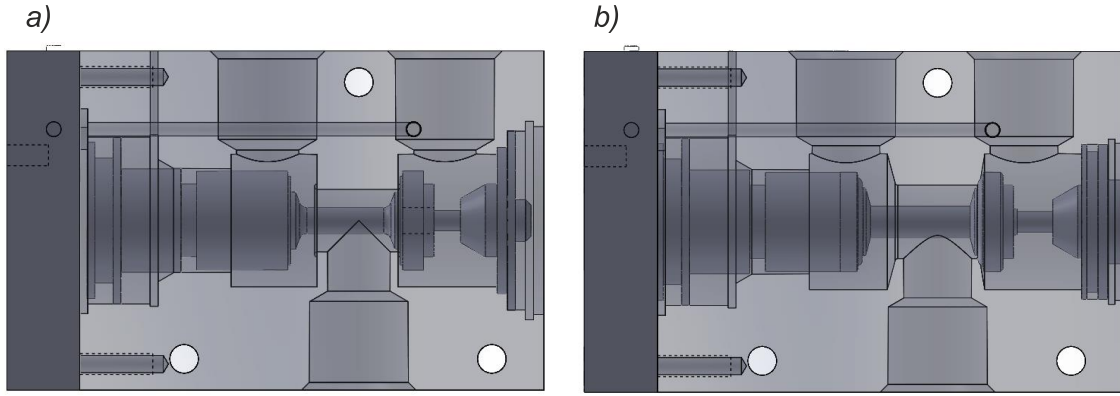


Fig. 2: Solid model of the 3/2 valve a) before modification, b) after modification.

$$\frac{\partial \rho}{\partial t} + \text{div}(\rho \mathbf{U}) = 0 \quad (1)$$

The Reynolds equations are:

$$\frac{\partial(\rho U)}{\partial t} + \text{div}(\rho U \mathbf{U}) = -\frac{\partial P}{\partial x} + \text{div}(\mu \text{grad} U) + \left[\frac{\partial(\rho \overline{u'^2})}{\partial x} - \frac{\partial(\rho \overline{u'v'})}{\partial y} - \frac{\partial(\rho \overline{u'w'})}{\partial z} \right] \quad (2)$$

$$\frac{\partial(\rho V)}{\partial t} + \text{div}(\rho V \mathbf{U}) = -\frac{\partial P}{\partial y} + \text{div}(\mu \text{grad} V) + \left[\frac{\partial(\rho \overline{u'v'})}{\partial x} - \frac{\partial(\rho \overline{v'^2})}{\partial y} - \frac{\partial(\rho \overline{v'w'})}{\partial z} \right] \quad (3)$$

$$\frac{\partial(\rho W)}{\partial t} + \text{div}(\rho W \mathbf{U}) = -\frac{\partial P}{\partial z} + \text{div}(\mu \text{grad} W) + \left[\frac{\partial(\rho \overline{u'w'})}{\partial x} - \frac{\partial(\rho \overline{v'w'})}{\partial y} - \frac{\partial(\rho \overline{w'^2})}{\partial z} \right] \quad (4)$$

The $k-\varepsilon$ model has become one of the most popular and definitely most commonly used models of turbulent flow. The two parameters ($k-\varepsilon$) require two additional transport equations, which can be written as:

$$\frac{\partial(\rho k)}{\partial t} + \text{div}(\rho k \mathbf{U}) = \text{div}\left(\frac{\mu_t}{\sigma_t} \text{grad } k\right) + \mu_t \phi - \rho \varepsilon \quad (5)$$

$$\frac{\partial(\rho \varepsilon)}{\partial t} + \text{div}(\rho \varepsilon \mathbf{U}) = \text{div}\left(\frac{\mu_t}{\sigma_t} \text{grad } \varepsilon\right) + C_1 \mu_t \frac{\varepsilon}{k} \phi - C_2 \rho \frac{\varepsilon^2}{k} \quad (6)$$

The parameter k denotes the turbulence kinetic energy, and ε is the turbulence kinetic energy dissipation rate. The above differential partial equations are implemented in the computational module of the Ansys CFX program. To effectively solve the system of equations describing the turbulent flow of the fluid, it is necessary to use boundary conditions that guarantee the uniqueness of the solution and affect the computational process in the area analyzed.

4. Numerical Analysis

This section discusses the results of a numerical analysis for a poppet valve to determine its performance before and after modifications to the design.

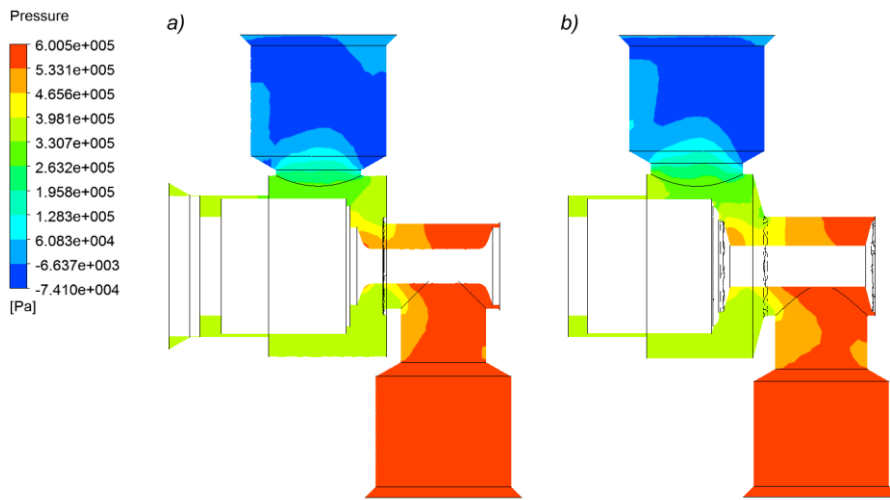


Fig. 3: Distributions of pressure.

As can be seen, the pressure distributions along the axis of symmetry are different for the two cases, i.e. before and after modifications (Figs. 1a and 1b, respectively). After the modification, the compression of the air takes place as early as in the inlet chamber; air reaches a pressure of approximately $4 \cdot 10^5$ [Pa]. The expansion occurs in the outlet port at the exit; the pressure of the air is nearly equal to the pressure of the environment.

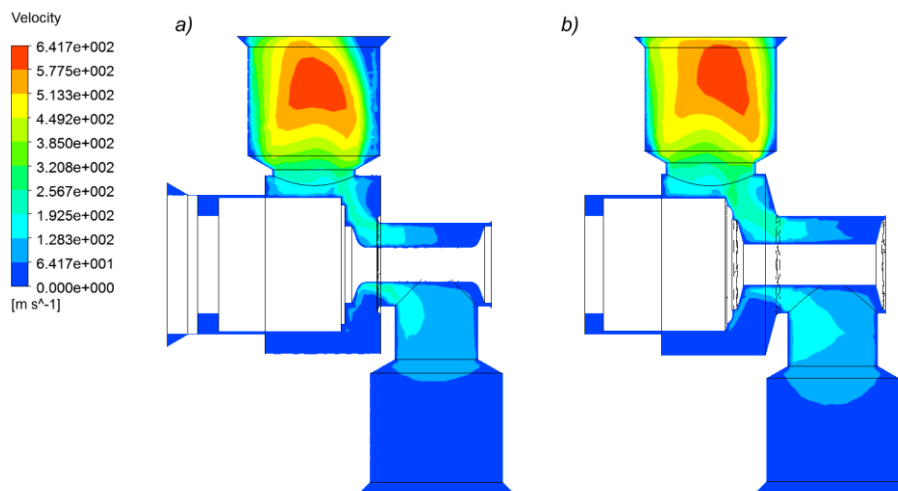


Fig. 4: Distributions of the flow rate.

It can be seen that, in the inlet and outlet ports, the rate of the air flow close to the walls is practically equal to zero and that the rate is the highest in the central part. As shown in Fig. 4, the air flow rate increases from a value close to zero to more than 640 [m/s] when the air passes from the second chamber to the outlet port.

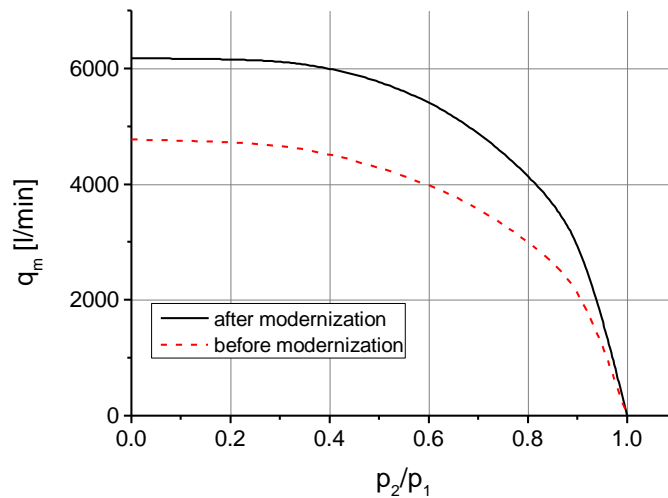


Fig. 5: Volumetric flow rate.

The curves in Fig. 5, based on the model analysis, illustrate the differences in the volumetric flow rate for the poppet valve before and after modifications to its design.

5. Conclusion

A numerical approach to fluid mechanics was used to optimize the flow of compressed air through the valve and determine the basic flow characteristics at the early design stage. This optimization method will enable us to produce pneumatic valves with improved operating parameters and functionality.

Acknowledgement

The numerical analysis was performed using software purchased for the LABIN Project (POPW.01.03.00-26-016/09) co-funded by the EU.

References

- Takosoglu, J. E., Dindorf, R. F. & Laski, P. A. (2009) Rapid prototyping of fuzzy controller pneumatic servo-system. *International Journal of Advanced Manufacturing Technology* Vol. 40, No. (3-4), pp. 349-361.
- Takosoglu, J. E., Laski, P. A. & Blasiak, S. (2012) A fuzzy controller for the positioning control of an electro-pneumatic servo-drive. *Proceedings of the Institution of Mechanical Engineers Part I-Journal of Systems and Control Engineering*, Vol. 226, No. 10, pp. 1335-1343.

ON PARALLELIZATION OF STIFFNES MATRIX ASSEMBLY

M. Bošanský*, B. Patzák**

Abstract: *The aim of this paper is to evaluate efficiency of different approaches to parallelization of sparse matrix assembly using OpenMP. The OpenMP platform is an Application Program Interface (API) for multi-platform shared-memory parallel programming in C/C++ and Fortran. The paper shows that parallelization can efficiently use modern available hardware, significantly reducing the needed computation time.*

Keywords: Assembly operation, Parallel efficiency.

1. Introduction

The development in computer hardware in last decades shows enormous progress, enabled by the introduction of parallel computers. Nowadays, the parallel technology is available even on desktop PC due to widespread use of multicore chips. The rapid development in hardware is, however, not accompanied by corresponding development in software technology. To fully utilize the potential of modern hardware, new algorithms and techniques have to be developed.

The aim of the paper is to study different approaches to parallelization of sparse matrix assemble operation using shared memory programming model using OpenMP library. The study has been done in OOFEM, which is a free finite element code with object oriented architecture for solving mechanical, transport and fluid mechanics problems (Patzak, 2002).

We focused our attention on sparse matrix assembly operation. During this phase, the individual characteristic matrices of individual elements are evaluated and assembled into a global problem matrix using element code numbers. This operation can be relatively demanding, especially, when nonlinear problems are taken into account. The parallelization strategy is based on decomposition of the total work into parts assigned to individual computing nodes. In the present context, the serial loop over all elements is split into disjoint parts assigned to individual computing nodes. The individual element matrices are computed in parallel on individual nodes and then assembled into global stiffness matrix, which is shared between individual nodes (shared memory). It is necessary to ensure, that multiple threads do not update the same value in the sparse matrix, as this will lead to unpredictable and incorrect results. The OpenMP provides different mechanisms that can be used to ensure consistency when accessing and updating shared memory. In this paper, we discuss the individual possibilities and compare their efficiency.

The paper is organized as follows. In Section 2 we briefly explain the assembly of the stiffness matrix and OpenMP API constructs which we use in Section 2. Results are shown and discussed in Section 3. Finally, we conclude the paper in Section 4.

2. Forming Stiffness Matrix with the Use of Parallel Directives

The typical (serial) implementation of sparse matrix assembly consists of loop over elements. Inside this loop, the individual element matrices are evaluated and assembled into a global matrix. The mapping between element local degrees of freedom and corresponding global degrees of freedom is described by code numbers. The individual values in element matrices are added to the corresponding global matrix entry, which row and column indices are determined using the element code numbers, see Tab. 1.

* Ing. Michal Bošanský, Department of Mechanics, Faculty of Civil Engineering, CTU in Prague, Thákurova 7/2077; 166 29, Prague; CZ, michal.bosansky@fsv.cvut.cz

** Prof. Borek Patzák, Department of Mechanics, Faculty of Civil Engineering, CTU in Prague, Thákurova 7/2077; 166 29, Prague; CZ, Borek.Patzak@fsv.cvut.cz

Tab. 1: Prototype code for serial sparse matrix assembly.

```

For elem=1, nelem
  Ke = computeElementMatrix(elem)
  Loc = geveElementCodeNumbers(elem)
  For i=1, K.rows
    For j=1, K.columns
      K(Loc(i), Loc(j)) += Ke (i, j)
    End
  End
End

```

2.1. Application of OpenMP platform

The OpenMP parallel constructs allow relatively straightforward parallelization of serial code, by providing construct enabling to parallelize the for-loops. This is achieved by marking such loop by a special compiler pragmas as parallel loop. The rest is done almost automatically by a compiler, which splits the loop into parts that are then assigned to individual threads of execution. The user can adjust certain parameters that affect the work assignment (static or dynamic), and the scope (local or shared) of variables inside the loop. In order to achieve the best scalability, the amount of serial code must be reduced to profit from parallel execution. It is therefore natural to parallelize the top level loop over individual elements in assembly operation. The parallel OpenMP loop construct allows to mark variables inside the loop as shared or private variables. Shared variables are shared among the individual computing nodes, which means that the data are visible and accessible by all threads simultaneously. On the other hand, the private variables are private to each thread and therefore each thread will have its own copy and use it as a temporary variable. The elements matrices and code number vectors were marked as private.

The consistency in accessing and updating shared data can be achieved by a number of different ways in OpenMP. The following approaches have been considered:

- A1.** The localization of element stiffness matrix is enclosed in critical section. The critical section ensures that the section can be processed by only a single thread in time.
- A2.** Only the update operation of global stiffness matrix entry enclosed in critical section.
- A3.** The update operation of global matrix entry marked as atomic. Atomic directive ensures that the memory update is atomic. A compiler might use special hardware instructions for better performance than when using *critical section*.
- A4.** The consistency ensured using lock or semaphore that lock particular part of code. When the lock is activated the code block which is locked can be executed by only one thread at a time that owns the lock. Single lock has been used.
- A5.** The consistency ensured using multiple locks. In this approach, the global matrix is divided in blocks, corresponding to a range of matrix rows (the number of blocks is a parameter) with dedicated lock. This approach does not locks the whole matrix for a single thread, it locks only specific block, so that the others threads can perform update in other rows.

Tab. 2: Prototype code for A1, A2 and A3 strategies.

<pre> #pragma omp parallel for For elem=1, nelem Ke = computeElementMatrix(elem) Loc = geveElementCodeNumbers(elem) #pragma omp critical (A1) For i=1, K.rows For j=1, K.columns #pragma omp critical (A2) K(Loc(i), Loc(j)) += Ke (i, j) End End End </pre>	<pre> #pragma omp parallel for For elem=1, nelem Ke = computeElementMatrix(elem) Loc= geveElementCodeNumbers(elem) For i=1, K.rows For j=1, K.columns #pragma omp atomic K(Loc(i), Loc(j)) += Ke (i, j) End End End </pre>
A1/A2: Sparse assembly with critical section	A3: Sparse assembly with atomic section

Tab. 3: Prototype code for A4 and A5 strategies.

<pre> omp_lock_t writelock; OMP_INIT_LOCK(&writelock); #pragma omp parallel for For elem=1, nelem Ke = computeElementMatrix(elem) Loc = geveElementCodeNumbers(elem) For i=1, K.rows For j=1, K.columns OMP_SET_LOCK(writelock); K(loc(i), loc(j)) += Ke (i, j) OMP_UNSET_LOCK(writelock); End End End OMP_DESTROY_LOCK(&writelock); </pre>	<pre> #define NBLOCKS 10 omp_lock_t writelock[NBLOCKS] For i=1, NBLOCKS OMP_INIT_LOCK(&writelock[i]) End // block size; note integer division blockSize = K.rows/NBLOCKS #pragma omp parallel for For elem=1, nelem Ke = computeElementMatrix(elem) Loc = geveElementCodeNumbers(elem) For i=1, K.rows For j=1, K.columns Bi = loc(i)/blockSize OMP_SET_LOCK(writelock[Bi]) K(loc(i), loc(j)) += Ke (i, j) OMP_UNSET_LOCK(writelock[Bi]); End End End </pre>
A4: Sparse assembly with single lock	A5: Sparse assembly with block locks

3. Testing Example, Results and Discussion

The individual approaches have been evaluated using a 3D finite element model of nuclear containment reactor. The mesh consists of 87320 nodes and 959700 tetrahedral elements with linear interpolation. The total number of equations was 260322. The stiffness matrix has been stored in compressed row sparse format. In this storage format, on floating-point array is needed to store actual nonzero values as they are traversed in a row-wise fashion. The other two integers arrays store the column indexes of the elements in the vector of values and the second stores the locations of those values that start a row. Instead of storing n^2 elements (where n is the number of equations), we need only $2nnz + n + 1$ storage locations, where nnz is number of nonzero entries.

The four described approaches (A1-A5) have been implemented and their efficiency compared on test example. The evaluations have been done on a desktop PC with 8 cores. The runtime, in terms of wall clock time, has been recorded for each strategy for varying number of processors. In the strategy A5, with multiple locks, each one for dedicated row blocks, the total number of blocks has been also changed.

In Table 4, the execution times for strategies A1-A4 are given. It can be clearly observed, that time needed for the execution is reduced with increasing number of threads. However, the gain is non-proportional, due to the overhead associated with resource sharing (data bus), data consistency (locking, critical sections), and thread management (creation, termination). The more threads are used, the less is the gained speed up. The best speedups and also absolute times are observed for A1 strategy, where the whole local matrix assembly block was contained within a critical section. Comparing to the A2, where only the update of global entry was in the critical section, it is clear, that the overhead associated with critical section is higher than possible gain, when the loops over local entries can be done in parallel. The strategy A5 with multiple locks for dedicated row blocks is efficient than the strategies A3 and A4 relying on simple lock strategy. The results show that there are significant differences between individual strategies. In general, the optimal strategy is problem dependent and must be evaluated on several examples. However, with each strategy one can achieve better performance compared to serial code.

4. Conclusions

The presented work evaluates the different strategies for parallel assembly of sparse matrix using OpenMP programming model. The individual strategies are based on critical sections, atomic constructs, and locks used to lock the whole matrix or its section. The strategies are compared on forming sparse stiffness matrix of a large scale engineering problem. The results show that using parallelization the computation time can be significantly reduced. The overhead costs of individual approaches can have a significant impact on overall computation time.

Tab. 4: Execution times for strategies A1 – A5.

execution times [s]	number of threads				
	1	2	4	6	8
A1	4.531	2.750	1.789	1.640	1.608
A2	5.019	3.124	5.553	7.487	8.488
A3	5.109	3.131	5.643	7.501	8.528
A4	5.002	3.120	5.553	7.417	8.345
A5 – NBLOCKS 50	5.134	3.175	2.539	2.482	2.451
A5 – NBLOCKS 100	5.152	3.159	2.429	2.383	2.359
A5 – NBLOCKS 500	5.155	3.151	2.306	2.175	2.131
A5 – NBLOCKS 1000	5.150	3.1722	2.299	2.172	2.126

Acknowledgement

This work was supported by the Grant Agency of the Czech Technical University in Prague, grant **No. SGS OHK1-089/14** “Advanced algorithms for numerical modeling in mechanics of structures and materials”.

References

- Patzak, B. (2002) OOFEM project home page, In: <http://www.oofem.org> [online], 2002-05-01 [cited 2014-26-1]. Available from: <http://www.oofem.org/en/documentation/manual.html>.
- Chapman, B., Jost, G., Pas, R. V. D. foreword Kuck, D. J. (2008) Using OpenMP – portable shared memory parallel programming The MIT press, Cambridge Massachusetts, London, England: ISBN-13: 978-0-262-53302-7.
- Stroustrup, B. (1997) The C++ programming language Third edition. Murray Hill, New Jersey: 1997 by AT T. ISBN 0-201 885954-4.

SIMULATION ASSESSMENT OF SUPPRESSION OF MACHINE TOOL VIBRATIONS

T. Březina^{*}, L. Březina^{*}, J. Marek^{**}, Z. Hadaš^{*}, J. Vetiška^{*}

Abstract: *The paper presents an approach for finding the locally optimal parameters of a mass which connected to a machine tool suppresses vibrations during machining process. The proposed approach is mainly based on simulation modeling of mechatronic systems with flexible bodies and consequent reduction of the obtained model order. Obtained parameters can be structurally interpreted and included in the model e.g. as a damper or an absorber. The complex model containing the machine tool model with the connected mass then makes possible to analyze the influence of the connected mass on the dynamic compliance of the machine tool.*

Keywords: Machine tool, Dynamic compliance, Flexible bodies, Simulation assessment, Mechatronic systems.

1. Introduction

The influence of a connected mass on the dynamic compliance of the whole system provides quite important information for a designer of a machine tool. The importance generally arises from consequent possibility of the revision and correction of the whole engineering design of the machine according to the obtained information.

The mentioned information was often based only on the experience of the design engineers. The proposed concept is on the contrary based on the simulation modeling of mechatronic systems which utilizes different simulation engines (Březina et al., 2011). The main advantage of the simulation modeling is then possibility of fast modifications of the model and its low cost compared to the experiments with the real machine.

However, finding the suitable locally optimal parameters of the connected mass, in order to tune the dynamic compliance of the system, might be quite complicated because its integration influences all of machine axes thus improvement of the behavior for one axis can lead to the worsening in the other axis. It should be also taken into account that the reliable model of the machine should contain flexible bodies which is leading to the dramatic increase of the model order.

The paper presents an approach to obtaining of the locally optimal parameters of the mass which is flexibly connected to the tool holder. The parameters of the mass are designed in a way to reduce the tool vibrations during the machining. The simulation modeling of the mechatronic systems concept is utilized for that purpose. The method based on the canonical form of the obtained LTI model of the system for the model order reduction is presented as well.

The modeled machine tool (Fig. 1) by TOSHULIN, a.s. producer was modeled in axes X, Y, Z at the center of gravity of the tool holder for the excitation frequency range 0 - 280 Hz. The asked correspondence with the real machine was up to 10% at both time and frequency domain.

^{*} Prof. Tomáš Březina; Lukáš Březina, PhD.; Zdeněk Hadaš, PhD.; Jan Vetiška, PhD.: Faculty of Mechanical Engineering, Brno University of Technology, Technická 2, 616 69, Brno; CZ, brezina@fme.vutbr.cz

^{**} Prof. Jiří Marek: TOSHULIN, a.s., Wolkerova 845, 768 24, Hulín; CZ, jiri.marek@toshulin.cz

2. Formulation of the Task

The connected mass A is described by mechanical parameter weight m_A . It is connected to an appointed place (the mass center of a tool holder) by an ideal damper with damping b_A and by an ideal spring with stiffness k_A (Fig. 2). The mass is moving in φ_A, θ_A direction (Fig. 2). φ_A, θ_A represent geometric parameters.



Fig. 1: Analyzed machine tool from TOSHULIN (Brezina et al., 2013).

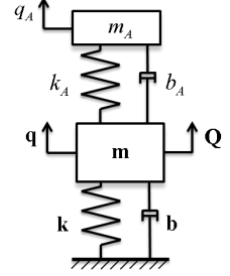
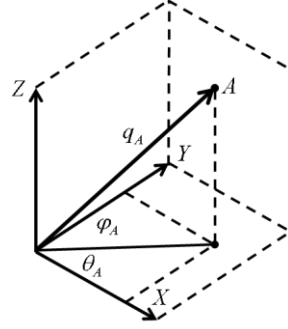


Fig. 2: Scheme of the integration of the mass A to the system (Brezina et al., 2013).

The dynamic compliance of the machine with the integrated mass A is described by following equations

$$\begin{aligned} (s^2 \mathbf{m} + s\mathbf{b} + \mathbf{k}) \mathbf{q} &= \mathbf{Q} - s^2 m_A \mathbf{q} + s^2 (\mathbf{h} m_A) q_A \\ (s^2 m_A + s b_A + k_A) q_A &= Q_A + s^2 (\mathbf{h} m_A)^T \mathbf{q} \end{aligned} \quad (1)$$

where \mathbf{m} , \mathbf{b} , \mathbf{k} mean one by one matrix of mass, matrix of damping, matrix of stiffness and $\mathbf{h} = [\cos(\varphi_A) \cos(\theta_A) \quad \cos(\varphi_A) \sin(\theta_A) \quad -\sin(\varphi_A)]^T$.

The improvement of the dynamic compliance of the machine tool with the connected mass A is formulated as a minimization of the objective function $g(\mathbf{p})$:

$$\begin{aligned} \mathbf{p} &= [m_A \quad b_A \quad k_A \quad \varphi_A \quad \theta_A] \\ \Delta_{i,j}(\mathbf{p}) &= \frac{\max_{\omega} |\alpha_{i,j}^A(\omega, \mathbf{p})|}{\max_{\omega} |\alpha_{i,j}(\omega, \mathbf{p})|} - 1 \\ g(\mathbf{p}) &= \max_{i,j} \Delta_{i,j}(\mathbf{p}) \\ \mathbf{p}_{opt} &= \arg \min g(\mathbf{p}) \end{aligned} \quad (2)$$

where $i, j = X, Y, Z$, $\max_{\omega} |\alpha_{i,j}^A(\omega, \mathbf{p})|$ is a dominant amplitude – maximum of the amplitude characteristics of the dynamic compliance of the machine with the integrated mass A and $\max_{\omega} |\alpha_{i,j}(\omega, \mathbf{p})|$ has the same meaning but the machine is considered without the mass A . There are considered following limitations:

$$\begin{aligned} m_A, b_A, k_A, \varphi_A, \theta_A &> (m_A)_{min}, (b_A)_{min}, (k_A)_{min}, 0, 0 \\ m_A, b_A, k_A, \varphi_A, \theta_A &\leq (m_A)_{max}, (b_A)_{max}, (k_A)_{max}, 360, 360 \\ \max_i \Delta_{i,i}(\mathbf{p}) &< 0 \end{aligned} \quad (3)$$

The first two conditions represent limitations of the magnitude of the parameters values and the last one is introducing requirement for the improvement of the dynamic compliance in the particular axis. The minimization of the objective function guarantees the least possible degradation of the dynamic compliance between the different axes. It is necessary to obtain the low order model of the dynamic compliance to implement the minimization process first of all.

3. Obtaining of the Low Order Model via CAD, FEM and MBS Models

To efficiently minimize the target function, a credible model of as low order as possible has to be used. The low order model is created according to the simulation modeling of mechatronic systems concept. The first step is to identify rigid and flexible parts in the CAD model. There are consequently created FEM models of the flexible parts (order around $10^5 - 10^6$) and modal analysis is performed. The high order is reduced by utilization of the Craig-Bampton method (Craig & Bampton, 1968) for the given frequency range. The reduced models (the order around $10^2 - 10^3$) are integrated to the multi-body machine model together with rigid bodies models. The order of the complete machine remains $10^2 - 10^3$. The final state LTI model $\alpha \equiv (\mathbf{A}, \mathbf{B}, \mathbf{C}, \mathbf{D} = \mathbf{0})$ is obtained by the linearization of the reduced model around the selected operation point. Let's note that L-image of α is for the zero initial conditions described as

$$\begin{aligned} s\mathbf{x}(s) &= \mathbf{A}\mathbf{x}(s) + \mathbf{B}\mathbf{Q}(s) \\ \mathbf{q}(s) &= \mathbf{C}\mathbf{x}(s) + \mathbf{D}\mathbf{Q}(s) \end{aligned} \quad (4)$$

where $\mathbf{x}(s)$, $\mathbf{Q}(s)$ and $\mathbf{q}(s)$ mean L-images of the vector of (inner) states, input vector of exciting force actions and output vector of corresponding displacements. The dynamic compliance of the machine tool or dynamic compliance only between axis j and i could be expressed simply as $\mathbf{q}(s) = \alpha(s)\mathbf{Q}(s)$, or $q_i(s) = \alpha_{i,j}(s)Q_j(s)$. The obtained model is of the 428th order. The asked correspondence with the real machine was according to measurements achieved.

4. Further Reduction of the LTI Model

There are many methods of reduction of the LTI order using similarity transformations based on the controllability and observability matrix (e.g. Antoulas & Sorensen, 2001; Moore, 1981) which, however, often disturb the original physical structure of the model. Therefore, the further reduction of the LTI model is performed by transforming the matrix \mathbf{A} into canonical modal form $\mathbf{A} = \text{diag}(\mathbf{A}_1, \mathbf{A}_2, \dots, \mathbf{A}_n)$. The matrices \mathbf{A}_k are 2/2 type and a couple of single eigenvalues of LTI $(\delta \pm i\sqrt{\omega_0^2 - \delta^2})_k$ or $(\delta \mp \sqrt{\delta^2 - \omega_0^2})_k$ is projected as

$$\mathbf{A}_k = \begin{bmatrix} \delta & \sqrt{\omega_0^2 - \delta^2} \\ -\sqrt{\omega_0^2 - \delta^2} & \delta \end{bmatrix}_k, \text{ or } \mathbf{A}_k = \begin{bmatrix} \delta - \sqrt{\delta^2 - \omega_0^2} & \\ & \delta + \sqrt{\delta^2 - \omega_0^2} \end{bmatrix}_k. \quad (5)$$

The symbol δ or expression $\delta \mp \sqrt{\delta^2 - \omega_0^2}$ means damping factors and ω_0 is the natural frequency of the couple. The application of such LTI form has two principal consequences: the original model can be decomposed into a set of partial models $\alpha_k \equiv (\mathbf{A}_k, \mathbf{B}_k, \mathbf{C}_k, \mathbf{D}_k = \mathbf{0})$ of the second order, for which applies

$$\begin{aligned} \mathbf{q}(s) &= \left(\sum_k \alpha_k(s) \right) \mathbf{Q}(s) \\ &= \sum_k \mathbf{q}_k(s) \end{aligned} \quad (6)$$

The modeled dynamic compliance $\alpha(s)$ is according to (6) a sum of partial dynamic compliances $\alpha_k(s)$. This can be utilized for the reduction of the LTI model $\alpha(s)$ which respects the structure of the original model of the mechanical system. It is possible to perform the reduction of $\alpha(s)$ by simple elimination of partial models $\alpha_k(s)$ with no significant contribution to the original model.

The order 428 of LTI model was reduced to just 80 with relative accuracy downgrade 7%. The minimization according to (2) and (3) is consequently performed for the reduced LTI. The found parameters are then used as initial parameters for the minimization on original LTI (order 428) because of the inaccuracy suppress.

The examples of the locally optimal solutions for the mass A (Fig. 3) are presented in (Brezina et al., 2013). There was observed significant suppression of the original dominant amplitudes (Fig. 3 - left).

Simultaneous worsening in some of the other axis also appeared (Fig. 3 - right) but outside the working range of the machine.

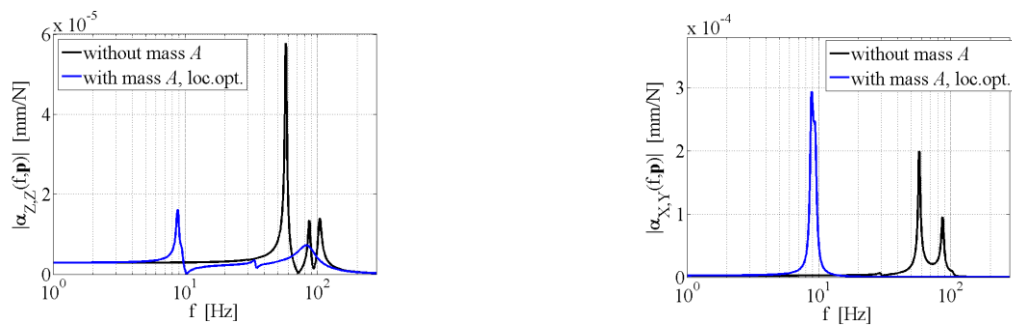


Fig. 3: The integration of the mass A with the locally optimal parameters, left - The amplitude characteristics of the dynamic compliance of the machine in the Z axis (the best integration influence), right - The amplitude characteristics of the dynamic compliance of the machine between the X and Y axis (the worst integration influence) (Brezina et al., 2013).

5. Conclusions

The proposed approach based on the modeling of mechatronic systems presents possible efficient way to the reduction of the obtained LTI model which contains also flexible bodies. The reduced model order reaches approximately 20% of the original one. The observed difference between the resonant frequencies of both models was typically up to 10%.

There was also presented an objective function for finding of the locally optimal parameters of the connected mass A which was integrated to the model in order to reduce the dominant amplitudes of the system. Initial locally optimal parameters are due to the decreasing of computational time found for the reduced model of the system. Final optimal parameters are then searched for the original non-reduced model. There was observed important decreasing of dominant amplitudes after the implementation of the mass A with the locally optimal parameters. Increasing of amplitudes in some other axes was observed outside the working range of the machine thus without an important impact on the machine function. Let's note that mass A can be practically implemented as a damper or an absorber.

Acknowledgement

This work is supported by project NETME Centre PLUS. The results of this project NETME CENTRE PLUS (LO1202) were co-funded by the Ministry of Education, Youth and Sports within the support programme „National Sustainability Programme I“.

References

- Antoulas, A. C. & Sorensen, D. (2001) Approximation of Large-Scale Dynamical Systems: an Overview. *Int. J. Applied Math. Computer Science*, 11, 5, pp. 1093-1121.
- Brezina, T.; Brezina, L.; Marek, J.; Hadas, Z. & Vetiska, J. (2013) Simulation Assessment of Suspension of Tool Vibrations during Machining, in: *Proc. 10th International Conference Mechatronics 2013*, Springer, London, pp. 273-280.
- Brezina, T., Vetiska, J., Hadas, Z. & Brezina, L. (2011) Simulation, Modelling and Control of Mechatronic Systems with Flexible Parts, in: *Proc. 9th Conf. Mechatronics 2011*, Springer Verlag, Berlin, pp. 569-578.
- Craig, R. R. & Bampton, M., C. (1968) Coupling of substructures for dynamics analyses. *AIAA Journal*, 6, 7, pp. 1313-1319.
- Moore, B.C. (1981) Principal Component Analysis in Linear Systems: Controllability, Observability and Model Reduction. *IEEE Trans. on Automatic Control*, AC-26, 1, pp. 17-31.

APPLICATION OF THE LATTICE BOLTZMAN METHOD FOR THE MODELLING OF PULSATILE FLOW IN IDEALISED BYPASS GEOMETRIES

O. Bublík*, A. Jonášová**, J. Vimmr***

Abstract: *This paper is focused on numerical simulations of pulsatile laminar blood flow using the lattice Boltzmann method. Compared to the traditional methods like the finite volume or finite element methods, the relatively new approach of the lattice Boltzmann method is simpler, faster and less memory-intensive. Because of these desirable properties, this method can be seen as an appropriate candidate for numerical simulations in the field of biomedicine, where large and complex flow problems have to be solved in short time. In this work, the lattice Boltzmann method is tested on a reference idealised bypass model. The obtained numerical results are compared with those computed using the finite volume method.*

Keywords: Lattice Boltzmann method, Finite volume method, Incompressible Newtonian fluid, Pulsatile blood flow, Idealised bypass geometry.

1. Introduction

The lattice Boltzmann method represents a relatively new approach for the modelling of fluid flow problems (Succi, 2001), (Chen et al., 1998). The principle of this method is based on the mesoscopic fluid description unlike the classical methods that utilise the macroscopic description. The lattice Boltzmann method originates from the lattice gas cellular automata (LGCA) representing a simplified molecular dynamics. However, unlike the LGCA, the lattice Boltzmann method operates with virtual particles. This approach makes it possible to solve various complex flow problems such as multiphase flow and free surface flow. Due to its simplicity, accuracy and computational efficiency, the lattice Boltzmann method has become very popular during the last decade.

Because any extra knowledge of the local hemodynamics prior to surgery can bring benefits not only to vascular surgeons in their pre-operative planning, but also to patients, the mathematical modelling of blood flow in patient-specific geometries has become very popular in recent years. A certain drawback of this approach is the need for very fast calculations in complex computational domains that are usually reconstructed from CT scans. From this point of view, the lattice Boltzmann method appears to be an appropriate numerical method for this type of computationally-demanding calculations. Its main advantages include robustness and ability to perform blood flow simulations directly in grids obtained from CT scans.

The aim of the present study is to compare the computational capabilities of the lattice Boltzmann method with those of the finite volume method for the numerical simulations of pulsatile Newtonian blood flow in a reference idealised bypass model taken from (Vimmr et al., 2012). Further numerical results for other bypass models with either tapered or widening grafts will be presented and discussed in detail at the conference.

* Ing. Ondřej Bublík: European Centre of Excellence NTIS – New Technologies for the Information Society, Faculty of Applied Sciences, University of West Bohemia, Univerzitní 22, 306 14 Pilsen, Czech Republic, obublík@ntis.zcu.cz

** Ing. Alena Jonášová: European Centre of Excellence NTIS – New Technologies for the Information Society, Faculty of Applied Sciences, University of West Bohemia, Univerzitní 22, 306 14 Pilsen, Czech Republic, jonasova@ntis.zcu.cz

*** Assoc. Prof. Jan Vimmr, PhD.: Department of Mechanics, Faculty of Applied Sciences, University of West Bohemia, Univerzitní 22, 306 14 Pilsen, Czech Republic, jvimmr@ntis.zcu.cz

2. Methods

The lattice Boltzmann method is derived from a special discretisation of the Boltzmann equation, describing the time evolution of the particle distribution function $f(\mathbf{x}, \mathbf{v}; t)$ in the phase space,

$$\frac{\partial f}{\partial t} + \mathbf{v}\nabla f = \frac{1}{\tau}(f^{eq} - f), \quad (1)$$

where the right hand side of Eq. (1) is the Bhatnagar-Gross-Krook model of the collision operator (Bhatnagar et al., 1954), the function $f^{eq}(\rho, \mathbf{v})$ is an equilibrium distribution function and τ is the single relaxation time. After a special space-time discretization of Eq. (1), the lattice Boltzmann equation is obtained

$$f_i(\mathbf{x} + \mathbf{e}_i\Delta t, t + \Delta t) = f_i(\mathbf{x}, t) - \frac{1}{\tau}(f_i(\mathbf{x}, t) - f_i^{eq}(\mathbf{x}, t)), \quad (2)$$

where $f_i, i = 1, 2, \dots, 19$ are the distribution functions corresponding to the i -th particle velocity \mathbf{e}_i . The spatial distribution of the particle velocities \mathbf{e}_i in 3D, which is denoted D3Q19, is shown in Fig. 1. In according to (Succi, 2001), the equilibrium functions $f_i^{eq}(\mathbf{x}, t)$ are defined as

$$f_i^{eq}(\mathbf{x}, t) = f_i^{eq}(\rho(\mathbf{x}, t), \mathbf{v}(\mathbf{x}, t)) = w_i\rho\left(1 + 3(\mathbf{e}_i \cdot \mathbf{v}) + \frac{9}{2}(\mathbf{e}_i \cdot \mathbf{v})^2 - \frac{3}{2}(\mathbf{v} \cdot \mathbf{v})\right), \quad (3)$$

where w_i are weights, $\rho = \rho(\mathbf{x}, t)$ is the density and $\mathbf{v} = \mathbf{v}(\mathbf{x}, t)$ is the velocity vector.

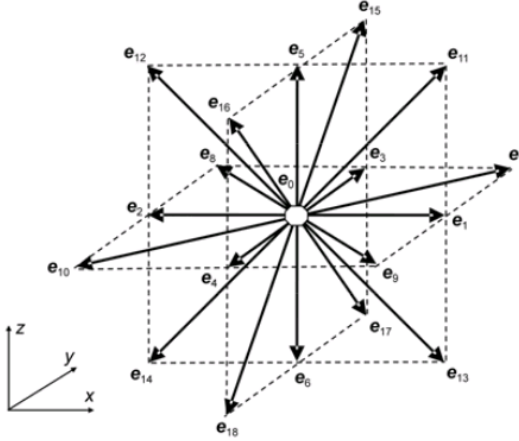


Fig. 1: D3Q19 lattice (3D space, 19 velocities).

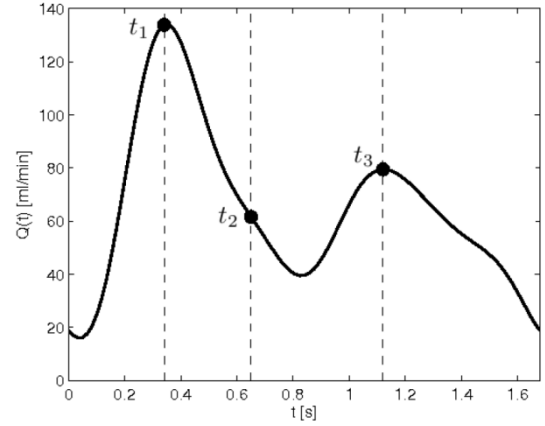


Fig. 2: Time-dependent inlet flow rate $Q(t)$.

The macroscopic variables $\rho(\mathbf{x}, t)$ and $\mathbf{v}(\mathbf{x}, t)$ can be recovered from the distribution functions $f_i(\mathbf{x}, t)$ as

$$\rho(\mathbf{x}, t) = \sum_{i=1}^{19} f_i(\mathbf{x}, t), \quad \mathbf{v}(\mathbf{x}, t) = \sum_{i=1}^{19} f_i(\mathbf{x}, t)\mathbf{e}_i.$$

The pressure $p(\mathbf{x}, t)$ is connected with the density $\rho(\mathbf{x}, t)$ through the following relationship

$$p = \frac{1}{3}\rho.$$

Using the Chapman-Enskog expansion (Succi, 2001), the nonlinear system of incompressible Navier-Stokes equations

$$\nabla \mathbf{v} = 0, \quad (4)$$

$$\rho\left(\frac{\partial \mathbf{v}}{\partial t} + \mathbf{v}\nabla \mathbf{v}\right) + \nabla p = \mu\nabla^2 \mathbf{v}, \quad (5)$$

can be recovered from the lattice Boltzmann equation (2). To demonstrate the computational capabilities of the lattice Boltzmann method, we compare the obtained results with those computed using the pressure-based second order finite volume method described in (Vimr et al., 2012).

3. Numerical results

The numerical simulations of pulsatile Newtonian blood flow are performed in an idealised bypass model, consisting of both proximal and distal anastomoses. The geometry of this model with average values shown in Fig. 3 is taken from (Vimmmr et al., 2012). At the inlet, a time-dependent velocity magnitude corresponding to the inlet flow rate, Fig. 2, is prescribed. At the outlet, the constant pressure boundary condition is considered. Figs. 4 and 5 show velocity profiles at selected cross-sections of the reference bypass model computed by the two numerical methods considered in this study at the time instant $t_3 = 1.12$ s. The comparison of longitudinal sections of the velocity profiles from Figs. 4 and 5 is displayed in Fig. 6. Tab. 1 lists the number of elements and CPU times necessary for the completion of two full cardiac cycle periods.

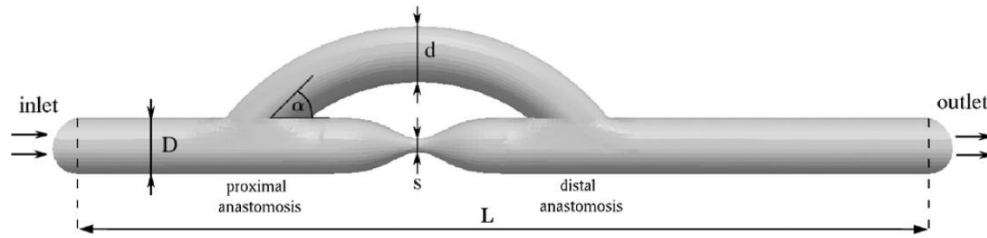


Fig. 3: Geometry of the reference 3D bypass model.

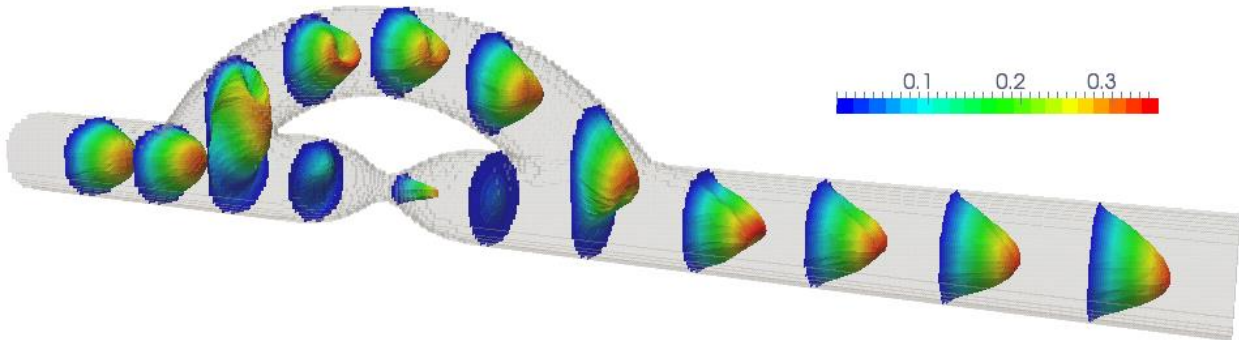


Fig. 4: Velocity profiles obtained using the lattice Boltzmann method at the time $t_3 = 1.12$ s.

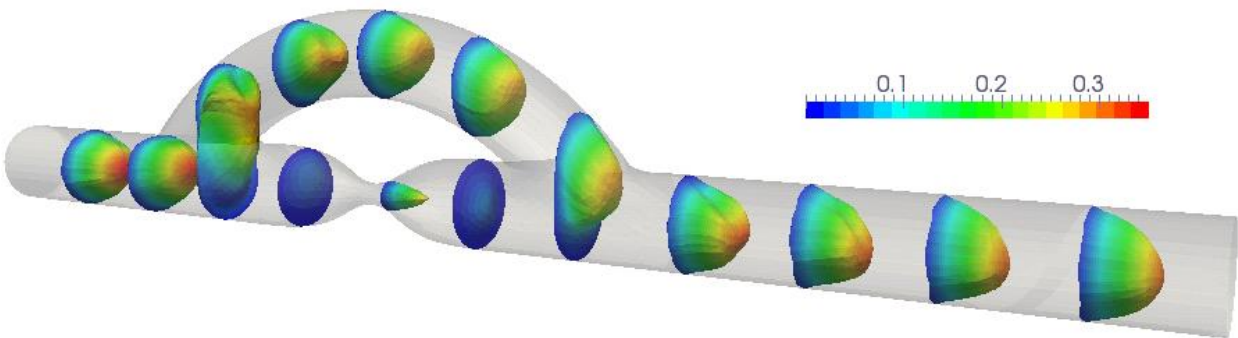


Fig. 5: Velocity profiles obtained using the finite volume method at the time $t_3 = 1.12$ s.

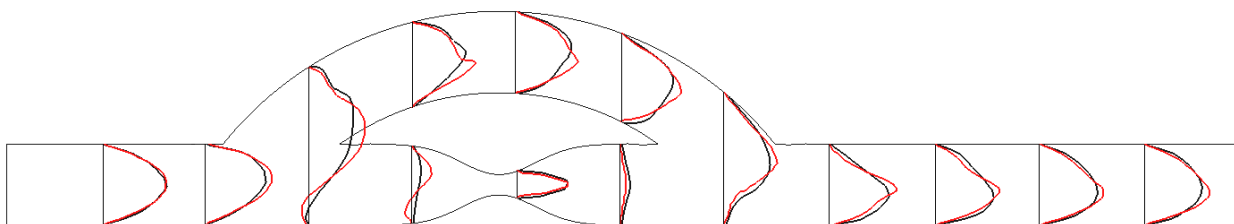


Fig. 6: Comparison of velocity profiles in the middle of the reference bypass model computed by the lattice Boltzmann method (red) and the finite volume method (black) at the time $t_3 = 1.12$ s.

The results obtained with the lattice Boltzmann method are in a relatively good qualitative agreement with those computed using the finite volume method, although several differences are present. The main differences are primarily caused by dissimilar computational meshes, see Fig. 7. Namely, the computational mesh used for the numerical computation with the finite volume method consisted of tetrahedral elements, which were able to precisely fit the boundary of the computational domain. By contrast, the computational grid used for the lattice Boltzmann method consisted of hexahedral bricks, which could only approximately fit the boundary of computational domain. This mesh difference results in different distributions of blood flow within the graft and the stenosed native artery.

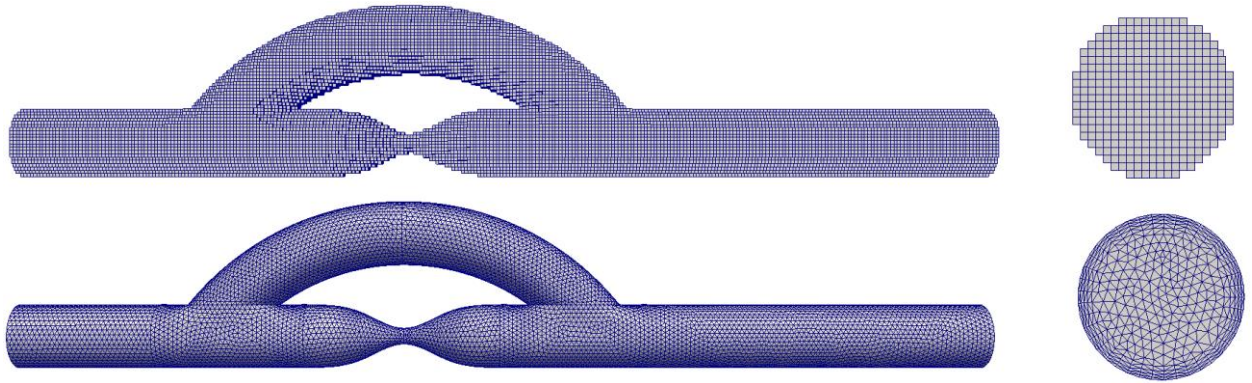


Fig. 7: Computational meshes used for the lattice Boltzmann method (top) and the finite volume method (bottom).

Tab. 1: CPU times for the two methods considered in this study. The listed time indicates the end of the computational process after reaching two full cardiac cycle periods.

method	number of cells	CPU time [s]
FVM	256461	174294
LBM	162779	36598

4. Conclusions

The lattice Boltzmann method represents an excellent tool for the solution of large and complex flow problems because of its simplicity, accuracy and high performance, Tab. 1. Some difficulties can be encountered when it is necessary to precisely capture the boundary of the computational domain, as shown in this study. In such cases, it is recommended to implement local grid refinement or apply a special boundary condition corresponding to the curvature of the boundary.

Acknowledgement

This work was supported by the European Regional Development Fund (ERDF), project ‘NTIS - New Technologies for the Information Society’, European Centre of Excellence, CZ.1.05/1.1.00/02.0090 and by the internal student grant project SGS-2013-036 of the University of West Bohemia.

References

- Bhatnagar, P. L., Gross, E. P., Krook, M. (1954) A Model for Collision Processes in Gases. I. Small Amplitude Processes in Charged and Neutral One-Component Systems, *Physical Review* 94 (3): 511-525.
- Chen, S. and Doolen, G. D. (1998) Lattice Boltzmann Method for Fluid Flows, *Annual Review of Fluid Mechanics*, vol. 30, pp. 329-364.
- Succi, S. (2001) *The Lattice Boltzmann Equation for Fluid Dynamics and Beyond*, Oxford university press
- Vimr, J., Jonášová, A., Bublík, O. (2012) Effects of three geometrical parameters on pulsatile blood flow in complete idealised coronary bypasses, *Computers & Fluids*, Volume 69, 30 October 2012, pp. 147-171.

MECHANICAL AND FILTERING PROPERTIES OF NON-SINTERED POROUS SOLIDS FOR FILTRATION APPLICATIONS

P. Bulejko^{*}, T. Svěrák^{**}

Abstract: *This work deals with the mechanical and filtering properties of porous materials based on silicon carbide and aluminate cement for filtration applications. Silicon carbide classified according to particle sizes was used as the main aggregate. The influence of granulometric composition and quantity of aggregate upon porous structure generation was studied and mechanical properties were characterized using a three-point bending test of columns with proportions of 20 × 20 × 100 mm prepared of testing mortars. The input materials were characterized using laser granulometry and X-ray diffraction; the porous structure was studied using mercury porosimetry, and scanning electron microscopy. Disc-shaped barriers with 90-mm diameters were prepared by uniaxial pressing in a mold. They were tested using air flux to determine their effective permeability. Additionally, capillarity testing of the materials was carried out.*

Keywords: Porous material, Porosity, Mechanical properties, Filtration.

1. Introduction

The production of porous supports for membranes as well as macroporous elements for filtration involves firing (Guocheng, et al., 2012). Firing is a basic process in ceramic technology and involves sintering to form strong ceramic bonds between the particles of raw materials (Hanykýř, 2000). The structure of the final product is mainly influenced by the firing temperature, which usually reaches 1100°C for inorganic membrane fabrication. With the increase in temperature, porosity is reduced and flexural strength is increased (Nandi, et al., 2008). The firing process itself can take several hours, and it is very expensive (Hlaváč, 1981, Dong, et al., 2009). The main effort in the field of membrane processes is to reduce the cost of membrane units and thereby reduce the cost of the overall process (Dong, et al., 2009, Sarkar, et al., 2012). One possibility is to skip the heat treatment step, which makes the final products more expensive. However, it is also necessary to preserve porosity and appropriate values of mechanical properties simultaneously. That is the main aim of this work.

2. Materials and Methods

2.1. Materials and preparation of samples

An aluminate cement, Secar 71, was mixed with silicon carbide (Carborundum Electrite a.s., Benátky nad Jizerou). Various particle sizes (Tab. 1) ranging from 33 to 500 μm were used to influence the porous structure of the final material.

Testing samples for evaluating mechanical properties were prepared by mixing water and cement for one minute. The aggregate was added and then homogenized for three minutes and casted in steel molds to form columns with measurements of 100 × 20 × 20 mm. The molds were enclosed in a polyethylene bag to avoid humidity outflow and then demolded. After demolding, the samples were cured at laboratory temperature and pressure in an enclosed plastic bath with increased humidity. Samples for permeability testing were prepared using the same mixing procedure above but the mixture was then pressed into a mold to form disks with 90-mm diameters and a thickness of 5 mm.

* Ing. Pavel Bulejko: Heat Transfer and Fluid Flow Laboratory, Faculty of Mechanical Engineering, Brno University of Technology (BUT), Technická 2896/2; 616 69, Brno; CZ, bulejko@lptap.fme.vutbr.cz

** Assoc. Prof. Ing. Tomáš Svěrák, CSc.: Institute of Material Chemistry, Faculty of Chemistry, BUT, Purkyňova 464/118, 612 00 Brno, CZ

2.2. Characterization methods

The phase composition of starting materials was determined using a PANalytical Empyrean X-ray diffraction spectrometer. Granulometric measurement to determine particle size distribution was performed with a Sympatec HELOS KR laser analyzer with a measuring range between 0.1 to 8750 μm .

Testing of flexural and compressive strengths was performed using the DESTTEST 4310 COMPACT A machine designed by Beton System, which is typically used for testing mechanical properties of building materials. Mechanical strengths were measured after 24 hours, 7 days and 28 days. Characterization of porous structure of the samples was carried out using a Micromeritics Poresizer 9310 mercury intrusion porosimeter. Cross-section of samples and their surfaces were analyzed using a Zeiss EVO LS 10 scanning electron microscope. Porosity was determined using the pycnometric method – the sample was dried at 105°C to a constant weight and left to cool in a desiccator. The sample was then weighed to an accuracy of 1 mg (m_1), put in a pycnometer, filled with distilled water and reweighed (m_2). Finally, the weight of the water-filled pycnometer was measured. Bulk density was calculated according to relation (1). The samples used for determination of bulk density were subsequently put into 50-cm³ beakers and these were filled with water to completely submerge the samples. The sample beakers were put on a hot plate and the water was boiled for an hour. After the samples were saturated with boiling water, their surfaces were wiped to remove water droplets and weighed (m_4). Absorbability was then calculated according to equation (2). Apparent porosity was calculated using equation (3) (Ptáček et al., 2012).

Finally, the permeability of the prepared materials was determined by air flux with a laboratory filtration apparatus. Mean pore (capillary) radius and the diffusion coefficient of water in the material was determined using a capillarity test. Permeability was tested using the 90-mm disks. The sample was placed into a chamber connected to a compressor air tank with a volume of 0.001 m³ and connected to the filtration apparatus, and the overpressure (Δp_0) in the range of 120 kPa (compared to atmospheric pressure) was set up. The beginning of the experiment was defined by turning on the valve to the chamber with the disk, and the time of the instantaneous overpressure (Δp) was measured until it was in equilibrium with atmospheric pressure. The results of the measurement were displayed as a linear dependence, described by equation (6). The effective permeability K_{eff} [$\text{mol}\cdot\text{m}^{-1}\cdot\text{s}^{-1}\cdot\text{Pa}^{-1}$] of the material was determined using the angular coefficient β [s^{-1}] of the linear dependence (equation 6), according to relation (7) where A is the disk surface area, h_b is its thickness, V_a is the volume of air tank, R is the molar gas constant ($8.314 \text{ J}\cdot\text{mol}^{-1}\cdot\text{K}^{-1}$) and T is the ambient temperature [K] (Kudová et al., 2004). For the determination of capillarity, a set of samples in the form of columns with dimensions $100 \times 20 \times 20$ mm was used. In a suitable dish, the specimens were put onto glass rods and the dish was filled with water up to the bottom edge of the columns. At the same time, the time measurement was initiated. The height of water raised in the specimen material was measured in three-minute intervals and the measurement was ended after 30 minutes. The values of measured height were used to determine the mean pore (capillary) radius (equation 4) and diffusion coefficient of water in the material of the samples according to relation (5) (Ptáček et al., 2012).

2.3. Equations

$$\rho_b = \frac{m_1}{m_3 - (m_2 - m_1)} \rho_{H_2O} \quad (1)$$

$$A_C = \frac{m_4 - m_1}{m_1} 100 \quad (2)$$

$$\varepsilon_a = \rho_b A_C \quad (3)$$

$$h = \frac{2\gamma \cos \varphi}{r_p g \rho_1} \cong \frac{1.49 \cdot 10^{-5}}{r_c} \quad (4)$$

$$h^2 = D_g t \quad (5)$$

$$\ln\left(\frac{\Delta p}{\Delta p_0}\right) = -\beta t \quad (6)$$

$$K_{\text{eff}} = \frac{\beta h_b V_a}{ART} \quad (7)$$

2.4. Figures and tables

AC-220-53 means sample prepared of aluminate cement (AC) and silicon carbide F220 (see Tab. 1) and AC content of 53 %.

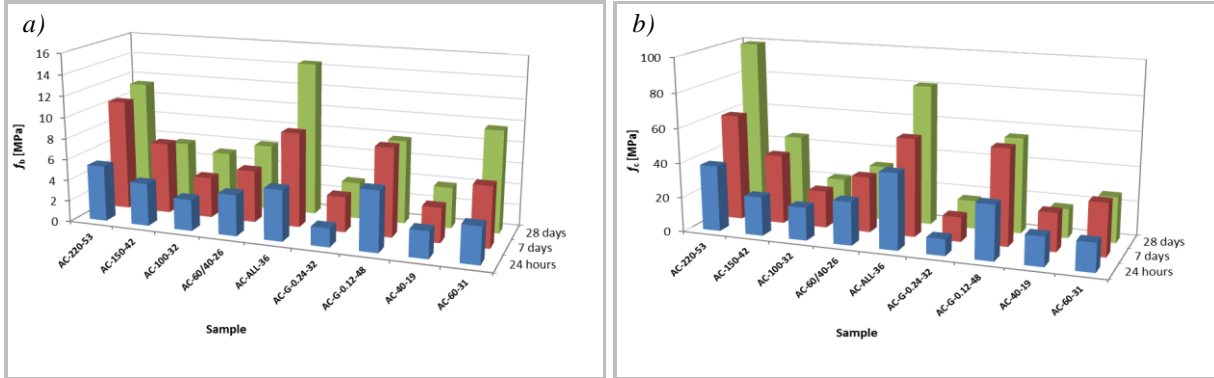


Fig. 1: Development of a) flexural and b) compressive strengths of samples.

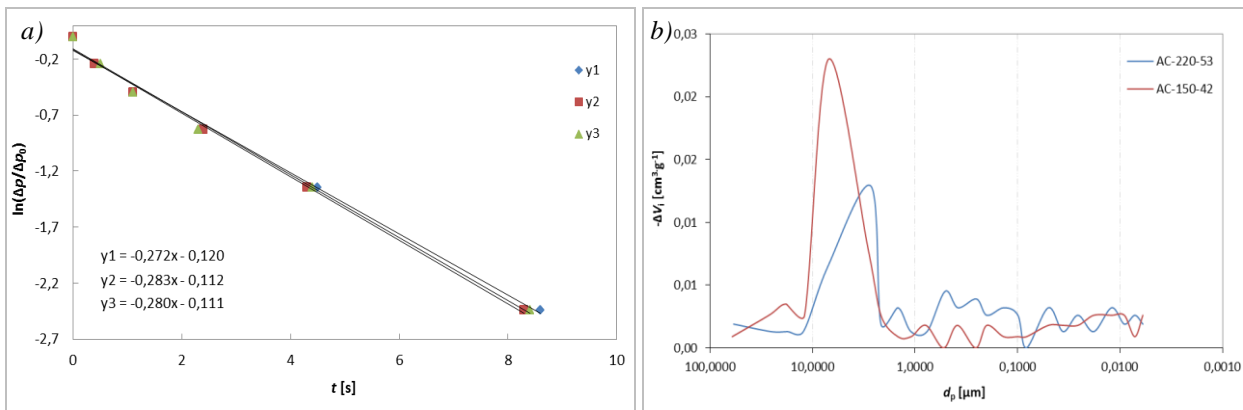


Fig. 2: a) Permeation measurement plot of sample AC-150-42 and b) incremental pore volume distribution of samples AC-220-53 and AC-150-42.

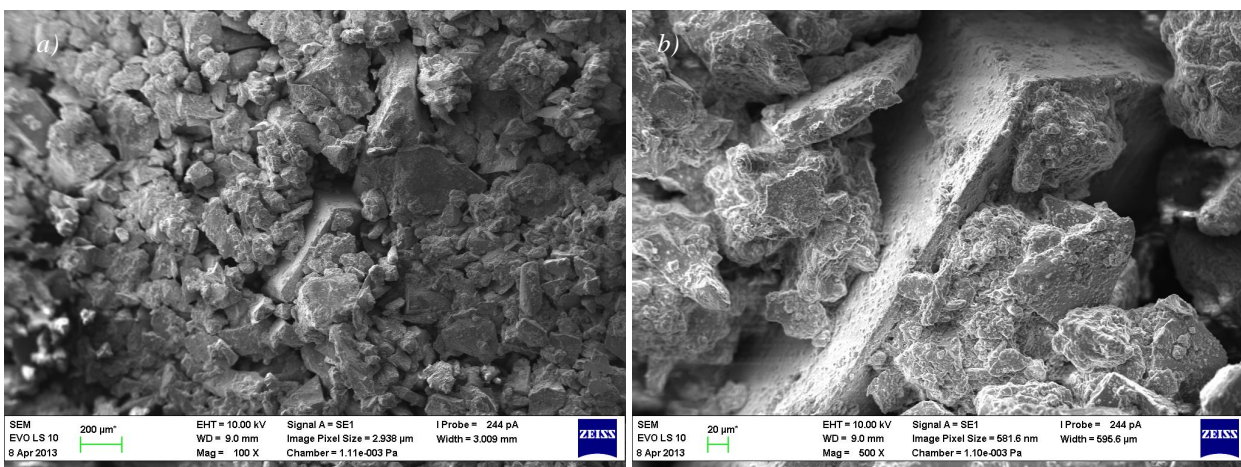


Fig. 3: Surface of sample AC-150-42 – SEM: a) Magnification: X 100; b) Magnification: X 500.

Tab. 1: Particle size of individual silicon carbide classes.

SiC	F40	F60	F100	F150	F220
d [μm]	500 ~ 425	300 ~ 250	150 ~ 125	106 ~ 75	75 ~ 33

3. Conclusions

With the combination of SiC F220, particle-size distribution within 75 – 33 μm and a binder content of 53 % (water-cement ratio = 0.40), an apparent porosity of 18.80 % and average pore diameter of 0.0540 μm were attained. At the same time, the compressive and flexural strengths for this sample were 99.43 MPa and 11.39 MPa, respectively (measured after 28 days). Based on these mechanical properties, the obvious utility for these materials is in filtration. Average pore diameter is decreased due to the high binder content, which had to be increased (compared to the other mixtures) to preserve the rheological properties of the blend. However, the incremental pore volume distribution (Fig. 2a) shows higher increments in the pore diameter range between 10 to 1 μm , so there is a higher amount of pores with diameters in this range, but the smaller pores generally prevail.

The results of permeation measurement show permeability at a relatively high level. The highest value was $3.168 \cdot 10^{-7} \text{ mol} \cdot \text{m}^{-1} \cdot \text{s}^{-1} \cdot \text{Pa}^{-1}$. The diffusion coefficient for the same sample was $0.034 \text{ cm}^2 \cdot \text{s}^{-1}$, which means good penetrability of fluid through the material and thus low resistance to fluid flow.

The filtration barriers based on this material have the potential to replace sintered metal or ceramic membranes in certain applications, especially where the use of the sintered materials is too cost-prohibitive.

Acknowledgement

This work was supported by a project of the Heat Transfer and Fluid Flow Laboratory of Faculty of Mechanical Engineering BUT HEATEAM CZ.1.07/2.3.00/20.0188 and the Material Research Center of Faculty of Chemistry BUT CZ.1.05/2.1.00/01.0012.

References

- Dong, Y. et al. (2009) Cost-effective tubular cordierite micro-filtration membranes processed by co-sintering. *Journal of Alloys and Compounds*. pp. 35-40.
- Guocheng, L. et al. (2012) Preparation and characterization of red mud sintered porous materials for water defluoridation. *Applied Clay Science*.
- Hanykýř, V., Kutzendorfer, J. (2000) *Ceramic technology*, Hradec Králové: Vega s.r.o., (in Czech).
- Hlaváč, J. (1981) *Fundamentals of silicates*, Praha SNTL, (in Czech).
- Kudová, J. et al. (2004) Porous ceramic elements for filtration of gases and related applications. *Chemické listy*, pp. 29-32, (in Czech).
- Nandi, B.K., Uppaluri, R., Purkait, M.K. (2008) Preparation and characterization of low cost ceramic membranes for micro-filtration applications. *Applied Clay Science*, pp. 102-110.
- Ptáček, P. et al. (2012) *Practicum of preparation and testing methods II*. Brno: Brno University of Technology, Faculty of Chemistry (in Czech).
- Sarkar, S. et al. (2012) New clay-alumina porous capillary supports for filtration application. *Journal of Membrane Science*. pp. 130-136.
- Spiratos, N. et al. (2003) *Superplasticizers for concrete: Fundamentals, technology, and practice*. Ottawa, Ontario: Supplementary Cementing Materials for Sustainable Development, Inc. ©2003.

SOME PROBLEMS WITH THE ESTIMATION OF PROJECTILE TRAJECTORY PERTURBATIONS

V. Cech^{*}, L. Jedlicka^{**}, J. Jevicky^{***}

Abstract: *The basis for the projectile trajectory analysis is the analysis of trajectories calculated for the standard conditions (Position, Material, and Weather). Trajectories calculated under the non-standard conditions are considered to be perturbed trajectories. The tools utilized for the analysis of perturbed trajectories are weighting factor functions (curves) – WFFs. The most important curves describe consequences of perturbation of meteorological conditions (WFF – wind, WFF – air density, WFF – virtual temperature, WFF – air pressure). The weighting factors (WFs) are calculated from the WFFs and obtained WFs are used for calculation of (meteorological) ballistic elements μ_B (ballistic wind w_B , density ρ_B , virtual temperature τ_B , pressure p_B). The tabular firing tables are prepared in such a way that the calculation of ballistic elements μ_B is required for the follow-up calculation. Ballistic elements μ_B are presented in the ballistic meteorological messages. The basis for creation of STANAG 4061 in 1957 were chosen WFFs. The original materials are not available today and therefore the corresponding WFFs were reconstructed to create conditions for the accuracy analysis of procedures based on the use of STANAG 4061. The article shows results of reconstructions – corresponding WFFs. In detail the WFF-virtual temperature will be analyzed.*

Keywords: Perturbation of the projectile trajectory, Weighting factor function (curve), Weighting factor, (meteorological) Ballistic elements, Firing Tables.

1. Introduction

The analysis of the procedure that was used for the reconstruction of the weighting factor functions (curves) – WFFs was presented in the article Cech et al. (2014). The analysis was limited to the type of met message: Surface-to-surface fire (K = 3).

The use of Weighting Factors $q(\mu)$ (particular magnitudes are presented in e.g. STANAG 4061) is based on linearization of the solution of projectile trajectories for non-standard trajectories that are close to standard ones. In practice the perturbation methods described in Molitz, H. and Strobel, R. (1963) can be used. The first step is always calculation of corresponding weighting (factor) function (WFF) $r(\mu)$. The weighting factors $q(\mu)$ are consequently derived from this function. The procedures of WFFs calculations gradually developed, see e.g. Curti (1945), Molitz and Strobel (1963). In the end the procedure proposed by Garnier (1929) and modified by Bliss (1944) became the most widespread. The procedure for WFFs calculation used by authors of this article is another modification of Garnier – Bliss procedure, e.g. Kovalenko and Shevkunov (1975), Logvin and Aleksandrov (1977), Petrovic (2005, 2006).

The reason for dealing with this issue is specific for the current time and countries that at the same time use the tabular firing tables in format defined in STANAG 4119 demanding the use of standard ballistic meteorological messages described in STANAG 4061 and also the tabular firing tables created in the former USSR and its satellites since the second half of the fifties of the last century. Their use requires utilisation of the Reference Height of Trajectory – RHT from corresponding WFFs and standardized met message

* Assoc. Prof. Ing. Vladimír Čech, CSc.: Oprox, Inc., Kulkova 8, Brno 615 00, Czech Republic and Trenčín University of A. Dubček, Studentska 2, 911 50 Trenčín, Slovakia, cech-vladimir@volny.cz

** Ing. Luděk Jedlička, PhD.: Department of Weapons and Ammunition, University of Defence, Kounicova 65, Brno 662 10, CZ, l.jedlicka@gmail.com

*** Assoc. Prof. RNDr. Jiří Jevický, CSc.: Department of Mathematics and Physics, University of Defence, Kounicova 65, Brno 662 10, CZ, jiri.jevicky@centrum.cz

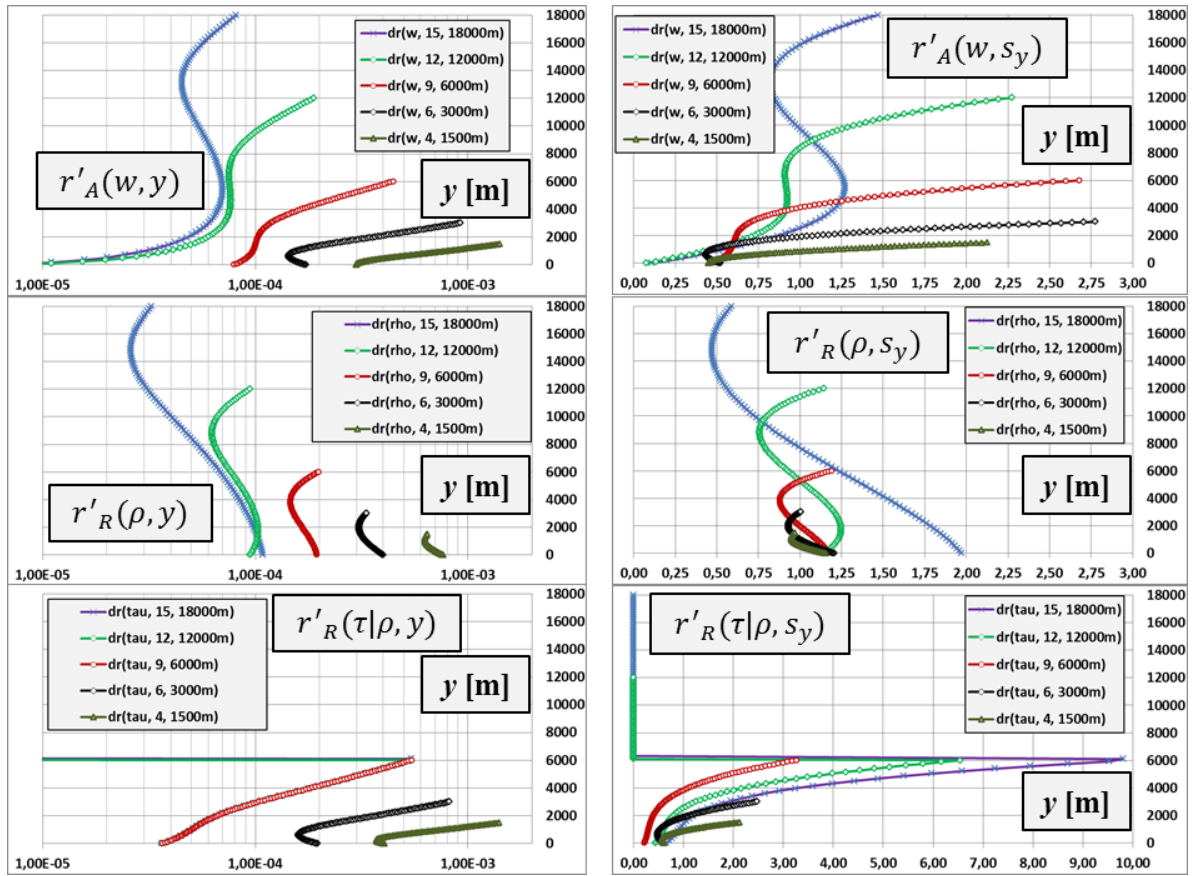


Fig. 1: Reconstructed derivatives of Weighting factor functions – WFFs with respect to y or relative height s_y – normalized form.

Meteo-11 or Meteo-44. The key is study of possibility of mutual conversion WFFs, WFs and RHTs and creation of methodology for mutual evaluation of accuracy of both procedures.

2. Weighting Factor Function

The following definitions hold true, e.g. Kovalenko, V. V. and Shevkunov, V. I. (1975)

$$\Delta\mu_B = \int_0^{Y_S} \Delta\mu(y) \cdot r'_A(y) \cdot dy = \int_0^1 \Delta\mu(s_y) \cdot r'_A(s_y) \cdot ds_y, \quad (1)$$

$$\delta\mu_B = \int_0^{Y_S} \delta\mu(y) \cdot r'_R(y) \cdot dy = \int_0^1 \delta\mu(s_y) \cdot r'_R(s_y) \cdot ds_y, \quad (2)$$

where:

$s_y = y/Y_S$ – relative magnitude of y coordinate,

Y_S – vertex height of trajectory [m],

$\Delta\mu(y) = \mu(y) - \mu_{STD}(y)$ - absolute deviation (index A) of met element μ at height y ,

$\delta\mu(y) = \Delta\mu(y)/\mu_{STD}(y)$ - relative deviation (index R) of met element μ at height y ,

$\mu(y)$ – real or measured magnitude of met parameter μ at height y ,

$r'_A(y) = \frac{\partial r_A}{\partial y}$ – partial derivative of WFF $r_A(\mu, y)$ with respect to y ,

$r'_R(y) = \frac{\partial r_R}{\partial y}$ – partial derivative of WFF $r_R(\mu, y)$ with respect to y .

It is obvious that the ballistic elements $\Delta\mu_B$ and $\delta\mu_B$ are calculated as weighted mean from the measured values $\mu(y)$. The conversion relation between WFF $r_A(\mu, y)$ and $r_R(\mu, y)$ is not presented here. It is rather common to show the graphs of WFF $r_A(\mu, s_y)$ and $r_R(\mu, s_y)$ – see Fig. 2.

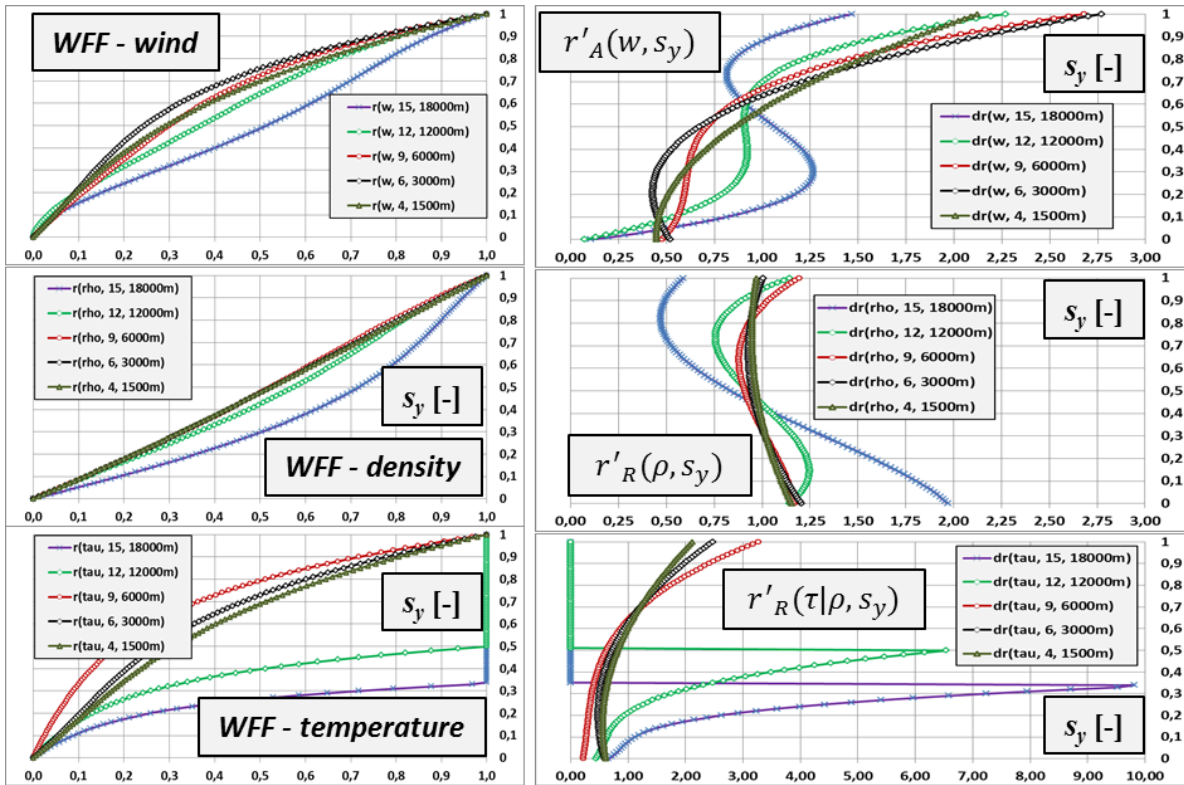


Fig. 2: Reconstructed Weighting factor functions (curves) – WFFs and their derivatives with respect to relative heights s_y – normalized form that is often used by number of authors.

Results of calculations – reconstructed WFFs and their derivatives – are presented in Fig. 1 and 2. The STANAG 4061 divides the atmosphere into height layers $n = 1, 2, \dots, 15$. Upper limit of the n -th zone is $y(n) = Y_S(n)$. The illustrative cases are chosen for layers $n = 4, 6, 9, 12, 15$ and their corresponding heights $y(n) = 1500, 3000, 6000, 12000$ and 18000 m.

3. Weighting Factor Function of the Virtual Temperature

The analysis of this issue concerning of WFF of the wind has already been done in Cech et al. (2014).

The untypical course of WFF of the virtual temperature (WFF - temperature) and its derivatives for zones $n = 10 - 15$ (illustrative case is for $n = 12$ and 15) is apparent from Fig. 1 and Fig. 2. This phenomena is known from the twenties of the last century and is sometimes labeled as “norm-effect”. Roth and Sägnér (1962) dealt with this issue in detail but simulation that has been carried out by authors imply that the issue is more complicated than these authors present.

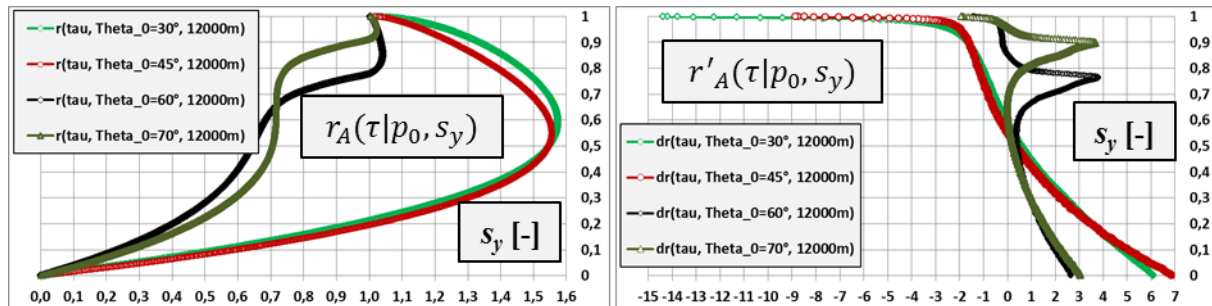


Fig. 3: Weighting factor functions – WFFs - temperature and their derivatives with respect to relative height s_y – normalized form for $Y_S = 12000$ m, $c_{43} = 0.43$ m²/kg and $\Theta_0 = 30^\circ, 45^\circ, 60^\circ$ and 70° ($v_0 = 1668, 1040, 802$ and 718 m/s).

Fig. 3 shows WFFs and their derivatives for $n = 12$ and $y(n) = 12000$ m, ballistic coefficient $c_{43} = 0.43$ m²/kg, angles of departure $\Theta_0 = 30^\circ, 45^\circ, 60^\circ$ and 70° and corresponding initial velocities v_0 . It is apparent that shapes of WFFs strongly depend on the angle of departure Θ_0 .

Following comparison based on the WFFs - temperature curves presented in Fig. 1, Fig. 2 and Fig. 3 is conditional and follows from the general analogies valid for the projectile trajectories. Immediate comparison is not possible because WFFs in Fig. 1 and Fig. 2 respecting STANAG 4061 suppose complementary WFFs-density that is expressed by notation $(\tau|\rho)$. Presented results of authors calculations suppose complementary met parameter air-pressure at the muzzle level p_0 , which is expressed by notation $(\tau|p_0)$. Deeper explanation can be find in Molitz and Strobel (1963) and also Cech et al. (2014).

As it has already been presented for the WFF-wind, the STANAG 4061 shows only one WFF curve for the given height $y(n)$ ("mean" WFF). It is apparently weighted mean of several WFFs curves. But used departure angles Θ_0 and ballistic coefficient c_{43} of these WFFs are not known just as used weights.

This "mean" WFF-temperature exceeds magnitude 1 and authors of STANAG 4061 simplified the problem by introducing the condition that for $r_R(\tau, s_y) > 1$ the magnitude of $r_R(\tau, s_y) = 1$. Unfortunately this simplification leads to distorted derivatives of WFFs courses with respect to y (compare Fig. 2 and Fig. 3). It follows from the relations (1) and (2) that the calculated relative deviation of ballistic virtual temperature $\delta\tau_B$ will be significantly different from the correct or more accurate magnitude.

4. Conclusions

It follows from the analysis of reconstructed WFFs and follow-up calculations that the weighting factors (WFs) presented in STANAG 4061 are sufficiently accurate as "average magnitudes" determined from "average" WFFs only for very narrow domain of combinations of magnitudes of departure angles and ballistic coefficients, i.e. particular weapons and projectiles. For the other combinations the sufficient accuracy in determination of ballistic elements μ_B is not guaranteed. The larges inaccuracies are caused by very simplified courses of "mean" WFFs-temperature for $Y_S > 6000\text{m}$. Further research will be focused especially on WFFs - temperature.

Acknowledgement

This work has originated under the support of financial means from the industrial research project of the Ministry of the Interior of the Czech Republic - project code VG20122015076: "Two survey points range-finding system utilization for perimeter security (screen)" and from the Research project for the development of the Department of Weapons and Ammunition, Faculty of Military Technology, University of Defence, Brno, PRO K-201.

References

- Cech, V., Jedlicka, L. & Jevicky, J. (2014) Problem of the reference height of the projectile trajectory as a reduced meteo-ballistic weighting factor. Defence Technology, in print.
- Curti, P. (1945) Introduction into Exterior Ballistics (in German). Frauenfeld: Verlag Huber and Co., p. 408.
- Kovalenko, V. V. & Shevkunov, V. I. (1975) Meteorological preparation of artillery fire (in Russian). Leningrad: Military Artillery Academy of M. I. Kalinin, p. 84.
- Logvin, A. M. & Aleksandrov, V.I. (1977) Gunnery and Exterior Ballistics (in Russian). Penza: Military Artillery Academy of N. N. Voronov, p. 255.
- Molitz, H. & Strobel, R. (1963) Exterior Ballistics (in German). Berlin: Springer-Verlag, p. 610.
- Petrovic, D. R. (2005) Mechanized procedure for the calculation of altitude coefficients. In.: Scientific-Technical Review, Vol. LV, No. 3-4, pp. 9-14.
- Petrovic, D. R. (2006) New procedure for calculating altitude coefficients. In.: Scientific-Technical Review, Vol. LVI, No. 3-4, pp. 47-51.
- Roth, E. & Sägner, R. (1962) Über den Einfluss der Temperatur auf die Flugbahn eines Geschosses. Zeitschrift für angewandte Mathematik und Physik (ZAMP), Vol. 13, Issue 2, pp. 175-181.
- STANAG 4044 MET Adoption of a Standard Atmosphere.
- STANAG 4061 MET Adoption of a Standard Ballistic Meteorological Message (METBKQ).
- STANAG 4119 Adoption of a Standard Cannon Artillery Firing Table Format.

DETERMINATION OF MATERIAL PARAMETERS OF RUBBER AND RUBBER COMPOSITES BY BIAXIAL LOADING

M. Čadek^{*}, B. Marvalová^{**}, I. Petříková^{***}, S. M. Samal^{****}

Abstract: *This paper describes a method, designed for measurement of material characteristics of rubber like materials, using biaxial loading device. We present the experimental measurement and FEA simulation in Comsol Multiphysics of the response of rubber specimens from conveyor belt used for the transport of overburden in a coal mine. The results of numerical simulation are verified by experimental measurements. This work is part of a broader project that aims to increase service life of the conveyor belts.*

Keywords: Rubber, Digital Image Correlation, Shear Modulus, Rubber material model, FEA.

1. Introduction

Rubber is a material capable of large deformation (100% at least) under relatively small load. Rubber, after load removal, quickly returns to almost its original state. Specimens of styrene-butadiene rubber, investigated in this work, were cut out of a covering layer of the conveyor belt. The material parameters of this covering layer are needed for the numerical simulation of the behaviour of the complete belt. Specimens were loaded in uniaxial and biaxial tension. Applied forces were measured by force sensors and large 2D displacements were measured by a non-contact, optical method - Digital Image Correlation - using Dantec Dynamics device and 2D strains were evaluated by Istra4D. Mooney-Rivlin hyperelastic material model with two parameters was chosen. The parameters were calculated by optimization methods in Matlab. The shear modulus was computed from these parameters and FEA of loading states specified above was performed in Comsol Multiphysics.

2. Experimental

Measurements are performed at room temperature using both special biaxial testing machine and universal testing machine TIRA for uniaxial loading. Measured variables are deformation and force. Force is measured by load cells placed on machine's grippers. Deformation is measured using Dantec Dynamics Q-400 system with Istra 4D software. As a result deformation is plane only one camera was used so the whole measurement is simplified to 2D. It is acceptable due to relatively thin specimens. All specimens were cut off from the same cover layer of belt. Specimens for uniaxial measurements are thin strips 300 x 28 x 3 mm. Specimens for biaxial measurement had a cruciform shape of 140 x 140 x 7 mm, with the width of cross arms 60 mm.

2.1. Uniaxial load

Uniaxial measurements were performed on 5 specimens of the same dimensions. The determined stress-strain diagram is represented in Fig. 1. These data were used for shear modulus determination. Mooney-

* Bc. Miloš Čadek: Department of Applied Mechanics, Technical University of Liberec, Komenského 314/2; 460 01, Liberec; CZ, milos.cadek@gmail.com

** Prof. Ing. Bohdana Marvalová, CSc.: Department of Applied Mechanics, Technical University of Liberec, Komenského 314/2; 460 01, Liberec; CZ, bohda.marvalova@tul.cz

*** Assoc. Prof. Ing. Iva Petříková, PhD.: Department of Applied Mechanics, Technical University of Liberec, Komenského 314/2; 460 01, Liberec; CZ, iva.petrikova@tul.cz

**** Dr. Sneha M. Samal: Department of Applied Mechanics, Technical University of Liberec, Komenského 314/2; 460 01, Liberec; CZ, samashneha@gmail.com

Rivlin parameters were computed in Comsol Multiphysics by optimization method $C_{01} = 1.72$ MPa, $C_{10} = 0.15$ MPa and shear modulus $G = 3.73$ MPa.

2.2. Biaxial load

Biaxial measurements were performed on special biaxial testing machine which can be seen on Fig. 3. Specimens were received from covering layer of conveyor belt. Measured data can be seen on Fig. 2. Mooney-Rivlin parameters were computed in Matlab by chapter 2.2.1. So $C_1 = 0.49$ MPa, $C_2 = 0.56$ MPa and shear modulus $G = 2.11$ MPa.

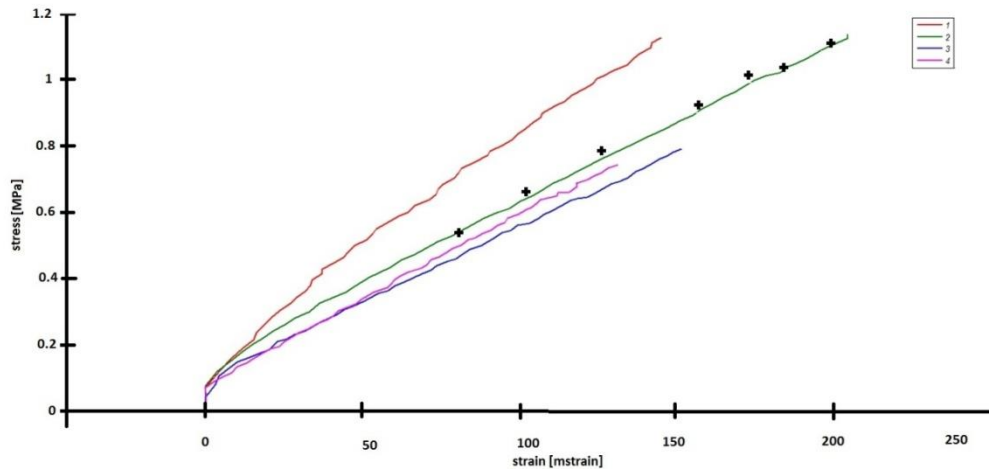


Fig. 1: Uniaxial tensile test. Full lines - measured data, points - FE simulation.

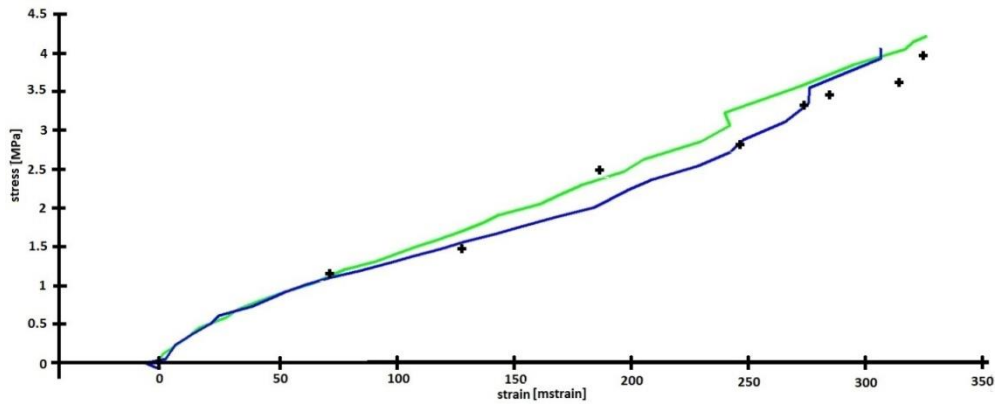


Fig. 2: Biaxial test. Full lines - measured data, points - FE simulation.

2.2.1. Shear Modulus

Elastomers are described by hyperelastic materials e.g. Ogden, Mooney-Rivlin or Neo-Hookean (Petříková, 2008). Each hyperelastic material is expressed by the strain energy density function. To determine shear modulus we use Mooney-Rivlin hyperelastic material with two parameters due to achieved elongation, using more parameters would lead to better fitting at higher deformations. Expression for strain energy density function in terms of the stretch ratios for Mooney-Rivlin material is represented by equation (1) and (2)

$$\Psi = C_1(\lambda_1^2 + \lambda_2^2 + \lambda_3^2 - 3) + C_2(\lambda_1^{-2} + \lambda_2^{-2} + \lambda_3^{-2} - 3) \quad (1)$$

$$\lambda_i^2 = 2E_{ij} + 1 \quad (2)$$

where C_1 , C_2 are Mooney-Rivlin parameters, λ_i are the stretch ratios and E_{ij} are components of Green Lagrange strain tensor. Equation (3) defines the relation between stress (4) and deformation.

$$\sigma_a = \lambda_a \frac{\partial \Psi}{\partial \lambda_a} - p \quad (3)$$

$$\sigma_a = \frac{F_a \lambda_a}{A_{0a}} \quad (4)$$

where F_a is measured load force and A_{0a} is cross-sectional area of undeformed specimen. If according to (Holzapfel, 2000) the incompressibility of the rubber is assumed, then

$$\lambda_1 \lambda_2 \lambda_3 = 1 \quad (5)$$

so
$$\lambda_3 = \frac{1}{\lambda_1 \lambda_2} \quad (6)$$

So the first and second principal stresses are determined as equations (7, 8).

$$\sigma_1 = 2C_1 \left(\lambda_1^2 - \frac{2}{\lambda_1^2 \lambda_2^2} \right) + 2C_2 (-\lambda_1^{-2} + 2\lambda_1^2 \lambda_2^2) \quad (7)$$

$$\sigma_2 = 2C_1 \left(\lambda_2^2 - \frac{2}{\lambda_1^2 \lambda_2^2} \right) + 2C_2 (-\lambda_2^3 + 2\lambda_1^2 \lambda_2^2) \quad (8)$$

Parameters C_1 and C_2 are determined by solving overdetermined system of equations (7 and 8) in Matlab. Lamé parameter is determined by equation (9), whereas according to (Holzapfel, 2000) Lamé parameter is equal to shear modulus G .

$$\mu = 2(C_1 + C_2) = G \quad (9)$$

The shear modulus of uni-axially loaded sample can be computed from optimization module in Comsol with more accuracy (COMSOL). Computation performed in Comsol is based on equivalent expression for strain energy density of equation (1), and Mooney-Rivlin material model. The inputs were measured stress- strain data to perform the computation of shear modulus. Output of the process are computed Mooney- Rivlin parameters, the fitting is displayed in the Fig. 4.

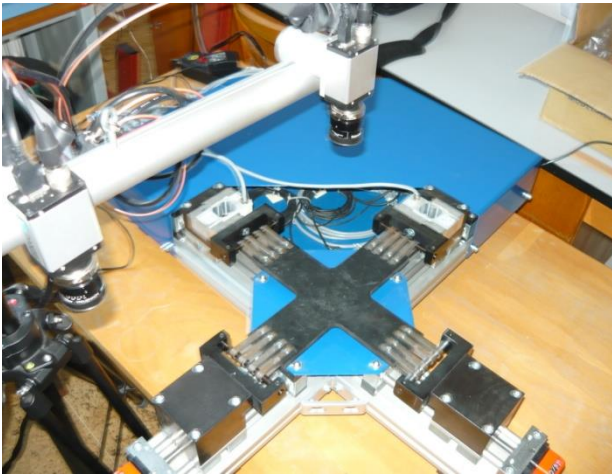


Fig. 3: Biaxial loading device.

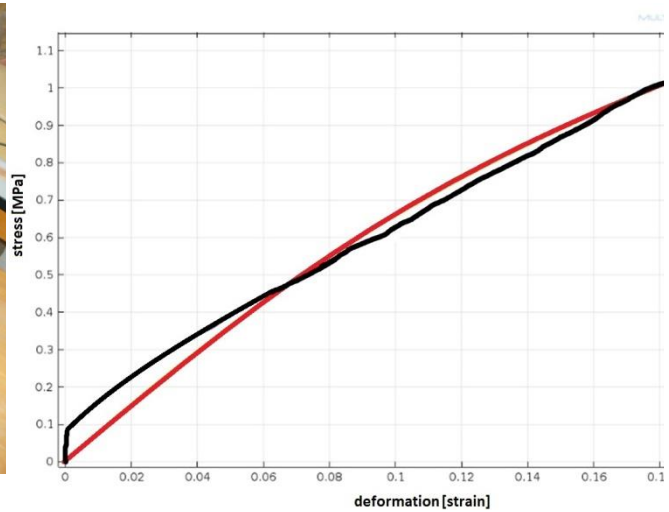


Fig. 4: Stress-strain diagram, -black experimental data, red - fitted curve.

2.2.2. FEA

Finite element analyses of both experiments were performed in Comsol Multiphysics. The comparison of measured and computed stress-strain fields is displayed in Figs. 5 and 6. Specific values from simulation can be found on Figs. 1 and 2. Simulations were performed in 2D with material parameters as computed in part 2.1. and 2.2., using Mooney-Rivlin material model.

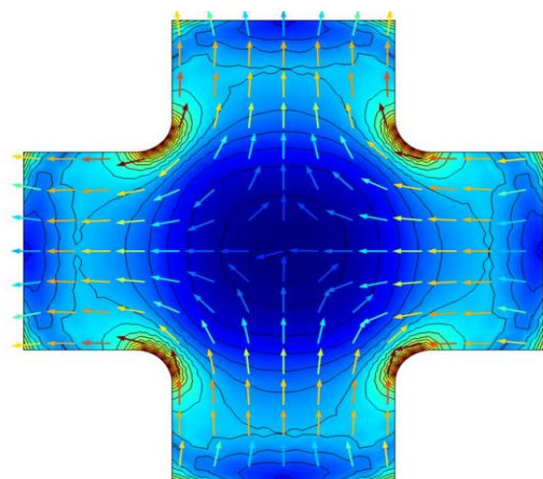


Fig. 5: FEA, displays first principal stress and first principal strain and its directions.

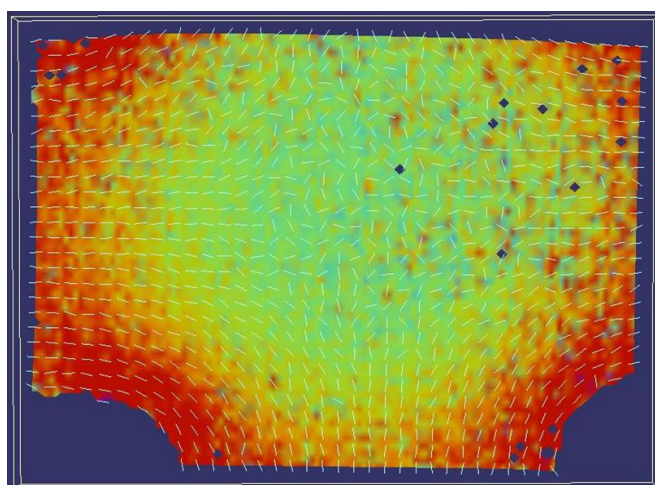


Fig. 6: Istra 4D image from deformation measurement, displays first principal strain.

3. Conclusions

This article includes measured stress-strain diagrams for two different types of experiments and five measured samples from covering layer of conveyor belt, calculation of shear modulus, and FEA of various experiments with the validity of described methods.

Material model used for uniaxial tension was Mooney-Rivlin. However, in the range of experimental deformation (under 100%) Neo-Hookean model with only one parameter could be sufficient to determine the shear modulus. On the contrary there was relatively higher deformation developed in the biaxial measurement, mainly due to stiffer clamping of the sample. This indicates a good fit of Mooney-Rivlin material model with two parameters. Homogeneous strain field is observed in the middle of the cruciform specimen designed for biaxial testing (Figs. 5 and 6). Similarly, first principal strain directions are the same both in FEA and measurement. The comparison of the values of stress calculated by FEA and determined by measurement showed a very small difference of 0.5 MPa. This indicates that methods used to determine shear modulus are valid for given material. The difference between computed shear modulus is given by measurement uncertainty, 2D simplification, numerical approximations and anisotropy that may arise in samples during the preparation. The work history of provided conveyor belt is unknown. Therefore computed values of shear modulus are valid just for this particular sample of conveyor belt and only to the amount of deformation achieved in experimental measurement with bi-axial or uni-axial tensile load.

Acknowledgement

The financial assistance of Ministry of Industry and Trade of Czech Republic, grant No FR-TI4/310 is gratefully acknowledged.

References

- Holzapfel, G. A. (2000) Nonlinear Solid Mechanics, John Wiley & Sons, Ltd.
- Petríková, I. (2008) The mechanical properties of rubber, TUL, KMP, Liberec (in Czech).
- COMSOL, The Nonlinear Structural Materials Module User's Guide.

INFLUENCE OF PROPELLER BLADE FORCE SPANWISE DISTRIBUTION ON WHIRL FLUTTER CHARACTERISTICS

J. Čeřrdle *

Abstract: *This paper is focused on the influence of the propeller blade lift spanwise distribution on whirl flutter stability. It gives the theoretical background of the whirl flutter phenomenon and the propeller blade forces solution. The problem is demonstrated on the example of a twin turboprop aircraft structure. The influences on the propeller aerodynamic derivatives and the influences on the whirl flutter speed and the whirl flutter margin respectively are evaluated.*

Keywords: Aeroelasticity, Flutter, Propeller blade force, Whirl flutter.

1. Introduction

Whirl flutter is the specific case of the flutter that includes additional dynamic and aerodynamic influences of propeller and engine rotating parts. Effect of a rotating mass increases the number of degrees of freedom and causes additional forces and moments. Moreover, rotating propeller causes a complicated flow field and interference effects between wing, nacelle and propeller. The essential fact is an unsymmetric distribution of forces on a transversely vibrating propeller. Whirl flutter may cause a propeller mounting unstable vibrations, even a failure of an engine, nacelle or whole wing.

2. Theoretical Background

The fundamental solution presented by Reed (1967) is derived for the system with 2 degrees of freedom as illustrated in Fig. 1. Engine system flexible mounting can be substituted by the system of two rotational springs (K_ψ , K_θ). Propeller is considered as rigid, rotating with angular velocity Ω . System is exposed to the airflow of velocity V_∞ .

Neglecting the propeller rotation and the aerodynamic forces, the two independent mode shapes will emerge with angular frequencies ω_ψ and ω_θ . Considering the propeller rotation, the gyroscopic effect makes two independent mode shapes merge to the whirl motion. The propeller axis shows an elliptical movement. The orientation is backward relative to the propeller rotation for the mode with lower frequency (backward whirl) and forward relative to the propeller rotation for the mode with higher frequency (forward whirl). The mode shapes of gyroscopic modes are complex, since independent yaw and pitch modes have a phase shift 90° . Gyroscopic mode shapes cause harmonic changes of propeller blades angles of attack. They give rise to unsteady aerodynamic forces, which may under the specific conditions induce whirl flutter. Provided that the air velocity is lower than critical value ($V_\infty < V_{FL}$), the system is stable and the motion is damped. If the airspeed exceeds the critical value ($V_\infty > V_{FL}$), the system becomes unstable and motion is diverging. The state of the neutral stability

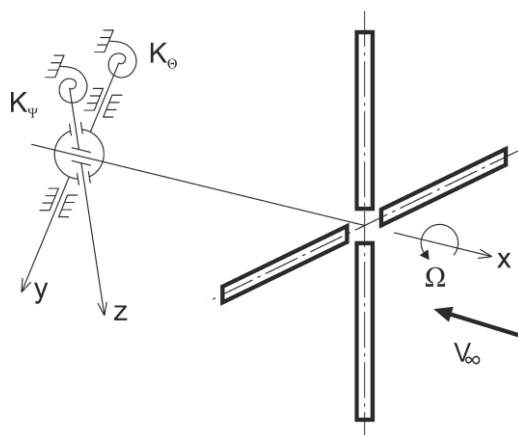


Fig. 1: Gyroscopic system with propeller.

* Ing. Jiří Čeřrdle, PhD.: Strength of Structures Dept., Aeronautical Research and Test Institute (VZLU), Beranovych 130; 199 05, Prague - Letnany; CZ, cecrdle@vzlu.cz

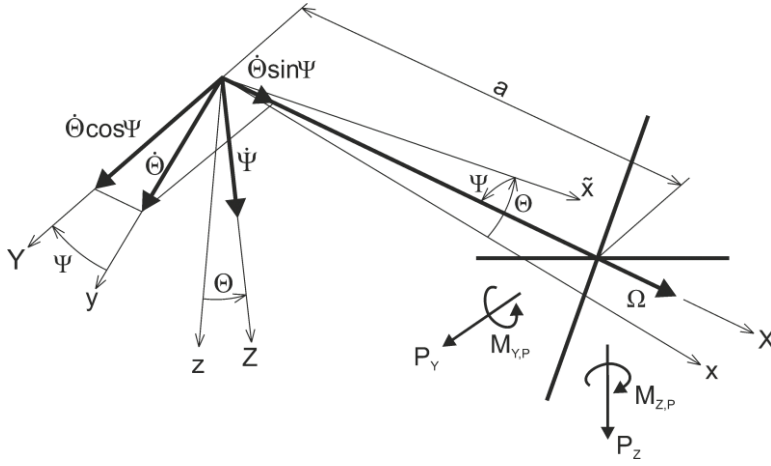


Fig. 2: Kinematical scheme of the gyroscopic system.

($V_\infty = V_{FL}$) with no total damping is called critical flutter state and V_{FL} is called critical flutter speed.

Basic problem consists in the determination of the aerodynamic forces caused by the gyroscopic motion for the specific propeller blades. The kinematical scheme including gyroscopic effects according Reed and Bland (1961) is shown in Fig. 2. The independent generalized coordinates are three angles (φ , θ , ψ). We assume the

propeller angular velocity constant ($\dot{\varphi} = \Omega t$), mass distribution symmetric around X-axis and mass moments of inertia $J_z \neq J_y$. Considering small angles the equations of motion become:

$$\begin{aligned} J_y \ddot{\theta} + \frac{K_\theta \gamma_\theta}{\omega} \dot{\theta} + J_x \Omega \dot{\psi} + K_\theta \theta &= M_{y,p} - a P_z \\ J_z \ddot{\psi} + \frac{K_\psi \gamma_\psi}{\omega} \dot{\psi} - J_x \Omega \dot{\theta} + K_\psi \psi &= M_{z,p} + a P_y \end{aligned} \quad (1)$$

We formulate the propeller aerodynamic forces by means of the aerodynamic derivatives as described later and make the simplification for the harmonic motion. Then the final whirl flutter matrix equation become:

$$\left(-\omega^2 [M] + j\omega \left([D] + [G] + q_\infty F_p \frac{D_p^2}{V_\infty} [D^A] \right) + ([K] + q_\infty F_p D_p [K^A]) \right) \begin{bmatrix} \bar{\theta} \\ \bar{\psi} \end{bmatrix} = \{0\} \quad (2)$$

The limit state emerges for the specific combination of parameters V_∞ and Ω , when the angular velocity ω is real. Whirl flutter appears at the gyroscopic rotational vibrations, the flutter frequency is the same as the frequency of the backward gyroscopic mode. The most critical state is $K_\theta = K_\psi$, it means $\omega_\theta = \omega_\psi$, when the interaction of both independent motions is maximal.

The fundamental solution of the propeller aerodynamic forces was derived by Ribner (1945). Later on, the modified solution of Houbolt and Reed (1962) became available as well. The propeller aerodynamic forces are expressed as:

$$\begin{aligned} P_y &= \pi \rho V_\infty^2 R^2 \left(c_{y\theta} \theta^* + c_{y\psi} \psi^* + c_{yq} \frac{\dot{\theta}^* R}{V_\infty} + c_{yr} \frac{\dot{\psi}^* R}{V_\infty} \right) \\ P_z &= \pi \rho V_\infty^2 R^2 \left(c_{z\theta} \theta^* + c_{z\psi} \psi^* + c_{zq} \frac{\dot{\theta}^* R}{V_\infty} + c_{zr} \frac{\dot{\psi}^* R}{V_\infty} \right) \\ M_{y,p} &= 2\pi \rho V_\infty^2 R^3 \left(c_{m\theta} \theta^* + c_{m\psi} \psi^* + c_{mq} \frac{\dot{\theta}^* R}{V_\infty} + c_{mr} \frac{\dot{\psi}^* R}{V_\infty} \right) \\ M_{z,p} &= 2\pi \rho V_\infty^2 R^3 \left(c_{n\theta} \theta^* + c_{n\psi} \psi^* + c_{nq} \frac{\dot{\theta}^* R}{V_\infty} + c_{nr} \frac{\dot{\psi}^* R}{V_\infty} \right) \end{aligned} \quad (3)$$

where ρ is a dynamic pressure and R is a propeller diameter. The effective angles (θ^* ; ψ^*) are basically expressed as the quasi-steady values ($(\theta^* = \theta + (\dot{Z}/V_\infty)$; $(\psi^* = \psi - (\dot{Y}/V_\infty)$) and the c_{ij} terms represent the aerodynamic derivatives. We neglect the aerodynamic inertia terms ($\theta^* \approx \theta$; $\psi^* \approx \psi$), make the simplification given by the symmetry ($c_{z\psi} = c_{y\theta}$; $c_{m\psi} = -c_{n\theta}$; $c_{mq} = c_{nr}$; $c_{zr} = c_{yq}$; $c_{z\theta} = -c_{y\psi}$; $c_{n\psi} = c_{m\theta}$; $c_{mr} = -c_{nq}$; $c_{yr} = -c_{zq}$) and we neglect the derivatives with low values ($c_{mr} = -c_{nq} = 0$; $c_{yr} = -c_{zq} = 0$). As the result, we obtain 6 independent values of aerodynamic derivatives expressed by the propeller blade integrals that integrate the aerodynamic forces in the blade spanwise direction.

The basic formulation was given by Houbolt and Reed (1962). It is limited to the 4-blade propeller and theoretical blade lift curve slope ($\alpha_0 = 2\pi$). It includes only 3 integrals accounting for the in-phase aerodynamic effects. Extended formulation of the blade integrals is presented by Rodden and Rose (1989). It includes the aerodynamic lift lag effect by means of the Theodorsen function ($F(k_p) + jG(k_p)$), the Prandtl - Glauert correction to the compressibility and the correction factor accounting for the compressible flow blade aspect - ratio effect. Final correction is applied to account for the number of blades. Integration range is reduced to the thrusting part of the propeller. The propeller lift curve slope (α_0) is treated as the effective (spanwise constant) value ($\alpha_0 = \alpha_{0eff}$). Contrary to Rodden's formulation, we use more precise approach, that treats the lift curve slope as the spanwise variable ($\alpha_0 = \alpha_0(\eta)$) accounting for the real propeller force distribution. In this case α_0 moves under the integrand and the propeller blade integrals become:

$$\begin{aligned}
I_1 &= \left(\frac{N_b}{4}\right) \left(\frac{1}{2\pi}\right) \frac{\mu^2 A_r}{c_r} \int_{\eta_0}^1 \frac{a_0(\eta) c(\eta) F(k_p)}{\sqrt{\mu^2 + \eta^2} \left[2 + A_r \sqrt{1 - M^2 \left(1 + \frac{\eta^2}{\mu^2}\right)}\right]} d\eta \\
J_1 &= \left(\frac{N_b}{4}\right) \left(\frac{1}{2\pi}\right) \frac{\mu^2 A_r}{c_r} \int_{\eta_0}^1 \frac{a_0(\eta) c(\eta) G(k_p)}{\sqrt{\mu^2 + \eta^2} \left[2 + A_r \sqrt{1 - M^2 \left(1 + \frac{\eta^2}{\mu^2}\right)}\right]} d\eta \\
I_2 &= \left(\frac{N_b}{4}\right) \left(\frac{1}{2\pi}\right) \frac{\mu A_r}{c_r} \int_{\eta_0}^1 \frac{\eta^2 a_0(\eta) c(\eta) F(k_p)}{\sqrt{\mu^2 + \eta^2} \left[2 + A_r \sqrt{1 - M^2 \left(1 + \frac{\eta^2}{\mu^2}\right)}\right]} d\eta \\
J_2 &= \left(\frac{N_b}{4}\right) \left(\frac{1}{2\pi}\right) \frac{\mu A_r}{c_r} \int_{\eta_0}^1 \frac{\eta^2 a_0(\eta) c(\eta) G(k_p)}{\sqrt{\mu^2 + \eta^2} \left[2 + A_r \sqrt{1 - M^2 \left(1 + \frac{\eta^2}{\mu^2}\right)}\right]} d\eta \\
I_3 &= \left(\frac{N_b}{4}\right) \left(\frac{1}{2\pi}\right) \frac{A_r}{c_r} \int_{\eta_0}^1 \frac{\eta^4 a_0(\eta) c(\eta) F(k_p)}{\sqrt{\mu^2 + \eta^2} \left[2 + A_r \sqrt{1 - M^2 \left(1 + \frac{\eta^2}{\mu^2}\right)}\right]} d\eta \\
J_3 &= \left(\frac{N_b}{4}\right) \left(\frac{1}{2\pi}\right) \frac{A_r}{c_r} \int_{\eta_0}^1 \frac{\eta^4 a_0(\eta) c(\eta) G(k_p)}{\sqrt{\mu^2 + \eta^2} \left[2 + A_r \sqrt{1 - M^2 \left(1 + \frac{\eta^2}{\mu^2}\right)}\right]} d\eta
\end{aligned} \tag{4}$$

where A_r is a blade aspect ratio, c is a blade local chord, k_p is a blade local reduced frequency. A propeller advance ratio is defined as $\mu = (\mathbf{V}_\infty / \Omega \mathbf{R})$ and a blade dimensionless radius is defined as $\eta = (r/R)$ where r is a blade local radius. M represent the forward flow Mach number. Aerodynamic derivatives are then expressed as:

$$\begin{aligned}
c_{z\theta} &= -\left(\frac{4\Omega c_r}{V_\infty}\right) I_1 \quad ; \quad c_{zq} = \left(\frac{4\Omega c_r}{V_\infty}\right) J_2 \quad ; \quad c_{m\theta} = -\left(\frac{2\Omega c_r}{V_\infty}\right) J_2 \quad ; \quad c_{mq} = -\left(\frac{2\Omega c_r}{V_\infty}\right) I_3 \\
c_{y\theta} &= -\left(\frac{4\Omega c_r}{V_\infty}\right) J_1 \quad ; \quad c_{yq} = -\left(\frac{4\Omega c_r}{V_\infty}\right) I_2 \quad ; \quad c_{n\theta} = -\left(\frac{2\Omega c_r}{V_\infty}\right) I_2 \quad ; \quad c_{nq} = -\left(\frac{2\Omega c_r}{V_\infty}\right) J_3
\end{aligned} \tag{5}$$

3. Application Example

The evaluation is performed on the structure of the **EV-55M** aircraft that is ordinary twin turboprop for **9 - 13** passengers powered by **PT6A-21** turboprop engines with Avia **AV-844** propellers. Firstly, the evaluation of the aerodynamic derivatives is provided. The blade lift curve slope spanwise distribution as well as the geometry of the blade cannot be reproduced here. The effective value extracted by means of the **RMS** method of $\alpha_{0eff} = 6.2478$ is slightly lower comparing to the profile theoretical value of 2π

Fig. 3 shows the example of aerodynamic derivative dependence on the flow velocity considering both a_{0eff} and $a_0(\eta)$. The derivative values considering $a_0(\eta)$ are lower comparing to the ones using a_{0eff} . This fact hold true also for the other ones which are not shown here.

The final evaluation of the whirl flutter speed was performed using the **NASTRAN** program system supported by the in-house **PROPFM** software code. The effective stiffnesses of the engine mount in both vertical and lateral directions were reduced by **50%** to reach the critical state within the reasonable velocity range wherever the standard analytical approach was employed. The results indicate the backward whirl flutter on the mode #2 that is the engine vertical vibrations mode. The flutter speed is $V_{FL} = 166.6 [m.s^{-1}]$ considering the effective value of the lift curve slope, whereas the flutter speed become $V_{FL} = 182.0 [m.s^{-1}]$ considering the real lift curve slope distribution. It represents the increase in the flutter speed by **9.2%**. The flutter frequency was $f_{FL} = 5.8 [Hz]$, the difference between both cases was barely noticeable.

Further explanation of the blade lift slope influence to the whirl flutter characteristics is provided in Fig. 4. It shows the stability margin defining the critical values of the structural parameters (e.g. vertical and lateral engine vibration mode frequencies) required to reach the neutral stability at the certain speed. Again, the real distribution of the lift curve slope gives the lower critical frequencies and thus higher reserve in terms of the whirl flutter stability with respect to the nominal state. The differences between both margins are ranging within **(5.5 - 7.1)%**.

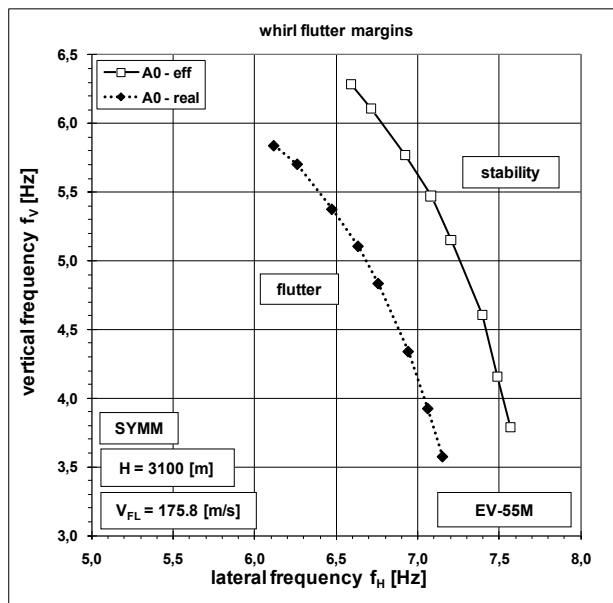


Fig. 4: Whirl flutter stability margins - blade lift slope: a_{0eff} ; $a_0(\eta)$.

References

- Ribner, H.S. (1945) Propellers in Yaw, NASA Rep. 820.
- Reed, W.H. & Bland, S.R. (1961) An Analytical Treatment of Aircraft Propeller Precession Instability, NASA, Technical Note, TN D-659.
- Houbolt, J.C & Reed, W.H. (1962) Propeller Nacelle Whirl Flutter, Journal of Aerospace Sciences, Vol.29, March 1962, pp. 333-346.
- Reed, W.H. (1967) Review of Propeller - Rotor Whirl Flutter, NASA Technical Report, TR R-264.
- Rodden, W.P. & Rose, T.L. (1989) Propeller / Nacelle Whirl Flutter Addition to MSC/NASTRAN, MSC World User's Conference, Universal City, CA, USA.

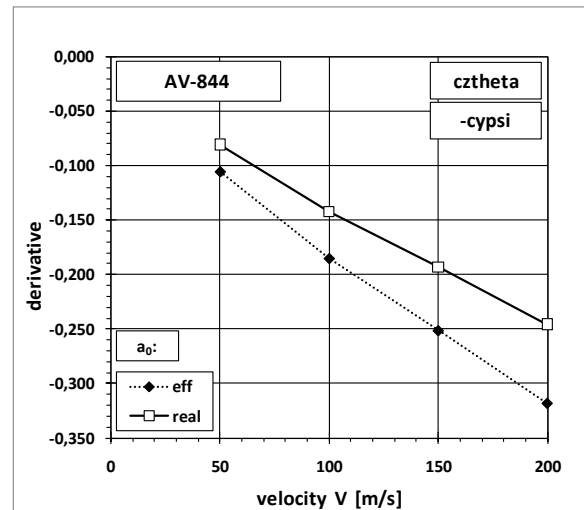


Fig. 3: Aerodynamic derivative $c_{z\theta}$ - blade lift slope: a_{0eff} ; $a_0(\eta)$.

4. Conclusion

Usage of the real propeller blade lift curve slope distribution increases the accuracy of results and raises the rate of reserve in terms of flutter stability. It causes decrease of the aerodynamic derivatives and, as the consequence, it increase the flutter speed and decrease the critical values of the structural parameters. Comparing to the usage of the effective value the derivatives may vary quite significantly.

SIMULATION OF MOTION OF MULTIPLE PARTICLES IN A CLOSED CONDUIT USING THE LBM BASED APPROACH

J. Dolanský*

Abstract: *The two-dimensional numerical model of motion of multiple circular particles in fluid flow based on the lattice Boltzmann method (LBM) is presented. The flow is driven by the power-law velocity profile at the inlet in a closed horizontal conduit. Motion of particles consists of free motion in the flow, particle-bed and particle-particle collisions. The simulation for both movements of particles and velocity field of the flow is developed. Stability issues of the simulation are considered and a resolution using the entropic LBM and extension of computational resources is proposed. Finally, an enhancement of the simulation for more complex processes is suggested.*

Keywords: Motion of particles, Hydrodynamic forces, Lattice Boltzmann method, Entropic LBM.

1. Introduction

The motion of multiple particles in the flow in a closed horizontal conduit is examined. It consists of free motion in the flow, mutual collisions of particles and collisions with the bed. Simulation – based on the LBM – of both motion of particles and velocity field of the flow is developed. It is shown that the simulation produces results comparable to the outputs derivable from the explicit expressions for hydrodynamic forces.

The mathematical model consists of equations for the fluid flow (e.g., Navier-Stokes), equations of motion for particles in the flow (Newton equations) and equations for velocities before and after (both particle-bed and particle-particle) collisions which can be derived from relations for impulse forces. Typically, the fluid flow and the particle motion are solved separately and coupled every time step. The fluid flow equations are usually solved by some of the CFD methods while the motion of particles can be treated for example by the discrete element method (DEM).

In contrast, the methods based on the lattice Boltzmann equation (LBM) represent a numerical strategy which allows to solve particle-fluid systems within a unique frame (e.g., Yu & Fan, 2010). The LBM is a two decade old numerical approach originating from the lattice gas automata methods (LGCA) used for the simulation of complex fluid flows (e.g., Succi, 2001). The LBM represents a second order, efficient computational scheme due to its inherent locality and explicitness. Moreover, the possibility of straightforward parallelization yields another considerable advantage of the traditional numerical approaches to fluid flow problems.

2. Mathematical Model

The flow is driven by the power-law velocity profile at the inlet in a closed horizontal conduit with smooth boundaries. The flow field is described by the incompressible Navier-Stokes equations. The two-dimensional conduit has boundaries of two types: open boundaries (inlet and outflow) and solid boundaries. Each type of boundaries is represented by a different boundary condition.

The no-slip boundary condition – identification of the fluid velocity adjacent to the surface with the velocity of the surface – is supposed at the boundaries of the conduit $\mathbf{u}(\mathbf{x}_{con}) = 0$ as well as on the surface of the moving particles $\mathbf{u}(\mathbf{x}_{part}) = \mathbf{v}(\mathbf{x}_{part})$. At the outflow, the Neumann free flow – the so called “do

* Ing. Jindřich Dolanský, PhD.: Institute of Hydrodynamics AS CR v. v. i., Pod Patankou 30/5; 166 12, Prague 6; CZ, dolansky@ih.cas.cz

nothing” – boundary condition is imposed which corresponds to the normal gradients of the velocity set to zero (e.g., Heywood, 1996).

The motion of a number (up to ten) of non-deformable particles in the flow is determined by actions of body and hydrodynamic forces. They are summed into the resultant net force

$$\mathbf{F}_{net} = -(m - m_f)\mathbf{g} + \rho A \frac{C_D}{2} v_r \mathbf{v}_r + m_f C_m \frac{dv_r}{dt} + \rho A \frac{C_L}{2} (v_{rT}^2 - v_{rB}^2) \mathbf{e}_L \quad (1)$$

where the first term stands for the gravitational force \mathbf{F}_g , the second term represents the drag force \mathbf{F}_d , the third term represents the force due to added mass \mathbf{F}_m and the last term corresponds to the lift force \mathbf{F}_L (Wiberg & Smith, 1985). The net force also develops a torque on the particles which determines their angular velocities ω .

Both the particle-bed and particle-particle collision models are derived from impulse equations of the form $m(\mathbf{v}' - \mathbf{v}) = \mathbf{J}$ which use the impulse force \mathbf{J} as the measure of change of momentum (the quote mark distinguishes velocities before and after collisions). It is supposed that collisions take place in a very short time and all external forces can be neglected. If rotation is taken into account the corresponding impulse equation for the angular velocities before and after the collision reads as $I(\omega' - \omega) = r J_t$ where I stands for momentum of inertia. The above relations enable to derive expressions for new velocities after collisions for both the particle-bed and particle-particle collisions (Czernuszenko, 2009; Lukerchenko et al., 2006, 2009).

3. D2Q9 Lattice Model

The numerical model based on the LBM corresponding to the mathematical description above is designed for the set of nine discrete velocities \mathbf{c}_i on two-dimensional square lattice – such a lattice is denoted by D2Q9. In the LBM the fluid is composed of fictive particles which propagate along the lattice links and interact in nodes. The fictive particles are represented by particle distribution functions $f(\mathbf{x}, \mathbf{c}_i, t)$ which give probabilities of finding of a fictive particle in a node \mathbf{x} with a certain discrete velocity \mathbf{c}_i in time t . The collision and propagation process follows from the lattice Boltzmann equation

$$f_i(\mathbf{x} + \mathbf{c}_i \Delta t, t + \Delta t) - f_i(\mathbf{x}, t) = \frac{1}{\tau} (f_i^{eq} - f_i)$$

where the Bhatnagar-Gross-Krook (BGK) collision operator on the right-hand side is applied on particle distributions f_i in nodes and expresses the tendency to local equilibriums f_i^{eq} (Δt is lattice time step). The collision operator has to fulfill the first law of thermodynamics, i.e., conservation of mass and momentum.

In the case of the BGK approximation the LBM is subject to numerical instabilities at the sub-grid scale caused dramatic fluctuations of distributions f_i in neighboring nodes (e.g., due to very low/high viscosity/Reynolds number). However, if the parameter τ (which expresses the rate of tendency to the local equilibrium f_i^{eq}) is replaced by the factor $\alpha/2\tau$ where the parameter α represents a non-trivial root of equation $H(f + \alpha(f_i^{eq} - f)) = H(f)$, and H is the Boltzmann H-function of the form $H(f) = \sum f_i \ln(f_i / w_i)$ and w_i represents weights of respective discrete velocities \mathbf{c}_i (Karlin et al., 2002, 2006). The collision term is then modified as $\alpha/2\tau (f_i^{eq} - f)$ which results in unconditionally stability of the method – even for high Reynolds number cases – while still retaining its locality and efficiency.

Boundary conditions mentioned above – for open boundaries of the inlet and the outflow, and the solid boundaries of the conduit – require the usage of different numerical schemes. Thus for the solid surface the so called bounce-back scheme is used $f_i(\mathbf{x}_{con}, t + 1) = f_{-i}(\mathbf{x}_{con}, t + 1/2)$ which consists in simple inversion of distributions along the directions incident to the boundary nodes. In the case of the moving surface the term $2w_i \rho(\mathbf{x}_{part}, t) / c_s^2 (\mathbf{c}_i \cdot \mathbf{v})$ corresponding to the exchange of momentum between fictive particles and the moving macroscopic particle is added to the inverted distributions. The specified velocity profile at the inlet is implemented by the Zou-He boundary scheme (Zou & He, 1996) which allows to impose velocity $\mathbf{u}(\mathbf{x}_in, t)$ or pressure $p(\mathbf{x}_in, t)$ on the boundary. In this case, only the non-equilibrium parts of distributions are bounced-back in the normal direction with respect to the boundary.

In the LBM frame motion of macroscopic particles in the flow is the effect of interaction of fictive particles with the solid surface of the macroscopic objects. The action of the objects on the flow is modeled as a special – moving – case of bounce-back boundary conditions considered above. Motion of

macroscopic objects is caused by the momentum transfer $\Delta \mathbf{p}$ from the fictive particles to these objects. Time rate of this momentum transfer $\Delta \mathbf{p} / \Delta t$ defines the hydrodynamic forces by which the flow acts on the objects. The hydrodynamic forces are calculated as a sum over momentum contributions from all fictive particles incident to the boundary nodes of the objects

$$\mathbf{F}_{part} = \frac{\Delta \mathbf{p}}{\Delta t} = \sum_{bn} \sum_i 2 \mathbf{c}_{-i} \left[f_{-i}^c(\mathbf{x}_{part}, t) + w_i \frac{\rho(\mathbf{x}_{part}, t)}{c_s^2} (\mathbf{c}_i \cdot \mathbf{v}(\mathbf{x}_{part}, t)) \right] \quad (2)$$

with $\Delta t = 1$ (Aidun et al., 1998). Another two contributions to the hydrodynamic forces must be mentioned which comes from nodes covered (the force \mathbf{F}_{cov} is exerted on the particle) or uncovered (the force \mathbf{F}_{ucov} forms the negative impulse force increment.) by motion of a particle. Thus the hydrodynamic forces can be expressed as the sum $\mathbf{F}_{net} - \mathbf{F}_g = \mathbf{F}_{bn} + \mathbf{F}_{cov} + \mathbf{F}_{ucov}$, compare with equation (1). To update the particle position $\mathbf{x}(t)$ and its velocity $\mathbf{v}(t)$ the left-hand side of the Newton equations has to be integrated every time step. For this purpose, the leap-frog algorithm is chosen as it is simple, possesses second order accuracy, is invariant under time reversal and has other favorable global properties (Allen & Tildeley, 1987).

4. Results

Particle motions are simulated by means of two different techniques. First approach employs the LBM scheme as a fluid solver which is coupled to exactly evaluated hydrodynamic forces based on explicit relations (1). In the second approach the forces are evaluated within the LBM frame as sum of contributions from momentum transfers of fictive particles (2). The trajectories resulting from both techniques are compared to test robustness and applicability of the LBM approach for simulating motion of multiple particles.

It is supposed that the process is performed in a horizontal conduit of the length $L = 1$ m and height $L/20$. The flow is driven by the power-law velocity profile with maximal value $u(0, L/10) = 0.3 \text{ m}\cdot\text{s}^{-1}$ at the inlet. The radii of the moving particles are assumed to be in range $r \in (L/400, L/200)$. The particles are released from different vertical positions of the conduit with zero translational and rotational initial velocity $(v_{x0}, v_{y0}) = (0, 0)$ and $\omega = 0$. The process is examined with the sand-like particle of density $\rho_p = 2.5 \times \rho_w$. However, most of the input parameters are adjustable within a range of values, e.g., maximal inlet velocity, radii of the moving particles, density of both the fluid and the particle or viscosity.

Segments of three particle trajectories $\mathbf{x}(t)$ with respect to the length and height of the conduit expressed in lattice space units are depicted in Fig. 1. The particles undergo both translational and rotational motion, collide with each other (collisions are illustrated by arrows connecting centers) and collide with the bed. Although the trajectories calculated in two ways (described above) are similar they also differ partially. This can be caused for example by presence of experimentally determined coefficients in exact expressions (1) or by insufficient refinement of the lattice grid.

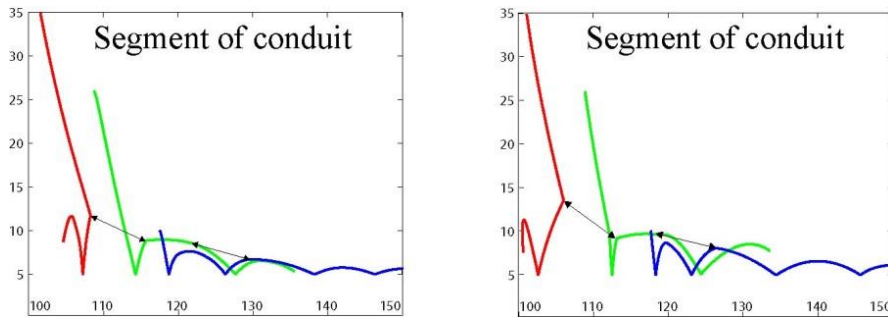


Fig. 1: Trajectories determined by forces: a) within the LBM frame or b) derived from exact expressions.

The low kinematic viscosity of water results in high Reynolds number $Re = uL/\nu \approx 10^5$ of the flow. The low value of the corresponding lattice viscosity ν^* means that the relaxation parameter $\tau \equiv \nu^*/c_s^2 + 1/2 \rightarrow 1/2$, and therefore the LBE method becomes potentially unstable because of incapability to dissipate the energy due to very large velocity gradients. The instability issues can be eliminated in various ways.

The entropic LBM represents a resolution of these issues due to its property of unconditional stability. However, calculation of the parameter α in each (potentially disruptive) node means solving the

mentioned non-linear equation. This equation is usually solved by combination of the bisection and Newton-Raphson method. To eliminate computational demands the parameter α is evaluated only in nodes exceeding a tolerance value for the deviation $|(f_i^{eq} - f_i) / f_i| < 10^{-2}$, i.e., in nodes with large deviations of the population f_i from local equilibrium f_i^{eq} . Thus the entropic approach is applied at quite larger scale (than in Dolanský, 2013) because of better usage of mentioned parallel features of the LBM.

Except the above considered entropic LBM better stability can be also achieved by refining the lattice grid. However, such a refinement also yields a significant grow in demands on computational resources. Due to the inherently parallel nature of the LBM it can be handled by employing the Parallel Computing Toolbox (MATLAB) and other transformations enabling usage of the CUDA GPU computing technology.

5. Conclusions

The LBM based two-dimensional simulation for movements of particles and velocity field of the flow in a closed horizontal conduit is described. The robustness of the method is tested by comparison of trajectories and hydrodynamic forces evaluated either within the LBM frame (2) or calculated from explicit expressions (1). It is shown that in both cases trajectories and forces are similar though there are differences which can be caused by various reasons and will be subject to other considerations. Stability issues of the simulation are considered and a resolution using an extended LBE model and enhancement of computational resources is proposed. The LBM is extended into the so called entropic LBM to guarantee the stability of the computation. The need for increase of computational resources results in employing the parallel features of the LBM. Thus, regarding stability and accuracy the LBM is shown to be suitable for ongoing development of the simulation. It is planned to extend it to motion of cluster of interacting particles in the fluid to observe mutual influence of the flow and the cloud of particles.

Acknowledgement

The support under the project No. P105/10/1574 of the GA CR and RVO: 67985874 of the Academy of Science of the Czech Republic is gratefully acknowledged.

References

- Aidun, C. K., Lu, Y. & Ding, E. J. (1998) Direct analysis of particulate suspensions with inertia using the discrete Boltzmann equation. *Journal of Fluid Mechanics*, 373, pp. 287-311.
- Allen, M.P., Tildesley, D. J. (1987) *Computer Simulation of Liquids*, Clarendon, Oxford.
- Czernuszenko, W. (2009) Model of particle-particle interaction for saltating grains in water. *Archives of Hydro-Engineering and Environmental Mechanics*, 56, pp. 101-120.
- Dolanský, J. (2013) Simulation of saltation motion using LBE based methods, in: *Proc. Int. Conf. on Experimental fluid mechanics* (T. Vít, P. Dančová & Petr Novotný eds), Tech. Univ. Liberec, Kutná Hora, pp. 170-177.
- Heywood, J. G., Rannacher, R. & Turek, S. (1996) Artificial boundaries and flux and pressure conditions for the incompressible Navier-Stokes equations. *International Journal of Numerical Methods in Fluids*, 22, pp. 325-352.
- Karlin, I. V., Ansumali, S. & Chikatamarla, S. S. (2006) Elements of the Lattice Boltzmann method I: Linear Advection Equation. *Communications in Computational Physics*, 1, pp. 616-655.
- Karlin, I. V. & Ansumali, S. (2002) Entropy Function Approach to the Lattice Boltzmann Method. *Journal of Statistical Physics*, 107, pp. 291-308.
- Lukerchenko, N., Chára, Z. & Vlasák, P. (2006) 2D numerical model of particle-bed collision in fluid-particle flow over bed. *Journal of Hydraulic Research*, 44, pp. 70-78.
- Lukerchenko, N., Piatsevich, S., Chára, Z. & Vlasák, P. (2009) 3D numerical model of the spherical particle saltation in a channel with rough bed. *Journal of Hydrology an Hydromechanics*, 57, pp. 100-112.
- Succi, S. (2001) *The lattice Boltzmann equation for fluid dynamics and beyond*, Clarendon, Oxford.
- Wiberg, P. L. & Smith J. D. (1985) A Theoretical Model for Saltating Grains in Water. *Journal of Geophysical Research*, 90, pp. 7341-7354.
- Yu, Z., Fan, L. S. Lattice (2010) Boltzmann method for simulating particle-fluid interactions. *Particuology*, 8, pp. 539-543.
- Zou, Q. & He, X. (1996) On pressure and velocity flow boundary conditions and bounceback for the lattice Boltzmann BGK model. *Physics of Fluids*, 9, pp. 1591-1598.

REDUCING PERIODICITY IN MICROSTRUCTURE RECONSTRUCTION OF HETEROGENEOUS MATERIALS

M. Doškář^{*}, J. Novák^{**}

Abstract: *An approach to modelling of heterogeneous materials by means of Wang tilings is outlined in the paper. The presented tiling concept can be understood as an extension to the widely accepted Periodic Unit Cell (PUC) approach. Unlike in the case of PUC, the microstructural information is compressed within a set of Wang tiles instead of a single cell, which allows us to eliminate periodicity and efficiently control long range orientation orders of a microstructure reconstruction. In this contribution tile morphology design based on the automatic tile design is used. Further enhancement reducing the repetitiveness by microstructural patch is proposed. A sensitivity study of automatic design parameters is performed in order to preserve spatial features of original microstructure.*

Keywords: Wang tilings, Microstructure compression and reconstruction, Automatic tile design, Patched tiles.

1. Introduction

Driven by the economic competition and worldwide trend in energy efficiency it is vital for manufacturers to produce high performance materials at low cost (both in sense of price and energy consumption). Composite materials are generally recognized way to meet these requirements. A capable model that links the properties of individual phases and their composition with the overall behaviour is thus desired, thereby allowing for an efficient virtual design of the materials. A widely accepted approach of microstructure representation is based on the concept of Periodic Unit Cell (PUC), in which the microstructure is substituted with a single cell assumed to be periodically extended in appropriate spatial directions. From this point of view, the presented concept of Wang tilings can be understood as a generalization since the microstructural information is, contrary to PUC, attributed to a set of smaller domains denominated as Wang tiles. The tilings allow to overcome the periodic nature of reconstructed microstructures bear upon the PUC concept.

2. Wang Tilings

The concept is named in honour of Hao Wang, who, in 1961, presented his tiling as a method to prove the validity of a certain type of mathematical statements by converting it into a corresponding set of Wang tiles and solving the task whether the set can tile an infinite plane or not (Wang, 1961; Wang, 1965). Wang's fundamental premise that the infinite plane can be covered with tiling only periodically was disapproved by his student Robert Berger who discovered the first set allowing only for aperiodic planar tilings. This finding triggered a pursuit of the smallest aperiodic set (Grunbaum & Shephard, 1986). The smallest set discovered to date (as of 2014) contains 13 tiles and was presented by mathematician Karel Čulík (Culik II, 1996). These sets have been used e.g. in modelling of quasi-crystals (Aristoff & Radin, 2011) or DNA self-assembly structures (Winfree et al., 1998). The appealing feature of Wang tilings of producing naturally looking less repetitive textures was first reported by Stam (Stam, 1997). This application inspired our current research that brings the tiling concept to Materials Engineering community (Novák et al., 2012).

^{*} Ing. Martin Doškář: Department of Mechanics, Faculty of Civil Engineering, Czech Technical University in Prague, Thákurova 7/2077, 166 29, Prague, CZ, martin.doskar@fsv.cvut.cz

^{**} Ing. Jan Novák PhD.: Institute of Structural Mechanics, Faculty of Civil Engineering, Brno University of Technology, Veveří 331/95, 602 00, Brno, CZ; Department of Mechanics, Faculty of Civil Engineering, Czech Technical University in Prague, Thákurova 7/2077, 166 29, Prague, novakj@cml.fsv.cvut.cz

The basic element of the concept is a square dominoe-like¹ tile with codes assigned to its edges; in Fig. 1b represented with different colours. In general, the edges are usually referred to the corresponding cardinal directions as W-west, N-north, E-east and S-south. In a valid² tiling all tiles are placed in such a manner that the adjacent tiles have the same codes on the congruent edges.

For the purposes of the Materials Engineering (Novák et al., 2012) as well as Computer Graphics (Cohen et al., 2003) stochastic tile sets are preferred to their strictly aperiodic counterpart. Albeit not strictly aperiodic they give more freedom in choice of the number of codes and their spatial permutations around the tile perimeter. This particular feature together with the stochastic tiling algorithm (Cohen et al., 2003) make them correspond better to the intended use in modelling of materials with random microstructures.

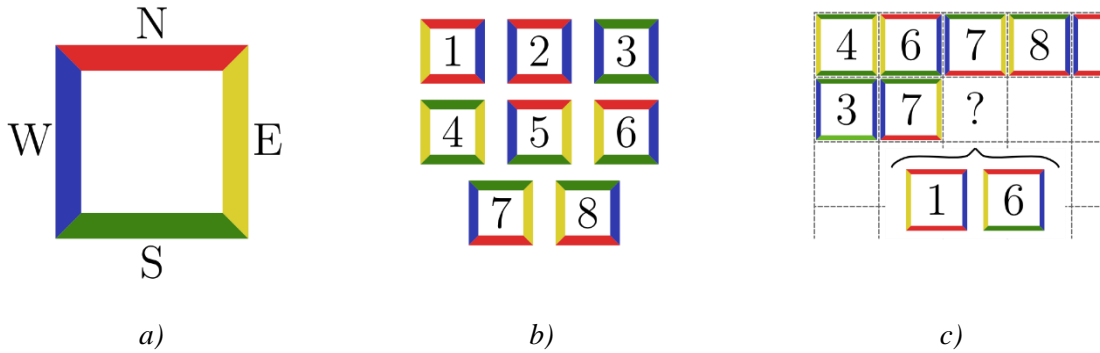


Fig. 1: Illustration of: a) Wang tile; b) Set of tiles W8/2-2; c) A step of stochastic tiling algorithm.

Reconstructed microstructure of arbitrary dimensions can be assembled from the given tiles by making use of the stochastic tiling algorithm proposed by Cohen et al. (2003). A regular tiling grid is filled with tiles in column-by-column, row-by-row order. In each loop, a subset of tiles satisfying edge constraints given by the previously placed tiles is filtered out of the tile set and a tile from the subset is randomly chosen and placed. The procedure is illustrated in Fig. 1c. To preserve the stochastic nature of the tiling yields the condition that at least a pair of tiles of each admissible NW edge code combination is present in the tile set.

3. Automatic Tile Design

Morphology of each tile, in the sense of the amount of microstructural information contained, has to be designed so that the reconstructed representation corresponds with the target system. Moreover, continuity of the morphology across the corresponding edges has to be guaranteed. Employing the optimization methods as reported by Novák et al. (2012) is general, however can be cumbersome from the computational efficiency point of view. Therefore, the automatic procedure proposed by Cohen et al. (2003), such as it makes the direct use of samples of reference microstructure, is reported in this work.

In brief, a number of samples is taken out from the given reference microstructure. Each sample corresponds to an edge code of the designed tile, which arises from the square cut-out of four partially overlapping samples positioned according to the desired edge code permutation, Fig. 2a. The diagonal cut through each sample ensures the compatibility of the microstructure morphology across the edges, assuming we store the remaining part for tiles involving opposite information. What remains is to fuse the samples in the overlap region without creating visible artefacts and errors in the morphology of the tile interior. For this purpose the Image Fusion algorithm (Efros & Freeman, 2001) modified to preserve inclusion shapes (Doškář, 2014) is used to locate a path along which the two samples are stitched together. In Fig. 2a, the path is highlighted in black. In order to split the microstructural information of the tile among edges and interiors, convenient from the viewpoint of spatial features of synthesized tilings, Novák et al. (2012), we further propose to stitch a patch to individual tiles as displayed in Fig. 2b.

The performance of the automatic tile design is governed by many parameters, width of the overlap region, dimension of the samples to be fused, and number of edge codes to name a few. Therefore, the sensitivity of results to those parameters was analysed for four reference microstructures, artificial and

¹ Alternatively called tetraminoe.

² Only valid tilings are assumed in the paper further on.

real. The proximity of reference and reconstructed media was quantified by means of spatial statistics. Namely, the volume fraction of phases, two-point probability and two-point cluster functions were calculated and compared.

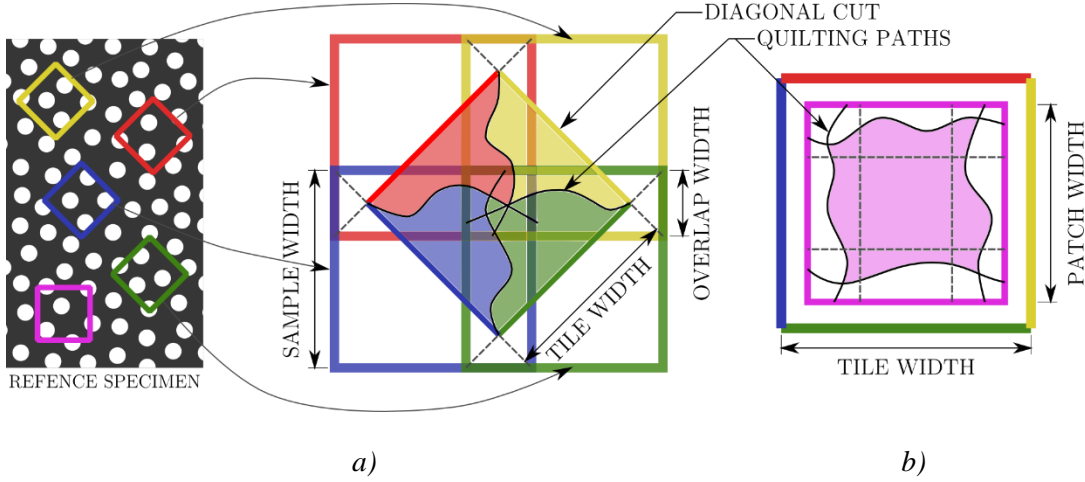


Fig. 2: Illustration of: a) Automatic tile design; b) Patch enhancement.

Based on this, the optimal width of the overlap region seems to be five to six times the mean the characteristic dimension of inclusions. Conversely, there seem not to exist a general rule for the number and dimension of the cut-outs; the same performance can be achieved either with smaller set of larger tiles or vice versa. The choice depends on a particular material composition or available computational resources. Therefore a similar analysis should be an integral part whenever a microstructure compression by making use of the tiling concept is planned.

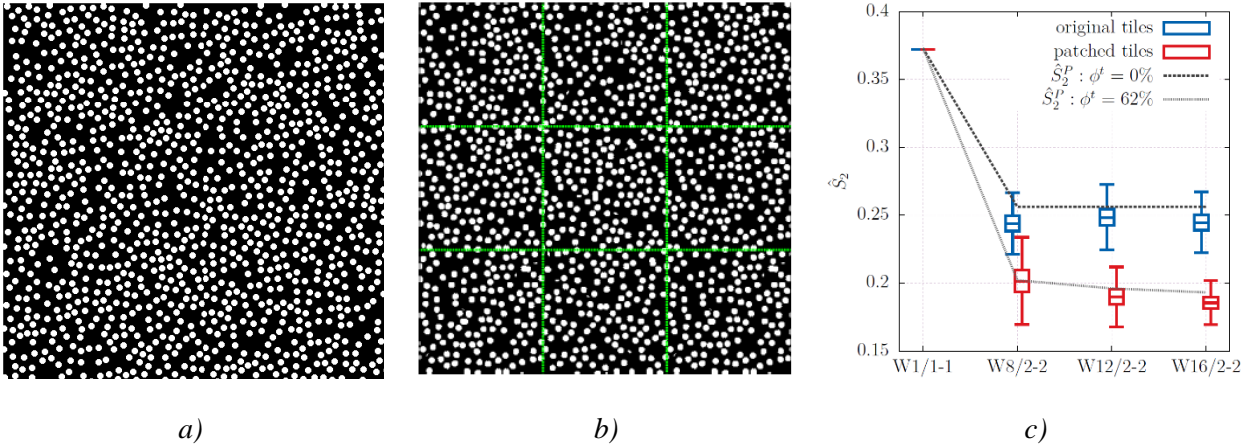


Fig. 3: Hard-disk monodispersion: a) Reference specimen; b) Reconstruction in 3x3 tiling; c) Comparison of predicted and actual values of local extremes \hat{S}_2^P .

4. Quantification of Long Range Orientation Orders

As was mentioned, the main goal of this contribution lies in efficient microstructure representation along with the reduction of the repetitive nature of the reconstruction. The parasitic Long Range Orientation Orders (LRO) induced, were quantified by means of local extremes \hat{S}_2 in the two-point probability function $S_2(\mathbf{x})$. In the case of reconstructions based on PUC these take place at a distance of the PUC dimension and are of the same magnitude as at the origin, i.e. $\hat{S}_2^{PUC} = S_2(\mathbf{0})$. If the tiling concept is applied the local extremes are reduced within the bounds due to Novák et al. (2012):

$$\hat{S}_2^P \approx \frac{\Phi^t}{n^t} [\Phi + (n^t - 1)\Phi^2] + \max_i \left\{ \frac{\Phi^e}{n_i^c} [\Phi + (n_i^c - 1)\Phi^2] \right\} \quad (1)$$

The reduction is governed by number of tiles n^t , number of distinct edge codes n_i^c in the set and the portion of unique information attributed either to the tile interior or to the tile edges, described with Φ^t and Φ^e , respectively, such that it holds $\Phi^t + \Phi^e = 1$. Since there is the entire microstructural

information attributed to edges when using the original automatic tile design, i.e. $\Phi^e = 1$, the magnitude of LRO depends solely on the number of edge codes. As the minimal stochastic set contains at least $n^t = 2n_1^c n_2^c$ tiles, adding edge codes leads to quadratic growth in number of tiles. Therefore the patched variant of the automatic tile design, presented in the previous section, seems the remedy as it allows for a significant reduction of LRO while keeping the number of tiles at feasible figures. On the other hand, patching requires additional inputs which raise demands on the quantity of reference microstructure samples. In Fig. 3 the comparison of the prediction given by Eq. (1) with the actual values of local extremes due to parasitic LRO is shown, namely for hard-disks monodispersion microstructure.

5. Conclusions

This contribution proposes a blend of techniques known in Discrete Mathematics (tiling), Computer Graphics (automatic tile design) and spatial statistics (sensitivity analysis) in order to build an efficient tool for microstructure compression and reconstruction. As shown in Fig. 3 employing the tiling concept significantly reduces the repetitive nature of the representation, especially when the patched tiles are used. Moreover, the automatic tile design is a faster alternative to optimization methods, time necessary to produce a tile set is of order of minutes. Note, that the automated processes can be also utilized to produce a Statistically Equivalent Periodic Unit Cell, the simplest Wang tile set W1/1-1. Despite the fact, that some guidance on design inputs is provided in the Section 3, to perform an analysis similar to the presented one is recommended whenever a microstructure is to be compressed via Wang tilings.

Besides the effective LRO control, the tiling concept proved to be a suitable way to model materials of which the Representative Volume Element dimensions are enormous, e.g. foams with high porosity, and cannot be effectively described by a single PUC (Doškář, 2014). Moreover, the potential of the tiling is further seen in evaluating the microstructure-informed enrichment functions for the Generalized Finite Element Methods (Novák et al., 2013).

Acknowledgement

The financial support by the Czech Science Foundation, grant No. 13-027024S (JN, MD), the European Social Fund, grant No. CZ.1.07/2.3.00/30.0005 “Creation of excellence interdisciplinary research teams at the Brno University of Technology” (JN), and the Grant Agency of the Czech Technical University in Prague, grant No. SGS14/028/OHK1/1T/11 “Modelling of random heterogeneous materials” (MD), are gratefully acknowledged.

References

- Aristoff, D. & Radin, C. (2011) First order phase transition in a model of quasicrystals. *Journal of Physics A: Mathematical and Theoretical*, 44, 25, pp. 255001.
- Cohen, M., Shade, J., Hiller, S. & Deussen, O. (2003) Wang tiles for image and texture generation. *ACM Transactions on Graphics*, 22, 3, pp. 287-295.
- Culik II, K. (1996) An aperiodic set of 13 Wang tiles. *Discrete Mathematics*, 160, 1, pp. 245-251.
- Doškář, M. (2014) Wang tilings for real world material systems, MSc thesis, CTU Press, Prague.
- Efros, A. & Freeman, W. (2001) Image quilting for texture synthesis and transfer, in: *Proc. 28th Ann. Conf. on Computer graphics and interactive techniques* (L. Poccock ed), ACM Press, pp. 341-346.
- Grunbaum, B. & Shephard, G. C. (1986) *Tilings and patterns*, W.H. Freeman & Company.
- Novák, J., Kučerová, A. & Zeman, J. (2012) Compressing random microstructures via stochastic Wang tilings. *Physical Review E*, 86, 4, pp. 040104.
- Novák, J., Kučerová, A. & Zeman, J. (2013) Microstructural enrichment functions based on stochastic Wang tilings. *Modelling and Simulation in Materials Science and Engineering*, 21, 2, pp. 025014.
- Somol, P. & Haindl, M. (2005) Novel path search algorithm for image stitching and advanced texture tiling, in: *WSGC's 2005 Full Papers Conference Proceedings*, Science Press, UNION Agency, Plzen, pp. 155-162.
- Stam, J. (1997) Aperiodic texture mapping. *European Research Consortium for Informatics and Mathematics*.
- Wang, H. (1961) Proving theorems by pattern recognition-II. *Bell Systems Technical Journal*, 40, 1, pp. 1-42.
- Wang, H. (1965) Games, logic and computers. *Scientific American*, 213, 5, pp. 98-106.
- Winfree, E., Liu, F., Wenzler, L. A. & Seeman, N. C. (1998) Design and self-assembly of two-dimensional DNA crystals. *Nature*, 394, 6693, pp. 539-544.

ANALYSIS OF SUBWAY WAGON ROLLER BEARING AXLE BOX STRESSES WITH MEDIUM OPERATION LOAD

S. Dowkontt*, W. Ostapski*, M. Tułodziecki*

Abstract: *The paper presents the stress-strain analysis of a bearing axle box of a subway wagon. Simulations were performed on a digital model using FEM for medium loads. Calculations were performed for the geometry of the roller with the standard outline.*

Keywords: Cylindrical roller bearings, FEA simulation, Contact stresses.

1. Introduction

The analysis concerns the subway wagon axle box roller bearings (Fig. 1). Bearing parameters: load $C_r = 84500$ daN, static load $C_{or} = 130200$ daN, axial clearance 0.6 to 1.1 mm, radial clearance $0.125 \div 0.165$ mm, the type of grease: Liten LT-4S3, bearing life $L_{10} = 600000$ km. Load to the axle box: [passengers], maximum 67.5 kN, speed: maximum 90 km/h, average 45 km/h.

Raceway of main rings is straightforward. A profile of roller (convex) is described with function:

$$P(x_k) = 0.00035 \cdot D_{we} \cdot \ln \left[\frac{1}{1 - (2 \cdot x_k / L_{we})^2} \right] \quad (1)$$

where: D_{we} - roller diameter, L_{we} - length of the roller

Permissible stresses contact: dynamic: $2800 \div 3000$ MPa, static: 4000 MPa.

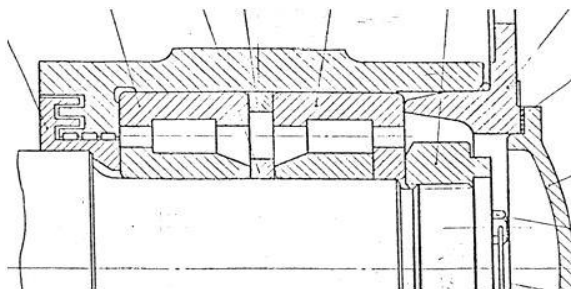


Fig. 1: Longitudinal section of the axle box.

2. Term of Substitute Loads

Tab. 1: The term of transverse substitute load.

Te - operation time of train %	Train weight P [kN]
9.5	540
23.8	340
66.7	440

* Szymon Dowkontt, PhD., Prof. Wiesław Ostapski, PhD., Maciej Tułodziecki, PhD: IPBM, Warsaw University of Technology, Narbutta 84; 02-524 Warszawa; Poland, sdowk@ipbm.simr.pw.edu.pl, wos@simr.pw.edu.pl, mtulo@simr.pw.edu.pl

Transverse substitute load [for average weight of wagon], is: $P_{sr} = 432.4 \text{ kN}$.

Radial substitute load of bearings set is: $P_{pz} = 54 \text{ kN}$. There are eight sets of bearings for four axles per wagon. Longitudinal substitute load for centrifugal force on the curve $P_{sw} = 8.918 \text{ kN}$. Longitudinal substitute load of bearings set $P_{wz} = 2.23 \text{ kN}$.

Simulations of stresses and strains in the developed FEM model of the axle box (Rakowski et al., 1993) were performed for these loads. Simulations considered neither overloading nor overheating.

3. Digital Model of Bearing Node

The digital model of axle box is shown on Fig. 2. Fig. 4 shows a global model with FEM mesh. The mesh contains 455827 nodes, and 454359 elements. The mesh is of hexagonal type. The boundary conditions and substitute loads are highlighted on Figure 4. Schematic transfer longitudinal forces of reaction or body shaft reactions [change the direction of the force] are shown on the Fig. 3.

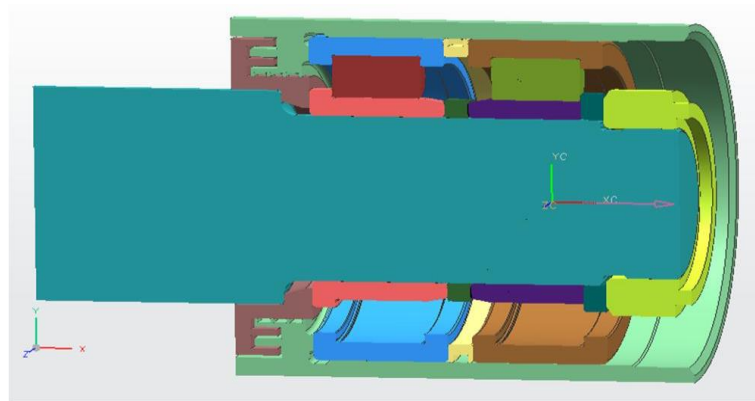


Fig. 2: 3D digital model of axle box.

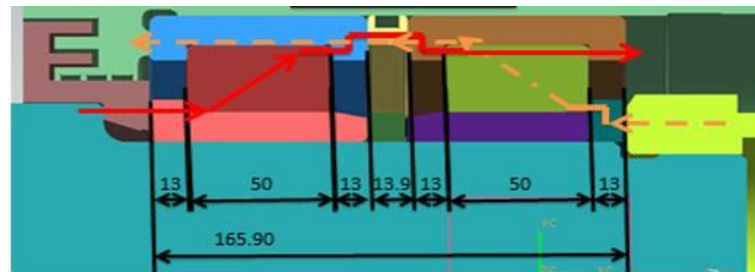


Fig. 3: Transfer of longitudinal force in axle box.

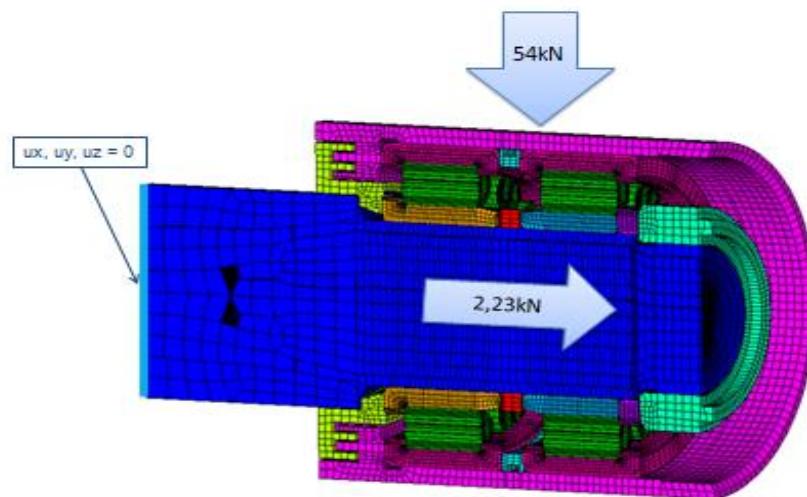


Fig. 4: 3D model with FEM mesh, loads and boundary conditions.

4. Simulation of Stresses and Strains on the Global Model

The simulation of stress and deformation of bearing was conducted for average substitute loads of the roller bearing set described in Chapter 2 and shown in Fig. 4.

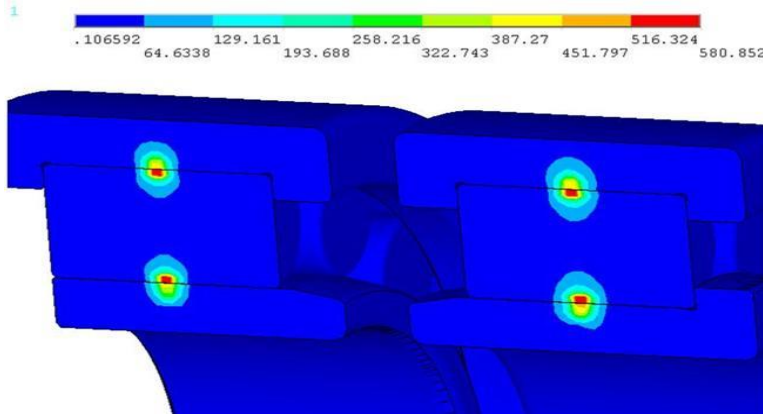


Fig. 5: Huber Mises equivalent stresses.

The maximum equivalent stresses, which occurred in the central zone of the roller contact with the track, were 580 MPa (Fig. 5).

The global 3D mesh model is too thin to provide more accurate results. It is, however, useful for preliminary estimation of stress distribution. It allows the area of the largest loads to be specified.

Thus it was necessary to build a submodel with enhanced mesh for better micro-geometry mapping in contact zone.

5. Submodel

The 3D Submodel (Fig. 7) was developed for micro-geometry mapping of maximum load zone of a standard roller outline (Rakowski et al., 1993), (Fig. 6).

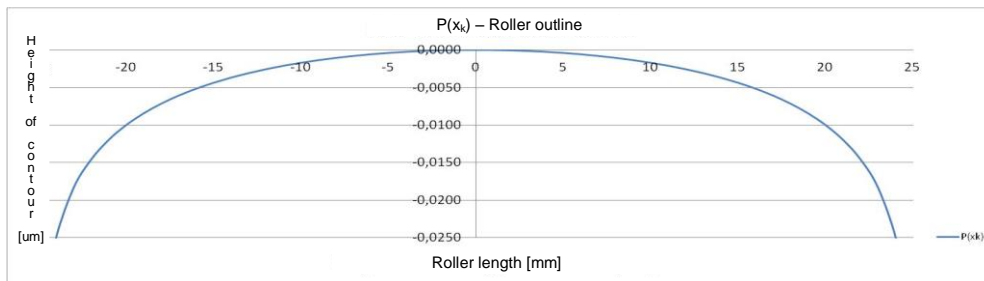


Fig. 6: Roller outline.

The number of nodes in submodel: 218954; the number of elements: 215363; hexagonal mesh (Hexahedra).

Submodel load conditions were determined based on results of simulation basis for the global model of maximum stress zone (Fig. 7).

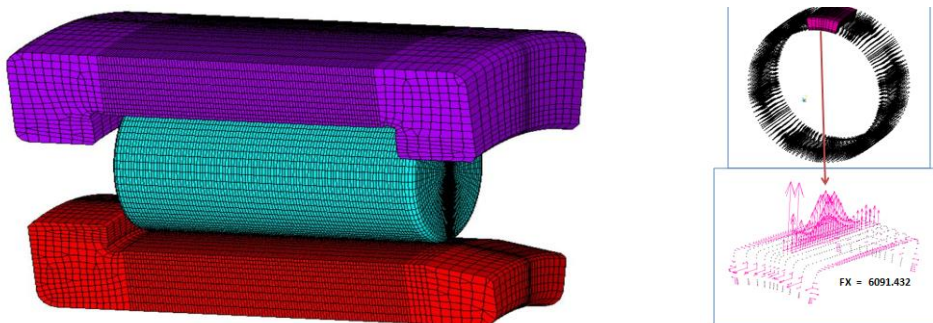


Fig. 7: Submodel with the distribution of forces in the zone of maximum load.

6. Simulation of Stress on the Developed Submodel

The simulation results of stress in submodel for the state of maximum load (Fig. 7) are shown in Figs. 8 and 9. The stresses in the rolling element contact with the inner race (Fig. 9) were calculated for the standard outline of the roller.

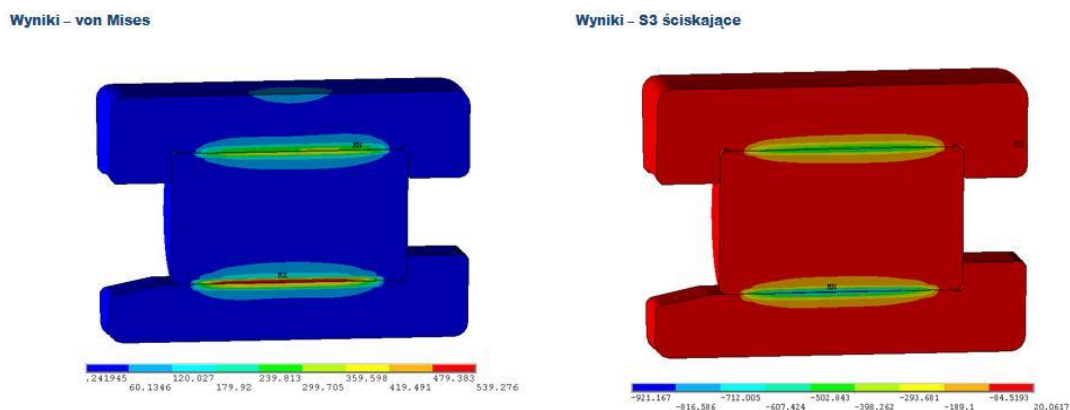


Fig. 8: Substitute loads [MPa] (left); Compressive stresses [MPa] (right).

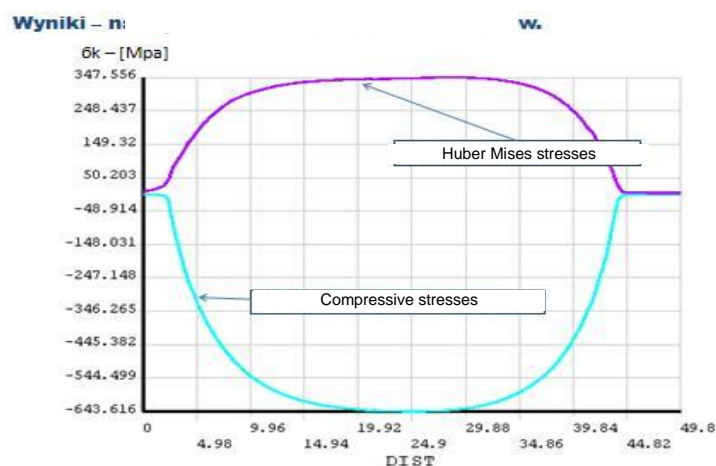


Fig. 9: The contact stresses - the inner ring raceway.

The resulting values of maximum substitute stress in the inner ring raceway do not exceed 400 MPa and compressive stress does not exceed 700 MPa. The amplitude of the maximum shear stress is 180 MPa. This is well below allowable contact stress values. It should be noted that these values are calculated for the average operating load condition. For states with maximum traction, load is expected to be higher. With the required time of operating $L_{10}=600000$ km, with proper installation and lubrication of bearings, durability of the axle box will be absolutely sufficient.

7. Conclusions

The developed digital model and the simulations on the FEM model of the axle box made possible the state of stress estimation of bearings for medium duty operation. In order to more accurately map the geometry, the submodel of the most loaded contact zone was developed. The area of maximum stress was determined as a result of global FEM model simulations. Stress distribution along a roller is uniform in both raceways which is beneficial to strength.

The result obtained is beneficial operationally in the specified load conditions. In the case of operating a wagon with a maximum number of passengers, the substitute load would increase by about 23%. The maximum stress increases, respectively, however, are still far below the limit values. The basis for the calculations were average loads. This article did not focus on thermal loads. Temperature differences in the axle box retain minimal radial clearance.

References

Rakowski, G., Kacprzyk, Z. (1993) Finite element method in engineering design. OWPW Warszawa (in Polish).

COMPARISON OF DYNAMIC INTERACTIONS IN THE DRIVE SYSTEM OF ELECTRIC LOCOMOTIVE EU07 BEFORE AND AFTER THE MODERNIZATION DRIVE UNIT

S. Duda^{*}, G. Gembalczyk^{*}, R. Lawniczek^{*}, T. Trawinski^{**}

Abstract: *This paper presents a research tool allowing to determine the state of the load in the drive system of electric locomotives. This tool was used to compare dynamic interactions in the drive system of locomotive EU07, where as a result of the modernization of the existing DC motors were replaced with AC induction motors. Developed models of combined engine were coupled to a rail vehicle model developed in the class of multibody system dynamics. Load the system comes from the moments generated by the electric motors and the forces generated at the interface between the wheels with guide rail. Developed mathematical models were implemented in Matlab / Simulink. Numerical simulations allow to determine the load of drive system for various vehicle dynamic states (startup, steady-state operation) depending on the locomotive load.*

Keywords: Rail vehicle, Electromechanical drive system, Vector control system.

1. Introduction

Since the beginning of the use of electric traction, DC motors are used to the drive rail vehicles. The main advantage of these drives is the control with ease in a wide speed range with high electromagnetic torque and the major disadvantage of these engines is to have a mechanical commutator and brushes, which is the cause reducing their durability and increases the need for regular maintenance and repairs. Lack of funds for the purchase of new rolling stock compels carriers to renovation and maintenance old ones. Modernization also concerns the drive system an example of it becomes installation of asynchronous motors in place of the DC motors in order to improve the operational performance, such as reducing failure and extending life. Replacement old one booting system based on resistance with new booting system based on frequency can yield significant energy savings. Determination of the actual state of charge the drive system on the basis of numerical simulations can be useful in planning modernizing the of the drive unit. This makes it necessary to construction of models which reflect the operation of a vehicle similar to the real ones. It was therefore necessary to use the at modernization with new approaches to the use of techniques and software tools that allow the use of modeling and simulation techniques, with a view to adjusting the drive model and vehicle model to the existing conditions at the operation.

2. Modelling the Electromechanical System of an Electric Locomotive

The electromagnetic and mechanical systems of the electric rail vehicle powertrain couple mutually through electromagnetic torque (M_e) and angular rotor velocity (ω). Because of the rail vehicle system, an analysis of dynamics in railway vehicles and the driving system coupled with it must take into account the analysis of electromagnetic and mechanical systems.

Taking into account the unique character of the solution for the electric locomotive driving system (type of its electric motor, number of motors and the configuration of their connections), further down the paper presents an electromagnetic model of the locomotive chosen for further analysis. For this purpose electric locomotive type EU07 has been chosen. Drive systems of the presented locomotives are DC motors,

^{*} Department of Theoretical and Applied Mechanics, Silesian University of Technology, ul. Konarskiego 18a 44-100 Gliwice, Poland, slawomir.duda@polsl.pl, grzegorz.gembalczyk@polsl.pl, rafal.lawniczek@polsl.pl

^{**} Department of Mechatronics Engineering Silesian University of Technology, ul. Akademicka 10a 44-100 Gliwice, Poland, tomasz.trawinski@polsl.pl

which as a result of modernization have been replaced by AC induction motors. Location of individual motors in carriers were shown in Fig. 1.

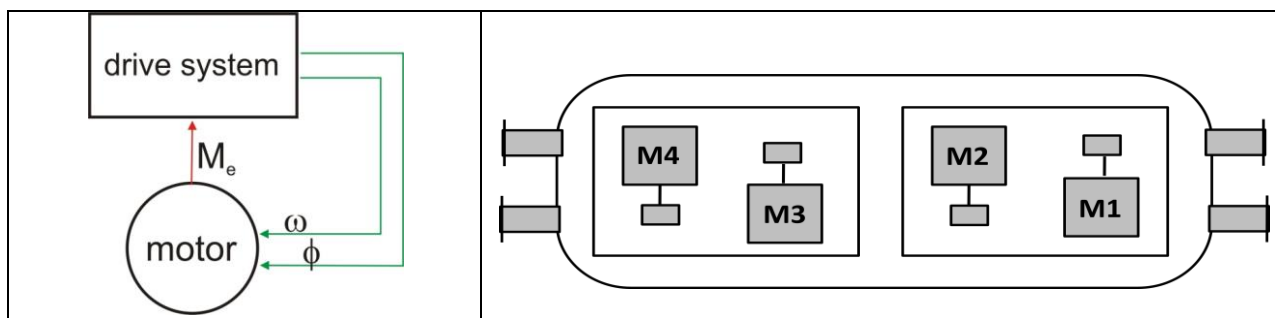


Fig. 1: Model of electromechanical system, structure of a driving system.

3. Development of Models of Electric Drives

In an operating cycle, the traction motors of the EU07 locomotive operate in two configurations. During the start-up phase, four motors are connected in series and, subsequently, to increase the voltage, switched over into a parallel circuit of two motors per branch. Equations describing the currents in electrical circuits, electromagnetic torque generated by the individual motors are further presented in (Duda, 2007).

As a result of the modernization drive systems EU07 locomotive used AC motors (locomotive EP07) in the modified current commutator motor housing. Proposed drive system of locomotives consists of following components: induction squirrel cage motor, mechanical system of wheels (with torque transmission chain) and inverter with control circuit. The internal couplings occurred in such a system are presented in Fig. 2.

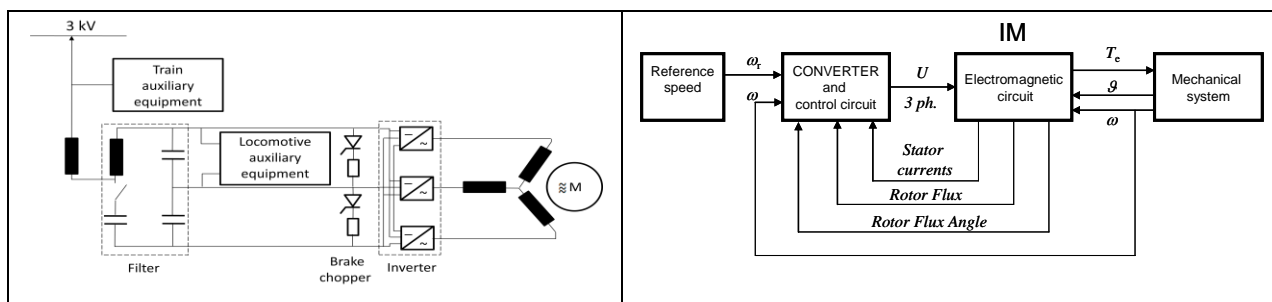


Fig. 2: Mutual coupling in drive system of locomotive with induction motor.

The electromagnetic circuit of induction machine is coupled with mechanical system by electromagnetic torque, angular displacement (of the rotor) and angular speed (Mezyk et al., 2007). Considering in mathematical model of drive system additional coupling, represented by angular displacement, gives more flexible chance to mathematical modeling of induction machine. It allows for taken into consideration mathematical models of induction machine which allows for electromagnetic reluctance or electromagnetic parasitic torque influence investigation on drive system properties. It is assumed that induction machine is fed from converter with vector control algorithms - so-called rotor field oriented control (RFOC). Practical realization of RFOC control system results in following couplings between induction motor, mechanical system and converter: as a input signal to converter are necessary stator currents, rotor flux and rotor flux angle (rotor flux vector may also be estimated based on stator voltage, currents and speed), and angular speed of the rotor.

Currently a complex study of the mechanical system – the rail – rail vehicle can be provided by numerical simulations, by using a computer as a tool. The numerical simulations of rail vehicles require implementing a mathematical model of the vehicle in a computer program that would describe it with a reasonable precision. Using the methods based on multibody system dynamics makes a very convenient approach for developing such models (Shabana et al., 2008). Model of the drive system together with the model of railway vehicle was developed using environment Matlab / Simmechanics in multibody convention (Duda, 2013).

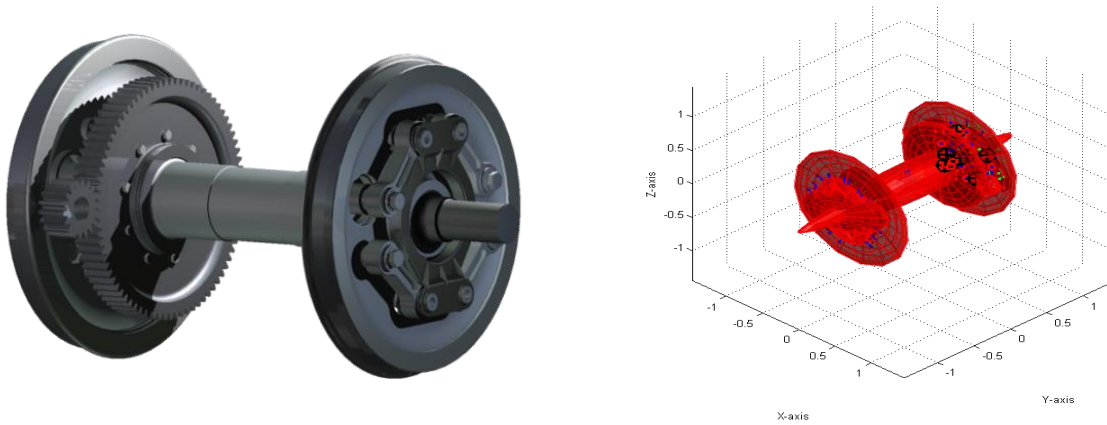


Fig. 3: CAD model of the driving system, visualization of multibody model of the driving system in Matlab/Simmechanics.

4. Numerical Simulation of a Rail Vehicle Travel and Dynamic Interactions in Drive System Kinematic Pairs

Studying the dynamics of electric rail vehicles requires creating three intercoupled models: a vehicle model including drive system models, a rail model, and a model for the wheel – rail interface. At the first stage of rail vehicle modeling process, during its travel on the railway track the subsystem models are built separately. Then, the models are interconnected to make a complete system. This method was implemented in proprietary software created in the Matlab environment.

The calculation algorithm used to analyze the rail vehicle travel on any railway track is presented in the form of a schematic diagram in Fig. 4.

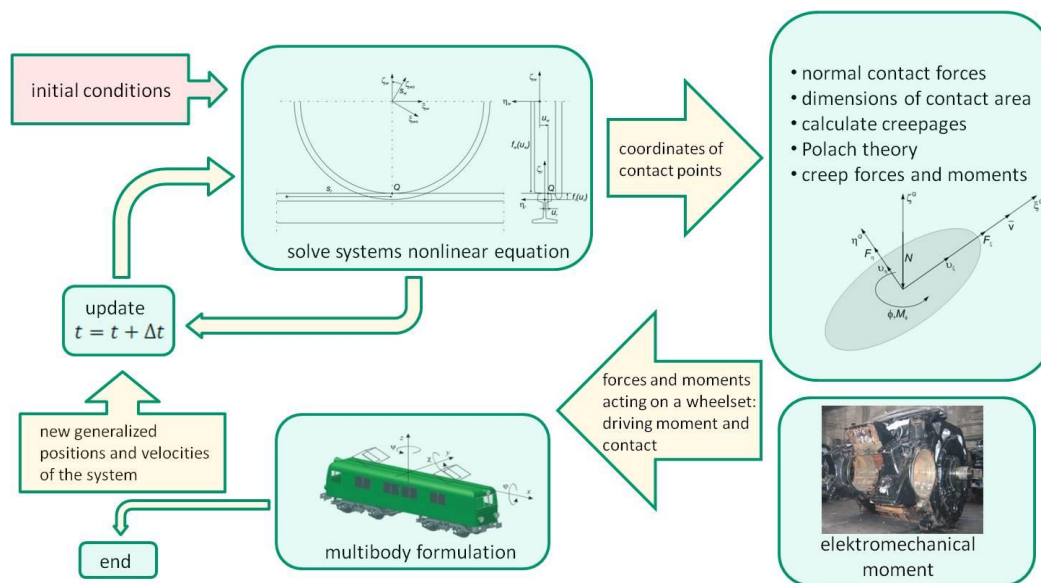


Fig. 4: Calculation algorithm used to analyze the rail vehicle travel dynamics on any railway track.

The presented algorithm (Fig. 4) used to develop the computer program for analyzing the rail vehicle travel dynamics on any railway track was developed based on literature (Lankarani et al., 1990), (Pombo et al., 2003) and (Polach, 1999).

The tool for simulating the travel of rail vehicles has been used to test various cases, showing the potential of the presented method in a variety of situations. These cases included the analysis of EU07 rail vehicle dynamics (before – DC motors and after modernization – asynchronous motors) during its travel on a straight railway track at various conditions.

In Fig. 5 the torques of DC motor and AC motor during start of locomotive are presented.

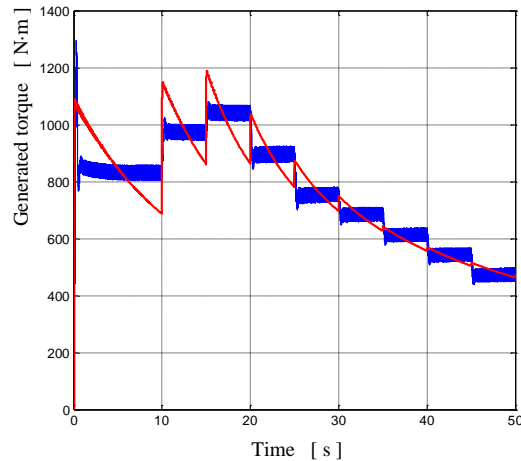


Fig. 5: Sawtooth like curve (red curve) - DC motor torque, square like curve (blue one) - AC motor torque.

5. Final Conclusions

Each mechanism has its operating life. Therefore, for economic reasons it is important to properly determine the dates of overhauls or just for routine periodic inspections. It can be obtained by having a thorough knowledge of dynamic phenomena occurring in the system under analysis, by applying numerical simulations performed on the adequate vehicle model. One of the most susceptible to wear and tear and important part of a rail vehicle is its drive system.

Using the methods of numerical modeling and simulation to provide dynamic analyses in the kinematic pairs of electric rail vehicle makes it possible to identify the state of loads for system components under different operating conditions and it can constitute a basis for forming vehicle traction characteristics effectively. Such studies can be successfully used both to modify the existing objects and to assist the design-construction process for the prototypes of new vehicles.

The developed models allow for the testing of dynamic phenomena occurring in power transmission systems, especially in transient states such as start-up or the change of loading conditions. The models serve the determination of optimal traction parameters for locomotives by e.g. the selection of the gear ratio of the power transmission system gear.

Acknowledgement

This paper is realized within the framework of research project No. 6700/B/T07/2011/40 funded by National Science Centre in Poland.

References

- Duda, S. (2013) Numerical modeling and simulating the dynamic interactions within the drive system of electric rail vehicles, in *Maintenance and Reliability*, 15 (4): 343-348.
- Duda, S. (2007) Nonlinear models of connected motors of the railway vehicle EU07, in *ZN 6/2007 Modelling and optimization of physical systems*, Gliwice, pp. 29-36.
- Lankarani, H. M , Nikraves, P. E. X (1990) A Contact Force Model with Hysteresis Damping for Impact Analysis of Multibody Systems, *AMSE Journal of Mechanical Design*, 112, pp. 369-376.
- Mężyk, A., Trawiński, T. (2007) Modeling of drive system with vector controlled induction machine coupled with elastic mechanical system, in *Recent Advances in Mechatronics*, ISBN 978-3-540-73955-5, Springer-Verlag Berlin Heidelberg, pp. 248-252.
- Pombo, J., Ambrósio, J. (2003) General Spatial Curve Joint for Rail Guided Vehicles: Kinematics and Dynamics, *Multibody Systems Dynamics*, 9, pp. 237-264.
- Polach, O. (1999) A Fast Wheel-Rail Forces Calculation Computer Code, *Vehicle System Dynamics*, Supplement 33, pp. 728-739.
- Shabana, A. A., Zaazaa, K. E., Sugiyama, H. (2008) *Railroad Vehicle. Dynamics. A Computational Approach*. Taylor & Francis Group.

SIMULATION AND EXPERIMENTAL STUDIES ON THE CONTROL SYSTEM FOR MECHATRONIC REHABILITATION DEVICE WITH KEEP-UP MOVEMENT

S. Duda*, G. Gembalczyk*, R. Lawniczek*

Abstract: *This work contains the results of simulation and experimental studies on crane control system with tracking movement system intended to support the rehabilitation process. This paper presents the kinematics and the basic elements of the drive system in one of the axes of the possible movement of the device. Based on this information the numerical model and the control algorithm of the system created in Matlab SimMechanics has been developed. The simulation results, based on the chosen optimal control mode settings, were compared with the results obtained during the test bench.*

Keywords: Numerical model, Mechatronics, Crane, Drive system.

1. Introduction

One of the conditions for the effective training of both sports and during rehabilitation, is a large repeatability of exercises. Therefore, in recent years the development of mechatronic devices supporting the process of rehabilitation are increasing. An example is the LOKOMAT Hocoma Company which enables simulation of the movement of the lower limbs or Zero-G device developed by Aretech. It allows the realization of different exercises in relieving (Hornby et al., 2005), (Hidler et al., 2011).

As part of the research work carried out at the Department of Theoretical and Applied Mechanics, in Silesian University of Technology was developed mechatronic device in the form of a crane, supporting the process of rehabilitation of patients learning to walk again. The idea of this device is shown in Fig. 1. This device provides the opportunity to work in various modes, and one of them is tracking movement after the moving load. Patient hanging system with adjustable length of rope is located on a gantry cart (indicated by symbol A), which can perform a translational motion in the horizontal plane (along directions OX and OY axes). The trolley moves along the OX-axis with entire crossmember, where drive system of OY-axis is mounted. The crane is driven in a horizontal plane, a motor controller for closed-loop operation responds to feedback with multi-axis sensor for measuring the deviation angles of the rope with added sling. The control system is based on a real-time controller in the steering of drive motors. Develop the best possible control algorithm to ensure optimal operation of the system according to the purpose of rehabilitation, safety and patient comfort (Ławniczek & Duda, 2013), (Gembalczyk & Duda, 2013).

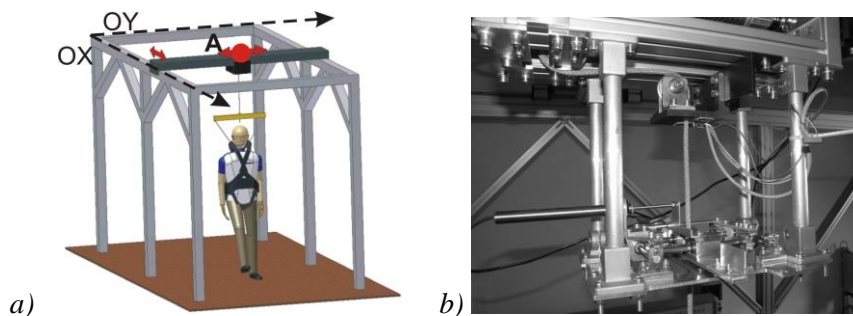


Fig. 1: a) Scheme of mechatronic devices to support walk reeducation;
 b) System for measuring deviations angles of rope.

* Department of Theoretical and Applied Mechanics, Silesian University of Technology, ul. Konarskiego 18b 44-100 Gliwice, Poland, slawomir.duda@polsl.pl, grzegorz.gembalczyk@polsl.pl, rafal.lawniczek@polsl.pl

2. The Structure of the Drive System

In order to demonstrate the correlation between the components of the mechatronic system that is proposed device for walk reeducation, was created a block diagram contains the most important elements. Developed diagram was shown in Fig. 2, is suitable for both drive axles.

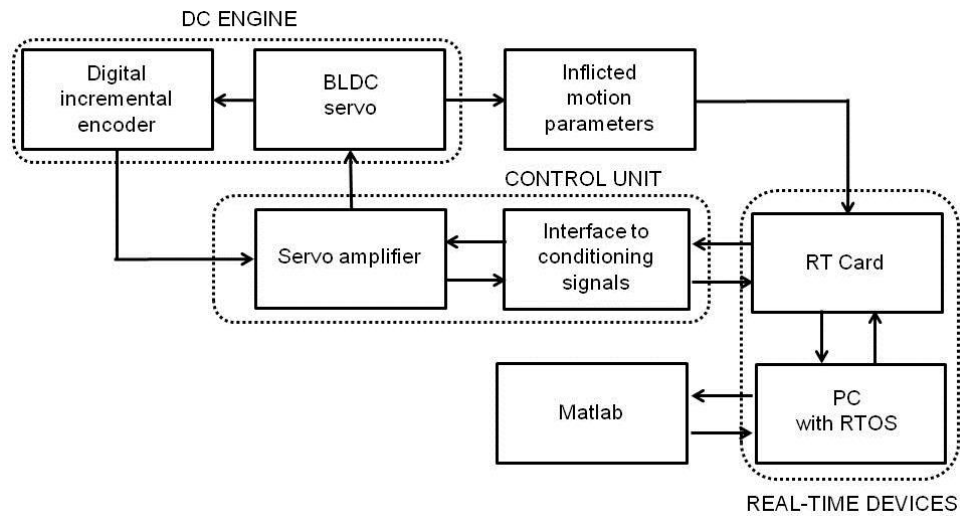


Fig. 2: Block diagram of the mechatronic control system on the laboratory stance.

Steering this mechanism is done using control algorithms developed in Matlab. The CPU where the real-time operating system is installed, using the digital signals (0-10 V), cooperate with real-time card. Real-time card communicates with the system executive. This system used two real-time cards RT-DAC4/PCI. Next elements included in this device is a servo amplifiers and cooperating with them BLDC servo motors equipped with a digital incremental encoders.

The numerical model of the electromechanical drive system was created using the software Matlab/SimMechanics. The mathematical model of BLDC motor (Brush Less Direct-Current Motor) was adopted in the form of simplified equations of motion (Glinka, 2002), (Ławniczek & Duda, 2013), (Świtoński et al., 2004).

Parameters of the motor model were estimated based on experimental studies. Mechanical part of this model was created in the convention of multibody system dynamics.

3. PID Control System

In the proposed tracking mode was used PID controller which on the basis of an error signal selects an appropriate value of the control signal of the drive motor speed. The error signal is equal to the deviation the crane rope from the vertical direction (set value of the inclination angle rope is equal to zero). This angle depends on the coordinates of gantry cart and the position of the patient. The idea of motion control algorithm follower mode of operation is shown in Fig. 3.

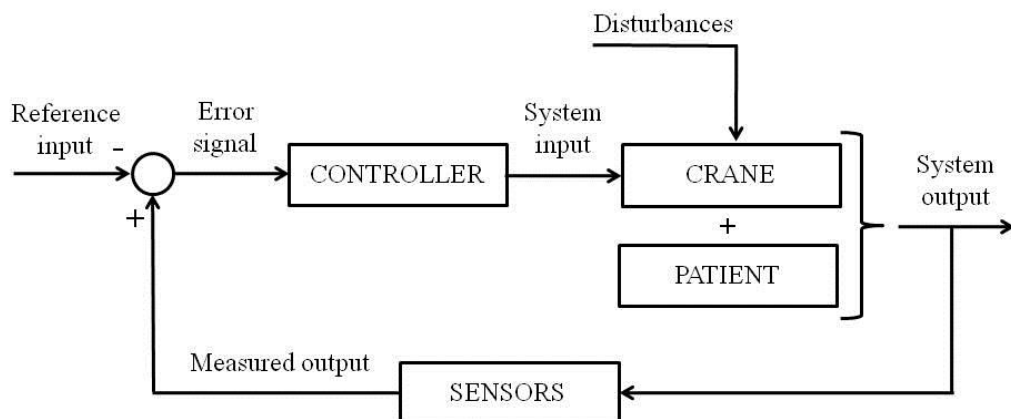


Fig. 3: Block diagram of the control system.

4. Tuning the Parameters of PID Controller

In order to analyse the control system at different values of PID controller gains in Matlab/Simulink was developed a numerical model of the tested device. Initially a displacement movement of the patient was modelled with a constant speed. During the initial selection of the control parameters, was noted that at too high value of proportional gain P indicated that gantry cart was ahead of the moving person. This leads to a situation in which hanging system starts to perform a reciprocating movement along the OX-axis with increasing speed. This situation is shown in the graphs below, which show the movement of the hanging mechanism and the patient (Fig. 4). The second graph (Fig. 5) shows changing the control signal values of the rotational speed of the drive engine.

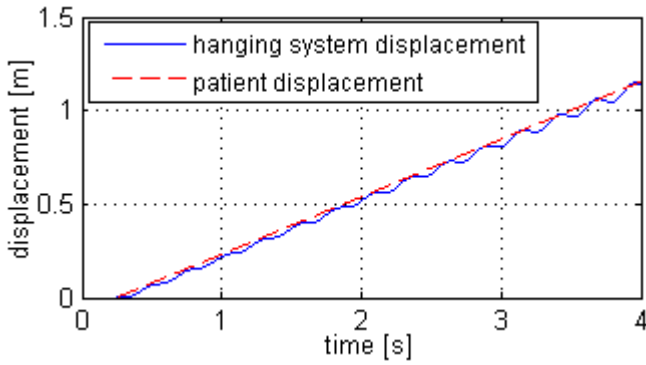


Fig. 4: Patient and trolley crane displacement as a function of time.

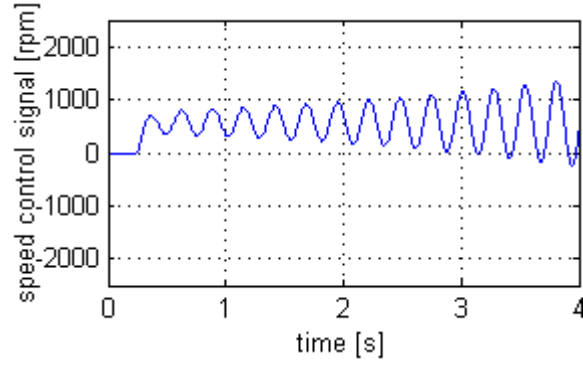


Fig. 5: A graph of speed control signal of the drive motor.

The same phenomenon was observed on a real object. Due to the patient safety and fear of mechanical damage of the device itself, tests of such settings were interrupted in the initial phase. An additional element of potentiating the action of gantry was distortion of signals from the measuring system of the deviation angles of rope – which was the feedback control signal.

Gantry movement discussed above causes both dangerous (can lead to the fall) and uncomfortable conditions for rehabilitation. When tuning the optimal values of PID controller gains was minimized both the angle of the rope and change the speed of the gantry cart while in motion (1). This was to ensure the smooth work as much as possible the vertical position of the rope (in this position hanging system has least impact on natural human movement).

$$F(\varphi) \cdot a + F(\dot{x}) \cdot b \rightarrow \min \quad (1)$$

$$F(\dot{x}) = \int_{t=0}^T \left| \frac{d^2x}{dt^2} \right| \quad (2)$$

T – the final simulation time; $F(\varphi)$ – the function of deviation angles of rope in time; $F(\dot{x})$ – the function that describes the change of the linear velocity of gantry cart in direction OX-axis; a, b – parameters defining the impact in functions of deflection angle of and changes the linear velocity gantry cart to minimize the objective function.

The parameters a and b are selected such that both functions (deflection angle of the rope and gantry cart speed changes) had a comparable effect on the objective function. For such formulated problem, assuming the patient's motion with a constant speed, the optimization process is carried out to tune the PID parameters using gradient method. The obtained values ($P = 300$, $I = 0$, $D = 10$) was implemented in the control system in real object. Obtained characteristics were different from received during the simulation, which was a result of the fact that man was not move with uniform motion. After taking into account the numerical model the patient's movement as recorded during the test, then re-attempt to the tuning of the optimal PID parameters. Results did not differ significantly from the previous ones. The results of numerical and experimental studies were similar nature. The graphs below show a comparison of the deviation angles of rope obtained during the simulation and the experiment (Fig. 6). In Fig. 7 shows the displacement of the patient and the gantry cart recorded during the tests on the real object.

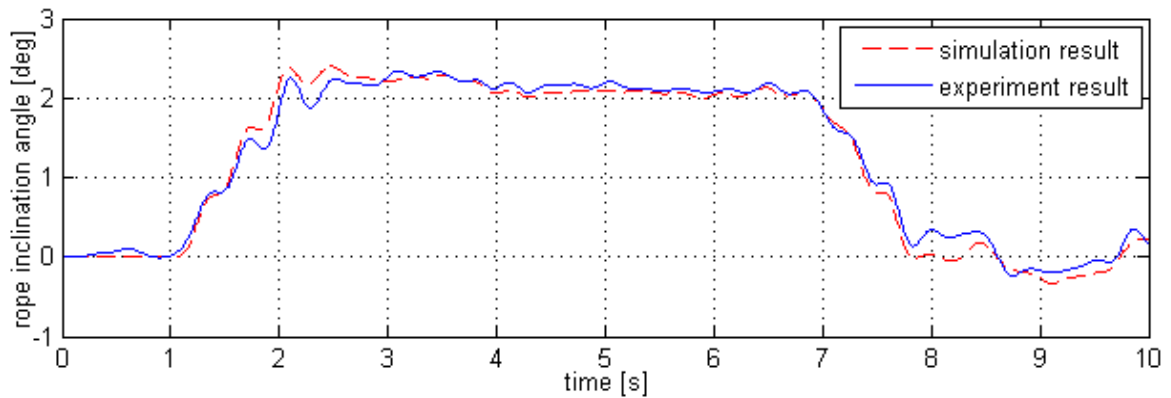


Fig. 6: Changing the angle of inclination rope in crane as a function of time.

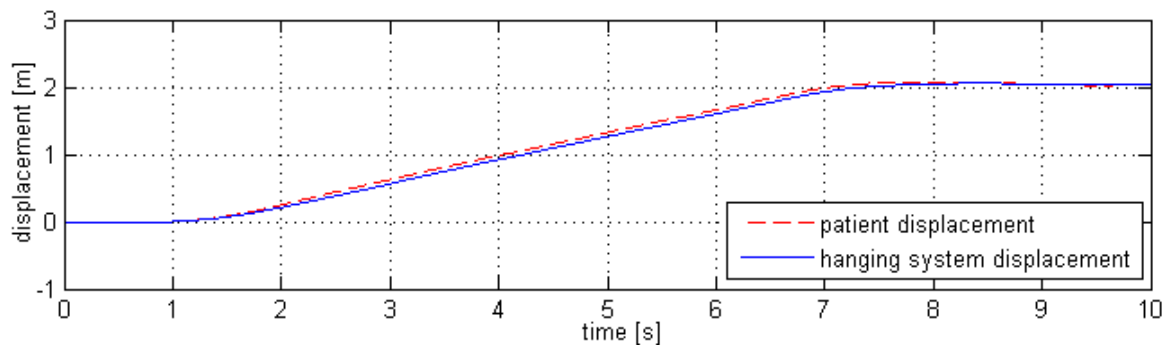


Fig. 7: Registered patient and the crane hanging system displacement as a function of time.

5. Conclusions

The developed control algorithm allows for the implementation of keep-up mode of rehabilitation crane movement after moving patient. It was designed for movement in the direction of one axis of the device, however, can easily be implemented in a second direction of action. The developed control system provides a small inclination angles of rope (less than 3 degrees), thus the force transmitted by the rope will act mainly on the vertical direction. Properly selected controller settings exclude the possibility of the patient's overtake by gantry cart, causing loss of balance and introduces entire structure to vibrate with a large amplitude.

The above conclusions show that the developed control algorithm provides the basic requirements for devices used in rehabilitation process.

The proposed numerical model, despite its simplifications (omitted drag force on the guides and simplifies motor control), shows a satisfactory convergence of the results obtained during the test bench.

Acknowledgement

This work was done with the supply of the research program NR03-0040-10/2010.

References

- Glinka, T. (2002) Electric machines, induced with permanent magnet. Gliwice: Wydawnictwo Politechniki Śląskiej. (in Polish)
- Ławniczek, R., Duda, S. (2013) Model of the control system for lifting mechanism in special purpose gantry crane. Gliwice : Wydaw. Katedry Mechaniki Teoretycznej i Stosowanej, (in Polish).
- Hornby, T.G., Zemon, D.H., Campbell, D. (2005) Robotic-Assisted, Body-Weight-Supported Treadmill Training in Individuals Following Motor Incomplete Spinal Cord Injury. *Physical Therapy*, Vol. 85, No. 1, pp. 52-66.
- Hidler, J., Brennan, D., Black, I., Nichols, D., Brady, K., Nef, T. Zero, G. (2011) Over ground gait and balance training system. *Journal of Rehabilitation Research & Development*, Vol. 48, No. 4, pp. 287-298.
- Świtoński, E. et al. (2004) Modeling of mechatronics drive systems. Monografia, Gliwice (in Polish).
- Gembalczyk G., Duda S. (2013) Design and validation of devices for measuring the force and the angle of inclination rope in crane. *Modelling in engineering*, Vol. 16, No. 47, pp. 76-81 (in Polish).

KINEMATICALLY EXCITED NON-LINEAR VIBRATION OF A BEAM ON ELASTIC SUPPORTS WITH CLEARANCES

Š. Dyk^{*}, V. Zeman^{**}, M. Byrtus^{***}

Abstract: *The paper deals with nonlinear vibration of a beam excited by harmonic movement of frame which the beam is fixed in. Except for supports of the ends of the beam, another supports along axis of the beam are considered. In these supports, there are clearances which cause nonlinear vibration of the system. A mathematical model of the beam is obtained using finite element method and decomposition of such a system is used to obtain a model including kinematical excitation. As an application, nonlinear vibration of a guide thimble in spacer grid of nuclear fuel assembly is shown. To get solution, numerical integration in time domain is used and quality of vibration is shown using orbits and phase trajectories of representative dynamical quantities.*

Keywords: Nonlinear vibration, Kinematical excitation, Clearance, Beam.

1. Introduction

In many engineering applications, non-linear vibration of beam type components appears. The non-linearity given by beam supports with clearances may cause that the vibro-impact motion occurs. This topic is very actual and it is widely studied with respect to structure reliability, see (Chena et al., 2014). Particularly, nuclear fuel assemblies consist of a large number of beam type components. The aim of this paper is to describe vibration of such a system in general and to define the admissible states of the beam motion. Let us suppose the fuel assembly components are fixed in the support plates and are kinematically excited. In the fuel assembly, there are rods (fuel rods and guide thimbles) which are fit into spacer grids of load-bearing skeleton (frame) with a clearance. Therefore, impacts occur between beam and the frame in levels of spacer grids which generate large impact forces during vibration which can lead to material stress increase and to degradation of surface of rods.

2. Mathematical Model of Kinematically Excited Beam on Elastic Supports with Clearances

A radial symmetric flexible fixed-ended beam is considered (see Fig. 1). One end of the beam is fixed in a rigid frame which moves harmonically with frequency ω and the second end moves harmonically as well with the same frequency ω but generally with different amplitude and with phase shift φ . Along axis of the shaft, there are m elastic supports with stiffnesses $k_i, i = 1 \dots m$, and there is a radial clearance Δ between the beam and a ring of support.

To get mathematical model of the beam, finite element method (FEM) is used. The beam is supposed to be one dimensional continuum satisfying Euler-Bernoulli theory – it is radially incompressible and there is no deplanation of a cross section in deformed position, see (Byrtus et al., 2010). One finite element has two nodes and in every one node, there are six degrees of freedom; displacement in axial direction u , lateral displacements v, w in sense of axes x, y , respectively, torsional rotation angle φ , and flexure rotation angles ψ, ϑ . The beam can then be divided to $N - 1$ elements with N nodes and it is chosen in the

* Ing. Štěpán Dyk: Department of Mechanics, University of West Bohemia; Univerzitní 22; 30614, Pilsen; CZ, stepan24@kme.zcu.cz

** Prof. Ing. Vladimír Zeman, DSc.: Department of Mechanics, University of West Bohemia; Univerzitní 22; 30614, Pilsen; CZ, zemanv@kme.zcu.cz

*** Ing. Miroslav Byrtus, PhD.: Department of Mechanics, University of West Bohemia; Univerzitní 22; 30614, Pilsen; CZ, mbyrtus@kme.zcu.cz

way that there is a node in each nonlinear support. The vector of generalized coordinates of whole system $\mathbf{q}(t)$ can be written in the form

$$\mathbf{q}(t) = [\dots, u_i, v_i, w_i, \varphi_i, \vartheta_i, \psi_i, \dots]^T \in \mathcal{R}^{6N}, \quad i = 1 \dots N. \quad (1)$$

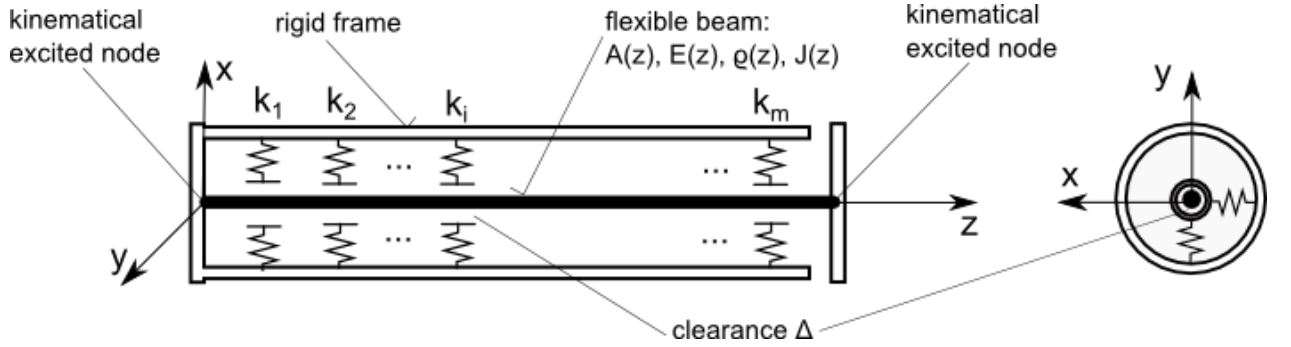


Fig. 1: System of kinematically excited rigid frame with flexible beam on elastic supports with clearances.

First, conservative mathematical model of the system will be derived and subsequently it will be extended to full nonlinear model. Conservative model can be derived in the following form

$$\mathbb{M}\ddot{\mathbf{q}}(t) + \mathbb{K}\mathbf{q}(t) = \mathbb{0}, \quad (2)$$

where $\mathbb{M}, \mathbb{K} \in \mathcal{R}^{6N, 6N}$ are mass matrix and stiffness matrix of the beam, respectively. To include kinematic excitation, the vector of generalized coordinates of the system in vertical position can be divided into three subvectors $\mathbf{q}_p, p = L, F, U$, where index L corresponds to lower kinematically excited node (fixed to the frame), index F corresponds to all free nodes and index U corresponds to generalized coordinates of upper kinematically excited node (fixed to the frame). System can be then written in decomposed form

$$\begin{bmatrix} \mathbb{M}_L & \mathbb{M}_{L,F} & \mathbb{0} \\ \mathbb{M}_{F,L} & \mathbb{M}_F & \mathbb{M}_{F,U} \\ \mathbb{0} & \mathbb{M}_{U,F} & \mathbb{M}_U \end{bmatrix} \begin{bmatrix} \ddot{\mathbf{q}}_L(t) \\ \ddot{\mathbf{q}}_F(t) \\ \ddot{\mathbf{q}}_U(t) \end{bmatrix} + \begin{bmatrix} \mathbb{K}_L & \mathbb{K}_{L,F} & \mathbb{0} \\ \mathbb{K}_{F,L} & \mathbb{K}_F & \mathbb{K}_{F,U} \\ \mathbb{0} & \mathbb{K}_{U,F} & \mathbb{K}_U \end{bmatrix} \begin{bmatrix} \mathbf{q}_L(t) \\ \mathbf{q}_F(t) \\ \mathbf{q}_U(t) \end{bmatrix} = \mathbb{0}. \quad (3)$$

After rewriting second row of (3), mathematical model is

$$\mathbb{M}_F \ddot{\mathbf{q}}_F(t) + \mathbb{K}_F \mathbf{q}_F(t) = -\mathbb{M}_{F,L} \ddot{\mathbf{q}}_L(t) - \mathbb{M}_{F,U} \ddot{\mathbf{q}}_U(t) - \mathbb{K}_{F,L} \mathbf{q}_L(t) - \mathbb{K}_{F,U} \mathbf{q}_U(t). \quad (4)$$

Now, the model (4) can be extended considering damping and nonlinear forces generated in supports with clearances. Damping is supposed to be proportional, so $\mathbb{B}_F = \alpha \mathbb{M}_F + \beta \mathbb{K}_F$, where $\alpha, \beta \in \mathcal{R}^+$ can be determined from estimation of damping ratio of first two eigenmodes. After inclusion of damping matrix and using vector of nonlinear forces $\mathbf{f}_N(\mathbf{q}_F)$, the model (4) can be completed in the form

$$\mathbb{M}_F \ddot{\mathbf{q}}_F(t) + \mathbb{B}_F \dot{\mathbf{q}}_F(t) + \mathbb{K}_F \mathbf{q}_F(t) = -\mathbb{M}_{F,L} \ddot{\mathbf{q}}_L(t) - \mathbb{M}_{F,U} \ddot{\mathbf{q}}_U(t) - \mathbb{K}_{F,L} \mathbf{q}_L(t) - \mathbb{K}_{F,U} \mathbf{q}_U(t) + \mathbf{f}_N(\mathbf{q}_F). \quad (5)$$

The vector $\mathbf{f}_N(\mathbf{q}_F)$ depends on generalized coordinates of free nodes and it is given as a sum of vectors of nonlinear forces in all supports

$$\mathbf{f}_N(\mathbf{q}_F) = \sum_j \mathbf{f}_N^{(j)}(\mathbf{q}_F), \quad j = 1 \dots m. \quad (6)$$

Vector $\mathbf{f}_N^{(j)}(\mathbf{q}_F)$ includes only lateral forces generated in j -th support and it can be written in a form

$$\mathbf{f}_N^{(j)}(\mathbf{q}_F) = [\dots, F_{Nx}^{(j)}, F_{Ny}^{(j)}, \dots]^T, \quad (7)$$

where forces $F_{Nx}^{(j)}$ and $F_{Ny}^{(j)}$ are placed in positions corresponding to transversal displacement of supported node „ j “ in direction x, y , respectively. These forces are given in the form

$$F_{Nx}^{(j)} = k_{jx}(u_{xj} - \Delta) \mathcal{H}(u_{xj} - \Delta), \quad (8)$$

$$F_{Ny}^{(j)} = k_{jy}(u_{yj} - \Delta) \mathcal{H}(u_{yj} - \Delta), \quad (9)$$

where k_{jx}, k_{jy} are contact stiffnesses in direction x, y in j -th support, u_{xj}, u_{yj} are relative displacements of center of the beam with respect to the frame in direction x, y in j -th node and $\mathcal{H}(\cdot)$ is Heaviside function.

3. Application to Vibration of Guide Thimble of Fuel Assembly of a Nuclear Reactor

The application part of the paper is aimed at vibration of fuel assembly TVSAT of the nuclear WWER 1000 type reactor which is in detail described in Sýkora (2009). Mathematical model of the reactor is built up in Hlaváč & Zeman (2013). The above theory was applied to nonlinear vibration of guide thimbles, which together with fuel rods, center tube and load-bearing skeleton (frame) with eight spacer grids make a fuel assembly. The guide thimbles are at both ends fixed in two support plates by means of lower and upper piece. All the rods are linked by the spacer grids which are transversal to their axes and the guide thimbles are inserted into spacer grids with a small clearance. One guide thimble is shown in the Fig. 2 with both lower and upper pieces. Further, only one guide thimble at the position r in 1st segment ($s=1$) will be considered. A generally spatial movement of the plates is given in configuration space $\mathbb{q}_X(t) = [x, y, z, \varphi_x, \varphi_y, \varphi_z]_X^T, X = L, U$ as shown in the Fig. 2 and vibration of a guide thimble in configuration space which is radially-tangential in x, y plane according to Zeman & Hlaváč (2011). Between these two systems, there is transformation which can be described by

$$\mathbb{q}_{r,X} = \mathbb{T}_{r,X}^{(s)} \mathbb{q}_X, \quad X = L, U, \quad (10)$$

where $\mathbb{T}_{r,X}^{(s)}$ is transformation matrix which transforms movement of lower and upper plates \mathbb{q}_X to movement of kinematical excited nodes of the guide thimble $\mathbb{q}_{r,X}$. It is dependent only on geometrical parameters, see Zeman & Hlaváč (2011). Only one chosen guide thimble is considered and indexes r and s will be omitted further.

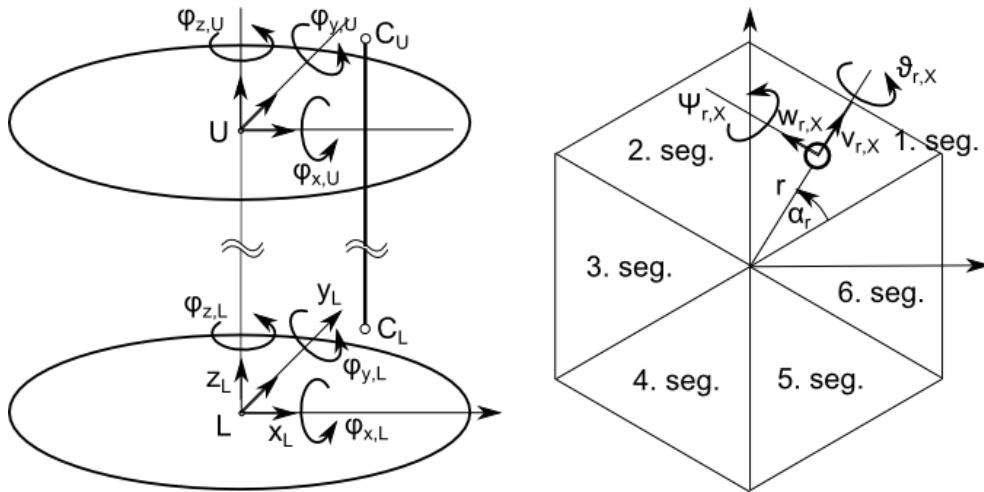


Fig. 2: Guide thimble in lower and upper piece and coordinate systems.

The considered guide thimble was divided into 18 finite elements. The lower C_L and upper C_U nodes are supposed to be ideally fixed and in every even free node, there are supports (spacer grids) with the same clearance considered. The geometry of spacer grids is shown in Hlaváč & Zeman (2013). In the first phase, only harmonic excitation with frequency ω and with phase shift $\varphi = 0$ was implemented. Mathematical model of the system can be written in the form

$$\begin{aligned} \mathbb{M}_F \ddot{\mathbb{q}}_F(t) + \mathbb{B}_F \dot{\mathbb{q}}_F(t) + \mathbb{K}_F \mathbb{q}_F(t) = & (\mathbb{M}_{F,L} \omega^2 - \mathbb{K}_{F,L}) \mathbb{T}_L (\mathbb{q}_L^S \sin \omega t + \mathbb{q}_L^C \cos \omega t) + \\ & + (\mathbb{M}_{F,U} \omega^2 - \mathbb{K}_{F,U}) \mathbb{T}_U (\mathbb{q}_U^S \sin \omega t + \mathbb{q}_U^C \cos \omega t) + \mathbb{f}_N(\mathbb{q}_F), \end{aligned} \quad (11)$$

where $\mathbb{q}_L, \mathbb{q}_U$ are vectors of amplitudes of harmonic excitation. To get solution of the system, numerical implementation in MATLAB was accomplished. To integrate mathematical model (11), fourth order Runge-Kutta method with adaptive step in time domain was implemented using ode45 MATLAB built-in function. For the simulation, important parameters are clearance $\Delta = 1$ mm, and frequency $\omega = 2\pi f$,

$f = 3$ Hz, contact stiffness in all spacer grids $k_j = 0.179 \cdot 10^6$ N/m, $j = 1 \dots 8$. Vectors of kinematical excitation are supposed in the form

$$\mathbb{q}_L^S = \mathbb{q}_U^S = [0,01; 0; 0; 0; 0; 0], \quad \mathbb{q}_L^C = \mathbb{q}_U^C = [0; 0,0075; 0; 0; 0; 0]. \quad (12)$$

Numerical integration results are shown in the Fig. 3. Orbits in plane x, y in chosen nodes of guide thimble are depicted (Fig. 3, on the left). It is evident, that boundary nodes which are close to kinematically excited nodes vibrate quasiharmonically. Nodes in the middle of the guide thimble vibrate with the largest amplitude and that is why impacts occur the most often there. There are phase trajectories depicted as well (Fig. 3, on the right). The impact motion can be well identified from these phase portraits. The impacts correspond to points at the trajectories where large changes in the velocity occur.

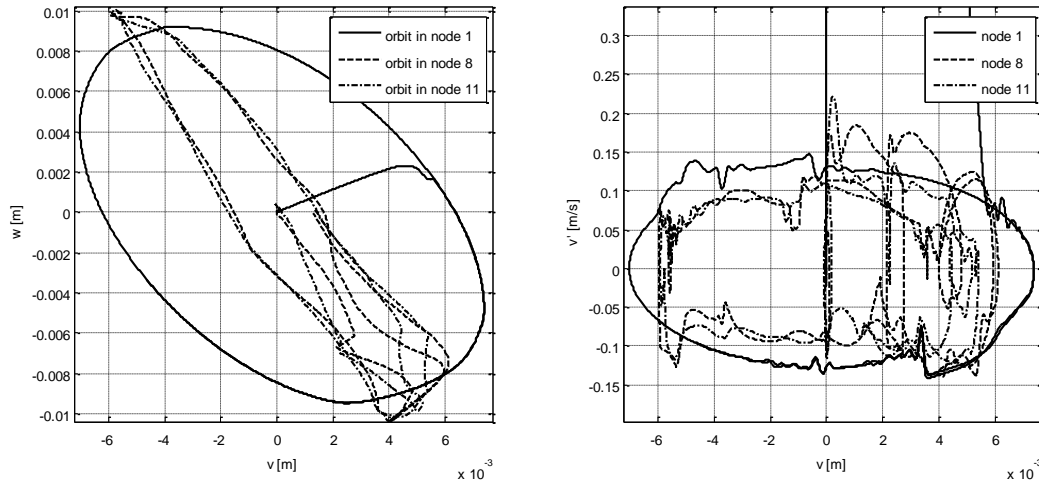


Fig. 3: Orbits in chosen nodes of guide thimbles (on the left) and example of phase trajectories.

4. Conclusion

The paper focuses on mathematical modelling of kinematically excited beam supported by nonlinear supports. The theory described above shows an approach to modelling of such a system. Particular application to guide thimble of nuclear fuel assembly is implemented in MATLAB and typical dynamical response of the system to harmonic kinematical excitation is shown.

Future analyses will be focused on optimization of parameters (clearances, contact stiffnesses, etc.) to reach lower impact forces between guide thimble and the spacer grids. Except for that, derived mathematical model and the display of impact motion are wide enough to represent dynamical response caused by another kind of excitation than only the harmonic one. Seismic excitation can be considered and a response of the system can be analyzed simulating seismic event in nuclear power plant.

Acknowledgement

This work was supported by the grant SGS-2013-36.

References

- Chena, H., Kurt, M., Leec, S., McFarland, D. M., Bergmand & L. A., Vakakis, A. F. (2014) Experimental system identification of the dynamics of a vibro-impact beam with a view towards structural health monitoring and damage detection, *Mechanical Systems and Signal Processing* 46, pp. 91-113.
- Byrtus, M., Hajžman, M. & Zeman, V. (2010) *Dynamics of rotating systems*. Západočeská univerzita v Plzni, ISBN 978-80-7043-953-1 (in Czech).
- Hlaváč, Z., Zeman, V. (2013) *Vibration of Nuclear Fuel Assemblies*. Lap Lambert Academic Publishing, Saarbrücken, Germany, ISBN 978-3-659-43122-7.
- Sýkora, M. (2009) *Reactor TVSA-T Fuel Assembly Insertion, Part 4*. Research Report Pp BZ1,2 ČEZ ETE (in Czech).
- Zeman, V., Hlaváč, Z. (2011) *Vibration of the Package of Rods Linked by Spacer Grids*. *Vibration of Problem ICOVP 2011*, Springer, pp. 227-233.

MODELLING AND INITIAL TESTS OF THE DYNAMIC PROPERTIES OF VIBROINSULATION MATS

W. Dzikowska^{*}, D. Żórawski^{**}, K. Peszyński^{***}

Abstract: *The paper demonstrates the mathematical model of polyurethane vibroinsulation mat tested using the dynamic mechanical analyser (DMA) method. The mechanical model is necessary to search for the analogy between different sample sizes of the objects tested. The aim of the study was to determine damping properties. The damping properties of vibroinsulation material are characterised by the loss factor $\tan \delta$. The value of the loss factor $\tan \delta$ was determined depending on the frequency of forced vibrations.*

Keywords: DMA, Loss factor, Polyurethane foam, Damping.

1. Introduction

The process of vibration transmission can be prevented mainly by installing flexible elements between the source of vibration and the surroundings (Adamczyk & Targosz, 2011). Modern flexible materials used for the vibroinsulation of solid materials and air vibrations, are the polyurethane mats made of spring part of composite with a mixed pore structure, i.e. open and closed pores.

The study of dynamic mechanical analyser (DMA) has been carried out to determine the usefulness of the polyurethane mats. The problem faced during the study is the high cost of testing equipment in accordance with the DIN 45673-5 standard. It is primarily the problem of samples sizes. The authors have at their disposal a very precise device DMA 242 NETZSCH that is adapted for testing even much smaller samples.

2. Mathematical Modelling of the Sample

Due to the fact that the test results have to be transferred to a much larger products than the samples, it is necessary to design a mathematical model of the sample. The sample in its basic part consists of polyurethane foam surrounded by coating which is formed in the modelling process of the sample (Fig. 1).

The equations of motion for the system are

$$\begin{aligned}
 m_3(\ddot{x}_3 - \ddot{x}_1) + b_3(\dot{x}_3 - \dot{x}_1) + k_3(x_3 - x_1) &= F(\omega) \\
 (m_1 + m_2)(\ddot{x}_1 - \ddot{x}_4) + (b_1 + b_2)(\dot{x}_1 - \dot{x}_4) + (k_1 + k_2)(x_1 - x_4) &= \\
 = m_3(\ddot{x}_3 - \ddot{x}_1) + b_3(\dot{x}_3 - \dot{x}_1) + k_3(x_3 - x_1) & \\
 m_4\ddot{x}_4 + b_4\dot{x}_4 + k_4x_4 = (m_1 + m_2)(\ddot{x}_1 - \ddot{x}_4) + (b_1 + b_2)(\dot{x}_1 - \dot{x}_4) + (k_1 + k_2)(x_1 - x_4) &
 \end{aligned} \tag{1}$$

where: $i = 1, 2, 3, 4$ is respectively upper layer of foam coating, basic foam, side layer of foam coating, and bottom layer of foam coating; x – displacement, m; m – mass, kg; b – damping coefficient, Ns/m; k – stiffness, N/m.

^{*} Weronika Dzikowska, MSc: PhD. student, Faculty of Mechanical Engineering, University of Technology and Life Sciences; al. Prof. S. Kaliskiego 7; 85-789 Bydgoszcz; Poland, weronika.dzikowska@wp.pl

^{**} Damian Żórawski, MSc: PhD. student, Faculty of Chemical Technology and Engineering, University of Technology and Life Sciences; ul. Seminaryjna 3; 85-326 Bydgoszcz; Poland, damzor000@utp.edu.pl

^{***} Assoc. Prof. Kazimierz Peszyński, CSc.: Mechanical Engineering Department, University of Technology and Life Sciences; al. Prof. S. Kaliskiego 7; 85-789 Bydgoszcz; Poland, peszyn@utp.edu.pl

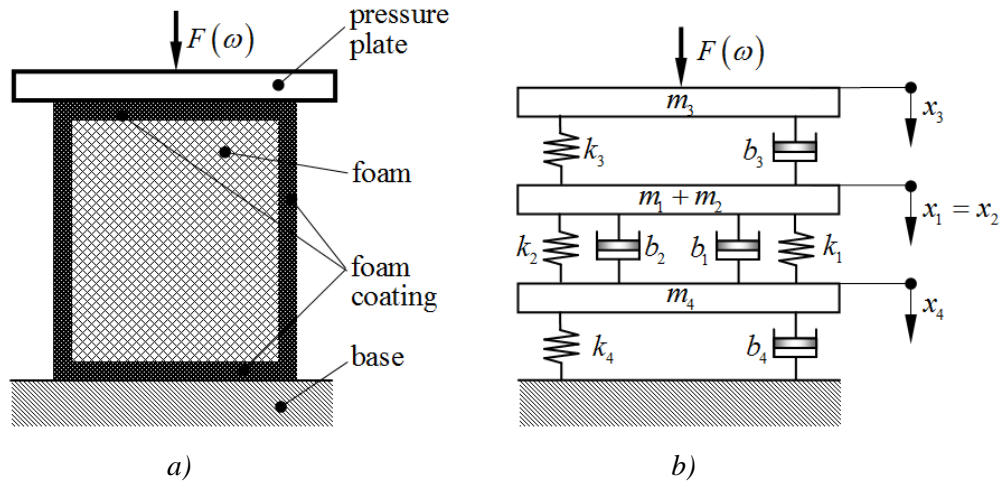


Fig. 1: Sample tested: a) Cross-section of the actual sample; b) Mathematical model.

The model defined by system (1) allows for determining the relationship between the input in the form of sinusoidal vibrations and the output in the form of transfer function. Spectral transfer function consists of real and imaginary part. The real part is an equivalent of storage modulus E' while the imaginary part refers to the loss modulus E'' known from the DMA method.

3. Materials and Methods

The research materials were vibroinsulation polyurethane mats with the density of 250 kg/m^3 and dimensions as $650 \times 650 \times 25 \text{ mm}$, produced in Polyurethane Foams Factory Ltd. in Bydgoszcz (Wytwórnia Pianek Poliuretanowych Sp z o. o. w Bydgoszczy). The cylindrical samples 20 mm in diameter and thickness of 5.6 mm were cut at randomly chosen locations of the polyurethane mat. Before testing, the samples were thermostated at $23 \pm 3^\circ\text{C}$ for 16 hours.

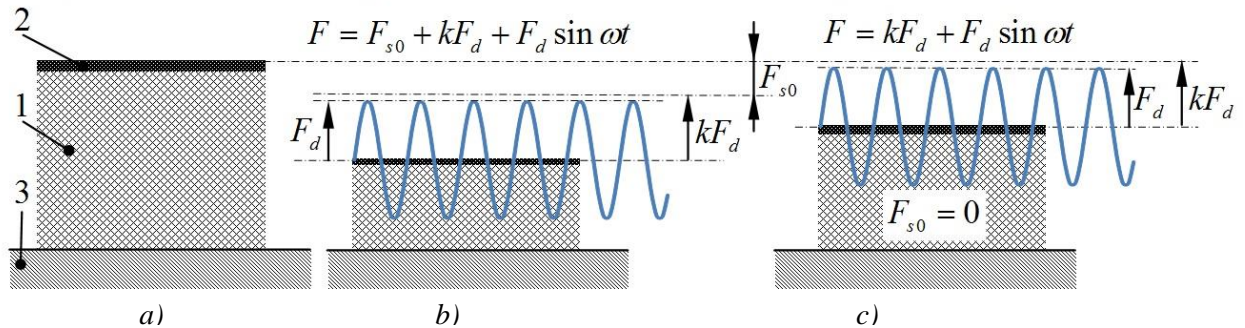
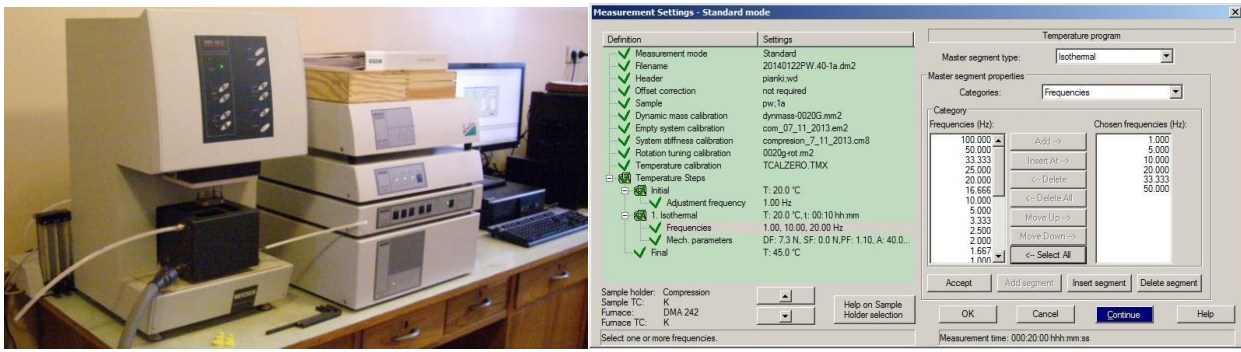


Fig. 2: Load scheme: a) Unloaded sample cut from mat; b) General load scheme; c) Scheme used during experiments.

Fig. 2 shows the sample and its load scheme. Fig. 2a presents the uncompressed sample cut from the mat. It is characterised by only one coating as opposed to the formed sample shown in Fig. 1. Fig. 2b demonstrates a possible course of excitation force used during testing of damping properties in accordance with the standard. That force consists of constant static load F_{s0} , static load which depends on the amplitude of sinusoidal dynamic force kF_d where k is a proportionality factor resulting from the fact that static force always has to be higher than the amplitude of change. As a result, at least a slight compression of the sample will be ensured during testing. Fig. 2c shows the course of excitation used during testing, where $F_{s0} = 0$, and $k = 1.1$.

Testing the dynamic properties of the vibroinsulation mat was carried out with the use of DMA 242 device produced by NETZSCH company (Fig. 3). The aim of this study was to determine a real part which corresponds to the spring properties of the material and the imaginary part corresponding to damping properties (energy dissipation). The analysis of the results was supported by NETZSCH Proteus software. The real part was designated as storage modulus E' while the imaginary part was designated as loss modulus E'' (Menczel & Prime, 2009).



a)

b)

Fig. 3: Test stand: a) Dynamic mechanical analyser DMA 242 NETZSCH; b) Research software settings.

An important issue in the evaluation of the dynamic properties of a material is the measurement of the damping properties (Koszkul et al., 2002). In DMA method, this size is expressed as the tangent of the angle of phase shift δ also known as the tangent of the angle of mechanical loss.

$$\operatorname{tg} \delta = \frac{E''}{E'} \quad (2)$$

The value of phase shift δ describes the ratio of the energy dissipated per cycle of ϵ strain to the energy stored during this process. The study consisted in the compression of the sample at specific frequencies. The German standard DIN 45673-5 Mechanical vibration - Resilient elements used in railway tracks - Part 5: Laboratory test procedures for under-ballast mats were used to determine research frequencies. Vibration frequencies 5, 10, 20, 30, and 40 Hz are used in the standard to examine the dynamic properties. In the research software, the parameters were established to be as close as possible to the recommended frequencies, i.e. 1 Hz, 5 Hz, 10 Hz, 20 Hz, 33.33 Hz and 50 Hz (Fig 4).

The amplitude of ϵ strain was $40 \mu\text{m}$ and the maximum dynamic force acting on the sample was 7.272 N. Isothermal conditions were maintained during testing, with the temperature at the level of $23^\circ\text{C} \pm 3^\circ\text{C}$. The measurement time was 10 minutes.

4. Results

Fig. 4 presents the course of changes in the storage modulus E' , loss modulus E'' , and $\tan \delta$ of an the angle of mechanical loss depending on the time. The figure shows the results of measurement at vibration frequencies of 1, 5, 10, and 20 Hz. The values of storage modulus as well as loss modulus and the angle

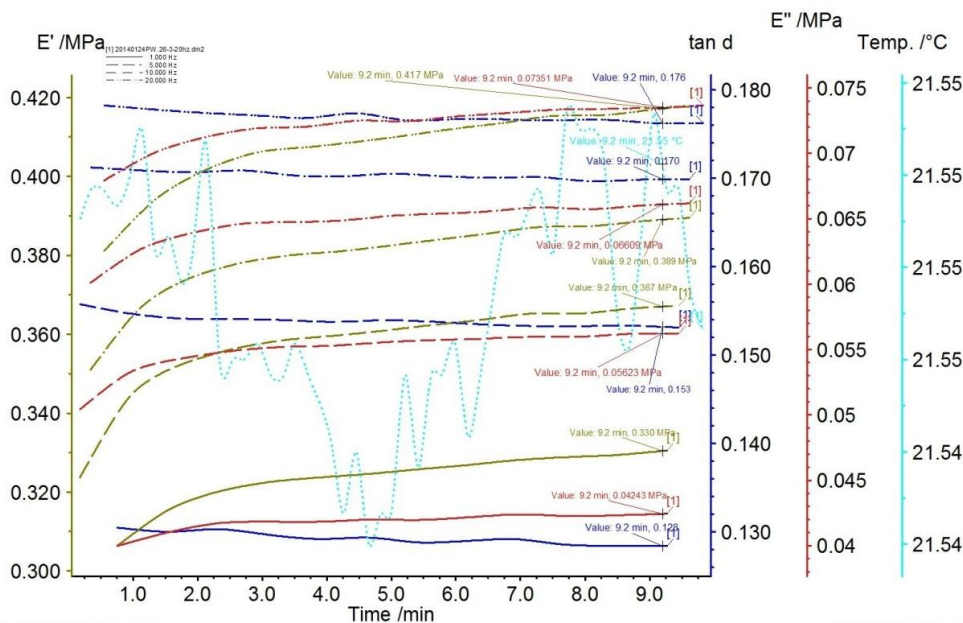


Fig. 4: Results of the sample obtained applying the NETZSCH Proteus software.

of mechanical loss depend on the vibration frequency. It is noted that the higher the frequency, the higher the values. After an increase of vibration frequencies from 1 Hz to 20 Hz there is observed an increase in value of $\text{tg}\delta$ by 37.5 %, loss modulus of approximately 26%. The largest increase is recorded for the measurement of mechanical loss modulus E'' , by 73%.

The results of $\text{tan}\delta$ measurements are shown in a diagram form, depending on the frequency selected (Fig. 5). Fig. 5 presents average values of five measurements for each frequency.

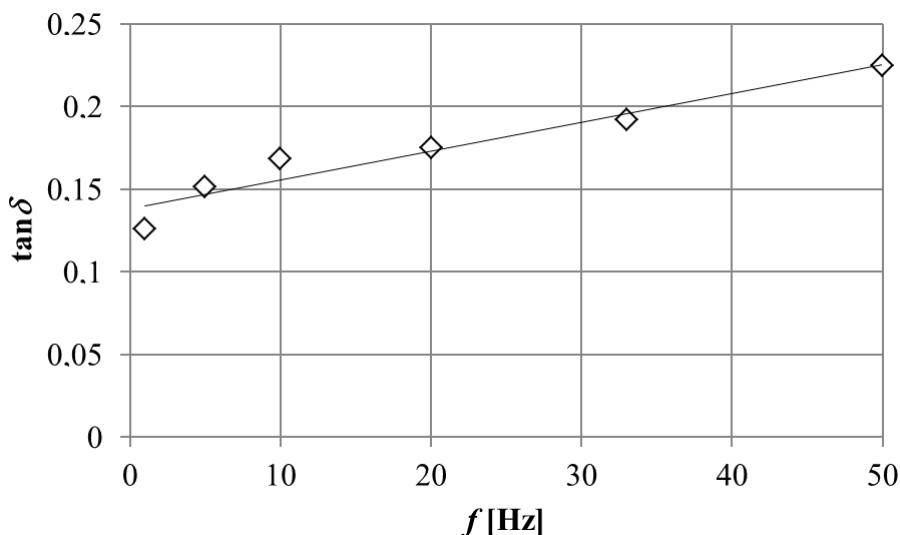


Fig. 5: Course of value $\text{tan}\delta$ depending on the frequency selected.

There can be seen a significant increase in value along with the frequency. The difference between the minimum and maximum value is 78% of the absolute value. The largest spread of the results between the extreme values, up to 27%, is observed for measurements of samples at the vibration frequency of 50 Hz. This frequency maybe is too high to obtain adequate repeatability of the results. It may also be related to the violation of the porous structure of the vibroinsulation mat during the measurement.

5. Conclusions

DMA is a measurement method which is increasingly used for the polyurethane material analysis. It allows testing the dynamic properties under the influence of an applied force in a function of temperature, frequency and time. This procedure allows the measurement of components of complex Young's modulus E^* – storage modulus and mechanical loss modulus. These values refer to damping characteristic of viscoelastic polymer properties.

According to the literature (Hatakeyama & ZhenHai, 1998) polymer materials are characterised by good damping properties if the value of the mechanical loss factor falls in the range $0.1 \leq \text{tg}\delta \leq 0.2$. Based on that it can be concluded that the tested vibroinsulation mats tested show the properties in the range of vibration frequency from 1 Hz to 33.3 Hz.

It should be noted that those are preliminary studies aiming to determine the relationship between dynamic properties and selected frequencies. Later the authors want to investigate the reaction of the vibroinsulation mat in variable temperature conditions as well as to find the correlation of the results in respect to laboratory tests according to DIN 45673-5.

References

- Adameczyk, J., Targosz, J. (2011) Diagnostics of physical and mechanical parameters of elastomer materials in aspect of applying them in railway vibroinsulation system. *Logistyka* 3, pp. 2777 – 2786.
- Hatakeyama, T., Zhenhai, L. (1998). *Handbook of thermal analysis*, John Wiley&Sons, New Jersey.
- Koszkul, J., Nitkiewicz, Z., Sobczak, R. (2002) Examination of the dynamic mechanical properties of polypropylene composites reinforced glass fibre. *Composites* 2, 3, pp. 78-80.
- Menczel, J. D., Prime, R. B. (2009) *Thermal Analysis of Polymers. Fundamentals and Applications*, John Wiley&Sons, New Jersey.

AN IMPROVED THERMAL-STRUCTURAL FINITE ELEMENT MODEL FOR MANUFACTURING PROCESSES WITH HEAT GENERATION

L. Écsi^{*}, R. Jančo^{**}, P. Élesztős^{***}

Abstract: *In this paper a universal mathematical model capable of predicting thermo-mechanical behaviour of various types of metal during their manufacturing using fully coupled thermal-structural finite element analysis is presented. The model takes into account the internal damping of the material, elastic and plastic heating and it can be used in wide range of strain rates that accompany the deformation of the body. In the model finite element implementation an improved heat equation, the updated Lagrangian formulation, the NoIHKH material model and the Jaumann rate in the form of the Green-Naghdi rate in the co-rotational Cauchy's stress tensor integration have been used. Cyclic tension of a notched aluminium specimen has been studied using prescribed axial deformation and a sine function with linearly increasing amplitude and 2 Hz frequency in the run-up stage of the test and a sine function with constant amplitude and linearly increasing frequency in the operation stage of the test. A few selected analysis results are presented and briefly discussed. The analysis results are very positive and the authors believe that the model might open new perspectives in the study and numerical simulations of metals.*

Keywords: Thermal-structural analysis, Strong coupling, Finite strain elastoplasticity, Internal damping, Elastic, Plastic and internal damping induced heating, Wide range of strain rates.

1. Introduction

Many manufacturing processes are accompanied by significant heat generation in real situations. Depending on the particular manufacturing process itself, the heat might stem from various sources. In the presented research we are interested in the study of such processes, where the heat originates from mechanical work. A few typical examples are machining of metallic materials, in which cutting a piece of raw metal into a desired shape and size is accompanied by severe heat generation, or friction-stir welding (FSW), in which the amount of heat generated between the tool and the welded material softens the nearby metal, which when intermixed at the presence of mechanical pressure, joins the two pieces of the welded metal. Numerical simulation of the aforementioned manufacturing processes represents a real challenge in contemporary computational mechanics, as it involves in it the simulation of contact between the workpiece and the tool, the heat generation, which either originates in friction or deformation, where the latter is large and usually strain rate dependent, thus the simulation requires rezoning and remeshing of the spatially discretized body.

The aim of this work is to present a universal mathematical model capable of predicting thermo-mechanical behaviour of various types of metal during their manufacturing.

2. Methods

In the study a fully coupled thermal-structural finite element (FE) analysis has been carried out using large strain / large deformation formulation, which employed an improved heat equation with elastic heating, plastic heating and internal damping induced heating (Écsi et al., 2012a).

^{*} Assoc. Prof. Ladislav Écsi, PhD.: Institute of Applied Mechanics and Mechatronics, Slovak University of Technology in Bratislava, Ná mestie slobody 17; 812 31, Bratislava; Slovakia, ladislav.ecsi@stuba.sk

^{**} Assoc. Prof. Roland Jančo, PhD.: Institute of Applied Mechanics and Mechatronics, Slovak University of Technology in Bratislava, Ná mestie slobody 17; 812 31, Bratislava; Slovakia, roland.janco@stuba.sk

^{***} Prof. Pavel Élesztős, PhD.: Institute of Applied Mechanics and Mechatronics, Slovak University of Technology in Bratislava, Ná mestie slobody 17; 812 31, Bratislava; Slovakia, pavel.elesztos@stuba.sk

The model is applicable to wide range of strain rates and it bases on our two former models utilizing an enhanced weak form for FE analysis that accounts for the strong coupling between the deformation field and the temperature field on the boundary of the body when convective or radiative heat transfer takes place on the boundary (Écsi et al., 2012b; Écsi et al., 2009). In the internal / material damping mathematical formulation we employed a modified Kelvin-Voight model which is capable of imitating the viscosity of the material during both, elastic and plastic deformations (Écsi et al., 2012b). The extended NoIHKH material model (Écsi et al., 2006), based on the original NoIHKH material model for cyclic plasticity of metal (Lemaitre, 2001), has been adapted to large strains / large deformations utilizing the updated Lagrangian formulation, the J_2 plasticity and the Jaumann rate in the form of the Green-Naghdi rate in the Cauchy's stress tensor integration. Using the co-rotational formulation the constitutive and evolution equations of the model are given with the following equations:

$${}^{n+1}\hat{\boldsymbol{\sigma}} = {}^{n+1}\hat{\boldsymbol{\sigma}}^{\text{el}} + {}^{n+1}\hat{\boldsymbol{\sigma}}^{\text{damp}}, \quad (1)$$

$${}^{n+1}\hat{\boldsymbol{\sigma}}^{\text{el}} = \Delta\hat{\boldsymbol{\sigma}}^{\text{el}} + {}^n\hat{\boldsymbol{\sigma}}^{\text{el}}, \quad (2)$$

$$\Delta\hat{\boldsymbol{\sigma}}^{\text{el}} = {}^{n+\frac{1}{2}}\hat{\mathbf{C}}^{\text{VJ}} : \left[\Delta t \left({}^{n+\frac{1}{2}}\hat{\mathbf{d}} - {}^{n+\frac{1}{2}}\hat{\mathbf{d}}^{\text{th}} \right) - x\Delta\tilde{\lambda} \frac{\partial f}{\partial \hat{\boldsymbol{\sigma}}} \right], \quad (3)$$

$${}^{n+1}\hat{\boldsymbol{\sigma}}^{\text{damp}} = {}^{n+1}\hat{\mathbf{C}}^{\text{VJdamp}} : \left[{}^{n+1}\hat{\mathbf{d}} - (1-x) \frac{\Delta\tilde{\lambda}}{\Delta t} \frac{\partial f}{\partial \hat{\boldsymbol{\sigma}}} \right], \quad (4)$$

$$f = \sigma_{\text{eq}} - \sigma_y - R \leq 0, \quad (5)$$

$$\sigma_{\text{eq}} = \sqrt{\frac{3}{2}(\hat{\boldsymbol{\Sigma}} - \boldsymbol{\Sigma}\hat{\mathbf{X}}) : (\hat{\boldsymbol{\Sigma}} - \boldsymbol{\Sigma}\hat{\mathbf{X}})}, \quad \hat{\boldsymbol{\Sigma}} = \hat{\boldsymbol{\sigma}} - \frac{1}{3}\text{tr}(\hat{\boldsymbol{\sigma}})\mathbf{I}, \quad \boldsymbol{\Sigma}\hat{\mathbf{X}} = \hat{\mathbf{X}} - \frac{1}{3}\text{tr}(\hat{\mathbf{X}})\mathbf{I}, \quad (6)$$

$$R = Q(1 - e^{-be^n}), \quad (7)$$

$${}^{n+1}\hat{\mathbf{X}} = \Delta t \cdot \left[{}^{n+\frac{1}{2}}\hat{\mathbf{C}}^{\text{VJcycl}} : {}^{n+\frac{1}{2}}\hat{\mathbf{d}}^{\text{pl-el}} - \gamma \left({}^{n+\frac{1}{2}}\boldsymbol{\varepsilon}^{\text{pl-el}} \right) {}^{n+\frac{1}{2}}\hat{\mathbf{X}} - {}^{n+\frac{1}{2}}\dot{\boldsymbol{\varepsilon}}^{\text{pl-el}} \right] + {}^n\hat{\mathbf{X}}, \quad (8)$$

$$\gamma(\boldsymbol{\varepsilon}^{\text{pl-el}}) = \gamma_{\infty} - (\gamma_{\infty} - \gamma_0)e^{-\omega\boldsymbol{\varepsilon}^{\text{pl-el}}}, \quad (9)$$

$${}^{n+\frac{1}{2}}\hat{\mathbf{d}}^{\text{pl-el}} = x \cdot \Delta\tilde{\lambda} \cdot \sqrt{\frac{3}{2}} \cdot \hat{\mathbf{N}}, \quad {}^{n+1}\hat{\mathbf{d}}^{\text{pl-damp}} = (1-x) \cdot \frac{\Delta\tilde{\lambda}}{\Delta t} \cdot \sqrt{\frac{3}{2}} \cdot \hat{\mathbf{N}}, \quad \hat{\mathbf{N}} = \frac{\hat{\boldsymbol{\Sigma}} - \boldsymbol{\Sigma}\hat{\mathbf{X}}}{\sqrt{(\hat{\boldsymbol{\Sigma}} - \boldsymbol{\Sigma}\hat{\mathbf{X}}) : (\hat{\boldsymbol{\Sigma}} - \boldsymbol{\Sigma}\hat{\mathbf{X}})}}, \quad (10)$$

$${}^{n+\frac{1}{2}}\mathbf{R} = \exp \left[\frac{\Delta t}{2} {}^{n+\frac{1}{2}}\mathbf{W} \right] \bullet {}^n\mathbf{R}, \quad {}^{n+1}\mathbf{R} = \exp \left[\Delta t {}^{n+\frac{1}{2}}\mathbf{W} \right] \bullet {}^n\mathbf{R}, \quad (11)$$

$$f \leq 0, \quad \Delta\tilde{\lambda} \geq 0, \quad f \cdot \Delta\tilde{\lambda} = 0. \quad (12)$$

In Eqns. (1)-(12) the left superscripts $n, n+1/2, n+1$ denote the physical quantity value at discrete times, corresponding to previous, mid and current configurations of the body within the current time step Δt . Here $\hat{\boldsymbol{\sigma}} = \mathbf{R}^T \cdot \boldsymbol{\sigma} \cdot \mathbf{R}$, $\hat{\boldsymbol{\sigma}}^{\text{el}}$, $\hat{\boldsymbol{\sigma}}^{\text{damp}}$ are the co-rotational Cauchy's stress tensor, its elastic part and its damping part, $\hat{\mathbf{X}} = \mathbf{R}^T \cdot \mathbf{X} \cdot \mathbf{R}$ is the co-rotational backstress tensor, in which objective integration there was employed the Jaumann rate in the form of the Green-Naghdi rate (De Souza Neto et al., 2008). We used an additive decomposition of the co-rotational strain rate tensor $\hat{\mathbf{d}} = \mathbf{R}^T \cdot \dot{\mathbf{d}} \cdot \mathbf{R}$ into an elastic part $\hat{\mathbf{d}}^{\text{el-el}}$, a thermal part $\hat{\mathbf{d}}^{\text{th}} = \alpha \dot{T} \mathbf{1}$ and a plastic part $\hat{\mathbf{d}}^{\text{pl-el}} = x(\Delta\tilde{\lambda} / \Delta t)(\partial f / \partial \hat{\boldsymbol{\sigma}})$ in Eqn. (3), and an additive decomposition of the co-rotational strain rate tensor $\hat{\mathbf{d}}$ into an elastic part $\hat{\mathbf{d}}^{\text{el-damp}}$ and a plastic part $\hat{\mathbf{d}}^{\text{pl-damp}} = (1-x)(\Delta\tilde{\lambda} / \Delta t)(\partial f / \partial \hat{\boldsymbol{\sigma}})$ in Eqn. (4), where x is the ratio of ductile and total damage, α is the

coefficient of thermal expansion, T is the absolute temperature, $\Delta\tilde{\lambda}$ is the plastic multiplier, $\mathbf{1}$ stands for a second order unit tensor and $\hat{\mathbf{C}}^{\nabla J_{damp}}$, $\hat{\mathbf{C}}^{\nabla J_{damp}}$, $\hat{\mathbf{C}}^{\nabla J_{cycl}}$ denote the fourth order co-rotational elastic material tensors of the model in the current configuration of the body along with the definitions of the accumulated plastic strain and the effective plastic strain as the measures of ductile and total damage (Écsi, L. & Élesztős, P., 2012a; Écsi, L. & Élesztős, P., 2012b). The corresponding rotation tensors (11) are expressed in terms of the time step size and a second order spin tensor \mathbf{W} . The extended NoIHKH material model for cyclic plasticity of metals that uses combined isotropic (7) and kinematic (8) hardening has been adapted for large strain elastoplasticity Eqns. (5)-(9). The loading/unloading criterions are defined with the discrete Khun-Tucker optimality conditions Eqn. (12).

2.1. Numerical experiment – Cyclic tension of a notched specimen

In our numerical experiment a 2024-T3 aluminium alloy notched specimen was studied using cyclic tension and zero stress ratio $R = 0$. One end of the specimen was fixed while there was a prescribed axial deformation applied to the second end of the specimen employing a sine function. The amplitude of the sine function increased linearly during the run-up stage of the test until the maximum amplitude, corresponding to 20% of the specimen length was reached, while the circular frequency was kept constant at 2 Hz. During the test, the amplitude of the sine function was kept constant and the circular frequency increased linearly with time. The dimensions of the specimen were 10 times smaller than the ones in the modelled experiment and the material properties were identical with the properties of the specimen used by Pastor, et. al. (2008) in their study. Only 1/4 of the body was modelled employing 2 planes of symmetry, which were meshed with 3D brick elements using linear shape functions. Convective and radiative heat transfer was considered through all free surfaces of the body using 273.15 K bulk temperature. At the moving end of the body, under the grip of the testing machine, the heat transfer coefficient value was increased to $h = 10^{22} \text{ W/m}^2 \cdot \text{K}$ to keep the temperature of the surfaces constant at these locations as in the test by Pastor et. al., 2008. Tab. 1 outlines the used material parameters.

Tab. 1: Material parameters of the specimen.

$E = 73100000000.0 \text{ Pa}$	$\gamma_0 = 0.002$
$E^{damp} = 73100.0 \text{ Pa}$	$\omega = 10.0$
$E^{cycl} = 73100000.0 \text{ Pa}$	$\rho_0 = 2770.0$
$\nu = \nu^{damp} = \nu^{cycl} = 0.33$	$c = 876.0 \text{ J/(kg} \cdot \text{K)}$
$\sigma_y = 345000000.0 \text{ Pa}$	$k_{xx} = k_{yy} = k_{zz} = 120.0 \text{ W/(m} \cdot \text{K)}$
$Q = 138000000.0 \text{ Pa}$	$\alpha_x = \alpha_y = \alpha_z = \alpha = 0.0000234 \text{ K}^{-1}$
$b = 3.0$	$h = 10.0 \text{ W/(m}^2 \cdot \text{K)}$
$\gamma_\infty = 0.001$	$\Psi = 1.0, \sigma_{EMS} = 11.343 \cdot 10^{-9} \text{ W/(m}^2 \cdot \text{K}^4)$

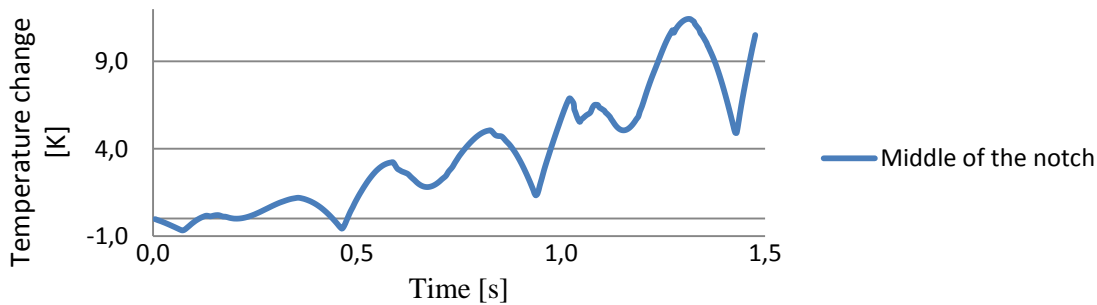


Fig. 1: Temperature change time history in the middle of the notch of the specimen.

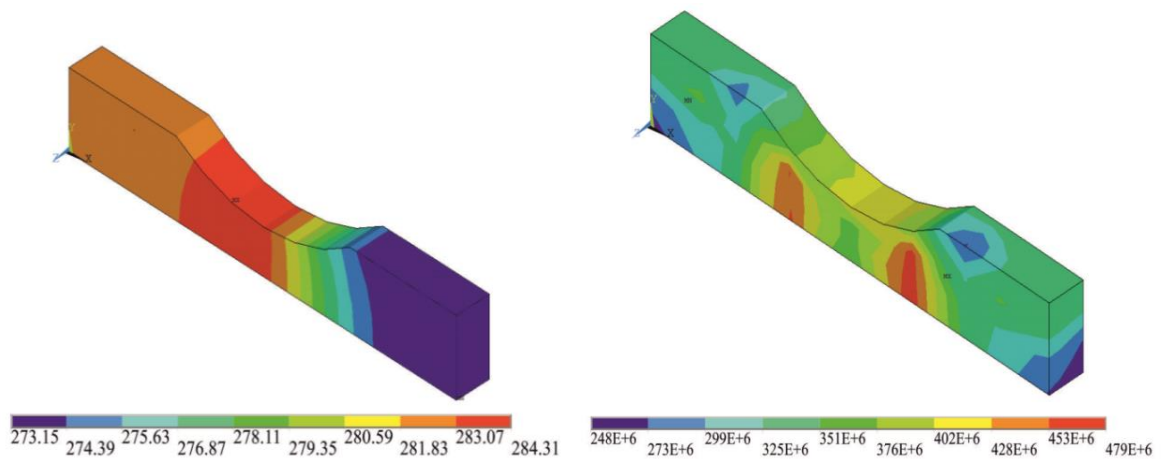


Fig. 2: Absolute temperature [K] and axial Cauchy's stress distribution [Pa].

Unfortunately at the time of writing the paper the analysis had not yet been finished, so that a few partial results only could be presented herein. They are the temperature change time history at the centre of the notch of the specimen (Fig. 1) and the absolute temperature and the axial Cauchy's stress distribution over the specimen body (Fig. 2). As can be seen in the figures, there is a significant temperature rise within less than 1.5 s of the analysis, the area of which gradually increases due to heat conduction toward the fixed end of the specimen near the origin of the coordinate system in Fig. 2 where the body is not cooled, while there is an insignificant change in temperature under the moving grips where the body is cooled. The beginning of the temperature time history agrees with the temperature time history reported by Pastor, et. al. (2008), which the authors consider to be very positive.

3. Conclusions

In this paper we have presented some recent developments in the research into fully coupled thermal structural finite element problems with convective heat transfer, radiation heat transfer, material damping within the framework of finite strain elastoplasticity. Cyclic tension of a notched specimen was studied. The analysis results are in agreement with available experiments. The authors consider the results positive and hope that the model might open new perspectives in the study and numerical simulation of metals.

Acknowledgement

The publication is the result of the "Research of friction stir welding (FSW) application as an alternative to melting welding methods" project, No. 26240220031, which has been supported by the Research & Development Operational Programme and funded by the ERDF. Funding from the VEGA 1/0627/13 project resources is also greatly appreciated.

References

- Écsi, L. & Élesztős, P. (2012a) An improved thermal-structural finite element model for ductile-to-brittle failure mode transition to model ductile material behaviour at high strain rates, In: CD - Proc. Europ. Congr. on Comput. Meth. in Appl. Sci. and Engrg. (ECCOMAS 2012) (J. Eberhardsteiner et.al. eds), Vienna.
- Écsi, L. & Élesztős, P. (2012b) Moving toward a more realistic material model of a ductile material with failure mode transition. *Mat.-wiss. u. Werkstofftech*, 43, 5, pp. 379-387.
- Écsi, L. & Élesztős, P. (2009) Constitutive equation with internal damping for materials under cyclic and dynamic loadings using a fully coupled thermal-structural finite element analysis. *Int. J. Multiphysics*, 3, 2, pp. 155-165.
- Écsi, L. & Élesztős, P. (2006) Extended NOIHKH model usage for cyclic plasticity of metals. *Engineering mechanics*, 13, 2, pp. 83-92.
- Lemaitre, J. (2001) *Handbook of material behaviour models*, Vol. 1, Def. of materials. Academic press, London.
- De Souza Neto, E.A., Perić, D. & Owen, D.R.J. (2008) *Computational methods for plasticity, Theory and applications*. John Wiley & Sons Ltd., Singapore.
- Pastor, M.L., Balandraud, X., Grédiac, M. & Robert, J.L. (2008) Applying infrared thermography to study the heating of 2024-T3 aluminium specimens under fatigue loading. *Infrared Phys. Techn*, 51, pp. 505-515.

DEM SIMULATION OF BALLAST OEDOMETRIC TEST

J. Eliáš*

Abstract: *The granular nature of the railway ballast in connection with fast dynamic loading makes it an ideal application of the Discrete Element Method (DEM). The contribution employs DEM to simulate the ballast behavior in large oedometric test. Ballast grains are represented by convex polyhedral particles with shape randomly generated via Voronoi tessellation. A novel algorithm to compute repulsive contact force based on intersecting volume of polyhedrons is presented. Crushing of grains is included via splitting the particles into smaller polyhedrons when some stress-based criterion is fulfilled.*

Keywords: Discrete Element Method, Polyhedrons, Crushing, Voronoi tessellation, Ballast.

1. Introduction

Power of modern computers is utilized to help engineers in designing and understanding of their technological solutions more frequently than ever. Dealing with various types of problems led to development of many different methods, among which the Discrete Element Method (DEM) is especially suitable when granular media under highly dynamic loading is studied. DEM treats every grain as an ideally rigid body which interacts with other particles through forces at their common contacts. In most cases, the simplest spherical elemental shapes are used. However, it has been reported that the particle shape has a strong influence on resulting behavior of the system. Therefore, more realistic elemental shapes are being considered. This is often achieved by clumping spheres into some more complex aggregations. Such a method has an advantage in simplicity and computational speed. Another approach lies in direct implementation of some non-spherical elements. There has been also extensive effort to use polyhedral particle shape. A technique developed by Cundall (1988) called *common plane* method is often used. It replaces contact between two polyhedrons by two plane-polyhedron contacts. This method was further improved by fast determination of the *common plane* (Nezami et al., 2006).

The railway ballast is used worldwide to support sleepers and rails on both normal and high speed railways. However, its short and long time behavior is still not fully understood. It is a highly heterogeneous material with strongly nonlinear behavior further complicated by its previous compaction and crushing. Robust models of the ballast are needed for better design of sleepers, under sleeper pads, and ballast itself as well as for determining optimal maintenance schedule of the tracks.

In this contribution, we present simulation of railway ballast experiment - large oedometric test - performed at the University of Nottingham (Lim and McDowell, 2005) using crushable polyhedral particles with random shape. Algorithms presented in the paper were implemented into the open source DEM software YADE (Kozicki and Donzé, 2008). Manipulation with polyhedrons as well as computation of convex hulls and least square fitting by plane is done via open source software CGAL (Kettner, 1999).

2. Generation of Randomly Shaped Polyhedral Particles

The particles are created using procedure that contains a random process; however, control of grain size and aspect ratio is kept. Initially, volume of size $5 \times 5 \times 5$ units is filled by nuclei with minimal mutual distance l_{\min} . Starting with central nucleus in the center of the volume, other nuclei with random coordinates are accepted if their distance to all previously placed nuclei exceeds l_{\min} . Voronoi tessellation

* Jan Eliáš: Institute of structural mechanics, Brno University of technology, Faculty of civil engineering, Veveří 331/95; 602 00, Brno; CZ, elias.j@fce.vutbr.cz.

is performed and the Voronoi cell associated with the central nucleus is extracted and used as a basic particle shape. The control of size and aspect ratio is ensured by scaling the Voronoi cell in all three directions according to user defined scaling vector. Finally, the particle is randomly rotated to prevent directional bias. Volume, centroid and inertia of the polyhedral particle is calculated through dividing the polyhedron into tetrahedrons. Contributions of tetrahedrons to each of the wanted quantity are found using analytical formulas.

3. Contact between Polyhedrons

In every time step, there is a loop seeking for all possible contacts between polyhedral elements. This is simply done through creation of bounding boxes around every polyhedron and detection of overlapping between the bounding boxes. If bounding box protrudes, one must examine the overlapping of polyhedrons \mathcal{P}_A and \mathcal{P}_B . This is solved here through searching for a separation plane.

The polyhedral intersection is assumed to exist until some separation plane is found. Only limited set of candidates for the separation plane must be tested to prove or disprove its existence. The minimal set of candidates contains bounding planes of both of the polyhedrons and planes determined by one edge from \mathcal{P}_A and another edge from \mathcal{P}_B . A loop over all these candidates is browsed. Every time, a trial separation plane is constructed so that centroid of the polyhedron \mathcal{P}_A lies at the positive side of the trial plane. Then, if all vertices from the first polyhedron \mathcal{P}_A lay at positive halfspace and all vertices from the second polyhedron \mathcal{P}_B lay in the negative halfspace, the trial plane is approved. If the loop is finished without approving any separation plane, there must be a contact between polyhedrons.

When two grains come into a contact, some repulsive force arises. In DEM simplification, the grains are ideally rigid and the contact is accompanied by overlapping of particles. In case of convex polyhedrons, the intersection is a convex polyhedron as well (Fig. 1). It is denoted \mathcal{P}_I , its volume is V_I . It is assumed that in the whole overlapping volume, constant repulsive *volume force* acts. Integrating this *volume force* over the intersecting volume gives us the total *normal force* \mathbf{F}_n and moment, that should be applied on both particles. Since the *volume force* is constant, the magnitude of the *normal force* is linearly proportional to the intersecting volume

$$|\mathbf{F}_n| = k_n V_I \quad (1)$$

where k_n [N/m^3] is a material parameter called volumetric stiffness. To eliminate the moment, the *normal force* acts at the centroid of the intersection. To find the exact polyhedral intersection, dual approach (Muller and Preparata, 1978) is used.

Besides the magnitude of the normal force, its direction must be determined as well. Normal direction is estimated to be perpendicular to a plane f taken as the least square fit of the shell intersection curve. After polyhedral intersection is found, its faces are divided to those belonging originally to the polyhedron \mathcal{P}_A and to the polyhedron \mathcal{P}_B , respectively. Edges on the boundary between these two groups (shell intersection curve) are then interpolated by a plane f using the least square fitting.

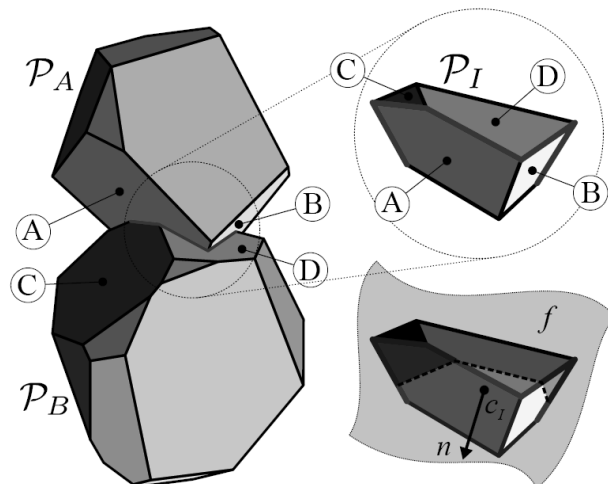


Fig. 1: Two polyhedral particles in contact.

Shear force is calculated by standard incremental algorithm. It consists in correction of the shear force from the last time step for changes in the normal direction and for the rigid-body motion. Then, an additional shear force increment caused by mutual movements and rotations of polyhedrons is added. Standard Coulomb friction is applied. Therefore, the shear force magnitude is limited by magnitude of normal force multiplied by tangent of internal friction angle.

4. Model of Crushing

Crushing of ballast grains is responsible for degradation of ballast and modelling should take it into account. Implementation of the crushing phenomenon is simply done via splitting the polyhedral particles into smaller polyhedrons whenever they fulfill some failure criterion. The criterion is based on comparison of equivalent splitting stress, σ_e , and size dependent strength, f_t . The average Cauchy stress tensor in the particle can be expressed as

$$\sigma_{ij} = \sum_c l_i^{(c)} F_j^{(c)} \quad (2)$$

where c runs over all contacts of the particle, $F^{(c)}$ is a force acting at the c -th contact at point with spatial coordinates $l^{(c)}$; $l_i^{(c)}$ and $F_j^{(c)}$ are i and j components of the coordinate vector or force, respectively. The stress tensor is symmetrized by averaging opposite non-diagonal members; then, principle stresses ($\sigma_I > \sigma_{II} > \sigma_{III}$) and their directions are found by eigenvalue analyses. The equivalent splitting stress entering the failure criterion is defined as

$$\sigma_e = -\frac{\sigma_{III}}{2} + \sigma_I \quad (3)$$

The equivalent splitting stress is compared with material strength f_t , which is (according to Lobo-Guerrero and Ballejo (2005)) dependent on particle size.

Whenever splitting stress exceeds strength of a particle, the polyhedron breaks. Polyhedron is cut through its centroid by two perpendicular planes that are parallel to the second principle stress, σ_{II} , and form angle $\pi/4$ with the remaining principal stresses. After the breakage, translational and rotational velocities are assigned to the polyhedral pieces according to the current velocities of the original particle.

5. Application to Oedometric Test

The proposed model was validated by simulating a large oedometric test on railway ballast performed and published by Lim and MCDowwel (2005). They tested several different ballasts, from which we chose variant A with ballast of grading 37.5-50 mm. A steel cylinder of diameter 300 mm and depth 150 mm was filled by the ballast and compacted on a vibration table with surcharge force 250 N. Then, it was loaded in compression up to force 1.5 MN (mean stress 21.2 MPa). Total duration of the experiment was about 40 minutes.

The same test was simulated with the polyhedral particles. Initially, randomly shaped polyhedrons were generated at random positions in a cylinder of magnified depth 1 meter with no overlapping. This was done by sequential placing of trial polyhedrons that were rejected whenever any collision with previously placed particles appeared. The polyhedrons then fall freely under 5 times magnified gravitational acceleration and reduced friction angle. Both gravity and friction changes were done to increase compaction of the assembly. After reaching low unbalanced forces, all polyhedrons exceeding depth limit 0.18 m were removed. To increase the compaction, the vibration table was mimicked via loading the sample by alternating acceleration in horizontal directions of magnitude equal to 5 times multiplied gravitation. Each vibration cycle consisted in four intervals of duration 0.02 s with constant acceleration in directions $+x$, $-x$, $+y$ and $-y$, respectively. Three vibration cycles were performed. Then, the simulation continued until low value of unbalanced forces was reached again. At that point, loading by sinusoidal wave started. The loading time was shortened to 1/3 s.

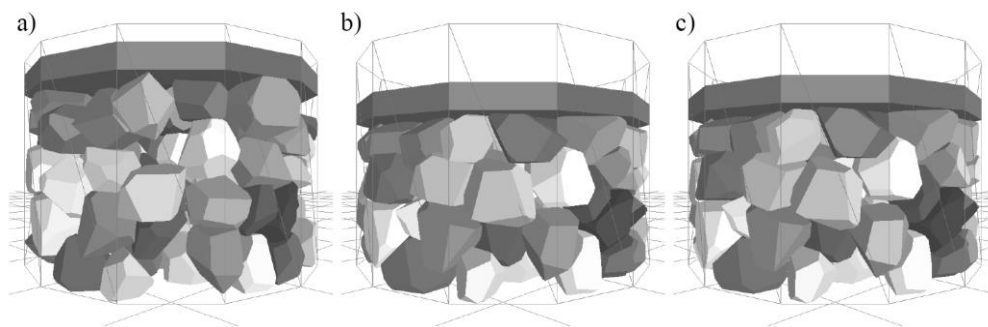


Fig. 2: Snapshots a) at the beginning of loading; b) at the maximum load; c) after releasing all the load.

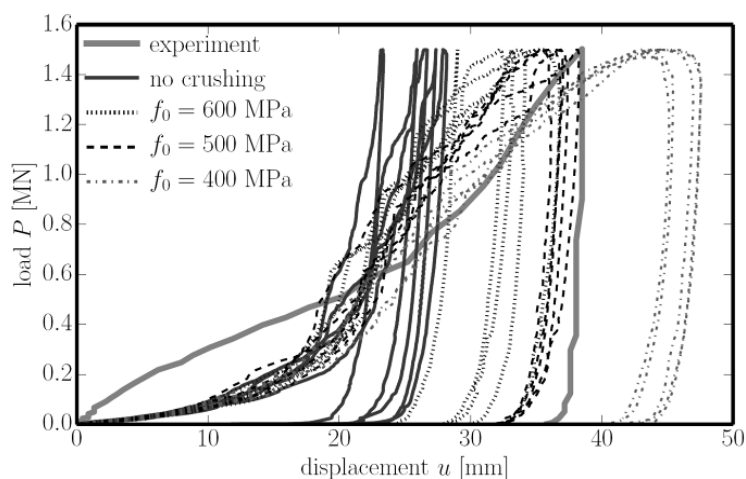


Fig. 3: Load-displacement response of the model with crushable particles.

The shear stiffness and friction angle were estimated; the normal volumetric stiffness of steel was assumed 10 times larger than the ballast normal stiffness, which was approximately identified in Eliáš (2013). Evaluation of the crushing criterion was run every 0.001 s during the simulation. Broken grains with volume lower than 1 cm³ were removed from the simulation as being less relevant to the overall response but slowing down the simulation substantially. Three variants of strength f_0 were tested: 400 MPa, 500 MPa and 600 MPa. Results are showed in Fig. 3. The value 500 MPa gives the best correspondence with the experimental record. It is interesting that crushing might occur also during unloading, especially for low strength close to the peak load.

Acknowledgement

The financial support received from Czech Ministry of Education, Youth and Sports under Projects No. CZ.1.07/2.3.00/20.0176 (IRICoN) and LH12062 is gratefully acknowledged.

References

- Cundall, P. (1988) Formulation of a three-dimensional distinct element model: Part I. A scheme to detect and represent contacts in a system composed of many polyhedral blocks. *Int. J. Rock. Mech. Min.*, 25:107-116.
- Eliáš J. (2013) DEM simulation of railway ballast using polyhedral elemental shapes. In: *Particle-Based Methods III: Fundamentals and Applications*, held in Stuttgart, Germany. pp. 247-256.
- Kettner, L. (1999) Using generic programming for designing a data structure for polyhedral surfaces. *Computational Geometry* 13:65-90.
- Kozicki, J., Donzé, F. (2008) A new open-source software developed for numerical simulations using discrete modeling methods. *Comput. Method. Appl. Mech.* 197:4429-4443.
- Lim, W. L., McDowell, G. R. (2005) Discrete element modelling of railway ballast. *Granular Matter.* 7:19-29.
- Lobo-Guerrero, S., Ballejo, L. E. (2005) Crushing a weak granular material: experimental numerical analyses. *Geotechnique* 55.
- Muller, D. E., Preparata, F. P. (1978) Finding the intersection of two convex polyhedra. *Theor. Comput. Sci.* 7:217-236.
- Nezami, E. G., Hashash, Y. M., Zhao, D., Ghaboussi, J. (2006) Shortest link method for contact detection in Discrete Element Method. *Int. J. Numer. Anal. Met.* 30:783-801.

SIMULATION AND IMPLEMENTATION OF TURBOCHARGING A 600CC ENGINE FOR FORMULA SAE

M. Farrugia^{*}, N. Grech^{**}, M. Chircop^{***}, J. P. Azzopardi^{****}

Abstract: *The aim of this work was to analyze turbocharging for a Kawasaki 600cc motorcycle engine using Ricardo WAVE® and the implementation of the turbocharger based on the findings of the engine simulations. The simulations showed that for the purposes of a FSAE® car, the Kawasaki 600cc engine should be equipped with the Pulse System Turbocharging (PST) rather than Constant Pressure Turbocharging (CPT). The turbocharger simulated and used was a Honeywell GT15V variable geometry unit. The optimum compression ratio found for the PST setup was 7. Implementation on the Kawasaki engine was done by placing a decompression plate between the cylinder block and crankcase. Experiments were also conducted on alternative cylinder head gasket designs. The engine was tested on a waterbrake dynamometer and using a programmable ECU. The turbocharger vane mechanism showed to highly effect the engine response and turbocharger spool up time. A cam sensor was integrated into the engine to run the electronic engine control in fully sequential mode. A charge air cooler was implemented to provide consistent air temperature even in the boosted operation during dynamometer testing.*

Keywords: Engine-downsizing, Turbocharging, FSAE., Pulse system turbocharging.

1. Introduction

Engine downsizing assisted by turbocharging has become an important aspect in engine technology. Engines not originally turbocharged must be modified before implementing a turbocharged setup. One such modification is the reduction of the compression ratio. The lowering of compression ratio for the engine leads to changes in the gasketing setup. Attard (2007) at the University of Melbourne preferred to go to a gasket-less setup providing the benefits of reduced crevice volumes and reusability without need for replacement gasket. However the gasket-less design did result in teething problems. At the University of Malta the used Kawaski 600cc Ninja engine provides a split at the engine block to crank case and therefore a decompression plate was placed there with the benefit of still using OEM head gasket. A PST setup was preferred versus CPT to utilize the kinetic energy in the exhaust pulses, reduce exhaust manifold weight, and require compact runners which allow a low centre of gravity installation of the relatively heavy turbocharger. The ignition timing, valve timing and other parameters are not the same for CPT and PST. Attard describes how when the turbocharging setup was changed from CPT to PST, engine torque reduced by as much as 20% with severe knock problems at previously determined Minimum spark timing for Best Torque (MBT). Boost levels had also to be reduced on the fixed geometry GT12 turbocharger used by Attard. A GT15V variable geometry turbocharged was chosen to be used at the University of Malta. A simulation study using Ricardo Wave® was conducted by Grech (2007) who determined that PST was the preferable setup for the GT15V on the Kawasaki 600cc engine.

2. Constant Pressure Versus Pulse System Turbochraging

The two turbocharging methodolgies sited by Watson and Janota are the Constant Pressure Turbocharging CPT and the Pulse System Turbocharging PST.

* Dr Ing Mario Farrugia: Mechanical Engineering Department, University of Malta, Msida MSD 2080, Malta
mario.a.farrugia@um.edu.mt

** Dr Nicholas Grech: Derby, England

*** Ing Marlon Chircop: Baxter Ltd. Malta

**** Jean Paul Azzopardi: Mechanical Engineering Department, University of Malta, Msida MSD 2080, Malta

In CPT, the exhaust ports from all cylinders are connected to a single exhaust manifold whose volume is large enough to dampen down the unsteady flow. As Watson and Janota (1984) describe, when the exhaust valve opens, the gas expands down to the constant pressure in the manifold without doing useful work. However the only energy lost is that due to heat transfer.

PST uses narrow pipes between the exhaust valves and the turbocharger's turbine. In this case a pressure build-up will occur during the exhaust blow-down period since flow of gases entering the manifold through the valve exceeds that of gases escaping through the turbine. Similar to CPT, just as the valve opens the pressure difference across the exhaust valve is above critical and hence flow through the valve will be sonic. Stagnation enthalpy remains constant and hence the flow from the valve is accompanied by an entropy increase. The gas then expands through the turbine to atmospheric pressure doing useful work. With pulse operation, a much larger portion of the exhaust energy can be made available to the turbine by considerably reducing throttling losses across the exhaust valve. It also causes a rapid fall in manifold pressure towards the end of the exhaust process improving scavenging and reducing piston pump work.

CPT causes steady flow to reach the turbine, losses from unsteady flow in the turbine are absent and this setup was preferred by Attard (2007) for use on his Wattard engine developed at Melbourne University.. However since it takes time for the pressure to rise in the large exhaust volume, the turbocharger response to an increase in throttle is slow *i.e.* it is not ideal for rapid changes.

3. Turbocharging Simulation in WAVE®

WAVE uses compressor and turbine components to model turbochargers. Each component is represented by a performance map produced by the TCMAP pre- and post-processor. Turbocharger models may be linked with engine models to fully simulate turbocharged engines. The turbine and compressor may also be operated in isolation as part of a simple system, *e.g.*, ambient-duct-compressor-duct-ambient. This is done to test the component alone.

The simulation relies on the data contained in steady-state maps typically obtained on a steady-state flow rig by the turbocharger manufacturer (it is of course a fact that the flow through a turbine and possibly the compressor is usually non-steady). Thus results from a PST simulation may have some level of inaccuracy.

The WAVE knock model is based on Douaud and Eyzat's induction correlation and is applicable to both the WAVE and IRIS cylinders. The Knock Model is applicable only to SI engines with two-zone combustion. The induction time (ignition delay) in seconds is calculated at every time step. In general, this induction time continually decreases as combustion progresses and the unburned zone temperature rises. The end-gas auto-ignites (knocks) if the induction time is less than the flame arrival time. When knock occurs, a spontaneous mass burning rate due to knock is determined and fed back to the cylinder, leading to rapid rise in cylinder pressure and temperature.

Turbocharging simulation was a development from the simulation study of a naturally aspirated restricted Kawasaki 600cc by Cauchi (2006). For each step the simulation took about 25 hours to complete. Such long computational times were required since WAVE was simulating the turbocharger and occurrence of knock, apart from the engine itself. Also, 220 simulation cycles were necessary for the simulation results to converge. Normal simulation of naturally aspirated engine would usually require 50 cycles.

3.1. Results for the Constant Pressure Turbocharging

Simulations of the CPT system showed that a boost of 1.7 bar was not achievable. On the other hand, instability was also noticeable at a boost pressure of 1.2 bar and below, especially at high engine speeds at which point the exhaust pressure was probably too high and the VGT stator vanes could not open enough to maintain a low boost. Hence the range of boost that was investigated was set from 1.2 to 1.5 bar. The model was then run at a boost pressure of 1.3 bar for different heat transfer coefficients (k) of the intercooling stage. The reduction in temperature affects the magnitude of the knock event. However the results showed that the intercooling stage did not effectively reduce knock levels, but slightly shifts the curve to lower engine speeds. The torque on the intercooled engine was higher as a result of the charge being denser. The intercooling stage was shown to be advantageous since for the same level of knock, the torque and b.h.p. were increased. The final set of simulations was to find the compression ratio that eliminated knock. The compression ratio was varied from 11 to 8 and the resulting engine performance is shown in Fig. 1.

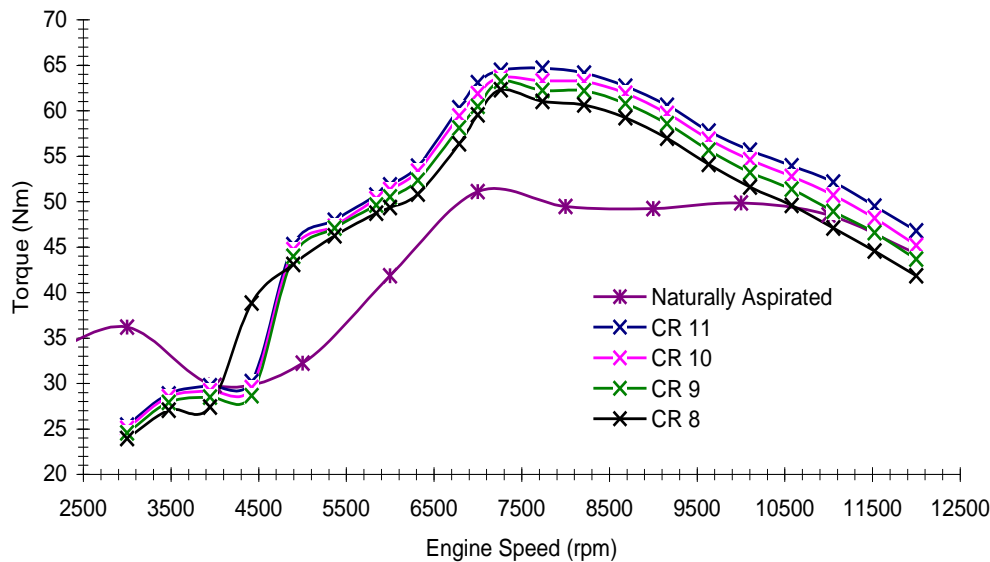


Fig. 1: CPT Torque curves for various compression ratios simulated.

3.2. Results for Pulse System Turbocharging

As in the CPT simulation, the PST setup was run under different boost pressures to check the range of boost achievable. The simulations showed that in a PST type setup, the boost pressures achieved are higher than for CPT confirming the statement by Attard (2007) that converting from CPT to PST caused problems in the engine including increased knock and worst torque characteristics. The simulations showed that stable boost pressures from 1.5 bar to 1.9 bar are possible. A boost of 1.4 bar could not be maintained throughout the entire engine speed while a pressure of 2 bar was very unstable. High boost pressures gave high peak power but over a narrow engine speed range apart from inducing high levels of knock. It was therefore determined that high boost pressures in this case provided no particular advantage and that low boost pressures will induce less knock, improve torque and power over a wider speed range while peak power is not much lower than for high levels of boost. With this reasoning, a boost pressure of 1.5 bar was selected for the PST setup. The last stage was that of determining the compression ratio to eliminate knock. Reducing the compression ratio obviously lowered the engine's performance but still give more power than the naturally aspirated version as shown in Fig. 2. A compression ratio of 7 was enough to totally eliminate knock throughout the entire engine speed range.

4. Experimental Setup

4.1. Decompression plate manufacture

The calculation of the required decompression plate thickness resulted in a value of 3.22 mm thicker than the stock gasket. The stock compression ratio was 11.8 while the target was 7. The OEM gasket found between the cylinder block and the crankshaft/transmission assembly had a thickness of 0.3 mm which implied that the total new thickness required was 3.52 mm. However, due to lack of availability from local suppliers and in order to facilitate machining, it was decided to machine the decompression plate from a 3mm thick aluminum sheet. This brought the compression ratio up to around 7.5, which was still within the knock prevention limits as determined by Grech (2007).

Due to excessive oil leaks from the compressor to the intake, a mechanical seal was integrated into the compressor side. For this reason a purposely designed compressor plate was manufactured to accept an off-the-shelf mechanical seal. This worked excellently and boost levels were still reached as before. A charge air cooler was also implemented to stabilize air temperatures downstream of the compressor. This is in contrast to Attard where he states that intercooling was found not to be necessary. Sequential operation of the engine electronic control was achieved by implementing a cam sensor onto one of the camshafts.

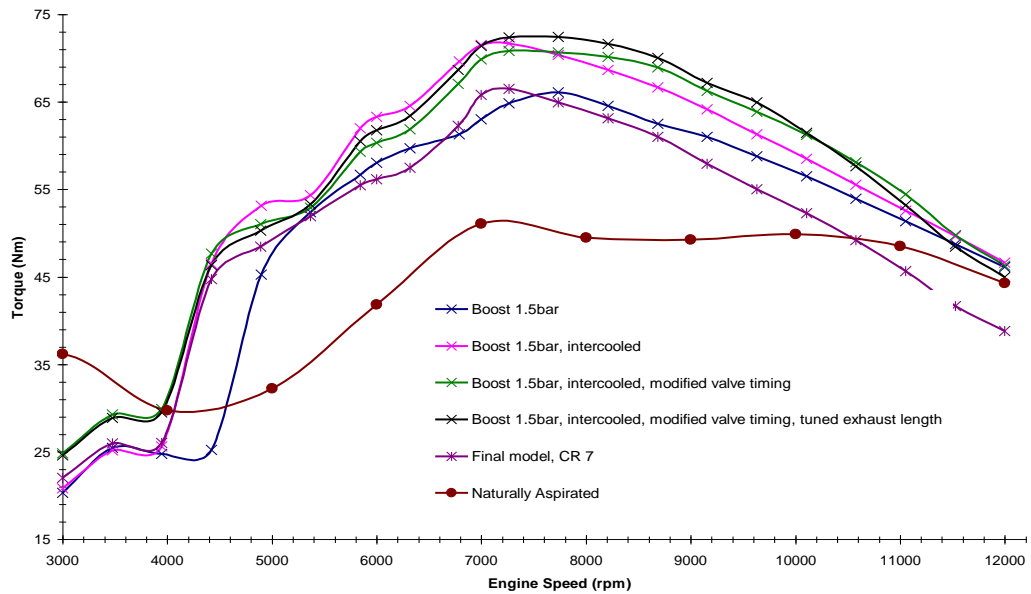


Fig. 2: Comparison of torque curves from various PST turbocharging stages.

4.2. Engine testing

The engine was started first using TPS as the load parameter and later changed to MAP. This was carried out since the TPS based map of the naturally aspirated engine was still valid for engine starting conditions and pre-boost operation

To safeguard the engine and reduce testing time, only sweep tests were carried out. The main aim of these tests was to indicate that the turbocharger actually produced boost and that the opening and closing of the vane system worked and produced a difference in turbocharger response time.

After proper engine warm up, the throttle was opened gradually and the variation in engine speed, MAP, air to fuel ratio and inlet air temperature were measured by a data acquisition system for both the closed vanes and open vanes situation. A maximum MAP value of around 170 kPa was obtained at 7200 rpm, while a rapid increase in MAP value above 5000 rpm occurred. The high boost pressures reached led to the decision to implement an external wastegate on the test stand so that boost levels other than the maximum can be stabilized in order to be able to experimentally determine proper fuel quantity and MBT timing. The testing of the external wastegate system together with the control system is currently being tested. Knock monitoring will be a next major goal in this development work. Changing of valve timing by design and production of our own camshafts is also another milestone to look forward to.

5. Conclusions

This study showed that a PST setup is more favourable for a Formula SAE vehicle. The one dimensional engine simulation software was used to find an optimal compression ratio, exhaust runner length and valve timing. The valve timing was not eventually modified but the compression ratio and exhaust runner lengths were implemented on the turbocharged engine. Experimental sweep tests on an engine dynamometer showed that the boost pressure reached 170 kPa with turbine vanes closed without any engine knock.

References

- Attard, W. (2007) Small Engine Performance Limits – Turbocharging, Combustion or Design, PhD Dissertation, University of Melbourne Australia.
- Cauchi, J., Farrugia, M. & Balzan, N. (2006) Engine Simulation of a Restricted Formula SAE® Engine, Focusing on Restrictor Modelling, SAE 2006-01-3651.
- Grech, N. (2007) S. I. Turbocharging Simulation and Fuel Injection Implementation, B.Eng Disser., Uni of Malta.
- Watson, N. & Janota, M. S. (1984) Turbocharging the Internal Combustion Engine, John Wiley & Sons, New York.

EXPERIMENTAL ANALYSIS OF A FIXED-SPEED AND A VARIABLE-SPEED AIR CONDITIONING SYSTEM

G. Fenech^{*}, M. Farrugia^{**}

Abstract: *A conventional air conditioning system is designed to satisfy the maximum load, and cycles on/off to match part load demand. A variable-speed or inverter driven system has the ability to regulate its cooling capacity by using a variable-frequency drive which continuously changes the speed of the motor and thus of the compressor. Variable-speed air conditioners are advertised as typically consuming 30 per cent less energy than conventional systems. This investigation is a continuation to a previous experimental investigation by Grech and Farrugia (2012) who used a belt driven open-type reciprocating compressor in both fixed and variable speed operation. In this experimental investigation a series of experiments on a conventional and an off-the-shelf inverter driven air conditioning system were performed. The aim of these experiments was to quantify the advertised part-load efficiency and reduced energy consumption of the off-the-shelf inverter driven air conditioner. The experimental results showed that the cooling coefficient of performance (based on refrigerant cooling effect) is higher for the inverter driven system at all refrigerant condenser out temperatures except at the highest temperatures at which the cooling coefficient of performance for the conventional system was better. This is to be expected since conventional systems are designed to satisfy the maximum load.*

Keywords: Air-conditioning, Inverter, Variable-speed, Part load, Coefficient of performance.

1. Introduction

As a consequence of the continuously rising energy prices, the need to control energy consumption has become a worldwide concern. Inverter driven air conditioners are systems designed with the main target of saving energy. Grech (2008) mentions that variable speed air conditioners are advertised as typically consuming 30 per cent less energy than conventional systems. This low energy consumption is achieved by the use of a variable-frequency drive which continuously changes the speed of the motor and thus of the compressor according to the cooling demand. In simple terms the variable-frequency drive will speed up the compressor when the demand is high and slow it down when the demand is low. Though their low energy consumption might be associated with a much higher initial cost, a well designed system is estimated to have a payback period that ranges between 3-4 years, Zubair et al. (1989). Inverter driven air conditioners both for residential and commercial applications were first implemented in Japan during the 1980s. Since then, variable-speed air conditioners have become widely popular owing to their energy saving and better performance in applications where part load is required. In fact in Japan sales of the inverter driven air conditioners account over 50 per cent of the air conditioning market and are still increasing, Zubair et al. (1989).

2. Experimental Setup

The experimental setup was based on instrumenting the air-conditioning system to have accurate measurements of electricity consumption, the flow of heat on both the hot and cold side, refrigerant flow, refrigerant pressures and many temperatures. The experimental setup used heat exchange to water on both the evaporator and condenser sides to give a better quantification of heat flow rather than cooling and heating of air. This involved the construction of two heat exchangers. The condenser side had the refrigerant coil immersed in a bath of water that was continuously stirred (through circulation) to maintain

* Ing Graziella Fenech: Lufthansa Technik, Malta

** Dr Ing Mario Farrugia: Mechanical Engineering Department, University of Malta, Msida MSD 2080, Malta
mario.a.farrugia@um.edu.mt

the desired refrigerant condenser out temperature. The heat was rejected from the bath by dumping the necessary amount of hot water and make-up with cold tap water to maintain a stable water level.

The evaporator side heat exchanger had two iterations in design, the first setup used a pipe-in-pipe configuration fed directly by mains water, but at low water flow rates the water froze which led to stagnation and trips. Hence an electrically heated bath setup was later used on the evaporator side as shown in Fig. 1. The cooling load was applied by switching on electrical heaters in the bath of water. This modification gave the added benefit that the temperature of the bath of water could be controlled to simulate the "room" temperature.

The experimental setup included the manufacture of small sized T-type thermocouples to have as little interference as possible with the thermal aspects of the refrigerant piping as detailed by Fenech (2009).

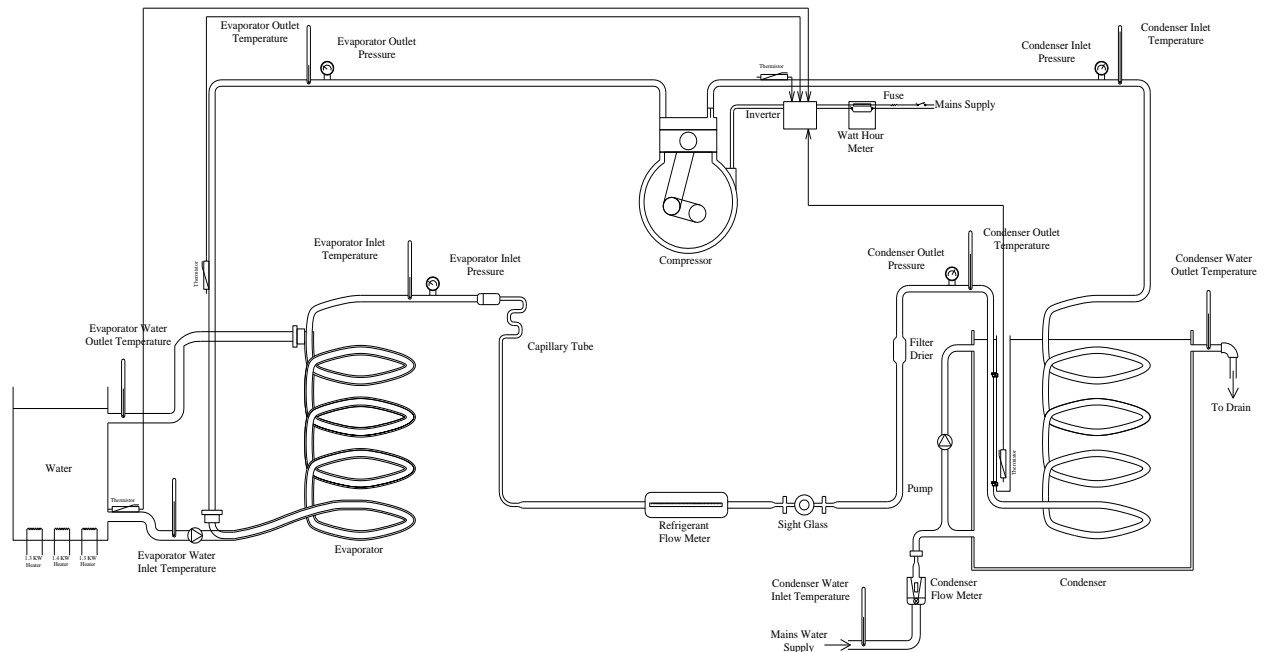


Fig. 1: Schematic diagram of the inverter driven air conditioning system.

3. Cooling Capacity

The variations of the cooling capacity with the refrigerant condenser out temperature obtained during experimentation are represented graphically in Fig. 2. As can be seen from the trends of Fig. 2 the cooling capacity exhibits a decrease as the refrigerant condenser out temperature is increased. This results from the fact that the enthalpy of the refrigerant at evaporator inlet increases at high condensing temperatures, thus the enthalpy difference across the evaporator decreases resulting in a lower refrigerant cooling capacity at high temperatures. The refrigerant mass flow rate also affects the cooling capacity. The refrigerant mass flow rate decreases as the refrigerant condenser out temperature increases. The decrease in refrigerant mass flow can be explained due to the fact that higher condenser out temperatures cause higher condenser pressures. Hence the compressor has to overcome a larger pressure rise which leads to a lowering of refrigerant flow. Thus the cooling capacity continues to decrease at the higher condenser temperatures. This decrease in the cooling capacity manifests itself as a low system coefficient of performance as will be discussed further in the next section.

Comparing the trends of the fixed-speed and variable-speed system, the former has a higher refrigerant cooling capacity due to the high volume of refrigerant that is delivered by the compressor. Considering the curves of the variable-speed system at the different loads, the largest cooling effect is obtained when the highest load was applied. Since the compressor had a larger load against which it had to work in order to maintain the "room" at the desired temperature, thus more refrigerant had to be delivered by the compressor. With the same argument the 1.4 kW load resulted in the lowest cooling capacity.

Grech's (2008) scaled trend also follows the same concept *i.e.* the cooling capacity decreases as the condensing temperature increases. This shows that the results of Grech's and those obtained from this study are in agreement. Additionally, the cooling capacity drop with condenser temperature rise for R 410 compared favourably to that given by Motta et al. (2000).

A comparison between the refrigerant and water cooling capacities was performed. Both show a decrease in cooling capacity as the refrigerant condenser out temperature is increased, thus it was concluded that a good energy balance was achieved between the refrigerant side and water side of the system. However there was a difference in magnitude between the refrigerant and water cooling capacity and this anomaly was attributed to the large amount of condensation that resulted on the outside of the evaporator heat exchanger. Additionally, the 1.4 kW, 2.0 kW and 2.7 kW trend lines should ideally have been horizontal representing the fixed loads to which the system is subjected. This would have indicated that no losses by convection were present during experimentation. It must also be pointed out that the losses for the case when 2.7 kW load was applied are much greater than for the other loads, since the change in temperature between the water temperature in the tank due to the heat source (heaters) and ambient conditions was larger.

The uncertainty analysis showed that the error associated with the volume measurement contributed the most in the final uncertainty value compared to the error in time measurement which were used in the water flow rate calibration. The error in temperature measurement was constant and determined by the grade of thermocouple wire used.

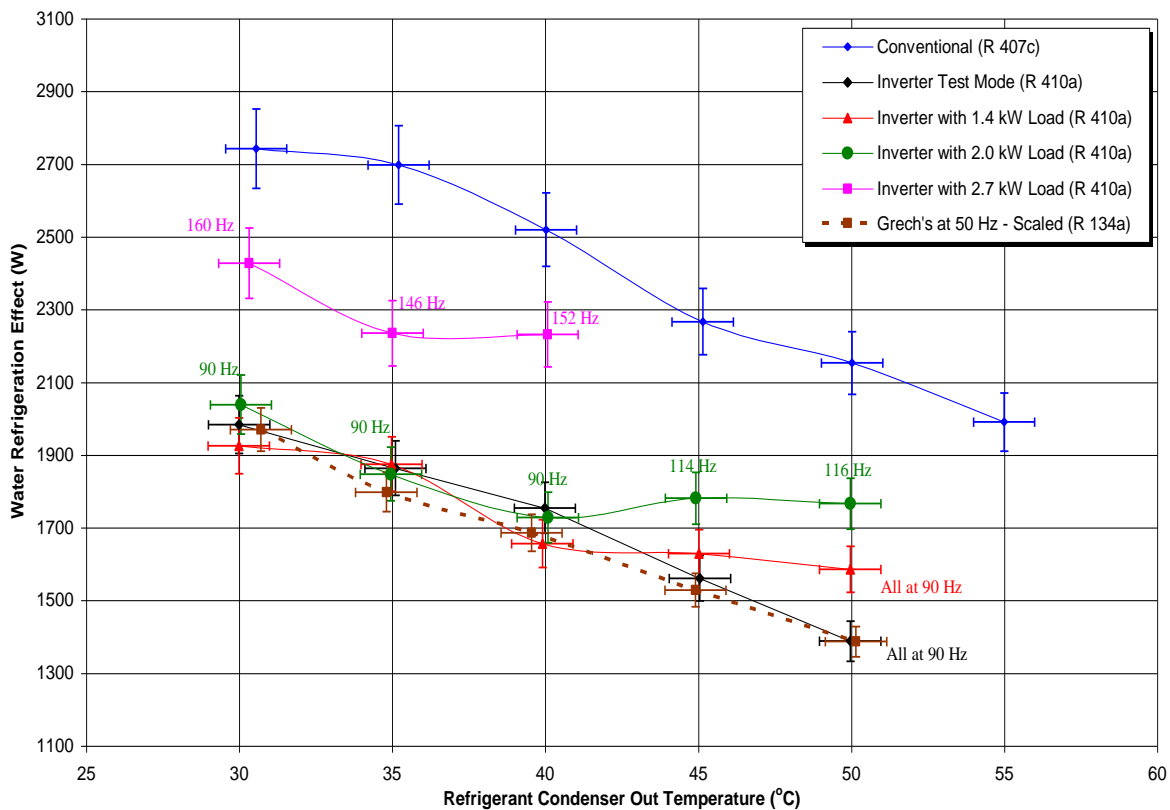


Fig. 2: Variation of water cooling capacity with refrigerant condenser out temperature.

4. Coefficient of Performance, COP

The trend of the electrical COP shown in Fig. 3 indicates that the electrical COP for all experiments performed worsens as the condensing temperature increases. From the figure it can be noted that the electrical COP of the conventional system is the lowest. This is mainly attributed to the large electrical power input that the conventional system requires all the time. It should be noted that the COP is dependent on the cooling capacity and hence its expected that the COP falls just like the cooling capacity does.

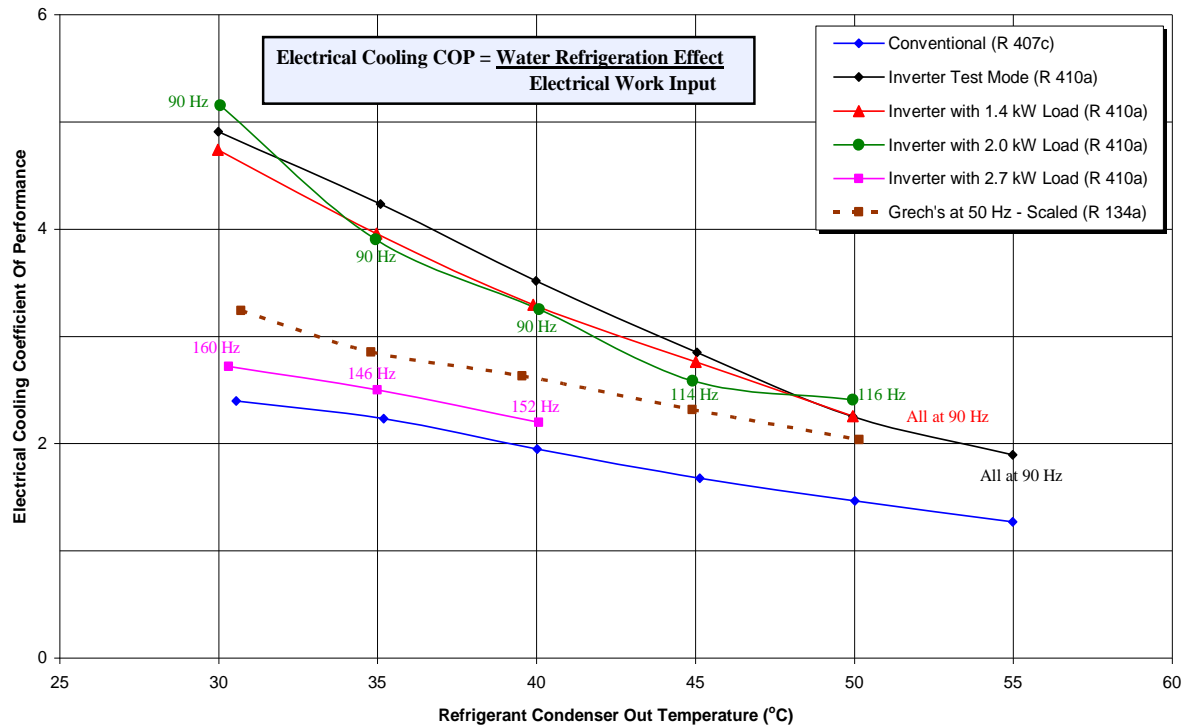


Fig. 3: Variation of electrical COP with refrigerant condenser out temperature.

5. Conclusions

The COP's from the experiments showed that larger COP's are obtained at lower condenser out temperatures. This is as expected as the reverse Carnot COP is higher for smaller temperature differences between the inside (evaporator) and outside (condenser) temperatures. This finding is also in agreement with observations by Motta et al. (2000). A comparative calculation based on the measured COP's for the off-the-shelf fixed-speed unit vs the off-the-shelf variable speed unit, at 20°C room temperature and an outside temperature of 35°C, and assuming the user switches on the air conditioner for 6 hours daily for an entire summer month, showed that a 30% reduction in electricity consumption by an inverter air conditioner is indeed a good ball park figure.

References

- Fenech, G. (2009) Experimental analysis of a fixed and variable speed air conditioning system, B.Eng. Dissertation, University of Malta, Malta.
- Grech, N. (2008) Investigation on variable speed operation of air conditioning, B.Eng. Dissertation, University of Malta, Malta.
- Grech, N & Farrugia, M. (2012) Experimental investigation on variable speed operation of air conditioning, In: Proc. 9th International Conference on Heat Transfer, Fluid Mechanics and Thermodynamics, Malta.
- Motta, S. F. Y. & Domanski, P. A. (2000) Performance of R-22 and its alternatives working at high outdoor temperatures, In: Proc. National Institute of Standards and Technology, pp. 47-54.
- Zubair, S., Bahel, V. & Arshad, M. (1989) Capacity control of air-conditioning systems by power inverters, Energy, Vol. 14, No. 3, pp. 41-151.

COMPARISON OF PROPELLER ANALYSIS METHODS AND EXPERIMENTAL DATA

J. Filipický*, V. Štorch**

Abstract: *An analysis of a propeller of known geometry was carried out using three various methods: vortex theory, vortex theory with lifting line correction (VT+LL) and a 3D panel method. Analysis results were compared with experimental data measured in a wind tunnel that was built for the purpose of propeller testing. The comparison indicates that the VT+LL method offers the best propeller efficiency prediction of the presented methods, although the 3D panel method has been used in a simplified way and will be further improved. The ambition of the work presented is to develop and validate a simple and reliable tool for propeller optimization.*

Keywords: Propeller, Vortex theory, 3D panel method.

1. Introduction

Vast expansion of powerful electrical propulsion units for UAVs and light sport crafts initiated a demand for propellers optimized for the new working conditions. Department of Fluid Mechanics and Thermodynamics of CTU in Prague is subsequently working on the development and validation of tools that can be reliably used for optimization of propellers and for their analysis. Three analysis methods are presented in this paper – vortex theory, vortex theory with lifting-line correction (VT+LL) and a 3D panel method. These methods have been used to analyse a 0.5 m in diameter propeller of known geometry and the results have been compared with experimental data measured in a wind tunnel that was built for the purpose of propeller testing.

2. Experiment

An open return wind tunnel with a 1.2 m circular test section and 150 kW of power was built by the Department in Letnany, Prague. The test section was equipped with custom made aerodynamic scales for torque and thrust measurement as well as devices for the measurement of RPM and power drawn by the electric motor powering the propeller. The tested propeller was designed by the authors using the vortex theory and manufactured based on 3D data in STL format. The geometry of the propeller was known at the entry to its manufacturing process and has been assumed to be made sufficiently geometrically precise without further check. The propeller's performance was measured for the RPM range of 600-6000 r/min and wind tunnel velocity range of 15-30 m/s. Finite size of the test section was taken in account by corrections according to Brandt (2011). The experimental data contain quite heavy scatter that is believed to be caused mostly by mechanical vibrations of the tested propulsion. Since insufficient resolution of the experiment did not reveal any dependency of the propeller's performance on Reynolds number and Mach number all further computations were carried out for constant RPM of 6000 r/min.

3. Vortex Theory

The vortex theory was introduced in 1912 by N. Y. Zhukovsky and until today remains a useful tool for the design and analysis of propellers (well covered by Alexandrov (1954)). The vortex theory substitutes

* Ing. Jakub Filipický: Department of Fluid Mechanics and Thermodynamics, Czech Technical University in Prague, Technická 4; 166 07, Prague; CZ, jakub.filipicky@fs.cvut.cz

** Ing. Vít Štorch: Department of Fluid Mechanics and Thermodynamics, Czech Technical University in Prague, Technická 4; 166 07, Prague; CZ, vit.storch@fs.cvut.cz

the propeller impact on the flow by a rigid vortex system that consists of helicoidal vortices blending into cylindrical vortex sheets as it supposes an infinite number of blades. The theory allows to easily compute the induced velocities at the propeller plane for a given circulation distribution. A sufficient propeller description that (along with the operating conditions) defines the vortex structure consists of one dimensional geometrical prescriptions for twist and chord length along blade radius and two dimensional airfoil data. In the approach described in this paper the airfoil data were obtained by M. Drela's Xfoil with a viscous and compressible computational model.

The vortex theory generally best describes propellers with small loading, for which the wake contraction downstream is low and the rigid cylindrical vortex structure gives a sufficient approximation. Another limiting aspect of the vortex theory is that it lacks interference between particular cylindrical vortices, as if each blade section acted independent on each other, which also means that no tip loss can be taken in account. This fact is very limiting for the optimization of propellers as it does not allow to compute the optimum circulation distribution along radius of the blade. To deal with this issue, the lifting line theory has been combined with the vortex theory. The lifting line theory describes the downwash distribution of a lifting line constructed by a system of horseshoe vortices and has been derived for the description of aircraft wing loading (described by McBain, 2012). Even though its assumptions of the vortex structure do not correspond to those of cylindrical vortices of the vortex theory, it has been proposed by the authors to offer a rough and simple way to overcome some of the issues of the vortex theory. The downwash computed by the lifting line theory is then simply added to axial velocity calculated by the vortex theory. Zero circulation condition has been prescribed at the blade's tip to accommodate for the tip losses.

4. Panel Method

Another useful tool for computing propeller aerodynamic properties is the panel method. The panel method solves Laplace's equation for potential flow. As a boundary condition, zero normal flow through blade surface discretized by panels is prescribed together with free stream velocity.

The implemented algorithm is a low order panel method using constant singularity distribution over each panel. The structured mesh is formed by quadrilateral panels. Potential doublet (dipole) was chosen as a singularity type for each panel. The velocity perturbation formulation of the panel method was selected instead of the more common potential perturbation formulation. This allows for easier velocity field calculations, especially away from the surface, while potential values are not immediately available. The basic concept of the different modifications of panel method is well covered in the book of Katz and Plotkin (2001). As was theoretically proven by Hess (1972), quadrilateral flat panel with constant doublet distribution is equivalent to a vortex ring made of vortex filament segments placed at the panel edges. The constant strength doublet panels are therefore represented by vortex rings, which is an equivalent substitution.

Proper lifting flow is realised using the Kutta condition. The Kutta condition in the form of zero circulation on the blade trailing edge is satisfied by adding wake panels to the trailing edge with such circulation to cancel the trailing edge circulation. The wake panels are of the same type as blade surface panels. For quasi-steady flow (i.e. when the propeller is maintaining constant rotation rate and forward velocity) all the wake panels shed by a pair of trailing edge panels maintain constant circulation. Practical realization of infinite free form wake is not possible, therefore the wake length is chosen as a compromise between precision and computation time.

The shape of the wake is initialized as a regular helical surface, which already gives satisfying results. An original iterative free wake modeling algorithm was implemented to align the wake panels with local velocity field (i.e create force free wake). The wake panel nodes are shifted according to the local velocity to satisfy the force free condition. This results in a slight change in circulation distribution on the blade surface, which together with a different wake panel position changes the induced velocity at each wake panel. The procedure is repeated until the wake is fully or at least reasonably well aligned with the flow.

The structured surface mesh is derived from the same data used for CNC machining of the propeller molds. The data consist of a set of equidistant propeller sections - airfoils. Since the implemented panel method is sensitive to meshing irregularities, especially sudden changes in paneling density and high aspect ratios of panels, it was necessary to interpolate the provided data using splines in order to create

proper mesh with arbitrary number of panels. The geometry of one blade is rotated to obtain the second blade so the effects of blade interactions are accounted for.

Convergence and sensitivity studies were performed in order to verify performance of the algorithms. In mesh density sensitivity study the result showed that the value of thrust was reasonably converged for 750 panels, while the value of shaft power (due to induced drag) was showing slight decreasing tendency even with 3400 panels per blade. This is in accordance with expectations that numeric integration of pressure over the surface estimates induced drag poorly. For more accurate results, the velocity field evaluation in the Trefftz plane as described by Katz and Plotkin (2001) would be necessary. Studying the effects of wake length showed that wake extending to at least one diameter distance behind propeller is sufficient and further increase in length has negligible effects on the solution.

The panel method has some advantages over simpler models. The method fully considers the actual blade geometry and provides results even for highly skewed and swept blades. It allows obtaining the velocity information throughout the whole domain, provides pressure distribution on the blade surface and is a great tool for simulating wake effects. Its advantages of simulating multi body interactions are especially useful in multiblade propeller designs. After some modification to accommodate the unsteady case, an off-axis free stream velocity may be defined to simulate aircraft flying in a side slip or a multicopter forward flight. On the other hand the panel method fails in predicting lift around stall conditions and without incorporating coupled viscous boundary layer model it will always underestimate the drag forces.

5. Data Comparison

Both experimental and computed thrust and shaft power were evaluated in dimensionless forms as thrust and power coefficients (c_t and c_p respectively) and plotted against dimensionless velocity (λ) related to the advance ratio:

$$c_t = \frac{T}{\rho n_s^2 D^4} \quad (1)$$

$$c_p = \frac{P}{\rho n_s^3 D^5} \quad (2)$$

$$\lambda = \frac{V_0}{\pi n_s D} = \frac{J}{\pi} \quad (3)$$

Propeller's efficiency is then defined as:

$$\eta = \frac{c_t}{c_p} \lambda \pi \quad (4)$$

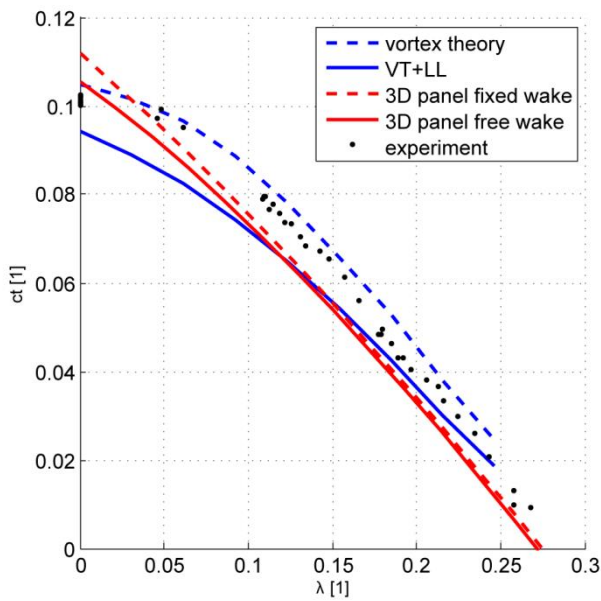


Fig. 1: Comparison of thrust coefficient.

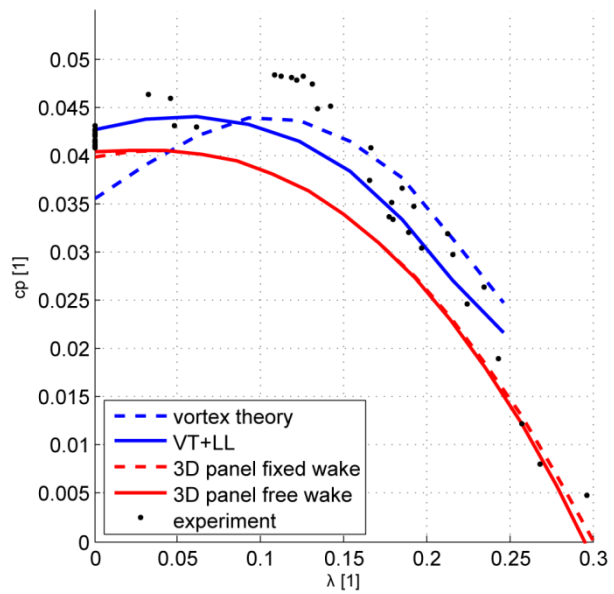


Fig. 2: Comparison of power coefficient.

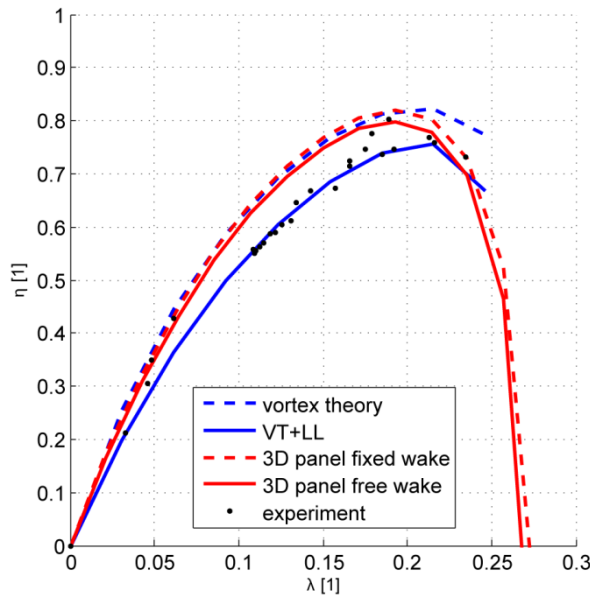


Fig. 3: Comparison of efficiency.

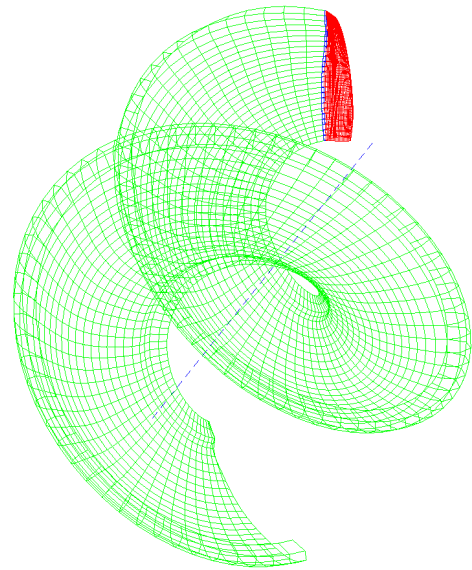


Fig. 4: 3D panel method – blade and free wake.

6. Conclusion

Three methods for propeller analysis were implemented and used to compute the performance of a propeller with a known geometry. An experiment has been carried out to provide experimental data for comparison. The thrust of the propeller was sufficiently predicted by all three methods. Even though the experimental data for shaft power are quite scattered it is clear that the vortex theory gives too optimistic results near static operation. VT+LL method gives very similar results for power as the 3D panel method, the curves are only offset from each other. The authors believe that the reason is the inviscid flow treatment of the 3D panel method. The propeller efficiency is best predicted by the VT+LL method. The Department of Fluid Mechanics and Thermodynamics will put additional effort to implement more sophisticated methods for analysis and optimization of propellers. The experimental facility is planned to be equipped with new measurement devices in the near future to allow for more reliable validation of computational models.

References

- Alexandrov, V. L. (1954) Aircraft Propellers. Státní nakladatelství technické literatury, Prague, pp. 193-207 (in Czech).
- Brandt, J. B. & Selig, M. S. (2011) Propeller Performance Data at Low Reynolds Numbers, 49th AIAA Aerospace Sciences Meeting, Orlando, FL. pp. 7-9.
- Deperrois, A. (2013) XFLR5 v6.09.06 [software] available at <http://www.xflr5.com>.
- Hess, J. L. (1972) Calculation of Potential Flow About Arbitrary Three-Dimensional Lifting Bodies, Final Technical Report MDC J5679-01, McDonnell Douglas, Long Beach, California.
- Katz, J. & Plotkin, A. (2001) Low speed aerodynamics. Cambridge, UK New York: Cambridge University Press. pp. 244-258.
- McBain, G. D. (2012) Theory of Lift. . Hoboken, NJ: Wiley, pp. 169-173.
- Technical Report MDC J5679-01, McDonnell Douglas, Long Beach, California.

BLAST PERFORMANCE OF FRC SPECIMENS WITH STEEL FIBERS OF LOW DUCTILITY

M. Foglar^{*}, M. Kovář^{**}

Abstract: Due to improved ductility, fibre-reinforced concrete (FRC) shows better performance under blast and impact loading compared to conventionally reinforced concrete. Also higher concrete strength shows better blast performance. The full scale blast tests of FRC and reinforced concrete specimens were performed in cooperation with the Czech Army corps in the military training area Boletice. The tests were performed using real scale reinforced concrete precast slabs (6x1.5x0.3m) with varying fiber content, fiber type, fiber strength and concrete strength class and 25 kg of TNT charges placed in distance from the slab for better simulation of real in-situ conditions. The paper presents conclusions from three sets of tests from years 2010, 2011 and 2013: eleven specimens were tested in total. Two specimens of different concrete strength were tested as reinforced concrete specimens to provide comparison to the nine FRC specimens of different fiber content (0.5% and 1%): polypropylen fibers (length 54 mm, strength of 600 MPa) and steel fibers (low ductility, 25 mm long, strength 400 MPa). This paper continues the contributions from years 2011 and 2012 and shows the results of the experiments from year 2013.

Keywords: Blast loading, Fiber reinforced concrete, Spalling of concrete subjected to blast loading.

1. Introduction

Due to improved ductility, fibre-reinforced concrete (FRC) shows better performance under blast and impact loading compared to conventionally reinforced concrete (Foglar & Kovar, 2013).

The experiments from year 2013 determine blast performance of FRC with low strength and low ductility steel fibers (strength 400 MPa).

This paper continues results presented in (Foglar et al., 2011) and (Foglar & Kovar, 2012)

2. Specimens and Materials

Dimensions of the specimens were designed in real scale of a small span bridge as concrete slabs, 6 m long, 1.5 m wide and 0.3 m thick.

The six specimens were tested in the year 2013, where three of them were made of C30/37 grade concrete ($f_{c,cyl} = 30$ MPa) (specimen No. 8, 9 and 10), three of C55/67 grade concrete ($f_{c,cyl} = 55$ MPa) (No. 6, 7 and 11). Steel fibers (FE) 25 mm long with strength 400 MPa and polypropylene (PP) 54mm long synthetic fibers with strength 600 MPa were used. The fiber dosage was following: specimen No. 6 80 kg/m³ FE fibers, No. 7 40 kg/m³ FE + 4.5 kg/m³ PP fibers, No.8 40 kg/m³ FE + 4.5 kg/m³ PP fibers, No.9 40 kg/m³ FE fibers, No. 10 80 kg/m³ FE fibers and No.11 40 kg/m³ FE fibers. The dosage of the fibers was kept low as it can be achieved on-site.

The layout of the experiment was practically the same as experiments from years 2010 and 2011.

* Ing. Marek Foglar, PhD.: Department of concrete and masonry structures, Czech Technical University, Thákurova 7; 166 29, Prague; CZ, marek.foglar@fsv.cvut.cz

** Ing. Martin Kovář: Department of concrete and masonry structures, Czech Technical University, Thákurova 7; 166 29, Prague; CZ, martin.kovar@fsv.cvut.cz

3. Results of the Experiments

The experiments were focused on the effect of different kinds of fibers, concrete compressive strength and its combination on blast performance of concrete. By means of performance, the dimensions of puncture and spalling of concrete is understood. The differences in puncture and spalling of concrete on the soffit of the slabs can be found in Tab. 1. In this section, the findings presented in Tab. 1 are described in detail.

The concrete of all specimens were tested for compressive strength. The results of probe cubes can be seen in Tab. 1.

The specimens tested in the years 2011 and 2012 are marked by “*”.

Tab. 1: The results of the experiments.

Specimen No.	1*	2*	3*	4*	5*	6	7	8	9	10	11
Concrete	C30/37	C30/37	C55/67	C55/67	C30/37	C55/67	C55/67	C30/37	C30/37	C30/37	C55/67
Concrete strength (cube)	49.9 MPa	41.8 MPa	80.0 MPa	82.5 MPa	41.9 MPa	65.0 MPa	58.3 MPa	45.0 MPa	48.0 MPa	46.5 MPa	65.7 MPa
Fibers	-	4.5 kg/m ³	-	4.5 kg/m ³	9.0 kg/m ³	80 kg/m ³	40 + 4.5 kg/m ³	40 + 4.5 kg/m ³	40 kg/m ³	80 kg/m ³	40 kg/m ³
Puncture – top surface	0.43 m ²	0.26 m ²	0.02 m ²	-	-	0.31 m ²	0.30 m ²	0.30 m ²	1.02 m ²	0.36 m ²	0.36 m ²
Concrete spalling (soffit) - < concrete cover	2.35 m ²	1.89 m ²	1.51 m ²	0.73 m ²	0.61 m ²	1.77 m ²	1.93 m ²	1.72 m ²	2.39 m ²	1.96 m ²	2.13 m ²
Concrete spalling (soffit) - > concrete cover	1.71 m ²	1.09 m ²	1.2 m ²	0.44 m ²	0.37 m ²	1.45 m ²	1.63 m ²	1.40 m ²	2.11 m ²	1.41 m ²	1.79 m ²
Concrete spalling (top surface) - < concrete cover	0.43 m ²	0.26 m ²	0.89 m ²	0.68 m ²	0.66 m ²	0.83 m ²	0.67 m ²	0.77 m ²	1.30 m ²	0.78 m ²	0.87 m ²
Concrete spalling (top surface) - > concrete cover	0.43 m ²	0.26 m ²	0.29 m ²	0	0.08 m ²	0.77 m ²	0.63 m ²	0.75 m ²	1.21 m ²	0.70 m ²	0.81 m ²
Concrete spalling (left side) - < concrete cover	0.52 m ²	0.05 m ²	0.08 m ²	0	0	0.04 m ²	0.04 m ²	0	0.23 m ²	0.06 m ²	0.06 m ²
Concrete spalling (left side) - > concrete cover	0.35 m ²	0	0.02 m ²	0	0	0.04 m ²	0.09 m ²	0	0.37 m ²	0	0.20 m ²
Concrete spalling (right side) - < concrete cover	0.34 m ²	0.16 m ²	0.08 m ²	0	0	0.07 m ²	0	0	0.24 m ²	0.11 m ²	0.06 m ²
Concrete spalling (right side) - > concrete cover	0.23 m ²	0.11 m ²	0.02 m ²	0	0	0.11 m ²	0.05 m ²	0.05 m ²	0.30 m ²	0.17 m ²	0.14 m ²
Volume of crushed concrete	0.23m ³	0.15m ³	0.20 m ³	0.05 m ³	0.06 m ³	0.20 m ³	0.25 m ³	0.26 m ³	0.45 m ³	0.24 m ³	0.27 m ³
Permanent deflection	0.31 m	0.37 m	0.28 m	0.30 m	0.26 m	0.31 m	0.30 m	0.45 m	-	0.45 m	0.32 m

The specimen No. 1 is determined as a reference specimen.

The specimen No. 6 was the one less damaged. The area of the puncture is 0.31 m^2 , volume 0.09 m^3 , which represents 3.4% of the total volume of the specimen. Total volume of the damaged concrete (puncture + spalling) is 0.20 m^3 , which represents 7.4% of the total volume of the specimen. The area of the puncture was reduced by 28% in comparison to specimen No. 1, the total volume of the damaged concrete was reduced by 13% in comparison to specimen No. 1. The damage of the left side of specimen No. 6 was reduced by more than 80%, the damage of the right side was reduced by more than 50%. The deflection was 310 mm. The shape of the deflection was similar to deflection from point loading in the mid-span of the specimen. The deflection was the same in comparison to specimen No. 1.

The specimen No. 7 was approximately equally damaged. The area of the puncture is 0.30 m^2 , volume 0.09 m^3 , which represents 3.3% of the total volume of the specimen. Total volume of the damaged concrete (puncture + spalling) is 0.25 m^3 , which represents 9.3% of the total volume of the specimen. The area of the puncture was reduced by 31% in comparison to specimen No. 1, total volume of damaged concrete was increased by 9% in comparison to specimen No. 1. The damage to the sides was reduced by 85%. The deflection was 300 mm. The shape of the deflection was similar to deflection from point loading in the mid-span of the specimen. The deflection was reduced by 3% in comparison to specimen No. 1.

The specimen No. 8 was approximately equally damaged. The area of the puncture is 0.30 m^2 , volume 0.09 m^3 , which represents 3.3% of the total volume of the specimen. Total volume of the damaged concrete (puncture + spalling) is 0.26 m^3 , which represents 9.6% of the total volume of the specimen. The area of the puncture was reduced by 31% in comparison to specimen No. 1, total volume of damaged concrete was increased by 10% in comparison to specimen No. 1. The damage to the sides was completely reduced by 95%. The deflection was 450 mm. The shape of deflection was similar to deflection from point loading in the mid-span of the specimen. The deflection was increased by 45% in comparison to specimen No. 1.

The specimen No. 9 did not sustain the loading and collapsed. The specimen No. 9 after blast can be seen in Fig. 1. The area of the puncture is 1.02 m^2 , volume 0.31 m^3 , which represents 11.3% of the total volume of the specimen. Total volume of the damaged concrete (puncture + spalling) is 0.45 m^3 , which represents 16.7% of the total volume of the specimen. The area of puncture was increased by 131% in comparison to specimen No. 1, total volume of damaged concrete was increased by 95% in comparison to specimen No. 1. The damage to the sides was 100% because area of puncture intervened over the whole width of slab. Cross-section of slab in mid-span was represented by steel reinforcement only.



Fig. 1: The specimen No. 9 after the blast.

The specimen No. 10 was approximately equally damaged as specimen No. 6. The area of the puncture is 0.36 m^2 , volume 0.11 m^3 , which represents 4% of the total volume of the specimen. Total volume of the damaged concrete (puncture + spalling) is 0.24 m^3 , which represents 8.9% of the total volume of the specimen. The area of puncture was reduced by 16% in comparison to specimen No. 1, total volume of damaged concrete was increased by 9% in comparison to specimen No. 1. The damage of the left side of specimen No. 10 was reduced by more than 85%, the damage of the right side was reduced by more than 75%. The deflection was 450 mm. The shape of deflection was similar to deflection from point loading in the mid-span of the specimen. The deflection was increased by 45% in comparison to specimen No. 1.

The specimen No. 11 was approximately equally damaged. The area of the puncture is 0.36 m^2 , volume 0.11 m^3 , which represents 4% of the total volume of the specimen. The total volume of the damaged concrete (puncture + spalling) is 0.27 m^3 , which represents 10% of the total volume of the specimen. The area of puncture was reduced by 16% in comparison to specimen No. 1, total volume of damaged concrete was increased by 17% in comparison to specimen No. 1. The damage of the left side of specimen No. 10 was reduced by more than 80%, the damage of the right side was reduced by more than 65%. The deflection was 320 mm. The shape of deflection was similar to deflection from point loading in the mid-span of the specimen. The deflection was increased by 3% in comparison to specimen No. 1.

4. Conclusions

The results from the experiments focused on determining blast performance of fiber reinforced concrete with low ductile steel fibers are described in this paper.

There is only slight positive effect of the added FE fibers on the damage of the specimens in comparison with reference specimen No. 1.

All specimens (No. 6–11) were more damaged at top surface than reference specimen No.1.

The extent of damage of all specimens (No. 6–11) was approximately the same as reference specimen No. 1.

The extent of damage slightly decreased with the increased fiber content, increased fiber strength and increased concrete strength. The combination of shear strength and fracture energy is the decisive material characteristics for determining the blast performance.

Acknowledgement

This paper was supported by the Czech Ministry of Interior project MVČR VG20132015114, the Grant Agency of the Czech Republic Grant Projects No. GAČR13-30441S.

References

- Foglar, M., Kovar, M. (2013) Conclusions from experimental testing of blast resistance of FRC and RC bridge decks, *International Journal of Impact Engineering*, Vol. 59, pp. 18-28, ISSN 0734-743X.
- Foglar, M., Sochorová, E., Křístek, V. (2011) Field tests of blast performance of reinforced concrete and fiber reinforced concrete specimens. In: *Proc. Inter. Conference Engineering Mechanics 2011* (V. Fuis ed), pp. 143-146. ISBN 978-80-87012-33-8.
- Foglar, M., Kovář, M. (2012) Blast performance of FRC composites. In: *Proc. Inter. Conference Engineering Mechanics 2012*. Prague: Institute of Theoretical and Applied Mechanics Academy of Sciences of the Czech Republic, 2012, pp. 269-279. ISBN 978-80-86246-39-0.

EXTERNAL AND INTERNAL FIXATORS FOR TREATMENT OF COMPLICATED FRACTURES IN TRAUMATOLOGY AND ORTHOPAEDICS

K. Frydryšek^{*}, L. Pleva^{**}, M. Pompach^{***}, O. Učeň^{****}, F. Fojtík[†], T. Kubín^{††},
G. Theisz^{†††}, L. Žilka^{††††}, Z. Poruba^{†††††}

Abstract: *In this paper, doctors want to draw attention to the possibilities of treatment of complicated fractures of limbs and pelvis. They present their own experiences with the treatment of these fractures by using various types of internal and external fixation. In this paper, engineers report about the new design, testing and numerical modelling of external and internal fixators invented at the VŠB - Technical University of Ostrava and at the Trauma Centre of The University Hospital in Ostrava and at the Pardubice Regional Hospital together with MEDIN a.s. company. These fixators are intended for the treatment of open, unstable, extraarticular or intraarticular and other types of complicated fractures in traumatology and orthopaedics for humans or animals limbs. The new design of external fixators is based on the development of Ilizarov and other techniques (i.e. shape and weight optimization based on composite materials, application of smart materials, nanotechnology, low x-ray absorption, antibacterial protection, patient's comfort, reduction in the duration of the surgical treatment, and cost). Similarly, the new intramedullary nail C-NAIL (i.e. an example of internal fixator) is intended for minimal-invasive fixation of intraarticular calcaneal fractures.*

Keywords: External and internal fixators, Traumatology, Design, Numerical modelling, Experiments, Calcaneal nail.

1. Introduction

Changes in lifestyle, wars in the world, increased age of population, accidents and development of endoprosthetics etc. are connected with increased occurrence of many types of unstable, opened, periprosthetic and other types of complicated fractures in recent years, see Figs. 1 and 2. There are descriptions of several possibilities of treatment of these fractures including their complications. Hence, the complicated fractures are an important therapeutical problem for their individual and specific character. Among the general risk factors we can include possible infects, osteoporosis, rheumatoid

* Assoc. Prof., M.Sc. Karel Frydryšek, PhD., ING-PAED IGIP: Department of Mechanics of Materials, Faculty of Mechanical Engineering, VŠB – Technical University of Ostrava, 17. listopadu 15/2172; 708 33 Ostrava; CZ, karel.frydrysek@vsb.cz

** Assoc. Prof., M.D. Leopold Pleva, PhD.: Trauma Centre, University Hospital in Ostrava, 17. listopadu 1790, 708 52 Ostrava, CZ, leopold.pleva@fno.cz

*** M.D. Martin Pompach: Department of Traumatology, Clinic of Surgery, Pardubice Regional Hospital, Kyjevská 44, 532 03 Pardubice, CZ

**** M.Sc. Oldřich Učeň, PhD.: Department of Production Machines and Design, Faculty of Mechanical Engineering, VŠB – Technical University of Ostrava, 17. listopadu 15/2172; 708 33 Ostrava; CZ, oldrich.ucen@vsb.cz

† M.Sc. František Fojtík, PhD.: Department of Mechanics of Materials, Faculty of Mechanical Engineering, VŠB – Technical University of Ostrava, 17. listopadu 15/2172; 708 33 Ostrava; CZ, frantisek.fojtik@vsb.cz

†† M.Sc. Tomáš Kubín, PhD.: Department of Production Machines and Design, Faculty of Mechanical Engineering, VŠB – Technical University of Ostrava, 17. listopadu 15/2172; 708 33 Ostrava; CZ, tomas.kubin@vsb.cz

††† M.Sc. Günther Theisz: Department of Mechanics of Materials, Faculty of Mechanical Engineering, VŠB – Technical University of Ostrava, 17. listopadu 15/2172; 708 33 Ostrava; CZ, gunther.theisz@vsb.cz

†††† M.Sc. Luboš Žilka, MEDIN, a.s., Vlachovická 619, 592 31 Nové Město na Moravě, Czech Republic, lubos.zilka@medin.cz

††††† M.Sc. Zdeněk Poruba, PhD.: Department of Mechanics, Faculty of Mechanical Engineering, VŠB – Technical University of Ostrava, 17. listopadu 15/2172; 708 33 Ostrava; CZ, zdenek.poruba@vsb.cz

arthritis, treatment with corticosteroids and naturally other diseases which may affect healing processes of patients. There is still continuing debate which treatment option is optimal for these patients. There is no consensus on the technique to be used but logically it must be minimally invasive to decrease mortality and morbidity. Stable osteosynthesis obtained by minimal invasive techniques assures more rapid fracture union. Therefore, treatment of fractures is a challenge for the surgeon, see for example Džupa et al. (2013), Pleva (1992), Seligson et al. (2012), Solomin et al. (2012), Stehlík et al. (2010) etc.

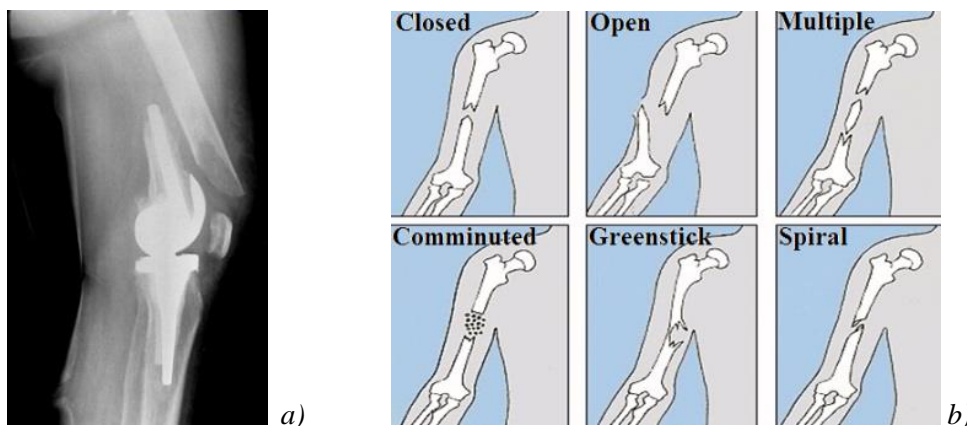


Fig. 1: a) X-ray Rorabeck type II fracture (periprosthetic) – lateral view; b) Musculoskeletal fractures.

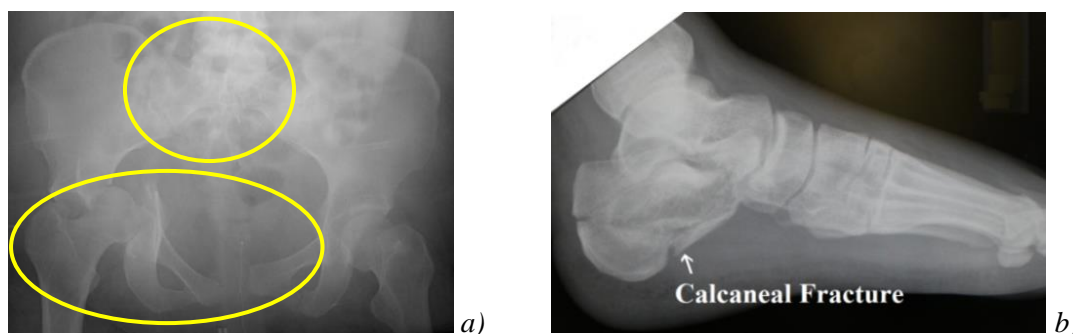


Fig. 2: a) X-ray of fracture of pelvis and its acetabulum (anteroposterior radiograph - transverse with posterior wall acetabular fracture), b) X-ray of a depressed calcaneal fracture.

Usually, there is no consensus on the surgical management of fractures (external fixation versus internal fixation etc.). However, this text is focused on the treatment of complicated fractures solved via external fixation (examples for limbs and pelvis, see Fig. 1 and 2a) and internal fixation (example for calcaneus, see Fig. 2b) and their engineering verification via numerical methods and laboratory testing. Hence, the authors report about their work, development and cooperation between the VŠB - Technical University of Ostrava, the Trauma Centre of The University Hospital in Ostrava, the Pardubice Regional Hospital and MEDIN a.s. company, for example see Frydrýšek et al. (2011, 2011a and 2013) and http (2014).

2. External Fixators

External fixators can be applied in traumatology, surgery and orthopaedics for treatments such as: open and unstable (complicated) fractures, limb lengthening, deformity correction, consequences of poliomyelitis, foot deformities, hip reconstructions, etc. Hence, external fixators can be used for treatment of humans and animals, for example see Fig. 3 (i.e. one story of a patient treatment in Ostrava), see Frydrýšek et al (2013).

In references Frydrýšek et al. (2011 and 2011a), the way for designing of a new external fixators which satisfy the new trends in medicine is presented (i.e. rtg. invisible of the outer parts of fixators, antibacterial protection, new materials and new design etc.).

Numerical modelling and laboratory experiments based on the previous skills, see references Frydrýšek et al. (2011, 2011a and 2013), as support for research and design, are very important parts of the solution, see Fig. 4 (i.e. applications of FEM and experiments – fixator for fractures of limbs) and Fig. 5 (i.e. applications of FEM – fixator for fractures of pelvis and its acetabulum).

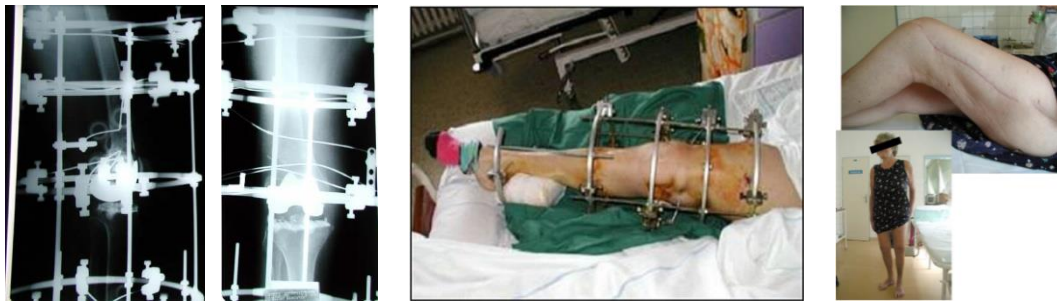


Fig. 3: Post-operative X-ray snapshot and a patient after the external fixation of periprosthetic fracture above the knee arthroplasty, see reference Frydryšek et al (2013).

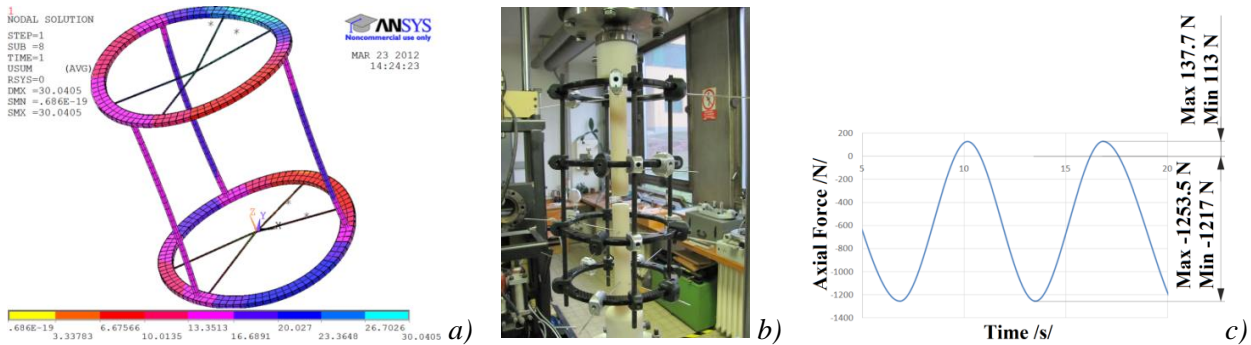


Fig. 4: External fixator for limbs: a) FEM – total displacements in the structure; b) Experiments in our laboratory; c) Quasi-static cyclic overloading of the fixator.

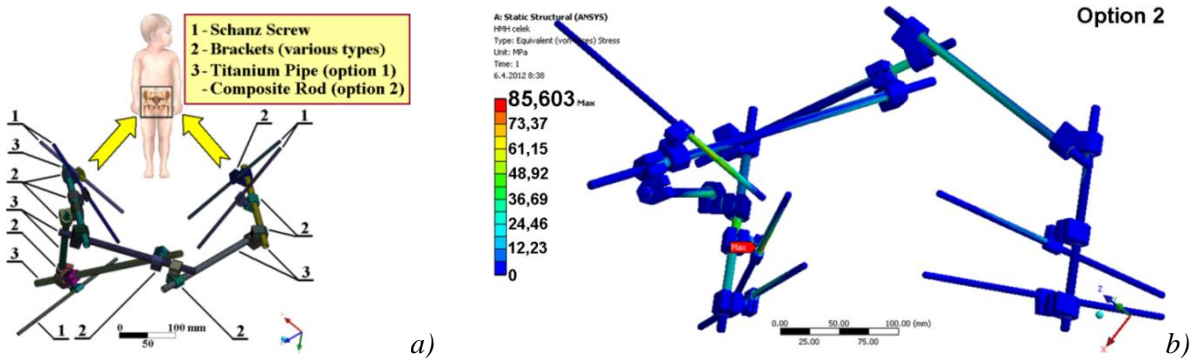


Fig. 5: External fixator for treatment of pelvis and its acetabulum: a) Design and application; b) FE modelling - equivalent stresses.

3. Internal Fixators

Internal fixation is an operation in orthopaedics and traumatology that involves the surgical implementation of implants for the purpose of repairing a bone. Usually, an internal fixator may be made of stainless steel or titanium. Types of internal fixators include bone screws and metal plates, pins, rods, Kirschner wires and intramedullary devices such as the Kuntscher nail and interlocking nail etc.

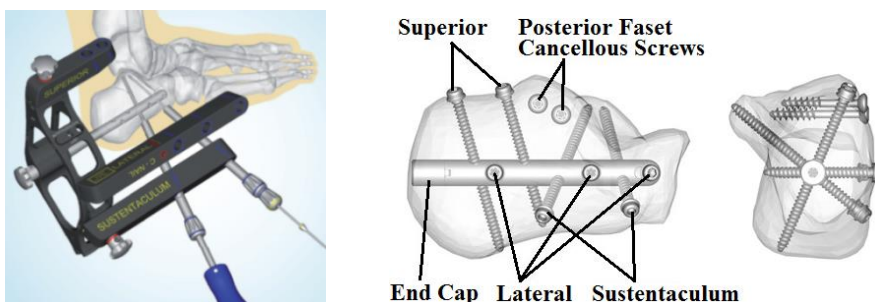


Fig. 6: C-NAIL and its application.

This chapter is focused mainly on the C-NAIL, see Fig. 6 and reference [http \(2014\)](http://www.c-nail.eu/), i.e. the intramedullary nail for minimal-invasive fixation of intraarticular calcaneal fractures. The principle is to stabilize with the nail the four to five main fragments of the fractured calcaneus in conjunction with up to seven interlocking screws and thus creating angular stable fixation. The maximum of stability is achieved by fixing the sustentacular fragment towards the nail with two interlocking screws guided by a very precise aiming device.

Numerical modelling for the C-NAIL rested in a broken calcaneus was performed, see Fig. 7 (i.e. applications of FEM – strength analyses).

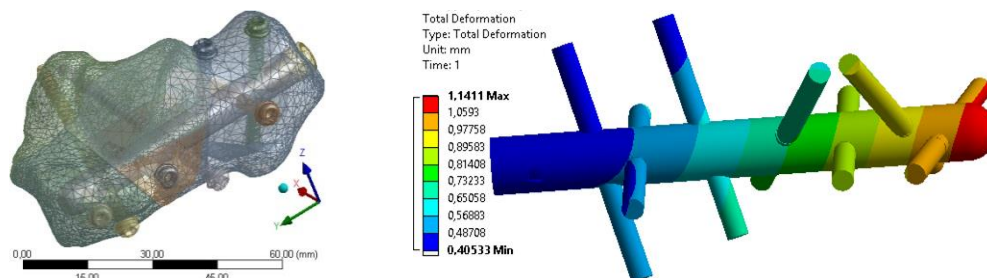


Fig. 7: C-NAIL (FE model of a broken calcaneus and acquired maximal displacement for dynamic overloading).

This is our first, but important, mention about our C-NAIL modelling. So far, in the world, there are not any numerical solutions (stress and displacement assessment etc.) for any type of intramedullary calcaneal nail.

4. Conclusion

According to the results and applications presented in this text (i.e. some examples of external and internal fixators), the verifications of these fixators are sufficient. Therefore, the fixators can be used for treatment of patients.

This is our first and original information about our C-NAIL modelling. Application of C-NAIL is a new and innovative trend in mini-invasive traumatology and orthopaedics. C-NAIL is a good alternative for older and typical treatments performed via calcaneal plating systems.

Acknowledgement

This work has been supported by Czech projects FR-TI3/818 and TA03010804.

References

- Džupa, V., Pavelka T., Taller, S. et al (2013) Treatment of Pelvic and Acetabular Fractures, Galén, Czech Republic, pp. 293, ISBN 978-80-7492-003-5, (in Czech).
- Frydrýšek, K., Jořenek, J., Učeň, O., Kubín, T., Žilka, L., Pleva, L. (2011) Design of external fixators used in traumatology and orthopaedics-treatment of fractures of pelvis and its acetabulum, J. Procedia Engineering, vol. 48, pp. 164-173.
- Frydrýšek, K., Košťál, P., Barabaszová, K., Kukutschová, J. (2011a) New ways for designing external fixators applied in treatment of open and unstable fractures, j. World Academy of Science, Engineering and Technology, vol. 76, pp. 697-702.
- Frydrýšek, K., Pleva, L., Učeň, O., Kubín, T., Šír, M., Madeja, R., Žilka, L. (2013) New External Fixators for Treatment of Complicated Periprosthetic Fractures, International Journal of Biology and Biomedical Engineering, Issue 2, Vol. 7, pp. 43-49.
- Pleva, L. (1992) External Fixation in Traumatology, Trauma Centre, University Hospital in Ostrava, Ostrava, Czech Republic, pp. 1-173, (in Czech).
- Seligson, D., Maufrey, C., Roberts, C. S et al (2012) External Fixation in Orthopedic Traumatology, ISBN 978-1-4471-2199-2, Springer-Verlag London Limited, 219 pp.
- Solomin, L. N. et al (2012) The Basic Principles of External Skeletal Fixation Using the Ilizarov and Other Devices, 2nd edition, ISBN 978-88-470-2618-6, Springer-Verlag Italia, 1593 pp.
- Stehlík, J., Štulík, J. (2010) Calcaneal Fracture, ISBN 9788072626595, Galén, pp. 1-107.
- <http://www.c-nail.eu/> (2014) web page of MEDIN, a.s. company, Czech Republic.

SHAPE DEVIATIONS ANALYSIS OF THE ALIGNED BARS

V. Fuis*

Abstract: This paper analyzes shape deviations of the bar surface, which was straightened in the straightening machine. Computational modelling of the straightening process is solved numerically using the finite element method (Skalka et al., 2014). The outer diameter of the bar is 20 mm and its length is 6 m. The original curvature of the bar had a curvature radius $R = 180$ m. The shape deviations were analysed using the algorithm that was developed within the framework of the stress state analysis performed in ceramic heads of total hip replacement (Fuis et al., 2009 and 2011).

Keywords: Oblique straightening machine, Finite element method, Shape deviations.

1. Introduction

Straightening of bars in the straightening machine is a technological standard way (Petruska et al., 2012). The principle of straightening is based on the passage of the bar through straightening rollers which alternately bend the bar. Computational modelling of straightening process is described in greater detail in the article (Skalka et al., 2014), including the setting of individual straightening rollers. A scheme of straightening is shown in Fig. 1 where the x -coordinate is given by the coordinate of bar axis. An analysis of dynamics and vibrations in the process of bar straightening are covered by the article (Lošák, 2014).

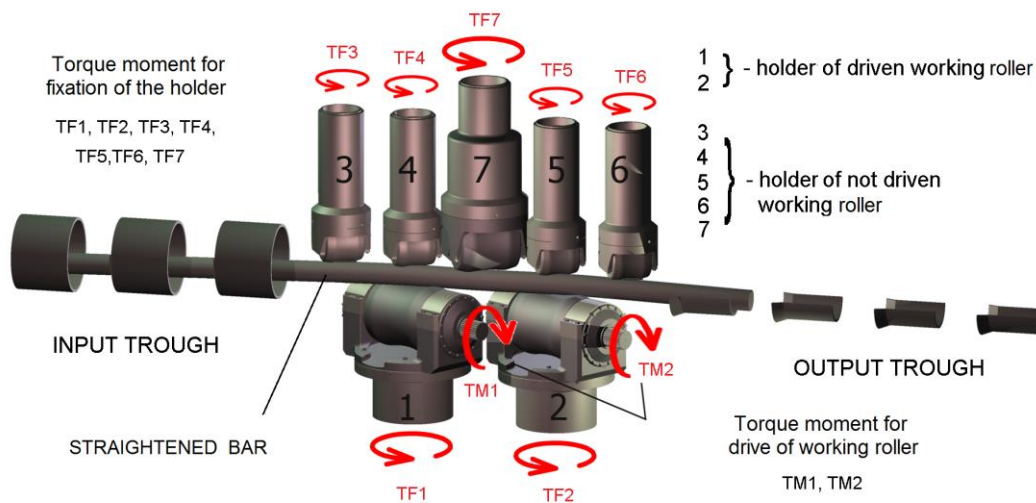


Fig. 1: Structure of oblique straightening machine (Skalka et al., 2014).

After the passage of curved bar (with model curvature $R = 180$ m and bar length of 6 m) through the straightening machine, it is possible to analyze both the macroscopic shape deviations from straightness (residual curvature) – Fig. 2, and also microshape deviations from a circular shape of the bar surface. These microshape deviations are caused by plasticization of bar surface layers. Fig. 3 shows the isosurfaces of von Mises equivalent stress in the straightened bar. It can be seen that on the surface there occur the regions with high values of stress (which acts only on the surface of the bar (under the surface are the value of the stresses low – Figs. 3 and 4); these regions are alternately repeated. High values of equivalent stress on the surface will also affect the final shape, which will not be circular any more, but microshape deviations will occur in it.

* Assoc. Prof. Ing. Vladimír Fuis, PhD.: Institute of Solid Mechanics, Mechatronics and Biomechanics, FME Brno University of Technology and Institute of Thermomechanics AS CR – branch Brno, Technická 2, 616 69 Brno, CZ fuis@fme.vutbr.cz

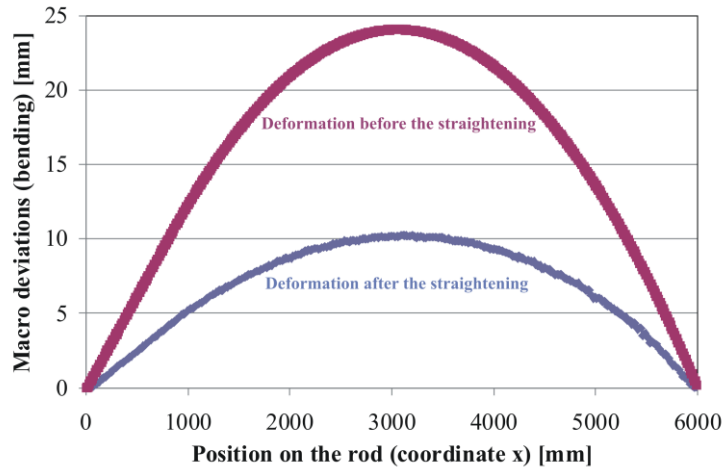


Fig. 2: Deformation of the bar before and after the straightening.

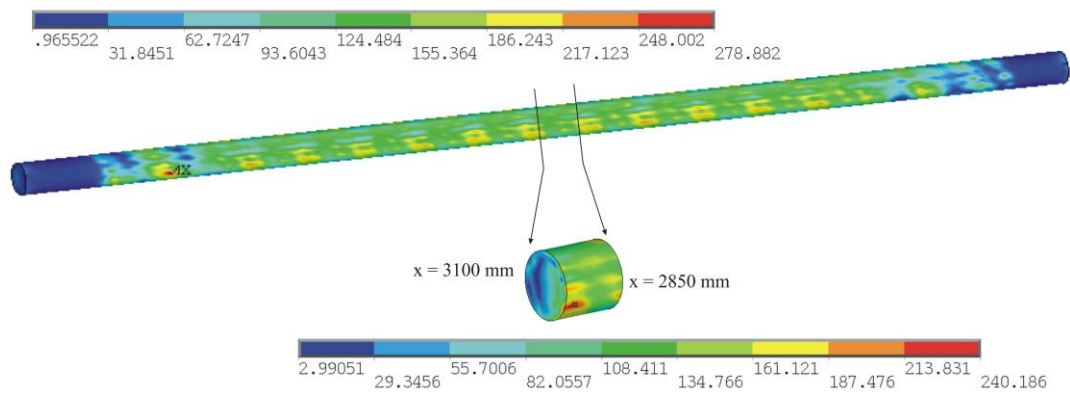


Fig. 3: Isosurface of Von Mises equivalent stress in the bar after straightening [MPa].

2. Methods

Microshape deviations on the bar will be analyzed by methodology that was developed for the analysis of the influence of shape deviations on the tapered surfaces of the head and stem of total hip replacement (Fuis et al., 2009 and 2011). In the first phase, a macroshape deviation of bar will be compared (deviation from straightness) before and after the passage through the straightener - Fig. 2. The maximum deviation before straightening was about 24 mm; after passing through the straightener, it was reduced to 10 mm.

In terms of microshape deviations we will focus on the centre of the bar, where between the coordinates x (2850 mm - 3100 mm) the values of equivalent stress on the bar surface are significantly changed (Fig. 3). Fig. 4 shows how a equivalent stress acts to the depth of the bar in the individual cross sections.

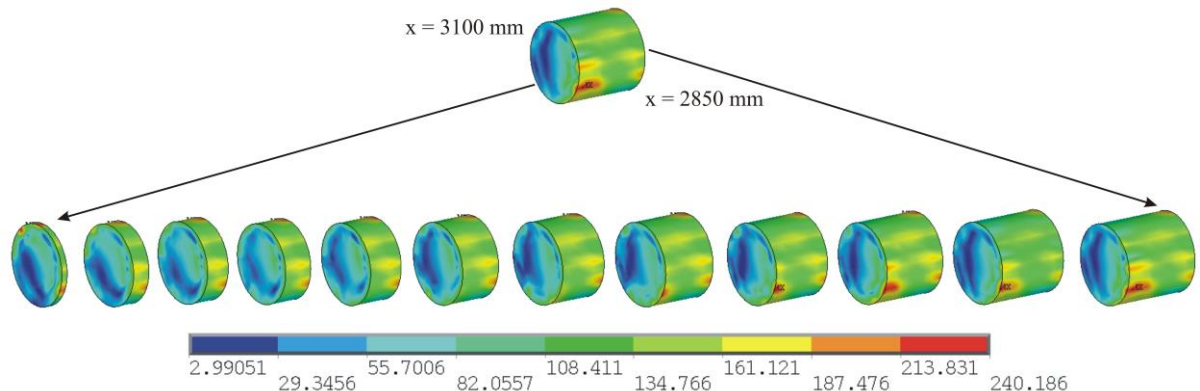


Fig. 4: Isosurface of Von Mises equivalent stress in the some sections of the bar after straightening [MPa].

3. Results and Discussions

Microshape deviations in the individual cross sections are shown in cylindrical coordinates (r and φ – Fig. 5) in order to compare them. These deviations are always quantified in the local coordinate system, which was newly created for each cross section (each x -coordinate). The reason is that after passing through the straightening machine, the bar is not straight (see Fig. 2) and thus it is not possible to use a global cylindrical coordinate system. The local cylindrical coordinate systems that were created from the nodes lying in the given plane show, however, deviations in the order of hundredths of degree (local axis z). This deviation is the most apparent in Fig. 5, where, in the given cross section, in addition to the radius, the value of axial displacement uz is also plotted (displacement in the direction perpendicular to the cross section and the extreme values uz are almost similar in absolute value). The deviation of normal (local axis z) causes the mean value of points of the outer surface of the bar (radius r in the Fig. 5) in the given cross section to oscillate circumferentially (along the angle φ – Fig. 5).

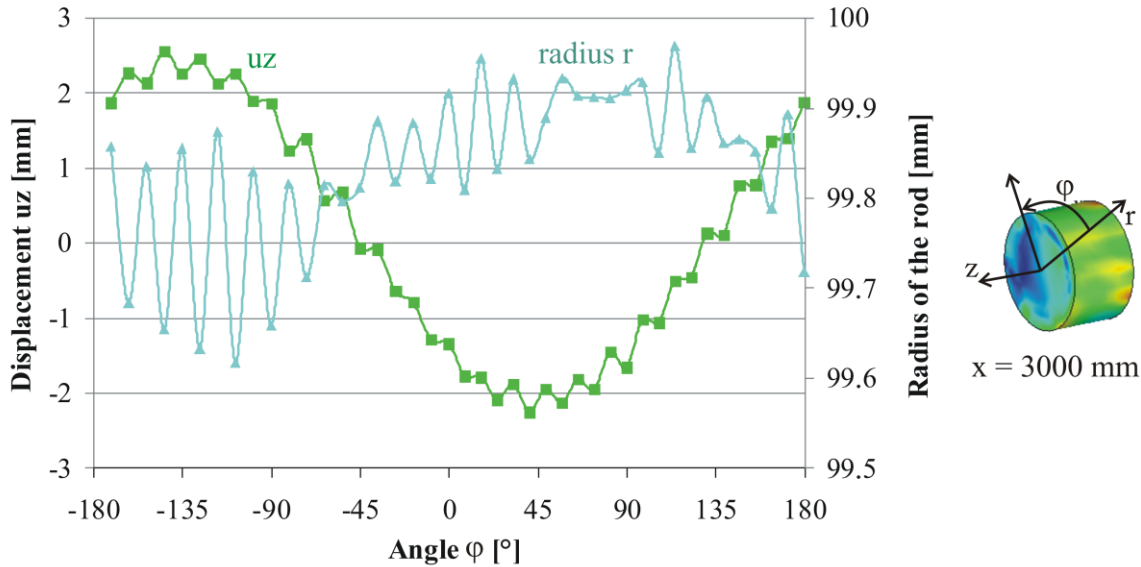


Fig. 5: Shape deviations (r and uz) of the bar's surface in the local coordinate system.

If the determined values of the radii are fitted with polynomial curve, we will obtain a curve that corresponds to the mean value of the radius – Fig. 6. If the local coordinate system is created exactly, this mean value of radius will be constant; however, this is not our case. Therefore, it is necessary to determine the value of the radius for a given angle φ as the distance from the mean value of radius - see Fig. 6. Thus we will obtain a course of radius value depending on the position (angle φ) for each cross section (in our case only for section $x = 3000 \text{ mm}$ – Fig. 7).

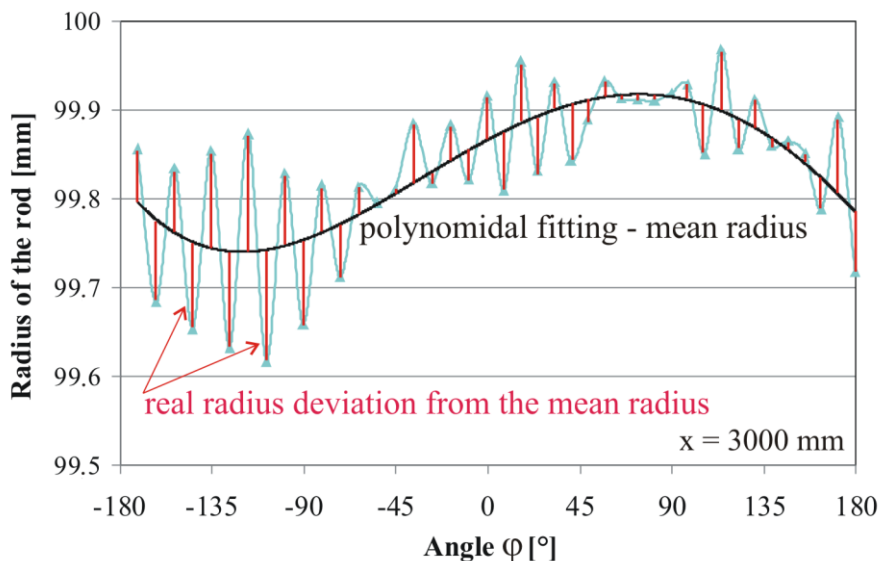


Fig. 6: Radius of the bar's surface in the local coordinate system and polynomial fitting.

Fig. 7 illustrates the high variability of the radius for different φ angles in the given cross section and a respective course of equivalent residual strains. The analysis of this figure shows that the radius of the bar in the given cross section can be found in a certain zone (zone width changes from -0.3 mm to 0.05 mm (minimal and maximal radius deviation – Fig. 7)) and it is oscillating a great deal, which may be caused by numerical calculation or by the vibrations of the bar during the straightening process. Moreover, no correlation has been proved between regions with high value of equivalent stress and the corresponding change in radius.

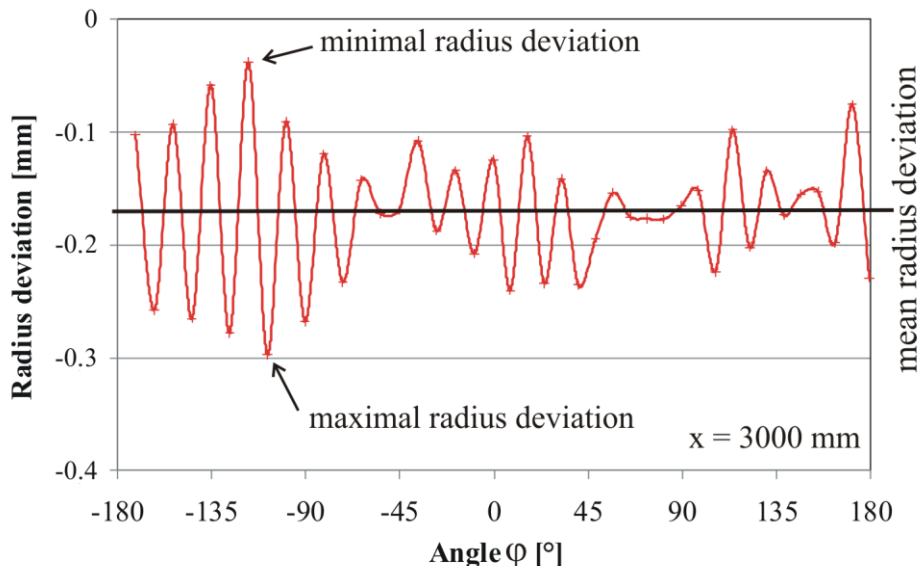


Fig. 7: Radius deviation around the cross section.

4. Conclusions

The performed analysis of reduced stress in the bar straightened in the straightener shows that the straightener was improperly set and this caused a non-uniform plasticization of the bar. The analysis of deviations of bar radius shows that it does not correspond to the reduced stress at the given location, which confirms the above conclusion.

Acknowledgement

This work was supported by Grant of Specific Research of Faculty of Mechanical Engineering – Brno University of Technology with the number FSI-S-14-2344.

References

- Skalka, P., Sobotka, J. (2014) Analysis of dynamic loading of bar straightening machine components. In: Proc. 20th Internat. Conference Engineering Mechanics, Svratka, Czech Republic, pp. 564-567.
- Lošák P. (2014) Identification of vibration causes based on spectrograms during the straightening process. In: Proc. 20th Internat. Conference Engineering Mechanics, Svratka, Czech Republic, pp. 368-371.
- Fuis, V., Koukal, M., Florian, Z. (2011) Shape Deviations of the Contact Areas of the Total Hip Replacement. In: Proc. 9th Inter. Conference on Mechatronics Location: Warsaw, Poland. Mechatronics: Recent Technological and Scientific Advances, pp. 203-212.
- Fuis, V. (2009) Tensile Stress Analysis of the Ceramic Head with Micro and Macro Shape Deviations of the Contact Areas. In: Proc. 8th Inter. Conference on Mechatronics, Luhacovice, Czech Republic, Recent Advances in Mechatronics: 2008-2009, pp. 425-430.
- Petruska, J., Navrat T., Sebek, F. (2012) A New Model for Fast Analysis of Leveling Process, In: Proc. 2nd Internat. Conference on Advanced Materials and Information Technology Processing (AMITP 2012), Taipei, Taiwan, Book Series: Advanced Materials Research, Vol. 586, pp. 389-393.

PROPOSITION OF CONSTITUTIVE MODEL FOR FIBRE-REINFORCED HYPERELASTIC MATERIALS

M. Gajewski*, S. Jemioło**

Abstract: *In the paper the class of relatively simple constitutive models of hyperelastic non-homogeneous composite materials with isotropic matrix reinforced with continuous fiber families is proposed. The model was formulated on the basis of strain energy additivity assumption. Proposed class of constitutive models reduce in approximation to the classical for linear theory models of fibrous composites, where full bounding between matrix and fibers is assumed. The strain energy potential for proposed model is a poly-convex function, what ensure existence of solution of boundary value problems for hyperelasticity and good numerical conditioning. Constitutive relationships expressed in objective incremental form are implemented in FORTRAN in user procedure UMAT of FEM system ABAQUS. The numerical tests were carried out to check correctness of the implementation, and two types of boundary value problems of tubes tension/compression tests are solved.*

Keywords: Anisotropy, Hyperelasticity, Fibre-reinforced materials, Constitutive models.

1. Introduction

Composite materials in the form of isotropic matrices reinforced with fibers are commonly used in technical applications because of their desirable mechanical properties. The main goal of fiber insertion into matrix is to obtain needed mechanical properties understood as desired stiffness and assumed strength. The fundamental condition to obtain planed mechanical properties of composite is a good coupling between components (in this case between fibers and matrix). And this assumption was a starting point several years ago for proposition of fiber composite theoretical model based on mixture theory, cf. Spencer (1972), Boehler (1987). Such models implemented in small deformation theory are very usefull in case of many engineering problems from geotechnical applications for geosynthetic grid modeling to aircraft skins modeling. The fundamental motivation for development of anisotropic hyperelastic constitutive models was and still is biomechanics and mechanics of woven materials. In case of biomechanics and soft tissue constitutive modeling, the application of large deformation theory is well-founded, cf. Bonet & Wood (1997). Unfortunately, in other mechanic disciplines the need for large deformation theory application is not always well understood. For example, geosynthetic grid becomes reinforcement for soil when soil deformation is large, when differences between configurations are significant. Then it follows that application of theory with nonlinear geometry is needed. On the other hand it is inadmissible in continuum mechanics to use so called “physically linear” constitutive models, because they are not fulfilling all basic requirements resulting from objectivity and energy conservation rules. The simplest theory in which all requirements are fulfilled is theory of hyperelastic materials, and a class of constitutive models for fiber reinforced materials considered herein is situated in group of anisotropic hyperelastic constitutive models (especially orthotropic and transversally isotropic hyperelastic materials, cf. Jemioło & Telega (2001)). The main goal of this paper is to extend previously presented constitutive model (Gajewski & Jemioło, 2007) in such a way that allows analysis of composites in which matrix is reinforced with many fiber families and its illustration on some non-trivial numerical examples.

* Marcin Gajewski, PhD. Eng.: The Institute of Building Engineering, Faculty of Civil Engineering, Warsaw University of Technology, Armii Ludowej 16; 00637, Warsaw; Poland, m.gajewski@il.pw.edu.pl

** Prof. Stanislaw Jemioło, PhD. D. Habil. Eng.: The Institute of Building Engineering, Faculty of Civil Engineering, Warsaw University of Technology, Armii Ludowej 16; 00637, Warsaw; Poland, s.jemioło@il.pw.edu.pl

2. Basic Assumptions and Constitutive Model of Anisotropic Hyperelasticity

Strain energy function (SEF) of hyperelastic material reinforced with several fiber families can be postulated in the following additive form:

$$\Psi = \left(1 - \sum_{n=1}^N p_n\right) \Psi_M + \sum_{n=1}^N p_n \Psi_{Rn}, \quad (1)$$

where Ψ_M is a strain energy function for matrix (SEFM), Ψ_{Rn} are elastic strain energy functions of fiber families (SEFR), and p_n stands for volume ratio of fibers in material volume unit. Matrix material is an isotropic material, for which SEF function is isotropic with respect to right deformation tensor $\mathbf{C} = \mathbf{F}^T \mathbf{F}$, and left deformation tensor $\mathbf{B} = \mathbf{F} \mathbf{F}^T$, where \mathbf{F} is so called deformation gradient tensor. The tensor \mathbf{F} has a positive determinant $J = \det \mathbf{F} > 0$, and symbol “T” in above relations stand for tensor transposition. According to the above assumption (isotropic function) the SEFM $\Psi_M = W(I_1, I_2, J)$ is a function of three non-reducing invariants of deformation tensor: $I_1 = \text{tr} \mathbf{C}$, $I_2 = \text{tr}(\text{cof} \mathbf{C})$ and $J = \det \mathbf{F} = \sqrt{\det \mathbf{C}}$. The SEFR function of n-th fiber family, which “works” in direction described with vector $\mathbf{m}_n(\mathbf{X})$, is approximated as:

$$\Psi_{Rn} = \frac{E_{Rn}}{4} (I_{4n} - 1)^2, \quad (2)$$

where $I_{4n} = \text{tr} \hat{\mathbf{M}}_n$. The $\hat{\mathbf{M}}_n$ tensors represent parametric tensors $\mathbf{M}_n = \mathbf{m}_n \otimes \mathbf{m}_n$ in actual configuration (e.g. $\hat{\mathbf{M}}_n = \mathbf{F} \mathbf{M}_n \mathbf{F}^T$). In (2) the E_{Rn} parameter have an interpretation of Young modulus of n-th fiber family. In this paper we are considering a special case of SEFM function, so called Ciarlet model for compressible materials:

$$\Psi_M = \frac{\mu_o}{2} [f(I_1 - 3) + (1-f)(I_2 - 3)] + \mathbf{A} J^2 - \left[\frac{\lambda_o}{2} + \mu_o \right] \ln J - \mathbf{A}, \quad (3)$$

also discussed in Jemioło (2002), where $\mathbf{A} = \frac{1}{4} [\lambda_o - 2\mu_o(1-f)]$. The parameters: μ_o and λ_o can be interpreted as Lamé constants. Function (3) is a poly-convex one and fulfills appropriate conditions of growth of elasticity potential if and only if $\mu_o > 0$, $f \in (0,1)$ and $\lambda_o > 2\mu_o(1-f)$, cf. Jemioło (2002). From local energy and mass conservation laws (altogether with balance equations of linear and angular momentum) one can obtain the Kirchhoff stress tensor for matrix made of Ciarlet model in the following form:

$$\boldsymbol{\tau}_M = \mu_o f \mathbf{B} + \mu_o (1-f) (I_1 \mathbf{B} - \mathbf{B}^2) + \left[\frac{1}{2} (\lambda_o - 2\mu_o(1-f)) J^2 - \frac{1}{2} \lambda_o - \mu_o \right] \mathbf{I}. \quad (4)$$

From (2) one can obtain the following relation for Kirchhoff stress in n-th fiber family:

$$\boldsymbol{\tau}_{Rn} = E_{Rn} (I_{4n} - 1) \hat{\mathbf{M}}_n. \quad (5)$$

So, the constitutive relationship for material reinforced with fiber families is as follows:

$$\boldsymbol{\tau} = J \boldsymbol{\sigma} = \left(1 - \sum_{n=1}^N p_n\right) \boldsymbol{\tau}_M + \sum_{n=1}^N p_n \boldsymbol{\tau}_{Rn}, \quad (6)$$

where $\boldsymbol{\sigma}$ is a Cauchy's stress tensor. The proposed constitutive model was implemented in the finite element method program ABAQUS through UMAT procedure for which constitutive relationship (6) has been rearranged into an incremental form, cf. ABAQUS (2000a and b).

3. Compression and Tension Tests of an Elastic Reinforced Tube

The problem of compression/tension of elastic reinforced tube in the direction of it's axis by applying displacement boundary conditions at the bottom and top base is considered. On the other parts of pipe outside surface the zero stress boundary conditions are assumed. The pipe is made of hyperelastic

material with fiber reinforcement, characterized by constitutive relationship expressed by (6). The four cases are considered, i.e. lack of reinforcement, the reinforcement overlaps with direction 3, reinforcement is placed circumferentially and reinforced is placed helicoidally, see Fig. 1. It is worth emphasizing that fiber placement directions are given in reference configuration, and during deformation undergo local changes.

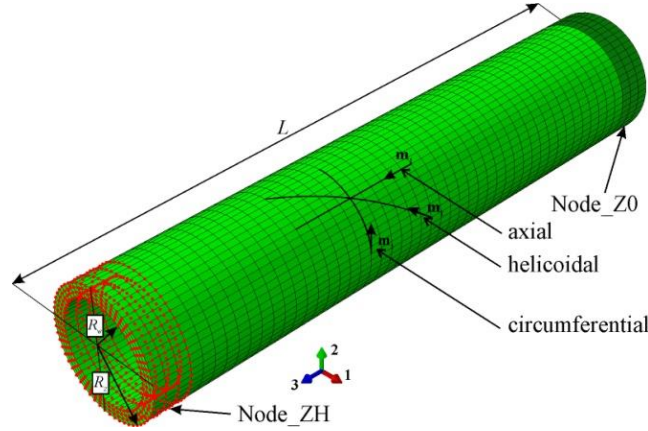


Fig. 1: FEM mesh for pipe of 100 mm length ($R_w=8$ mm, $R_z=10$ mm) with indication of node groups where boundary displacement conditions were assumed.

For the node group marked as Node_ZH (all nodes belonging to the top base of the pipe together with nodes laying on interior and exterior side surfaces but not further from the edge than 6 mm) the zero displacement boundary conditions for all three displacement components are assumed. Next, all nodes marked as Node_Z0, cf. Fig. 1, were joined with some reference node by applying multi-point constraints (MPC) option which gives the possibility to assume displacement boundary conditions for all nodes through reference node. In that case, in reference node the zero displacement boundary conditions for components u_1 and u_2 (preserving circular shape) and for all rotation angles were assumed. The pipe compression is obtained by assuming non-zero displacement $u_3 = -20$ mm, and in case of tension test $u_3 = 50$ mm. The following material data were assumed: $p = 0.05$, $\mu_0 = 1.0 E_M$, $\lambda_0 = 1.5 E_M$, $E_z = 26 E_M$, where E_M is an initial Young's modulus of matrix material, and $f = 0.2$.

All tasks were solved using standard Newton-Raphson incremental algorithm. The graphs of resulting cumulative compression and tension forces (denoted as F_{cc} and F_{ct} , respectively) in reference node as a function of displacement u_3 are shown in Fig. 2. In Fig. 3 the contour graphs of Mises stresses on deformed compressed tubes configurations are presented for minimum obtained forces (beginning of local or global buckling). The main goal of this example is a comparison of solutions obtained for hyperelastic isotropic material with solutions obtained for implemented constitutive models of hyperelastic materials reinforced with differently placed fiber families.

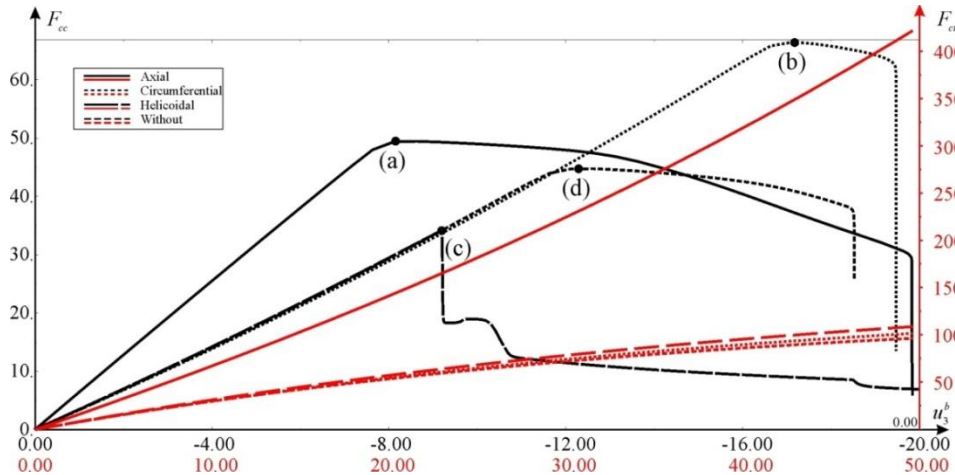


Fig. 2: The compression/tension cumulative force as a function of displacement u_3 for different types of fibre reinforcement.

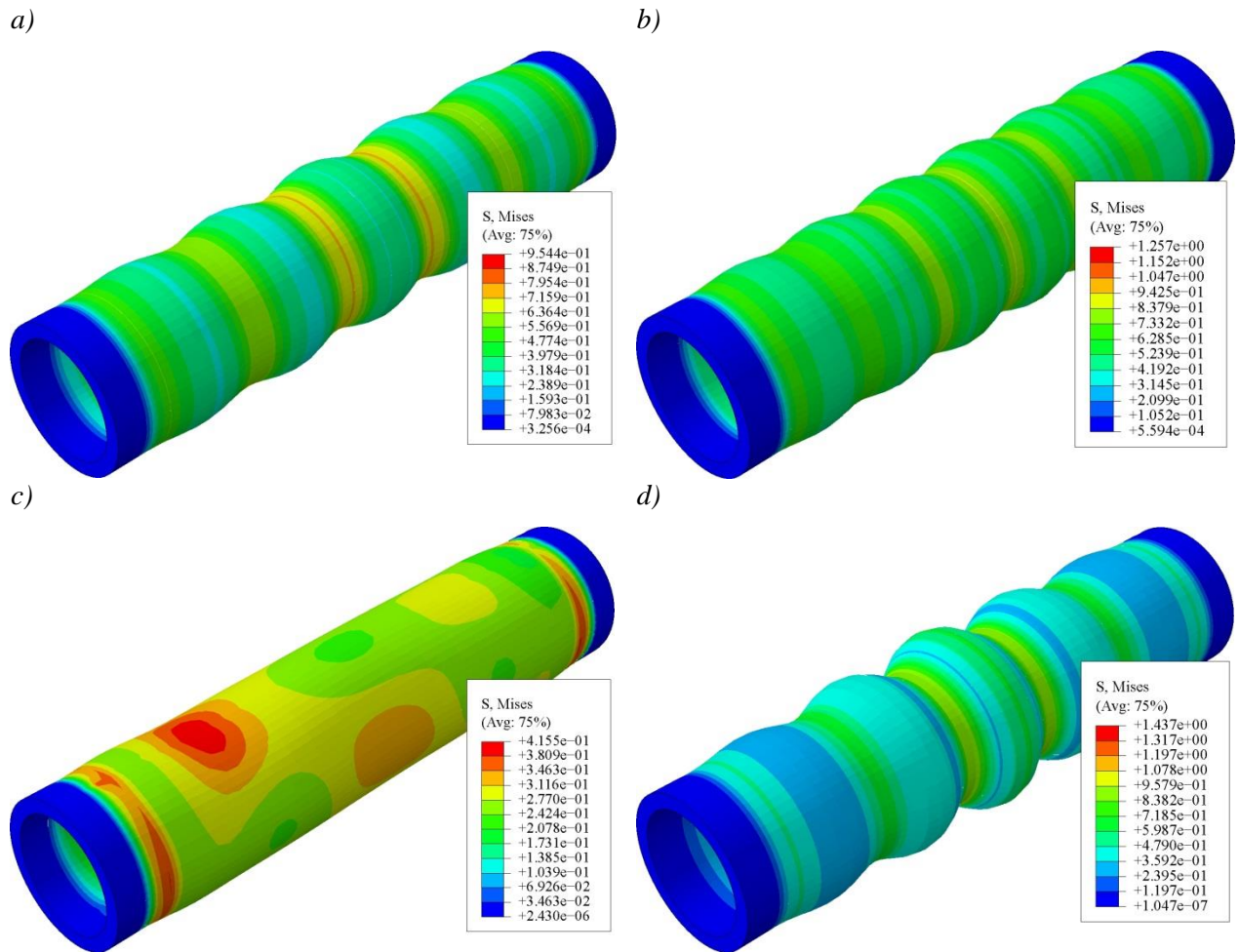


Fig. 3: Contour graphs of Mises stresses for compression tests in the configuration corresponding to minimum force, as indicated in Fig. 2.

4. Final Remarks

In the paper the constitutive relationship for anisotropic hyperelasticity in case of fibre reinforced materials has been shown altogether with its numerical implementation in FEM system ABAQUS. Some example applications illustrating the compression/tension of the differently reinforced tube is presented proving correctness and robustness of the implementation. The most suitable application area for proposed relationship is probably biomechanics, and modeling of vasculature consisting of a complex system of arteries, arterioles, capillaries and veins.

References

- ABAQUS (2000a) Theory manual, Version 6.1, Hibbit, Karlsson and Sorensen, Inc., Pawtucket.
 ABAQUS (2000b) Standard User's manual, Version 6.1, Hibbit, Karlsson and Sorensen, Inc., Pawtucket.
 Boehler, J. P. (ed) (1987) Applications of tensor functions in solid mechanics. CISM Courses and Lectures, No. 292, Wien-New York, Springer-Verlag.
 Bonet, J., Wood R.D. (1997) Nonlinear continuum mechanics for finite element analysis, Cambridge University Press.
 Gajewski, M., Jemioło, S. (2007) FEM implementation of hyperelastic constitutive models of reinforced materials, XVI Slovak-Polish-Russian Seminar Theoretical Foundation of Civil Engineering, Žilina, pp. 119-126, Moscow, (in Polish).
 Jemioło, S. (2002) A study of the hyperelastic properties of isotropic materials. Modelling and numerical implementation, Prace Naukowe, Budownictwo z. 140, pp. 1-308, OWPW, (in Polish).
 Jemioło, S., Telega, J. J. (2001) Modelling elastic behaviour of soft tissues, Part II. Transverse isotropy, Eng. Trans., Vol. 49, No. 2-3, pp. 241-281.
 Spencer, A. J. M. (1972) Deformations of fibre-reinforced materials, Oxford, Clarendon Press.

BASE ISOLATION SYSTEMS IN BUILDING STRUCTURES

I. Gołębiowska^{*}, W. Sakiewicz^{**}

Abstract: *This paper shows review of base isolation techniques and other ones used around the world. The basic idea of base isolation is to decouple the building structure from damaging components of the harmful motion. This paper summarizes a review of articles on base isolation techniques in building structures. Rubber bearing, lead rubber bearing, friction pendulum and other types of isolators will be described.*

Keywords: Base isolation, Vibration control, Damping.

1. Introduction

Base isolation separates the structures from the harmful motion of the ground by providing flexibility and energy dissipation capability through the insertion of the devices so called isolators between the foundation and the building structure (Ismail et. al., 2010).

Various vibration control strategies are employed to reduce the effect of harmful vibrations. They can be divided into four categories: passive, semi-active, active and hybrid control (Fig. 1).

There are following systems of passive control:

- (1) base isolation (elastomeric rubber bearing, elastomeric lead rubber bearing, elastomeric high damping rubber bearing, friction pendulum, sliding with restoring force, sliding with yielding devices),
- (2) energy dissipation devices (viscous damper, viscoelastic damper, hysteretic damper, friction damper, electro-magnetic damper),
- (3) mass dampers (tuned mass dampers, tuned liquid dampers, impact damper).

Energy dissipation devices are generally installed as integral parts of building structures (Gołębiowska & Rojek, 2010).

Tuned mass damper (TMD) consists of the mass, spring and damping element. The frequency of the TMD is generally tuned to the fundamental frequency of the primary structure. They are placed in buildings, chimneys, masts, towers and other tall structures (Gołębiowska & Sakiewicz, 2008).

In this paper, a brief description of the basic construction, mechanical behaviour of selected type base isolation is presented.

2. Base Isolation

A variety of base isolation bearings have been developed and implemented around the world for many years. In general, base isolation is classified into two categories: (1) bearing (elastomeric, sliding), (2) others systems (spring, rollers, sleeved piles, hybrid systems, etc.). The main concept base isolation is explained in Fig. 2. The shift of the fundamental period of the structure out of the range of dominant excitation frequencies is the base of this concept. The local soil conditions have a great impact on the reliability of the base isolation (Symans, 2004).

^{*} Prof. Irena Gołębiowska, PhD.: Faculty of Civil and Environmental Engineering and Architecture, University of Technology and Life Sciences in Bydgoszcz, ul. Prof. S. Kaliskiego 7; 85-796, Bydgoszcz; Poland, irena_golebiowska@wp.pl

^{**} Wioletta Sakiewicz, M.Sc.: Faculty of Civil and Environmental Engineering and Architecture, University of Technology and Life Sciences in Bydgoszcz, ul. Prof. S. Kaliskiego 7; 85-796, Bydgoszcz; Poland, wioletta.sakiewicz@utp.edu.pl

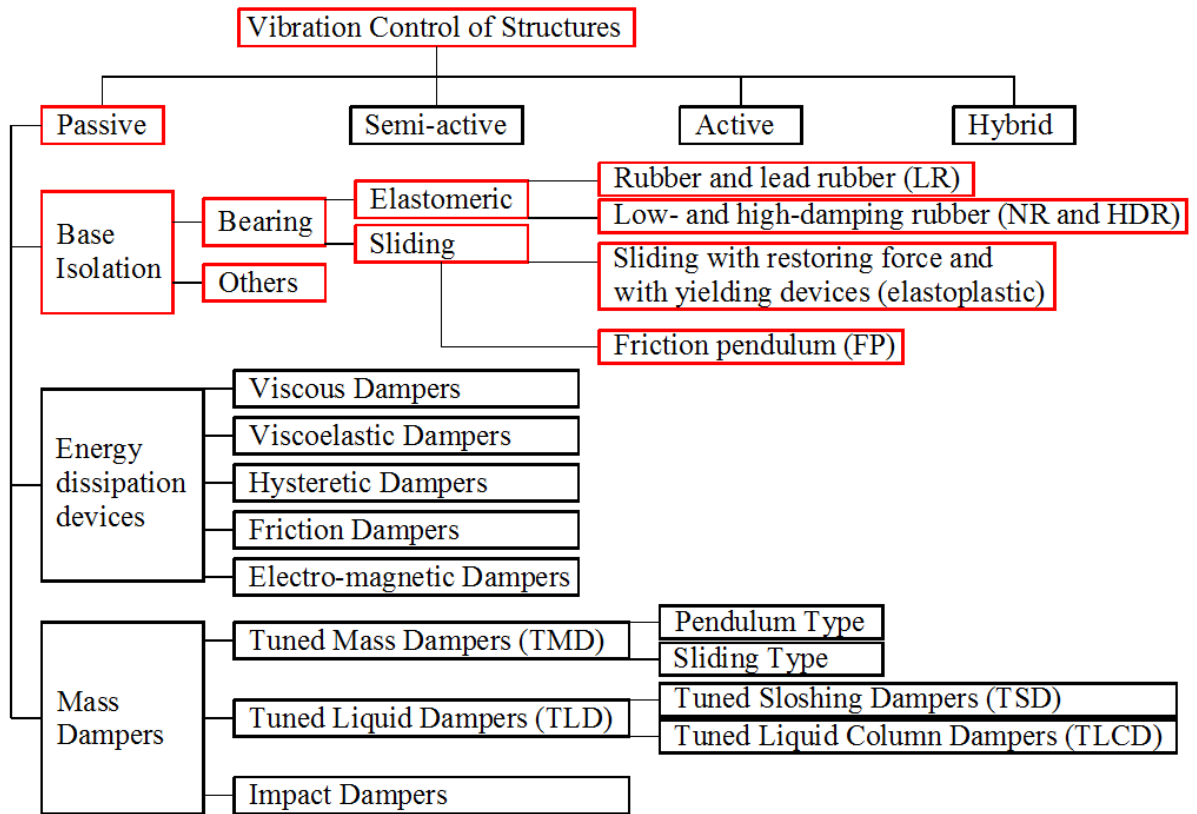


Fig. 1: Various types of vibration control.

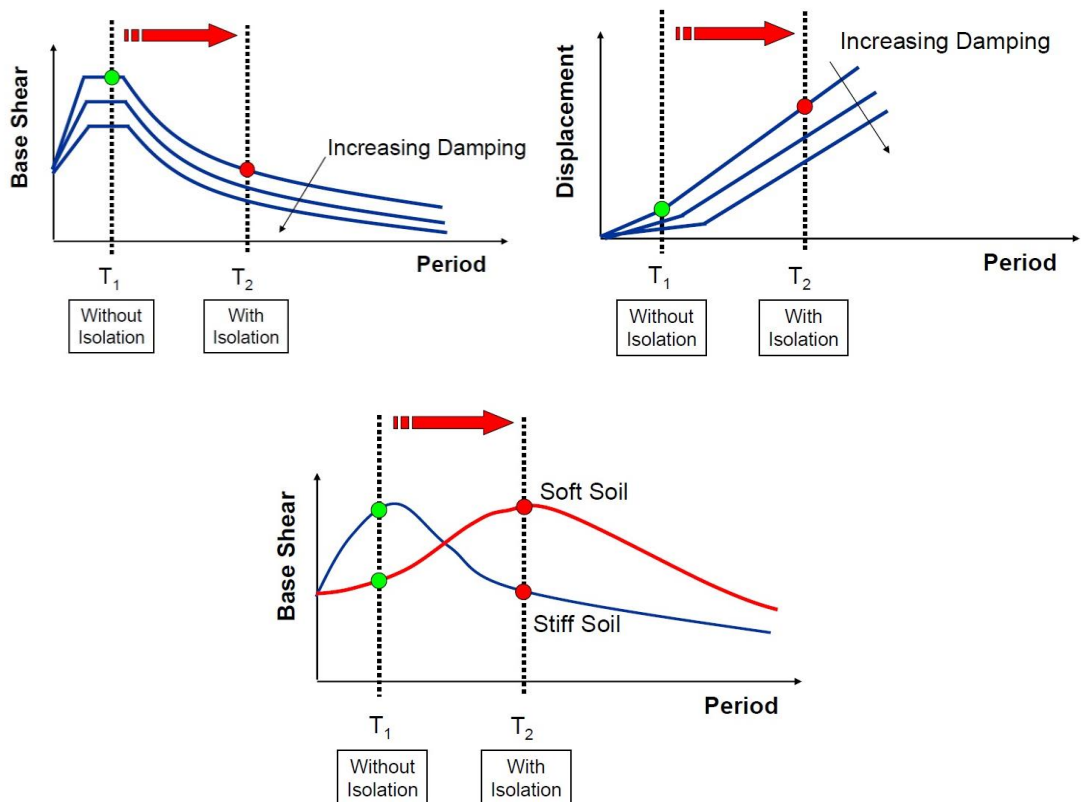


Fig. 2: Concept of base isolation (Symans, 2004).

Elastomeric bearing is composed of alternating layers of natural, or synthetic, rubber bonded to intermediate steel shim plates (Fig. 3). Elastomeric bearing can be classified into two categories: low-damping rubber and high-damping rubber.

Fig. 4 shows improved version of elastomeric rubber bearing where a centrally located lead core inside is introduced, which has energy dissipating capacity. Then, isolator essentially works as hysteretic damping device.

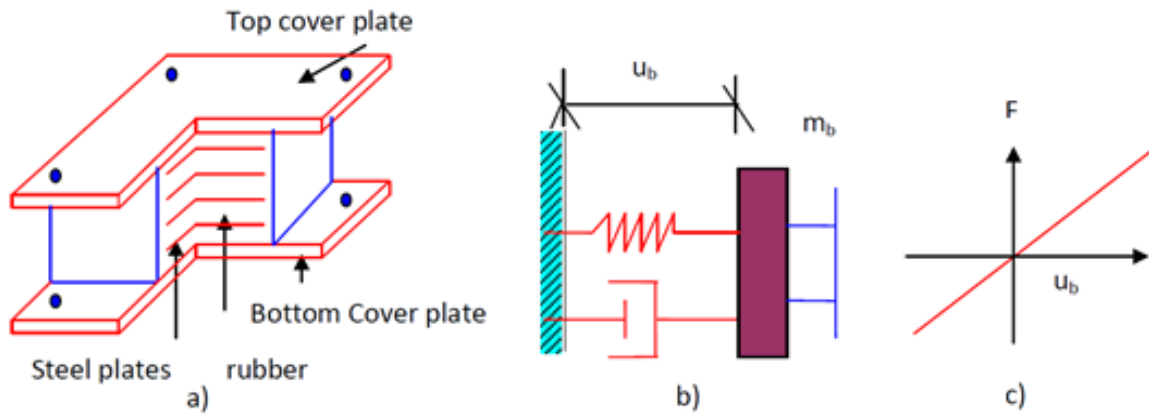


Fig. 3: Elastomeric rubber bearing: a) Sectional details; b) Schematic diagrams; c) Force deformation behavior (Patil & Reddy, 2012).

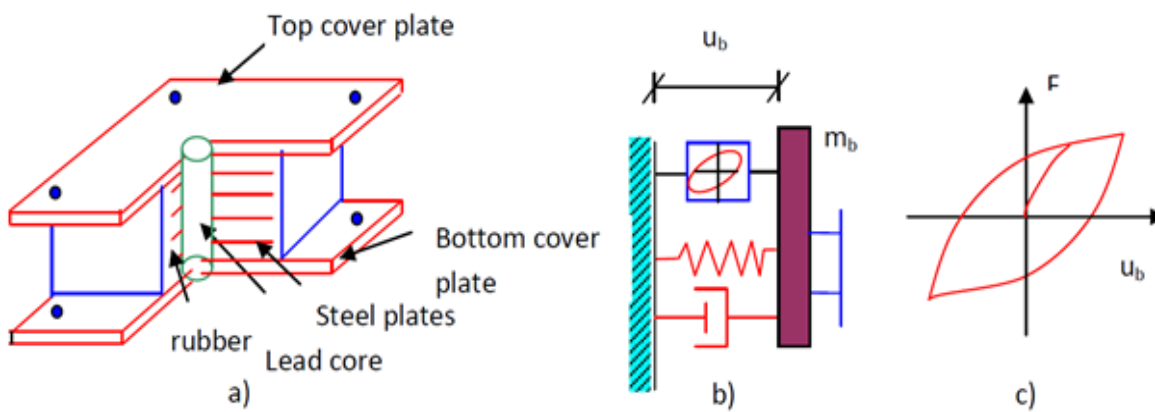


Fig. 4: Lead rubber bearing: a) Sectional details; b) Schematic diagrams; c) Force deformation behavior (Patil & Reddy, 2012).

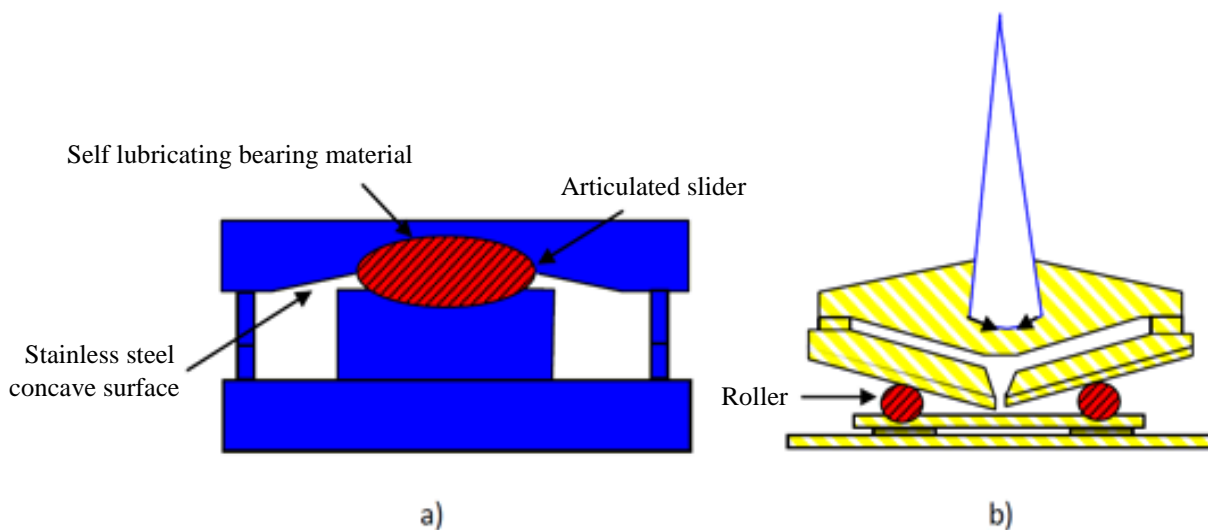


Fig. 5: Friction pendulum base isolator: a) Friction pendulum system; b) Roller pendulum system (Patil & Reddy, 2012).

Sliding bearing support the weight of structure on a bearing that rest on a sliding interface. Most sliding bearings use polytetrafluorethylene type material and stainless steel for bearing material at the sliding interface. The single friction bearing consists of a base plate, an articulated slider and a spherical concave dish (Fig. 5). Sliding bearing dissipates energy by friction, and may use a separate mechanism to provide a self-centering capability or employ a curved sliding surface that may be spherical, conical or of varying curvatures.

There are some other types of isolators: springs, rollers and sleeved piles. Spring isolators and rollers are used for machinery isolation. The disadvantage of springs is little damping. Rollers are more resistant to service load as springs. Sleeved piles provide flexibility but no damping.

Nowadays hybrid isolation systems are often used, because they are high performance in reducing vibration, possess the ability to adapt to different loading conditions and are able to control multiple vibration modes.

3. Conclusion

Common vibration control systems in use today include elastomeric and sliding bearings with and without energy dissipation devices and/or mass dampers. The benefit of base isolation is that the damping capacity can be obtained in one device. However, because the nonlinear vibration characteristics of base isolation devices the vibration reduction is not optimal for a wide range of input ground motion intensities. For wide range of excitation the hybrid control strategies can be effective, consisting of a base isolation combined with passive energy dissipation devices and mass dampers. Due to limit of paper sheets, in this article only the important selected isolators were shown.

References

- Gołębiowska, I. & Rojek, J. (2010) Devices passive vibration control in buildings. *Ekologia i Technika*, Vol. XVIII, Nr 5, pp. 290-298, (in Polish).
- Gołębiowska, I. & Sakiewicz, W. (2008) Control systems for vibrating structures. *Lightweight Structures in Civil Engineering*, Local Seminar of IASS Polish Chapter XIV LSCE, Warsaw, pp. 40-43.
- Ismail, M., Rodellar, J. & Ikhouane, F. (2010) An innovative isolation device for aseismic design. *Engineering Structures* 32, pp. 1168-1183.
- Patil, S.J. & Reddy, G.R. (2012) State of art review – base isolation systems for structures. *International Journal of Emerging Technology and Advanced Engineering*, Vol. 2, Issue 7, pp. 438-453.
- Symans, M.D. (2004) *Seismic Protective Systems. Seismic Isolation. Instructional Material Complementing FEMA 451, Design Examples.*

CONCRETE DETERIORATION DUE TO AGGRESSIVE ENVIRONMENT AND CYCLIC LOADING – THEORETICAL STUDY

J. Göringer^{*}, M. Foglar^{**}

Abstract: *With the usage of modern cementitious materials, structural elements are designed more slender. For structures subjected to cyclic loadings this means higher stress ranges and thus higher probability of fatigue failure. Structures of transport infrastructure which are mainly exposed to cyclic loading are often located in places of aggressive environment. The paper presents a theoretical study, part of a long-term experimental research focused on the effect of coupled deterioration by aggressive environment and cyclic loading on the concrete specimens. The evaluation of the deteriorative effect of aggressive environment is based on kinetics of chemical reaction between concrete and aggressive solution of hydrochloric acid.*

Keywords: Concrete, Deterioration, Aggressive environment, Cyclic loading.

1. Introduction

Fatigue can be defined as a process of permanent progressive changes in the structure of material subjected to cyclic loading. The influence of fatigue on changes in material structure has been studied by many authors as has been described in Foglar & Göringer (2013). The influence of cyclic loading on the deflections of concrete samples was developed by Holmen (1979) and further extended by Foglar (2010).

The influence of aggressive environment can be divided into two types of deterioration mechanism, mechanical – agents contained in aggressive environment crystallize in the pores of the material and cause pore pressures and consequently lead to the formation and propagation of cracks in the material matrix, chemical – the material is exposed e.g. to acid solution which reacts with concrete components and successively weakens composition of the binder. The phenomenon of chemical deterioration has been extensively investigated with regard to the effect of acid rain on concrete structures, the summary can be found in Göringer & Foglar (2014).

Both areas of material damage (fatigue caused by cyclic loading, deterioration due to the aggressive environment) are widely explored. However, the interaction of these two adverse effects has not yet been properly quantified.

For evaluation of the interaction of the mentioned phenomena, a long-term experimental program was proposed.

2. Methodology

2.1. Aggressive environment and its definition

The set of European standards, namely EN 206-1, defines the exposure classes of aggressive environment. The most severe class XA3 is defined as environment with value of pH equals to 4.0 which corresponds to concentration of H^+ ions, which cause the acidity of solution, $c_{H^+} = 10^{-4} \text{ mol/dm}^3$.

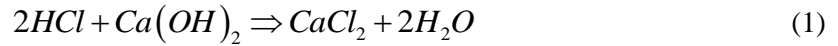
In the developed (and below described) experimental program, an aggressive environment consisting of hydrochloric acid (*HCl*) solution of pH 2.0 is considered to speed up the deterioration process.

^{*} Ing. Jakub Göringer: Faculty of Civil Engineering, Czech Technical University in Prague, Thakurova 7; 166 29, Prague; CZ, jakub.goringer@fsv.cvut.cz

^{**} Ing. Marek Foglar, PhD.: Faculty of Civil Engineering, Czech Technical University in Prague, Thakurova 7; 166 29, Prague; CZ, marek.foglar@fsv.cvut.cz

2.2. Chemical deterioration of concrete

The rate of chemical deterioration of concrete is primarily affected by the concentration of H^+ ions. As a main deteriorative reaction which weakens the composition of binder, the neutralization defined in (1) can be assumed. The dissolution of ferrite or aluminate hydrates occurs at lower values of pH and in a lesser extent than the dissolution of calcium hydroxide ($Ca(OH)_2$). This assumption was proposed and verified by Pavlík (1994). This assumption will be used in the research.



With the depletion of calcium hydroxide from the concrete surface layers, it can be assumed that the rate of deterioration of the concrete ceases to be primarily dependent on the solution pH and that it will switch to the diffusion phenomenon that is mainly influenced by the concrete permeability.

2.3. Formulation of the problem to be solved

Let it be assumed that the major effect on the strength of the concrete can be attributed to the content of calcium hydroxide (CaO) in the cement, which during the hydration process changes to hydration products. When using the known concrete mix design, it is possible to determine the initial concentration of Ca^{2+} ions and thus determine the maximum capacity for neutralization from the amount of cement and its content of $Ca(OH)_2$.

To determine the kinetics of reaction it is appropriate to use the rate equation, which in the case of neutralization according to (1) has the following form:

$$-\frac{dc_{Ca}}{dt} = k_{Ca} c_H^\alpha c_{Ca}^\beta \quad (2)$$

where c_{Ca} , $c_H = Ca^{2+}$, H^+ ions concentration, $t =$ time, $k_{Ca} =$ rate constant, α , $\beta =$ reaction order.

In the case, that the proposed mechanism is correct and corresponds to the experimental data set, it is possible to use the relation established in (2) for further calculations e.g. loss of calcium ions. The rate constant k_{Ca} have to be determined experimentally using additive properties, for example the change of pH over time, or with use of chemical analysis methods as flame atomic absorption spectroscopy (AAS).

Returned to the assumption that the total amount of CaO in the mixture affects the compressive strength of the concrete, it is possible to develop the relationship between the time loss of Ca^{2+} ions from the material matrix caused by the aggressive environment and decrease of the compressive strength. The result of the chemical deterioration process is from this viewpoint primarily the reduction of compressive strength as outlined below.

For the description of fatigue deterioration the compressive strength is used in all previously mentioned approaches for modeling fatigue damage. Prerequisite for coupled deterioration due to aggressive environment and fatigue caused by cyclic loading is to combine reduction of compressive strength of both damage components. The principle of interaction of both types of damage can be seen in Fig. 1.

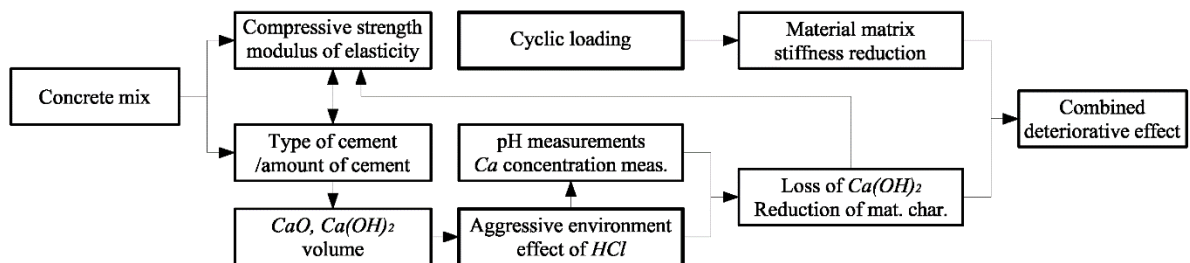


Fig. 1: Principle of interaction of damage components due to fatigue and material deterioration.

2.4. Diffusion and corroded layer

Due to the nature of concrete as a material, the basic problem for evaluation of specimen deterioration degree is diffusion of aggressive agents through material matrix.

Pavlík (1994) states that the transport of H^+ ions may be considered as steady-state diffusion due to slow increase of the corroded layer thickness. Two boundary conditions are proposed – on the surface of the concrete specimen the concentration of H^+ ions is equal to concentration of aggressive solution; in contact of the corroded and uncorroded layer the concentration pH value is due to neutralization around 7 ($c_{H^+} = 10^{-7} \text{ mol/dm}^3$). The gradient dc_{H^+}/dx is nearly constant. The pH distribution through the corroded layer according to mentioned assumptions can be seen in Fig. 2.

From the viewpoint of the conventional diffusion it is possible to describe the transport process of H^+ ions with the Fick's second law of diffusion (3). Mathematical solution considering constant diffusion coefficient, boundary and initial conditions is stated respectively in (3).

$$\frac{\partial c}{\partial t} = D \frac{\partial^2 c}{\partial x^2} \quad \Rightarrow \quad c(x,t) = c_0 \left[1 - \operatorname{erf} \left(\frac{x}{2\sqrt{Dt}} \right) \right] \quad (3)$$

where c = is concentration, D = diffusion coefficient, x = location from surface, c_0 = solution concentration, erf = Gauss error function.

The time and location dependent pH distribution according to (3) and the comparison of the pH distribution according to (3) and Pavlík (1994) for time $t = 365$ days and initial concentration $c_0 = 10^{-4} \text{ mol/dm}^3$ (pH = 4) can be seen in Fig. 2. This comparison shows disagreement in both mentioned approaches. The suitability of the applicable approaches will be tested in the experimental program.

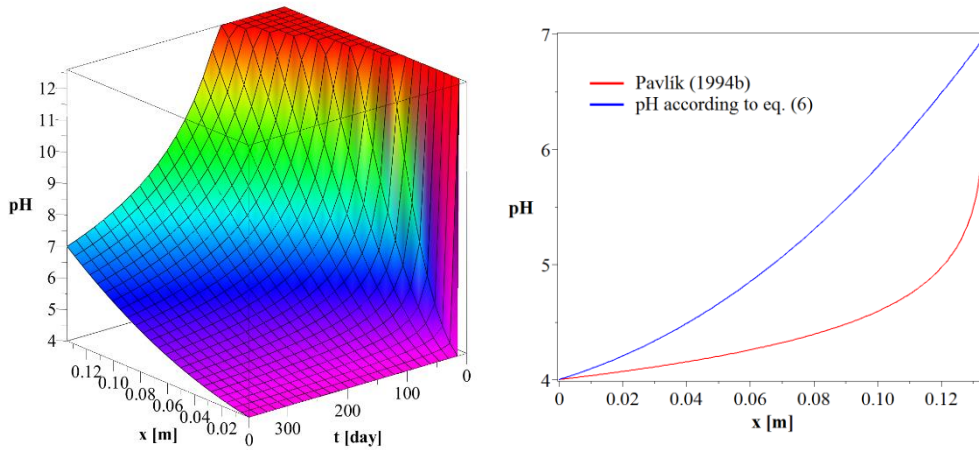


Fig. 2: In time pH distribution for (4) (left), comparison of (4) and approach in Pavlík (1994) (right).

If the pH distribution through the corroded layer according to Pavlík (1994) proves to be valid, there is a possible presumption that for the deterioration degree evaluation, the time variable surface exposed to aggressive environment can be used. At the basis of the kinetics of chemical reaction (1) (experimental data are required) the amount of dissolved Ca^{2+} ions can be determined. For known mix design, it is then possible to identify the possible thickness of the layer with almost none Ca^{2+} ions. This layer may be eliminated from further diffusion process.

Evaluation of the compressive strength. The compressive strength is the decisive characteristics both for its fatigue and deterioration performance. For the mix design of concrete the F eret equation (F eret, 1892) for compressive strength of concrete is commonly used (4).

$$f_{ck}(t) = k_f(t) f_{mc} \left[\frac{v_c}{v_c + v_w + v_a} \right]^2 \quad (4)$$

where f_{ck} = compressive strength of concrete (function of time) k_f = F eret coefficient (function of time), f_{mc} = resistance of cement in 28 days, v_c, v_w, v_a = cement, water and air volume in mix design.

With the mentioned assumption, that the compressive strength of concrete is dependent on total amount of CaO in concrete volume the value of v_c in (4) can be modified by amount of dissolved Ca^{2+} from concrete matrix into the aggressive storage solution. With a constant pH of aggressive environment the

solution of (2) substituted into (4) yields the function of compressive strength of concrete as a function of time and H^+ ions concentration, thus the value of pH of aggressive storage solution (5).

$$f_{ck} = k_f f_{mc} \left(\frac{X_{cem} V_c \exp(-k_{Ca} C_H t)}{V_c (X_{cem} \exp(-k_{Ca} C_H t) + X_w + X_a)} \right)^2 \quad (5)$$

where X_{cem} , X_w , X_a = volume fraction of cement, water, air in mix, V_c = volume of specimen.

The Féret coefficient k_f is evaluated from the tests of compressive strength of cube specimens. The rate constant k_{Ca} is evaluated from the analysis of periodic sampling of storage aggressive solution. As a comparative data, some cubes are stored separately in aggressive solutions of different pH. According to (1) and (2) the rate constants k_{Ca} is to be evaluated from the time development of the pH value.

3. Experimental Program

Several sets of concrete specimens (strength class C25/30-X0) were designed for the long-term experimental program. All sets are stored in dry or aggressive environment and consequently exposed to cyclic loading. To maintain the stable value of the pH = 2 during the storage of specimens in aggressive environment, the pH value was regularly measured. According to these measurements hydrochloric acid was added each time. Based on the pH measurements and the amount of added acid, the volumes of dissolved Ca^{2+} ions were calculated as well as determined using AAS. The comparison of calculated and measured volumes can be seen in Tab. 1. The values correspond with assumptions from section 2.2.

Tab. 1: The Calculated and analyzed volumes of Ca^{2+} , Al^{3+} , Fe^{3+} and Si^{4+} ions

Specimen no.	Added HCl [cm ³]	Calculated volume of Ca^{2+} ions [g]	AAS volume of Ca^{2+} ions [g]	AAS vol. of Al^{3+} , Fe^{3+} , Si^{4+} ions [-]
A1	1240	238.764	235.660	2.8 / 1.2 / 5.1
A2	1720	390.264	402.612	4.4 / 1.3 / 5.5
A3	1085	246.197	248.643	0.9 / 0.1 / 3.0

4. Conclusions

This paper described the theoretical study, part of a long-term experimental program focused on the interaction of deterioration caused by aggressive environment and cyclic loading. The paper presented the outline of a new approach to describe the coupled problem of both types of deterioration which will be based on an ongoing experimental program.

Acknowledgments

The financial support of the Czech Science Foundation grant project 13-30441S is gratefully acknowledged.

References

- Göringer, J. & Foglar, M. (2014) Experimental and theoretical study of the performance of reinforced concrete specimen subjected to cyclic loading and aggressive environment, *Adv. Material Research*, 891, pp. 494-499.
- Holmen, J. (1979) Fatigue of concrete by constant and variable amplitude loading, *NTH Bulletin*, 79, pp. 71-110.
- Foglar, M. (2010) The strain development in concrete under cyclic loading, In: Proc. 5th international conference of bridge maintenance, safety and management, Balkema, Philadelphia, pp. 3185-3189.
- Foglar, M. & Göringer, J. (2013) Investigation of the combined effect of fatigue and aggressive environment on concrete, In: Proc. 7th Int. Conf. on Concrete under Severe Conditions (Z.J.Li, W.Sun & C.W.Miao eds), RILEM, Bagneux, pp. 1065-1075.
- Pavlík, V. (1994) Corrosion of hardened cement paste by acetic and nitric acids part II: Formation and chemical composition of the corrosion products layer, *Cement and Concrete Research*, 24, pp. 1495-1508.
- Féret, R. (1892) Sur la compacité des mortiers hydrauliques, *Annales des Ponts et Chaussées*, 2, pp. 5-61.

INFLUENCE OF REDUCER DISK BALANCE ON FLEXURAL VIBRATION OF PROPELLER SHAFT

M. Hać, W. Ostapski*

Abstract: *In the paper vibration analysis of a propeller shaft of a light airplane piston engine is considered. The bending vibration of the shaft occurs due to unbalanced assembly: reducer disk – shaft as a consequence of machining tolerance. The finite element method is used for determination of the shaft deflection and the geometric non-linear model is considered. The dynamic equations for rotating shafts are developed and the results for bending vibration of the shaft are presented.*

Keywords: Bending vibration, FEM, Propeller shaft, Airplane piston engine.

1. Introduction

The object considered in the present paper is a propeller shaft of a light airplane. The drive unit consists of new-generation, multifuelled airplane piston engine, planetary reducer, and propeller shaft (Ostapski, 2012). The design of the reducer involves the use of a planetary gear, thus a disk with the ring gear is embedded on the propeller shaft (see Fig. 1). For safety reasons it is very important to properly balance this assembly since the shaft speed during operation is high (approx. 2600 rpm). Moreover, during operation the roller bearings develop additional clearance due to wear, which also influences the shaft balance. Therefore it is important to analyze the bending vibration of the shaft due to unbalanced elements.

In order to estimate the possible imbalance of the reducer the machining tolerance of the splined connection of the shaft and the disk is taken into account. The line of deflection of the shaft is determined using the finite element method. The axis of symmetry for the shaft pin and the disk cannot be ideally coaxial (within the area of machining tolerance) and this is the reason for vibrations appearing during rotation of the shaft. These vibrations cause additional deflection of the rotating shaft and influence the gear wheel meshing. This problem was carefully addressed in (Hać, 2005) and the method of calculation of the load distribution corrections along gear width was also presented.

The propeller shaft is designed for torque transmission from engine to the propeller and dominant strains are those from conveying torque. However, the presence of heavy elements – such as a reducer disk – causes the possibility of bending vibration to develop, which is highly dangerous when not controlled.

The model of the propeller shaft presented in Fig. 1 for further consideration is simplified to the form presented in Fig. 2

2. Modelling of Shafts by FEM

The finite element method is used in order to analyze elastic transverse deformation of the propeller shaft. The planar Bernoulli-Euler beam finite elements are used and the nodal displacement vector consists of both transverse and longitudinal displacements of nodes and nodal angular deformations.

2.1. Modelling of articulated joint (hinge)

Usually for modelling a hinge joint an additional very short finite element (compared to other elements used in construction) is used. In this way the deformation angle at the left side of the hinge is different

* Dr. hab. Michał Hać, PhD., Prof. Wiesław Ostapski, PhD.: Institute of Machine Design Fundamentals, Warsaw University of Technology, Narbutta 84, 02-524 Warsaw, Poland, mha@simr.pw.edu.pl, wos@simr.pw.edu.pl

than at the right side. In order to avoid introducing additional elements, the node (number 2) at the articulated joint (hinge) is modelled by assuming two independent rotational degrees of freedom (left and right) - see Fig. 3.

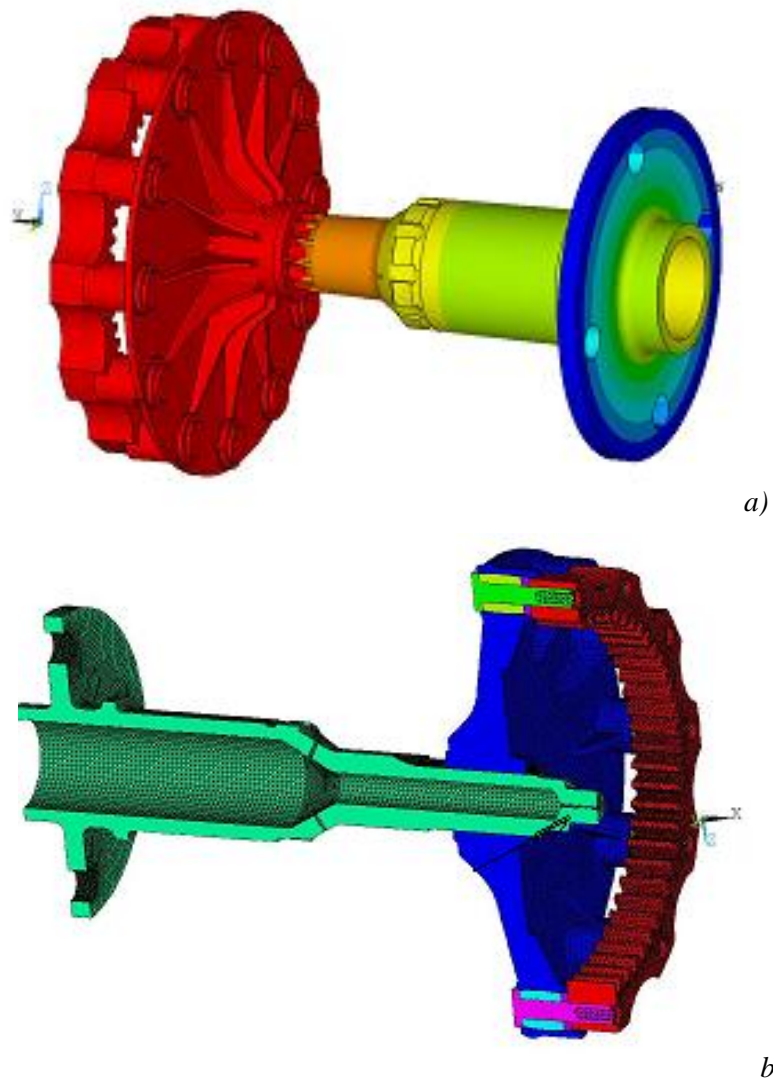


Fig. 1: Propeller shaft of airplane engine: a) 3D view; b) Its cross-sectional view.

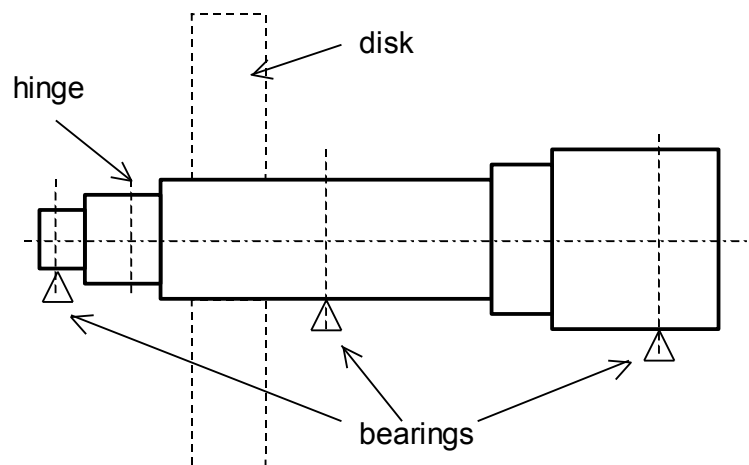


Fig. 2: Model of propeller shaft for finite element analysis.

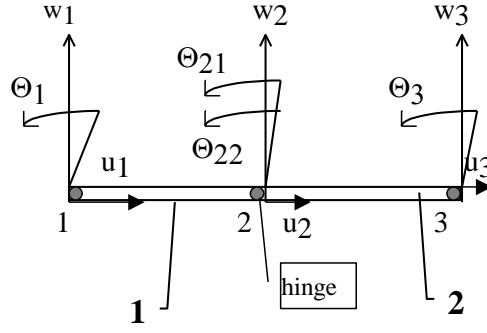


Fig. 3: Displacements of nodes of two finite elements connected by the hinge.

Nodal displacement vectors for elements 1 and 2 connected in the hinge are as follows

$$\{\delta_1\}^T = [u_1, w_1, \Theta_1, u_2, w_2, \Theta_{21}] \quad (1)$$

$$\{\delta_2\}^T = [u_2, w_2, \Theta_{22}, u_3, w_3, \Theta_3] \quad (2)$$

where: Θ_{21}, Θ_{22} are the left and the right angular deformations of the hinge node, respectively.

In this way the articulated joint is modelled in a precise way (no artificial elements in the hinge are used). Moreover, the size of the problem is reduced because the global stiffness matrix compared to the problem without hinge joint is increased by only 1 (i.e. additional deformation angle in the hinge). In the case when additional element is used the size of the problem increases more (co-ordinates of additional node). In most cases longitudinal displacements of nodes of finite element neighboring with the hinge joint are equal – the hinge does not transfer longitudinal force and the neighboring finite elements are not longitudinally loaded. In such case it can be assumed: $u_1 = u_2 = u_3$.

3. Equations of Motion of Rotating Shaft

The equations of motion of rotating shafts can be obtained by any method used in derivation of motion of dynamic systems such as the principle of virtual work, the Gibbs-Appel equations of motion, or Lagrangian equations of motion. The equations of motion of rotating shaft in the global coordinate system can be expressed as follows (Brown and Shabana, 1997):

$$[M]\{\ddot{x}\} + [C]\{\dot{x}\} + [C_g]\{\dot{x}\} + ([K] + [K_c])\{x\} = \{F\} \quad (3)$$

where coefficient matrices are global matrices obtained from appropriate element matrices: $[M_e]$ is the element inertia matrix, $[C]$ is the global damping matrix, $[C_g]$ is the gyroscopic matrix, $[K]$ is the global stiffness matrix, $[K_c]$ is the centrifugal matrix, $\{F\}$ represents generalized forces, and $\{\ddot{x}\}$, $\{\dot{x}\}$ and $\{x\}$ represent acceleration, velocity, and displacement vectors (in nodal points). Matrices $[C_g]$ and $[K_c]$ are obtained from element matrices $[C_{ge}]$ and $[K_{ce}]$ defined as follows:

$$[C_{ge}] = 2\omega\rho A \int_0^L [N_e]^T [\Omega] [N_e] d\zeta, \quad [K_{ce}] = -\omega^2 \rho A \int_0^L [N_e]^T [N_e] d\zeta \quad (4)$$

where ω is the angular velocity of the shaft, ρ is mass density, A is the cross-sectional area, $[N_e]$ is the beam finite element shape function, $0 \leq \zeta \leq L$, L is the length of the beam finite element, and $[\Omega] = [0, -1; 1, 0]$ is the Boolean type operator matrix.

The damping matrix can be presented as a linear combination of the mass and stiffness matrices

$$[C] = \alpha[M] + \beta[K] \quad (5)$$

where α and β are constants to be determined from first few natural frequencies of the system. Usually damping proportional to stiffness is considered (i.e. “structural” damping), and in that case $\alpha = 0$, and β is obtained based on natural frequencies and assuming material damping coefficient for steel in the range of 0.02÷0.03.

In order to calculate the natural frequencies of the system the homogeneous version of equation of (3) is considered. In the further analysis the structural damping (proportional to stiffness) is considered and the damping matrix is formulated as $[C] = \beta[K]$.

4. Numerical Results and Conclusions

Dynamic behavior can significantly influence the deflection of the shaft. In order to conduct the vibration analysis the damping coefficient β for determination of the damping matrix $[C]$ (see Eqn (5)) should be calculated. The coefficient β is calculated based on the first two natural frequencies of the system. For the given data of the propeller shaft the natural frequencies are as follows [Hz]: 39; 99.

In our case of steel shaft the damping ratio ξ_β is assumed to be 0.02 for the first two modes. The coefficient β is calculated from the formula (Rakowski & Kacprzyk, 1993):

$$\beta = 2\xi_\beta / (\omega_1 + \omega_2) \quad (6)$$

For the obtained natural frequencies this yields $\beta = 2.897 \cdot 10^{-4}$.

In the dynamic analysis it is assumed that the imbalance of the shaft-disk assembly results from the shaft and the disk axes not being coaxial (within the assumed tolerance of the joint). Thus additional centrifugal forces act on the shaft and influence its deflection. The deflection graph of the shaft obtained for the highest inertia force possible is presented in Fig. 4.

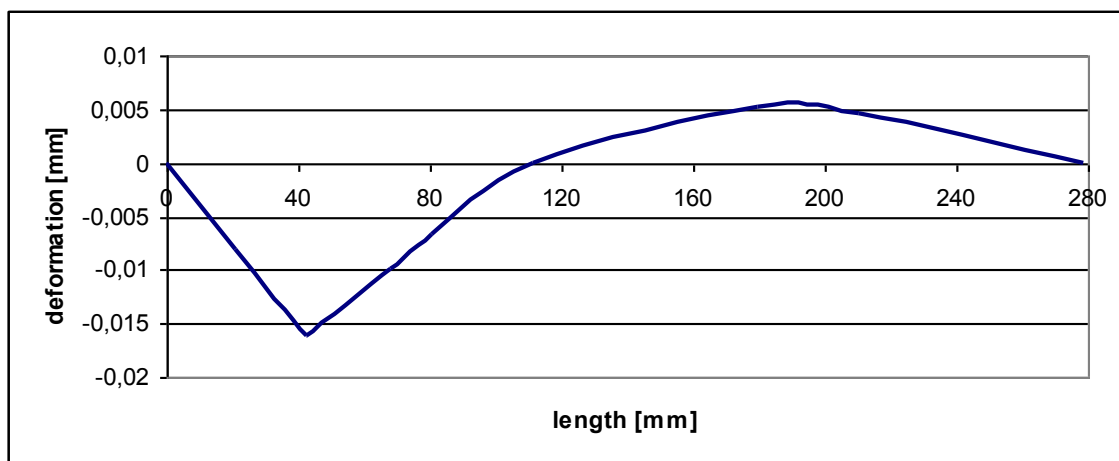


Fig. 4: Shaft deflection.

The results show that, within the given tolerance of shaft – disk connection, significant centrifugal forces (approximately 60 times the weight of the disk) may occur, which cause additional deflection of the shaft. It should be noted that the presented analysis does not contain additional dynamic response due to clearances in bearings. The problem is very important since the bending vibration of shafts is often the reason for destruction of the structure in both piston and jet airplane engines.

References

- Brown, M.A., Shabana, A.A. (1997) Application of multibody methodology to rotating shaft problems, *Journal of Sound and Vibration*, 204, 3, pp. 439-457.
- Hać, M. (2005) Influence of static and dynamic deflection of shaft pins on strength parameters of toothed gear. *Machine Dynamic Problems*, Vol. 29, 1, pp. 65-76.
- Ostapski, W. (2012) Report of the target project nr 6ZR62008C/07057: “Developing and implementing eco-friendly, multifuelled new generation airplane piston engine of power N = 200 kW”, Warsaw, (in Polish).
- Rakowski, G., Kacprzyk, Z. (1993) *Finite element method in structural mechanics*, WPW, Warszawa (in Polish).

ENERGY HARVESTING ANALYSIS OF BODY MOTION AS ENERGY SOURCE FOR BIOMEDICAL DEVICES

Z. Hadas^{*}, J. Vetiska^{**}

Abstract: *This paper deals with an energy harvesting analysis for a development of an efficient energy harvesting system for the artificial cochlea. The artificial cochlea could be used for a compensation of deafness. This artificial cochlea consists of a MEMS sensor based on banks of mechanical filters, electronics for sensing and electrodes, power supply and packaging. The energy harvesting systems are used for biomedical devices in present time and using of energy harvesting in head area for powering of the artificial cochlea is convenient. There are several types of energy which can be used as a source of energy for this biomedical application. Only 3 types of energy converters are suitable in the head area and the sufficient output power is expected. There are thermal gradient between skin and surroundings, mechanical movement of the head (shocks and vibrations) and bending movement of neck muscles and an artery. The energy harvesting from mechanical movement in head area is analysed in this paper.*

Keywords: Energy harvesting, Mechanical energy, Mechatronics, Biomedical device, Cochlea.

1. Introduction

This paper deals with an analysis and development of an efficient energy harvesting system for the artificial cochlea. The artificial cochlea is a biomedical device for a compensation of deafness. The operation of our artificial cochlea is based on the active MEMS sensor with bank of mechanical filters. Therefore, the power consumption of the active MEMS sensor is lower than using of passive sensor with a microphone and speech processor. The mentioned artificial cochlea consists of the MEMS structure with mechanical filters, electronics for sensing and electrodes, power supply and packaging. Batteries are usually used as the power supply for biomedical devices in present time. However several biomedical devices with very low power consumption are assumed for using with energy harvesting system (Beker et al., 2013). The energy harvesting is an alternative way how to provide electricity to any autonomous devices from surroundings without any fuel consumption or physical connection to outside power supply. The energy harvesting systems in head area can be used for sufficient powering of the developed artificial cochlea.

The whole artificial cochlea is mechatronic system based on several engineering's domains and our aim is the development of this complex device with respect on the mechatronic approach. The correct operation of the artificial cochlea depends on the sufficient power source and simultaneously the artificial cochlea has to operate in very low level of power consumption because the level of ambient energy in the head area is very low. The aim of this paper is analysis of harvested power for biomedical device in the head area.

There are several types of energy which can be used as a source of energy for this biomedical application, e.g. (Abdi et al., 2013), (Khaligh, 2010), (Delnavaz and Voix, 2014), (Lay-Ekuakille et al., 2009). On the base on the initial analyses and experience with energy harvesting systems only 3 types of energy converters in the head area appears as sufficient power sources. There are thermal gradient, mechanical movement (shocks and vibrations) and bending movement of neck muscles and an artery in the head area. The energy harvesting from any mechanical movement in the head area is analysed in this paper. The energy harvesting from mechanical movement can be harvested by these physical principle of electro-

* Ing. Zdeněk Hadaš, PhD.: Institute of Solid Mechanics, Mechatronics and Biomechanics, Faculty of Mechanical Engineering, Brno University of Technology, Technická 2896/2; 616 69, Brno; CZ, hadas@fme.vutbr.cz

** Ing. Jan Vetiška, PhD.: Institute of Production Machines, Systems and Robotics, Faculty of Mechanical Engineering, Brno University of Technology, Technická 2896/2; 616 69, Brno; CZ, vetiska@fme.vutbr.cz

mechanical conversions: piezo-electric, electro-magnetic, electro-static and magnetostriction physical principle.

2. Analysis of Body Motion

The mechanical energy harvester is usually based on a resonance mechanism which is excited by ambient energy of mechanical movements (Hadas & Singule, 2011). The movement can be in a form of vibrations (usually in engineering applications) or in a form of body shocks (movement acceleration). The inertia forces provide a relative movement of a seismic mass in the resonance mechanism. This relative movement is converted by any physical principle of the electro-mechanical conversion. This principle is shown in Fig. 1.

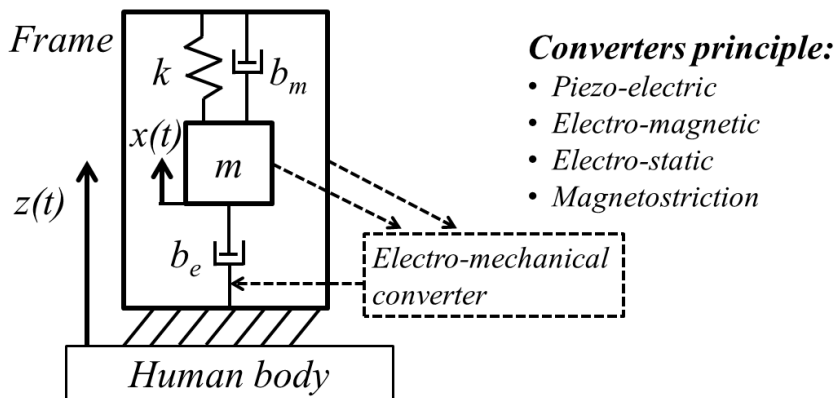


Fig. 1: Energy Harvesting Principle from Human Body Motion.

The second order differential equations of moving mass (1) is ordinary used for solving of displacement x , velocity \dot{x} and acceleration \ddot{x} of the mass m . The system operation is effected by mechanical damping b_m and stiffness of the mechanism k . During harvesting of electrical energy this dissipation of energy provides feedback by electro-mechanical damper b_e . This system is excited by ambient vibrations or shocks with acceleration \ddot{z} .

$$m\ddot{x}(t) + b_m\dot{x}(t) + b_e\dot{x}(t) + kx(t) = m\ddot{z}(t) \quad (1)$$

The energetic analyses of this differential equation of the mechanical energy harvester was published several times, e.g. (Hadas et al., 2010) and (Williams and Yates, 1996). This model corresponds with lab results and it can be used in technical engineering projects. However, the human body is not a machine from steel and the human body reacts against the relative oscillation inside resonance mechanism. The human muscles and skeleton provide damping forces which effects ordinary motion equations and this equation cannot be used for power analyses. Unfortunately several papers, e.g. (Accoto et al., 2009) and (Goll et al., 2011), do not reflect this fact and analyses presented in this paper are biased.

This effect can be presented on a simple experiment. The commercial piezo-electric converter from Company MIDE was used. This piezo converter consists of flexible beam and two thin film layers from piezo-electric material with electrodes. Electrodes of the piezo layers are connected in series. The beam of piezo converter provides stiffness of the resonance mechanism with own mechanical damping. The seismic mass 8 grams was fixed on the beam end.

This simple energy harvesting system is used for energy harvesting analysis in our paper. This system was excited by initial displacement of the beam end and the system response was measured for different places. These responses are shown in Fig. 2. The first response, labelled "Table", was measured with energy harvesting system on the hand and the hand was propped on a table. The second response, labelled "Hand", was measured in free hand and the last response, labelled "Head", was measured on the head in an ear area. The measured responses confirm that using of the motion equation (1) is not correct for energy harvesting analyses in case of biomedical devices. The human body damps energy harvester oscillation. The differential equation (1) has to be extended to a model of the human body behaviour and this model has to be verified for design of harvester parameters.

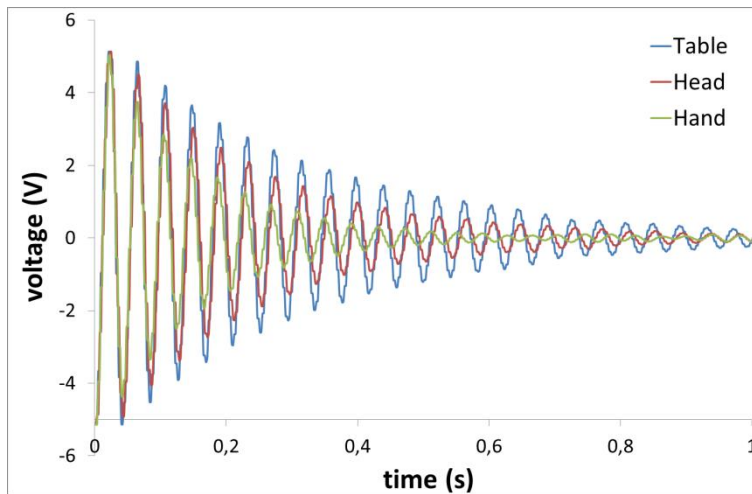


Fig. 2: Response of Piezo-electric converter on initial displacement; for different position of energy harvester (fixed on head, in hand and in hand propped on table).

3. Experimental Analyses of Energy Harvesting from Human Motion

However the presented piezo converter can be used for experimental analyses of energy harvesting from human body motion. The piezo energy harvesting system was fixed in head area and voltage responses were measured. The example of the voltage measurement is shown in Fig. 3. This measurement provides response of piezo energy harvesting system during a fine walking.

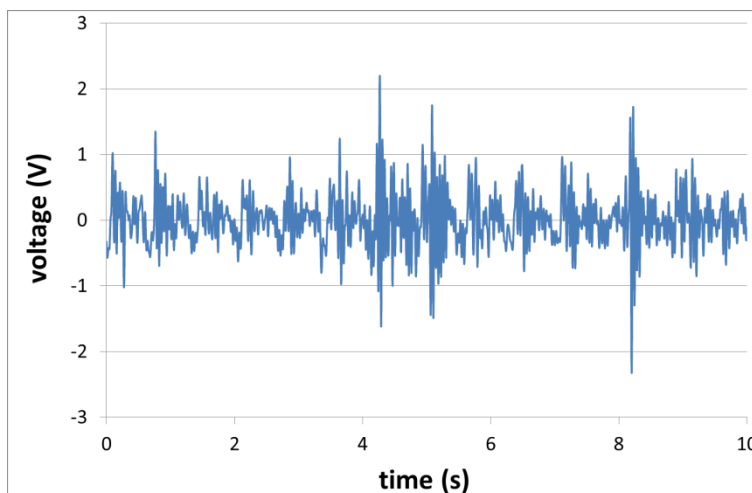


Fig. 3: Response of piezo-electric converter on human walking.

There is advantage than a head area does not provide such damping effect as hands, legs or back. This experiment shows that very low excitation can provide significant voltage response of piezo energy harvester. Several human body behaviours were analysed and the results are presented in Tab. 1. The presented values are range of maximal voltage peak in open circuit for different human body behaviours.

Tab. 1: Generated voltage (open circuit) for different body behaviour.

Body behaviour	Generated voltage peaks
<i>breathe</i>	200 mV
<i>breathe deeply</i>	300 - 400 mV
<i>facial gestures</i>	400 - 600 mV
<i>speech</i>	600 - 800 mV
<i>walking</i>	1 - 1.2 V
<i>jumping</i>	3 - 5 V

4. Conclusions

The analytical analysis of harvester power from the ordinary motion equation is not suitable for predict of harvested power from human behaviour such for engineering's applications. This analytical model has to be extended to active human body behaviour for correct energy harvesting analysis for biomedical analyses. Otherwise the presented experimental results are useful for energy harvesting analysis without energy harvester model with correct excitation and human body feedbacks.

The experimental results of the simple piezo energy harvesting system shows that voltage response of thin film piezo element are sufficient for processing with current ultra-low power electronics. Recent advances in integrated circuit technology provides ultra-low power systems for biomedical applications (Chandrakasan et al., 2008) with power consumption approximately in range 10 – 100 μ W. The results promise that the energy harvesting system in the head area can provide enough energy for powering of the developed artificial cochlea.

However only open voltage responses were measured and next step of our development is design of power management circuit which can provide optimal power point tracking and output power of the energy harvesting system will be analysed. Generally output power of these mechanical converts depends on their mass. Output power in range 10 – 100 μ W are expected from volume for the artificial cochlea but this power is not provided continuously, only in a burst mode such is shown in Fig. 3.

The experimental results during different human body behaviours provided a preliminary view on energy harvesting technology in biomedical applications. Energy harvesting technologies are logical concept for powering of biomedical devices which can improve life of patients, it depends on clinical needs. However there is long way to implement energy harvesting system to biomedical devices.

Acknowledgement

This paper has been supported by the project "Research of the Micro Electro Mechanical Artificial Cochlea Based on Mechanical Filter Bank" GAČR 13-18219S under the Czech Science Foundation (CSF).

References

- Abdi, H., Mohajer N., Nahavandi S. (2013) Human Passive Motions and a User-Friendly Energy Harvesting System. *Journal of Intelligent Material Systems and Structures* .
- Accoto, D., Calvano, M., Campolo, D., Salvinelli, F., Euglielmelli, E. (2009) Energetic Analysis for Self-Powered Cochlear Implants. *Annual International Conference of the IEEE Engineering in Medicine and Biology Society. IEEE Engineering in Medicine and Biology Society. Conference 2009*, pp. 4860-4863.
- Beker, L., Zorlu, O., Goksu, N., Kulah, H. (2013) Stimulating Auditory Nerve with MEMS Harvesters for Fully Implantable and Self-Powered Cochlear Implants. In: *2013 Transducers & Eurosensors XXVII: 17th International Conference on Solid-State Sensors, Actuators and Microsystems (Transducers & Eurosensors XXVII)*, pp. 1663-1666.
- Delnavaz, A., Voix, J. (2014) Energy Harvesting for In-Ear Devices Using Ear Canal Dynamic Motion. *IEEE Transactions on Industrial Electronics* 61 (1), pp. 583-590.
- Goll, E., Zenner, H-P., Dalhoff, E. (2011) Upper Bounds for Energy Harvesting in the Region of the Human Head. *IEEE Transactions on Bio-Medical Engineering* 58 (11), pp. 3097-3103.
- Hadas, Z., Singule, V. (2011) Energy Harvesting - Opportunity for Future Remote Applications. Edited by V Fuis. *Engineering Mechanics 2011*, pp. 167-170.
- Hadas, Z., Ondrusek, C., Singule, V. (2010) Power Sensitivity of Vibration Energy Harvester. *Microsystem Technologies* 16 (5), pp. 691-702.
- Chandrakasan, A., P, Naveen Verma, Daly D.C. (2008) Ultralow-Power Electronics for Biomedical Applications. *Annual Review of Biomedical Engineering* 10, pp. 247-274.
- Khaligh, A. (2010) Kinetic Energy Harvesting Using Piezoelectric and Electromagnetic Technologies—State of the Art. *IEEE Transactions on Industrial Electronics* 57 (3), pp. 850-860.
- Lay-Ekuakille, A., Vendramin, G., Trotta, A., Mazzotta G. (2009) Thermoelectric Generator Design Based on Power from Body Heat for Biomedical Autonomous Devices. In *2009 IEEE International Workshop on Medical Measurements and Applications*, pp. 1-4.
- Williams, C.B., Yates, R.B. (1996) Analysis of a Micro-Electric Generator for Microsystems. *Sensors and Actuators A: Physical* 52 (1-3), pp. 8-11.

EXPERIMENTAL EVALUATION OF THE EFFECTS OF A CONCRETE BARRIER TO PRESSURE WAVE PROPAGATION

R. Hájek^{*}, M. Foglar^{**}

Abstract: *This paper presents the results of an experimental program focused on measuring the parameters of the blast wave resulting from explosive detonation and possibilities of influencing propagation of this blast wave in order to minimize risk of injury of people near the explosion. Multiple arrangements of solid blast barriers are proposed and experimentally evaluated. The results obtained from the experiments are presented and explained. Thanks to the use of TNT charge, the experimental results can be directly compared to data derived from other blasts without barriers. That presents a valid basis for determination of the overall barrier effectiveness in reducing overpressure at the front of the blast wave.*

Keywords: Blast Wave, Experiment, Barrier.

1. Introduction

Due to rise of the threat of terrorist attack, the research in the field of blast loading of structures and their interiors has gained considerable attention in the recent years. Buildings such as railway stations, airports or embassies ought to be designed to ensure as much safety of the users as possible. The structure shall not collapse due to any of the considerable design situations. Furthermore, measures shall be taken to reduce the severity of the explosion, i.e. the magnitude of the pressure wave coming from epicentre of the explosion and the amount of potentially harmful flying debris.

An experimental program was proposed in order to determine ways to influence propagation of the blast wave by a system of concrete blast barriers.

2. Experimental Program

The experimental program was performed by the Institute of Energetic Materials, Faculty of Chemical Technology, University of Pardubice, Czech Republic. Prior to the experiment itself, a numeric study was conducted to predict the behaviour of the pressure wave in interaction with solid barrier and multiple arrangements of blast barriers which were designed. The pure TNT charge was used as an explosive. That means the results obtained could be easily compared with experimental data from other authors. Pachman et al. (2013) and Foglar and Kovář (2013) conducted series of experiments with varying yield and standoff distance from the explosive charge.

2.1. Scaling

Given typical dimensions of public building and predicted maximal weight of an explosive charge to be carried by a single person, it was decided to conduct experiments in reduced scale 1: n . Widely used scaling laws (Henrych, 1973) state:

$$A_{real.} = A_{model} \cdot n \quad (1)$$

$$W_{real.} = W_{model} \cdot n^3 \quad (2)$$

where n is a scaling factor, A is any parameter of length and W is weight of the explosive.

^{*} Ing. Radek Hájek: Department of Concrete and Masonry Structures, Czech Technical University in Prague, Thákurova 2077/7, 166 29, Prague; CZ, radek.hajek@fsv.cvut.cz

^{**} Ing. Marek Foglar, PhD.: Department of Concrete and Masonry Structures, Czech Technical University in Prague, Thákurova 2077/7, 166 29, Prague; CZ, marek.foglar@fsv.cvut.cz

One additional arrangement was considered (1C). Five precast walls were positioned in line and were equipped with custom made steel console pointing at 45 degree angle towards the explosive. This arrangement was added to the original set because the numerical study predicted greater effectiveness of angled shape than basic rectangular shape used in arrangements 1A, 1B, 1D and 1E.

2.3. Data collection and results

During the experiments, the pressure sensors were used to measure the peak overpressure at the front of passing pressure wave. For each arrangement, the sensors were placed in multiple distances with step of 1000 mm as shown in Fig. 1. Each experimental arrangement was repeated at least twice.

The obtained results are summarized in Fig. 3 and Fig. 4. The figures show comparison of the measured peak overpressure on the front of passing blast wave for each considered arrangement and for situation without any barrier. Rectangular barriers (Fig. 3) do not appear to have any significant effect on the value of peak overpressure. On the other hand, the angled barrier (Fig. 4) has proven that there is a possibility of influencing the propagation of the pressure wave with rigid barriers.

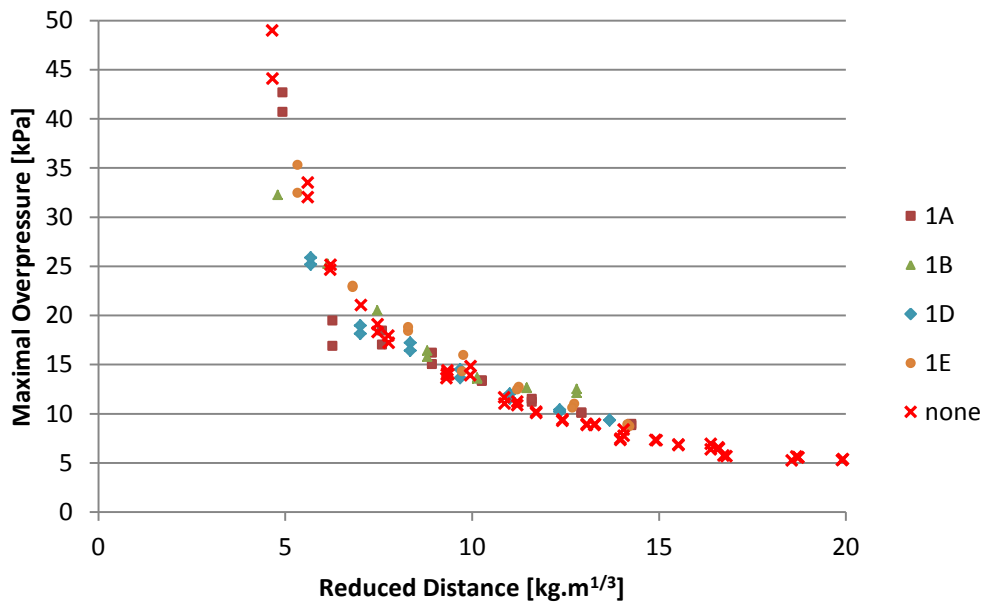


Fig. 3: Comparison of the measured peak overpressure behind barriers type 1A, 1B, 1D and 1E with experiment without barriers (Pachman et al., 2013).

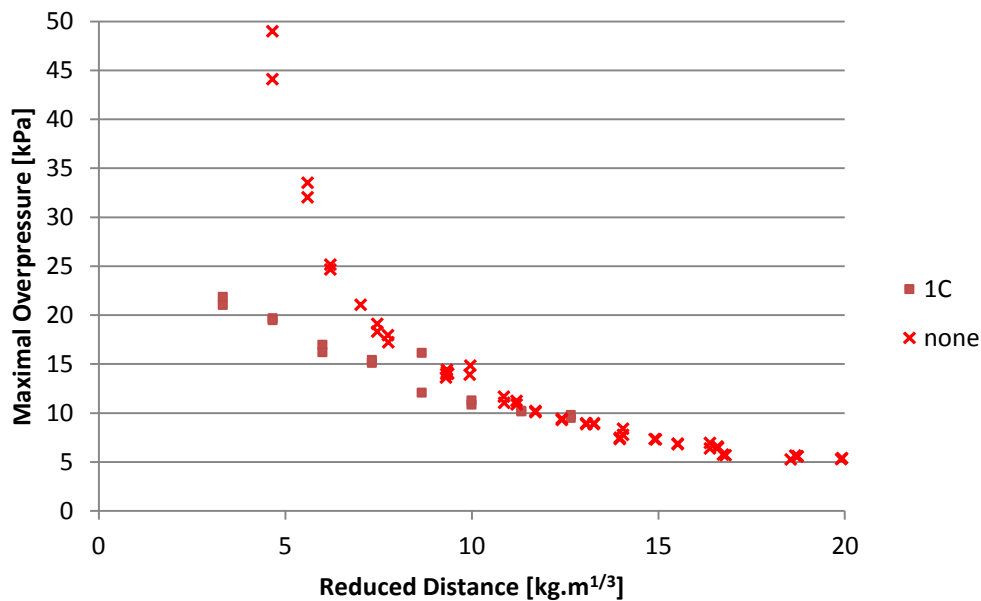


Fig. 4: Comparison of measured peak overpressure behind barrier type 1C with experiment without barriers (Pachman et al., 2013).

3. Conclusions

Although experiments were executed as planned, the results failed to prove predicted effectiveness of solid rectangular barriers. However the angled design of barrier type 1C showed some optimistic results and will most likely determine direction of further research in field of barrier arrangement optimization.

The results also indicate that even if barrier type 1C has some effect on lowering the peak overpressure, the effect is limited to the area directly behind the barrier. In greater distance the effect diminishes rapidly and pressure wave resumes its original strength. That leads to the assumption, that the very effective reduction of the peak overpressure in greater area is not achievable with rigid barriers. The main benefit of such barriers would be the absorption of potentially harmful flying debris carried by the blast wind.

Experimental data will be subsequently used for calibration of numerical FEM models used to predict pressure wave propagation. If satisfactory agreement between experiment and numerical model would be achieved, the need for expensive experiments would be reduced. Computer modelling of experiments presented in this paper can be found in Hájek & Foglar (2014).

Acknowledgements

The support of the Ministry of the Interior of the Czech Republic project no. VG20132015114 and the Czech Republic Grant Agency project no. 13-30441S is kindly acknowledged.

References

- Foglar, M., Kovář, M. (2013) Conclusions from experimental testing of blast resistance of FRC and RC bridge decks, *International Journal of Impact Engineering*, Volume 59, pp. 18-28, ISSN 0734-743X.
- Hájek, R. & Foglar, M. (2014) Numerical modelling of interaction between pressure wave and rigid barrier, In: *Proc. 20th International Conference Engineering Mechanics 2014*, Svratka, Czech Republic, pp. 212-215.
- Henrych, J. (1973) *The dynamics of explosion and its use*. Academia, Prague. 412 p., (in Czech).
- Huang, Y., Willford, M. R. (2012) Validation of LS-DYNA® MMALE with Blast Experiments. In: *12th International LS-DYNA Users Conference*. Detroit, USA.
- Makovička, D., Janovský, B. (2008) *Handbook of antiexplosion protection of structures*, CTU Press, Prague. ISBN 978-80-01-04090-4.
- Pachman, J., Šelešovský, J., Künzel, M. (2013) Blast wave parameters of small charges: trinitrotoluene (TNT) and urea nitrate (UNi), In: *Proc. of New trends in Research of Energetic Materials (NTREM)*, Pardubice, pp. 818-826.

NUMERICAL MODELLING OF INTERACTION BETWEEN PRESSURE WAVE AND RIGID BARRIER

R. Hájek^{*}, M. Foglar^{**}

Abstract: *This paper is focused on computer modelling of blast wave propagation in interaction with rigid blast barriers. The 3D numerical FEM model was created using LS-DYNA software. The pressure wave reflections are also studied. Suitable material model of explosive charge and equations of state for TNT and air are presented. The paper also includes validation of FEM analysis results in comparison to experimental data and FEM model calibration to ensure accuracy of obtained results in various arrangements. If FEM modelling produces sufficiently accurate results, the need for many expensive experiments will be eliminated and experiments only limited to validation tests.*

Keywords: Blast Wave, FEM modelling, Barrier, LS-DYNA.

1. Introduction

Explosions can occur because of number of reasons, most likely by an accident or a terrorist attack. Public buildings such as railway stations, airports or embassies should be constructed to provide safety to the people inside. That could be arranged for example by an installation of blast barriers.

An experimental program was conducted in order to determine ways of influencing the propagation of the blast wave by a system of concrete blast barriers. Due to high cost, it is appropriate to replace experiments with computer modelling. However the accuracy of computer model can vary significantly so it is imperative to validate results of such model by comparison with actual experiment. When properly calibrated, the FEM model can be useful, fast and cheap tool for an optimization process.

2. Computer Modelling

The proposed experiments were performed by Institute of Energetic Materials, Faculty of Chemical Technology, University of Pardubice, Czech Republic. Prior to the experiment itself a preliminary numerical study was conducted to predict behaviour of pressure wave in interaction with solid barrier and multiple arrangements of blast barriers were designed. Four blast barrier arrangements were then chosen for experimental measuring of the peak overpressure at the front of passing blast wave after explosion of TNT charge in standoff distances from 1 to 8 m behind the barriers.

2.1. Model calibration

Pure TNT charge was used as an explosive. This means that obtained results can be easily compared with experimental data from other authors. Pachman et al. (2013) conducted series of experiments with varying yield and standoff distance from the explosive charge, the same as and Foglar and Kovář (2013). The results were used for calibration of the material models of air and explosive on elementary computer model without any barriers. Equations of state used to define both materials had to be also properly calibrated. The Barriers were then added and the model with barriers was evaluated again based on data obtained from experimental program (Hájek & Foglar, 2014).

* Ing. Radek Hájek: Department of Concrete and Masonry Structures, Czech Technical University in Prague, Thákurova 2077/7, 166 29, Prague; CZ, radek.hajek@fsv.cvut.cz

** Ing. Marek Foglar, PhD.: Department of Concrete and Masonry Structures, Czech Technical University in Prague, Thákurova 2077/7, 166 29, Prague; CZ, marek.foglar@fsv.cvut.cz

2.1.1. Meshing and element type

A finite element mesh was created using ANSYS and LS-DYNA software. There were two separate meshes defined; first for air and explosive, second for barriers. The contact between the two meshes is automatically generated by the LS-DYNA solver. The air and explosive are modelled using ALE (Arbitrary Lagrangian-Eulerian) elements, barriers are modelled using standard solid elements. Mesh size and timestep of the explicit dynamics solver engine have dramatic impact on model accuracy. The size of the air and explosive ALE elements was determined based on scale of the experiment and comparison with experimental data from Pachman et al. (2013). Maximal length of element edge is 25 mm. Hexahedral mesh is used for air and explosive, tetrahedral mesh for concrete barriers.

2.1.2. Modelling of air and explosive material

Material model 009-NULI was defined for air elements and model 008-HIGH_EXPLOSIVE_BURN was defined for the TNT charge.

The equation of state for ideal gas (1) was used to model the air. Parameters of the equation were defined according to Huang & Willford (2012).

$$P = (C_4 + C_5 \mu) e_{ipv0} = (\gamma - 1) \frac{\rho}{\rho_0} e_{ipv0} \quad (1)$$

where:

$$C_4 + C_5 = \gamma - 1 = 0.4$$

$$P_0 = 101.3$$

$$v_0 = 1.0$$

$$e_{ipv0} = P_0 v_0 / (\gamma - 1)$$

For TNT the JWL (Jones-Wilkins-Lee) equation of state was used (2). Calibration of this equation of state is quite difficult. The parameters were derived from Zukas & Walters (1997) and Toussaint & Durocher (2008).

$$p = A \left(1 - \frac{\omega}{R_1} \frac{\rho}{\rho_0} \right) e^{-R_1 \frac{\rho_0}{\rho}} + B \left(1 - \frac{\omega}{R_2} \frac{\rho}{\rho_0} \right) e^{-R_2 \frac{\rho_0}{\rho}} + \omega E \frac{\rho}{\rho_0} \quad (2)$$

2.1.3. Modelling of concrete barriers

The deformations of the barriers have an unintended impact on results. It was decided to model the concrete barriers as rigid structures. The simplified material model of barrier is linear elastic, but the value of modulus of elasticity E is significantly increased to provide rigid-like behaviour. The interaction between air and barrier was in question, but results clearly prove that blast wave is reflected of the barrier surface properly (Fig. 1).

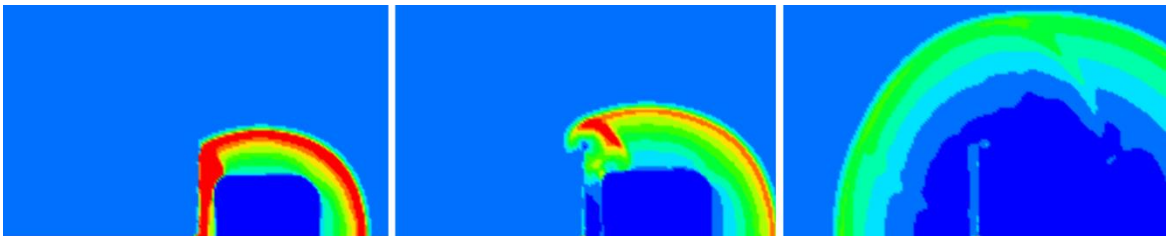


Fig. 1: Contours of overpressure: Blast wave interacting with rigid barrier.

2.2. Experimental program

Given typical dimensions of public building and predicted maximal weight of explosive charge to be carried by single person, it was decided to conduct experiments in reduced scale 1:n. Four arrangements were chosen for the reduced scale experiments (Fig. 2). Reinforced concrete precast panels were used to

model solid barriers (Fig. 3). Thorough information and complete results of the experiments can be found in Hájek & Foglar (2014).

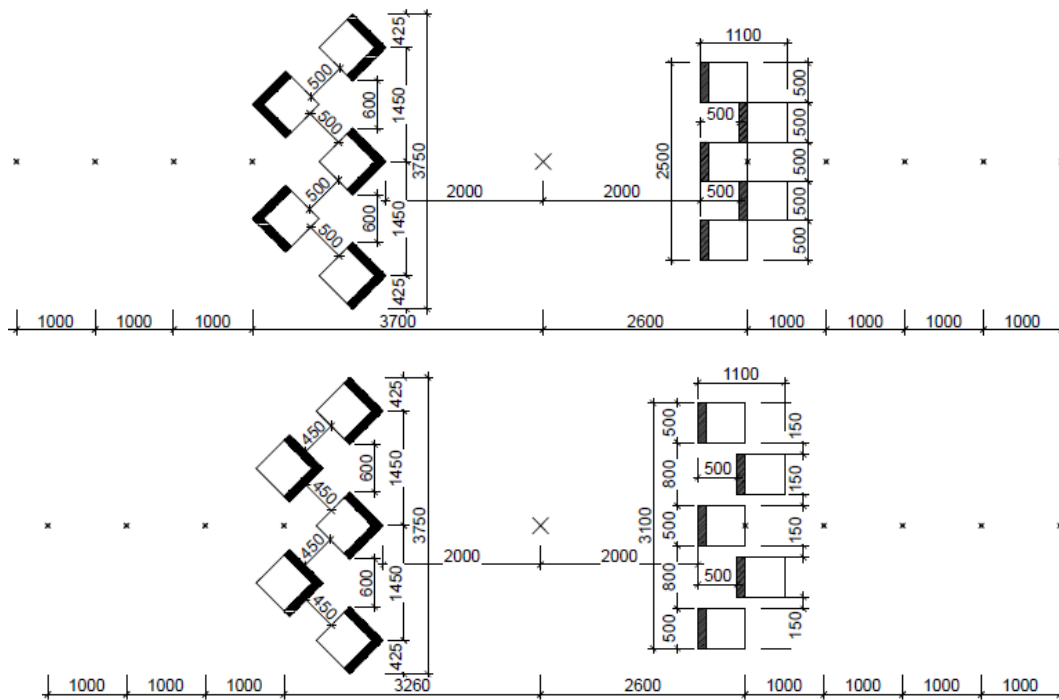


Fig. 2: Tested Arrangements of Concrete Barriers: 1A (top left), 1B (top right), 1D (bottom left), 1E (bottom right). Dimensions in mm.



Fig. 3: Barrier Layout 1A set up on site.

2.3. Validation of computer models with experimental results

During the experiment, pressure sensors were used to measure the peak overpressure at the front of passing pressure wave. For each arrangement, sensors were placed in multiple distances with step of 1000 mm as shown in Fig. 1. Each experimental arrangement was repeated at least twice. Values of element pressure at corresponding coordinates were obtained from the FEM model and compared to experimental data. The comparison is summarized in Fig. 4.

The results indicate that computer model is capable of predicting the peak overpressure with relatively high accuracy in most cases. The time difference between peaks in standoff distance of 0 m and 1 m was also predicted correctly.

Based on the acquired data, it can be assumed that the model is calibrated correctly enough to be used for optimization of barrier shape and arrangement. This way a large number of possibilities can be studied without the need for many expensive experiments.

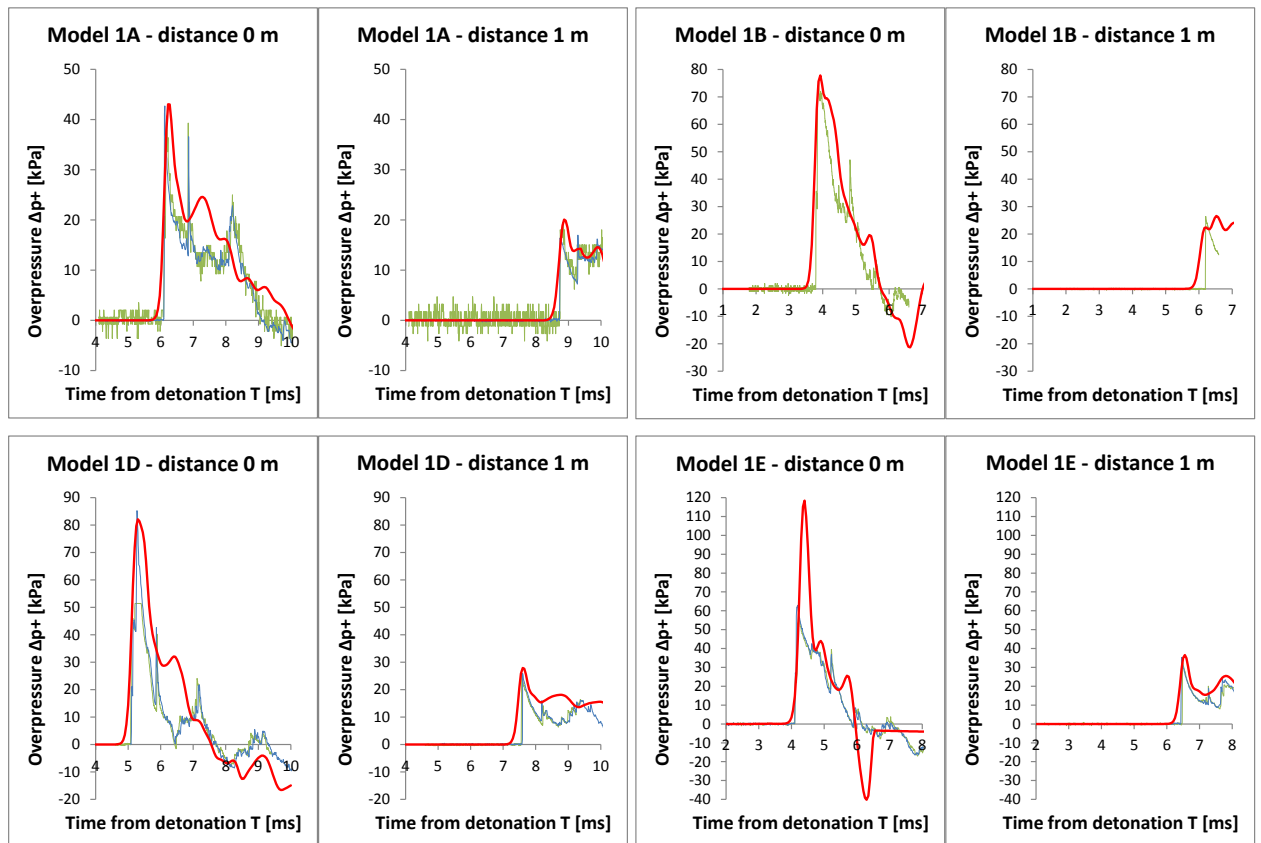


Fig. 4: Comparison of the measured and computed overpressure behind barrier for multiple arrangements (FEM results red, experiments blue and green).

3. Conclusions

Comparison of computer modelling results and experimental data shows that FEM modelling of a blast event can in particular cases and boundary conditions substitute the experimental measuring. The credibility of the results is defined by the configuration of the model. The calibrated model can be useful when optimizing the barrier arrangement because it can dramatically reduce cost of the experiment. On the other hand, at least one validation test should still be performed for each change in materials or major change in arrangement of the experiment.

Acknowledgements

The support of the Ministry of the Interior of the Czech Republic project no. VG20132015114 and the Czech Republic Grant Agency project no. 13-30441S is kindly acknowledged.

References

- Foglar, M., Kovar, M. (2013) Conclusions from experimental testing of blast resistance of FRC and RC bridge decks, *International Journal of Impact Engineering*, Vol. 59, pp. 18-28, ISSN 0734-743X.
- Hájek, R., Foglar, M. (2014) Experimental evaluation of effects of a concrete barrier to pressure wave propagation, In: *Proc. 20th International Conference Engineering Mechanics 2014*, Svratka, Czech Republic, pp. 208-211.
- Huang, Y., Willford, M. R. (2012) Validation of LS-DYNA® MMALE with Blast Experiments. In: *Proceedings of 12th International LS-DYNA Users Conference*. Detroit, USA, 3 - 5 June 2012.
- Pachman, J., Šelešovský, J., Künzel, M. (2013) Blast wave parameters of small charges: trinitrotoluene (TNT) and urea nitrate (UNi), In: *Proc. New trends in Research of Energetic Materials (NTREM)*, Pardubice, pp. 818-826.
- Toussaint, G., Durocher, R. (2008) Finite Element Simulation using SPH Particles as Loading on Typical Light Armoured Vehicles, In: *Proc. 10th International LS-DYNA Users Conference*, Dearborn, MI, USA, 8 - 10 June 2008. ISBN 0-9778540-4-3.
- Zukas, J. A., Walters, W. P. (1997) *Explosive Effects and Applications*. Springer-Verlag, New York. 460 p., ISBN 9780387982014.

EXPERIMENTAL VERIFICATION OF THEORETICAL MODELS TO CALCULATE THE HEAT TRANSFER COEFFICIENT IN THE SHELL-AND-TUBE HEAT EXCHANGER

J. Havlík*, T. Dlouhý**

Abstract: *This paper experimentally verifies the validity of theoretical models to calculate the heat transfer coefficient in shell-and-tube heat exchangers. Determination of the HTC is a complex problem, as a large deviation in the comparison of theoretical models and experiments commonly occurs. The methods by Kern, Bell-Delaware and Flow-stream analysis method for the evaluation of HTC in a vertical shell and tube condenser are compared with the results of measurements in the range of Reynolds number from 1200 to 6300. The HTC values by the Kern method reach the top boundary of the experimental results while the results of the Bell-Delaware method and the Stream-flow analysis method are at the bottom. Therefore, usage of the Bell-Delaware method and the Stream-flow analysis method is suitable in accordance with the design assurance.*

Keywords: Heat transfer coefficient, Shell-and-tube heat exchanger.

1. Introduction

The heat transfer coefficient (HTC) is an important parameter for the design of heat exchangers. Its value depends on the technical solution of the heat exchanger and the thermo-mechanical properties of the flowing fluid. This paper deals with shell and tube heat exchangers (Fig. 1). Methods commonly recommended for the calculation of shell-side coefficient values are the Kern method, the Bell-Delaware method and the Flow-stream analysis method (Hewitt et al., 1994). The Kern method, which has been the conventional method for a long time, is still used due to its simplicity, although its results are significantly higher in comparison with the other two methods (see Fig. 2). Determination of the HTC is a complex problem, as a large deviation in the comparison of theoretical models and experiments commonly occurs. Experimental values of the HTC for shell-and-tube heat exchanger may prove the difference between the theoretical methods and the real operation of the heat exchanger.

2. Experiment

Experiments are carried out on a vertical shell-and-tube heat exchanger (Fig. 1) in which the condensing water vapor flows downwards in vertical tubes and a cooling water countercurrent flows in the shell part. The vapor outlet is open to the atmosphere, thus the steam condenses at atmospheric pressure. The tube bundle is formed by 49 tubes with a length of 865 mm, an outside diameter of 28 mm and an inside diameter of 24 mm. The tubes are arranged in staggered arrays with a triangular tube pitch of 35 mm. The cross-section of the shell is rectangular in shape with a size of 223 mm by 270 mm. Seven segmental baffles (223x230mm) are used in the shell section, the tube-to-baffle diametral clearance is 1 mm and there is no shell-to-baffle diametral clearance. The material is stainless steel 1.4301 (AISI 304).

2.1. Measurements

Measured parameters are the outlet and inlet cooling water temperature, the cooling water flow, the inlet vapor pressure, the inlet vapor temperature and the amount of vapor condensate.

* Ing. Jan Havlík: Department of Energy, Engineering, Czech Technical University in Prague, Technická 4; 166 07, Prague; CZ, jan.havlik@fs.cvut.cz

** Assoc. Prof. Ing. Tomáš Dlouhý, CSc.: Department of Energy, Engineering, Czech Technical University in Prague, Technická 4; 166 07, Prague; CZ, tomas.dlouhy@fs.cvut.cz



Fig. 1: Vertical shell-and-tube condenser.

2.2. Determination of the heat transfer coefficient

The HTC is calculated from the heat balance of the exchanger. The total heat transfer rate of the heat exchanger is given by

$$Q = M_w \cdot c_w \cdot (t_{w,out} - t_{w,in}) \quad (1)$$

where M_w is the total cooling water mass flow, c_w is the specific heat capacity, $t_{w,out}$ is the outlet cooling water temperature and $t_{w,in}$ is the inlet cooling water temperature. The total heat flow rate of the heat exchanger is also given by

$$Q = U \cdot S \cdot \Delta t_{log} \quad (2)$$

where U is the overall heat transfer coefficient, S is the total area of the outside of the tubes and Δt_{log} is the logarithmic mean temperature difference. The shell-side HTC α_w is given from the following equation to calculate the overall heat transfer coefficient:

$$U = \frac{1/D_e}{\frac{1}{d_i \cdot \alpha_p} + \frac{1}{2k} \ln\left(\frac{D_e}{d_i}\right) + \frac{1}{D_e \cdot \alpha_w}} \quad (3)$$

where d_i is the inside diameter of the tubes, α_p is the tube-side HTC (vapor condensation), k is thermal conductivity (material 1.4301), D_e is the outside diameter of the tubes. The heat transfer coefficient α_p is calculated according to the Nusselt model for filmwise condensation on vertical surfaces (Incropera & DeWitt, 1996 or Hewitt et al., 1994).

The value of the overall HTC primarily depends on the third term of the right side of Eq. (3), where the value of thermal resistance ($1/\alpha_w$, see Fig. 2) is significantly higher than the value of thermal resistance of the first and the second terms (approximately $1/10^4 \text{ m}^2\text{K/W}$). Therefore, these terms do not significantly influence the result of Eq. (3) and it is possible to well determine the value α_w .

3. Theoretic Methods

Hewitt et al. (1994) represent the methods as follows. The first attempt to provide methods for calculating the shell-side heat transfer coefficient was the Kern method, which was an attempt to correlate data for standard exchangers by a simple equation analogous to equations for the flow in the tubes. Although the Kern method is not particularly accurate, it does allow a very simple and rapid calculation of shell-side coefficients to be carried out and is still successfully used.

In the Bell-Delaware method, correction factors for the specific configuration were introduced. Nevertheless, empirical correction factors are limited to the range of configuration for which the database was obtained.

A more generic method, covering the full range of possible arrangements, is the Flow-stream analysis method in which fluid streams were designed for each of the possible flow routes through the exchanger. The stream-analysis technique is particularly suitable for computer calculation. Therefore, a simplification for calculating it by hand has been developed.

Generally speaking, the Kern method offers the simplest route, the Bell-Delaware method offers the most widely accepted method and the Flow-stream analysis method offers the most realistic method.

3.1. Kern method

Based on data from industrial heat transfer operations and for a fixed baffle size (75 % of the shell diameter), the following equation was introduced:

$$\alpha_w = \frac{k}{D} \cdot 0.36 \cdot Re^{0.55} \cdot Pr^{0.33} \quad (4)$$

where k is fluid thermal conductivity, D is the relevant characteristic dimension. No change in viscosity from the bulk to the wall is assumed.

3.2. Bell-Delaware method

In this method, correction factors for the following elements were introduced:

- 1) Leakage through the gaps between the tubes and the baffles and the shell, respectively.
- 2) Bypassing of the flow around the gap between the tube bundle and the shell.
- 3) Effect of the baffle configuration (i.e., a recognition of the fact that only a fraction of the tubes are in pure cross-flow).
- 4) Effect of the adverse temperature gradient on heat transfer in laminar flow.

The ideal cross-flow heat transfer coefficient is given by

$$\alpha_c = \frac{k}{D} \cdot 0.273 \cdot Re^{0.653} \cdot Pr^{0.34} \quad (5)$$

then the shell side heat transfer coefficient is given by

$$\alpha_w = \alpha_c \cdot J_C \cdot J_L \cdot J_B \quad (6)$$

where J_C is the correction for the baffle configuration, J_L is the correction factor for leakage, J_B is the correction factor for bypass in the bundle-shell gap.

3.3. Flow-stream analysis (Wills and Johnson) method

This method analyses in detail the flow in a heat exchanger. The fluid flows from place A to place B via various routes. Leakage flows occur between the tubes and the baffle and between the baffle and the shell. Part of the flow passes over the tubes in cross-flow and part bypasses the bundle. The cross-flow and bypass streams combine to form a further stream that passes through the window zone. A correction factor F_{cr} , which adjusts the mass flow calculation (the Reynolds number), takes these effects into account. Then the shell-side heat transfer coefficient is given by

$$\alpha_w = \frac{k}{D} \cdot 0.273 \cdot Re_{cr}^{0.653} \cdot Pr^{0.34} \quad (7)$$

where

$$Re_{cr} = F_{cr} \cdot Re \quad (8)$$

4. Results

The experiments are carried out in the range of heat exchanger thermal power from 20 to 60 kW, with a logarithmic mean temperature difference from 6 to 28 °C and the Reynolds number from 1200 to 6300

(76 measured states). The comparison of the experimental results with the results of the theoretical methods is shown in Fig. 2. The deviation of the measurements ranges from 4 % up to 7 % in the dependence on operation parameters.

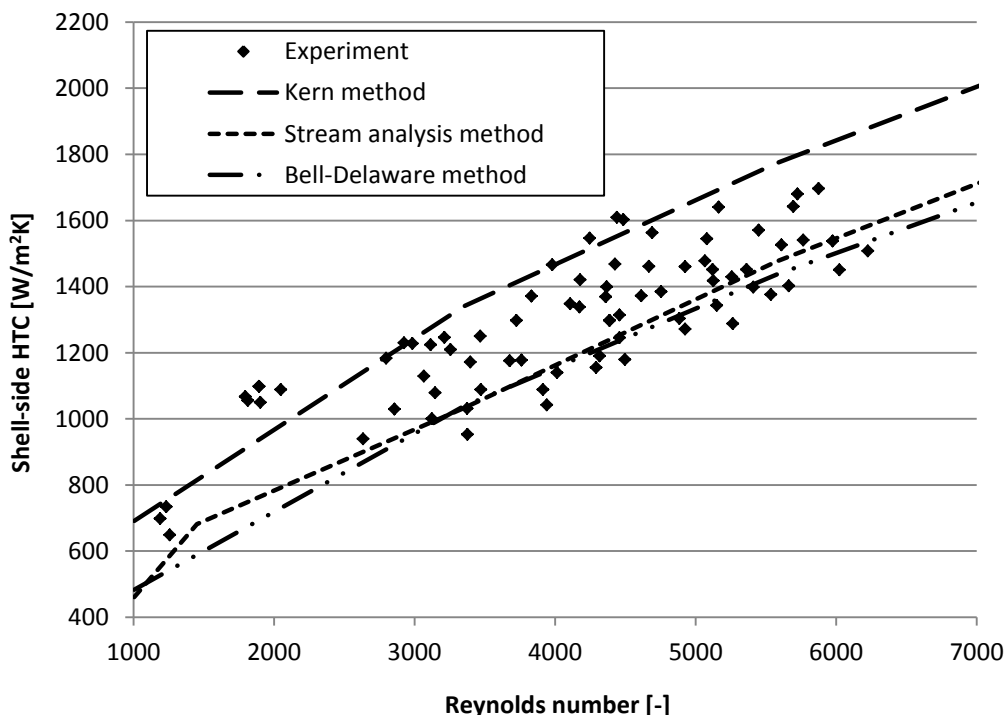


Fig. 2: Comparison of experimental and theoretical results.

The total variance in the experimental results is assumed concerning the complexity of the heat transfer process and various operation parameters.

5. Conclusions

This paper experimentally verifies the validity of theoretical models to calculate the HTC in shell and tube heat exchangers. The Kern, Bell-Delaware and Stream-flow analysis methods for evaluation of HTC in a vertical shell and tube condenser are compared with the results of experimental measurements in the range of the Reynolds number from 1200 to 6300.

The HTC values by the Kern method reach the top boundary of the experimental results while the results of the Bell-Delaware method and the Stream-flow analysis method are at the bottom. Therefore, usage of the Bell-Delaware method and the Stream-flow analysis method is suitable in accordance with the design assurance.

Acknowledgement

This work was supported by the Grant Agency of the Czech Technical University in Prague, grant No. SGS13/134/OHK2/2T/12 and the Ministry of Education, Youth and Sports CR, a research project MSM 6840770035.

Reference

- Hewitt, G. F., Shires, G. L., Bott T. R (1994) Process Heat Transfer, Begell house, New York.
 Incropera, F. P. & DeWitt, D. P. (1996) Introduction to heat transfer, Wiley-Academy, New York.

MODIFIED COMPACT TENSION TEST: THE INFLUENCE OF THE STEEL BARS POSITION

T. Holušová^{*}, S. Seitl^{**}, A. Fernández-Canteli^{***}

Abstract: *Testing and analysis of fatigue behavior of homogeneous materials, such as concrete or other cement based composites, are one major problem being studied in this scientific field. In this contribution, adaptation of the compact tension test, well known its use in the testing of metallic materials, is pursued for crack propagation rate measurement on cement based composites using cylindrical specimens. In particular, the influence of the steel bars position on the fracture parameters is studied in the modified compact tension test. The numerical study is performed by ATENA 2D. The results are compared by Load-COD diagrams and the variation of the fracture parameters values is discussed.*

Keywords: Modified compact tension test, Concrete, Fracture parameters of concrete, FEM.

1. Introduction

The fatigue behavior of quasi-brittle materials is still a fairly unexplored scientific field. Several different setups for the experimental testing of cement based materials are available for fracture mechanics purposes, such as the three or four point bending test (RILEM, 1991), or the recently postulated wedge-splitting test (Brühwiller & Wittmann, 1990) for determination of the fracture-mechanics parameters of quasi-brittle materials (Karihaloo, 1995). Such configurations can be adopted for determining experimentally the fatigue resistance of the constructions under cyclic loads.

To obtain the adequate parameters, the specimens can simply be extracted from the real construction as a drill core without or with a small amount of reinforcement, and subsequently cut into several small cylindrical specimens. Though this specimen shape is suitable for cylindrical wedge-splitting static tests, the test setup is unfortunately unsuitable for a cyclic load since the test configuration is relatively complicated and the use of the wedge equipment is involved for repeated load, although preparation of the test specimens is very easy. The CT specimen (compact tension specimen) is well known from fatigue testing on metallic materials and after a convenient modification (see Fig. 1b) can be properly engaged for compact tension tests. A hole is drilled perpendicular to the specimen notch, through which two steel bars of 8 or 10 mm diameter are introduced and fixed by hart epoxy resin. Once the resin is hardened, the steel bars are gripped by their ends into the load machine and loaded under cyclic load.

In this paper, a numerical study of the influence of the steel bars position on the results of the modified compact tension test is performed by means of the finite element method (FEM) software ATENA 2D (Červenka Consulting, 2005). Three different positions of the steel bars are considered, which are marked as W (see Fig. 1) where W is the distance from the load axis to the opposite side of the specimen.

2. Numerical Model

According to the ASTM Standard E-399-06 (2006) recommendations for CT specimens, a ratio $D/W \approx 1.25$ between the load position parameter (W) and specimen diameter (D) was used, whereas by

^{*} Ing. Táňa Holušová: Institute of Physics of Materials, Academy of Science of the Czech Republic, v. v. i., Žitkova 22, 616 62 Brno, and Brno University of Technology, Faculty of Civil Engineering, Veveří 331/95, 602 00 Brno, CZ, holusova.t@fce.vutbr.cz

^{**} Ing. Stanislav Seitl, PhD.: Institute of Physics of Materials, Academy of Science of the Czech Republic, v. v. i., Žitkova 22, 616 62 Brno, CZ, seitl@ipm.cz

^{***} Prof. Alfonso Fernández-Canteli: University of Oviedo, Dept. of Construction and Manufacturing Engineering, Campus de Viesques, 332 03 Gijón, ES, afc@uniovi.es

Kim et al. (2009) this ratio was $D/W \approx 1.35 W$.

In Fig. 1 two possibilities are shown for creation of the modified compact tension test for cement based composites, although the shape of the specimen in Fig. 1a) was already used in the previous literature (Kim et al., 2009, Xu & Reinhardt, 1999).

Three sizes of parameter W are considered in this contribution: 100, 110 and 120 mm. For numerical study, configuration with steel bars gripped into the specimen (positions of steel bars see Fig. 1b) is modeled. For all positions of steel bars, the relative starting crack lengths α were 0.1; 0.15; 0.2; 0.3; 0.4 and 0.5. The symbol a in equation (1) indicates the starting notch length (notch thickness is around 3 mm) measured from the load axis. All these values are summarized in Tab. 1.

$$\alpha = \frac{a}{W} \quad (1)$$

Tab. 1: All considered dimensions for model of compact tension test.

W [mm]	α [-]	0.1	0.15	0.2	0.25	0.3	0.4	0.5
100	a [mm]	10	15	20	25	30	40	50
110	a [mm]	11	16.5	22	27.5	33	44	55
120	a [mm]	12	18	24	30	36	48	60

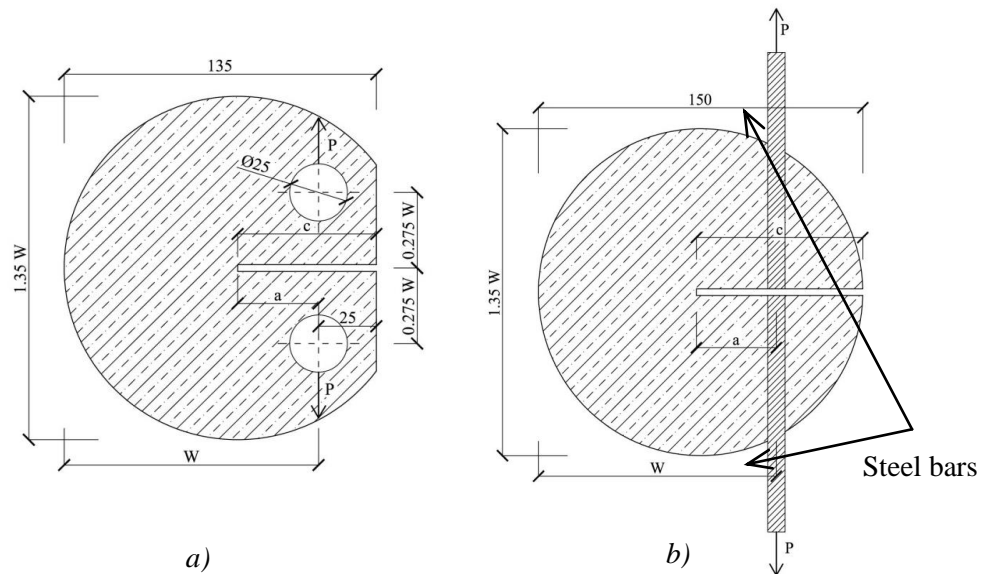


Fig. 1: Specimen for compact tension test: a) Standard one for metal materials (based on Knésl & Bednář, 1998); b) Modified specimen for cement based composites.

3. Numerical Calculation

The finite element software ATENA 2D was performed for calculation. The thickness of the specimens was in all cases equal to 100 mm. This value is relatively small, so the models were subjected under plane stress. For that occasion the concrete parts were modeled by the material model called SBETA and for modeling steel bars the material Plane stress elastic isotropic was used. Model SBETA is the material model recommended by software developers for modeling of concrete in ATENA 2D. The input values for both materials are summarized in Tab. 2.

For all models, the same finite element mesh with densification around starting crack (notch) to 0.1 mm was used, see Fig. 2. The basic element size for the model was 2 mm. In Fig. 2a), the model of the cylindrical specimen with diameter $D = 150$ mm, the position of the steel bars $W = 120$ mm and relative crack length $\alpha = 0.1$ is shown. Fig. 2b) shows a cylindrical specimen with the same diameter ($D = 150$ mm), but the position of the steel bars is $W = 100$ mm and relative crack length $\alpha = 0.5$.

Tab. 2: Input parameters of concrete and steel for ATENA 2D.

	Cube strength f_c [MPa]	Tensile strength f_t [MPa]	Young's modulus E [GPa]	Density ρ [kg/m ³]
Concrete	30	2.317	30.32	2300
Steel	-	-	210	7850

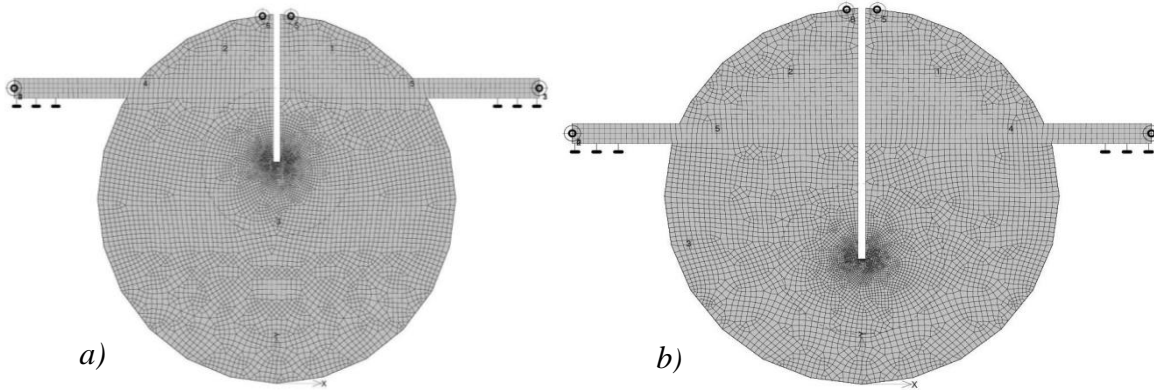


Fig. 2: Finite element mesh (2 mm with densification to 0.1 mm) and boundary conditions:
a) $D = 150$ mm, $W = 120$ mm, $\alpha = 0.1$; b) $D = 150$ mm, $W = 100$ mm, $\alpha = 0.5$.

4. Results and Discussion

The obtained numerical results are performed by Load-COD (Load – Crack Opening Displacement) diagram. For better visualization, selected Load-COD curves for relative notch length $\alpha = 0.1$; 0.25 and 0.5 are shown in Fig. 3. Loading curves for $\alpha = 0.1$ are marked by black lines, for $\alpha = 0.25$ are marked by double black lines and for $\alpha = 0.5$ gray lines were used.

In elastic parts of the loading curves in the diagram, the values are similar and trends of the decreasing parts are relatively parallel. There are two influences caught in Fig. 3. The first one is the influence of the starting relative crack length α and the second one is the influence of the steel bars position W according to the values of fracture energy calculated from loading curves in Fig. 3. The obtained values of fracture energy are not the final ones and are shown in Fig. 4.

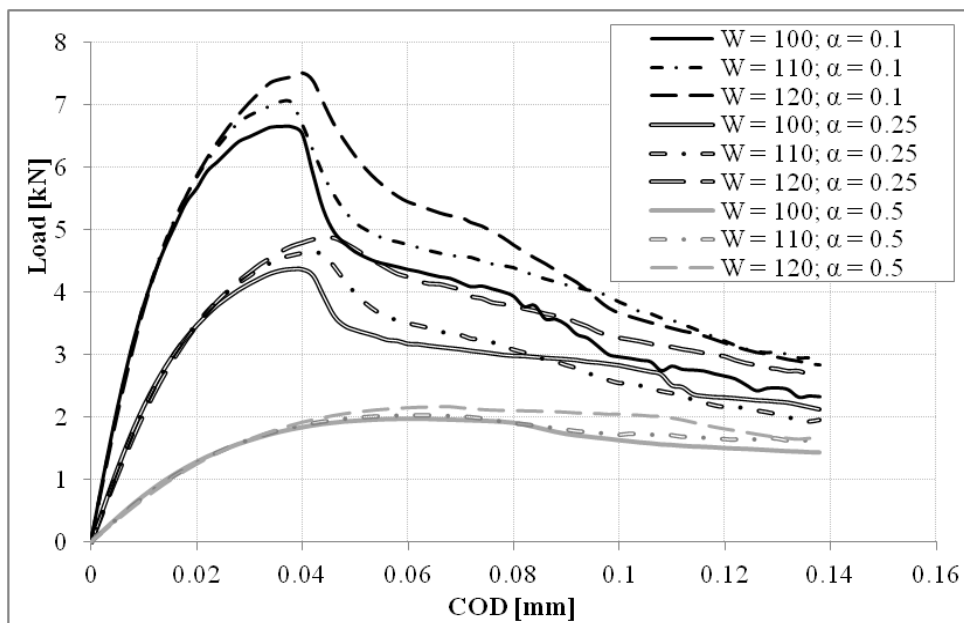


Fig. 3: Loading diagrams of selected CT configurations.

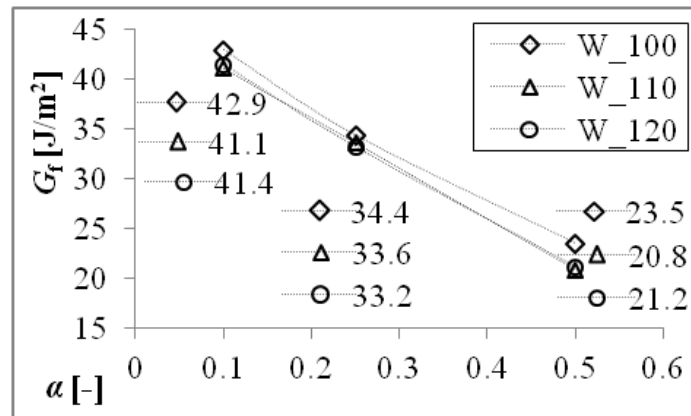


Fig. 4: Values of fracture energy obtained from the loading curves.

5. Conclusions

This contribution presents a part of the investigation of the compact tension test modification for use on cement based composites. The influence of the steel bars position was investigated. The results were presented and compared by loading diagrams and a diagram of the fracture energy values dependent on relative crack/notch length. The following conclusions can be drawn:

The values of maximum load are dependent on the position of the steel bars. A lower position means lower resistance to fatal damage. On the other hand, all three mentioned position of steel bars can be used in future investigations.

According to this numerical study preparation of an initial relative crack/notch length between 0.1 and 0.3. is recommended.

According to these values the results are independent of the steel bars position W , otherwise the position of the steel bars has an influence on the resistance of the specimens to fatal damage.

Acknowledgement

The paper was written by the support of the MEYS of the Czech Republic Nr. CZ.1.07/2.3.00/20.0214 and grant project Nr. M100411204 and by the Spanish Ministry of Science and Innovation, Ref. BIA2010-19920, and Ref. SV-PA-11-012 of the Dept. of Education and Sciences of the Asturian Regional Government.

References

- ASTM International Standard E399-06 (2006) Standard test method for linear-elastic method of plane-strain fracture toughness K_{IC} of metallic materials, pp. 1-32.
- Brühwiler, E. & Wittmann, F. H. (1990) The Wedge Splitting test, a new method of performing stable fracture mechanics tests, *Engineering Fracture Mechanics* Vol. 35, pp. 117-125.
- Červenka Consulting, s. t. o. - www.cervenka.cz.
- Karihaloo, B. L. (1995) *Fracture mechanics of concrete*, Longman Scientific & Technical, New York.
- Kim, H., Wagoner, M. P. & Buttlar, W. G. (2009) Numerical fracture analysis on the specimen size dependency of asphalt concrete using a cohesive softening model. *Construction and Building Materials* 23, pp. 2112-2120.
- Knésl, Z. & Bednář K. (1998) Two-parameter fracture mechanics: calculation of parameters and their values, IPM ASCR, Brno.
- RILEM Report 5 (1991) *Fracture Mechanics Test Methods for Concrete* (S. P. Shah & A. Carpinteri eds.), Chapman and Hall, London.
- Xu, S., Reinhardt, W. (1999) Determination of double-K criterion for crack propagation in quasi-brittle fracture, Part III: Compact tension specimen and wedge splitting specimens. *International Journal of Fracture* 98, pp. 179-193.

MEASUREMENT OF VIBRATION, FLOW AND ACOUSTIC CHARACTERISTICS OF A HUMAN LARYNX REPLICA

J. Horáček*, V. Bula*, V. Radolf*, T. Vampola**, M. Dušková***

Abstract: *The study presents results of in vitro measurements of voicing performed on the developed artificial larynx based on the CT images of human larynx taken during phonation. The measured phonation characteristics are in good agreement with the values found in human larynges. The knowledge of these characteristics for the vocal folds replica can be useful for experimental verification of developed sophisticated 3D computational finite element models of phonation due to relatively exactly defined input material and geometrical parameters, which is problematic to obtain reliably in humans.*

Keywords: Fluid-structure interaction, Flutter, Biomechanics of voice modeling, Phonation.

1. Introduction

The vocal folds, excited by the airflow, generate a primary laryngeal tone whose fundamental frequency corresponds to the vibration frequency of the vocal folds. In the airways above the vocal folds, i.e. in the vocal tract, the acoustic resonant phenomena modify the spectrum of the primary laryngeal tone, especially the higher harmonics. Understanding the basic principles of voice production is important for better interpretation of clinical findings, detection of laryngeal cancers or other pathologies and treatment of laryngeal disorders. Considering the inaccessibility of the vocal folds in humans exact airflow or tissue measurements in vivo are very restrained or impossible. Therefore, the physical models of the voice production are important tools in development and validation of theoretical models of phonation.

2. Model of the Human Larynx

The CT examination was performed for male trained singer (34 years old) after warm-up exercises. The subject was placed in a CT scanner in supine position and phonated a sustained vowel [a:] in a habitual pitch and comfortable loudness. The CT images were acquired by Toshiba–Aquilion CT machine with the time of the rotation 0.5 s and 510 slices of thickness 0.5 mm. The CT images were segmented and processed into volume model of the vocal tract (Vampola et al., 2014), which was used for preparation of the mould on a 3D printer, see Fig. 1.



Fig. 1: The mould produced by 3D-printing and the casted larynx model made of silicone rubber.

* Ing. Jaromír Horáček, DrSc., Ing. Vítězslav Bula, Ing. Vojtěch Radolf, PhD., Institute of Thermomechanics, ASCR, Dolejškova 5, 18200 Prague, CZ, jaromirh@it.cas.cz, bula@it.cas.cz, radolf@it.cas.cz

** Assoc. Prof. Dr. Ing. Tomáš Vampola, Department of Mechanics, Biomechanics and Mechatronics, Faculty of Mechanical Engineering, Czech Technical University, Technická 4, 16607, Prague; CZ, Tomas.Vampola@fs.cvut.cz

*** Dr. Ing. Miroslava Dušková-Smrčková, Institute of Macromolecular Chemistry, ASCR, Heyrovského nám. 1888/2, 16206 Prague, CZ, m.duskova@imc.cas.cz

The dynamic viscoelastic properties of the silicone rubber were measured by oscillatory rheometer (Gemini HR Nano, Malvern, UK) as a frequency sweep in linear viscoelasticity region (LVR) in strain control mode. For dynamic measurement in lower frequency range: 0.1-10 Hz, standard plate-plate geometry was used. This test was performed with disc-like silicone rubber specimen of thickness 3 mm and diameter 25 mm. A rubber sheet of that thickness was casted from the same reactive mixture (Ecoflex 00-10) separately between two glasses with Teflon distance. After complete cure, the samples for dynamic mechanical analysis (DMA) were cut with a sharp puncher. For DMA measurement in a special high-frequency mode using so called piezzo-rotational vibration geometry (PRV attachment supplied by Malvern) that allows to reach loading frequencies of several kHz, thin rubber disks were made: their thickness was below 1 mm and the diameter was 40 mm (the dimension of specimen is varied due to increase of stiffness of tested material). In both tests, conventional DMA and high frequency DMA (using PRV) a shear dynamic oscillatory deformation was applied on the rubber and the force response was monitored in linear viscoelasticity region of the rubber that had to be determined separately prior to the DMA test. From the stress-strain ratio and rheometer response, the complex shear modulus $G=G'+iG''$ and loss factor $\tan \delta$ were calculated as function of frequency, Fig. 2. The measurement was performed at laboratory temperature. The shear moduli of model silicone rubber Ecoflex 00-10 at frequency 100 Hz at PRV mode were $G'=11$ kPa, and $G''=3.5$ kPa with the loss angle around 20 degree. These values suggest the rubbery behavior and the material at frequencies close to phonation range reveals significant viscous response. At loading frequencies over 104 Hz, the model silicone starts approaching its vitrification (frequency) area.

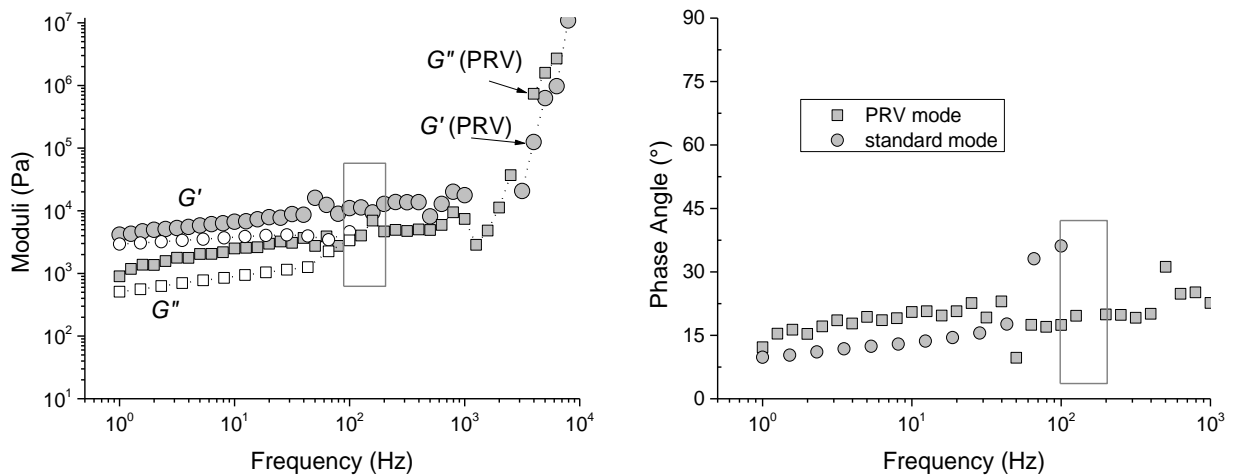


Fig. 2: Shear moduli of material for larynx model, G' , G'' and the phase (loss) angle measured by dynamic mechanical oscillatory shear test. Two measurements combined in one plot: in low frequency range (1-100 Hz) by standard shear test - open symbols; and in high frequency range using special piezzo-rotational vibration mode (PRV, 1-10⁴ Hz) – filled symbols.

The experiments with the artificial larynx were performed in a test rig that enables synchronous registration of the airflow induced vocal fold vibrations using a high speed camera, measurement of contact stress between the vocal folds during collisions, the subglottic dynamic and mean air pressure and the generated acoustic signal, see Horáček et al. (2013).

3. Results of the Phonation Measurement

Example of the simultaneously recorded time signals for the (IS) measured by a miniature pressure transducer, the subglottal pressure (P_{sub}) and the glottis opening (GO) evaluated from the images of the self-oscillating vocal folds are presented in Figs. 3 and 4. When the glottis was opened during the vibration period T , the contact sensor measured the intraglottal air pressure of about 2.5 kPa in the airflow between the vocal folds. As a result the maximum of contact (impact) stress was $MaxIS \cong 2.6$ kPa .

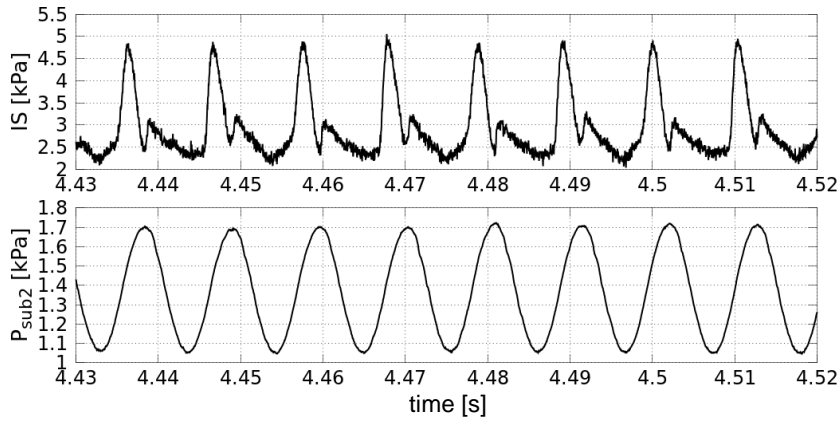


Fig. 3: Impact stress (IS) measured by the contact sensor during the vocal folds self-oscillations and the subglottic pressure (P_{sub}) measured by the pressure transducer mounted on the model of trachea for the mean flow rate $Q=0.3$ l/s and the mean subglottic pressure $\bar{P}_{sub}=1.47$ kPa.

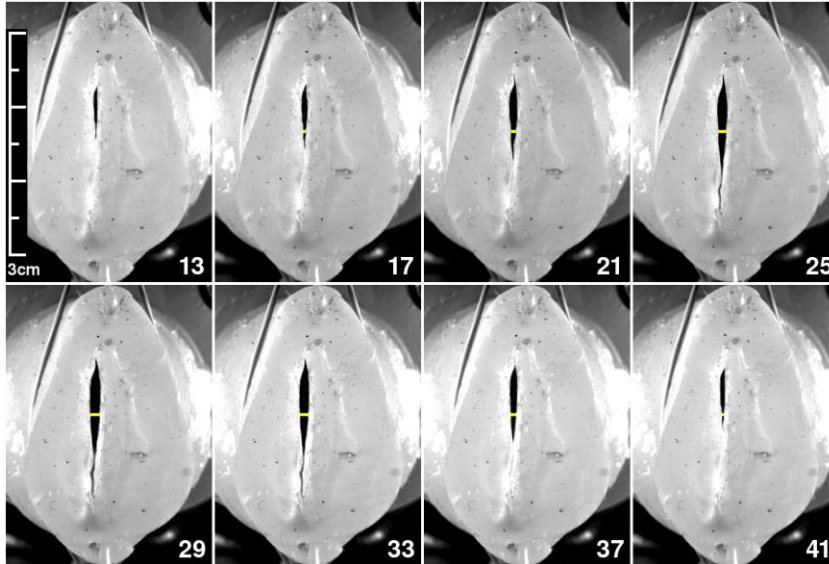
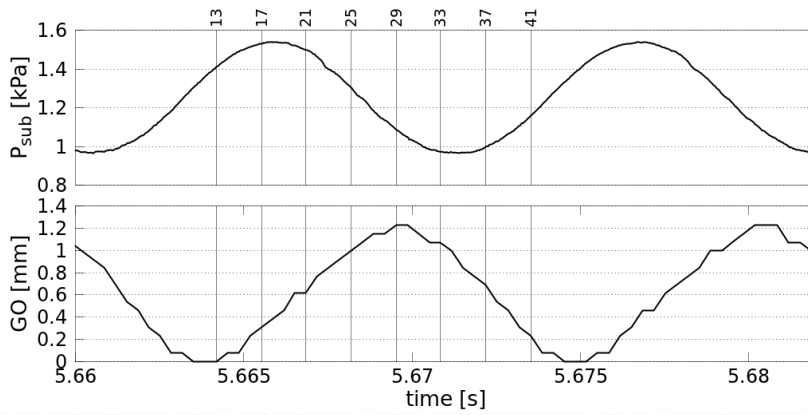


Fig. 4: The subglottic pressure (P_{sub}) and the glottal opening (GO) of the vibrating vocal folds evaluated from the images taken by the high speed camera at the time instants marked by numbers 13-41.

The maximum of $P_{sub} \cong 1.7$ kPa was delayed after the $MaxIS$ of about $T/5$ (Fig. 3) and the maximum GO was delayed behind P_{sub} by about $T/3$, see Fig. 4, where the vibration pattern of the vocal folds is shown during one period. The results summary of the vibration and acoustic characteristics of the larynx in the measured phonation range is shown in Fig. 5. We note that the airflow rate was the controlled parameter in the experiments and the phonation onset, where $IS \approx 0$ and sound pressure level $SPL \approx 0$, was found at $Q \approx 0.15$ l/s.

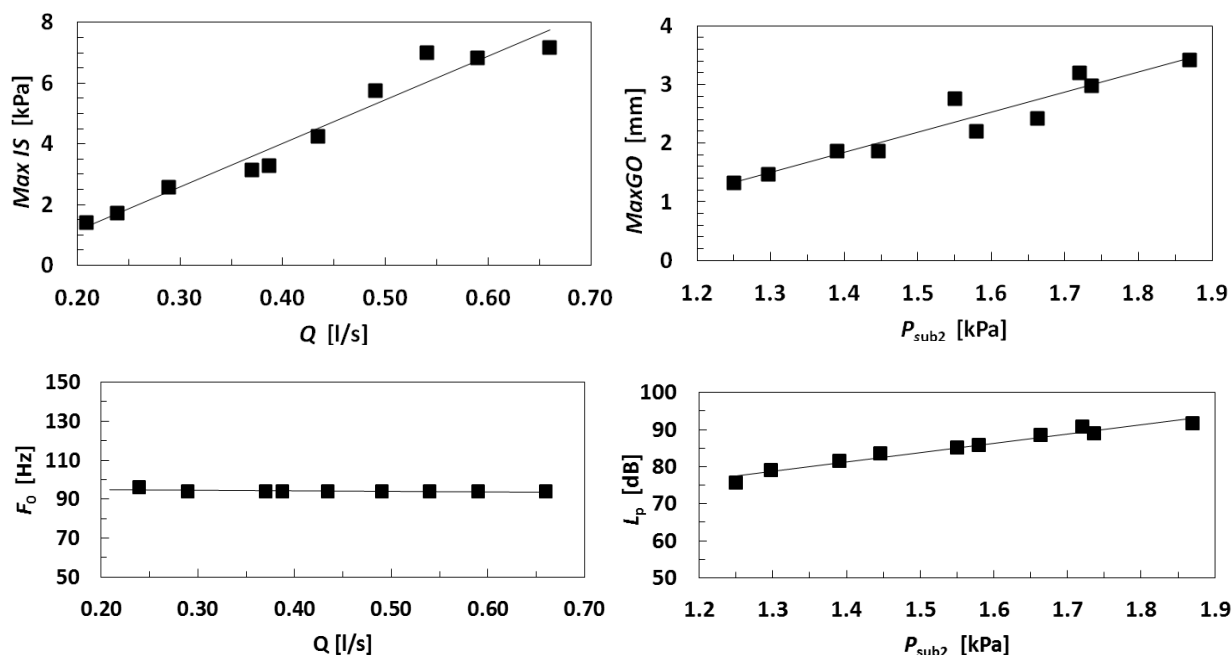


Fig. 5: Measured maxima of the impact stress ($MaxIS$) and the glottis opening ($MaxGO$), the fundamental phonation frequency (F_0) and peak sound level (L_p) as functions of the airflow rate (Q) and mean subglottic pressure (P_{sub}).

4. Conclusions

Depending on the mean flow rate $Q=0.2-0.7$ l/s the measured $MaxIS \cong 0-7.5$ kPa and the peak sound level $L_p \cong 75-92$ dB of the acoustic signal in a distance of 20 cm from the vocal folds were increasing approximately linearly. The mean subglottic pressure varied in the interval $\bar{P}_{sub} \cong 1.2-1.9$ kPa and the fundamental frequency of the vocal folds self-oscillations varied in the interval $F_0 \cong 94-96$ Hz.

The measured phonation characteristics are in good agreement with the values found in human or canine excised larynges, see e.g. Titze (2006). The knowledge of these characteristics for a vocal folds replica can be useful for experimental verification of developed sophisticated 3D computational finite element models of phonation due to relatively exactly defined input material and geometrical parameters, which is problematic in case of real human vocal folds.

Acknowledgement

The work has been supported by the grant project GACR No P101/12/1306 Biomechanical modeling of human voice production – a way to artificial vocal folds.

References

- Horáček, J., Bula, V., Radolf, V., Šidlof, P. (2013) Impact stress in a self-oscillating model of human vocal folds, In: Proc. 11th International Conference On Vibration Problems (ICOVP 2013), Z. Dimitrovová et al. (eds.), Lisbon, Portugal, CD-ROM 10 p.
- Titze, I.R. (2006) The Myoelastic-Aerodynamic Theory of Phonation. National Center for Voice and Speech, Denver, CO.
- Vampola, T., Horáček, J., Laukkanen, A.M., Švec, J.G. (2014) Human vocal tract resonances and the corresponding mode shapes investigated by three-dimensional finite-element modelling based on CT measurement. Logopedics Phoniatrics Vocology. 2014; Early Online: 1–10 DOI: 10.3109/14015439.2013.775333 (in press).

NUMERICAL SOLUTION OF INVISCID TRANSONIC FLOW IN A CHANNEL WITH COMPLEX EQUATION OF STATE

V. Hric, J. Halama, J. Fürst*

Abstract: *The presented paper deals with the incorporation of complex (non-ideal) equation of state into the Euler model which describes dynamics of inviscid fluid. We have performed numerical experiments for the steady transonic flow of steam in the 2D GAMM channel (channel with the 10% thick circular arc bump on the lower wall). The using of complex equation of state allows the more accurate prediction of thermodynamic quantities, mainly in the regions where compressibility factor differs from unity. The results achieved by the van der Waals, Redlich-Kwong-Aungier, one-coefficient virial and special gas IAPWS equation of state are compared with the traditional perfect gas model. All of these models are implemented into in-house CFD code based on the finite volume method in 2D along with the AUSM+ flux scheme. The results confirmed the necessity of using more complex equations of state, especially when higher pressures are considered.*

Keywords: Real gas, Euler inviscid model, GAMM channel, Finite volume method.

1. Introduction

Major part of CFD codes frequently limit attention to the perfect gas model (PG). This approach is justified only if thermodynamic quantity ranges are relatively narrow and the compressibility factors do not differ too much from unity. It is usually true if pressures are relatively low and (or) temperatures are higher. It yields significantly reductions in computational times. However, not negligible errors can be occurred in some non-ideal state regions. To remedy this, more complex equations of state must be used.

2. Flow Model and Equations of State

The dynamics of inviscid fluid flow in 2D is described by the system of time dependent Euler equations

$$\mathbf{W}_t + \mathbf{F}_x + \mathbf{G}_y = \mathbf{0},$$

where $\mathbf{W}(t, x, y) = (\rho, \rho u, \rho v, \rho E)^T$ is vector of conservative variables, $\mathbf{F}(\mathbf{W}) = (\rho u, \rho u^2 + p, \rho uv, \rho uH)^T$, $\mathbf{G}(\mathbf{W}) = (\rho v, \rho uv, \rho v^2 + p, \rho vH)^T$ are vectors of fluxes in which ρ, u, v, E, p, H is density, x- and y-component of velocity, specific total (internal) energy, static pressure and specific total enthalpy, respectively. This system of equation must be closed by the relation for pressure $p = p(\mathbf{W})$. Analytical form of the pressure equation exists only in the case of PG model. In cases where more complex equations of state are used we obtain the pressure value only by some iterative procedure. In this paper we adopted the Newton-Raphson method (NR) which solves firstly nonlinear algebraic equation for temperature $T = T(\rho, e) = T(\mathbf{W})$ from known values of density $\rho(\mathbf{W})$ and internal energy $e(\mathbf{W})$. Static pressure is then evaluated from relation $p = R\rho_c T_c (1 + \delta\phi_\delta^{res}) \delta/\tau$.

In the following we briefly summarize one of the possible techniques for evaluation of thermodynamic quantities in the case of non-ideal gases. The value of certain thermodynamic quantity $Q(\rho, T)$ is given as the contribution of its ideal part $Q^{id}(\rho, T)$ computed with the means of PG model from the known value of density and temperature. This ideal value is then corrected by the residual correction $Q^{res}(\rho, T)$, cf. Fig. 1, for which the following integral formula reads (Novák, 2007)

* Ing. Vladimír Hric (vladimir.hric@gmail.com), Assoc. Prof. Ing. Jan Halama, PhD, Assoc. Prof. Ing. Jiří Fürst: Department of Technical Mathematics, Faculty of Mechanical Engineering, CTU Prague, Karlovo náměstí 13, 121 35 Prague, CZ

$$Q^{res} = Q - Q^{id} = \int_0^\rho \left(\frac{\partial Q}{\partial \rho} - \frac{\partial Q^{id}}{\partial \rho} \right) d\rho.$$

There are actually two equations required for evaluation of all thermodynamic quantities. The first is the thermal equation of state typically in the form $p = p(\rho, T)$. It is the so-called incomplete equation of state since it lacks caloric description. The second is the temperature dependent relation for specific isobaric heat capacity in the ideal gas state $c_p^{id} = c_p^{id}(T)$. However, in the last decades the approach with so-called fundamental equations of state became popular. In this paper we use the form with non-dimensional Helmholtz (free) energy $\phi(\delta, \tau)$, where $\delta = \rho/\rho_c$, $\tau = T_c/T$ and $(\cdot)_c$ designates critical state. This function has two parts. The first part is the ideal contribution ϕ^{id} only stemmed from the ideal specific internal energy e and the ideal specific entropy s along with some supplied equation for $c_p^{id}(T)$. In the case of steam we adopted the relation from (Wagner & Pruss, 2002). The second part is the residual correction ϕ^{res} stemmed from some non-ideal equation of state. In the paper all of the used traditional equations of state in the form $p = p(\rho, T)$ are transformed to its corresponding residual Helmholtz energy part via the relation borrowed from (Novák, 2007)[†]

$$\phi^{res}(\rho, T) = \int_0^\rho \frac{z - 1}{\rho} d\rho,$$

where $z = p/\rho RT$ is the compressibility factor and R is the specific gas constant. All thermodynamic properties can be derived by using the appropriate combinations of ϕ^{id} and ϕ^{res} and their first and second derivatives. Details can be found e. g. in (Wagner & Pruss, 2002).

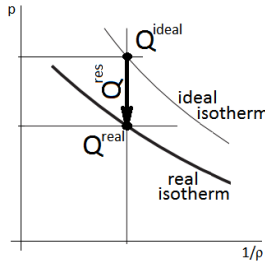


Fig. 1: Residual correction.

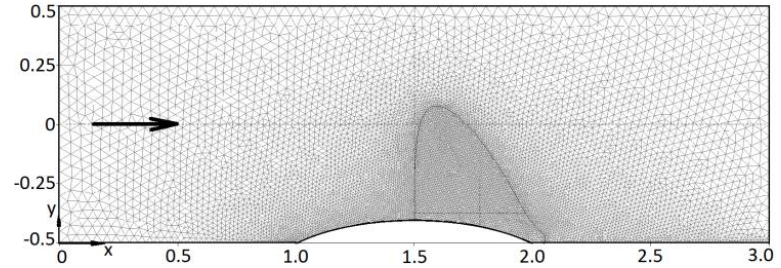


Fig. 2: Computational mesh of GAMM channel.

PG model is both thermally and calorically perfect. This model predicts constant value of compressibility factor which consequences in validity of Mayer's relation. Furthermore, the specific isobaric heat capacity is constant too. This limitation naturally causes vanishing of residual part ϕ^{res} , and so reduces thermodynamic concept to simple analytical form. The residual part relation for others used equations of state along with their coefficients which were computed in this paper are briefly summarized in the following part where e. g. in the case of vdW model for its coefficients holds $n = -a\rho_c/RT_c$, $d = b\rho_c$ where a, b are classical coefficients of this model.

- **Van der Waals (vdW)**

$$\phi^{res}(\delta, \tau) = n\delta\tau - \ln(1 - d\delta) \quad n = -1.838708, \quad d = 0.544802$$

- **Redlich-Kwong-Aungier (RKA)**

$$\phi^{res}(\delta, \tau) = n\tau^t \ln(1 - d_1\delta) - \ln(1 - d_2\delta)$$

$$n = -4.933962, \quad t = 1.958391, \quad d_1 = -0.377615, \quad d_2 = 0.367840$$

- **One-coefficient virial (1-VIR)**

$$\phi^{res}(\delta, \tau) = \delta \sum_{i=1}^4 n_i \tau^{t_i} \quad t_i \text{ given in (Harvey \& Lemmon, 2004)}$$

- **Special gas equation IAPWS-95 (GE-IAPWS-95)**

$$\phi^{res}(\delta, \tau) = \sum_{i=1}^7 n_i \delta^{d_i} \tau^{t_i} \quad n_i, d_i, t_i \text{ given in (Wagner \& Pruss, 2002)}$$

[†] Owing to consistency and comparison with the special gas equation provided by IAPWS

3. Numerical Method

The computational domain of the test GAMM channel is discretized by using Gmsh mesh generator (Geuzaine & Remacle, 2009). The mesh is unstructured triangular (set frontal meshing algorithm) and contains 9247 nodes, 18144 cells and 27390 interfaces, cf. Fig. 2. The cell-centered finite volume method with piece-wise constant reconstruction of cell data is used for discretization of spatial derivatives. Fluxes through common cell interfaces are computed applying AUSM+ scheme. The resulting system of ordinary differential equations is solved by 3-stage low-storage Runge-Kutta method with $CFL = 1.5$. Time step for this method is estimated by the relation borrowed from (Blazek, 2006). Subsonic inlet flow is considered, and so we prescribed stagnant pressure $p_{stg} = 12 \text{ MPa}$, stagnant temperature $T_{stg} = 675 \text{ K}$ and zero y-component of velocity at the inlet boundary. Prescription of high pressure is due to effort to simulate flow in non-ideal state region. The value of stagnant entropy along with extrapolated static pressure from interior is used for calculation of density and temperature in ghost cells where the system of two nonlinear algebraic equations must be solved (NR method applied). Considering outlet flow in subsonic regime, we prescribed back pressure p_{out} , via the pressure ratio $p_{out}/p_{stg} = 0.7463$; density and velocity components are extrapolated from interior. NR method is applied for evaluation of temperature from known density and pressure. At the inviscid wall boundary zero normal velocity component is prescribed. Initial estimates for all NR calculations are taken from previous time level.

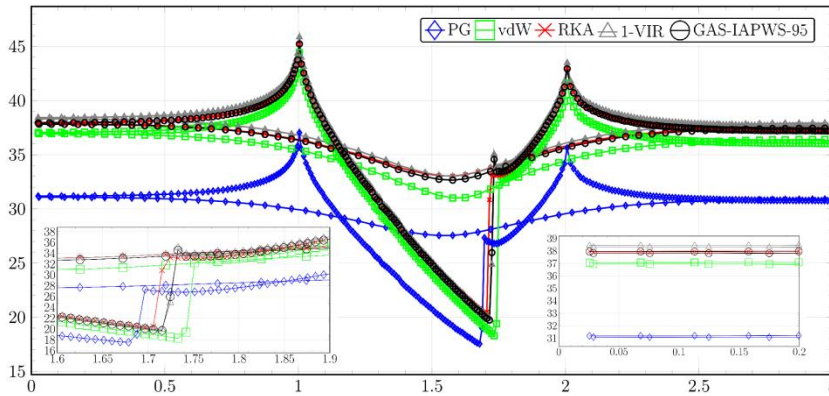


Fig. 3: Lower and upper wall density [kg m^{-3}] distribution.

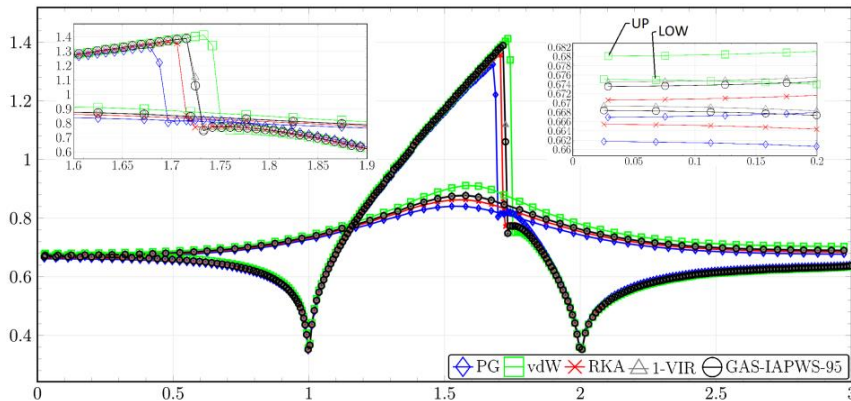


Fig. 4: Lower and upper wall Mach number [-] distribution.

4. Results

Fig. 3 shows distribution of density along the upper and the lower wall. Real gas models give significantly higher values and they shift location of shock wave downstream. Fig. 4 presents distribution of Mach number. Deviations from PG model are on either walls relatively small. However, this is not true in the vicinity of shock wave along the lower wall and in the middle of the upper wall. Shifting of shock wave location on the lower wall resulted in higher peak values of Mach number (PG 1.32, vdW 1.41, RKA 1.36, 1-VIR and GE-IAPWS-95 1.39) and in lower values in the location of so-called Zierep's singularity (= stronger shock waves). Maximum Mach number values on the upper wall are as follows, PG 0.84, vdW 0.91, RKA 0.86, 1-VIR and GE-IAPWS-95 0.88.

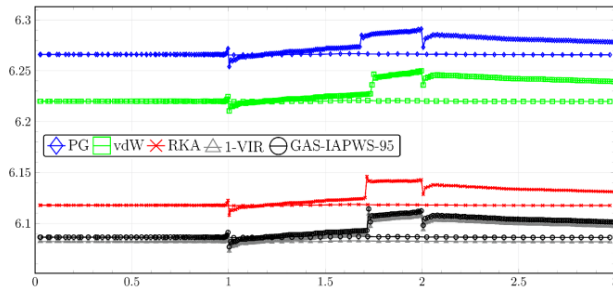


Fig. 5: Entropy [$\text{kJ kg}^{-1} \text{K}^{-1}$] distribution.

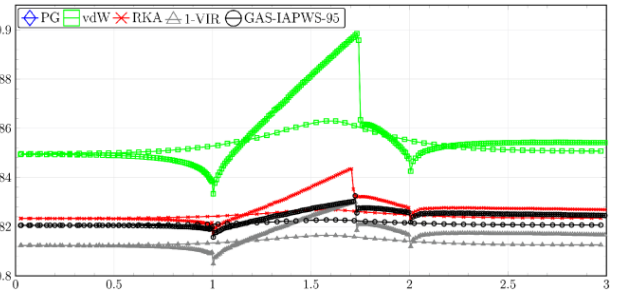


Fig. 6: Compressibility factor [-] distribution.

Fig. 5 depicts distribution of entropy. Real gas models give lower values. From physical point of view it is known that in the case of inviscid fluid flow entropy should grow only as a result of shock wave formation. Non-physical entropy increase and decrease on the bump surface up to the shock wave location and wiggles at the bump inlet and outlet in our results are caused by imperfection and numerical viscosity of used flux scheme. Fig. 6 shows distribution of the compressibility factor. All real gas models give substantially lower values and range between 0.805 and 0.845 (except vdW model). The comparison of real gas total CPU time per one cell and per one time step related to the same quantity in the case of PG model is summarized in Tab. 1. The most CPU time consuming operation (relative to the real gas model implementation) is repeated numerical solution of temperature from known internal energy and density (temperature is required for evaluation of pressure and other quantities like e. g. sound speed). In this case the average number of iterations in NR method ranges between 1.55 and 2.15. The maximum values are in the vicinity of shock wave.

Tab. 1: Relative CPU time comparison

EQUATION OF STATE	PG	vdW	RKA	1-VIR	GE-IAPWS-95
RELATIVE CPU TIME	1.00	2.08	3.04	4.37	6.13

5. Conclusion Remarks

Results confirmed necessity of using more complex equations of state when flow simulations include non-ideal state regions. It was presented on distributions of selected parameters. Drawbacks of this augmentation are loss of explicitness in thermodynamic concept and higher CPU time demands.

Acknowledgement

This work was supported by the grant No. SGS13/174/OHK2/3T/12 of the Grant Agency of the Czech Technical University in Prague.

References

- Aungier, R. H. (1994) A fast, accurate real gas equation of state for fluid dynamic analysis applications. *J. Fluids Eng.*, 117, 2, pp. 277-281.
- Blazek, J. (2006) *Computational fluid dynamics – principles and applications*. Elsevier, Amsterdam.
- Geuzaine, Ch. & Remacle, J. F. (2009) Gmsh – a three-dimensional finite element mesh generator with built-in pre- and post-processing facilities. *International Journal for Numerical Methods in Engineering*, 79, 11, pp. 1309-1331.
- Harvey, A. H. & Lemmon, E. W. (2004) Correlation for the second virial coefficient of water. *J. Phys. Chem. Ref. Data*, 33, 1, pp. 369-376.
- Novák, J. P. (2007) *Thermodynamic properties of gases*. ICT Press, Prague, (in Czech).
- Wagner, W. & Pruß, A. (2002) The IAPWS formulation 1995 for the thermodynamic properties of ordinary water substance for general and scientific use. *J. Phys. Chem. Ref. Data*, 31, 2, pp. 387-535.

A STABILITY CRITERION OF AN ORTHOTROPIC BI-MATERIAL NOTCH BASED ON THE STRAIN ENERGY DENSITY

M. Hrstka^{*}, T. Profant^{**}, J. Klusák^{***}, O. Ševeček^{****}, M. Kotoul^{*****}

Abstract: A bi-material notch composed of two orthotropic materials is considered. The stress and displacement fields are expressed using the Lekhnitskii-Eshelby-Stroh formalism for plane elasticity and as the result of an application of the Ψ -integral method. Knowledge of the basic stress concentrator characteristics such as stress singularity exponent and corresponding regular and auxiliary eigenvectors allows the Ψ -integral to evaluate the generalized stress intensity factor of the studied stress concentrator. The achieved results are used for the next analysis such as assessment of the potential direction of the crack initiation and for notch stability criteria assessment as an extension of standard crack fracture mechanics.

Keywords: Fracture mechanics, Bi-material notch, Stability criteria, Singular stress concentrator, Stress intensity factor, Ψ -integral.

1. Introduction

Joints of different materials, such as layered composite materials, fiber reinforced ceramics or construction with protective surface layer may occur in practical engineering structures. They enable to achieve the properties which could not be attained by means of homogeneous materials. In the case of composite materials, parts of the joints often exhibit orthotropic material properties. The stress field in closed vicinity of these material joints has a singular character and complicated form. In a comparison to a crack in homogeneous media, in the case of bi-material joints, the stress singularity exponent is different from $1/2$ and generally can be complex. The stress is mostly characterized by more singular terms and at the same time each singular term covers combination of both normal and shear modes of loading (Broberg, 1999).

Despite a presence of stress concentrators like a notch, it precludes any application of the fracture mechanics approaches which were originally developed for a crack in isotropic homogeneous materials, the assessment of such singular stress concentrators becomes topical (Klusák & Knésl, 2007; Susmel & Taylor, 2008; Marsavina & Sadowski, 2008; Profant et al., 2010).

Most such discontinuities can be mathematically modeled as bi-material notches composed of two orthotropic materials given by angles ω_1 and ω_2 , as can be seen in Fig. 1a.

2. Materials and Methods

The necessary step for the crack initiation assessment is detailed knowledge of the stress distribution. Within plane elasticity of anisotropic media the Lekhnitskii-Eshelby-Stroh (LES) formalism based on complex potentials (Hwu, 2010) can be used. Complex potentials satisfying the equilibrium and the

* Ing. Miroslav Hrstka: Institute of Solid Mechanics, Mechatronics and Biomechanics, Brno University of Technology, Technická 2896/2, 616 69, Brno; CZ, y72539@stud.fme.vutbr.cz

** Assoc. Prof. Ing. Tomáš Profant, PhD.: Institute of Solid Mechanics, Mechatronics and Biomechanics, Brno University of Technology, Technická 2896/2, 616 69, Brno; CZ, profant@fme.vutbr.cz

*** Assoc. Prof. Ing. Jan Klusák, PhD.: High Cycle Fatigue Group, Institute of Physics of Materials, Žitkova 22, 616 62, Brno; CZ, klusak@ipm.cz

**** Ing. Oldřich Ševeček, PhD.: Institute of Solid Mechanics, Mechatronics and Biomechanics, Brno University of Technology, Technická 2896/2, 616 69, Brno; CZ, sevecek@fme.vutbr.cz

***** Prof. RNDr. Michal Kotoul, DSc.: Institute of Solid Mechanics, Mechatronics and Biomechanics, Brno University of Technology, Technická 2896/2, 616 69, Brno; CZ, kotoul@fme.vutbr.cz

compatibility conditions as well as the linear stress-strain dependence and given boundary conditions are the basis for the determination of stress and deformation fields. In the case of general plane anisotropic elasticity all the components of the stress and deformation tensors have to be considered.

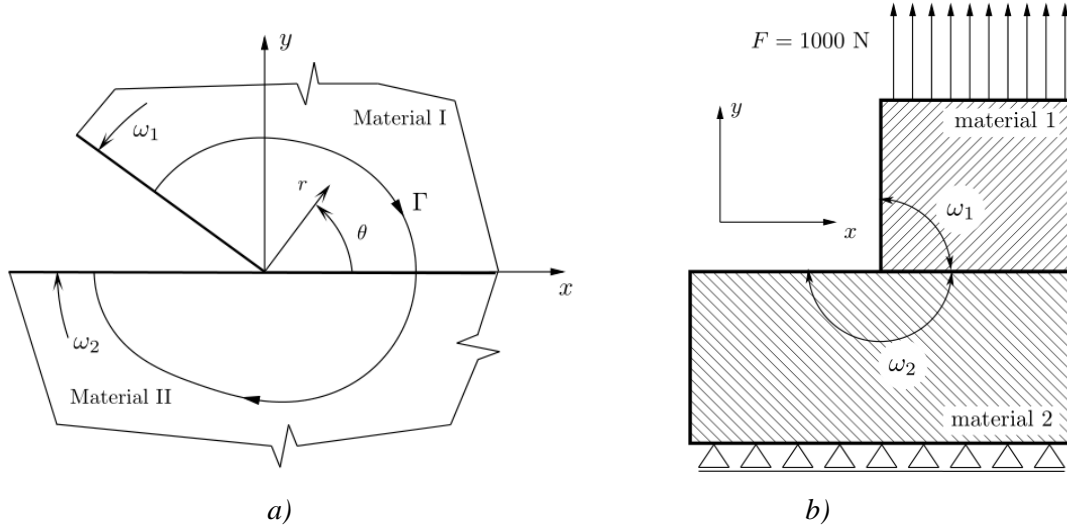


Fig. 1: a) A bi-material notch given by angles ω_1 , ω_2 and composed of two orthotropic materials. An integration path Γ is surrounding the bi-material notch tip, r and θ are polar coordinates. b) A bi-material configuration with angles $\omega_1=90^\circ$, $\omega_2=180^\circ$ and under external loading.

2.1. Stress distribution

In terms of material with orthotropic properties, symmetry occurs in the stiffness and in the compliance matrices. Thus, the stress and strain tensor is significantly reduced. According to the LES theory for an orthotropic material, the relations for displacements and stresses can be written as follows

$$u_i = 2\Re\{A_{ij}f_j(z_j)\}, \sigma_{2i} = 2\Re\{L_{ij}f_j'(z_j)\}, \sigma_{1i} = -2\Re\{L_{ij}\mu_j f_j'(z_j)\}, \quad (1)$$

where $i, j = 1, 2$, \Re denotes the real part of the complex expression and $z_j = x + \mu_j y$. Complex numbers μ_j are the eigenvalues of the material. For matrices A_{ij} and L_{ij} holds

$$\mathbf{A} = \begin{bmatrix} s_{11}\mu_1^2 + s_{12} & s_{11}\mu_2^2 + s_{12} \\ s_{12}\mu_1 + s_{22}/\mu_1 & s_{12}\mu_2 + s_{22}/\mu_2 \end{bmatrix}, \mathbf{L} = \begin{bmatrix} -\mu_1 & -\mu_2 \\ 1 & 1 \end{bmatrix}, \quad (2)$$

where s_{ij} are the elastic compliances.

In the case of the studied notch, the potential $f_j(z_j)$ has the following form

$$\mathbf{f} = H\langle z_*^\delta \rangle \mathbf{v}, \quad (3)$$

re H is the generalized stress intensity factor, \mathbf{v}_i is an eigenvector corresponding to the eigenvalue δ representing the exponent of the stress singularity at the notch tip. Eigenvector \mathbf{v}_i and eigenvalue δ are the solution of the eigenvalue problem leading from the prescribed notch boundary and compatibility conditions. The expression $\langle z_*^\delta \rangle$ denotes a diagonal matrix $\langle z_*^\delta \rangle = \text{diag}[z_1^\delta, z_2^\delta]$. In most practical cases, there are two singular terms corresponding to two stress singularity exponents.

2.2. Determination of the generalized stress intensity factor

In order to determine the final stress distribution around the notch, it is important to find out the value of the generalized stress intensity factors (GSIF) from the analytical-numerical solution to a concrete situation with given geometry, materials and boundary conditions. The GSIFs can be determined using the so-called Ψ -integral (Kotoul et al., 2010; Hwu, 2010). This method is an implication of Betti's reciprocity theorem, which in the absence of body forces states that the following integral (4) is path-independent and equals

$$\Psi(\mathbf{u}, \hat{\mathbf{u}}) = \int_\Gamma \{\sigma_{ij}(\mathbf{u})n_i \hat{u}_j - \sigma_{ij}(\hat{\mathbf{u}})n_i u_j\} ds, \quad (i, j = 1, 2) \quad (4)$$

The contour Γ , as shown in Fig. 1a, surrounds the notch tip and the displacements \mathbf{u} are considered as the regular and $\hat{\mathbf{u}}$ as the auxiliary solutions of the notch eigenvalue problem. For the corresponding exponents it holds $\hat{\delta} = -\delta$. If the contour Γ closely surrounds the notch tip, the Ψ -integral can be written as

$$\begin{aligned}\Psi(\mathbf{u}, \hat{\mathbf{u}}) &= - \int_{-\omega_2}^{\omega_1} \{ \varphi_{i,\theta}(\mathbf{u}) n_i \hat{u}_j - \varphi_{i,\theta}(\hat{\mathbf{u}}) n_i u_j \} d\theta = \\ &= H(c_1^I + c_2^I - c_3^I - c_4^I + c_1^{II} + c_2^{II} - c_3^{II} - c_4^{II})\end{aligned}\quad (5)$$

where the constants c_1^I, \dots, c_4^{II} are given by definite integrals independent of the coordinate r .

Because of their complicated form, they are not stated here. The superscript I or II corresponds to the material regions bounded by the angles ω_1 and ω_2 . The comma in the subscript means the derivation with respect to θ . Because of the path independency of the integrals, the left hand side integral in (4) can be computed numerically along the path, which is any remote integration path with finite diameter. Since the exact solution \mathbf{u} in this case is not known, a finite element solution can be used as its approximation.

2.3. Stability criterion

The stress field around a bi-material notch inherently covers combined normal and shear modes of loading. In the present paper where the two orthotropic materials are assumed as perfectly bonded, only crack propagation into materials I or II is supposed.

There are different methods to determine a stability criterion, for example as shown in (Erdogan & Sih, 1963; Profant et al. 2013). In present paper, a strain energy density factor (SEDF) is used, (Sih, 1977). Strain energy density is defined as

$$\Sigma(r, \theta) = r \frac{dW}{dV} = r \int_0^{\varepsilon_{pq}} \sigma_{ij} d\varepsilon_{ij}, \quad (6)$$

where W is the strain energy, dV is differential volume and ε_{ij} is strain. The integrand in (6) has to be total differential to provide the integral to be path-independent. Using the constitutive laws and substituting into (1) one can obtain

$$\Sigma(r, \theta) = \frac{1}{2} r^{2\delta_1 - 1} H_1^2 F_{H_1}(\theta) + r^{\delta_1 + \delta_2 - 1} H_1 H_2 F_{H_{1,2}}(\theta) + \frac{1}{2} r^{2\delta_2 - 1} H_2^2 F_{H_2}(\theta), \quad (7)$$

where the F_{H_1} , $F_{H_{1,2}}$, F_{H_2} are functions of the parameters δ and θ and can be found in (Profant et al., 2010). The strain energy density depends on the distance r from the notch tip. To make this dependence weaker, it is convenient to introduce a mean value of the SEDF over some distance d , which equals

$$\bar{\Sigma}(r, \theta) = \frac{1}{d} \int_0^d \Sigma(r, \theta) dr \quad (8)$$

A potential crack can initiate in both materials and the crack direction is determined from the minimum of the mean value of the strain energy density. The resulting direction is then used for stability criterion estimation.

The critical value of the generalized stress intensity factor H_C is consequently determined from the strain energy density factor corresponding to the critical conditions, i.e. a crack initiates. A crack will not initiate at the tip of a bi-material notch if the value H is lower than its critical value H_C , i.e.

$$H(\sigma^{appl}) < H_C(K_{IC}), \quad (9)$$

where σ^{appl} is an applies load and K_{IC} the fracture toughness.

3. Results and Discussion

The procedure discussed above can be used to make a parametric study of the notch with geometry and external loadings given in Fig. 1b. The rectangular bi-material orthotropic notch is characterized by angles $\omega_1 = 90^\circ$ and $\omega_2 = 180^\circ$; this configuration often occurs in engineering constructions. The Young's moduli in Cartesian coordinate system according to the materials I, II are $(E_x)_I = 100$ MPa, $(E_y)_I = 50$ MPa, $(E_x)_{II} = 400$ MPa, $(E_y)_{II} = 50$ MPa. The eigenvalues corresponding to the stress singularity exponents are equal to $\delta_1 = 0.570$ and $\delta_2 = 0.939$ and GSIFs hold the values of $H_1 = 0.00348$ MPa $m^{1-\delta_1}$ and $H_2 = 0.07039$ MPa $m^{1-\delta_2}$. The evaluation of SEDF $\bar{\Sigma}$ around the notch tip is depicted in the Fig. 2.

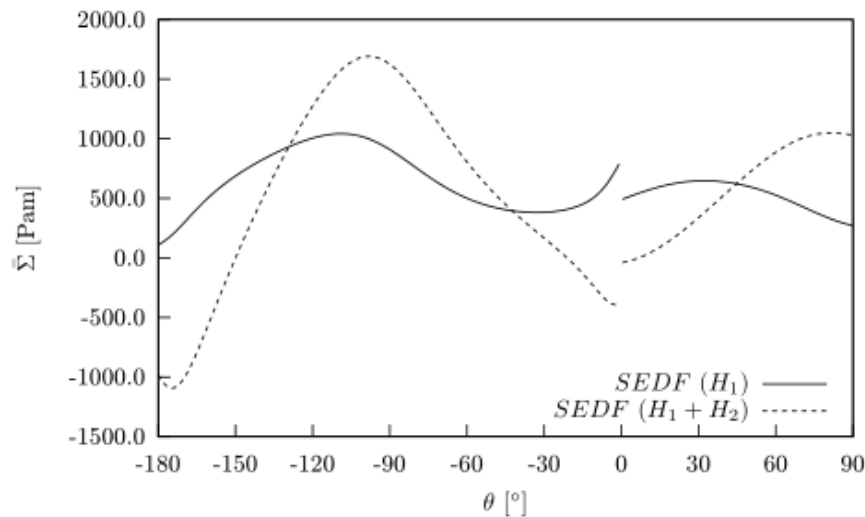


Fig. 2: Strain energy density factor as a function of the polar coordinate θ . The distance $d = 0.01$ mm. The minimal value determines the angle of crack initiation.

4. Conclusion

Composite structures involving interfaces, notches and free edges generally develop a singular elastic stress field near the intersection of lines of material and geometrical discontinuities. These localized regions of severe stress state are possible sites of failure initiation and growth. The aim of the present paper was to determine the stability criterion of the bi-material notch tip using a combination of analytical and numerical approach. As the stability criterion, the critical value of the generalized stress intensity factor was introduced. Using of this criterion is conditioned by the capable mathematical theory for the evaluation of those parameters, which characterize the stress singularity in notch tip vicinity and consequently allow to compute relevant concentrator characteristics. Because of the generalization of the stress singularity character at the notch due to its geometry, the Ψ -integral method and Lekhnitskii-Eshelby-Stroh were chosen.

Acknowledgement

The authors are grateful for financial support through the specific academic research grant of the Ministry of Education, Youth and Sports of the Czech Rep. No. FSI-S-14-2311 provided to Brno University of Technology, Faculty of Mechanical Engineering.

References

- Broberg, Bertram K. (1999) Cracks and fracture. San Diego : Academic Press, ISBN 01-213-4130-5.
- Erdogan, F., Sih, G. C. (1963) On the crack extension in plates under plane loading and transverse shear. Transactions of the ASME, Journal of Basic Engineering, 85D, pp. 519-527.
- Hwu, Ch. (2010) Anisotropic elastic plates, Springer, New York, ISBN 987-1-4419-5914-0.
- Klusák, J., Knésl, Z. (2007) Determination of crack initiation direction from a bi-material notch based on the strain energy density concept. Comp. Mater. Sci., Vol. 39(1), pp. 214-218.
- Kotoul, M., Ševeček, O., Profant, T. (2010) Analysis of multiple cracks in thin coating on orthotropic substrate under mechanical and residual stresses. Eng. Fract. Mech., Vol. 77, pp. 229-248.
- Marsavina, L., Sadowski, T. (2009) Fracture parameters at bi-material ceramic interfaces under bi-axial state of stress. Computational Materials Science, 45, pp. 693-697.
- Profant, T., Klusák, J., Kotoul, M. (2010) A study of the stability of sharp notches in the orthotropic heterogeneous media. The Ninth International Conference on Multiaxial Fatigue & Fracture, University of Parma, pp. 733-740.
- Profant, T., Klusák, J., Ševeček, O., Hrstka, M., Kotoul, M. (2013) Energetic criterion for a micro-crack of finite length initiated in orthotropic bi-material notches. Engineering fracture mechanics, pp. 396-409.
- Sih, G. C. (1977) A special theory of crack propagation. Mechanics of Fracture – Methods and Analysis and Solutions of Crack Problems, Noordhoff International Publishing, Leyden, The Netherlands.
- Susmel, L., Taylor, D. (2008) The theory of critical distances to predict static strength of notched brittle components subjected to mixed-mode loading. Eng. Fract. Mech., 75, pp. 534-550.

HEAT TRANSFER SIMULATION OF HEAT EXCHANGERS MADE BY POLYMERIC HOLLOW FIBERS

V. Hřibová*, J. Komínek*, I. Astrouski*, M. Raudenský*, A. A. Tseng**

Abstract: Heat exchangers have been used for a broad range of industrial applications. Due to its good thermal conductivity and mechanical strength, metal has been widely applied for making the heat exchangers. Recently, however, because of their superior characters, including corrosion resistance, cost-effectiveness, light-weight, high ratio of surface-area to volume, dual transport ability, and less fouling ability, polymeric hollow fibers (PHFs) have been used for fabricating heat exchangers for many applications. The purpose of this paper is to present a versatile numerical model, which can be conveniently used for designing PHF heat exchangers (PHFHEs) and reliably used to predict the thermal characteristics of the heat exchangers, including fluid outlet temperatures, external, internal, and overall heat transfer coefficients, and total heat transfer rate as well as the thermal efficiency.

Keywords: Numerical model, Heat exchanger, Heat transfer, Polymeric hollow fibers.

1. Introduction

Polymers began to be used in the construction of heat exchangers over 40 years ago (Whitley, 1957). Polymers offer several advantages over metal. Their lower price; ease of shaping, forming and machining; and lower densities are the reasons for their much lower construction, transportation and installation costs. They are environmentally attractive because the energy required to produce a unit mass of plastics is about 2 times lower than that of common metals. Because of the smooth surface of polymers, the friction factors and thus pressure drops are smaller and there is less fouling than with commercial metal tubes. Polymers have excellent chemical resistance to acids, oxidizing agents, and many solvents. Moreover, drop-wise condensation caused by the smooth surface of hydrophobic plastics instead of film-wise condensation leads to a much higher heat transfer coefficient.

The main disadvantage of using polymers is their low thermal conductivity, which is usually between 0.1 and 0.4 Wm⁻¹K⁻¹ and thus 100-300 times lower than thermal conductivity of metals. This limits the use of polymers for heat exchangers due to high magnitude of wall thermal resistance (Zarkadas & Sirkar, 2004). Additionally, the high thermal expansion of plastics requires special design considerations. On the other hand, this expansion can also be a benefit because repeated expansion and contraction of the plastic tubes can lead to scale detachment (Githens, 1965).

Two main approaches exist to achieve performance comparable with metal heat exchangers. The first is to increase the thermal conductivity of the material and the second one is to decrease the wall thermal resistance by using thin walls between heat transfer mediums. That is why PHFHEs are proposed as a new type of heat exchanger for lower temperature/pressure applications (Zarkadas & Sirkar, 2004).

Besides the advantages mentioned above, PHFHEs are easily and inexpensively formed even into complex shapes, which enables their mass production. They are recyclable, which is a benefit from an ecological point of view.

* Bc. Veronika Hřibová, Ing. Jan Komínek, Ing. Ilya Astrouski, prof. Ing. Miroslav Raudenský, CSc.: Heat Transfer and Fluid Flow Laboratory, Faculty of Mechanical Engineering, Brno University of Technology, Technická 2896/2; 616 69, Brno; CZ; komínek@lptap.fme.vutbr.cz

** Dr. Ampere A. Tseng: School for Engineering of Matter, Transport and Energy, 501 E. Tyler Mall, ECG301, Arizona State University, Tempe, AZ 85287-6106 USA; E-mail: ampere.tseng@asu.edu

2. Calculation Method

A simple iterative analytical model is used to calculate the estimation of the heat transfer between the hot fluid in the tubes of the heat exchanger and the air flow in the shell side. It is very important to have an approximation of the behavior of polymers for designing an appropriate PHFHE.

2.1. Equations

For any other considerations the subscript t is used for values related to the tube inside, s for values related to the shell side, i for inputs and o for outputs.

2.1.1. Heat Transfer in the Tube Side

The average Nusselt number of a circular tube at a laminar condition under a constant wall temperature $T_{t,w}$ can be correlated as (Whitaker, 1972):

$$\overline{Nu}_t = \frac{\bar{h}_t d_t}{k_t} = 1.86 \left[\frac{Re_t Pr_t}{\left(\frac{L}{d_t}\right)} \right]^{1/3} \left(\frac{\mu_t}{\mu_w} \right)^{0.14}, \quad (1)$$

where $Re_t = \rho_t V_t d_t / \mu_t$ is the Reynolds number and $Pr_t = c_{p,t} \mu_t / k_t$ is the Prandtl number. All properties, density ρ_t , dynamic viscosity μ_t , specific heat at constant pressure $c_{p,t}$, thermal conductivity k_t and velocity V_t , are evaluated at the arithmetic mean of the tube fluid inlet and outlet temperatures $T_{t,am} = (T_{t,mi} + T_{t,mo})/2$. Dynamic viscosity μ_w is calculated at $T_{t,w}$. The above equation (1) can be used if both assumptions $0.48 \leq Pr_t \leq 16.7$ and $0.0044 \leq \mu_t / \mu_w \leq 9.75$ are fulfilled.

If it is true that $[Re_t Pr_t / (\frac{L}{d_t})]^{1/3} (\frac{\mu_t}{\mu_w})^{0.14} < 2$ the Nusselt number can be considered as a constant and the equation (2) can be applied (Incropera & DeWitt, 1996):

$$Nu_t = \frac{h_t d_t}{k_t} = 3.66 \text{ or } h_t = 3.66 \frac{k_t}{d_t}. \quad (2)$$

The equation (3) (Dittus and Boelter, 1930) should be used for smooth tubes with a fully-developed turbulent flow, i.e. $Re_t > 4,000$:

$$Nu_t = \frac{h_t d_t}{k_t} = 0.023 Re_t^{0.8} Pr_t^{0.3}. \quad (3)$$

The equation (2) can often be used for calculations of PHFHEs because d_t is less than 1 mm, which means the entry region and Re_t are relatively small under normal operating conditions.

The outlet temperature can be found as

$$T_{t,mo} = T_{t,w} + (T_{t,mi} - T_{t,w}) \exp[-\pi d_t L \bar{h}_t / (\dot{m} c_{p,t})], \quad (4)$$

where L is the length of the tube and $\dot{m} = \rho_t V_t \pi d_t^2 / 4$ is the mass flow rate.

The heat transfer rate from the tube can be found as:

$$q_t = \dot{m} c_{p,t} (T_{t,mi} - T_{t,mo}) = \bar{h}_t \pi d_t L \Delta T_{t,lm}, \quad (5)$$

where $\Delta T_{t,lm}$ is the log-mean temperature difference in the tube side:

$$\Delta T_{t,lm} = \frac{(T_{t,w} - T_{t,mi}) - (T_{t,w} - T_{t,mo})}{\ln[(T_{t,w} - T_{t,mi}) / (T_{t,w} - T_{t,mo})]}. \quad (6)$$

The total heat transfer rate from all tubes in the heat exchanger should be:

$$Q_t = N_t q_t, \quad (7)$$

where N_t is the total number of tubes.

2.1.2. Heat Transfer in the Shell Side

The most common correlation for the average heat transfer coefficient of the air flow across tube bundles in an in-line arrangement is (Zukauskas, 1972):

$$\overline{Nu}_s = \frac{\bar{h}_s d_s}{k_s} = C_{Z1} Re_{s,max}^m Pr_s^{0.36} \left(\frac{Pr_s}{Pr_w} \right)^{0.25}, \quad (8)$$

where properties k_s , Pr_s and $Re_{s,max}$ are evaluated at the arithmetic mean of air inlet and outlet temperature $T_{s,am} = (T_{s,i} + T_{s,o})/2$ and Pr_w is evaluated at $T_{s,w}$. Calculation of $Re_{s,max}$ is based on the maximum air velocity which is for aligned arrangement approximately equal to $V_{s,max} = P_T V_s / (P_T - d_s)$, where $P_T = p_{tr}/d_s$ and p_{tr} is a distance between centers of the tubes in the perpendicular direction to the air flow.

The equation (8) is valid only for tube banks having 17 or more rows of tubes in the air flow direction ($N_r \geq 17$), otherwise a correction factor C_{Z2} has to be added (Zukauskas, 1972):

$$\overline{Nu}_s|_{N_r < 17} = C_{Z2} \overline{Nu}_s|_{N_r \geq 17}. \quad (9)$$

The equation (8) can be used only for $10 \leq Re_{s,max} \leq 100$ and $1.000 \leq Re_{s,max} \leq 2 \cdot 10^6$. For $100 \leq Re_{s,max} \leq 1.000$ the equation (10) for a single tube can be applied (Zukauskas, 1972):

$$\overline{Nu}_s = \frac{\overline{h}_s d_s}{k_s} = 0.51 Re_s^{0.5} Pr_s^{0.37} \left(\frac{Pr_s}{Pr_w} \right)^{0.25}. \quad (10)$$

The values of all the constants can be found in tabular form in most heat transfer books (e.g. Incropera & DeWitt, 1996).

The total heat transfer rate from the tube bank to the air can be calculated as:

$$Q_s = N_t q_s = N_t \overline{h}_s \pi d_s L \Delta T_{s,lm}, \quad (11)$$

where $\Delta T_{s,lm}$ is the log-mean temperature difference:

$$\Delta T_{s,lm} = \frac{(T_{s,w} - T_{s,i}) - (T_{s,w} - T_{s,o})}{\ln[(T_{s,w} - T_{s,i}) / (T_{s,w} - T_{s,o})]}. \quad (12)$$

Based on the principle of conservation of energy, $T_{s,o}$ can be found as:

$$T_{s,o} = T_{s,w} - (T_{s,w} - T_{s,i}) \exp \left[- \frac{\pi d_s N_t \overline{h}_s}{\rho_s V_s N_p p_{tr} c_{p,s}} \right]. \quad (13)$$

Using area of the tube side or area of the shell side, the overall heat transfer coefficients can be evaluated and $U_t A_t = U_s A_s = UA$ (Incropera & DeWitt, 1996):

$$U_t = \frac{1}{\frac{1}{h_t} + r_f^t + \frac{d_t \ln(\frac{d_s}{d_t})}{2k_w} + r_f^s \left(\frac{d_t}{d_s} \right) + \frac{d_t}{h_s}}, \quad (14)$$

$$U_s = \frac{1}{\frac{1}{h_s} + r_f^s + \frac{d_s \ln(\frac{d_s}{d_t})}{2k_w} + r_f^t \left(\frac{d_s}{d_t} \right) + \frac{d_s}{h_t}}. \quad (15)$$

In the equations (14) and (15) r_f represents a fouling factor. Its value is negligible for PHFHEs and does not need to be considered in the present calculation.

2.2. Iterative Model

An iterative model is based on the equations from the above subsection. The superscript denotes the iteration.

Step 1: Start with the assumption that $T_{t,w}^1 = (T_{t,mi} + T_{s,i})/2$ for the first iteration so all h_t^1 , $T_{t,mo}^1$ and q_t^1 can be calculated using equations (1-6).

Step 2: Assume $T_{s,w}^i = T_{t,w}^i - q_r \ln(\frac{d_s}{d_t}) / (2\pi L k_w)$ and h_s^i , q_s^i and $T_{s,o}^i$ can be calculated using equations (8-13). Note that $q_i = q_t$ for $i=1$.

Step 3: Evaluate next temperatures of the wall as $T_{t,w}^{i+1} = T_{t,w}^i + T_{t,w}^i (q_t^i - q_s^i) / [s(q_t^i + q_s^i)]$ and $T_{s,w}^{i+1} = T_{s,w}^i - T_{s,w}^i (q_s^i - q_t^i) / [s(q_s^i + q_t^i)]$ and using them, recalculate h_t^{i+1} , h_s^{i+1} , $T_{t,mo}^{i+1}$, $T_{s,o}^{i+1}$, q_t^{i+1} and q_s^{i+1} .

Step 4: If both $|T_{t,w}^{i+1} - T_{t,w}^i| < \delta$ and $|T_{s,w}^{i+1} - T_{s,w}^i| < \delta$, where δ is a small non-negative number, stop and go to step 5. Otherwise, $q_r = (q_t^{i+1} + q_s^{i+1})/2$ and $i = i+1$. Then go to step 2 using the updated $T_{t,w}^{i+1}$.

Step 5: Evaluate total heat transfer rate Q_t , Q_s using equations (7) and (11) and overall heat transfer coefficient U_t and U_s using equations (14) and (15).

The iterative model is developed to find the outlet temperatures $T_{t,mo}$ and $T_{s,o}$, the heat transfer rate Q_t and Q_s and the overall heat transfer coefficients U_t and U_s . In order to preserve the principle of conservation of energy, i.e. $Q_t \approx Q_s$, several iterations are expected to obtain a convergent value of q_r , which should be close to q_t and q_s and $(q_t - q_s)^2$ should be smaller than a preselected allowed error ϵ .

3. Results

The iterative model was tested for two same proportional PHFHEs with different diameters of fibers. As you can see in Fig. 1 the total heat transfer rate is much better for PHFHE with a smaller diameter if the same proportional PHFHEs used with constant velocity (0.15 m/s) and the same input temperature (60°C) of 50% ethylene-glycol/water and in tubes and the same input temperature of air (20°C) outside. These results confirm opinions mentioned in the first section.

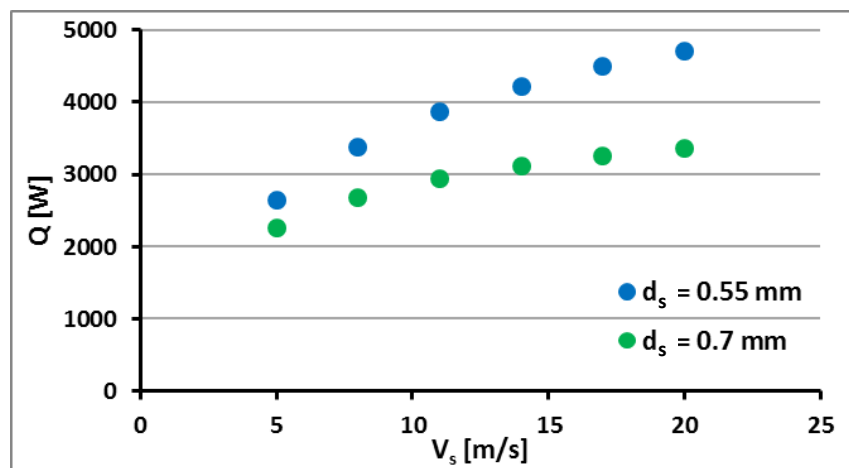


Fig. 1: Dependency of the total heat transfer rate on velocity of air outside.

4. Conclusions

As described in the first section, using polymers for heat exchangers has many advantages but also some problems which require further close study. However, this theoretical iterative model can approximately show the behavior of the PHFHE and processes of heat transfer that take place in polymer fibers. That can help to choose or create the best heat exchanger for the conditions required.

Acknowledgements

The present work has been supported by the European Regional Development Fund within the framework of the research project NETME Centre, CZ. 1.05/2.1.00/01.0002, under the Operational Programme Research and Development for Innovation.

References

- Dittus, F. W., Boelter, L. M. K. (1930) Heat transfer in automobile radiators of the tubular type, University of California Publications on Engineering, 2, 443-461, Berkeley, CA.
- Githens, R. E., Minor, R. W., Tomsic, V. J. (1965) Flexible tube heat exchangers. Chem. Eng. Prog., 61 (7), 55.4.
- Incropera, F. P. & DeWitt D. P. (1996) Fundamentals of Heat and Mass Transfer, 4th ed., Wiley, New York.
- Whitaker, S. (1972) Forced convection heat transfer correlations for flow in pipes, past flat plates, single cylinders, single spheres, and for flow in packed beds and tube bundles, AIChE J., 18(2), 361- 71.
- Whitley, D. M. (1957) Plastic heat exchangers gain in severe service. Chem. Eng. 64 (9), 308.
- Zarkadas, D. M. & Sirkar K. K. (2004) Polymeric hollow fiber heat exchangers: An alternative for lower temperature applications. Ind. Eng. Chem. Res. 43, pp. 8093-8106.
- Zukauskas, A. (1972) Heat transfer from tubes in crossflow, Adv. Heat Transfer, 8, 93-160.

DEVELOPMENT OF MATHEMATICAL MODEL OF RAIN ZONE

T. Hyhlik*

Abstract: *The article deals with the development of one of the key part of the complex CFD model of natural draft wet-cooling tower flow namely model of rain zone. The physical phenomena occurring in the natural draft cooling tower can be described by the combined Eulerian-Lagrangian model with additional model of film type fill. The Eulerian part is the model of the flow of homogeneous mixture of dry air and water vapour. The Lagrangian part is the model of transport of liquid water droplets. The heat and mass transfer between Lagrangian phase and Eulerian phase is included via source terms in the model of homogeneous mixture of dry air and water vapour. The simplified model of rain zone based on the solution of boundary value problem for the system of ordinary differential equation is also derived.*

Keywords: Natural draft wet-cooling tower, Eulerian-Lagrangian model, Rain zone, Evaporative cooling.

1. Introduction

The aim of the wet-cooling tower is transfer of heat from cooled water into the moist air. The cooling of flowing water is connected with warming up of flowing moist air and with increase of its humidity. The density of warmed air is decreasing unlike of surrounding air and this density difference produce natural draft.

Cooled water is sprayed above the fill using the set of sprayers. In the channels of counterflow cooling tower fill water flows vertically down as a liquid film. Air is driven by tower draft and flows in the opposite direction. Evaporation and convective heat transfer cool down the water. The water is leaving the fill zone and falling down in the form of rain to the pond at the bottom part of the cooling tower. This work concentrates mainly on the development of the model of heat and mass transfer in the rain zone. The water droplets are considered as Lagrangian phase and moist air is considered as Eulerian phase.

2. Eulerian Model of Moist Air Flow

Moist air can be considered as homogeneous mixture of dry air and water vapour. Continuity equation for dry air can be written as

$$\frac{\partial(\rho_a)}{\partial t} + \frac{\partial(\rho_a v_k)}{\partial x_k} - \frac{\partial}{\partial x_k} \left[D_{a,v} \frac{\partial \rho_a}{\partial x_k} \right] = 0, \quad (1)$$

where $D_{a,v}$ is diffusion coefficient of dry air in the water vapour. We can express the continuity equation of water vapour in the form

$$\frac{\partial(\rho_v)}{\partial t} + \frac{\partial(\rho_v v_k)}{\partial x_k} - \frac{\partial}{\partial x_k} \left[D_{v,a} \frac{\partial \rho_v}{\partial x_k} \right] = \sigma_v(x_k, t), \quad (2)$$

where $\sigma_v(x_k, t)$ represents the density of source of vapour and diffusion coefficient of water vapour in the air is $D_{v,a} = D_{a,v}$. The system of momentum equations can be written in the form

$$\frac{\partial(\rho v_i)}{\partial t} + \frac{\partial}{\partial x_k} [\rho v_i v_k - \sigma_{ik}] = -\rho g \delta_{i3} - \zeta(x_k, t) \rho \frac{|v|^2}{2} \delta_{i3} + \sigma_h(x_k, t) \delta_{i3}, \quad (3)$$

* Ing. Tomáš Hyhlik, PhD.: Department of Fluid Dynamics and Thermodynamics, Faculty of Mechanical Engineering, Czech Technical University in Prague, Technická 4; 166 07, Prague; CZ, tomas.hyhlik@fs.cvut.cz

where $-\rho g \delta_{i3}$ represents gravitational force acting on the flowing moist air, σ_{ik} is the stress tensor in a flowing fluid, ζ represents a loss coefficient per meter of the fill zone and $\sigma_h(x_k, t)$ is momentum source. The energy equation is written in the form

$$\frac{\partial(\rho e)}{\partial t} + \frac{\partial}{\partial x_k} [\rho v_k e - \sigma_{kj} v_j + q_k] = \sigma_q(x_k, t) - g \rho v_3, \quad (4)$$

where $\sigma_q(x_k, t)$ is density of heat source where the only sensible part of heat source is considered because of the definition of total energy

$$\rho e = \rho \left(c_v T + \frac{v_k v_k}{2} \right) = \left(\frac{r}{\kappa - 1} T + \frac{v_k v_k}{2} \right), \quad (5)$$

where κ is Poisson coefficient

$$\kappa = \frac{c_p}{c_v}. \quad (6)$$

Pressure can be expressed using the equation of state as

$$p = \frac{\rho R T \left(1 + \frac{M_a x}{M_v} \right)}{M_a (1 + x)} = \rho R T \left(\frac{M_v - w_v (M_v - M_a)}{M_a M_v} \right), \quad (7)$$

where x is specific moisture and w_v is water vapour mass fraction. Detailed description of the model of the flow of homogeneous mixture of air and water vapour is in reference Hyhlík (2014).

3. Lagrangian Model of Water Droplets

There is flow of moist air with droplets in the rain zone and in the spray zone. Mean diameter of droplet falling down in the rain zone and in the spray zone is in the order of millimeters. It is stated in the reference Kroger (2004) that mean diameter in rain zone is 3.5 mm. Pierce (2007) measured mean diameter 3.22 mm and Sauter mean diameter 5.73 mm in rain zone. Viljoen (2006) measured droplet mean diameter for medium pressure spray nozzles about 2 mm and Sauter diameter was between 2.4 and 3.4 mm in spray zone. For low pressure spray nozzles Viljoen (2006) measured in spray zone mean diameter about 3.2 mm and Sauter mean diameter was about 7.4 mm.

Equation of motion of a single droplet falling down can be derived by using Newton's second law

$$m_d \frac{dv_d}{dt} = -\frac{4}{3} \pi R^3 g \rho_w + c_x (Re) \pi R^2 \rho_{ma} \frac{[v_a - v_d(z)]^2}{2}, \quad (8)$$

where first term on the right side represents gravitational force and second term is drag force with relative velocity of air to droplet $|v_a - v_d(z)|$, m_d is droplet mass, v_d is droplet velocity, R is droplet radius, g is gravitational acceleration, ρ_w is density of water, $c_x(Re)$ is drag coefficient and ρ_{ma} is moist air density.

3.1. Droplet heat and mass transfer

In the case of dilute mixture the rate of change of mass of single droplet can be expressed as

$$\frac{dm_d}{dt} = -h_m \rho_{Ama} 4\pi R^2 \left(x''(t_d(z)) - x(z) \right), \quad (9)$$

where h_m is mass transfer coefficient, ρ_{Ama} is averaged density of moist air, $x''(t_d(z))$ is specific humidity of saturated moist air at the temperature of droplet and $x(z)$ is specific humidity of moist air flowing around the droplet. If we assume uniform drop temperature, then convection heat transfer can be expressed using Newton's law of cooling

$$\dot{Q} = \alpha 4\pi R^2 (t_a - t_d(z)), \quad (10)$$

where α is heat transfer coefficient, t_a is moist air temperature and $t_d(z)$ is droplet temperature. Rate of change of internal energy of single droplet can be then expressed as

$$\frac{d}{dt} (m_d c_w t_d) = m_d c_w \frac{dt_d}{dt} + c_w t_d \frac{dm_d}{dt} = \dot{Q} + \frac{dm_d}{dt} h_v(t_d), \quad (11)$$

where c_w is specific heat capacity of water and $h_v(t_d)$ is enthalpy of water vapour at droplet temperature. Heat and mass transfer can be evaluated using correlations of Ranz and Marshall (1952)

$$Nu = 2 + 0.6Re^{1/2}Pr^{1/3}, \quad (12)$$

$$Sh = 2 + 0.6Re^{1/2}Sc^{1/3} \quad (13)$$

which are based on Nusselt number Nu , Reynolds number Re , Prandtl number Pr , Sherwood number Sh and Schmidt number Sc .

4. Simplified Model of Rain Zone

The definition of droplet velocity can be used to modify system of equations (8-11) to get similar equations like Fisenko et al. (2002). The equation describing the change in radius can be derived from equation (9)

$$\frac{dR}{dz} = -\frac{h_m \rho_{Ama}}{v_d(z) \rho_w} [x''(t_d(z)) - x(z)]. \quad (14)$$

The equation for the velocity of falling droplet is based on equation (8)

$$\frac{dv_d}{dz} = -\frac{g}{v_d(z)} + \frac{3}{8} \frac{c_x(Re)}{R v_d(z)} \frac{\rho_{ma}}{\rho_w} [v_a - v_d(z)]^2. \quad (15)$$

The equation for temperature of droplet is based on equation (11)

$$\frac{dt_d}{dz} = \frac{3[\alpha(t_a - t_d) - h_m \rho_{Ama} [x''(t_d(z)) - x(z)] (l_0 + t_d(c_{pv} - c_w))]}{v_d(z) R c_w \rho_w}. \quad (16)$$

The density of water droplets per meter of the rain zone can be defined as

$$N_D(z) = \frac{\dot{m}_w}{\frac{4}{3} \pi R_i^3 \rho_w |v_d(z)|}, \quad (17)$$

where \dot{m}_w is water mass flow rate at rain zone inlet and R_i is droplet radius at the inlet. Mass balance of incremental step of rain zone can be expressed from the point of view of flowing moist air as

$$\dot{m}_a \frac{dx}{dz} = -N_D(z) v_d(z) \frac{dm_d}{dz}, \quad (18)$$

where \dot{m}_a is dry air mass flow rate. The change in moist air total enthalpy of incremental step of rain zone can be expressed like

$$\dot{m}_a \frac{dh_{1+x}}{dz} = -N_D(z) v_d(z) \left[\frac{dQ}{dz} + \frac{dm_d}{dz} h_v(t_d) \right], \quad (19)$$

The change in specific moisture can be expressed from equation (18) and by using equation (14) as

$$\frac{dx}{dz} = \frac{4\pi R^2 N_D(z) h_m \rho_{Ama}}{\dot{m}_a} [x''(t_d(z)) - x(z)]. \quad (20)$$

The change in moist air temperature is expressed using derivation of moist air enthalpy definition

$$\frac{dt_a}{dz} = \frac{1}{c_{pa} + x c_{pv}} \left[\frac{dh_{1+x}}{dz} - (l_0 + c_{pv} t_a) \frac{dx}{dz} \right]. \quad (21)$$

After substitution of equation (19), (20), (9) and (10) we get

$$\frac{dt_a}{dz} = \frac{-4\pi R^2 N_D}{\dot{m}_a (c_{pa} + x c_{pv})} [\alpha(t_a - t_d) + h_m \rho_{Ama} (x''(t_d) - x) c_{pv} (t_a - t_d)]. \quad (22)$$

Equations (14), (15), (16), (20) and (22) form our model of rain zone. We have boundary value problem for the system of ordinary differential equations in rain zone. We should prescribe droplet radius, droplet velocity and temperature on the upper boundary. Moist air temperature and specific humidity should be stated on the lower boundary of the rain zone.

5. Source Terms

From the point of view of Eulerian model given by equations (1), (2), (3) and (4) it is necessary to solve them iteratively together with initial value problem for the system of equations (14), (15) and (16) and prescribe source terms. The density of water vapour source is

$$\sigma_v(x_k, t) = \frac{4\pi R^2 N_D(z) h_m \rho_{Ama}}{A(z)} [x''(t_d(z)) - x(z)]. \quad (23)$$

The source in the system of momentum equations can be expressed as

$$\sigma_h(x_k, t) = -c_x(Re)\pi R^2 \rho_{ma} \frac{[v_a - v_d]^2 N_D(z)}{2 A(z)}. \quad (24)$$

The density of heat source where only sensible part of heat source is considered is

$$\sigma_{qs}(x_k, t) = \frac{-4\pi R^2 N_D(z)}{A(z)} \left(\alpha(t_a - t_d) - h_m \rho_{Ama} (x''(t_d(z)) - x(z)) c_{pv} t_d \right). \quad (25)$$

Because of the definition of total energy (5) the density of heat source should be calculated as

$$\sigma_q(x_k, t) = \sigma_{qs}(x_k, t) + 273.15 c_{pv} \sigma_v(x_k, t). \quad (26)$$

6. Conclusions

The Eulerian-Lagrangian model of moist air flow with droplets falling down is developed. The key part of the proposed model is the calculation of sources of mass, momentum and energy defined by equations (23), (24), (25) and (26). The developed model is an extension of previously developed model of natural draft cooling tower by Hyhlik (2014) where heat and mass transfer in rain zone was omitted. Byproduct of the development is rain zone model given by equations (14), (15), (16), (20) and (22). Practically it is the model of counterflow rain zone. We have boundary value problem for the system of ordinary differential equations in this case. Not least should be mentioned that proposed model is ignoring droplet distribution function and the influence of droplet deformation on the heat and mass transfer. The more complex models will be probably developed in future.

Acknowledgement

This work has been supported by Technology Agency of the Czech Republic under the project Advanced Technologies for Heat and Electricity Production –TE01020036.

References

- Hyhlik, T. (2014) Concept of CFD model of Natural Draft Wet-Cooling Tower Flow, submitted to European Physical Journal Web of Conferences.
- Kroger, D. G. (2004) Air-Cooled Heat Exchangers and Cooling Towers, Pen Well Corporation, Tulsa.
- Pierce, D. J. (2007) Evaluation and Performance of Cooling Tower Rain Zones, M.Sc. Thesis, University of Stellenbosch.
- Viljoen, D. J. (2006) Evaluation and Performance Prediction of Cooling Tower Spray Zones, M.Sc. Thesis, University of Stellenbosch.
- Ranz, W. E., Marshall, W.R. (1952) Evaporation from Drops, Part I, Chemical Engineering Progress, Vol. 48, No. 3, pp. 141-146.
- Fisenko, S. P., Petruhic, A. I., Solodukhin, A. D. (2002) Evaporative cooling of water in a natural draft cooling tower, International Journal of Heat and Mass Transfer, Vol. 45, pp. 4683-4694.

IDENTIFICATION OF THE AEROELASTIC PROFILE BASED ON OPTICAL MEASUREMENT

Š. Chládek^{*}, I. Zolotarev^{*}

Abstract: *This paper introduces an identification of an aeroelastic profile as n – degrees of freedom linear system. The common identification is based on the excitation of the system with an impact hammer and the measurement of the response by an acceleration sensor and using the transfer functions the modal properties are evaluated. This approach gives a disadvantage in the sense of influence of the system structural properties. In this paper the identification of the dynamical system is based on the optical measurement of the system response. The great advantages of this approach are both the low influence of the measuring devices to the system properties and the high precision of the measurement. The theory has been verified on the aeroelastic profile NACA 0012 with 2 degrees of freedom and the results are presented.*

Keywords: System identification, Aeroelastic profile, Optical measurement.

1. Introduction

The identification of the real object means to derive its mathematical model. The mathematical model has to fulfill certain criterion; the most important one is that the model describes the object properties as close as possible. Identification of the dynamical system is widely spread field of study, when the most methods are based on the system excitation and its response measurement and using the transfer function the modal properties are evaluated, see Kozánek (1982). There have to be performed more measurements for the complete system description. This approach gives a disadvantage in the sense of added mass (weight of the sensor) and added damping (the sensor's wire attachment). The mentioned disadvantages influence the profile's modal and structural properties and these changes can cause a difference between numerical simulation and real experiment results. This paper describes an identification method based on the optical measurement of the system response. The great advantage of the optical measurement is a minimal impact on the system properties and the requirement of one measurement only.

2. System Identification

The linear system can be described by the equation of motion

$$\mathbf{M}\ddot{\mathbf{z}}(t) + \mathbf{B}\dot{\mathbf{z}}(t) + \mathbf{K}\mathbf{z}(t) = \mathbf{F}(t), \quad (1)$$

where $\mathbf{z}(t)$ is the position vector, $\mathbf{F}(t)$ is the excitation vector and \mathbf{M} , \mathbf{B} , \mathbf{K} are the mass, damping and stiffness matrices, respectively. The acceleration, velocity and displacement responses can be expressed using the modal transformation

$$\dot{\mathbf{z}}(t) = \mathbf{V}\dot{\mathbf{q}}(t), \quad \dot{\mathbf{z}}(t) = \mathbf{V}\dot{\mathbf{q}}(t), \quad \mathbf{z}(t) = \mathbf{V}\mathbf{q}(t), \quad (2)$$

where \mathbf{V} is the matrix of modal vectors. Coupling the equations (1), (2), using the equalities $\mathbf{M}^{-1}\mathbf{B} = \text{diag}(2b_{ri}\Omega_{0i})$, $\mathbf{M}^{-1}\mathbf{K} = \text{diag}(\Omega_{0i}^2)$, $i = 1, 2, \dots, n$, where n is the number of degrees of freedom and the assumption the modal vectors matrix is orthogonal, the resulting equation of motion in modal coordinates can be written in the form

$$\ddot{q}_i(t) + 2b_{ri}\Omega_{0i}\dot{q}_i(t) + \Omega_{0i}^2q_i(t) = V_{ji}^T F_i(t), \quad (3)$$

^{*} Ing. Štěpán Chládek, Ing. Igor Zolotarev, CSc.: Institute of Thermomechanics AS CR, v. v. i., Dolejškova 1402/5, 182 00 Prague, CZ, chladek@it.cas.cz, igor@it.cas.cz

where b_{ri}, Ω_{0i} is the damping ratio and natural frequency, respectively. The modal coordinate $q_i(t)$ can be derived from the natural coordinates using a suitable data processing, i.e. appropriate data filtration. The relation between the structural matrices and modal properties can be expressed in the form

$$\mathbf{M} = \mathbf{V}^{-1}, \mathbf{B} = \text{diag}(2b_{ri}\Omega_{0i})\mathbf{V}^{-1}, \mathbf{K} = \text{diag}(\Omega_{0i}^2)\mathbf{V}^{-1} \quad (4)$$

where $i = 1, 2, \dots, n$ denotes the number of degrees of freedom. The damping ratios b_{ri} , undamped natural frequencies Ω_{0i} and modal vector matrix \mathbf{V} are determined from the modal coordinates. The natural frequencies Ω_i of the damped system are calculated using the Fourier transformation. The Hilbert transformation of the modal coordinate q_i is used for calculation of b_{ri} in the sense of relation

$$b_{ri} = \sqrt{\frac{1}{1 + \left(\frac{\Omega_i}{k_i}\right)^2}} \quad (5)$$

where k_i is the slope of the envelope of the modal coordinate q_i when it is depicted in semi logarithmic coordinates. Similar approach based on Hilbert-Huang transformation is described in Yang et al. (2003). The natural frequency of undamped system is determined as

$$\Omega_{0i} = \sqrt{\frac{\Omega_i}{b_{ri}^2 - 1}} \quad (6)$$

The element $V_{i,j}$ of the matrix \mathbf{V} is calculated from the mean value of the ratio of the modal coordinate q_i in the position 1 and j .

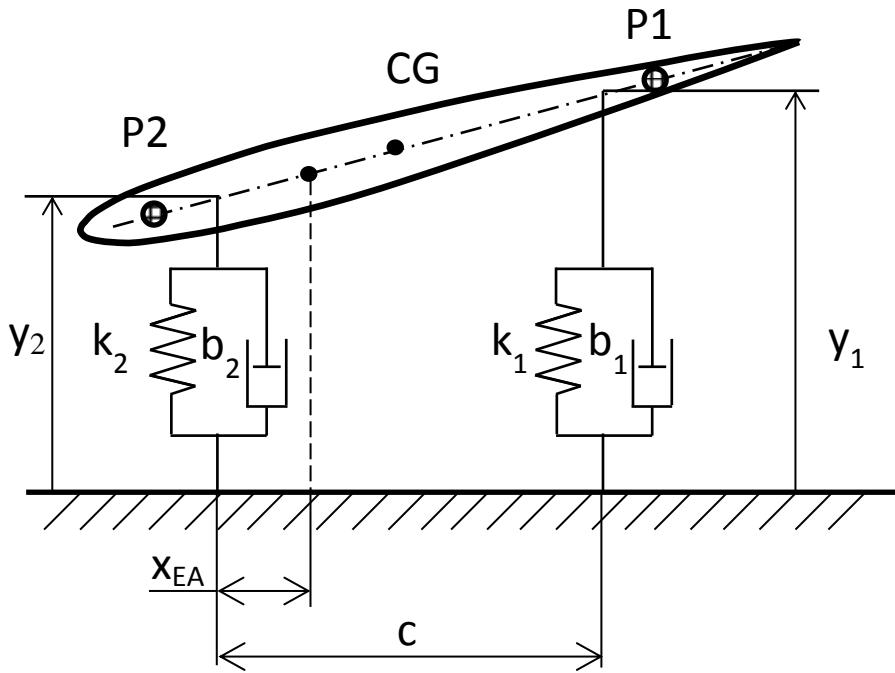


Fig. 1: Scheme of the profile NACA 0012 attached to the frame. Points P1, P2 denote the positions of targets, which have been recorded by camera. CG means center of gravity, EA denotes the elastic axis.

3. Experimental Measurement

It has been chosen a profile NACA 0012 with two degrees of freedom for the theory verification. The length of the chord is 100 mm and the span of the wing is as well 100 mm. The wing is attached with two leaf springs to the frame, see Chládek et al., (2012). The scheme of the profile is in the Fig. 1.

There has been attached a white paper with two black points P1, P2 on one side of the profile. The black points have been chosen to increase the contrast to the white background and these points have been used for the instantaneous position determination. The number of black points has to be equal to the number of

degrees of freedom. The paper with the weight of less than 0.2 g is the only one influence to the profile. The position of the points has been captured with high frequency camera Dantec NanoSense. The sampling frequency has been set up to $f_s = 2000 \text{ Hz}$ and the record time as non-optional parameter has been calculated as $t = 11.3 \text{ s}$. One picture from the camera is shown in the Fig. 2. The profile has been deflected from its equilibrium position and its response has been measured. Based on the Fourier transform of the signal the natural frequencies Ω_i have been computed and the digital filters have been designed. It has been chosen a bandpass type filter with the finite impulse response.



Fig. 2: Picture of the targets recorded by the high frequency camera with the points P1 (right), P2 (left).

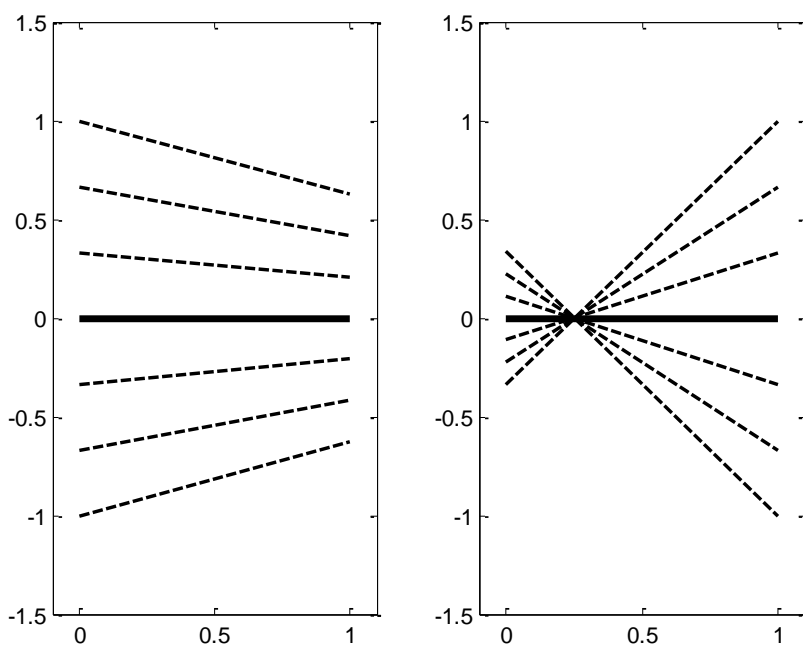


Fig. 3: Eigenmodes related to the 1st natural frequency (left) and to the 2nd natural frequency (right).

Tab. 1 Comparison of modal properties of the system evaluated from the time record of the position measured in the points P1 and P2.

	Record point P1	Record point P2
f_{01} [Hz]	31.62	31.62
f_{02} [Hz]	38.88	38.88
f_1 [Hz]	31.62	31.62
f_2 [Hz]	38.88	38.88
b_{r1} [-]	323×10^{-5}	324×10^{-5}
b_{r2} [-]	190×10^{-5}	190×10^{-5}

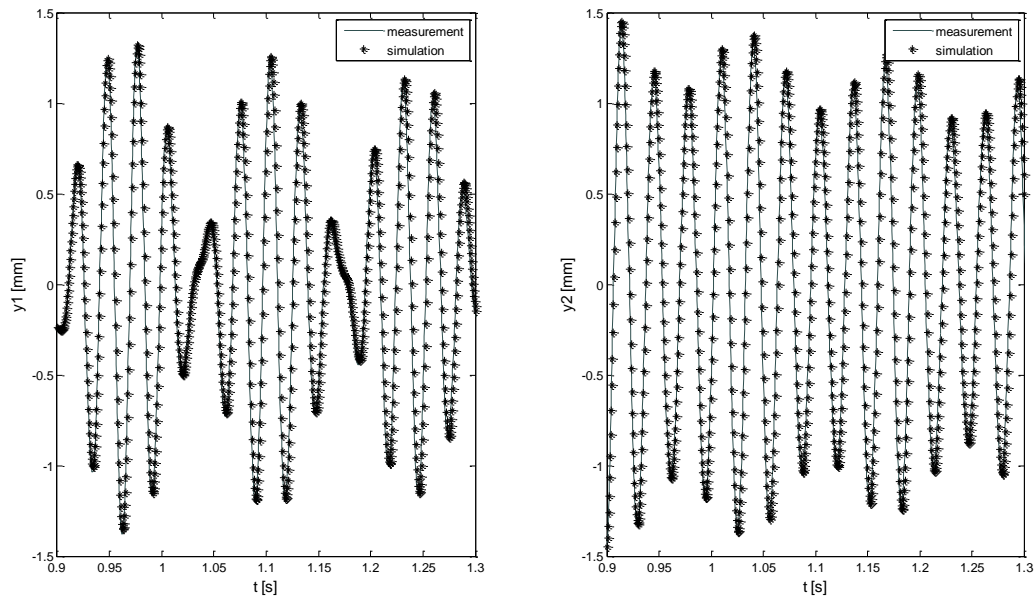


Fig. 4: Comparison of experiment (solid line) and numerical simulation (discrete points) in time record of the profile movement.

The modal coordinates have been derived applying the suggested filters to the original signals. The modal properties have been computed using (5), (6) and they are listed in the Tab. 1. This table has two columns due to the fact that all modal properties have been calculated twice from the signal measured at the point P1 and P2 as well. The eigenmodes related to the natural frequencies are plotted in the

Fig. 3. The structural matrices have been calculated using (4). The possible way for the matrices verification is the computation of (1) with the initial conditions corresponding to the real experiment and the excitation vector $F(t) = \mathbf{0}$. The numerical integration has been performed with the time $t = (t_0, t_1)$ and the results are compared with the experiment in the Fig. 4.

4. Conclusions

Identification method based on the optical measurement of the system displacement has been introduced. There have been performed both numerical simulation and experiments for the theory verification. The results have demonstrated high accordance of the real system with its mathematical model. Considering the Tab. 1 it can be concluded that the measurement has been performed with very high precision, because the differences of calculated modal properties are negligible. The most important results of introduced identification process are the correct structural matrices, which have been proved by comparing the real experiment and the numerical simulation of system response to the given initial conditions. The major disadvantage of the submitted method is the requirement of an expensive high frequency camera while the widespread used acceleration sensors are significantly cheaper.

Acknowledgement

The research was supported by the project of the Grant Agency of the Czech Republic GA13-10527S „Subsonic flutter analysis of elastically supported airfoils using interferometry and CFD“.

References

- Chládek, Š., Zolotarev, I. & Uruba, V. (2012) Numerical Simulation and Experiments with the Profile NACA 0012. In: Proc. Inter. Conference Engineering Mechanics 2012, Svratka, Czech Republic, pp. 523-529, paper #78.
- Kozánek, J. (1982) Evaluation of transfer function from experimental data. Strojnický časopis, 33, pp. 281-288. (in Czech).
- Yang, J., N., Lei, Y., Pan, S., Huang, N. (2003) System Identification of linear structures based on Hilbert-Huang Spectral Analysis. Part 1: normal modes. Earthquake engineering and structural dynamics, 32, pp. 1443-1467.

PARAMETER IDENTIFICATION IN INITIAL VALUE PROBLEMS FOR NONLINEAR ORDINARY DIFFERENTIAL EQUATIONS

J. Chleboun^{*}, K. Mikeš^{**}

Abstract: *Nonlinear initial value problems (IVPs) for ordinary differential equations are considered. As a representative, a cement hydration model is chosen. The model equation depends on a few parameters that are to be identified on the basis of hydration-related measurements at a sequence of time points. This is done through the minimization of a cost function defined as the sum of squared differences between the measured values and the model response at the same time points. To minimize the cost function, a gradient based algorithm is used. The gradient of the cost function can be calculated either by numerical differentiation or via solving auxiliary initial value problems. The minimization algorithm tends to find a local minimum. Therefore, it is run from different starting points to increase the chance of finding the global minimum. Algorithms are coded in the Matlab environment, and Matlab IVP solvers as well as Matlab Optimization Toolbox and Symbolic Math Toolbox are utilized. The latter makes the derivation of the auxiliary IVPs easy and reliable.*

Keywords: Identification of parameters, Initial value problem, Matlab, Sensitivity analysis.

1. Introduction

Identification of parameters is a frequent problem in modeling real-world phenomena. In a common situation, a phenomenon is observed and its features are quantified through measurements. Next, a mathematical model is formulated that, inevitably, depends on parameters that can be general and known (as general physical constants, for instance) or rather special and known only approximately. Parameters can also determine the basic hypothesis of the mathematical model. As an example, take a possible uncertainty in the relationships between quantities involved in the model. These relationships can be described by, for instance, linear, quadratic, or exponential mathematical expressions, and the first goal of modeling is to identify the classes of dependencies that constitute the model.

In this paper, we focus on the identification of parameters in initial value problems for ordinary differential equations. This subject has been widely studied in the literature. An easily accessible introductory material (Munster, 2009) can serve as an appropriate starting point for beginners in the field. A more advanced application is the subject of the paper (Babadzanjanz et al., 2003). Let us note that we will deal with a problem that is not ill-posed and that can be treated in a straightforward way similar to that used in the papers cited above.

We were motivated by the report (Mareš, 2012), where four parameters of a cement hydration model are identified through a neural network approach. The initial value problem is, see (Mareš, 2012),

$$\frac{d\alpha}{dt}(t) = B_1 \left(\frac{B_2}{\alpha_\infty} + \alpha(t) \right) (\alpha_\infty - \alpha(t)) \exp\left(\frac{\eta}{\alpha_\infty} \alpha(t) \right) C, \quad (1)$$

$$\alpha(0) = 0, \quad (2)$$

where α is the time dependent degree of hydration, B_1 and B_2 are coefficients related to the cement chemical composition, α_∞ is the limit value of the hydration degree, η represents the microdiffusion of free water through formed hydrates, and C is a constant originating from an expression comprising some

^{*} Jan Chleboun: Faculty of Civil Engineering, Czech Technical University in Prague, Thákurova 7; 166 29 Prague; CZ, chleboun@mat.fsv.cvut.cz

^{**} Karel Mikeš: Faculty of Civil Engineering, Czech Technical University in Prague, Thákurova 7; 166 29 Prague; CZ, karel.mikes.1@fsv.cvut.cz

physical constants such as the universal gas constant, for instance. The initial condition $\alpha(0) = 0$ stands for the hydration degree at time $t = 0$ that is assumed to be zero though a positive value less than α_∞ is also possible. The degree of hydration is measured at time points t_i , in this way, values $m_i, i = 1, 2, \dots, n$, are produced. To take account of possibly different importance of the measurements, nonnegative weights w_i can be considered. In the sequel, the hydration initial value problem will also be referred to as the state equation, especially in the context that is not limited to the hydration equation but includes other initial value problems too.

Constant C is known, but the values of α_∞, B_1, B_2 , and η are to be identified through the minimization of the cost function defined as follows

$$f(\alpha_\infty, B_1, B_2, \eta) = \sum_{i=1}^n w_i (m_i - \alpha(t_i))^2 \quad (3)$$

The range of these input parameters is given in Table 1 taken from (Mareš, 2012). As a consequence, we arrive at a constrained minimization of f , where, to obtain the value of f for different inputs, the hydration initial value problem (1)-(2) has to be repeatedly solved.

Tab. 1: Lower and upper bounds for input parameters α_∞, B_1, B_2 , and η .

Parameter	Minimum	Maximum
α_∞	0.7	1.0
B_1	10^6	10^7
B_2	10^{-6}	10^{-3}
η	-12	-2

2. Methods

Various approaches are possible for solving the constrained global minimization problem described in the end of Section 1. We have chosen an SQP (sequential quadratic programming) method implemented as the optimization procedure `fmincon` in the Matlab Optimization Toolbox, see (Optimization, 2012). This Matlab function is designed to find a minimum of a constrained nonlinear cost function. The algorithm asks for the gradient of the minimized cost function. The gradient can be either calculated automatically by a numerical differentiation of the cost function or delivered by a user-written Matlab function. To use the latter option, it is necessary to derive and solve auxiliary initial value problems that represent the sensitivity of the solution of the state equation to the input parameters. The sensitivity is, in fact, the derivative of the state solution with respect to an input parameter. The background theory for the derivation of these problems is described in (Kurzweil, 1978), Chapter 14, for instance.

2.1. Sensitivity equations

The aforementioned initial value problems have the same form, namely

$$\frac{dv}{dt}(t) = g(t)v(t) + p(t), \quad (4)$$

where $g(t)$ and $p(t)$ are known functions containing the state solution $\alpha(t)$ the derivative of which we wish to calculate. The equation is equipped with $v(0) = 0$, the initial condition. In detail,

$$g(t) = B_1 \exp\left(\frac{\eta}{\alpha_\infty} \alpha(t)\right) \left(\alpha_\infty - \frac{B_2}{\alpha_\infty} - 2\alpha(t) + \left(\frac{B_2}{\alpha_\infty} + \alpha(t)\right) (\alpha_\infty - \alpha(t)) \eta \alpha_\infty^{-1} \right) C \quad (5)$$

is shared by all the sensitivity equations but p is more input parameter dependent. If the sensitivity (that is, the derivative) to α_∞ is required, then

$$p(t) = B_1 \alpha(t) \exp\left(\frac{\eta}{\alpha_\infty} \alpha(t)\right) C \alpha_\infty^{-3} \\ \times (\alpha_\infty B_2 + \alpha_\infty^3 - \eta \alpha_\infty B_2 + \eta B_2 \alpha(t) - \eta \alpha_\infty^2 \alpha(t) + \eta \alpha^2(t) \alpha_\infty). \quad (6)$$

If B_1 is in the focus of sensitivity analysis, then

$$p(t) = \left(\frac{B_2}{\alpha_\infty} + \alpha(t) \right) (\alpha_\infty - \alpha(t)) \exp\left(\frac{\eta}{\alpha_\infty} \alpha(t) \right) C. \quad (7)$$

For B_2 , we obtain

$$p(t) = B_1 (\alpha_\infty - \alpha(t)) \exp\left(\frac{\eta}{\alpha_\infty} \alpha(t) \right) C \alpha_\infty^{-1}. \quad (8)$$

Finally, the differentiation with respect to η results in

$$p(t) = B_1 \left(\frac{B_2}{\alpha_\infty} + \alpha(t) \right) (\alpha_\infty - \alpha(t)) \alpha(t) \exp\left(\frac{\eta}{\alpha_\infty} \alpha(t) \right) C \alpha_\infty^{-1}. \quad (9)$$

To facilitate the process of the derivation of the sensitivity initial value problems, Matlab Symbolic Math Toolbox, see (Symbolic, 2012), was employed. By using this tool, we automatically both derive the sensitivity formulae and obtain the respective Matlab functions that are then called from a sensitivity calculation routine.

The sensitivity of the cost function, represented by the partial derivative of f with respect to $\omega \in \{\alpha_\infty, B_1, B_2, \eta\}$, is as follows

$$\frac{\partial f}{\partial \omega} = 2 \sum_{i=1}^n w_i (m_i - \alpha(t_i)) \alpha'_\omega(t_i), \quad (10)$$

where α'_ω , the derivative of α with respect to ω , is obtained through solving the sensitivity initial value problems (4)-(9), that is, $\alpha'_\omega \equiv v$.

The key point of the calculation is to solve the initial problems. This is done by the ordinary differential equation solver `ode45`, a standard Matlab function. Although its use in the main program as well as in its subroutines is easy and comfortable, it has turned out that the accuracy the gradient calculation is affected by the values of the inner parameters that control the setting of the `ode45` solver. Tuning of these parameters is recommended.

2.2. Results and comments

Outputs of two identification program runs are depicted in Fig. 1. The data were generated from a known state solution, the parameters of which were then “lost” and identified again.

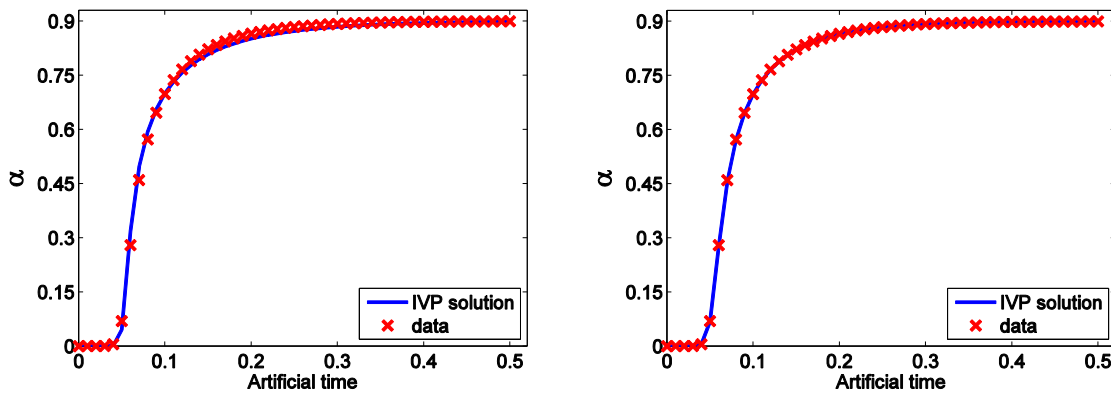


Fig. 1: Measured data and the solution of the hydration problem corresponding to the identified parameters α_∞ , B_1 , B_2 , and η .

In the left graph, one can see that the data points are not exactly matched. The initial cost of 181.932 was reduced to 4.086, which falls short of expectations. The minimization method got stuck at a local minimum. The right graph results from the optimization run starting at a different initial point. The initial cost of 3 408.858 was reduced to 0.0000222.

3. Conclusions

The coupling of a purely numerical software with a computer algebra tool has proved to be effective. It substantially reduces the danger of erroneous derivation of the sensitivity equations and saves coding time. Since the identification problem is a sort of global minimization problem, one has to be careful when using a gradient-based optimization algorithms. A set of different starting points has to be chosen.

Acknowledgements

The authors appreciate the support of the Grant Agency of the Czech Technical University in Prague, grant No. SGS14/003/OHK1/1T/11. The authors also wish to thank Karel Hájek and Ondřej Petlík for their assistance in the project.

References

- Babadzanjan, L. K., Boyle, J. A., Sarkissian, D. R. & Zhu, J. (2003) Parameter identification for oscillating chemical reactions modelled by systems of ordinary differential equations. *Journal of Computational Methods in Science and Engineering*, 3, pp. 223-232.
- Kurzweil, J. (1978) *Ordinary Differential Equations*. SNTL – Nakladatelství technické literatury, Praha (in Czech).
- Mareš, T. (2012) Artificial neural networks in calibration of nonlinear models. Report. Department of Mechanics, Faculty of Civil Engineering, Czech Technical University in Prague, pp. 1-11. Available at http://mech.fsv.cvut.cz/wiki/index.php/Sout%C4%9B%C5%BE_o_Cenu_akademika_Ba%C5%BEanta#2012
- Munster, D. (2009) Parameter Identification: A Comparison of Methods. Report. Dept. of Mathematics, College of Science, Virginia Tech, pp. 1-29.
Available at http://www.math.vt.edu/ugresearch/munster_draxton.pdf.
- Optimization Toolbox (2012) <http://www.mathworks.com/help/optim/ug/fmincon.html>.
- Symbolic Math Toolbox (2012) <http://www.mathworks.com/help/symbolic/index.html>.

OPTIMISATION IN THE EXPLICIT ANALYSIS OF THE ROAD BARRIERS

L. Iván^{*}, M. Popović^{**}

Abstract: *The aim of this project was to setup a surrogate process that is able to substitute a real crash test of road barriers. As a standardized vehicle was used a typical city bus. The sensitivity analysis was performed due to detailed understanding of the parameters limits and their relations. The sensitivity study enables to check more than one crash test loadcase. Two variants of optimization were used, the standard optimization procedure and optimization with meta-model based on the previous sensitivity study. Both of them used the evolutionary algorithm. The goal was to increase a maximum internal energy of the barrier. Apart from that the vehicle maximum deceleration was improved. The optimized barrier model was verified in the thorough explicit numerical study due to investigation of the detailed interaction between the barrier model and the vehicle model. The effect of the testing vehicle on the crash barriers can be evaluated in tens of impact directions and impact velocity values. Apart from that the design of barriers was improved. The detailed numerical analysis of the “best” variant confirms a good relation between numerical simulations and real tests.*

Keywords: ANSYS, Explicit Analysis, Road barriers, OptiSLang, LS-Dyna.

1. Introduction

The safety in road traffic is a long-term problem in most countries regardless their actual state of economy or political situation. There are many types of technical resources that can help to reduce undesirable consequences of very frequent road accidents. One of the most difficulties in a production of these technical resources is to estimate their capability to decrease unfavorable results of traffic accidents. Many kinds of possible real situations lead to many analyzed loadcases.

The aim of this project was to setup a standard process of a numerical simulation that is able to substitute a real crash test of road barriers which is whenever expensive. Two points of a view are included in this project. The first is to build a simple and quick numerical model of the crash test that can be used in optimization process with hundreds of variants. The second point of view is to build the accurate numerical model as much as possible. This kind of model has to be used as a substitution of a real test. Both models can be used as a part of a development process.

2. Crash Test Configurations – Sensitivity

The simple model of the crash test, see Fig. 1, was built due to the investigation of the worst loading case that barrier has to satisfy. It brings a general overview of relations between the vehicle impact velocity, the impact angle and structural results on the barrier. A typical city bus that is most common in this area was used as a standardized vehicle. It represents a body with 13 tons of mass impacted to the barrier under defined angle.

The sensitivity analysis was performed with next input parameters:

- impact velocity,
- impact angle between vehicle and barriers,
- thickness of the barriers (two parameters).

^{*} Ing. László Iván, PhD.: SVSFEM Ltd., Skrochova 42; 615 00, Brno; CZ, livan@svsfem.cz

^{**} Ing. Miloslav Popović: SVSFEM Ltd., Skrochova 42; 615 00, Brno; CZ, mpopovic@svsfem.cz

Next output parameters were investigated:

- internal energy of the barrier assembly,
- residual velocity of the vehicle,
- maximum deceleration of the vehicle.

More input parameters were investigated in previous analyses. Moreover during the barriers geometry design some local parts were parameterized together with global parameters of the barrier (material thickness). All parameters were evaluated in a form of correlation coefficients. It enables to exclude redundant parameters from a complex study (Saltelli, 2008). With respect to this previous investigation only thickness parameters were used in the final optimization study.

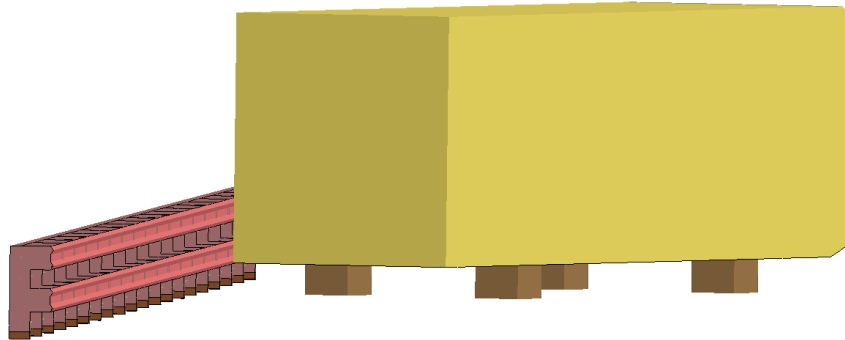


Fig. 1: Simple numerical model.

All investigated parameters were analyzed in maximal important on their limits with regards to manufacturing of barriers and all possible load cases in the crash test.

A very common approach in parameters choice is random sampling, which is called Monte Carlo Simulation (MCS). For design exploration the design variables are assumed to follow a uniform distribution with given lower and upper bounds. However this method fills the limit space not so much effectively. Many parameters sets are doubled. The better method was used, the advanced Latin Hypercube Sampling (Fig. 2). This method is able to setup parameters values more uniformly around the whole limit space.

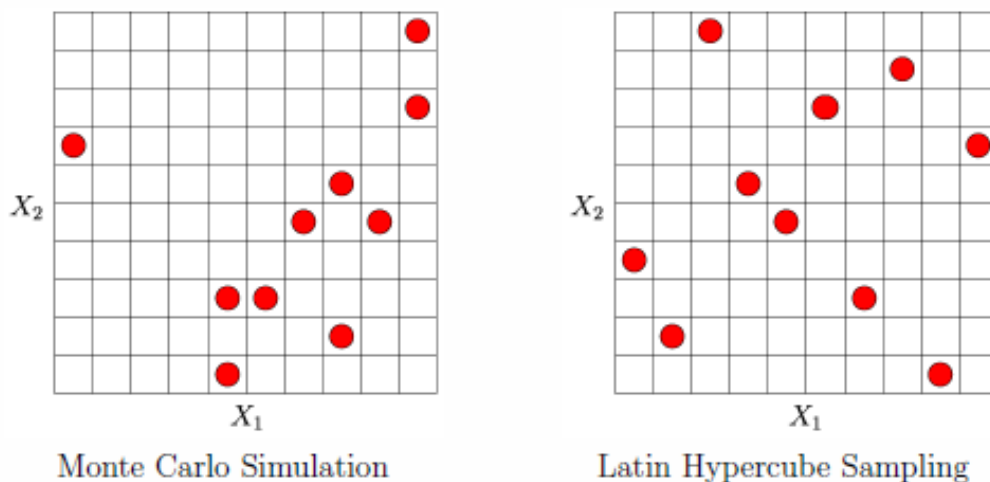


Fig. 2: Stochastic sampling schemes.

The performed sensitivity study confirms a high influence of the vehicle impact angle to all output parameters, especially to the maximal deceleration and residual velocity of the vehicle. This was quantified by correlation coefficients. The particular distribution of the influence of input parameters to output parameters was described by coefficients of importance.

3. Road Barriers Optimization

The previous sensitivity model was used as a base for next optimization. The goal was to increase a maximum internal energy of the barrier. It represents an energy that is absorbed in the barrier assembly mainly by its deformation. Not only absorbed energy but also the vehicle maximum deceleration was used as a significant goal of the optimization study. Apart of that the residual velocity of the vehicle was investigated as well.

Two variants of the optimization were used, the standard optimization procedure and the optimization with meta-model (Most, 2008) based on the previous sensitivity study. Both of them used the Evolutionary algorithm (Kelley, 1999).

Evolutionary algorithms are stochastic search methods that mimic processes of natural biological evolution. These algorithms have been originally developed to solve optimization problems where no gradient information is available, like binary or discrete search spaces, although they can also be applied to problems with continuous variables.

The prediction quality of an approximation model may be improved if unimportant variables are removed from the model. This idea is adopted in the Metamodel of Optimal Prognosis (MOP) which is based on the search for the optimal input variable set and the most appropriate approximation model (polynomial or MLS with linear or quadratic basis). Please see Fig. 2 for an optimization procedure.

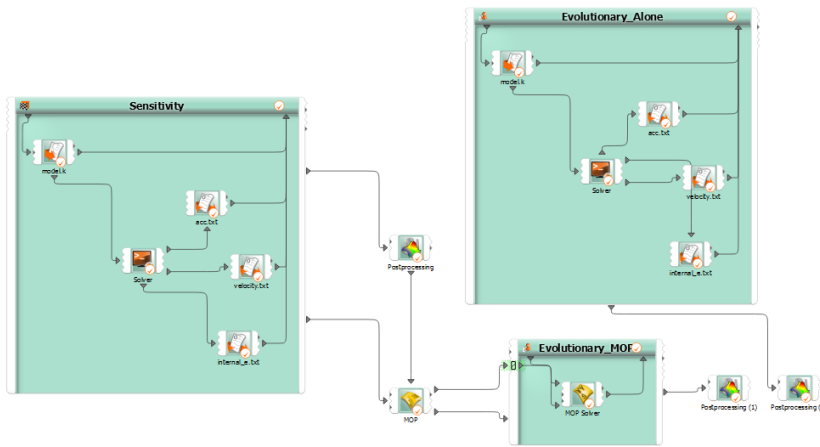


Fig. 3: Optimization procedure with MOP model.

Two thickness parameters of the road barriers were used as discrete input parameters (longitudinal part and vertical part thickness). The impact velocity and angle were fixed according standards for that kind of tests.

The optimization study used with the advance the evolutionary algorithm with two optimized objectives (Branke, 2008) – maximal energy absorbed in road barriers and the maximum deceleration of the vehicle. Those two results are naturally in the opposite. The optimization enables to evaluate a pareto front from all design points at the start, Fig. 4. Afterwards next optimization steps come near this line. It significantly improved desirable energy value.

During the optimization some steps bring good value of absorbed energy but the vehicle deceleration cross the value about 10G.

The internal energy absorbed in the road barriers was increased about 28% to 1.4e6 J (the initial kinetic energy of the vehicle is about 2.5e6 J).

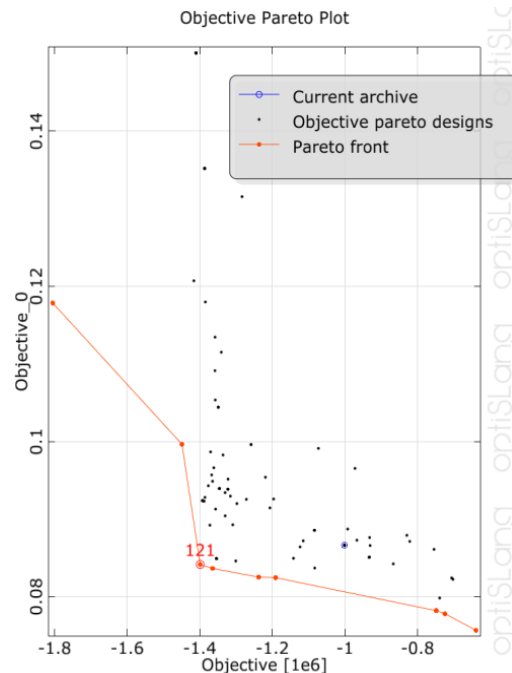


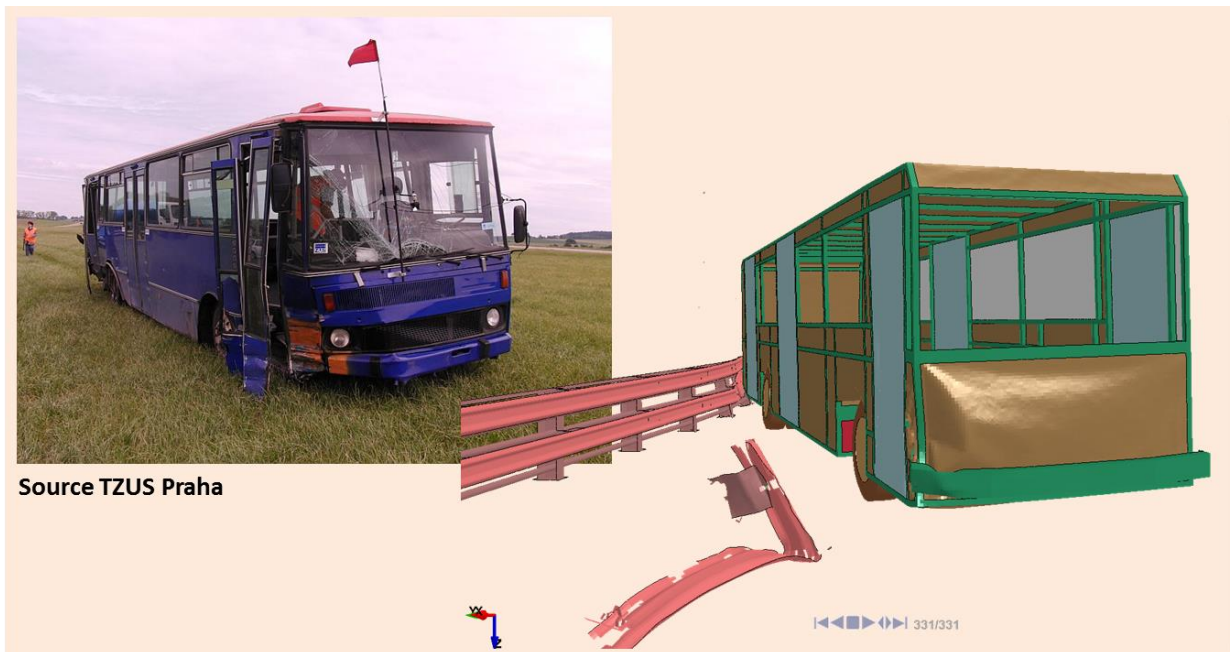
Fig. 4: Multiobjective optimization assessment.

The residual velocity in the optimized variant was kept close to the minimum value about 14 km/h (the impact velocity was defined about 70 km/h).

4. Verification Test in Numerical Simulation

The optimized barrier model was verified in the explicit numerical study due to the investigation of the detailed interaction between the barrier model and the vehicle model. This analysis was compared with the crash test of the real vehicle, see Fig. 5. More than 500k nodes were used for the modeling of the vehicle body and the barrier assembly. All materials were prescribed with parameters that enable a material erosion and plasticity behavior as well (Hallquist, 2006 and 2012).

The test results confirm supposed deformations from numerical simulation and the vehicle and barrier interaction as well.



Source TZUS Praha

Fig. 5: Verification test of the numerical model.

5. Conclusion

The optimization brings two significant benefits in the road barriers investigation. At first, the previous sensitivity study enables to check more than one crash test load case. The effect of the testing vehicle on the road barriers was evaluated in tens of impact directions and impact velocity values. At second, the design of the road barrier was improved with the respect to the energy absorbed in barriers and undesirable deceleration in the vehicle body.

The detailed numerical analysis of the “best” variant confirms a good relation between numerical simulations and real tests.

References

Hallquist, John O. (2006) LS-DYNA theory manual, LSTC, Livermore, California.
Hallquist, John O. (2012) LS-DYNA keyword user manual, LSTC, Livermore, California.
Most, T. and Will, J. (2008) Metamodel of Optimal Prognosis - an automatic approach for variable reduction and optimal metamodel selection. In Proc. Weimarer Optimierungs- und Stochastiktage 5.0, Weimar, Germany.
Saltelli, A. et al. (2008) Global Sensitivity Analysis. The Primer. Chichester, England: John Wiley & Sons, Ltd.
Kelley, C. T. (1999) Iterative Methods for Optimization. Philadelphia: Siam, Society for Industrial and Applied Mathematics.
Branke, J., K., Deb, K. Miettinen, and R. Slowinski (2008) Multiobjective Optimization. Springer.

SIMULATION OF DROP TESTS OF THE CASK FOR RADIOACTIVE WASTE

V. Ivančo^{*}, M. Orečný^{**}, R. Huňady^{***}

Abstract: *The paper deals with finite element simulation of steel cask drop test. The analyzed cask is designed for transport of solid radioactive waste. The paper describes simulation when the cask is falling down from a height of 9 meters on the side part. The main attention of the paper is devoted to procedures and methods of evaluation of the results. The performed simulation revealed that the design is insufficient for qualification of the cask according to relevant rules.*

Keywords: Cask, Radioactive waste, Drop test, Simulations, Finite Element Method.

1. Introduction

In order to eliminate risk of radioactive pollution, special conditions defined by international rules as International Atomic Energy Agency regulations and national decrees (e.g. NRA 2006) have to be satisfied. The rules define conditions for storage and transport of shipments containing radioactive materials. Important parts of the rules are requirements of shipments resistance in accidental conditions. They define some hypothetical accidents as a drop of the shipment from a given height, specific action of fire etc. Resistance is usually evaluated by testing, computations or by employing both methods. Tests performed for full-scale prototypes or for their models of appropriate scale (Droste, 2007, YooJeong-Hyoun et al., 2011, Trebuňa et al., 2012) are demanding and expensive as special testing facilities are necessary. Moreover, specimens used in tests are damaged and more specimens have to be manufactured for repeated tests. This is a reason for numerical simulation of tests by Finite Element Analysis (FEA). If tests are performed, simulations represent very useful tools for improving knowledge and for better understanding of the test results. Simulations usually serve for the assessment of cask resistance during the design process to reduce time and cost required to develop a final product (e.g. Rueckert et al., 1993, Jakšič and Nilsson, 2007). As it follows from comparison of experimental and simulation data, FEA based simulations can give good agreement with tests and realistic estimation of product resistance (Qiao et al., 2011, YooJeong-Hyoun et al., 2011). This paper deals with assessment of resistance of the steel cask exposed to a drop from height of 9 m. The simulations were performed using drop test simulation module of CAD system SolidWorks 2012. Described and discussed are methods of results evaluation for the assessment of the cask applicability. Description is limited to the initial engineering design and of the cask.

2. Computational Model

The initial engineering design of the cask intended for transport of radioactive waste is schematically drawn in Fig. 1. The cask consists of cylindrical body (1) covered with lid (2). Thicknesses of these parts were determined from requirements on shielding of radioactive radiation. Upper end of the lid is equipped with deformation elements serving also for manipulation. Deformation zone with a plate for fixing the cask to a transport device is at bottom part of the cask body. Both main parts of the cask are joined with

* Assoc. Prof. Ing. Vladimír Ivančo, CSc.: Faculty of Mechanical Engineering, Technical University of Košice, Letná 9; 042 00, Košice; Slovakia, vladimir.ivanco@tuke.sk

** Ing. Martin Orečný: Faculty of Mechanical Engineering, Technical University of Košice, Letná 9; 042 00, Košice; Slovakia, martin.orecny@tuke.sk

*** Ing. Róbert Huňady, PhD.: Faculty of Mechanical Engineering, Technical University of Košice, Letná 9; 042 00, Košice; Slovakia, robert.hunady@tuke.sk

bolts (4) to enable loading and unloading transported waste placed in a standard steel barrel (3). Transported waste, mostly pieces of structural parts, can vary from case to case; hence the barrel was modeled as a cylinder of homogenous material with density following from cargo maximum allowable weight and volume of the barrel. Finite element mesh consisting of ten node tetrahedrons is in Fig. 2. As obvious from figure (2), smaller elements had to be used to model bolts and their connections to body and lid.

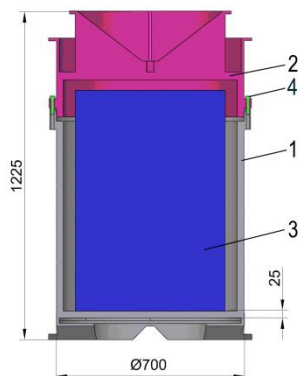


Fig. 1: Scheme of the cask initial design.

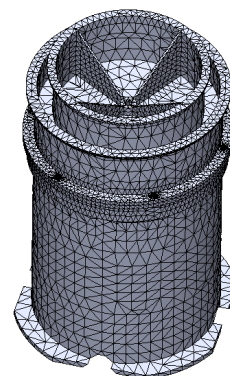


Fig. 2: Finite element mesh.

Simulations were performed by explicit method. The mesh refinement then brought some complications to computations as velocity c of stress waves in a 3D continua modeled by solid finite elements is

$$c = \sqrt{\frac{E(1-\mu)}{\rho(1+\mu)(1-2\mu)}}, \quad (1)$$

where E , μ and ρ are modulus of elasticity, Poisson's number and material density respectively. In order to achieve stability of the method, time increments Δt had to be less than $\Delta t = h/c$, where h is the size of the smallest element in the mesh.

The cask and lid were designed to be made of welded hot-rolled steel. Designed material of bolts was heat treated steel, with high tensile strength and low ductility. For these parts a bilinear elasto-plastic material model with kinematic hardening was used. The corresponding material properties are listed in Tab. 1, where R_e , R_m and A are the yield strength, ultimate strength and ductility respectively. The impact pad was considered as rigid; hence no material properties were needed to define.

Tab. 1: Material properties.

	E (MPa)	μ (-)	R_e (MPa)	R_m (MPa)	A (-)	ρ (kg/m ³)
Cask	200 000	0.30	345	625	0.3	7 850
Barrel	14 400	–	–	20	–	1 600
Bolts	200 000	0.30	1 100	1450	0.08	7 800

3. Results Evaluation

Evaluations were based on stress plots in individual time instances, plots of stress envelopes (i.e. their maximal values from all time instances), plots of strains and time courses of stress and strain in selected points of the model specified as sensors.

The cask impacted onto its left side and the contact between the impact pad and the bottom and upper part of the cask occurred at same time. Progression of stress wave is observable from stress fields in Fig. 3 and Fig. 4. As color scale was set from zero to yield strength, it is visible that the von Mises stress reached and in some areas exceeded the yield strength of the material. This implies that plastic strains of the cask will occur after the impact. As an accidental situation is investigated, permanent deformation of cask jacketed can be tolerated (or they cannot be avoided) providing that they have no effect on its integrity. To check structural integrity of the cask jacket the maximum values of nodal von Mises stresses are depicted in Fig. 5. Setup of color map is such that the red color represents the values of stress equal to the ultimate strength 625 MPa. It is obvious that the values of stresses are less than 418 MPa i.e. slightly above the yield strength but markedly under the ultimate strength. Deformation of the cask is notable in Fig. 5. On

Fig. 3 the stress wave is moving from the impact zone to the upper side of the container. The maximum value of the von Mises stress in time $50 \mu\text{s}$ is 347.4 MPa in the contact zones.

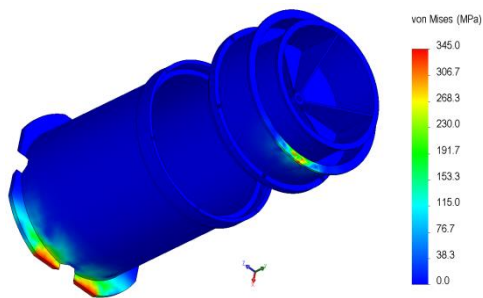


Fig. 3: Von Mises stresses at time $50 \mu\text{s}$.

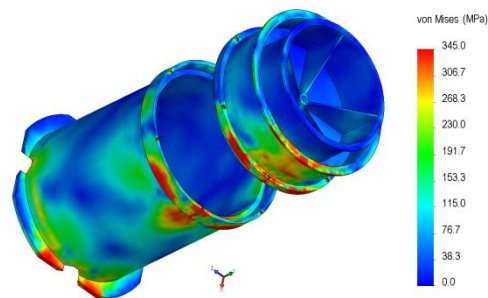


Fig. 4: Von Mises stresses at time $750 \mu\text{s}$.

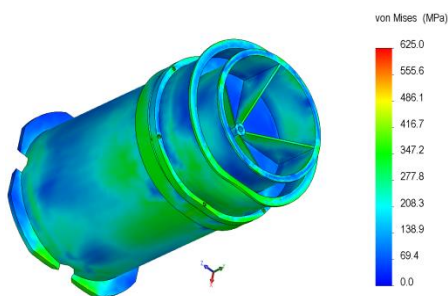


Fig. 5: Envelope of von Mises stresses.

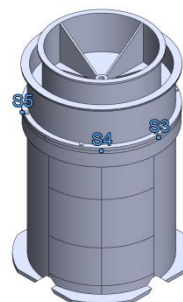


Fig. 6: Sensors on flange of the cask.

In order to acquire more information about the cask behavior during impact, other sensors were inserted on flanges of the cask, see Fig. 6. Time course of the von Mises stress in sensor S3 (see Fig. 7) shows that after sudden increase at beginning of impact, the stress does not change almost at all. This is caused by continual deformation of contact zones. The maximal value of the von Mises stress is over the yield stress of the material, therefore the cask will deform plastically. In contrary, values of stress in sensor S4 changes more frequently, see Fig. 8. The maximal value of stress is below the yield strength of the material.

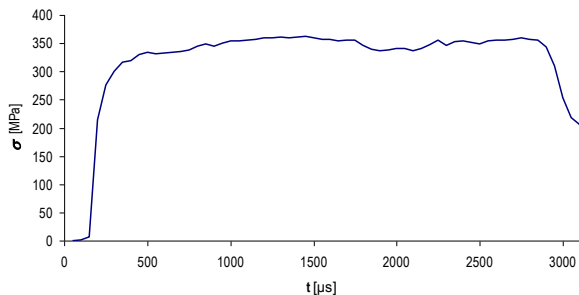


Fig. 7: Time course of stress in sensor S3.

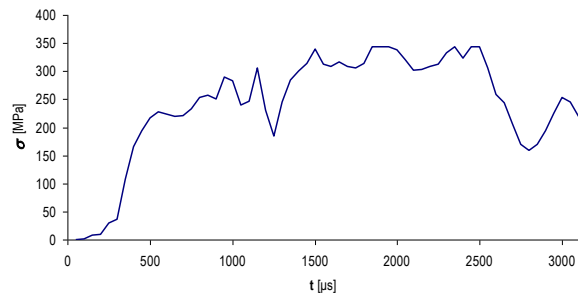


Fig. 8: Time course of stress in sensor S4.

For better understanding of the cask behavior after impact it is necessary to evaluate displacements. Full contact of both bodies occurred after time $3000 \mu\text{s}$. This is visible in Fig. 9 displaying resultant displacements at time $5000 \mu\text{s}$. As deformed shape is drawn in true scale, comparatively large gap between cask body and lid flanges is obvious.

To investigate origination of the gap, time courses of displacements in the y-axis direction of two adjacent nodes of both flanges are drawn in Fig. 10. It is clear that gap originated after $2500 \mu\text{s}$ from impact. As stresses in flanges are small, the only explanation is that plastic deformation originated in bolts. This is documented by envelopes of tensional stresses in bolts in Fig. 12.

Stress range in Fig. 11 was set from 0 to 1200 MPa . It is visible that tensile stresses in all six bolts exceeded the yield strength of material which is 1200 MPa . Bolts deformed plastically which caused origination of a gap between flanges. The maximal node value of the tensile stress is 1569 MPa . This value is above the tensile strength of the material, meaning that the bolts would rupture. It should be noted that simulation program does not enable modeling damage and rupture of a material, hence stress values could be larger than the ultimate strength.

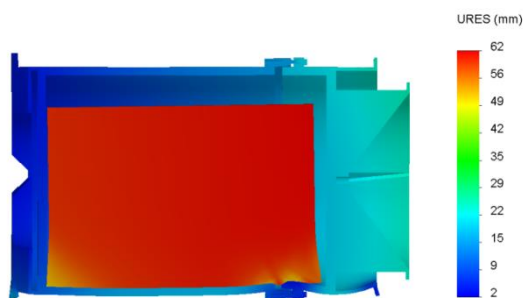


Fig. 9: Displacements at time 5000 μs .

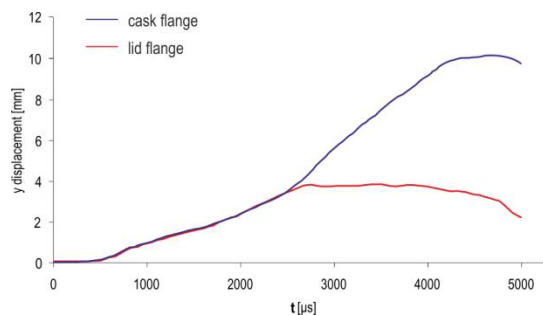


Fig. 10: Displacements of adjacent nodes of both flanges.

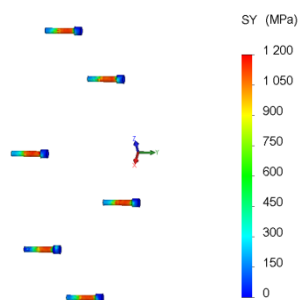


Fig. 11: Maximum tensional stress in bolts.

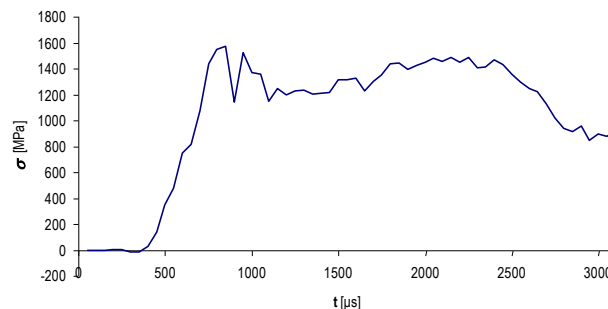


Fig. 12: Time course of normal stress in maximally loaded bolt.

4. Conclusions

Drop tests simulated with initial engineering design of the cask for transport of radioactive waste were studied. The two of tests demanded by relevant rules are described and methods of results evaluations are presented. From evaluations of results it follows that the design did not meet conditions of its qualifications and therefore changes of the design were necessary. The subsequent design modifications are beyond the scope of this paper.

Acknowledgement

The work has been accomplished under the research project financed by the grant 1/0090/12 of the Scientific Grant Agency of the Ministry of Education of the Slovak Republic and Slovak Academy of Science and the faculty project O-06-103/0008-00.

References

- Droste, B. (2007) Testing of type B packages in Germany to environments beyond regulatory test standards, Packaging, Transport, Storage and Security of Radioactive Material, Vol. 18, No. 2, 73-85.
- Jakšič, N., Nilsson, K. F. (2007) Numerical simulation of the one meter drop test on a bar for the Castor cask, DG JRC Institute for Energy, Petten (the Netherlands).
- NRA (Nuclear Regulatory Authority of the Slovak Republic) (2006) Decree 57/2006 of the Nuclear Regulatory Authority of the Slovak Republic, Collection of laws Nr 57/2006.
- Qiao, L., Zencker, U., Musolff, A., Komann, S. (2011) Dynamic Finite Element Analyses of a Spent Fuel Transport and Storage Cask with Impact Limiters by 9 Meter Drop Tests, In: Proc. SIMULIA Customer Conference, Barcelona, Spain, pp. 932-945.
- Rueckert, J., Diersch, R., Marcault, P. (1993) Assessment of Cask Loading in Drop Tests with Finite Element Methods, Structural Mechanics in Reactor Technology, In: Proc. 12th International Conference, Vols. J; Stuttgart, pp. 109-114.
- YooJeong-Hyoun et al. (2011) Arising Technical Issues in the Development of a Transportation and Storage System of Spent Nuclear Fuel in Korea, Nuclear Engineering and Technology, Vol. 43, Issue 5, 413-420.
- Trebuňa, F., Šimčák, F., Huňady, R., Pástor, M., Bobovský, Z. (2012) Modal analysis of transport complex and drop tests of container for transport of spent nuclear fuel, In: Proc. 50th International conference on Experimental Stress Analysis 2012, Tábor, Czech Republic, pp. 493-500.

STRESS-STRAIN ANALYSIS OF CERAMIC HEADS IN THE DESTRUCTION DEVICE

P. Janicek*

Abstract: This article deals with the issues of modification of destructive device for ceramic heads of total hip replacement based on the analysis of tensile stress state in the head. The goal of device modification is a shift of the location with extreme value of σ_{1max} from the region of head's hole bottom to its opening. This modification will increase the credibility of the obtained material properties of bioceramics, which will be determined from a set of head destructions using the Weibull weakest link theory.

Keywords: Material parameters of bioceramics, Destruction tests, Weibull weakest link theory, Endoprosthesis ceramic heads.

1. Introduction

Material properties of bioceramic material are determined by standard 3 or 4-points bending tests using the Weibull weakest link theory (Jiang et al., 2011; Basu et al., 2009). This method is useful when samples cut out of the ceramic part guarantee the standardized minimum dimensions. If the sample dimensions are smaller than those given by standards, they show material characteristics of higher values than in reality. This phenomenon is due to the fact that with a decreasing sample volume the probability of a critical length crack decreases; this, under a given stress state, causes a sample fracture.

2. Methods

The above problem will be eliminated if not the sample is destroyed, but a specific element of a brittle material, in our case of bioceramics. It is necessary to expose the entire element to such a load that is close to operational load and generates a tensile stress state in the element. A global objective is to determine the material properties of bioceramics, from which hip replacement heads are manufactured. This hip replacement is attached to the stem taper and loaded on its spherical surface by contact pressure of the cup. This method shows variations and depends on the physiology of the individual patient and on the process of his/her physical activity. Therefore, for the destruction test, we prefer the load used to test the static strength of ceramic heads ISO 7206-5 (Willmann, 1993; Weisse et al., 2003). During this test, the head is pressed on the stem in the direction of the system axis and thus the created character of stress state is suitable for both the assessment of head static strength and also for determination of material properties.

In the process of solving the stress state in the ceramic head of total hip replacement loaded according to ISO 7206-5, it was found out that the stress state in the head is heavily dependent on micro and macro shape deviations of tapered contact surfaces (Andrisano et al., 1990; Teoh et al., 2002; Fuis et al., 2001, 2002, 2004 and 2009a). When determining the material properties, it is necessary to carry out destructions of at least 35 samples in which the stress field σ_1 .

When destructing the head, it is necessary to know the value

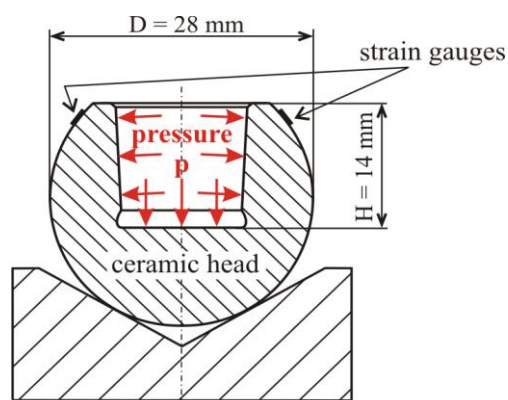


Fig. 1: Head's loading.

* Prof. Ing. Přemysl Janiček, DSc.: Institute of Thermomechanics AS CR – branch Brno, Technická 2, 616 69 Brno; CZ, janicek@fme.vutbr.cz

of tensile strain in order to subsequently determine the stress field. Therefore, two strain gauge transducers (about 1 mm from the edge – Fig. 1) are bonded on the outer surface of the spherical area; these transducers measure circumferential strain of the head under pressure loading (Fuis et al., 2006 and 2010). The entire head is in a special destructive device and the pressure load is exerted by a piston which acts on the rubber disposed in a tapered hole of the head. Rubber acts on the head by internal pressure p ; this causes the circumferential tensile strain in the head to destroy it subsequently.

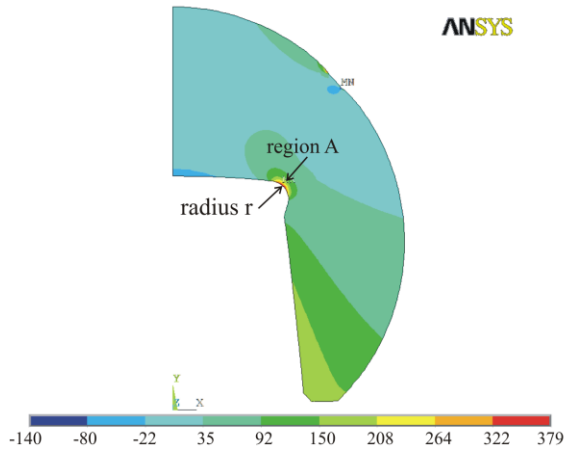


Fig. 2: First principal stress in the head under the pressure loading in MPa.

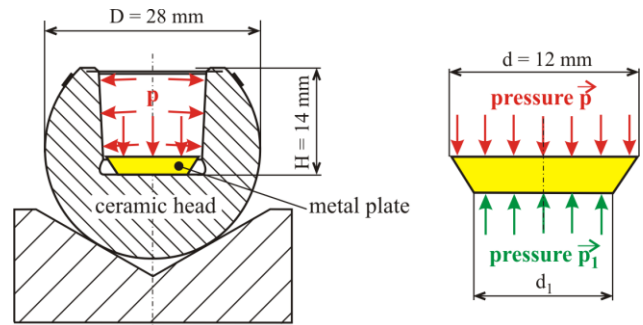


Fig. 3: Treatment of the head's loading in the destruction device..

Isosurfaces of the first principal stress σ_1 in the head under a given pressure load are described in Fig. 2 (Fuis et al., 2004, 2011). This figure shows that the maximum value of σ_1 (379 MPa) is at the transition region of the tapered hole into its bottom (region A) and is dependent on the radius of this transition r . After the destruction of each head, it is possible to measure the specific value of the radius and to determine the stress field for specifically measured radius. However, for destruction of 40 heads, this method is time-consuming and computational methodology of material characteristics specified in (Bush, 1993; McLean et al, 1991) is also more complicated. Therefore, efforts have been made to eliminate the stress concentration at the transition region of the taper into the bottom.

One of the options how to eliminate the stress concentration is to prevent the pressure acting in the transition region of the taper into the bottom and also into the part of the bottom of head hole. A metal plate (pad) with a trapezoidal cross-section is inserted into the region of the head bottom, as shown in Fig. 3 (thickness $t = 2$ mm). The pressure of rubber acts on a pad with a diameter $d = 12$ mm. This pad is in contact with the head bottom only on the diameter d_1 , which can vary. The aim of the analysis is to determine for which diameter d_1 the maximum value of σ_1 in the head will move out of stress concentrator (the opening of the tapered hole).

Computational modelling is performed using the finite element method - ANSYS. Due to the axis symmetry of the analyzed body, the head is discretized by axis symmetric elements. A bond on the spherical surface is modelled as rigid and pressure load is applied to the inner hole of the head - pressure $p = 100$ MPa acts on the whole tapered part (including the hole termination); pressure p_1 acts in the contact region with the pad – Fig. 3. The value of pressure p_1 is determined from the force balance of trapezoidal pad in the axial direction.

In terms of head geometry it is a variant with an outer diameter of 28 mm, taper of 12/14mm and hole depth of 14 mm (Fig. 1). This type of head has been destroyed by a special destructive device described in greater detail in (Fuis et al., 2006). The head is made of bioceramics Al_2O_3 characterised by the value of modulus of elasticity $E = 3.9$ GPa and Poisson's ratio $\mu=0.23$ (Fuis et al., 2009 and 2011a).

3. Results and Discussions

Isosurfaces of the first principal stress in the head for pad different diameter d_1 are shown in Fig. 4. With a decreasing size of diameter d_1 , the maximum stress is still located in the region A (Figs. 1 and 4) and it almost always obtains extreme values of about 280 – 290 MPa. However, this value is lower than in the

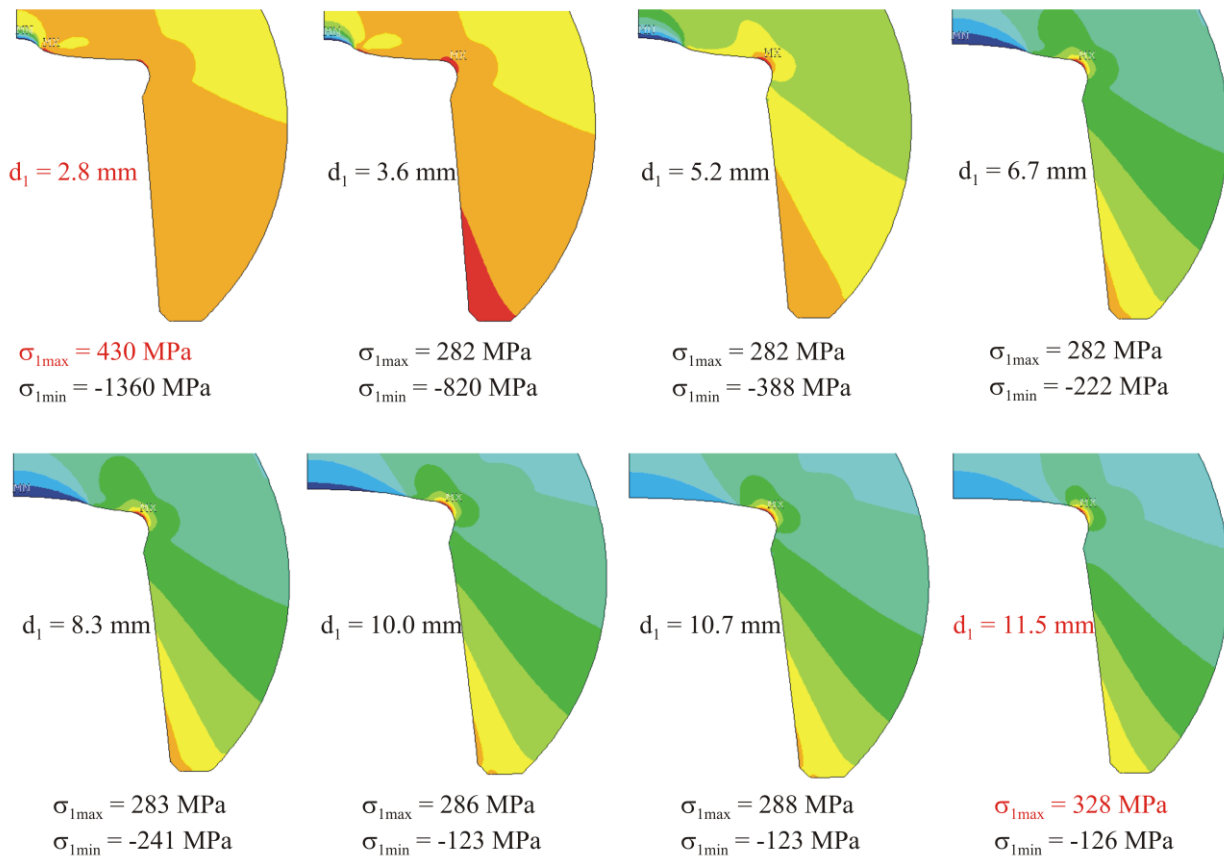


Fig. 4: Isosurfaces of stress σ_1 for different values of the pad diameter d_1 ($d = 6$ mm, $p = 100$ MPa).

case of loading of the entire hole by pressure $p = 100$ MPa (Fig. 4). With a decreasing size of diameter d_1 , the pressure p_1 acting between the pad and the head bottom increases. Moreover, with a decreasing size of diameter d_1 , the values of tensile stress also increase in the lower portion of the head (in the region of the largest diameter of tapered hole). An exception is the case when d_1 is in the interval between 12.5 and 11.5 mm - in this case the maximum stress is higher than the above 280 MPa due to the fact that the pressure p_1 acts in the vicinity of the stress concentrator, thereby increasing the stress state. If we reduce the size of diameter d_1 up to 2.25 mm, a change in the nature of stress state occurs in the region of the head bottom and the maximum stress is shifted to the region where load pressure p_1 has ceased (maximum value is significantly higher than in the previous cases and it is about 430 MPa). The analysis shows that in this case it is not possible to achieve the elimination of effects of stress concentration in the transition region of the taper into the head bottom.

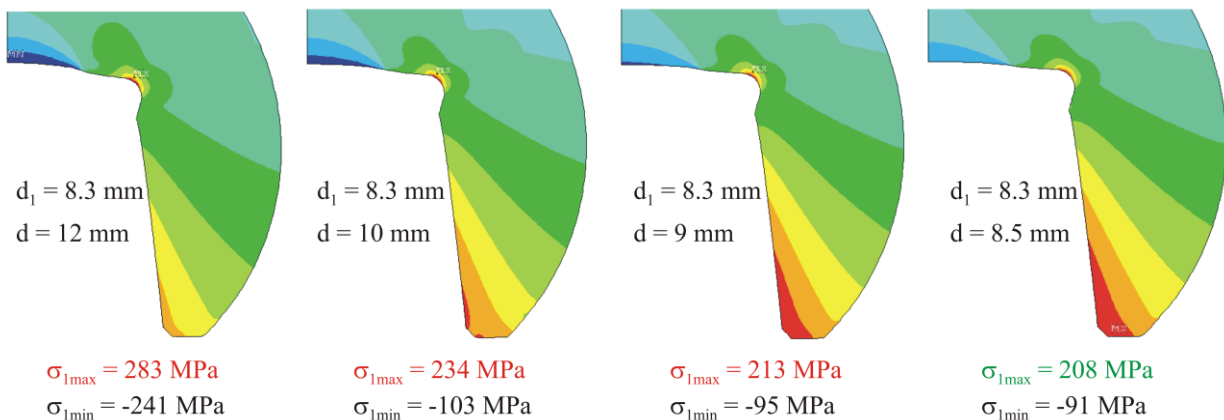


Fig. 5: Isosurfaces of stress σ_1 for different values of the pad diameter d ($d_1 = 8.3$ mm, $p = 100$ MPa).

Now there is a possibility to determine for a given diameter d_1 the value of diameter d so that the maximum stress is shifted from the transition region of the taper into the head bottom. The size of diameter d_1 was selected 8.3 mm and Fig. 5 shows the isosurfaces of σ_1 for different pad diameter d_1 (12;

10; 9 and 8.5) mm with corresponding pressure p_1 . The results of computational modelling suggest that for the pad having a diameter $d_1 = 8.3$ mm and the diameters $d < 9.8$ mm, the position of maximum stress has shifted from the hole bottom region (region A) to its opening, as shown in Fig. 5 completely right.

4. Conclusions

The aim of this study was to change the way of destroying the heads so that the position of extreme values of tensile stresses has moved from the region of the head bottom to its opening. To achieve this goal it is necessary to insert a trapezoidal pad into the head, which will change the pressure acting in the region of head bottom.

Acknowledgement

The research has been supported by the project of the Czech Science Foundation GA CR nr. 13-34632S.

References

- Andrisano, A. O., Dragoni, E., Strozzi, A. (1990) Axisymmetric mechanical analysis of ceramic heads for total hip replacement. *Proc. Inst. Mech. Engrs, Part H, Vol. 204*, pp. 157-167.
- Fuis, V., Janicek, P. (2002) Stress and reliability analyses of damaged ceramic femoral heads, *Conference on Damage and Fracture Mechanics, Maui Hawaii, Structures and Materials Vol. 12*, pp. 475-485.
- Weisse, W., Zahner, M., Weber, W., Rieger, W. (2003) Improvement of the reliability of ceramic hip joint implants. *Journal of Biomechanics 36*, pp. 1633-1639.
- Fuis, V., Koukal, M., Florian, Z. (2011) Shape Deviations of the Contact Areas of the Total Hip Replacement, In: 9th International Conference on Mechatronics, Warsaw, Poland pp. 203-212.
- Bush, D. (1993) Designing Ceramic Components for Structural Applications, *J. Mater. Eng. Perf. ASM Int., Vol. 2*, pp. 851-862.
- Fuis, V., Malek, M., Janicek, P. (2011a) Probability of destruction of Ceramics using Weibull's Theory, In: *Proc. 17th International Conference on Engineering Mechanics, Svratka, Czech Republic*, pp. 155-158.
- Teoh, S. H., Chan, W. H., Thampuran, R. (2002) An Elasto-plastic Finite Element Model for Polyethylene Wear in Total Hip Arthroplasty, *J Biomech 35*: 323-330.
- Fuis, V., Janicek, P., Houfek L. (2008) Stress and Reliability Analyses of the Hip Joint Endoprosthesis Ceramic Head with Macro and Micro Shape Deviations, In: *Proc. International Conference on Biomedical Engineering, Singapore, IFMBE Proceedings Vol. 23, Iss. 1-3pp. 1580-1583*.
- Fuis, V. (2004) Stress and reliability analyses of ceramic femoral heads with 3D manufacturing inaccuracies, In: *Proc. 11th World Congress in Mechanism and Machine Science, Tianjin, China* pp. 2197-2201.
- McLean, A. F., Hartsock, D. L. (1991) Engineered materials handbook, Vol. 4, Ceramics and Glasses. ASM International, pp. 676-689.
- Fuis, V., Navrat, T., Hlavon, P., et al. (2006) Reliability of the Ceramic Head of the Total Hip Joint Endoprosthesis Using Weibull's Weakest-link Theory, In: *Proc. World Congress on Medical Physics and Biomedical Engineering, Seoul, South Korea, IFMBE Proc. Vol. 14*, pp. 2941-2944.
- Fuis, V. (2009) Tensile Stress Analysis of the Ceramic Head with Micro and Macro Shape Deviations of the Contact Areas, *Recent Advances in Mechatronics: 2008-2009*, In: *Proc. International Conference on Mechatronics, Brno, Czech Republic*, pp. 425-430.
- Jiang, R. Murthy, D. N. P. (2011) A study of Weibull shape parameter: Properties and significance. *Reliability Engineering and System Safety 96*, pp. 1619-1626.
- Fuis, V., Varga, J. (2009a) Stress Analyses of the Hip Joint Endoprosthesis Ceramic Head with Different Shapes of the Cone Opening. In: *Proc. 13th International Conference on Biomedical Engineering, IFMBE Proceedings Vol. 23, Iss. 1-3*, pp. 2012-2015.
- Basu, B., Tiwari, D., Kundu, D., Prasad, R. (2009) Is distribution the most appropriate statistical strength distribution for brittle materials? *Ceramics International, Vol. 35, Iss. 1*, pp. 237-246.
- Fuis, V., Navrat, T., Vosynek, P. (2010) Analyses of the Shape Deviations of the Contact Cones of the Total Hip Joint Endoprostheses. In: *Proc. 6th World Congress of Biomechanics (WCB 2010) Singapore, IFMBE Proceedings Vol.: 31*, pp. 1451-1454.
- Fuis, V., Janicek, P. (2001) Stress and reliability analyses of ceramic femoral heads with axisymmetric production inaccuracies. In: *Proc. 9th Mediterranean Conference on Medical and Biological Engineering and Computing, Pula, Croatia, IFMBE Proceedings Pts. 1 and 2*, pp. 632-635.
- Willmann, G. (1993) The principle of taper fitting of ceramic articular heads of hip joint endoprostheses. Internal Report, CERASIV GmbH, Plochingen, Germany.

EFFICIENT BAYESIAN PARAMETER IDENTIFICATION

E. Janouchová^{*}, A. Kučerová^{**}, J. Sýkora^{***}

Abstract: *Many important parameters influencing structural behaviour involve unacceptable uncertainties. An extensive development of efficient methods for stochastic modelling enabled reducing these uncertainties in input parameters. According to Bayes' rule, we obtain a more accurate description of the uncertain parameter involving an expert knowledge as well as experimental data. The aim of this contribution is to demonstrate two techniques for making the identification process more efficient and less time consuming. The first technique consists in replacement of the full numerical model by its polynomial approximation in order to reduce the computational effort. The particular approximation is based on polynomial chaos expansion constructed by linear regression based on Latin Hypercube Sampling. The obtained surrogate model is then used within Markov chain Monte Carlo sampling so as to update the uncertainty in the model inputs based on the experimental data. The second technique concerns a guided choice of the most informative experimental observation. Particularly, we apply sensitivity analysis to determine the most sensitive component of the structural response to the identified parameter. The advantages of the presented approach are demonstrated on a simple illustrative example of a frame structure.*

Keywords: Bayesian identification, Markov chain Monte Carlo, Stochastic modelling, Polynomial chaos expansion, Sensitivity analysis.

1. Introduction

Bayesian approach allows us to reduce uncertainties in parameters influencing structural reliability such as material or structural properties. The principal idea of Bayesian identification is based on a common way of thought when the resulting belief about a random event is given by a combination of all the available information (Gelman et al., 2004). An initial expert knowledge formulates prior distribution of the uncertain parameters and likelihood function contains new data obtained from experiments. The result of Bayesian identification is posterior distribution whose formulation includes the whole structural model. For this reason, the corresponding statistical moments cannot be generally computed analytically, but their computation can be done by Markov chain Monte Carlo (MCMC), see e.g. Geyer (2011). The disadvantage of this method is its high computational effort resulting from necessity of high number of model simulations. In order to accelerate the sampling procedure, a polynomial approximation of the model response can be used instead of the full numerical model.

Here, we employ polynomial chaos expansion (PCE) for the approximation of the model response in the stochastic space (Matthies, 2007; Stefanou, 2009; Marzouk et al., 2007). The efficiency of this technique depends on computational requirements of the PCE construction and its consequent accuracy. PCE can be used to approximate the response with respect to the probability distribution of the random variables. The convergence of the approximation error with the increasing number of polynomial terms is optimal in case of orthogonal polynomials of a special type corresponding to the probability distribution of the underlying variables (Xiu & Karniadakis, 2002). In particular, we employ Hermite polynomials associated with the Gaussian distribution. A comparison of several methods for the construction of the PCE-based approximation of a model response can be found in Janouchová et al. (2013). In this contribution we focus on linear regression (Blatman & Sudret, 2010), which is a very general method of

* Ing. Eliška Janouchová: Faculty of Civil Engineering, Czech Technical University in Prague; Thákurova 7/2077; 166 29, Prague; CZ, eliska.janouchova@fsv.cvut.cz

** Ing. Anna Kučerová, Ph.D.: Faculty of Civil Engineering, Czech Technical University in Prague; Thákurova 7/2077; 166 29, Prague; CZ, anicka@cml.fsv.cvut.cz

*** Ing. Jan Sýkora, Ph.D.: Faculty of Civil Engineering, Czech Technical University in Prague; Thákurova 7/2077; 166 29, Prague; CZ, jan.sykora.1@fsv.cvut.cz

computing the PCE coefficients based on a set of model simulations. The samples are drawn according to a stratified procedure called design of experiments (DoE), in particular well-known Latin hypercube sampling (LHS) which is able to respect the prescribed probability distributions (Janouchová & Kučerová, 2013).

Global sensitivity analysis (SA) is an important tool for investigating properties of complex systems. It is a valuable part of solution of an inverse problem such as a parameter identification. SA provides some information about the relationship between the system parameters/model inputs and the system response/model outputs. Several approaches to SA have been developed, see e.g. Saltelli et al. (2000) for an extensive review. The presented contribution is focused on widely used sampling-based approaches (Helton et al., 2006), particularly aimed at an evaluation of Spearman's rank correlation coefficient (SRCC). The aim of sensitivity analysis in the identification process is to determine the most sensitive component of the structural response to the identified parameter.

2. Bayesian Approach

Consider a stochastic problem

$$z \approx M(\mathbf{m}) \quad (1)$$

with uncertain model parameters \mathbf{m} and random observable data z , which can be predicted by a function M of the parameters. In Bayesian statistics, probability represents a degree of belief about the values of the parameters. Combining the initial knowledge in the form of the prior distribution $p(\mathbf{m})$ and the experimental data as the likelihood function $p(z | \mathbf{m})$ according to Bayes' rule

$$p(\mathbf{m} | z) = \frac{p(z | \mathbf{m})p(\mathbf{m})}{p(z)} = \frac{p(z | \mathbf{m})p(\mathbf{m})}{\int_{\mathbf{m}} p(z | \mathbf{m})p(\mathbf{m})d\mathbf{m}}, \quad (2)$$

we obtain the posterior distribution of the parameters.

3. Illustrative Example

In order to demonstrate a performance of Bayesian identification on an engineering structure, we have chosen a simple frame presented in Marek et al. (2003). The geometry and load distribution of the frame are shown in Fig. 1.

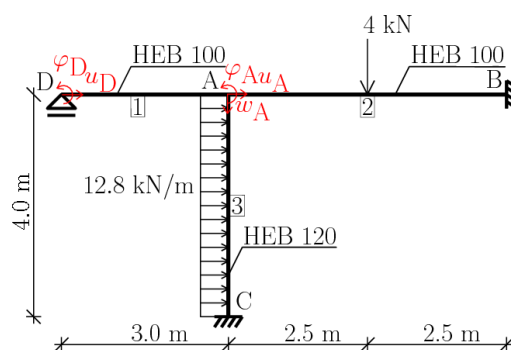


Fig. 1: Scheme of a frame structure.

Material of the frame is steel with uncertain Young's modulus E . Prior of this parameter is lognormal distribution with parameters $\mu_m = 210$ GPa and $\sigma_m = 110$ GPa. Likelihood is based on the displacements and their normally distributed measurement errors.

3.1. Markov chain Monte Carlo with polynomial chaos expansion

MCMC is based on a creation of an ergodic Markov chain of required stationary distribution equal to the posterior. There are different algorithms for the construction of this chain (Spall, 2003). In this contribution we employ Metropolis algorithm with a symmetric proposal distribution. Suitable setting of the proposal distribution is important and can be evaluated on the basis of acceptance rate AR (Rosenthal, 2011) or autocorrelation which is required to be minimal, as you can see in Fig. 2.

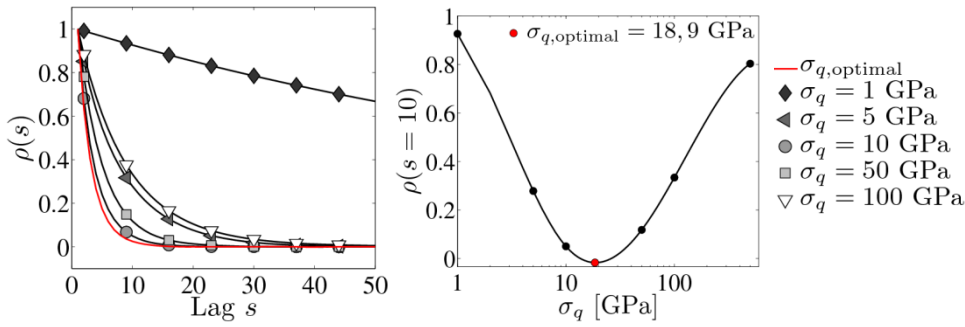


Fig. 2: A choice of the proposal standard deviation σ_q according to autocorrelation of the chain.

The computational effort of MCMC is reduced by using the polynomial approximation. A comparison of the time requirements and resulting accuracy of PCE and the full model (FM) is in Fig. 3.

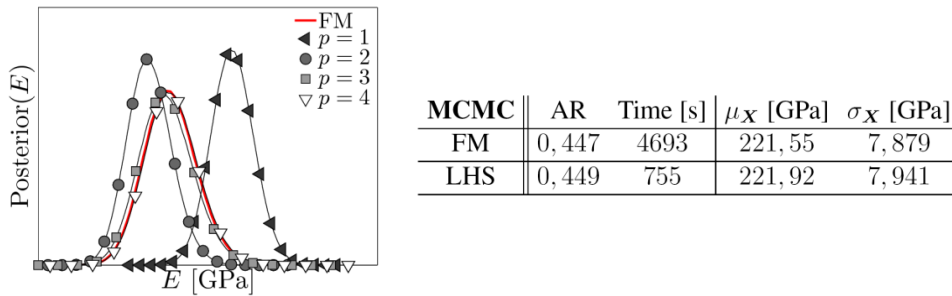


Fig. 3: Posteriors based on PCE of a degree p and FM. Numerical results for PCE of $p = 4$ and FM.

3.2. Sensitivity analysis

The remaining question concerns a choice of model response component to be measured. The answer can be obtained with the help of SRCC-based sensitivity analysis due to the monotonic dependence of the outputs on E . The examples of obtained results are depicted in Fig. 4.

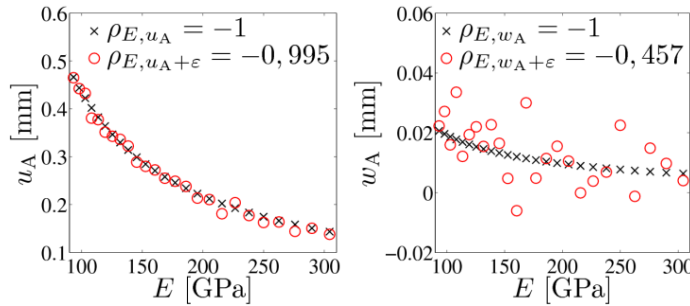


Fig. 4: Sensitivity expressed by SRCC in the case of the most and least sensitive displacements.

If we measure the exact values of the displacements, SRCC is the same in the both cases. By taking into account the measurement errors – assumed to have one value equal for all the displacements and another value equal for all the rotations – SRCC is lower in the case of the displacement with a smaller prior variance. The most sensitive structural response is then displacement u_A .

3.3. Parameter identification

Final characteristics of the posterior distribution strongly depend on the mentioned options. Fig. 5 shows results for several cases of input data for the identification process. In each graph there is a vertical black line denoting the true value of the parameter corresponding to the experiments. A significant difference in using the most or least sensitive output can be seen in Fig. 5a. The mean value of the red posterior belonging to the most informative data practically equals to the true value and the variance expresses the uncertainty which we have about this value. In the second case, the identification is not efficient and our uncertainty remains great. There are shown two variants of parameter updating in the next graphs. Fig. 5b shows a case with sequential measuring one to five of different components of the structural response while Fig. 5c presents a variant with measuring the same displacement one to five times. The both cases lead to a considerable reduction of the uncertainty in the input parameter.

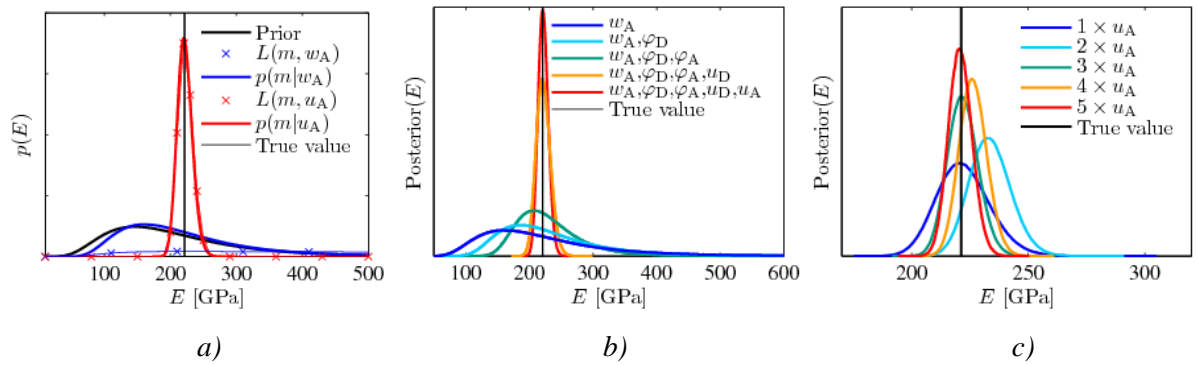


Fig. 5: Posteriors based on differently informative data a), one to five variant observations b) and one to five observations of the same variable c).

4. Conclusions

Bayesian identification provides a simple and effective approach for minimization of the uncertainty in the input parameters using all the available information. In order to obtain statistical moments of the posterior, Markov chain Monte Carlo is used. The computationally exhaustive process is accelerated by replacing the model response by its polynomial approximation. The coefficients of polynomial chaos are computed with the help of linear regression based on LHS. The efficiency of the identification depends on the choice of observed data. The best input data for the identification are chosen according to sensitivity analysis based on Spearman's rank correlation coefficient.

Acknowledgement

This outcome was financially supported by the Czech Science Foundation, project No. 105/12/1146, and the Grant Agency of the Czech Technical University in Prague, grant No. SGS14/028/OHK1/1T/11.

References

- Blatman, G. & Sudret, B. (2010) An adaptive algorithm to build up sparse polynomial chaos expansions for stochastic finite element analysis. *Probabilistic Engineering Mechanics*, 25, 2, pp. 183-197.
- Gelman, A., Carlin, J. B., Stern, H. S. & Rubin, D. B. (2004) *Bayesian data analysis*. Chapman & Hall/CRC.
- Geyer, C. J. (2011) *Handbook of Markov Chain Monte Carlo*. Chapman & Hall/CRC.
- Helton, J. C., Johnson, J. D., Sallaberry, C. J. & Storlie, C. B. (2006) Survey of sampling-based methods for uncertainty and sensitivity analysis. *Reliability Engineering and System Safety*, 91, 10-11, pp. 1175-1209.
- Janouchová, E., Kučerová, A. & J. Sýkora (2013) Comparison of Numerical Methods for Uncertainty Quantification, in: *Proc. of Engineering Mechanics 2013*, Institute of Thermomechanics, Academy of Sciences of the Czech Republic, Prague, pp. 235-246.
- Janouchová, E. & Kučerová, A. (2013) Competitive Comparison of Optimal Designs of Experiments for Sampling-based Sensitivity Analysis. *Computers & Structures*, 124, pp. 47-60.
- Marek, P., Brozzeti, J., Guštar, M. & Tikalsky, P. (2003) Probabilistic assessment of structures using Monte Carlo simulation. Institute of Theoretical and Applied Mechanics, Academy of Sciences of the Czech Republic, Prague.
- Marzouk, Y. M., Najm, H. N. & Rahn, L. A. (2007) Stochastic spectral methods for efficient Bayesian solution of inverse problems. *Journal of Computational Physics*, 224, 2, pp. 560-586.
- Matthies, H. G. (2007) *Encyclopaedia of Computational Mechanics*. John Wiley & Sons Ltd.
- Rosenthal, J. S. (2011) Optimal Proposal Distributions and Adaptive MCMC, in: *Handbook of Markov Chain Monte Carlo*. Chapman & Hall/CRC, pp. 93-140.
- Saltelli, A., Chan, K. & Scott, E. M. (2000) *Sensitivity analysis*. NY: Wiley.
- Spall, J. C. (2003) Estimation via Markov Chain Monte Carlo. *IEEE Control Systems Magazine*, 23, 2, pp. 34-45.
- Stefanou, G. (2009) The stochastic finite element method: Past, present and future. *Computer Methods in Applied Mechanics and Engineering*, 198, 9-12, pp. 1031-1051.
- Xiu, D. & Karniadakis, G. E. (2002) The Wiener-Askey Polynomial Chaos for Stochastic Differential Equations. *SIAM Journal on Scientific Computing*, 24, 2, pp. 619-644.

STUDY OF EXTERNAL COOLING OF STEAM GENERATOR PGM-1000M COLLECTORS POCKET WELD № 111 FOR SUPPRESSING OF STRESS CORROSION CRACKING

L. Joch^{*}, R. Krautschneider^{**}

Abstract: *The subject of this report is to assess different rates of cooling the bottom of the collector region, specifically the outer surface of the weld JS1200 (also known as weld 111) and the surrounding area. Based on the experience from Russia (OKB Hidropress) it is possible by external cooling of the outer surface of the weld area to reduce tensile stresses in the weld and in the outer radius of collectors pockets, or even change them into compressive stresses. The presence of tensile stresses in the outer radius of collectors pocket in combination with a corrosive environment in the collectors pocket support the possibility of crack initiation and propagation mechanism of stress corrosion cracking (SCC).*

Keywords: Fluid structure interaction, Steam generator, CFD thermal analysis, Stress corrosion cracking.

1. Introduction

One of the most important components of a nuclear power plant is steam generator (SG) which produce steam to turbogenerator for electricity production. Nuclear power plants in Czech Republic operate with pressurized water reactors and horizontal steam generators, same like in Russian federation or Ukraine. SG is constructed as horizontal cylindrical vessel and horizontal tube bundles which are built into the vertical collectors (Figs. 1, 2).

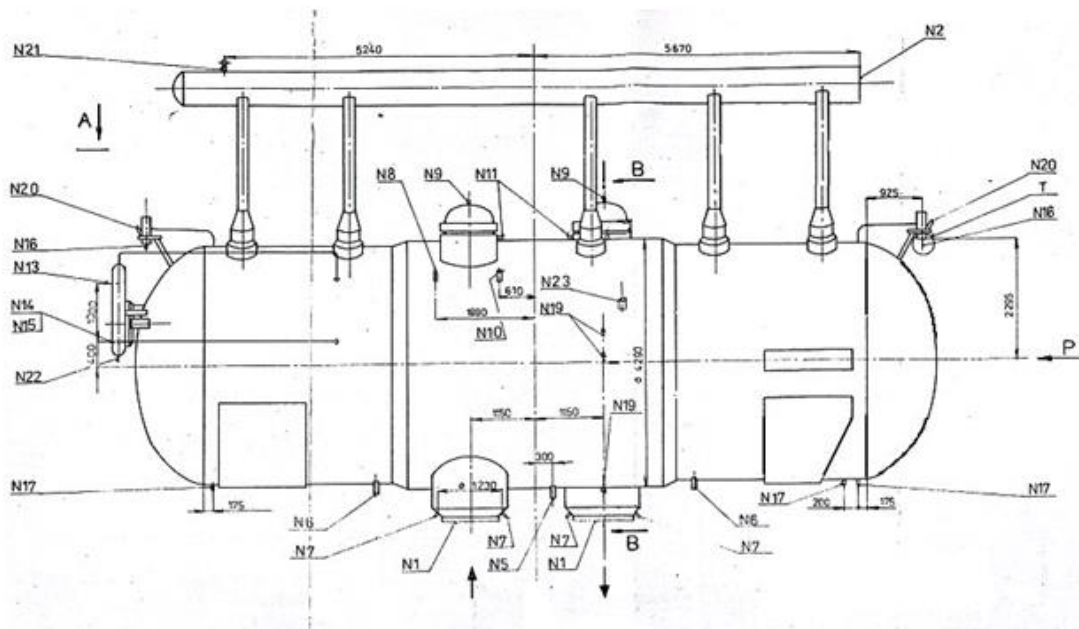


Fig. 1: Steam generator (SG) PGM-1000M.

^{*} Ing. Lukáš Joch: Energy Institute, Faculty of Mechanical Engineering, Brno University of Technology, Technická 2896/2; 616 69, Brno; CZ, jochl@uam.cz

^{**} Ing. Roman Krautschneider, PhD.: Institute of Applied Mechanics Brno, Ltd.; Resslova 972/3; 602 00, Brno; CZ, krautschneider@uam.cz

Horizontal steam generator, contrary to vertical SG used in PWR nuclear power plants, often works with worse water quality. This could be one of the reasons of pilling up deposits in collector pockets and the creation of corrosive environment.

As a result of stress corrosion cracking and growth of cracks in steam generator collector pockets (Fig. 2), it was necessary to replace or repair steam generators in several VVER nuclear power plants abroad.

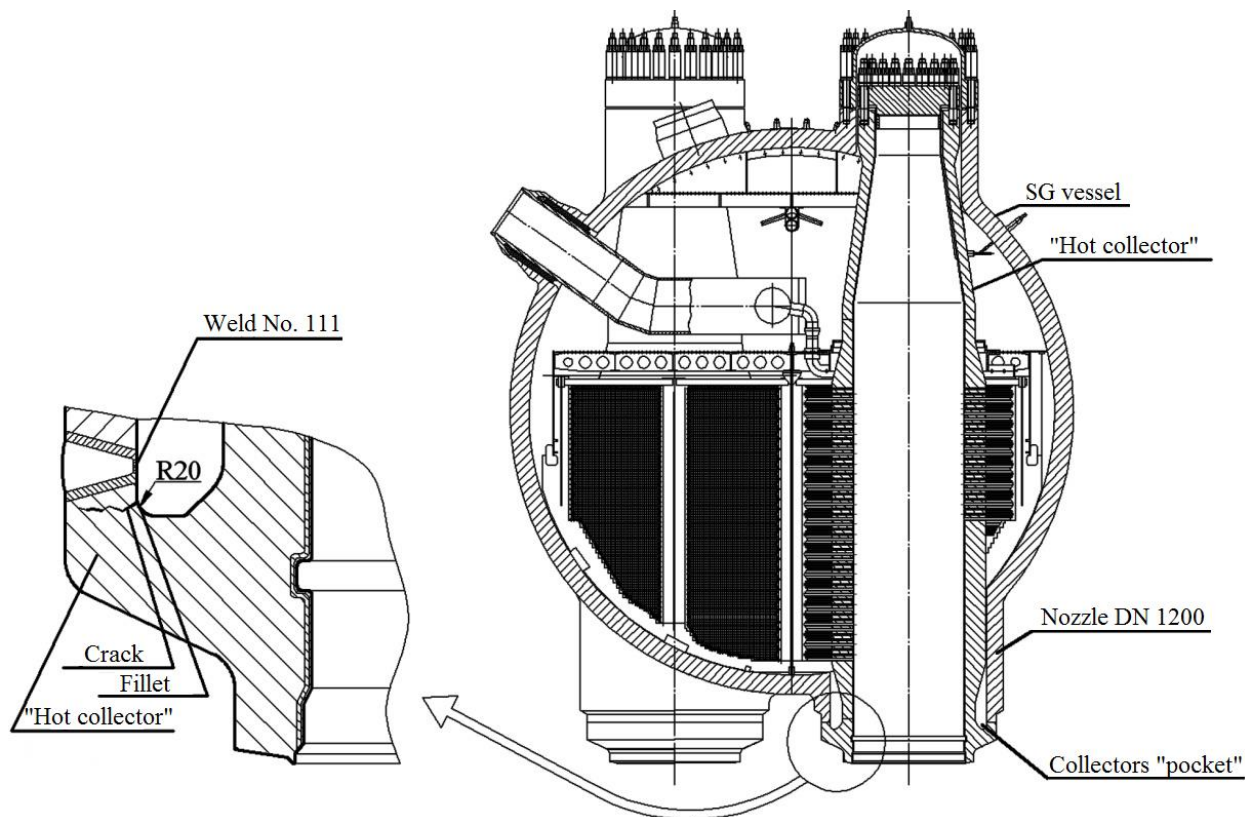


Fig. 2: Steam generator cross section view with detail of collectors pocket (Lyakishev et al., 2009).

This work is based on studies carried out in Russia (OKB Hidropress) where they deal with the possibility of reducing tensile stress in the pocket of the steam generator collectors which should lead to prevent occurrence and growth of these defects.

Decreasing tensile stresses or even converting them into compressive stresses can be achieved by local cooling of the external surface area of the collector.

For the collector cooling was used a similar model as the cooling sleeve referenced in publications of OKB Hidropress (Fig. 3) (Lyakishev et al., 2009) (Kutdusov et al, 2013).

Subsequently it was developed a CFD numerical model. For the numerical structural analysis exported temperature fields from CFD analysis were used.

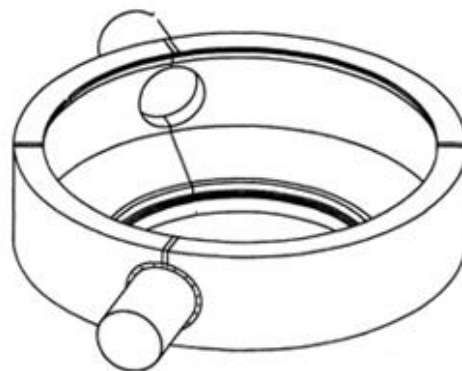


Fig. 3: Cooling sleeve (Kutdusov et al., 2013).

2. Methods

2.1. Fluid-structure interaction

Fluid-structure interaction (FSI) problems describe the coupled dynamics of fluid mechanics (CFD) and structure mechanics (FEM). There exist two approaches to coupling of CFD and FEM, one-way and two-way FSI, in this case was used one-way fluid-structure interaction to transfer temperature fields from CFD analyses to FEM structural analyses.

One-way FSI is typically created by the pure mapping of physical properties resulting from the CFD analysis to FEM. CFD and FEM models typically do not rely on matching meshes (e.g. mapping temperature field onto a structural Finite Element model). However in our case of one-way FSI the mapping of the physical properties does not include the modification of any of the meshes.

2.2. Computational model

The first step was to create a 3D model of the steam generator with cooling sleeve, which was placed around the area of collector and SG vessel connection (around surrounding the connection weld No. 111). The model covered the lower half of the SG vessel (Fig. 1).

CFD computational model considered three medium regions. Inside the collector is water from the primary circuit, the secondary side of SG vessel considered saturated water-steam and the cooling sleeve contained the cooling air medium of ambient temperature and pressure.

In the second step CFD calculated temperature fields were mapped as a boundary condition for finite element analysis model. Numerical model for stress-strain analysis was created using quadratic (mid-side node) elements. The areas of FE mesh, which were used for evaluation of stresses, were appropriately refined.

3. Results

3.1. CFD results

In Fig. 4 two of the modeled temperature fields, which give some idea of the change of temperature fields due to external cooling, are shown. We are interested of course mainly in the area around the connection of the collector with SG vessel. This temperature field was mapped onto a structural Finite Element model.

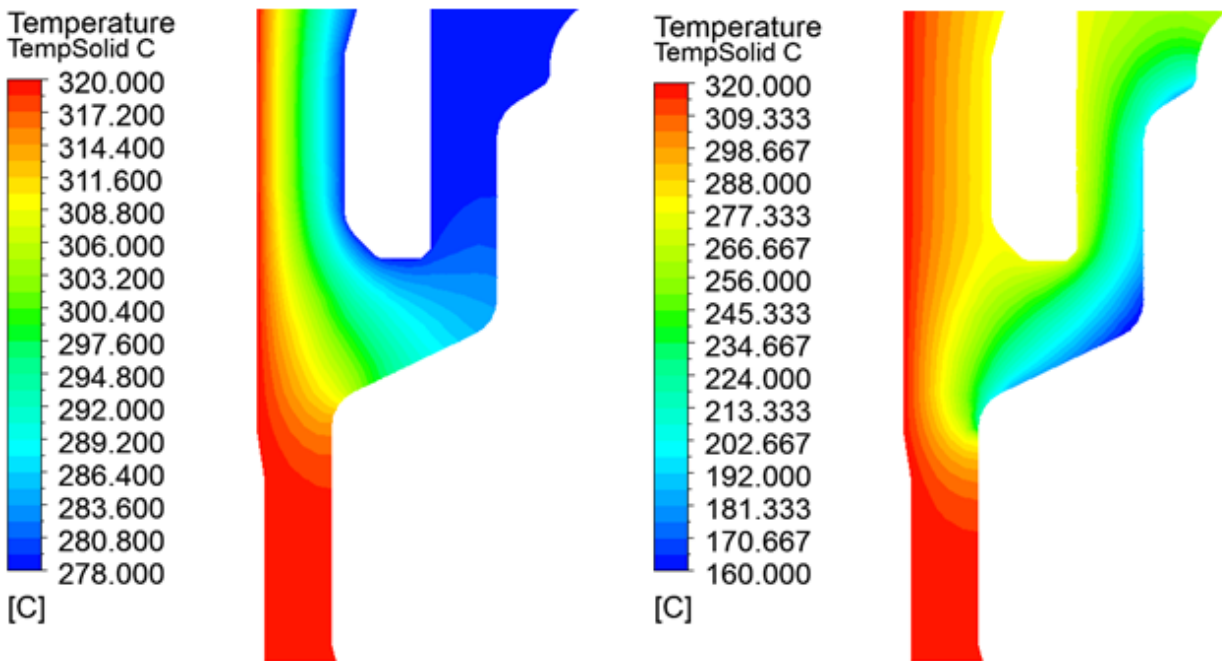


Fig. 4: Temperature field in the area of collectors pocket without cooling (left) a and with external cooling $5\text{ m}^3/\text{s}$ (right).

3.2. FEM results

Fig. 5 shows that by appropriate external cooling it is possible to lower tensile stresses in the collectors pocket area and even change the tensile stresses into compressible (coolant flow of $5\text{ m}^3/\text{s}$). Unfortunately, it is connected with growth of temperature gradients in this area, which is increasing stress intensity in collector pocket.

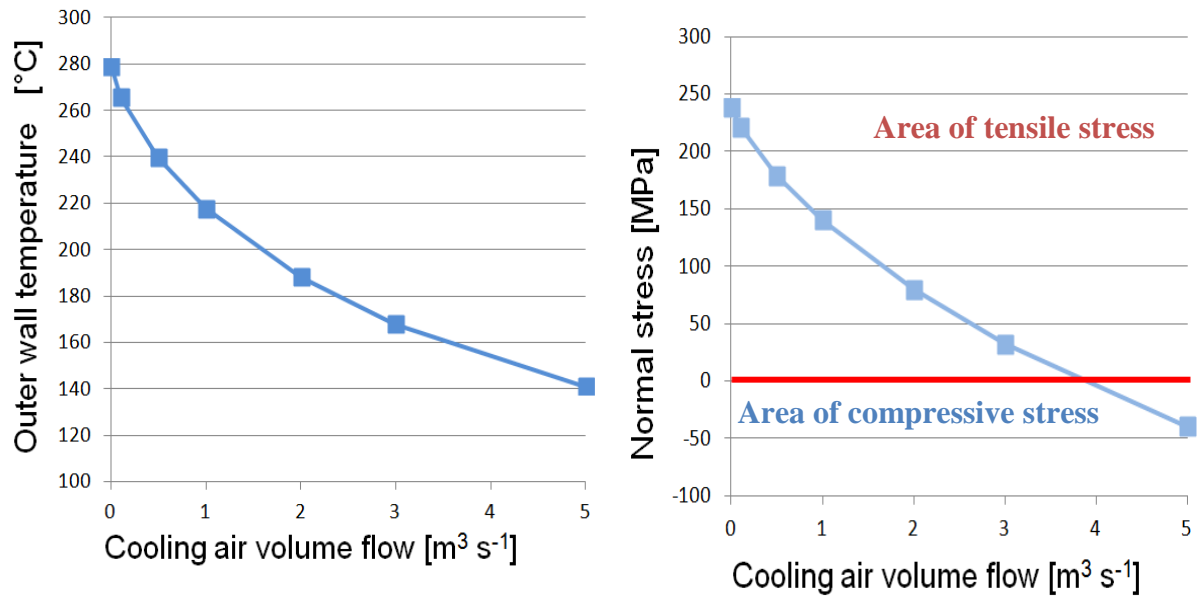


Fig. 5: Calculated outer wall temperature in the area of collectors pocket (left) and calculated normal stresses in the collectors pocket area (right).

4. Conclusions

This paper deals with the influence of external cooling of the area of steam generator collector pocket on normal stresses in this area. The greater the tensile stresses are, the bigger is the danger of stress corrosion cracking occurrence. By appropriate external cooling of this area, it is possible to influence not just the stresses level, but also the character.

External cooling of the outer surface of the area of interest was made by placing “cooling sleeve” around this area. The cooling sleeve has an inlet and outlet nozzle and as the cooling medium is used air of ambient temperature and pressure (air from the NPP containment around 30°C).

This study used the one-way fluid structure interaction (FSI) approach. First the CFD analysis was done and then temperature fields were transferred onto FEM model to calculate stresses. Then calculated stresses were evaluated in the area of steam generator pocket. Four different rates of cooling were analyzed (coolant flow 0 m³/s (no cooling), 1 m³/s, 3 m³/s and 5 m³/s).

The article concludes that by appropriate external cooling it is possible to lower normal tensile stresses in the SG collector pocket area and even change them into compressible one. This will positively affect the possibility of stress corrosion cracking in this critical area.

Acknowledgement

The study was performed as a part of the research the possibility of risk components of nuclear power and therefore the authors are grateful to all consultants who contributed to this topic.

References

- Kutdusov, Yu.F. et al. (2013) Innovation of devices for stress reduction in welding joint 111 of welding unit of “hot” heat-transfer manifold and socket Du1200 of SWG 1000 by air blowing method on Rostov and Balakovo nuclear power plants. In: 8-th International Scientific and Technical Conference "Safety Assurance of NPP with WWER" (OKB "GIDROPRESS"), (in Russian).
- Lyakishev, S.L. et al. (2009) Development and justification of measures on assurance of reliable and safe operation of welded joints no. 111 of steam generator PGV-1000M. In: 6th International Scientific and Technical Conference "Safety Assurance of NPP with WWER" (OKB "GIDROPRESS"), (in Russian).
- Michejev, M. A. (1952) Fundamentals of Heat Transfer, Industrial Publishing House, Prague, 382 p. (in Czech).

SIMULATION OF CONTRAST MEDIUM PROPAGATION BASED ON 1D AND 3D PORTAL HEMODYNAMICS

A. Jonášová^{*}, O. Bublík^{**}, E. Rohan^{***}, J. Vimmr^{****}

Abstract: *The mathematical modelling of 3D blood flow coupled with contrast medium propagation in patient-specific human vessels ranks among the most computationally-demanding tasks, especially if a large vessel network is considered. With this in mind, some measure of simplification for potential use in clinical practice is usually inevitable and often also desired. In the present study, the main interest lies in the quantitative comparison between 3D and 1D models of portal hemodynamics and contrast medium propagation in two hepatic portal vein networks reconstructed from CT scans provided by the courtesy of the University Hospital Pilsen. To approximate the flow resistance of the downstream vascular bed and hepatic tissue, the mathematical model of Newtonian blood flow is coupled with the three-element Windkessel model. The numerical simulations of 3D and 1D blood flow and contrast medium propagation under average flow conditions are carried out using own in-house software. The obtained results show that, although the 1D model can never completely imitate the computational capabilities of the 3D model, its easy implementation, time-saving model preparation and almost no demands on computer technology dominate as advantages over obvious but moderate modelling errors arising from the dimensional reduction.*

Keywords: Patient-specific model, Blood flow, Contrast medium, Finite volume method, Windkessel model.

1. Introduction

In the last two decades, medicine has experienced a boom in the field of computer-aided imaging methods. Now the efforts of the bioengineering community are directed toward computational software that would aid surgeons during difficult surgeries or help them find an optimal surgical solution that would increase the chance of complete recovery for the patient. Compared to the numerical simulations performed in industry, where a computation may take days or even weeks, the clinical practice, however, requires results within a short time period and with minimal computational demand. With such strict requirements in mind, a development of clinical software is not easy and it is only natural that some model simplifications are usually inevitable.

This study, which is focused on quantitative comparison between 3D and 1D models of blood flow and contrast medium propagation in realistic hepatic portal vein networks, is a result of research performed at the University of West Bohemia in close co-operation with the University Hospital Pilsen. The main objective of this co-operation is the development of software for microstructurally-oriented multiscale modelling of tissue perfusion (Rohan et al., 2012), which would accelerate liver resection and make it more exact. In this regard, it is crucial to understand the impact of model simplification on the overall simulation accuracy, especially if the importance of blood supply to each part of the liver through the hepatic portal vein is taken into account. Fig. 1 shows selected preliminary data of contrast medium propagation in a patient-specific liver model, where the networks of the hepatic portal vein and hepatic veins are modelled by means of the 1D model.

^{*} Ing. Alena Jonášová: European Centre of Excellence NTIS – New Technologies for the Information Society, Faculty of Applied Sciences, University of West Bohemia, Univerzitni 22; 306 14, Pilsen; CZ, jonasova@ntis.zcu.cz

^{**} Ing. Ondřej Bublík: European Centre of Excellence NTIS – New Technologies for the Information Society, Faculty of Applied Sciences, University of West Bohemia, Univerzitni 22; 306 14, Pilsen; CZ, obublik@ntis.zcu.cz

^{***} Prof. Dr. Ing. Eduard Rohan, DSc.: European Centre of Excellence NTIS – New Technologies for the Information Society, Faculty of Applied Sciences, University of West Bohemia, Univerzitni 22; 306 14, Pilsen; CZ, rohan@kme.zcu.cz

^{****} Assoc. Prof. Ing. Jan Vimmr, PhD.: European Centre of Excellence NTIS – New Technologies for the Information Society, Faculty of Applied Sciences, University of West Bohemia, Univerzitni 22; 306 14, Pilsen; CZ, jvimmr@kme.zcu.cz

The main objective of this study is to determine the differences between the 3D and 1D network models by adopting the assumptions of impermeable and inelastic vessel walls and blood as an incompressible Newtonian fluid with density of 1050 kg/m^3 and dynamic viscosity of $0.00345 \text{ Pa}\cdot\text{s}$.

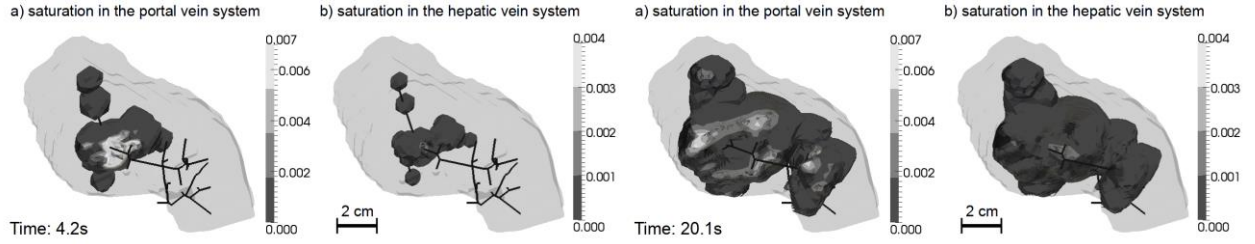


Fig. 1: Example of contrast medium propagation in patient-specific model of human liver at two selected time instants: $t_1 = 4.2 \text{ s}$ (left) and $t_2 = 20.1 \text{ s}$ (right). The results, which are based on the modeling approach introduced in (Rohan et al., 2012), show the local concentration of the contrast medium in the: a) portal and b) hepatic vein systems of the hepatic tissue. Here, the vessels involved in the tissue perfusion and contrast medium propagation are represented by 1D venous networks (black lines).

2. Methods and Results

2.1. Patient-specific hepatic portal vein networks

In this study, the numerical simulations of blood flow and contrast medium propagation are carried out in two realistic portal vein geometries with different levels of complexity (9 outlets vs. 39 outlets), Fig. 2 (left). Both models are reconstructed from CT scans provided by the courtesy of the University Hospital Pilsen. For the reconstruction process, we employ the semi-automatic segmentation software DICOM2FEM (Jiřík & Lukeš, 2013), which is currently being developed at the University of West Bohemia, in combination with the well-known Taubin smoothing algorithm. The computational meshes for the two 3D hepatic portal vein models are generated with the help of the software package HyperMesh v11.0 (Altair Engineering, Troy, USA). The number of tetrahedral cells required to model the simple and complex venous networks is 816,547 and 2,042,156, respectively.

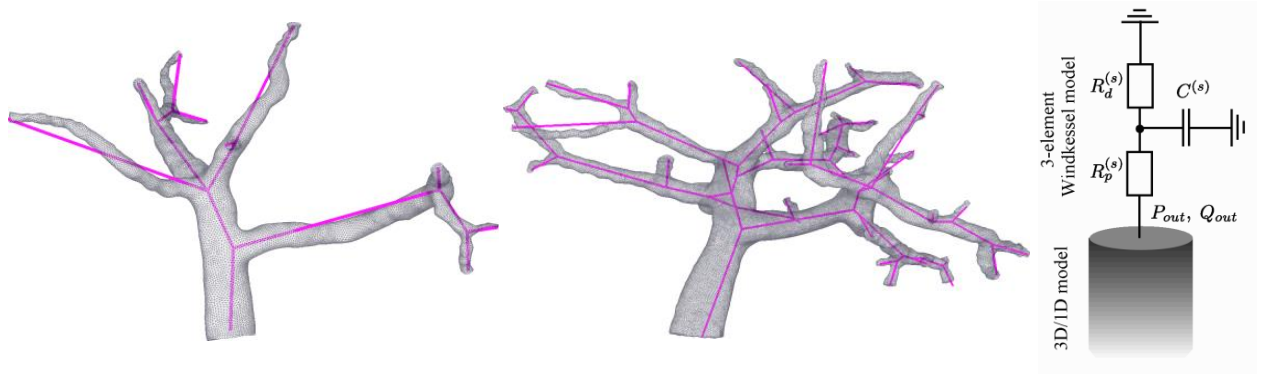


Fig. 2: Left – 1D and 3D reconstructions of simple (9 outlets) and complex (39 outlets) hepatic portal vein networks. Right – The three-element Windkessel model as an outflow boundary condition. For more details on the principle of this lumped model, see, for example, (Westerhof et al., 2009).

2.2. Blood flow in 3D and 1D models

For the description of the blood flow in the 3D venous networks, the non-linear system of Navier-Stokes equations for an incompressible Newtonian fluid is used

$$\frac{\partial v_j}{\partial x_j} = 0, \quad (1)$$

$$\frac{\partial v_i}{\partial t} + \frac{\partial}{\partial x_j} (v_i v_j) + \frac{1}{\rho} \frac{\partial p}{\partial x_i} = \frac{1}{\rho} \frac{\partial^2 v_i}{\partial x_j \partial x_j}, \quad i, j = 1, 2, 3, \quad (2)$$

where t is the time, v_i is the i -th component of the velocity vector \mathbf{v} corresponding to the Cartesian component x_i of the space variables vector \mathbf{x} , p is the pressure, and ρ is the density. The mathematical model is numerically solved using our own computational algorithm based on a stabilised variant of the projection method in combination with the cell-centred finite volume method formulated for hybrid unstructured tetrahedral grids. The principle of this algorithm, which we have successfully implemented for the solution of various hemodynamical problems in the past, is described in (Vimr et al., 2013).

Compared to the 3D flow problem, we assume the blood flow in one inelastic segment of the 1D venous network to be governed by the continuity equation and the Bernoulli equation

$$A_{i-1}u_{i-1} = A_i u_i, \quad (3)$$

$$\frac{1}{2}\rho u_{i-1}^2 + p_{i-1} = \frac{1}{2}\rho u_i^2 + p_i + e_i^{\text{loss}}, \quad (4)$$

where A_i is the cross-sectional area of the i -th segment and u_i is the velocity in this segment. To approximate the losses originating from the viscous resistance, the Bernoulli equation (4) is completed with the term e_i^{loss} corresponding to friction loss in inelastic tubes, which is known to be proportional to the local velocity magnitude. In general, the description of blood flow in a 1D venous network results in a system of non-linear algebraic equations, which is solved with the help of the Newton method.

The numerical simulations of 3D and 1D blood flow are carried out for steady boundary conditions. At the inlet of the hepatic portal vein, we prescribe an average physiological velocity of 0.325 m/s. Because of the difficulties associated with clinical determination of physiological pressure in portal vein networks, each outlet of the two models considered in this study is coupled with a well-known lumped model – the three-element Windkessel model, schematic drawing of which is shown in Fig. 2 (right). Compared to other modelling approaches such as the prescription of one constant outlet pressure, the Windkessel model is able to approximate the flow resistance of the downstream vascular bed and to provide a physiological value of pressure at all network outlets. For one outlet, the Windkessel model is mathematically described by the following two equations for unknown pressures p_d and p_o :

$$\frac{d}{dt}p_d(t) + \frac{p_d(t)}{CR_d} = \frac{1}{C}Q_o(t), \quad p_o(t) = p_d(t) + R_p Q_o(t), \quad (5)$$

where p_o and Q_o are the pressure and flow rate determined at this specific outlet of the 3D/1D models and p_d is the distal pressure representing the pressure in arterioles and capillaries of the downstream vascular bed. Note that the remaining parameters known as the lumped parameters of proximal R_p and distal R_d resistance and capacitance C have to be calculated for each outlet prior to the numerical simulation.

Selected outflow results for the simple and complex venous networks are listed in Tab. 1 with corresponding cross-sectional areas (CSA) and absolute Δ [ml/s] and relative errors σ [%] defined as

$$\Delta = |Q_{3D} - Q_{1D}|, \quad \sigma = \frac{|Q_{3D} - Q_{1D}|}{Q_{3D}} \cdot 100\%, \quad (6)$$

where Q_{3D} and Q_{1D} are the flow rates in the 3D and 1D models, respectively. In general, it is possible to say that the flow rates computed with the 1D blood flow model sufficiently approximate the ones determined using the 3D model.

Tab. 1: Overview of selected outlet results for the simple (left) and complex (right) portal vein networks. Here, the abbreviation CSA stands for cross-sectional area of the outlet.

outlet No.	CSA [mm ²]	abs error Δ [ml/s]	rel error σ [%]	outlet No.	CSA [mm ²]	abs error Δ [ml/s]	rel error σ [%]
1	6.23	0.63	12.95	1	1.39	0.21	15.32
3	6.67	0.57	8.85	9	1.51	0.09	4.54
5	8.36	0.79	12.01	10	1.46	0.24	12.10
6	4.97	0.34	7.11	20	1.03	0.05	6.64
9	4.15	0.32	9.77	36	1.92	0.10	3.52

2.3. Contrast medium propagation

For the purpose of this study, the propagation of the contrast medium dissolved in the blood and transported through the venous network is modelled in analogy to the mathematical model introduced in Rohan et al. (2012). Taking into consideration only the convection of the contrast medium, the local concentration of the tracer expressed by the saturation S is described as

$$\frac{\partial S}{\partial t} + \frac{\partial}{\partial x_j}(S v_j) = 0, \quad (7)$$

where t is the time. The numerical solution of Eq. (7) in the 3D portal vein model is based on the upwind cell-centered finite volume scheme formulated for unstructured tetrahedral grids in combination with the two-stage Runge-Kutta method of second order accuracy in time. To simulate the propagation of the contrast medium based on the portal hemodynamics computed previously, we apply an external source saturation given in the form of a time bolus. Selected numerical results for the simple venous network are shown in Fig. 3. From the graph in Fig. 3 (right), it can be noted that the difference between the 1D and 3D outlet tracer rates is non-zero (22% at $t = 2.5$ s) because of tracer accumulation near the walls of the 3D model.

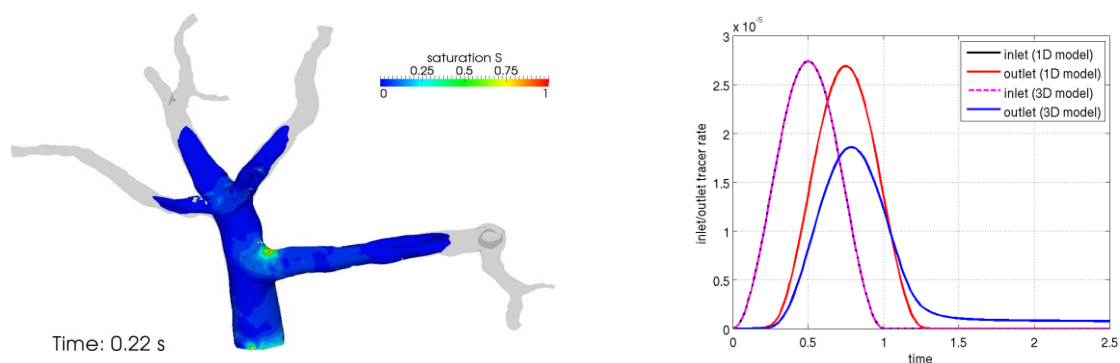


Fig. 3: Left – Propagation of the contrast medium in the 3D model with 9 outlets at the time $t = 0.22$ s. Right – Time development of inlet and outlet tracer rates in the simple 3D and 1D venous networks.

3. Conclusions

Comparing not only the results obtained for both the 3D and 1D models, several advantages and disadvantages of each modelling approach can be noted. First of all, there is the matter of model preparation: Before a 3D venous network can be used for any numerical simulation, quite many time-consuming preparation steps are necessary (reconstruction from CT scans, geometry 'cleaning', remeshing etc.), whereas the 1D network requires only one step – the 'cleaning' (removal of non-anatomical branches and loops). Another issue is the computational demand of the 3D and 1D models: In the case of the 1D network, the simulation of blood flow and contrast medium propagation takes only seconds to complete and requires no special computer technology. On the other hand, the 3D simulation is computationally very demanding even assuming up-to-date computer technology is available. Thus, despite the existing result differences between both models, the benefits of the 1D approach clearly outweigh its slight inaccuracy.

Acknowledgement

This study was supported by the project NT13326 of the Ministry of Health of the Czech Republic.

References

- Jiřík, M. & Lukeš, V. (2013) DICOM2FEM software (<https://github.com/vlukes/dicom2fem>).
- Rohan, E., Lukeš, V., Jonášová, A. & Bublík, O. (2012) Towards microstructure based tissue perfusion reconstruction from CT using multiscale modeling, In: Proc. 10th World Congress on Computational Mechanics (WCCM2012), Universidade de Sao Paulo, Sao Paulo, pp. 1-18.
- Vimr, J., Jonášová, A. & Bublík, O. (2013) Numerical analysis of non-Newtonian blood flow and wall shear stress in realistic single, double and triple aorto-coronary bypasses. International Journal for Numerical Methods in Biomedical Engineering, 29, 10, pp. 1057-1081.
- Westerhof, N., Lankhaar, J.-W. & Westerhof, B. E. (2009) The arterial Windkessel. Medical & Biological Engineering & Computing, 34, 8, pp. 1049-1064.

REDUCTION FOR HIGH-RISE BUILDINGS SEISMIC ANALYSIS

J. Kabeláč*, S. Rossier**

Abstract: *This paper presents reduction as a special case of static condensation. The reduction was designed for checking seismicity of high-rise buildings. A reference point is assigned to each floor. Mass matrix and the stiffness matrix of the original structure are reduced to these reference points. The presented procedure is based on the requirements of design codes and engineering practice.*

Keywords: Modal analysis, Dynamic reduction, Seismicity, High-rise buildings, Sensitivity analysis.

1. Introduction

The seismic design of buildings is a part of the standard design procedures in many countries nowadays, even those with low or moderate seismic risk. Design codes (Eurocode EC-EN 1998, 2004) are increasingly demanding about it and efficient analysis tools are therefore necessary. The increasing complexity of structures requires the use of 3D finite element modelling to provide realistic distribution of design internal forces in complex shear-resisting systems. Most design codes recommend – or, in some cases, even request – the use of the response spectrum method, which implies a modal analysis of the structure.

Using a full 3D modelling of a building for dynamic analysis tends to be computationally heavy. Moreover, the FE discretization of all structural members introduces many DoF in the modelling which correspond to local eigenmodes and are uninteresting regarding the overall seismic behavior of the structure. Those local modes mostly correspond to very small parts of the modal mass of the structure, but their important number makes it difficult to reach the typical 90% of cumulated modal mass within a reasonable number of modes. The computation of a very high number of modes might thus be required in order to ensure that all relevant modes are indeed taken into account in the modal superposition, thus making the process unaffordable.

Another typical issue is the so-called accidental eccentricity. Design codes require that some mass eccentricity is introduced in the analysis to account for an irregular distribution of the non-structural masses (dead and live loads). As classical modal analysis uses a diagonal mass matrix to reduce the computation effort, that eccentricity cannot be taken into account directly in a full 3D FE analysis.

The Improved Reduced System technique presented in this paper addresses directly the issues above. The reduced system is directly generated from a classical 3D FE mesh, which means that no dedicated input is necessary for it, apart from the actual definition of the reference points for each storey. Not only the floor slabs, but also all supporting members are reduced at once and mapped to the closest reference point, leading to a reduced model with only 6 DoF per storey. This extremely compact analysis model automatically leads to a solution including only relevant eigenmodes for the seismic behaviour. After resolution, the end results (displacements, stresses) can be expanded back to the original FE mesh, providing detailed output in the entire structure. Additionally, the use of a full mass matrix for the reduced model allows for implicit mass eccentricity without modifying the geometry of the system. Finally, because of its ideal topology, the reduced system can provide directly results at the mass center of each storey, such as displacements, accelerations and inter-storey drift. Those are required for the seismic assessment of a building.

* Ing. Jaromír Kabeláč: FEM Consulting, Veveří 331/94; 602 00, Brno, CZ, jaromir.kabelac@seznam.cz

** Ing. Stéphane Rossier, PhD.: Nemetschek Scia, Dürrenbergstrasse 24, 32112 Gurmels, Switzerland, s.rossier@scia.ch

2. Method

The proposed dynamic reduction should meet the following conditions. The resulting eigenmodes shall approximate significant eigen modes of the original building. With the classical reduction to the point there is a not realistic concentration of stresses (Guyan, 1965, O'Callahan et al., 1989). This is very inconvenient for the following checks seismicity. Other methods are more accurate in loading from seismicity (O'Callahan et al., 1989, Paz, M. 1984, and their modification). The resulting reduced system should also respect the mass distribution along the structure reduced to points at each storey. It is very suitable for the following sensitivity analysis and close to engineering practice. However, the mentioned methods partially conceal it. The chosen process is illustrated in Fig. 1. Most of the original node structure is allocated to the floor. The method does not require the identification of all nodes especially between floors. A reference point is chosen for each storey. This point represents the movement of the storey as a whole.

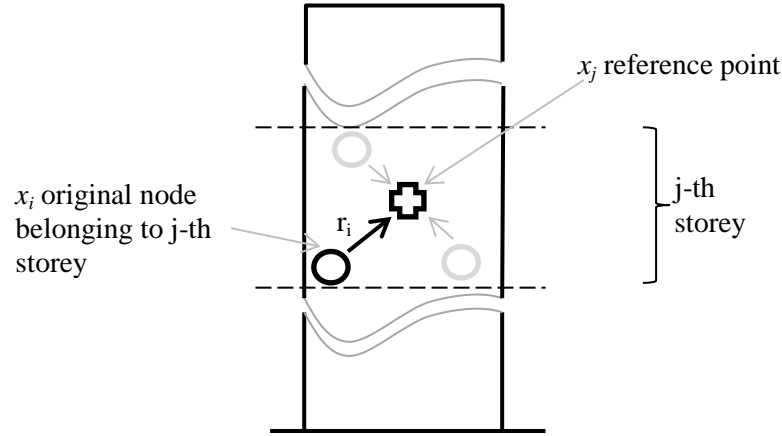


Fig. 1: Schema of method.

2.1. Main reduction

Inputs are symmetric sparse positive definite stiffness matrix \mathbf{K} and sparse symmetric mass matrix \mathbf{M} , which are determined by classic FEM model over original construction. Third input is sparse matrix \mathbf{H} . Matrix \mathbf{H} defines linear relationships between forces in reduced DOF \mathbf{F}_r and forces in original DOF \mathbf{F}_o by following equation:

$$\mathbf{F}_o = \mathbf{H}\mathbf{F}_r \quad (1)$$

Using the matrix \mathbf{H} does not imply any artificial reinforcement structure. Moreover, it may even better describe the structure load caused by its own mass without any concentration. If we use Lagrange multiplier, we can write the following system of equations as a special case of static condensation. Where \mathbf{u}_r is deformation in reference node and \mathbf{u}_o is deformation on original construction.

$$\begin{bmatrix} \mathbf{K} & -\mathbf{H} \\ -\mathbf{H}^T & \mathbf{0} \end{bmatrix} \begin{bmatrix} \mathbf{u}_o \\ \mathbf{F}_r \end{bmatrix} = \begin{bmatrix} \mathbf{0} \\ \mathbf{u}_r \end{bmatrix} \quad (2)$$

$$\mathbf{F}_r = (\mathbf{H}\mathbf{K}^{-1}\mathbf{H})^{-1} = \mathbf{K}_r \cdot \mathbf{u}_r \quad (3)$$

$$\mathbf{u}_o = \mathbf{K}^{-1} \cdot \mathbf{H}\mathbf{K}_r \cdot \mathbf{u}_r = \mathbf{T}\mathbf{u}_r \quad (4)$$

Using the transformation matrix \mathbf{T} , reduced mass matrix can be obtained.

$$\mathbf{M}_r = \mathbf{T}^T \mathbf{M} \mathbf{T} \quad (5)$$

Both reduced matrix \mathbf{M}_r , \mathbf{K}_r are full and small. Now it is possible to solve reduced eigenvalue problem over reduced matrixes.

$$\{\mathbf{M}_r, \mathbf{K}_r\} \Rightarrow \{\boldsymbol{\Lambda}, \mathbf{V}_r\} \quad (6)$$

And eigen vectors \mathbf{V} of original construction can be approximated by transformation matrix \mathbf{T} and eigen vectors of reduced problem \mathbf{V}_r at final.

$$\mathbf{V} = \mathbf{T} \cdot \mathbf{V}_r \quad (7)$$

2.2. Relation matrix H

Creating the matrix H is based on the following simplifying assumption. We reduce the original nodes x_i belonging to that storeys to the storey reference point (see Fig. 1.). The acceleration of each relevant original node is dependent on the acceleration of the reference node as in rigid body. This can be written classically by a kinematic relationship (where $\hat{\mathbf{r}}$ is antisymmetric matrix representing vector \mathbf{r}_i at Fig. 1).

$$\ddot{\mathbf{x}}_i = \begin{bmatrix} \mathbf{E} & \hat{\mathbf{r}} \\ \mathbf{0} & \mathbf{E} \end{bmatrix} \ddot{\mathbf{x}}_j = \mathbf{R}_i \ddot{\mathbf{x}}_j \quad (8)$$

For inertia force in the original node x_i caused by acceleration in the reference node can be written

$$\mathbf{F}_i = \mathbf{M}_i \cdot \mathbf{R}_i \cdot \ddot{\mathbf{x}}_j \quad (9)$$

Force in reference node caused by acceleration in reference node is given by summation of forces in original node.

$$\mathbf{F}_j = \sum_i \mathbf{R}_i^T \cdot \mathbf{F}_i = \left(\sum_i \mathbf{R}_i^T \mathbf{M}_i \cdot \mathbf{R}_i \right) \cdot \ddot{\mathbf{x}}_j = \mathbf{J}_j \cdot \ddot{\mathbf{x}}_j \quad (10)$$

Exclude $\ddot{\mathbf{x}}_j$ from (10) and substitute to (9).

$$\mathbf{F}_i = \mathbf{M}_i \cdot \mathbf{R}_i \cdot \mathbf{J}_j^{-1} \cdot \mathbf{F}_j = \mathbf{H}_{ij} \cdot \mathbf{F}_j \quad (11)$$

This is founded part of matrix \mathbf{H} , which represents relationship between j-th reference node and i-th reduced node and respects mass distribution over construction.

2.3. Some remarks about sensitivity analysis

Each floor can have a variable center of gravity from operational mass. The resulting eccentricity up can lead to significant torsional load of the building. It is reflected also in building design codes. To check the structural element it is necessary to select the most adverse mass distribution. In practice this leads to the evaluation of the many mass combinations. It is possible to use the reduced stiffness matrix \mathbf{M}_r here. It is not difficult to find a sensitivity of the reduced mass matrix to change the center of gravity Δx_{ij} of each floor. Linear estimation can be applied for the modification.

$$\tilde{\mathbf{M}}_r = \mathbf{M}_r + \Delta x_{ij} \frac{\partial \mathbf{M}_r}{\partial x_{ij}} \quad (12)$$

Now we can use a sensitivity analysis (for example in Choi and Kim, 2005).

$$\left\{ \mathbf{M}_r, \frac{\partial \mathbf{M}_r}{\partial x_{ij}} \mathbf{K}_r, \mathbf{\Lambda}, \mathbf{V}_r \right\} \Rightarrow \left\{ \frac{\partial \mathbf{\Lambda}}{\partial x_{ij}}, \frac{\partial \mathbf{V}_r}{\partial x_{ij}} \right\} \quad (13)$$

The resulting sensitivity of eigenvalues can be used to quickly find the extreme load of the part of structure.

3. Example

This 7-storey building is a part of the training centre of the ACPC in Fribourg (Switzerland). The modal behaviour of the original, full mesh model and that of the reduced system have been compared. The frequencies and modal masses of the most relevant eigenmodes are listed in the table below. The corresponding eigenshapes (not represented here) show excellent concordance for low order modes (see modes 1-2-3 in the table). For higher order modes, the full mesh analysis tends to exhibit local vibrations

and spread modal mass across several modes, whence the reduced model tends to more smooth the response and group similar behaviours and corresponding modal mass. Internal forces in the main shear walls after modal superposition exhibit no significant differences. As it is a real building with an important structural eccentricity, all relevant modes have combined translational and torsional behaviour.

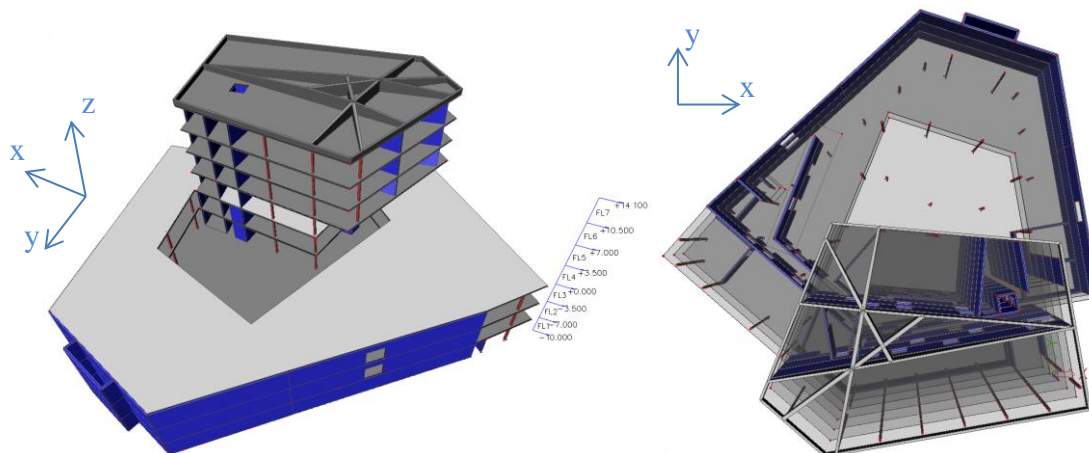


Fig. 2: Example of building.

Eigenvalue	Original model				Reduced model			
	Freq [Hz]	Modal mass [%]			Freq [Hz]	Modal mass [%]		
		X	Y	Rz		X	Y	Rz
Translation Y	1.71 (1)	0.3	17.9	5.1	1.71 (1)	0.3	17.9	5.1
Translation Y	2.44 (2)	5.1	11.6	1.8	2.44 (2)	5.1	11.6	1.8
Translation X	3.09 (3)	30.0	2.4	10.7	3.10 (3)	30.7	2.6	10.9
Translation X	7.12 (21)	11.2	2.5	1.1	8.06 (15)	11.5	11.6	0.2
Torsion Rz	12.83 (92)	0.2	0.1	10.2	12.85 (30)	9.9	3.4	29.9

4. Conclusions

The method corresponds to engineering practice of dividing the building into individual floors. It reflects the requirements of design codes. The reduced model can directly obtain mass characteristics, the relative motion and acceleration of the floors. In addition, modification of the position of center of gravity of the floor in the calculation model is easy. The reduced model can be directly used for seismic analysis and next sensitivity analysis. More accurate methods of reduction are known. However, numerical simulations confirmed its sufficient robustness for real buildings with low or moderate seismic risk. The presented method has been implemented in the CAE software SCIA Engineer for building applications.

Acknowledgement

This contribution has been prepared with the financial support of the companies FEM Consulting and Nemetchek SCIA.

References

- Eurocode EC-EN 1998 (2004) Design of structures for earthquake resistance, chapter 4.3 Structural Analysis for Design of Buildings.
- O'Callahan, J. (1989) A Procedure for an Improved Reduced System (IRS) Model, In: Proc. 7th International Modal Analysis Conference, Las Vegas, Nevada.
- O'Callahan, J., Avitabile, P., Riemer, R. (1989) System Equivalent Reduction Expansion Process (SEREP), In: Proc. 7th International Modal Analysis Conference, Las Vegas, Nevada.
- Guyan, R.J. (1965) Reduction of Stiffness and Mass Matrices, AIAA Journal, Vol. 3.
- Paz, M. (1984) Dynamic Condensation, AIAA Journal, pp. 724-727.
- Choi, K.K., Kim, N.H. (2005) Structural sensitivity analysis and optimization 1, Linear systems, Springer.

LATERAL-TORSIONAL BUCKLING OF I-SECTION BEAMS WITH INITIAL RANDOM IMPERFECTIONS

Z. Kala^{*}, J. Valeš^{**}

Abstract: *The paper deals with a statistical analysis of load carrying capacity of a simply supported straight I-beam with equal end moment with cross-section IPE 220, solved by geometrically nonlinear solution influenced by lateral-torsional buckling. The beam was modelled applying the programme ANSYS on behalf of the element BEAM188. Imperfections were considered to be random quantities. The initial curvature and the axis rotation are considered to have the shape of one half-wave of the sine function. The correlation between the amplitudes of initial curvature and initial rotation of the axis is considered as the parameter of solution within the interval from -1 to 1. The influence of this correlation on the change of mean value and standard deviation of random load carrying capacity is studied, the other imperfections being considered to be random quantities resulting from experiments. Realizations of initial imperfections are simulated applying the Latin Hypercube Sampling method. The conclusion presents a discussion of need of paying attention to initial torsion of the axis, when creating stochastic computational models.*

Keywords: Lateral-torsional buckling, Load-carrying capacity, Imperfection, Beam, Steel, Slenderness.

1. Introduction

The paper presented deals with the stochastic analysis of load carrying capacity of a simply supported straight IPE 220 beam with equal end moment. The influence of lateral-torsional buckling on load carrying capacity of the beam the non-dimensional slenderness of which equals 1 is studied. The beam was solved by means of geometrically nonlinear solution so that it would be possible to take into consideration the influence of initial imperfections on load carrying capacity. The first initial geometrical imperfections are assumed to follow the shape of the first eigenmode pertaining to lateral-torsional buckling. This imperfection consists of lateral buckling of the beam in the direction perpendicular to the minor axis of cross-section, and of the rotation of the axis of rotation of cross-sections directed at the beam centre. The beam curvature according to its first eigenmode of lateral-torsional buckling supposes that the lateral-torsional buckling and the rotation of beam axis are functionally dependent. It is not clear to what extent this assumption corresponds with the results which would be obtained from experiments.

The majority of laboratory measurements pay attention more to measurement of initial curvature of the beam axis than to measurement of initial rotations of cross-sections (Fukumoto et al., 1976). However, in case of lateral-torsional buckling, both imperfections can be of importance. It is a question which correlation can be considered to exist between them. The consideration of the correlation by the value 1 need not correspond with the reality accurately. The correlation between them is primarily given by manufacturing processes. To get an idea about to how large extent the correlation value can influence statistical characteristics of load carrying capacity, this problem is studied on behalf of a nonlinear computational model in the present paper.

The computational model was realized out in the ANSYS programme, the random influence of all initial imperfections having been taken into consideration.

^{*} Prof. Ing. Zdeněk Kala, PhD.: Brno University of Technology, Faculty of Civil Engineering, Institute of Structural Mechanics, Veveří 331/95 602 00 Brno, kala.z@fce.vutbr.cz

^{**} Ing. Jan Valeš: Brno University of Technology, Faculty of Civil Engineering, Institute of Structural Mechanics, Veveří 331/95 602 00 Brno, vales.j@fce.vutbr.cz

2. Computational Model

A computational model of a two-hinged beam of IPE 220 profile was created. Its length L was calculated in dependence on non-dimensional slenderness according to EUROCODE 3 as $L = 3.323$ m. The model was created applying the programme ANSYS applying the beam element BEAM188. This element is suitable for analysing slender beam structures. It is based on Timoshenko beam theory which includes shear-deformation effects and it is well-suited for linear, large rotation, and large strain nonlinear applications. BEAM188 has seven degrees of freedom at each node (these include translations in the x , y and z directions and rotations about the x , y and z directions, the seventh degree of freedom is a warping magnitude). At both ends, the model was loaded by bending moments of the same size, and of opposite sign. The beam diagram is in Fig. 1.

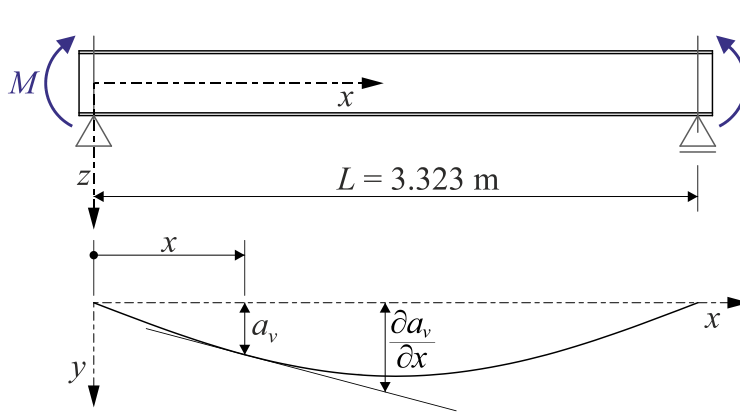


Fig. 1: Beam diagram.

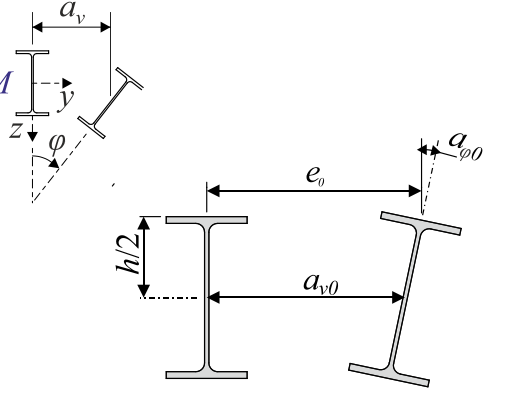


Fig. 2: Curvatures in the middle span.

2.1. Initial imperfections

The beam axis rotation in the direction of the major axis, i.e., in the plane xy , is described by the function:

$$a_v = a_{v0} \sin\left(\frac{\pi x}{L}\right), \quad (1)$$

and the rotation of cross sections along the beam length is given as

$$a_\varphi = a_{\varphi 0} \sin\left(\frac{\pi x}{L}\right), \quad (2)$$

a_{v0} and $a_{\varphi 0}$ being the amplitudes (Kala, 2013), see Fig. 2. If the beam is curved according to the first eigenmode, it is then valid that

$$a_{v0} = \frac{e_0}{1 + \frac{h}{2} \frac{P_z}{M_{cr}}}, \quad (3)$$

$$a_{\varphi 0} = a_{v0} \frac{P_z}{M_{cr}}, \quad (4)$$

where e_0 is the amplitude of one half-wave of the sine function relating to the upper flange, and for force P_z , the following relation is valid:

$$P_z = \pi^2 \frac{EI_z}{L^2}, \quad (5)$$

When generating the random quantities and subsequently creating the computational model, various values of correlations are considered between initial curvature e_0 and initial cross-section rotation $a_{\varphi 0}$, and namely within the interval -1 to 1 with the step 0.1. The initial curvature is simulated by random input quantity e_0 , from which the axis curvature a_{v0} is calculated according to the formula (3). The random imperfection $a_{\varphi 0}$ is selected as being correlated with imperfection e_0 . As there was not the

information on standard deviation of initial rotation $a_{\varphi 0}$, this was calculated on behalf of (3) and (4) on condition that e_0 was a random quantity, and h, P_z, M_{cr} were deterministic quantities given by nominal geometrical characteristics of the cross-section. As the mean value of e_0 is zero, so the mean value of $a_{\varphi 0}$ is zero as well. Let us remark that for the calculation, the quantity $a_{\varphi 0}$ is not considered as the functionally depending on e_0 , as it would be indicated by (3) and (4), but these formulae serve only for calculation of standard deviation of the amplitude of initial rotation of cross-section $a_{\varphi 0}$ as a random input quantity correlated with e_0 .

Calculations of load carrying capacity are thus carried out for series of random realizations with 21 different correlations between both initial imperfections. Let us remark that neither mean values nor standard deviations of initial imperfections e_0 or $a_{\varphi 0}$ change with the correlation change. Examples of initial curvature in combination with the rotation of cross-sections modelled applying the ANSYS are schematically presented in Fig. 3.

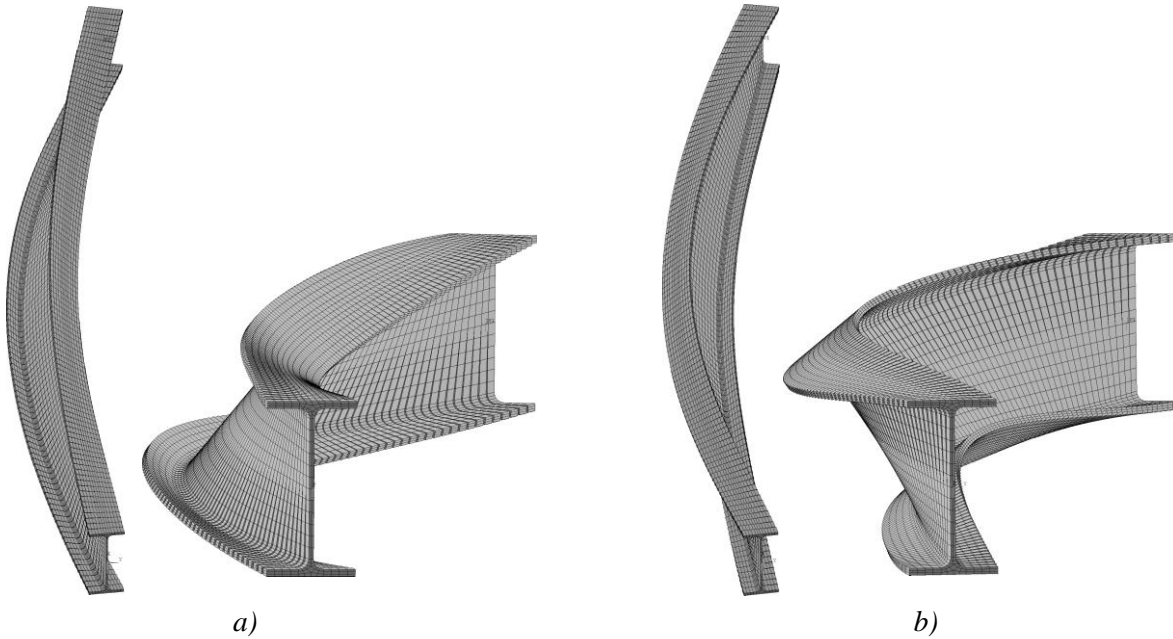


Fig. 3: Diagram of computational model: a) Initial curvature combined with rotation of cross-sections with correlation -1; b) Initial curvature combined with station of cross-sections with correlation 1.

3. Stochastic Analysis of Load Carrying Capacity

3.1. Random input quantities

In general, the load carrying capacity M_d is a random quantity which is a function of random geometrical and material characteristics, and can be studied by applying simulation methods of the Monte Carlo type, see, e.g., (Gottvald & Kala, 2012; Kala, 2012). For the presented problem, 500 random realizations were simulated for each of the series of 21 correlations considered between input imperfections by the Latin Hypercube Sampling method (Iman, 1980), (McKey, 1979).

The dimensions of the profile IPE 220 (Fig. 4), material characteristics of the steel grade S 235 (Melcher, 2004), and initial imperfections e_0 and $a_{\varphi 0}$ were random input quantities. The Gaussian distribution of probability density is considered for all input random quantities. Residual stresses were not considered. With the exception of initial imperfections e_0 and $a_{\varphi 0}$, all the quantities are mutually statistically independent.

3.2. Random output quantities

As the load carrying capacity value M_d , such value of the bending moment M (see Fig. 1) is considered at which the von Mises stress, at the most stressed point of the beam, is equal to yield strength f_y . The possibility of cross-section to plasticize is not considered, and thus, M_d is the value of elastic load-carrying capacity. The statistics of load carrying capacities is illustrated by the diagram in Fig. 4.

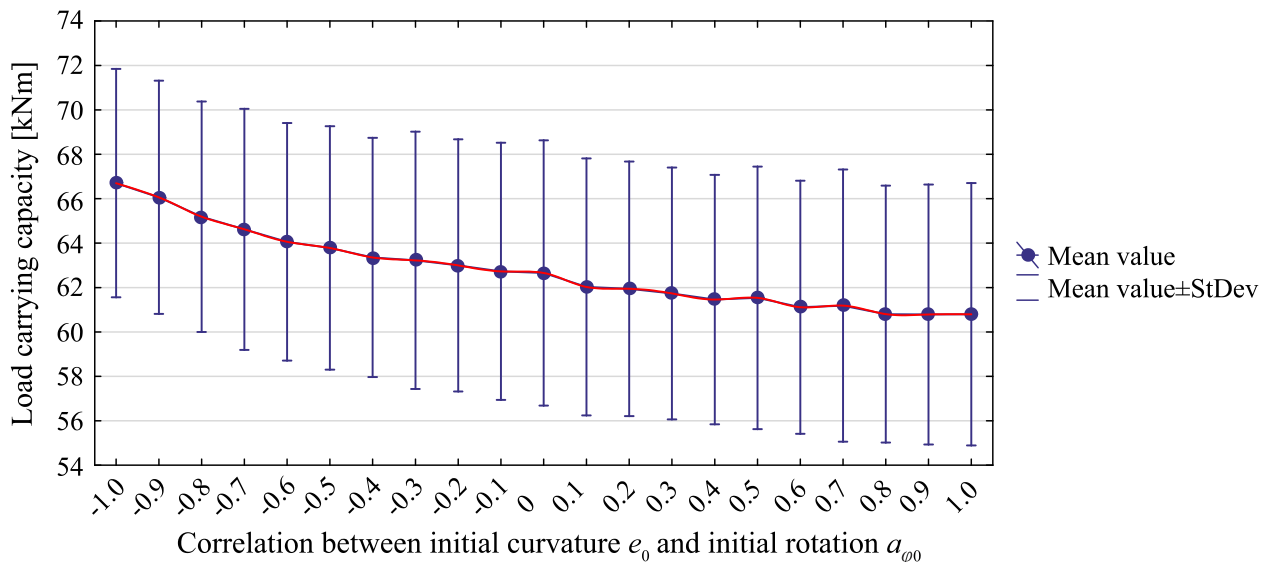


Fig. 4: Mean values with standard deviations of load carrying capacities for correlations considered.

4. Conclusions

It is evident from the diagram in Fig. 4 that the mean load carrying capacity value decreases with increasing correlation between initial curvature e_0 and initial rotation of cross-sections $a_{\phi 0}$, whereas the standard deviation shows the increasing tendency. At the same time, the decrease in mean value shows a moderate nonlinear trend decreasing in the region in which correlations approach 1. The lowest mean value of load carrying capacity was obtained for the correlation 1, i.e., for complete functional dependence between these two imperfections. It confirms the fact that initial rotation of beams is an imperfection not to be neglected. For the correlation 1, not only the lowest value of average load carrying capacity but, at the same time, high value of standard deviation of load carrying capacity will be obtained. The mean value of load carrying capacity is, for this correlation, by approximately 9.84 % lower than the mean value of load carrying capacity for the correlation -1. If the design load carrying capacity were calculated as 0.1 percentile, the low mean value and the high standard deviation would lead to a low value of 0.1 percentile. The curvature of the beam axis according to the first eigenmode pertaining to lateral-torsional buckling (correlation 1) is conservative from the point of view of design reliability; to get more accurate calculation, it would be needed to know the real value of the correlation between e_0 and $a_{\phi 0}$ found on the basis of large number of experiments.

Acknowledgement

The article was elaborated within the framework of projects GAČR 14-17997S.

References

- Fukumoto, Y., Kajita, N. & Aoki, T. (1976) Evaluation of column curves based on probabilistic concept, In: Proc. Int. Conf. on Stability, Prelim. Rep., publ. by Gakujutsu Bunken Fukyu - Kai, Tokyo, pp. 1-37.
- Gottvald, J. & Kala, Z. (2012) Sensitivity analysis of tangential digging forces of the bucket wheel excavator SchRs 1320 for different terraces. Journal of Civil Engineering and Management, 18, 5, pp. 609-620.
- Kala, Z. (2012) Geometrically non-linear finite element reliability analysis of steel plane frames with initial imperfections. Journal of Civil Engineering and Management, 18, 1, pp. 81-90.
- Kala, Z. (2013) Elastic lateral-torsion buckling of simply supported hot-rolled steel I-beams with random imperfections, Procedia Engineering, 57, pp. 504-514.
- Iman, R.C. & Conover, W.J. (1980) Small sample sensitivity analysis techniques for computer models with an application to risk assessment. Communications in Statistics – Theory and Methods, 9, 17, pp. 1749-1842.
- McKey, M.D, Conover, W.J, Beckman, & R.J. (1979) A comparison of the three methods of selecting values of input variables in the analysis of output from a computer code. Technometrics, 1, 2, pp. 239-245.
- Melcher, J., Kala, Z., Holický, M., Fajkus, M. & Rozlívka, L. (2004) Design characteristics of structural steels based on statistical analysis of metallurgical products. Journal of Constructional Steel Research, 60, 3-5, pp. 795-808.

COMPUTER NUMERICAL SOLUTION OF VON MISES PLANAR TRUSS BY THE POTENTIAL ENERGY

M. Kalina *

Abstract: *The task of the von Mises planar truss is to examine the effect of load located on top joint oriented in vertical direction. The mathematical concept of large displacement elastic analysis of the von Mises truss specified for computers is described. The model consists of finite nodes, tensile stiffness, and rotation stiffness. The formulas for the evaluation of displacements of nodes and rotations of segments were derived using geometric and physical conditions. Formulae for the determination of potential energy of the system are presented. Using search for the minimum potential energy, we can find the deformation of the model. The solution is searched step by step, using the Newton-Raphson iteration. The presented computational algorithm allows to model the von Mises truss using a finite amount of segments. Such solution is suitable for the load-deflection curve computation of a limit load model.*

Keywords: Von Mises truss, Nonlinear solution, Potential energy, Newton-Raphson method, Discrete model, Computational algorithm.

1. Introduction

The study of the two-bar truss, also known as the von Mises planar truss, is important to define the main stability characteristics of framed structures as well as flat arches, and of many other phenomena associated with bifurcation buckling. The von Mises planar truss is an example of a classical elastic system having numerous references in the literature (von Mises, 1923; von Mises & Ratzersdorfer, 1925; Kwasniewski, 2009).

The objective of the solution is an analysis of the load-deflection curve of top joint. The load-deflection curve of the top joint has been attempted with use of the computer programme which calculates the change of the potential energy for individual nodes of the model.

The deflection for the specific node, which was used in past, was attempted to be calculated by a static method. Using this method for calculation of any node could be more difficult in terms of time and accuracy of the result. Contrastingly, using the potential energy is important to analyze the deflection of any nodes.

The solution is useful for plotting the load-deflection curves of asymmetrical trusses with random imperfection. Let us note that imperfections are generally random variables, realizations of which can be simulated by methods of type Monte Carlo; it can be seen in the following publications (Karmazínová et al., 2009; Gottvald & Kala, 2012; Kala, 2012; Kala, 2013). In the design of steel structure, it is important to count with the influence of imperfection, see, e.g., (Kala, 2008; Gottvald, 2010; Kala & Kala, 2010; Kala, 2012). Their effect has the significance for both static and economic designs of the structure, see, e.g., (Gottvald, 2010; Kala et al., 2012). The mathematical concept described in this article is suitable for the analysis of load-deflection curves of asymmetrical trusses with random imperfection.

* Ing. Martin Kalina: Institute of Structural Mechanics, Brno University of Technology, Veveří 331/95; 602 00, Brno; CZ, kalina.M1@fce.vutbr.cz

2. Geometry of the Model

Two slender struts connected by means of top joints form the model of von Mises truss, see Fig. 1. The geometry is characterized by the span L , angle α and Young's modulus of elasticity E . If the span L and angle α are known, it can be evaluated the height of the von Mises truss H , see (1):

$$H = \frac{1}{2} \cdot L \cdot \operatorname{tg} \alpha \quad (1)$$

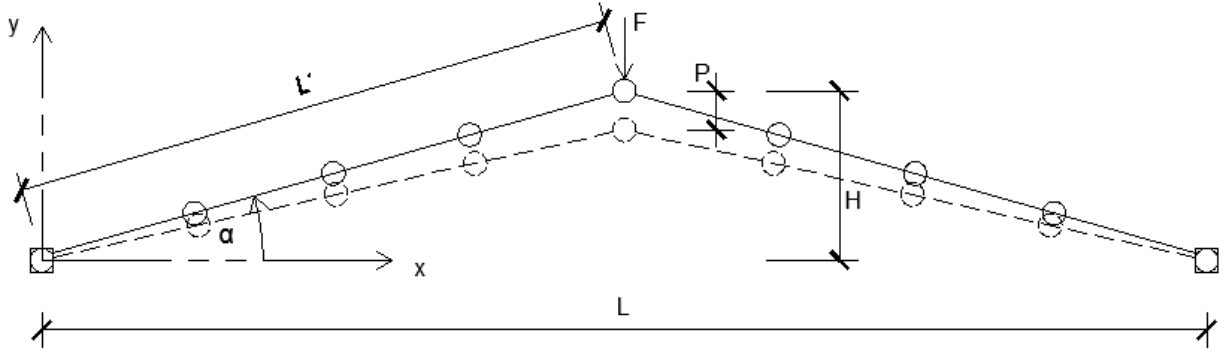


Fig. 1: Model of von Mises planar truss.

In the first step, the model is divided into a finite number of segments. The model is loaded with force F in the top joint, see Figure 1. Initial coordinates of individual mass points of the model are evaluated, see (2), (3).

$$x_i = L_i \cdot \cos \alpha \quad (2)$$

$$y_i = x_i \cdot \operatorname{tg} \alpha \quad (3)$$

where L_i is the segment length (distance between the initial node and the i^{th} node). It is obtained according to the following equation:

$$L_i = \frac{2 \cdot i \cdot L'}{m} \quad (4)$$

where i is the index of the node, L' is the length of one strut, m is the finite number of segments into which the structure was divided (m is an even number for symmetrical models). If coordinate y_i is evaluated for the top joint, then (3) is adjusted to the following equation stemming from (1) and (2):

$$y_i = H - (x_i \cdot \operatorname{tg} \alpha - H) \quad (5)$$

3. Solution by Potential Energy

The energy principle is applied to solve internal forces, taking into account geometrical non-linearity. The movement of individual points of the von Mises truss can be observed by means of the computer programme. At the beginning, coordinates of nodes are fixed as the initial state. Subsequently, a dislocation will be attributed to a chosen node, and potential energy of the system will be calculated for this state.

$$E_p = \frac{1}{2} \left(K_u \sum u_i^2 + K_\varphi \sum \varphi_i^2 \right) \quad (6)$$

where K_u is axial stiffness of the model, u_i is the matrix of the distance between actual and previous positions of the i -th node, K_φ is bending stiffness of the model, and φ_i is the rotation of individual parts

which can be calculated as the difference between two angles formed by two segments. Calculation of axial stiffness will be obtained according to the following relation.

$$K_u = \frac{E \cdot A}{L'} \quad (7)$$

where E is Young's modulus, A is cross-section area, and L' is hypotenuse length formed by bending units. The calculation of bending stiffness will be determined according to the following formula:

$$K_\phi = \frac{E \cdot I}{L'} \quad (8)$$

where E is Young's modulus, I is the second moment of the area, L' is the length of hypotenuse formed by bending units.

4. Newton Iteration Method

To search for the extreme values of the potential energy method, the Newton-Raphson iteration, for example, can be used as it was carried out in the journal; it is described in (Frantik, 2007). In the case of position change of initial coordinates, the equation will have the following forms:

$$J(x_i^n) \cdot v(x_i^n) = -f(x_i^n) \quad (9)$$

$$J(y_i^n) \cdot v(y_i^n) = -f(y_i^n) \quad (10)$$

where $J(x_i^n)$, $J(y_i^n)$ are matrices of partial derivations of vector functions f in points with coordinates x_i , y_i in steps n . The vector functions $f(x_i^n)$, $f(y_i^n)$ are numerical central derivations of the vectors of potential energies, see (11), (12):

$$f(x_i^n) = \frac{E_{p_x}^U - E_{p_x}^L}{2s} \quad (11)$$

$$f(y_i^n) = \frac{E_{p_y}^U - E_{p_y}^L}{2s} \quad (12)$$

where s is parameter of solutions (1×10^{-8}), and $E_{p_x}^U$, $E_{p_x}^L$, $E_{p_y}^U$, $E_{p_y}^L$ are potential energies with changes by parameter s . As the matrices $J(x_i^n)$, $J(y_i^n)$ are regular, the vector of unknown dislocations of coordinates will have just only one solution for the step $v(x_i^n)$, $v(y_i^n)$ searched for. This solution can be obtained from relations (9), (10), for example by means of the Gaussian elimination method, and subsequently, the positions of new nodes can be determined.

$$x_i^{n+1} = x_i^n + v(x_i^n) \quad (13)$$

$$y_i^{n+1} = y_i^n + v(y_i^n) \quad (14)$$

After having calculated (13), (14), the new coordinates will change by the parameter s , and the calculation of potential energy will be repeated. Checking the coordinates of individual points continues from the step 1 to n . In the course of calculation, the programme saves the values of coordinates of nodes.

5. Conclusions

The mathematical solution determined to create a computer programme based on finite numbers of segments is developed. The objective of the solution is an analysis of the load-deflection curve of top point. The solution is applicable to drawing the load-deflection curves of asymmetrical trusses with random imperfections. The axes of struts are, in general, curves which can be modelled by means of random quantities or random fields; it was applied (Kala, 2007). Geometrical and material characteristics,

as well, should correspond with the real data obtained from experimental measurements as accurately as possible, as described in (Melcher et al., 2004; Strauss et al., 2006; Kala et al., 2009). Applying the Newton method of tangents, the computer programme can check the coordinates of any node. It represents a possibility of more detailed analysis enabling to take into consideration all important imperfections. The statistical analysis can apply advanced methods of reliability analyses based on the methods of type Monte Carlo, see, e.g., (Kala, 2010a; Kala, 2010b).

Acknowledgement

The article was elaborated within the framework of project GAČR 14-17997S.

References

- Frantik, P. (2007) Simulation of the stability loss of the von Mises truss in an unsymmetrical stress state, *Journal Engineering Mechanics*, 14, pp. 155-162.
- Gottvald, J. (2010) The calculation and measurement of the natural frequencies of the bucket wheel excavator SchRs 1320/4x30. *Transport*, 25, 3, pp. 269-277.
- Gottvald, J. & Kala, Z. (2012) Sensitivity analysis of tangential digging forces of the bucket wheel excavator SchRs 1320 for different terraces. *Journal of Civil Engineering and Management*, 18, 5, pp. 609-620.
- Kala, Z. (2007) Stability problems of steel structures in the presence of stochastic and fuzzy uncertainty. *Thin-Walled Structures*, 45, 10-11, pp. 861-865.
- Kala, Z., Melcher, J. & Puklický, L. (2009) Material and geometrical characteristics of structural steels based on statistical analysis of metallurgical products. *Journal of Civil Engineering and Management*, 15, 3, pp. 299-307.
- Kala, Z. (2010a) Sensitivity analysis in advanced building industry. *Procedia-Social and Behavioral Sciences*, 2, 6, pp. 7682-7683.
- Kala, Z. & Kala, J. (2010) Resistance of plate girders under combined bending and shear, in: *Proc. Int. Conf. on Engineering Mechanics, Structures, Engineering Geology*, In: *Proc. International Conference on Geography and Geology*, pp. 166-171.
- Kala, Z. (2010b) Reliability of steel members designed in accordance with the code design concepts, In: *Proc. Int. Conf. on Numerical Analysis and Applied Mathematics (G.Psihoyios & C.Tsitouras eds)*, AIP Conference Proceedings, 1281, pp. 579-582.
- Kala, Z. (2008) Sensitivity analysis of carrying capacity of steel plane frames to imperfections, In: *Proc. Int. Conf. on Numerical Analysis and Applied Mathematics (T.E.Simos, G.Psihoyios, C.Tsitouras, eds)*, AIP Conference Proceedings, 1048, pp. 298-301.
- Kala, Z. (2012) Geometrically non-linear finite element reliability analysis of steel plane frames with initial imperfections. *Journal of Civil Engineering and Management*, 18, 1, pp. 81-90.
- Kala, J., Salajka, V. & Hradil, P. (2012) Investigation of eigenvalue problem of water tower construction interacting with fluid. *Journal of Vibroengineering*, 14, 3, pp. 1151-1159.
- Kala, Z. (2013) Elastic lateral-torsional buckling of simply supported hot-rolled steel I-beams with random imperfections. *Procedia Engineering*, 57, pp. 504-514.
- Karmazinová, M., Melcher, J. & Kala, Z. (2009) Design of expansion anchors to concrete based on results of experimental verification. *Advanced Steel Construction*, 5, 4, pp. 390-405.
- Kwasniewski, L. (2009) Complete equilibrium paths for von Mises trusses. *International Journal of Non-Linear Mechanics*, 44, 1, pp. 19-26.
- Melcher, J., Kala, Z., Holický, M., Fajkus, M. & Rozlívka, L. (2004) Design characteristics of structural steels based on statistical analysis of metallurgical products. *Journal of Constructional Steel Research*, 60, 3-5, pp. 795-808.
- von Mises, R. (1923) Über die Stabilitätsprobleme der Elastizitätstheorie, *ZAMM* 3, pp. 406-422.
- von Mises, R. & Ratzersdorfer, J. (1925) Die Knicksicherheit von Fachwerken, *ZAMM* 5, pp. 218-235.
- Strauss, A., Kala, Z., Bergmeister, K., Hoffmann, S. & Novák, D. (2006) Technologische Eigenschaften von Stählen im Europäischen Vergleich. *Stahlbau*, 75, Heft 1, pp. 55-60.

BIOLOGICAL SOFT TISSUES: MECHANICAL CHARACTERIZATION, DATA ANALYSIS, AND MODELS' EVALUATION

R. Kazakevičiūtė-Makovska*

Abstract: *Mechanical test procedures and a systematic data analysis of soft tissues are discussed with the view of providing experimental bases for the evaluation and validation of constitutive models for this class of biological materials. A new methodology and measures are presented for the quantitative and qualitative characterization of the mechanical response of soft tissues under monotonic (J-shape response) and quasi-static cyclic loading (stress softening effect) in different deformation modes. The general structure of constitutive theory and special models are shortly discussed within the same conceptual framework.*

Keywords: Soft tissues, Multiple-axial tests, Elasticity, Stress softening, Viscoelasticity.

1. Introduction

Soft tissues such as arteries muscle, skin, lung, mesentery, etc. exhibit qualitatively similar mechanical properties (Fung, 1993). They are inelastic (no single-valued relationship between stresses and strains exists), their stress-strain history relationships are nonlinear, they show hysteresis when subjected to cyclic loading-unloading, they exhibit stress relaxation and creep when held at constant strain and stress, respectively. Soft tissues are anisotropic and inhomogeneous, their properties vary with the sites, aging, etc. When all these factors are coupled, the problem of how to experimentally characterize and theoretically describe the mechanical properties of soft tissues becomes quite acute. Two main issues, which must be addressed in this respect, are: 1) advanced and efficient experimental methods to guarantee a high quality of comprehensive data for soft tissues; 2) reliable constitutive models with physically identified material parameters that represent mechanisms occurring in these biological materials.

There is a wide range of testing techniques available to characterize the mechanical behavior of soft tissues. These differing experimental methods and testing protocols have resulted in a large variance in the reported data making comparison of the mechanical behavior of soft tissues difficult and sometimes even impossible. In order to address these issues, this paper discusses in a unified way testing procedures under monotonic and quasi-static cyclic loading together with suitable methods of data analysis that provide a firm experimental basis for the evaluation of theoretical models for the biological soft tissues.

2. Test Procedures and Data Analysis

Mechanical properties of soft tissues can be experimentally studied by different test procedures, e.g. a) monotonic loading up to failure, b) cyclic pre-stressing to an assigned strain, c) cyclic pre-stressing to a fixed stress, and d) pre-stressing to successively higher strains or stresses. In addition, the viscoelastic behavior of these biological materials can be experimentally studied in the standard creep and relaxation tests as well as by the dynamical mechanical analysis. Moreover, all these tests may be performed in various deformation modes such as uniaxial tension (compression), equi-biaxial tension, pure or simple shear, planar tension, and multi-axial straining. A typical behavior of soft tissues observed under monotonic and cyclic loading is schematically shown in Fig. 1.

Under monotonic loading, most soft tissues exhibit characteristic J-shape stress-strain curves with three main phases. The best way to qualitatively describe this phenomenon is to measure the slope of the stress-strain curves and to plot this quantity as a function of strain or stress. This analysis of the monotonic

* Rasa Kazakeviciute-Makovska, PhD.: Institute of Mechanics, Mechanics-Continuum Mechanics, Ruhr-University Bochum, Universitätsstr. 150; 44780, Bochum; Germany, Rasa.Kazakeviciute-Makovska@rub.de

tension data lies at the basis of the famous Fung model for the elastic behavior of soft tissues (Fung, 1993).

Under cyclic loading, all biological soft tissues exhibit the so-called stress softening phenomenon, first observed in elastomers (natural and synthetic rubber) where it is referred to as the Mullins effect. The main problem in qualitative characterization of this phenomenon is the variety of ways of expressing the degree of stress softening.

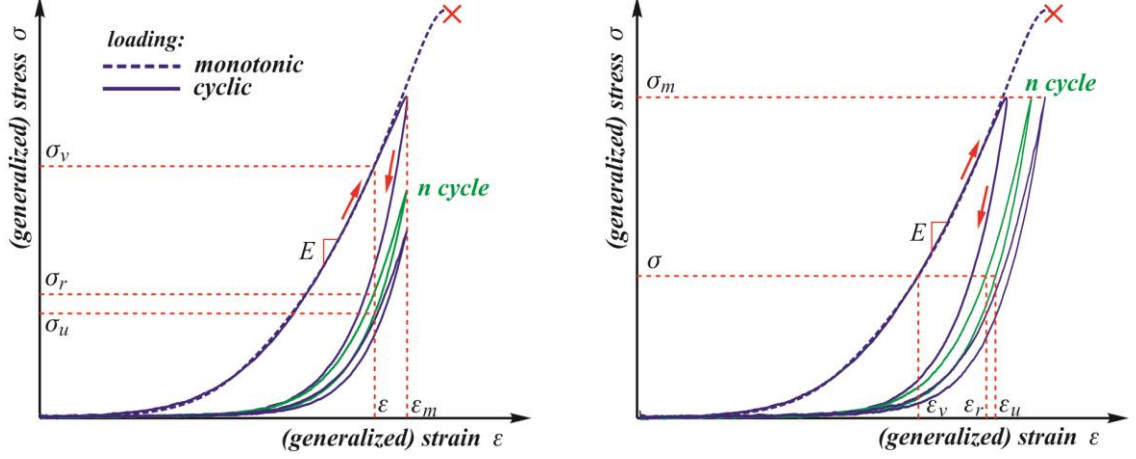


Fig. 1: Schematic response of soft tissues under monotonic and quasi-static cyclic loading to pre-scribed strain (left) and to pre-scribed stress (right).

In this study, the stress-strain response of soft tissues under monotonic and cyclic loading is characterized by the tangential modulus E defined as the slope of the stress-strain curve during loading, unloading, and reloading with E denoted by $E_v(\varepsilon)$, $E_u(\varepsilon; \varepsilon_m)$ and $E_r(\varepsilon; \varepsilon_m)$, respectively. The reduction of modulus caused by successive stretching serves as a measure of the amount of stress softening. In addition, this quantity during each deformation cycle for the specified value of pre-strain ε_m and pre-stress σ_m is described by the stress and strain retention $s(\varepsilon; \varepsilon_m)$ and $e(\sigma; \sigma_m)$, respectively, defined as (see Fig. 1)

$$s(\varepsilon; \varepsilon_m) = \frac{\sigma_s(\varepsilon; \varepsilon_m)}{\sigma_v(\varepsilon)}, \quad e(\sigma; \sigma_m) = \frac{\varepsilon_s(\sigma; \sigma_m)}{\varepsilon_v(\sigma)}. \quad (1)$$

Here σ_s is a common notation for σ_u and σ_r (ε_s for ε_u and ε_r , respectively). Plots of $s(\varepsilon; \varepsilon_m)$ and $e(\sigma; \sigma_m)$ as functions of the normalized strain $\varepsilon / \varepsilon_m$ and stress σ / σ_m for different values of ε_m and σ_m , respectively, provide qualitative and quantitative measures of the stress softening in the tested soft tissues. These plots should be compared with corresponding theoretical results predicted by various models proposed in the literature.

Most experimental studies of the stress softening in soft tissues are confined to uniaxial tension tests. However, this phenomenon is also evidenced in cyclic compression, equi-biaxial tension, and shear deformation modes. The methodology of characterizing the stress softening described above applies to all these deformation modes with the uniaxial stress and strain replaced by their generalized counterparts. For example, the axial strain may be replaced by the measure of the deformation extent discussed below.

3. Modeling and Models' Evaluation

Macroscopic behavior of soft tissues may effectively be modeled within the thermodynamic framework of continua with internal variables or micro-forces (Kazakevičiūtė-Makovska and Steeb, 2011). For first order (local) models with time effects neglected or at constant strain rates, the latter theory reduces to the former one and the general constitutive law for the stress takes the form

$$\mathbf{T} = \tilde{\mathbf{T}}(\mathbf{F}, \boldsymbol{\alpha}) + \mathbf{T}_R, \quad \tilde{\mathbf{T}}(\mathbf{F}, \boldsymbol{\alpha}) = J^{-1}(\partial \Phi(\mathbf{F}, \boldsymbol{\alpha}) / \partial \mathbf{F})(\mathbf{F}^{-1})^T, \quad J = \det \mathbf{F}. \quad (2)$$

Here $\Phi = \Phi(\mathbf{F}, \boldsymbol{\alpha})$ is the energy potential (free energy in isothermal processes or internal energy in adiabatic processes), which is a function of the deformation gradient \mathbf{F} and a set of internal variables $\boldsymbol{\alpha} = (\alpha_1, \dots, \alpha_n)$. Moreover, \mathbf{T} denotes the Cauchy (true) stress tensor and \mathbf{T}_R is a constitutively

indeterminate reactive stress due to possible material constraints (e.g. incompressibility of bulk material or fibre inextensibility). For unconstrained materials, $\mathbf{T}_R = \mathbf{0}$. The internal variables $\boldsymbol{\alpha} = (\alpha_1, \dots, \alpha_n)$ represent the state of deterioration (stress softening, permanent strain, etc.) of a material and their evolution during deformation process must be specified by additional constitutive laws. In general, the functional form of the constitutive relations (2) is delimited only by the frame-indifference principle and possible material symmetries. They can be rewritten in terms of the first (engineering) and second Piola-Kirchhoff stress tensors \mathbf{P} and \mathbf{S} using classical relations.

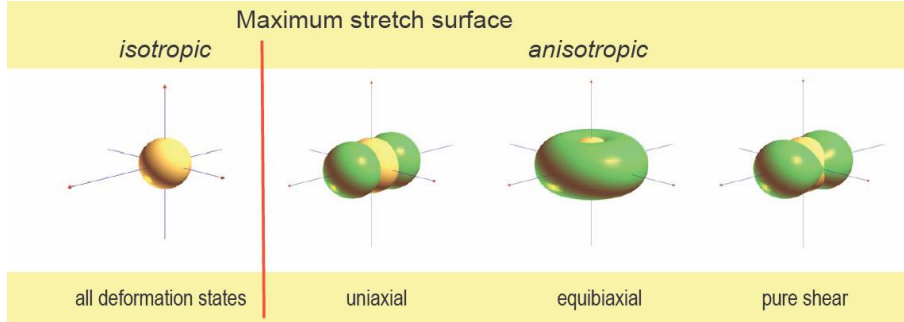


Fig. 2: Quantification of deformation extent under general loading conditions.

In formulating the evolution law for the softening and permanent set variables $\boldsymbol{\alpha} = (\alpha_1, \dots, \alpha_n)$, it is generally assumed that the response of soft tissues to cycling loading depends only on the maximum previous strain experienced during the deformation history (Horný et al., 2010; Peña et al., 2011). Accordingly, a suitable measure must be introduced to quantify the maximum strain experienced by the material during the entire deformation process for the three-dimensional state of strain. In general, such a measure is defined as $v = \hat{v}(\mathbf{F})$ subject to certain physically justified assumptions (Kazakevičiūtė-Makovska, 2007a). For both isotropic and anisotropic response of materials, the deformation extent may be defined as the maximum of stretches computed over all directions and the past history (this definition is graphically represented in Fig. 2). Most of models proposed in the literature for the stress softening of soft tissues use a single softening variable in which case the evolution law may be assumed in the following general form: $\alpha = \hat{\alpha}(v; v_m)$, $0 \leq v \leq v_m$. Here v is a measure of deformation extent at the current time instant t and v_m denotes the maximum value of v experienced by material during deformation process up to time t . The function $\hat{\alpha}(v; v_m)$ may be called the softening function because it determines the measure of softening in the tissue during the whole deformation process. It has been shown by Kazakevičiūtė-Makovska (2007, 2007a) that two broad classes of the evolution laws for the softening variable may be distinguished for elastomeric materials. It turns out that the same forms of the evolution law are used for soft tissues (e.g. Peña et al., 2011; Gultova et al., 2011; Maher et al., 2012):

$$\alpha = \begin{cases} \hat{\alpha}(v) \equiv \tilde{\alpha}(v; v) & \text{if } v = v_m \quad (\text{primary loading path}), \\ \alpha_m \equiv \hat{\alpha}(v_m) & \text{if } v < v_m \quad (\text{unloading / reloading paths}), \end{cases} \quad (3)$$

or (e.g. Weisbecker et al., 2012)

$$\alpha = \begin{cases} 0 & \text{if } v = v_m \quad (\text{primary loading path}), \\ \tilde{\alpha}(v; v) & \text{if } v < v_m \quad (\text{unloading / reloading paths}). \end{cases} \quad (4)$$

With evolution law assumed in either form (3) or (4), it remains to specify the dependence of the response function $\tilde{\mathbf{T}}(\mathbf{F}, \alpha)$, equivalently the energy function $\Phi = \Phi(\mathbf{F}, \alpha)$, on α but leaving the dependence on \mathbf{F} arbitrary. The general assumption is that for $\alpha = 0$ the relations (2) reduce to the constitutive equation of the nonlinear elasticity $\mathbf{T}_0 = \tilde{\mathbf{T}}_0(\mathbf{F}) + \mathbf{T}_R$ with the elastic response function $\tilde{\mathbf{T}}_0(\mathbf{F}) \equiv \tilde{\mathbf{T}}(\mathbf{F}, \mathbf{0})$ derived from the strain energy density $W(\mathbf{F})$. In the context of elastomers, that there are four basic classes of models that differ in the manner the response function $\tilde{\mathbf{T}}(\mathbf{F}, \alpha)$ depends on the internal (softening) variable α (Kazakevičiūtė-Makovska, 2007, 2007a). The same classification applies to models proposed in the literature for the soft tissues.

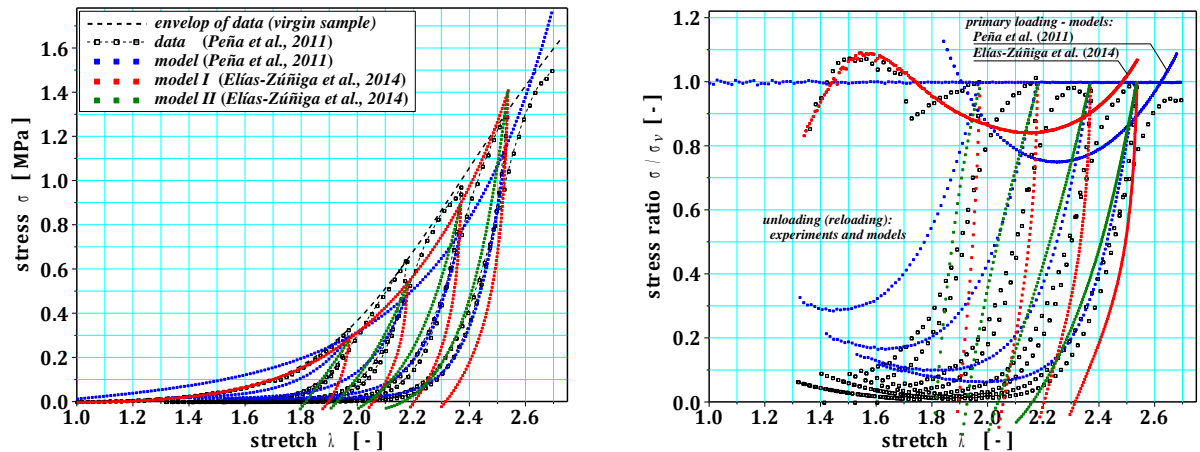


Fig. 3: Comparison of data with different models prediction: Conventional comparison of stress-strain curves (left); plots of stress ratio $(1)_I$ defined in this work (right).

4. Conclusions

Characterising and modelling the mechanical behaviour of soft tissues are an essential step in development of predictive computational models to assist research for a wide range of applications in medicine, biology, tissue engineering, pharmaceuticals, consumer goods or cosmetics. Therefore, it is critical that constitutive models capture the main characteristic properties of this class of biological materials so that the proposed models are adapted for their intended applications. Results of this work provide reliable methods for the quantitative and qualitative evaluation of the theoretical models aiming to describe the response of soft tissues under monotonic and cyclic loading in different deformation modes. The proposed methodology is far more reliable than the usual comparison of theoretical and measured stress-strain curves. This is illustrated in Fig. 3 for the measured data and theoretical model prediction presented in Peña et al. (2011) and two models proposed by Eliás-Zúñiga et al. (2014).

References

- Eliás-Zúñiga, A., Baylón, K., Ferrer, I., Serenó, L., García-Romeu, M., Bagudanch, I., Grabalosa, J., Pérez-Recio, T., Martínez-Romero, O., Ortega-Lara, W. & Elizalde, L. (2014) On the rule of mixtures for predicting stress-softening and residual strain effects in biological tissues and biocompatible materials. *Materials*, 7, pp. 441-456.
- Fung, Y.C. (1993) *Biomechanics: Mechanical Properties of Living Tissues* (Second Edition). Springer, New York.
- Gultova, E., Horny, L., Chlup, H. & Zitny, R. (2011) A comparison between the exponential and limiting fiber extensibility pseudo-elastic model for the Mullins effect in arterial tissue. *Journal of Theoretical and Applied Mechanics*, 49, pp. 1203-1216.
- Horný, L., Gultová, E., Chlup, H., Sedláček, R., Kronek, J., Veselý, J. & Žitný, R. (2010) Mullins effect in human aorta described with limiting extensibility evolution, In: *Proc. XII Mediterranean Conference on Medical and Biological Engineering and Computing*, 29, pp. 768-771.
- Kazakevičiūtė-Makovska, R. & Steeb, H. (2011) Micromechanical bases of superelastic behavior of certain biopolymers. In: *Mechanics of Generalized Continua* (H. Altenbach, G. Maugin, V. Erofeev, eds), Series: *Advanced Structured Materials*, Vol. 7, Part 3, pp. 175-192, Springer-Verlag, Berlin, Heidelberg.
- Kazakevičiūtė-Makovska, R. (2007) Experimentally determined properties of softening functions in pseudo-elastic models of the Mullins effect. *International Journal of Solids and Structures*, 44, pp. 4145-4157.
- Kazakevičiūtė-Makovska, R. (2007a) Stress-softening in elastomers: Physical mechanisms and phenomenological modeling, In: *Constitutive Equations in Mechanics of Continua*, Technical University of Gdansk, pp. 35-45.
- Maher, E., Creane, A., Lally, C. & Kelly, D.J. (2012) An anisotropic inelastic constitutive model to describe stress softening and permanent deformation in arterial tissue. *Journal of the Mechanical Behavior of Biomedical Materials*, 12, pp. 9-19.
- Peña, E., Martins, P., Mascarenhas, T., Natal Jorge, R.M., Ferreira, A., Doblaré, M. & Calvo, B. (2011) Mechanical characterization of the softening behavior of human vaginal tissue. *Journal of the Mechanical Behavior of Biomedical Materials*, 4, pp. 275-283.
- Weisbecker, H., Pierce, D.M., Regitnig, P. & Holzapfel, G.A. (2012) Layer-specific damage experiments and modeling of human thoracic and abdominal aortas with non-atherosclerotic intimal thickening. *Journal of the Mechanical Behavior of Biomedical Materials*, 12, pp. 93-106.

CFD ANALYSIS OF FLOWS IN A HIGH-PRESSURE NATURAL GAS PIPELINES WITH DIFFERENT SHAPES OF ORIFICE PLATES

R. Kiš^{*}, M. Malcho^{**}, M. Janovcová^{***}

Abstract: *This work aims to present the numerical analysis of the natural gas which flows through the high-pressure pipelines and the orifice plate by using CFD methods. The paper contains CFD calculations of the flowing natural gas in the pipe with different geometry of used orifice plates. One of them has a standard geometry and a shape without any deformation and the others are deformed by the action of the pressure differential. It shows behaviour of the natural gas in the pipeline by the pressure fields of the gas in all models and their differences. This research is based on the fact, that small deformation of the orifice plate can cause differences in the measured pressure differentials from what is mass flow calculated.*

Keywords: Orifice plate, High-pressure pipeline, Natural gas, CFD analysis, Pressure fields.

1. Introduction

Worldwide raising requirements for the heat and the energy have huge influence on decreasing amounts of the mineral resources and on increasing tendency of their prices. It is necessary to deal with them responsibly. One of these cases is using natural gas as an energy and heat source. Nowadays there are billions of normalized cubic meters of natural gas transferred and used every day all around the world. The most common flow measurement type, used in high-pressure pipelines, is measuring by pressure differential, which mainly uses orifice plates inserted in the pipelines. This paper tries to focus on behaviour of the natural gas flowing in the high pressure pipeline with installed orifice plate used as a flow meter. This type of measuring is still most common for the flow measurements in the transit gas lines in Slovakia and the other European countries (Malcho, 2006).

This paper shows differences in pressure differentials, pressure fields and velocity streams between undeformed and deformed orifice plates. For those analyses were prepared 3 models. The undeformed model is not loaded by the action of any tensions. The geometry of the deformed models is affected by the action of pressure differential, which causes shift and deformation of the orifice plate. In this comparison analysis was chosen pressure differential of 30 kPa and 50 kPa and a thickness of the plate was 10 millimeters. Maximum shifts caused by the deformation were 0.75 mm for 30 kPa and 1.23 mm for 50 kPa (Fig. 1) (Kiš, 2013).



Fig. 1: Cut through undeformed and deformed model of the orifice plate ($\Delta p = 50 \text{ kPa}$, $t = 10 \text{ mm}$).

* Ing. Roman Kiš: Department of Power Engineering, University of Zilina, Univerzitna 1; 010 01, Zilina; Slovakia, roman.kis@fstroj.uniza.sk

** Prof. RNDr. Milan Malcho, PhD.: Department of Power Engineering, University of Zilina, Univerzitna 1; 010 01, Zilina; Slovakia, milan.malcho@fstroj.uniza.sk

*** Ing. Martina Janovcová: Department of Power Engineering, University of Zilina, Univerzitna 1; 010 01, Zilina; Slovakia, martina.janovcova@fstroj.uniza.sk

2. Model Preparation

The model analysis is calculated in ANSYS Workbench. All models consist of three parts, two straight pipes and the orifice plate in the middle of them. In one model is the orifice plate modelled as undeformed one and in the other is the orifice plate deformed by the action of the pressure differential. In the analysis there is used only the inverted solid volume, what is the fluid flowing through the pipes and the orifice plate. In this case the natural gas is the fluid medium. The model is axisymmetric to reduce a number of the cells and to simplify the calculation. Because of the axial symmetry the geometry contains only one half of the section. The height of the pipe is 365 millimetres, the inlet length is 2000 millimetres and the outlet length is 10000 millimetres long (Fig. 2). Thickness of the orifice plate is 10 millimetres.

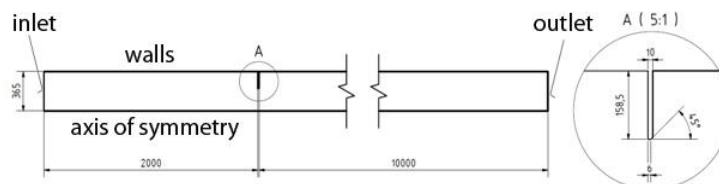


Fig. 2: Geometry of the model.

3. Mesh

The mesh of all three models consists of 527740 quadrilateral cells and it has 530078 nodes. The surface of the model is split into the ten blocks. Two blocks are for the orifice plate's part and four blocks are for each pipe (Fig. 3a). This splitting is necessary to make the mesh thicker in the areas around the orifice plate (areas no.: 1, 2, 3, 4, 7, 8) and the pipe walls (areas no.: 4, 5, 8, 9). In the areas 6 and 10 it is not important to have too many cells and that is the reason why the mesh is thinner there. Lower spacing near the walls and around the orifice plate is significant to obtain the behaviour of the natural gas flow more realistic. In the Fig. 3b there is a detail of the mesh around the orifice plate (Kiš, 2012).

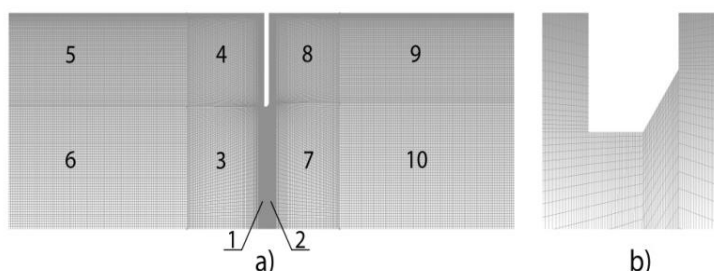


Fig. 3: a) Mesh with the geometry splitting; b) Mesh detail around the orifice plate edge.

4. Boundary Conditions and Model Solver

Behaviour of the model was set for the high-pressure pipe with the flowing methane as the fluid part. All boundary conditions are the same in both analyses. The value of the mass flow was $80 \text{ kg}\cdot\text{s}^{-1}$. Boundary condition for the inlet was set to the mass flow and for the outlet was set to the pressure outlet. All boundary conditions in the inlet to the pipe are in the Tab. 1.

Tab. 1: Boundary conditions in the inlet to the pipe.

Pressure	Temperature	Density	Mass flow rate
p [Pa]	T [K]	ρ [$\text{kg}\cdot\text{m}^{-3}$]	m [$\text{kg}\cdot\text{s}^{-1}$]
$5\cdot 10^6$	288.0	34.1	90.0

Because of the low Mach numbers, the compressible fluid was changed into the incompressible and the density-based model solver into the pressure-based. Due to the high Reynolds numbers and the necessity of the modelling flow near the wall was chosen standard k- ϵ model (Lenhard, 2010).

5. Pressure Analysis

The measuring of the pressure differentials at the orifice plate is fundamental for the measurement of the mass flow rate. In the Fig. 4 is shown the layout of the pressure fields in the section around the orifice plate for models with undeformed and deformed orifice plate.

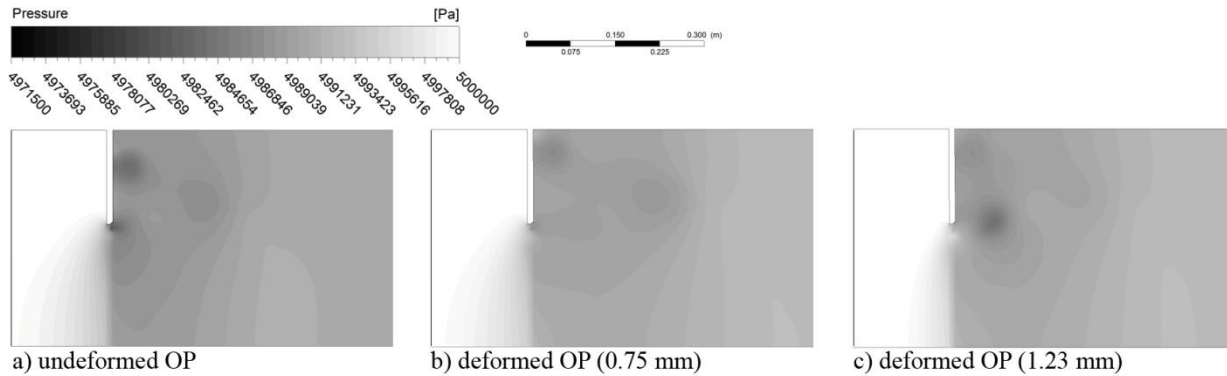


Fig. 4: Pressure fields in the section around the orifice plate: a) undeformed; b+c) deformed.

From the Fig. 4 is visible, that the pressure fields in front of the orifice plate start dropping closer to the plate and the pressure field behind the orifice plate are changed by the deformation of the orifice plate too. The area of the pressure fields with lower pressures became larger, what causes different pressures measured in the downstream. Finally it changes pressure differential from which is the volumetric flow calculated. The place where to measure pressures correctly in the system with the orifice plate is given in the standard ISO 5167-2:2003.

The standard ISO 5167-2:2003 mentions rules how to correctly measure with the orifice plates. For orifice plates with D and D/2 tapings, the spacing l_1 of the upstream pressure tapping is nominally equal to D. The spacing l_2 of the downstream pressure tapping is nominally equal to 0.5D (Fig. 5.), where D is diameter of the pipe connected to the orifice plate. The other possibility is to measure with flange tapings, where pressure values are taken from the distances 25.4 ± 1 mm in both sides from the surface of the orifice plate.

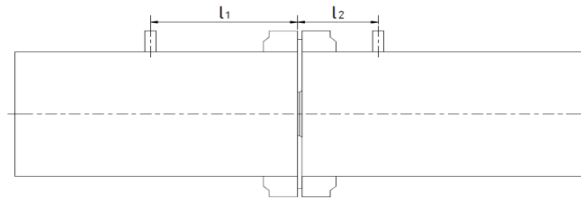


Fig. 5: Spacing of the pressure tapings for the orifice plates with D and D/2 tapings.

Dependence of the pressure on the distance measured near the wall is shown for all three models below in the Fig. 6.

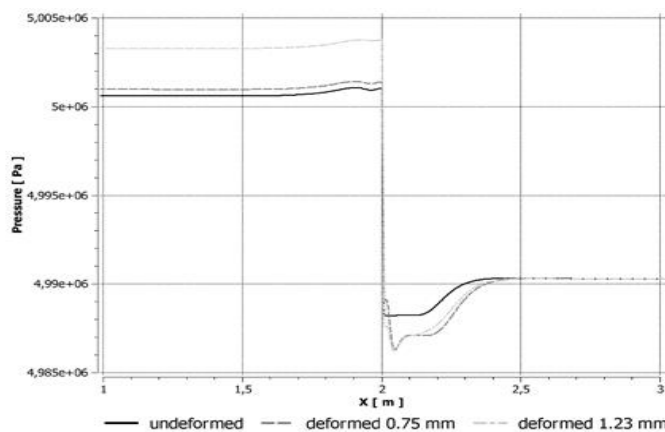


Fig. 6: Dependence of the pressure on the distance from the inlet to the pipe (area near the orifice plate).

It can be seen, that the deformation of the geometry causes the difference in the pressure differentials. With the increasing deformation the value of pressure differential increased too. There are two different values of the pressure differential for each kind of deformation. One value is valid for D and D/2 tapings and the other is for flange tapings. In the Fig. 7 there is a graphical dependence of the deformation on the pressure differential for all three models.

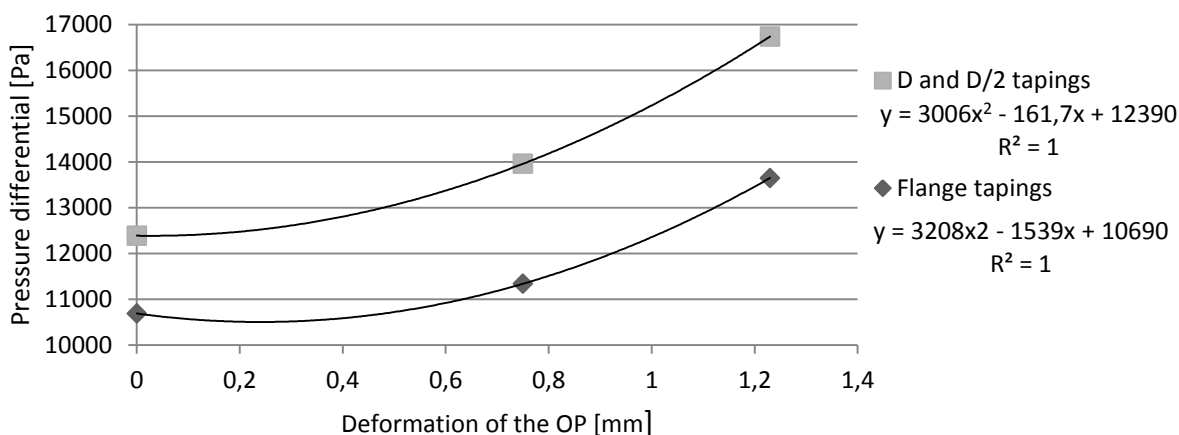


Fig. 7: Graphical dependence of "the deformation of the orifice plate on the pressure differential".

If trend lines are inserted through values in the graph, it will be received two different polynomials of the second grade with reliability equation $R^2 = 1$. Numerical dependence for D and D/2 tapings is valid in (1), for flange tapings is valid in (2):

$$y = 3006x^2 - 161.7x + 12390 \quad (1)$$

$$y = 3208x^2 - 1539x + 10690 \quad (2)$$

6. Conclusion

The analysis shows, that the deformation has a great impact on the stream field in the high-pressure pipeline. The shape deformation causes different behaviour of the natural gas stream. It causes different values of pressure differentials however boundary conditions of all three models are identical. The final accuracy of the measurement could be affected if the deformation is not included in the calculation of the final volumetric flow. Next research will show behaviour of the natural gas in the 3-dimensional space. The results of axisymmetric and 3-dimensional analyses will be compared, if the dimensional difference has impact to the natural gas flow.

Acknowledgment

This paper was prepared within the project APVV-0577-10 Cooling of power systems by cooling cycles without mechanical drive.

References

- Kiš, R., Janovcová, M., Malcom, M. (2013) The impact of the orifice plate thickness on the deformation of the orifice plate, TRANSCOM 2013, pp. 173-176.
- Malcho, M., Jandačka, J., Papučík, Š. (2006) Analyse influence on measuring of volume flow of natural gas in membrane gas-meters, Acta Metallurgica Slovaca, pp. 233-238.
- Lenhard, R. (2010) Numerical simulation device for the transport of geothermal heat with forced circulation of media, Power control and optimization: proceeding of fourth global conference, pp. 4.
- ISO 5167-2:2003, "Measurement of fluid flow by means of pressure differential devices inserted in circular cross-section conduits running full – Part 2: Orifice plates." International organization of Standardization, Slovakia.
- Kiš, R., Janovcová, M., Malcho, M. (2012) Pressure deformation of the orifice plate for measuring flow. The application of experimental and numerical methods in fluid mechanics and energy, pp. 136-140.

LASER TRACKER MEASUREMENT FOR PREDICTION OF WORKPIECE GEOMETRIC ACCURACY

J. Knobloch^{*}, M. Holub^{**}, M. Kolouch^{***}

Abstract: *The primary objective of this paper is to present a new method for measuring of geometric errors in the machine tool workspace in order to predict the accuracy of investigated workpiece. A general methodology for a three axis machine tool is described to map the volumetric errors and based on this map to evaluate the dimensional and geometric workpiece parameters. A measurement strategy uses a portable coordinate measurement system Laser Tracker and is intended principally for middle-size and large milling machines. For purposes of testing the strategy was applied on a small machine tool first. The relative discrepancies between the tool and the workpiece were estimated from the separate table and spindle measurements in contrast to application in large machine tools and other strategies. Based on the results and according to the required accuracy parameters, this method is used for locating the optimal workpiece position in the machine volume.*

Keywords: Optical alignment, Laser Tracker, Machine accuracy, Error prediction.

1. Introduction

As a basis to improve machining accuracy of machine tools (MTs), it is important to develop a methodology to measure it in an efficient manner. There are many error sources presented in a MT that affect the accuracy of a workpiece depending on factors such as kinematics, cutting conditions, workpiece material and dimensions (Aguado et al., 2012). The knowledge of MT accuracy is for MT manufactures essential, although the importance of geometric error measurement is by many of them not fully understood yet. It is a feedback that could affect both design and assembly. However, typical MT users concern accuracy when the MT performs actual machining. This paper therefore considers the strategy for measuring geometric errors in order to predict investigated workpiece accuracy. This strategy is the output of the project motivated by industrial demands solved in cooperation between the industrial partner TOSHULIN, a. s. and the Institute of Production Machines, Systems and Robotics (Brno University of Technology).

A laser tracker is a portable system that measures a position of a reflector in spherical coordinates. Among many benefits are easy setup and large range of possible applications. However, acquisition costs remain high and measuring accuracy that is affected by many error sources in spite of development in laser tracker technology (Aguado et al., 2013) and is lower than by standard measurement systems that are used for calibration of MTs nowadays. As a result, MT builders use laser tracker mainly for measuring, aligning and assembling of large parts (Holub et al., 2013). The application in measurement of volumetric accuracy, which is presented in this paper, is connected with many obstacles - expenses in raw costs and in lost production, for the time consuming procedure is mostly hard to find a space in demanding delivery terms and finally, the common measurement methods require a high degree of technical expertise. Finding a measurement strategy for geometric calibration of MTs, that is efficient, has low time requirements and is easy to apply, is the aim of this research project. Unlike other methods that

^{*} Ing. Josef Knobloch, M.Sc.: Institute of Production Machines, Systems and Robotics, Brno University of Technology, Technická 2896/2; 619 69, Brno; CZ, knobloch@fme.vutbr.cz

^{**} Ing. Dipl.-Ing. Michal Holub, PhD.: Institute of Production Machines, Systems and Robotics, Brno University of Technology, Technická 2896/2; 619 69, Brno; CZ, holub@fme.vutbr.cz

^{***} Dr.-Ing. Martin Kolouch, PhD.: Institute for Machines Tool and Production Processes, Chemnitz University of Technology, Reichenhainer Straße 70; D-09126, Chemnitz; Germany, martin.kolouch@mb.tu-chemnitz.de

concern calibration and compensation of MTs, this strategy presents different approach - direct evaluation of workpiece geometric parameters.

Eman (1987) stated that quasi-static errors constitute 60-70% of the final error and affect the MT repeatability. Based on this fact, the main object of this method is to find a relation between the results from static measurement and the final accuracy of an investigated workpiece. Undisputedly, other error sources presented in a MT depending on factors such as kinematics, stiffness, cutting conditions, workpiece material, etc. affect the accuracy of a workpiece too. However, these sources were in the first phase of the research neglected.

This paper presents the results from the first measurement. The positioning accuracies of the table and the spindle are measured separately. Another measurement of the clamping face is suggested as the workpiece is also affected by its flatness. After the data are collected, they are merged into a three-dimensional lattice where each point represents a tool position relative to the workpiece. These points are compared to their nominal positions and the discrepancies are considered as errors. Finally, based on the results of the first measurement, the paper suggests a new proposal for measurement strategy that eliminates the occurrence of systematic errors and enhances reachable accuracy of laser tracker measurement.

2. Method of Measurement

In principle, measurement conditions should be close to real working conditions. However, neither application of static and dynamic forces on the spindle or loading the table simulating the weight of a workpiece is applied because of the required space keeping left for the laser beam. Nevertheless, measuring of different load conditions is allowed fundamentally. Geometric errors as a result of the method are therefore valid under assumption of low static and dynamic forces during machining.

In order to map 3D errors in the working volume of the MT, both the table and the spindle are measured. This method presents an option to choose whether the whole or only a frequently used part of the machine space is measured and what accuracy is required. Both these factors significantly influence the overall time demands. The size of the machine volume does not allow placing the tracker directly on the table and it was attached next to the machine (Fig. 1). Because of the assumption that errors of the spindle (Z axis) and the table (X and Y axis) are independent, they could be obtained in separate measurements. First the reflector was attached to the table center point (1P). This position represented the most frequent placement of the workpiece on the table. The machine table was measured in two ways – at first, the measured points were approached in direction of X axis and then similarly in direction of Y axis. After both cycles were repeated three times, the reflector was moved and clamped in the spindle with an offset that corresponded to the tool center point of a preferred milling tool (2P). The data of Z axis were captured three times as well. The influence of different tool lengths was ignored since the determination of the spindle angular errors from one-point measurement is not possible.

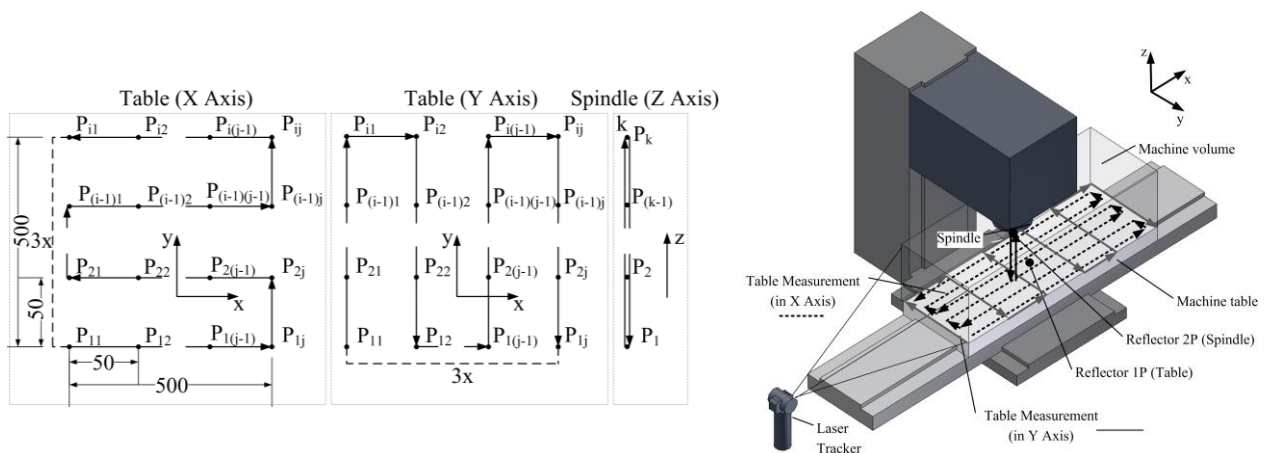


Fig. 1: Setup on the three axis MT.

All three-axis of the tested machine are equipped with high-precision ball screws and the movements are performed on linear guide ways with rolling elements. The measurement of positions is realized by means

of direct linear measuring units with activated thermal compensation. The measurement was performed with a laser tracker, which accuracy is specified according the standards with MPE value as $\pm 15 \mu\text{m} + 6 \mu\text{m/m}$. The achievable accuracy is, to the author's knowledge, improved when the rotational movements of the tracker measuring head are decreased to a minimum; thus to place the laser tracker in the direction of the longest axis is suggested, the X axis in the case of tested machine.

Since the flatness of the clamping face is also considered, the measured points are captured manually in positions constantly spread across the table face (Tab. 1). Before the machine volume is measured, the size of step is chosen with respect to the investigated workpiece. The fact of the constantly spread points makes more difficult to determine regular occurring systematic errors such as those caused by lead of the ball-screw. Nevertheless, the constant step is required for data processing and the occurrence of systematic errors is therefore neglected. Though, the reflector is attached in the table center point, an error in any other workpiece location on the table can be recalculated from the results of flatness measurement of the clamping face.

Tab. 1: Measurement setup summary.

	$X[\text{mm}]$	$Y[\text{mm}]$	$Z[\text{mm}]$	Step [mm]	No. of Rep.	Total No. of Points
Table (in X Axis)	500	500	0	50	3	3x132
Table (in Y Axis)	500	500	0	50	3	3x132
Spindle	0	0	600	50	3	3x12
Flatness	500	500	-	-	1	16

3. Results of the Original Measurement

The data are captured according to the method described in section 2. For further processing, mean values of each measured point are considered. Solely the result of the table measurement will be discussed as it showed up to be the critical part of the measuring strategy. Fig. 2 and Fig. 3 show the captured points of both sets of the table measurement; each set was interpolated with a quadratic polynomial surface to improve the clarity. Comparing the data of both sets in Fig. 2 and Fig. 3 together regular discrepancy in the measured motions occurs, although the sets should correspond to each other. The direction of the surface peaks corresponds to the direction that the measured points were approached. This occurrence of systematic error is explained by the hysteresis of drive mechanism in the laser tracker.

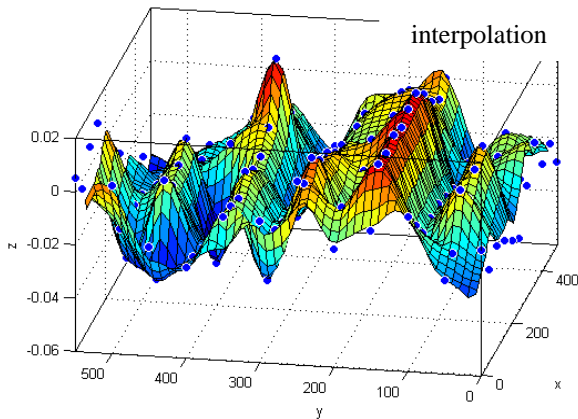


Fig. 2: Interpolated results of table measurement (in X axis direction).

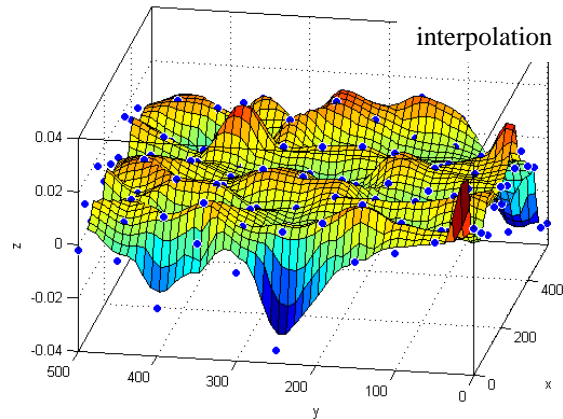


Fig. 3: Interpolated results of table measurement (in Y axis direction).

The matrix of ideal points P_{Id} was subtracted from the points obtained during the axis measurements according to Eqs. (1)–(2). The results were two three-dimensional lattices of errors $\Delta P_{dev,1}$ and $\Delta P_{dev,2}$ that describe the discrepancies in the machine volume.

$$\Delta P_{dev,1} = (P_{Table,X} - P_{Spindle}) - P_{Id} \quad (1)$$

$$\Delta P_{dev,2} = (P_{Table,Y} - P_{Spindle}) - P_{Id} \quad (2)$$

A distribution of errors in $\Delta P_{dev,1}$ and $\Delta P_{dev,2}$ differs significantly in both sets of data (Fig. 4 and Fig. 5).

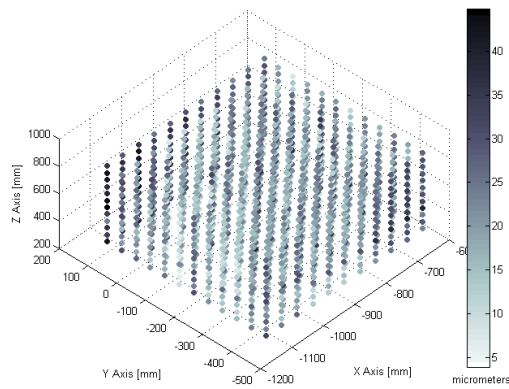


Fig. 4: 3D error lattice ($\Delta P_{dev,1}$).

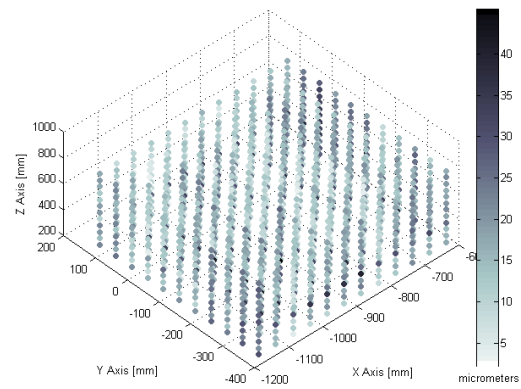


Fig. 5: 3D error lattice ($\Delta P_{dev,2}$).

4. Proposal of the New Method of Axis Measurement and Conclusion

Based on the results of the original measurement, a new proposal of a measuring strategy is developed that has its basis in the standard ISO 230-2. It was determined during the first measurement that it is necessary to approach the points from counter directions to minimize the impact of hysteresis. Furthermore, the number of the measurement repetitions must be increased to improve the resulting accuracy. Based on these facts, the new method suggests the measurement strategy as shown in Fig. 6, where P_{ij} and P_k refer to measured positions, r to reversal path, k to number of measuring repetitions and s to the size of a step.

A simplified method of machine measurement for workpiece accuracy prediction was developed and tested.

Based on results the new proposal is suggested that is tailored to the laser tracker specific demands with the aim of increasing achievable measurement accuracy. This new method of measurement will be applied in further work on the project with the main objective of locating the most suitable workpiece position in a machine volume and is intended primarily for the middle-size and large MTs as the small MTs operate generally with high accuracy that is beyond the common laser tracker measuring capacity.

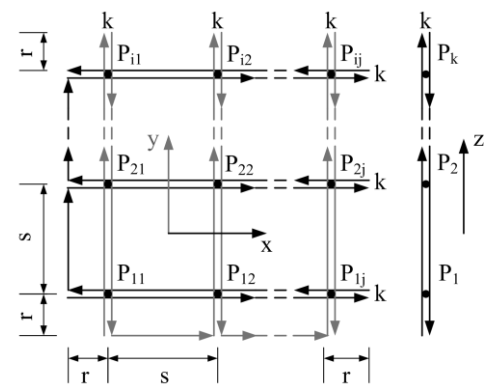


Fig. 6: New measurement strategy.

Acknowledgement

This work has been supported by Brno University of Technology, FME, Czech Republic (Grant No. FSI-S-11-5) and by European Regional Development Fund in the framework of the research project NETME Centre under the Operational Programme Research and Development for Innovation. Reg. Nr. CZ.1.05/2.1.00/01.0002. The results of this project NETME CENTRE PLUS (LO1202) were co-funded by the Ministry of Education, Youth and Sports within the support programme „National Sustainability Programme I. The machine and the measurement device for the measurement were supported by the industry partner TOSHULIN, a.s.

References

- Aguado, S., Santolaria, J., Samper, D. and Aguilar, J. J. (2013) Influence of Measurement Noise and Laser Arrangement on Measurement Uncertainty of Laser Tracker Multilateration in Machine Tool Volumetric Verification. *Precision Engineering* 37 (4): 929-943.
- Aguado, S., Samper, D., Santolaria, J. and Aguilar, J. J. (2012) Identification Strategy of Error Parameter in Volumetric Error Compensation of Machine Tool Based on Laser Tracker Measurements. *International Journal of Machine Tools and Manufacture* 53 (1): 160-169. doi:10.1016/j.ijmactools.2011.11.004.
- Eman, K. F., Wu, B. T. and DeVries, M. F. (1987) A Generalized Geometric Error Model for Multi-Axis Machines. *CIRP Annals - Manufacturing Technology* 36 (1): 253-256. doi:http://dx.doi.org/10.1016/S0007-8506(07)62598-0.
- Holub, M., Michalicek, M., Vetiska, J. and Marek, J. (2013) Mechatronics 2013 Recent Technological and Scientific Advances. In *Prediction of Machining Accuracy for Vertical Lathes*, edited by Tomas Brezina and Ryszard Jablonsky, 41-48. Springer.

IMPLEMENTATION OF STABILIZED FORMULATION FOR LEVEL SET EQUATION

F. Kolařík^{*}, B. Patzák^{**}

Abstract: *This paper presents an implementation and verification of stabilized mass-conserving level set formulation. This formulation is suitable for further use in combination with XFEM for two phase flow simulations. The whole numerical scheme is based on finite element method and can be easily augmented into existing code for level set equation as a post-processing. Capability of the method is tested on a simple one dimensional numerical example.*

Keywords: Free-surface flow, Level set, Mass conservation, Fluids, Finite elements.

1. Introduction

This paper deals with implementation and verification of conservative level set method as an interface capturing technique for two-fluid flow problem. From a wider perspective, our interest lies in numerical simulations of fresh concrete casting, in particular with applications to Self-Compacting Concrete (SCC). Simulation of fresh concrete casting is naturally a free surface flow. We consider concrete as a single homogeneous fluid. Therefore, as it is standard in CFD, its motion is described within the Eulerian framework, in which free surface flow is modeled as a flow of two immiscible fluids in a fixed domain. One of the fluids represents the concrete, which is modeled as a non-Newtonian fluid using two-parametric Bingham model. The second fluid represents the air, which is modeled as a standard Newtonian fluid. In the context of Eulerian framework, description of the interface between the two fluids plays a key role in the whole problem and a proper interface-capturing method has to be chosen to deal with the interface. The problem can be solved using many well known techniques, for example level set method, volume of fluid method (VOF) and recently their combination, known as conservative level set and VOF method (CLSVOF). All of the aforementioned approaches have their own advantages and drawbacks. VOF based methods have superior conservation properties, while the interface reconstruction requires an additional effort (for example PLIC or least-squares techniques, see (Kees et al., 2011) for further reference). On the other hand, level set based methods can easily represent even very complicated interfaces, but suffer from being non-conservative, and an additional effort has to be made in order to enforce the conservation properties. However, for further use together with eXtended Finite Element Method (XFEM), the level set method is a natural choice. In the level set method, interface is represented implicitly as a zero level set of a suitable higher dimensional scalar function. In connection to XFEM, it is useful to choose that scalar function as a signed distance function, measuring the distance from the interface. Level set function with this property can be beneficially used in XFEM as a core of enriching approximation functions.

There are two main problems connected to level set method. One is that the level set function ϕ loses its signed distance property with evolution of the time. This represents a problem especially in combination with XFEM, where the signed distance property plays an important role. To reconstruct this property, proper reinitialization technique has to be employed. In this work, eikonal equation for the level set function is solved in order to recover the signed distance property. The second problem is that numerical schemes for evolution of the level set function generally do not conserve the mass. There are a few methods how to preserve the mass conservation, see Olsson & Kreiss (2005) for further reference. In this

* Ing. Filip Kolařík: Faculty of Civil Engineering, CTU in Prague; Thákurova 7; 166 29, Prague; CZ, filip.kolarik@fsv.cvut.cz

** Prof. Dr. Ing. Bořek Patzák: Faculty of Civil Engineering, CTU in Prague; Thákurova 7; 166 29, Prague; CZ, borek.patzak@fsv.cvut.cz

work, we employ an approach proposed in paper by see (Kees et al., 2011), where the evolution equation for the level set function is coupled with volume fraction equation through a correction to the level set function in order to preserve the mass conservation. This technique is described in the latter section.

2. Description of the Interface

In this section, description of the interface and its motion using level set method is given. In the level set method, the interface is described geometrically as a zero level set of an appropriate, higher dimensional scalar function ϕ (called level set function). Its motion due to the given velocity field is governed by following equation

$$\frac{\partial \phi}{\partial t} + \mathbf{v} \cdot \nabla \phi = 0 \quad (1)$$

In general, ϕ can be chosen as an arbitrary differentiable function. However, especially in combination with XFEM, it is common to choose the level set function as a sign distance function, measuring the distance from the interface. In other words, ϕ has to satisfy following condition

$$\phi(\mathbf{x}) = \pm \min_{\mathbf{x}^* \in \Sigma} \|\mathbf{x} - \mathbf{x}^*\| \quad (2)$$

where Σ denotes the interface between both fluids. Numerical solution of equation (1) causes that level set function ϕ to gradually lose the signed distance property. This is a problem for future combination with XFEM, where the signed distance property plays an important role. The usual and widely applied way how to reinitialize the signed distance property is to solve iteratively the following equation

$$\frac{\partial \phi}{\partial \tau} = S(\phi_0)(1 - |\nabla \phi|) \quad (3)$$

until it reaches the steady state. In the equation (3), $S(\phi_0)$ is regularized signum function, ϕ_0 represents level set function computed by (1) and is used as initial condition to (3). Parameter τ is a pseudo time.

The main problem of the numerical solution of (1) is that it is in general non-conservative and therefore it can produce unacceptable mass conservation errors. To solve this problem, we employ an approach proposed in a paper by (Kees et al., 2011). The level set equation is coupled with mass conservation equation through a correction ϕ' to the level set function ϕ . This approach is suitable for our purposes, since all the solutions are based on Galerkin formulation and could be easily solved by FEM. Therefore, the presented approach can be easily integrated into existing code for solving flow problems in OOFEM, see Patzák & Bittnar (2011). OOFEM is free finite element code with object oriented architecture for solving mechanical, transport and fluid mechanics problems, which is developed at Department of Mechanics, Faculty of Civil Engineering, CTU in Prague.

The mass conservation equation, which was mentioned above, can be expressed in terms of the Heaviside function $H(\phi)$. The total mass of fluid (denoted as f) can be computed as

$$M(t) = \int_{\Omega_f} \rho_f dx = \int_{\Omega} \rho_f H(\phi) dx \quad (4)$$

With this notion, the conservation of mass can be then expressed using the following continuity equation

$$\frac{\partial(\rho_f H(\phi))}{\partial t} + \nabla \cdot (\rho_f H(\phi) \mathbf{v}) = 0 \quad (5)$$

In (4), $H(\phi)$ does not conserve the mass, since ϕ does not. If we denote the mass conserving approximation of volume fraction as \hat{H} , then we want to compute a correction ϕ' to the level set function ϕ such that

$$\int_{\Omega} [H(\phi + \phi') - \hat{H}] dx = 0 \quad (6)$$

To do so, authors (Kees et al., 2011) proposed to couple level set equation (1) and volume fraction equation (5) through the ϕ' into the following problem

$$\kappa \Delta \phi' = H(\phi + \phi') - \hat{H} \quad (7a)$$

$$\nabla \phi' \cdot \mathbf{n} = 0 \quad (7b)$$

The correction ϕ' is therefore computed as a post-processing step after the level set equation (1) is solved and it is added to ϕ in order to obtain corrected, mass conserving level set function.

3. Numerical Solution

In this section, numerical solution of the problem will be briefly described. In the latter, we assume that the velocity field, which arises in all presented equations, is given. Of course, in real simulations, the velocity field is obtained as a result of solving the Navier-Stokes equations. However, as it is not in the center of our attention, we will skip its precise description. Here, for the sake of brevity, the numerical procedure will be presented only in a schematical way. Few notes about the full discretization will be provided.

Given solution values at time t_n , we integrate the equations (1), (3), (5), (7) to time t_{n+1} gradually as follows. Assume that the velocity field \mathbf{v}^{n+1} was already computed, we use it to advance the level set equation and volume fraction equation:

$$\frac{\phi_0^{n+1} - \phi^n}{\Delta t} + \mathbf{v}^{n+1} \cdot \nabla \phi_0^{n+1} = 0 \quad (8)$$

$$\frac{\hat{H}_0^{n+1} - \hat{H}^n}{\Delta t} + \nabla \cdot (\hat{H}_0^{n+1} \mathbf{v}^{n+1}) = 0 \quad (9)$$

where ϕ_0^{n+1} and \hat{H}_0^{n+1} is the solution of the level set and volume fraction equation, respectively. Note that the computed level set function ϕ_0^{n+1} has lost the signed distance property and it does not conserve the mass in the sense that $H(\phi_0^{n+1}) \neq \hat{H}_0^{n+1}$. Next, the signed distance property of ϕ_0^{n+1} is recovered by solving the eikonal equation:

$$\|\phi_d^{n+1}\| = 1 \quad (10a)$$

$$\phi_d^{n+1} = 0 \text{ on } \Sigma_0 = \{\mathbf{x} \in \Omega; \phi_0^{n+1}(\mathbf{x}) = 0\} \quad (10b)$$

The final step consists of solving nonlinear equation for mass-conservation correction ϕ' to ϕ_d^{n+1} as follows

$$H_\varepsilon(\phi_d^{n+1} + \phi') - \hat{H}_0^{n+1} = \kappa \Delta \phi' \quad (11a)$$

$$\nabla \phi' \cdot \mathbf{n} = 0 \text{ on } \partial \Omega \quad (11b)$$

Here, H_ε is regularized Heaviside function, ε is regularization parameter, which determines the width of smeared discontinuity and κ is another parameter, which penalizes deviation of ϕ' from global constant. After computation of ϕ' , the final value of level set and volume fraction functions is given as

$$\phi^{n+1} = \phi_d^{n+1} + \phi' \quad (12)$$

$$\hat{H}^{n+1} = H_\varepsilon(\phi_d^{n+1} + \phi') \quad (13)$$

Note that in equations (8)-(13), backward Euler method was used for the sake of simplicity. In our implementation, generalized mid-point rule is adopted. Spatial discretization of all presented equations is done in terms of finite element method. Note that because of the convective character of equations (8), (9) and (10) in the aforementioned form (3), additional stabilization technique has to be employed. In our case, SUPG and YZ β discontinuity capturing stabilizations were used. Precise description of spatial discretization will be skipped because of the abstract length limitation, interested reader can find the details in (Bazilevs et al., 2007).

4. Numerical Example

At this point, only simple 1D example, demonstrating capability of a prototype MATLAB implementation will be shown. More complex examples will be presented at the conference. To illustrate the problem, we consider a propagation of a square wave on a periodic domain for a volume fraction equation. This corresponds to propagation of a kink function on the same domain for the level set function, see Fig. 1. The problem can be described as follows

$$\Omega = [0,4] \quad (14a)$$

$$\hat{H}(x, 0) = \hat{H}(\phi) \quad (14b)$$

$$\hat{H}(0, t) = \hat{H}(4, t) \quad (14c)$$

$$\phi(x, 0) = \frac{1}{2} - |x - 2| \quad (14d)$$

$$\phi(0, t) = \phi(4, t) \quad (14e)$$

The Fig. 1, illustrates the deformation of the level set profile for different numerical schemes for advecting the level set function. It can be seen, that stabilized Galerkin formulation provides totally incorrect solution. If the redistancing equation (10) is employed, the solution is much better, but from the Fig. 2 is clear, that for long time simulations, there is still a loss of mass. On the other hand, with the help of conservation correction equation (11), the total mass oscillates around the exact solution with error less than 0.1%.

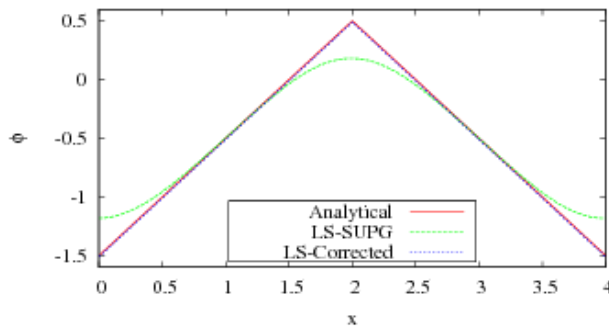


Fig. 1: Level set profiles after $t = 10$ s.

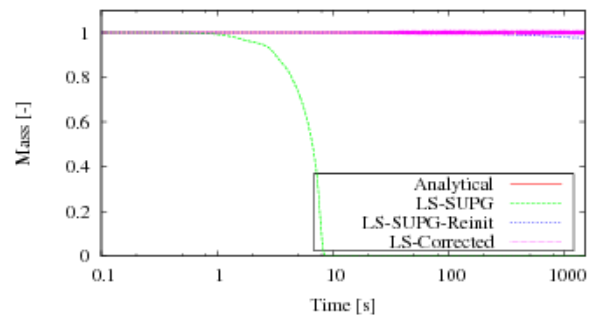


Fig. 2: Illustration of mass loss.

5. Conclusions

A prototype implementation and verification of stabilized mass-conserving level set formulation is presented. A simple numerical example is used for demonstration of the method's capability. It seems to be stable for long time simulations, which makes the method suitable for use in modeling of fresh concrete casting as a two fluid flow problem.

Future work lies in implementation of the method into OOFEM code.

Acknowledgement

The research was carried out within the project SGS14/029/OHK1/1T/11 – “Pokročilé algoritmy pro numerické modelování v mechanice konstrukcí a materiálů”.

References

- Bazilevs, Y., Calo, V. M., Tezduyar, T. E., Hughes, T. J. R. (2007) $YZ\beta$ discontinuity capturing for advection-dominated processes with application to arterial drug delivery. *Int. J. Numer. Meth. Fluids*, 54, pp. 593-608.
- Kees, C. E., Akkerman, I., Farthing, M. V., Bazilevs, Y. (2011) A conservative level set method suitable for variable-order approximations and unstructured meshes. *Journal of Computational Physics* 230, pp. 4536-4558.
- Olsson, E., Kreiss, G. (2005) A conservative level set method for two phase flow. *Journal of Computational Physics*, 210, pp. 225-246.
- Patzak, B., Bittnar, Z (2001) Design of object oriented finite element code. *Advances in Engineering Software*, 32, pp. 759-767.

INTERACTION BETWEEN BENDING MOMENT AND SHEAR FORCE IN ALUMINIUM PLATED STRUCTURAL ELEMENTS

Y. Koleková*, I. Baláž**

Abstract: Resistance of aluminium plated structural elements under interaction between bending moment and shear force according to EN 1999-1-1 compared with various interaction formulae. Critical analysis of the current interaction formulae given in Eurocode EN 1999-1-1 and proposals for their improvement, which may be used in the new Eurocode generation available in the year 2019.

Keywords: Resistance, Local buckling, Interaction, Bending moment, Shear force, Aluminium structure.

1. Introduction

Design requirements of stiffened and un-stiffened aluminium plates which are subject to in-plane forces are given in Eurocode EN 1999-1-1. Interaction between bending moment and shear force are treated in EN 1999-1-1 in the following clauses:

a) clause 6.2.8 related to resistance of cross-section. Where a shear force is present allowance should be made for its effect on the moment resistance. If the shear force V_{Ed} is less than half the shear resistance V_{Rd} its effect on the moment resistance may be neglected except where shear buckling reduces the section resistance, see 6.7.6. Otherwise the reduced moment resistance should be taken as the design resistance of the cross-section, calculated using a reduced strength.

$$f_{o,V} = f_o \left[1 - (2V_{Ed}/V_{Rd} - 1)^2 \right] \quad (1)$$

where for non-slender sections with $h_w/t_w < 39\sqrt{250\text{MPa}/f_o}$ the shear resistance is

$$V_{Rd} = A_v \frac{f_o}{\sqrt{3}\gamma_{M1}} \quad (2)$$

The shear area A_v may be taken as:

$$A_v = \sum_{i=1}^n \left[(h_w - \sum d)(t_w)_i - (1 - \rho_{o,haz})b_{haz}(t_w)_i \right] \quad (3)$$

b_{haz} - total depth of HAZ (Heat Affected Zone) material occurring between the clear depth of the web between flanges. For sections without welds, $\rho_{o,haz} = 1$. If the HAZ extends the entire depth of the web panel $b_{haz} = h_w - \sum d$.

d - diameter of holes along the shear plane

n - number of webs.

* Assoc. Prof. Ing. Yvona Koleková, PhD.: Department of Structural Mechanics, Faculty of Civil Engineering, Slovak University of Technology, Radlinského 11; 813 68, Bratislava; Slovakia, yvona.kolekova@stuba.sk

** Prof. Ing. Ivan Baláž, PhD.: Department of Metal and Timber Structures, Faculty of Civil Engineering, Slovak University of Technology, Radlinského 11; 813 68, Bratislava; Slovakia, ivan.balaz@stuba.sk

In the case of an equal-flanged I-section classified as class 1 or 2 in bending, the resulting value of the reduced moment resistance $M_{v,Rd}$ is:

$$M_{v,Rd} = t_f b_f (h - t_f) \frac{f_o}{\gamma_{M1}} + \frac{t_w h_w^2}{4} \frac{f_{o,V}}{\gamma_{M1}} \quad (4)$$

where h is the total depth of the section and h_w is the web depth between inside flanges.

In the case of an equal-flanged I-section classified as class 3 in bending, the resulting value of $M_{v,Rd}$ is given by expression (4) but with the denominator 4 in the second term replaced by 6.

For slender webs and stiffened webs, for sections classified as class 4 in bending or affected by HAZ softening, see 6.7.6.

b) clause 6.2.10 related to interaction between bending moment, shear and axial force. Influence of axial force is not taken into account in this paper.

Where shear and axial force are present, allowance should be made for the effect of both shear force and axial force on the resistance of the moment. Provided that the design value of the shear force V_{Ed} does not exceed 50% of the shear resistance V_{Rd} no reduction of the resistances defined for bending and axial force in 6.2.9 need be made, except where shear buckling reduces the section resistance, see 6.7.6. Where V_{Ed} exceeds 50% of V_{Rd} the design resistance of the cross-section to combinations of moment and axial force should be reduced using a reduced yield strength

$$(1 - \rho) f_o \quad (5)$$

for the shear area A_v , where reduction factor $\rho = \left(\frac{2V_{Ed}}{V_{Rd}} - 1 \right)^2$ (6)

NOTE: Instead of applying reduced yield strength, the calculation may also be performed applying an effective plate thickness.

c) clause 6.5.6 (defined in Amendment A1 to EN 1999-1-1) related to resistance of un-stiffened plates under combined in-plane loading.

If the combined action includes the effect of a coincident shear force, V_{Ed} , then V_{Ed} may be ignored if it does not exceed $0.5 V_{Rd}$ (see 6.5.8). If $V_{Ed} > 0.5 V_{Rd}$ the following condition should be satisfied:

$$\frac{N_{Ed}}{N_{c,Rd}} + \frac{M_{Ed}}{M_{c,Rd}} + \left(\frac{2V_{Ed}}{V_{Rd}} - 1 \right)^2 \leq 1.00 \quad (7)$$

d) clause 6.7.6 related to plate girders. Interaction between bending moment, shear force and axial force. Influence of axial force is not taken into account in this paper.

Provided that the flanges can resist the whole of the design value of the bending moment and axial force in the member, the design shear resistance of the web need not be reduced to allow for the moment and axial force in the member, except as given in 6.7.4.2(10).

If $M_{Ed} > M_{f,Rd}$ the following two expressions should be satisfied:

$$\frac{M_{Ed} + M_{f,Rd}}{2M_{pl,Rd}} + \frac{V_{Ed}}{V_{w,Rd}} \left(1 - \frac{M_{f,Rd}}{M_{pl,Rd}} \right) \leq 1.00 \quad (8)$$

$$M_{Ed} \leq M_{c,Rd} \quad (9)$$

where: $M_{c,Rd}$ - design bending moment resistance according to 6.7.2 (4).

$M_{f,Rd}$ - design bending moment resistance of the flanges only, see 6.7.5(9).

$M_{pl,Rd}$ - plastic design bending moment resistance.

2. Parametrical Study and Comparison of Various Procedures

The complete results of the parametrical study may be found in the full text paper on CD. The graphical interpretations of EN 1999-1-1 interaction formulae are shown in Fig. 1. Relative resistances valid for the I-section calculated in the following numerical example are indicated in the diagram by symbols and numerical values.

Formula (7) for $N_{Ed} = 0$, and formula (8) may be rewritten in the following forms

$$\frac{V_{Ed}}{V_{bw,Rd}} = \frac{1}{2} \left[\sqrt{1 - \frac{M_{Ed}}{M_{c,Rd}}} + 1 \right], \quad \frac{V_{Ed}}{V_{bw,Rd}} = \frac{1}{2} \left[\frac{1 - \frac{M_{Ed}}{M_{pl,Rd}}}{1 - \frac{M_{f,Rd}}{M_{pl,Rd}}} + 1 \right] \quad (10a, b)$$

3. Numerical example

Graph in the Fig. 1 is valid for:

material: aluminium alloy EN AW-7020 T651, buckling class A:

$$E = 70 \text{ GPa}, \quad \nu = 0.3, \quad f_o = 280 \text{ MPa}, \quad f_u = 350 \text{ MPa}, \quad \gamma_{M1} = 1.1,$$

extruded I-section (class 4):

$$h = 650 \text{ mm}, \quad \text{flange (class 1): } b = 120 \text{ mm}, \quad t_f = 25 \text{ mm}, \quad \text{web (class 4): } h_w = 600 \text{ mm}, \quad t_w = 10 \text{ mm},$$

radius of fillet: $r = 5 \text{ mm}$.

Such high profile would be welded. For the sake of simplification we suppose that aluminium I-section is extruded profile. Influence of welds is not investigated in this paper. This enable us to compare pocedures used in Eurocode EN 1993-1-5 for steel and in EN 1999-1-1 for aluminium structures.

Ratio of bending moment resistances of the flanges and the gross I-section $M_{f,Rd} / M_{pl,Rd} = 0.676$.

For simply supported girder loaded in the midspan by the transverse force F_{Ed} , with a transverse stiffener under F_{Ed} , we obtain for girder geometry $L = 5h_w$ the following values of the resistances F_{Rd} :

a) according to EN 1993-1-5, formula (7.1), formula (7) in (Baláž & Koleková, 2014): $F_{Rd,EN} = 1058 \text{ kN}$,

$$M_{Ed,EN} / M_{pl,Rd} = 0.899, \quad V_{Ed,EN} / V_{bw,Rd,EN} = 0.779,$$

$$M_{eff,Rd,EN} / M_{pl,Rd} = 0.783,$$

b) according to EN 1999-1-1, formula (6.147), here the formula (10b): $F_{Rd,EN} = 997.5 \text{ kN}$,

$$M_{Ed,EN} / M_{pl,Rd} = 0.847, \quad V_{Ed,EN} / V_{bw,Rd,EN} = 0.735,$$

$$M_{eff,Rd,EN} / M_{pl,Rd} = 0.783,$$

c) according to EN 1999-1-1, formula (6.90b), here the formula (10a): $F_{Rd,EN} = 858 \text{ kN}$,

$$M_{Ed,EN} / M_{pl,Rd} = 0.729, \quad V_{Ed,EN} / V_{bw,Rd,EN} = 0.632,$$

d) according to EN 1999-1-1, from the formula (9): $F_{Rd,EN} = 2 M_{eff,Rd,EN} / (0.5L - 0.5d) = 922.3 \text{ kN}$.

e) according to EN 1999-1-1, from the formula: $F_{Rd,EN} = 2 V_{bw,Rd,EN} = 1357 \text{ kN}$.

Comparison of the final resistances F_{Rd} calculated according to:

EN 1993-1-5, formula (7.1): $\min(1058 \text{ kN}; 922.3 \text{ kN}; 1357 \text{ kN}) = 922.3 \text{ kN}$,

EN 1999-1-1, formula (6.147): $\min(997.5 \text{ kN}; 922.3 \text{ kN}; 1357 \text{ kN}) = 922.3 \text{ kN}$,

EN 1999-1-1, formula (6.147): $\min(858 \text{ kN}; 922.3 \text{ kN}; 1357 \text{ kN}) = 858 \text{ kN}$.

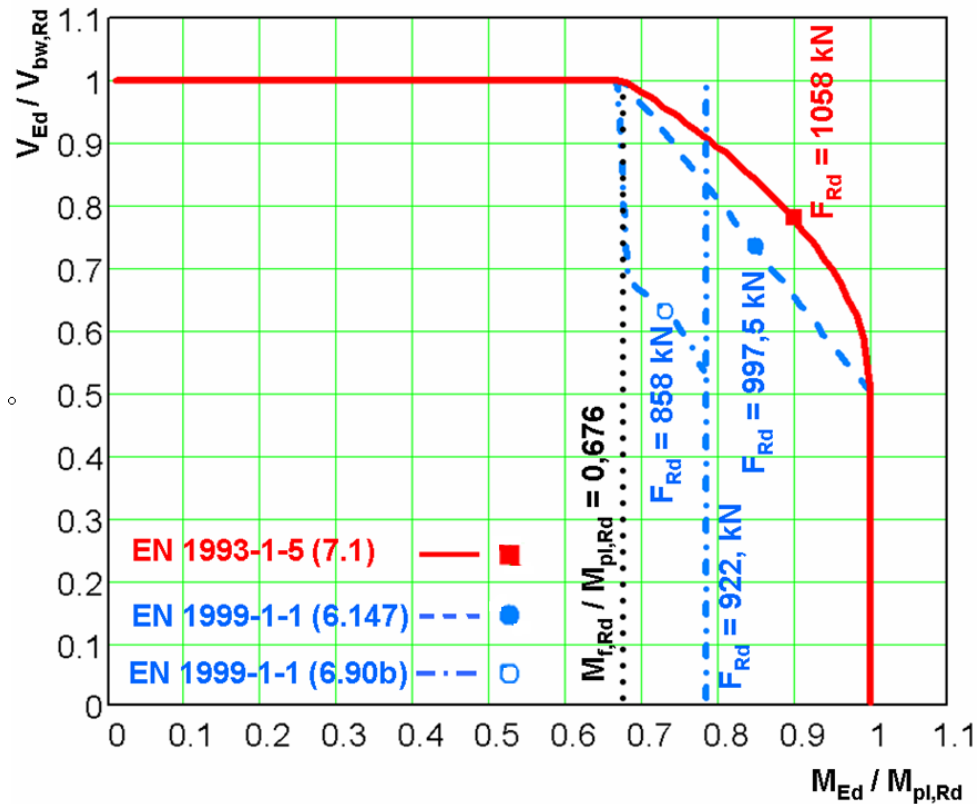


Fig. 1: Resistances calculated according to EN 1999-1-1 for aluminium I-profile web under combination of bending moment M_{Ed} and shear force V_{Ed} . Values of resistances F_{Rd} for extruded I-profile (125 mm x 25 mm + 600 mm x 10 mm + 125 mm x 25 mm, EN AW-7020 T651) are indicated by coordinates of symbols ○, ● and ■. Influence of M_{Ed} and V_{Ed} is characterised by the relationships $M_{Ed} = F_{Ed} L / 4$, $V_{Ed} = F_{Ed} / 2$, $L = 5 h_w$, $M_{Ed} / V_{Ed} = 2,5h_w = 3.75$ m.

4. Conclusion

An empirical model based on observations from tests was first developed by Basler. His formula was later modified by Höglund and others. The Eurocode formulae are based on these results.

Comparison of the resistances in Fig. 1 calculated according to EN 1993-1-5, formula (7.1), EN 1999-1-1, formula (6.147) and EN 1999-1-1, formula (6.90b) shows that:

- formula (6.90b) should be deleted from EN 1999-1-1. Use of the formula in its partial form (for $N_{Ed} = 0$ kN) leads to unrealistic small cross-section resistances. Use of the formula in its full form (for $N_{Ed} \neq 0$ kN) leads to incorrect results.
- formula (6.147) from EN 1999-1-1 gives more conservative results than formula (7.1) from EN 1993-1-5. The formulae of these two Eurocodes should be harmonised.

Acknowledgement

Project No. 1/0748/13 was supported by the Slovak Grant Agency VEGA.

References

- Baláž, I., Koleková, Y. (2014) Interaction between bending moment and shear force in steel plated structural elements. In: Proc. 20th International conference Engineering Mechanics 2014, (V. Fuis ed.), Svratka, Czech Republic, pp. 60-63.
- EN 1993-1-5 (2006) and Corrigendum AC (2009) Eurocode 3 - Design of steel structures. Part 1-5: Plated structural elements.
- EN 1999-1-1 (2007) and Amendment A1 (2009) and Amendment A2 (2013) Eurocode 9 - Design of aluminium structures. Part 1-1: General structural rules.

THE INFLUENCE OF FROST RESISTANCE ON UHPC PLATES WITH DIFFERENT TYPES OF TEXTILES ARMATURES

M. Kostecká^{*}, J. Kolísko^{**}, T. Bittner^{**}, P. Huňka^{**}, T. Mandlík^{**}

Abstract: High strength concrete and ultrahigh performance concrete (UHPC) develops quickly and applications appear in many countries. The UHPC are high performance concretes with exceedingly high strengths and durability. These materials include Portland cement, silica fume, quartz flour, fine silica sand, high-range water-reducer, water and either steel or organic fibres. Depending on the type of fibres used can influence the compressive strength. The article describes the tests of frost resistance on UHPC plates with different types of textiles armatures, such as referential matrix without armature, 3D glass fabric, PVA fibres and glass fibre mesh fabric. The aim of the testing is describe influence of textiles armatures in UHPC matrix in extreme conditions. These conditions are typical by practical use of UHPC for architectural building panels.

Keywords: UHPC concrete, Textiles armatures, Frost resistance, Bending strength, Plates.

1. Introduction

UHPC (Ultra High Performance Concretes) are ultra high-grade concretes with fine-grained macrostructure and high consistency. This implies its high resistance to the penetration of liquids and high durability. Due to its high compression strength greater than 150 MPa and improved durability, these represent significant advances in concrete technology. This highly advanced and sophisticated material offers a number of interesting applications such as the production of facade panels, which promotes more abroad. In this article the frost test is presented on thin UHPC slabs that are reinforced by a new type of armature. It is a textile armature, which should replace the classic metal (steel) armature. Textile armature should not only reduce the cost of production, but, because it is not susceptible to corrosion as conventional steel armature, panels can be designed with significantly less cover thickness in achieving similar or longer lifetime of these elements. The combination of UHPC concrete with a minimum thickness of cover and textile armature allows to design elements weighing up to 70 % lower compared to conventional concrete elements with conventional armature. This can achieve significant savings and benefits not only in economic aspects, but also in environmental aspects (Novotná et al., 2013).

2. Test Specimens

The four concrete test plates with sizes 700 x 250 x 15 mm were produced for comparative experiments (see Fig. 1) on May 20, 2013. All four plates were made from the same type UHPC with similar recipe matrix. The difference was only in the type of textile armature.

The recipe matrix for 1 cubic meter did consist: cement CEM I 52.5 N – white (650 kg), calcite + TiO₂ (132 kg), sand +milled silica, max. fraction 1.6 mm (1264 kg), water (164 kg), superplasticizer (37.6 kg).

The first plate was without armature (marked M), the second one contain PVA fibres with length 20 mm (marked PVA). The third plate use alkali-resistant glass fibre mesh fabric with mesh dimension 5 mm (marked Perl). The last one contains the 3D glass alkali-resistant armature with mesh dimension 20 mm (marked 3D).

* Ing. Michaela Kostecká.: Klokner Institute, Czech Technical University in Prague, Šolínova 7, 166 08, Prague; CZ, michaela.kostecka@klok.cvut.cz

** Assoc. Prof. Ing. Jiří Kolísko, PhD., Ing. Tomáš Bittner, Ing. Petr Huňka, Ing. Tomáš Mandlík: Klokner Institute, Czech Technical University in Prague, Šolínova 7, 166 08, Prague; CZ, {name.surname}@klok.cvut.cz

Each plate was further cut into 6 smaller test plate specimens with dimensions: width 124 mm, length 232 mm and thickness 13 mm. A set of 6 test specimens was created from one plate with the specific type of armature. There were thus prepared 24 test specimens. Half of them were then subjected to cycles of freezing, half served as a reference.

Basic characteristics of the used materials are: for the matrix without armature and matrix reinforced by glass fibre mesh armature and 3D glass fabric armature tested on solids with dimensions 40 x 40 x 160 mm after 28 days of ageing, the compressive strength was 125 MPa, a bending strength was 19 MPa and a volume weight was 2410 kg/m³. For the matrix with PVA fibres the solid of the same size and age the compressive strength was 112 MPa, bending strength was 25 MPa and a volume weight was 2400 kg/m³.

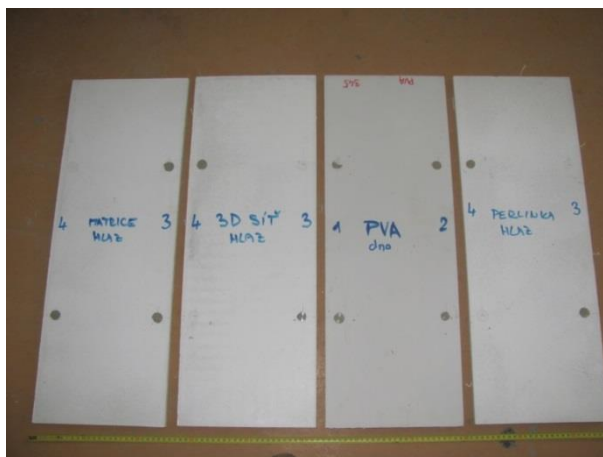


Fig. 1: UHPC plates with (from left) – referential matrix without armature, 3D glass fabric, PVA fibres, glass fibre mesh fabric.

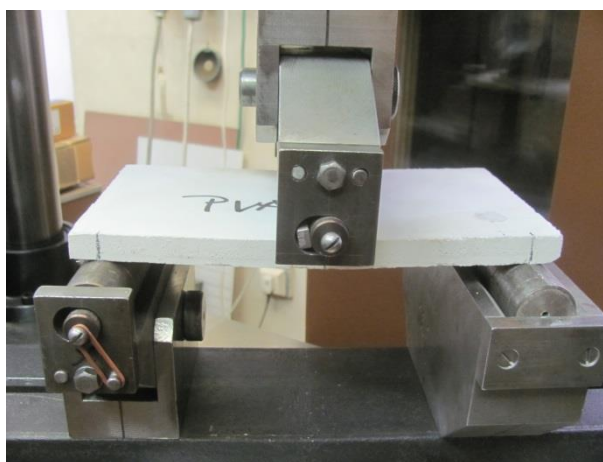


Fig. 2: Testing device for bending strength TIRATEST 2300 during test.

3. Procedure of Monitoring the Frost Resistance Test

The purpose of this test was to specify tensile strength when bending the testing samples by selected freezing cycles.

The bending strength was determined according standard ČSN EN 12467 in three-point bending strength.

The tests were performed on the test device TIRATEST 2300 (see Fig. 2). The support distance was 200 mm. The rate of loading of specimens was 1 mm/min, the rupture did occur in time between 10 and 30 seconds.

Results were determined by comparing the two sets of samples:

- 1. set – unexposed (reference) testing plates after storage in water at 20 ± 2 °C,
- 2. set – exposed testing plates after cycling – 2 hours freezing in -20 ± 4 °C and 2 hours defrosting in water 20 ± 4 °C.

The cycling was done automatically in a freezing chamber. After the required number of 150 cycles, the testing samples were conditioned in the water 20 ± 2 °C during 7 days. Subsequently, the bending test was carried out (ČSN EN 12467, 2005; ČSN EN 1170-5, 1999; Kostelecká et al., 2013).

4. Results of Comparative Experiment

A summary of the results of mechanical tests are shown in Tab. 1 and in Figs. 3 a 4.

Tab. 1: Coefficient of frost resistance and the average of bending strength determined at the reference set of specimens (1 set) and set of frozen samples after 150 cycles (2 set).

Specimens	Volume weight [kg/m ³]	MOR _f
		[MPa]
Specimens without armature - marked M – average from three tests		
specimens M – reference	2437	14.6
specimens M – after freezing	2459	12.8
Coefficient of frost resistance - specimens M – ratio of bend. strength		0.9
Specimens with PVA fibres armature – marked PVA – average from three tests		
specimens PVA – reference	2363	14.4
specimens PVA – after freezing	2464	13.9
Coefficient of frost resistance - specimens PVA – ratio of bend. str.		1.1
Specimens with glass fibre mesh fabric armature – marked Perl – average from three tests		
specimens Perl – reference	2472	12.7
specimens Perl – after freezing	2415	11.4
Coefficient of frost resistance - specimens Perl – ratio of bend. str.		0.9
Specimens with 3D glass fabric armature – marked 3D – average from three tests		
specimens 3D – reference	2392	19.0
specimens 3D – after freezing	2335	14.0
Coefficient of frost resistance - specimens 3D – ratio of bend. str.		0.7

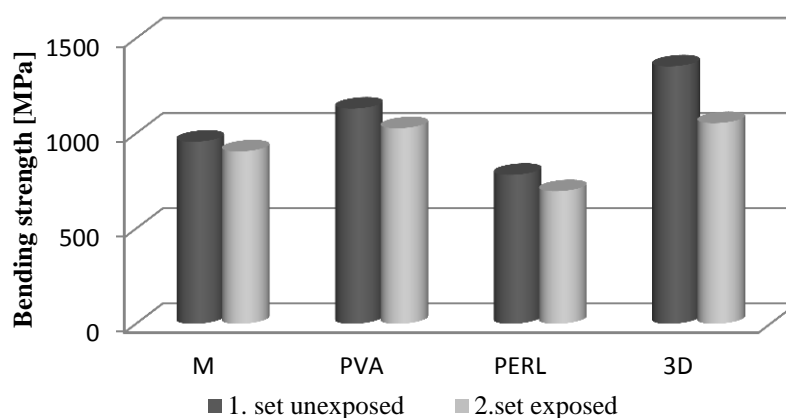


Fig. 3: The frost resistance test – comparison of average values of bending strength.

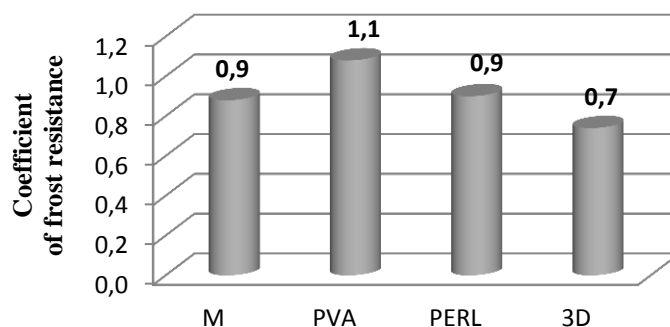


Fig. 4: Coefficient of frost resistance-the ratio of bending strength (of both set 1+2).

The results of tests of frost resistance of thin UHPC plates were presented in this article. The UHPC plates were reinforced with different types of textile armatures: PVA fibres, glass fibre mesh fabric and 3D glass fabric. Each type of test samples was divided into two sets. First set contained unexposed (reference) samples (7 days conditioning in water at 20 ± 4 ° C). The second set contained samples exposed (cycling two hours of freezing at -20 ± 4 ° C and 2 hours of putting into water at 20 ± 4 ° C in 150 cycles and after 7 days conditioning in water at 20 ± 4 ° C). Results were determined by comparison of the two sets of test specimens.

From the measured values we can see that the greatest strength values were obtained for samples with 3D glass fabric armature, then the samples reinforced with PVA fibres and the lowest values were obtained for samples with glass fibre mesh armature. The bending strength of samples with 3D glass fabric armature and PVA fibres armature were higher than the strength of the matrix without armature. For specimens with 3D glass fabric armature was bending strength higher by 37 %, and samples with PVA fibres armature by 15 %. Only samples reinforced with glass fiber mesh reached a lower bending strength values than the matrix without armature by 21 %.

When we compare exposed and unexposed sets, the exposed sets have lower strength values, but the differences are not so significant. The differences are 28% for 3D glass fabric armature, 10% for PVA fibres armature, 11% for glass fibre mesh armature and 5% for the matrix without armature. The value of 28 % for 3D specimens could be lower. The problem was with 3D specimen No. 1, which was mechanically damaged when cycling in the laboratory.

5. Conclusions

The presented results indicate that the greatest strength values were obtained for the test plates reinforced with 3D glass fabric armature. From this it follows that the best use of unconventional textile armature is a 3D glass fabric armature. The advantage of this armature is its alkali-resistance against aggressive environments. The disadvantage is that it is most expensive of all of the tested textile armatures.

Acknowledgement

The research has been supported by the Grant Agency of the Czech Republic No. 13-12676S.

References

- ČSN EN 1170-5(1999) Precast concrete product – Test method for glass-fibre reinforced cement – Part 5: Measuring bending strength, “Complete bending test” method.
- ČSN EN 12467 (2005) Fibre-cement flat sheets – Product specification and test methods.
- Kostecká, M., Kytýř, D., Doktor, T. (2013) Study of Degradation of Fibre – Cement Plates with Different Types of non-Metalic Fibres, in: 10th Youth Symposium on Experimental Solid Mechanics, Technische Universität Chemnitz, Chemnitz, pp. 61-62, ISBN 978-3-941003-34-7.
- Novotná, M., Kostecká, M., Hodková, J., Vokáč, M. (2013) Use of Textiles Reinforced Concrete – Especially for Façade Panels, In: CRRB-15th International Conference on Rehabilitation and Reconstruction of Building, Vědeckotechnická společnost pro sanace staveb a péči o památky, Prague, pp. 264, ISBN 978-80-02-02502-3.

CORROSION OF REINFORCEMENT VERSUS RELIABILITY OF RC GIRDERS

P. Koteš*, J. Vičan**

Abstract: Corrosion is the destructive attack on metal by chemical or electrochemical reaction with its environment. The quality and the durability of the concrete structures are affected a lot by the degradation processes. Reinforced concrete is considered as a versatile, economical and successful construction material. Usually it is durable and resistant material, performing well throughout its service life. The corrosion of reinforcing steel in concrete, due to invasive environment, is the phenomenon that highly affects the reliability and durability of reinforced concrete structures. The paper deals with reinforcement corrosion and its influence on reliability of the existing bridge concrete structures. In conclusion, changes of the failure probability and reliability index of the structure with time, influenced by reinforce corrosion, are shown.

Keywords: Corrosion, Reinforcement, Concrete, Reliability, Existing structure.

1. Introduction

Deterioration by physical causes is not called corrosion, but is described as erosion, galling or wear. The term of corrosion is restricted to chemical attack on metals. There are three areas of concern when corrosion and its prevention are considered (Revie & Uhlig, 2008; Sastri et al., 2007). The three major factors are economics, safety and environmental damages. Metallic corrosion indeed affects many sectors of a nation's economy.

This paper deals with a problem of actual material degradation and its influence on reliability in time of existing bridge reinforced concrete structures. Two types of calculations are considered in this paper: during the passive stage and during the active stage of corrosion.

2. Corrosion of Reinforcement and Resistance - Theory

Analysis of corrosion influence on reinforced concrete (RC) members' reliability subjected to bending was performed using the engineering probability method. In that method, the reliability margin $G(t)$ (Mrázik, 1987) is the basic parameter of structural reliability and it is described by formula

$$G(t) = R(t) - E(t) \quad (1)$$

where $R(t)$ is the generalized function of random variable structural resistance,
 $E(t)$ are random variable load effects of the same element.

From formula (1) follows, that the random variable resistance $R(t)$, the random variable load effect $E(t)$ and the reliability margin $G(t)$ are variables dependent on time t . The resistance $R(t)$ could change in time due to many factors. The different types of RC structure degradation are the best-known factors causing the resistance change with time. The most significant way of degradation of concrete structures is reinforcement corrosion as a consequence of diffusion of CO_2 to the concrete member called carbonatization or penetration of the chloride ions, Cl^- .

The process of CO_2 diffusion consists of two phases (Tuutti, 1982; Broomfield, 1997). The first phase is the passive stage, during the time period $(0, t_0)$, when CO_2 penetrates through the concrete cover. During

* Assoc. Prof. Peter Koteš, PhD.: Department of Structures and Bridges, University of Zilina, Univerzitna 8215/1; 010 26, Zilina; Slovakia, kotes@fstav.uniza.sk

** Prof. Josef Vičan, PhD.: Department of Structures and Bridges, University of Zilina, Univerzitna 8215/1; 010 26, Zilina; Slovakia, vican@fstav.uniza.sk

that time, the resistance of element is not changed since the material and geometric parameters do not change (slight increase and following decrease of concrete strength in compression is neglected). Length of the passive stage depends on the cover depth. The second phase – active stage during the time period (t_0, T) , from the instance when CO_2 has penetrated through the concrete cover and reached reinforced bars until the end of the member's life, $T_d = 100$ years. During that time, the corrosion of reinforced bars occurs. The RC element subjected to bending was considered in this parametric study. The resistance $R(t)$ of the bent concrete element is given by formula based on Eurocodes (STN EN 1992-1-1)

$$R(t) = M_{Rd,pl}(t) = A_s(t) \cdot f_y \cdot \left[\left(h - c - \frac{\phi(t)}{2} \right) - \frac{1}{2} \cdot \frac{A_s(t) \cdot f_y}{b \cdot f_c} \right] \quad (2)$$

where f_c is the concrete strength [$\text{N}\cdot\text{mm}^{-2}$],
 f_y is the reinforcement yield strength [$\text{N}\cdot\text{mm}^{-2}$],
 h is the cross-section height [m],
 b is the cross-section width [m],
 c is the concrete cover thickness [mm],
 $\phi(t)$ is the reinforcement diameter, dependent on time [mm],
 $A_s(t)$ is the reinforcement cross-section area, dependent on time [m^2]

$$A_s(t) = n \cdot \frac{\pi}{4} \cdot \phi^2(t) \quad (3)$$

Input parameters b , c , h , f_c and f_y are considered as random variables and their notation is shown in Fig. 1.

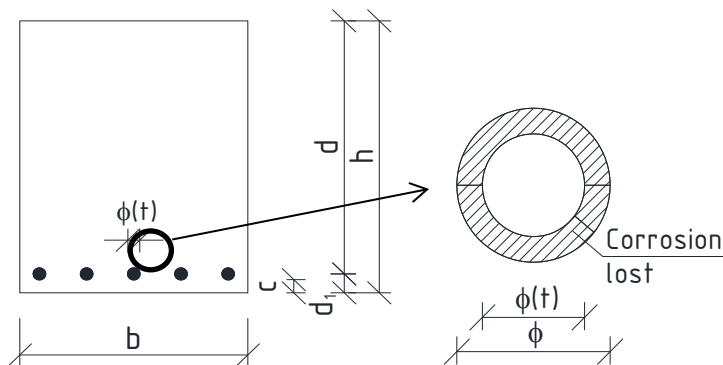


Fig. 1: Scheme of the profile parameters notation and loss of cross/section area due to corrosion.

The change of resistance $R(t)$ with time depends on the loss of the reinforcement cross-section area. The corrosion model according to Andrade et al. (1996) (see Fig. 1) was considered in the parametric study. This model is one of the most used corrosion models. The diameter loss, $\phi(t)$, for the planar uniform corrosion is described by formula

$$\phi(t) = \phi - 0.0232 \cdot (t - t_0) \cdot i_{corr} \quad (4)$$

where i_{corr} is the corrosion current density [$\mu\text{A}/\text{cm}^2$] ($1 \mu\text{A}/\text{cm}^2$ is equal to $11.6 \mu\text{m}/\text{year}$ of corrosion),
 t_0 is period of the passive stage.

The corrosion current density i_{corr} was measured on the real bridge structures (Andrade et al., 1996) and used values are shown in Tab. 1.

The beginning of the resistance changing with time depends on the length of the passive stage. The process of CO_2 diffusion is described by the second Fick's law (Matoušek & Drochytka, 1998). Many CO_2 diffusion models were derived for practical use. Those models depend on various factors. Only one model of passive stage calculation was used in this parametric study. In that model is assumed that the length of the passive stage depends on the concrete cover c and material constant D . This model is simple and it is cited in many references. Length of the passive stage is given by formula

$$t_0 = \frac{c^2}{2.D} \quad (5)$$

where D is a material constant presented in Tab. 1.

3. Influence of Corrosion of Reinforcement on Reliability in Time - Parametric Study

The parametric study was performed in order to find the influence of reinforcement corrosion on RC member's reliability subjected to bending. The values of h , b , c , ϕ , f_c , f_y and i_{corr} in relations (2-4) were considered as normally distributed random variables in the parametric study. The statistical characteristics of variables are given in Tab. 1.

Tab. 1: Statistical characteristics of RC cross-section.

Variables	mean value	standard deviation	coefficient of variation
Yield strength – f_y [$N.mm^{-2}$]	400.81480	23.96686	0.06800
Strength of concrete – f_c [$N.mm^{-2}$]	24.64000	2.68000	0.10877
Height – h [m]	0.797800	0.01360	0.01705
Width – b [m]	0.49570	0.00740	0.01493
Bar diameter – ϕ [mm]	19.770	0.223	0.01128
Number of bars – n [pieces]	7	-	-
Concrete cover – c [mm]	24.00	1.30	0.05417
Corrosion current density – i_{corr} [$\mu A/cm^2$]	1.00	0.20	0.20
	3.00	0.60	0.20
	5.00	1.00	0.20
Material constant – D [$mm^2.s^{-1}$]	$4.82 \cdot 10^{-7}$	-	-

Numerical calculation of the resistance $R(t)$ time dependence was realized by simulation by the Monte-Carlo method. It is possible to use other methods for simulation, also, for example LHS, Important sampling (Kala, 2001) etc. The results of simulation are shown in Fig. 2 and Fig. 3.

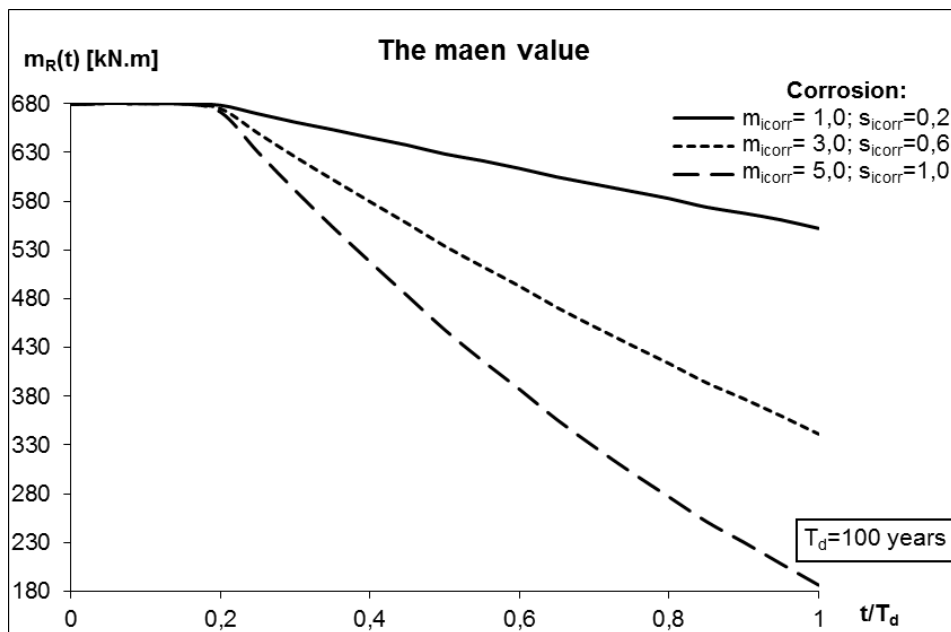


Fig. 2: Change with time of the resistance mean value $m_R(t)$.

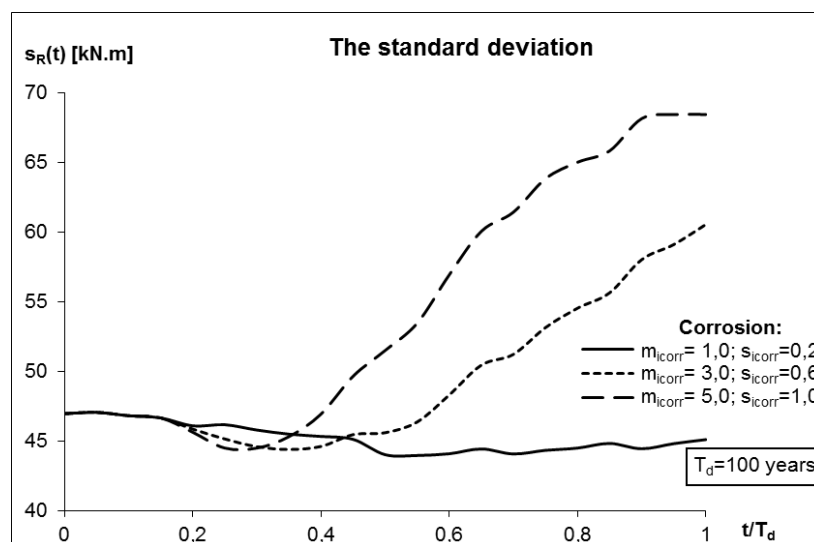


Fig. 3: Change with time of the resistance standard deviation $s_R(t)$.

If the designed lifetime of the bridge member, equals to $T_d = 100$ years, and the reliability level for the newly designed bridge members, equals to $\beta_d = 3.652$, are considered, the corresponding load effects are given by (normally distributed) parameters $m_E(t = t_0) = 464.752 \text{ N.mm}^{-2}$; $s_E(t = t_0) = 35.237 \text{ N.mm}^{-2}$.

4. Conclusions

In this paper is presented the influence of reinforcement corrosion on the resistance and reliability of the concrete bridge element, subjected to bending. The values of the corrosion current density i_{corr} significantly affect the mean value and standard deviation of resistance $R(t)$. Higher value of i_{corr} corresponds to higher decrease of the resistance mean value. The highest value of i_{corr} should not be applied in our region (it corresponds to very aggressive conditions). The resistance standard deviation $R(t)$ depends greatly on standard deviation of corrosion current density i_{corr} . The resistance standard deviation increases in time with higher standard deviation of i_{corr} . The failure probability $P_f(t)$ and reliability index $\beta(t)$ are changed significantly after the half of their lifetime.

Acknowledgement

The research is supported by European regional development fund and Slovak state budget by the project "Research Centre of University of Žilina", ITMS 26220220183 and by the Slovak Research and Development Agency under contract No. APVV-0106-11 and by Research Project No. 1/0517/12 of Slovak Grant Agency.

References

- Revie, R.W., Uhlig, H.H. (2008) Corrosion and Corrosion Control. An Introduction to Corrosion Science and Engineering. A John Wiley & Sons, Inv., Hoboken New Jersey.
- Sastri, V.S., Ghali, E. & Elboudjaini, M. (2007) Corrosion Prevention and Protection. Practical Solution. John Wiley & Sons, Ltd., West Sussex, England.
- Mrázik, A. (1987) Reliability theory of steel structures. VEDA Bratislava, 360 p. (in Slovak).
- Tuutti, K., (1982) Corrosion of Steel in Concrete. Swedish Cement and Concrete Research Institute, Stockholm, CBI forskning research, 04-82, 1982.
- Broomfield, J.P. (1997) Corrosion of steel in concrete. Understanding, investigation and repair. E&FN Spon, London, 240 p.
- STN EN 1992-1-1, Eurocode 2: Design of Concrete Structures, Part 1-1: General rules for buildings, SÚTN, 2006, 200 p.
- Andrade, C., Sarria, J., Alonso, C. (1996) Corrosion rate field monitoring of post-tensioned tendons in contact with chlorides. In: Conference Durability of building materials and components, Stockholm, pp. 959-967.
- Matoušek, M., Drochytka, R. (1998) Atmospheric corrosion of concrete. IKAS Prague.
- Kala, Z. (2001) Approximation and Advanced Numerical Simulation Methods. In: II. Conference "Reliability of Structures", Ostrava, pp. 97-100.

FITTING MODEL PARAMETERS OF PRESTRESSED CONCRETE BRIDGE: COMPUTATIONAL ASPECTS

T. Koudelka^{*}, J. Kruis^{**}, M. Lepš^{***}, J. Nosek^{****}

Abstract: *Many tasks, in our case fitting parameters of a numerical model, need enormous computing time that is not usually easily accessible. Here enormous means many days or months when a common computer is used. Nowadays there exists a possibility to utilize distributed resources like grid or volunteer computing. This contribution is focused on an application of distributed computing for fitting model parameters of a real structure. We are focused on a three-span prestressed concrete bridge in Mělník. This 23 years old bridge has a serious problem with an excessive deflection. The evaluation of monitoring results clearly shows that after 23 years since putting the bridge into operation the deflection is still growing.*

Keywords: Grid computing, Volunteer computing, Parallel processing, Prestressed concrete, SIFEL.

1. Introduction

This paper presents fitting of finite element model parameters of the bridge over the Labe river in Mělník. It is a box girder road bridge from prestressed concrete with three spans of lengths 72 m, 146 m and 72 m, see Fig. 1. Since its erection in 1994, the midspan deflection of the bridge is still increasing, see publications (Vodsloň, 2008; Urban et al., 2009; Vráblík et al., 2009). Suspected causes are relaxation of prestressing steel (Bažant & Yu, 2013) and creep of concrete (Bažant et al., 2011). Up to now, a rate of their influence and more importantly, their interaction is not known. Therefore, this contribution is a part of a pathway to the identification of the main causes of the excessive deflection of the bridge.



Fig. 1: Bridge in Mělník.

^{*} Tomáš Koudelka, PhD.: Department of Mechanics, Czech Technical university in Prague, Thakurova 7, 166 29, Prague; CZ, tomas.koudelka@fsv.cvut.cz

^{**} Assoc. Prof. Jaroslav Kruis, PhD.: Department of Mechanics, Czech Technical university in Prague, Thakurova 7, 166 29, Prague; CZ, kruis@fsv.cvut.cz

^{***} Assoc. Prof. Matěj Lepš, PhD.: Department of Mechanics, Czech Technical university in Prague, Thakurova 7, 166 29, Prague; CZ, leps@cml.fsv.cvut.cz

^{****} Josef Nosek: Department of Mechanics, Czech Technical university in Prague, Thakurova 7, 166 29, Prague; CZ, Josef.nosek@fsv.cvut.cz

2. Finite Element Model

The bridge was analyzed with the help of a finite element method. Three-dimensional model was based on hexahedral finite elements used for concrete and one-dimensional bar (tension/compression) elements used for tendons. Mesh contains 73 765 nodes, 48 896 hexahedral elements and 10 448 bar elements, see Fig. 2. With respect to general position of tendons in the structure, hanging nodes were used for nodes defining the bar elements. Displacements of the hanging nodes are obtained as a linear combination of the master nodes, in our case the master nodes are nodes of the hexahedral elements.

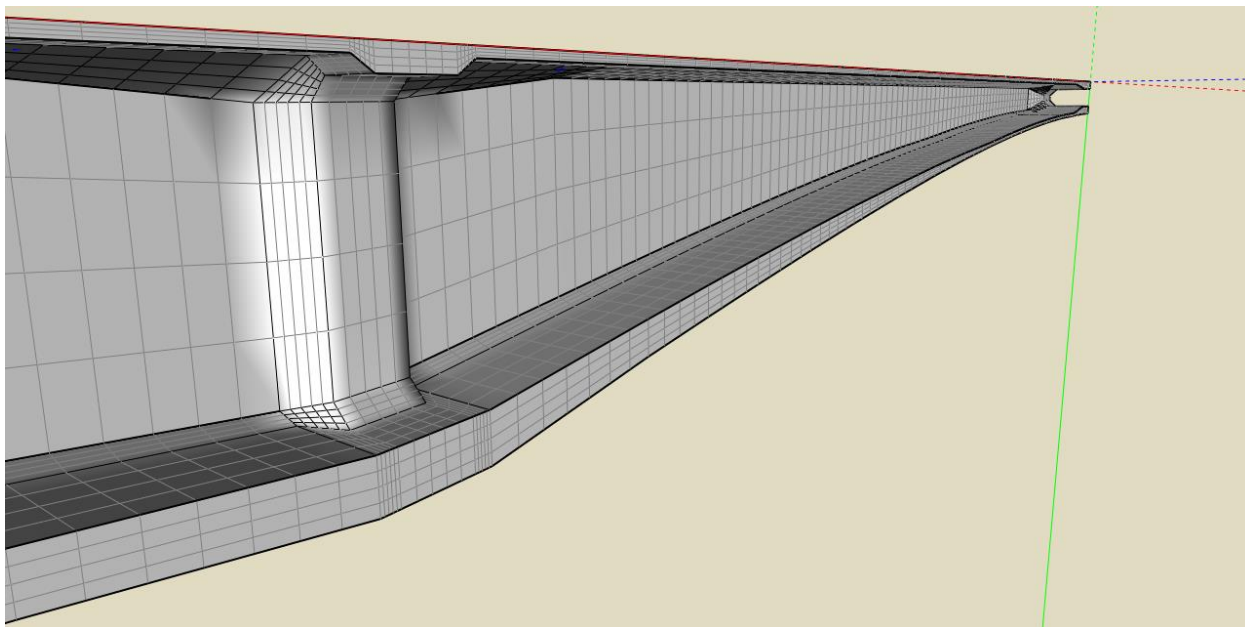


Fig. 2: Mesh on bridge.

The aim of the analysis was to describe long term behavior of the bridge. B3 creep material model (Bažant & Baweja, 2000) was used for concrete and relaxation of stresses in tendons was described by a model of relaxation based on Eurocode standard. The numerical model took into account construction phases of the bridge. All nodes and finite elements were equipped with a time function. The nodes or elements were taken into account only when the time function had the value 1.

3. Solver

Calculation of the model was performed in an open finite element software SIFEL (Krejčí et al., 2011; Kruis et al., 2001-2014). SIFEL offers analysis of various mechanical problems, e.g. simple elasticity, plasticity, dynamics, visco-elasticity, geomechanics and many others. Results can be exported to commercial graphical postprocessor GiD which provides robust environment for their visualization. SIFEL is written in C++ with respect to portability and extensibility, therefore it can be run on both Linux and Windows platforms.

4. Searching for Parameters

To assess the influence of individual parameters and to fit the long term deflection, it is necessary to perform global sensitivity analysis. Particularly, individual parameters are varied inside estimated bounds. The individual combinations then form so called Design of Experiments (DoE); see e.g. (Myšáková & Lepš, 2012) for more details on DoE as well as on applied methodology of DoE creation.

Then the computational demands are following: we have prepared a DoE comprising of 3000 combinations. In average, one evaluation takes around 4 hours of CPU time. Therefore, 12 000 CPU/hours are needed, i.e. we need 500 CPU/day. Two possibilities of distributing computational burden over many computers are described in the following text.

5. Volunteer Computing Project

“Volunteer computing” is a type of distributed computing in which computer owners can donate their spare computing resources (processing power, storage and Internet connection) to one or more research projects. Volunteer desktops and laptops can be connected to form the equivalent of a single huge super computer. Volunteers are motivated by various factors: support for the goals of the research, participation in online communities, and competition based on computational power. Our project CONVECTOR (Nosek, 2013-2014) is based on BOINC middleware (BOINC, 2010). At the time of writing, the project contains more than 3000 computers worldwide.

Tab. 1: Percentage of operation systems.

Operating system	Number of hosts	%
Windows based	2905	85.11
Linux based	414	12.13
Other	94	2.76

One disadvantage of a volunteer project is a requirement of availability of compiled applications for more than one software platform. A current representation of individual platforms shown is in Tab. 1. For these reasons, it was necessary to port SIFEL software to windows systems. Despite the great support of SIFEL authors, the 32 bit windows version was not able to correctly allocate all data into memory. Hence, we have decided to try to solve the task via grid computing in MetaCentrum under a Linux platform.

6. Grid Computing

MetaCentrum is a Czech national grid. It is widely open grid computing network for an academic research where all computers are running under Linux. However, each task must be entered by PBS (Portable Batch System). PBS is a batch job and computer system resource management package. It accepts batch jobs (shell scripts with control attributes), preserves and protects a job until its end, runs a job, and finally, delivers an output back to the submitter. Each task is assigned to a specific queue. Each queue has priority, an allowed maximum time length and a number of tasks in each queue. Most free is a queue called “Backfill” where we can have up to 1000 tasks at one time. Moreover, maximum running time is limited to 24 hour for each task. But this freedom queue has one disadvantage. If another queue with higher priority needs more CPU, it can kill your task immediately. If this happens one must identify this case and again to create a new task with same parameters at the end of the queue. Despite this complication we were able to finish all computations in a few days.

In detail, the work needed to process a task is as follows. A short bash script for reservation via PBS was built, and the task (also called work unit) was copied to a destination machine. Work unit contains an input data file, a main program and a set of instructions how to handle an output file. The task also contains minimal requirements for hardware. At least, one core of CPU, 3 GB RAM memory and 8 GB of free space on HDD was required for each task. A multiple core CPU can run more than one task if the computer has enough memory. A time limit for each work unit was set to 20 hours. If any task exceeded this time, such work unit has been aborted. Note that abortion of some tasks also happened few times for unknown reasons.

7. Conclusion

One of the main goals was to find out suitability of volunteer computing for this type of engineering problems. The main disadvantage of volunteer computing is heterogeneity of available computers. For instance, 1563 computers with Windows 7 are currently connected to our project CONVECTOR. But in fact there are 27 different versions of Windows 7 system. Although the task of fitting parameters of the prestressed concrete bridge seems big enough for distributed computing, in fact it is too small for a volunteer computing project and concurrently, too big for a standalone cluster. Apart from these two possibilities, grid computing looks very promising. Main advantages of grid computing are (i) good knowledge about each computer and (ii) huge flexibility. On the other hand the capacity of a grid

computing cluster is rather more limited in comparison to a volunteer computing project. However, both these computing methods can find utilizations in demanding engineering tasks.

Second important task was to calculate model of the bridge with varying input parameters for optimal fitting these parameters to available measurements. A typical output of such procedure is shown in Fig. 3.

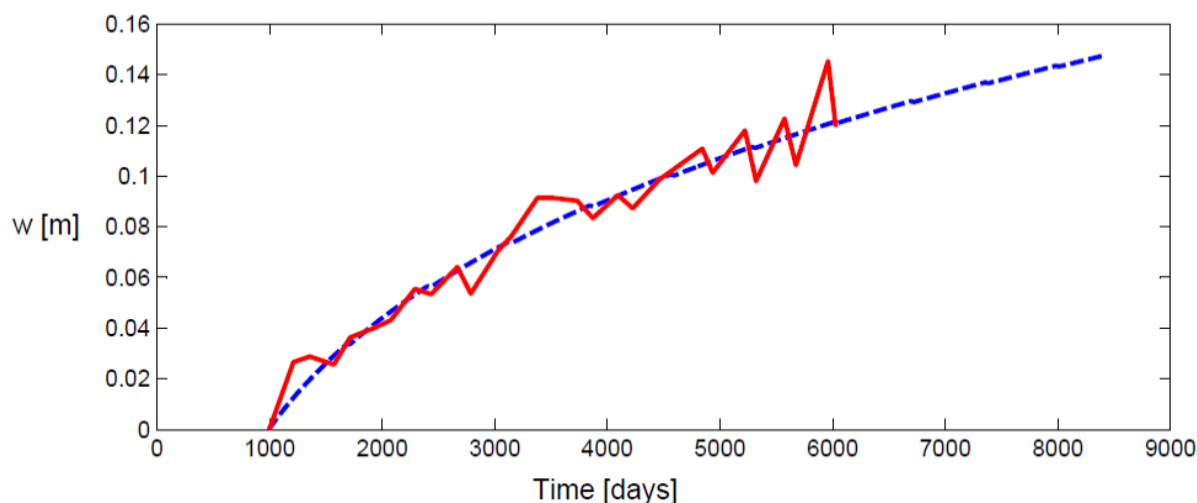


Fig. 3: Fitted deflection at midspan.

Acknowledgement

This work was supported by the Grant Agency of the Czech Technical University in Prague, grant No. SGS14/028/OHK1/1T/11 and from the Technology Agency of the Czech Republic through the project TA01030733.

Access to computing and storage facilities owned by parties and projects contributing to the National Grid Infrastructure MetaCentrum, provided under the programme "Projects of Large Infrastructure for Research, Development, and Innovations" (LM2010005), is greatly appreciated.

References

- Bažant, Z. P., Baweja, S. (2000) Creep and shrinkage prediction model for analysis and design of concrete structures: Model B3, ACI Special Publication Creep and Shrinkage of Concrete.
- Bažant, Z.P., Yu, Q., Kim, K.-T., Hubler, M.H., Šmilauer, V., Vráblik, L., Lepš, M., Křístek, V. (2011) Excessive multi-decade deflections of prestressed concrete bridges: How to avoid them and how to exploit their monitoring to improve creep prediction model, In: Proc. *fib* Symposium Prague 2011.
- Bažant, Z.P. & Yu, Q. (2013) Relaxation of prestressing steel at varying strain and temperature: Viscoplastic constitutive relation, *Journal of Engineering Mechanics*, 139:814-823.
- BOINC (2010) Berkeley open infrastructure for network computing. <http://boinc.berkeley.edu/>
- Krejčí, T., Koudelka, T., Kruis, J. (2011) Modeling of building constructions in SIFEL environment. 1. ed. Czech Technical University in Prague.
- Kruis, J., Koudelka, T., Krejčí, T. (2001-2014) SIFEL package, <http://mech.fsv.cvut.cz/~sifel/>.
- Myšáková, E., Lepš, M. (2012) Comparison of Maximin LHS Design Strategies. In: Proc. 3rd Conference Nano and Macro Mechanics.
- Nosek, J. (2013-2014) CONVECTOR project, <http://convector.fsv.cvut.cz/>.
- Urban, R., Štroner, M., Vráblik, L. (2009) Measurement of bridge body across the river Labe in Mělník. In: Proc. of Workshop 2009, Czech Technical University in Prague.
- Vodsoň, J. (1995-2007) Time evaluation of large, permanent deflections of prestressed concrete bridges in time; Reports on the results of long-term monitoring of selected road bridges in 1995–2007, (in Czech).
- Vráblik, L., Štroner, M., Urban, R. (2009) Measurement of bridge body across the river Labe in Mělník, *Acta Montanistica Slovaca*, 14, No. 1, 79-85.

METHODS OF A BUILDING STONE INTERNAL STRUCTURE STUDY

K. Kovářová*, R. Ševčík**

Abstract: Building stone is during its “life” influenced by actions of weathering processes which usually lead to changes in the internal structure of the stone which influences its durability. For this reason, studies of a stone internal structure are very important. There are many methods to determine effective porosity and provide porosity values in a percentage, nevertheless, these methods do not enable visualization of the internal structure. The visualization can be useful for better understanding of the durability phenomenon. Therefore, the methods of X-Ray microtomography and microscopy in ultraviolet light were used in our research of three Czech sandstones. Both methods also provide different values of porosity which are given due to their limitation. The main aim of this contribution is to present basic information about both methods and to compare their results, advantages and disadvantages.

Keywords: Building stone, Internal structure, X-Ray microtomography, UV microscopy, MicroOpis.

1. Introduction

Building stone is during its “life” influenced by actions of weathering processes which usually lead to changes in the internal structure of the stone. According to studies by many authors (e.g. Fitzner & Kalde, 1991; Kovářová, 2012), once these changes are initiated they influence the stone's durability. For this reason studies of a stone internal structure are very important. There are many methods to determine effective porosity, such as mercury porosimetry, helium pycnometry and determination of open porosity according to the national standards. These methods provide porosity values in a percentage (by helium pycnometry after the conversion of the gained material real density); however, they do not enable the visualization of the internal structure. The visualization can be useful for better understanding of the durability phenomenon.

For these purposes we used the methods of X-Ray microtomography and microscopy in ultraviolet light (UV) in the research of three Czech sandstones. Both methods are described and the obtained results are mentioned and discussed in this article.

2. Experimental Material and Methods

2.1. Experimental material

Three types of commonly used Czech cretaceous sandstone were studied in our research – Božanov, Hořice and Kocbeře. Although all quarries are situated relatively close to each other, each type looks macroscopically as well as microscopically different. The Hořice and Kocbeře sandstones are fine-grained, mostly formed from quartz grains, whereas the Božanov sandstone is coarse-grained and contains higher amounts of feldspar. Each type has a different mineralogical composition of cement binder and also a different organization of the pore space, i.e. the internal structure. Finally, each type also reacts to the weathering action in a different way from the point of view of physical-mechanical properties changes (Kovářová, 2012).

* Mgr. Kateřina Kovářová, PhD.: Czech Technical University in Prague, Faculty of Civil Engineering, Thákurova 7; 166 29, Prague; CZ, katerina.kovarova@fsv.cvut.cz

** Mgr. Robert Ševčík, PhD.: Slovak Academy of Science, Institute of Measurement Science, Department of Optoelectronics, Dúbravská cesta 9; 841 04, Bratislava; Slovakia, umersevc@savba.sk

2.2. Methods

2.2.1. X-Ray microtomography

The method of X-ray microtomography belongs to non-destructive test methods, which were used to obtain information about porosity and organization of internal structure in general. X-Ray microtomography is a characterization method based on the investigation of internal sample structure by image analysis (e.g. Appoloni et al., 2007). X-Ray microtomography is composed of two basic steps - acquisition of projections and volume reconstruction. In the phase of acquisition the object is turned around the rotation axis at a selected small angle and so called X-ray projections are measured. The absorption of X-ray beams as they pass through a material is a logarithmic function of the absorptivity of the material and the distance through which the light must travel (so called Beer's law).

Projections are X-ray attenuation images which are created on a two-dimensional detector after the beam transmission through the object. To accomplish the measurement, the sample can be rotated at 180° or 360°, the latter being used in our case. In one turn the selected number of projections is captured. The three dimensional image of the object is reconstructed after obtaining all projections, when two-dimensional detector is used as in our case (Hain et al., 2011). This method enables to create 3-D video and so a detailed visualization of pore space is possible.

Small cylinder samples with the diameter 1 cm and the height 1.5 cm were prepared from every sandstone type. Samples were measured by microCT phoenix|x-ray nanoton180 with 5 Mpx 2D detector at 90 kV, 100 μ A with timing 2 s and 2880 projections. Voxel size was 5 μ m (Kovářová et al., 2012). This experimental arrangement enables to evaluate pores with diameter > 5 μ m.

2.2.2. Microscopy in ultraviolet light

Microscopy in ultraviolet light is usually used for better description of pore space. The method enables to study the pore size, connectedness, pore types and presence of microcracks. Pores and cracks are highlighted by a fluorescence dye contained in the resin which is excited by captured ultraviolet radiation (Jornet et al., 2002). The polarizing microscope Olympus BX-51 with a mercury lamp enabling observation in ultraviolet light was used for the study of stone thin sections.

The program MicroOpis (Kovářová & Kovář, 2011) was used for the study and evaluation of obtained pictures. This software performs color analysis contained in the photo. Photos saved in a raster (dot) graphical format are composed of individual discrete points, pixels. Each point is characterized by a record describing the color of the point. The application MicroOpis passes the photo point to point and counts points which correspond with the selected color condition. The percentage of points complying with the selected condition is calculated from the number of satisfactory points and total points in the photo. The total number of photo points is defined by the photo resolution. The MicroOpis application allows the user to select a "reference color" which is the closest to the desired area in the photo. Consequently, it is necessary to choose the "threshold", the number in the same range as those defined in the representation of each color component, which defines the maximum distance of tested colors from the reference color (Kovářová, 2012).

3. Results and Discussion

The three-dimensional reconstruction of pore space and cross-sections were done by X-Ray microtomography in each stone type (Figs. 1 and 2). The porosity values determined by both methods are given in Tab. 1. As it is obvious from the following figures, each type of sandstone has a different organization of the pore structure. This phenomenon was also confirmed using microscopy in ultraviolet light (Fig. 3). The sample of processed image in ultraviolet light of the Božanov sandstone using MicroOpis application is shown in Fig. 4.

The differences of porosity values determined by both methods are caused by limitations of both methods. Both methods enable the detection of total porosity, i.e. open and closed pores, but each has a different detection limit. The detection limit of X-Ray microtomography in this experimental arrangement is 5 μ m and the detection limit of microscopy in ultraviolet light depends on the used enlargement. The results of image analysis using the MicroOpis application also strongly depend on the ability of individual assessors to accurately determine the grain/pore boundary. The analysis of UV images is also time-

consuming. Because of the above mentioned limitations of the methods, it is useful to determine the porosity also by another method, i.e. the mercury porosimetry (Kovářová et al., 2012).

Tab. 1: Porosity values (%) of studied sandstone using both methods of determination.

Sandstone	X-Ray microtomography	UV microscopy
<i>Božanov</i>	<i>16.00</i>	<i>21.14</i>
<i>Hořice</i>	<i>22.00</i>	<i>30.22</i>
<i>Kocbeře</i>	<i>15.61</i>	<i>23.15</i>

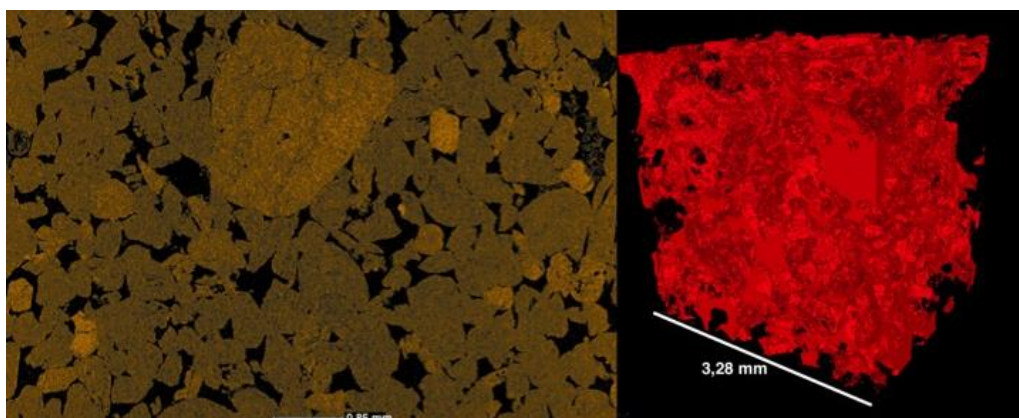


Fig. 1: Cross-section (on the left) and three-dimensional reconstruction (on the right) of Božanov sandstone.

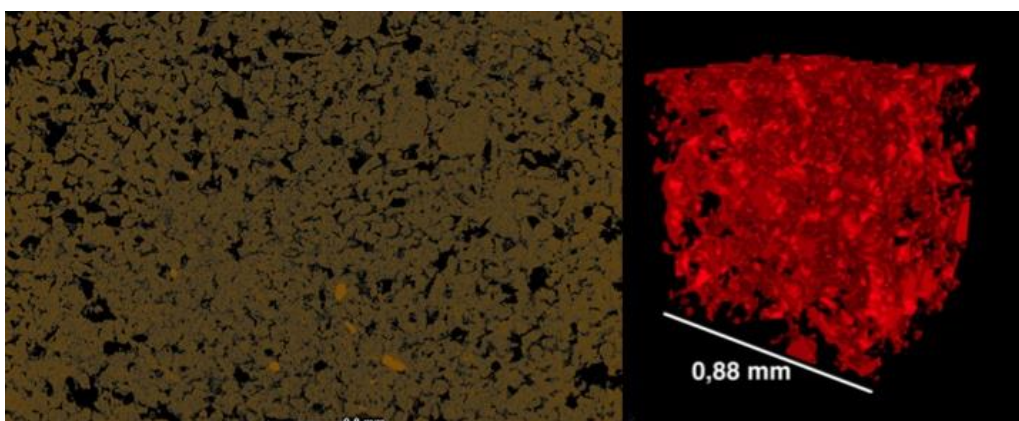


Fig. 2: Cross-section (on the left) and three-dimensional reconstruction (on the right) of Hořice sandstone.

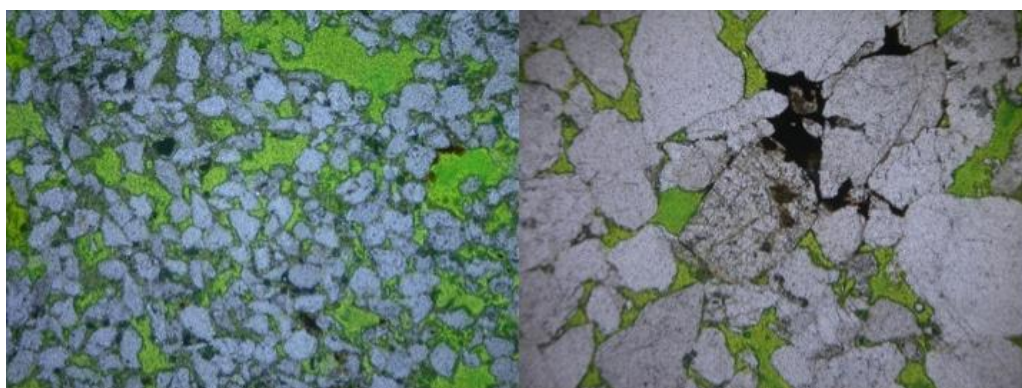


Fig. 3: The Hořice sandstone (on the left) and Božanov sandstone (on the right) in ultraviolet light (4x enlargement).

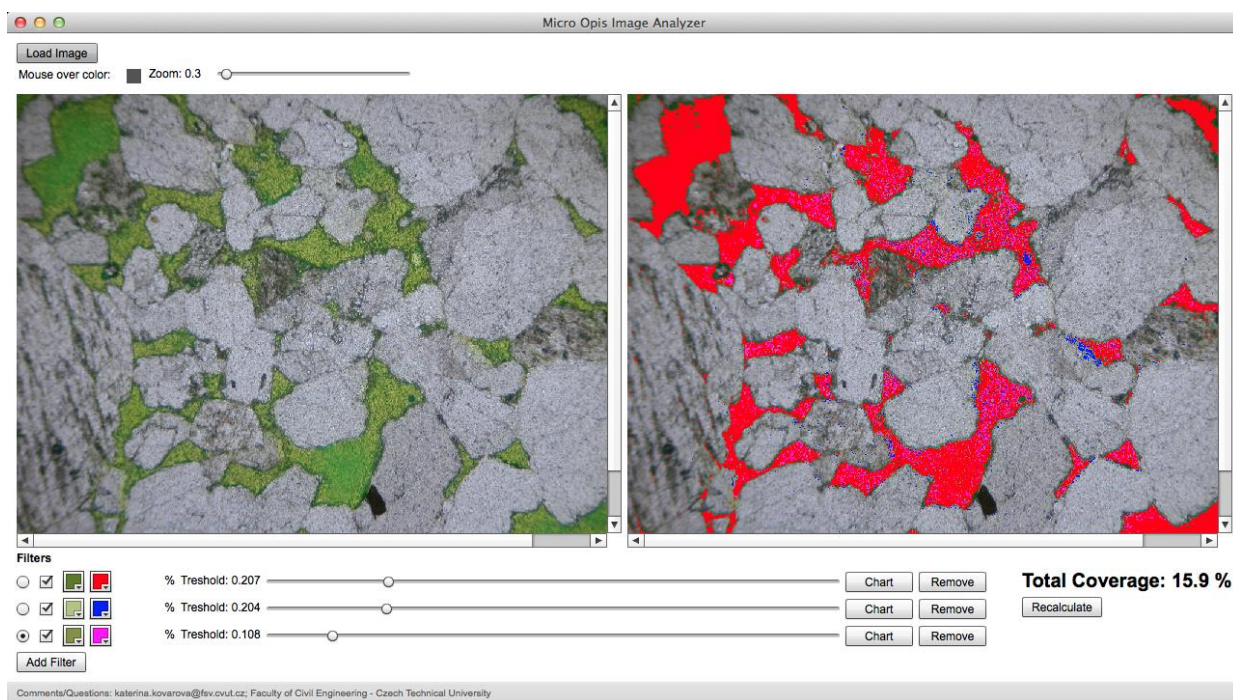


Fig. 4: The processed UV image of the Božanov sandstone using the MicroOpis application – the UV image of the stone thin section (on the left); the image after the color highlight of pore area, incl. their percentage (on the right).

4. Conclusions

To sum up, both mentioned methods enabling the study of the internal structure have their own limitations. The main disadvantage of both methods is their detection limit but the main advantage is the possibility to visualize the internal structure which is not possible using another method.

Acknowledgement

This paper has been supported by the project: “A comprehensive methodology for the selection and processing of a stone intended for replacements and repairs of the ashlar masonry of historic buildings” (Project No. DF12P01OVV020, supported by the Ministry of Culture of the Czech Republic). Establishment of Microtomographic laboratory was financially supported by the European Regional Development Fund under the project CEKOMAT (ITMS-26240120006, ITMS-26240120020).

References

- Appoloni, C.R., Fernandes, C.P., Rodrigues C.R.O. (2007) X-ray microtomography study of a sandstone reservoir rock. *Nuclear instruments and methods in physics research A*, 580, pp. 629-632.
- Fitzner, B., Kalde, M. (1991) Simulation of frost-thaw cycle and salt weathering - nature adapted material tests, In: *La détérioration des matériaux de construction, Colloque International, La Rochelle (France)*, pp. 103-114.
- Hain, M., Nosko, M., Simančík, F., Dvořák, T., Florek, R. (2011) X-Ray microtomography and its use for non-destructive characterisation of material, In: *Proc. 8th International Conference on Measurement (Maňka, J., Witkovský, V., Tyšler M. & Frollo, I. eds)*, Institute of Measurement Science, SAS, Bratislava, pp. 123-126.
- Jornet, A., Teruzzi, T., Rück, P. (2002) Bowing of Carrara marble slabs: comparison between natural and artificial weathering, In: *Understanding and managing of stone decay (Přikryl R. & Viles H. eds)*, Karolinum, Prague, pp. 161-169.
- Kovářová, K. (2012) Influence of weathering processes on physical-mechanical properties of sandstones. PhD. thesis, CTU Prague.
- Kovar, J., Kovarova, K. (2011) *MicroOpis 1.0*.
- Kovářová, K., Ševčík, R., Weishauptová, Z. (2012) Comparison of mercury porosimetry and X-Ray microtomography for porosity study of sandstones. *Acta Geodyn. Geomater.*, 9, 4 (168), pp. 541-549.

ENERGY ABSORPTION OF CELLULAR FOAMS IN HIGH STRAIN RATE COMPRESSION TEST

V. Králík^{*}, J. Němeček^{**}, A. Jíra^{***}, T. Fíla^{****}, P. Zlámal^{*****}

Abstract: Aluminum foams are structural materials with excellent energy absorption capacity jointed with very low specific weight and high stiffness. Products of aluminum foams are used in a wide range of structural and functional applications (e.g. as a part of composite protection elements) due to its attractive properties. Full characterization of deformation behaviour under high-strain rate loading is required for designing these applications. The aim of this study is to compare stress-strain behaviour and energy absorption of the aluminium foam structure with conventional energy absorbing materials based on polystyrene and extruded polystyrene commonly used as protective elements. The compressive deformation behaviour of the materials was assessed under impact loading conditions using a drop tower experimental device.

Keywords: Impact test, Energy absorption, Alporas, Polystyrene, Extruded polystyrene.

1. Introduction

In recent years there has been a significant increase of interest in products made of aluminum foams. Due to their exceptional mechanical and physical properties, they are used in a wide range of industries, ranging from automotive (e.g. bumpers) to building industry (e.g. sound proofing panels). This highly porous material is characterized by closed cellular structure with large pores (~1-13 mm in diameter) and very thin cell walls (~0.1 mm). Mechanical properties of aluminum alloys foam in quasi-static conditions (such as compressive strength, tensile strength and elastic modulus) have been extensively studied and reviewed by many authors (Paul et al., 2000; Gibson et al., 1997; Koudelka et al., 2012). The foam has a long and well-defined phase of plastic straining stress-strain diagram under compression (Gibson et al., 1997), which is recognized by the “plateau stress“ and densification strain in the stress-strain diagram (Gibson et al., 1997). This plateau region is responsible for a high ability of the material to absorb deformation energy, which can be used also for the construction of composite protective devices such as motorcycle and bicycle helmets (Pinnoji et al., 2010). For such a use, it is necessary to know an exact deformation behavior of the foam and accurately evaluate energy dissipation under the high strain rate loading. Mechanical properties of aluminum alloy foams in quasi-static conditions (such as compressive strength, tensile strength and elastic modulus) have been extensively studied and reviewed (Paul et al., 2000; Gibson et al., 1997; Koudelka et al., 2012).

The most widely used technique to investigate material behavior at different high strain rates is a split Hopkinson pressure bar (SHPB) (Ma et al., 2009; Yi et al., 2001; Shen et al., 2010). Some authors (Shen et al., 2010; Paul et al., 2000) dealt with the strain rate effect on the energy dissipation capacity of an aluminum foam. These studies showed that the energy dissipation capacity of the foam significantly

* Ing. Vlastimil Králík: Faculty of Civil Engineering, Department of Mechanics, Czech Technical University in Prague, Thákurova 2077/7; 166 29, Prague; CZ, vlastimil.kralik@fsv.cvut.cz

** Assoc. Prof. Ing. Jiří Němeček: PhD.: Faculty of Civil Engineering, Department of Mechanics, Czech Technical University in Prague, Thákurova 2077/7; 166 29, Prague; CZ, jiri.nemecek@fsv.cvut.cz

*** Ing. Aleš Jíra, PhD.: Faculty of Civil Engineering, Department of Mechanics, Czech Technical University in Prague, Thákurova 2077/7; 166 29, Prague; CZ, jira@fsv.cvut.cz

**** Ing. Tomáš Fíla: Institute of Theoretical and Applied Mechanics (ITAM) ASCR, v. v. i., Prosecka 76, 190 00, Prague; CZ, fila@itam.cas.cz

***** Ing. Petr Zlámal: Faculty of Transportation Sciences, Department of Mechanics and Materials, Czech Technical University in Prague, Konviktská 20; 110 00, Prague; CZ, xzlamal@fd.cvut.cz

increases with the increasing strain rate. However, studies on the deformation behavior of aluminum foams with direct impact loading (with the strain rate not constant) are rare (Merrett et al., 2013).

The objective of the presented research was to perform an experimental investigation of the deformation behaviour and energy absorption capacity of commercially produced aluminum alloy Alporas (Shinko Wire Ltd., Japan) under impact loading conditions using a drop tower experimental device and to compare the characteristics with the behaviour of widely used protective materials like plain and extruded polystyrene in the same testing conditions.

2. Experimental Methods

Three types of energy absorbing materials were used for testing and evaluation - closed-cell aluminum foam Alporas (Shinko Wire Ltd., Japan) with the mass density of $260 \pm 15 \text{ kg/m}^3$, polystyrene EPS 200 S with the mass density $\sim 30 \text{ kg/m}^3$ and extruded polystyrene foam Styrodur ROOFMATE SL-A with the mass density $\sim 33 \text{ kg/m}^3$. The density of Alporas was detected by weighing of samples with the known volume assuming the density of walls to be equal to pure aluminum (2700 kg/m^3). An example of the test samples is shown in Fig. 1. Morphological features and detailed microstructural description of the Alporas samples have been previously studied by the authors and can be found in (Němeček et al., 2013). Rectangular specimens having $60 \times 60 \text{ mm}^2$ cross-sectional dimensions and thickness 40 mm for polystyrene and extruded polystyrene and 35 mm for Alporas were cut from larger material blocks.



Fig. 1: Samples for impact tests – polystyrene, extruded polystyrene foam, Alporas foam (left to right).

Impact tests were conducted using a drop tower experimental device. This drop-weight rig can be used to generate impact velocities up to 5.4 m/s. A sledge with impactor is guided during free fall by rollers on three rails. The rig is equipped by triaxial accelerometer (EGCS3, Measurement Specialties, USA) and high speed camera (NX3, Integrated Design Tools, Inc., USA) to capture deformation of the sample. A photograph of the experimental setup is shown in Fig. 2. Specimens were placed on the bottom compression plate and the impactor was positioned at a defined distance from the top of the sample to achieve the required impact velocity. Sample was fixed on the bottom platen to avoid any possible slip of the specimen. The total mass of the impactor used in this study was 5020 g and the potential energies related to the top surface of the specimens were 16.5 J (for impact velocity 2.5 m/s) and 30.8 J (for impact velocity 3.5 m/s). Each specimen was impacted only once.

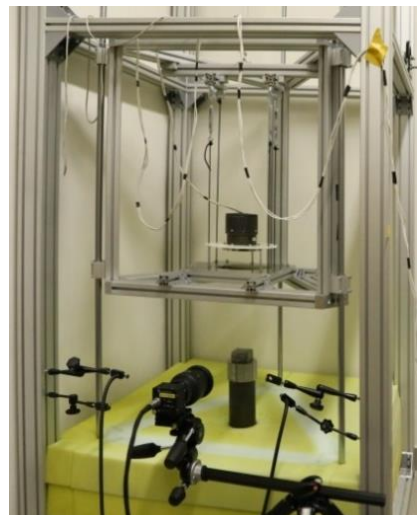


Fig. 2: Photograph of the experimental set up for impact tests.

3. Results and Discussions

The acceleration of the impactor was recorded in time during its drop. An average displacement of the top sample surface and compression force were calculated from the acceleration. Overall engineering strain in the sample was assessed taking into account the sample height. Finally, the engineering stress-strain curve was constructed as shown in Fig. 3. Three tests were conducted for each material. The compressive stress–strain curve of Alporas foam, either quasi-static or dynamic one, exhibits three deformation regions (Yi et al., 2001): an initial linear-elastic response; an extended plateau region with a nearly constant flow stress and a final densification region in which the cells collapse and are compacted together. The final region is not present in our stress-strain curves due to an insufficient impact velocity. Polystyrene and Styrodur are characterized by similar qualitative behaviour to Alporas (Fig. 3).

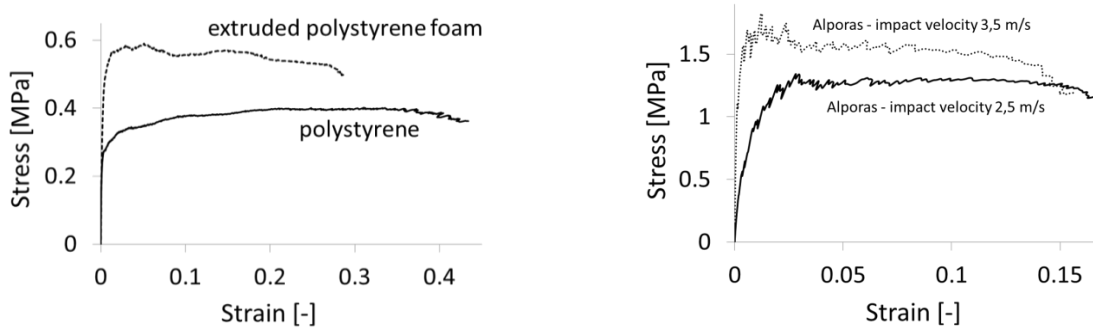


Fig. 3: Dynamic compressive stress-strain curve of tested samples.

Fig. 3 also shows large differences in yield stress for the studied samples. This difference is quite large for polystyrene and extruded polystyrene foam (impact velocity 2.5 m/s) in contrast to small difference in their mass densities. In the case of Alporas foam, which was measured at two impact velocities, the yield stress is (as expected) much higher. It also increases with the impact velocity. Fig. 3 further shows that linear elastic part of the stress-strain diagram only appears at very low strains for the studied cases (smaller than about 0.001).

The energy absorption capacity is defined as the energy necessary to deform a given specimen volume to a specified strain. The absorption energy per unit volume of a sample up to a strain ϵ_0 can be evaluated by integrating the area under the stress–strain curve as follows:

$$W = \int_0^{\epsilon_0} \sigma(\epsilon) d\epsilon \quad (1)$$

Fig. 4 and Tab. 1 show the absorption energy for different tested material at compression strains of 0.05, 0.10, 0.15, 0.20, 0.25, 0.30, 0.35 and 0.40 and at different strain rates.

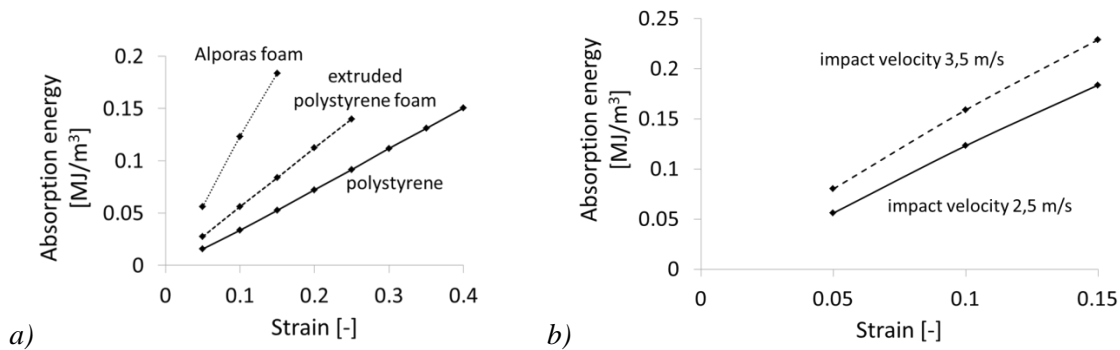


Fig. 4: Absorption energy for: a) Impact velocity 2.5 m/s and b) Alporas foam at two different impact velocities.

The experimental results show that the yield stress of Alporas foam increases with the impact velocity, so the area under the stress–strain curve also increases. The difference between the absorbed energy of Alporas foam with impact velocity 2.5 m/s against impact velocity 3.5 m/s is about 24% for strain 0.15 for the respective averages (Tab. 1). Mean values of the energies fluctuated within approx. 10% between the samples of the same category and are summarized in Tab. 1. The difference in the obtained energies

points out the importance of the impact velocity which has to be known when designing the protective foam layers in a specific application.

Tab. 1: Absorbed energy (mean values) of tested samples at different strains [MJ/m³].

Type of material	Impact velocity	Strain								
		[m/s]	0.05	0.1	0.15	0.2	0.25	0.3	0.35	0.4
Polystyrene	2.5		0.016	0.034	0.053	0.072	0.092	0.112	0.131	0.151
Styrodur			0.027	0.056	0.084	0.112	0.140			
Alporas			0.056	0.123	0.184					
Alporas	3.5		0.080	0.159	0.229					

4. Conclusion

Dynamic impact tests were performed for three types of energy absorbing materials (Alporas, polystyrene and extruded polystyrene foams) using a drop tower experiment device. The energy absorption capacity was evaluated for all materials. Two impact velocities (2.5 and 3.5 m/s) were tested in the case of Alporas. The dynamic compressive stress-strain curves of the materials were determined from the record of acceleration. Both yield stress and the absorbed energy of Alporas increased with increasing impact velocity and it was significantly larger than in the case of polystyrene and extruded polystyrene (tested for impact velocity of 2.5 m/s). Interestingly, the yield stress of extruded polystyrene foam was also significantly larger than for polystyrene even if there is a small difference in their mass densities.

It was proven by the presented investigations that the Alporas foam can absorb significantly higher energies compared to conventional materials and its behaviour at high impact velocities can be very useful for designing new impact protective devices.

Acknowledgement

Support of the Czech Science Foundation (GAČR P105/12/0824) and the Grant Agency of the Czech Technical University in Prague (SGS12/163/OHK2/2T/16 and OHK1-042/14) is gratefully acknowledged.

References

- Gibson, L. J., Ashby, M. F. (1997) Cellular solids – Structure and properties. Cambridge University Press, Cambridge.
- Koudelka, P., Zlámal, P., Kytýř, D., Fíla, T., Jiroušek, O. (2012) Experimental study on size effect in quasi-static compressive behavior of closed cell aluminium foams, In: Proc. 13th Bilateral Czech/German Symposium (CTU in Prague, Faculty of Transportation Sciences), pp. 115-118.
- Merrett, R.P., Langdon, G.S., Theobald, M.D. (2013) The blast and impact loading of aluminium foam, *Materials and Design*, 44, pp. 311-319.
- Němeček, J., Králík, V., Vondřejc, J. (2013) A two-scale micromechanical model for aluminium foam based on results from nanoindentation, *Computers and Structures*, 128, pp. 136-145.
- Paul, A., Ramamurty, U. (2000) Strain rate sensitivity of a closed-cell aluminum foam, *Materials Science and Engineering A*, 281, 1-2, pp. 1-7.
- Pinnoji, P.K., Mahajan, P., Bourdet, N., Deck, C., Willinger, R. (2010) Impact dynamics of metal foam shells for motorcycle helmets: Experiments & numerical modeling, *International Journal of Impact Engineering*, 37, pp. 274-284.
- Shen, J., Lu, G., Ruan, D. (2010) Compressive behaviour of closed-cell aluminium foams at high strain rates, *Composites: Part B-Engineering*, 41, 8, pp. 678-685.
- Yi, F., Zhu, Z., Zu, F., Hu, S., Yi, P. (2001) Strain rate effects on the compressive property and the energy-absorbing capacity of aluminum alloy foams, *Materials Characterization*, 47, pp. 417- 422.

ANALYSIS OF DYNAMIC RESPONSE OF FOOTBRIDGE VEVEŘÍ ON PEDESTRIAN LOAD

O. Kratochvíl*, J. Křížan**

Abstract: *The paper deals with dynamic response of footbridge Veverčí which is induced by the movement of people. Measurement of response induced by the movement of people was carried out on this footbridge. Graphs of acceleration in chosen points in time were results of measurement. The pedestrians who cross footbridge in specific numbers and in different types of walk were source of vibrations. On site measurements were compared with calculations of individual load states.*

Keywords: Footbridge, Dynamic analysis, Vibration serviceability of footbridges, Damping, stiffness, Dynamic force, Force model, Walking force, Natural frequencies and vibration modes.

1. Description of Measurement

The response of the bridge deck is recorded for walk of one, two, four, six and sixteen pedestrians. The pedestrians move either unorganized (free walk) or organized (synchronized walk).

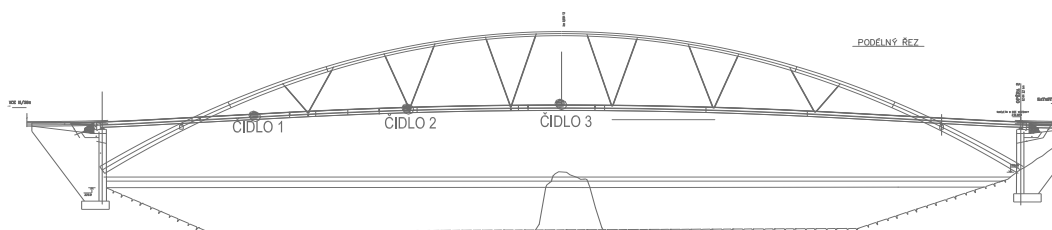


Fig. 1: Scheme of accelerometer placement on footbridge.

Two sets of measurement were carried out. Each set contained several load states. Main difference between sets is in positions of sensors (Kala et al., 2012a). The first set has placing of sensors on three places of bridge deck. The acceleration in vertical direction was recorded.

2. Introduction and Aims

Large attention was devoted to computations of dynamic response of footbridge in recent years. The response is assessed in terms of vibration influence on structure but also and above in terms of influence on pedestrian. Recent experiences showed necessity to check response of structure on a pedestrian walk comfort. Acceleration and size of oscillation are assessed. If these variables are exceeded, a certain degree of discomfort is felt by pedestrian. In worst case it can come to disabling of walk. The goal of paper was verify conformity computations of dynamic response with measurement in-site. Size of the conformity is a key to assess dynamic response in terms of pedestrian comfort. Measurement in-site, which serves to calibrate computational model, was available in this case. These details are not available in construction time. Executed conformity of results of numerical analysis with measurement can show which parameters of structure and calculation are the most important to reach exact results.

* Ing. Ondřej Kratochvíl: Institute of Structural Mechanics, Brno University of Technology, Faculty of Civil Engineering, Veverčí 95; 602 00, Brno; CZ, ondrej.kratochvil@seznam.cz

** Ing. Jiří Křížan: Institute of Structural Mechanics, Brno University of Technology, Faculty of Civil Engineering, Veverčí 95; 602 00, Brno; CZ, krizan.j@fce.vutbr.cz

Tab. 1: Load states for the first set of measurement.

Set of measurement 1								
N. Measurement	N.of person	Type of movement	Transition time	Speed	Stride length	frequency	Stride length	frequency
			[s]	[m.s ⁻²]	[m]	[Hz]	[m]	[Hz]
1	2	fast walk	62	1.616	0.8	2.020	0.840	1.924
2	2	synchronized brisk walking	60	1.670	0.8	2.088	0.706	2.365
3	6	normal walk	84	1.193	0.8	1.491	0.723	1.650
4	6	synchronized walk with stomping	68	1.474	0.8	1.842	0.719	2.050
5	16	normal walk	91	1.101	0.8	1.376	0.605	1.820
6	16	synchronized walk	72	1.392	0.8	1.740	0.631	2.207

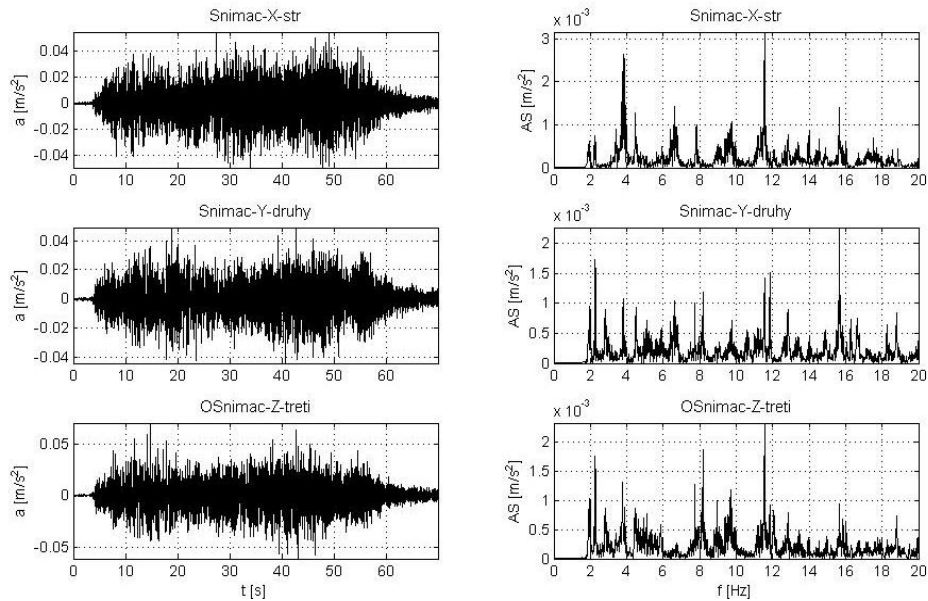


Fig. 2: Record of dynamical response of footbridge – measurement 1-1, left side describes acceleration in time, right side describes frequencies.

Tabs. 1 and 2 show list of measured cases dynamical response of footbridge. Two details for step frequency are in the table. Each is related to different length of step. First value step frequency is calculated on the base length of step 0.8 m.

It is given by equation, $v = 0.8xf$ [m.s⁻²]. Length of step is determined by measurement for normal walk. The second value was calculated for specific case of measurement. Walk velocity was determined from graph of acceleration. This graph shows also time to pass over the footbridge. Frequency was determined from frequency representation of record measurement. This is the first peak in the graph.

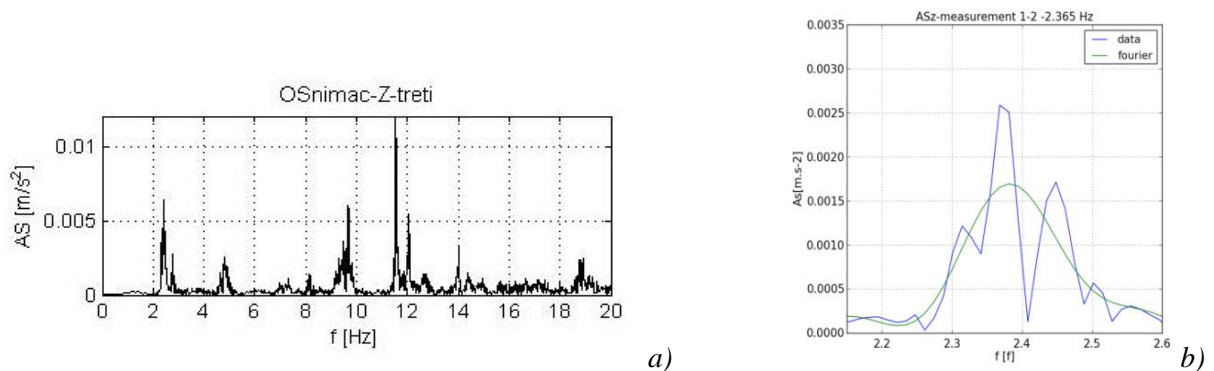


Fig. 3: a) Record of dynamical response – measurement 1-2, frequency zone; b) Detail with step frequency.

Tab. 2: Load states for the second set of measurement.

Set of measurement 2								
N. Measurement	N.of person	Type of movement	Transition time	Speed	Stride length	frequency	Stride length	frequency
			[s]	[m.s-2]	[m]	[Hz]	[m]	[Hz]
1	2	fast walk	66	1.518	0.8	1.898	0.787	1.930
2	2	synchronized brisk walking	53	1.891	0.9	2.101	0.834	2.268
3	1	normal walk	34	2.947	1	2.947	1.053	2.800
4	1	running	27	3.711	1	3.711	1.088	3.410
5	4	normal walk	41.7	2.403	0.9	2.670	0.910	2.640
6	4	running	27	3.711	1	3.711	1.108	3.350
7	6	normal walk	77.7	1.290	0.8	1.612	0.713	1.808
8	6	synchronizovaná chůze	72	1.392	0.8	1.740	0.710	1.961
9	16	normal walk	85.8	1.167	0.8	1.459	0.686	1.701
10	16	synchronized walk	80	1.253	0.9	1.392	0.653	1.917
11	7	lateral excitation - vandalism	40					2.140
12	16	lateral excitation - vandalism	30					1.760

Modal analysis was performed to description behaviour of structure in dynamical load. Lower stiffness is evident in horizontal direction upright to longitudinal axis of footbridge. Mode shapes and corresponding eigen frequency are shown on Fig. 4. This result is given by configuration of structure support system (Kala et al., 2012b). The bridge deck is suspended by ropes to arcs which have large stiffness in vertical direction.

Damping, which is caused by dispersion of mechanical energy, was considered uniform and constant damping. Damping model for numerical analysis was modeled by Rayleigh damping. Damping value was determined from the damping ratio $\xi = 0.007$.

Tab. 3: Load states for the second set of measurement.

Modal structure charakteristic		
No.	Frequency	Shape description
1	1.321	Lateral
2	1.68	Lateral
4	2.764	Vertical
6	4.044	Vertical

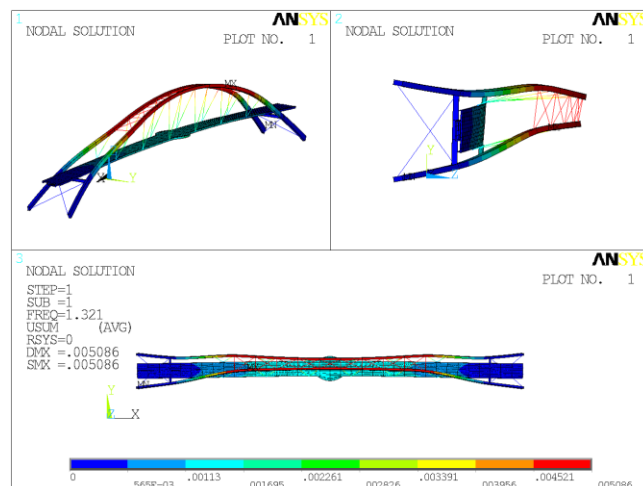


Fig. 4: Mode shape of structure with frequency 1.321 Hz.

3. Evaluation of Dynamical Response – Numerical Analysis Result

Process of response in graph on the left side shows acceleration in chosen point for given direction. Longitudinal direction is marked as “x”, transverse “y” and vertical “z”. Corresponding step frequency and step length are marked on the top of graph.

Dependence acceleration in time is on the left side, Fourier transformation to frequency zone is on the right side.

Process of response which is from the first measurement set is only for vertical direction.

Numerical analysis is in appropriate conformity with measurement. Large result difference which is in the middle time response can be ascribed to method of computation. Although the model is taking into account flexible supports, the bridge deck is softening (Kala et al., 2012c). Regardless it is not possible to completely eliminate large amplitude, when the pedestrians (represented by the forces) cross the chosen point.

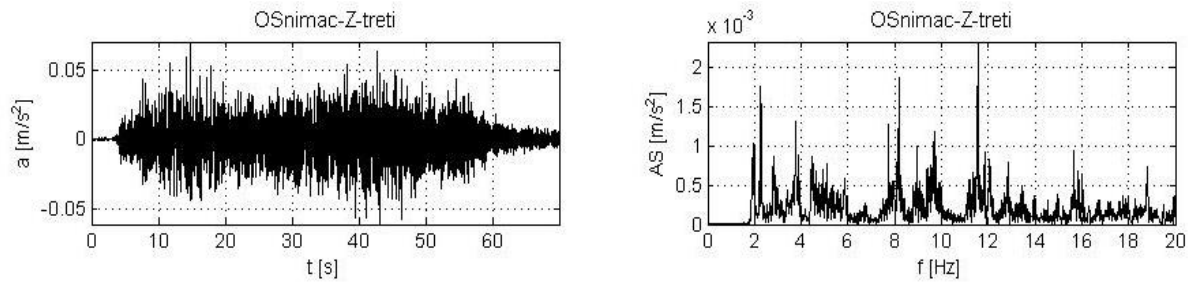


Fig. 5: Measurement record 1-1, walk, direction „z“.

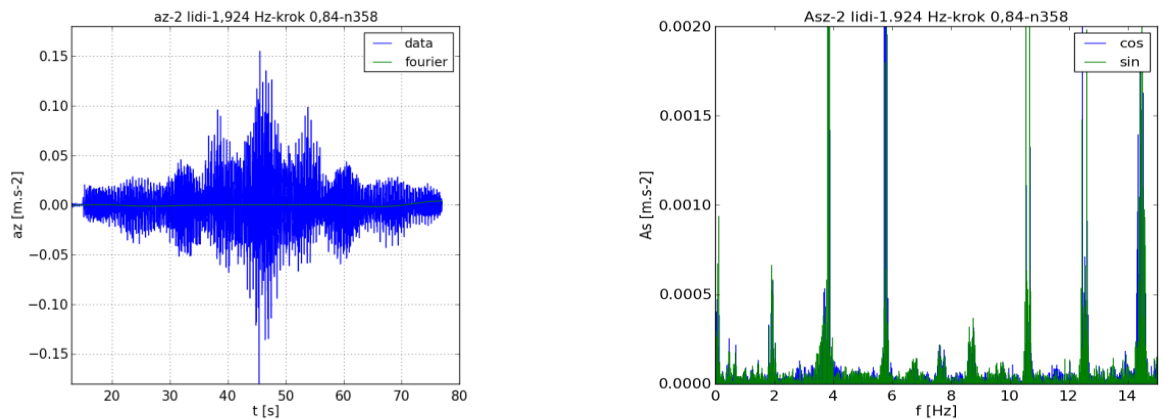


Fig. 6: Walk 2 pedestrians, $f = 1.924$ Hz, step 0.84 - direction “z”.

The graph, which shows transformation of result in time dependency to frequency zone, confirms correctness step frequency. Step frequency is 1.924 Hz for this case. Conformity of values is especially in frequency 1.924 Hz and further in frequency 3.84 Hz. This fact is confirmed by the most significant part of the first two members Fourier series for step force.

4. Conclusion

The paper presents measurement of dynamical response of bridge structure and comparison with results of numerical analysis. Result differences between measurement and computation are given by the damping model. Presented comparison measurement and computation demonstrates appropriate conformity of results. This fact proves good prediction of behavior of structure loaded by the movement of pedestrians.

Acknowledgement

The article was elaborated within the framework of research project GACzR 14-25320S.

References

- Kala, J., Salajka, V., Hradil, P. (2012) Sensitivity Investigation of eigenvalue problem of water tower construction interacting with fluid, Journal of Vibroengineering, 2012, Vol. 14, Issue 3, pp. 1151-1159, ISSN 1392-8716.
- Kala, Z., Kala, J. (2012) Lateral-Torsional Buckling Analysis of I-Beams using Shell Finite Elements and Nonlinear Computation Methods, In: Proc. International Conference of Numerical Analysis and Applied Mathematics (ICNAAM), Greece, pp. 2066-2069, DOI: 10.1063/1.4756596, ISSN: 0094-243X, ISBN: 978-0-7354-1091-6.
- Kala, J., Kala, Z. (2012) The Interaction of Local Buckling and Stability Loss of a Thin-Walled Column under Compression, In Proc. International Conference of Numerical Analysis and Applied Mathematics (ICNAAM), Greece, pp. 2074-2077, DOI: 10.1063/1.4756598, ISSN: 0094-243X, ISBN: 978-0-7354-1091-6.

ASSESSMENT OF THE CONSTITUTIVE PROPERTIES OF REACTOR STEEL USING AN INVERSE ANALYSIS ON THE SMALL PUNCH TEST

M. Krčmář*, A. Materna**

Abstract: *This paper presents a method for parameter identification based on the small punch test and inverse analysis. During the small punch test a miniaturized disk specimen was deformed by a spherical punch in a manner similar to deep drawing. The experimental outcome was a force – displacement curve, which indirectly contains information concerning the mechanical properties of the tested material. The parameter identification was carried out by means of an inverse analysis which was based on the finite element modeling of the small punch test. The finite element models have to maintain the required accuracy with reasonable computational costs. The inverse analysis consists of an iterative method which minimizes error between the experimental load – displacement curve and the curves obtained via finite element modeling. The identification procedure was applied to 15Ch2MFA steel in order to estimate the true stress – true strain relationship. The identified curve was compared with the one obtained from the standard tensile test.*

Keywords: Small punch test, Inverse analysis, Finite elements, Parameter identification.

1. Introduction

Parameter estimation of irradiated materials based on small-scale specimen techniques is currently a subject of interest worldwide. Despite the fact that the small-scale specimen brings with it certain difficulties, its use is required for several reasons. Firstly, there are severe limitations on specimen size in irradiated-material testing facilities. Secondly, the small specimen can be extracted from in-service components in a semi-destructive way, i.e. the component can be kept operative without a need for sampling place repair. This allows for an estimation of the residual life of a component and keeping it in-service beyond its designed life.

Over recent decades a number of different techniques applied onto non-standard small specimens have been developed in order to assess material properties. Among them the small punches test (SPT) has been shown to be an extremely attractive and promising technique. In small punch testing a disk sample (usually 0.5 mm thick and 8 mm diameter) is clamped between dies and punched with a spherical indenter in a miniaturized deep drawing test. The experimental outcome is the relationship between the applied force and the tip displacement of the sample – load-displacement curve (LDC). SPT was developed by Manahan et al. (1982) for postirradiation mechanical behavior determination. SPT has been used thus far in order to extract the true stress – true strain relationship, the ductile-brittle transition temperature, tensile strength, fracture toughness, creep properties and others (Chang, 2008).

The aim of this paper is to invent the parameter estimation procedure based on an inverse analysis of the small punch test. The function and validity of the procedure is demonstrated by estimating the true stress – true strain relationship of the 15Ch2MFA steel.

2. Experimental Tests

The material under investigation was 15Ch2MFA steel which is used as a base material for pressure vessels in a nuclear reactor VVER-440. Young's modulus $E = 213 \pm 3$ GPa and the yield strength

* Bc. Michal Krčmář: Czech Technical University in Prague, Faculty of Nuclear Sciences and Physical Engineering, Dept. of Materials, Trojanova 13; 120 00 Prague; CZ, Michal.Krcmar01@gmail.com

** Ing. Aleš Materna, PhD.: Czech Technical University in Prague, Faculty of Nuclear Sciences and Physical Engineering, Dept. of Materials, Trojanova 13; 120 00 Prague; CZ, ales.materna@fjfi.cvut.cz

$R_{p0.2} = 499 \pm 5$ MPa was measured with a standard tensile test. The true stress – true strain relationship is plotted in Fig. 4.

The SPTs was performed on a tensile testing machine Inspekt 100 kN, Hegewald & Peschke. The tests were carried out at room temperature. The schematic of the small punch testing device is shown in Fig. 1. The specimen is a small disk with dimensions 8 mm in diameter and 0.5 mm in thickness which was clamped to a die by means of a down-holder with the force $F \sim 14.5$ kN. The final specimen surface was grinded with sand paper (grit size P1200) and no lubrication between the punch and the specimen was used. Over the course of the test, the punch with a spherical head was pushed downward with a constant speed $v = 0.5$ mm/min. The test was completed when a sudden force drop caused by a crack extension occurred. The disk was symmetrically deformed in a deep drawing manner. Using the down holder, the specimen was prevented from cupping upward and therefore, the plastic deformation was concentrated into the region below the punch. Further information about the specimen preparation, testing device and test procedure can be found in Janča (2013).

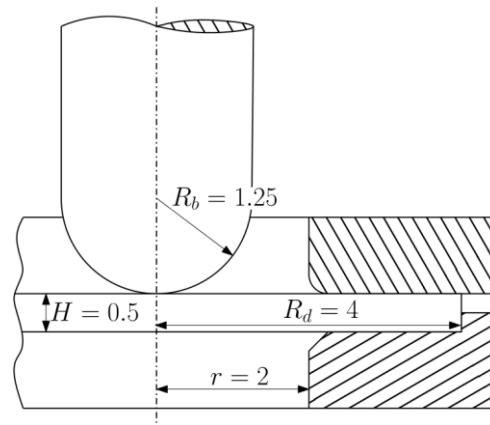


Fig. 1: Schematic illustration of the SPT device.

The displacement of the central point on the bottom side is monitored as a function of applied force during the test. This load-displacement curve (LDC) contains information about the material properties of the sample. The typical LDC for the ductile material can be divided into several regions based on the main deformation process (Baik et al., 1986): elastic bending (I), plastic bending (II), plastic membrane stretching (III) and plastic instability (IV). The linear elastic deformation in region I is followed by an expansion of the plastic deformation from the punch tip to the entire specimen in region II. In region III the deformation mechanism changes from bending to biaxial stretching. The local reduction of thickness in region IV causes a micro-cracking and load decrease followed by a final rupture.

3. Parameter Estimation

LDC contains information indirectly concerning the elasto-plastic deformation behavior and about the strength and fracture properties of the material. There are two basic ways to extract unknown material parameters from LDC: (I.) determine the empirical relationship in order to relate the results from SPT and unknown parameter for a given class of materials; (II.) perform an inverse analysis based on finite element simulations. The latter is presented in this paper to obtain a true stress – true strain curve.

3.1. Finite element modeling of SPT

FE simulations have become an inseparable tool for parameter estimation by means of inverse analysis. During the inverse analysis, tens or even hundreds of finite element models have to be evaluated, thus models should maintain the required accuracy with a reasonable computation costs.

Since the test geometry, loading, deformation and damage evolution up to the crack initiation are axisymmetric, a 2D FE model is sufficient to calculate the LDC. A typical finite element mesh is plotted in Fig. 2a, four node axisymmetric elements of full integration with an edge 0.04 mm in length were used. The contact between the specimen, punch and dies was modeled with a friction coefficient $\mu = 0.1$. The punch and dies were modeled as rigid bodies. Neither damage nor failure were taken into account in the FE model, thus LDC is only valid in first three regions before micro-cracking occurs.

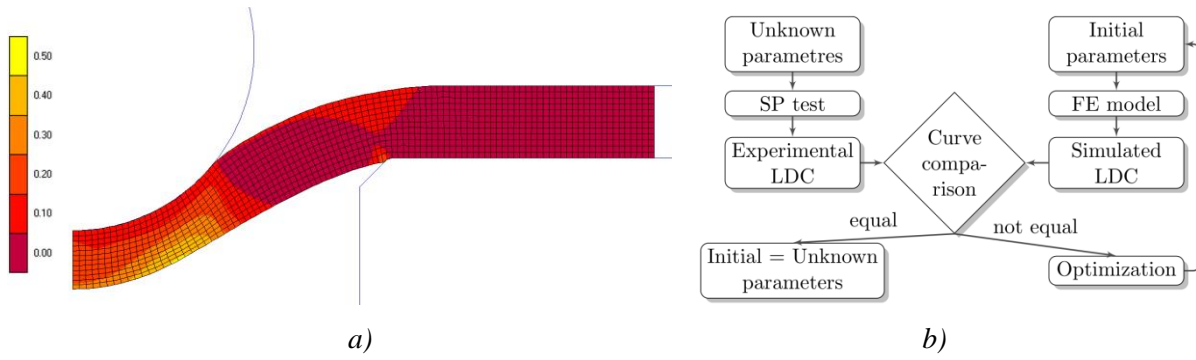


Fig. 2: a) Typical FE mesh used in the simulations. The scale shows the equivalent logarithmic strain.
b) Scheme of inverse analysis.

3.2. Inverse Analysis

Obtaining a true stress – true strain relationship by SPT requires an inverse analysis. The principal scheme of the parameter estimation procedure is shown in Fig. 2b. The iterative procedure compares the experimental and simulated LDC by means of the cost function

$$err(x) = \frac{1}{N} \sum_{i=1}^N [F^{MKP}(x, u_i) - F^{EXP}(u_i)]^2 \quad (1)$$

in which N is the number of points considered in the optimization. $F^{MKP}(x, u_i)$ is the force value at displacement u_i calculated by the FE model which is dependent on unknown parameters x . $F^{EXP}(u_i)$ is the force value at displacement u_i from the experimental SPT. The cost function is minimized by means of a gradient-based algorithm, namely the Levenberg–Marquardt method (Andrade-Campos et al., 2007).

The unknown parameters (x) represent in this case the true stress – true strain curve defined as a piecewise function

$$\sigma_{true} = \begin{cases} K\varepsilon_{true}^n + \sigma_0 & \varepsilon_{true} \leq \varepsilon_0 \\ A(\varepsilon_{true} - \varepsilon_0) + K\varepsilon_0^n + \sigma_0 & \varepsilon_{true} > \varepsilon_0 \end{cases} \quad (2)$$

in which there are four unknown parameters K, n, σ_0, B and parameter ε_0 is kept fixed at value 0.29.

4. Application and Results

The aforementioned procedure was implemented via Matlab which governed the optimization procedure as well as the FE simulations carried out with the MSC.Marc software. An inverse analysis has been performed in order to estimate the four unknown parameters of the true stress – true strain curve defined by equation (2) for the 15Ch2MFA steel.

The LDC obtained during the inverse analysis are plotted in Fig. 3 and compared with the experimental one. Only regions I–III of the LDC are used for the parameter identification. It is apparent that the iterations steadily converge towards the experimental curve. The convergence was reached in 13 iterations and 103 FE models in all were calculated. The entire curve is approximated quite well with a slight misalignment remaining in the early stages of deformation.

The corresponding true stress – true strain curves are shown in Fig. 4. The predicted curve underestimated the value of the yield strength, although it on the whole provided close agreement with the curve obtained by the classic tensile test which was corrected after necking by Bridgman’s correction method.

5. Conclusions

The characterization of material for the pressure vessel in the nuclear reactor has been carried out in this paper by means of an inverse analysis on a small punch test. Both the experimental tests as well as the optimization routine with finite element simulations have been carried out in order to validate the parameter estimation based on an inverse analysis.

The developed identification routine was applied to extract the true stress – true strain curve from the outcome of the SP test (load-displacement curve). The estimated curve provided a satisfactory approximation of the curve from the standard tensile test with a maximum deviation 6%.

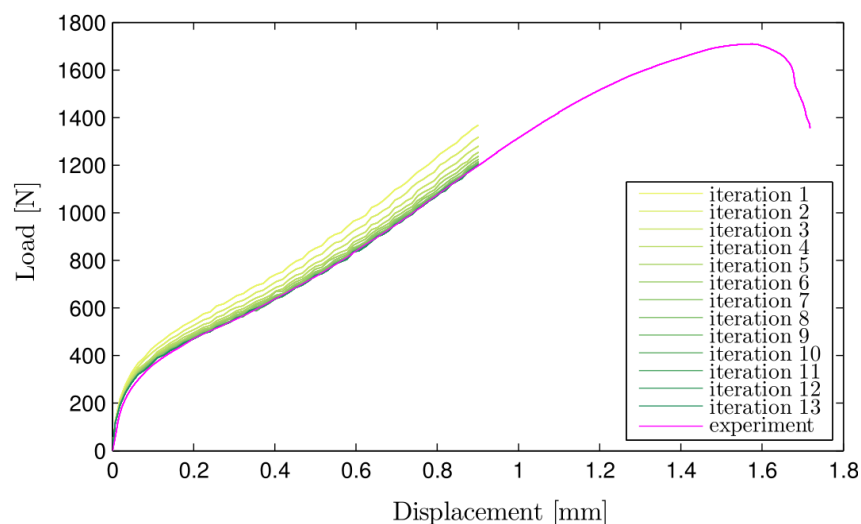


Fig. 3: Experimental LDC and numerically estimated curves during the inverse analysis.

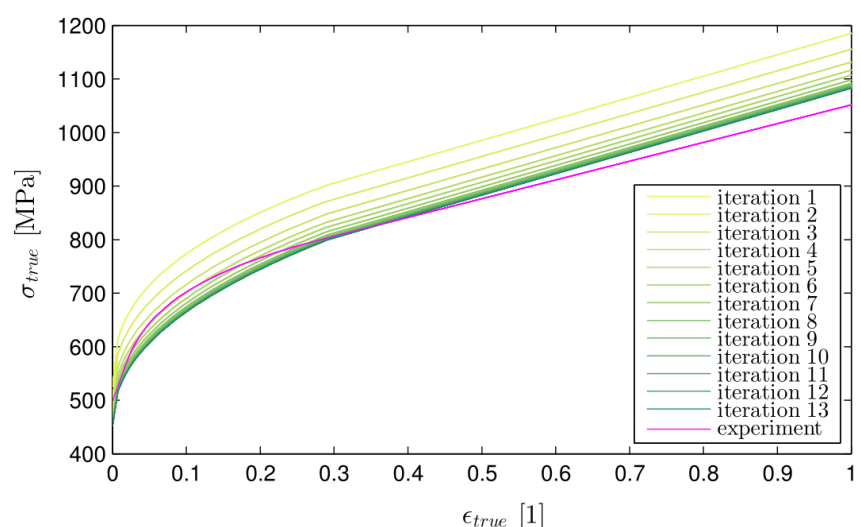


Fig. 4: Hardening curves corresponding to LDC in Fig. 3.

Acknowledgements

This work was carried out within the framework of the research projects TA02020811 (Technology Agency of the Czech Republic) and SGS13/223/OHK4/3T/14 (Grant Agency of the Czech Technical University in Prague).

References

- Andrade-Campos, A., Thuillier, S., Pilvin, P., Teixeira-Dias, F. (2007) On the determination of material parameters for internal variable thermoelastic-viscoplastic constitutive models. *International journal of plasticity*, 23, 8, pp. 1349-1379.
- Baik, J. M., Kameda, J., Buck, O. (1986) Development of small punch test for ductile–brittle transition temperature measurement of temper embrittled Ni–Cr Steels, In: *The use of small-scale specimens for testing irradiated material* (W.R.Corwin & G.E.Lucas eds), ASTM STP 888, Philadelphia, pp. 92-111.
- Chang, Y.-S., Kim, J.-M., Choi, J.-B., Kim, Y.-J., Kim, M.-C., Lee, B.-S. (2008) Derivation of ductile fracture resistance by use of small punch specimens. *Engineering Fracture Mechanics*, 75, 11, pp. 3413-3427.
- Janča, A. (2013) *Methodology of the small punch test*, Bachelors Thesis, Prague, (in Czech).
- Manahan, M., Argon, A., Harling, O. (1982) The development of a miniaturized disk bend test for the determination of post-irradiation mechanical-properties. *Journal of Nuclear Materials*, 103, 1-3, pp. 1545-1550.

MULTIPLE INDOOR ROBOT LOCALIZATION USING INFRARED BEACONS

J. Krejsa^{*}, S. Vechet^{**}, K. Chen^{***}

Abstract: Mobile robot localization based on active artificial landmarks is well established robust technique in indoor mobile robotics. This paper explores the extension of the method to multiple robot localization, with the key idea of using the robots themselves as the artificial landmarks, supplying other robots in the group with its estimate of position. The method uses nonlinear version of Kalman filter for determination of position estimate in 2D space, x - y coordinates and angle with respect to global coordinate system, with the estimate represented by mean values and corresponding covariances. Simulation results based on model well verified with the real system suggest that while only small reduction of number of fixed active landmarks can be achieved, the main advantage of the method is in increased robustness of localization technique with respect to obscured landmarks fields of view.

Keywords: Mobile robot, Indoor localization, Kalman filter, Infrared beacons.

1. Introduction

Determination of autonomous mobile robot position – localization – is essential task in robot navigation. There is a number of approaches to the task, most common ones include some kind of landmark detection, with active artificial landmarks being the most reliable in spite its disadvantage of the need to put such landmarks into environment.

In past few years the focus of robotic community moves towards the multiple robots cooperation, used e.g. for advanced mapping, when a group of robots maps the surrounding areas with either vision or rangefinder based systems and such information is fused to get complete map of environment (Saedi et.al. 2011). Regarding localization, artificial landmarks approach is ideal for multiple robots, see e.g. Park & Kee (2011), proposing an indoor localization system for a wide service area divided into multiblocks for reliable sensor operation.

The idea behind the method introduced in this paper is to place active artificial landmark onto each robot in the group, creating moving beacon, that can serve as additional source of information for localization. On contrary to relative localization (Mao, 2013), the moving beacon information is fused with the static beacons to enhance the robustness of global localization.

2. Infrared Beacons Based Localization

Infrared beacons based localization determines the position $\mathbf{x}_k = [x_k^R, y_k^R, \varphi_k^R]^T$ of the robot on 2D plane in k step using the model of the robot response to actions $\mathbf{u}_k = [u_k^t, u_k^r]$ represented by translational u_k^t and rotational u_k^r velocities and the measurement of relative angle between the robot and detected beacon,

* Assoc. Prof. Ing. Jiří Krejsa, PhD.: Institute of Thermomechanics, v.v.i. AS CR – branch Brno, Technická 2, 616 69, Brno, CZ, krejsa@fme.vutbr.cz

** Ing. Stanislav Věchet, PhD.: Institute of Thermomechanics, v.v.i. AS CR – branch Brno, Technická 2, 616 69, Brno, CZ, vechet.s@fme.vutbr.cz

*** Prof. Kuo-Shen Chen, PhD.: National Cheng Kung University, Department of Mechanical Engineering, No.1, Ta-Hsueh Road, Tainan 701, Taiwan

placed in known position $\mathbf{x}_{bi} = [x_{bi}, y_{bi}]$, $i = 1, 2, \dots, N$, see Fig. 1. The position of the robot is represented by simple unimodal Gaussian approximation.

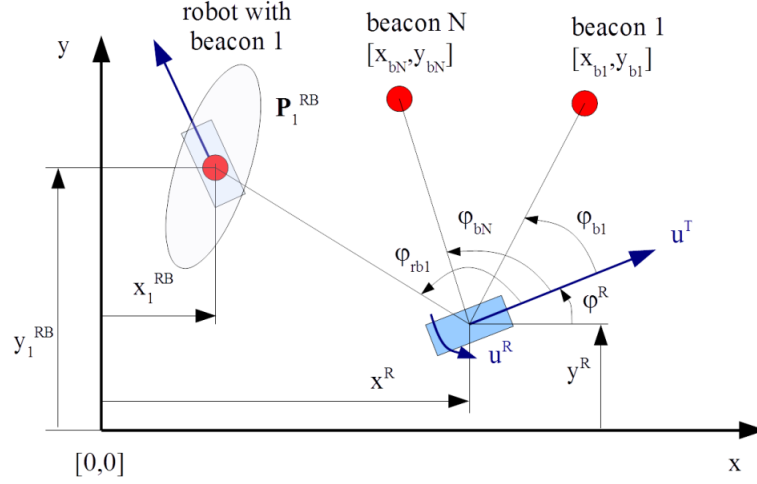


Fig. 1: Robot state definition, static beacons and additional robot with beacon attached.

The model is defined in (1) and (2), where \mathbf{v}_k is white Gaussian process noise with zero mean and covariance matrix \mathbf{V}_k , \mathbf{y}_k is system output, \mathbf{w}_k is corresponding measurement noise with zero mean and covariance matrix \mathbf{W}_k and f and h are continuously differentiable nonlinear functions. The state transition function f defines how the state changes when action is applied:

$$\mathbf{x}_{k+1} = f(\mathbf{x}_k, \mathbf{u}_k) + \mathbf{v}_k = \begin{bmatrix} \cos \varphi_k^R u_k^t \Delta t + x_k^R \\ \sin \varphi_k^R u_k^t \Delta t + y_k^R \\ u_k^r \Delta t + \varphi_k^R \end{bmatrix} + \mathbf{v}_k \quad (1)$$

and for N measurements of beacon relative angle the output is:

$$\mathbf{y}_k = \begin{bmatrix} h_1(\mathbf{x}_k, \mathbf{x}_{b1}) \\ \vdots \\ h_N(\mathbf{x}_k, \mathbf{x}_{bN}) \end{bmatrix} + \begin{bmatrix} \mathbf{w}_{1k} \\ \vdots \\ \mathbf{w}_{Nk} \end{bmatrix} \quad (2)$$

with single beacon measurement

$$h_1(\mathbf{x}_k, \mathbf{x}_{b1}) = \left[\text{atan2}(y_k^R - y_{b1}, x_k^R - x_{b1}) - \varphi_k^R \right] \quad (3)$$

As the state can not be determined exactly, the state estimate is used instead, defined by its mean $\hat{\mathbf{x}}_k$ and covariance matrix \mathbf{P}_k . Nonlinear version of Kalman filter, either EKF or UKF can be used to find such estimate, see the details in Krejsa & Vechet (2012).

3. Multiple Robots Localization

The simple extension for multiple robots localization is trivial, all the robots will receive successive measurements from all the beacons. The beacon identification problem is solved by one way communication from the robot to the beacon, therefore the only issue with the extension is to select one robot as the group leader, communicating with the beacons, while other robots receive the issued emitting command and consequently read the relative angle measured.

This simple approach can be further extended by placing additional beacon on top of each robot. The motivation is straight-forward: such dynamic beacon can provide other robots with additional information, that is particularly advantageous in cases when some of the beacons are out of receivers field of view, or remaining visible static beacons are in undesirable geometric configuration (keep in mind that only bearing information is available for infrared beacons, not the distance).

However, some issues arise when dynamic beacons are introduced. First of all, the communication between the robots has to enable to transmit and receive the estimate of i -th robot position $\hat{\mathbf{x}}_{ik}^{RB}$, \mathbf{P}_{ik}^{RB} . As the robots have to receive the beacon identification commands anyway, it is not difficult to extend the communication protocol. Second issue arises with the increased number of beacons increasing the time delay in single round through all the beacons, therefore the number of robots is limited due to technological limitations. The last remaining issue arises from the uncertainty in dynamic beacon position. The measurement from dynamic beacons therefore has to be handled differently, taking into account the covariances \mathbf{P}_{ik}^{RB} .

In Extended Kalman filter correction step, the update is given as:

$$\begin{aligned}\hat{\mathbf{x}}_{k+1|k+1} &= \hat{\mathbf{x}}_{k+1|k} + \mathbf{K}_{k+1} \tilde{\mathbf{y}}_{k+1} \\ \mathbf{P}_{k+1|k+1} &= \mathbf{P}_{k+1|k} - \mathbf{K}_{k+1} \mathbf{H}_{k+1} \mathbf{P}_{k+1|k}\end{aligned}\quad (4)$$

where Kalman gain $\mathbf{K}_{k+1} = \mathbf{P}_{k+1|k} \mathbf{H}_{k+1}^T \mathbf{S}_{k+1}^{-1}$ needs the partial derivatives of measurement function h and $\mathbf{S}_{k+1} = \mathbf{H}_{k+1} \mathbf{P}_{k+1|k} \mathbf{H}_{k+1}^T + \mathbf{W}_{k+1}$. The covariance matrix \mathbf{W}_{k+1} for static beacons is simply consisting of variances in each beacon detection, see Krejsa & Vechet (2012) for technical details. For dynamic beacons there are two variances that need to be taken into account. The one from the measurement itself and the one from the uncertain position of the dynamic beacon. The state of the beacon carrying robot is available, it consists of the mean $\hat{\mathbf{x}}_{ik}^{RB}$ and covariance matrix \mathbf{P}_{ik}^{RB} . Due to the nature of infrared beacons and corresponding receiver, the information about the angle is irrelevant, therefore the problem is narrowed to determination of the variance in position. To do so, let's extract the position information $\mathbf{x}_{ij}^{RBP} = \hat{\mathbf{x}}_{ik}^{RB} (1, 2) = [x^{RBP} \quad y^{RBP}]^T$ and $\mathbf{P}_{ik}^{RBP} = \mathbf{P}_{ik}^{RB} (1, 1) \dots \mathbf{P}_{ik}^{RB} (2, 2)$. With position of the robot we are investigating being $\mathbf{x}_k^R = \hat{\mathbf{x}}_k^R (1, 2) = [x^R \quad y^R]$, the variance is determined as:

$$\mathbf{W} = \mathbf{C} \mathbf{P}_{ik}^{RBP} \mathbf{C}^T \quad (5)$$

where matrix \mathbf{C} corresponds to unit vector perpendicular to the direction vector from the robot to dynamic beacon, calculated from the means of corresponding position estimates. In particular $\mathbf{C} = [-y^{RBP} + y^R \quad x^{RBP} + x^R]$.

4. Simulations and Results

The above described approach was implemented in Matlab and number of simulations were performed. Simulation model is based on the model developed for presentation robot Advee (Krejsa et al., 2012) and as such the model was thoroughly modified to correspond with the real robot, including the localization method. Therefore in spite the fact that following results are based on simulation only, we have high level of confidence in overall correctness.

The experiments were organized as follows. Each robot was placed on random initial position. Goals were generated for each robot randomly, whenever the goal was reached the new goal was generated. Motion planner used was simple FSM based with obstacle avoidance, including other robots, no dynamic obstacles apart from the robots were present. Four static beacons were placed in map corners and beacon detection took into account the visibility of the beacon. Independently on beacon visibility the probability of the beacon to be detected was gradually increased in $\langle 0, 1 \rangle$ interval. Dynamic beacons visibility was also taken into account and the probability of dynamic beacon to emit the signal was set to 0.5. Experiments were performed in two groups, with and without the use of dynamic beacons.

Example of localization courses with 5 robots without and with dynamic beacons is shown on left of Fig. 2. Ellipses correspond to 99% confidence interval. Localization error is clearly reduced for the case with dynamic beacons and more importantly, the size of confidential ellipses shows that uncertainty is reduced as well.

The overall results are shown on graph in right side of Fig. 2. Total of 1000 simulations were performed for each configuration. Shown results use percentage of maximum error exceeding given limit in distance error; angular error is much smaller, as the available information is angular. The improvement is obvious, however there is not much difference between 3 and 5 dynamic beacons, partially due to the uncertainty in robots position and partially due to delays in data processing caused by higher number of measurements.

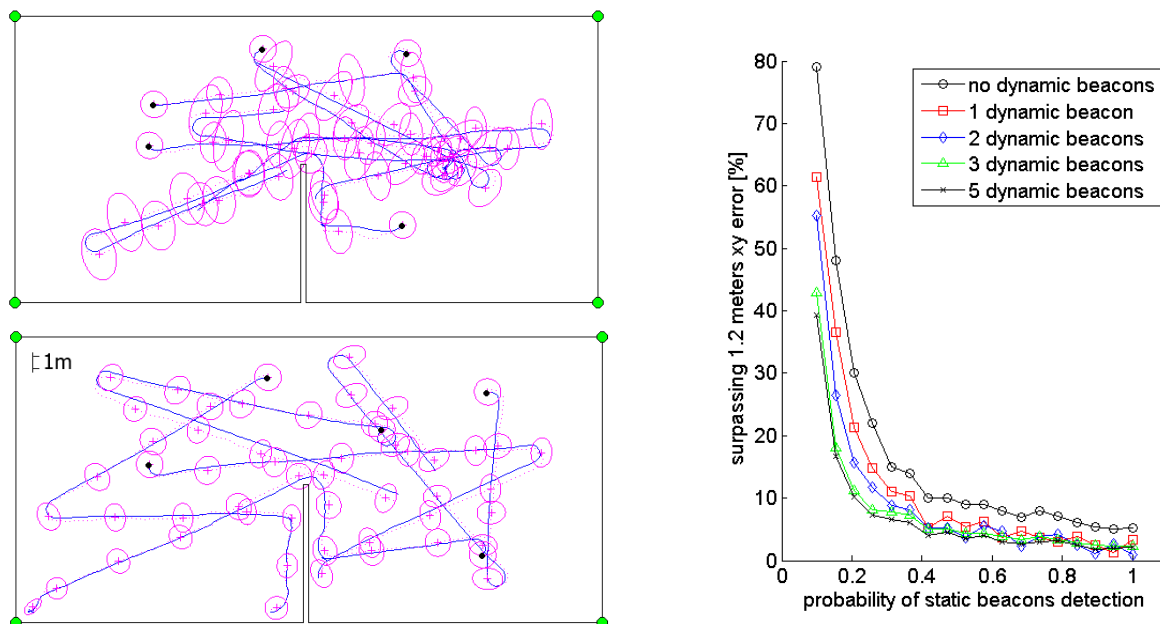


Fig. 2: Example of localization courses of individual robots, with static beacons only (top left), static+dynamic (bottom left). Quality of localization in percentage of surpassing certain maximum error.

5. Conclusions

The paper presented method improving the bearing only beacon based localization for multiple robots by introducing dynamic beacons carried by the robot themselves. Incorporation of dynamic beacon uncertainty in robot position was presented, extracting the necessary variation as linear function of 3D normal probability distribution.

The results show that improvement of precision and robustness is achieved, on the cost of higher technological demands on inter-robot communication. The method is suitable mainly for larger areas with obstacles covering certain portions of static beacons field of view.

Acknowledgement

Published results were acquired with the support of the Academy of Sciences of the Czech Republic with institutional support RVO:61388998.

References

- Krejca J., Věchet S., Hrbáček J., Ripel T., Ondroušek V., Hrbáček R., Schreiber P. (2012) Presentation robot Advee, Engineering Mechanics, Vol. 18, No. 5, pp. 1-16.
- Krejca, J., Vechet, S. (2012) Infrared beacons based localization of mobile robot, Electronics and Electrical Engineering, 1(117), pp. 17-22.
- Mao, L., Chen, J.P., Li, Z.B., Zhang, D.W. (2013) Relative Localization Method of Multiple Micro Robots Based on Simple Sensors, International Journal of Advanced Robotic Systems, Vol. 10.
- Saeedi, S., Paull, L., Trentini, M; Li, H. (2011) Neural Network-Based Multiple Robot Simultaneous Localization and Mapping, IEEE Transactions on Neural Networks, Vol. 22, Iss. 12, pp. 2376-2387.
- Park, J., Lee, J. (2011) A Beacon Color Code Scheduling for the Localization of Multiple Robots, IEEE Transactions on Industrial Informatics, Vol. 7, Iss. 3, pp. 467-475.

MORPHOMETRY AND RECONSTRUCTION OF HEPATIC LOBULES IN PIG BASED ON SERIAL HISTOLOGICAL SECTIONS

T. Kubíková^{*}, K. Witter^{**}, V. Liška^{***}, Z. Tonar^{****}

Abstract: *Aims of our study were as follows: 1) to perform a 3D reconstruction of parts of the adjacent classical hepatic lobules, 2) to compare the histomorphometric techniques available for estimating the volume of the lobules using 3D reconstruction and interactive stereological techniques, 3) to assess the volume fraction of liver parenchyma, connective tissue, and blood vessels, 4) to quantify the shrinkage in tissue blocks porcine liver. The morphometric parameters were assessed using serial histological sections and stereological methods. Volume of the sampled portions of the lobules ranged between 0.282-0.498 mm³. The volume fraction of parenchyma in liver was 0.867, the volume fraction of connective tissue was 0.077 and the fraction of blood vessels was 0.026. The mean volume shrinkage of porcine liver was 55.23%. This value can be used for correcting the data based on paraffin-processed histological sections. For further quantitative studies, we suggest the nucleator technique as a fast, robust and reliable method for estimating the volume of the lobules. For biomechanical modelling, the absolute volumes resulting from histological studies have to be corrected due to the tissue shrinkage affecting the paraffin-processed tissue samples.*

Keywords: Liver, Stereology, Volume, Point grid, Nucleator.

1. Introduction

Advanced biomechanical models of biological organs should be based on statistical morphometry of their microscopic architecture. Quantitative description of the microscopic properties of real tissues sample is an advantage when devising computer models that are statistically similar to biological tissues under physiological or pathological conditions (Králičková, 2013). Biomechanical models of liver have already proved to be useful when clarifying biological problems such as liver perfusion, ontogenetic growth, fibrosis and cirrhosis, metastatic spread, and remodeling or regeneration after surgical resection (Debbaut et al, 2014; Marcos et al., 2012). The research of the liver is often done using porcine model (Ekataksin and Wake, 1991; Králičková, 2013; Lehmann et al., 2008) due to its similarity with human liver.

Description of hepatic blood circulation gives an insight into liver pathology and may be used to inspire or modify surgical techniques as well. Corrosive vascular casts and micro-computed tomography are used for three-dimensional reconstruction of the hepatic circulation (Debbaut et al., 2014). A simplified liver microstructure may be characterized by periodically repeating morphological units known as representative volume elements (REVs). Naturally occurring REVs in liver are the classical polygonal hepatic lobules surrounding the central veins. In rat, three-dimensional (3D) reconstruction of these units revealed their volume to range between 0.094 and 0.621 mm³ (Teutsch et al., 1999).

Another morphometric parameter of liver tissue is the ratio between the functional parenchyma and the structural supporting connective tissue. This ratio may greatly vary, e.g., in hepatic fibrosis or cirrhosis. However, all 3D reconstructions and morphometric studies based on routine formalin-fixed and paraffin-embedded histological sections are biased by a significant and hardly predictable tissue shrinkage (Dorph-Petersen et al., 2001). Therefore the aims of our study were as follows: 1) to perform a 3D reconstruction

* Mgr. Tereza Kubíková: Department of Histology and Embryology and Biomedical centre, Faculty of Medicine in Pilsen, Charles University in Prague, Karlovarská 48, 301 66 Pilsen, CZ; kubikova@lfp.cuni.cz

** Priv. Doz. Dr. med.vet. Kirsti Witter, PhD.: Institute of Anatomy, Histology and Embryology, Department for Pathobiology, University of Veterinary Medicine Vienna, Vienna, Austria; Kirsti.Witter@vetmeduni.ac.at

*** MUDr. Václav Liška, PhD.: Department of Surgery, Faculty of Medicine in Pilsen and University Hospital in Pilsen, Alej Svobody 80, 304 60 Pilsen, CZ; liskav@fnplzen.cz

**** Assoc. Prof. MUDr. Mgr. Zbyněk Tonar, PhD.: European Centre of Excellence NTIS, Faculty of Applied Sciences, University of West Bohemia, Pilsen, CZ; tonar@ntc.zcu.cz

of parts of the adjacent classical hepatic lobules as REVs, 2) to compare the histomorphometric techniques available for estimating the volume of the lobules using 3D reconstruction and interactive stereological techniques, 3) to assess the volume fraction of liver parenchyma, connective tissue, and blood vessels, 4) to quantify the shrinkage in tissue blocks representing porcine liver.

2. Methods

Four tissue blocks (approx. $1 \times 1 \times 1$ cm) were taken from the liver of a healthy pig (age 14 weeks, weight 25 kg). The animal received humane care in compliance with the European Convention on Animal Care and the whole project was approved by the Faculty Committee for the Prevention of Cruelty to Animals. For 3D reconstruction, one sample was fixed in 10% formaldehyde, rinsed in 70% ethanol, and dehydrated. The cutting plane was randomized and the blocks were embedded in paraffin. The block was cut into a series of consecutive 3- μ m-thick 50 histological sections, every second of them was stained with aniline blue and nuclear fast red. All sections were photographed using a $2\times$ objective. The images were registered in order to correct the shift and rotation deviation between the serial sections using the Imagreg software (Jiri Janacek, The Academy of Sciences of the Czech Republic, Prague). Using the Polygon tool of the Ellipse software (ViDiTo, Košice, Slovak Republic), five classical lobules as well as the central veins were outlined (Figs. 1a and 1b) and their areas were recorded. Using the Surface module of the Ellipse software, a 3D model connecting the contours was rendered and used for both visualization (Figs. 1c and 1d) and quantification of the reconstructed parts of lobules.

Next, profiles of the same lobules used for reconstruction were measured using the Nucleator plugin in the Ellipse software. The nucleator method has been devised as a local stereological probe to estimate volume of objects provided that each object has a unique arbitrary point and the sections are either isotropic uniform or vertical uniform (Gundersen et al., 1998; Marcos et al., 2012). Briefly, in any n -dimensional space, the distance l between an arbitrary fixed point measure and the object boundary in any isotropic direction provides an unbiased estimate of the object content as follows:

$$\text{content} = c \cdot \overline{l^n} \quad (1)$$

where for $n = 1, 2, 3$, the content is length, area, or volume and $c = 2, \pi, \text{ or } 4\pi/3$ (Gundersen et al. 1998). In our case, a two-dimensional (2-D) nucleator was used. Therefore $n=2$ for a sample of two-dimensional isotropic uniform sections and content gives an estimate of mean area of the profile of morphological lobules. We used a 2-D nucleator probe with four isotropically oriented rays (Fig. 2c). Next, we estimated the volume of the sampled portions of classical lobules using the Cavalieri principle (Mouton, 2002) by multiplying the sum of there are as from the serial sections by the distance between the sections. We used the stereological point grid (Mouton, 2002) to quantify the volume fractions of the parenchyma, connective tissue and the blood vessels (Figs. 2a and 2b). The variation between the serial sections was assessed with use of the coefficient of error CE calculated with the quadratic approximation formula of Matheron, modified for use in a stereological context (Gundersen & Jensen, 1987).

Three tissue blocks were taken using punch biopsy (10-mm diameter) to estimate the tissue shrinkage. The dimensions of each biopsy was precisely measured using a caliper and their volume was calculated and labelled as $V(\text{primary volume})$. The samples were fixed in 10% formaldehyde, rinsed in 70% ethanol, dehydrated and routinely embedded in paraffin. Tissues blocks were exhaustively cut into series of consecutive 5- μ m-thick histological sections, every tenth section was stained with hematoxylin and eosin. The volume of each processed tissue block $V(\text{volume_after_processing})$ was estimated using the stereological point grid (Fig. 2d) and Cavalieri principle. The volume shrinkage was calculated using the formula $1 - V(\text{volume_after_processing})/V(\text{primary})$.

3. Results and Discussion

Volume of the sampled portions of the classical lobules ranged between 0.282 mm^3 and 0.498 mm^3 .

The volume fraction of parenchyma in liver was 0.867 (CE = 0.009), the volume fraction of connective tissue in liver was 0.077 (CE = 0.021) and the fraction of blood vessels in liver was 0.026 (CE = 0.021).

The volume shrinkage was 56.8% in sample #1, 59.4 in sample #2, and 49.5% in sample #3. The mean volume shrinkage of porcine liver was 55.23%. Shrinkage of hepatic tissue was substantial, probably due to the large blood supply. This value can be used for correcting the data based on paraffin-processed

histological sections. The final volume of the structures before histological processing $V(final)$ can be calculated as $V(final)=V(primary\ volume)*(1-volume\ shrinkage)$.

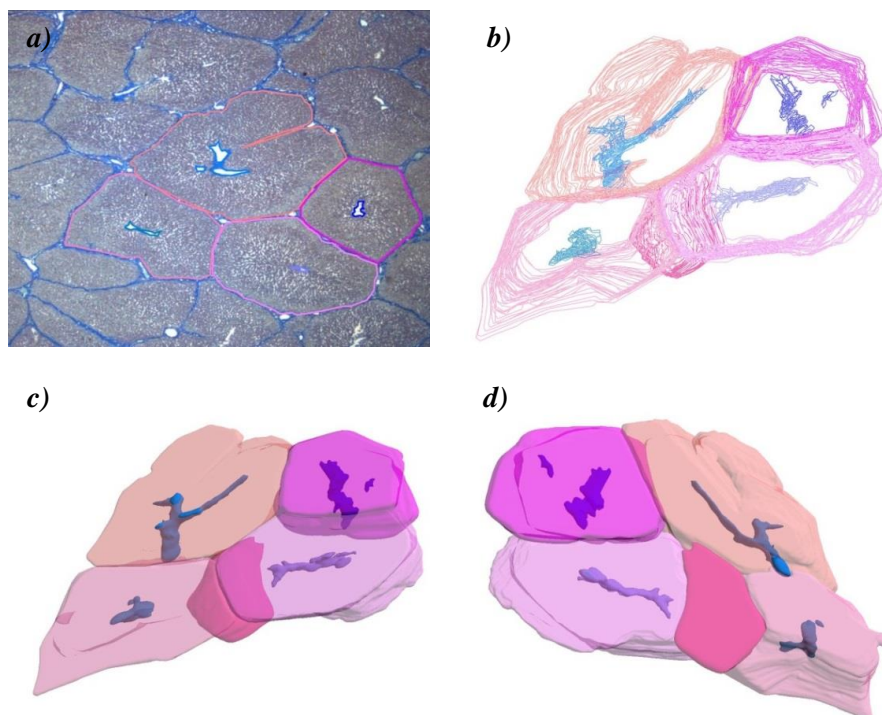


Fig. 1: Three-dimensional reconstruction of hepatic lobules: a) Tracing the contours; b) 3D view of the contours; c), d) 3D reconstruction of classical lobules and their central veins.

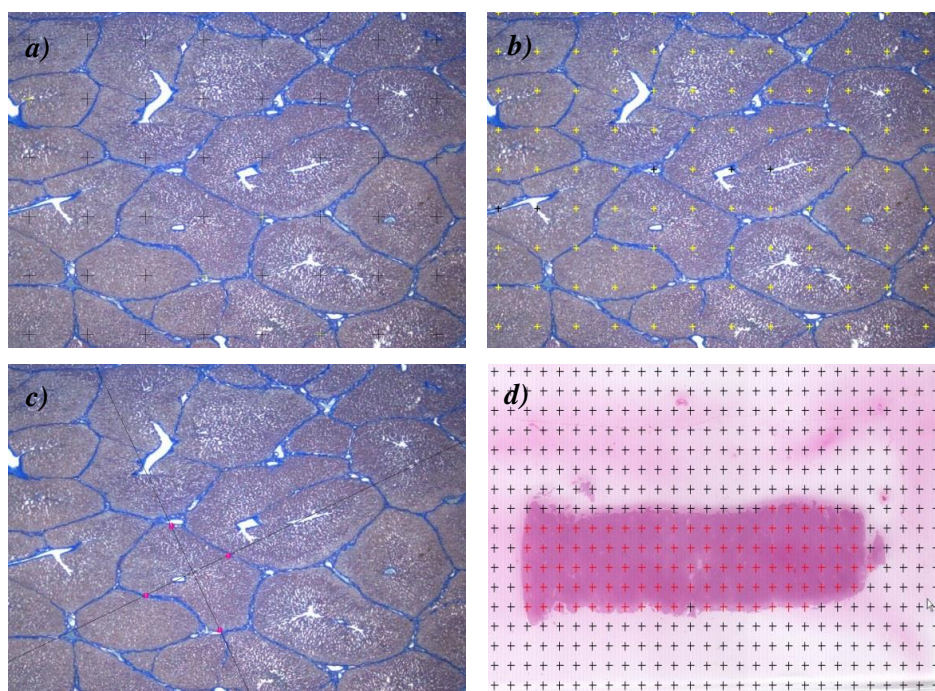


Fig. 2: Estimating volumes and areas using stereological point grid (a),b,d)) and the nucleator technique (c): a) – Points hitting the interlobular connective tissue were marked yellow and used for estimating the volume fraction of the connective tissue. Each point represents the same predetermined area. B) Points hitting the functional parenchyma were labelled yellow. c) The sectional area of a lobule quantified using a two-dimensional nucleator probe with four isotropically oriented rays. The intersections of the probe rays with the borders of the lobule are marked. d) Using point grid for quantifying the volume after histological the processing to quantify the tissue shrinkage.

Tab. 1: Volume of sampled portions of hepatic lobules assessed by three methods: planimetry ($V(\text{contours})$), 3D reconstruction ($V(3D)$) and the nucleator method ($V(\text{nucleator})$). The variability of the volume estimates is characterized by the coefficient of error (CE).

	$V(\text{contours})$ [mm ³]	CE (contours)	$V(3D)$ [mm ³]	$V(\text{nucleator})$ [mm ³]	CE (nucleator)
lobule#1	0.498	0.008	0.493	0.491	0.017
lobule#2	0.282	0.009	0.279	0.275	0.017
lobule#3	0.372	0.008	0.366	0.363	0.014
lobule#4	0.305	0.008	0.299	0.297	0.010
lobule#5	0.050	0.020	0.046	0.472	0.037

4. Conclusions

Using 3D reconstruction and stereological methods, we visualized portions of five adjacent classical hepatic lobules and the corresponding central veins, thus partially demonstrating their spatial relations. We compared three techniques for estimating the volume of the lobules. For further quantitative studies, we suggest the nucleator technique as a fast, robust and reliable method. Next, we quantified the volume fractions of the major constituents of the liver, namely the functional parenchyma, the connective tissue, and the blood vessels. For biomechanical modelling, the absolute volumes resulting from histological studies have to be corrected due to the tissue shrinkage affecting the paraffin-processed tissue samples.

Acknowledgement

Supported by the project ED2.1.00/03.0076 and partially funded by the Charles University in Prague, Project No. SVV 266801 and Project No. P36.

References

- Debbaut, C., Segers, P., Cornillie, P., Casteleyn, C., Dierick, M., Laleman, W., Monbaliu, D. (2014) Analyzing the human liver vascular architecture by combining vascular corrosion casting and micro-CT scanning: a feasibility study. *Journal of Anatomy*. In Press, doi: 10.1111/joa.12156.
- Dorph-Petersen, K.A., Nyengaard, J.R., Gundersen, H.J. (2001) Tissue shrinkage and unbiased stereological estimation of particle number and size. *Journal of Microscopy*, 204, pp. 232-246.
- Ekataksin, W., Wake, K. (1991) Liver units in three dimensions: I. Organization of argyrophilic connective tissue skeleton in porcine liver with particular reference to the "compound hepatic lobule." *American Journal of Anatomy*, 191, pp. 113-153.
- Gundersen, H.J., Bagger, P., Bendtsen, T.F., Evans, S.M., Korbo, L., Marcussen, N., Moller, A., Nielsen, K., Nyengaard, J.R., Pakkenberg, B. (1988) The new stereological tools: disector, fractionator, nucleator and point sampled intercepts and their use in pathological research and diagnosis. *Acta Pathologica, Microbiologica et Immunologica Scandinavica*, 96, pp. 857-881.
- Gundersen, H.J., Jensen, E.B. (1987) The efficiency of systematic sampling in stereology and its prediction. *Journal of Microscopy*, 147, pp. 229-263.
- Králíčková, A. (2013) Quantification of Liver Microcirculation Using X-Ray Microtomography of Vascular Corrosion Casts. *Key Engineering Materials*, pp. 505-508.
- Lehmann, K.S., Ritz, J.-P., Valdeig, S., Schenk, A., Holmer, C., Peitgen, H.-O., Buhr, H.-J., Frericks, B.B. (2008) Portal vein segmentation of a 3D-planning system for liver surgery--in vivo evaluation in a porcine model. *Annals of Surgical Oncology*, 15, pp. 1899-1907.
- Marcos, R., Monteiro, R.A., Rocha, E. (2012) The use of design-based stereology to evaluate volumes and numbers in the liver: a review with practical guidelines. *Journal of Anatomy*, 220, pp. 303-317.
- Mouton, P.R. (2002) *Principles and Practices of Unbiased Stereology. An Introduction for Bioscientists*, The Johns Hopkins University Press, Baltimore.
- Teutsch, H.F., Schuerfeld, D., Groezinger, E. (1999) Three-dimensional reconstruction of parenchymal units in the liver of the rat. *Hepatology (Baltimore, Md.)*, 29, pp. 494-505.

A COMPUTATIONAL MODEL OF POWERTRAIN COMPONENTS IN SIMULINK

P. Kučera^{*}, V. Pištěk^{**}

Abstract: *The article deals with the development of a computational model of an engine, a transmission and a clutch. These parts of the powertrain were created using blocks from the libraries of the Simulink software while the input parameters for individual components were set on the basis of constructional CAD documentation of the vehicle. The creation of the computational model is described and some of the results of the Simulink simulations are presented. Furthermore, examples of the simulations of gear ratio change and cranktrain torsional vibration analysis are shown at the end of this article.*

Keywords: Diesel Engine, Torsion Model, Transmission, Clutch, Computational Model, Simulink.

1. Introduction

In order to accelerate the development and lower the expenses of prototype realization, advanced computational models of a vehicle's powertrain are used with rising frequency. As a result, the problems often associated with the first prototype running can be significantly reduced. Nowadays, software developers offer many different forms of development support for computational models, including some well-equipped libraries which make the creation of various model parts easier.

This article deals with the creation of computational models of parts included in a heavy commercial vehicle's powertrain. The following chapters describe the creation of engine computational models and transmission computational models meant to represent the 8-cylinder diesel engine and the accompanying transmission in the vehicle. The aim was to develop computational models which are able to simulate the relevant part of a powertrain with a sufficient level of detail, including torsional vibrations. The models assembled have a modular structure and will be gradually enhanced by models of powertrain additional substructures, which will allow real-time simulations of the complex model and the development of mechatronical systems for this vehicle.

The model was assembled using the Simulink software environment, which can serve for the creation of own computational models and simulation calculations, including real-time simulations. In the article there are described two examples computations which simulate a cranktrain torsional vibrations and the process of gear ratio change.

2. Fundamental Input Parameters for Computational Model Creation

The input parameter for a computational engine model is the course of indicated pressure inside a cylinder. From this pressure, the engine torque can be calculated (Kožoušek, 1983). Therefore, a script to create a 3D matrix of the engine torque depicted in Fig. 1a was written in the Matlab software. The dimensions of the matrix are 13x720x2 and it is composed of two 2D matrices which represent the maximum and minimum fuel supply. 13 rows of the 2D matrix contain engine torque curves during one working cycle which corresponds to the engine speed range from 800 rpm to 2 000 rpm. Consequently, the resulting engine torque value is determined by the crank angle, engine speed and fuel supply.

* Ing. Pavel Kučera: Brno University of Technology, Faculty of Mechanical Engineering, Institute of Automotive Engineering, Technická 2896/2, 616 69 Brno, CZ, kucera@iae.fme.vutbr.cz

** Prof. Ing. Václav Pištěk, DSc.: Brno University of Technology, Faculty of Mechanical Engineering, Institute of Automotive Engineering, Technická 2896/2, 616 69 Brno, CZ, pistek.v@fme.vutbr.cz

In order to allow the computational engine model to perform also a torsional vibrations analysis, it was devised as a dynamic torsional system. The motion equations obtained according to the Lagrangian method are written as

$$M\ddot{\varphi} + K\dot{\varphi} + C\varphi = T(t) \quad (1)$$

where the vector of generalised coordinates φ contains angular displacements of system elements, M is the mass matrix, C is the stiffness matrix, K is the damping matrix and $T(t)$ is the vector of excitation engine torques. The input parameters of the computational engine model are the values of the moments of inertia, torsional stiffness values and damping coefficient values. The kinetic energy of the reciprocating masses depends on the crank angle. For the calculation of the mass matrix is used the mean value, so the mass matrix elements are constant. The damping coefficient values were set according to the measurement results on a similar powertrain. The calculation of the eigenfrequencies is carried out as an eigenvalue problem according to the literature (Píštěk & Štětina, 1993).

The computational model of a clutch which transfers the engine torque can be assembled in two ways, both described in (Budynas & Nisbett, 2006). One follows the even clutch wear assumption, while the other uses the assumption of even pressure distribution on the clutch friction lining. In this computational model, the even wear assumption was adopted. The transmission of a heavy commercial vehicle is composed of several parts. The first one is a gearbox, where normal and reduction gears are changed. The second one is the main gearbox used for the selection of 5 forward gear ratios and 1 reverse gear ratio. The main gearbox is followed by an auxiliary gearbox with 2 further gear ratios which further enhance the gear ratio range. The driver can therefore choose from 7 forward gear ratios. The first 5 are selected in the main gearbox and the additional 6th and 7th are selected as a combination of main and auxiliary gearboxes' ratios. The input parameters are the individual gear ratio values, moments of inertia of rotating components, torsional stiffness of the shafts and values describing synchronizers, as they are also included in the computational transmission model. To define the torque transfer through the synchronizer, the same two assumptions applicable for the clutch can be used. For the computational model, the even wear assumption was used in this case as well. The model also describes the forces transferred by the spring through the ball contained in the synchronizer to increase the accuracy of the simulation. The equations for the synchronizer calculations are described in details in (Budynas & Nisbett, 2006).

3. Computational Models

Individual computational models were assembled from the basic blocks included in Simulink software libraries. The user guide and tutorials for modelling in Simulink were gathered from (Dabney & Harman, 2004; Grepl, 2007). The computational models of the powertrain contain many modules, only some of which will be mentioned here, namely the engine and transmission subsystems models.

3.1. Computational model of the engine

The structure of the computational engine model is presented in Fig. 1b. Fundamental parts of the model are blocks which describe the parameters of rotational parts and torsional springs and a torque generator.

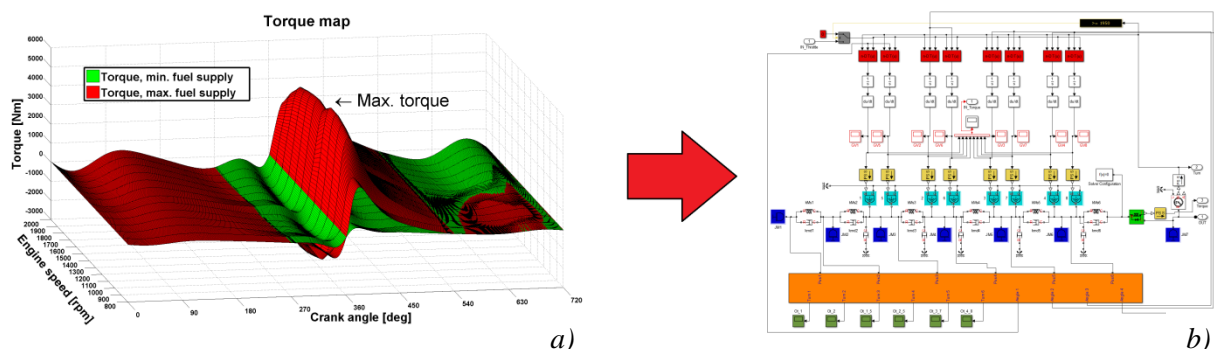


Fig. 1: Input values and computational model of the engine.

Using these blocks, a torsional system is assembled as a dynamic model of a real engine. The 3D matrices defined in Chapter 2 are connected to the mentioned blocks generating the torque in the torsional system. This torsional model enables to determine the rotational speeds of parts during the simulation. Therefore

the speed sensor is placed at the engine output and the value serves as an input to the 3D matrix. The orange submodel in Fig. 1b reports the exact crank angle value which is the second input to the 3D matrix. The last input is the accelerator pedal position which is controlled by the user. Using these inputs, the torque on each crank throw can be calculated. Individual 3D matrices are also shifted according to the ignition sequence of the engine cylinders.

3.2. Computational model of the transmission

The computational transmission model is composed of blocks similar to those used in the engine model. It contains blocks representing rotational parts, synchronizers, gears and other elements which serve to control the selection of individual gear ratios. On the other hand, this model does not contain torsional springs as the loaded shaft length depends on various gear ratios; therefore, the torsional stiffness is not constant. However, these torsional stiffnesses as well as gear couplings are by orders of magnitude higher than the other shafts in the powertrain.

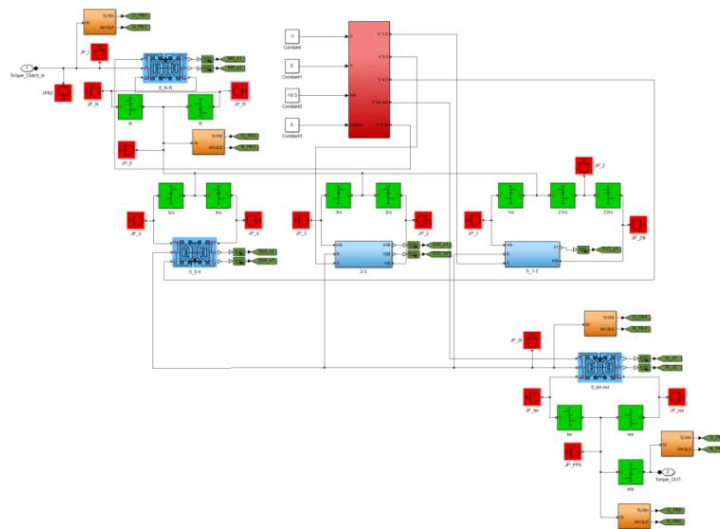


Fig. 2: Computational model of the transmission.

4. Examples of Computational Simulations

Computational models were used to perform braking simulations of the engine with and without the transmission connected to a virtual dynamometer. In the following subchapters the results of engine torsional vibrations simulation and gear change simulation are presented.

4.1. Torsional vibrations simulation

The simulation was carried out with fixed throttle position. The engine speed settled at 1 487 rpm and the torque at the engine output was being monitored and subsequently processed by the Fourier Transform with Hann window according to (Zaplatilek & Doňar, 2006). The results are the harmonic components of the resulting engine torque measured after the flywheel.

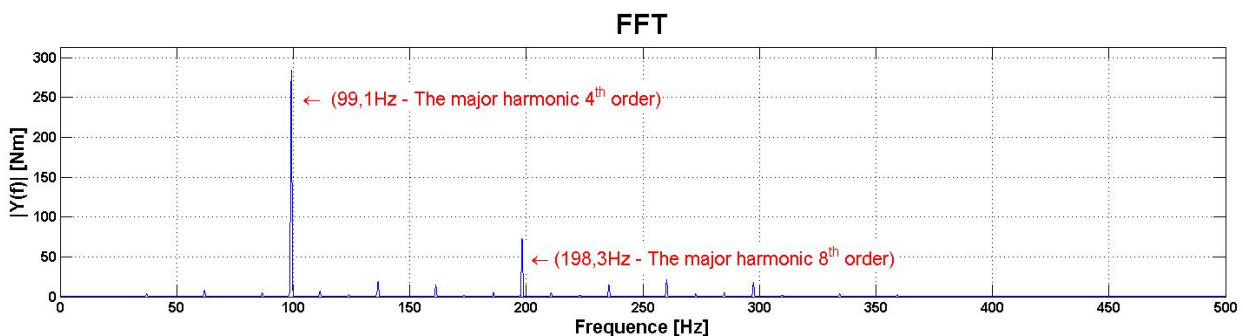


Fig. 3: FFT analysis of engine torque at 1 487 rpm.

4.2. Gear change simulation

In order to conduct the gear change simulation, engine and transmission computational model were joined together and controlled by additional algorithm, which simulates gradual rise of engine speed followed by a clutch pedal depression, engine speed drop and gear change. The clutch pedal is then let loose and the engine speed rises again. This is repeated until the highest gear is selected. Resulting engine speed curves and transmission output speed curves are given in Fig. 4.

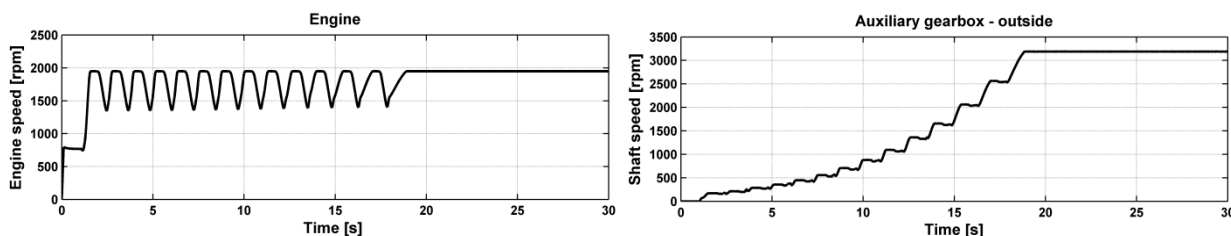


Fig. 4: Speed curves of individual driveline parts.

5. Conclusions

The computational models of an engine, a transmission and a clutch were assembled using the blocks from the libraries of Simulink software. The aim was to create computational models able to represent real parts of a vehicle powertrain of known construction parameters with sufficient accuracy.

In the second chapter, the description of input parameter preparation is given, while the third chapter presents the main subsystems of computational models and their assembly in the Simulink environment. The final chapter then describes selected simulations of an engine and a gear change. The results prove that the behaviour of these models is correct.

The described computational models will be enhanced by further modules in the future, which will allow the simulation of the whole powertrain of a commercial vehicle. This complex computational model will then be used for the development of mechatronical systems aimed at commercial vehicles' powertrains and undercarriages. It will also be possible to run the simulations in real-time. Some of these have already been run using the real-time testing hardware supplied by National Instruments.

Acknowledgement

This work is an output of research and scientific activities of NETME Centre, regional R&D centre built with the financial support from the Operational Programme Research and Development for Innovations within the project NETME Centre (New Technologies for Mechanical Engineering), Reg. No. CZ.1.05/2.1.00/01.0002 and, in the follow-up sustainability stage, supported through NETME CENTRE PLUS (LO1202) by financial means from the Ministry of Education, Youth and Sports under the „National Sustainability Programme I“.

References

- Budynas, R. G., Nisbett, J. K. (2006) Shigley's Mechanical Engineering Design. 9st ed. United States of America: The McGraw Hill Companies, 1059 p. ISBN 0-390-76487-6.
- Dabney, J B., Harman T. L. (2004) Mastering Simulink. Upper Saddle River: Pearson Prentice Hall, 376 p., ISBN 0-13-142477-7.
- Grepl, R. (2007) Modeling of mechatronic systems in Matlab SimMechanics. 1st ed. Prague: BEN, 151 p., ISBN 978-80-7300-226-8, (in Czech).
- Kožoušek, J. (1983) Calculation and construction of combustion engines II. 1st ed. Prague: SNTL, 483 p., (in Czech).
- Píštěk, V., Štětina, J. (1993) Strength and durability. 1st ed. Brno: VUT Brno, 205 p., ISBN 80-214-0474-4, (in Czech).
- Zaplátilek, K., Doňar, B. (2006) MATLAB: Getting Started with signals. 1st ed. Prague: BEN, 271 p., ISBN 80-7300-200-0, (in Czech).

STOCHASTIC MODELLING OF HETEROGENEOUS MATERIALS BASED ON IMAGE ANALYSIS

A. Kučerová^{*}, J. Sýkora^{**}, J. Zeman^{***}

Abstract: *Macroscopically heterogeneous materials, characterized mostly by comparable heterogeneity lengthscale and structural sizes, can no longer be modelled by deterministic approach. It is convenient to introduce stochastic approach with uncertain material parameters quantified as random fields. Nevertheless, introduction of random fields brings higher demands on quality of input data, especially on inputs of covariance functions representing the spatial randomness. The present contribution is devoted to the construction of random fields based on image analysis utilizing statistical descriptors, which were developed to describe the different morphology of two-phase random material. The whole concept is demonstrated on a simple numerical example of stationary heat conduction where interesting phenomena can be clearly understood.*

Keywords: Stochastic finite element method, Random fields, Two-point probability density function, Covariance function.

1. Introduction

Nowadays, the stochastic finite element method (SFEM) is very popular approach to modelling of heterogeneous materials. SFEM is an extension of the classical deterministic finite element approach to the stochastic framework i.e. to the solution of stochastic (static and dynamic) problems involving finite elements whose properties are random, see (Stefanou, 2009). The Monte Carlo (MC) method is the most widely used technique in simulating of these problems. Unfortunately, MC simulations require thousands or millions samples because of relatively slow convergence rate, thus the total cost of these numerical evaluations quickly becomes prohibitive. To meet this concern, the surrogate models based on the polynomial chaos expansion (PCE), see (Xiu & Karniadakis, 2002), were developed as promising alternative. The PC-based surrogates are constructed by different fully-, semi- or non-intrusive methods based on the stochastic Galerkin method (Ghanem & Spanos, 2012; Matthies 2010), stochastic collocation (SC) method (Babuška et al., 2004; Xiu, 2009) or DoE (design of experiments)-based linear regression (Blatman & Sudret, 2010).

When the input parameters are defined as random fields, the additional mathematical formulations are introduced to describe the spatial randomness. The Karhunen-Loève expansion (KLE) allow for representation of random fields utilising surprisingly few orthogonal modes from spectral decomposition of covariance matrix, see (Adler & Taylor, 2007). Several analytical covariance functions (CF) were created to describe the spatial covariance, but their relevance in describing real material properties remains questionable and poorly justified. Therefore, relatively new concepts of extracting the spatial covariance from images were established, see (Soize, 2006; Jürgens et al., 2012). Here, we propose a novel construction of CF obtained from two-point probability density function, which is calculated from the given image.

* Ing. Anna Kučerová, PhD.: Czech Technical University in Prague, Faculty of Civil Engineering, Thákurova 7, 166 29, Prague, CZ, anicka@cml.fsv.cvut.cz

** Ing. Jan Sýkora, PhD.: Czech Technical University in Prague, Faculty of Civil Engineering, Thákurova 7, 166 29, Prague, CZ, jan.sykora.1@fsv.cvut.cz

*** Assoc. Prof. Ing. Jan Zeman, PhD.: Czech Technical University in Prague, Faculty of Civil Engineering, Thákurova 7, 166 29, Prague, CZ, zemanj@cml.fsv.cvut.cz

2. Methodology

Due to the lack of space it is impossible to introduce whole methodology. Therefore, we focus here only on the construction of random fields. Other topics, such as implementation of heat conduction problem into the stochastic framework using the stochastic Galerkin are presented elsewhere; see (Kučerová & Matthies, 2010; Kučerová et al., 2012). As a preamble, we utilise KLE for modelling the spatial randomness. Based on the spectral decomposition of covariance function $C(\mathbf{x}, \mathbf{x}')$ and the orthogonality of eigenfunctions ϕ_i , the real-valued random field $\lambda(\mathbf{x}, \omega)$ truncated after M terms can be written as

$$\lambda(\mathbf{x}, \omega) \approx \mu_\lambda(\mathbf{x}) + \sum_{i=1}^M \sqrt{\zeta_i} \xi_i(\omega) \phi_i(\mathbf{x}), \quad (1)$$

where $\mu_\lambda(\mathbf{x})$ is the mean value, ζ_i are the positive eigenvalues and $\xi(\omega)$ is a set of uncorrelated random variables of zero mean and unit variance. It is obvious that the CF plays a key role in the construction of random field. Therefore, we introduce following relations: The first two belong to classical analytical approaches and third one is a novel strategy utilizing the information from images:

- Gaussian CF in two-dimensional space is given as

$$C(\mathbf{x}, \mathbf{x}') = \sigma_\lambda^2 \exp\left(-\frac{(x-x')^2}{2L_x^2} - \frac{(y-y')^2}{2L_y^2}\right), \quad (2)$$

where $\mathbf{x} = (x, y)$ and $\mathbf{x}' = (x', y')$ are arbitrarily chosen two points, σ_λ^2 is the variance of $\lambda(\mathbf{x}, \omega)$ and $\mathbf{L} = (L_x, L_y)$ are the correlation lengths.

- Exponential CF is defined as

$$C(\mathbf{x}, \mathbf{x}') = \sigma_\lambda^2 \exp\left(-\left|\frac{x-x'}{L_x}\right| - \left|\frac{y-y'}{L_y}\right|\right). \quad (3)$$

Image-based CF – here we focus in particular on two-point probability function $S_2(\mathbf{x}, \mathbf{x}')$, see (Torquato, 2002), and two-phase medium with constant value $\lambda^{(i)}$ over the domain of the phase (i). According to (Lombardo et al., 2009), the CF is derived as

$$C(\mathbf{x}, \mathbf{x}') = \left(S_2^{(1)}(\mathbf{x}, \mathbf{x}') - (c^{(1)})^2\right) (\lambda^{(1)} - \lambda^{(2)})^2, \quad (4)$$

where $c^{(1)}$ is volume fraction of the phase (1).

3. Numerical Example

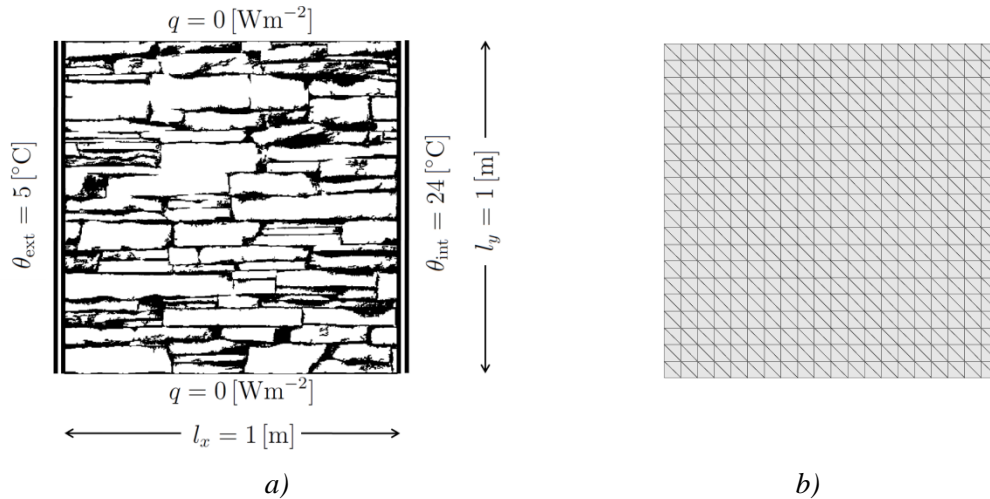


Fig. 1: a) Heterogeneous structure with boundary conditions (θ is the temperature [$^\circ\text{C}$], q is the heat flux [Wm^{-2}] and l is the length [m]) and b) its finite element discretisation with 441 FE nodes.

This section supports the proposed methodology through numerical study of heat conduction problem in irregular masonry, where energy balance equation leads to

$$-\nabla \cdot (\lambda(x) \nabla \theta(x)) = f(x), \quad x \in \mathcal{G} \subset \mathbb{R}^2, \quad (5)$$

$$\theta(x) = g(x), \quad x \in \partial \mathcal{G}, \quad (6)$$

where θ is a temperature, f stands for a head source or sink and g is a prescribed boundary conditions. Thermal conductivity is assumed to be $\lambda^{(1)} = 1.9 \text{ Wm}^{-1}\text{K}^{-1}$ for bricks (white phase) and $\lambda^{(2)} = 0.9 \text{ Wm}^{-1}\text{K}^{-1}$ for mortar (black phase). We consider the geometry obtained from a photograph of irregular masonry. Its black-and-white variant together with the loading conditions is depicted in Fig. 1a, while the employed finite element discretisation is given in Fig. 1b.

While the image-based CF is fully defined by the image and conductivity in particular phases, the Gaussian and exponential CFs need a calibration of correlation lengths L_x and L_y and variance σ_λ^2 . Moreover, the expansion of the field in Eq. (1) also requires mean value μ_λ . The latter two moments can be obtained simply as mean and variance of conductivity values $\lambda^{(1)}$ and $\lambda^{(2)}$ prescribed to both phases weighted by their corresponding volume fractions $c^{(1)}$ and $c^{(2)}$. Determination of correlation lengths is, however, not trivial and commonly requires some expert knowledge about the modelled material. Here we exploit our knowledge about image-based CF and optimise the values of correlation lengths so as to fit the analytical CFs to the one obtained from image. The optimisation process resulted in $L_x = 47.6 \text{ mm}$ and $L_y = 4.07 \text{ mm}$ in case of Gaussian CF and $L_x = 83.3 \text{ mm}$ and $L_y = 5.69 \text{ mm}$ in case of exponential CF. The shape of resulting CFs is shown in Fig. 2, where inadequacy of Gaussian or exponential approximation of image-based CF is clearly visible.

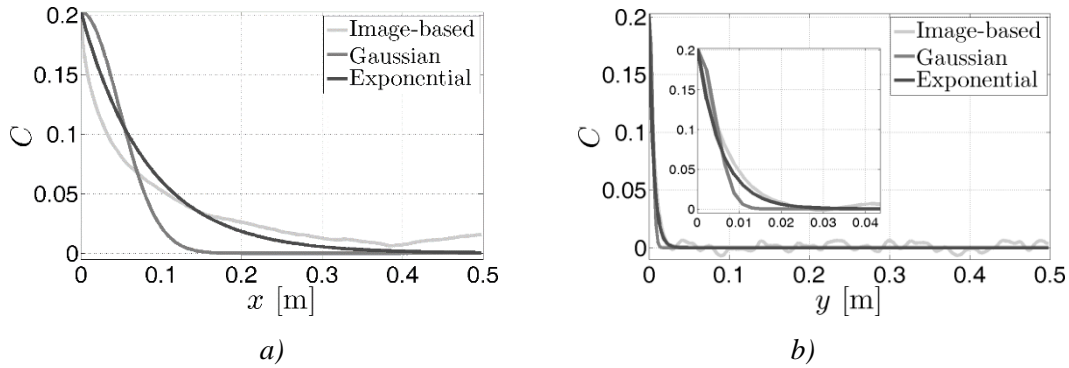


Fig. 2: CFs corresponding to given microstructure: a) Cut along the axis x ; b) Cut along the axis y .

The impact on the shape of random field is given by shape of particular eigenfunctions, which are depicted in Fig. 3. One can see the low oscillation of first eigenfunctions obtained from Gaussian and exponential CFs, while the image-based eigenfunctions clearly describe higher frequencies.

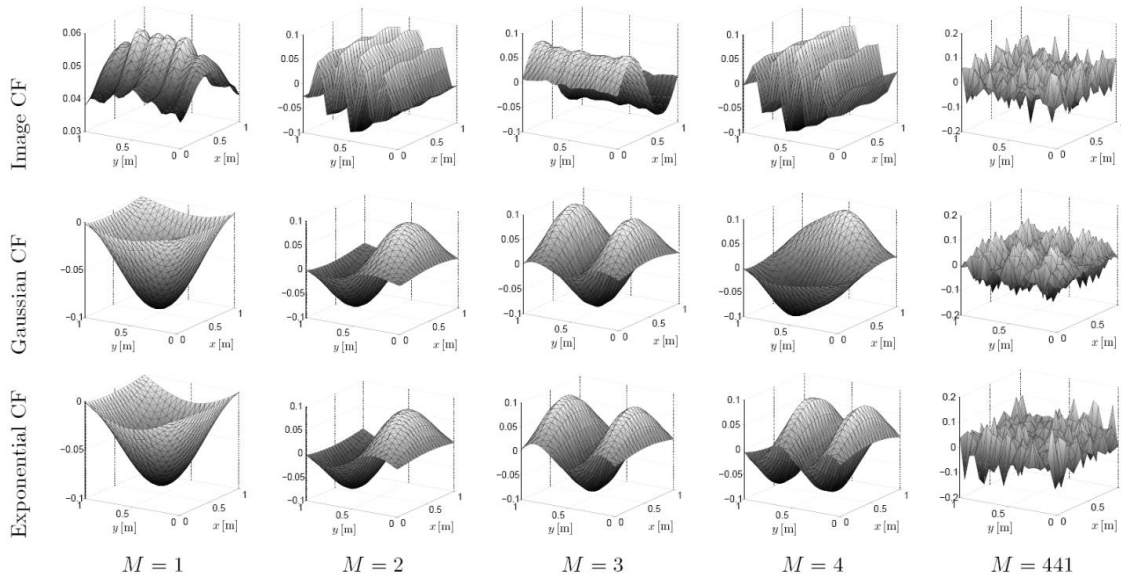


Fig. 2: KL modes ($M = 1, M = 2, M = 3, M = 4, M = 441$) for given CFs.

Finally, we computed the relative error of temperature fields defined as

$$\epsilon(\theta) = \frac{\|\theta_M - \theta_{441}^{\text{image}}\|_{L^2(\mathcal{G} \times \Omega)}}{\|\theta_{441}^{\text{image}}\|_{L^2(\mathcal{G} \times \Omega)}}, \quad (7)$$

where θ_M denotes the temperature field obtained using a given CF described by M modes, $\theta_{441}^{\text{image}}$ denotes the temperature field obtained using image-based CF and all 441 modes, and l^2 is the Euclidean norm computed over the spatial domain \mathcal{g} and stochastic domain Ω discretized into 1000 randomly generated realisations of random variables $\xi(\omega)$. The evolution of resulting errors is shown in Fig. 4 with remarkable divergence of errors obtained using Gaussian and exponential CFs.

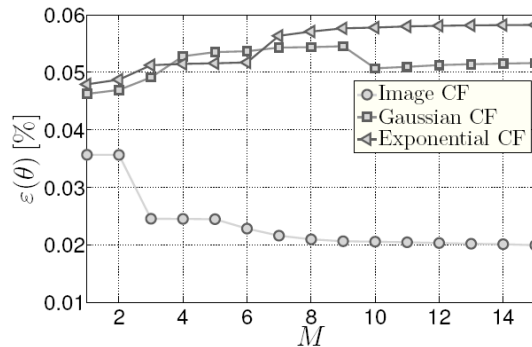


Fig. 3: Relative error of temperature.

4. Conclusions

In this contribution, we present different strategies for construction of random fields. A comparison of classical approach based on the analytical CFs and a novel methodology based on image analysis was shown to assess the quality and accuracy of obtained random fields. The whole concept was demonstrated on the stationary heat conduction problem with spatial random material parameters.

Acknowledgement

This outcome has been achieved with the financial support of the Czech Science Foundation, project Nos. 105/11/P370 and 105/12/1146.

References

- Adler, R. J., Taylor, J. E. (2007) Random Fields and Geometry. Springer, 2007.
- Babuška, I., Tempone, R., Zouraris, G. E. (2004) Galerkin Finite Element Approximations of Stochastic Elliptic Partial Differential Equations. SIAM Journal on Numerical Analysis, 42, 2, pp. 800-825.
- Blatman, G., Sudret, B. (2010) An adaptive algorithm to build up sparse polynomial chaos expansions for stochastic finite element analysis. Probabilistic Engineering Mechanics, 25, 2, pp. 183-197.
- Ghanem, R. G., Spanos, P. D. (2012) Stochastic Finite Elements: A Spectral Approach. Dover Publications.
- Jürgens, D., Krosche, M., Niekamp, R. (2012) A Process for Stochastic Material Analysis based on Empirical Data. Technische Mechanik, 32, 2-5, pp. 303-306.
- Kučerová, A., Sýkora, J., Rosić, B., Matthies, H. G. (2012) Acceleration of uncertainty updating in the description of transport processes in heterogeneous materials. Journal of Computational and Applied Mathematics, 236, 18, pp. 4862-4872.
- Kučerová, A., Matthies, H. G. (2010) Uncertainty updating in the description of heterogeneous materials. Technische Mechanik, 30, 1-3, pp. 211-226.
- Lombardo, M., Zeman, J., Šejnoha, M., Falsone, G. (2009) Stochastic modeling of chaotic masonry via mesostructural characterization. Int. Journal for Multiscale Computational Engineering, 7, 2, pp. 171-185.
- Matthies, H. G. (2010) Encyclopedia of Computational Mechanics, chap. Uncertainty Quantification with Stochastic Finite Elements. John Wiley & Sons, Ltd., 2007.
- Soize, C. (2006) Non-Gaussian positive-definite matrix-valued random fields for elliptic stochastic partial differential operators. Computer Methods in Applied Mechanics and Engineering, 195, pp. 26-64.
- Stefanou, G. (2009) The stochastic finite element method: Past, present and future. Computer Methods in Applied Mechanics and Engineering, 198, 9-12, pp. 1031-1051.
- Torquato, S. (2002) Random heterogeneous materials: Microstructure and macroscopic properties. Springer-Verlag.
- Xiu, D., Karniadakis, G. E. (2002) The Wiener Askey Polynomial Chaos for Stochastic Differential Equations. SIAM Journal on Scientific Computing, 24, 2, pp. 619-644.
- Xiu, D. (2009) Fast Numerical Methods for Stochastic Computations: A Review, Communications in Computational Physics, 5, 2-4, pp. 242-272.

PERFORMANCE COMPARISON OF LOCALIZATION LIMITERS

J. Květoň*, J. Eliáš**

Abstract: *It is well known, that simulation of crack propagation using the finite element method is dependent on mesh discretization. The contribution compares two approaches that are designed to reduce the mesh influence: (I) the crack band model and (II) the nonlocal model. These localization limiters are applied to simulate three-point-bent beam with and without notch. The model of the beam is made with several variants of mesh discretization differing in finite element size and inclination. Performance of both localization limiters is discussed.*

Keywords: Quasi-brittle materials, Strain softening, Localization, Crack band model, Nonlocal model.

1. Introduction

Behaviour of quasi-brittle materials is usually represented in FEM software by material models with strain-softening. When using such a model, after reaching the tensile strength, strain continues to increase while stress decreases. In consequence, crack localizes into a band of width of one finite element and computed results become dependent on mesh discretization. There are several approaches that try to avoid such an unwanted behaviour. The most known are the Crack band model (Bažant & Oh, 1983) and Nonlocal model (Jirásek, 1998). Both approaches should theoretically ensure correct energy dissipation during the crack propagation and therefore also similar load-deflection response of FEM models irrespectively of chosen discretization.

Desired independency is unfortunately hard to achieve in reality, especially when the crack is inclined from the mesh direction. This contribution shows performance of both localization limiters on simulation of three-point-bending test with and without central notch using several variant of mesh discretization.

2. Model of the Beam

The approaches are compared on a model of the three-point-bent beam. The beam dimensions are following: span $s = 400$ mm, total length $l = 1.1 \times s = 440$ mm, depth and thickness are both $D = t = 100$ mm. If notch is present, its depth is $1/3$ of beam depth D .

Three element meshes differing in density of the discretization were generated for each beam variant (with and without the notch). The element size was chosen as 10, 5 and 2.5 mm, respectively. Another three element meshes for each beam variant were made to study effect of inclined mesh, and were inclined by angle of 30, 45 and 60 degrees. The element size for the inclined meshes was 5 mm. Some of the meshes are shown in Fig. 1.

The loading was done via prescribed deformation at two nodes above the beam center. The two nodes were necessary to ensure symmetric boundary condition. The total loading force F was measured as sum of forces at the loaded nodes, deflection d was taken as an average of vertical movement of two nodes at the bottom surface at the midspan.

* Josef Květoň: Institute of structural mechanics, Brno University of technology, Faculty of civil engineering, Veveří 331/95; 602 00, Brno; CZ, kvetonj@study.fce.vutbr.cz

** Ing. Jan Eliáš, PhD.: Institute of structural mechanics, Brno University of technology, Faculty of civil engineering, Veveří 331/95; 602 00, Brno; CZ, elias.j@fce.vutbr.cz

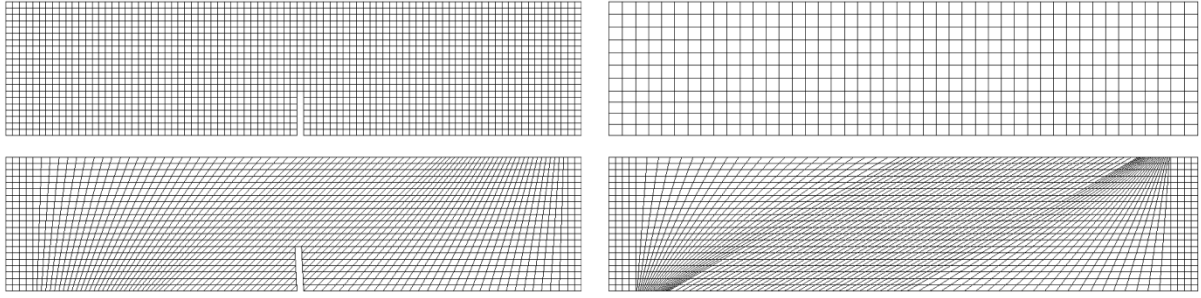


Fig. 1: Examples of straight and inclined meshes with and without notch.

Material parameters were chosen to represent behaviour of concrete in tension: Young's modulus $E = 30$ GPa, tensile strength $f_t = 2.5$ MPa, Poisson's ratio $\nu = 0.18$, linear strain-softening represented by isotropic damage variable. Self weight was omitted in this study. Equivalent stress was defined according to Mazars (1984)

$$\bar{\varepsilon} = \sqrt{\sum_{I=1}^3 \langle \varepsilon_I \rangle^2} \quad (1)$$

where ε_I are principle strains and brackets $\langle \cdot \rangle$ returns positive part of the argument inside. FEM analyses were computed in open-source program Oofem (Patzák & Bittnar, 2001).

3. Demonstration of Discretization Density Effect

To demonstrate the influence of localization, the first study was performed using local constitutive law with constant value of the final strain $\varepsilon_f = 0.004$, which is the strain that corresponds to fully opened crack. Fig. 2 you can see that the response is different for the different finite element discretization density. Load-deflection diagrams obtained from unnotched (notched) beam simulations are shown in gray (black) color, respectively. Both peak loads and descending parts of the diagrams are different for different mesh densities. Demand for more efficient model is obvious.

4. Crack Band Model

The first tested remedy is the *crack band* model developed by Bažant & Oh (1983). The crack band model does not actually eliminate the localization; it just helps us get rid of the localization influence on the results. The crack still propagates through the thin band of one layer of finite elements. The main idea is to ensure the constant value of energy dissipated in the unit of the area. This constant value is called fracture energy G_f [N/m²] and it is understood as a material parameter. The energy dissipated in one finite element must be equal to the fracture energy multiplied by the area of the finite element. The final strain in the constitutive law is not constant anymore and it is dependent on the fracture energy and the element width. For the linear softening, it can be calculated as

$$\bar{\varepsilon}_f = \frac{2 G_f}{h_b f_t}, \quad (2)$$

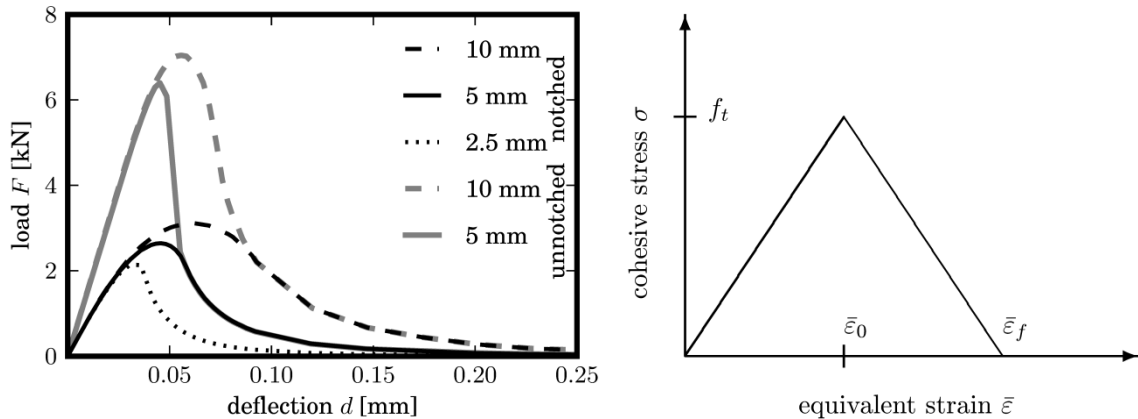


Fig. 2: Dependency of local material model with constant final strain.

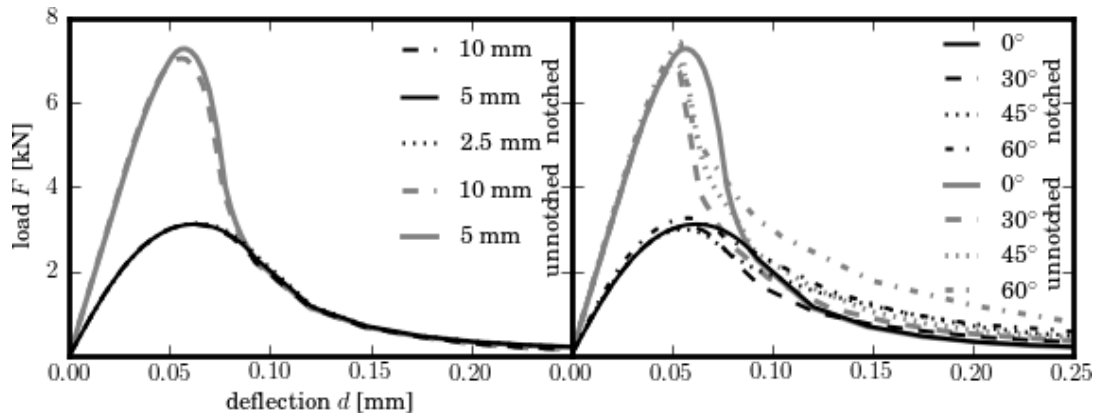


Fig. 3: Crack band model applied on meshes differing in element size and inclination.

where h_b is the band width. When crack is aligned with mesh direction, the width can be taken as size of the finite elements. But the crack does not always propagate in the same direction as the finite elements are aligned. In such cases, the band width must be artificially estimated (Jirásek & Bauer, 2012).

The *crack band* model was applied on the same three point bended beam with the same set of mesh geometries. In addition, the performance of the crack band model was verified on set of inclined mesh geometries. Fracture energy was chosen to correspond to constitutive law of the 10 mm element from Sec. 2; its value was 50 N/m^2 . The results are shown in Fig. 3, the left hand side shows load-deflection diagrams for various mesh densities, whereas the right hand side displays results on meshes with different inclination angle.

Performance of the *crack band* model on aligned meshes is excellent; curves for different discretization densities almost coincide. Poorer results are obtained for inclined meshes, where calculation of the band width is not that simple. Peak load is not affected by the inclination at all.

5. Nonlocal Model

The nonlocal model does not allow the crack to localize into band of one element width. It enforces the crack to propagate through zone of constant width irrespectively of meshing. The constitutive law is not modified, it has constant final strain ε_f . However, the nonlocal equivalent strain is used and it is computed as an average of equivalent strains using some weight function α_0 . The weight function can be any function that decreases with increasing distance. Besides different type of weight functions, there are also nonlocal models that average other variable instead of equivalent strain, such as damage, stress, etc.

In this contribution, nonlocal equivalent strain is considered; weight function was chosen bell shaped function according to

$$\alpha_0(s) = (1 - s^2/R^2)^2, \quad (3)$$

where s is distance and R is range of the weight function. For any point outside of the range ($s > R$), the value of the weight function is considered as zero. The function needs to be normalized to ensure, that the sum of its values is equal to 1. The nonlocal equivalent strain is then calculated from

$$\bar{\varepsilon}(x) = \sum_V \alpha(s_i) \bar{\varepsilon}(\gamma_i) \quad (4)$$

where x is coordinate of the examined point and γ_i is coordinate of any point in the range of weight function

The range R was chosen as 10 mm. The final strain in constitutive law in $\bar{\varepsilon}_f = 0.002$ was chosen to provide the response comparable with the crack band model results. We applied the nonlocal model on the same geometry as was done with the crack band model. The performance on the aligned meshes (left part of the Fig. 4) is worse than what we got with the crack band localization limiter. For inclined meshes, the results look more or less the same as those provided by the crack band model. For 60 degrees inclination angle, quite poor agreement is found.

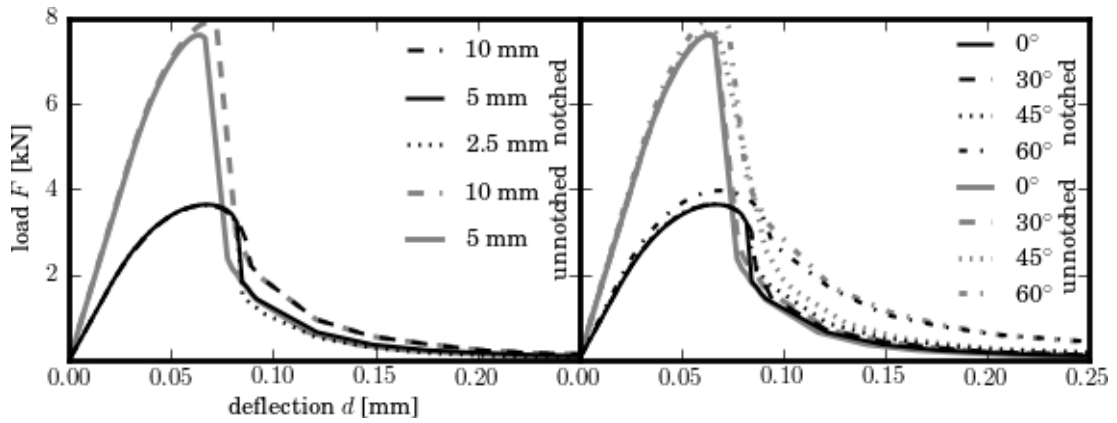


Fig. 4: Nonlocal model applied on meshes differing in element size and inclination.

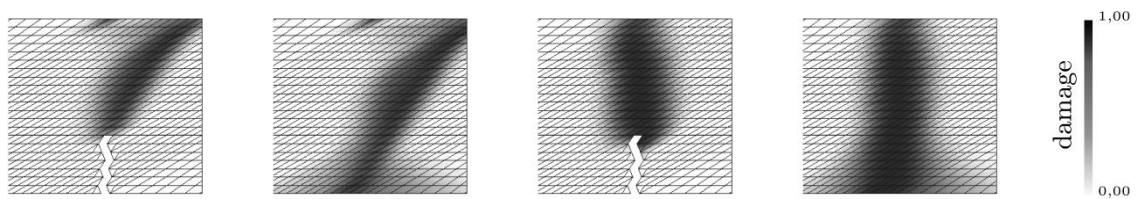


Fig. 5: Crack patterns for Crack band (left) and Nonlocal model (right) for notched and unnotched beam with mesh inclined by 60 degrees.

Besides the load-deflection curves, the crack path was compared as well. Fig. 5 displays damage variable at the end of the simulation. There are only shown central parts of the beams, the depth is not trimmed. Two figures in the right were computed using the nonlocal model, other two figures at the left by crack band model. Crack band allows the localization and the damaged band goes through only a few elements. The nonlocal model avoids such localization. In case of the crack band model and inclination angle 60 degrees, the crack pattern is spuriously skewed along the mesh orientation.

6. Conclusion

Both approaches provide reduction of dependency of the results on the finite element size. When inclined mesh is used, independency of the response seems to be more efficiently provided by the *nonlocal* formulation, especially when considering the crack pattern. On the mesh with inclination angle of 60 degrees, the crack spuriously propagates along the mesh orientation when using the *crack band* model.

Acknowledgement

The financial support received from the Ministry of Education, Youth and Sports of the Czech Republic under Project No. LH12062 is gratefully acknowledged.

References

- Bažant, Z. P., Oh, B.-H. (1983) Crack band theory for fracture of concrete. *Materials and Structures*. Rilem, Paris, 16:155-177.
- Jirásek, M. (1998) Nonlocal models for damage and fracture: comparison of approaches. *Solid structures*, 35:4133-4145.
- Patzák, B., Bittnar, Z. (2001) Design of object oriented finite element code. *Advances in Engineering Software*, 32(10-11):759-767.
- Jirásek, M., Bauer, M. (2012) Numerical aspects of the crack band approach. *Computers and structures*, 19:60-78.
- Mazars, J. (1984) Application of the damage mechanics to the nonlinear behavior and the fracture of structural, the Doctorate concrete of state of Université Paris VI.

NUMERICAL SIMULATION OF THE TURBULENT COMPRESSIBLE GAS FLOW IN THE VANELESS MACHINES

M. Kyncl^{*}, J. Pelant^{**}

Abstract: We work with the numerical solution of the turbulent compressible gas flow. We show the numerical simulation of the effect observed in the special vaneless stator-rotor system. The considered axis-symmetrical problem is solved numerically. The system of the Reynolds-Averaged Navier-Stokes equations with the k - ω turbulent model is reformulated into the cylindrical coordinates. The finite volume method is used for the solution of the resulting system of equation in meridian planes. At the boundary, the classical Riemann problem is modified to yield physically relevant boundary conditions, with the aim to keep the conservation laws. Suggested procedures were programmed into the own software, and used on examples. The described method can be used for flow simulation in symmetrical channels of arbitrary apparatuses.

Keywords: Turbulent Gas Flow, 3D RANS, Finite Volume Method, Axis-symmetrical Problems, Boundary Conditions.

1. Introduction

The aim of this contribution is to simulate the viscous compressible gas flow in the slot which is formed by the gap between two coaxial cones. The considered geometry is shown in Fig. 1. The inner cone here acts as a rotor, and outer cone is the stator. The gas enters this shaped channel with the essentially small tangential velocity, and exits with relatively high tangential velocity component. The resulting viscous stresses turn the rotor. In order to simulate this 3D nonstationary process we numerically solve the system of the Navier-Stokes equations for the turbulent flow. We assume the problem to be axis-symmetrical. Therefore we simplify the governing equations and compute 3D solution in the two-dimensional meridian plane. Numerical example of this approach is shown. In our simulation we consider the Reynolds-Averaged Navier-Stokes equations with the k - ω model of turbulence, rewritten into the axis-symmetrical form.

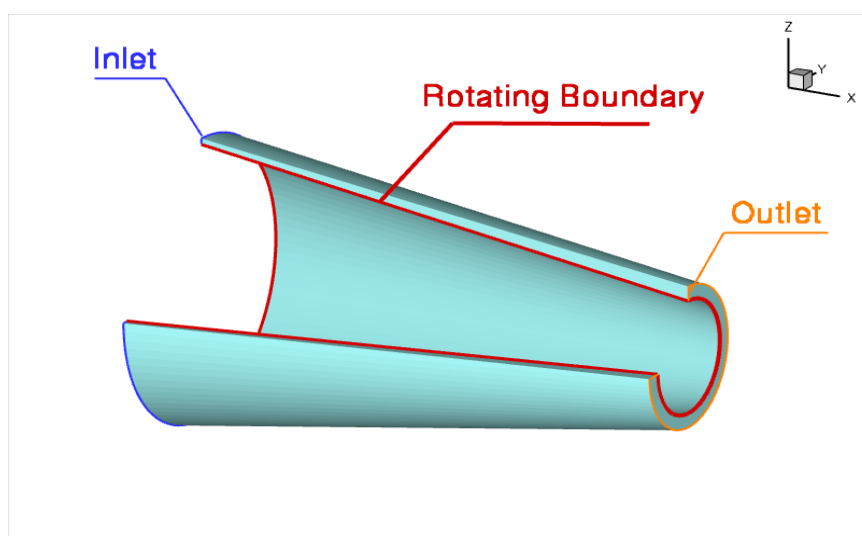


Fig. 1: 3D geometry shape, inner boundary rotates along the x -axis.

^{*} RNDr. Martin Kyncl, PhD.: VZLU Praha a.s., Beranových 130, 199 05 Prague, CZ, kyncl@vzlu.cz

^{**} RNDr. Jaroslav Pelant, CSc.: VZLU Praha a.s., Beranových 130, 199 05 Prague, CZ, pelant@vzlu.cz

2. The Formulation of the Equations

For the symmetrical three dimensional flow we use the following system of the equations

$$\frac{\partial}{\partial t} q + \frac{\partial}{\partial x} f(q) + \frac{\partial}{\partial y} g(q) - \left(\frac{\partial}{\partial x} r(q) + \frac{\partial}{\partial y} s(q) \right) = -\frac{1}{y} F(q) + \frac{1}{y} G(q), \quad (1)$$

where $q = (\rho, \rho u, \rho v, \rho w, E)$ denotes the state vector, and

$$\begin{aligned} f(q) &= [\rho u, \rho u^2 + p, \rho uv, \rho uw, (E + p)u], \\ g(q) &= [\rho v, \rho vu, \rho v^2 + p, \rho vw, (E + p)v], \\ r(q) &= \left[0, \tau_{xx}, \tau_{xy}, \tau_{xz}, u\tau_{xx} + v\tau_{xy} + w\tau_{xz} + \gamma \left(\frac{\mu}{Pr} + \frac{\mu_T}{Pr_T} \right) \frac{\partial \varepsilon}{\partial x} \right], \\ s(q) &= \left[0, \tau_{xy}, \tau_{yy}, \tau_{yz}, u\tau_{xy} + v\tau_{yy} + w\tau_{yz} + \gamma \left(\frac{\mu}{Pr} + \frac{\mu_T}{Pr_T} \right) \frac{\partial \varepsilon}{\partial y} \right], \\ F(q) &= [\rho v, \rho uv, \rho(v^2 - w^2), 2\rho vw, (E + p)v], \\ G(q) &= \left[0, \mu_x \left(\frac{1}{3} \frac{\partial v}{\partial x} + \frac{\partial u}{\partial y} \right), \mu_x \frac{4}{3} \left(\frac{\partial v}{\partial y} - \frac{v}{y} \right), \mu_x \left(\frac{\partial w}{\partial y} - \frac{w}{y} \right), \right. \\ &\quad \left. \mu_x \left(-\frac{4}{3} v \frac{\partial u}{\partial x} + \frac{1}{3} u \frac{\partial v}{\partial x} + u \frac{\partial u}{\partial y} - w \frac{\partial w}{\partial y} \right) + \gamma \left(\frac{\mu}{Pr} + \frac{\mu_T}{Pr_T} \right) \frac{\partial \varepsilon}{\partial y} - \frac{2\rho k}{3} v \right], \end{aligned}$$

with $\mu_x = \mu + \mu_T$, and

$$\begin{aligned} \tau_{xx} &= \left(+\frac{4}{3} \frac{\partial u}{\partial x} - \frac{2}{3} \frac{\partial v}{\partial y} \right) \mu_x - \frac{2\rho k}{3}, \\ \tau_{yy} &= \left(-\frac{2}{3} \frac{\partial u}{\partial x} + \frac{4}{3} \frac{\partial v}{\partial y} \right) \mu_x - \frac{2\rho k}{3}, \\ \tau_{xy} = \tau_{yx} &= \left(\frac{\partial v}{\partial x} + \frac{\partial u}{\partial y} \right) \mu_x, \\ \tau_{xz} = \tau_{zx} &= \left(\frac{\partial w}{\partial x} \right) \mu_x, \quad \tau_{yz} = \tau_{zy} = \left(\frac{\partial w}{\partial y} \right) \mu_x. \end{aligned}$$

Here p is the pressure, ρ the density, (u, v, w) is the average value vector of velocity: u is the velocity in the direction x , the components v, w are radial and circle velocities, x, y, z denote the cylindrical coordinates: y denote the radius, z the angle of rotation, and t the time. Further, k is the turbulent kinetic energy of flux components of the velocity, ω is the specific turbulent dissipation, Pr is laminar and Pr_T is turbulent Prandtl constant number, μ is the dynamic viscosity coefficient dependent on temperature, $\mu_T = \rho k / \omega$ is the eddy-viscosity coefficient. In the energy equation, E denotes the total energy $E = \rho \varepsilon + \rho k + \frac{1}{2} \rho (u^2 + v^2 + w^2)$, where $\varepsilon = p / \rho (\gamma - 1)$ is the internal energy of a unit mass of the fluid where the constant $\gamma > 1$. Using the integral form of the system (1) we can study a flow with shock waves, too. In this work we assume the system (1) equipped with the $k - \omega$ two-equation turbulent model described in (Kok, 2000), and rewritten into the cylindrical coordinates in (Kyncl & Pelant, 2013).

3. Numerical Time Step Method

For the discretization of the system (1) we used the finite volume method. The time interval of interest is divided using the set of partial time-steps (each of them restricted by the so-called CFL condition). The finite volume mesh is constructed as a polygonal approximation of the area studied. In this work we used the structured quadrilateral mesh. The system (1) is integrated over each element and time interval, the Green's theorem is used to compose the finite volume formulation. In order to compute the piecewise constant approximation of the solution at each time instant (and each quadrilateral element) we must evaluate the state on the edges of each quadrilateral. We use the so-called Riemann solver for the inner edges. At the boundary edges we use boundary modifications of this initial-value problem. We applied analysis from (Kyncl & Pelant, 2006), Chapters 4-8. for the inlet and outlet edges. For the edges corresponding to the wall surface we applied (Kyncl & Pelant, 2008), Chapter 2. The dual mesh was used for the approximation of the higher order terms. In order to achieve higher accuracy in space we used the higher-order scheme with the VAN ALBADA limiter.

4. Examples

The computation was made for geometry in Fig. 1, the apparatus is 0.17 m long. The gas flows from the left towards the right side. We simulated gas rotating at inlet around axis at 960 Rad. s⁻¹. Inner boundary (referring to geometry shown in Fig. 1), representing the rotor, had the velocity fixed at 960 Rad. s⁻¹. We chose T₀ = 293 K, p₀=105000 Pa at inlet (left in Figs. 1 and 2), average pressure p = 100000 Pa at the outlet (the right-hand side in Figs. 1 and 2). Mesh consisted of 88x44 quadrilaterals, 1.000.000 iterations were computed.

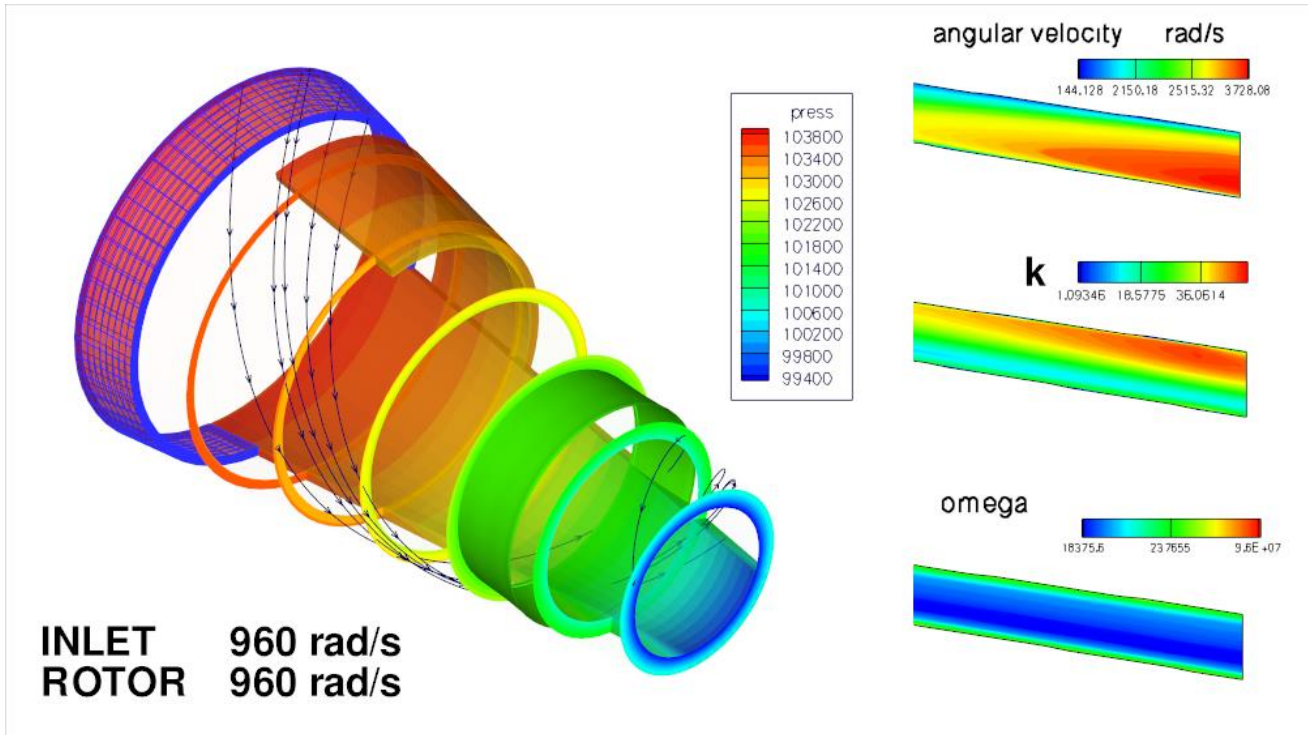


Fig. 2: Turbulent flow, angular velocity, density, and entropy isolines shown at the outlet part, 2D cut, pressure isolines and velocity streamlines shown in 3D.

Further test cases involve the increased rotor speed to 960 Rad. s⁻¹, 1440 Rad. s⁻¹, 1920 Rad. s⁻¹, and the rotor with the slip (inviscid) surface. The aim of these computations was to compare the kinetic energy of the surface velocity component of the gas in the vicinity of the rotor. The Fig. 3 shows the comparison of this restricted part of the kinetic energy $Ek = 0.5\rho w^2$, where w is the surface (rotational) component of the velocity.

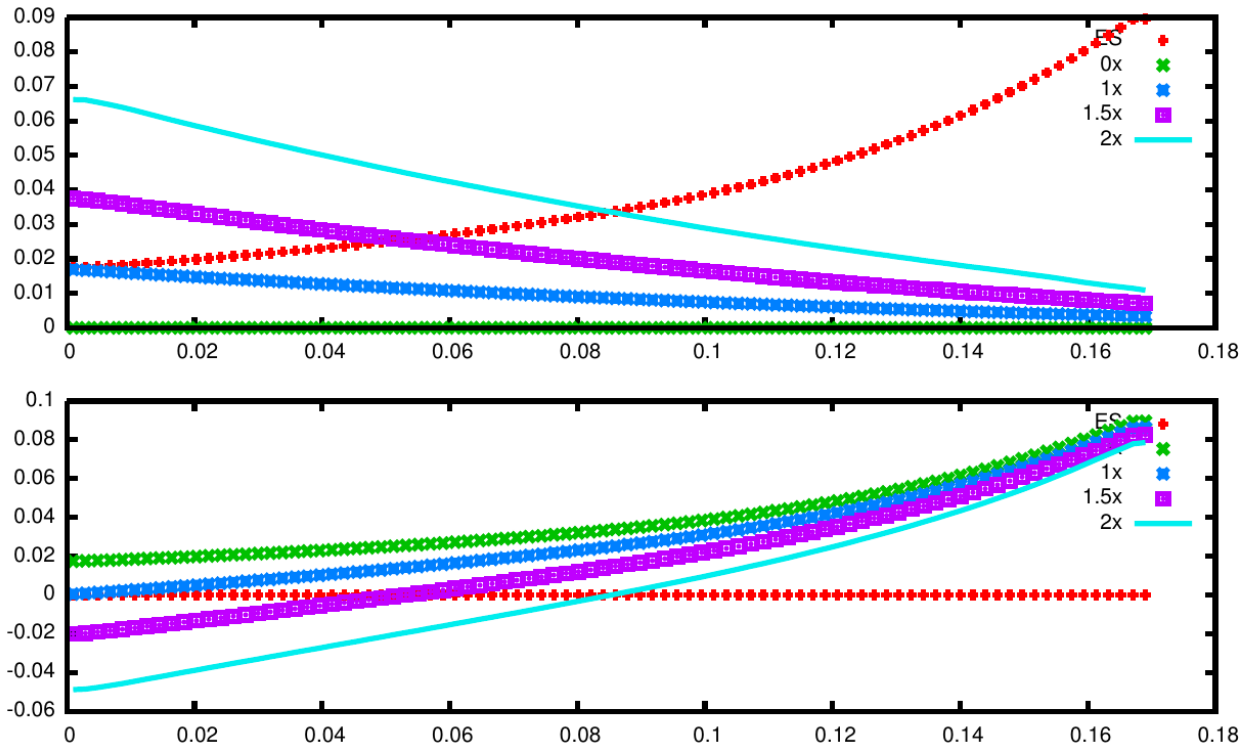


Fig. 3: Computational results for the selected cases with the slip rotor (ES), and the rotor with angular velocities 0 Rad. s^{-1} (0x), 960 Rad. s^{-1} (1x) 1440 Rad. s^{-1} (1.5x), 1920 Rad. s^{-1} (2x). Horizontal axis is the x-axis, the vertical axis shows the rotational component of the kinetic energy $E_k = 0.5\rho\omega^2$. The bottom picture shows the difference of this energy E_k and the energy E_k in the case of the slip rotor.

5. Conclusions

We presented the numerical method suitable for solving the 3D Navier-Stokes equations with $k-\omega$ turbulence model for axis-symmetrical flow in two-dimensional meridian plane. The turbulent closure equations were transformed into the cylindrical coordinates. The originality of this result lies also in the use of the modified Riemann problem for the construction of the boundary conditions. Described method can be used for the flow simulation in symmetrical channels of arbitrary apparatuses. The presented example shows the flow through the real gas turbine with the simple design (without any blades). The shown method can be used for the further optimization of such apparatuses.

Acknowledgement

This result originated with the support of Ministry of Industry and Trade of Czech Republic for the long-term strategic development of the research organization. The authors acknowledge this support.

References

- Kyncl, M., Pelant, J. (2006) Applications of the Navier-Stokes Equations for 3d Viscous Laminar Flow for Symmetric Inlet and Outlet Parts of Turbine Engines with the Use of Various Boundary Conditions, Report VZLÚ R3998, Prague.
- Kyncl, M., Pelant, J. (2008) Applications of the Navier-Stokes Equations for 2d Viscous, Compressible Turbulent Flow on Steady Grids with the (EARS) Turbulent Model, Report VZLÚ R4300, Prague).
- Kok, J. C. (2000) Resolving the Dependence on Free-stream Values for $k-\omega$ Turbulence Model. In AIAA Journal, Vol. 38, No. 7, pp. 1292-1295.
- Kyncl, M., Pelant, J. (2013) Simulation of the Propeller Disk Inside the Symmetrical Channel, in Proc. EFM 2013, Kutná Hora, pp. 404-410.
- Feistauer, M., Felcman, J., Straškraba, I. (2003) Mathematical and Computational Methods for Compressible Flow. Oxford University Press, Oxford
- Pelant, J. (1996-2000) ARTI Reports VZLÚ, Z-65, Z-67 to Z-73. Prague.

A DELTA TYPE CLOSED KINEMATICS CHAIN WITH PNEUMATIC MUSCLE ACTUATOR MANIPULATOR

P. A. Laski^{*}, J. E. Takosoglu^{**}, S. Blasiak^{***}

Abstract: *In this paper electropneumatic with closed kinematic chain, three degrees of freedom with pneumatic actuators muscle delta type manipulator is presented. The paper presents the components and design of proposed control system with the results.*

Keywords: Parallel pneumatic manipulator, Pneumatic muscles, Simple and inverse kinematics.

1. Introduction

The need for rehabilitation of persons with disabilities requires the involvement of substantial resources as well as highly qualified personnel. The main objective of the robot design was to create construction with corresponding to human limbs movements. It was assumed that the structure will be characterized by a gentle start and stop, and high overload (Takosoglu et al., 2012). Moreover, the design should have a low weight. The proposed construction delta type robot with closed kinematic chain is usually driven by electric rotary actuator. The authors have proposed replacing the rotary drives by the pairs of pneumatic muscles working alternately. Pneumatic artificial muscles are characterized by considerable dynamics and at the same time allow you to perform gentle movements. The work of robot relies on the introduction by a qualified person (physiotherapist) selected movement trajectory and play repeatedly with the specified parameters by a person who is rehabilitated. The relatively low cost of implementation of the parallel manipulator based on the pneumatic muscle actuators allow for its use in the home.

The manipulator constructed in accordance with a delta structure includes a movable platform connected to the fixed base by three kinematic chains acting simultaneously. Each chain includes rotary drive actuated by a combination of a pair of pneumatic muscles acting antagonistic. The ends of the muscles were connected with the fixed base. To pass movement to the working platform are used three parallelograms ended by spherical joints. Single kinematic chain of 3-RSS manipulator contains the rotary type joints (R) and spherical type joints (S).

2. Inverse and Forward Kinematics

To control the robot in real time is necessary to solve the tasks of simple and inverse kinematics. Determination of the current position and orientation of the robot working platform is based on the measurement of angular displacement of arm and feedback in the control system while driving (Laski & Dindorf, 2007). Fig. 1. shows a diagram of a robot with visible local coordinate systems necessary to solve the tasks of kinematics.

For considered manipulator kinematics equations requires a designation of parameters according to the notation of DH (Denavit-Hartenberg) for working platform and arms. Tab. 1 includes the kinematic parameters of the work platform, while the Tab. 2 contains the parameters for the manipulator arm.

* Pawel Anrzej Laski, PhD.: Department of Automation and Robotics, Faculty of Mechatronics and Machine Design, Aleja Tysiaclecia Panstwa Polskiego 7; 25-314 Kielce; Poland, pawell@tu.kielce.pl

** Jakub Enamuel Takosoglu, PhD.: Department of Mechatronic Devices, Faculty of Mechatronics and Machine Design, Aleja Tysiaclecia Panstwa Polskiego 7; 25-314 Kielce; Poland, qba@tu.kielce.pl

*** Slawomir Blasiak, PhD.: Department of Mechanical Engineering and Metrology, Faculty of Mechatronics and Machine Design, Aleja Tysiaclecia Panstwa Polskiego 7; 25-314 Kielce; Poland, sblasiak@tu.kielce.pl

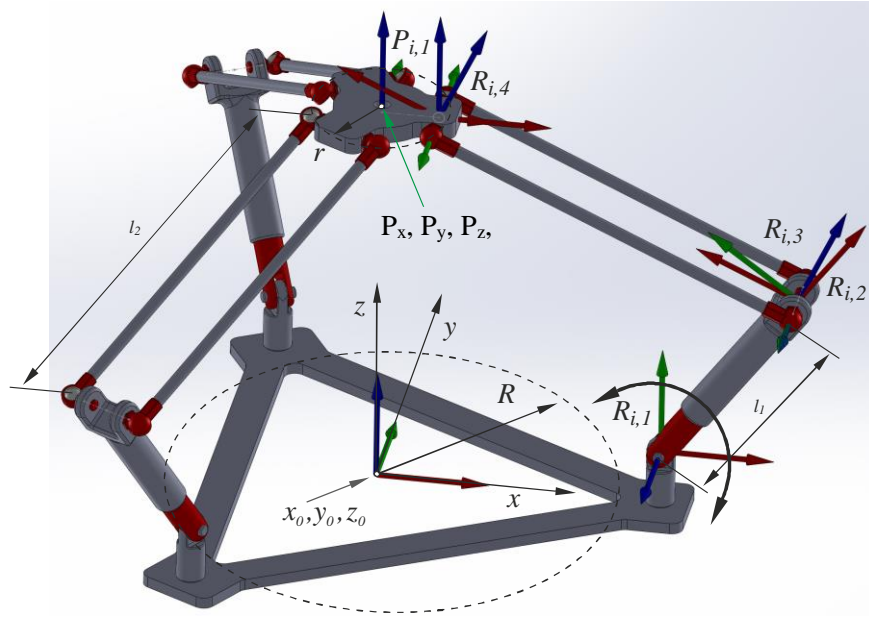


Fig. 1: Kinematic diagram of the delta type manipulator.

Tab. 1: DH parameters for the working platform.

Coordinate system	Rot_{z,θ_i}	$Trans_{z,d_i}$	$Trans_{x,a_i}$	Rot_{x,α_i}
$P_{i,1}$	ζ_i	0	r	0

Tab. 2: DH parameters for the next arms i -te; $i = 1, 2, 3$.

Coordinate system	Rot_{z,θ_i}	$Trans_{z,d_i}$	$Trans_{x,a_i}$	Rot_{x,α_i}
$R_{i,1}$	ξ_i	H	R	$\frac{\pi}{2}$
$R_{i,2}$	$\theta_{i,1}$	0	l_1	0
$R_{i,3}$	$\theta_{2,1}$	0	0	$\frac{\pi}{2}$
$R_{i,4}$	$\theta_{3,1}$	0	l_2	0

To solve the equations of kinematics (0.1) and (0.2) were used numerical procedure based on the Newton-Raphson method for nonlinear equations using Gaussian elimination. Platform joint i – ty ($i = 1, 2, 3$)

$$\begin{cases} Wsp_{i,x} = P_x + r \cos(\zeta_i) \\ Wsp_{i,y} = P_y + r \sin(\zeta_i) \\ Wsp_{i,z} = P_z \end{cases} \quad (1)$$

Arm i – te ($i = 1, 2, 3$)

$$\begin{cases} f(\theta_{i,1}, \theta_{i,2}, \theta_{i,3}) = -Wsp_{i,x} + \cos(\xi_i)(l_1 \cos(\theta_{i,1}) + l_2 \cos(\theta_{i,3}) \cos(\theta_{i,1} + \theta_{i,2}) + R) + l_2 \sin(\theta_{i,3}) \sin(\xi_i) = 0 \\ f(\theta_{i,1}, \theta_{i,2}, \theta_{i,3}) = -Wsp_{i,y} + \sin(\xi_i)(l_1 \cos(\theta_{i,1}) + l_2 \cos(\theta_{i,3}) \cos(\theta_{i,1} + \theta_{i,2}) + R) - l_2 \sin(\theta_{i,3}) \cos(\xi_i) = 0 \\ f(\theta_{i,1}, \theta_{i,2}, \theta_{i,3}) = -Wsp_{i,z} + H + l_1 \sin(\theta_{i,1}) + l_2 \cos(\theta_{i,3}) \sin(\theta_{i,1} + \theta_{i,2}) = 0 \end{cases} \quad (2)$$

Dimensions:

- l_1, l_2 - arm lengths,
- R - the radius of the circle on which are arranged arms,
- $\xi_1 = 0^\circ; \xi_2 = 120^\circ; \xi_3 = 240^\circ$ - angles of the distribution of arms on a circle,

- r - radius of the circle on which joints of platform are distributed,
- $\zeta_1 = 0^\circ; \zeta_2 = 120^\circ; \zeta_3 = 240^\circ$ - angles of joints of platform placed on the circle.

2.1. Workspace analysis

One of the most important traits of robots is the range and shape of the workspace. Fig. 2 shows the space of designed delta type robot. In comparison to the open-chain robot kinematic with similar geometric dimensions the workspaces are much smaller.

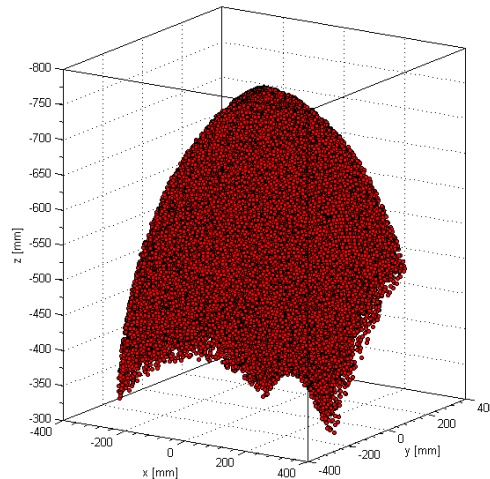


Fig. 2: Working space of delta type manipulator.

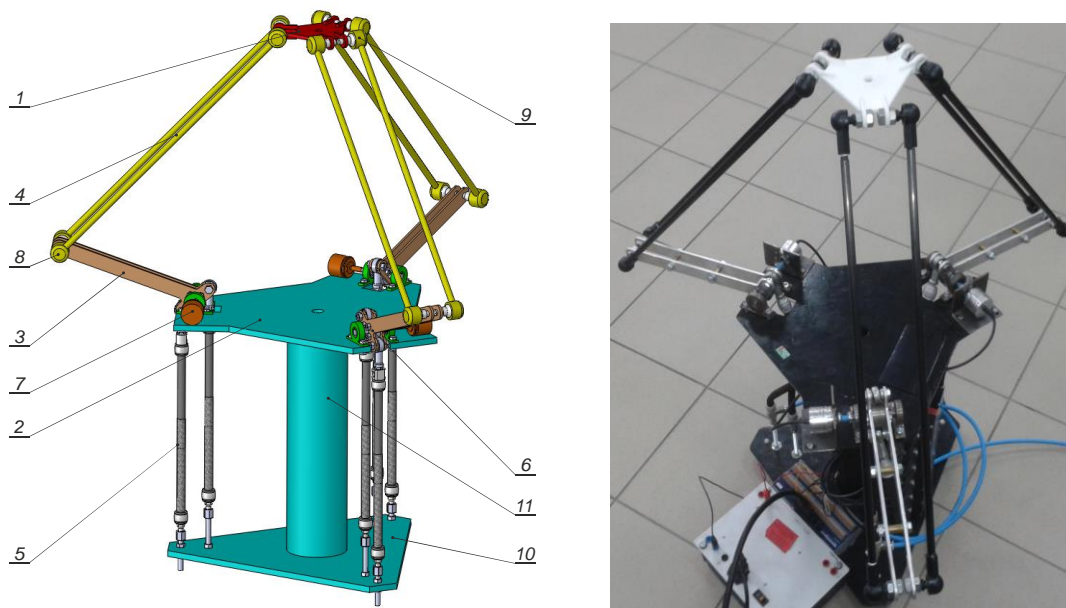


Fig. 3: Solid model of parallel delta type manipulator: 1 - working platform, 2 - upper platform, 3 - active arms, 4 - passive arms, 5 - muscles drive, 6 - revolution joints, 7 - angular position sensors, 8, 9 - ball joints, 10 - base, 11 - support column.

2.2. The construction of delta type manipulator

In most delta type robots, rotary drive motors are mounted on the fixed base. Because the delta robot drives perform only limited moves with a certain angular range the drives were replaced by pneumatic muscles. In order to obtain angular movements of the joint muscles were paired to work alternately (antagonistic). Calling the rotational movement is a result of interaction of the two muscles on lever which is change progressive movement to the rotational. In order to obtain the movement one of the muscle is shrinking while the opposite relaxes and vice versa just as it is in human hand movements for the biceps and triceps muscles. Actuators of the robot arm transmit movement to the work platform via passive arms made of rods and ball joints connecting them (Krzysztofik & Koruba, 2012). The use of a

ball joint kinematic chain causes the passive arms carry rods transmits only the tensile and compressive loading preferable from the viewpoint of strength of materials. This kinematic structure has a small mass resulting in significant dynamic robot (Laski et al., 2010). The main drive robot arms are made of aluminum. Passive arms are made of carbon fiber and the work platform is made of polyamide by SLS rapid prototyping technology. Used ball joints are also made of plastic with a small weight. Fig. 3 shows the solid model and the prototype of robot (Laski et al., 2009). To control the muscles pneumatic six ultra high-speed proportional pressure valves controlled by piezoelectric actuator were used (Takosoglu, Dindorf & Laski, 2009). Since the pneumatic muscles are nonlinear objects, control of each muscles is realized by PID controllers (Takosoglu et al., 2010). PID tuning was carried out using the method of Ziegler-Nichols (Cedro, 2013). A single muscle is controlled using a Hoerbiger proportional pressure valve, which is activated by voltage between 0-10V (tecnoplus model). The control system and kinematic models have been implemented in Matlab / Simulink environment. The system designed constitutes an integrated environment for designing mechatronic systems, motion control, power electronics and signal conversion. xPC Target with the Education Real-Time Target Machine is a ready-to-use platform with embedded A/D and D/A cards. It is possible to control, tune and alter the parameters of the designed compensation-measurement system directly from Simulink in real time while the system is operating. All available functions of pneumatic valve terminal operate in real time (Blasiak et al., 2013). In the literature, there is no delta type pneumatic muscle robot solution. At this stage of construction it is difficult to compare the efficiency of the manipulator with the other structures of this type but with a different drive.

3. Conclusions

The paper presents the parallel delta type manipulator with the pneumatic muscle actuators. Structure with a description of the geometrical shape of the workspace is showed. Experimental studies have confirmed the assumption that the manipulator is characterized by high dynamics, soft start and stop, Robots of this construction can be used in medical rehabilitation processes of lower limb injuries and also in packaging processes, palletizing installation. In a further stage of construction the authors will performs experimental studies of positioning accuracy under different load mass of manipulator for classical and intelligent controllers.

Acknowledgement

The work was performed within the framework of the research project No. N514 217038 financed by the Ministry of Science and Higher Education.

References

- Blasiak, S., Laski, P. A., Takosoglu, J. E. (2013) Parametric analysis of heat transfer in non-contacting face seals, *International Journal of Heat and Mass Transfer*, Vol. 57, No. 1, 2013, pp. 22-31.
- Cedro, L. (2013) Identification of the manipulator with electric drive. *Electrical Review*, ISSN 0033-2097, R. 88 NR 9a/2012, pp. 208-212 (in Polish).
- Laski, P., Dindorf, R. (2007) Prototype of pneumatic parallel manipulator. *Hydraulika a Pneumatika* (1):22-24.
- Krzysztofik, I., Koruba, Z. (2012) Model of Dynamics and Control of Tracking-Searching Head, Palced on a Moving Object. *Journal of Automation and Information Sciences*, Vol. 44, Issue 5, ISSN 1064-2315, DOI: 10.1615/JAutomatInfScien.v44.i5.40, pp. 38-47.
- Takosoglu, J. E., Dindorf, R. F., Laski, P. A. (2009) Rapid prototyping of fuzzy controller pneumatic servo-system. *International Journal of Advanced Manufacturing Technology* Vol. 40, No. (3-4), pp. 349-361.
- Takosoglu, J.E., Dindorf, R.F., Laski, P.A. (2010) Fuzzy logic positioning system of electro-pneumatic servo-drive. In: Jimenez A, Al Hadithi BM (eds) *Robot Manipulators, Trends and Development*. In-Tech, Croatia, pp. 298-320.
- Laski, P. A., Dindorf, R, Takosoglu, J. E., Wos, P (2010) Project of pneumatic parallel manipulator type Delta with pneumatic muscle actuators. *Acta Mechanica et Automatica* 4(1):61-65.
- Laski, P. A., Dindorf, R, Takosoglu, J. E. (2009) Virtual project of parallel manipulator with pneumatic muscle actuators. . In: Macha E, Robak G. (eds) *Transfer of Innovation to the Inter-disciplinary Teaching of Mechatronics for the Advanced Technology Needs*. Opole University of Technology, Opole, pp. 209-216.
- Takosoglu, J. E., Laski, P. A., Blasiak, S. (2012) A fuzzy controller for the positioning control of an electro-pneumatic servo-drive. *Proceedings of the Institution of Mechanical Engineers Part I-Journal of Systems and Control Engineering*, Vol. 226, No. 10, pp. 1335-1343.

INVESTIGATION OF PROCESS DYNAMICS OF TBM EXCAVATION

E. Lazarová^{*}, V. Krúpa^{**}, L. Ivaničová^{***}, M. Kruľáková^{****}

Abstract: Full-profile tunnelling with TBM enables to monitor the excavation process data, serving for further investigation of rock cutting mechanism. The monitored data provides calculation of the specific cutting energy, the contact stress of the disc cutter acting on rock surface in the instant of rock disintegration, which defines the rock compressive strength, or other useful variables. The paper discusses the relation of such calculated rock strength and specific energy in the dynamic process of rock excavation in natural conditions of rock formation. Process dynamics was described by first order linear differential equation with constant coefficients.

Keywords: Mechanized tunnelling, Rock mass, Dynamics of rock cutting.

1. Introduction

Excavation of highway tunnels in Slovakia delivered the deployment of TBM technology. The tunnelling machines were installed with monitoring systems that were recording the data on tunnelling process variables, which were later confronted with the engineering-geological prospecting information. Large databases of acquired data were used for the investigation of the rock cutting mechanism of TBM excavation in the in-situ conditions. TBM tunnelling involves an interesting feature - the dynamics of the interaction of disc cutters with the rock on the excavated tunnel face. The synergy of disc operation is determined by the TBM's cutterhead structure, by the wear condition of the individual disc cutter contact surface, and by the applied regime of TBM operation. All of these parameters affect the excavation effectiveness in the present geological formation.

2. Theoretical Background

TBM excavation is delivered by the simultaneous action of disc cutters installed on the TBM cutterhead. During their operation, the intervals of alternated loading and relieving of the rock under the pressing disc cutter induce the increase of rock stress, which, after crossing the rock strength limit, causes chipping of rock from the compact rock mass. The mechanism of rock chipping is characterized by the crushing of rock under the disc cutter. The size of rock chips is limited by the distance or span of the neighbouring disc cutters' tracks and by the disc penetration depth. Such mechanism uses the tensile and shear stresses, making the rock chipping a less energy-consuming mechanism, as the rock shear and tensile strength is lower than the rock compressive strength.

When speaking about the energy-consumption of the rock cutting/excavation process, the issue is described as the specific energy SE, expressed by the formula

$$SE = \frac{2\pi.n.M_k(F)}{S.v(F)} \quad [MJ.m^{-3}] \quad (1)$$

^{*} Ing. Edita Lazarová, PhD.: Institute of Geotechnics, Slovak Academy of Sciences, Watsonova 45; 040 01, Košice; Slovakia, lazarova@saske.sk

^{**} Visiting Prof. Ing. Vítazoslav Krúpa, DSc.: Institute of Geotechnics, Slovak Academy of Sciences, Watsonova 45; 040 01, Košice; Slovakia, krupa@saske.sk

^{***} Ing. Lucia Ivaničová, PhD.: Institute of Geotechnics, Slovak Academy of Sciences, Watsonova 45; 040 01, Košice; Slovakia, ivanic@saske.sk

^{****} Ing. Mária Kruľáková, PhD.: Institute of Geotechnics, Slovak Academy of Sciences, Watsonova 45; 040 01, Košice; Slovakia, krulakova@saske.sk

where n [s^{-1}] – revolutions of the TBM cutterhead, M_k [kNm] – torque of TBM cutterhead, and v [$mm.s^{-1}$] – advance rate of TBM cutterhead. Revolutions, torque and advance rate represent the regime variables affected by the applied thrust force F [kN] acting on the tunnel face. S [m^2] is the face area and it is a constant parameter for the respective TBM.

Specific cutting energy has become a universal parameter for the assessment of total energy demand in a rock cutting process during previous years, (Bilgin et al., 2006). SE is commonly used for the quantification of the cutting process, as it determines the size of strength and deformation in the moment of rock breaking. It is a parameter that can be determined in real time from the data recording of the cutting process by TBM. There is a correlation SE to the mechanical properties of the rock mass. In case of rock cutting regime with minimum SE, there is a relationship between the specific cutting energy and the rock strength characteristics.

Specific energy of rock cutting by a normal pressure SE_T is determined by the rock compressive strength, as described in the following equation

$$SE_T = \frac{E}{V} = \frac{1}{2} \frac{F_N}{S_N} \frac{h}{h} = \frac{1}{2} \sigma, \quad [MJ.m^{-3}] \quad (2)$$

where E [MJ] is the energy necessary for rock cutting under pressure, V [m^3] is the volume of cut rock, the ratio F_N/S_N represents the contact pressure of the disc cutter pressing on rock in the instant of rock chipping, i.e. contact stress in the direction of normal force F_N and h is the penetration depth of disc cutter in the rock.

Theoretically, the graphic interpretation of the relation $SE_T = f(\sigma)$ is given by the line (Fig. 1). The real conditions however involve the partial action of shear and tensile stresses.

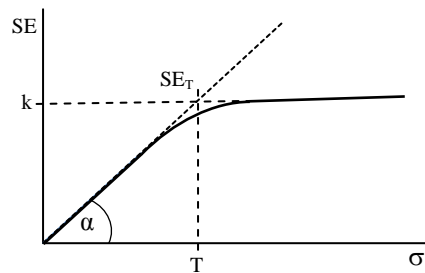


Fig. 1: Relation of specific energy and stress of rock cutting.

3. Data Processing Method

First order linear differential equation with constant coefficients and non-zero right-hand side was used for the modelling of the dependence curve of specific energy on calculated rock strength σ or the specific energy SE_T in the following form

$$SE = k \left(1 - e^{-\frac{\sigma}{T}} \right), \quad [MJ.m^{-3}] \quad (3)$$

where the parameter k expresses the maximum value of specific energy for the selected dataset and parameter T determines the value of rock compressive strength with the SE_T value equal to maximum SE (as in Fig. 1).

The rock cutting effectiveness assessment implies from the assumption that the less energy-consuming cutting is defined by a lower k -value and higher T -value. If $k=T$, the $tg\alpha$ of the line $SE_T = f(\sigma)$ equals 1, i.e. 45° .

4. Results and Analysis

The initial database for analysis comprised monitored data from excavation of the exploratory tunnel Branisko. Rock mass of the tunnel was classified by engineering-geological survey into the quasi-homogeneous geological sections according to the dominant rock type occurring in the respective section, (Bohyník, 1998). The paper describes analysis of the geological sections from GC5 to GC27, with the sequence of paleogene rocks, transiting to crystalline rocks through significantly mylonitized zones

further to the compact amphibolite formation. Five rock types (RT) were identified in the sections 5-27: mylonites (Kmy), biotitic gneisses (Rbp), amphibolic gneisses (Rab), granitoids (G) and prevailing amphibolites (A). Table 1 shows mean values of individual parameters for geological sections 5-27: GC – geological section; L – chainage; ΔL – section length; k – calculated parameter expressing maximum SE; T – rock mass strength value with SE_T equal to maximum SE; σ - calculated modelled rock compressive strength, SRH – compressive strength derived from Schmidt rebound hammer test by engineering-geological survey; PLT – compressive strength rebound hardness and PLT – rock strength derived from point load test by engineering-geological survey; α - angle of SE_T line. The table also contains mean values of monitored regime parameters in respective section: SE – specific energy; F – thrust force of cutterhead; M_k – torque of cutterhead; h – calculated penetration depth.

Tab. 1: Mean monitored and calculated values of excavation parameters from Branisko exploratory tunnel.

GC	L	ΔL	k	T	σ	SRH	PLT	α	SE	F	M_k	h	RT
	[m]	[m]	[-]	[-]	[MPa]	[MPa]	[MPa]	[°]	[MJm ⁻³]	[kN]	[kNm]	[mm]	
GC5	226	70	30	52.5	127	101	107	31	26	1410	116	3.38	G
GC6	297	49	27.5	39	48	41	62	35	18	1015	112	3.38	Rbp
GC7	345	64	35	39.5	66	50	69	42	23	1200	118	3.85	Rbp
GC8	453	26	36	38.5	75	53	75	43	26	1305	121	3.51	Rab
GC9	493	34	40.5	58	83	68	90	35	26	1337	113	3.26	Rab
GC10	527	14	31	29.5	20	6	35	46	12	592	75	5.15	Kmy
GC11	541	49	50	68.5	90	62	96	36	27	1279	104	3.05	A
GC12	590	62	33.5	38	63	62	96	41	22	1001	85	3.02	A
GC13	652	29	58.5	83	52	43	65	35	20	1060	104	4.21	Kmy
GC14	680	39	48	65.5	83	81	114	36	29	1461	125	3.29	A
GC15	720	51	47.5	66.5	108	75	116	36	33	1617	116	2.73	A
GC16	770	80	40	44	83	62	72	42	32	1473	116	2.80	A
GC17	851	67	41	40.5	93	81	114	45	33	1459	126	2.91	A
GC18	917	30	40.5	37	62	40	55	48	33	1440	123	2.95	A
GC19	947	43	51.5	55.5	119	87	88	43	42	1645	120	2.19	A
GC20	1033	20	47.5	38.5	78	56	57	51	36	1376	123	2.74	Kmy
GC21	1053	18	54	56.5	55	77	70	44	32	1089	110	2.55	A
GC22	1071	37	56	56.5	66	46	77	45	37	961	11	2.20	A
GC23	1109	48	44.5	43	118	70	81	46	38	1255	112	2.00	A
GC24	1193	34	57	88	147	98	136	33	44	1917	128	2.24	A
GC25	1242	1	57	88	84	54	78	33	32	1506	115	2.59	A
GC26	1274	21	48.5	54.5	147	92	140	42	44	2072	130	2.17	A
GC27	1295	4	44	41	141	105	129	47	42	2083	133	2.30	A

Torque M_k , which is affected by size of the tangential force F_t , is a determining variable for calculation of specific energy SE according to the Eq. (1). Calculation of the specific energy of rock disintegration under pressure load SE_T involves the applied thrust force F as a determining variable ($F = F_N \cdot N$, where N - number of disc cutters on TBM cutterhead; F_N – normal force of individual disc cutter). There is a non-linear relation between the variables F_t and F_N , which is transformed into the relation of specific energy on rock strength $SE = f(\sigma)$ and defined by the Eq.(3).

All the above-mentioned factors affect the resulting values of searched parameters k and T by various shares. The values of specific energy and measured rock strength change dynamically according to the instant condition of the regime parameters (thrust force, torque and penetration depth).

The value of the applied thrust force has risen with sequential advance to the middle of the excavated tunnel due to preserving the effective disc penetration depth. The sections with higher thrust force show also higher values of SE (Fig. 2). Such results provided graphic identification of unfavourable excavation regime in the geological sections 20 – 23, which resulted in emergent changes of worn disc cutters. This section long 123 m required 25 discs changes.

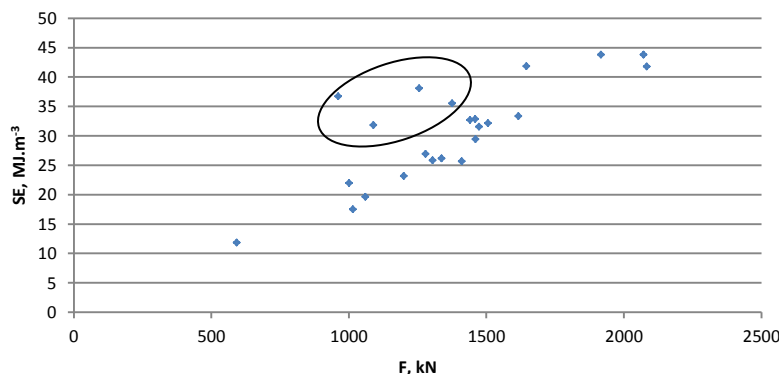


Fig. 2: Relation of specific energy on thrust force.

Averaged values of k and T for different rock formations (G, Rab, Rbp, Kmy, A) are presented in Tab. 2 and the relations of specific energy to rock strength are shown in the Fig. 3.

<i>RT</i>	<i>K</i> [-]	<i>T</i> [-]	<i>A</i> [°]
<i>G</i>	30	52	30
<i>Rbp</i>	31	39	39
<i>Rab</i>	56	61	43
<i>Kmy</i>	45	49	42
<i>A</i>	46	54	40

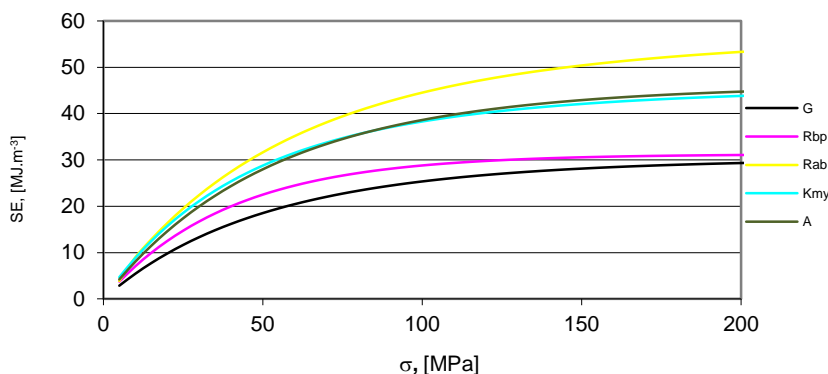


Fig. 3: Graphic interpretation of the Eq.3 for rock formations: *G* – granitoids, *Rbp* - biotitic gneisses, *Rab* - amphibolic gneisses, *Kmy* - mylonites, *A* - amphibolites.

The most energy-convenient excavation occurred in granitoids, the most unfavourable situation was during the excavation in amphibolic gneisses.

5. Conclusions

Obtained results confirmed the validity of theoretical assumptions on energy interpretation of rock strength. Even the TBM tunnelling process involves a number of affecting factors, the presented method provided visual identification of differences in energy consumption of the excavation in different rock types in the in-situ conditions.

Acknowledgement

The contribution was prepared within the projects nr. 2/0105/12 of Scientific Grant Agency VEGA.

References

- Bilgin, N., Demircin, M. A., Copur, H., Balci, C., Tuncdemir, H., Akcin, N. (2006) Dominant rock properties affecting the performance of conical picks and the comparison of some experimental and theoretical results, *International Journal of Rock Mechanics & Mining Sciences* 43, pp. 139-156.
- Bohnyik, et al. (1998) Detailed engineering-geological and hydrogeological survey a highway D1 Behárovce-Branisko, part B - tunnel Branisko. Partial report Number 6, INGEО, a.s., Žilina.

IDENTIFICATION OF VIBRATION CAUSES BASED ON SPECTROGRAMS DURING THE STRAIGHTENING PROCESS

P. Lošák*

Abstract: This paper deals with dynamic analysis of straightening machine loading during straightening process. During it, a crooked bar passing through the machine and the rollers and holders are subjected to the dynamic loadings. The roller's moment amplitudes depend, among others, on straightening speed, size of the bar curvature, bar's diameter, and on friction between the bar and the rollers. The loading is time-varying and knowledge of the frequencies of the moment is important; it can be used for verification of the numerical simulation or for the straightening machine design. Machine operation close to resonance state can cause excessive vibration which can subsequently cause noise and adversely affect the life of the machine and also straightening accuracy. This paper is aimed to analyze frequency spectra of the moments, which are obtained from the computational simulation and find the possible causes of vibration. Although, the straightening process is complex, it was possible to identify three main causes of vibration which are presented as the results of this paper.

Keywords: Spectrogram, Dynamic Loading, Straightening Machine, Straightening Simulation.

1. Introduction

The straightening machine, analyzed in this paper, is intended for a straightening of crooked cylindrical bars. The machine's configuration is schematically shown in Fig. 1. The scheme consists of seven parabolic rollers in two sizes. Two of them (number 1 and 2) are driven by electromotor. An important element of the design of the machine is that the rollers axes are inclined relative to the straightened bar by angle of 26°. This angle ensures that the rollers circumferential velocity is decomposed into the circumferential (rotation) and axial direction (translation) of the bar. Rollers 1, 2 and 7 have diameter of 580 mm and rollers 3, 4, 5 and 6 have diameter of 370 mm. The bar has diameter of 200 mm. More details of the machine construction and operation conditions can be found in Skalka & Sobotka (2014).

The numerical simulation of the straightening process is performed and described in detail in Skalka & Sobotka (2014). Their work is focused on the loading of the straightening machine in terms of maximum moments during the simulated process. The bar passing speed is controlled by angular velocity of the roller 1 and 2. The friction is considered between the bar and the rollers. The simulation is done for two cases of friction coefficient – 0.1 and 0.2. The history of drive moments (M_{d1} and M_{d2} in Fig. 1) and moments M_{f1} through M_{f7} in Fig. 1 is recorded. This paper extends the work of Skalka & Sobotka (2014) by the analysis of frequency spectra of the moments records. Detailed analyses of shape deviations after bar straightening is described in Fuis (2014), which is based on Fuis et al. (2009 and 2011).

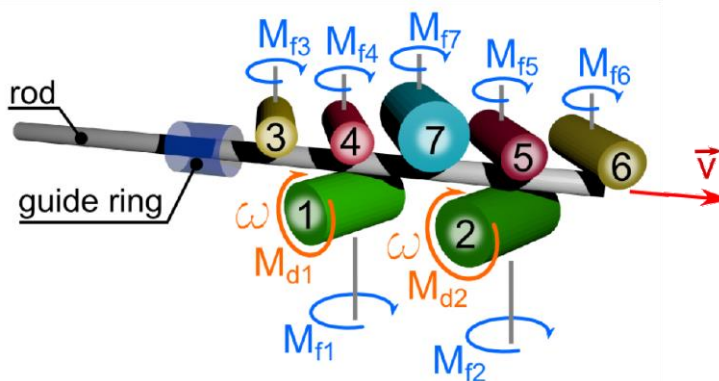


Fig. 1: Schematic layout of the straightening machine.

* Ing. Petr Lošák PhD.: Institute of Solid Mechanics, Mechatronics and Biomechanics, University of Technology Brno, Technická 2896/2; 616 69, Brno; CZ, losak@fme.vutbr.cz

2. Visualization of the Time-Varying Frequency Spectra

The moments, obtained from simulation, are in the time domain (Fig. 2). The plots can be useful for determination of maximum moments during straightening process; however, information about frequencies is not clear from them.

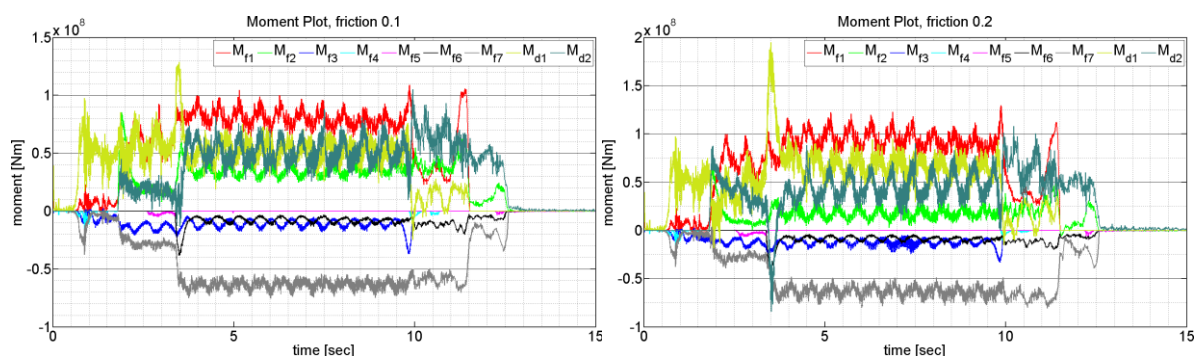


Fig. 2: Time record of the moments for the friction coefficient 0.1 (left) and 0.2 (right).

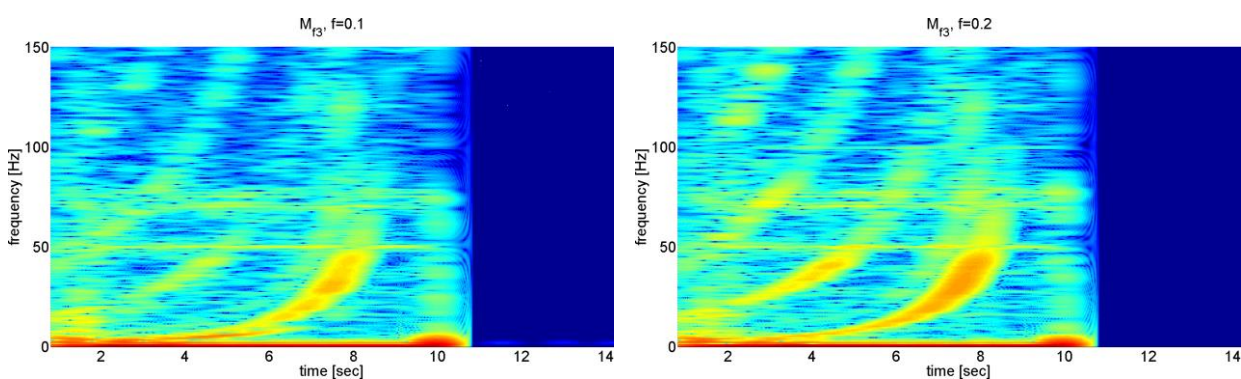


Fig. 3: Spectrogram of the moment M_{f3} for the friction coefficient 0.1 (left) and 0.2 (right).

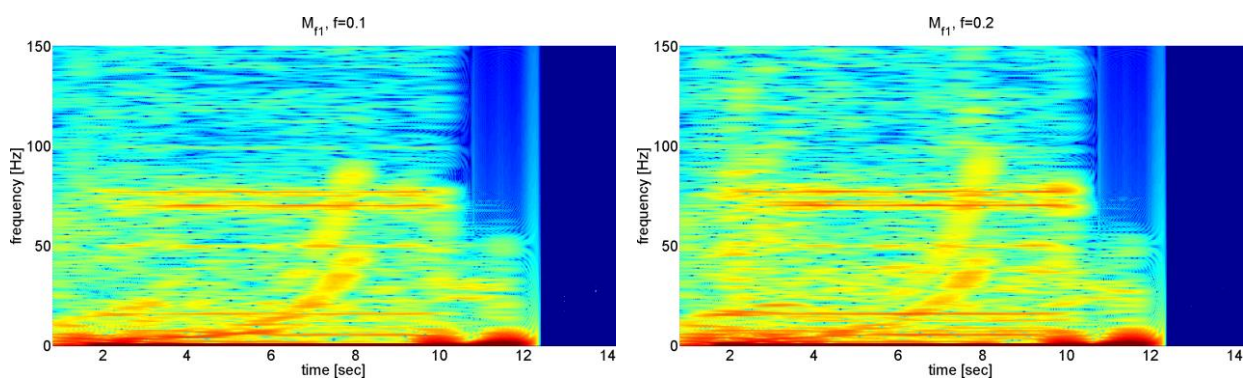


Fig. 4: Spectrogram of the moment M_{f1} for the friction coefficient 0.1 (left) and 0.2 (right).

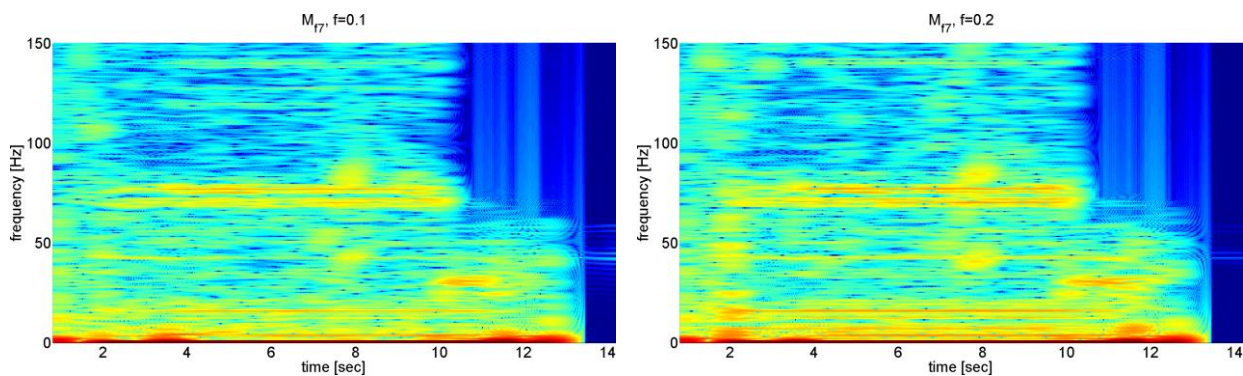


Fig. 5: Spectrogram of the moment M_{f7} for the friction coefficient 0.1 (left) and 0.2 (right).

The spectrogram is one of the best way how to display the frequency spectra of the time-varying signal (more about spectrograms could be found e.g. in Mertins (1999)). They show how the amplitudes and frequencies are changing over the time. The spectrogram of each moment record is computed and some results are shown in Figs. 3, 4 and 5. The horizontal axis represents time, on vertical one is for frequency. Amplitudes of vibration are marked by colors - dark blue stands for zero amplitude, dark red for highest amplitude in the spectrum.

Based on the time it is possible to determine the bar position in the straightening machine. Some of the significant time points are shown in Fig. 6. The position of the bar in the straightening machine is related to the spectrograms and also to causes of vibrations.

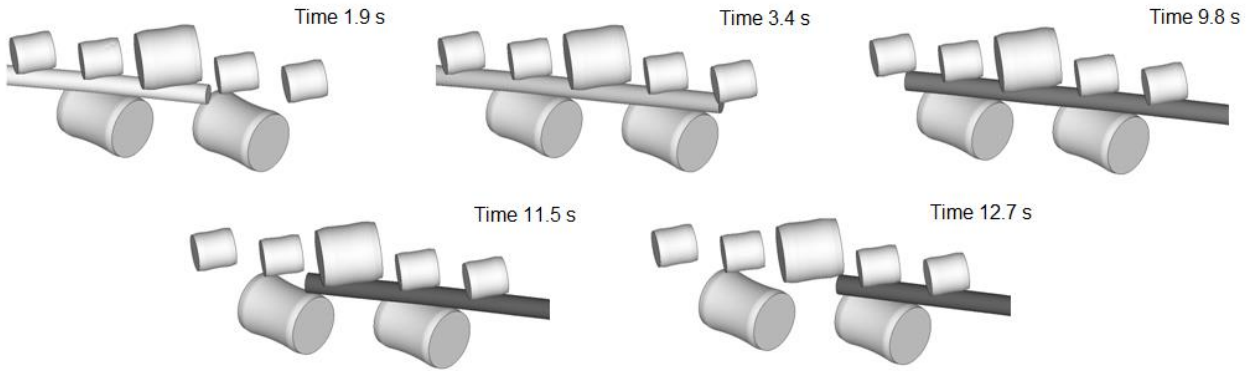


Fig. 6: Bar position in the specific time points.

3. Analysis of the Frequency Spectra

When the bar passes through straightening rollers, the excitation of rollers occurs due to inertia and rotational motion. The most significant vibrations are observed at the free end of crooked side. The displacements are so large that the bar impacts into the guide ring from Fig. 1. The friction coefficient between the bar and rollers has also impact on the frequency spectra.

Three regions of significant amplitudes can be observed in the spectrograms. Regions are highlighted in Fig. 7 and labeled as region A, B and C. Each of these regions is related to one cause of vibration.

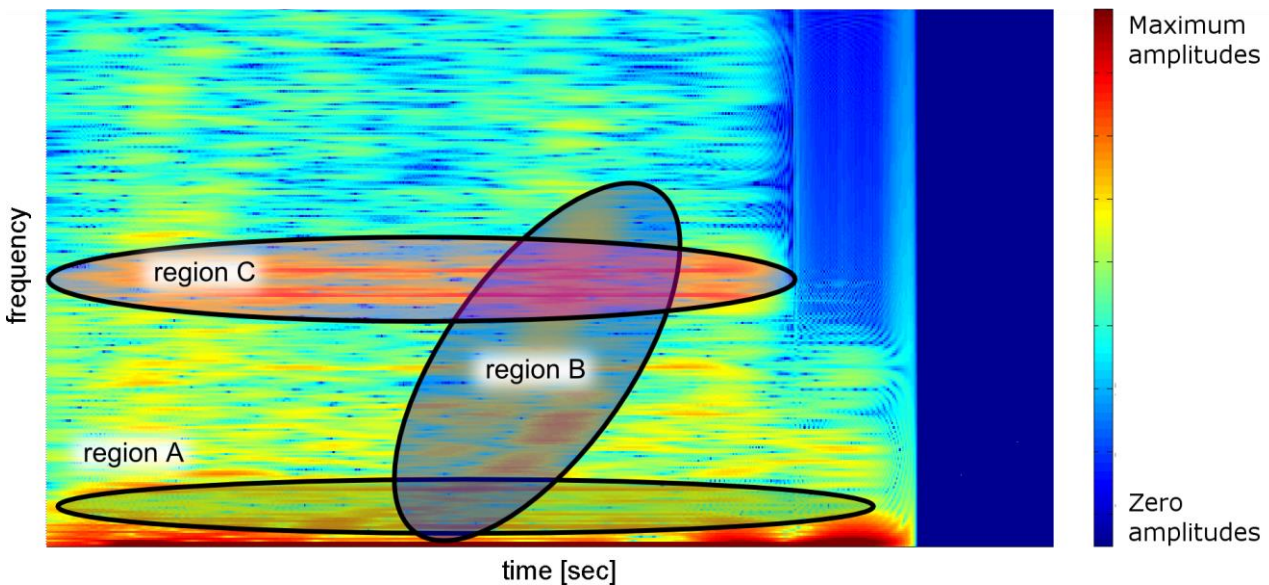


Fig. 7: Significant regions in the figure.

3.1. Region A - Rotation of the bar

The frequencies in the region A are excited by the rotation of the crooked bar. Its curvature causes that the vibrations are transferred into the rollers per each rotation. The frequencies are dependent on inclination rollers axes, their diameters and rollers angular velocity.

3.2. Region B – Natural frequencies of the bar

The numerical simulation shows that the maximum displacement's amplitudes of the free end of the bar are so large that the bar hits the guide ring sometimes. It yields to an excitation of a free response vibration. Then, frequencies in this area are given by natural frequencies of the straightened bar. As the bar free end becomes shorter in the straightening process also the natural frequencies increase. Evidence of this fact is given in Fig. 8.

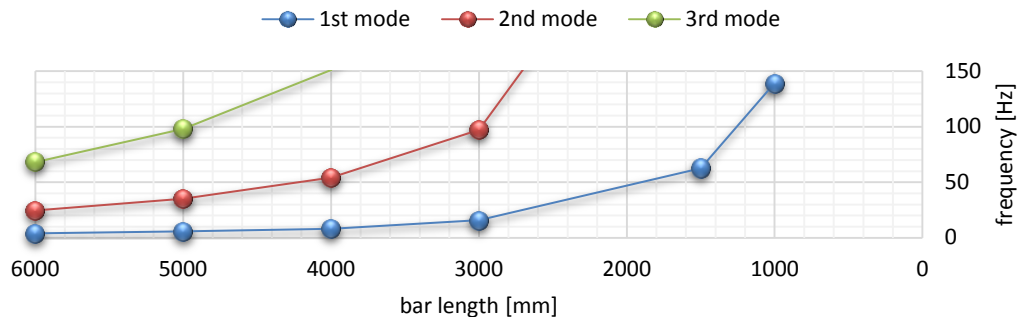


Fig. 8: Dependence of the natural frequencies on the bar length.

This figure indicates an exponential rising trend in the first three natural frequencies of one-side fixed bar for the varying bar length. The same trend can be observed in the spectrograms (mainly in Figs. 3 and 4).

3.3. Region C – Slips of the bar

The simulation shows that the frequencies of the region C are related to modal properties of the bar section, which links rollers 1 and 2. These two rollers are driven. Due to the vibration of bar on the roller 1 there is a slight speed phasing of the bar between the cylinders. This difference is compensated by the bar slips on the one of the rollers. Frequencies in the region C correspond to the natural frequencies of the bar with a length equal to the roller's pitch.

In addition to the three regions, there can be observed the frequencies in the spectrograms without obvious dependence on the known circumstances. But since the straightening process is complex, full of nonlinear phenomena, then other minor excitation actions can occur.

4. Conclusion

This paper was focused on the dynamic analysis of the moments obtained by the numerical simulation of the straightening process. The spectrograms were calculated and areas with significant moment amplitudes were found. These areas were examined in details and the specific causes of excitation were identified. Knowledge of these characteristics can help to prevent undesirable vibrations of the machine already in the design stage.

Acknowledgement

This paper was written with the support of project FSI-S-14-2311.

References

- Mertins, A. (1999) Signal Analysis: Wavelets, Filter Banks, Time-Frequency Transforms and Applications, John Wiley & Sons Ltd., ISBN 0-471-98626-7.
- Skalka, P., Sobotka, J. (2014) Analysis of Dynamic Loading of Bar Straightening Machine Components, In: Proc. 20th Int. Conference Engineering Mechanics, Svratka, Czech Republic, pp. 564-567.
- Fuis, V. (2014) Shape deviations analysis of the aligned bars. In: Proc. 20th Int. Conference Engineering Mechanics, Svratka, Czech Republic, pp. 184-187.
- Fuis, V., Koukal, M., Florian, Z. (2011) Shape Deviations of the Contact Areas of the Total Hip Replacement. In.: Proc. 9th Inter. Conference on Mechatronics Location: Warsaw, Poland. Mechatronics: Recent Technological and Scientific Advances, pp. 203-212.
- Fuis, V. (2009) Tensile Stress Analysis of the Ceramic Head with Micro and Macro Shape Deviations of the Contact Areas. In: Proc. 8th Inter. Conference on Mechatronics, Luhacovice, Czech Republic, Recent Advances in Mechatronics: 2008-2009, pp. 425-430.

STUDY ON SHEAR CONNECTION BETWEEN BRIDGE STEEL TRUSS AND CONCRETE SLAB

J. Machacek^{*}, M. Charvat^{**}

Abstract: *Behaviour of shear connection between steel and concrete parts of steel and concrete composite truss bridges from elastic phase up to plastic collapse is presented. The primary interest concerns the elastic and elastic-plastic distribution of longitudinal shear flow along the connection corresponding to design level of bridge loading. Results of 3D materially non-linear analysis using ANSYS software package is demonstrated together with approximate 2D elastic frame modelling of the shear connection used by designers. Results of both models are mutually compared and confronted with provisions of Eurocode 4 for composite bridges. The non-uniform distribution of the longitudinal shear required for design of shear connection of composite steel and concrete bridges (in both ultimate limit state including fatigue and serviceability limit state) significantly depends on rigidities of the shear connection, steel/concrete parts and concentration of the shear connectors above truss nodes. The most important results from parametric studies are presented and recommendations for practical design suggested.*

Keywords: Steel and concrete composite, Truss girder, Longitudinal shear, Shear connection.

1. Introduction

Composite steel and concrete trusses are used both in buildings as primary or secondary beams and in bridge structures. In ninetieth the comprehensive research (Skidmore et al., 1992) resulted in design recommendations showing wide range of design aspects. In accordance with these recommendations the plastic design can be performed correspondingly to the one of a common plate girder, including the design of a steel-concrete shear connection, provided the shear connectors are ductile.

The elastic design however, is necessary for class 3 and 4 cross sections, rigid shear connectors and generally in bridges (in both ultimate and serviceability limit states). In consequence the highly non-uniform distribution of longitudinal shear along steel truss/concrete slab interface caused by transmitting truss node forces into the concrete slab needs to be taken into account. Local effects of the concentrated longitudinal force introduced into concrete slab of a composite continuous girder due to prestressing were investigated by Johnson & Ivanov (2001) and introduced into Eurocode 4 for bridges (Johnson, 1997). Designers of bridges commonly use shear (vertical) force to calculate longitudinal shear, to which roughly add local effects due to differences of chord forces in truss nodes along estimated length. The detailed experimental and theoretical analysis of composite trusses behaviour both in elastic and plastic region was presented by Machacek & Cudejko (2009). The numerical model using ANSYS software and described briefly below proved to correspond excellently with the tests results.

In this paper the distribution of the shear flow along concrete-steel interface of composite truss bridge girders is analysed by 3D nonlinear analysis (MNA) using ANSYS software and simplified 2D elastic analysis (LA) by SCIA Engineer software. Results of vast parametric studies are shown and discussed.

2. Theoretical Analysis (3D MNA and 2D LA)

Several real bridges were studied, e.g. in city of Pilsen, Fig. 1. First the 3D MNA (materially non-linear analysis) using ANSYS software was applied, Fig. 1. The 3D reinforced concrete elements (SOLID65)

* Prof. Ing. Josef Machacek, DSc.: Faculty of Civil Engineering of the Czech Technical University in Prague, Thakurova 7, 164 00, Prague; CZ, machacek@fsv.cvut.cz

** Ing. Martin Charvat: Faculty of Civil Engineering of the Czech Technical University in Prague, Thakurova 7, 164 00, Prague; CZ, martin.charvat@fsv.cvut.cz

were used for concrete slab, while beam (BEAM24) and shell (SHELL43) elements for steel parts of the truss. Shear connection using the load-slip stud connector diagram given by Oehlers & Coughlan (1986) was modelled by non-linear springs (COMBIN39) located at a suitable spot between the anticipated shear connector and concrete slab (no uplift effects were considered, see Machacek & Cudejko (2009) for more details). The model was applied to experimental trusses employing real steel and concrete properties and load-slip diagram of used shear connector. Both numerical and experimental central deflections and slips between steel truss and concrete parts were nearly identical and therefore the model may be considered as a benchmark for other models.

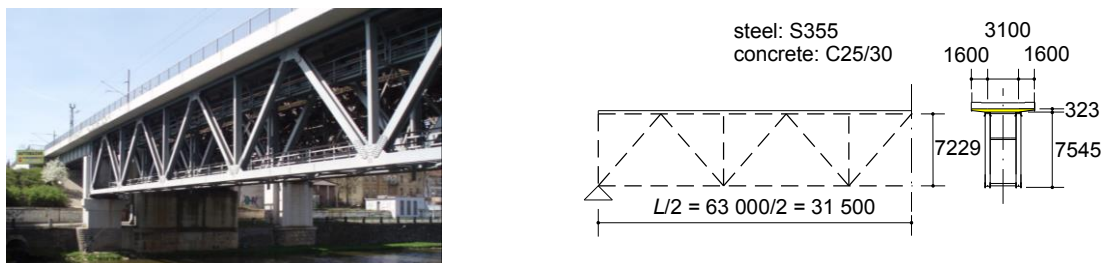


Fig. 1: View of the composite railway bridge and basic data.

For uniformly distributed loading and uniformly distributed shear connectors (headed studs of 19 mm dia, ultimate strength $f_u = 450$ MPa, located in 4 parallel rows and longitudinally in distance of 400 mm) the distribution of shear forces per connector is shown in Fig. 2 (left). After commencing plasticity in the bottom chord of the truss (approx. loading $q = 270$ kN/m) and following plastification of shear connectors (at approx. 82 kN) a rapid plastic shear flow redistribution yields into truss collapse at $q = 325$ kN/m.

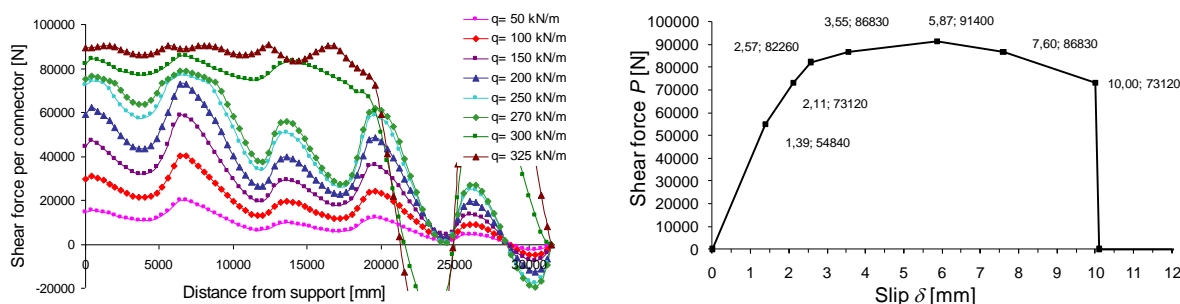


Fig. 2: Shear forces per connector and load-slip diagram of one stud.

Due to rather demanding 3D MNA another study using simplified elastic 2D LA with help of SCIA Engineer common frame software modelling shear connection as short cantilevers between steel truss and concrete slab was performed, which is considered convenient for bridge shear connection design. Only first linear parts of the relationships for both steel and concrete (Young's modulus E , E_{cm}) and linear substitution representing 4 studs at parallel position in accordance with first branch of diagram in Fig. 2 (right) were employed. The shear connectors were modelled as cantilevers of due stiffness sticking out from steel flange axis and pin connected at mid-plane of concrete slab represented by a concrete strut (neglecting slab tension zone) see Fig. 3 (left). Such approach relates to study of longitudinal shear only.

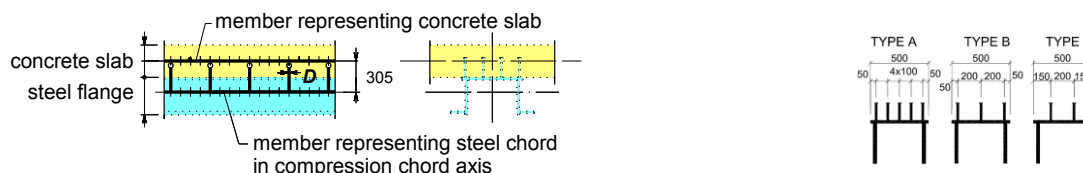


Fig. 3: Left: 2D model of shear connection. Right: Arrangement of studs in parametric study (Chapter 3).

Comparison of shear forces per connector resulting from simplified 2D LA under loading 200 kN/m (which is near to design bridge loading) and non-linear 3D MNA is shown in Fig. 4 (left). The simplified analysis reasonably imitates the ANSYS analysis, while conservativeness (higher values in shear peaks) of simplified elastic solution is obvious. Nevertheless, the simplified analysis seems to be appropriate for

both practical design and parametrical studies. Eurocode 4 (EN 1994-2) distribution of the shear flow for loading 200 kN/m is also shown for both non-ductile shear connectors (inclined, trapezoidal distribution) and ductile ones (rectangular distribution) in Fig. 4 (right). Enormous conservativeness of the Eurocode is evident. Eurocode approach is based on brilliant 3D elastic studies by Johnson & Ivanov (2001), but apparently after abnormal simplification.

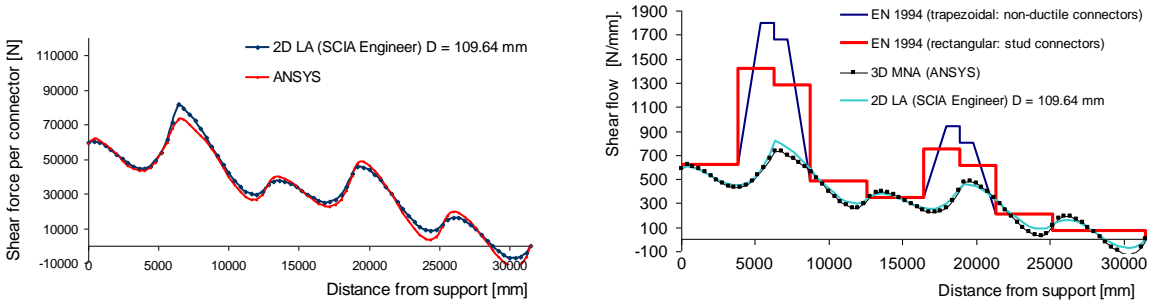


Fig. 4: Left: Shear forces per connector from 2D LA and 3D GMNA, loading 200 kN/m. Right: Comparison of shear flow from both analyses with Eurocode 4, loading 200 kN/m.

3. Parametrical Studies

Detailed parametrical studies in simplified 2D LA were performed for various real bridge structures. Here only those concerning railway bridge shown in Fig. 5 are presented to show the fundamental significance of relevant parameters. Arrangement of shear connectors placed on upper truss chord is shown in Fig. 3 (right). Load-slip relationship of welded studs with characteristic/design strength $P = 81.6/65.3$ kN was linearized up to 48.9 kN.

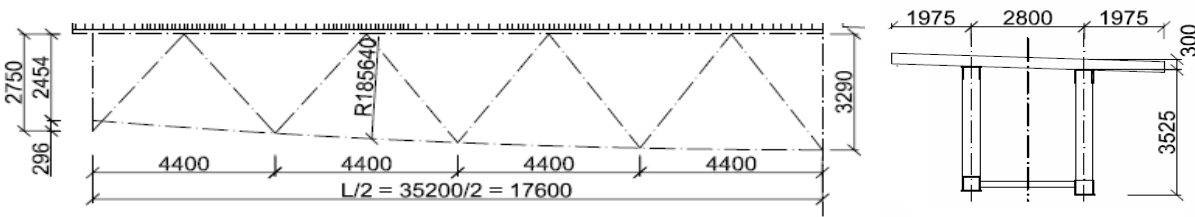


Fig. 5: Layout of the bridge.

This study deals with bridge loading LM71 in central position according to Fig. 6 (left) only, i.e. under unpropped construction and without supplemental dead loadings. Distribution of the shear flow (instead of shear force per connector) for various number of parallel studs uniformly distributed at 200 mm spacing is shown in Fig. 6 (right).

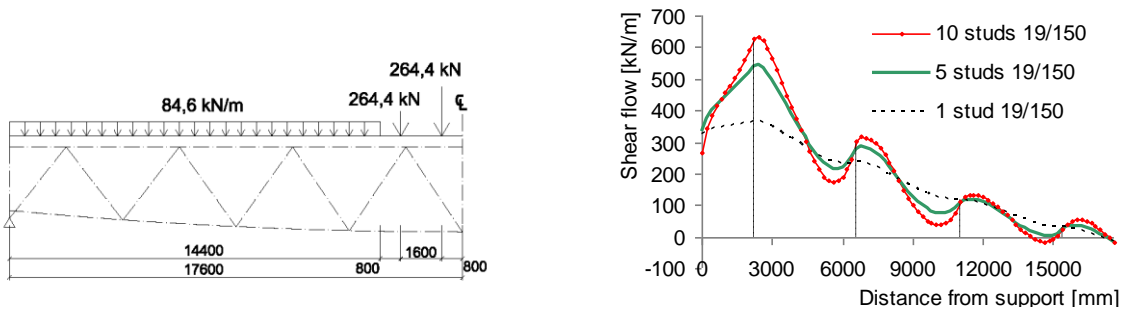


Fig. 6: Left: Relevant design Eurocode bridge loading LM71. Right: Influence of shear connection stiffness (number of parallel studs).

The actual shear forces per one stud arranged as Type A (Fig. 3, right) depending on stiffness of the upper steel chord (second moment of area and corresponding area) and effective width of the concrete slab (initially 3375 x 300 mm) which were rearranged into half or doubled are shown in Fig. 7. In practice the shear peaks are covered by concentrated shear connectors. The densification necessary for successful design of shear connection produces considerable redistribution of the shear flow and attracts the shear flow to concentrated (more rigid) areas. Design of an optimum densification requires an iteration process.

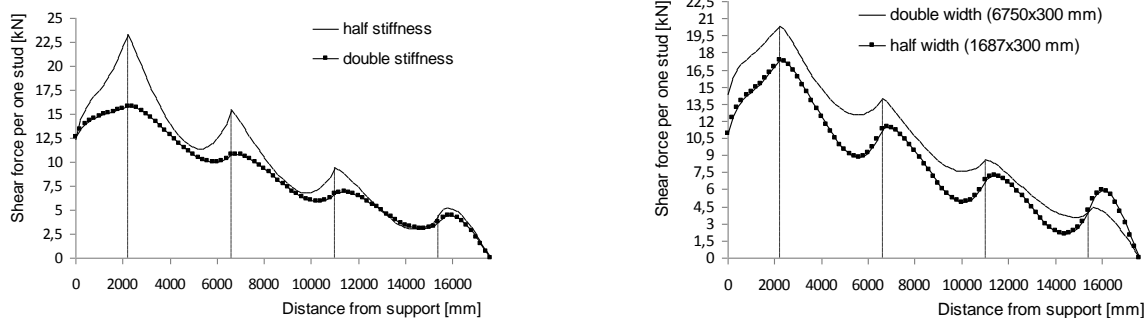


Fig. 7: Left: Influence of stiffness of the upper steel chord. Right: Influence of the slab effective width.

An example of shear forces per one stud, where initial 5 parallel studs in uniform 200 mm distance were densified above the first and second node, is shown in Fig. 8 (left). The concentration of studs within one quarter of node distances (proved to be optimal and marked as densified areas) corresponds to initial ratios of respective shear forces above the first and second node to the force at the third node (2.44 or 1.64, respectively). Obviously the redistribution is not fully optimal and need the second iteration. Other studies were focused on creep and temperature effects. E.g. creep effects on shear forces per connector for uniform supplemental dead loading 94.05 kN/m are illustrated in Fig. 8 (right).

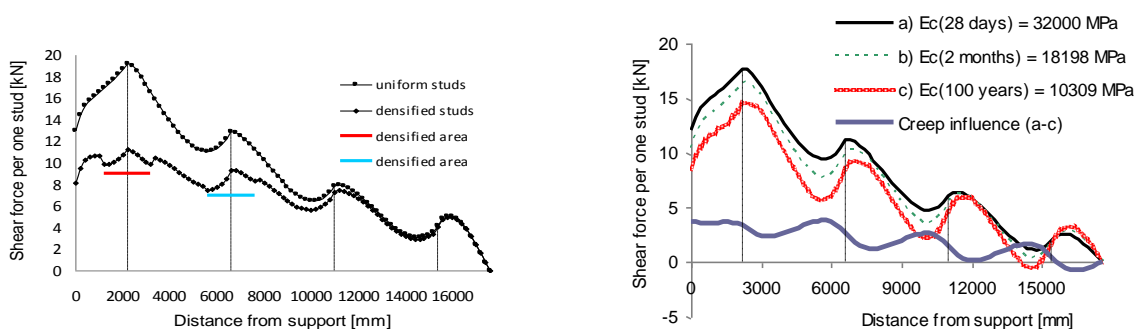


Fig. 8: Left: Shear forces due to densification of studs above the first two truss nodes. Right: Influence of concrete modulus of elasticity (5 parallel studs 19/150, 200 mm spacing).

4. Conclusions

Proposed 2D LA model proved to be an efficient tool for parametric studies and correct design practice. The studies point to following results: The longitudinal shear peaks are more distinct for higher stiffness of the shear connection, less stiff steel chord and wider/thicker concrete slab. Optimum densification of shear connectors within a quarter of node distances is recommended and requires an iteration process. Effects of temperature and creep are similar as in common plated composite steel and concrete bridges.

Acknowledgement

Support of the Czech Grant Agency GACR, grant No. 103/13/25781S, is gratefully acknowledged.

References

- Johnson, R. P. (1997) Shear connection for composite bridges and Eurocode 4: Part 2, In: Proc. Conf. Composite Construction - Conventional and Innovative, Innsbruck, pp. 573-578.
- Johnson, R. P., Ivanov, R. I. (2001) Local effects of concentrated longitudinal shear in composite bridge beams, The Structural Engineer, 79, 5, pp. 19-23.
- Machacek, J., Cudejko, M. (2009) Longitudinal shear in composite steel and concrete trusses, Eng. Structures, 31, 6, pp. 1313-1320.
- Oehlers, D. J., Coughlan, C. G. (1986) The shear stiffness of stud shear connections in composite beams. J. Construct. Steel Research, 6, pp. 273-284.
- Skidmore, Owings, Merrill (1992) Design of composite trusses. Publication 83, SCI (Steel Construction Institute), Ascot.

NUMERICAL ESTIMATION OF MICRO-CRACK PATHS IN POLYMER PARTICULATE COMPOSITE

Z. Majer^{*}, L. Náhlík^{**}

Abstract: *Determination of composite mechanical behavior is one of important part during the composite tailoring. The aim of the present work was to estimate a micro-crack behavior in a polymer particulate composite. The composite was investigated by means of the finite element method - using ANSYS software. A two-dimensional three-phase finite element model was developed to analyze the crack growth behavior. The assumptions of the linear elastic fracture mechanics were considered and the Maximum Tangential Stress (MTS) criterion was used to predict the direction of the crack propagation. The effect of the elastic modulus of the interphase on the micro-crack propagation was investigated. The properties of matrix and particles were taken from experiment. It was shown that the interphase properties influence the stress intensity factor K_I as well as the micro-crack paths. The results of this paper can contribute to a better understanding of the micro-crack propagation in particulate composites with respect to the interphase.*

Keywords: Polymer Composite, Fracture Mechanics, Interphase, Finite Element Method.

1. Introduction

Generally, composites are vastly used in many engineering applications. The main advantage of composites is that mechanical properties can be adapted according to the needs of individual applications. There are many different types of composite materials. One of them is particulate composites, especially the composite with rigid particles and soft matrix, where the particles are used to reinforce the material properties of the matrix. The mechanical behavior of the composite depends on many factors which are associated with particles size, matrix properties, volume filler fraction, etc. (Demjen et al., 1998; Park et al., 2004; Majer et al., 2013). The polymer particulate composites are studied by many authors experimentally (Muratoglu et al., 1995), analytically (Pal, 2005) as well as numerically (Majer et al., 2012). The analytical description of these structures is relatively complicated and the experiments are expensive and time consuming. On the other hand, the numerical approach is easily accessible and could solve many issues in a very short time. Of course, the numerical results should be compared with experimental data (observation) to confirmation.

During the production of the polymer composites the rigid mineral particles are added to the soft polymer matrix. In addition, the mineral particles are usually chemically treated on surface by stearic acid to better dispersion in matrix. This process causes creation of the third phase of the matrix-particle interface, generally called “interphase” (Fu et al., 2008; Kozak et al., 2004). The interphase is a region of a few up to a few hundred nanometers in size. In fact, the interphase controls the adhesion between the matrix and the fillers. The interphase can affect the behavior of the polymer particulate composites. An estimation of interphase properties is not simple due to size of interphase. The properties can be estimated indirectly but the results are significantly dependent on the method of determination (Mesbah et al., 2009). In the paper (Moczko et al., 2002) the interphase thickness was correlated with the work of adhesion and for the polypropylene particulate composite the interphase thickness t of 100 nm was determined.

The aim of the present work was to estimate a crack behavior in a polymer particulate composite using the finite element method. The stress intensity factor K_I versus the crack length was shown.

* Ing. Zdeněk Majer, PhD.: Faculty of Mechanical Engineering, Brno University of Technology, Technická 2; 616 69, Brno; CZ, majer@fme.vutbr.cz

** Assoc. Prof. Ing. Luboš Náhlík, PhD.: CEITEC IPM, Institute of Physics of Materials; Žitkova 22; 616 62, Brno; CZ, nahlik@ipm.cz

2. Computational Model

2.1. Numerical model

A two-dimensional three-phase numerical model was developed, see Fig. 1a. The particles were uniformly dispersed in the matrix with a distance between the particle centers d of 1.25 μm . The diameter D of the round particles was chosen as 1 μm and the thickness of interphase t of 100 nm was used. The initial crack was modeled at a distance c of 0.55 μm from the center line and with an initial length a_i of 0.5 μm .

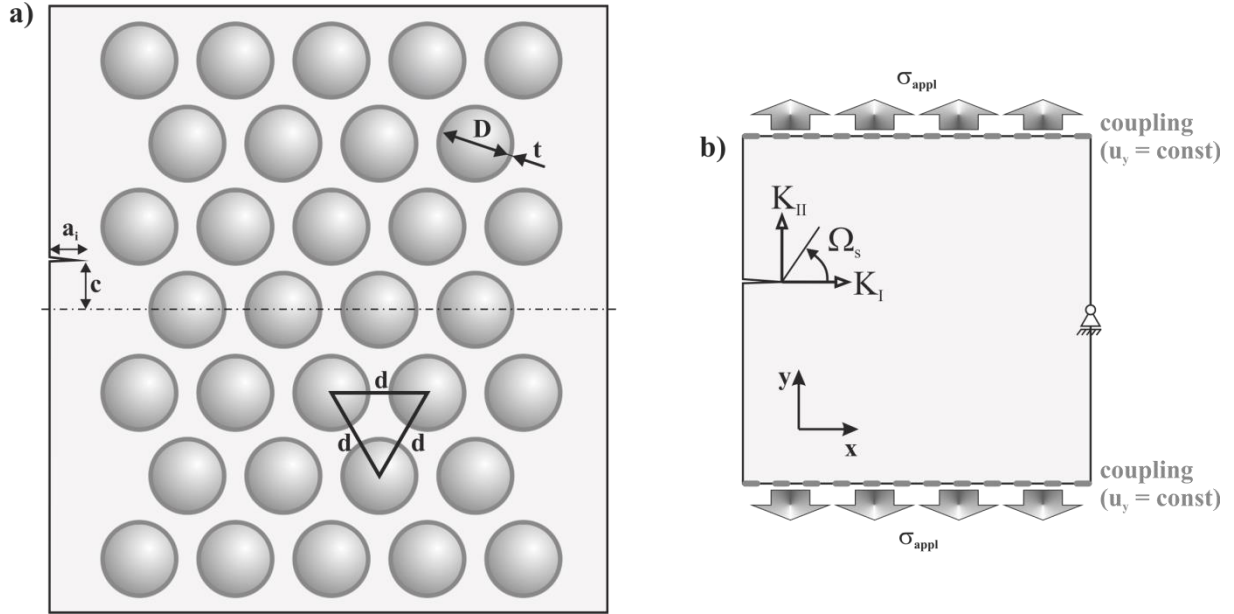


Fig. 1: a) Geometry of the finite element model; b) Used boundary conditions and scheme of the crack propagation direction Ω_s .

Ideal adhesions between matrix, particles and interphase were assumed in the model. The nodes on the top and at the bottom of the model were coupled in the y -direction, see Fig. 1b. A mean stress σ_{appl} of 100 MPa was applied in those regions and held constant throughout the calculation (Majer, 2013). A node on the right of the model was constrained in y direction, as shown in Fig. 1b. Only elastic behavior of the matrix and the particles was considered.

Plane strain condition and elements with quadratic displacement function (ANSYS type “PLANE183”) have been used. The high stress distribution is usually situated around the micro-crack tip and it is important significantly refine the mesh in this area. Moreover, special “crack” finite elements with shifted mid-nodes to capture the stress singularity at the crack tip were used. The values of the stress intensity factors K_I and K_{II} were calculated using the standard KCALC procedure implemented in ANSYS. Obtained values K_I and K_{II} were used for estimation of the direction of the crack propagation.

2.2. Maximum Tangential Stress (MTS) criterion

The propagation of a micro-crack in the matrix of the particulate composite is influenced by its interaction with particles. To describe of the interaction the micro-crack propagation direction has to be known. For the determination of crack propagation direction, numbers of criteria exist in the literature (Sih, 1991). In this paper the Maximum Tangential Stress criterion has been used (Erdogan and Sih, 1963). The criterion assumes that the crack propagates in the direction leading to zero K_{II} values. Determination of crack propagation direction Ω_s can then be expressed by the following equation:

$$\Omega_s = \arccos \left(\frac{3K_{II}^2 + K_I \sqrt{K_I^2 + 8K_{II}^2}}{K_I^2 + 9K_{II}^2} \right) \quad (1)$$

where Ω_s is micro-crack propagation direction and K_I and K_{II} are stress intensity factors for mode I and II, respectively.

2.3. Material properties

The experiments were performed at the Institute of Material Science and Engineering, Faculty of Mechanical Engineering, Brno University of Technology in cooperation with the Polymer Institute Brno, spol. s.r.o. A co-polymer well known as PP SHAC KMT 6100 was used as the matrix (produced by Shell International Chemical Co. Ltd.) and its behavior under different load conditions was measured (Mollikova, 2003; Majer & Novotna, 2011).

The Young's modulus of matrix E_m of 4 GPa was measured (at temperature -50°C) and corresponds value for particles E_p of 72 GPa. The interphase Young's modulus was considered in range from 0.5 GPa to 4 GPa. The value of Poisson's ratio ν of 0.29 was considered for all phases. The particle size was determined from experiment as $1\ \mu\text{m}$.

3. Results and Conclusions

A simplified finite element model of micro-crack growth in polymer particulate composite has been developed and stress intensity factors K_I and K_{II} were calculated on the base of the linear elastic fracture mechanics. Only the selected results are shown.

Influence of stress intensity factor K_I (mode I) on the micro-crack length a was determined, see Fig. 2. The values K_I were calculated for four configurations; interphase Young's modulus of 500, 1000, 2000 and 4000 MPa (in fact without interphase). With decreasing of interphase Young's modulus the value of stress intensity factor increases. It means that the micro-crack could propagate faster in composite with any kind of softer interphase. This effect of interphase is negative.

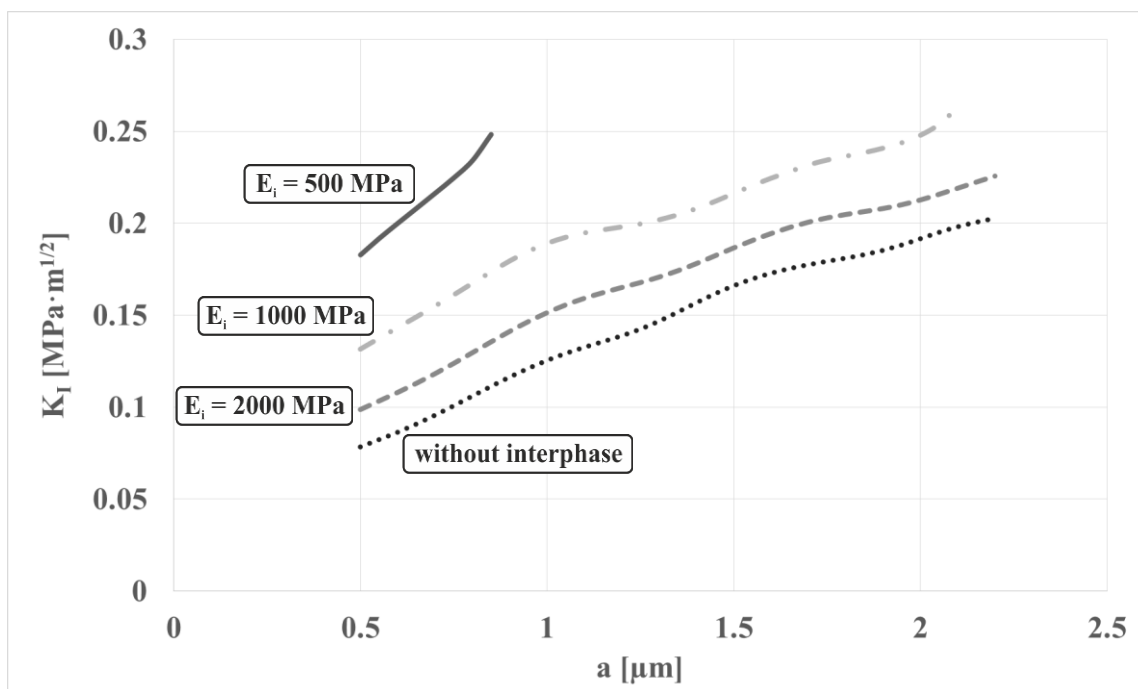


Fig. 2: Calculated values K_I for particulate composite. The initial crack at the distance c of $0.55\ \mu\text{m}$ from the middle plane was considered. Four values of interphase Young's modulus were considered.

On other hand, micro-crack paths influenced by interphase are shown in Fig. 3. It is seen that for two softest interphases (500 and 1000 MPa) the micro-crack is practically attracted to the rigid particle. In fact, for interphase with Young's modulus of 500 MPa the micro-crack touches immediately to the closest particles covered by interphase. For 1000 MPa the micro-crack is not so strongly attracted; nevertheless, micro-crack encounters to other particle. Consequently, the particle can be fully debonded because of high stresses in the interphase which is damaged. As a result, the micro-crack is blunted and stays arrested on the particle. For re-initiation it needs some time and much more energy. The blunting of micro-cracks in connection with debonding can contribute to an increase in the fracture toughness of the composite. The results of this paper can contribute to a better understanding of the micro-crack propagation in particulate composites with respect to the interphase.

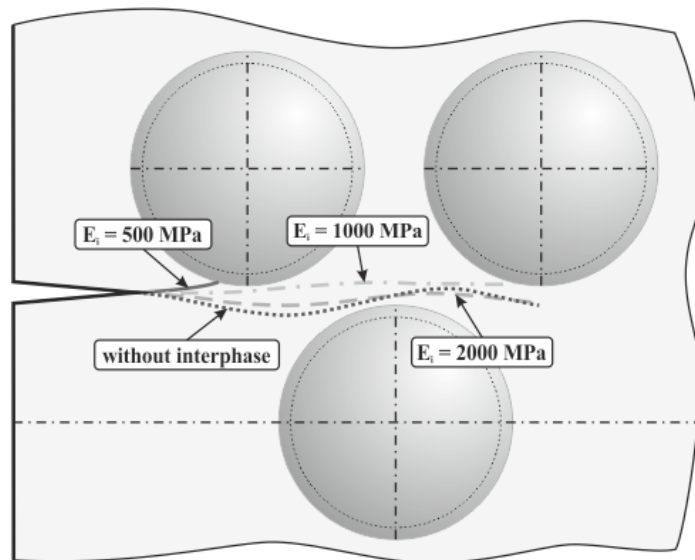


Fig. 3: The paths of the micro-cracks for the distance c of $0.55 \mu\text{m}$ are shown.

Acknowledgement

The investigation has been supported through project No. CZ.1.07/2.3.00/30.0039 of Operational Program Education for Competitiveness of Ministry of Education, Youth and Sport of the Czech Republic.

References

- Demjen, Z., Pukanszky, B., Nagy, J. (1998) Evaluation of interfacial interaction in polypropylene/surface treated CaCO_3 composites. *Composites*, 29A, pp. 323-329.
- Erdogan, F., Sih, G.C. (1963) On the Crack Extension in Plates under Plane Loading and Transverse Shear. *Journal of Basic Engineering*, 85, pp. 519-527.
- Fu, S.Y., Feng, X.Q., Lauke, B., Mai, Y.W. (2008) Effects of particle size, particle/matrix interface adhesion and particle loading on mechanical properties of particulate-polymer composites. *Composites: Part B*, 39, 6, pp. 933-961.
- Kozak, M., Danch, A., Osoba, W., Domka, L., Stelzer, F., Jurga, S. (2004) Relationship between filler loading and morphology of the interphase in polyethylene-chalk composites. *Polymers and Polymer Composites*, 12, pp. 409-416.
- Majer, Z., Novotna, E. (2011) The Effect of Various Non-linear Matrix Types on Mechanical Properties of Particulate Composite. *Chemické Listy*, 105, 17, pp. 830-831.
- Majer, Z., Nahlik, L., Hutar, P. (2012) The Estimation of Micro-crack Behavior in Polymer Particulate Composite with Soft Interphase. *Advanced Materials Research*, 482-484, pp. 1660-1663.
- Majer, Z. (2013) Load Influence on the Behavior of Micro-crack in the Particulate Composite. *Key Engineering Materials*, 525-526, pp. 173-176.
- Majer, Z., Hutar, P., Nahlik, L. (2013) Determination of the Effect of Interphase on the Fracture Toughness and Stiffness of a Particulate Polymer Composite. *Mechanics of Composite Materials*, 49, 5, pp. 475-482.
- Mesbah, A., Zaïri, F., Boutaleb, S., Gloaguen, J.M., Naït-Abdelaziz, M., Xie, S., Boukharouba, T., Lefebvre, J.M. (2009) Experimental characterization and modeling stiffness of polymer/clay nanocomposites within a hierarchical multiscale framework. *Journal of Applied Polymer Science*, 114, pp. 3274-3291.
- Moczo, J., Fekete, E., Pukanszky, B. (2002) Acid-Base Interactions and Interphase Formation in Particulate-Filled Polymers. *The Journal of Adhesion*, 78, 10, pp. 861-875.
- Mollikova, E. (2003) The relationship between technology, structure and mechanical properties of polypropylene filled with magnesium hydroxide. PhD. thesis, Brno (in Czech).
- Muratoglu, O.K., Argon, A.S., Cohen, R.E. (1995) Toughening mechanism of rubber-modified polyamides. *Polymer*, 36, 5, pp. 921-930.
- Pal, R. (2005) New models for effective Young's modulus of particulate composites. *Composites Part B: Engineering*, 36, 6-7, pp. 513-523.
- Park, J., Hong, S.H., Choa, Y., Kim, J. (2004) Fabrication and magnetic properties of LTCC NiZnCu ferrite thick films. *Physica Status Solidi (A) Applied Research*, 201, pp. 1790-1793.
- Sih, G.C. (1991) *Mechanics of Fracture Initiation and Propagation*. Kluwer.

IMPACT OF MISSILE ON CONCRETE OR SOIL OBSTACLE

D. Makovička^{*}, D. Makovička^{**}

Abstract: *Missile-Target interaction analysis is usually based on three essential assumptions and simplifications used to analyze this problem. In this paper the problem of interaction analysis is applied to impact of large body (an airplane, vehicle or a rocket) or small body (concrete fragments) of cylindrical shape as a rule, on concrete obstacle or on soil ground (soils, hard rocks, layered bedrock). In this sense, the paper focuses on impacts of flying body on building structure or on soil in its vicinity. A moving body or its parts may hit various types of structures, and missiles may also enter inside areas of objects through light structures. The impact theory was used to solve the residual mass and velocity of impacting missile, kind of target failure and missile penetration in obstacle. This methodology is based on kinetic energy transfer of the hitting object to the building structure. In this sense, contact areas of the building structure and of the moving object usually need to be specified, based on simplifications of the impact surface of its solid parts.*

Keywords: Missile, Obstacle, Impact, Concrete, Soil.

1. Introduction

In general, upon impact of a moving object on a massive slab-type obstacle the impact surface gradually changes (increases or decreases) as the hitting object is compacted or hits and penetrates the obstacle. When an object hits walls or the ceiling of various structures of an obstacle, parts of the falling object are apparently cut off (for example, wings of airplanes, mudguards and rear-view mirrors of vehicles, etc.). Upon such an impact, total kinetic energy of the falling object is partially consumed for deformation or also for crushing or breaking off of a part of the obstacle. However, the missile still continues to enter the structure at a reduced speed, which is equivalent to energy loss of the whole object upon its impact on a building structure of this type (DOE-STD, 1996). If the object falls on steel beam structures, both the object and its wrecks are slowed down upon impact on load-bearing sections of the structures, which are then deformed or damaged, and the remaining parts continue to further enter the structure at a reduced speed. Similarly, upon impact on concrete walls and boards (or those made of other materials, such as masonry or the ground), engines of vehicles are usually blown off and enter the structure.

Immediately after the impact, the impact is resisted by the structure mass, which corresponds to the area of the impact (collision); this assumption is very conservative and leads to higher velocities of motion of the wrecks upon impact on the structure. The assumption that rather double mass of the impact area resists the impact is apparently closer to reality in flat, large-sized structures.

2. Impact Theory Application

Normal shock of two bodies, an airplane or its wrecks against a building structure, is adapted for nuclear power industry by a DOE (1996) regulation in the U.S. and IAEA (2003) standard, and apparently this regulation can also be applied to other structures. The shock solution methods correspond to procedures commonly used in next publications focused on structure dynamics.

Based on energy comparison, the impact energy E_a transferred to the obstacle is:

^{*} Assoc. Prof. Ing. Daniel Makovička, DSc.: Klokner Institute, Czech Technical University in Prague, Šolínova 7; 166 08, Prague; CZ, daniel.makovicka@klok.cvut.cz

^{**} Ing. Daniel Makovička, Jr.: Static and Dynamic Consulting, Šultysova 170; 284 01 Kutná Hora; CZ, d.makovicka@makovicka.cz

$$E_a = \frac{1}{2} M_e V_t^2 \text{ if } \frac{m}{M_e} \leq e \text{ or } E_a = \frac{1}{2} M_e V_t^2 + \frac{1}{2} m V_m^2 \text{ if } \frac{m}{M_e} > e \quad (1)$$

velocities after impact:

$$V_m = \frac{V_0 \left[\frac{m}{M_e} - e \right]}{1 + \frac{m}{M_e}} \text{ and } V_t = \frac{m / M_e}{1 + (m / M_e)} [V_0 (1 + e)] \quad (2)$$

where m is effective (inertial) mass of missile (inertial mass); M_e is effective (inertial) mass of obstacle; V_0 is normal component of missile velocity before impact; V_m is missile velocity after impact and factor of restitution is:

$$e = \frac{V_t - V_e}{V_e} \quad (3)$$

According to the modified NDRC empiric formula (Bangash, 1993, Durchstanzen, 2002) the perforation thickness of reinforced concrete slab caused by a flying solid object is:

$$t_p = \left(\frac{U}{V} \right)^{0.25} \left(\frac{MV^2}{Df_c'} \right)^{0.5} \quad (4)$$

where U is the reference velocity 200 ft/s; V is the missile impact velocity [ft/s]; $M = W / g$ is the missile mass determined based on its gravity W [lb] and gravitational acceleration $g = 32.2 \text{ ft/s}^2$; D is missile effective diameter [ft] and f_c' is the limit pressure strength of the concrete [lb/ft²].

Shear stress needed to penetrate the reinforced concrete slab is approximately: $4\sqrt{f_c'}$ [psi], or potentially up to $10\sqrt{f_c'}$ [psi]. Using the formula to determine the perforation thickness, the penetration thickness for a missile is equal approximately to 50% of the thickness. On the contrary, if the purpose of using the formula above is to prevent perforation, a slab thickness higher than or equal to $1.2 t_p$ should be used.

For dynamic analysis of interaction of both bodies is possible to use FEM procedure. Example of this solution see (Makovička, 1994) but the truth of the directly dynamic solution and/or energetic method is comparable, especially if the mechanical characteristic of the soil or the form of disturbed missile (by passage through barrier) is determined only very roughly.

3. Fall of Missile on Hard Surface of the Ground

Hard surface is understood either as solidified ground surface, e.g. a road, or hard rock or semi-rock ground. Assuming that the time course of the impact force F_d acting on a solid obstacle, and the time duration of its action $\tau_{ef} = \tau_+ = \Delta t$ are known. Let us assume an impulse $F_d \times \Delta t$ acting approximately on the impact area A ; however, considering pliability of various grounds, it is more suitable to consider the area A as a double impact area. Thus for example, for a solid missile (airplane) and its impact at the speed 450 m/s: impact force $F_d = 300 \text{ MN}$; time of duration $\Delta t = 0.031 \text{ s}$ and impact area $A = 2 \times 16.8 \text{ m}^2$.

Substituting the elasticity modulus E of the bedrock with the deformation modulus $E_{\text{def}} = 8500 \text{ MPa}$ (rock class R2 based on ČSN 73 1101) per height of the cover over the hard bedrock or over a massive concrete structure ($h \approx 1.0 \text{ m}$), the result provides general stiffness of the soil (rock) column:

$$k_{\text{soil}} = E \times A / h = 8500 \times 2 \times 16.8 / 1.0 = 285600 \text{ MN/m} \quad (5)$$

The airplane will thus sink into the ground at the value:

$$y = F / k_{\text{soil}} = 300 / 285600 = 0.001 \text{ m} \quad (6)$$

Apparently, the hard bedrock is able to resist an airplane fall, and the sinking depth is virtually negligible.

Considering clay-sandy soil, the deformation modulus is $E_{\text{def}} = 20 \text{ MPa}$ and the result stiffness and penetration are as follows: $k_{\text{soil}} = 672 \text{ MN/m}$ and $y = 0.446 \text{ m}$. Thus upon impacting on the ground at this velocity, the missile is virtually crashed (compacted) without exerting any rather significant influence on the structure of the ground obstacle. In this case, let us estimate the sinking (penetration) rate from kinetic energy of the impact of the airplane on the clay and sandy ground surface:

$$E_k = \frac{1}{2} m v_r^2 = 0.5 (12 \times 450^2) = 1\,215\,000 \text{ tm}^2/\text{s}^2 \quad (7)$$

And let this energy be consumed only for sinking of the missile into the ground without any considerable damage of the missile, thus:

$$k_{\text{soil}} = E \times A / h = 20 \times 2 \times 16.8 / 1.0 = 672 \text{ MN/m} \text{ and } E_k = F_d x_p \quad (8)$$

Substituting F_d with the design force for an impact on a solid obstacle $F_d = 300 \text{ MN}$, the depth of penetration is as follows: $x_p = E_k / F_d = 1\,215\,000 / 300\,000 = 4.05 \text{ m}$. Taking into account the initial assumptions (in particular, no damage to the missile), the determined penetration depth is markedly increased. The probable penetration value will be significantly lower considering compaction of the missile; let us estimate it as half the value (see a similar assumption in (Durchstanzen von Triebwerken, 2002)). Apparently, even thus recalculated penetration depth x_p will be lower taking into account various losses, but it may also be slightly higher (the fall may not follow the normal line; the missile may hit the ground with an edge, wing, etc.), thus approximately in the range from 0.5 m to 3.5 m. Thus upon hitting a pliable ground, the airplane sinks into the ground given that load capacity of the bedrock at the airplane sinking place is exceeded. This sinking will also cause the stress to distribute to the sides, away from the place of impact.

4. Example

The theory above was used for an impact of chosen airplanes on reinforced concrete wall. Results of the calculated parameters are presented in the following Tab. 1.

Tab. 1: Missile impact on RC transversal wall in thickness 900 m.

Airplane (missile)			Airliner		Airliner		small plane		Fighter	
			unit		engine		unit		unit	
Missile mass	m	[t]	43.6		7.96		3.27		7.96	
Angle of incidence	α	[deg]	30		60		50		60	
Incidence velocity	V	[m/s]	81.3		312		104		312	
Missile diameter	D	[m]	3.75		4.62		3.00		4.62	
Impact area	A	[m ²]	103.8		16.8		11.9		16.8	
Effective mass of obstacle	M_e	[t]	269	538	18.4	36.8	30.8	61.6	43.5	87.0
Missile and obstacle velocity after impact	V_m, V_t	[m/s]	11.3	6.1	8.6	4.6	10.0	5.2	48.3	26.2
Mass of missile after impact	M	[t]	39.2		2.45		2.94		7.96	
Obstacle velocity after impact	V_t	[m/s]	11.3	6.1	8.6	4.6	10.0	5.2	48.3	26.2
Thickness of obstacle	t	[m]	0.90		0.90		0.90		0.90	
Pressure strength of obstacle material	f'_c	[MPa]	10.5		10.5		10.5		10.5	
Perforation depth	t_p	[m]	1.26		0.76		0.46		1.33	

The effect of mass of obstacle is considered in two variants (single and double multiple). This shows that for the big airplane and for fighter the thickness of obstacle is not sufficient. The same may be used for soil barrier; for penetration depth it is possible to use for sandy-clays approximately $f_c' \approx 4$ MPa.

5. Conclusions

Design criteria (DOE, 1996, IAEA 1982 and 2003), used in the world are based particular on the US, Japan and Germany namely experimental investigations. Purpose of these works is development of safety thickness of RC or soil structures on the basis of impact theory and determination of perforation depth into the obstacle. For NPP structures are usually used an airplane and its engine. In our case we used the simplified methods in accordance with international published recommendations and own experiences (Makovička, 1994, 2010 and 2012). The initial kinetic energy of the missile under relatively high speed crash is used for structure solution. Depth of missile penetration into the RC wall or soil layers is function of limit pressure strength of RC or soil materials. The dynamic force of missile, acting on barrier, is then proportion of its kinetic energy and dynamic deflection.

Upon inclined impact of missile and its wrecks on a structure it is assumed that whether or not the structure is broken through depends on the normal component of the part impacting on the surface of the obstacle that is most hazardous for the structure as a rule, and if penetrated, the wrecks together with wrecks of the penetrated building structure continue moving further in the direction of their impact on the structure. However, considering that these phenomena are very fast, the conservative adoption of certain simplifications may be considered.

Acknowledgement

The study is based on outcomes of the research project VG20122015089 supported by the Ministry of the Interior of the Czech Republic.

References

- Bangash, M. Y. H. (1993) Impact and Explosion. Blackwell Scientific Publications, Oxford.
- Durchstanzen von Triebwerken, Grundlagen (2002) Bundesamt für Energie, Hauptabteilung für die Sicherheit der Kernanlagen, Zürich.
- DOE-STD-3014-96 (1996) Accidental analysis for aircraft crash into hazardous facilities. E.S. Department of Energy, Washington, D.C. 20585I.
- Durchstanzen von Triebwerken, Grundlagen (2002), Bundesamt für Energie, Hauptabteilung für die Sicherheit der Kernanlagen, Zürich.
- IAEA Safety Guides No. 50-SG-S5 (1982): External man-induced events in relation to power plant siting. International Atomic Energy Agency (IAEA), Vienna.
- IAEA Standard Guide, NS-G-1.5 (2003) External events excluding earthquakes in the design of nuclear power plants, Vienna.
- Makovička, D., Makovička, D. (1994) Dynamic analysis of reactor containment to airplane crash. Building Research Journal, Vol. 42, No. 1, pp. 15-33.
- Makovička, D., Makovička, D. (2010) Simplified evaluation of a building impacted by a terrorist explosion, In: Jones, N., Brebbia, C.A.: Structures Under Shock and Impact XI, WIT Press, Southampton, pp. 93-104.
- Makovička, D., Makovička, D. (2012) Blast resistant design and limits of the response of a structure to an external explosion, In: Schleyer, G. & Brebbia, C.A.: Structures Under Shock and Impact XII, WIT Press, Southampton, pp. 229-239.

PLASTIC ZONE EXTENT IN A CCT SPECIMEN DETERMINED FROM THE CRACK-TIP STRESS FIELD APPROXIMATED BY MEANS OF THE WILLIAMS EXPANSION

L. Malíková*

Abstract: *A plate with a central crack under uniaxial tension is studied in this work in order to discuss the influence of the number of terms considered in the Williams expansion (derived for approximation of the crack tip stress field) on the plastic zone size. Two criteria are introduced: Rankine criterion and von Mises criterion. Comparison between FEM solution and results obtained by means of the Williams expansion shows that whereas for short cracks the classical one-parameter fracture mechanics can be used, the plastic zone extent estimated via the Williams expansion for longer cracks agrees better to the numerical solution if more than only the first term of the series is considered.*

Keywords: Williams power expansion, Plastic zone extent, Crack-tip field, Over-deterministic method, Multi-parameter fracture mechanics.

1. Introduction

There exists a large group of materials that fail in a brittle manner and whose fracture behavior can be described satisfactorily by means of the well-known stress intensity factor (SIF). On the other hand, a lot of engineering structures is made of materials whose fracture response is more complicated and the SIF as the single-controlling parameter is not sufficient. Some energetic parameters are very often searched in this case in order to assess the fracture behavior properly. Extent of the nonlinear zone around the crack tip, where the fracture processes occur, seems to be one of the important parameters. Furthermore, if a relation between the nonlinear zone extent and boundary condition and/or specimen size and shape is found, the typical phenomenon what is referred to as the size/geometry/boundary effect (Berto & Lazzarin, 2010; Karihaloo et al., 2006) could be minimized/eliminated. In this paper, a multi-parameter approach of approximation of the crack-tip stress field is presented. The so-called Williams expansion (Williams, 1957) is used in order to describe the stress state in a plate with a central crack under uniaxial tension and it is utilized for better estimation of the plastic zone extent.

2. Methodology

Several basic terms and ideas should be presented before the results are introduced.

2.1. Williams power expansion

Williams (1957) derived a power series that can express the stress/displacement crack-tip field in a linear-elastic material with a plane crack with traction-free faces subjected to arbitrary remote loading. If only mode I of loading is considered the expansion for stress tensor components can be written in a form:

$$\sigma_{ij} = \sum_{n=1}^{\infty} \frac{n}{2} r^{\frac{n}{2}-1} A_n f_{ij}^{\sigma}(\theta, n). \quad (1)$$

For further explanations the expression for the displacement vector components shall be known as well:

* Ing. Lucie Malíková, PhD.: Brno University of Technology, Faculty of Civil Engineering, Institute of Structural Mechanics, Veveří 331/95; 612 00, Brno; CZ, malikova.l@fce.vutbr.cz

$$u_i = \sum_{n=0}^{\infty} r^{n/2} A_n f_i^u(\theta, n, E, \nu) . \quad (2)$$

Symbols with the following meanings are used in Eq. (1) and (2):

σ_{ij} stress tensor components; $i, j \in \{x, y\}$;

u_i displacement vector components; $i \in \{x, y\}$;

r, θ polar coordinates centered at the crack tip;

A_n unknown coefficients of the Williams expansion (WE) terms (depend on the specimen geometry, relative crack length α and loading conditions); they have to be determined numerically;

E, ν material properties (Young's modulus and Poisson's ratio);

f_{ij}^σ known functions corresponding to the stress distribution;

f_i^u known functions corresponding to the displacement distribution.

Note that for the presented study only up to ten initial terms of the infinite series are considered, i.e. the expansion has a finite number of terms N .

2.2. Over-deterministic method

The over-deterministic method, ODM, (described in more detail for instance in Ayatollahi & Nejati, 2011) was chosen as a tool for calculation of the coefficients of the Williams expansion terms, A_n . This method is based on the Eq. (2) and it requires knowledge of the displacements field determined by means of the conventional FE analysis in a set of nodes around the crack tip. Efficiency and accuracy of the method have been tested and several recommendations can be found in the paper Šestáková (2013).

2.3. Estimation of the plastic zone size

Two various conditions/criteria for estimation of the plastic zone extent were applied: the Rankine criterion and the von Mises criterion.

2.3.1. Rankine criterion

The Rankine criterion is also known as the normal stress, Coulomb, or maximum stress criterion and it is often used for brittle/quasi-brittle materials. The plastic zone size is estimated by means of the comparison of the principal stress, σ_1 , with a critical stress value, σ_c , that is a material property (tensile strength, yield strength, etc.):

$$\sigma_1 \geq \sigma_c . \quad (3)$$

2.3.2. Von Mises criterion

The von Mises criterion is also referred to as the HMH criterion and it applies best to ductile materials, such as metals. Based on the criterion, the plastic zone size is defined again through the equation between the equivalent (von Mises) stress, σ_{HMH} , and a critical stress value, σ_c :

$$\sigma_{\text{HMH}} \geq \sigma_c . \quad (4)$$

The equivalent (von Mises) stress can be defined for instance as:

$$\sigma_{\text{HMH}} = \frac{1}{\sqrt{2}} \sqrt{(\sigma_{xx} - \sigma_{yy})^2 + (\sigma_{yy} - \sigma_{zz})^2 + (\sigma_{xx} - \sigma_{zz})^2 + 6(\sigma_{yz}^2 + \sigma_{zx}^2 + \sigma_{xy}^2)} . \quad (5)$$

3. Numerical Model of the CCT Configuration

Dimensions of the specimen, see Fig. 1, as well as the material properties (of an aluminium alloy) were taken from the paper written by Tay (1995) in order to verify the analysis: $W = 50$ mm, $h = 100$ mm, $a = 15.6$ mm, $\sigma = 82$ MPa; $E = 73$ GPa, $\nu = 0.3$, $\sigma_c = 370$ MPa. Because of the small specimen thickness ($t = 2.5$ mm) the plane stress conditions were applied in the finite element model. Due to the symmetry, only one quarter of the specimen could be simulated. The commercial FE software

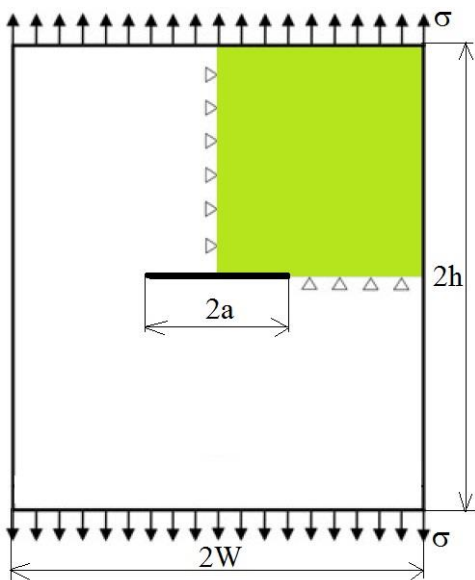


Fig. 1: Schema of the CCT specimen; only the colored quarter of the specimen was modeled.

Ansys was used for the numerical calculations; particularly, PLANE183 elements were applied in order to model the cracked specimen. The crack-tip singularity was simulated via the shifted mid-side nodes in the first row of the triangular elements around the crack tip. The distance of nodes from the crack tip used for application of the ODM was chosen to be 7.8 mm.

4. Results

First, the verification of the method was performed. In Fig. 2a, the comparison of the plastic zone sizes published in Tay (1995) and results calculated by means of the WE when only the first term (as it is usual) is considered. It can be seen that the mutual agreement is very good for both criteria used (note that in the assumed configuration the Rankine criterion is identical to the Tresca criterion). The difference of the experimental data is caused by the nature of the criteria applied, because no redistribution of the stress at the crack tip is considered (it is to be one of the next research areas of the author's collective). Nevertheless, another kind of results shall be shown in this work.

Fig. 2b and 2c (for Rankine and von Mises criterion, respectively) show the plastic zone calculated numerically via FEM together with results calculated by means of the WE under consideration of various numbers of terms used for the reconstruction of the stress field and for determination of the plastic zone.

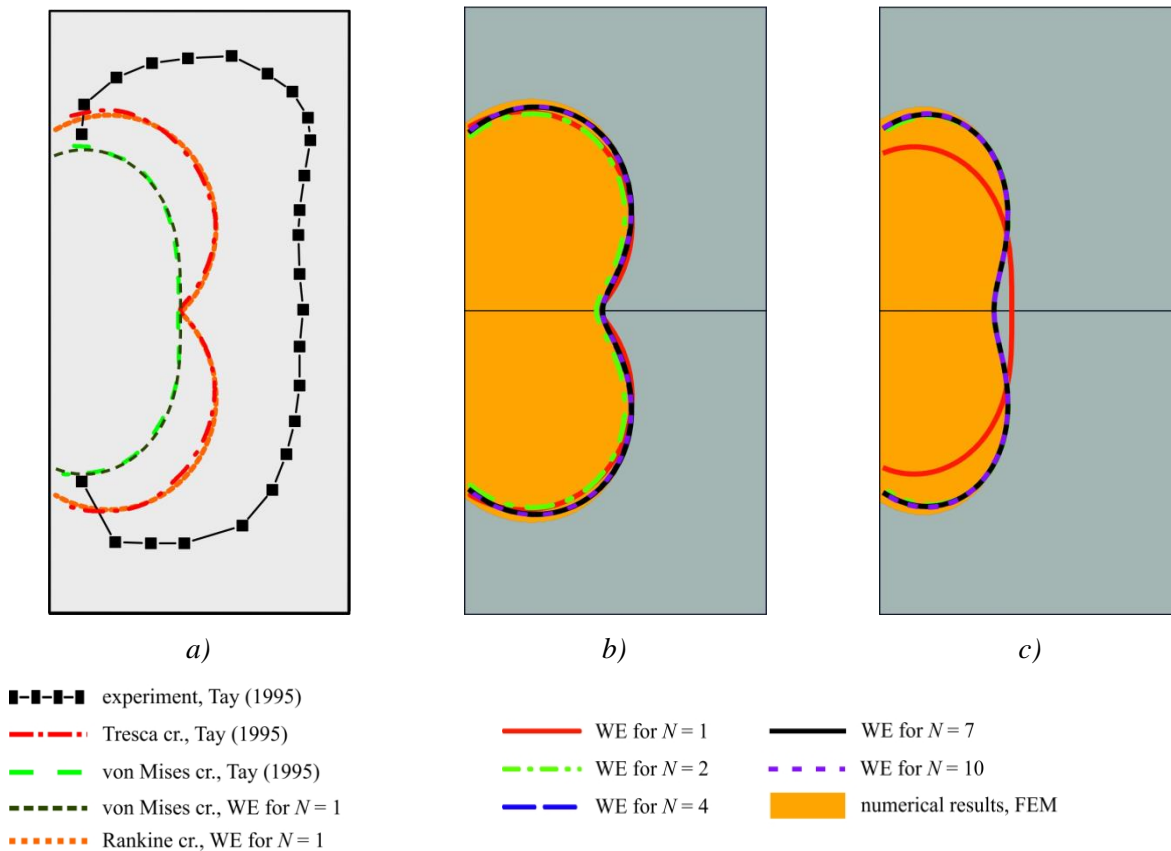


Fig. 2: Comparison of the plastic zone extents: a) Verification of the methodology, i.e. comparison of the data published in Tay (1995) with data calculated by means of the Williams expansion considering only the first term ($N = 1$); b) Plastic zone determined through FEM vs. plastic zone size calculated by means of the Williams expansion from the Rankine criterion; c) ditto b) from the von Mises criterion.

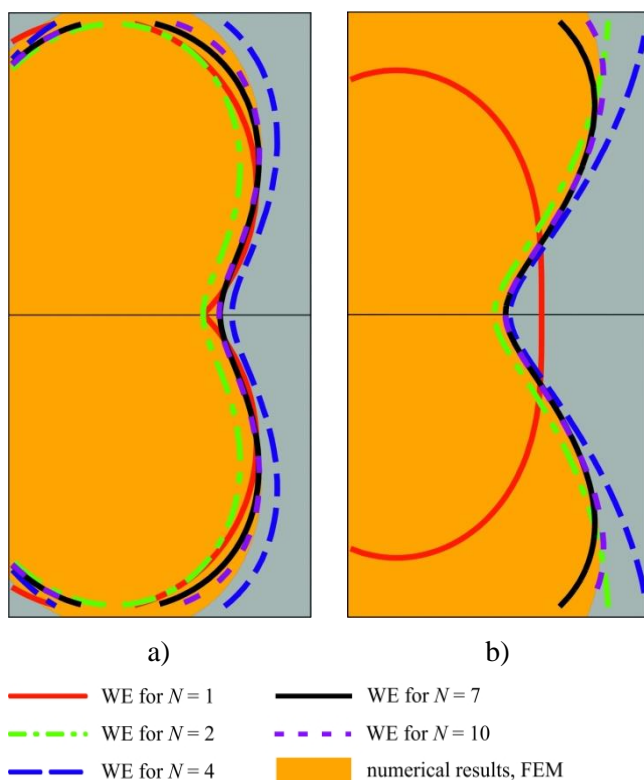


Fig. 3: Comparison of the plastic zone extent for a long crack ($a = 40$ mm) in CCT specimen calculated via FEM with results determined by means of the Williams expansion with various numbers of terms considered ($N = 1, 2, 4, 7$ and 10): a) Rankine criterion; b) Von Mises criterion.

tested, i.e. the stress distribution around the short cracks is not affected by any boundary conditions (e.g. free surface). This is proved on a configuration with a very long crack, where the plastic zone extent calculated from the WE depends on the number of terms considered and the biggest differences are observed between the FEM solution and the conventional one-parameter fracture mechanics approach when the von Mises criterion is applied.

Acknowledgement

Financial support from the Czech Science Foundation (project No. P105/12/P417) is gratefully acknowledged.

References

- Ayatollahi, M.R., Nejati, M. (2011) An over-deterministic method for calculation of coefficients of crack tip asymptotic field from finite element analysis. *Fatigue & Fracture of Engineering Materials & Structures*, 34, pp. 159-176.
- Berto, F., Lazzarin, P. (2010) On higher order terms in the crack tip stress field. *International Journal of Fracture*, 161, pp. 221-226.
- Karihaloo, B.L., Abdalla, H.M., Xiao, Q.Z. (2006) Deterministic size effect in the strength of cracked concrete structures. *Cement and Concrete Research*, 36, pp. 171-188.
- Šestáková, L. (2013) How to enhance efficiency and accuracy of the over-deterministic method used for determination of the coefficients of the higher-order terms in Williams expansion. *Applied Mechanics & Materials*, 245, pp. 120-125.
- Tay, T.E., Yap, C.M., Tay, C.J. (1995) Crack tip and notch tip plastic zone size measurement by the laser speckle technique. *Engineering Fracture Mechanics*, 52, 5, pp. 879-893.
- Williams, M.L. (1957) On the stress distribution at the base of a stationary crack. *Journal of Applied mechanics*, 24, pp. 109-114.

As can be seen in Fig. 2a and 2c, the numerical results agree well with the approximation by means of the WE. Furthermore, there are almost no differences regardless of the number of the WE terms considered. Most likely, this is a consequence of the specimen configuration, because the stress field is not affected by the free surface or other boundary conditions. In order to validate this hypothesis, a CCT configuration with a very long crack ($a = 40$ mm) was modeled, see results in Fig. 3.

Fig. 3 shows that the plastic zone extent for a very long crack calculated by means of the WE differs in dependence on the number of the terms considered. The biggest difference from the FEM solution is clearly apparent if only the first term of the WE is taken into account and the von Mises criterion is applied.

5. Conclusions

In the paper, the plastic zone extent is investigated in a CCT specimen, i.e. in a configuration loaded in mode I. It is shown that for short cracks the size of the plastic zone calculated via FEM is identical to that determined by means of the Williams power expansion considering an arbitrary number of terms of the series. This conclusion is in contradiction to authors experience and it is explained by the configuration of the specimen

AN ALGORITHM FOR COMPUTATIONAL SIMULATION OF MANDIBLE BONE MODELING AND REMODELING AROUND DENTAL IMPLANTS

P. Marcián^{*}, L. Borák^{*}, N. Narra^{**}, P. Skalka^{*}, J. Kaiser^{***}, J. Wolff^{****}

Abstract: *Clinically, dental implants induce diverse stresses on surrounding bone; however, when excessive forces are applied implant failure can occur. The stress and strain fields around dental implants are affected by the bone quality and quantity and the remodeling processes at the bone-implant interface. Computational simulation of the bone remodeling around dental implants still remains a challenge. In this study, a microCT-based 2-D geometry of mandibular segment is used to simulate the remodeling of bone in response to contact with a screw implant. The remodeling process is simulated using an adaptive feedback algorithm which is based on "Mechanostat" strain thresholds, i.e. the initial trabecular architecture changes depending on the loading and boundary conditions and results in the final distribution of the trabeculae within the cancellous bone. The aim of this study is to introduce a novel computational FE model for the simulation of trabecular bone remodeling around dental implants. Computational simulation of the bone remodelling process is strongly dependent on the boundary conditions and thus performing 3-D simulations with more sophisticated boundary conditions is necessary.*

Keywords: Mandible, Bone, Dental implant, Mechanostat theory, FEM.

1. Introduction

Modeling and remodeling of bone tissue is a biomechanical phenomenon that is currently still not fully understood. Furthermore computational simulation of bone remodeling is still at a very early stage of development. The first study that described structural changes in bone caused by mechanical stimuli was presented by Julius Wolff in 1892 (Wolff, 1892). Wolff described the implications of external loading on the trabecular architecture in long bones. In 2004 an American orthopedist and surgeon Harold M. Frost (Frost, 2004) explored how mechanical stimuli can influence the remodeling of bone.

In dental implantology, after the placement of an implant, the surrounding bone tissue undergoes changes in its architecture. The inserted implant is typically in contact with both cortical and cancellous bone tissues. Post-operatively, when the implant is loaded the surrounding bone changes its shape and structure according to Wolff's law. That is, the stresses transferred by the loaded implants induce strain in the adjacent bone which stimulates the modeling/remodeling processes. Additionally, an ideal post-operative healing would involve the osseointegration of the implant into the bone matrix. This process creates a firm/stable connection at the bone-implant interface without mutual relative movement/displacement.

The aim of this study is to model the adaptive changes that the cancellous bone undergoes in response to external loading of an adjacent dental implant. The following sections describe the bone modeling/remodeling algorithm based on the Mechanostat theory and developed using principles of dental biomechanics and computational simulation procedures. Special attention is paid to the level of

^{*} Ing. Petr Marcián, PhD., Ing. Libor Borák, PhD., Ing. Petr Skalka, PhD.: Institute of Solid Mechanics, Mechatronics and Biomechanics, Faculty of Mechanical Engineering, Brno University of Technology, Technická 2896/2, 616 69 Brno, CZ, marcian@fme.vutbr.cz, liborborak@seznam.cz, sklaka@fme.vutbr.cz

^{**} M.Sc. Nathaniel Narra: Department of Electronics and Communications Engineering, Tampere University of Technology, 33520 Tampere; Finland, nathaniel.narragirish@tut.fi

^{***} Prof. Jozef Kaiser, PhD.: X-ray micro CT and nano CT research group, CEITEC - BUT, Brno University of Technology, Technická 2896/2, 616 69 Brno, CZ, kaiser@fme.vutbr.cz

^{****} Jan Wolff, DDS, PhD.: Department of Oral and Maxillofacial Surgery, VU University Medical Center Amsterdam, Amsterdam; Netherlands, Jan.wolff@uta.fi

detail of cancellous bone and the critically important bone-implant interface. The micro-level approach used in this study is not commonly undertaken within the field; thus the results presented in this paper, to the best of our knowledge, have not yet been published in the literature.

2. Methods

In this preliminary study, the 2D model of a mandibular section with the inserted dental implant was based on a single micro-CT (μ CT) cross-sectional image (Fig. 1a). The appropriate image was selected from a tomographic image volume dataset of a mandibular segment with missing teeth. The imaged mandible was obtained from a patient who had bequeathed his body to the Anatomical Institute of Masaryk University in Brno for medical-scientific research and training purposes. The μ CT images of the bone segment were acquired using a unique μ CT device TOMOLAB (Synchrotron Elettra, Trieste, Italy (Bernardini et al., 2012)); with a $17\ \mu\text{m}$ pixel size. Using an in-house software - ROI Analysis (Valášek et al., 2010), the bone volume fraction (BVF) of the cancellous bone was determined to be 0.377 ± 0.056 , which corresponds to groups D2 and D3 of the bone density classification according to Misch (Prášilová et al., 2012).

Subsequently, a 2D geometric model was manually created in ANSYS 14 by a simple tracing of the cortical bone boundary. Thus, bone tissue was segmented into two regions - cortical bone and cancellous bone (Fig. 1b)). The cross-section of a typical dental implant was inserted into the model geometry using Boolean operations and the appropriate commands in ANSYS. It should be noted that the implant geometry is not associated with any specific implant brand, rather it is a general representation of a screw implant. This generalization aids in the qualitative study of the developed method and thus, is in keeping with the scope of this paper. All three areas are glued together. The geometry was discretized using quadratic element PLANE183 with an approximate size of 0.08 mm. The fine mesh consisted of approximately 60 000 elements and 160 000 nodes. The trabecular architecture was created on the final FE mesh by defining the material properties as explained below.

All components of the model were defined as linear isotropic material. Young's moduli of the bone tissues, inter-trabecular pores, and dental implant was 13 700 MPa, 5 MPa and 110 000 MPa, respectively (Mellal et al., 2004; Natali et al., 2003). Poisson's ratio was set in all cases at 0.3. The pores were segmented as a separate region consisting of zero pixel intensities in the processed μ CT image. This region was correspondingly meshed into elements and the material properties defined (Fig. 1c). The plane stress assumption was adopted in the 2D analysis.

The FE model of a unit thickness was loaded by a force of 36 N acting on the dental implant in the axial direction. The value was determined to be "the 2D-equivalent" of 200 N acting on the 3D assembly of bone with implant (Marcián et al., 2013).

The model was simulated under three different boundary conditions (Fig. 2a, b, c):

1. The segment is constrained in the middle of buccal as well as lingual cortical bone boundary;
2. The segment is constrained around the whole bone perimeter except at the alveolar region;
3. The segment is constrained in the basal boundary only.

In the first step, the bone has the initial cancellous bone architecture (and therefore the material properties distribution) as described above. In the following steps, the Mechanostat-based algorithm is employed to predict the trabecular architecture changes throughout the loading (Fig. 3). The algorithm is as follows: After each step, the strain intensity distribution in the bone is determined and the values in all elements are compared to the Mechanostat strain thresholds (Frost, 2004). Strain intensity (ε_{int}) is an invariant defined as the largest of the maximum values of $|\varepsilon_1 - \varepsilon_2|$, $|\varepsilon_1 - \varepsilon_3|$, $|\varepsilon_2 - \varepsilon_3|$, where ε_1 , ε_2 , and ε_3 are the principle strains. Three cases may arise (the thresholds are proposed by Frost): 1. If $\varepsilon_{int} < 250\ \mu\varepsilon$ then the element acquires the properties of pores; 2. If $250\ \mu\varepsilon < \varepsilon_{int} < 4000\ \mu\varepsilon$ then no change in the element properties occurs; 3. If $4000\ \mu\varepsilon < \varepsilon_{int}$ then the element acquires the properties of bone. These cases represent the bone atrophy, bone maintenance, and bone growth, respectively. The solution was performed for 100 steps (cycles) which were identified to be sufficient for the stabilization of the structure. It should be emphasized that this is a preliminary study and the quasistatic character of solution may be questioned. Nevertheless, the work presented in this paper is a springboard to the more sophisticated applications of the Mechanostat-based algorithm which take into account the time factor, typical chewing record etc.

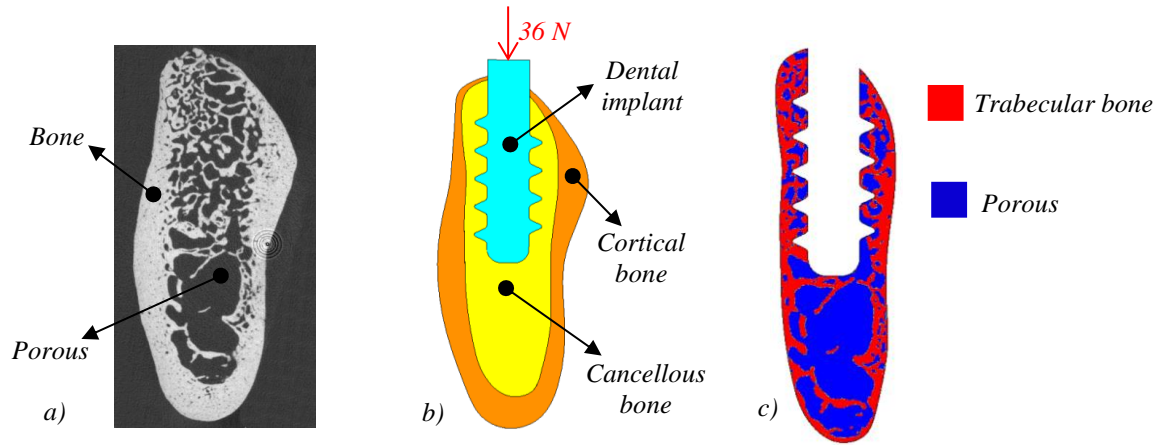


Fig. 1: a) Micro-CT slice; b) Geometry model; c) Trabecular architecture of cancellous bone.

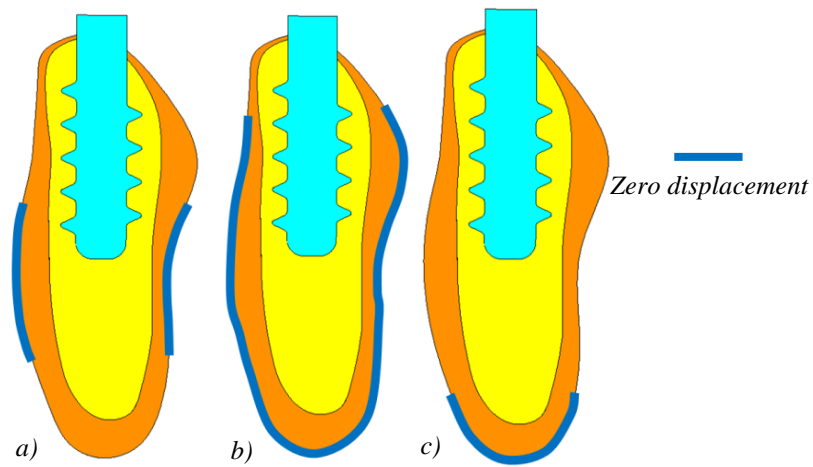


Fig. 2: Three different variants of boundary conditions.

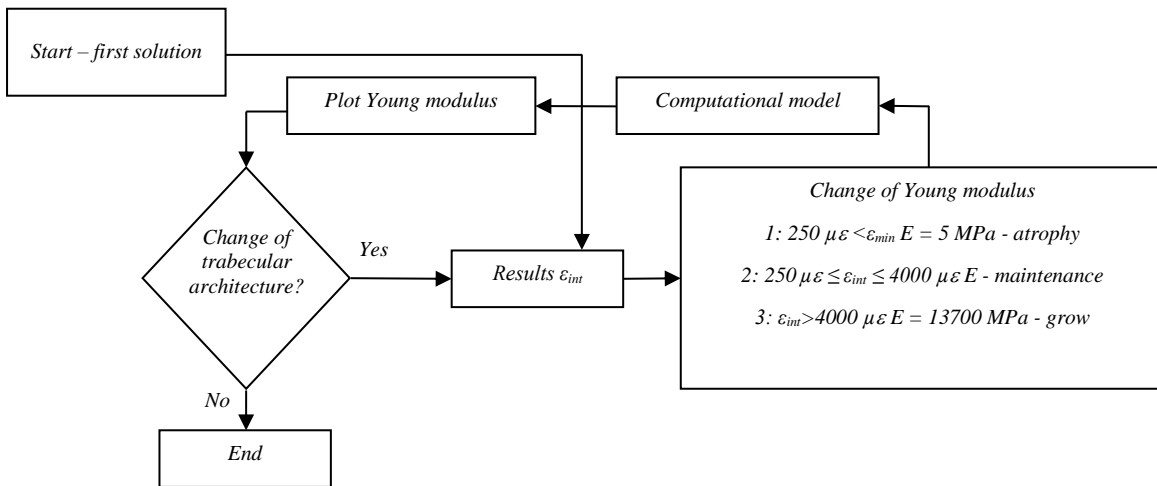


Fig. 3: Algorithm of bone modeling and remodeling.

3. Results

Fig. 4 shows the final shape of the trabecular architecture for all three variants of boundary condition. It is apparent that in cases 1 and 2 the trabecular network, which initially was present in the basal part of the segment, erodes after 100 cycles. In these cases, the cancellous bone adapted to the specific boundary conditions constraining the sides of the segment, i.e. the trabeculae developed in close proximity to the implant only. In case 3, the segment is simply supported in the basal region and the results indicate this to be favorable for the modeling of the trabecular bone.

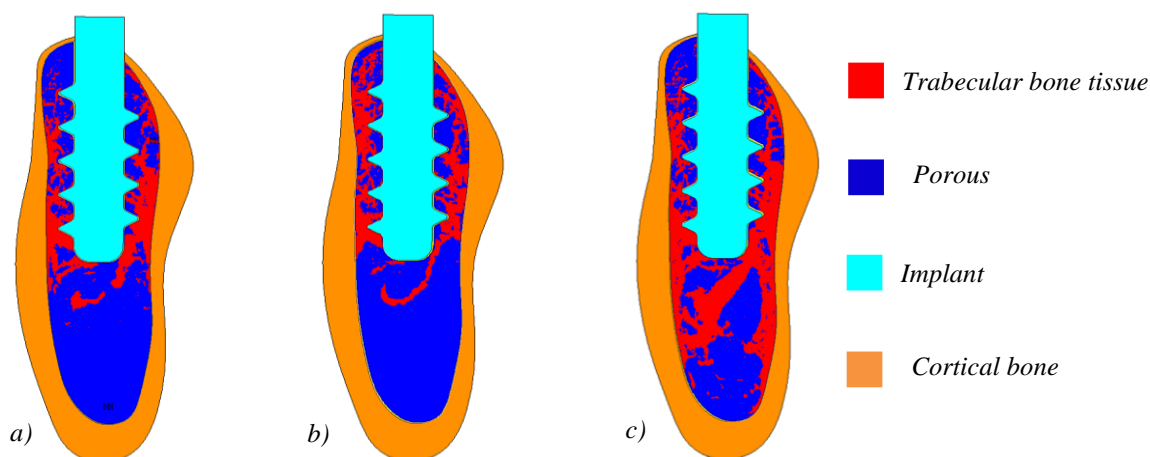


Fig. 4: Finish shape of trabecular bone architecture.

4. Conclusion

This paper describes an initial study of the simulation of bone adaptation to the loading of a dental implant inserted in its proximity. The tissues and regions within the bone are modeled at the microstructure level. Using the Mechanostat-based algorithm the cancellous bone architecture is modeled for 100 cycles over the simulation-adaptation loop under static loading of the implant. Per literature review, the Mechanostat-based algorithm was already applied in bone adaptation prediction. However, to the best of our knowledge, there are no published studies which apply this on a detailed bone and dental implant assembly. The authors are aware that this is the very first step in this specific research direction. The time aspect of the bone modeling/remodeling, the typical loading record, the proper boundary conditions, and other relevant factors must be thoroughly discussed and implemented into the model in order to provide a reliable prediction of the bone adaptation to the external loading. In the near future we aim to integrate all these factors into a 3D geometrical model to develop a more realistic simulation.

Acknowledgement

This work is an output of research and scientific activities of NETME Centre, regional R&D centre built with the financial support from the Operational Programme Research and Development for Innovations within the project NETME Centre (New Technologies for Mechanical Engineering), Reg. No. CZ.1.05/2.1.00/01.0002 and, in the follow-up sustainability stage, supported through NETME CENTRE PLUS (LO1202) by financial means from the Ministry of Education, Youth and Sports under the „National Sustainability Programme I“.

References

- Wolff, J.D. (1892) *Das Gesetz der Transformation der Knochen*. Berlin: Hirschwald.
- Frost, H.M. (2004) A 2003 update of bone physiology and Wolff's law for clinicians. *The Angle orthodontist*, 74, pp. 3-15.
- Bernardini, F., Tuniz, C., Coppa, A., Mancini, L., Dreossi, D., et al. (2012) Beeswax as Dental Filling on a Neolithic Human Tooth. *PLoS ONE*, 7, 9, pp. e44904.
- Valášek, J., Marcián, P., Krpalek, D., Borák, L., Florian, Z., Konečný, O. (2010) Material Properties of Bone Tissue Obtained from CT for Biomechanics Purposes. In *MENDEL 2010*. Mendel Journal series, 1, pp. 483-490.
- Prášilová, E., Marcián, P., Krpalek, D., Řehák, K., Malina, R., Konečná, V. (2012) Comparative Study of Mechanical Properties of Bone Tissue Based on the CT and the micro-CT Slices. *Applied Mechanics and Materials*, 232, pp. 152-156.
- Natali, A.N., Hart, R.T., Pavan, P.G., Knets, I. (2003) Mechanics of bone tissue, in: A.N. Natali (Ed.), *Dental Biomechanics*, Taylor & Francis, London.
- Mellal, A., Wiskott, H.W., Botsis, J., Scherrer, S.S., Belser, U.C. (2004) Stimulating effect of implant loading on surrounding bone. Comparison of three numerical models and validation by in vivo data. *Clinical Oral Implants Research*, 15, pp. 239-248.
- Marcián, P., Borák, L., Konečný, O., Navrátil, P., Florian, Z. (2013) Computational Modeling of Interaction of Dental Implant with Mandible. *Applied Mechanics and Materials*, 245, pp. 57-62.

ON AN ESTIMATION OF THE EXPONENT OF THE STRESS SINGULARITY: THREE DIMENSIONAL PROBLEMS AND EFFECT OF RESIDUAL STRESSES ON A CRACK ARRESTED ON THE INTERFACE

B. Máša^{*}, L. Náhlík^{**}, P. Hutař^{***}

Abstract: *The main aim of this paper is an investigation of the crack behavior in the ceramics laminates. Especially, the problem of the estimation of the stress singularity exponent in such a material using different approaches is closely described. Since analytical approach is a suitable tool for two dimensional problems, introducing residual stresses, which can be result of used procedures during composite production, may influence value of the stress singularity exponent. Unfortunately, there is formally no analytical tool available to introduce residual stresses. Moreover, when the three dimensional geometry is investigated, effects of complicated stress distribution in front of the crack tip are of crucial importance for crack behavior. Hence using numerically obtained stress distribution appears to be the only way, how to capture the effect of residual stresses and three dimensional geometry of the crack front. The stress singularity exponent can be directly determined from stress components in front of the crack tip and/or from displacements at faces of the crack. Both can provide good results and give us a solution, which cannot be obtained analytically. In following text the procedure will be described in more detail and shown results obtained on ceramic laminate.*

Keywords: Stress singularity exponent, Residual stress, Singular stress concentrator, Material interface, Ceramic composites.

1. Introduction

One of the most important material parameters, in terms of fracture mechanics, is fracture toughness. For example usage of ceramics is fairly limited for its brittleness. However, using special technologies and composite design it is possible to prepare ceramic materials with fracture toughness increased three times compared to single ceramic layer without special treatment (e.g. Bermejo et al., 2007). The main idea is to introduce residual stresses, which are closing the crack tip and retard further crack propagation. The interfaces are also barriers for crack propagation – the crack could extend across the interface at some angle; it could extend along the interface; reflect back into the originating material, or arrest. Therefore, the knowledge of the crack behavior in the vicinity or at the interface is of crucial importance.

The stress singularity exponent p of the crack propagating in isotropic, elastic and homogeneous material is $p = 0.5$ (e.g. Williams, 1957). Nevertheless, when the crack terminates the material interface, the classical square root singular field changes its value within the interval $0 < p < 1$. Both, residual stresses and material mismatch may influence the exponent of the stress singularity. This problem occurs also in the place, where the crack front extends to the free surface of the body (e.g. Hutař et al., 2010). Thus, this effect should be included in further considerations about crack behavior near the free surface. Therefore, there is the need to have a suitable tool to evaluate all these effects, either analytically or numerically.

2. Analytical Approach

According to the literature (Knésl et al., 2003; Náhlík et al., 2009), the stress singularity exponent $p = 1 - \lambda$ is given by the solution of the characteristic equation following from the boundary conditions:

* Ing. Bohuslav Máša: Brno University of Technology, Technická 2896/2, 616 69, Brno, CZ, masa@ipm.cz

** Assoc. Prof. Ing. Luboš Náhlík, PhD.: Institute of Physics of Materials, AS CR, Žitkova 513/22, 616 62, Brno, CZ, nahlik@ipm.cz

*** Assoc. Prof. Ing. Pavel Hutař, PhD.: Institute of Physics of Materials, AS CR, Žitkova 513/22, 616 62, Brno, CZ, hutar@ipm.cz

$$\lambda^2(-4\alpha^2 + 4\alpha\beta) + 2\alpha^2 - 2\alpha\beta + 2\alpha - \beta + 1 + (-2\alpha^2 + 2\alpha\beta - 2\alpha + 2\beta)\cos(\lambda\pi) = 0, \quad (1)$$

where α and β are the composite parameters (Meguid et al., 1995) given as follows:

$$\alpha = \frac{\frac{E_1}{E_2}(1+\nu_2) - (1+\nu_1)}{4}, \beta = \frac{E_1}{E_2} \quad \text{for plane stress conditions,} \quad (2)$$

$$\alpha = \frac{\frac{E_1}{E_2} \frac{1+\nu_1}{1-\nu_1} - 1}{4(1-\nu_1)}, \beta = \frac{E_1}{E_2} \frac{1-\nu_1^2}{1-\nu_2^2} \quad \text{for plane strain conditions,} \quad (3)$$

E_1, E_2 are Young moduli, and ν_1, ν_2 are Poisson's ratios of materials, which create the interface.

2.1. Numerical approach

The stress distribution around a crack tip of a crack perpendicular to the interface can be written in the form:

$$\sigma_{ij} = \frac{H_I}{\sqrt{2\pi}} r^{-p} f_{ij}(p, \theta), \quad (4)$$

where H_I [MPa.m^p] is a generalized stress intensity factor and r, θ are polar coordinates with origin at the crack tip. Thus, one of the possible approaches is to estimate the stress singularity exponent directly from numerically obtained stress distribution in front of the crack tip. For given geometry, boundary conditions and polar angle θ the stress components correspond to:

$$\sigma_{ij} \approx r^{-p}. \quad (5)$$

The stress singularity exponent corresponds directly to the tangent of the stress distribution (5) expressed in log-log coordinates. Similar approach can be used for the stress singularity exponent determination from numerically obtained displacements on the crack faces. The relation between displacement components and the stress singularity exponent is:

$$u_{ij} \approx r^{1-p}. \quad (6)$$

Let us note that estimation of the stress singularity exponent using these approaches is quite accurate and is suitable for problems, where analytical solution is not defined, e.g. for 3D problems, where the complicated stress distribution is expected. The disadvantage is dependence on the mesh density – numerical model has to contain fine mesh around the crack tip and this will cause important increase in time for model preparation, high hardware requirements and the calculation is time consuming.

3. Numerical Modeling

For estimation of the stress singularity exponent a ceramic composite was chosen in order to capture an effect of the 2D and 3D crack front geometry and how the residual stresses can influence its value. The composite design was a laminate with A-B-A architecture, which consists of 5 ATZ layers (alumina with tetragonal zirconia) $t_{\text{ATZ}} = 0.52$ mm and 4 AMZ layers (alumina with monoclinic zirconia) $t_{\text{AMZ}} = 0.10$ mm (Fig. 1). Material properties (see Tab. 1) of the laminate layers were taken from the works (Bermejo et al., 2007; Náhlík et al., 2009).

Tab. 1: Material properties of the studied laminate (Bermejo 2007, Náhlík 2009).

PROPERTY	UNITS	ATZ	AMZ
Young's modulus E	GPa	390	280
Poisson's ratio ν	-	0.22	0.22
Coefficient of thermal expansion α_t	10^{-6}K^{-1}	9.82	8.02

For the stress distribution around the crack tip numerical 2D and 3D models were created in commercial FEM software Ansys 13.0. However, two dimensional models represent the crack passing through the entire layer, which is not in agreement with experimental observations. The crack propagating in a plate exhibits approximately a semi-elliptical crack front shape. Thus, parametrically controlled 3D models with semi-elliptical crack front were developed. On the crack front numerous locations were selected and the stress intensity factor K_I was computed using the direct method (extrapolation of stress component to the crack tip). Under assumption of the constant stress intensity factor along the crack front, the real crack front shape was iteratively found (Hutař et al., 2010; Ševčík et al., 2012), see Fig. 2.

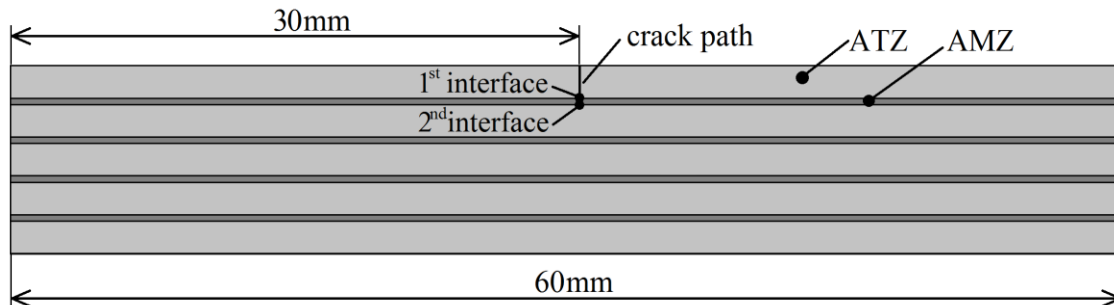


Fig. 1: Design scheme of the laminate with predefined crack path and evaluated interfaces.

Let us note that the residual stresses were prescribed to the numerical model using different thermal coefficients for ATZ and AMZ layer. The specimen is during preparation cooled down from the stress free temperature 1250°C to the room temperature. After this procedure strong residual stresses are developed in the laminate layers (for given case ATZ = +110 MPa, AMZ = -715 MPa), which are able to open/close the crack tip and influence the crack behavior, see Fig. 3.

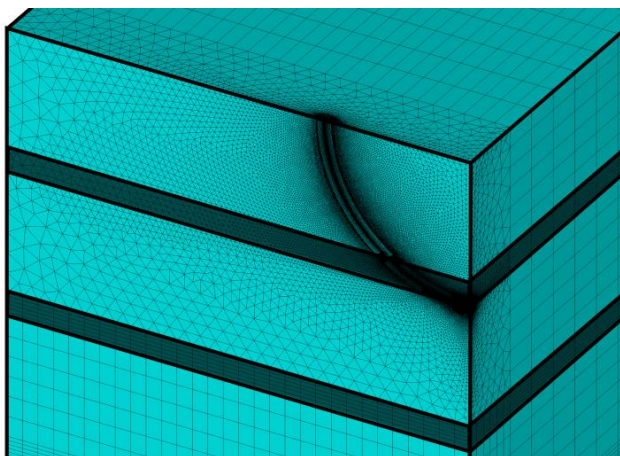


Fig. 2: The real crack front shape numerically estimated for the 3D geometry.

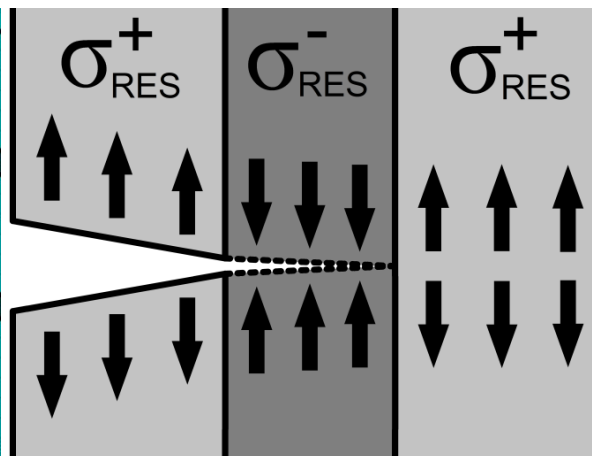


Fig. 3: Effect of the residual stresses distributed in ATZ and AMZ layers.

4. Results

Following previous methodology, analytical solution was used for the 2D geometry where the first 2 interfaces were considered. Also, numerical modeling was performed for the 2D and 3D configurations for the same interfaces, where following loading of the laminate was chosen: a) external bending loading only, b) internal residual stresses only, c) combination of the external and internal loading. The results for the first ATZ/AMZ interface are summarized in the Tab. 2. It is evident that the 2D numerical solution differs slightly from the analytical solution and error is less than 2% for all three loadings considered. When 3D models were evaluated, differences are about 10%. This is due to different stress distribution caused by semi-elliptical shape of the crack front touching the interface.

For the AMZ/ATZ interface analytical solution is in a good agreement with 2D model with external loading only. This situation represents a state, for which is the analytical approach derived and match of these two results was expected. Three-dimensional numerical model shows again a slight difference from the analytical solution. Nevertheless, the strong compressive stresses of 715 MPa cause that no crack opening is obtained and exponent of the stress singularity could not be evaluated clearly (or with a

significant error) using extrapolation of the opening stress to the crack tip. Moreover, determination from numerically obtained displacements on the crack faces fails completely, because of negative values of displacement were computed. This, again, physically means that no crack opening occurs.

Tab. 2: Estimation of the stress singularity exponent for the crack on ATZ/AMZ and AMZ/ATZ interfaces.

APPLIED LOADING		SOLUTION FOR ATZ/AMZ INTERFACE		
External loading	Residual stresses	Analytical	2D numerical	3D numerical
Yes	no	0.54008	0.54826	0.60185
No	yes	0.54008	0.54956	0.60461
Yes	yes	0.54008	0.54874	0.60265
External loading	Residual stresses	SOLUTION FOR AMZ/ATZ INTERFACE		
Yes	no	0.46451	0.47240	0.54650
No	yes	0.46451	X	X
Yes	yes	0.46451	X	X

5. Conclusions

This paper deals with an estimation of the stress singularity exponent. Analytical approach was presented and used for the exponent evaluation. This procedure is able to capture the effect of material mismatch on the composite interface accurately. Nevertheless, does not correspond to the 3D problems. Moreover, when the effect of residual stresses needs to be captured, this method has no option to incorporate this effect to the solution. When the 3D problem with consideration of residual stresses is investigated, the numerical approach for the stress singularity exponent evaluation is needed. This approach takes into account all effects which may influence a stress field around the crack tip - this leads to the more accurate value of the exponent. Disadvantage of this approach is requirement for the fine mesh in the vicinity of the crack, which increase the computation time. Nevertheless, based on the results, no significant difference on the value of the stress singularity exponent was observed between analytical and 2D numerical solution for all considered types of loading. On the other hand, when 3D crack is investigated, the exponent should be evaluated numerically.

Acknowledgement

This work was supported through the Specific academic research grant No. FSI-S-11-11/1190 provided to Brno University of Technology, Faculty of Mechanical Engineering and grant No. CZ.1.07/2.3.00/30.0063 of the Ministry of Education, Youth and Sports of the Czech Republic.

References

- Williams, M.L. (1957) On the Stress Distribution at the Base of a Stationary Crack. *Journal of Applied Mechanics*, 24, pp. 109-114.
- Knésl, Z., Náhlík, L., Radon, J.C. (2003) Influence of interface on fatigue threshold values in elastic bimetals. *Computational Materials Science*, 28, pp. 620-627.
- Náhlík, L., Šestáková, L., Hutař, P. (2009) Estimation of apparent fracture toughness of ceramic laminates. *Computational Materials Science*, 46, pp. 614-620.
- Meguid, S.A., Tan, M., Zhu, Z.H. (1995) Analysis of cracks perpendicular to biomaterial interfaces using a novel finite element. *International Journal of Fracture*, 73, pp. 1-23.
- Hutař, P., Náhlík, L., Knésl, Z. (2010) The effect of a free surface on fatigue crack behavior, *International Journal of Fatigue*, 32, pp. 1265-1269.
- Bermejo, R., Torres, Y., Baudín, C., Sánchez-Herencia, A.J., Pascual, J., Anglada, M., Llanes, L. (2007) Threshold strength evaluation on an Al₂O₃-ZrO₂ multilayered system. *Journal of the European Ceramic Society*, 27, pp. 1443-1448.
- Ševčík, M., Hutař, P., Knésl, Z., Náhlík, L., Zouhar, M. (2012) Estimation of the critical configuration of a crack arrested at the interface between two materials. *Computational Materials Science*, 64, pp. 225-228.

FRACTURE MECHANICS ASSESSMENT OF CRACKED WELDED POLYOLEFIN PIPES

J. Mikula^{*}, M. Ševčík^{**}, P. Hutař^{***}, L. Náhlík^{****}

Abstract: *The aim of this paper is to present methodology for estimation of fracture mechanics parameters in polyolefin pipes with an axially oriented crack using three dimensional numerical analyses. Linear elastic fracture mechanics is used for description of fracture behavior. In the paper, three different variants of pipe weld with an internal axial semi-elliptical crack are studied. Numerical models correspond to a cracked pipe containing material nonhomogeneity in the welding area caused by welding process. A critical locations of the crack initiated along the pipe wall is found and the stress intensity factor for such cracks with real crack shape are numerically estimated in these critical locations. The methodology presented here can be used for estimation of residual lifetime of welded polymer pipes containing crack.*

Keywords: Polyolefin pipes, Butt weld, Stress intensity factor, Numerical modeling.

1. Introduction

Nowadays, polyolefin materials are common material in piping industry. Polyolefin materials show high resistance to corrosion, abrasion or chemicals and are therefore suitable for those applications, rather than metallic or ceramic materials. In service, a high functionality is required and thus the pipes are usually designed with a lifetime exceeding 50 years. A new generation of pipes should be able to survive up to 100 years. The pipes are usually connected using butt welding process. Once the welding is finished a material nonhomogeneity takes place in the heat affected zone. Such a change in material properties may accelerate the failure processes. Thus the purpose of this paper is to study the contribution of presence of material nonhomogeneity caused by welding process on the fracture parameter of the crack growing in weld area.

One of the typical failure modes of pressurized polyolefin pipes is quasi-static failure that represents slow (creep) crack growth of a crack initiating at the internal pipe surface. Creep failure testing of the pipes in real time is not practical as the test would be extremely long and expensive. For these reasons numerical models of cracked pipes are being developed in order to study the fracture behavior in reliable time. Even though the material exhibits viscoelastic behavior the slow crack growth regime can be evaluated using linear elastic fracture mechanics (LEFM) approach as the plastic zone in the vicinity of the crack is small and the crack growth rate is slow.

2. Numerical Model

For finite element calculations (FE) of polyolefin pipes a three dimensional model has been developed using the commercial package ANSYS. The pipe dimensions used in the calculations were: outer pipe diameter $d = 125$ mm and pipe wall thickness $s = 7.4$ mm.

^{*} Bc. Jakub Mikula: Institute of Physics of Materials Academy of Science of the Czech Republic, v. v. i., Žižkova 22, 616 62 Brno; and Brno University of Technology, Faculty of Mechanical Engineering, Technická 2896/2, 616 69 Brno; CZ mikula_jakub@centrum.sk

^{**} Ing. Martin Ševčík, PhD.: Institute of Physics of Materials Academy of Science of the Czech Republic, v. v. i., Žižkova 22, 616 62 Brno; Czech Republic, sevcik@ipm.cz

^{***} Assoc. Prof. Ing. Pavel Hutař, PhD.: Institute of Physics of Materials Academy of Science of the Czech Republic, v. v. i., Žižkova 22, 616 62 Brno; Czech Republic, hutar@ipm.cz

^{****} Assoc. Prof. Ing. Luboš Náhlík, PhD.: Institute of Physics of Materials Academy of Science of the Czech Republic, v. v. i., Žižkova 22, 616 62 Brno; Czech Republic, nahlik@ipm.cz

The pipe was loaded by an internal pressure $p_{int} \approx 0.8$ MPa acting at both inner pipe surface and crack faces that results in hoop stress of $\sigma_{hoop} = 6$ MPa.

A distribution of Young's modulus in the welding area can be roughly estimated based on the micro-indentation tests along the pipe weld (Lach et al., 2013). The distribution of Young's modulus along the weld can be modeled by the double power-law function (Chi and Chung, 2003) as follows:

$$E(z) = h_1(z)E_{max} + [1 - h_1(z)]E_{min} \text{ for } 0 \leq z \leq w/2, \quad (1a)$$

$$E(z) = h_2(z)E_{max} + [1 - h_2(z)]E_{min} \text{ for } w/2 \leq z \leq w,$$

where function $h_{1,2}(z)$ are:

$$h_1(z) = \frac{1}{2} \left(\frac{z}{w/2} \right)^p \quad 0 \leq z \leq w/2, \quad (1b)$$

$$h_2(z) = 1 - \frac{1}{2} \left(\frac{w-z}{w/2} \right)^p \quad w/2 \leq z \leq w;$$

and where p is an exponent describing the change of material properties and w is the half-width of the weld region, see Fig. 1. Based on experimental results, performed on the same pipe geometry as analysed in this paper, the exponent $p = 2$ and the width of the weld region $2w = 14$ mm were considered for the numerical analyses. The ratio E_{max}/E_{min} corresponds mainly to pipe materials being welded, e.g. polypropylene pipes exhibit ratio $E_{max}/E_{min} = 1.32$. The Young's modulus of the base pipe material was considered as $E_{min} = 180$ MPa (corresponds to working temperature of 80°C). The Poisson's ratio of $\nu = 0.35$ has been kept constant along the weld.

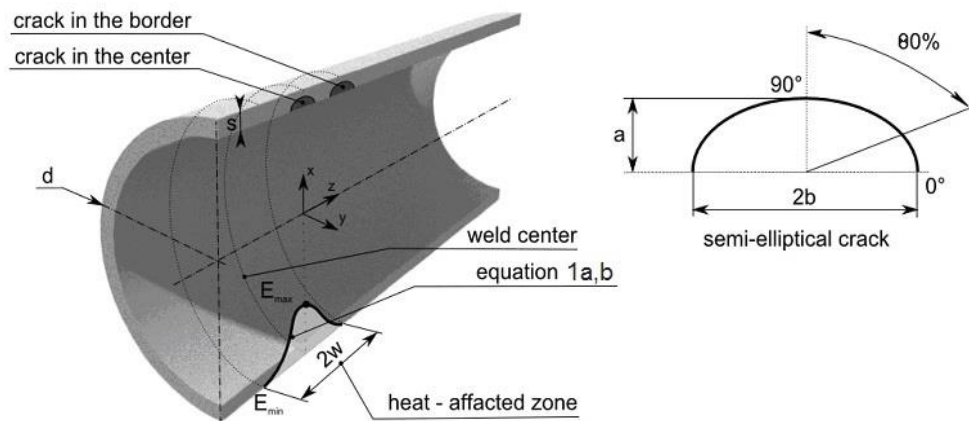


Fig. 1: Scheme of the pipe with a crack considered in the work.

In this study, three different models of the cracked welded pipe have been compared:

- Homogeneous pipe with a crack (PIPE 1),
- Nonhomogeneous pipe weld with a crack in the center of the weld (WELD 1),
- Nonhomogeneous pipe weld with a crack in the border of the weld (WELD 2).

For the homogeneous pipe only the value of E_{min} was considered for the whole numerical model. A preview of finite element mesh with a detail of mesh refinement near the crack front is shown in Fig. 2.

Due to existence of two planes of symmetry only one-quarter of the welded pipe was evaluated in the case of PIPE 1 and WELD 1 model. Due to the crack not lying in the center of the weld, only one plane of symmetry exists for WELD 2 model so that one-half of the welded pipe was considered. The finite element mesh was created by 20-nodes iso-parametrical quadratic element (denoted by number 186 in ANSYS) taken for the calculations and the density of mesh used was depending on the crack length varying from 550 000 to 650 000 elements in the first two cases and about twice as much in the third

case. The highest mesh density was concentrated near the crack front in order to describe the stress state near the crack front properly.

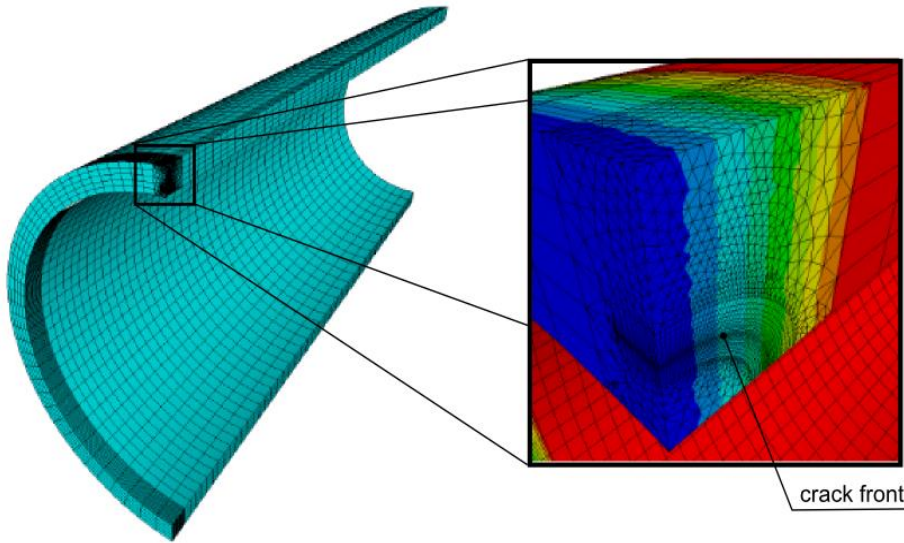


Fig. 2: Finite element mesh with a detail of mesh refinement near the crack front (colors represents different material properties in weld area).

The stress intensity factor for different crack lengths was numerically estimated, from which the lifetime of the pipe can be estimated. The stress intensity factor was evaluated using so called direct method, which is based on extrapolating the opening stress values to the crack tip. It should be mentioned that a few points closest to the crack front are influenced by the numerical error and should be omitted from the extrapolation. To get closer to the real crack propagation a real crack front shape can be found using numerical methods. For a general case of the semi-elliptical crack in the body the distribution of the stress intensity factor (SIF) over the crack front is not constant. It can be assumed the real crack propagates in the continuum when the distribution of the SIF is constant along the crack front. It is possible e.g. to estimate the SIF in 30 points along the crack front and change the aspect ratio of the semi-elliptical crack shape in order to find the real crack front shape. However, the extrapolation paths along the crack front should not be close to the free surface of the body. The reason for this is the vertex singularity (Bažant et al., 1979; Pook, 1994; Hutař et al., 2009) near the free surface that significantly changes the stress field in the vertex point at the free surface so that SIF cannot be estimated correctly by classical approaches of LEFM. Hutař et al., 2011 published an approximative relation for the development of the semi-elliptical crack front in the homogenous polymer pipe as follows:

$$b = a \left[-0.1936 \left(\frac{a}{s} \right)^2 + 0.6628 \left(\frac{a}{s} \right) + 1.0919 \right], \quad (2)$$

where a and b are lengths of major and minor axis of the ellipse representing the crack front shape, see Fig. 1. The crack front shape determined by Eq. (2) is quite similar to those crack front shapes numerically estimated using to the procedure described above for all studied locations of the crack.

3. Results

The stress intensity factor has been numerically estimated for a cracked polymer pipe welds for various position of the crack initiation. An initial defect of 0.1 mm has been considered. The change of the crack front shape during the crack growth was also taken into account. The comparison of stress intensity factor estimated for various crack positions is shown in Fig. 3. An approximative relation for calculation of the stress intensity factor in internally cracked pressurized polymer pipe found in (Hutař et al., 2011) in the following form was used for comparison:

$$K_I = \frac{p_{int} d}{s} \sqrt{\pi a} \left[0.3417 + 0.0588 \left(\frac{a}{s} \right) - 0.0319 \left(\frac{a}{s} \right)^2 + 0.1409 \left(\frac{a}{s} \right)^3 \right]. \quad (3)$$

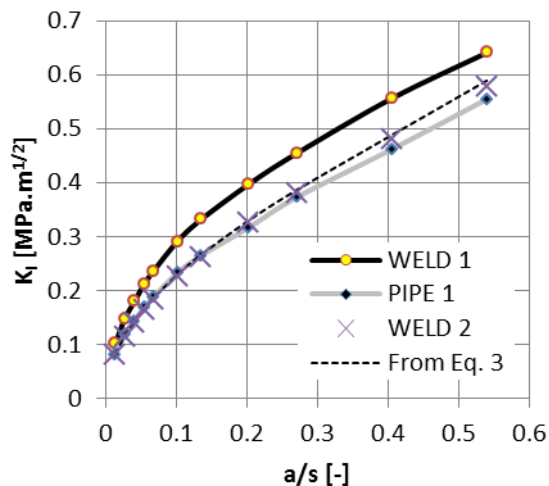


Fig. 3: SIF estimated for different crack position in the weld.

4. Conclusions

The work presented here describes numerical analysis of axially oriented cracks in polyolefin pipes and evaluates the contribution of material nonhomogeneity as a consequence of butt welding process on fracture parameters. The developed three-dimensional model demonstrated capability to predict correctly the stress intensity factor for pressurized cracked polymer pipe weld. It can be concluded that positive Young's modulus ratio E_{max}/E_{min} results in increase of the SIF values in comparison with a cracked homogeneous pipe. From the performed calculations it may be also concluded that the closer the crack to the weld center is the more critical configuration it produces.

The results obtained in the paper may be used to an estimation of critical crack length or lifetime of internally pressured welded pipes with axially oriented cracks subjected to quasi-brittle failure mode.

Acknowledgement

This work was supported through the grant P108/12/1560 of the Czech Science Foundation and by the Ministry of Education, Youth and Sports of the Czech Republic throughout the Project No. CZ.1.07/2.3.00/30.0063 "Talented postdocs for scientific excellence in physics of materials".

References

- Bažant, Z.P., Estenssoro, L.F. (1979) Surface singularity and crack propagation, *International Journal of Solids and Structures*, 15, pp. 405-426.
- Chi, S.-ho and Chung, Y.-L. (2003) Cracking in coating-substrate composites with multi-layered and FGM coatings, *Engineering Fracture Mechanics*, Vol. 70 No.10, pp. 1227-43.
- Hutař, P., Náhlík, L., Knésl, Z. (2009) Quantification of the influence of vertex singularities on fatigue crack behavior, *Computational Materials Science*, 45, pp. 653-657.
- Hutař, P., Ševčík, M., Náhlík, L., Pinter, G., Frank, A. (2011) A numerical methodology for lifetime estimation of HDPE pressure pipes, *Engineering Fracture Mechanics*, Vol. 78, pp. 3049-3058.
- Lach, R., Hutař, P., Veselý, P., Nezbedová, E., Knésl, Z., Koch, T., Bierögel, Ch., Grellmann, W. (2013) Assessment with indentation techniques of the local mechanical behavior of joints in polymer parts, *Polimery* 58, pp. 900-905.
- Pook, L.P. (1994) Some implications of corner point singularities, *Engineering Fracture Mechanics*, 48, pp. 367-378.
- Ševčík, M., Hutař, P., Náhlík, L., Lach, R., Knésl, Z. (2012) Crack propagation in a welded polyolefin pipe, *International Journal of Structural Integrity*, Vol. 3, 2, pp. 148-157.

The obtained results of the SIF for the homogeneous pipe are in a very good agreement with Eq. (3) as the maximum error is less than 5% for crack length ratio $a/s = 0.5$. This implies that the numerical model gives sufficient accuracy for subsequent analyses containing nonhomogenous distribution of Young's modulus in the weld area.

In the case of models of cracked pipe weld (WELD 1 and WELD 2) the SIFs were estimated in the deepest point of the crack and the crack front shape was considered to fulfill Eq. (2). For the crack in the border of the weld (WELD 2) values of SIF are very similar to those estimated on homogeneous pipe with the crack. Concerning the crack in the center of the weld it has been found that the SIF is significantly increased due to the material nonhomogeneity and it is therefore the most critical position of an axially oriented crack in the welded pipe.

COMPARATIVE ANALYSIS OF BURZYŃSKI-TORRE STRENGTH HYPOTHESIS FOR DENTINE AND ENAMEL

G. Milewski*

Abstract: *The paper presents the analysis of Burzyński-Torre strength hypothesis application for hard tissues of teeth, i.e. dentine and enamel. Comparative analysis was done with regards to the well-known strength hypotheses, as Huber-von Mises, Tresca-Guest and de Saint-Venant theories. Numerical simulations as well as the finite element modeling were done by means of ANSYS® program. The calculations have been done for the features of the normal occlusal loadings respectively for anterior and lateral teeth. The numerical stress field analyses in dental and enamel were compared with the relevant experimental and clinical data. The effort estimation according to the Burzyński-Torre hypothesis produces the relatively wide spread out of the obtained results, both in the dentine and enamel. As the result of the large negative values of the first invariant of the stress tensor for the proper occlusal loadings the obtained reduced stress values are relatively low when comparing with Huber-von Mises and Tresca-Guest assessments. For the cases of strong bending effects for anterior teeth and for mastication loadings in lateral teeth the respective values of Burzyński-Torre reduced stress rapidly increase. Those effect also seem to be a result of the strong asymmetry of the dentine, and especially enamel, at tension and compression.*

Keywords: Burzyński-Torre strength hypothesis, Dental, Enamel.

1. Introduction

The problem of application of strength hypotheses for the tooth structures seems to be very rare in the dental biomechanical literature. However dentine and enamel are very similar to the bone tissues teeth characterize with the endodermal genesis, as for instance nails or hair. With reference to the bone structures, both compact and trabecular, hard tissues of teeth are highly mineralised. In the case of enamel the rate of the mineral phase reaches even more than ninety percent. Such a structure of dentine and enamel results in treating them also as highly isotropic materials (Craig and Peyton, 1958, Currey, 1995, Powers and Sakaguchi, 2008). Tab. 1 presents a set of strength properties for hard tissues of tooth.

Tab. 1: Strength properties of dentine and enamel.

Tooth structure	Dentine*	Enamel
Modulus of elasticity E [GPa]	18.6	84.1
Poisson's ratio ν	0.31	0.33
Tensile strength σ_r [MPa]	105.5	10.3
Compressive strength σ_c [MPa]	297	382
Tangential strength σ_s [MPa]	138	90.2

* for demineralized dentine: E [GPa] = 0.26; σ_r [MPa] = 29.6

The aim of the paper was to analyze the stress distributions for the chosen strength hypotheses as well as to compare them with the experimental and clinical data in order to select the best fitting of theoretical effort estimation in dental and enamel to the relevant experimental and clinical data. A special attention was paid to the Burzyński-Torre strength hypothesis, which is considered to be the best and the most effective hypothesis for both ductile and brittle materials (Życzkowski, 1999).

* Grzegorz Milewski, PhD, DSc.: Institute of Applied Mechanics, Cracow University of Technology, Warszawska 24; 31-155, Cracow; Poland, milewski@mech.pk.edu.pl

2. Methods

In general the hypothesis of Burzyński-Torre describes the material effort as a function of three stress invariants (Życzkowski, 1999)

$$s = \frac{1}{3} s_I = \frac{1}{3} (\sigma_x + \sigma_y + \sigma_z) \quad (1)$$

$$t = \frac{\sqrt{2}}{3} \sqrt{s_I^2 - 3s_{II}} = \frac{\sqrt{2}}{3} \sqrt{\sigma_x^2 + \sigma_y^2 + \sigma_z^2 - \sigma_x \sigma_y - \sigma_y \sigma_z - \sigma_z \sigma_x + 3(\tau_{xy}^2 + \tau_{yz}^2 + \tau_{zx}^2)} \quad (2)$$

$$u = \sqrt[3]{s_{III}} = \sqrt{\sigma_x \sigma_y \sigma_z + 2\tau_{xy} \tau_{yz} \tau_{zx} - \sigma_x \tau_{xy}^2 - \sigma_y \tau_{yz}^2 - \sigma_z \tau_{zx}^2} \quad (3)$$

As the influence of the third invariant u could be neglected, the reduced stress with the sufficient accuracy is formulated as a function of two invariants: mean stress s and deviatoric stress t . In practise two approximations, linear and parabolic, are being used:

$$\sigma_{B-T} = \frac{1}{2\kappa_c} \left\{ 3(\kappa_c - 1)\sigma_m + \sqrt{\left[9(\kappa_c + 1)^2 - 12 \frac{4\kappa_c^2}{3\kappa_s^2} \right] \sigma_m^2 + \frac{4\kappa_c^2}{3\kappa_s^2} \sigma_e^2} \right\} \quad (4)$$

where $\kappa_c = \sigma_c / \sigma_f$ and $\kappa_s = \sigma_s / \sigma_f$ are the relevant strength parameters.

Comparative analyses of Burzyński-Torre reduced stress distributions in hard tissues of tooth were done with respect to the well-known Huber-von Mises (σ_{H-vM}), Tresca-Guest (σ_{T-G}) and de Saint-Venant (ϵ_I) theories. Numerical simulations as well as the finite element modelling were done by means of ANSYS® program. The calculations have been done for the features of the normal occlusal loadings respectively for anterior and lateral teeth. The same types of occlusions were applied for the strength tests carried out for the removed teeth by means of INSTRON 4465 strength machine. The numerical models of incisor and premolar were taken after Milewski, 2002. A separate code done in Ansys Parametric Design Language for Burzyński-Torre strength hypothesis was joint to the postprocessor part of ANSYS program.

The detailed stress and strain analysis were done in the areas of the teeth crowns structures which characterize with the maximal effort. Tab. 2 presents a comparison of the maximal values of the reduced stress in the incisor dentine and enamel for the considered strength hypotheses. The comparison was done with the reference to the variable occlusion angle ϕ in the characteristic areas: occlusal contact zone (A), base of a tooth crown near the gingival line: lingual site (B), buccal site (C) and dentine close to the apical region of pulp chamber (D). Calculations were done for the total occlusion 500 N.

Tab. 2: Comparison of the maximal values of effort in the incisor dentine and enamel for Burzyński-Torre reduced stress and other typical strength hypotheses.

ϕ [°]	Area	Tooth structure	σ_{B-T} [MPa]	σ_{H-vM} [MPa]	σ_{T-G} [MPa]	ϵ_I [$\times 10^{-4}$]	σ_m [MPa]
0	A	Enamel	13.2	160.0	174.3	8.4	-105.5
	B	Dentine	5.5	15.5	15.9	3.6	-2.3
20	A	Enamel	5.7	168.2	192.2	10.8	-77.0
	D	Dentine	16.7	41.6	45.2	8.3	-20.9
25	A	Enamel	5.2	158.8	182.5	10.8	-69.8
	D	Dentine	19.2	47.6	52.0	9.9	-23.7
30	A	Enamel	4.8	149.8	172.7	12.6	-63.4
	D	Dentine	20.6	51.2	56.2	10.9	-25.4
45	B	Enamel	313.6	224.1	256.4	26.1	104.8
	D	Dentine	24.2	60.5	66.9	18.0(B)	-29.4
90	B	Enamel	624.6	450.9	514.0	52.9	208.6
	B	Dentine	45.5	80.8	86.9	30.3	8.0

The examples of Huber-von Mises and Burzyński-Torre reduced stress distributions in the incisor dentine and enamel for chosen occlusal angles are given respectively in Fig. 1.

The results of the numerical stress analysis in the hard tissues of teeth were compared with the experimental strength tests carried out for the removed teeth. Fig. 1 shows typical two ways of crown

fractures for anterior teeth for various ways of occlusal loadings. The first case, the oblique fracture line (Fig. 1a), is characteristic for the proper occlusions (for ϕ up to 30°), while the second one, fracture of the crown base (Fig. 1b), appears more often for higher occlusal angle ϕ , where bending effects dominate.

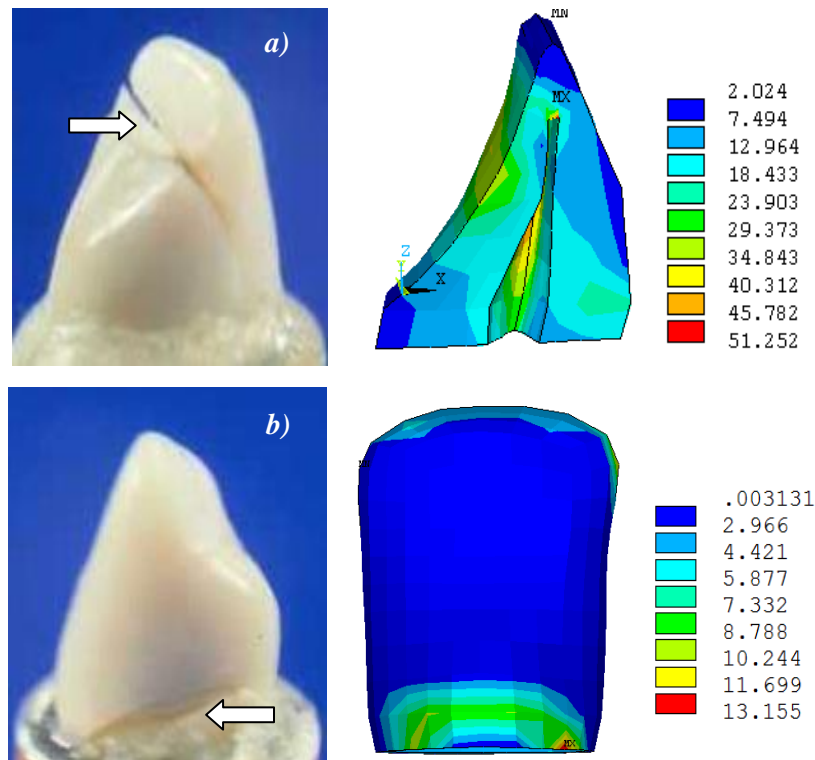


Fig. 1: Typical anterior teeth crowns fractures: a) Oblique line; b) Tooth crown base at gingival base.

For the lateral teeth (premolars and molars) a comparison of the considered strength hypotheses is presented in Tab. 3. With the reference to the described above localisation of the effort areas (A to D), additionally E stands for the dentine areas in the upper part of the crown, close to the mastication surface.

Tab. 3: Burzyński-Torre reduced stress and other strength hypotheses comparison for the maximal effort in premolar dentine and enamel for proper occlusion 500 N.

Tooth structure; Area	σ_{B-T} [MPa]	σ_{H-vM} [MPa]	σ_{T-G} [MPa]	$\epsilon_1 [x 10^{-4}]$	σ_m [MPa]
Enamel; A	1.4	45.9	48.1	2.0	-18.5
Enamel; B	0.6	25.3	25.9	1.1	-7.3
Dentine; E	5.9	16.8	17.7	3.5	-5.5
Dentine; D	6.1	16.6	18.3	3.9	-6.5
Dentine; B	9.3	15.9	16.7	1.4	-14.3

On the other hand the examples of the accompanying strength tests for the removed lateral teeth are shown in Fig. 2. The total teeth crowns destructions characteristic for the normal occlusions (Figs. 2a, 2b) and for the masticatory movements (destructions of the separate cusps - Fig. 2c) were in majority.

Further analysis of application of Burzyński-Torre approach was done with the regards to the influence of the strength hypothesis parameters on the values of the reduced stress estimation. The calculations were done for the enamel for the case of incisor at proper occlusion ($\phi = 30^\circ$). The results of the numerical calculations are presented in Tab. 4.

The analysis of Burzyński-Torre hypothesis sensitivity for variable values of κ_c and κ_s parameters shows that κ_c changes has almost no influence on the values of the reduced stresses while for the coefficient κ_s that influence is noticeable for relatively low values of mutual ratio of tangential to tensile strength.

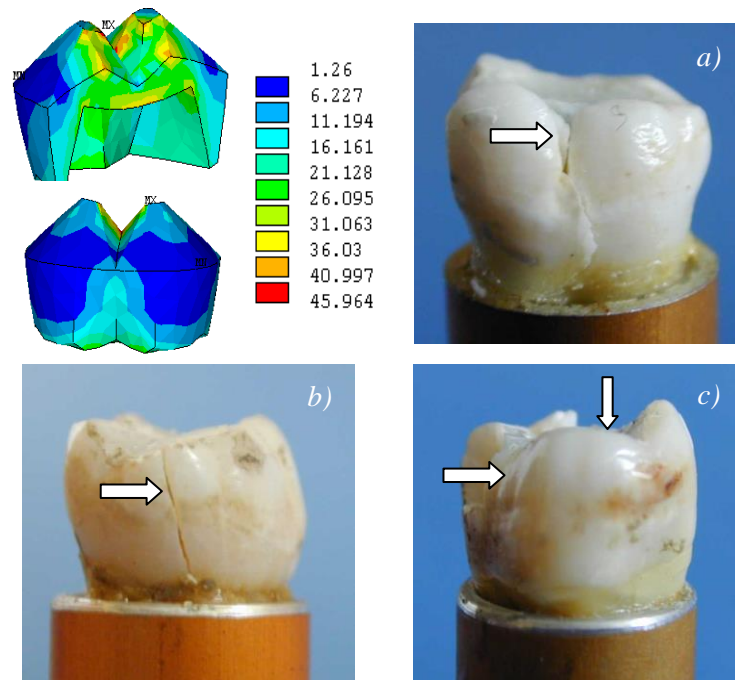


Fig. 2: Characteristic lateral teeth crowns fractures: a) In buccal-lingual plane; b) In distal-mesial plane; c) Separate cusps fractures; total occlusion in numerical calculations 500 N.

Tab. 4: Burzyński-Torre strength hypothesis sensitivity for variable values of κ_c and κ_s parameters.

κ_c	σ_{B-T} [MPa] for $\kappa_s = 8.72$	κ_s	σ_{B-T} [MPa] for $\kappa_c = 37.28$
37.28	101.448	8.72	101.448
30	101.450	8	101.403
25	101.451	6	101.190
20	101.453	4	100.577
10	101.463	2	97.130
8.72	101.466	1.5	93.271

3. Conclusions

Numerical simulations and experimental strength tests prove that, especially for dentine, the areas of maximal effort correspond to the distributions of the maximal tangential stresses. It implies the correctness of application of both the von Mises and Tresca-Guest strength hypotheses. Initiations of cracks in the enamel in the occlusal contact zone as well as in the area of the crown base point out the usefulness of the hypothesis of the maximal principal strain ϵ_1 . It is also worth underlining a relatively wide spread out of the effort estimation according to the Burzyński-Torre hypothesis, both in the dentine and enamel. As the result of the large negative values of the I invariant of the stress tensor (mean value) for the proper occlusal loadings the obtained σ_{B-T} reduced stress values are relatively low when comparing with σ_{H-vM} and σ_{T-G} values. For the cases of strong bending effects for anterior teeth and for mastication loadings in lateral teeth the respective values of σ_{B-T} rapidly increase. Those effect also seem to be a result of the strong asymmetry of the dentine, and especially enamel, at tension, compression and shearing.

References

- Craig, R. G., Peyton, F. A. (1958) Elastic and mechanical properties of human dentine, J. Dent. Research, Vol. 37, No. 4, pp. 661-668.
- Currey, J. D., et al. (1995) In: Proc. Bone Cell and Tissue Mechanics, C.I.S.M., Udine.
- Milewski, G. (2002) Strength aspects of biomechanical interaction hard tissue-implant in dentistry, DSc Thesis, Cracow University of Technology, s. Mechanics, No. 89, Kraków.
- Powers, J. M., Sakaguchi, R. L. (2008) Dental Materials, Elsevier Urban & Partner, Wrocław.
- Życzkowski, M. (1999) Discontinuous bifurcation in the case of the Burzyński-Torre yield condition, Acta Mechanica, Vol. 132, pp. 19-35.

INVESTIGATION OF THE SPRAY GENERATED BY A Y-JET ATOMIZER

M. Milkvik^{*}, M. Zaremba^{**}, J. Jedelský^{***}, G. Wigley^{****}

Abstract: *The presented research is based on the application of optical diagnostics to determine the quality of a liquid fuel spray generated by a Y-type nozzle designed according to the works of Mullinger (1974) and Madsen (2006). Two non-intrusive optical measurement techniques were used to characterize the spray in terms of droplet velocity and size, PDA (Phase Doppler Anemometry), and flow structure, PIV (Particle Image Velocimetry). PDA measurements were made in the downstream region of the fully atomized spray, where uniform spherical droplets were expected. The velocity and drop size profiles were measured by PDA in a plane at a distance of 100 mm downstream from the nozzle. These velocity measurements were assumed as a reference for later comparison with the PIV flow measurements. The main application of the PIV technique was to determine the velocity field of the spray in the near nozzle region where the presence of the ligaments and large non-spherical droplets were expected. The simultaneous use of the two measurement techniques provides a more complete understanding of the fluid mechanic processes occurring in the spray. The spray quality produced by the nozzle design has been judged in terms of the Sauter mean droplet diameter and spray velocity profiles.*

Keywords: Y-jet atomizer, Spray characteristics, PDA, PIV, Sauter mean diameter.

1. Introduction

Y-jet atomizers are widely used for the atomization of the liquids in the combustion applications. The goal of the atomization is to increase the effective surface of the liquid. That means that the liquid stream must be disintegrated into small droplets. The spray quality is often evaluated using the criterion called the Sauter Mean diameter, SMD, which is the diameter of a sphere with the equivalent surface to volume ratio as a particle of interest, D_{32} . The quality of the spray from the Y-jet atomizer depends mainly on the flow in the internal mixing chamber. The relationship between the internal and external flows was studied by Song and Lee (1996). The SMD value is a dependent variable which is affected mainly by the hydraulic parameters, the geometrical parameters of the atomizer nozzle and the physical properties of the fluids. The flow in the mixing chamber can be described using the criterion, based on the hydraulic parameters, the Gas/Liquid Ratio, GLR.

2. Experimental Equipment and Methods

Experiments were conducted on a cold test bench equipped with Y-jet atomizer. The flow and spray quality were investigated by PDA and PIV.

2.1. Test bench

The Y-jet atomizers were operated on a test bench which was equipped with pressurised fuel and air supplies. The fuel supply system consisted of a pressurised fuel tank, a filter, a regulator valve and a Siemens Mass 2100 Coriolis flow meter fitted with Mass 6000 Ex Transmitter. Light heating oil (LHO) was used as the atomized liquid. Pressurised air was taken from the central compressed air supply system

* Ing. Marek Milkvik, PhD.: Brno University of technology, Technická 2896/2, 616 69 Brno, CZ, mlkvik@fme.vutbr.cz

** Ing. Matous Zaremba: Brno University of technology, Technická 2896/2, 616 69 Brno; CZ, y116215@stud.fme.vutbr.cz

*** Assoc. Prof. Jan Jedelský, PhD.: Brno University of technology, Technická 2896/2, 616 69 Brno; CZ, jedelsky@fme.vutbr.cz

**** Dr. Graham Wigley: Loughborough University, LE11 3TU, United Kingdom, g.wigley@lboro.ac.uk

which provided a maximum pressure of 0.8 MPa. The air flowed through a dehumidifier and a filter into a regulator valve. Pressure sensors (BD sensors DMP 33li) and thermometers (resistance temperature sensor Omega SPRTX-S1) were mounted in both fuel and air loops.

2.2. Atomizer

The design of Y-jet atomizer was based on the findings of Mullinger (1974) and Madsen (2006). The schematic layout is shown in the following figure:

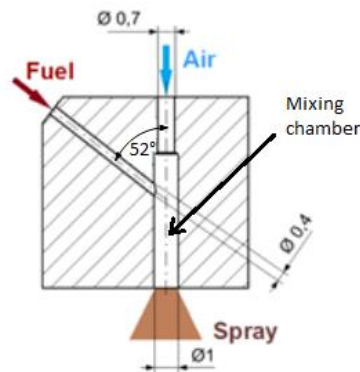


Fig. 1: Y-jet atomizer scheme.

Liquid is injected into the mixing chamber by a radial fuel port entry. Two phase flow is created inside mixing chamber and it is disintegrated when it reaches the exit orifice and expands into ambient air.

2.3. PDA system

A two component fiber based PDA system by Dantec Dynamics was used to measure velocity (in the axial and radial direction of the nozzle's main axis) and the droplet size distribution. The system consists of Spectra Physics Stabilite 2017 argon ion laser, 60X41 transmitter with Bragg cell, 60X81 2D 85 mm transmitting optics, 57X50 112 mm diameter fiber PDA receiver optics which is connected to the fiber PDA detector unit and signal is processed in BSA P80 flow and particle processor.

2.4. PIV system

A standard PIV system from TSI was used for the investigation of the flow. The illumination was provided by the New Wave Research PIV MiniLase, dual cavity Nd:YAG Laser System with attached sheet optics. The spray images were captured by the TSI PIVCAM 13-8 CCD camera. The image pairs were processed by the INSIGHT 3G software.

2.4.1. PIV measurements in spray

Atomization produced by twin fluid nozzles is driven by breakup of the initial structures i.e. ligaments and large droplets. It can be seen in the Fig. 2a, that these formations are created in regions close to the exit orifice of the nozzle and they disintegrate into smaller droplets further downstream.

From a light scattering point of view, the different liquid forms and varying droplet sizes cause problems for optical diagnostics since the amount of scattered light is related to the square of the droplet size. The differences in the scattered light intensities between the small and large droplets means that, for PIV, where the optimal droplets would be spherical with a small uniform size, the detectability of these droplets is going to be low. In the opposite situation, when the smaller droplets are made visible on the images, by increasing the camera gain, the large droplets and ligaments would be over exposed, especially in the central part of the spray which leads to complications in the image processing.

Another problem is caused by the heterogeneous distribution of the droplets. Most of the liquid mass is present in central regions of the spray, whereas, only a low amount of droplets is present in peripheral regions. The PIV system is tuned to obtain data from regions with defined range of the density of droplets. Visual data from regions where droplet density is out of this range cannot be processed by the PIV algorithm. Statistical analysis can be used to determine the distribution of the mass in spray over the long time period. The Root Mean Square (RMS) value of pixel intensity can be calculated over the set of

captured images. Information about the mass distribution on the final RMS image is expressed by the intensity of each pixel. Further processing, for example, conversion of the grey-scale intensity into a colour spectrum, can help recognize regions in the spray.

If ligaments and large droplets are present in the spray, as in Fig. 2a, then small droplets cannot be captured due to the low intensity of the scattered light. Whereas, Fig. 2b demonstrates, that most of the captured droplets were in the central region of the spray. Different distribution of the mass influences the instrumental parameters of image acquisition. Hence the PIV system must be realigned for each regime.

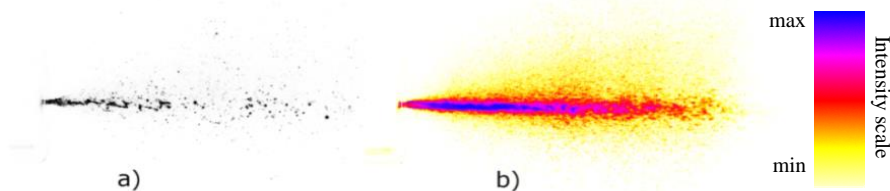


Fig. 2: Comparison of the inverted instantaneous PIV image and the RMS image created from 100 PIV double images ($\Delta p = 0.035$ MPa, GLR = 2.5%).

3. Results and Discussion

The PDA and PIV experiments were performed for eight different operating regimes. Two pressure values (0.035 and 0.07 MPa) and four values of GLR (2.5, 5, 10, 20%). The PDA results are reported, according to Jedelský (2009), with an integral value of the Sauter mean diameter (ID_{32}) which characterizes drop size distributions with one value.

As expected, higher fuel pressure leads to lower values of ID_{32} which is consistent with Madsen (2006). At low pressure regimes, fuel inside the mixing chamber has lower potential energy which leads to lower velocities and higher values of ID_{32} . As mentioned above, the nozzle performance is also dependent on GLR. An increase in GLR leads to lower values of ID_{32} which is consistent with the work of Zhou (2010).

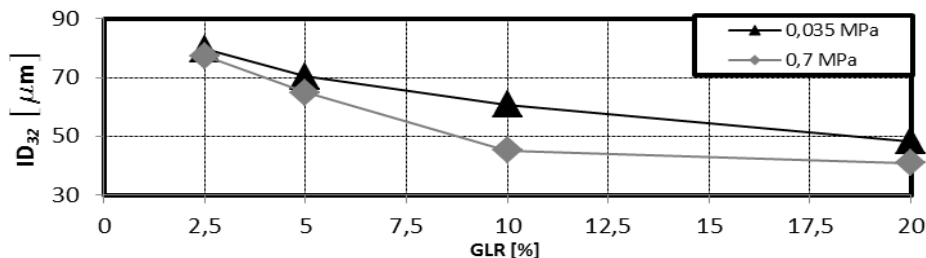


Fig. 3: Integral values of ID_{32} for different working regimes of the atomizer.

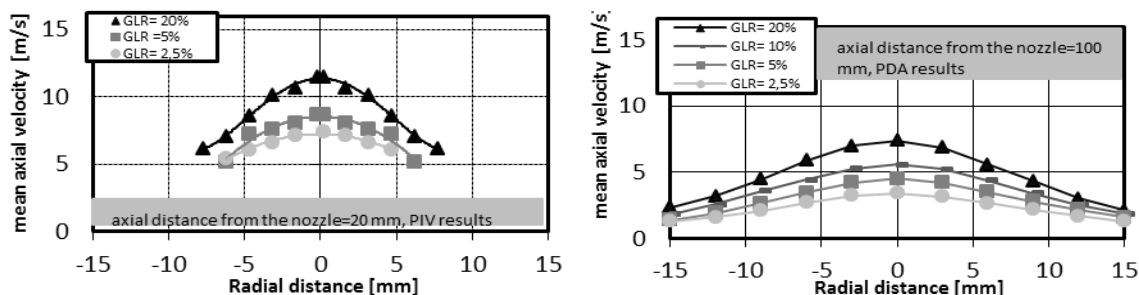


Fig. 4: Axial velocity profile at different distances from the nozzle ($\Delta p = 0.035$ MPa, measured using PIV and PDA).

The PIV measurements, presented on the left hand side in Fig. 4 and Fig. 5 show the velocity profile at a distance of 20 mm downstream from the exit orifice of the nozzle. It can be observed that information about the velocity field in outer regions of the spray is missing. These regions of the spray consist mostly of small droplets which cannot be captured along with the ligaments and large droplets. Thus, the velocity

profiles from the PIV in Fig. 4 and Fig. 5 are valid only for large droplets which can be found in central region of the spray near the nozzle. It can be expected that the velocity of the droplets in the outer regions decreases, due to momentum transfer with the surrounding air, and that the velocity profiles would be similar to the distribution of the velocity profiles measured by the PDA technique and shown in the right side of Fig. 4 and Fig. 5.

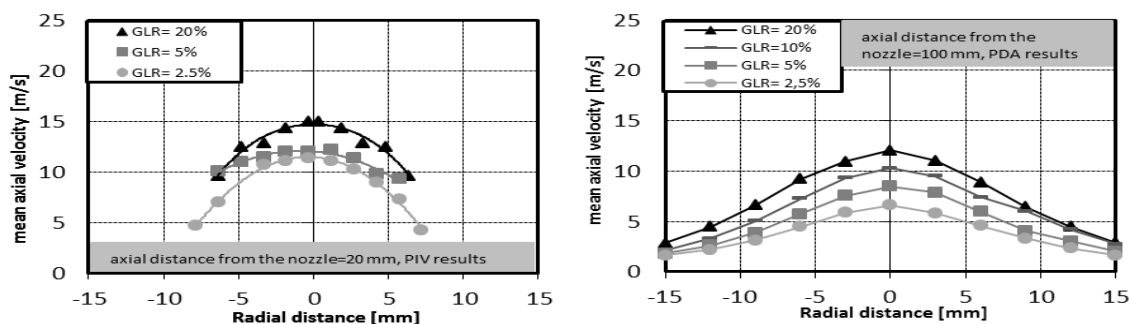


Fig. 5: Axial velocity profile at different distances from the nozzle ($\Delta p = 0.07$ MPa, measured using PIV and PDA)

4. Conclusion

The PDA measurements were made at a distance of 100 mm from the nozzle where atomization was expected to be complete and all droplets spherical. In the region from the nozzle to an axial distance approximately 60 mm, the PIV measurements have been used to characterise the spray.

From presented results it can be stated that the flow field in the spray is symmetric in all measured regimes. The nozzle generates a stable spray with a narrow drop size distribution which is represented by the ID_{32} values. However, it can be seen that spray stability is related to the initial pressure of fluids. With higher pressure values, spray stability is increased from a visual point of view, due to the higher potential energy of the atomizing liquids.

Although, the PIV velocity measurements show the velocity profile in region near to the exit orifice of the nozzle. Further PIV experiments are indicated to be desirable especially with higher spatial resolution. This can be achieved, for example, by macro-imaging of the regions with different droplet size classes. It must be mentioned that this method is not only time-consuming in the experimental phase but also in the image processing phase. A second approach will be to reprocess the PDA data with the mean droplet velocity being calculated as a function of different drop size classes.

Acknowledgement

Authors acknowledge financial support from project № 101/11/1264 funded by the Czech Grant Agency, from project NETME CENTRE PLUS (LO1202) co-funded by the Ministry of Education, Youth and Sports within the support programme „National Sustainability Programme I“ and project № CZ.1.07/2.3.00/30.0005 of Operational Program Education for Competitiveness of Ministry of Education, Youth and Sport of the Czech Republic.

References

- Jedelsky, J. et al. (2009) Development of an Effervescent Atomizer for Industrial Burners, Energy Fuels, pp. 6121-6130.
- Madsen, J. (2006) Computational and Experimental Study of Sprays from the Breakup of Water Sheets. PhD. Thesis Aalborg University Esbjerg.
- Mullinger, P. J., Chigier, N. A. (1974) The design and performance of internal mixing multijet twin fluid atomizers. Journal of the Institute of Fuel 47, pp. 251-261.
- Neya, K., Sato, S., Hatori, K. (1975) Study of Y-jet Twin Fluid Atomizer, Rep. Ship Res. Inst, pp. 1-19.
- Si Hong Song, Sang Young Lee (1996) Study of Atomization Mechanism of Gas/Liquid Mixtures Flowing Through Y-jet Atomizers, Atomization and Sprays, Vol. 6, pp. 193-209.
- Zhou et al (2010) Experimental investigation and model improvement on the atomization performance of single-hole Y-jet nozzle with high liquid flow rate, Powder Technology 199. pp. 248-255.

COMPARISON OF METHODS FOR CONSTRAINED DESIGN OF COMPUTER EXPERIMENTS

E. Myšáková*, M. Lepš**

Abstract: A design of experiments creates an essential part in any experimentation, development of meta-models, sensitivity analysis or probability calculations. The creation of the design of experiments is determined by the shape of a design domain. In case of dependent input variables the design domain is constrained. Therefore classical designs developed for regular hypercubes cannot be applied here. This contribution presents comparison of several methods for designs in constrained design domains in terms of space-filling properties of the resulting designs and time required for their generation. Examples are focused on a special type of experiments called a mixture experiment, where individual parameters (ingredients) form a unit volume or unit weight. This condition leads to a simplex or a convex polytope shape of the design domain.

Keywords: Design of Experiments, Space-filling, Constraints, Maximin, MiniMax.

1. Introduction

Design of experiments (DoE) creates an essential part in experimentations, surrogate modeling and many other fields such as sensitivity analysis or probability computations. The design of experiments consists of a set of design points whose coordinates correspond to combinations of input parameters values. The aim of the design of experiments is to gain maximal information about the solved system with a minimal number of executions. Therefore the basic requirements placed on the experimental design are orthogonality and space-filling of the design domain.

The shape of the design domain is firstly affected by presence of limiting conditions (constraints) and secondly by their form. In case of no constraints, the design domain has a regular shape, so-called hypercube. One special case of constrained design space is a mixture experiment. Here a sum of input variables (relative proportions of components) forms a unit volume or unit weight:

$$x_1 + x_2 + \dots + x_n = 1, \quad 0 \leq x_i \leq 1, \quad i = 1, \dots, n \quad (1)$$

Then the design domain is a simplex and the design points can be described by barycentric coordinates as shown in Fig. 1. The additional limiting conditions lead to the design domain in shape of a polytope.

Except of the shape of the design domain the method for generation of experimental design is influenced by other factors. The essential is the distinction between real (physical, chemical...) experiments and computer experiments called simulations. This contribution is aimed at designs for computer experiments. The experimental designs for real experiments are described in detail for example in (Montgomery, 2000). Methodology is influenced also by the difference between experiments with continuous parameters and experiments with discrete parameters. Here we focus on experiments with continuous parameters.

The quality of the designs can be evaluated by many criterions (Janouchová & Kučerová, 2013). Those aimed at orthogonality are for example a condition number or correlation coefficients. Criterions evaluating the space-filling are for example Audze-Eglais criterion, discrepancy, Euclidean Maximin distance or miniMax criterion. The last two criterions are used in this contribution.

* Ing. Eva Myšáková: Faculty of Civil Engineering, Czech Technical University in Prague, Thákurova 7, 166 29, Prague, CZ, eva.mysakova@fsv.cvut.cz

** Assoc. Prof. Ing. Matěj Lepš, PhD.: Faculty of Civil Engineering, Czech Technical University in Prague, Thákurova 7, 166 29, Prague, CZ, leps@cml.fsv.cvut.cz

Euclidean Maximin distance (*EMM*) is the shortest among all distances between the design points:

$$EMM = \min \{ \dots, L_{ij}, \dots \}, \quad i = 1, \dots, np, \quad j = (i + 1), \dots, np, \quad (2)$$

where np is a number of design points and L_{ij} is the distance between points i and j . This criterion indicates undesirable proximity of points in the design. The higher the *EMM* value the better.

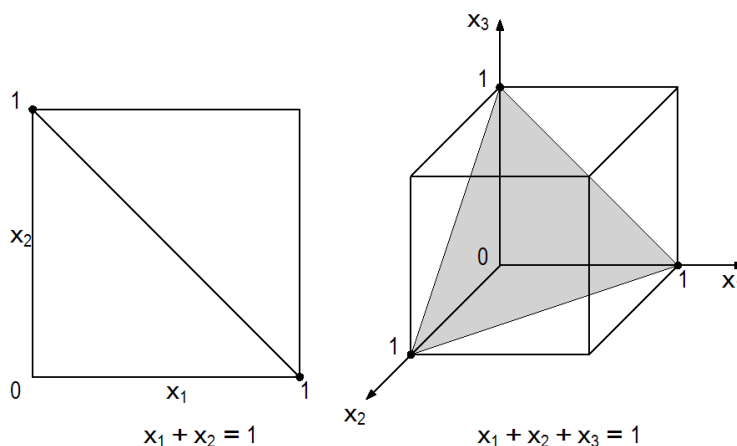


Fig. 1: The design domain for mixture experiment with two and three components.

Criterion miniMax (*mM*) corresponds to the *Largest Empty Sphere problem* (*LES*). The objective is to find the largest (hyper) sphere that includes no design point and whose center lies in the solved design domain. The value of the miniMax criterion is then equal to the radius of this largest sphere. MiniMax criterion serves for detection of unexplored areas inside the domain. The smaller the value is the better.

The paper follows (Myšáková, 2013) and is organized as follows: Chapter 2 presents several methods for generation of experimental designs in constrained domains. Two illustrative examples of mixture experiments used for comparison of the methods are described in Chapter 3 and Chapter 4 brings results and conclusions.

2. Methods for Design Generation

Methods for generation of the experimental design in generally irregular design space can be divided into two categories. The first one uses the bounding box – the regular domain (in shape of hypercube or hypercuboid) circumscribing the solved constrained domain. In this regular domain we can easier generate the design and then just extract the points lying in original irregular domain. Contrary, the second category is based on division of the constrained domain into simplices by Delaunay triangulation. In these simplices the generation of the points is also easier than in the whole irregular domain, so we can generate the design points in individual simplices and then create the design by union of these design points.

2.1. Generator of random points

The first method belongs to the second category mentioned above. The solved constrained domain is decomposed by Delaunay triangulation into simplices. Here the random points are generated with exponential distribution and then normalized (Devroy, 1986). The number of points generated in each simplex is given by its relative volume.

2.2. LHS on bounding box

Another method uses the bounding box of the domain. Here the LHS design is created and only points lying in solved irregular domain are extracted. Non-optimized and optimized LHS design can be used.

2.3. Removal of superfluous points

The third presented method involves removal of points from intentionally overcrowded initial designs. In each step one of points from the actual mutual closest pair is removed. There are two variants which

differ in determination of a removed point. In the first variant the removed point is chosen from the pair randomly, in the second variant the point whose second shortest distance to other design points is removed.

2.4. Distmesh tool

The last method uses the Distmesh tool (Persson & Strang, 2004). It is a heuristic algorithm for generation of meshes for Finite Element Method (FEM). The quality meshes should have evenly distant nodes; therefore we can use this tool for creation of space-filling design of experiments. The algorithm is based on dynamical system of an expanding truss structure.

3. Applications

For comparison of presented methods two examples of mixture experiments were used. The first one is a three-component mixture (Snee, 1979). The corresponding design domain is a 2D irregular polygon with 6 vertices. The second example involves six-component mixture (Simon et al., 1997) with a 5D irregular polytop design domain with 51 vertices.

4. Results and Conclusions

The comparison of methods is shown in Figs. 2 and 3. The bottom graphs present the quality of resulting designs evaluated by criterions Maximin (*EMM*) and miniMax (*mM*). The top graphs show the corresponding time demands where the horizontal axis is *EMM* as in graphs below. The utopia (ideal) point lies in right bottom corner of both graphs.

The legend for the graphs is showed below:

- the random points generator
- non-optimized LHS design in the bounding box
- ★ optimized LHS design in the bounding box
- ◆ the removal – random point removed from the closest pair
- ★ the removal – “worse” point removed from the closest pair
- ▼ the Distmesh tool I
- ▲ the Distmesh tool II

Note: In methods with points removal several levels of overcrowding was tried.

The results clearly indicate a correlation between criterions *EMM* and *mM*. Optimization of one of them improves the design also in the terms of the other.

In 2D the dominance of the Distmesh tool is evident. On the other hand in higher dimensions the Distmesh tool cannot be practically used. Its time demands rise rapidly with the dimensions due to repeated Delaunay triangulations within the algorithm. More severe issue is that the quality of the resulting designs also deteriorates with grow of dimensions. In 5D the Distmesh tool even generates designs with duplicated points.

The random points generator is the fastest method but its designs have the worst quality in almost every case. Better results were achieved with the method using extraction of the points from LHS designs in the circumscribed domain. It was confirmed that usage of optimized LHS designs leads to better constrained designs; of course in cost of some additional time.

The method applying removal of points from overcrowded designs reached very good results. The more overcrowded the initial design is the better final design is created. But there are some limits for the level of overcrowding. In examples used in this paper the level of overcrowding larger than 30 does not worth the increasing time demands.

Finally, the results can be summarized as follows: in low dimensions the Distmesh tool is effective; in higher dimensions the usage of removal from the overcrowded designs can be recommended.

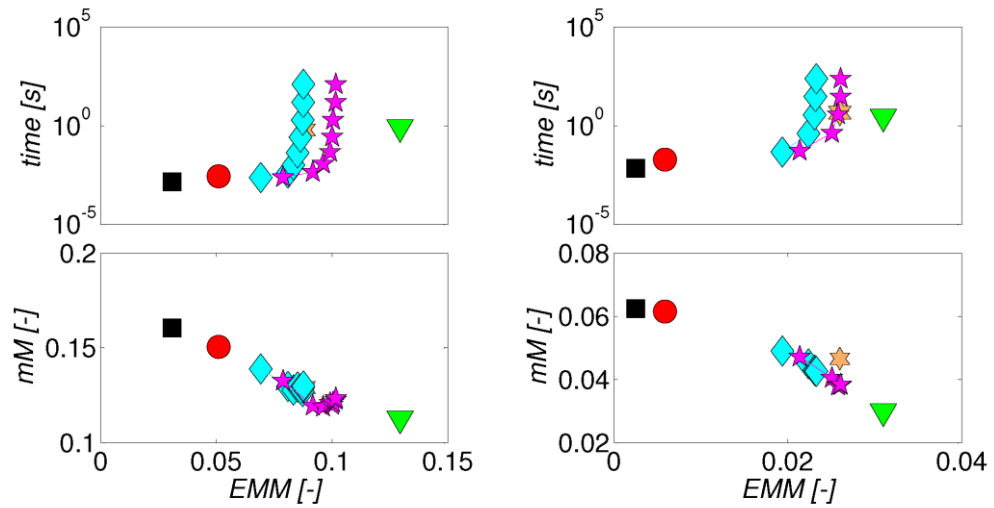


Fig. 2: Results of methods in example with three-component mixture. Left: DoE with 10 design points; Right: DoE with 100 design points.

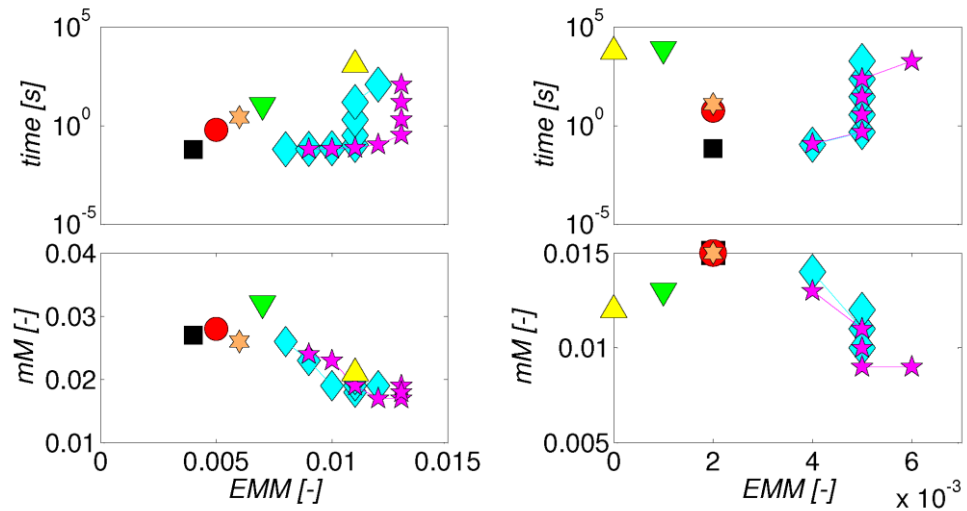


Fig. 3: Results of methods in example with six-component mixture. Left: DoE with 10 design points; Right: DoE with 100 design points.

Acknowledgement

The authors gratefully acknowledge the financial support from the Grant Agency of the Czech Technical University in Prague, the grant SGS14/028/OHK1/1T/11.

References

- Devroy, L. (1986) Non-uniform Random Variate Generation. Springer-Verlag.
- Janouchová, E., Kučerová, A. (2013) Competitive Comparison of Optimal Designs of Experiments for Sampling-based Sensitivity Analysis. Computers & Structures, 124, pp. 47-60.
- Montgomery, D. C. (2000) Design and Analysis of Experiments, 5th edition. Wiley.
- Myšáková, E. (2013) Optimization of Uniformity of Computer Experiments for Constrained Design Spaces. Diploma Thesis. Faculty of Civil Engineering, Czech Technical University in Prague.
- Persson, P. O., Strang, G. (2004) A Simple Mesh Generator in MATLAB. SIAM Review, 46, 2, pp. 329-345.
- Simon, M. J., Lagergreen, E. S., Snyder, K. A. (1997) Concrete Mixture Optimization Using Statistical Mixture Design Methods. In Proceedings of the PCI/FHWA, New Orleans, Louisiana, pp. 230-244.
- Snee, R. D. (1979) Experimental Designs for Mixture Systems with Multicomponent Constraints. Communications in Statistics - Theory and Methods, 8, 4, pp. 303-326.

ESTIMATION OF CRITICAL STRESS VALUES FOR CRACK INITIATION FROM SHARP V-NOTCHES

L. Náhlík*, K. Štegnerová**, P. Hutař***

Abstract: *The aim of the paper is to estimate a critical value of an applied stress for a crack initiation from sharp tip of the V-notch using a procedure based on linear elastic fracture mechanics (LELM). The V-notch represents singular stress concentrator with the stress singularity exponent different from 0.5, therefore the generalized form of LELM for stress distribution description in the vicinity of the sharp V-notch was used. The stress singularity exponent depends on the V-notch opening angle, in general. A stability criterion based on the average value of the tangential stress component across a critical distance d from the V-notch tip is used in the paper. Resultant values of the critical applied stress are compared with experimental data.*

Keywords: Failure initiation, Stress singularity, V-notch, Generalized stress intensity factor.

1. Introduction

V-notches are one of the most frequent stress concentrators occurring in engineering structures. They cause a decrease of the critical applied stress value which leads to the crack initiation. Therefore, stability criteria for the crack initiation from the tip of V-notch have been formerly developed. Also the problems of the brittle fracture of structural components with sharp V-notches have been considered in papers (e.g. Knésl, 1991; Knésl, 1993; Seweryn, 1994; Seweryn, 2002; Gómez, 2003).

V-notches are singular stress concentrators with stress singularity exponents different from 0.5, which depend on the V-notch opening angle. Therefore, the standard procedures of LELM should be generalized for stress singularity exponents in the range from 0 to 0.5 (Knésl, 1991; Seweryn, 2002).

The aim of this paper is to estimate the critical value of an applied stress for the crack initiation from sharp V-notch. Two different kinds of materials, different geometries, V-notch opening angles and notch depths are considered. The stability criterion used is based on the averaged value of the tangential stress component across a critical distance d from the notch tip. Results obtained are compared with experimental data taken from the literature (Seweryn, 1994; Gómez, 2003).

2. Theoretical Background

2.1. Stress distribution around the sharp tip of a V-notch

In the first step it is necessary to estimate the stress singularity exponent and stress distribution around the sharp tip of a V-notch. The singular stress field around the V-notch tip can be expressed by (Knésl, 1991):

$$\sigma_{ij} = \frac{H_I}{\sqrt{2\pi}} \cdot r^{-p} \cdot f_{ij}(\alpha, p, \theta), \quad (1)$$

where H_I is generalized stress intensity factor corresponding to mode I of loading, p is stress singularity exponent, $f_{ij}(\alpha, p, \theta)$ are known shape functions, r and θ are polar coordinates with the origin at the

* Assoc. Prof. Ing. Luboš Náhlík, PhD.: CEITEC IPM, Institute of Physics of Materials, Academy of Science of the Czech Republic; Žitkova 22; 616 62, Brno; CZ; Faculty of Mechanical Engineering, Brno University of Technology; Technická 2896/2; 616 69, Brno; CZ, nahlik@ipm.cz

** Ing. Kateřina Štegnerová: CEITEC IPM, Institute of Physics of Materials, Academy of Science of the Czech Republic; Žitkova 22; 616 62, Brno; CZ; Faculty of Mechanical Engineering, Brno University of Technology; Technická 2896/2; 616 69, Brno; CZ, stegnerova@ipm.

*** Assoc. Prof. Ing. Pavel Hutař, PhD.: CEITEC IPM, Institute of Physics of Materials, Academy of Science of the Czech Republic; Žitkova 22; 616 62, Brno; CZ, hutar@ipm.cz

V-notch tip and α is opening angle of the V-notch (see Fig. 1). The stress singularity exponent p depends on the angle α only and can be obtained by solving of characteristic equation (Knésl, 1991):

$$\sin(2(1-p)(\pi-\alpha)) + (1-p)\sin(2(\pi-\alpha)) = 0. \quad (2)$$

Generalized stress intensity factor H_I can be determined numerically using finite element (FE) method, e.g. by using of so-called direct method, see Fig. 2.

2.2. The criterion of stability

Conditions of the sharp V-notch stability depend on the stress state near the V-notch tip and on material resistance to the fracture. Criterion development following an idea that the mechanism of the crack initiation from pre-crack and the crack initiation from the sharp V-notch is the same and it is controlled by variable L , which has a clear physical meaning and is well defined in both cases, for body with a crack as well as for body containing V-notch. Then, the critical values L_C for the crack and V-notch can be compared:

$$L_C(\dots, K_{IC}, \dots) = L_C(\dots, H_{IC}, \dots), \quad (3)$$

where K_{IC} [MPa.m^{0.5}] is a fracture toughness and H_{IC} [MPa.m^p] is a critical value of generalized stress intensity factor. As the variable L an average stress calculated across the distance d from the notch tip can be used (Knésl, 1991). The average stress $\bar{\sigma}$ represents average value of the tangential stress component $(\sigma_{\theta\theta})_{max}$ acting in front of the notch tip and can be related to the quantity σ_{crit} , i.e. to the critical stress. The crack doesn't propagate for:

$$\bar{\sigma} = \frac{1}{d} \int_0^d (\sigma_{\theta\theta})_{max} dr < \sigma_{crit} = \frac{2K_{IC}}{\sqrt{2\pi d}}. \quad (4)$$

The value of the critical stress σ_{crit} for the crack can be obtained from Eq. (4) as a function of K_{IC} . The critical stress in the case of the sharp V-notch can be obtained by similar way, i.e. by integration of Eq.(1) for H_I equal to H_{IC} :

$$\sigma_{crit} = \frac{H_{IC}}{\sqrt{2\pi}} \frac{(2-p)(1+q)}{d^p}, \quad (5)$$

where $q = -\cos(p(\pi-\alpha))/\cos((2-p)(\pi-\alpha))$. By comparison of Eq. (4) and (5):

$$H_{IC} = K_{IC} \frac{2d^{p-\frac{1}{2}}}{(2-p)(1+q)}. \quad (6)$$

Several expressions for estimation of the critical distance d exist (Zouhar, 2012). The expression published by Yosibash (2010), $d = \frac{2}{\pi} \left(\frac{K_{IC}}{\sigma_C}\right)^2$, was used in calculations. σ_C is a tensile strength.

The applied stress σ_{appl} represents a remote loading of the body with V-notch, see Fig. 3. The critical value of applied stress $\sigma_{appl,crit}$ necessary for the crack initiation from the V-notch can be expressed as:

$$\sigma_{appl,crit} = \frac{H_{IC}}{H_I} \sigma_{appl}. \quad (7)$$

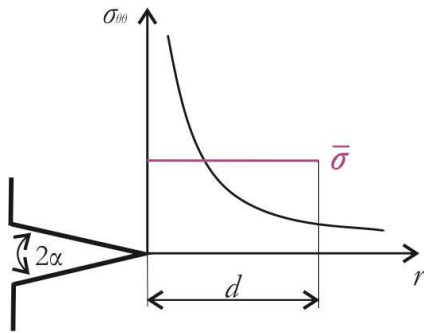


Fig. 1: Averaged tangential stress value in front of the V-notch.

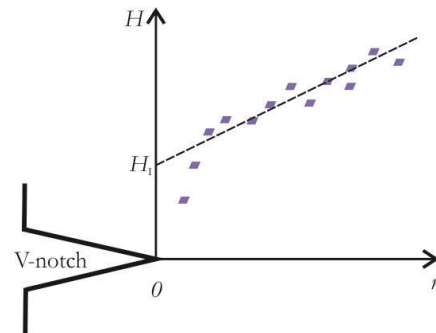


Fig. 2: Determination of H_I value by the direct method.

3. Numerical Model

Three different sets of experiments were modeled by finite element method according to Seweryn (1994) and Gómez (2003). Two sets were specimens with sharp V-notch in the middle of each side (DENT) (Fig. 3) made of polymethylmethacrylate (PMMA) and duraluminum, respectively. The third set represents single edge notch tensile (SENT) specimens (Fig. 3) made of PMMA.

The dimensions of the DENT specimens were: length $L = 192$ mm, width $4w = 109$ mm, notch depth $a = 27$ mm and V-notch opening angle $\alpha = 0 \div 70^\circ$ (changing with step of 10°). The thickness of PMMA specimen was $t = 4$ mm and the thickness of duraluminum specimen was $t = 5$ mm. Both kinds of specimens were loaded by tension. The eighth of the specimen was modeled, because of the symmetry in geometry and loading conditions. Conditions of plane strain were considered in all cases.

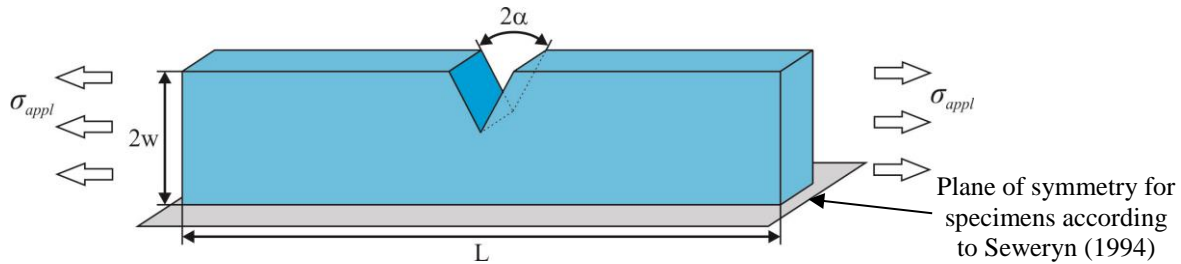


Fig. 3: Geometry of the model used for finite element calculations.

The dimensions of the SENT specimens were: length $L = 196$ mm, width $2w = 28$ mm, notch depths $a = 5, 10, 14, 20$ mm and V-notch opening angle $\alpha = 30^\circ, 45^\circ, 60^\circ, 75^\circ$, the thickness was $t = 14$ mm. The influence of the V-notch opening angle α and V-notch depth a on the critical applied stress was studied. The quarter of the specimen was modeled, because of the symmetry in geometry and loading conditions.

Following material properties were considered: PMMA - Seweryn (1994): Young's modulus $E = 2.3$ GPa, Poisson's ratio $\nu = 0.36$, fracture toughness $K_{IC} = 1.9$ MPa.m^{1/2} and tensile strength $\sigma_c = 70$ MPa; duraluminum - Seweryn (1994): $E = 70$ GPa, $\nu = 0.33$, $K_{IC} = 54.3$ MPa.m^{1/2} and $\sigma_c = 454$ MPa; PMMA - Gómez (2003): $E = 3.0$ GPa, $\nu = 0.40$, $K_{IC} = 1.0$ MPa.m^{1/2} and $\sigma_c = 75$ MPa.

Both materials were considered as homogenous linear-elastic and isotropic. The critical distance d was 0.451 mm for PMMA according to Seweryn (1994), 0.113 mm in the case of PMMA according to Gómez (2003) and 9.026 mm in the case of duraluminum (Seweryn, 1994).

4. Results and Discussion

Using FE analysis the critical applied stresses for the crack initiation from sharp V-notch was estimated and compared with the experimental data. V-notch stability conditions depend on the applied load and on the material resistance to the fracture.

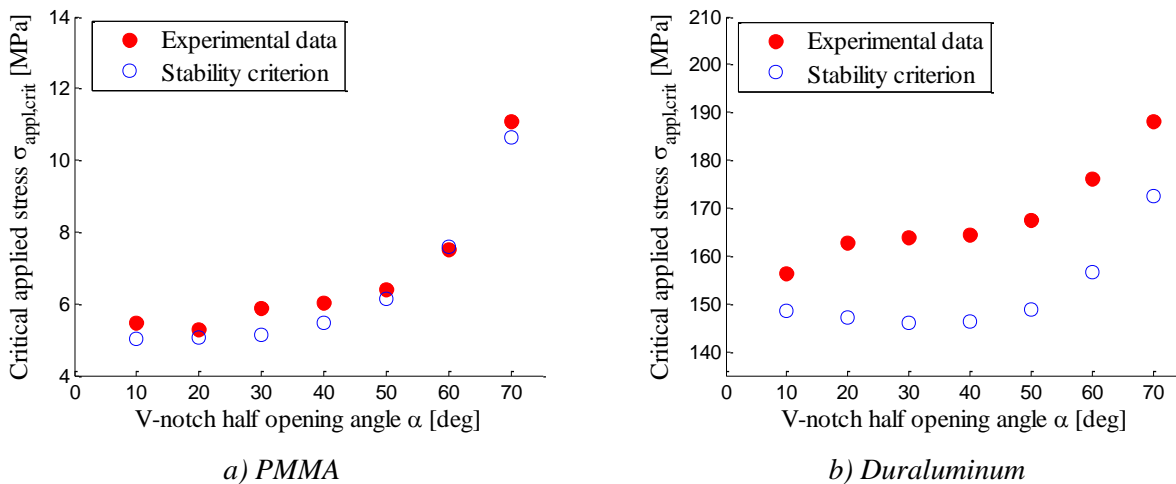


Fig. 4: Comparison of estimated critical values of applied tensile stress $\sigma_{appl,crit}$ and experimental data taken from Seweryn (1994).

Very good agreement between calculated critical applied stress values and experimental data was found in the case of PMMA specimens for V-notch opening angle α less than 70° (see Fig. 4a and Fig. 5a), and for depth of the V-notch a higher than 10 mm (see Fig. 5b). Vicinity of the free surface influenced calculated results for V-notch depth a equals or less than 10 mm.

The criterion described above is not convenient for ductile materials (see Fig. 4b). The difference between calculated and experimental data is caused by substantial plastic behavior of duraluminum.

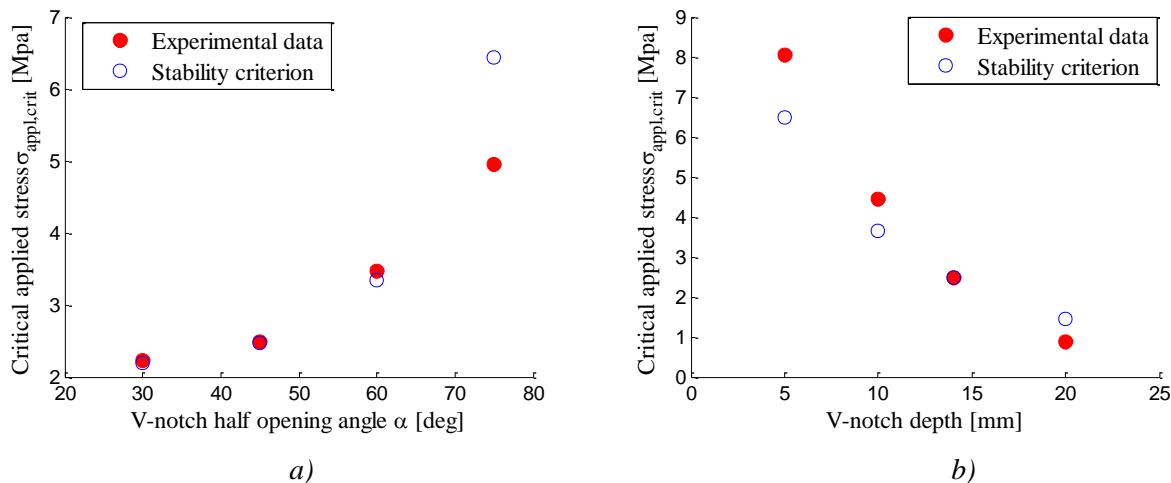


Fig. 5: Comparison of estimated critical values of applied tensile stress $\sigma_{app,crit}$ and experimental data taken from Gómez (2003).

5. Summary

The critical value of the applied stress necessary for the crack initiation from sharp V-notch was estimated in the paper. Tensile specimens with V-notches were modeled by numerical simulations and two different materials were considered: PMMA and duraluminum. Influence of the V-notch opening angle α and the V-notch depth a was studied. A criterion based on average value of the tangential stress in front of the sharp concentrator was applied. Estimated values of the critical applied stress were compared with experimental data taken from the literature and good agreement was found for brittle PMMA. The paper represents an example of the use of the generalized form of LELM in the case of general singular stress concentrators.

Acknowledgement

This work was supported through the grant No. CZ.1.07/2.3.00/30.0063 of the Ministry of Education, Youth and Sports of the Czech Republic.

References

- Knésl, Z. (1991) A criterion of V-notch stability. *International Journal of Fracture*, 48, pp. 79-83.
- Knésl, Z. (1993) The application of the strain energy density concept to the determination of a crack propagation direction initiated at a sharp notch tip. *Acta Technica ČSAC*, 38, pp. 221-234.
- Seweryn, A. (1994) Brittle fracture criterion for structures with sharp notches. *Engineering Fracture Mechanics*, 47, 5, pp. 673-681.
- Seweryn, A., Lukaszewicz, A. (2002) Verification of Brittle fracture criteria for elements with V-shaped notches. *Engineering Fracture Mechanics*, 69, pp. 1487-1511.
- Gómez, F. J., Elices, M. (2003) Fracture of components with V-shaped notches. *Engineering Fracture Mechanics*, 70, 14, pp. 1913-1927.
- Zouhar, M., Náhlík, L., Hutař, P., Ševčík, M., Knésl, Z. (2012) The effect of critical distance in stability condition for the crack at the interface between two materials. *Engineering Mechanics*, 19, 2/3, pp. 155-164.
- Yosibash, Z. (2010) *Singularities in elliptic boundary value problems and elasticity and their connection with failure initiation*. Springer Science Business Media.

POST-CRITICAL MULTI-MODAL VIBRATION OF A CONTINUOUS INVERSE PENDULUM TYPE SYSTEM

J. Náprstek*, C. Fischer*

Abstract: Auto-parametric effects are processes endangering structures during a seismic attack. Tall structures exposed to a strong vertical component of an earthquake excitation nearby the epicenter can collapse due to auto-parametric resonance effect. Vertical and horizontal response components being independent in the linear regime get into a complex interaction due to non-linear terms in post-critical regime. Two generally different types of the post-critical regimes are presented: (i) post-critical state with possible recovery; (ii) exponentially rising horizontal response leading to a collapse. A special attention is paid to processes of transition from semi-trivial to post-critical state in case of time limited excitation period as it concerns the seismic processes. Solution method combining analytical and numerical approaches is developed and used. Its applicability and shortcomings are commented. A few hints for engineering applications are given.

Keywords: Auto-parametric systems, Dynamic stability, Semi-trivial solution, Multi-modal vibration, Post-critical states.

1. Outline of the System

Non-linear dynamic effects are the most dangerous processes endangering structures during a seismic attack. Among them auto-parametric non-linear vibration in state of post-critical auto-parametric resonance, see Tondl et al. (2000), Hatwal et al. (1983) or Bajaj et al. (1994), can lead to collapse particularly in case of high slender systems or large dynamically sensitive structures. Auto-parametric resonance caused in the past heavy damages or collapses of towers, bridges and other structures. The main cause of these effects is a strong vertical component of an earthquake excitation in epicenter area. In sub-critical linear regime vertical and horizontal response components are independent and therefore in such a case no horizontal response component is observed. If the amplitude of a vertical excitation in a structure foundation exceeds a certain limit, a vertical response component loses dynamic stability, e.g. Benettin et al. (1980) and dominant horizontal response component arises and can lead to failure of the structure.

The seismic type broadband random non-stationary excitation can be particularly dangerous and amplify these effects. From viewpoint of rational dynamics the problem is of the inverse pendulum type. Authors are involved in this topics related with earthquake engineering for a long time, see e.g. Náprstek and Fischer (2009, 2010, 2011) and others.

In principle easily deformable tall structures are the most sensitive regarding effects of auto-parametric resonance (chimneys, towers, etc.). Therefore the structure itself is modeled as a console with continuously distributed mass and stiffness in order to respect the whole eigen-value and eigen-form spectrum, see Fig. 1. The subsoil model enables to respect vertical and rocking component of the response including internal viscosity of the Voight type. Mathematical model is deduced by Hamiltonian functional including kinetic and potential energies as well as the Rayleigh function:

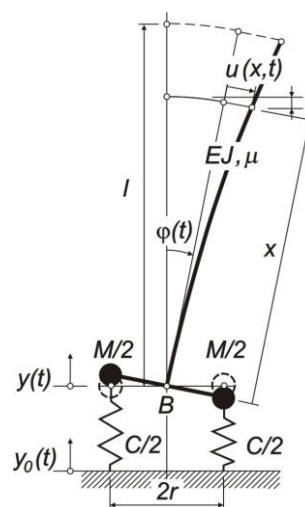


Fig. 1: Outline of the 3-DOF autoparametric system.

* Ing. Jiří Náprstek, DSc., RNDr. Cyril Fischer, PhD., Institute of Theoretical and Applied Mechanics, Prosecká 76, 190 00 Prague, naprstek@itam.cas.cz

$$T(t) = \frac{1}{2}M(\dot{y}^2(t) + r^2\dot{\varphi}^2(t)) + \frac{1}{2}\mu \int_0^l [(\dot{\varphi}(t)x + \dot{u}(x,t))^2 + \dot{y}^2(t) - 2\dot{y}(t)(\dot{\varphi}(t)x + \dot{u}(x,t)) \sin \varphi(t)] dx, \quad (1a)$$

$$U(t) = Mg \cdot y(t) + \frac{1}{2}C((y(t) - y_0(t))^2 + r^2\varphi^2(t)) + \mu g \int_0^l [y(t) - x(1 - \cos \varphi(t)) - u(x,t) \sin \varphi(t)] dx + \frac{1}{2}EJ \int_0^l u''^2(x,t) dx. \quad (1b)$$

Hamiltonian functional provides Lagrangian differential system linking strongly non-linear two-degree of freedom (TDOF) part with multi-degree of freedom (MDOF) part modeling continuous console to the simultaneous governing system, see e.g. Náprstek and Fischer (2009,2010), or Náprstek and Fischer (2011). The material damping of the console is proportional. Therefore the deformation of that can be expressed in a form of a convergent series:

$$u(x,t) = \sum_{i=1}^n \alpha_i(t) \cdot \psi_i(x) \Rightarrow \psi(\xi,t) = \sum_{i=1}^n \alpha_i(t) \chi_i(\xi), \quad (2)$$

where $(x) = l \cdot \chi_i(\xi)$ and basis functions $\chi_i(\xi)$ are eigen functions (eigen forms) of the differential equation:

$$\chi_i''''(\xi) + \lambda_i \chi_i(\xi) = 0, \quad (\lambda_i/l)^4 = \mu \omega_i^2/EJ \quad (3)$$

with boundary conditions for a console beam: $\chi_i(0) = 0$, $\chi_i'(0) = 0$, $\chi_i''(1) = 0$, $\chi_i'''(1) = 0$.

The Lagrangian system for components $\zeta(t)$, $\varphi(t)$ and components $\alpha_i(t)$ arithmetizing coordinates $\chi_i(\xi)$ reads:

$$\begin{aligned} \ddot{\zeta}(t) - \frac{1}{4}\kappa_0(\varphi^2(t))'' - \kappa_0 \sum_{i=1}^n [(\varphi(t)\dot{\alpha}_i(t))' \Theta_{0,i}] + \omega_0^2 [\zeta(t) - \zeta_0(t) + \eta_c (\dot{\zeta}(t) - \dot{\zeta}_0(t))] &= 0 \\ \ddot{\varphi}(t) - \frac{1}{2}\kappa_1\dot{\zeta}(t)\varphi(t) + \kappa_1 \sum_{i=1}^n [\ddot{\alpha}_i(t) \Theta_{1,i} + (\dot{\zeta}(t)\dot{\alpha}_i(t) - \omega_2^2\alpha_i(t)) \Theta_{0,i}] + \omega_1^2[\varphi(t) + \eta_c\dot{\varphi}(t)] &= 0 \\ \ddot{\alpha}_i(t) \cdot \Theta_{2,i} + \ddot{\varphi}(t) \cdot \Theta_{1,0} - [(\dot{\zeta}(t)\varphi(t))' + \omega_2^2\varphi(t)] \cdot \Theta_{0,i} + \omega_3^2[\alpha_i(t) + \eta_e\dot{\alpha}(t)]\Theta_{3,i} &= 0 \end{aligned} \quad (4)$$

where

$$\zeta_0(t) = y_0(t)/l, \quad \zeta(t) = y(t)/l, \quad \varphi(t), \quad u(x,t)/l = \psi(\xi,t), \quad \xi = x/l, \quad \rho = r/l, \quad m = \mu l \quad (5)$$

Solution method combining analytical and numerical approaches is presented in the final text together with its applicability and shortcomings. A wide parametric analysis is provided and regular and special cases indicated, quantified and commented. A few hints for engineering applications being motivated by these results are given.

2. Post-Critical Response Types and Transition Effects

The system shows that horizontal and vertical response components are independent in the semi-trivial regime, which is linear in such a case. Their interaction takes place due to non-linear terms in post-critical regime only. Interaction of nonlinear modes provided by the console and subsoil is investigated, as it comes to light that sub- and super-harmonic resonances can produce a number of effects typical for nonlinear approach particularly when internal resonances arise, see Fig. 2, where the sub-harmonic resonance effect is obvious.

Complicated inter-resonance effects of quasi-periodic type are verified in order to detect an existence of possible beating processes related with a possible periodic energy transfer among degrees of freedom. A number of non-linear effects related with MDOF character of the rather weak console and its interaction with bottom part of the system is discussed, in the best knowledge of authors, for the first time. Various post-critical deterministic as well as chaotic types of the response are investigated as well. Attractive and repulsive post-critical limit cycles are typical and will be carefully discussed in the full text. Investigation being conducted using Lyapunov exponent testing makes possible to identify a number of interaction types of eigen-modes.

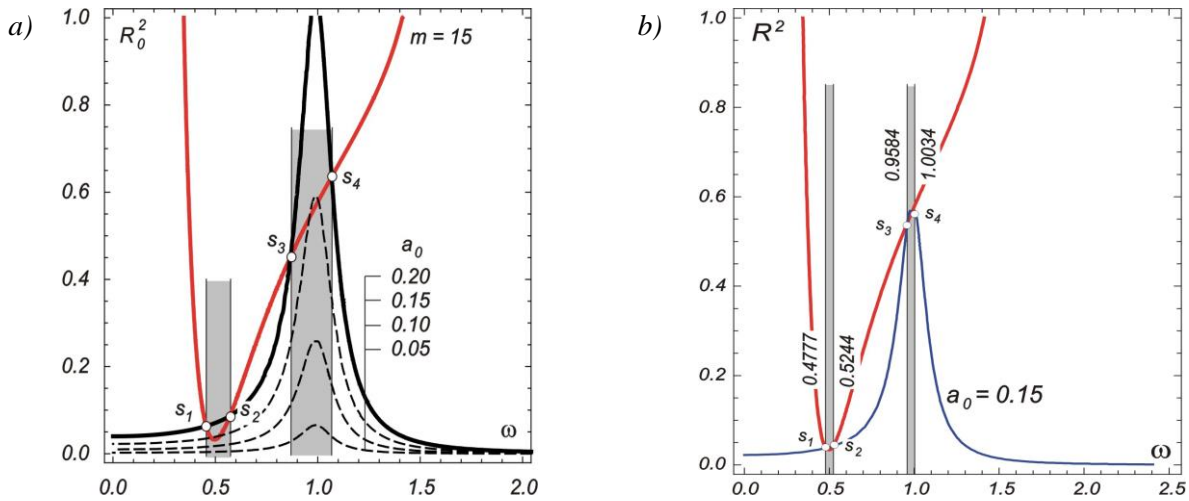


Fig. 2: Instability intervals: a) Large excitation amplitude ($a_0 = 0.20$);
b) Medium excitation amplitude ($a_0 = 0.15$).

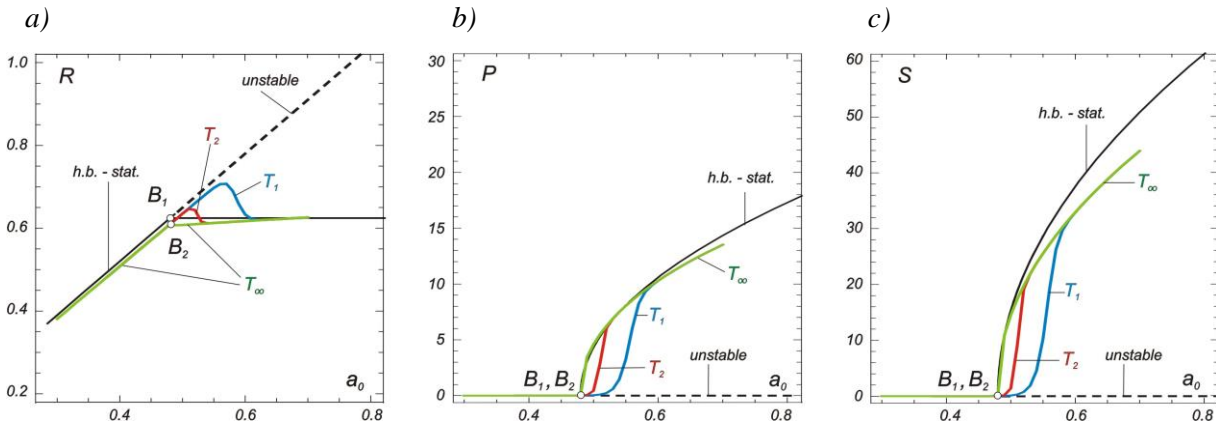


Fig. 3: Process of the stability loss and of the post-critical response:
a) Bifurcation diagram of the vertical response component P - amplitude R ;
b) and c) Bifurcation diagrams of horizontal (rotation) components φ, ψ - amplitudes P, S .

Two generally different types of the post-critical regimes are presented in the paper: (i) the close neighbourhood of the stable state (area between the semi-trivial solution stability limit and the limit of irreversibility); despite the response is strongly non-linear, structure can regain the stable state, when excitation drops below a certain limit; (ii) if the response leaves beyond the limit of irreversibility, the rocking response component loses any periodic character and rises exponentially leading inevitably to a failure of the structure without possibility of any recovery. In such a case an avalanche process throughout eigen-modes can emerge releasing accumulated energy in the system before the post-critical processes occurs.

A special attention is paid to processes of transition from semi-trivial to post-critical state in case of time limited excitation period as it concerns the seismic processes, see Fig. 3. In the picture (a) the bifurcation point B_1 is an origin of two branches: stable and unstable. It is obvious that for a short excitation interval (blue curve) the response follows the unstable branch for higher excitation amplitudes than it corresponds to B_1 and only after a certain time it drops asymptotically to nearly horizontal stable branch. Similarly in pictures (b) and (c) we can observe that the response for a short excitation interval is nearly zero following the unstable branch and only later is rising to stable branch demonstrating large horizontal amplitudes. Due to this effect a significant increase of admissible excitation amplitude is provided contributing for the sake of the structure safety.

3. Conclusions

Authors deal with easily deformable tall structures, which are very sensitive to effects of auto-parametric resonance (chimneys, towers, etc.). If the amplitude of a vertical excitation in a structure foundation exceeds a certain limit, a vertical response component loses stability and dominant horizontal response component arises. This post-critical regime (auto-parametric resonance) follows from the non-linear interaction of vertical and horizontal response components and can lead to a failure of the structure.

In principle solution methods combining analytical and numerical approaches have been developed and used. Their applicability and shortcomings are commented. A few hints for engineering applications in a design practice are given. Some open problems are indicated.

Acknowledgement

The kind support of the Czech Science Foundation project GA CR 13-34405J and of the RVO 68378297 institutional support are gratefully acknowledged.

References

- Bajaj, A. K., Chang, S. I., Johnson, J. M. (1994) Amplitude modulated dynamics of a resonantly excited autoparametric two degree of freedom system, *Nonlinear dynamics*, 5, pp. 433-457.
- Benettin, G., Galgani, L., Giorgilli, A., Strelcyn, M. (1980) Lyapunov characteristic exponents for smooth dynamical systems and Hamiltonian systems: A method for computing all of them. Part 2, Numerical application, *Meccanica*, 15, 21-30.
- Hatwal, H., Mallik, A. K., Ghosh, A. (1983) Forced nonlinear oscillations of an autoparametric system, *ASME Jour. Applied Mechanics*, 50, pp. 657-662.
- Náprstek, J., Fischer, C. (2009) Auto-parametric semi-trivial and post-critical response of a spherical pendulum damper, *Computers & Structures*, 87, 19-20, pp. 1204-1215.
- Náprstek, J., Fischer, C. (2010) Post-critical response types of a non-linear autoparametric structure due to seismic excitation, In: *Proc. 14th Eur. Conf. Earthq. Eng. (Garevski M. ed)*, Macedonian Assoc. For Earthq. Eng., Ohrid, Macedonia, paper 223, 8 p.
- Náprstek, J., Fischer, C. (2011) Auto-parametric Stability Loss and Post-critical Behavior of a Three Degrees of Freedom System, *Computational Methods in Stochastic Dynamics*, M. Papadrakakis et al. (Editors), Springer, Chapter 14, pp. 267-289.
- Tondl, A., Ruijgrok, T., Verhulst, F., Nabergoj, R. (2000) *Autoparametric Resonance in Mechanical Systems*, Cambridge University Press, Cambridge.

AEROELASTIC DIVERGENCE MODELED BY MEANS OF THE STOCHASTIC RESONANCE

J. Náprstek^{*}, S. Pospíšil^{*}

Abstract: *The divergence is one of the most important and dangerous phenomenon of aeroelastic post-critical states occurring at a prismatic slender beam in a cross-flow. This phenomenon manifests by stable periodic hopping between two nearly constant limits perturbed by random noises. Experimental observation and numerical simulation motivates an idea to model this process as the effect of the stochastic resonance. Being observed and practically used in a number of disciplines in physics (optics, plasma physics, atd.) its mathematical basis follows in the most simple case from properties of the Duffing equation with negative linear part of the stiffness. The occurrence of this phenomenon depends on certain combinations of input parameters, which can be determined theoretically and verified experimentally in the wind tunnel. Parameter combinations leading to the stochastic resonance (or divergence) should be avoided in practice in order to eliminate any danger of the bridge deck collapse due to aeroelastic effects.*

Keywords: Stochastic resonance, Interwell hopping, Non-linear vibration, Aeroelastic divergence, Post-critical states.

1. Phenomenon of the Stochastic Resonance

Stochastic resonance is a phenomenon, which has been surmised in physical chemistry in early forties, see e.g. Kramers (1940). Many years later several branches in theoretical and experimental physics identified this phenomenon and applied this one in optics and plasma physics, see e.g. Inchiosa & Bulsara (1996), or review paper Gammaitoni et al. (1998). Hundreds papers more have been published until now, including also a couple of monographs, for instance McDonnell et al. (2008). Authors outlined some basic properties of the stochastic resonance quite recently, Náprstek (2014). Stochastic resonance represents in principle a very stable interwell hopping of the non-linear oscillator of the Duffing type under suitable combination of the deterministic (harmonic) and white noise related random excitation. Many physical effects can be modeled using this approach.

Let us assume the nonlinear mass-unity oscillator with one degree of freedom under additive excitation, which consists of harmonic and random components:

$$\begin{aligned} \dot{u} &= v; \\ \dot{v} &= -2\omega_b \cdot v - V'(u) + P(t) + \xi(t). \end{aligned} \quad (1)$$

$V(u)$ - potential energy being introduced in a form corresponding with the Duffing equation:

$$V(u) = -\frac{\omega_0^2}{2}u^2 + \frac{\gamma^4}{4}u^4 \quad \Rightarrow \quad V'(u) = dV(u)/du = -\omega_0^2 \cdot u + \gamma^4 \cdot u^3 \quad (2)$$

$\xi(t)$ - Gaussian white noise of intensity $2\sigma^2$ respecting conditions:

$$E\{\xi(t)\} = 0 ; \quad E\{\xi(t)\xi(t')\} = 2\sigma^2 \cdot \delta(t - t') \quad (3)$$

$P(t) = P_0 \exp(i\Omega t)$ - external harmonic force with frequency Ω . Amplitude P_0 should be understood per unit mass. Symbols ω_0 and ω_b have a usual meaning of the circular eigen-frequency and circular damping frequency of the associated linear system. The linear part of the $V'(u)$ is negative making the system metastable in the origin, while the cubic part acts as stabilizing factor beyond a certain interval of displacement u .

^{*} Ing. Jiří Náprstek, DSc., Assoc. Prof. Ing. Stanislav Pospíšil, PhD.: Institute of Theoretical and Applied Mechanics, Prosecká 76, 190 00 Prague, CZ naprstek@itam.cas.cz

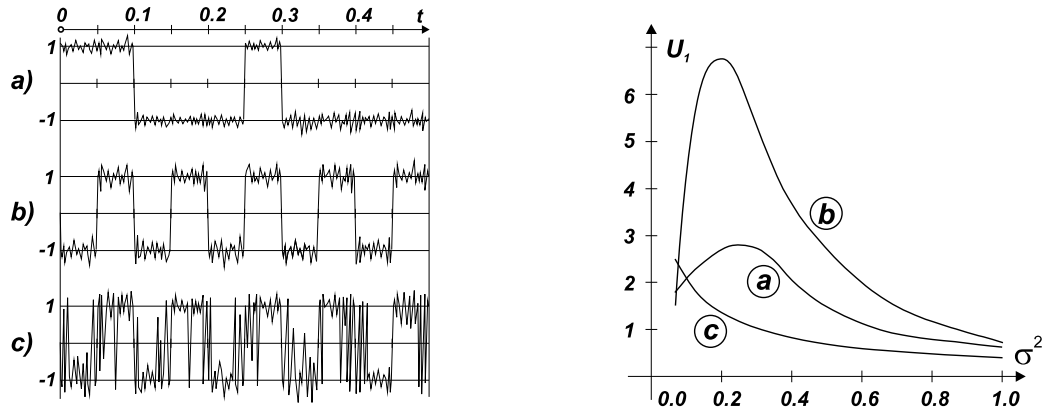


Fig. 1: Response of the system with combined excitation - white noise and harmonic (left). The spectral amplification of the system response due to stochastic resonance effect (right).

Taking into account that random noise in Eq. (1) has an additive character, the appropriate Fokker - Planck (FP), e.g. Pugachev & Sinitsyn (1987), equation can be easily written out:

$$\kappa_u = v ; \quad \kappa_v = -2\omega_b \cdot v - V'(u) + P(t) ; \kappa_{vv} = 2\sigma^2 \quad (4)$$

$$\frac{\partial p(u,v,t)}{\partial t} = -v \frac{\partial p(u,v,t)}{\partial u} + \frac{\partial}{\partial v} [2\omega_b \cdot v + V'(u) - P(t)]p(u,v,t) + \sigma^2 \frac{\partial^2 p(u,v,t)}{\partial v^2} \quad (5)$$

together with boundary conditions:

$$\lim_{u,v \rightarrow \pm\infty} p(u,v,t) = 0 ; \quad p(u,v,0) = \delta(u,v). \quad (\text{Dirac function}) \quad (6)$$

Some illustrative numerical results have been outlined in Fig. 1. It presents numerical simulations using the basic system Eq. (1). In individual parts the influence of rising white noise intensity σ^2 , which acts together with a harmonic force onto the system, can be seen. For very low level of the noise the harmonic component is hardly able to overcome the inter-well barrier and therefore only seldom irregular jumps between stable points occur. In local regimes the system response is relatively small and nearly linear, see Fig. 1 - left (a). Optimal ratio of the noise intensity and the amplitude of the harmonic force results for its certain frequency in the system response containing a visible periodic part corresponding with the frequency of the external harmonic excitation component. The response is not harmonic and contains many higher harmonics. However the basic frequency of the interwell hopping is stable making possible to reconstruct the original harmonic component hidden in the background, see Fig. 1 - left (b). Fig. 1 - left (c) demonstrates the state of a large superiority of the noise. Increasing the noise level can counteract the aforementioned process and thereby the stochastic resonance effect vanishes. However, the useful harmonic component could be still detected when stiffness parameters (ω_o^2, γ^4) and damping (ω_b) are adjusted appropriately with respect to the deterministic excitation component frequency.

General characteristics of the response can be obtained investigating the FP equation (5) together with conditions Eqs (6). Examining the right side of Eq. (5), it is obvious that stationary solution cannot exist due to time dependent coefficient κ_v . This factor is given by deterministic excitation component. Otherwise the stationary solution exists and can be carried out for Hamiltonian systems using the Boltzmann's formula, e.g. Cai & Lin (1988) or Pugachev & Sinitsyn (1987). A number of methods can be used to solve Eq. (1), however an evolution character should be kept at this case. Fig. 1 shows the sensitivity of the system.

2. Example - Harmonically Excited Beam Under Influence of Turbulence Noise

The response of a beam, loaded by the wind with turbulent component, known as the aeroelastic divergence, see e.g. Náprstek & Pospíšil (2012) and many others, initiated the idea to use the theory of stochastic resonance for the explanation of hopping of the beam in between two meta-stable positions, see e.g. Gammaitoni et al. (1998), McDonnell et al. (2008) or Náprstek (2014). This kind of the response has been observed during the wind tunnel measurement focused on the self-induced vibration with the large amplitudes in the non-linear range using the special experimental stand. It represents the working

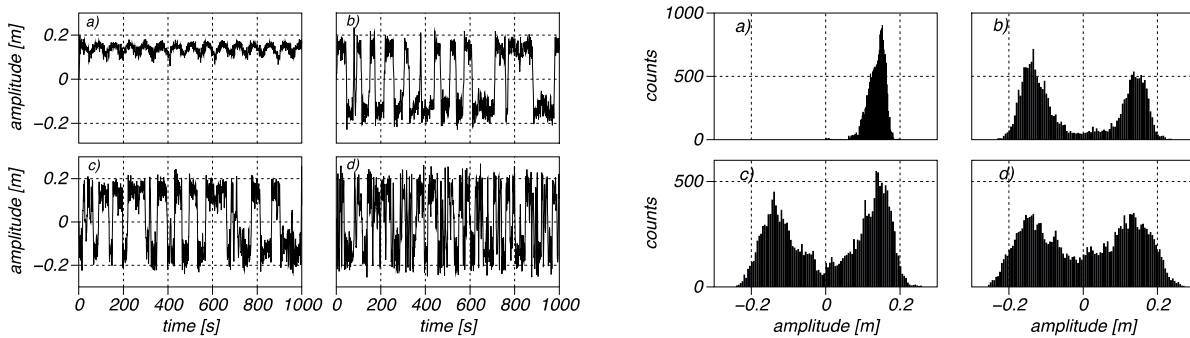


Fig. 2: Time history and probability density functions (histograms) of the response due to change of the noise intensity.

mechanism sensitive to the excitation by the wind. The stand and the experiments are described more in detail in the paper Král et al. (2013).

The effect of the stochastic resonance has been demonstrated by means of numerical simulation on the special experimental stand mentioned above. It accommodates a sectional model of a slender prismatic beam tested in a cross-flow in a wind tunnel. As it can be seen in Fig. 2 - left, time histories for various levels of the noise component are adequate with those demonstrated in Fig. 1 - left. Influence of the noise intensity increase manifests itself from a local nearly linear effect running around one of two semi-stable system positions as far as complex nonlinear process passing through the domain of both semi-stable positions. This result is even more obvious regarding Fig. 2 - right presenting the response probability density for input noise intensities corresponding with the left picture. In particular the probability density shape changes from the local concentration rather of the Gaussian like curve until bimodal probability density being symmetrical and typical for Duffing oscillator with a high level white noise excitation and almost without any harmonic excitation component.

3. Conclusions

The phenomenon of the stochastic resonance has been introduced as a theoretical tool of aeroelastic divergence description. This way reveals to be adequate observing carefully experimental results obtained by comprehensive measurements in a wind channel. With respect to those, the divergence manifests phenomenologically as a periodical hopping between two quasi-static positions with weak random perturbation. This effect can emerge under a relevant combination of periodic (nearly harmonic vortex shading) and random (white noise type) additive excitation as it has been observed experimentally. Conditions of the theoretical stochastic resonance occurrence at the Duffing equation are qualitatively identical and therefore it has been adopted as an adequate theoretical model of the divergence phenomenon. The relevance of this model has been verified analytically by means of the Fokker-Plack equation as well as by numerical solution of corresponding Ito stochastic system. The paper describes also the numerical simulation of the experimental stand used for the aeroelastic testing of profiles, before it has been tested in the turbulent flow. It shows, that under certain "optimal" value of the parameters, the signal-to-noise ratio of the response increases and the resonant-like peak occurs in the amplitude spectra. This makes an optimistic perspective for the experimental analysis, which together with the analytical and numerical ones should continue to obtain better insight into the general tendencies when individual parameters of the system and the input signal are changed.

Acknowledgement

The kind support of the Czech Scientific Foundation No. GA CR 13-34405J and RVO 68378297 institutional support are gratefully acknowledged.

References

- Cai, G. Q., Lin, Y.K. (1988) On exact stationary solutions of equivalent non-linear stochastic systems. International Journal of Non-Linear Mechanics, Vol. 23, 4, pp. 315-325.
- Gammaitoni, L., Hänggi, P., Jung, P., Marchesoni, F. (1998). Stochastic resonance. Reviews of Modern Physics, 70, 1, pp. 223-287.

- Inchiosa, M. E., Bulsara, A. R. (1996) Signal detection statistics of stochastic resonators. *Physical Review E*, 53, 3, pp. 2021-2024.
- Kramers, H. A. (1940) Brownian motion in a field of force and the diffusion model of chemical reactions. *Physica*, VII, 4, pp. 284-304.
- McDonnell, M. D., Stock, N. G., Pearce, C. E. M., Abbott, D. (2008) *Stochastic Resonance*, Cambridge University Press, Cambridge, New York.
- Náprstek, J. (2014) Stochastic resonance in a simple Duffing equation. In: *Proc. Dynamics of Machines 2014* (L. Pešek ed.). Institute of Thermomechanics, Prague, 2014, in print.
- Pugachev, V. S., Sinitsyn, I. N. (1987) *Stochastic Differential Systems - Analysis and Filtering*. J. Willey, Chichester.
- Náprstek, J., Pospíšil, S. (2012) Response types and general stability conditions of linear aero-elastic system with two degrees-of-freedom. *J. Wind Eng. Ind. Aerodyn*, 111, pp. 1-13.
- Král, R., Pospíšil, S., Náprstek, J. (2013) *Experimental set-up for advanced aeroelastic tests on sectional models*. *Experimental Techniques*, SEM Wiley, doi:10.1111/ext.12056.

BIOMECHANICAL TESTING OF SPINAL SEGMENT FIXED BY ARCOFIX SYSTEM

T. Návrát^{*}, Z. Florian^{*}, J. Kočíš^{**}, P. Vosynek^{*}

Abstract: *The aim of this study was to compare the mechanical properties of the spinal segment in the intact state, destabilized (injury) state and the state after fixation by implant ArcoFix. The problem was solved by using the experimental modelling ZWICK testing machine. The study was based on in vitro biomechanical testing. Ten test samples were prepared for the experiment. Mechanical properties were described by the value of force couple needed to twist the specimen during the applied tensile force. Statistical analysis of measured results confirmed the hypothesis of different behavior of the states of intact, injured and fixed samples. Analysis did not confirm different mechanical behavior of intact and fixated specimens when comparing by the couple moment.*

Keywords: ArcoFix, Spine stabilization, Lateral stabilization, Biomechanics.

1. Introduction

The reconstruction of the anterior column of the thoracolumbar spine has become more common in the last few years. ArcoFix is an implant and instrument system for the anterior stabilization of the thoracolumbar spine. It can be used in combination with a bone graft or a vertebral body (ArcoFix, Technique Guide).

Testing criteria for spinal implants and similar biomechanical studies have been described by Kocis (2010), Wilke (1998), Panjabi (1982, 1992), Manohar (2003), Janů (2011), Urbanová (2010). The aim of this study was to compare the mechanical properties of the spinal segment in the intact state, destabilized (injury) state and the state after fixation by implant ArcoFix.

2. Methods

Test specimens were taken from domestic pig. A total of 10 specimens were prepared for the purposes of the experiment. For the purposes of mechanical tests, spinal segment had to be modified so that it could be tightened into jaws of a testing machine. As the specimens are of organic origin, it was not possible to use fixtures designed for tests of technical materials. Both ends of the specimen were fixed in duracryl blocks that were tightened through plates with clamping pins into jaws of a standard testing machine using six-jaw lathe chucks. The specimen tightened into jaws of a testing machine is demonstrated in Fig. 1.

The Zwick testing machine with basic equipment made it possible to subject specimens to tension or torsion load, or the combination of both. Our Institute has rich experience with this combination of loads used for experimental modelling of spinal elements. Tension load selected for this experiment is rather unusual, as it almost does not occur during normal movements of a human body. However, tension load is suitable for the purpose of the experiment, as it exposes the specimen to mechanical states that can be considered as more adverse as compared with pressure load.

^{*} Ing. Tomáš Návrát, PhD., Assoc. Prof. Ing. Zdeněk Florian, CSc., Ing. Petr Vosynek: Institute of Solid Mechanics, Mechatronics and Biomechanics, Faculty of Mechanical Engineering, Brno University of Technology, Technická 2896/2; 616 69, Brno; CZ, navrat@fme.vutbr.cz, florian@fme.vutbr.cz, vosynek@fme.vutbr.cz

^{**} Assoc. Prof. MUDr. Ján Kočíš, PhD.: Department of Traumatology, Faculty of Medicine, Masaryk University Brno; Ponávka 2; 662 50, Brno; CZ, jankocis@seznam.cz

The tests were performed for intact (physiological state, Fig. 2a), injury (state of instability, Fig. 2b) and fixed (stabilization by the implant, Fig. 2c) specimen. In each state, the specimen was subjected to tension load of a prescribed force and, subsequently, twisted by a given angle. Load values were defined based on the experience with measurements of similar nature. Force load was 200 N. Torsion load had a deformation character, i.e. control variable was twisting angle and measured variable was the moment. The amplitude of load alternating cycle was 3 deg. The value of amplitude was established based on the initial tests with regard to maximum allowed torque of 20 Nm (as limited by the sensor).

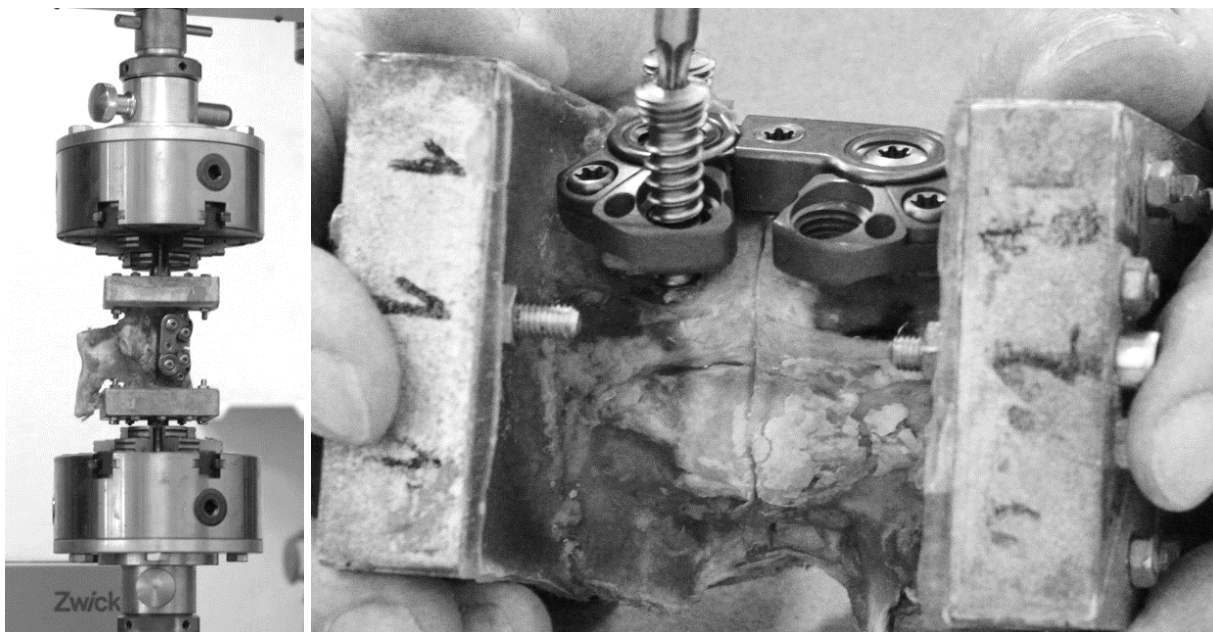


Fig. 1: The specimen tightened in jaws of a testing machine.

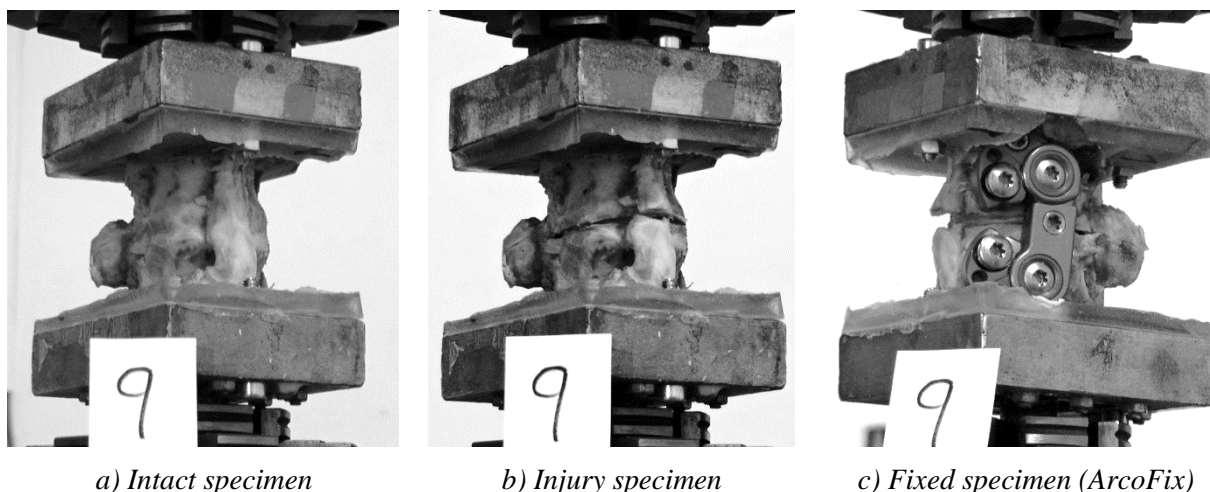


Fig. 2: Statuses of the specimen.

3. Results

During measurements, values of a couple necessary to twist the specimens were evaluated. An example of the behavior of moment in dependence on twisting angle for specimen 4 is demonstrated in Fig. 3.

The behavior of the specimens under rotation (both sides) can be seen in Fig. 4 which shows the mean value and standard deviation of torque needed for twisting the specimens of +3 and -3 degrees.

The measured maximum moments divided to three classes according to the specimen state are summarized in Fig. 5. It has to be decided whether the differences between classes are statistically

significant or, in other words, whether the impairment of specimens and the application of fixators affect the moment necessary to twist the specimens. The paired t-test was used to evaluate the differences.

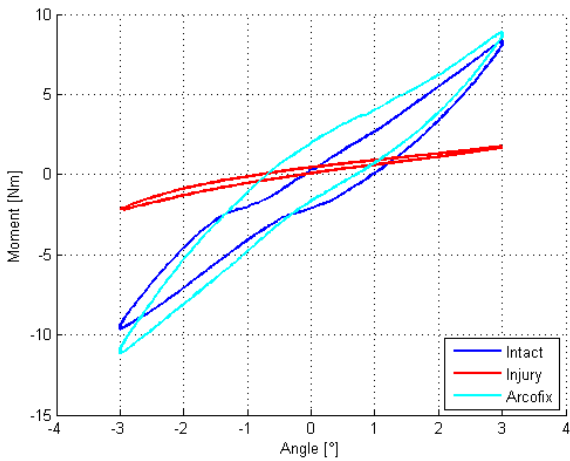


Fig. 3: Dependence of couple moment on twisting angle for specimen 4.

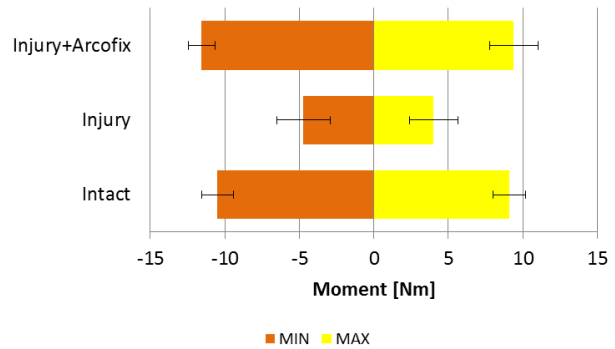


Fig. 4: The values of the moments for right and left rotation. Mean ± standard deviation.

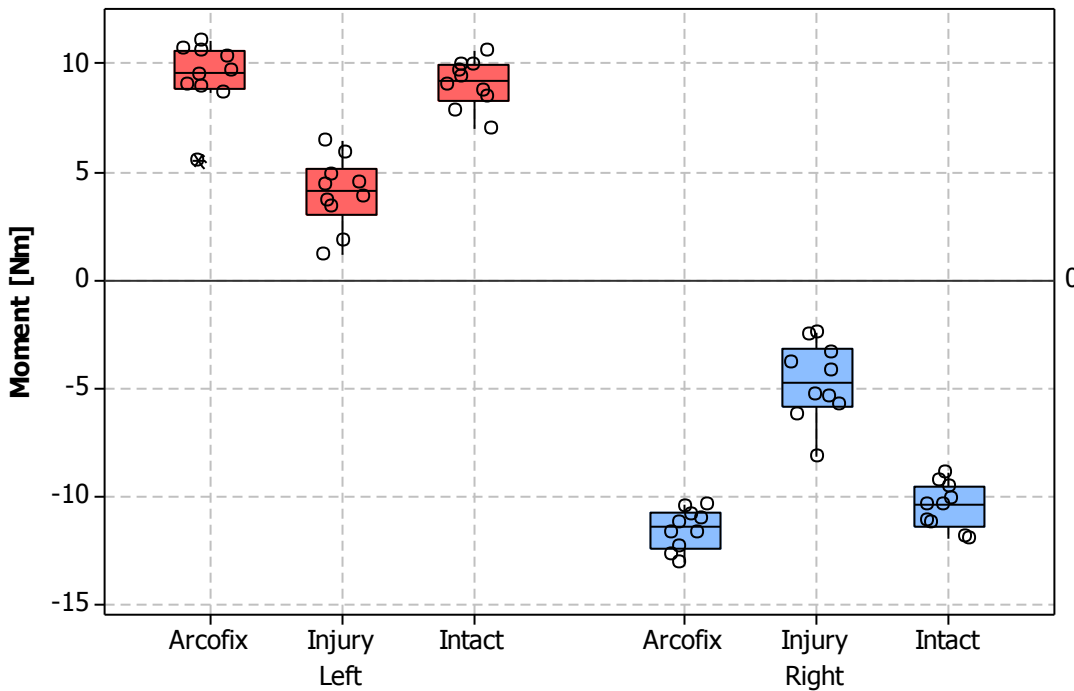


Fig. 5: Boxplot of maximum values of moment. Circle symbols – individual values.

The calculated p-values are summarized in Tab. 1. The test of normality at the significance level of 5% rejected the hypothesis that the data come from a normal distribution. The equality of the standard deviations and variances between two populations was determined using Bartlett's Test (p-value = 0.264).

Statistically significant difference was found between the state of the sample Intact and Injury and between the Injury and ArcoFix, both comparisons in positive and in negative twisting angle. The torque magnitude decreases for the damaged sample to about 45% of the value of the state ArcoFix and Intact. The different behaviour of specimens was also confirmed in state Intact and ArcoFix for positive and negative twisting angle. This indicates an asymmetric behaviour of the sample when rotation occurs. Statistically insignificant difference was found between the state Intact and ArcoFix. Implant therefore returns the stability of the injured sample to physiological state.

Tab. 1: P-values of paired t-test.

p-value		Left			Right		
		Intact	Injury	ArcoFix	Intact	Injury	ArcoFix
Left	Intact	X	< 0.0005	0.404	0.004	< 0.0005	< 0.0005
	Injury	< 0.0005	X	< 0.0005	< 0.0005	0.118	< 0.0005
	ArcoFix	0.404	< 0.0005	X	0.078	< 0.0005	< 0.0005
Right	Intact	0.004	< 0.0005	0.078	X	< 0.0005	0.008
	Injury	< 0.0005	0.118	< 0.0005	< 0.0005	X	< 0.0005
	ArcoFix	< 0.0005	< 0.0005	< 0.0005	0.008	< 0.0005	X

4. Conclusions

Statistical analysis of measured results confirmed the hypothesis of different behaviour of the states of intact, injured and fixed samples. Analysis did not confirm different mechanical behaviour of intact and fixated specimens when comparing by the moment. Behaviour of the fixed segment by ArcoFix implant is close to physiological state. The experimentally determined data were statistically processed using MINITAB 15 software.

Acknowledgement

This work is an output of research and scientific activities of NETME Centre, regional R&D centre built with the financial support from the Operational Programme Research and Development for Innovations within the project NETME Centre (New Technologies for Mechanical Engineering), Reg. No. CZ.1.05/2.1.00/01.0002 and, in the follow-up sustainability stage, supported through NETME CENTRE PLUS (LO1202) by financial means from the Ministry of Education, Youth and Sports under the „National Sustainability Programme I“.

References

- ArcoFix. Anterior-only reduction plate. Technigue Guide. Available from: <http://www.synthes.com/>
- Kocis, J., Navrat, T., Florian, Z., Wendsche, P. (2010) Biomechanical Testing of Spinal Segment Fixed by Thoracolumbar Spine Locking Plate on The Swine Lumbar Spine, Biomed Pap Med Fac Univ Palacky Olomouc Czech Repub. 154(4):345-354.
- Panjabi, M.M. (1992) The Stabilizing System of the Spine. Part II. Neutral Zone and Instability Hypothesis. J Spinal Disord, 5(4):390-6.
- Panjabi, M., GHoel, V. (1982) Relationship between chronic instability and disc degeneration. International Society for the Study of the Lumbar Spine, Toronto, Canada.
- Manohar M. Panjabi (2003) Clinical spinal instability and low back pain, Journal of Electromyography and Kinesiology, Vol. 13, Iss. 4, pp. 371-379.
- Wilke, H. J., Wenger, K., Claes, L. (1998) Testing criteria for spinal implants: recommendations for the standardization of in vitro stability testing of spinal implants, Eur Spine J. 7, pp. 148-154.
- Urbanová, L., Srnec, R., Proks, P., Stehlík, L., Florian, Z., Návrat, T., Nečas (2010) A. Comparison of the Resistance to Bending Forces of the 4.5 LCP Plate-rod Construct and of 4.5 LCP Alone Applied to Segmental Femoral Defects in Miniature Pigs. Acta Veterinaria Brno. 79(4). pp. 613-620.
- Janů, I., Kočíš, J., Návrat, T., Florian, Z., Wendsche, P. (2011) Comparative analysis screws Socon CS and Socon in the treatment of osteoporotic thoracolumbar spine fractures - a biomechanical study. Acta Chirurgie Orthopaedicae et Traumatologie Českoslovaca. 78(4). pp. 334-338, (in Czech).

ANALYSIS OF DAMAGED CONNECTION PIPING

R. Nekvasil^{*}, P. Lošák^{**}, P. Lukáč^{***}

Abstract: *The following paper analyses a cracking of a superheater connection piping which occurred after a general repair. Pipes repeatedly detached in the area of welding to the collector nozzles. Connection piping was subjected to a thorough FEM analysis and flow simulation using CFD software.*

Keywords: Piping, Nozzles, Boiler, Crack, FEM, CFD.

1. Introduction

Boiler superheaters and their connection piping are the soft spots of boilers and often get damaged, which is caused by high operating temperature and pressure inside the system where every slight change in operation significantly decreases system life. Fig. 1 shows a damaged piping. Design of the vertical connection piping is given in the figures throughout the paper.



Fig. 1: Detachment of DN 100 connection piping in the area of welding to the chamber nozzle.

In order to detect the cause of pipe cracking, structural calculation of the design was examined at first. The design flaws, which make up approximately 30 to 40 per cent of all equipment damage in the industry, may be eliminated. Major design flaws are revealed soon (several days or months), minor flaws show after several years. Examination of structural calculation of the design proved that the calculation complies with all requirements of boiler design standards (EN 12952, 2012).

^{*} Ing. Richard Nekvasil, PhD.: Institute of Process and Environmental Engineering, Brno University of Technology, Technická 2896/2; 616 69, Brno; CZ, nekvasil@fme.vutbr.cz

^{**} Ing. Pavel Lošák: Institute of Process and Environmental Engineering, Brno University of Technology, Technická 2896/2; 616 69, Brno; CZ, losak@upei.fme.vutbr.cz

^{***} Ing. Peter Lukáč, PhD.: Department of Power Engineering, Technical University of Košice; Vysokoškolská 4; 042 00, Košice; Slovakia, peter.lukac@tuke.sk

2. Stress State Analysis of Connection Piping for Operating Conditions

Analysis of operating conditions revealed that there are two basic regimes for operating conditions, i.e. summer and winter regimes. With respect to the loading, operating conditions in winter regime proved to be more significant (steam capacity reaches 20 to 30 t/h).

Following operating conditions were selected for analysis of the connection piping: 32.1 t/h capacity, 3.5 MPa working external pressure in steam superheater piping, 302.8 °C temperature at the outlet from first convective superheater, and 240 °C temperature at the inlet to second convective superheater. Temperature distribution was designed using standard methods of linear distribution along connection piping height. Fixing of chambers (collectors and vertical chamber) was modelled using sleeves, according to design of these parts.

Provided operating conditions helped to model stress distribution in the piping (given in Fig. 2).

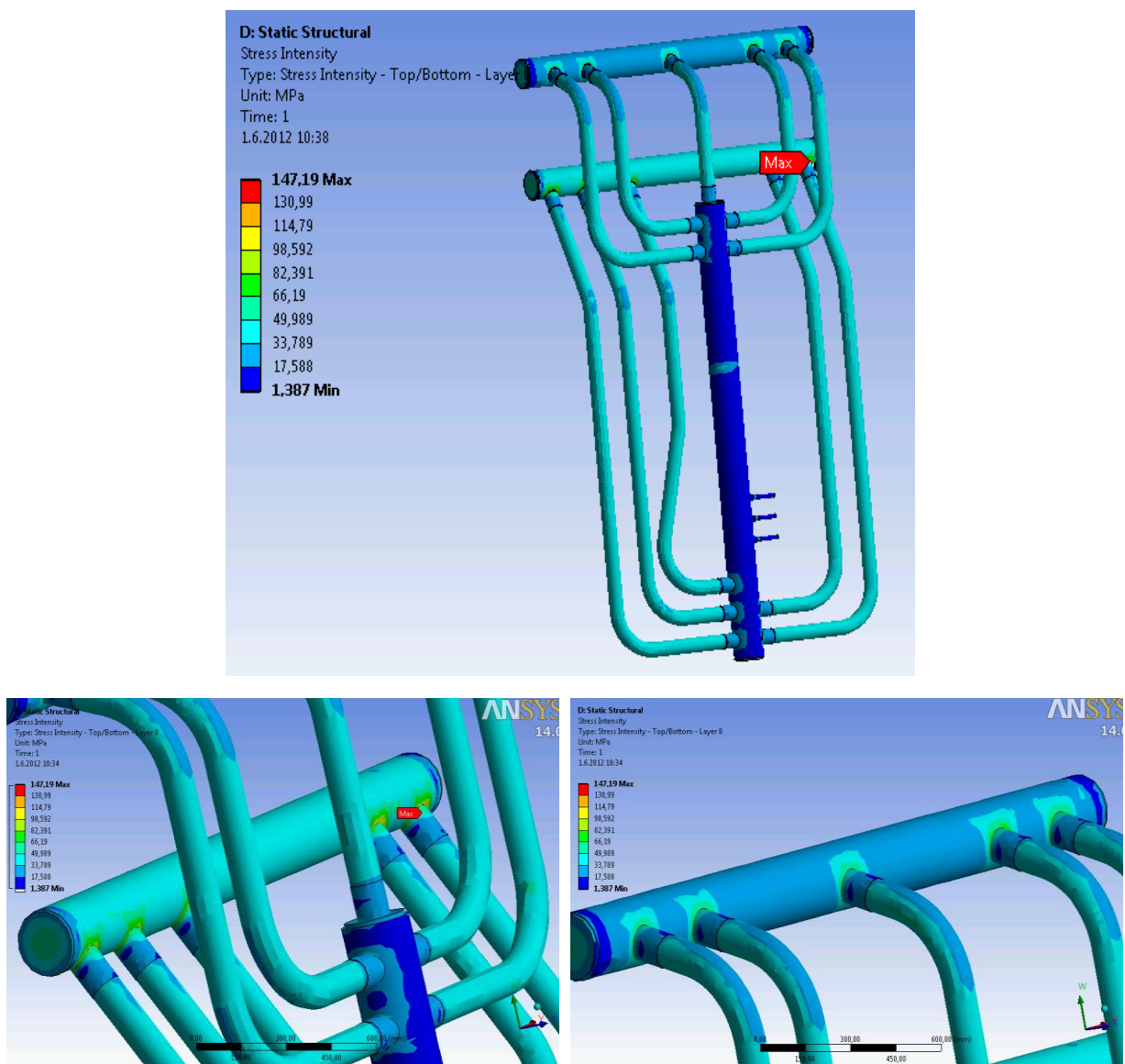


Fig. 2: Stress distribution in chambers and connection piping.

Stress values peak at 147.2 MPa, which is significantly lower than 165 MPa (Annaratton, 2007), the permissible values for membrane and bending stress (piping is made of steel 12022). Therefore, we may conclude that these normal operating conditions could not cause the damage of critical areas.

3. Analysis of Various Distributions of Heat Flux

With respect to the fact that the equipment is operated at a lower capacity than the capacity designed, it is assumed that velocity flows in individual branches of connection piping are not identical. This has further impact on different heat fluxes in individual branches, and creation of additional stress. CFD simulation was performed so that temperature distribution upon injection of water into main pipe of connection piping may be identified. Analysis revealed the nature of velocity distribution which has direct impact on heat transfer coefficient in individual areas, and on temperature distribution itself (Moinereau et al., 2001).

Analysis used identical conditions that were used in the previous chapter, i.e. 32.1 t/h capacity. Following parameters of the saturated steam were applied in the analysis: 14.16 kg/m^3 density, $2.10^{-5} \text{ Pa}\cdot\text{s}$ viscosity. Injection was calculated to equal 1.6 t/h and temperature of condensate cooler (998.2 kg/m^3 density, $1.003 \cdot 10^{-3} \text{ Pa}\cdot\text{s}$ viscosity) was ca. $190 \text{ }^\circ\text{C}$. Even steam distribution at the chamber inlet was the only simplification in the analysis.

Following figure presents velocity distribution in individual parts of the connection piping. Velocity profiles indicate uneven mixing and distribution of media flows (for both saturated steam and injected condensate). These facts had a major impact on temperature distribution in the pipes.

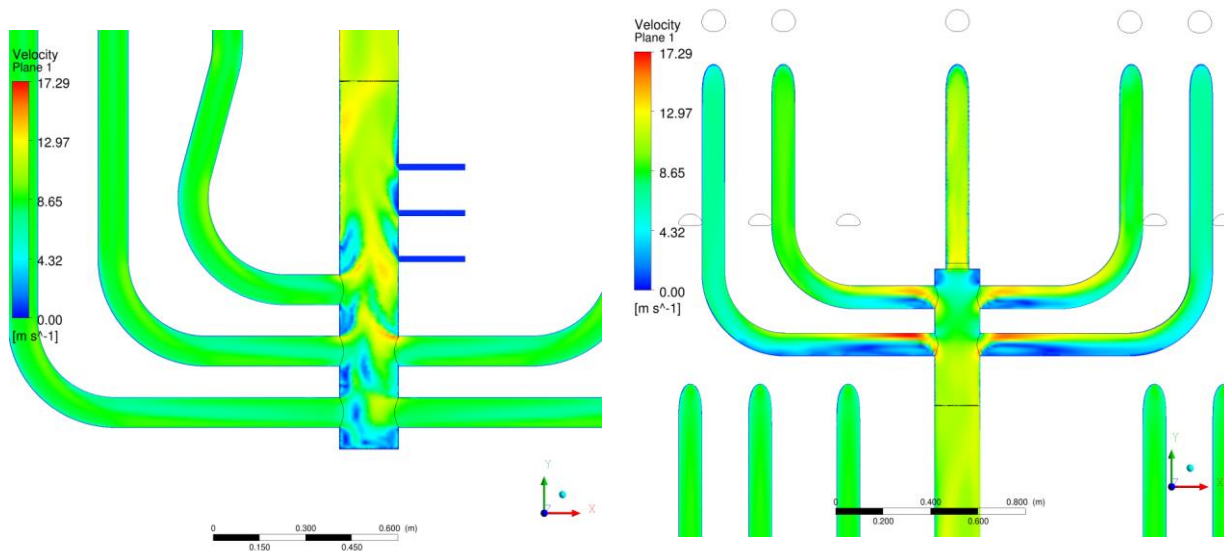


Fig. 3: Velocity distribution during mixing of steam flows and injection of condensate (left), and steam distribution in individual branches (right).

Analysis of uneven heating/cooling of connection piping was performed using acquired results. Temperatures in outer pipes differ from inner pipes and thus the outer pipes may have higher/lower temperatures. Temperature distribution was used for stress state analysis (Fluid Structure Interaction method) along with provided boundary conditions. Stress state distribution in connection piping is given in Fig. 4. Stress state peaks in the area of welding of the pipe and nozzle which are critical. Stress state reached 165.9 MPa in the critical spot, which is a permissible value. Consequently, even more specific operating conditions did not help in identification of a damage cause.

Therefore, it is recommended that the samples are taken for material analysis, and technology compliance of the equipment repair is examined.

4. Conclusion

Based on the check analysis, no cause for the pipe cracking was identified and the design of the connection piping was verified as correct. Individual samples were afterwards taken for material analysis which also did not show any major irregularities in operation of the equipment. Failure to comply with repair technology was identified as the only possible cause of the damage. Due to inconsistencies in the drawings, two different structures may have been manufactured (in terms of dimensions) and shift of nozzles and tubes prior to welding may have reached up to 25 mm . These inconsistencies are usually

disposed of by proper fitting of the pieces during the installment process. In this case, the welding then caused serious stress in the welding area, which was manifested in the cracking of the equipment.

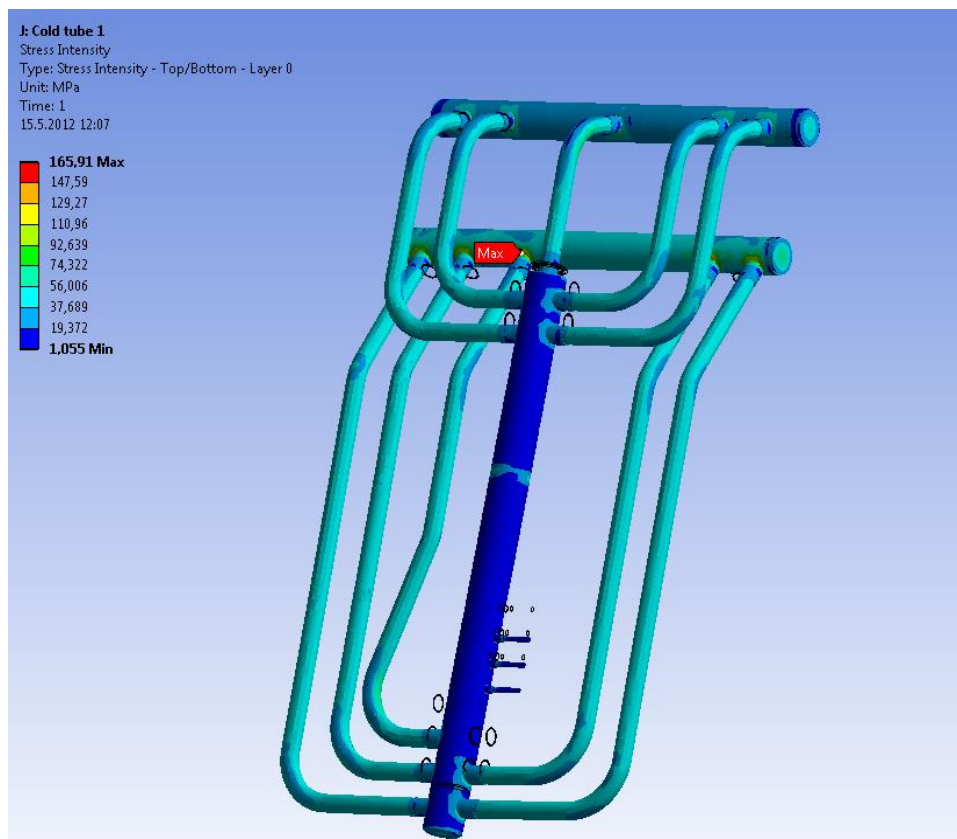


Fig. 4: Stress state distribution in connection piping.

Acknowledgement

The results of this project NETME CENTRE PLUS (LO1202) were co-funded by the Ministry of Education, Youth and Sports within the support programme „National Sustainability Programme I“.

References

- Annaratton, D. (2007) Pressure Vessel Design. Springer, Berlin.
- EN 12 952. (2012) Water tube boilers and auxiliary installations, CEN, Prague.
- Moinereau, D., Bezdikian, G., Faidy, C. (2001) Methodology for pressurized thermal shock evaluation, International Journal of Pressure Vessels and Piping, 78, pp. 69-83.

EFFECTIVENESS OF KINETIC ENERGY RECOVERY EXPLORED BY MEANS OF EXPERIMENTAL STAND

J. Nevrlý*, Z. Němec**, M. Jurík***

Abstract: *The presented paper deals with efficiency determination of kinetic energy recovery explored by means of experimental stand installed in the Institute of Machine and Industrial Design, Faculty of Mechanical Engineering, Brno University of Technology. Transfer of kinetic energy to pressure hydraulic energy was carried out by means of this stand and research was aimed to the use of results in transport, especially in heavy horse commercial vehicles operating in start-stop regime. The main purpose of stand experiments is to find conditions for the most economical operation of vehicles using two-way energy recovery.*

Keywords: Effectiveness, Energy, Recovery, Hydraulic, Stand.

1. Introduction

The basic idea of kinetic energy recovery is to use the kinetic energy of the braked vehicle which is commonly lost by braking and uselessly changed in heat. This can be done by the change of the kinetic energy to hydraulic energy that can be used at the following start of the vehicle. This system is especially suitable in vehicles working in frequent cycle braking-start as e. g. road rollers (Fig. 1), forklift trucks, garbage trucks, city busses etc. Value of efficiency serves as a criterion of optimum parameters settings and the recovery process effectiveness (Pourmovahed et al. (1992, 1992a)).



Fig. 1: The road roller.



Fig. 2: The experimental stand.

* Prof. RNDr. Ing. Josef Nevrlý, CSc.: Faculty of Mechanical Engineering, Brno University of Technology, Technická 2, 616 69 Brno, CZ, nevrlj@fme.vutbr.cz

** Assoc. Prof. Ing. Zdeněk Němec, CSc.: Faculty of Mechanical Engineering, Brno University of Technology, Technická 2, 616 69 Brno, CZ, nemec@fme.vutbr.cz

*** Ing. Miroslav Jurík, Težební 1238/2, 627 00 Brno, CZ, Bosch Rexroth, miroslav.jurik@boschrexroth.cz

2. Structure of the Experimental Stand

The main tasks for the new experimental stand were (Nevrlý, 2011, 2012):

- testing of operation states,
- measuring of the most important operation quantities for further analysis, mathematical modeling and computer simulation leading to size optimization of substantial parameters and elements and to optimization of valves control,
- finding suitable methods for efficiency determination as a measure of the system effectiveness.

The hydraulic motor drives the dynamometer that represents inertia of the real vehicle. The axial piston motor equipped with the electronic control is connected to the valve block. The electric motor of 22 kW is attached to the frame and drives the axial piston pump equipped with the proportional flow control. The pump block is connected to the valve block that contains six electromagnetic controlled valves. The valves of this block control a flow of oil into the corresponding branches of the hydraulic circuit according to the set operation regime (Nevrlý, 2012a, 2013a).

The stand for research of kinetic energy recovery is depicted in Fig. 2. The details can be seen in the hydraulic scheme in Fig. 3.

2.1. Operation regimes of the stand

- The regime STOP is the initial regime.
- The regime Set RPM serves for setting of output revolutions of hydraulic motor.
- The regime Decel causes a fly-wheel to brake.
- The regime Accel starts a fly-wheel to be driven by pressure of working liquid flowing from the high pressure accumulator.

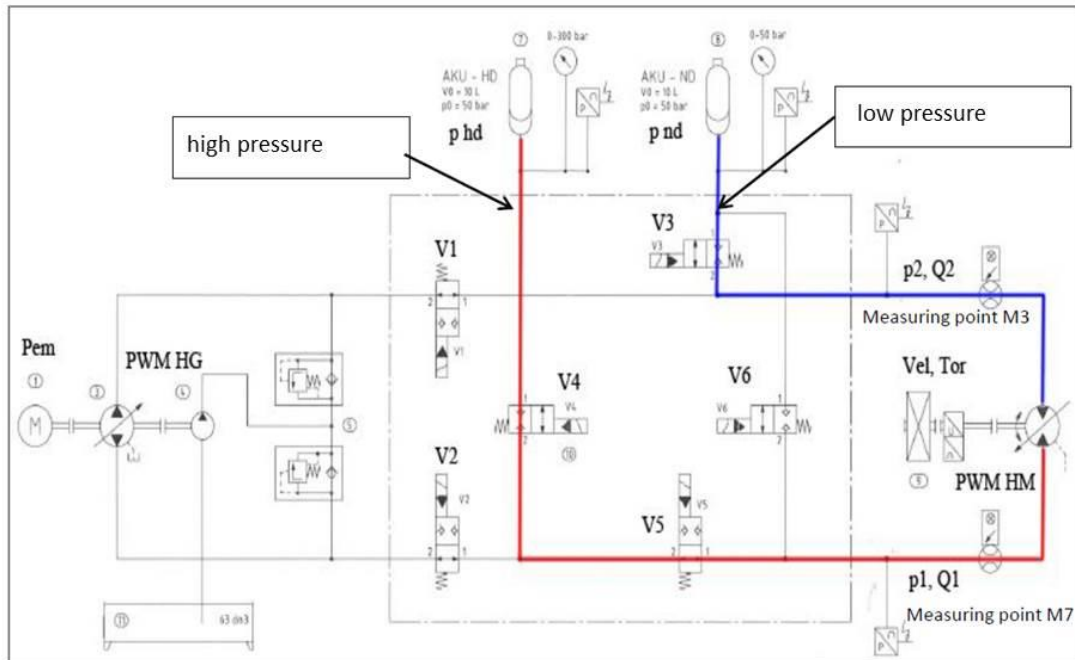


Fig. 3: Simplified scheme of the stand for operation regime Decel.

2.2. Example of efficiency determination

An example of measured high pressure and low pressure courses at regime Decel can be seen in Fig. 4 showing important trends during this operation mode.

Efficiency of the regime Decel is defined as relation of energy coming in the process and energy going out of him. Efficiency has been determined by computation and by measuring of electric power input (Němec, 2013, 2013a).

$$\eta = \frac{E_1}{E_2} = \frac{E_{phd} - E_{pnd}}{E_k + E_{em}} = \frac{\int Q_2 \cdot p_{hd} \cdot dt - \int Q_1 \cdot p_{nd} \cdot dt}{\int P_{E_k} \cdot dt + \int P_{em} \cdot dt}$$

$$P_{E_k} = \frac{d\left(\frac{I \cdot \omega^2}{2}\right)}{dt}$$

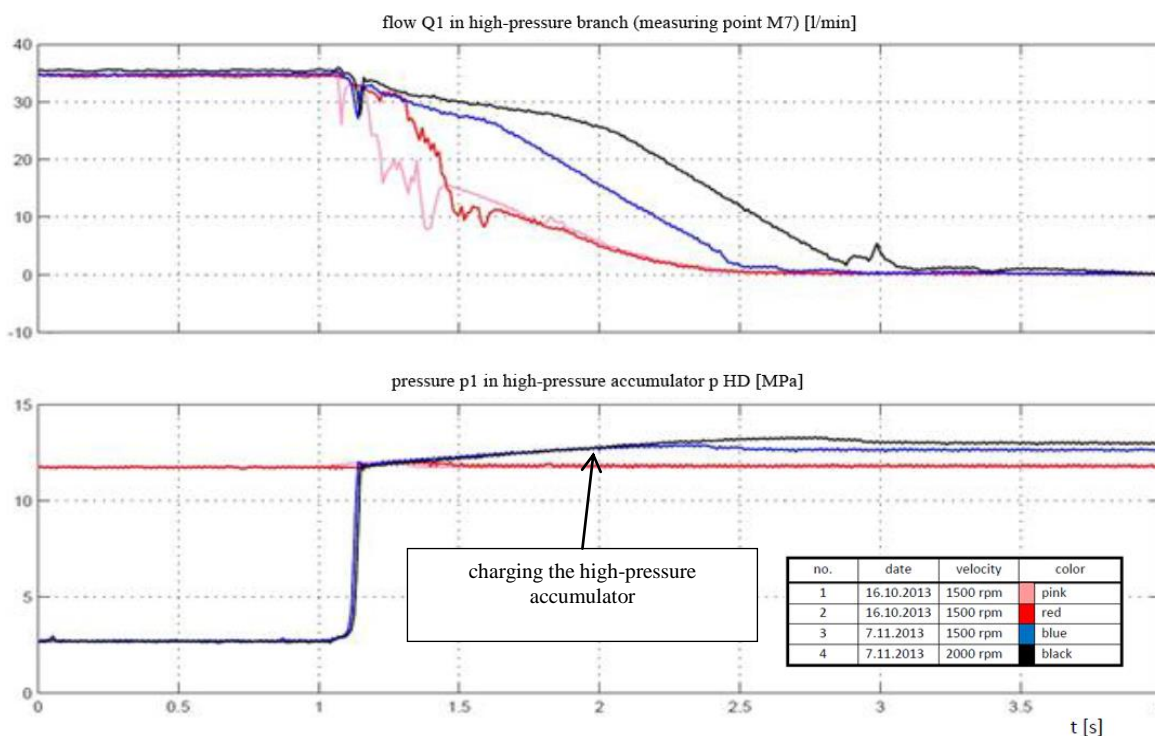


Fig. 4: Example of measured high pressure and low pressure courses at regime Decel.

Tab. 1: Determination of energy recovery effectiveness in cyclic regime by means of electric power input measuring.

	recovery start	recovery end	recovery difference	standard start	standard end	standard difference	saving	saving
velocity	el.energy consump.	el.energy consump.	el.energy consump.	el.energy consump.	el.energy consump.	el. energy consump.		
min ⁻¹	Wh	Wh	Wh	Wh	Wh	Wh	Wh	%
1500	49.90	132.62	82.72	46.40	138.45	92.04	9.32	10.12
2000	84.53	177.61	93.07	20.03	125.86	105.82	12.75	12.04

3. Conclusions

Measuring of energy recovery effectiveness during cyclic operation by means of electric power input measuring (Tab. 1) proved the following positive results (Nevrlý, 2013b):

- 1) Saving of **10 % till 12 %** shows maximum energy saving in stand till **18 %** at 3500 rpm.
- 2) Prospect of real energy saving in road roller AP 240 H is about **15 %**.

Acknowledgment

The present work has been supported by the Ministry of Education, Youth and Sports of the Czech Republic in the framework of the research project Eureka – LF12029 and by European Regional Development Fund in the framework of the research project NETME Centre under the Operational Programme Research and Development for Innovation - NETME Centre, ED0002/01/01, CZ. 1.05/2.1.00/01.0002.

References

- Němec, Z. (2013) Models and simulation for recovery stand equipped by hydrostatic drive (in Czech). Chapter 4.4 in (Nevrlý, 2013b).
- Němec, Z. (2013a) Valves timing of in recovery stand of FME. Partial research report. FME BUT, (in Czech).
- Nevrlý, J. (2011) Kinetic Energy Recovery at Heavy Cycle-rate Operating Commercial Motor Vehicles. Research report. Institute of Machine and Industrial Design, Faculty of Mechanical Engineering, Brno University of Technology, (in Czech).
- Nevrlý, J. (2012) Hydraulic Energy Recovery Stands for Vehicles. In: Proc. 53rd International Conference of Machine Design Departments. Conference Proceedings, ISBN 978-80-214-4533-8. Brno University of Technology, Faculty of Mechanical Engineering, Institute of Machine and Industrial Design. Mikulov, pp. 199-206.
- Nevrlý, J. (2012a) Recovery hydrostatic module for utility vehicles. Periodical report 2012 of the project LF12029. Institute of Machine and Industrial Design, Faculty of Mechanical Engineering, Brno University of Technology, Brno, (in Czech).
- Nevrlý, J. (2013a) Experimental Hydrostatic Stand to Energy Recovery Research for Vehicles. In: Proc. 54th International Conference of Machine Design Departments. ICMD 2013, Liberec, Czech Republic. pp. 137-142.
- Nevrlý, J. (2013b) Recovery hydrostatic module for utility vehicles (in Czech). Periodical report 2013 of the project LF12029. Institute of Machine and Industrial Design, Faculty of Mechanical Engineering, Brno University of Technology, Brno.
- Pourmovahed, A., Beachley, N. H., Fronczak, F. J. (1992) Modeling of Hydraulic Energy Regeneration System – Part I: Analytical Treatment. Journal of Dynamic Systems, Measurement, and Control. Vol. 114, pp. 155-159.
- Pourmovahed, A., Beachley, N. H., Fronczak, F. J. (1992a) Modeling of Hydraulic Energy Regeneration System – Part II: Experimental Program. Journal of Dynamic Systems, Measurement, and Control. Vol. 114, pp. 160-165.

CORRELATION BETWEEN ENHANCED MECHANICAL STRENGTH AND MICROSTRUCTURE RELIABILITY OF GEO-COMPOSITE

P. T. Nhan^{*}, S. M. Samal^{*}, I. Petrikova,^{*} B. Marvalová^{*}

Abstract: A correlation between increase in mechanical strength and the microstructure reliability of fabric reinforced geo-composite is established in elevated temperature range. The mechanical strength of the fabric reinforced geo-composite is investigated at elevated temperature in terms of physical, fire testing and thermal conductivity. The strength of carbon based geo-polymer increased towards higher temperature that strongly correlated with development of various microstructures. Fire testing was conducted on 15 mm thick panels with surface exposure of region 100 x 100 mm. The fires rating more than half an hour were achieved with resistance to shrinkage cracking exhibited as important parameter. The microstructure of geo-composite shows large pores towards 600 °C, that indicated lower in mechanical strength. On increasing the temperature, microstructure of carbon based geo-composite shows oxidized layer and very homogenous layer with less porosity. As a result the mechanical strength increases on increasing the temperature and developing oxidized layer. Fiber reinforced composites may be considered as an alternative to improve flexural strength and fracture toughness at elevated temperature. The carbon reinforced geo-composite proves as one of the suitable candidate for the high temperature applications such as thermal barrier and fire resistant panels.

Keywords: Mechanical strength, Geo-composite, Carbon fabric, Geo-polymer, High temperature.

1. Introduction

Materials designed for the high temperature application should withstand for prolonged period of time (Davidovits, 1991, 2008a, 2008b). Geo-polymers are the most promising green and eco-friendly alternatively to cementitious materials due to their proven durability, mechanical strength, and thermal properties with economically lower in cost (Barbosa and MacKenzie, 2003). However, despite these features the poor tensile and bending strengths has been exhibited by the materials due to their brittle nature that leads to the main obstacle at high temperature applications (Pachego-Torgal et al., 2008; Xu, Van, 2000). Fiber reinforced polymer can replace as the better alternative for improved mechanical strength and fire resistant properties with better thermal behavior (Giancaspro et al., 2009, 2010).

This study investigates the effect of various fibers reinforced in a geo-polymer matrix at elevated temperature. High Tenacity (HT) carbon, E-glass and basalt were chosen and several tests have been carried out in order to determine the adhesion of fiber to the matrix and their ability to improve the mechanical, fire testing and thermal properties of the geo-composite.

A correlation between fiber types and the microstructure evolution is investigated for the performance of geo-composite at elevated temperature.

2. Methods

Tab. 1 represents the fabrication of geo-composite. Compressive strength testing was conducted on samples (with dimension $3 \times 15 \times 220$ mm) using universal tester TIRA test 2810 (U.K.) and INSTRON model 4202. Firing test was conducted in accordance with the standard ASTM C1314-06. The test was performed in the electric furnace from the temperature varies in the range 200 to 1000 °C with a 25 kW/ m² heat source for a duration of 30 min. The samples were of dimension $3 \times 14 \times 90$ mm with the

^{*} Sneha Manjaree Samal, PhD., Ing. Phan Thanh Nhan, Assoc. Prof. Ing. Iva Petriková, PhD., Prof. Ing. Bohdana Marvalová, CSc.: Technical University of Liberec, Liberec 46001, CZ, phanthanhhan240670@yahoo.com.vn, Sneha.Manjaree.Samal@tul.cz, iva.petrikova@tul.cz, bohda.marvalova@tul.cz

geo-polymer matrix and with fabric reinforcement volume ratio around 40 %. The surface morphology of the samples was carried out by scanning electron microscope (SEM, ZEISS) with field emission source.

3. Results

Based on the following equation, using the value of the deflection, we can calculate the stress, strain and modulus of elasticity of a beam

$$\sigma = \frac{3.P.S}{2.b.t^2} \quad (1)$$

$$\varepsilon = \frac{6.D.t}{S^2} \quad (2)$$

$$E = \frac{\Delta\sigma}{\Delta\varepsilon} = \frac{S^3}{4.b.t^3} \cdot \frac{\Delta P}{\Delta D} \quad (3)$$

where: σ - maximum stress in the outer fiber,

S - support span,

b - width,

t - thickness of the sample,

D - deflection of the beam center,

ε - maximum strain in the outer fiber,

E - modulus of elasticity in bending,

$\Delta P/\Delta D$ - ratio of force difference and deflection difference at the beam center, measured at the linear segment of the graph.

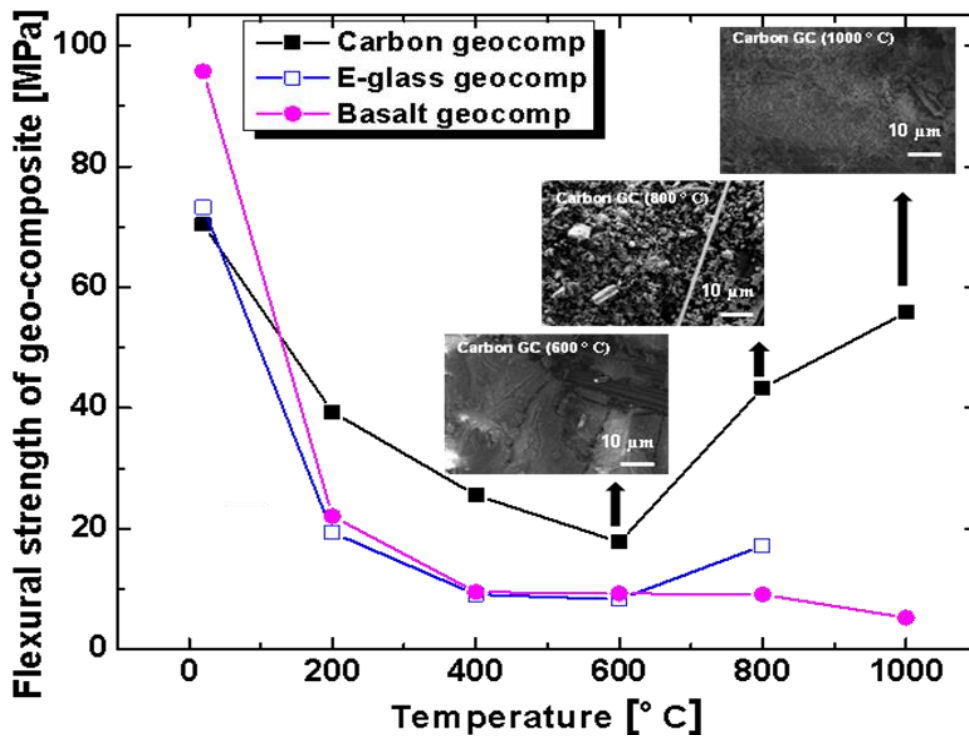


Fig. 1: Flexural strength of fabric reinforced geo-composite as the function of firing temperature. (Inset: microstructure of carbon fabric reinforced geo-composite with respect to temperature 600, 800, and 1000 °C.).

Tab. 1: Fabrication of fabric-in-plane reinforced geo-composite synthesis.

Sample	Matrix (polymer) content (Vol. %)	Fiber content (Vol. %)	Void content (Vol. %)	T (°C) (cured)
Carbon GC	40	39	21	70
E-glass GC	37	41	22	70
Basalt GC	45	40	15	70

Fig. 1 presents residual mechanical properties of various composites with exposure to different temperature ranges. Carbon reinforced geo-composite maintains the strength at 400 °C. The remaining strength increases with increase in the temperature. This may be attributed towards the good wetting properties exhibited between carbon fiber and polymer matrix. In case of E-glass and basalt fabric, a strong interaction exhibited and dissolution of the fiber inside the geocomposite observed at elevated temperature at 1000 °C.

4. Micro-Structural Evolution

Fig. 1 (inset) shows the microstructure of the geo-composite after fire test around 600, 800 and 1000 °C. After fire test, the porosity enlarges and wettability between the matrix and the fiber varies widely. The gap between the fiber and the matrix increases during the firing due to the shrinkage and dehydration of the moisture from the matrix. Carbon fiber exhibits good adhesion between the fiber and the matrix. Thermal stability in carbon reinforced geo-composite increases with the temperature with increasing the homogenities of the matrix within the fiber distribution. The carbon induced the mechanical strength of the composite with increasing temperature, although some mass loss was observed during the high temperature. After the firing, the binding phase appeared more homogeneous and dense due to the sintering at high temperatures. Oxidized layer creation at elevated temperature prevents further disintegration and degradation of the fabric in carbon based geo-composite.

5. Conclusion

Carbon-reinforced fiber was found to have good adhesion properties, being able to control micro-cracks propagation along the matrix and creating a favorable bridging effect. At elevated the temperature carbon reinforced geo-composite exhibited higher strength, better homogeneity, and most suitable geo-composite for high temperature application. The creation of oxidized layer improves the bridging and prevents the degradation of fabric. The mechanical strength increases on increasing towards elevated temperature around 1000 °C. Carbon-reinforced geo-composite may be suitable candidate for thermal insulation with wide potential application in industrial fields at elevated temperature.

Acknowledgement

This work was supported by ESF operational programme "Education for Competitiveness" in the Czech Republic in the framework of project "Support of engineering of excellent research and development teams at the Technical University of Liberec" No. CZ.1.07/2.3.00/30.0065.

References

- Davidovits, J. (1991) Geopolymers: Inorganic polymeric new materials, Journal of thermal analysis, 37, pp. 1633-1656.
- Davidovits, J. (2008a) Geopolymers: Chemistry and Applications, 2nd ed. Geopolymer Institute, Saint Quentin, p. 21.

- Davidovits, J. (2008b) *Geopolymers: Chemistry and Applications*, 2nd ed. Geopolymer Institute, Saint Quentin, pp. 498-500.
- Barbosa, V. F., MacKenzie, K. J. (2003) Thermal behaviour of inorganic geopolymers and composites derived from sodium polysialate. *Materials Research Bulletin*, 38, pp. 319-331.
- Pacheco-Torgal, F, Castro-Gomes, J, Jalali, S. (2008) Alkali-activated binders: A review, Part 1. *Construction and Building Materials*, 22, pp. 1305-1314.
- Xu H, Van Deventer, J. S. J. (2000) The geopolymerisation of alumino-silicate minerals. *International Journal of Mineral Processing*, 59, pp. 247-266.
- Giancaspro, J. W., Papakonstantinou, C. G., Balaguru, P. N. (2009) Mechanical behavior of fire-resistant biocomposite. *Composites Part B: Engineering*, 40, pp. 206-211.
- Giancaspro, J. W., Papakonstantinou, C. G., Balaguru, P. N. (2010) Flexural Response of Inorganic Hybrid Composites with E-Glass and Carbon Fibers. *Journal of Engineering Materials and Technology*, 132, pp. 1-8.

PASSIVE ELEMENTS FOR PRECISE DIRECTION AND MANAGEMENT OF AIR IN DATA RACKS

J. Novotný*, J. Matěcha*, P. Pohan**

Abstract: The goal of the presented work is to enable the increase of energy load in one data rack up to 15 kW. The work aims to find and subsequently optimize such passive elements for directing the air flow inside the data rack, which lead to the mass flow rate increase in the data rack while keeping the pressure loss. Target value of the mass flow rate in the data rack was $1 \text{ m}^3\text{s}^{-1}$ of air assuming a fifteen-degree temperature drop on IT devices fitted in the data rack. The work resulted in two optimized deflectors that serve for directing the air flow through the floor to the front of the IT device. Further increase of the mass flow rate in the data rack was solved with the help of additional side zones. All passive elements were first verified with the help of numerical simulations and subsequently also by experiments. The final optimized variant indicates, at the same pressure drop, an increase of the mass flow rate by 79%; the resultant mass flow rate of $0.97 \text{ m}^3\text{s}^{-1}$ enables to fit the data rack with device with a total capacity of 15 kW.

Keywords: Data rack, Side zones, CFD, Measurement, Simulation.

1. Introduction

Solving the problem of passive elements for directing the air flow inside the data rack is included in a three-year TAČR project called: Research and development of data rack, cooling and transport systems for data centers. Solving the problem is currently very topical with regard to growing demands on increasing the density of heat flow rate in the data rack (AlLee, 2007; Demetriou, 2011; Hassan 2012, 2013). Based on last two years of solving the project several variants of data racks with passive elements for directing the air flow (Novotny, 2012) have been proposed. For subsequent optimization of the passive elements, data racks with cooling air supply to data rack within a double floor were selected where a greatest impact of optimization on the resulting energy consumption was anticipated. At this variant, cold and hot aisle are separated (see Fig. 1). In this data rack configuration the air cooled by CRAC unit is supplied through the floor into space under the data rack and conducted by deflector into space in front of particular IT devices, which consume the cold air in order to cool the produced heat output. Within the original solution, the air was improperly directed to the data rack space by 1U and 3U deflectors that were completely unsuitable from the

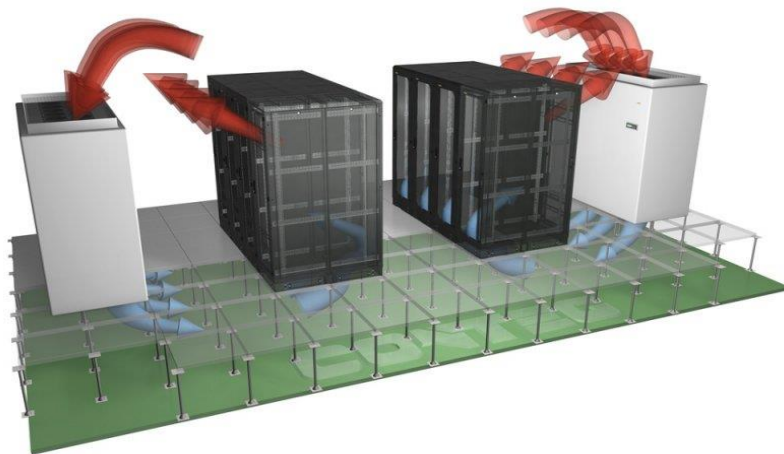


Fig. 1: Arrangement of data center with air supply to data rack within a double floor.

* Ing. Jan Novotný, PhD.: CTU in Prague, Technická 4, Prague 6, 160 00, Street 559/7; 140 00, Prague; jan.novotny@fs.cvut.cz,

** Ing Petr Pohan, Conteg s.r.o.

aerodynamic point of view. For this reason, it was necessary to optimize the deflectors in order to minimize the pressure loss at the data rack inlet. Since the resulting increase of the mass flow rate was insufficient, it was necessary to look for other ways to increase the total mass flow rate in the data rack. The new solution of distribution of cooled air inside the data rack through additional space proved to be such solution. This solution consists in using the side walls that are "hollow" in the original variant of the data rack and are not used for distribution of the cooled air inside the data rack. By using these side walls together with optimized deflectors the cooled air flow rate was increased by 100% according to first numerical simulations. Since the proposed solution satisfied the original aims, it was necessary to proceed to final development of particular components with respect to the production capacity of the manufacturer.

2. Deflectors by Optimized Side Zone

The original proposed solution of the side zones inside the data rack anticipated the use of the entire depth of the data rack cabinet. The resulting solution uses only the front part of the data rack. The reason for the change was the effort to propose uniform solution that can be installed into data rack of any depth, including the data racks already installed and in operation. The newly proposed solution of deflectors including the side cooling zone is shown in Fig. 2. The side zone is indicated by yellow and the front zone by blue color. Effects of supporting braces at the inlet were also included in the numerical model so that the results corresponded to the final solution as much as possible.

A new numerical model was created out of the newly proposed shape of the side cooling zones, which respect the production capacities and enable to install the side zones in all types of data rack.

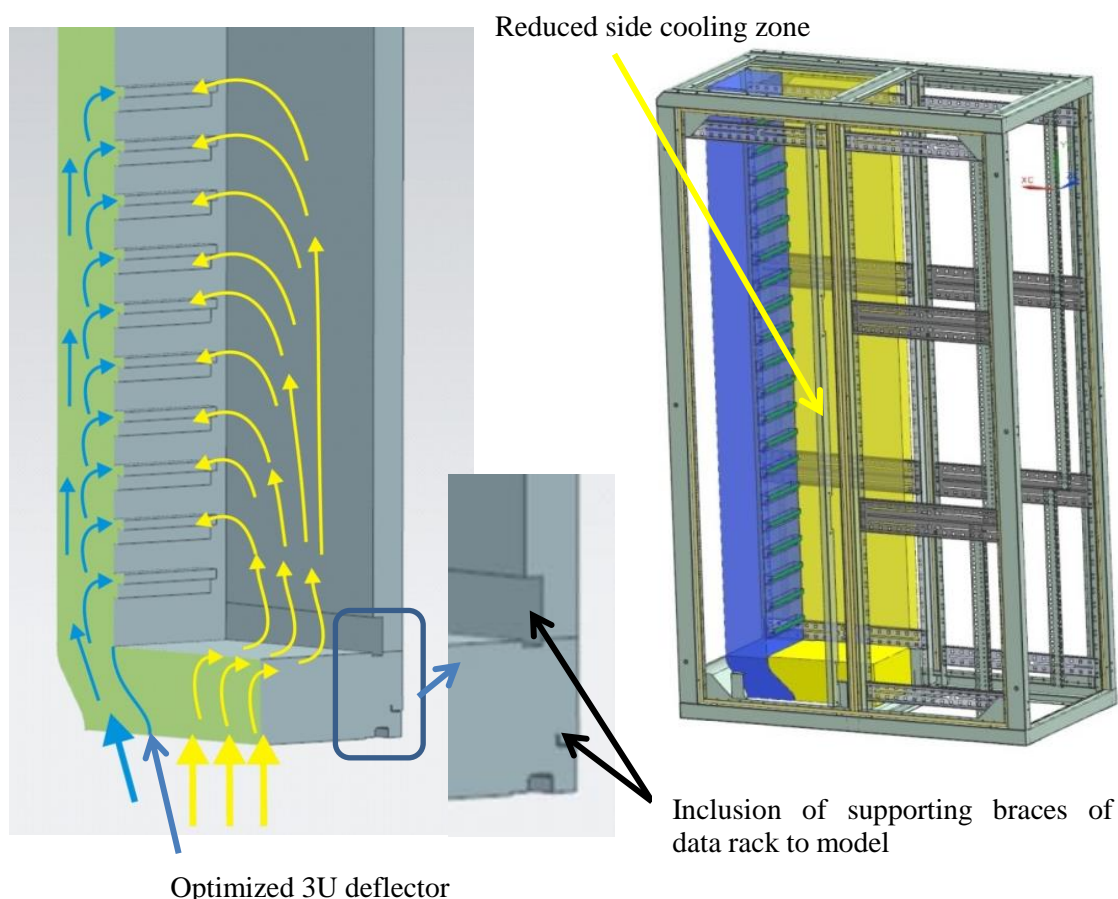


Fig. 2: Newly designed solution of side zones. Reduction of active depth, including supporting braces of data rack. On the left - volumetric model from which numerical model was subsequently developed. On the right - indication of location of side cooling zone and optimized deflector including splitter of air inside data rack.

Tab. 1: Comparison of original and optimized variants of the data rack. The resulting mass flow rate of particular variants and mutual comparison for final variants of deflectors and side zones.

Deflector	$\dot{m}[\text{kgs}^{-1}]$	Position of U in data rack without recirculation	\dot{m}/\dot{m}_i
1U original	0.512	15-42	100 %
1U optimized	0.664	9-42	129 %
1U Optimized with a side zone	0.79	3-42	154 %
3U original	0.54	15-42	100 %
3U optimized	0.72	9-42	133 %
1U Optimized with a side zone	0.97	3-42	179%

Unlike the original model, the model of the air inlet into the IT devices was modified, in addition to modification of the shape of the side zones. Setting of numerical solver was performed identically as in the previous solution. In the simulation, a "pressure" condition at the inlet to the IT devices - underpressure related to the atmosphere – 100 Pa was used. IT devices are once again not part of the numerical model and are replaced by the "pressure outlet" condition. The inlet to the space under the data rack is replaced by the boundary condition of pressure inlet type (atmospheric pressure at the inlet). The task is solved as stationary using a two-equation k-epsilon model (realizable). The boundary layer is simulated with a minimum wall thickness of 0.02 mm, the number of layers 10 with a growth factor 1.1. The calculation was terminated when the value of the mass flow rate in the data rack was constant. Heat flow rate in the data rack was not considered. When calculating the flow characteristics for other modifications, the same boundary conditions at the inlet and outlet surfaces were used. Consequently, the total mass flow rate in the data rack was determined from the calculated flow characteristics in front of the IT devices together with estimation of the percentage difference in pressure loss at the same mass flow rates in the data rack.

3. Measurement of the Mass Flow Rate in Data Rack

Verification of numerical analyzes has been performed in previous years only with the help of measurement of the velocity fields inside the data rack by the PIV method. The results of the PIV measurement do not allow for obtaining information on the mass flow rate of cooling air in the data rack. This was the reason why the resulting increase of the mass flow rate for new solution of air distribution in the data rack had to be verified by experiment. For the purpose of verification of numerical simulations an experimental setup allowing for measurement of the mass flow rate entering the space under the data rack was built. The mass flow rate was measured using the pressure drop across the nozzle against the atmosphere. The pressure at the narrowest point of the nozzle was measured with the help of a pressure transducer as a mean value of four samples of static pressure. View of the experiment is shown in Fig. 3. The 27U tested data rack was fitted with ten heat simulators. During the actual measurement of dependence of the mass flow rate on particular configurations 14 variants were measured. The mass flow rate was also measured depending on set performance of heat simulators.



Fig. 3: Measurement of the mass flow rate in data rack using the pressure drop measurement across the nozzle.

4. Conclusions

Based on the performed numerical experiments new optimized shapes of deflectors, which direct the air flow from the bottom part of the data rack in front of the IT device fitted in the data rack have been proposed. The original shaping of deflectors was proposed with regard to minimum production costs. Due to this requirement, however, the influence of the deflector shape on the total pressure loss was ignored. New optimized deflectors reduced the pressure loss and allowed for an increase of the mass flow rate in the data rack at same energy requirements for air distribution by 29 %, with data rack fitted with a 1U deflector. With a data rack fitted with 3U deflector, the mass flow rate increase is by 33%. The mass flow rate increase of 30 percent may be significant but it allows fitting the data rack with IT device of capacity up to 10 kW. One of the main requirements of customers ordering data centers is to increase the maximum value of IT device capacity, which a single data rack can be fitted with. However, the optimized deflectors do not satisfy this requirement. For this reason, using side zones for controlled air distribution was proposed. When using the side zones together with optimized deflectors the mass flow rate in the data rack increased by 54%, alternatively 79% for 3U deflector. The resulting variant of 3U optimized deflector together with the usage of side zones thus provides the mass flow rate of the cooling air about 1kgs-1. The mass flow rate is already sufficient so that the data rack could be fitted with IT device with a total capacity of 15 kW. Comparison of resulting variant with the original deflectors are shown in Table 1: Energy savings of the proposed solution consists in the fact that the already existing data center, which will be fitted with new deflectors and side cooling zones, can be fitted with a more powerful IT device and this will provide primary energy savings in production of the new data center. The proposed solution, however, in addition to reduced one-off production costs, also reduces the fixed costs of electrical energy consumption necessary for the air distribution. Since the pressure loss is proportional to second power of velocity and considering the fact that the mass flow rate increase for new solution is known to be about 80 %, it is possible to count the energy performance requirements of the new solution and its change compared to the original solution. It follows that if the original data rack was to be fitted with IT device with a total capacity of 15 kW the costs of air distribution in the IT device would increase up to three times compared to the original state where the data rack is fitted with IT device with a capacity of about 8 kW. With a 15% efficiency of fans fitted in IT devices the resulting consumption of these fans is 1800 W. Electric power consumption necessary for power supply of the fans for the newly proposed solution, where the data rack is fitted with IT device with a total capacity of 15 kW, is only 550 W. The energy savings of the newly proposed solution is, compared to the original solution, 1250 W for one fully fitted data rack. The energy savings when fitting the data center with forty data racks with a total installed capacity of 600 kW shall be 50 kW. The energy savings with fully loaded data center for one year period shall be 438 MW hours.

Acknowledgment

This project has been supported by the TACR TA01010184: Research and Development of IT Racks, Cooling and Transport Systems for Data Centers.

References

- AllLee, G., Milenkovic, M., Song, J. (2007) Data center energy efficiency, Research @ Intel Day June 20 [ftp://download.intel.com/pressroom/kits/research/poster Data Center Energy Efficiency.pdf](ftp://download.intel.com/pressroom/kits/research/poster/Data%20Center%20Energy%20Efficiency.pdf).
- Demetriou, D. W., Khalifa, H. E., Iyengar, M., Schmidt, R. (2011) Development and experimental validation of a thermo-hydraulic model for data centers. *HVAC&R Research*, 17(4):540-55.
- Hassan, N. M. S., Kha, M. M. K., Rasul, M. G. (2013) Temperature monitoring and CFD Analysis of Data Centre, *Procedia Engineering*, ELSEVIER 05/2013; 56:551-559. DOI:10.1016/j.proeng.2013.03.159.
- Hassan, N. M. S., Khan, M. M. K., Rasul, M.G., MTO Amanullah (2012) Thermal Performance Modelling of Data Centre – A case study, In: *Proc. 9th International Conference on Heat Transfer, Fluid Mechanics and Thermodynamics (HEFAT)*, Malta.
- Novotný, J., Matěcha, J., Nováková, L., Manoch, L., Pohan, P. (2013) Optimizing air supply into data rack through the floor. In: *Proc. 8th World Conference on Experimental Heat Transfer, Fluid Mechanics and Thermodynamics*, Lisboa, Portugal.
- Niles, S., Donovan, P. (2008) Virtualization: Optimized power and cooling to maximize benefits. *American Power Conversion White Paper 118*, Schneider Electric, France. [www.apcmedia.com/salestools/SNIS-7AULCP R3 EN.pdf](http://www.apcmedia.com/salestools/SNIS-7AULCP_R3_EN.pdf).

ANALYSIS OF SLIDE BEARING COMPUTATIONAL MODELS CONSIDERING ELASTIC DEFORMATIONS AND ROUGH SURFACES

P. Novotný*, O. Maršálek**, M. Zubík***, L. Drápal****

Abstract: *The paper presents computational simulation strategies of the slide bearing lubrication as a fluid-structural problem. Finite difference method is proposed for a solution of the fluid problem described by Reynolds differential equation and Finite Element Method is used for a solution of the structural problem. Bearing loads are calculated by the Virtual Engine model assembled and solved in Multibody System. The proposed approaches include temperature and pressure dependent viscosity and density of bearing lubricant. All the computational approaches are applied on a main bearing of modern in-line three-cylinder engine.*

Keywords: Elastohydrodynamics, Rough surface, Stiffness matrix, Coupled solver, Viscosity.

1. Introduction

In the course of time, the hydrodynamic (HD) theory has been developed by a relative large number of authors. Subsequently, the HD has been enhanced by elastic deformation influences (EHD) and this theory has been extended for many mechanical components, for instance gears etc.

HD theory presumes that a bearing shell and a pin are without any deformations. Therefore, a relative eccentricity can reach a maximal value of 1. Slide bearings of present combustion engines are highly loaded and the relative eccentricity sometimes exceeds value of 1. This is caused by elastic deformations, mainly of the bearing shell nevertheless, in general, also by the pin deformation. These conditions can be found in some modern turbocharged diesel engines.

One important effect takes place when local bearing clearance values drop to extremely low levels, surface asperities on a pin and a bearing shell start interaction with each other and thereby create boundary lubrication conditions. This effect should also be incorporated into the computational model.

2. Theoretical Background

A slide bearing solution can be presumed as the coupled structural-fluid problem and it covers a solution of three basic equations (1, 2, 4). These equations have to be solved simultaneously.

In general, if the modified Navier-Stokes equation and continuity equation are transformed for cylindrical forms of bearing oil gap together with restrictive conditions, e.g. Novotny (2009), the behaviour of oil pressure can be now described by Reynolds differential equation. This frequently used equation is derivated for a bearing oil film gap and can be written in the form:

$$\frac{\partial}{\partial x} \left(\frac{\rho h^3}{12\eta} \frac{\partial p}{\partial x} \right) + \frac{\partial}{\partial y} \left(\frac{\rho h^3}{12\eta} \frac{\partial p}{\partial z} \right) - \frac{\partial(u\rho h)}{\partial x} - \frac{\partial(\rho h)}{\partial t} = 0, \quad (1)$$

* Assoc. Prof. Ing. Pavel Novotný, Ph.D.: Institute of Automotive Engineering, Brno University of Technology, Technická 2896/2; 616 69, Brno; CZ, novotny.pa@fme.vutbr.cz

** Ing. Ondrej Maršálek: Institute of Automotive Engineering, Brno University of Technology, Technická 2896/2; 616 69, Brno; CZ, marsalek@fme.vutbr.cz

*** Ing. Martin Zubík: Institute of Automotive Engineering, Brno University of Technology, Technická 2896/2; 616 69, Brno; CZ, zubik@iae.fme.vutbr.cz

**** Ing. Lubomír Drápal: Institute of Automotive Engineering, Brno University of Technology, Technická 2896/2; 616 69, Brno; CZ, drapal@fme.vutbr.cz

where p is a pressure, x and y are coordinates, t is time, h is oil film gap, η is dynamic viscosity of oil, ρ is density of oil and u is an effective velocity.

Generally, oil properties and oil viscosity respectively are dependent on the pressure, temperature or shear stress. High viscosity differences can be achieved especially when machinery parts include point or line contact (roller bearings or a cam/tappet contact). Roelands (1966) formula is one of the simplest descriptions of oil viscosity vs. pressure.

The influence of oil temperature on its viscosity is also significant. Therefore, it is necessary to incorporate the temperature dependence in a form of a computational model. In practice, the oil temperature is not constant. However, variable oil temperatures considerably increase a model complexity. Therefore, oil temperature is rated as constant for the model for every temperature cycle.

The oil film thickness including elastic deformations is calculated by introduction of stiffness matrices of a shell or a pin respectively as:

$$\mathbf{h}(x, z) = \mathbf{h}_{rigid} + \mathbf{K}_{shell}^{-1}(\mathbf{p}_{hydro} + \mathbf{p}_{rough}) + \mathbf{K}_{pin}^{-1}(\mathbf{p}_{hydro} + \mathbf{p}_{rough}), \quad (2)$$

where \mathbf{K}_{shell} and \mathbf{K}_{pin} are stiffness matrices of the shell and the pin respectively, \mathbf{p}_{hydro} is a matrix of hydrodynamics pressures and \mathbf{p}_{rough} is a matrix of pressures due to a contact of surface roughness. FE model of the pin is relative simply one (cylinder under boundary conditions) and it is generated by a user written macro. FE model used for a generation of the shell stiffness matrix is based on 3D CAD model of an engine block. Ideally, the oil film gap h_{rigid} , considering a rigid pin and shell, is defined as:

$$h_{rigid} = R - r + e \cos(\varphi - \delta) + B \sin(\varphi - \delta) \tan \alpha_x + B \cos(\varphi - \delta) \tan \alpha_y, \quad (3)$$

where B is bearing width, R is shell radius, r is pin radius, e is eccentricity, φ is circumferential angle, δ is angle of minimal oil film thickness and α_x and α_y are tilting angles.

The third fundamental equation is force equilibrium and it can be presented as:

$$\sum_{i=1}^n F_i = 0, \quad (4)$$

External load, hydrodynamic and rough contact forces are only forces considered for the force equilibrium of slide bearing solution. External loads include also inertial and other forces and they are completely obtained by a solution of Virtual Engine in Multibody software, presented by Novotny (2009).

3. Numerical Methods

To simplify the writing and to improve the numerical solution of equation (1), the following variables can be used

$$\begin{aligned} H &= \frac{h}{R-r} = \frac{h}{c}, & \varphi &= \frac{x}{R}, & Z &= \frac{z}{B}, & P &= \frac{pc^2}{R^2\eta_0}, & \xi &= \frac{\bar{\rho}H^3}{12\bar{\eta}}. \\ k &= \frac{B}{R} = \frac{2B}{D}, & \bar{\eta} &= \frac{\eta}{\eta_0}, & \bar{\rho} &= \frac{\rho}{\rho_0}, & \omega_e &= \omega - 2\dot{\delta}. \end{aligned} \quad (5)$$

The symbol H denotes a dimensionless thickness of the oil gap, D is bearing diameter, η_0 is dynamic viscosity at atmospheric pressure and room temperature and ρ_0 is the density at atmospheric pressure. By using equations (5), equation (1) can be written in the form:

$$\frac{\partial}{\partial \varphi} \left(\xi \frac{\partial P}{\partial \varphi} \right) + \frac{1}{k^2} \frac{\partial}{\partial Z} \left(\xi \frac{\partial P}{\partial Z} \right) - \omega_e \frac{\partial(\bar{\rho}H)}{\partial \varphi} - \frac{\partial(\bar{\rho}H)}{\partial t} = 0. \quad (6)$$

The transient term (time derivative of $\bar{\rho}H$) of equation (6) is now neglected if only a comparison of different approaches is required. Otherwise, this term is also important because slide bearing operates under highly time variable conditions.

For the discretization of equation (6), the finite difference method (FDM) is used and for numerical solution, Gauss-Seidel method supplemented by strategies (e.g. SOR – Successive over relaxation

method) to accelerate the calculation is used. Equation (6) is discretized and solved for each point of the grid according to the relationship:

$$\bar{P}_{i,j} = \bar{P}_{i,j}(1 - \omega_{opi}) + \omega_{opi} \delta_{i,j} \quad \text{and} \quad \bar{P}_{i,j} = 0 \quad \text{if} \quad \bar{P}_{i,j} < 0. \quad (7, 8)$$

The $\delta_{i,j}$ is defined as

$$\delta_{i,j} = \frac{a_1(\bar{\xi}_{i+1/2,j} P_{i+1,j} + \bar{\xi}_{i-1/2,j} P_{i-1,j}) + a_2(\bar{\xi}_{i,j+1/2} P_{i,j+1/2} + \bar{\xi}_{i,j-1/2} P_{i,j-1/2}) - a_3(\bar{\rho} H_{i+1,j} - \bar{\rho} H_{i-1,j})}{a_1(\bar{\xi}_{i+1/2,j} + \bar{\xi}_{i-1/2,j}) + a_2(\bar{\xi}_{i,j+1/2} + \bar{\xi}_{i,j-1/2})}, \quad (9)$$

where

$$a_1 = \frac{1}{h_\phi}, \quad a_2 = \frac{1}{(kh_z)^2}, \quad a_3 = \frac{1}{2h_\phi}. \quad (10)$$

Coefficients h_ϕ and h_z are the integration steps, the way line indicates the value of the previous iteration, the overline denotes the value of the current iteration. ω_{opi} is over-relaxation parameter.

The nature of the coupled fluid-structural problem is non-linear, therefore the Newton-Raphson algorithm (NRA) is used for a solution of two dimensional problem.

The pure boundary lubrication according to Greenwood and Tripp (1970) is used when oil supply is insufficient. The nominal pressure can be calculated as

$$p_{rough} = K_{GT} E' F_{h/\sigma}, \quad (11)$$

where

$$K_{GT} = \left(8\pi \frac{\sqrt{2}}{15} \right) (N\beta\sigma)^2 \left(\sqrt{\frac{\sigma}{\beta}} \right) \quad \text{and} \quad E' = \frac{E_1 E_2}{E_2(1-\nu_1^2) + E_1(1-\nu_2^2)}. \quad (12)$$

E_1 and E_2 denotes Young's modulus of the pin and shell respectively, ν_1 and ν_2 are Poisson numbers, σ is composite summit height standard deviation, β is radius at asperity summit and N is number of asperities per unit area.

4. Results

The relative eccentricity, total friction moment, maximal hydrodynamic pressure, minimal oil film thickness and oil flow are the results selected to present different computational approaches.

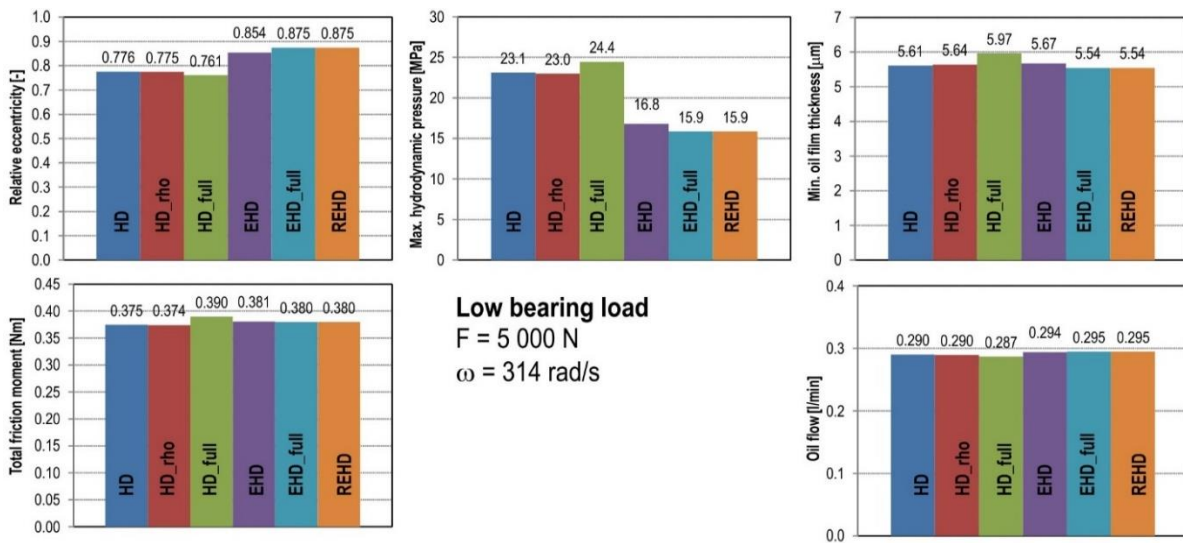


Fig. 1: Result comparisons for low bearing load.

For comparison, these computational approaches are considered: the hydrodynamic solution (HD); the hydrodynamic solution under variable oil density (HD_rho); the hydrodynamic solution under variable oil density and dynamic viscosity (HD_full); the elastohydrodynamic solution (variable viscosity and

density) with rigid pin approach (EHD); the elastohydrodynamic solution considering also elastic pin (EHD_full); the elastohydrodynamics and contacts of rough surfaces solution (REHD). The REHD approach considers variable density, viscosity and elastic deformations of the pin and the shell, this approach is taken as a base for all comparisons.

The results are presented for the main bearing of 1.2 litre SI engine. The engine speed of 3000 rpm is always applied. Different loads are used to demonstrate the results: 5 kN as an example of relative low bearing loads (Fig. 1); and 15 kN as a peak bearing load for the target engine (Fig. 2).

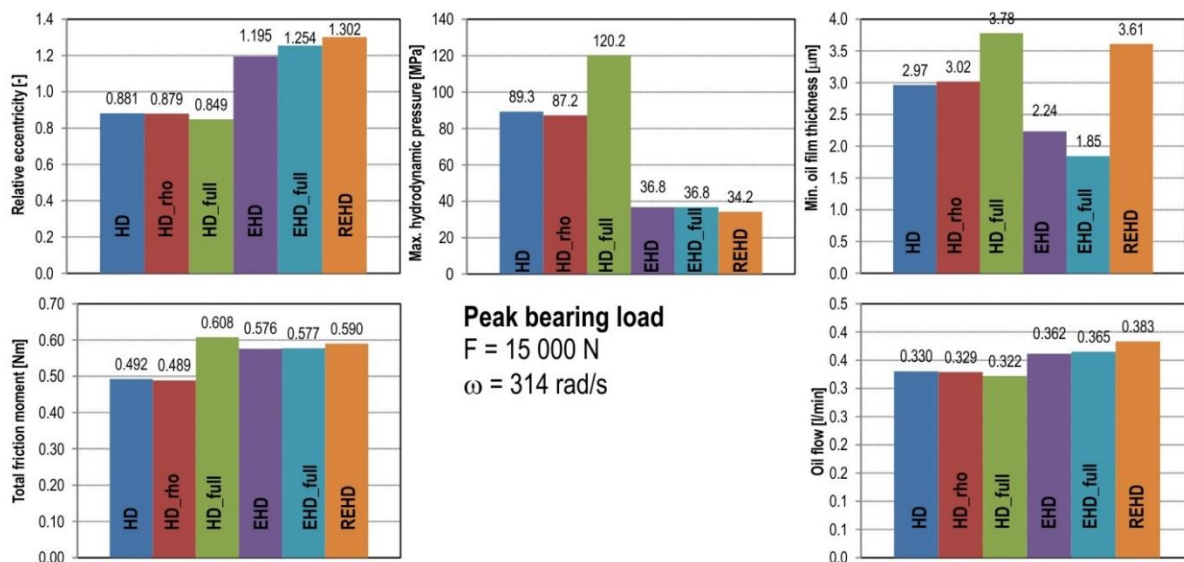


Fig. 2: Result comparisons for peak bearing load.

5. Conclusions

The comparison of the different computational strategies shows that for low bearing load the more complex models based on EHD with rough contacts do not introduce any decisive differences. On the other hand if the load increases, the importance of elastic deformations and contacts of roughness peaks (mixed lubrication conditions) requires more sophisticated computational models.

Of course, there is much more parameters describing the solved system (shear stress influences, design of the engine block, surface treatment etc.) that influences the complexity of appropriate computational models but future approaches for a solution of the slide bearing are evident: full thermoelastohydrodynamic solution incorporating contacts of surface roughness of anisotropic properties.

Discretisation using FDM, FEM, or FVM (Finite Volume Method) solved iteratively by Gauss-Seidel method with SOR are the ways how we have to solve the coupled fluid-structural problem.

Acknowledgement

This work is an output of research and scientific activities of NETME Centre, regional R&D centre built with the financial support from the Operational Programme Research and Development for Innovations within the project NETME Centre (New Technologies for Mechanical Engineering), Reg. No. CZ.1.05/2.1.00/01.0002 and, in the follow-up sustainability stage, supported through NETME CENTRE PLUS (LO1202) by financial means from the Ministry of Education, Youth and Sports under the „National Sustainability Programme I“.

References

- Greenwood, J. A., Tripp, J. H. (1970) The Contact of two Nominally Flat Rough Surfaces, In: Proc. Instn. Mech. Engrs., pp. 625-633. ISSN 0954-4100.
- Novotný, P. (2009) Virtual Engine – A Tool for Powertrain Development. Inaugural Dissertation, Brno: Brno University of Technology.
- Roelands, C. J. A. (1966) Correlational Aspects of the Viscosity-Temperature-Pressure Relationship of Lubricating Oils. PhD. Thesis, Delf: Technical University Delft, The Netherlands.

REVITALISATION OF INDUSTRIAL ROBOT CONTROL SYSTEMS

K. Nowicki^{*}, P. Kolber^{**}, D. Perczyński^{***}, S. Wawrzyniak^{****}

Abstract: *The paper demonstrates the way of adapting control system of welding industrial robot produced by ASEA company. The aim was to adapt it to parameters of welding process using a new generation of welding machines. Control system based on card with FPGA processor made by National Instruments company was built instead of old system based on integrated circuit with a low integration scale and using signals from rate generators and transformers of angular position. Moreover, encoders were installed as positional and rotational speed sensors. For controlled system identification, there was used a model created in SimMechanics tool which is included in MATLAB environment. Data concerning location of centre of gravity, masses and moments of inertia for blocks of SimMechanics tool were obtained from independently made three-dimensional model of manipulation working parts of robot in Catia system. There were also used data on drivers features based on information from their rating plates.*

Keywords: Control system, Controlled system, MATLAB, SimMechanics, Direct-current motor.

1. Introduction

The research work is a result of cooperation with Hydrapres S.A. company that asked five universities in Northern Poland to modernise control systems of welding robots. One welding robot IRB-6, produced by ASEA, was given to each university.

The reason of research, presented by representatives of the ordering company, was a necessity to adapt control system of robots to the parameters of welding process using a new generation of welding machines (Morecki et al., 2002). The representatives stated that the robot producer was not interested in adapting robots to factory requirements. According to the robot producer, the only possibility was to purchase new robots. However, whole robots replacement was economically unjustified.

An expected result of the research was a control system with functionality similar to factory system which is characterised by higher speed of trajectory with maintaining or increasing the positioning accuracy of robot end-of-arm. Another requirement was a necessity of keeping the original robot motors.

2. Task of Revitalisation

The task of revitalisation is the control system of welding industrial robot IRB produced by ASEA presented in Fig. 1. The primary control system is based on a low integration scale circuits. The functions of the control system can be divided into three groups:

- **Low-level functions:** independently control of five direct-current motors carried by PID controllers based on feedback signals of resolver and rate generators placed on motor axes.
- **High-level functions:** implementation of any trajectory with set speed by using linear interpolation in three-dimensional space while controlling the welding process.

^{*} Assist. Prof. Krzysztof Nowicki, PhD.: Institute of Mechanics and Machinery Design, University of Technology and Life Sciences, Kaliskiego 7/2.3; 85 789, Bydgoszcz; Poland, krzysztof.nowicki@utp.edu.pl

^{**} Assist. Prof. Piotr Kolber, PhD.: Institute of Mechanics and Machinery Design, University of Technology and Life Sciences, Kaliskiego 7/2.3; 85 789, Bydgoszcz; Poland, piotr.kolber@utp.edu.pl

^{***} Assist. Prof. Daniel Perczyński, PhD.: Institute of Mechanics and Machinery Design, University of Technology and Life Sciences, Kaliskiego 7/2.3; 85 789, Bydgoszcz; Poland, daniel.perczyński@utp.edu.pl

^{****} Assist. Prof. Sylwester Wawrzyniak, PhD.: Institute of Mechanics and Machinery Design, University of Technology and Life Sciences, Kaliskiego 7/2.3; 85 789, Bydgoszcz; Poland, sylwester.wawrzyniak@utp.edu.pl

- **Control functions:** monitoring the state of robot during operation, programming work movements, manual control.

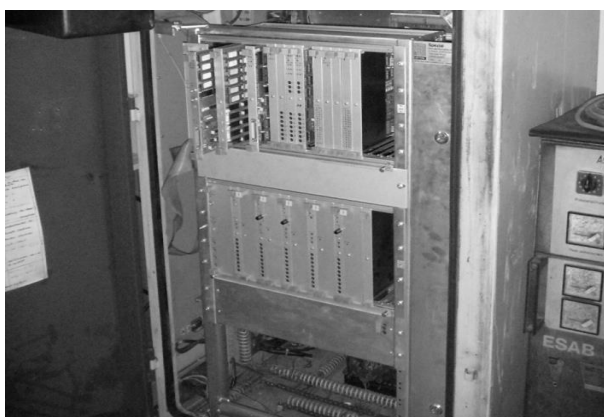


Fig. 1: Primary robot control system – inside view.

3. Controlled System

Manipulation working parts of robot IRB-6 consist of base, body, arm, forearm and wrist ended by flange end-of-arm which is used for adjusting welding devices. Such design of segments provides to five degrees of freedom: rotation around the base, arm rotation, forearm rotation, wrist inclination, and flange end-of-arm rotation. Each motion of manipulation working parts are performed by actuators, which include direct-current motors as well as driven gears and tie bars. Each motor also includes a transformer of angular position and rate generator.

4. Specification of the Design of the Revitalised Control System

The basis for the development of a new control system was a decision of ordering company representatives regarding lack of economic prerequisites for purchase and adapting factory system. For technical reasons, modernisation of current control system was rejected, mainly because of the lack of suitable systems as well as no data about standards using in its build.

It was decided that FGPA processor (Field Programmable Gate Array) would be used for building a control system (Kozłowski at al., 2003). The processor is a type of programmable logic circuit. It has the same functionality as integrated circuit which is designed to implement a very specific task (such as installed into factory control systems of robots). However, it can be repeatedly reprogrammed after it has already been produced, purchased and installed in a target device.

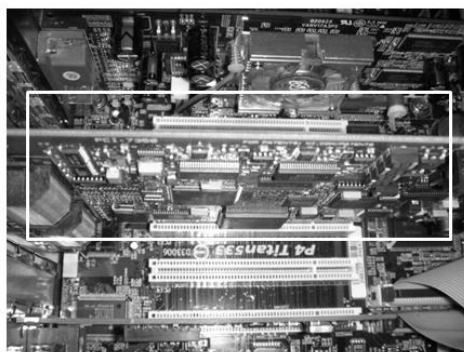


Fig. 2: The new control system. Card with FPGA processor (marked by white frame) placed in PC housing.

Due to financing from the Research and Development Funds in Kuyavian-Pomeranian Province, the card with FPGA processor produced by National Instruments company was used. This card can control eight electric drives in development version (powered and programmed by typical PC computer) within software used for its programming. A view of the new control system placed in PC housing is presented in Fig. 2.

Power-supply systems of direct-current motors were replaced. Power supplies that use power transistor were applied instead of power supplies based on transformers, which is presented in Fig. 3. The new power-supply system is several times smaller and the housing shown in Fig. 3 contains power supplies for four drives. Moreover, the new power-supply system provides a change of feed current parameters with higher accuracy (by one order of magnitude) and higher frequency to 200 Hz.

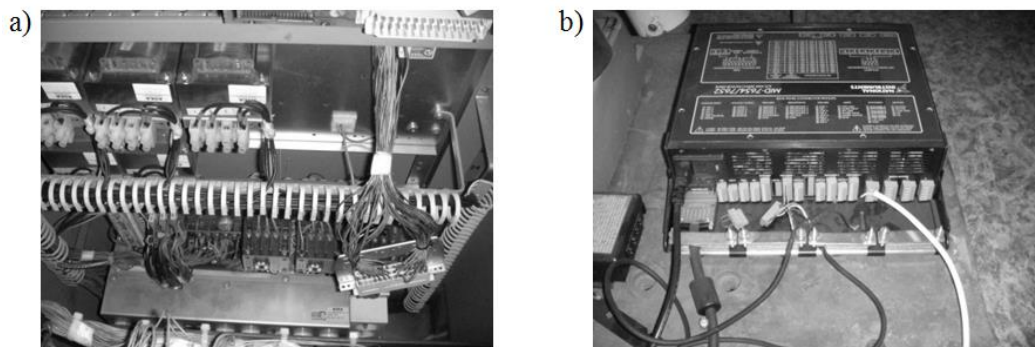


Fig. 3: Drive power-supply system of robot IRB-6: a) original; b) new.

The last elements of the control system were positional and rotational speed sensors placed on motor axes of robot. Instead of resolvers and rate generators, there were installed encoders with a resolution of 3600 positions per rotation. Installation of sensors required a development of interface system with dimensions selected in the way that new sensors fit the actuators housings, which is presented in Fig. 4.



Fig. 4: Encoder with interface system placed on motor axis.

5. Identification of Controlled System

The main research issue was a necessity to perform an identification of controlled system, indispensable for correct programming of control system. A significant difficulty was an inability to obtain proper dynamic characteristics based on system dismantling and independent analysis its components. There was also no ability to analyse the controlled system because of no possibility of launching it.

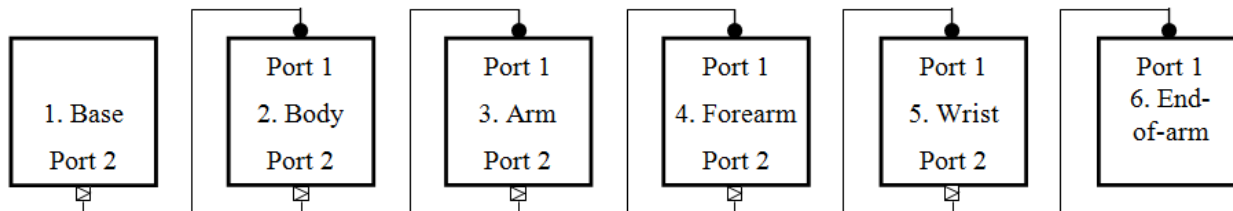


Fig. 5: Simulation model of robot manipulating working parts in SimMechanics tool.

SimMechanics tool, which is included in MATLAB environment, was used for controlled system identification. In a recognition tool, SimMechanics is a set of blocks libraries and special features of the simulations which symbolises physical bodies, constraints, actuators, powers and sensors that model their respective parts of devices. Created simulation model of robot is presented in Fig. 5.

Each block contains data about actual robot part. Basic blocks are built of elementary blocks. Each of them defines mechanical features of selected structural part of manipulator. Fig. 6 presents a sample block schemes of flange end-of-arm.

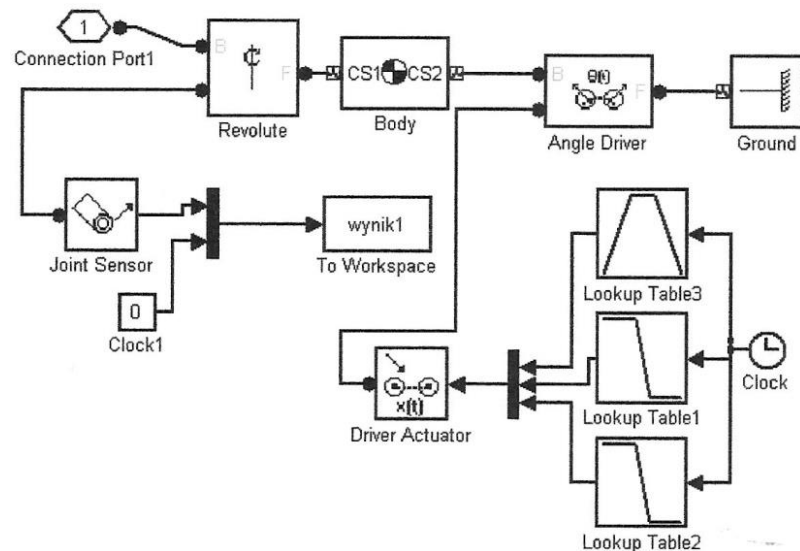


Fig. 6: Block scheme of end-of-arm in SimMechanics tool.

In Fig. 6, the blocks are connected by lines, each of which symbolises a different structural part of manipulator. The most important blocks are those with CS1 and CS2 symbols which determine mass as well as moment of inertia for robot working parts. Blocks of B and F symbols determine characteristic features of connections between parts and blocks labelled as 'Driver' define characteristic features of actuators (including clutches and gears). The other blocks are used for creating connections between working parts as well as entering parameters and observing results of simulation.

The data regarding centre of gravity location, masses and moments of inertia for blocks of SimMechanics tool were obtained from independently made three-dimensional model of manipulation working parts of robot in CATIA system. Basic data about features of actuators were obtained from rating plates placed on their housings.

This approximate model of robot manipulating working parts was put between the new control system and manipulating parts in the feedback loop. The purpose of this procedure was to obtain data from encoders. By iteratively performing series of basic motions of robot parts, while knowing their target position, feedback signal was observed. By entering feedback signal as a control signal into simulation model, model response was observed in the form of coordinates of robot end-of-arm location (or other characteristic point). By comparing the actual location of robot end-of-arm with coordinates from simulation, simulation variables were corrected and the results were corresponding to their values. Multiple repeating of this process for different working parts of robot as well as expected coordinates of characteristic robot parts obtained identification of controlled system.

6. Conclusions

Suggested way of controlled system identification, which involves creating an adapting simulation model, allows specifying a characteristic of dynamic objects for which the well know methods have failed. This is particularly important in the case of robots (systems) revitalisation, because the design documentation is often not known. Obtained simulation model allows design a new control system and its verification by "black box" method.

The cost of suggested control system is one third the cost of repair/replacement the primary control system. Additional sensors replacement allows increasing the accuracy of control system positioning. Application of FPGA processor allows increasing the speed of robot motions without sacrificing the accuracy of positioning while maintaining original actuators.

References

- Kozłowski, K., Dudkiewicz, P., Wróblewski, W. (2003) Robots modeling and control. Warszawa, PWN (in Polish).
 Morecki, A., Knapczyk, J., Kędzior, K. (2002) Mechanisms and manipulators theory. Warszawa, Wydawnictwa Naukowo – Techniczne (in Polish).

SIMULATION TESTS OF IRB6 ROBOT

K. Nowicki^{*}, D. Perczyński^{}, P. Kolber^{***}, K. Peszyński^{****}**

Abstract: Robots operated in industrial plants are characterised by out-of-date control systems. In the purpose of designing suitable control system, there must be carried out the simulation tests that provide to determine its kinematic features. The simulation tests presented in the paper were carried out in MATLAB environment. Part of this environment includes SimMechanics tool which is an environment for design and simulation of kinematic rigid members of machines and devices. Data concerning location of centre of gravity, masses and moments of inertia for blocks of SimMechanics tool were obtained in CATIA system.

Keywords: Simulation tests, MATLAB, SimMechanics, Industrial robot.

1. Introduction

The large part of industrial plants is faced with a problem of operated equipment modernisation. This issue also applies to robots. Operated robots have in principle sufficiently good power transmission systems, however, the control systems are out-of-date. Control Group of Faculty Mechanical Engineering is specialised in modernisation of analysing robots.

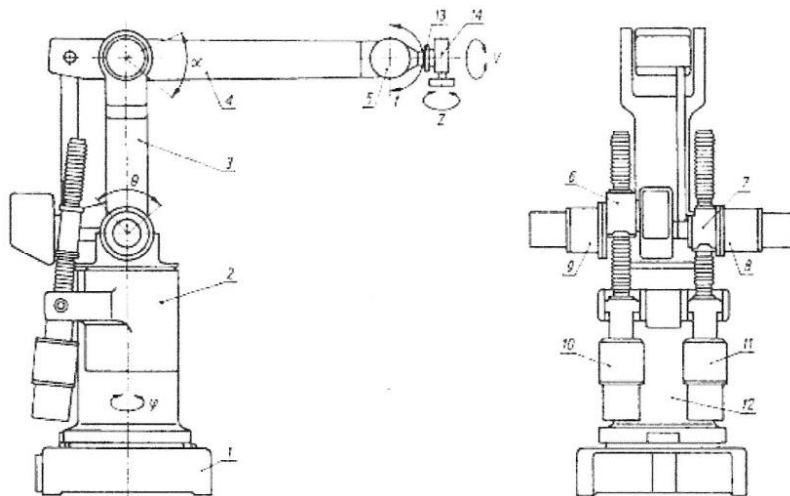


Fig. 1: Components of IRB6 robot: 1- base, 2 - body, 3 - arm, 4 - forearm, 5 – wrist, 6, 7 – working helical gear, 8, 9, 10, 11 – actuators, 12 – actuator for body rotation, 13 – flange, 14 end-of-arm.

The task of the research is IRB6 robot. Manipulation working parts of robot are presented in Fig. 1. They consist of base, body, arm, forearm and wrist ended by flange end-of-arm which is used for adjusting welding devices. Such design of segments provides to five degrees of freedom: rotation around the base, arm rotation, forearm rotation, wrist inclination, and flange end-of-arm rotation. Each motion of

^{*} Assist. Prof. Krzysztof Nowicki, PhD.: Institute of Mechanics and Machinery Design, University of Technology and Life Sciences, Kaliskiego 7/2.3; 85 789, Bydgoszcz; Poland, krzysztof.nowicki@utp.edu.pl

^{**} Assist. Prof. Daniel Perczyński, PhD Institute of Transport and Machine Operation, University of Technology and Life Sciences, Kaliskiego 7/2.3; 85 789, Bydgoszcz; Poland, daniel.perczynski@utp.edu.pl

^{***} Assist. Prof. Piotr Kolber, PhD, Institute of Transport and Machine Operation, University of Technology and Life Sciences, Kaliskiego 7/2.3; 85 789, Bydgoszcz; Poland, piotrl.kolber@utp.edu.pl

^{****} Assoc. Prof. Kazimierz Peszyński, PhD, Institute of Transport and Machine Operation, University of Technology and Life Sciences, Kaliskiego 7/2.3; 85 789, Bydgoszcz; Poland, kazimierz.peszyński@utp.edu.pl

manipulation working parts are performed by actuators which include direct-current motors as well as driven gears and tie bars. Each motor also includes a transformer of angular position and rate generator.

The paper demonstrates the way of determining kinematic parameters of IRB6 robot by computer simulation method in SimMechanics tool.

2. Modelling the Geometry Components of Manipulator

Modelling the three-dimensional geometry robot (Jeziarski, 2006; Morecki et al., 2002), showed in Fig. 2, was carried out by using V5R16 Catia system. It allowed obtaining data about centre of gravity locations, masses and moments of inertia for blocks of SimMechanics tool.

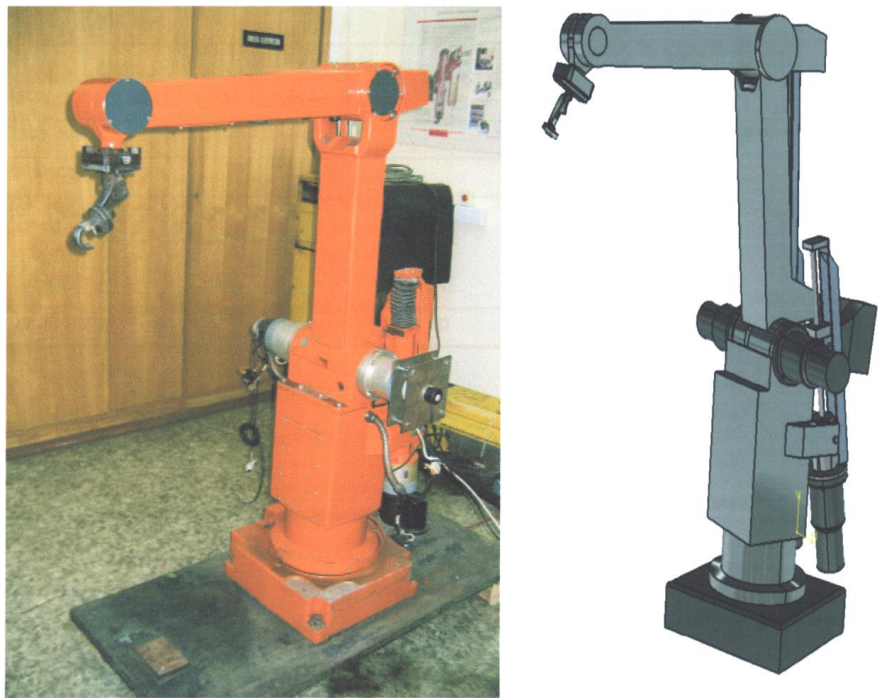


Fig. 2: Industrial robot and its three-dimensional model.

3. Simulation Tests

Simulation tests were carried out in MATLAB environment (Kozłowski et al., 2003). It combines calculations, visualisation and programming in an friendly environment to use.

SimMechanics tool is an addition to MATLAB environment. It is an environment for design and simulation of kinematic rigid elements of machines and devices using Newtonian analysis of force and moments, both directly and inversely. Simulations of mechanical systems can be modelled and carried out in SimMechanics. Blocks of this tool represent physical objects and their relations.

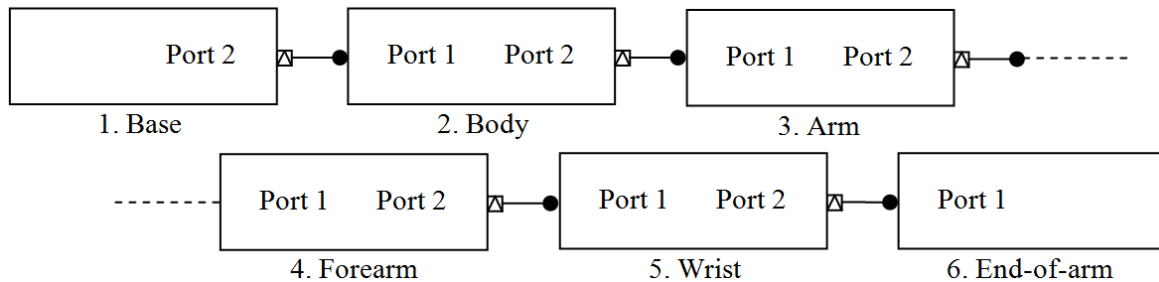


Fig. 3: Simulation model of IRB6 robot.

A model has two meaning in SimMechanics tool. One of them refers to physical object that contains at least one rigid component. The second one applies to a different and separate block. Each block represents one physical device. It means that a model can consist of one or many devices. A model

created in SimMechanics tool represents physical structure of a device, its geometric and kinematic relations which later is transformed into structural representation to inside and equivalent mathematic model.

The various stages of modelling (Tarnowski & Bartkiewicz, 2003) in SimMechanics tool:

- selection of basis and connection of blocks,
- distribution of blocks,
- configuration of solids in the individual blocks,
- selection, connection and configuration of sensors and actuators,
- model connection (as a subsystem) into major model.

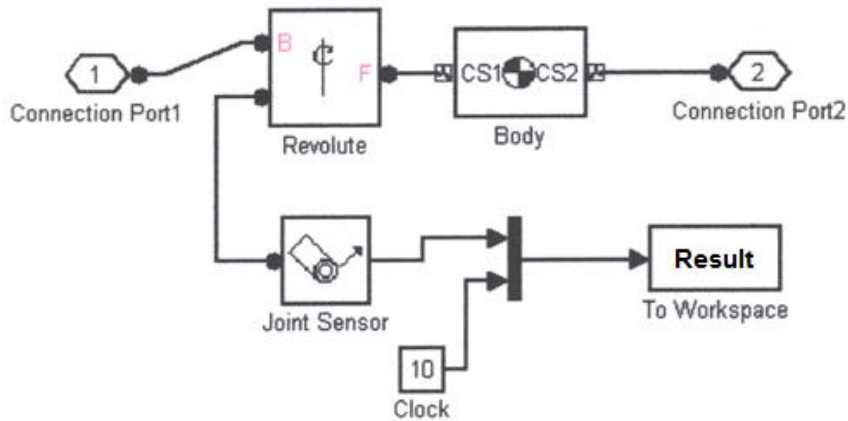


Fig. 4: Flow chart of IRB6 robot body created in SimMechanics tool.

Each block includes data regarding specific component. All of the blocks are connected by ports. The basis is connected only to the body, while the body has two connections, both basis and arm. The next parts are connected in the same way until the end-of-arm which is not connected to any other part. The following figure presents an example of body flow chart.

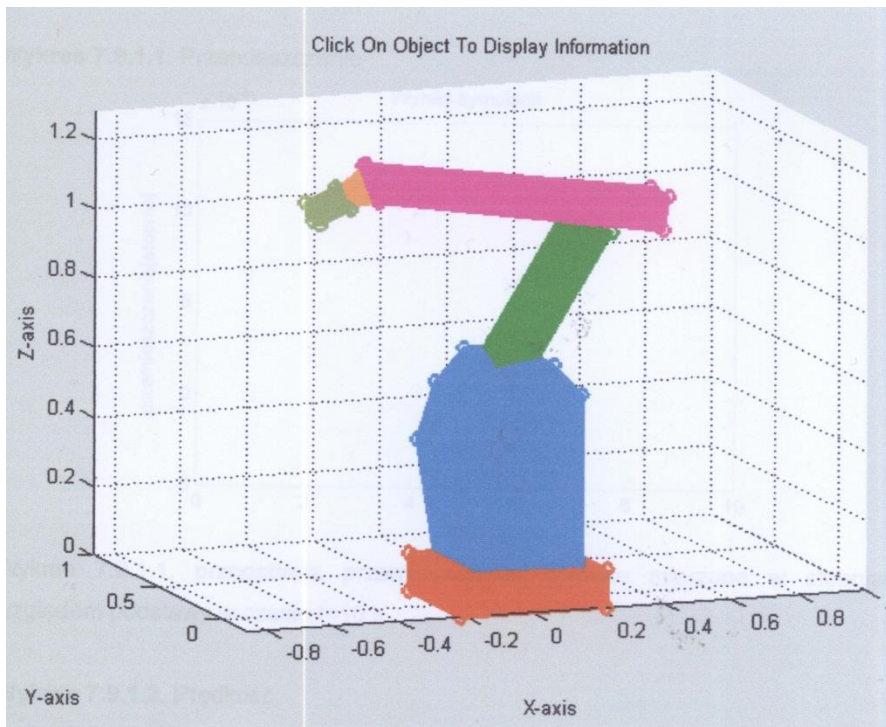


Fig. 5: Three-dimensional model of IRB6 robot in SimMechanics.

After entering all data in SimMechanics tool, the flow chart was obtained. The model, presented in Fig. 5, is in the initial position, i.e. in the way it was entered in the simulation. In the purpose of simplification of the model, motors that were installed on the body of actual object, were entered into the body block. Therefore, apparent lack of motors during the visualisation is not a mistake.

4. Selected Results of Simulation Tests

After the simulation, the calculation results were obtained as graphs of displacement and speed of analysed robot parts. Selected results of tests are presented in Figs. 6 and 7.

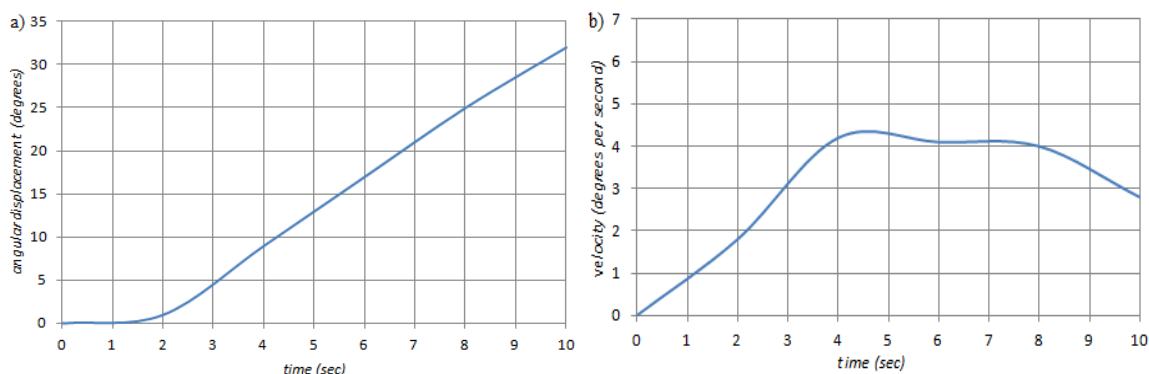


Fig. 6: Simulation of robot arm: a) angular displacement, b) angular velocity.

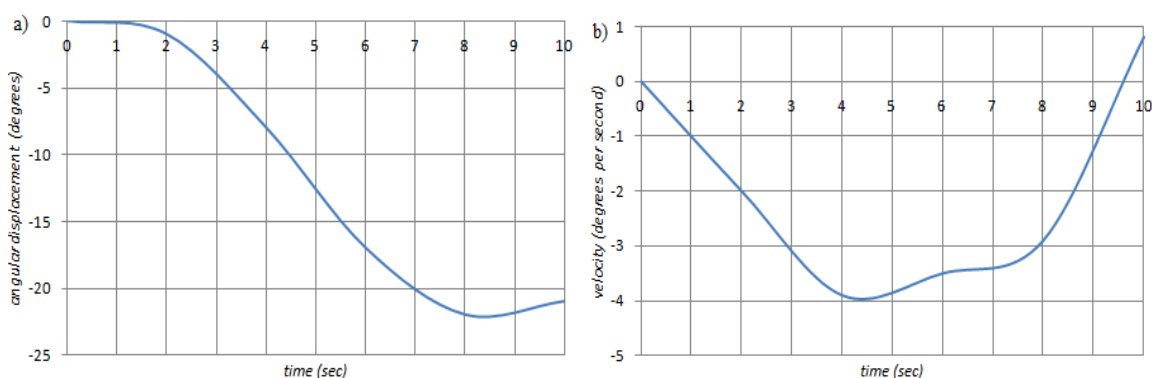


Fig. 7: Simulation of robot forearm: a) angular displacement; b) angular velocity.

5. Conclusions

MATLAB environment as well as its tools, such as SimMechanics, Simulink, and SimDriveline, were used for the simulation calculations of kinematic properties. Those tools allowed building model of robot kinematic chain. On that basis, simulation model of IRB6 robot was obtained and provided to determine its kinematic features.

In the purpose of correct robot modelling, it was necessary to determine the parameters values such as mass, moments of inertia, centre of gravity, and overall dimensions. The aim was achieved by accepting the modelled values in CATIA V5R16.

Simulation calculations, presented in the paper, were used for further studies, which aim was to determine any trajectory of end-of-arm which reflects robot motions in practice (welding, painting) and then they were used for selection appropriate time constants of control system.

References

- Jeziński, E. (2006) Robots Dynamics. Wydawnictwa Naukowo-Techniczne, Warszawa (in Polish).
- Kozłowski, K., Dudkiewicz, P., Wróblewski, W. (2003) Robots Modelling and Control. PWN, Warszawa (in Polish).
- Morecki, A., Knapczyk, J., Kędzior, K. (2002) Mechanisms and Manipulators Theory. Wydawnictwa Naukowo – Techniczne, Warszawa (in Polish).
- Tarnowski, W., Bartkiewicz, S. (2003) Mathematical Modeling and Numeric Simulation of Continues Dynamic Processes. Wydawnictwo Uczelniane Politechniki Koszalińskiej, Koszalin (in Polish).

MODEL OF THE RELIABILITY PREDICTION OF MASONRY WALLS

B. Nowogońska*

Abstract: *The suitable repair forecasting is needed for proper maintenance of the buildings. The appropriate maintenance planning should be based on the prognostic analysis of the repair needs. However, in Poland, maintenance planning is currently not seen as a long-term system. Repairs are understood as extemporary works and are carried out exclusively on the basis of intermittent inspections and controls. One of the numerous factors determining maintenance planning is exploitation reliability conditioned by durability. This article presents a proposal to determine the prediction of operational reliability of the building constructed using traditional technology. The method of behaving and changing the reliability of the building throughout its use will be useful in planning renovations. The presented analysis includes apartment buildings erected in a traditional technology and regards them as technical objects. For such approached buildings it is proposed to apply rules applied for mechanical and electrical objects. The probability of the exploitation of a building without any breakdowns in a given period of time is defined as exploitation reliability.*

Keywords: Exploitation reliability, Prediction, Degree of technical wear.

1. Introduction

The presented analysis includes apartment buildings erected in a traditional technology and regards them as technical objects. For such approached buildings it is proposed to apply rules applied for mechanical and electrical objects. The probability of the exploitation of a building without any breakdowns in a given period of time is defined as exploitation reliability.

The examined material comprises 260 residential buildings performed in the traditional technology, situated within the area of the town of Gorzow Wlkp. (Lubuskie Voivodeship in Poland). The applied building materials and the structural solutions are similar in all the buildings. The masonry walls were made of solid bricks; the floors over the ceilings – masonry, Klein type; the remaining floors – wooden beams; the stairs and the roof structure – wooden, rafter framing – purlin-collar-tie type and in some cases – collar-beam type; roofing – flat tiles or roofing paper.

The technical states of all the buildings were periodically inspected by experts. The periodic monitoring, consisting in the examination of technical wear, resulted in the reports containing the information on the percentage wear of 25 components of the buildings.

2. Methods

To model a situation for the needs of the survival analysis, when the probability changes in time, the Weibull distribution is most frequently used as a distribution of random variable of the time of the building's usefulness (Walpde and Myers, 1985; Nowak and Collins, 2000; Runkiewicz, 1998, Zaidi et al., 2012). The probability density function for the Weibull distribution is determined with the relation:

$$f(t) = \alpha \beta^\alpha t^{\alpha-1} \exp [-(\beta t)^\alpha] \quad \text{for } t \geq 0 \quad (1)$$

where: t -the exploitation period,
 α -scale parameter (a real number) $\alpha > 0$,
 β -the shape parameter (a real number), $\beta > 0$.

* Dr. Beata Nowogońska, PhD.: Institute of Building Engineering, University of Zielona Góra, ul. Prof. Z. Szafrana 1, 65-516 Zielona Góra, Poland, b.nowogonska@ib.uz.zgora.pl

Parameter α of the distribution determines the probability of a breakdown in time:

- for $\alpha < 1$ the probability of breakdown decreases in time, which suggests that, when the object breakdown is modeled, some specimen may have production defects and slowly fall out of the population,
- for $\alpha = 1$ (exponential distribution) the probability is constant, it indicates the fact that breakdowns are caused by external random events,
- for $\alpha > 1$ the probability grows in time, which suggests that time-related technical wear of elements is the main cause of breakdowns,
- for $\alpha = 2$ (the Rayleigh distribution) the probability grows linearly in time.

Distribution parameter β is a coefficient characterising the rate of the reliability obsolescence:

$$\beta = 1/ T_R \quad (2)$$

where T_R denotes the period of the object durability.

The distribution function for the Weibull distribution obtained after integration:

$$F(t) = 1 - \exp [-(\beta t)^\alpha] \quad (3)$$

In the literature, the distribution function is called the probability of damage, a destruction function, breakdown or a failure function and is determined with the relation:

$$F(t) = P (t < T_R) = 1 - R(t) \quad (4)$$

where: T_R - period of object durability,

$R(t)$ - reliability function, also called the probability of proper operation, or durability function.

The object's reliability is defined as the ability to fulfil the task resulting from the purpose it was intended for. It means that the object is demanded to fulfil a determined function in determined time t in determined conditions of operation. The measure of the reliability of an object, in terms of the task, is the probability of the task completing. Such determined reliability measure is a function of time of the building's reliable performance and is called reliability function.

Exponential distribution is a particular case of the Weibull's distribution, where shape parameter $\alpha = 1$. Exponential distribution is frequently used in the examination of a proper performance time (Nowogońska, 2011; Salamonowicz, 2001). The relation defining the reliability functions for the i -th component of a building for known parameters α and β may take the form:

$$R_i(t) = \exp [-(t/T_{Ri})] \quad (5)$$

where:

$R_i(t)$ - exploitation reliability for the i -th component of a building,

t - exploitation time,

T_{Ri} - durability period of the i -th element of a building.

Another particular case of Weibull distribution, where $\alpha = 2$ is the Rayleigh distribution. The application of the Rayleigh distribution for buildings seems to be the best choice. All buildings and their components are subject to technical wear and the Rayleigh distribution is applied when the object's wear increases in time. For this case, the reliability function takes the form:

$$R_i(t) = \exp [-(t/T_{Ri})^2] \quad (6)$$

2.1. Exploitation reliability of components building

To determine the exploitation reliability of a building with the use of relation (6), the building, erected in the traditional technology, was divided into 25 components. A determined material-structure solution with characteristic theoretical average durability periods T_{Ri} (T_{Ri} by Ściślewski, 1995) was assumed for each component. Relation (6) was applied to examine the change in the exploitation reliability of all the components within the assumed a 100-year period of exploitation. The selected results of calculations are presented in Figs. 1 and 2.

MASONRY WALLS

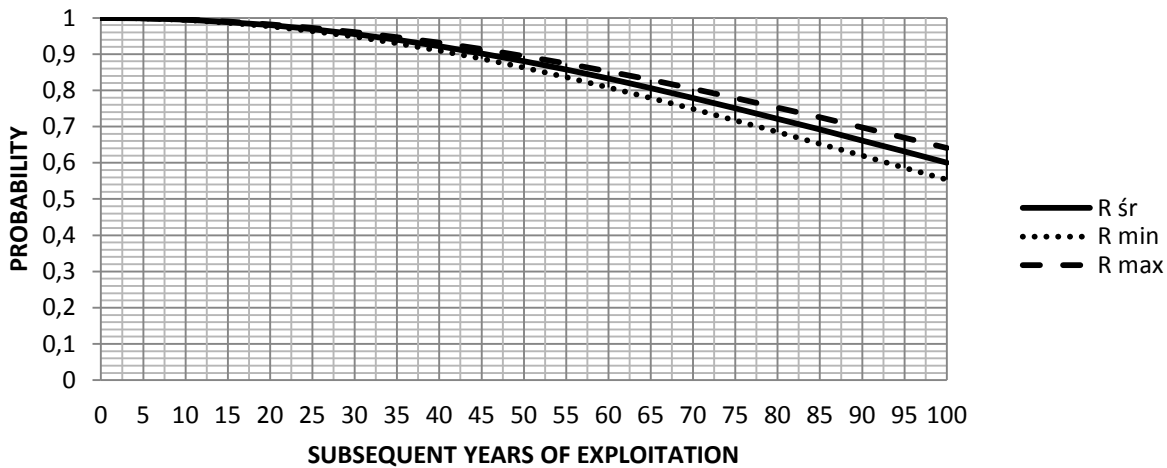


Fig. 1: Exploitation reliability of masonry walls according to the Rayleigh distribution.

WOODEN FLOORS

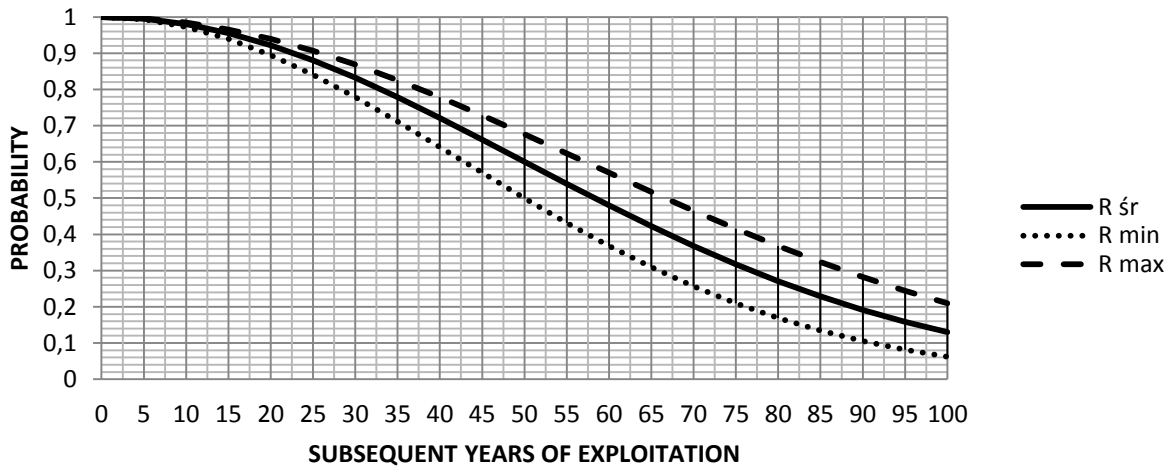


Fig. 2: Exploitation reliability of wooden floors according to the Rayleigh distribution.

Methods derived from the theory of exploitation of machines and electrical appliances were applied to examine the properties of apartment buildings. The results obtained at the present stage of the realisation of the exploitation reliability problem may be helpful in maintenance planning.

2.2. Prediction of the degree of technical wear of masonry walls

The bibliography on reliability of electronic devices attributes the intensity of failure to technical (Salamonowicz, 2001) wear as described in:

$$S_z = \int_0^t \lambda(t) dt \quad (7)$$

The technical wear according to the exponential distribution, where the intensity of failure is constant (7) is expressed with a linear function:

$$S_z = t / T_R \quad (8)$$

where:

- S_z – the degree of technical wear of an object expressed in percentage,
- t – the age of the object,
- T_R – the expected durability period of an object expressed in years.

For the Rayleigh distribution, where $\alpha = 2$, $\beta = 1/T_R$, the degree of technical wear equals:

$$S_Z = t^2 / T_R^2 \quad (9)$$

For each building element, it is possible to determine the prediction of the technical wear in any arbitrary exploitation period, the prediction of the degree of technical wear may be obtained according to the exponential distribution and the Rayleigh distribution. For brick masonry walls, the durability period is determined within the limits 130 – 150 years. The degrees of technical wear were determined for the minimum (130) and the maximum (150) values, with the use of the exponential distribution (formula 8) and according to Rayleigh distribution (formula 9). The obtained results are presented in Fig. 3.

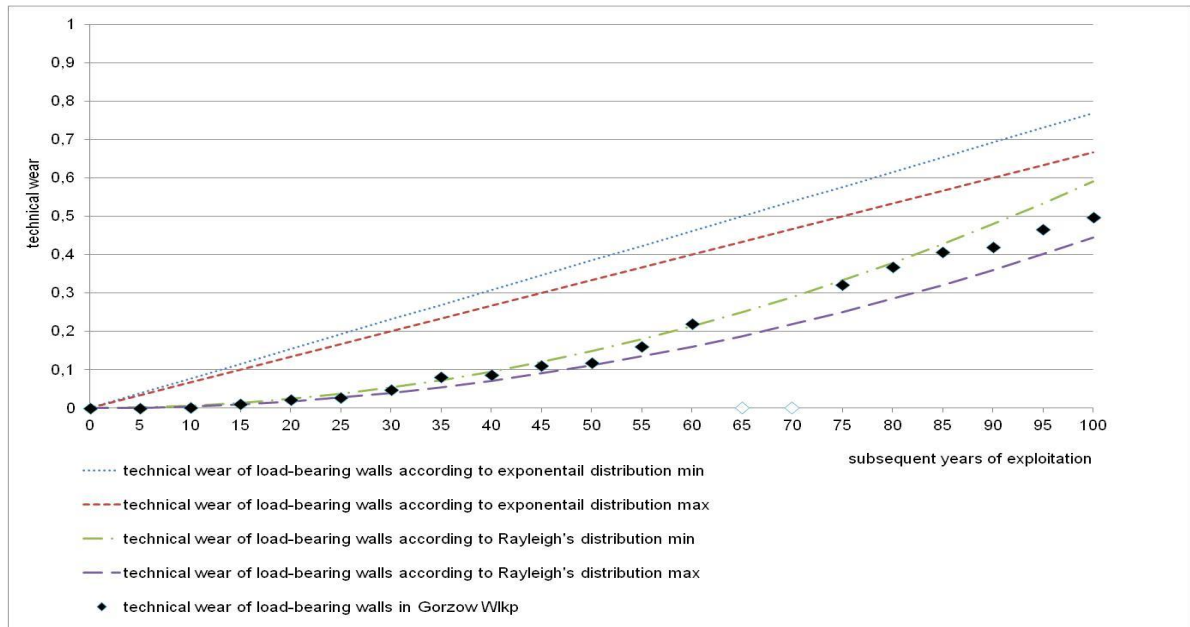


Fig. 3: Comparison between the degrees of technical wear of masonry walls according to exponential and Rayleigh distributions and the average results obtained in the evaluation.

3. Conclusions

The values of the degree of wear of the walls by the Rayleigh distribution was verified using Student t test. Assuming a 5% chance of error in applying ($p = 0.05$), and the number of degrees of freedom is 19, the critical value of the test is 2.0930. The test result in the study was 2.16817, which means that the results are statistically significant for the level of $p = 0.05$.

The results of technical wear of buildings in Gorzow Wlkp. confirm the effectiveness of the proposed method of the determination of the degree of technical wear with the use of Rayleigh distribution. The average values of the degree of technical wear determined in situ inconsiderably varied from the proposed charts in Rayleigh distribution.

References

- Nowak, A. S., Collins, K. R. (2000) Reliability of Structures, Mc Graw-Hill Int. Edition.
- Nowogońska, B. (2011) Reliability of building determined by the durability of its components. Civil Environmental Engineering Reports, No 6, pp. 173-180.
- Runkiewicz, L. (1998) Evaluation of the quality of materials in historic buildings. In: IV Proc. of the Conference on Scientific and Technological Sciences and PZITB on "Engineering Problems of the Old Town Historic Restoration", Cracow.
- Salamonowicz, T. (2001) Models reliability serviceable objects of preventive service. The Journal Issues machine operation, issue 2/2001.
- Ścisławski, Z. (1995) Life building. Kielce University of Technology Press, Kielce.
- Walpde, R. E., Myers, R. H. (1985) Probability and Statistics for Engineers and Scientists, Macmillan Publishing Company, London.
- Zaidi, A., Bouamama, B., Tagina, M. (2012) Bayesian reliability models of Weibull systems: state of the art. International Journal of Applied Mathematics and Computer Science, Vol. 22, No 3, pp. 585-600.

COMPARISON OF MODAL PARAMETER ESTIMATION TECHNIQUES FOR EXPERIMENTAL MODAL ANALYSIS

V. Ondra^{*}, P. Lošák^{*}

Abstract: *This paper deals with comparison of three commonly used modal parameter estimation methods (Pick Picking, Least Square Complex Exponential and Eigensystem Realization Algorithm) in order to judge about their accuracy and limitation. There have been invented a great amount of modal parameter estimation techniques in the field of experimental modal analysis. However, there is not universal method which would be suitable for every possible structure and/or with acceptable accuracy. As a test structure, 15 degrees of freedom plane with given mass, damping and stiffness was chosen. The foundations of discussed methods are described, their implementation on the test structure is shown and finally, natural frequencies and damping obtained by analytical approach are compared with those estimated using mentioned techniques. In addition, mode shapes differences are illustrated by means of Modal Assurance Criterion. Based on these comparisons, an accuracy and limitation of the methods is summarized in the conclusion.*

Keywords: Experimental Modal Analysis, Modal Parameter Estimation, Modal Assurance Criterion.

1. Introduction

Experimental modal analysis is used for the fast determination of the modal properties, determination of the structure vibration behavior or verification of finite element model and its correlation. There can be found a lot of methods that are used in an experimental modal analysis for determination of the modal properties (natural frequencies f_r , damping b_r and mode shapes) from Frequency Response Function (FRF). None of those methods is perfect and none of them is suitable for all cases with guarantee of accuracy (Avitabile, 2001). The aim of this paper is to compare three commonly used modal parameter estimation techniques in order to judge their accuracy on the test structure, which is represented by simulated 15 degrees of freedom plane.

2. Modal Parameter Estimation Methods

According to operation domain, the modal parameter estimation methods can be divided into time-domain and frequency-domain methods. There can be found methods, which work on single degrees of freedom (SDOF) systems only, and also more complex algorithms which work on multi degrees of freedom (MDOF) systems. As the representative of frequency-domain method, Least Square Complex Exponential (LSCE) was chosen. Eigensystem Realization Algorithm (ERA) is from group of the time-domain methods and Pick Picking (PP) method stands for classical, SDOF system method.

2.1. Pick Picking method

This method is sometimes referred also as peak-amplitude method (Ewins, 1986). It is one of the simplest modal parameter estimation methods. Pick Picking method belongs to SDOF methods group and from this fact yields its great limitation. It works well just for structures with well-separated (uncoupled) modes and in addition, for structures with a “good” damping. For heavily damped systems the response at a resonance is influenced by more than one mode. On the other hand the accurate measurements at resonance are difficult to obtain for light-damped structures. The detailed description of the Peak Picking method can be found in Ewins (1986).

^{*} Bc. Václav Ondra, Ing. Petr Lošák PhD.: Institute of Solid Mechanics, Mechatronics and Biomechanics, Brno University of Technology, Technická 2896/2; 616 69, Brno; CZ, y126251@stud.fme.vutbr.cz, losak@fme.vutbr.cz

2.2. Least Square Complex Exponential method

Least Square Complex Exponential (LSCE) method is representative of the frequency-domain methods. It operates on MDOF systems directly. This means that it is able to find all modes in frequency range of interest at once. Basically, this method fits a theoretical expression for frequency-domain transfer function on the measured data. The process itself is very sophisticated and has been optimized into time efficient and robust algorithm (Verbover, 2002; Cauberghe, 2004). Results of this method are natural frequencies, damping and, in this case, complex mode shapes. The only problem here is an unknown order of the system. This deficit is removed by using of a stabilization chart (Cauberghe et al., 2005).

2.3. Eigensystem realization algorithm

The Eigensystem realization algorithm (ERA) is the typical time-domain method, which was published by Juang and Pappa (1985). All details, together with mathematical proofs, can be found in this publication. The core of this method lies in finding state-space matrices of the system from a time-domain data. In case of the experimental modal analysis, an impulse response function (IRF) can be used instead of the time-domain data. The IRF is computed from FRF by means of inverse Fourier transform (Ewins, 1986). Again, the problem is to determinate the system order, so similar stabilization chart has to be used as in case of LSCE.

3. Application of the Methods on the Test Structure

3.1. Description of the test structure

The simulated plane with 15 DOF was used as a test structure. The rectangular plane (Fig. 1) has fixed supports on two sides and free edges on another two sides. Properties of the plane (mass and stiffness) were chosen and proportional viscous damping model was used for determination of the damping matrix. The exact modal properties of the plane were computed and will be used for comparisons. The theoretical frequency response functions (Fig. 1) were calculated by direct inverse method (Ewins, 1986). Seven close coupled modes of vibration can be found in frequency range 270 Hz – 370 Hz.

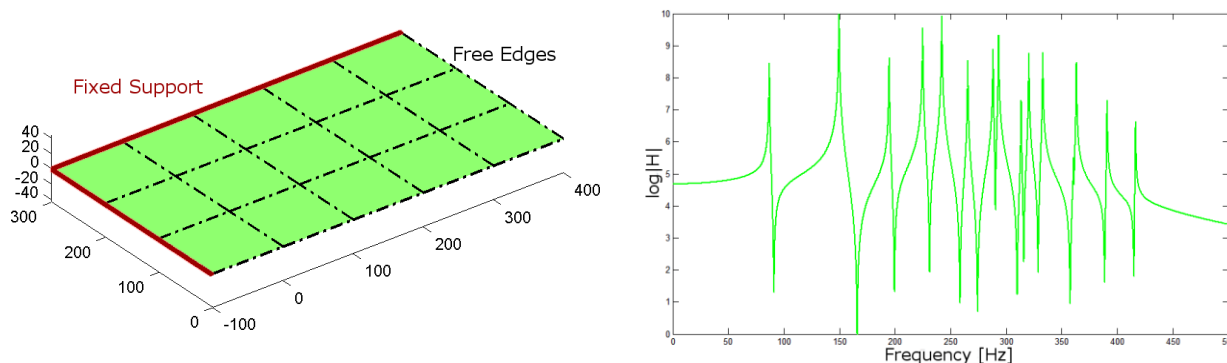


Fig. 1: Simulated test structure (left: Geometry, right: Frequency Response Function).

3.2. Setting of used modal parameter estimation techniques

Every modal parameter estimation technique requires an influence of analysts (Avitabile, 2001). It needs to be judged about system order or choose an individual peak in the FRF. When we deal with MDOF systems identification techniques we have to define the system order. In general, this is not easy task since we don't know the number of modes which are included in measured frequency range. Stabilization charts are constructed in order to remove this little disadvantage. It is convenient to mark a stable frequencies and damping in the stabilization charts. The stable, in this content, means that the frequencies and damping change just in small range of their values (usually 1% for frequency and 2% for damping) with different system order (Cauberghe et al., 2005).

For the test structure, we were able to identify all 15 peaks in FRF using manual peak picking. The stabilization charts of ERA and LSCE for our test structure can be seen in Fig. 2. ERA products cleaner stabilization diagram, however, the setting of ERA for successful identification (Caicedo, 2011) is more

complicated than setting of LSCE. In every case, both methods were able to identify all 15 modes with required accuracy.

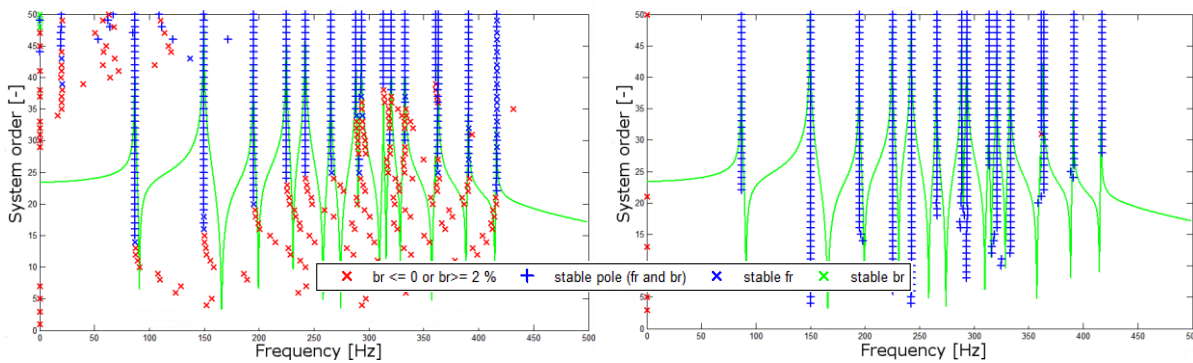


Fig. 2: Stabilization charts (left: LSCE, right: ERA).

3.3. Comparison of natural frequencies and damping

The comparison of natural frequencies and damping is made by graphical method that is described in Ewins (1986) and the results are plotted in Fig. 3.

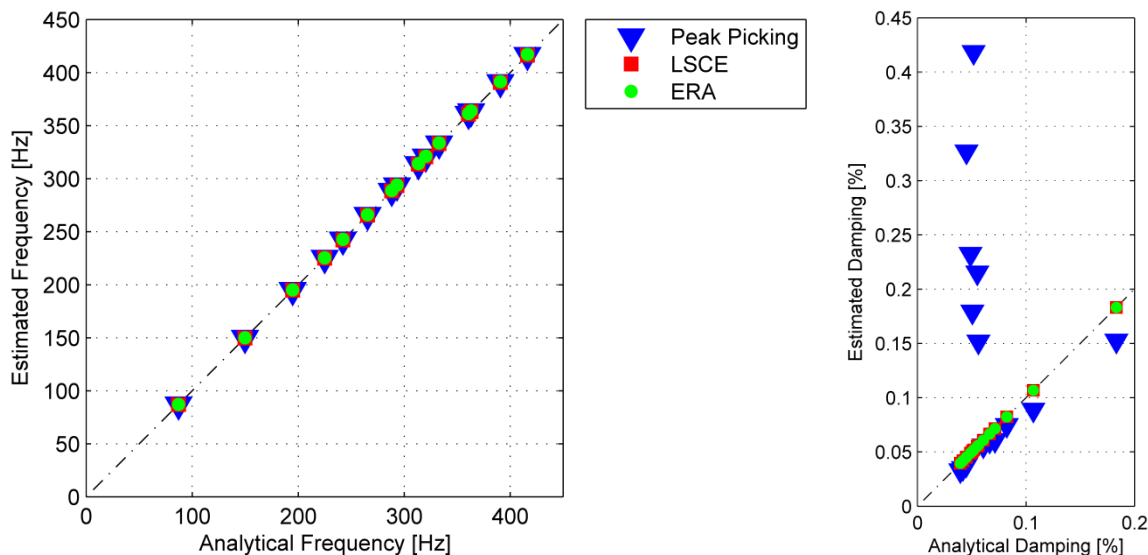


Fig. 3: The comparison of natural frequencies and damping.

It can be seen from these graphs that estimated natural frequencies are almost independent on the used estimation method. On the other hand, the damping, which is estimated by PP method, varies from analytical, LSCE and ERA values. The most differences can be found in the close coupled modes where the values of estimated damping are different of up to 300% from analytically calculated damping.

3.4. Comparison of mode shapes

Naturally, it would be possible to compare mode shapes from different method by overlap them into one graphs. But picture like this would be confusing and comparison would be uneasy (Ewins, 1986). Therefore, numerical methods have been developed for comparison of the mode shapes. One of the most used parameter is a Modal Assurance Criterion (MAC). The MAC is scalar value designed for two mode shapes from different sets (e.g. predicted vs. measured). It can be used for real and even for complex mode shapes. Modal Assurance Criterion indicates the degree of correlation between two mode shapes (Ewins, 1986). If the mode shapes are similar (or identical) the MAC values is equal or close to one, different mode shapes produce zero or almost zero MAC value. The MAC values from different combinations of mode shapes can be written into matrix and subsequently plotted. Comparison of the mode shapes obtained by PP and LSCE with analytical mode shapes is made in Fig. 4.

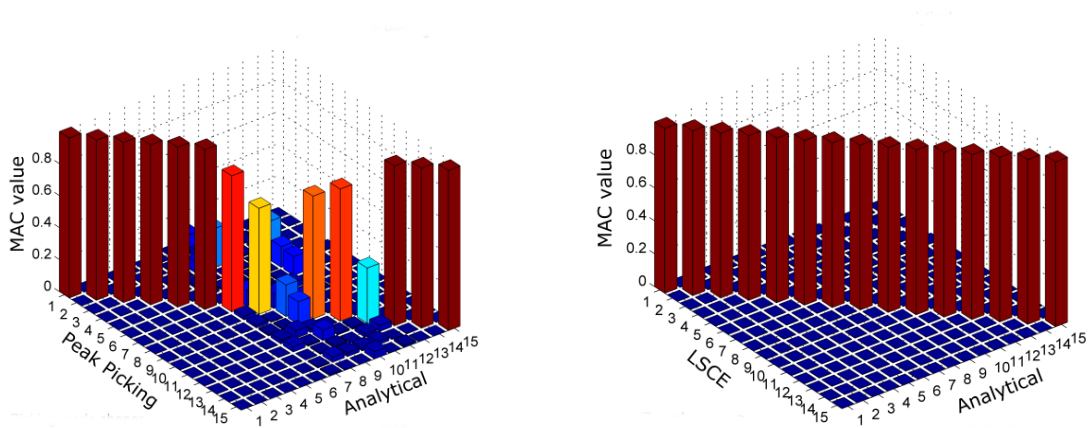


Fig. 4: The comparison of mode shapes (left: Analytical vs. PP, right: Analytical vs. LSCE).

From Fig. 4 can be observed that mode shapes produced by PP are very inaccurate in area of coupled modes. Mode shapes produced by LSCE are highly similar with analytical mode shapes.

4. Conclusion

The paper presented the comparison of modal parameter estimation methods. Three commonly used methods were chosen – Pick Picking, Least Square Complex Exponential and Eigensystem Realization Algorithm. The assessment about the quality of methods was based on comparison of modal properties. All frequencies estimated by these methods corresponded with analytical very well. However, the damping was different in the case of Pick Picking method. From the comparison of mode shapes by means of Modal Assurance Criterion it could be found the same trend i.e. the mode shapes estimated by Pick Picking method were not determined very well.

From these comparisons clearly state that Pick Picking method fails in case of the close coupled modes of vibration. Least Square Complex Exponential method and Eigensystem Realization Algorithm show very good performance in area of close coupled mode shapes, but the estimation itself requires more computing time and has higher demands on the quality of the measured FRFs.

Acknowledgement

This paper was written with the support of project FSI-S-14-2311 – “Problems of strength and dynamics of modern materials and structures II”.

References

- Avitabile, P. (2001) Experimental Modal Analysis – A Simple Non-Mathematical Overview, Sound & Vibration, Vol. 35, pp. 20-31.
- Caicedo, J. M. (2011) Practical Guidelines for the Natural Excitation Technique (NExT) and the Eigensystem Realization Algorithm (ERA) for Modal Identification Using Ambient Vibration, Experimental Techniques, Vol. 35, pp. 52-58.
- Cauberghe, B. (2004) Applied Frequency-domain System Identification in the field of Experimental and Operation Modal Analysis, PhD Thesis, Vrije University, Brussel.
- Cauberghe, B. et al. (2005) On the influence of the parameter constraint on the stability of the poles and the discrimination capabilities of the stabilization diagrams, Mechanical Systems and Signal Processing, Vol. 19, pp. 989-1014.
- Ewins, D. J. (1986) Modal Testing: Theory and Practice, Research Studies Press, London.
- Juang, J. N., Pappa, R. S. (1985) An Eigensystem Realization Algorithm for Modal Parameter Identification and Model Reduction, Journal of Guidance, Control and Dynamics.
- Verboven, P. (2002) Frequency-domain System Identification for Modal Analysis, PhD Thesis, Vrije University, Brussel.

KINEMATIC MODEL OF A MECHANICAL DEVICE FOR THE SUPPORT HUMAN LOWER LIMB

M. Ostaszewski^{*}, F. Siemieniako^{**}

Abstract: *The paper presents the structure of a mechanical device for the support of a human lower limb or for rehabilitation in the sagittal plane. The device has a parallel - serial mechanical structure. Three linear actuators with indirect displacements were used as executive devices. Inverse kinematics model was built for the mechanical design. The input signals for the model are angular displacements in the joints of the human lower limb. The outputs of the model are the displacements of the rods pistons actuators. The article presents the results of measurements of angular displacements using of the laboratory station for the determination of angular displacement in the joints of the lower limb. The paper also presents the displacement of the actuators in a function of angular displacements.*

Keywords: Inverse kinematic, Rehabilitation, Support system.

1. Introduction

The subject of the paper is the kinematic analysis of the mechatronic device, which is designed to assist the human lower limb motion in a plane perpendicular to the axis of rotation of the knee joint of human. The mechanical structure is show in Fig. 1a. In Fig. 1b the kinematic diagram of the device is presented.

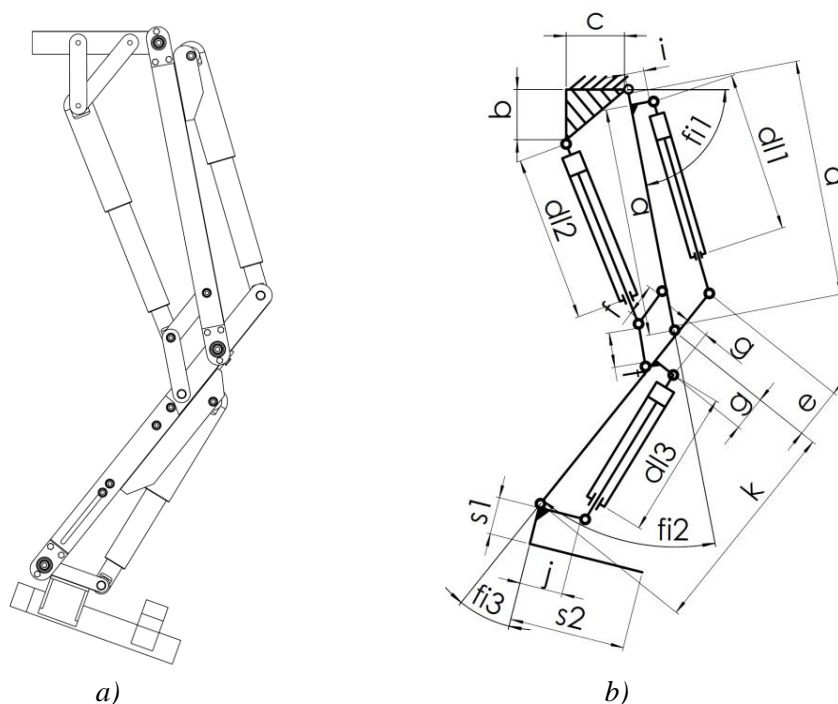


*Fig. 1: The device for the rehabilitation of the human lower limb: a) mechanical structure;
 b) Kinematic diagram of the device.*

^{*} Michal Ostaszewski, MSc.: Department of Automatic Control and Robotics, Faculty of Mechanical Engineering, Bialystok University of Technology Wiejska 45C, 15-351 Bialystok, Poland, m.ostaszewski@pb.edu.pl

^{**} Prof Franciszek Siemieniako: Department of Automatic Control and Robotics, Faculty of Mechanical Engineering, Bialystok University of Technology Wiejska 45C, 15-351 Bialystok, Poland, f.siemieniako@pb.edu.pl

The device was designed to support the muscular system and to enforce the correct movements in the respective joints of the lower limb of a man during rehabilitation. The correct movements and trajectories are forced by the person which coordinate the rehabilitation by using the test station for angular displacements.

The device consists of components connected in joint in class V. Groups of components consist of two serial and one parallel structures. The used parallel structure increases the operating range of the device. In the mechanical design three electric linear actuators with indirect displacement are placed (Siemieniako, 2013). The input signals for the model are the angular displacement in the joints of the human lower limb. The outputs of the model are the displacements of the rods pistons actuators. The required range of motion and orientation of the executive actuator are determined experimentally using laboratory station for angular displacements in the joints of the lower extremities in the sagittal plane. (Ostaszewski, 2013).

2. Mathematical Model

To determine the inverse kinematic model for the mechanical structure the equations of motion of piston rod actuators as functions of angular displacements φ_1 , φ_2 , φ_3 have been designated:

$$\begin{aligned} w_1 &= f_1(\varphi_1, \varphi_2), \\ w_2 &= f_2(\varphi_1, \varphi_2), \\ w_3 &= f_3(\varphi_3), \end{aligned} \quad (1)$$

where: w_1 , w_2 , w_3 - displacements of piston rods of the actuators 1, 2, 3.

In order to determine the equations of inverse kinematics the simplified model equations of angular displacements have been developed, as a function of the displacements relative to axes OX, OY, and the orientations of feet relative to the initial base:

$$\begin{aligned} \varphi_1 &= f_4(x, y, \varphi), \\ \varphi_2 &= f_5(x, y, \varphi), \\ \varphi_3 &= f_6(x, y, \varphi). \end{aligned} \quad (2)$$

The final form of the equations describing the inverse kinematics of the support mechanical device have been written as follows:

$$\begin{aligned} \varphi_1 &= \arctan 2(y + \sin(\sigma_6)\sqrt{s_1^2 + s_2^2}, x - \cos(\sigma_5)\sqrt{s_1^2 + s_2^2}) - \arctan 2\left(b\sqrt{\frac{\sigma_1^2}{4d^2k^2} - 1}, d + \frac{\sigma_1}{2d}\right), \\ \varphi_2 &= \arctan 2\left(b\sqrt{\frac{\sigma_1^2}{4d^2k^2} - 1}, d + \frac{\sigma_1}{2d}\right), \\ \varphi_3 &= -(\varphi - \varphi_1 - \varphi_2), \end{aligned} \quad (3)$$

where

$$\begin{aligned} \sigma_1 &= (x - \cos(\arctan\left(\frac{s_2}{s_1}\right) - \varphi)\sqrt{s_1^2 + s_2^2})^2 + (y - \sin(\arctan\left(\frac{s_2}{s_1}\right) - \varphi)\sqrt{s_1^2 + s_2^2})^2 - d^2 - k^2, \\ \sigma_6 &= \arctan\left(\frac{s_2}{s_1}\right) - \varphi. \end{aligned}$$

$$w_1 = \sqrt{a^2 + e^2 + i^2 - 2e \cdot \cos(\arcsin\left(\frac{i}{a}\right) - \varphi_2)} \sqrt{a^2 + i^2} - dl_1,$$

$$w_3 = \sqrt{j^2 + l^2 + m^2 - 2j \cdot \cos(\arcsin\left(\frac{m}{l}\right) + \varphi_3 - \frac{\pi}{2})} \sqrt{l^2 + i^2} - dl_3, \quad (4)$$

$$w_2 = \sqrt{b^2 + c^2 - \sigma_3 + f^2 + (d-h)^2 + 2\cos(\arccos\left(\frac{2(d-h)^2 - \sigma_3}{2(d-h)\sigma_2}\right) + \varphi_1 + \sigma_5)} \sqrt{b^2 + c^2} \sigma_2 - dl_2,$$

where

$$\sigma_2 = \sqrt{\sigma_3 + f^2 + (d-h)^2},$$

$$\sigma_3 = 2f \cos(\arccos\left(\frac{h+g \cos(\sigma_2)}{\sigma_4}\right) + \arccos\left(\frac{\sigma_4}{2f}\right))(d-h),$$

$$\sigma_4 = \sqrt{g^2 + 2\cos(\varphi_2)g h + h^2},$$

$$\sigma_5 = \arccos\left(\frac{b}{c}\right) - \frac{\pi}{2}.$$

3. Range of Motion of the Device

In order to verify the device for the support of the lower limb the simulations of the required range have been performed. Schematic structure of the simulation was shown in Fig. 2.

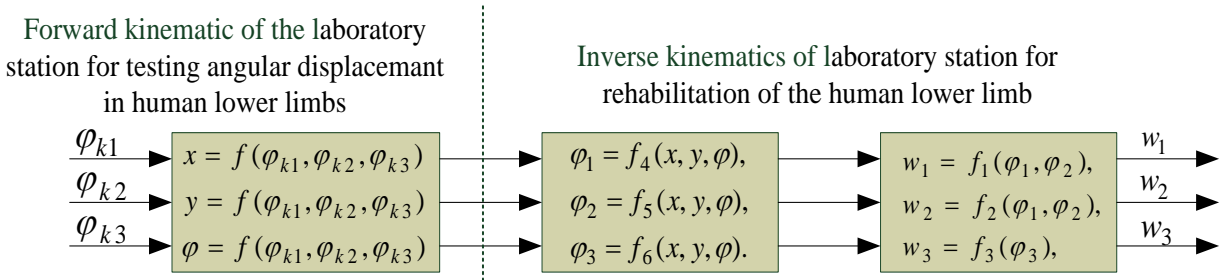


Fig. 2: Schematic structure of the simulation model.

The input signals to the system are displacement in the joints for the human lower limb. Signals have been collected using the laboratory station to measure the position of the angular displacement. The process of measurement and the laboratory station is described in (Ostaszewski, 2013). Using the station measurements of angular displacements are realized by six 12 bit hall effect absolute encoder. The encoder is installed in the joints of measurement station. The joints directly map the movements of individual joints (hip, knee, ankle) lower limb during the test. Sampling frequency was equals was 1 kHz. The maximum height of persons who have been subjected to the tests is 1.95 meter. In the procedure angular displacement which was collected on the measuring station were converted to global coordinates of movement and orientation of the human feet. Then by using the equitation inverse kinematics the signal were transformed into angles and then the displacements of rod cylinders mounted on the devise.

Fig. 3 presents measurements of the position and orientation of the human foot in XOY plane for the left leg in normal walking phase at a speed of 0.15 m/s. The measurement was for 1.95 meter high person. The distance between the hip joint and the knee joint was 0.47 meter and between the knee joint and the ankle was 0.5 meter. Required displacements for the actuators are shown the Fig. 4.

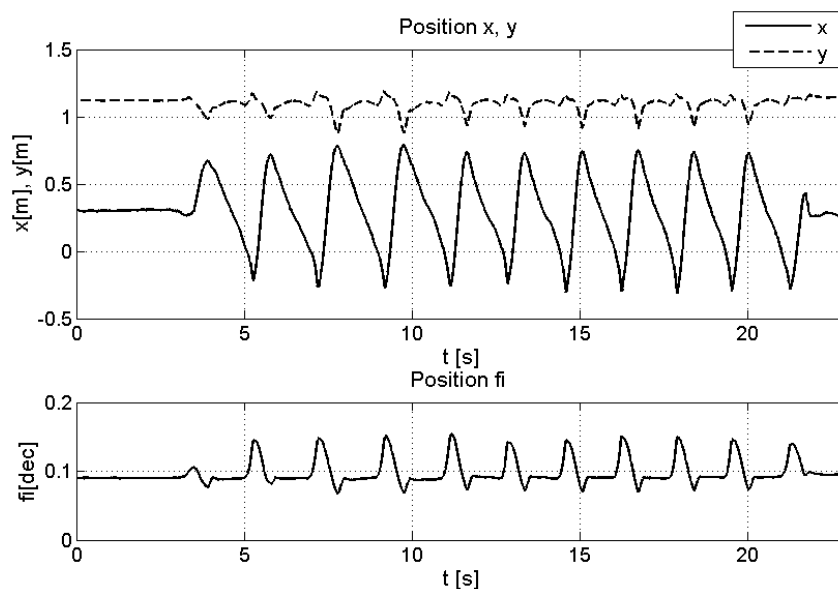


Fig. 3: Time charts of angular displacements during normal walk.

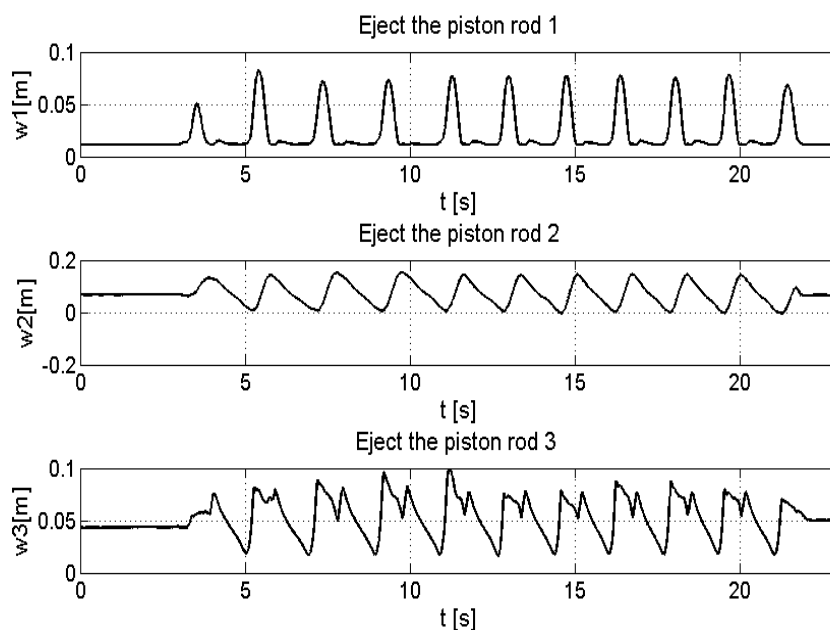


Fig. 4: Time charts of the movements of the actuators as answer to the angular displacement.

4. Conclusions

The rehabilitation device for the lower limb is equipped with actuators of the maximum rod output stroke equal, respectively for actuator 1 - 0.15 m, actuator 2 - 0.15 m, actuator 3 - 0.10 m based on the designed inverse kinematics model. We can observe that the designed structure and the maximum displacements for actuators are in allowable ranges. A further step will be design of a dynamic model of device for rehabilitation. The dynamic model will be used to investigate the regularity of selected cylinders due to the generated power.

References

- Ostaszewski, M., Siemieniako, F. (2013) Laboratory Station for Research on Angular Translocation in Human Lower Limbs, Solid State Phenomena, Trans-Tech Publications, Durnten-Zurich, Vol. 199, pp. 326-331.
- Siemieniako, F., Ostaszewski, M. (2013) Identification of in-line electric actuator, In: Proc. 14th International Carpathian Control Conference ICC'2013, Rytro, pp. 280-283, DOI 10.1109/CarpathianCC.2013.6560553.

OPTIMIZATION OF VALVE MANIFOLD TIMING SEQUENCE USING DIFFERENTIAL EVOLUTION ALGORITHM

T. Panáček^{*}, M. Klapka^{**}, Z. Němec^{***}

Abstract: *The present article deals with time optimization of the valve manifold by differential evolution algorithm. The adjustable valve manifold is a part of the experimental energy regeneration circuit for heavy vehicles with hydrostatic drive. The optimization process is based on a numerical model of the experimental rig, which is a scaled model of the real hydrostatic drive of the heavy vehicle.*

Keywords: Differential evolution algorithm, Optimization, energy regeneration, Efficiency.

1. Introduction

Reduction of vehicle fuel consumption is nowadays a significant technical problem in many heavy vehicle categories, e.g. construction vehicles described by Baseley et al. (2007). Recently, Brno University of Technology and Bosch Rexroth Company have been collaborating on the device for energy regeneration for heavy vehicles equipped with a hydrostatic drive. An experimental rig was assembled to simulate the hydrostatic drive of the real vehicle in a particular scale (Nevrlý et al., 2013). A correct operation of suggested device depends on the valve manifold which selects between the normal operation and the energy regeneration. Therefore a certain degree of optimization of the process is required to achieve high efficiency of device operation. This article deals with time optimization of the valve manifold by differential evolution algorithm. The acceleration mode of the experimental rig with energy regeneration is the subject of the optimization process.

2. Experimental Rig and its Simulation Model

Fig. 1a shows a simplified hydraulic circuit of the experimental rig. There are depicted all the valves (V1 to V6) in the valve manifold; its time sequence setting is the subject of the proposed optimization.

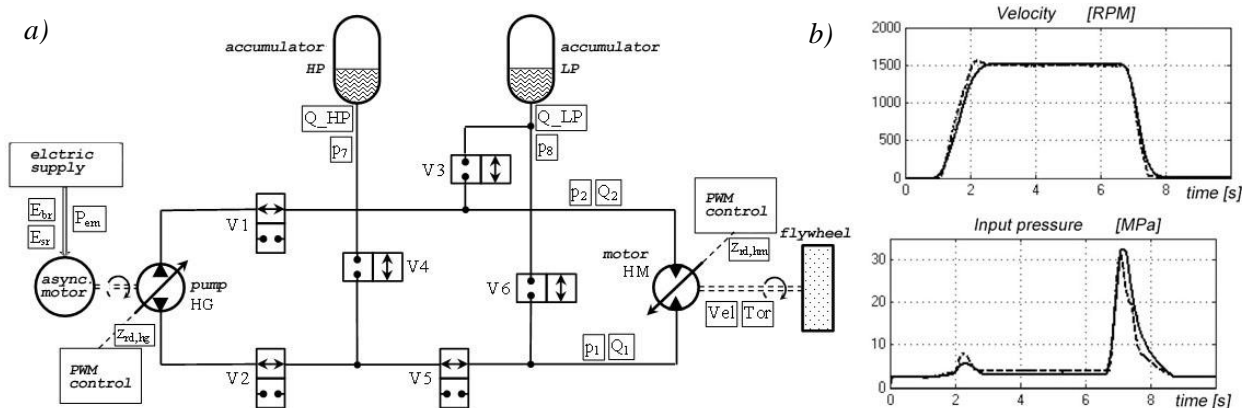


Fig. 1: a) Experimental rig diagram; b) Time response of selected quantities for the model verification.

^{*} Ing. Tomáš Panáček: Institute of Solid Mechanics, Mechatronics and Biomechanics, Brno University of Technology; Technická 2; 616 69, Brno; CZ, ypanac00@stud.fme.vutbr.cz

^{**} Ing. Milan Klapka, PhD.: Institute of Machine and Industrial Design, Brno University of Technology; Technická 2; 616 69, Brno; CZ, klapka.m@fme.vutbr.cz

^{***} Assoc. Prof. Zdeněk Němec, CSc.: Institute of Automation and Computer Science, Brno University of Technology; Technická 2; 616 69, Brno; CZ, nemec@fme.vutbr.cz

A simulation model of the rig was assembled in the Matlab/Simulink/SimHydraulics. It was verified by comparison of the results obtained by simulation and by measurement on the experimental rig in various operational modes. Time responses of the selected physical quantities depicted in Fig. 1b confirm a good agreement between the simulated and measured results. Thus the suggested simulation model is suitable for the optimization of valve timing.

3. Optimization of the Valve Control Signal Timing for *Accel* and *SetRPM* Mode Transitions

The experimental rig is capable to simulate the same operational modes as those found a real vehicle. The operational mode, which simulates the hydrostatic drive, is called *SetRPM*. It is possible to change the settings of the throttle which controls output revolutions of the hydraulic motor. Another operational mode called *Decel* simulates braking with active energy regeneration where the energy of braking is stored into the high pressure accumulator. The operational mode called *Accel* simulates acceleration of the experimental rig with active energy regeneration which utilizes previously stored energy. The article deals with the optimization of the acceleration process with energy regeneration; therefore transitions between *SetRPM* and *Accel* are considered. This operational mode is the most significant regarding the highest possible efficiency to be achieved.

3.1. Working cycle

The *SetRPM* mode with a zero throttle is the initial state of simulation. After 0.5 s, it is switched to the *Accel* mode with 51% throttle which is approx. 1 500 RPM of the motor. There are only two valves in the manifold switched (namely V4 and V6) within this transition, the other valves remain in the initial state. The accumulator becomes discharged after 1 s, therefore *Accel* switches back to *SetRPM* mode with the throttle remaining at 51%. This time, valves V4, V5 and V6 are switched if it is required.

3.2. Control signal timing

The timing vector is defined as follows:

$$\mathbf{t}_{R1,R2} = (t_{R1,R2,V1}, t_{R1,R2,V2}, \dots, t_{R1,R2,V6}) \quad (1)$$

Where $R1$ represents the initial operational mode and $R2$ is the mode to which the experimental rig is switched. Elements of the vector $\mathbf{t}_{R1,R2}$ determine a time delay of the valve control signal in milliseconds. The time delay is calculated from the moment of change of the operational mode from $R1$ to $R2$.

3.3. Purpose function

Maximum efficiency of the system is required providing:

$$\eta = \frac{E_2}{E_1} \quad (2)$$

where kinetic energy E_2 of the flywheel is determined by angular velocity and moment of inertia:

$$E_2 = \int_0^{t_{max}} P_2(t) dt \quad (3)$$

$$P_2(t) = \frac{d(\frac{1}{2}I\omega^2)}{dt} \quad (4)$$

and E_1 is energy consumption of the electromotor driving the test rig. This energy is replaced by energy E_0 for the optimization purposes. E_0 is defined as an integral of the true input power of the electromotor P_{em} decreased of true input power of the steady state P_{st} (losses):

$$E_0 = \int_0^{t_{max}} (P_{em}(t) - P_{st}(t)) dt \quad (5)$$

$$P_{st}(t) = P_{st1} + \omega(t) \frac{P_{st2} - P_{st1}}{\omega_{st2} - \omega_{st1}} \quad (6)$$

where P_{st1} and P_{st2} are true input power values of the electromotor in steady states before and after the experiment. In similar way, ω_{st1} and ω_{st2} are values of the flywheel angular velocity before and after the experiment.

The purpose function formula based on equations (3, 5) is:

$$f = k_p \frac{E_2}{E_0} \quad (7)$$

Some penalization is needed of non-feasible solutions. The criterion of the solution feasibility is met when there is zero flow $Q_{saf}(t)$ through the safety valves. Therefore coefficient k_p is introduced.

$$k_p = \begin{cases} 1, & Q_{saf}(t) = 0, t \in \langle 0; t_{max} \rangle \\ 0, & \text{other cases} \end{cases} \quad (8)$$

The time of the experiment is expressed by interval $\langle 0; t_{max} \rangle$.

3.4. Description of optimization algorithm

The algorithm of differential evolution (Price and Storn, cited 2013) was used for optimization of time vectors $t_{SetRPM,Accel}$ and $t_{Accel,SetRPM}$ and their elements. It is a stochastic population based optimization algorithm. The algorithm works over a set of candidate solution vectors P_g , where g represents a number of iteration. New elements of the solution vector group P_{g+1} are obtained from N vectors from previous solution P_g by the following method:

1. Assembly of the noise vector (Wang and Jiang, 2009):

$$v_{i,g+1} = x_{i,g} + F(x_{rand1,g} - x_{rand2,g}) \quad (9)$$

where $i = 1..N$, $x_{i,g}$ is base vector, $x_{rand1,g}$ and $x_{rand2,g}$ are random vectors selected from P_g . The amplification factor F affects the rate of convergence.

2. Assembly of the trial vector $u_{i,g+1}$ with regarding that the elements of the vector $v_{i,g+1}$ should be swapped with corresponding elements of the vector $x_{i,g}$ with probability P_c .
3. Calculation of the purpose function $f(u_{i,g+1})$.
4. Vector with the highest value of the purpose function is selected from $x_{i,g}$ and $u_{i,g+1}$. The selected vector is placed into a group of new solution vectors.

The algorithm was implemented on .NET platform. An assessment of quality of the optimization output (calculation of the criterion value) was conducted with verified simulation model in Matlab/Simulink. The group of solutions contained 150 solution vectors. The terminal condition of the process was a zero increase of the purpose function value after 50 iterations. The F factor has a constant value of 0.5 during the entire solution process.

4. Results

At first, a simulation was conducted of the efficiency of pure hydrostatic drive in acceleration according to the working cycle. Only the *SetRPM* operational mode is used. Thus all valves remain in the initial state and no time vector is needed. The energy consumption of the electromotor is $E_1 \cong 25.85 \text{ kJ}$ and kinetic energy of the flywheel is $E_2 \cong 7.68 \text{ kJ}$. Overall efficiency of the cycle obtained according to the equation (2) is $\eta = 29.75\%$.

Subsequently the working cycle with active energy regeneration was simulated. Provided there is no particular timing of the valve control signals, thus

$$t_{SetRPM,Accel} = (0, 0, 0, 0, 0, 0), t_{Accel,SetRPM} = (0, 0, 0, 0, 0, 0)$$

the energy consumption of the electromotor is $E_1 \cong 20.39 \text{ kJ}$ and obtained kinetic energy of the flywheel is $E_2 \cong 7.72 \text{ kJ}$. Overall efficiency is $\eta = 37.88\%$. Therefore the energy regeneration system is capable to increase the overall efficiency of the hydrostatic drive by 8.13%. The efficiency of driveline can be further improved by the optimization of the energy regeneration process.

Introducing optimized time vectors

$$t_{SetRPM,Accel} = (0, 0, 0, 160, 0, 20), t_{Accel,SetRPM} = (0, 0, 0, 60, 200, 80)$$

we can obtain the electromotor energy consumption $E_1 \cong 19.203 \text{ kJ}$ and flywheel kinetic energy $E_2 \cong 7.735 \text{ kJ}$. The overall efficiency is $\eta = 40.28\%$. Optimization of the process yields another 2.4% increase in the efficiency according to the operational conditions used.

A comparison of simulated results is shown in Fig. 2. There are time responses of the electromotor true power and time response of the velocity.

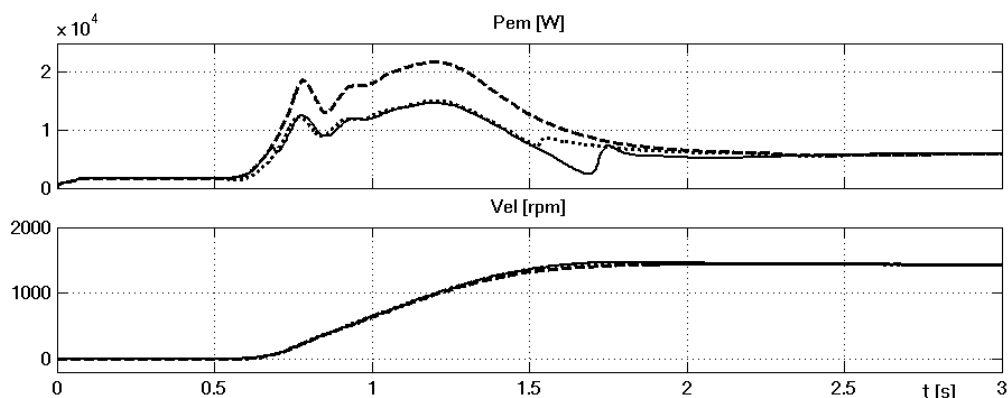


Fig. 2: Time response of selected simulated quantities. Hydrostatic drive mode – dashed; Energy regeneration active – dotted; Energy regeneration active and optimized – full.

5. Conclusions

The optimization of the selected operational mode with differential evolution algorithm results in 10.5% increase in the overall efficiency of the system in contrast to a non-optimized system. Another process which requires a similar optimization is the *Decel* operational mode where a pressure accumulator is charged with the energy of braking. The volume of the pressure accumulator should also be optimized. Considering the aforementioned optimization, there is a good possibility to achieve up to 16% increase in simulated efficiency of the drive with energy regeneration in comparison to the pure hydrostatic drive. Subsequently, simulated results should be verified by experiments on a testing rig. It is expected that the experimentally obtained efficiency of the system should be a maximum of 3% lower due to some minor simplifications of the mathematical model.

Acknowledgement

This work is an output of cooperation between Ministry of Education, Youth and Sports of the Czech Republic in the framework of the research project Eureka – LF12029 and NETME Centre, regional R&D centre built with the financial support from the Operational Programme Research and Development for Innovations within the project NETME Centre (New Technologies for Mechanical Engineering), Reg. No. CZ.1.05/2.1.00/01.0002 and, in the follow-up sustainability stage, supported through NETME CENTRE PLUS (LO1202) by financial means from the Ministry of Education, Youth and Sports under the „National Sustainability Programme I”.

References

- Baseley, S., Ehret, C., Greif, E., Kliffken, M. (2007) Hydraulic Hybrid Systems for Commercial Vehicles. SAE Technical Paper 2007-01-4150, doi:10.4271/2007-01-4150.
- Nevrlý, J. et al. (2013) Use of experimental stand for research of kinetic energy recovery. In: Proc. 22nd International Conference on Hydraulics and Pneumatics. Prague, Czech Republic, pp. 195 - 202. ISBN 978-80-248-3136-7.
- Price, K., Storn, R. (2013) Differential Evolution for Continuous Function Optimization [online] (cit. 2.8.2013). Available at <http://www.icsi.berkeley.edu/~storn/code.html>.
- Wang, X., Jiang, J. (2009) Optimization matching of wheel drive hydraulic hybrid vehicle components based on adaptive simulated annealing genetic algorithm. In: Proc. International Conference on Mechatronics and Automation, ICMA 2009, pp. 1962-1967.

THERMODYNAMICS PROPERTIES OF COPPER HALIDE ALLOY ($\text{CuBr}_{0.5}\text{Cl}_{0.5}$)

E. Parham*

Abstract: *Ab initio density functional theory (DFT) has been used to investigate the thermal properties of the $\text{CuBr}_{0.5}\text{Cl}_{0.5}$ alloys over a wide range of temperature. Using the quasiharmonic approximation (QHA) for the some physical quantities of interest such as heat capacity at constant volume and entropy are calculated and discussed. The theoretical results show good agreement with the available experimental data for CuBr and CuCl. The present results show that symmetric and asymmetric structure of $\text{CuBr}_{0.5}\text{Cl}_{0.5}$ have a good agreement with the calculatingly value for heat capacity.*

Keywords: DFT, PWSCF, Thermodynamics properties, $\text{CuBr}_{0.5}\text{Cl}_{0.5}$.

1. Introduction

During the last three decades, the CuX (X = Br, Cl and I) have been a subject of many theoretical and experimental studies. The CuX compounds are big direct gap semiconductors, which crystallise at ambient condition in the cubic NaCl structure, and possess 10 valence electrons instead of eight for common zinc-blend and wurtzite III-V and II-VI compounds. The copper halides are prototype materials for nonlinear optical experiments (Konigsberg and Schrunner, 1989). They found renewed interest because of the possibility of producing microcrystals (Frohlich et al., 1971). As promising candidates for photosensitive and semiconducting materials, copper halides attract much attention and several theoretical and experimental results have been reported (Blacha et al., 1986; Hsueh and Maclean, 1995). The copper halides CuBr and CuCl crystallize under ambient conditions in the zinc-blende structure. A closer look at the structural properties of I-VII semiconductor alloys made possible by more measurements (Endo et al., 1993) reveals, however, that these alloys form a complete solid solution. In 1998 the band structures of $\text{CuCl}_{1-x}\text{Br}_x$ (Heireche et al., 1998), $\text{CuCl}_{1-x}\text{I}_x$ (Bouhafs et al., 1998) and $\text{CuBr}_{1-x}\text{I}_x$ (Bouhafs et al., 1998) alloys are used tight-binding (TB) theory within the virtual crystal approximation (VCA) studied. The miscibility of copper halides is studied by using a three-body potential (Sekkal et al., 1999). The electronic structure and disorder effects in copper halides alloys are studied by using the full potential linearized augmented plane wave (FLAPW) method (El Haj Hassan and Zaoui, 2001). It is shown that X-ray diffraction patterns of $\text{CuBr}_{1-x}\text{I}_x$ crystals indicated a cubic zinc-blende structure and is shown that the lattice parameter changed linearly without changes in the crystal structure (Bouhafs et al., 1998).

In this paper we present a first principles study of the ground state and thermodynamic properties of $\text{CuBr}_x\text{Cl}_{1-x}$ compounds by employing plane wave pseudo-potential method and density-functional theory. The paper is organized as follows. In Section 2, we briefly review the computational method used. In Section 3, the result of our calculations are presented and discussed. Finally, a summary of the work will be given in Section 4.

2. Methods

The present theoretical calculations are performed using the PWSCF software package (Baroni et al., 2001). During first-principles calculations, the exchange-correlation functional is treated with GGA Perdew–Wang 91 (Perdew and Wang, 1992; Perdew et al., 1992), in which the expansion of the augmentation charges is required. The core-valence electron interaction is described via ultrasoft pseudopotential (Vanderbilt, 1990). For the eight atom supercell considered here (Fig. 1), many possible

* Elnaz Parham, M.Sc.: Department of Physics, Najafabad Branch, Islamic Azad University, Isfahan, Iran, parham_elnaz@yahoo.com

atomic arrangements may exist for the alloy. The unit cell contains four Cu atoms, two atoms of Cl and two atoms of Br, where the tetrahedral nearest neighbor environment of each Cl or Br atom is 4 Cu atoms in the symmetrical type that showed in Fig. 1a and the Asymmetric type that showed in Fig. 1b. The basis set is truncated to a kinetic energy cutoff of 36 Ry for Symmetrical type of alloy and a kinetic energy cutoff of 37 Ry for Asymmetric type. The Brillouin-zone integrations are performed using a $5 \times 5 \times 5$ grid mesh of Monkhorst-Pack scheme for both. With QHA, a fourth-order finite strain equation of state (EOS) (Silveira et al., 2006; Karki and Wentzcovitch, 2000; Wu and Wentzcovitch, 2008; Sun and Umemoto, 2008; Li et al., 2012) is used to obtain the Helmholtz free energy $F(T,V)$ at various temperatures. From the Helmholtz free energy, several physical quantities of interest are obtained, which are as a function of temperature.

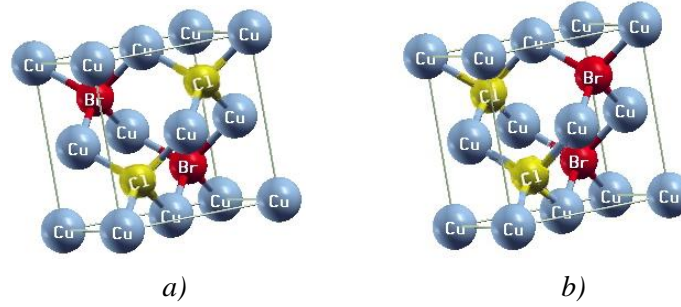


Fig. 1: Schematic picture of the possible atomic arrangements of Cu in the $\text{CuBr}_{0.5}\text{Cl}_{0.5}$ cubic supercell. (a) shows the symmetrical and (b) shows the Asymmetric type.

3. Results and Discussion

3.1. Structural properties

$\text{CuBr}_{0.5}\text{Cl}_{0.5}$ has two CsCl-type simple cubic structures with space group of $F43m$ (Dwight, 1959). As shown in Fig. 1, its unit cell has three kinds of atom with lattice constant $a = 5.62 \text{ \AA}$ for asymmetrical type and $a = 5.61 \text{ \AA}$ for symmetrical type. We first determine the ground-state structural parameters of symmetrical and asymmetrical of $\text{CuBr}_{0.5}\text{Cl}_{0.5}$. The ground state properties are obtained by minimization of the total energy with respect to the unit cell volume V , which is directly related to the lattice constant. Our results of $\text{CuBr}_{0.5}\text{Cl}_{0.5}$ crystals indicated a cubic zinc-blende structure and showed that the lattice parameter changed linearly with Br: Cl concentration ratio without changes in the crystal structure.

3.2. Thermodynamic properties

The thermodynamic properties of $\text{CuBr}_{0.5}\text{Cl}_{0.5}$ can be determined in detail by the entire phonon spectrum. The quasi-harmonic approximation can describe such properties quite satisfactorily. In the present work, the more explicit forms of the phonon contribution to the entropy S , and constant-volume specific heat C_v , at temperature T , in the harmonic approximation per unit cell are given (Lee and Gonze, 1995) as follows:

$$C_v = 3nNk_B \int_0^{\omega_{\max}} \left(\frac{\hbar\omega}{2k_B T} \right)^2 \text{csch}^2 \left(\frac{\hbar\omega}{2k_B T} \right) g(\omega) d\omega \quad (1)$$

$$S = 3nNk_B \int_0^{\omega_{\max}} \left[\frac{\hbar\omega}{2k_B T} \coth \frac{\hbar\omega}{2k_B T} - \ln \left\{ 2 \sinh \frac{\hbar\omega}{2k_B T} \right\} \right] g(\omega) d\omega \quad (2)$$

Where k_B is the Boltzmann's constant, h is the Planck's constant, n is the number of atoms per unit cell, N is the number of unit cells, ω is the phonon frequencies, ω_{\max} is the largest phonon frequency, and $g(\omega)$ is the normalized phonon density of states.

The variation of entropy with temperature for $\text{CuBr}_{0.5}\text{Cl}_{0.5}$ is given in Fig. 3. Entropy is a measure for the disorder of the micro-particle in thermodynamic system. The change of entropy can determine whether a thermodynamic process is a reversible process. The lattice contribution to the C_v is calculated and shown in Fig. 2. In the low-temperature limit, the specific heat exhibits the expected T^3 power-law behavior and

approaches at high temperatures the Dulong- Petit limit of $C_v = 3nNk_B = 74.830$ J/mol K. Due to the lack of experimental or other theoretical values existing on the thermodynamics for comparison with our results, we have calculated the thermodynamic properties for a number of materials such as CuBr and CuCl to further test of our computational methodology. Theory and experiment show satisfactory agreement within the limitation of the PWSCF program and the harmonic approximation. Here, we just list the calculated results S and C_p for CuBr and CuCl in Tab. 1 together with the corresponding experimental data (Cox et al., 1989; Pedley, 1994; Gurvich, 1994). CuBr has a cubic symmetry structure and two kinds of atoms with lattice parameters of $a = 6.695\text{\AA}$, the Cu atom occupies the (0, 0, 0) site and Br atoms occupy the (1/4, 1/4, 1/4) site. The calculated lattice parameters are 6.706\AA . Compared with the experimental results, the maximal deviation is only 0.16%, a normal agreement by GGA standards. The good agreement for CuBr can predict that the calculated thermodynamic properties of $\text{CuBr}_{0.5}\text{Cl}_{0.5}$ can also be at the same level of accuracy. Our calculated results can be seen as a prediction for the future investigations.

Tab. 1: The calculated thermodynamic functions for CuBr and CuCl compared with experimental results.

	S(J/molK)		Cp(J/molK)		ΔH (kJ/mol)	
	Cal.	Exp.	Cal.	Exp.	Cal.	Exp.
CuBr	95.7	96.1	54.1	54.7	-104.1	-104.6
CuCl	85.8	86.2	48.1	48.5	-136.9	-137.2

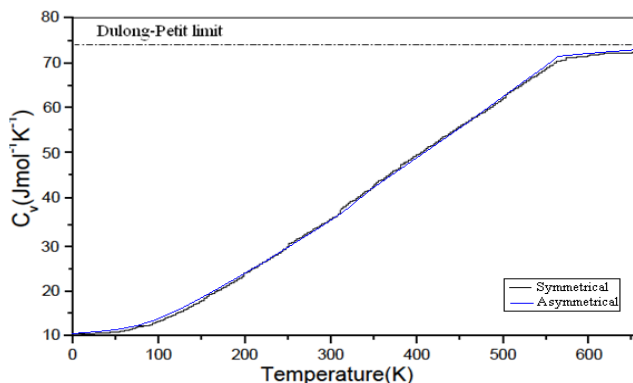


Fig. 2: Calculated temperature dependence of heat capacity of $\text{CuBr}_{0.5}\text{Cl}_{0.5}$ at constant volume (C_v) for symmetrical and asymmetrical type.

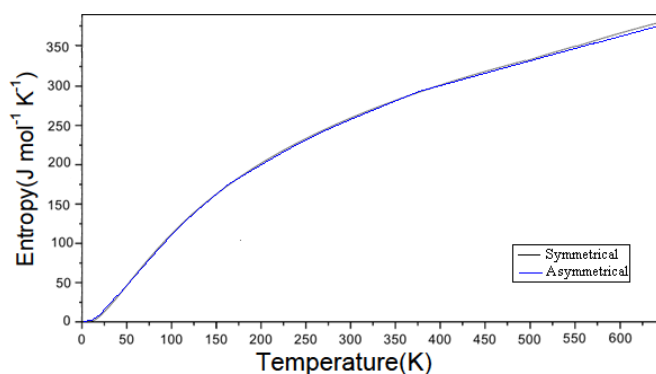


Fig. 3: Variation of entropy S with temperature T for symmetrical and asymmetrical type.

4. Conclusions

In summary, the calculation of thermodynamic properties of $\text{CuBr}_{0.5}\text{Cl}_{0.5}$ using DFT and pseudo-potential methods are performed. The heat capacity is found to be in good agreement with the calculatingly value (dulong petit value) with the error less than 0.19%. Finally, we predicate the important thermodynamics properties including the entropy and constant-volume specific heat within the quasi harmonic

approximation (QHA). Our thermodynamic calculations of $\text{CuBr}_{0.5}\text{Cl}_{0.5}$ compound is showed similar in symmetrical and asymmetrical type and will certainly be very useful for the interpretation of future experiments.

References

- Baroni, S., de Gironcoli, S., Dal Corso, A., Giannozzi, P. (2001) Phonons and related properties of extended systems from density-functional perturbation theory, *Rev. Mod. Phys.* 73, pp. 515-562.
- Blacha, A., Christensen, N. E., Cardona, M. (1986) Electronic structure of the high- pressure modifications of CuCl, CuBr, *Cul. Phys. Rev. B*, 33, 2413-2421.
- Bouhafs, B., Heireche, H., Sekkal, W., Aourag, H., Ferhat, M., Certier M. (1998) Electronic and optical properties of copper halide mixed crystals $\text{CuBr}_{1-x}\text{I}_x$, *Phys. Status Solidi. B* ,209, pp. 339-352.
- Bouhafs, B., Heireche, H., Sekkal, W., Aourag, H., Certier M. (1998) Electronic and optical properties of copper halides mixed crystal $\text{CuCl}_{1-x}\text{I}_x$, *Phys. Lett. A*, 240, pp. 257-264.
- Cox, J. D., Wagman, D. D., Medvedev, V. A. (1989) CODATA Key Values for Thermodynamics, Hemisphere Publishing Corp., New York.
- DaSilveira, P. R., DaSilva, C. R., Wentzcovitch, R. M. (2006) Metadata Management for Distributed First Principles Calculations in VLab: a Collaborative Grid/Portal System for Geomaterials Computations ,American Geophysical Union, Fall Meeting 11A-1151.
- Dwight, A. E. (1959) CsCl-type equiatomic phases in binary alloys of transition metals, *Trans. Met. Soc. AIME*, 215, pp. 283-286.
- El Haj Hassan, F., Zaoui, A. (2001) Electronic structure of $\text{CuCl}_x\text{Br}_{1-x}$, $\text{CuCl}_x\text{I}_{1-x}$ and $\text{CuBr}_x\text{I}_{1-x}$ alloys, *Superlattices and Microstructures*,30, 2, pp. 75-80.
- Endo K, Yamamoto, K., Deguchi, K. (1993)Structure analysis of metal(I) halide mixed crystal by ^{63}Cu MASNMR and X-Ray diffraction methods. III. $\text{CuCl}_x\text{Br}_{1-x}$ crystal, *J. Phys. Chem. Solids*, 54, pp. 357-364.
- Frohlich, D., Mohler, E., Wiesner, P. (1971) Observation of exciton polariton dispersion in cucl *Phys. Rev. Lett.* 26,10, pp. 551-556.
- Gurvich, L. V., Veyts, I. V., Alcock, C. B. (1994) Thermodynamic Properties of Individual Substances, Fourth Edition, Vol. 3, CRC Press, Boca Raton, FL.
- Heireche, H., Bouhafs, B., Aourag, H., Ferhat, M., M. Certier (1998) Electronic and optical properties of copper halides mixed crystal $\text{CuCl}_{1-x}\text{Br}_x$, *J. Phys. Chem Solids*, 59 ,6 , pp. 997-1007.
- Hsueh, H. C., Maclean J. R., Guo, G. Y., Lee, M. H., Clark, S. J., Ackl, G. J., Crain, J. (1995) Pressure-induced polymorphism in CuCl: An ab initio study. *Phys. Rev.*, B, 51, 18, pp. 12216-12222.
- Karki, B. B., Wentzcovitch, R. M., de Gironcoli, S., Baroni, S. (2000) High-pressure lattice dynamics and thermoelasticity of MgO, *Phys Rev. B*, 61, pp. 8793-8800.
- Königsberger, E., Schrunner, H. (1989) On lattice parameters and enthalpies of mixing of alkali halide solid solutions. *physica status solidi (b)*, 151 (1). pp. 101-109.
- Lee, C., Gonze, X. (1995) Ab initio calculation of the thermodynamic properties, *Phys. Rev. B* 51, pp. 8610-8613.
- Li, G., Zhou, H., Gao, T. (2012) Structural, vibrational and thermodynamic properties of Zirconium–cobalt: First-principles study, *Journal of Nuclear Materials* 424, pp. 220-223
- Pedley, J. B. (1994) Thermochemical Data and Structures of Organic Compounds, Thermodynamic Research Center, Texas A & M University, College Station, TX.
- Perdew, J. P., Chevary, J. A., Vosko, S. H., Jackson, K. A., Pederson, M. R., Singh, D. J., Fiolhais, C. (1992) Atoms, molecules, solids, and surfaces: Applications of the generalized gradient approximation for exchange and correlation, *Phys. Rev. B*, 46, 11, pp. 6671-6687.
- Perdew, J. P., Wang, Y. (1992) Perdew-Wang '92 Local Spin Density Approximation, *Phys. Rev. B*, 45, pp. 13244–13249.
- Sekkal, W., Laref, A., Zaoui, A., Aourag, H., Certier, M. (1999) The Miscibility of Copper Halides Using a Three-Body Potential. I. $\text{CuCl}_x\text{Br}_{1-x}$ Crystal, *Mol. Simul.* 23, pp. 127-142.
- Sekkal, W., Zaoui, A., Laref, A., Aourag, H., Certier, M. (2000) The miscibility of $\text{Cu}_x\text{Ag}_{1-x}\text{I}$ using a Tersoff potential, *Superlatt. M.*, 28,1, pp. 55-66.
- Sun, T., Umemoto, K. (2008) Lattice dynamics and thermal equation of state of platinum, *Phys. Rev. B*, 78,2, 024304.
- Vanderbilt, D. (1990) Soft self-consistent pseudopotentials in a generalized eigenvalue formalism *Phys. Rev. B*, 41, 11, pp. 7892-7895.
- Wu, Z. Q., Wentzcovitch, R. M. (2008) Pressure-volume-temperature relations in MgO: An ultrahigh pressure-temperature scale for planetary sciences applications *J. Geophys. Res*,113, B06204.

SENSITIVITY OF ACTION POTENTIAL TO CHANGES OF INWARD RECTIFIER POTASSIUM CURRENT I_{K1} IS DIFFERENT IN RECENT MODELS OF HUMAN VENTRICULAR CARDIOMYOCYTES

M. Pásek*, J. Šimurda**, G. Christé***

Abstract: *The inwardly rectifying potassium current I_{K1} is one of the principle ionic currents responsible for repolarization phase of mammalian action potentials (APs). To estimate the impact of individual ionic currents on AP configuration, mathematical models have been widely used. In this study, we compare the effects of alcohol-induced changes of I_{K1} on AP duration (APD) as simulated in four recently published computer models of human ventricular cells. As expected, increasing or decreasing I_{K1} conductance by 20% respectively caused a shortening or a lengthening of APD. However, the effect was largely model-dependent, ranging from 1% to about 15% change of APD. Given the conflicting available experimental data on the features of I_{K1} in human ventricular myocytes there is a need for a set of well-established end-point constraints for a reliable human ventricular myocyte model to be generated.*

Keywords: Cardiac cell, Action potential, Inward rectifier potassium current, Quantitative modelling.

1. Introduction

In our recent work, we studied the effects of ethanol on the inward rectifier potassium current (I_{K1}) in adult rat ventricular myocytes (Bébarová et al., 2013). The results showed that ethanol affects I_{K1} in dual ways; it causes an inhibition of I_{K1} at very low concentrations up to 0.8 mM (equivalent to ~0.37‰ of ethanol in the blood) and an increase at concentrations above 20 mM (equivalent to ~0.92‰ of ethanol in the blood). To simulate the functional consequences of these changes of I_{K1} on human cardiac cells we decided to use our own and three other recently published models of human ventricular myocytes (Hrabcová et al., 2013; O'Hara et al., 2011; Fink et al., 2008; Iyer et al., 2004) for comparison. Surprisingly, changes of I_{K1} led to substantially different effects on AP in these four models indicating different sensitivities of the models to I_{K1} variations.

2. Methods

To compare the sensitivity of action potential (AP) to changes of I_{K1} in recently published models selected for this study (Hrabcová et al., 2013; O'Hara et al., 2011; Fink et al., 2008; Iyer et al., 2004), we performed simulations of APs and I_{K1} at 1Hz stimulation at steady-state (after 300 s stimulation – control conditions) and after an increase and decrease of I_{K1} -channels conductivity (g_{K1}) by 20%. In each case, AP duration at 90% repolarisation (APD₉₀) and relative change of APD₉₀ were evaluated.

The simulations on our model (Hrabcová et al., 2013) were performed using the computational system MATLAB 7.2 (MathWorks, Natick, MA, USA) and the solver for stiff systems ODE-15s. Simulations on the other models (O'Hara et al., 2011; Fink et al., 2008; Iyer et al., 2004) were performed using the computational environment for cellular modelling, CORv.0.9.31.1409 (Dr. Alan Garny), and the CellML codes of the models available at <http://models.cellml.org/electrophysiology>.

* Assoc. Prof. Ing. Michal Pásek, PhD.: Institute of Thermomechanics, AS CR - branch Brno; Technická 2; 616 69 Brno and Department of Physiology, Medical Faculty of Masaryk University, Kamenice 5; 625 00 Brno; CZ; pasek.avcr@centrum.cz

** Assoc. Prof. RNDr. Ing. Jiří Šimurda, CSc.: Department of Physiology, Medical Faculty of Masaryk University, Kamenice 5; 625 00; Brno; CZ; simurda@med.muni.cz

*** Dr. Georges Christé: Laboratoire de Neurocardiologie, EA4612, Université Lyon 1, F-69003 Lyon; France; georges.christe@inserm.fr

3. Results

Fig. 1 shows the simulated APs using all four models under conditions described in methods. In all cases, as expected, the 20% decrease of g_{K1} caused a reduction of I_{K1} and, consequently, a prolongation of AP duration. Analogically, the 20% increase of g_{K1} resulted in an increase of I_{K1} and subsequent shortening of AP duration. However, as evident from the figure, the potencies of the I_{K1} changes to affect AP were substantially different in these models.

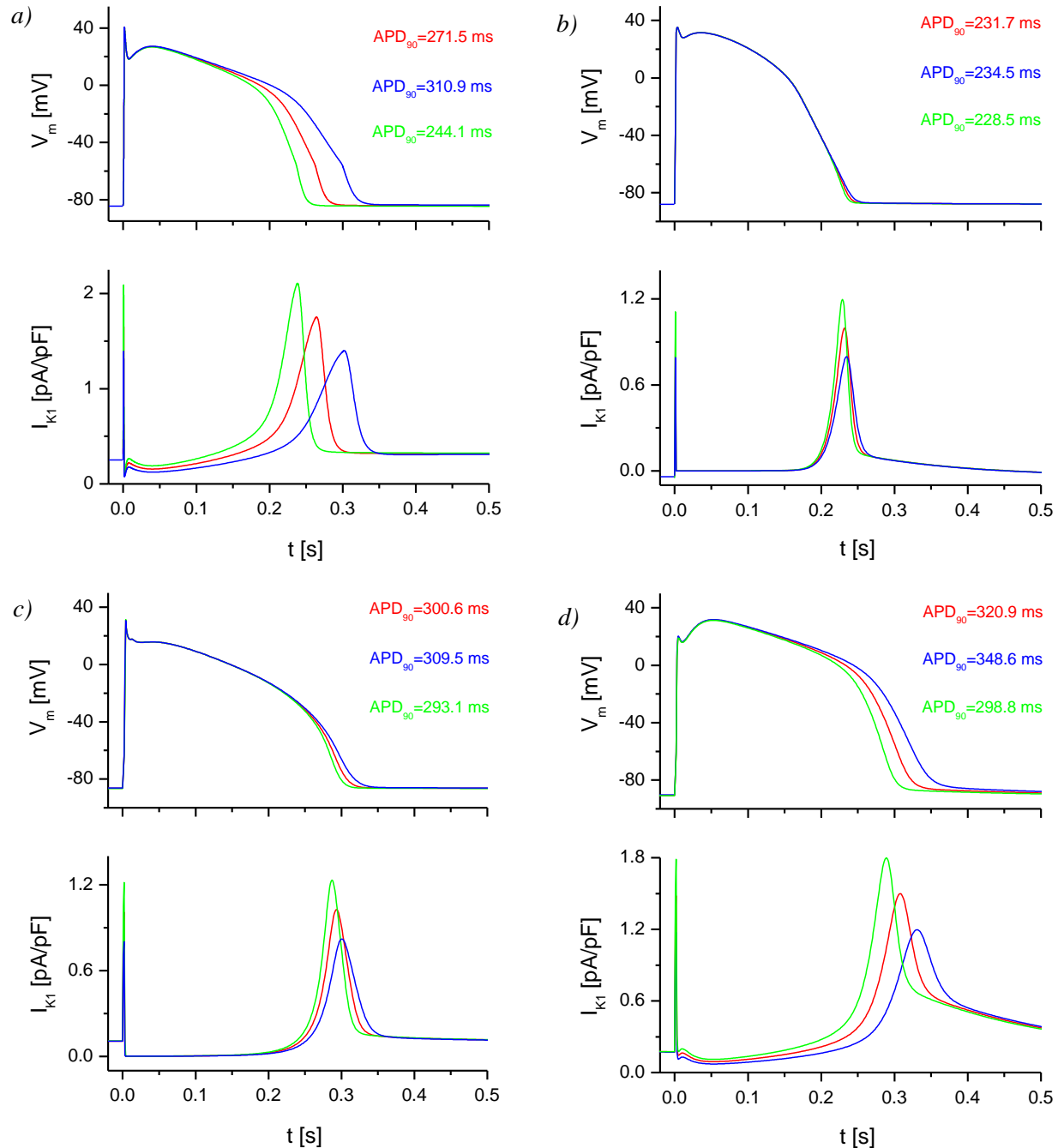


Fig. 1: Simulations of APs and I_{K1} in 1Hz steady-state (control conditions - red lines) and after decrease or increase of g_{K1} by 20% (blue and green lines respectively) using the models of human ventricular cardiomyocytes recently published by: a) Hrabcová et al. (2013); b) O'Hara et al. (2011); c) Fink et al. (2008); and d) Iyer et al. (2004). APD₉₀ stands for the duration of action potential at 90% of repolarisation.

Fig. 2 shows that the highest sensitivity of AP to changes of I_{K1} was found in the model of Hrabcová et al. (2013) where the 20% decrease of g_{K1} caused a relative increase of APD₉₀ by 14.5% and the 20% increase of g_{K1} caused a relative decrease of APD₉₀ by 10.1%. On the contrary, the lowest sensitivity of AP to

changes of I_{K1} was exhibited by the model of O'Hara et al. (2011) where the same changes of g_{K1} resulted in only 1.2% increase and 1.4% decrease of APD_{90} , respectively.

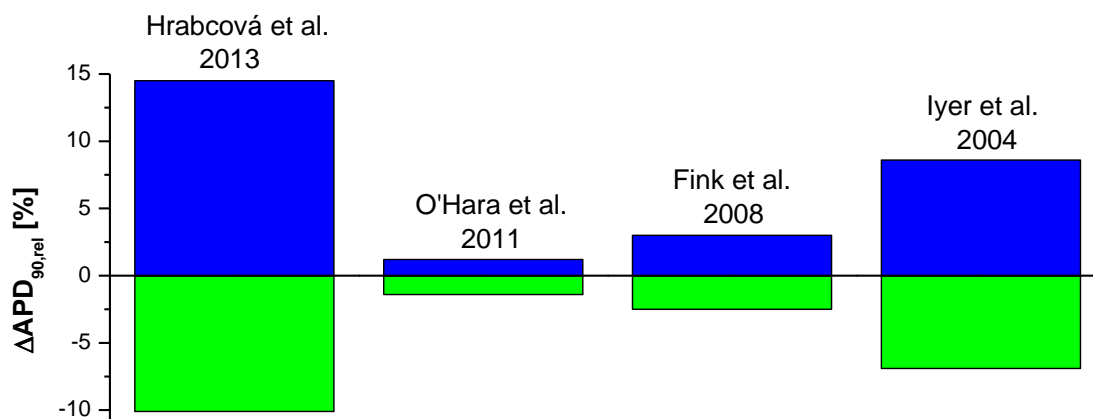


Fig. 2: Comparison of relative increase and decrease of APD_{90} (blue and green columns respectively) evoked respectively by a decrease or increase of g_{K1} by 20% from control values in the models of human ventricular cardiomyocytes recently published by Hrabcová et al. (2013), O'Hara et al. (2011), Fink et al. (2008) and Iyer et al. (2004).

4. Discussion and Conclusions

The prominent differences between sensitivities of APD to changes of I_{K1} in the explored models reflect the inconsistencies in mathematical description of I_{K1} properties due to the lack of experimental data from human ventricular cardiomyocytes gathered up to date. The highest sensitivity was observed in the model of Hrabcová et al. (2013) with formulation of I_{K1} based on the description in Iyer et al. (2004) while the lowest sensitivity was found in the model of O'Hara et al. (2011).

During the last decade, other comparative studies have been published in an effort to define the contribution of individual components of potassium current to repolarization of the AP. For example, Fink et al. (2006) have compared ten Tusscher et al. (2004) and Iyer et al. (2004) models and have concluded that the effects of a fixed percentage reduction of I_{K1} give rise to significantly different prolongation of AP in these two models. However, they noted that it was not possible to determine unequivocally which of these models would be more reliable for simulation of AP repolarization because reliable data on I_{K1} in human ventricle were not available in the whole range of physiological voltages. In 2008, Fink et al. reformulated I_{K1} to better reproduce the data obtained from human ventricular myocytes in their new model. Later on, Grandi et al. (2010) proposed an improved computational model of the human epicardial and endocardial myocytes, based on some of the best features of previous models combined with newer data. I_{K1} blockade increases APD rather modestly in these two later models consistently with other published experimental data (Rudy et al., 2008).

Nevertheless, the experimental results related to the properties of I_{K1} in human ventricular myocytes are not yet complete, and the sample size of available data sets is too small so far. Because of ethical reasons, it is practically impossible to study sufficient numbers of normal human cardiac cells to fully characterize their electrophysiological properties. On occasion, experimental animal models can help to fill important gaps in the missing data. They should be, however, used with caution. For example, I_{K1} changes appear to affect the APD considerably more in guinea pig (Miake et al., 2003) and dog (Jost et al., 2013) than in human cardiomyocytes.

In conclusion, the formulation of I_{K1} in the models of Fink et al. (2008) and Grandi et al. (2010) seem to be currently best adjusted to available measured experimental data from human cardiomyocytes and will likely provide the most reliable view on the effect of ethanol induced block of I_{K1} on action potential in human ventricular cells.

Acknowledgement

This study was realized with institutional support RVO: 61388998 and with support of the project NT14301-3/2013 from the Ministry of Health of the Czech Republic. Georges Christé's work was supported by Université Lyon 1 research allowances to the EA4612 Neurocardiology Unit.

References

- Bébarová, M., Matejovič, P., Pásek, M., Šimurdová, M., Šimurda, J. (2013) Ethanol and its principle metabolite acetaldehyde affect inward rectifier potassium current IK1 in rat ventricular myocytes (abstract). Biomedical Papers of the Faculty of Medicine and Dentistry of Palacky University Olomouc, Czech Republics, 157, pp. S1.
- Fink, M., Giles, W. R., Noble, D. (2006) Contributions of inwardly rectifying K⁺ currents to repolarization assessed using mathematical models of human ventricular myocytes. *Philosophical Transactions of the Royal Society A*, 364, pp. 1207-1222.
- Fink, M., Noble, D., Virag, L., Varro, A., Giles, W. R. (2008) Contributions of HERG K⁺ current to repolarisation of the human ventricular action potential. *Progress in Biophysics and Molecular Biology*, 96, pp. 357-376.
- Grandi, E., Pasqualini, F. S., Bers, D. M. (2010) A novel computational model of the human ventricular action potential and Ca transient. *Journal of Molecular and Cellular Cardiology*, 48, pp. 112-121.
- Hrabcová, D., Pásek, M., Šimurda, J., Christé, G. (2013) Effect of ion concentration changes in the limited extracellular spaces on sarcolemmal ion transport and Ca²⁺ turnover in a model of human ventricular cardiomyocyte. *International Journal of Molecular Sciences*, 14, pp. 24271-24292.
- Iyer, V., Mazhari, R., Winslow, R. L. (2004) A computational model of the human left-ventricular epicardial myocyte. *Biophysical Journal*, 87, pp. 1507-1525.
- Jost, N., Virág, L., Comtois, P., Ordög, B., Szuts, V., Seprényi, G., Bitay, M., Kohajda, Z., Koncz, I., Nagy, N., Szél, T., Magyar, J., Kovács, M., Puskás, L. G., Lengyel, C., Wettwer, E., Ravens, U., Nánási, P. P., Papp, J. G., Varro, A., Nattel, S. (2013) Ionic mechanisms limiting cardiac repolarization reserve in humans compared to dogs. *Journal of Physiology*, 591, pp. 4189-4206.
- Miake, J., Marbán, E., Nuss, H. B. (2003) Functional role of inward rectifier current in heart probed by Kir2.1 overexpression and dominant-negative suppression. *The Journal of Clinical Investigation*, 111, pp. 1529-1536.
- O'Hara, T., Virág, L., Varró, A., Rudy, Y. (2011) Simulation of the undiseased human cardiac ventricular action potential: Model formulation and experimental validation. *PLoS Computational Biology*, 7, e1002061.
- Rudy, Y., Ackerman, M. J., Bers, D. M., Clancy, C. E., Houser, S. R., London, B., McCulloch, A. D., Przywara, D. A., Rasmusson, R. L., Solaro, R. J., Trayanova, N. A., Van Wagoner, D. R., Varró, A., Weiss, J. N., Lathrop, D. A. (2008) Systems approach to understanding electromechanical activity in the human heart: a national heart, lung, and blood institute workshop summary. *Circulation*, 118, pp. 1202-1211.
- Ten Tusscher, K. H., Noble, D., Noble, P. J., Panfilov, A. V. (2004) A model for human ventricular tissue. *American Journal of Physiology*, 286, pp. H1573-H1589.

PRINCIPLES OF VIBRATION IMPACT ON CRACKED METHANE-BEARING COAL SEAM

M. V. Pavlenko*

Abstract: *The present article deals with the results of research into vibration impacts on a low-permeable coal seam. A method is described of how to create additional systems of cracks for array degassing to ensure its safe preparation. The result of vibration impact of on the coal seam was an increase in internal surface and pore volume of coal. Experimental vibration impacts on the coal seams have shown an increase in its absorption capacity, which ensured the extra impregnation of micro-pore volume of working fluid. With resonance system, the amplitude of the pressure fluctuations may significantly exceed its static value; for its assessment, however, it is necessary to know the characteristics of fluid viscosity, as they will determine the value of this amplitude. A proposed method of vibration impact is used to excite waves in a well filled with fluid, to transfer energy to the coal seam and to create new systems of formation of additional cracks for methane release from remote parts of coal seam.*

Keywords: **Vibration impact, Coal seam, Crack, Methane release, Well, Permeability, Hydrodynamics.**

1. Introduction

The problem of effectively controlled impact on low-permeable coal seam for intensification of methane release from coal is a very current issue. A coal seam should be seen as a typical example of a cracked porous medium. A coal seam always has a block structure caused by the presence of cracks of different origin. The coal seam subjected to hydrodynamic impacts appears to subsequently develop a network of cracks; thus the seam acquires the properties of block-cracked medium. A distinctive feature of such a medium is that the releasing methane is filtered out of the micro-cracks of that part of the blocks; these cracks are artificially created during hydrodynamic impacts in the seam, along the large cracks to the well, and then - via the system of trunk cracks - through the well to the surface (Shcherban et al., 1958). The output of well hydro-impacting in this medium is defined as the permeability of cracks, and the rate of gas release from the blocks. The resulting average size of blocks in the seam is estimated 5-15 m.

The main disadvantage of the method of hydro-impacted coal seams is non-uniform processing of the array associated with on-going use of only basic systems of natural cracks in the coal seam, which significantly limits the number of ways how to avoid sudden outbursts of coal and gas and how to achieve a deep and uniform degassing of coal-bearing stratum. Therefore, apart from advantages, hydro-impacting has significant drawbacks.

The objective of this research is to use vibration impacts as part of a comprehensive impact, joining together and using all the advantages. Vibration impacts combine the advantages of all the above methods, while avoiding their main disadvantages.

2. Results of Vibration Impact on Low-Permeability Coal Seam

The research carried out into vibration impacts on a low-permeability coal seam both via surface wells and also via underground holes showed that this is the way how to create additional systems of cracks for degassing of the array to ensure its safe preparation. The result of vibration impact on the coal seam was

* Prof. Michail V. Pavlenko: Moscow State Mining University, Leninsky avenue. 6, 119991, Moscow, Russia, mihail_mggy@mail.ru

an increase in internal surface and pore volume of coal. Experimental works related to the impact of vibration on coal seams have shown an increase in its absorption capacity, which ensured the extra impregnation of micro-porous volume of working fluid. This caused the increase of moisture content in micro-porous volume of coal and the subsequent extra desorption of coal-bed methane, which resulted in the increase of depth of degassing in coal seam. The article refers to the results of research into changes in hydrodynamics during vibration impacts on a low-permeability coal seam through a well from the surface. When impacting through the well from the surface, the increase in permeability of the coal seam is evident; this is confirmed by the change in seam hydrodynamics and the increase in gas-releasing surface.

If the system resonates, the amplitude of pressure fluctuations may significantly exceed its static value; however, for its assessment, it is necessary to know the characteristics of fluid viscosity in the well, because in particular they will determine the value of this amplitude.

The proposed method of vibration impact is used to excite waves in a well filled with fluid with the aim to transfer energy to the coal seam to create new additional systems for formation of cracks enabling the methane release from remote parts of coal seam (Ettinger, 1966).

According to this, in the lower part of the well, the conditions are created for resonance and transfer of vibration energy to the coal seam, which ultimately leads to the increase in seam permeability of up to 30-60%, formation of additional (2-3) systems of cracks, and after removal of water from the well, methane is released in the amount of 40-70%.

Laboratory experiments in low-frequency range of 1-100 Hz established that in the initial period of impacting (frequency 10-20 Hz) and in the final period (frequency 60-80 Hz), the activity of methane release from coal samples was low. When coal samples were exposed to vibrations in the range of 30-40 Hz, the methane release is enhanced, a maximum of degassing occurs, which is confirmed by the occurrence of the additional system of coal cracks (Pavlenko, 1999).

At the same time, depending on the frequency and amplitude and on the ratio of these values, a different energy impact occurs, which was established by the intensity and rate of methane release.

It is necessary to mention that the main characteristic of degree of impact on the medium is not the amplitude but the energy of vibrations E and, to some extent, vibration acceleration G , which are proportional, as follows:

$$E \approx A^2 \omega^2; \quad G \approx A \omega^2,$$

where: A is amplitude of vibrations,

ω is frequency of vibrations.

A characteristic of the equipment used is such that the amplitude of the emitted signal decreases with the increasing frequency. This dependence in the specified range of frequencies can be approximated as follows:

$$A = a - b\omega.$$

On the basis of experimental data (the triangles in Fig. 1), the coefficients a and b are equal, $a = -4.6 \cdot 10^{-5}$ and $b = 4.5 \cdot 10^{-3}$ respectively, where a is the amplitude independent of the frequency (reference frequency); b – the value of amplitude decrease depending on the frequency.

Dependences of vibration energy and vibration acceleration on the frequency are presented in Fig. 1. As follows from these graphs, in the used frequency range, the energy maximum falls on frequencies of order 40 - 50 Hz and acceleration of vibrations is 60-70 Hz.

With the aim to achieve qualitative assessments, it is necessary to consider the simplest model - a coal particle lying on a vibrating base. As noted above, an effective impact requires a separation of coal particles from the surface of vibrating base and their subsequent collision. If this impact is totally inelastic (which fully corresponds to the conditions inside the coal seam), optimum of G is achieved at maximum difference of speeds in the moment of impact.

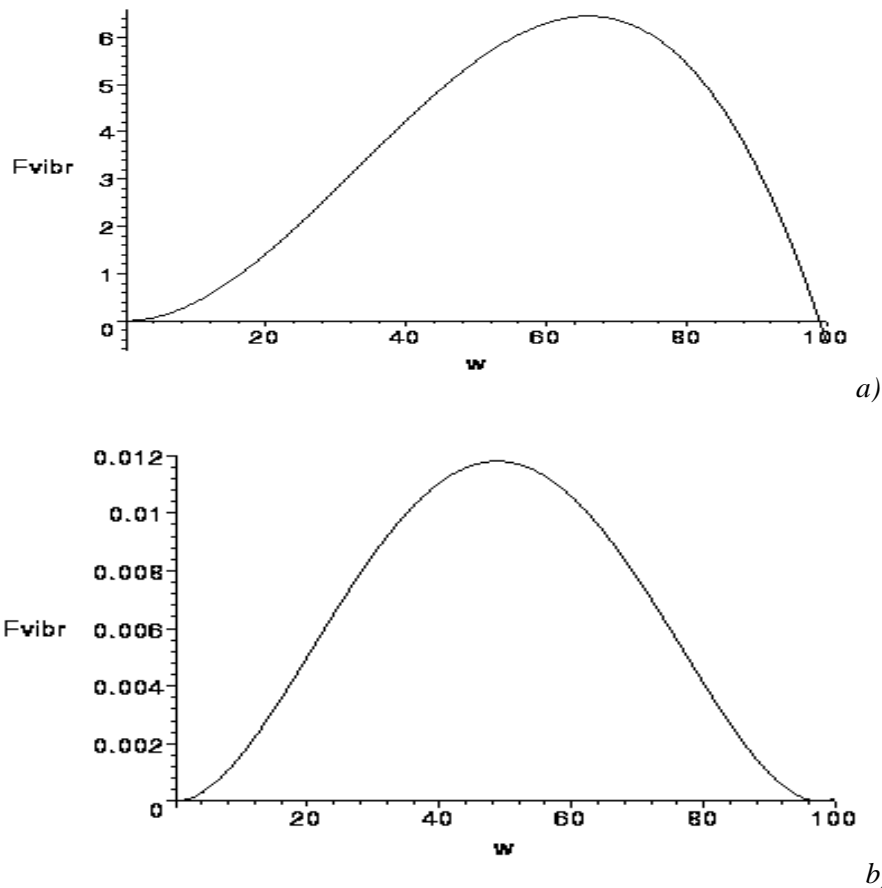


Fig. 1: Dependence of: a) energy of vibrations and b) acceleration of vibrations on frequency.

A separation condition is determined by the ratio of vibrating basis acceleration $A\omega^2$ and free-fall acceleration:

$$A\omega_c^2 \geq g,$$

where ω_c - critical frequency when the coal is separated from the colliding basis

$$\omega_c = \sqrt{\frac{g}{A}}.$$

Accordingly, if the average amplitude of vibrations in the experiments was 3.5 mm, the critical frequency was equal to $\omega \sim 35$ Hz. It is this frequency that determines the lower limit of the range of optimal impact.

As noted above, in relation to coal seam conditions, the existence of resonant frequencies, the impact on which is the most effective, is explained by internal structural changes of coal.

The experiments conducted in this way confirm the increase in the rate of gas filtration in the area of elastic vibrations, which can be explained by the improvement of filtration-capacitive properties.

To summarize, it is possible to state that the conducted experiments confirm the conclusion about a high sensitivity of coal seam to vibration impacts while the response of low-permeable coal seam to vibration impacts essentially depends of the frequency of waves generated by the source.

3. Conclusion

When solving the task of enhancing the gas release from coal, we were allowed to set sufficiently precise parameters for enhancement of methane release from coal depending on the parameters of vibration impact on a low-permeable coal seam. A proposed physical model of the interaction between coal and a vibrating surface qualitatively describes the experimentally observed samples of methane release from coal. Each volume of a coal sample has the optimal characteristics of gas release at a respective amplitude

and frequency of vibrations, at which the methane release from coal increases due to vibrations. The basic requirements to enhance the methane release from the coal seam using vibration impacts are to establish a particular relation between the amplitude and the frequency of vibrations, which creates a condition not only for initiation of cracks, but also enables us to preserve them for a given time. The proposed principles of constructing a vibration device to create an effective impact that uses a column of fluid filling the well with the aim to change the status of coal-bearing strata, to increase its intake capacity and, as a consequence, to increase permeability to create gas conductive cracks.

This goal is achieved by the formation of uniform artificial cracks across a vast area of coal seam, by transfer of vibration energy to the "coal-methane" system with a subsequent filtering using the gas conducting cracks united in a single filtering network drilled on the seam through one or a group of underground wells. The area of vast artificial cracks is created by the transfer of vibration energy through the seam underground wells and also by excitation of reflective elastic waves of high intensity in the seam from the lateral rocks of the coal seam. These elastic waves, concentrically propagating from the well along the coal seam, create a uniform network of artificial cracks in the seam. Energy of vibration impact, spreading via a network of cracks in the coal seam, violates the structure of the coal seam, and methane is released from the free and sorption volume that fills the cracks and micro-pores in coal, which is on the same network of newly formed cracks, and is released through the parallel drilled underground well (Rodionov et al., 1976). Therefore, the selection of objects subjected to vibration impact was subordinated to the main purpose of impact – a selection of optimal parameters for vibration impact and, as consequence, for a decrease of high gas content in the processed coal seam.

A proposed methodology of designing the technological schemes for preparation of a mine field, which is based on a comprehensive use of active impact, seems to be a priority alternative for the preliminary preparation as for the sequence and types of active impacts, and the use of degasification wells and vibration impacts in the final stage, leading to an intensive formation of cracks and gas permeability in the coal seam. It is established that methane release from block media of coal seam is conditioned by the development of cracks oriented along the maximal basic system of formed cracks followed by formation of systems of new cracks in the domain of seam hydro-impacting where the rate of gas release and its distribution within the blocks of coal under optimal impact frequencies is estimated by values of the order of 30-40 Hz (Pavlenko, 1999).

Science research-based methodical recommendations have been proposed on the selection of appropriate technological systems to control the gas release through a comprehensive impact. These systems take into account the parameters of a coal seam; this determines a selection of frequency characteristics of the coal seam to ensure the required degree of gas release from the coal seam when preparing the array of rocks, up-to-date speeds of preparatory excavations, as well as a high load on coal slaughtering. A technology of vibration impacts on gas-bearing coal seam has been developed.

Acknowledgements

The work was performed pursuant to the geological tasks to carry out the works in the Pechora coal basin on the facility of open society "Vorkutaugol": "Experimental and methodical works on estimation of the resources and development of technologies for extraction of coal methane".

References

- Pavlenko, M. V. (1999) Characteristics of methane release from coal using wave action. *Sat. Trudy inst. "Modern problems of coal mine methane"*. Moscow state mining University. pp. 203-205.
- Shcherban, A. N., Cerulnikov, A. S. (1958) *Gas Permeability of coal seams*. Kiev: Nauka, 79 p.
- Rodionov, V. N, Spivak, A. A., Tsvetkov, V. M. (1976) Method of determining filtration properties of rocks in the array. *Physical-technical problems of development of mineral resources*. No. 5, pp. 92-96.
- Ettinger, I. L. (1966) *Gas capacity fossil coal*. Nedra.

ACOUSTIC FREQUENCIES OF COOLANT IN PRIMARY CIRCUIT OF NPP TEMELIN AND POSSIBILITY OF RESONANCES WITH FUEL ASSEMBLY TVSA-T

L. Pečínka*, M. Švrček*

Abstract: *On the basis of electromechanical analogy is as criterion of possible interaction of acoustic waves in primary circuit of NPP Temelin derived so-called quality factor Q . The Q value determines a range of coolant acoustic frequencies in which there is a natural frequency of fuel assembly and in which resonance is realized. The range of fuel assembly frequency is named as pass band. Estimated values of Q and pass band are given. The developed methods algorithms of calculation and quantitative estimations of coolant pulsation frequencies, Q factor and pass band allow developing coolant parameter control actions necessary for prevention of resonances.*

Keywords: **Electromechanical analogy, Quality factor Q , Coolant acoustic frequencies, Fuel assembly natural frequency, Resonances.**

1. Introduction

In primary circuit of PWR reactors the three types of standing acoustic waves exist:

- in primary piping including steam generator and reactor,
- in primary piping, steam generator, reactor and pressurizer,
- only in the hot leg between output from reactor and input in pressurizer.

Calculation of eigen frequencies is possible to perform either using of electromechanical analogy (Pecinka, 2004) or solution of coolant momentum equation and Euler equation (Pecinka, 2006) in all possible operation states. From the experimental point of view the coolant pressure pulsation are measured using pressure sensors installed on the primary piping (cold leg and hot leg).

2. Electromechanical Analogy

Acoustic scheme of primary coolant in reactor core is illustrated in Fig. 1 where denote: R acoustic resistance, m acoustic mass, C acoustic compliance, V_0 volumetric coolant flow in reactor core, ΔP pressure drop in reactor core.

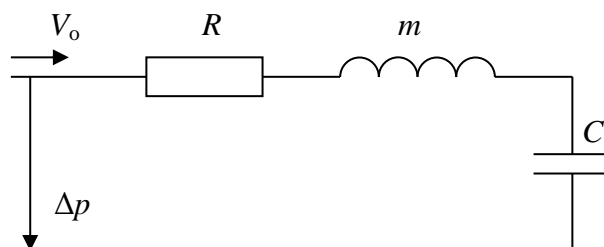


Fig. 1: Acoustic scheme of coolant in reactor core.

Analogy between acoustic and electronic parameters is illustrated in next Tab. 1.

* Ing. Ladislav Pečínka, CSc.: ÚJV Řež, a. s.; Hlavní 130, 250 68 Husinec-Řež; CZ, ladislav.pecinka@ujv.cz

** Ing. Miroslav Švrček: ÚJV Řež, a. s.; Hlavní 130, 250 68 Husinec-Řež; CZ, miroslav.svrcek@ujv.cz

Tab. 1: Electromechanical analogy.

Acoustical hydraulic parameters			Electrical parameters		
Parameters	Symbol	Dimension	Parameter	Symbol	Dimension
Pressure drop	ΔP	N m^{-2}	Voltage	U	Volt
Volumetric flows	V_0	$\text{m}^3 \text{s}^{-1}$	Current	I	Ampere
Acoustic compliance	C	$\text{m}^4 \text{s}^2 \text{kg}^{-1}$	Capacitance	C	Farad
Acoustic mass	m	kg m^{-4}	Inductance	L	Henry
Acoustic resistance	R	$\text{kg s}^{-1} \text{m}^4$	Active resistance	R	Ohm
Differential characteristic resistance	R_d	$\text{kg s}^{-1} \text{m}^4$	Differential characteristic resistance	Z_c	Ohm

3. Resonance Operational State of Pressure Pulsations in Primary Circuit Induced by Sinusoidal Changes of Volumetric Flow

Two types of resonant operation states exist (Proskuriakov, 2013):

- main, i.e. resonance states of pressure pulsations,
- parallel, i.e. resonance states of volumetric flow.

Resonance operation state exists in such case, when acoustic mass and acoustic compliance are in series, see Fig. 1. In such case the following equations are valid (Gependin, 1974).

$$Z_{inlet} = R + i\left(m\omega - \frac{1}{C\omega}\right), \quad (1)$$

$$P_{inlet} = V_0 \cdot Z_{inlet}, \quad (2)$$

$$Z_{inlet} = \sqrt{R^2 + \left(m\omega - \frac{1}{C\omega}\right)^2} = \sqrt{R^2 + X^2}, \quad (3)$$

where $X = m\omega - 1/(C\omega)$.

The resonance condition requires zero of reactive component of input resistance, i.e. $X_{input} = 0$ and $Z_{input} = R_{input}$. After some rearrangement equation (2) takes the final form:

$$V_0 = \frac{\Delta P_{input}}{\sqrt{R^2 + \left(m\omega - \frac{1}{C\omega}\right)^2}} = \frac{\Delta P_{input}}{\sqrt{R^2 + X^2}}. \quad (4)$$

4. Derivation of the quality factor Q

Quality factor Q is defined as ratio of the pressure on the element m or C (see Fig. 1), i.e. P_{m0} or P_{e0} to the input pressure P_{inlet0} . In the case when characteristic resistance Z_c (see Table 1) represent resistance of the acoustic compliance or acoustic mass in the resonant state, i.e. if:

$$Z_c = m\omega_0 = \frac{1}{\omega_0 C} = \sqrt{\frac{m}{C}}, \quad (5)$$

where $\omega_0 = (mC)^{-1/2}$ then using equations (2), (4) and (5) after some rearrangement we obtain:

$$Q = \frac{P_{m0}}{P_{inlet0}} = \frac{P_{C0}}{P_{inlet0}} = \frac{V_{0,0} Z_c}{V_{0,0} R} \Rightarrow P_{m0} = Q \cdot P_{inlet0}; P_{C0} = Q \cdot P_{inlet0} = \frac{\sqrt{\frac{m}{C}}}{R} = \frac{Z_c}{R}. \quad (6)$$

Volumetric flow ratio to volumetric flow in the resonant operation state (V_0 / V_{inlet}) depend on the angular frequency ω . After some rearrangement the following equation takes the form:

$$V_1 = \frac{\Delta P_{inlet}}{\sqrt{R^2 + \left(m\omega - \frac{1}{C\omega}\right)^2}} = \frac{\Delta P_{inlet}}{R\sqrt{1 + \frac{1}{R^2}\left(m\omega - \frac{1}{C\omega}\right)^2}} = \frac{V_{0,0}}{\sqrt{1 + \frac{R_C^2}{R_0^2}\left(\frac{\omega}{\omega_0} - \frac{\omega_0}{\omega}\right)^2}}$$

$$V_1 = \frac{V_{0,0}}{\sqrt{1 + Q^2\left(\frac{\omega}{\omega_0} - \frac{\omega_0}{\omega}\right)^2}}. \quad (7)$$

As the result we obtain:

$$\frac{V_0}{V_{input}} = \frac{1}{\sqrt{1 + Q^2\left(\frac{\omega}{\omega_0} - \frac{\omega_0}{\omega}\right)^2}} = \frac{1}{\sqrt{1 + \frac{X_{input}^2}{R^2}}}, \quad (8)$$

where $X_{input} = \omega m - 1/(C\omega)$.

Resonance curves of the coolant volumetric flow are illustrated on the Fig. 2.

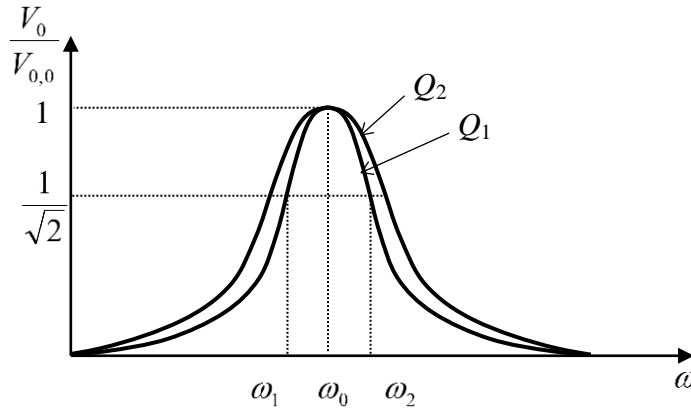


Fig. 2: Resonant curves of the coolant volumetric flow.

5. Definition of the Frequency Pass Band

According Fig. 2, the frequencies ω_1 and ω_2 defined the frequency pass band based on the ratio $V_0/V_{0,0} = 0.707$. As the result can be written:

$$\frac{V_0}{V_{0,0}} = \frac{1}{\sqrt{1 + \frac{1}{R^2} X_{vstup}^2}} = \frac{1}{\sqrt{2}}. \quad (9)$$

Finally $1 + X_{input}^2/R^2 = 2 \Rightarrow X^2/R^2 = 1 \Rightarrow X = R$.

Correlation between bounding frequencies ω_1 , ω_2 , resonant frequency ω_0 and Q factor may be derived as follows:

$$\frac{V_0}{V_{0,0}} = \frac{1}{\sqrt{1 + Q^2\left(\frac{\omega}{\omega_0} - \frac{\omega_0}{\omega}\right)^2}} = \frac{1}{\sqrt{2}}, \quad \frac{\omega_{1,2} - \omega_0}{\omega_0} = \pm \frac{1}{Q}, \quad \text{where } \omega_1 < \omega_0 < \omega_2.$$

As the result we obtain:

$$\begin{aligned}\frac{\omega_2}{\omega_0} - \frac{\omega_0}{\omega_2} &= +\frac{1}{Q}, \\ \frac{\omega_1}{\omega_0} - \frac{\omega_0}{\omega_1} &= -\frac{1}{Q}.\end{aligned}\quad (10)$$

After some rearrangement as the results we obtain:

$$\omega_0 = \sqrt{\omega_1 \omega_2}, \quad (11)$$

$$Q = \frac{\omega_0}{\omega_1 - \omega_2}. \quad (12)$$

Assessment of the reactor V1000 ETE core Q factor using equation (4) and (6), the Q factor is defined as:

$$Q = \frac{\sqrt{\frac{m}{C}}}{\frac{\Delta P}{V_0}}. \quad (13)$$

The following expressions may be used (Pecinka, 2004):

$$m = \frac{\rho \cdot l}{A}; \quad C = \frac{A \cdot l}{\rho \cdot c^2}.$$

As the result we obtain:

$$Q = \frac{\rho \cdot c \cdot V_0}{\Delta P \cdot A}. \quad (14)$$

In the next will be performed application to core of reactor V1000 ETE in level A Service limit. Input data of coolant and core are follows: $\rho = 726 \text{ kg}\cdot\text{m}^{-3}$; $c = 940 \text{ m}\cdot\text{s}^{-1}$; $A = 7.84 \text{ m}^2$; $\Delta P = 0.5 \text{ MPa}$; $V_0 = 23.6 \text{ m}^3\cdot\text{s}^{-1}$.

As the results we obtain quality factor $Q = 4.1$. The lowest acoustic frequency of the coolant in the loop without pressurizer is $f_0 = 6.95 \text{ Hz}$ (Pecinka, 2006). Using equation (12) the related frequency pass band is $f_2 - f_1 = 6.95 / 4.1 = 1.7 \text{ Hz}$. The first bending frequency of the fresh fuel assembly is 4.94 Hz . According Fig. 2 left and right half of the frequency pass band is $1.695 / 2 = 0.85 \text{ Hz}$. It means that the lower boundary of the frequency band is $4.97 - 0.847 = 4.123 \text{ Hz}$ and upper boundary is $4.97 + 0.847 = 5.82 \text{ Hz}$. We can conclude that coolant frequency 6.95 Hz is out of frequency pass band.

Similar situation exists for the loop with pressurizer and the fuel assembly at the end of fuel cycle. In this case the lowest frequency is 1.066 Hz (Pecinka, 2004) and the first bending frequency of the fuel assembly decrease to 2.63 Hz . Using the same methodology as in previous case, the upper frequency of the frequency pass band is 1.19 Hz . It means that the fuel assembly 2.63 Hz is out of the frequency pass band.

6. Conclusion

Using electromechanical analogy the so called quality factor Q has been derived as the criterion of the acoustic waves interaction with reactor internals. This methodology represents specific branch in fluid-structure interactions. Practical applications exist in PWR reactors of Russian type.

References

- Pecinka, L. (2004) Assessment of acoustic frequencies in primary circuit of NPP Temelin, units 1 and 2. Report UJV Rez, (in Czech).
- Pecinka, L. (2006) Exact solution of acoustic resonant operation states in primary circuit of nuclear reactor. In: Colloquium Dynamics of Machines 2006, Prague, (in Czech).
- Proskuriakov, K. N. (2013) Elimination of resonant vibrations of fuel assemblies with coolant acoustic pulsations. Private communication, (in Russian).
- Lebedin, L. F. (1978) Acoustic, Moscow, University press, (in Russian).

MINIMISING OF THE OPERATION COSTS OF POWER TRANSFORMERS

D. Perczyński^{*}, P. Kolber^{**}, S. Wawrzyniak^{***}

Abstract: *The paper demonstrates the problem of profitability of 15/0.4 kV transformers replacement. The transformers work with a small coefficient of peak loads on the units with a lower power rating. The discussion includes fixed and variable costs of the transformers and the costs of their replacement under operating conditions.*

Keywords: Power transformer, Operating costs, Peak load coefficient.

1. Introduction

Power distribution networks are an important part of power system. The networks are characterised by a large number of network devices and receiving nodes. They are time-varying complex dynamic systems. The way of distribution networks operation significantly affects the quality of the power system operation. This is due to their significant participation in fixed assets system, high labour consumption of operating procedures as well as the decisive influence on the efficiency and reliability of electricity supply. They are also the cause of most of losses in the power system.

MV/LV (middle voltage / low voltage) transformers are the important component of power distribution networks. This is due to a significant number of these network elements operating in the public power system.

MV/LV transformers, unlike other basic components of power distribution networks, are easily replaceable and their durability does not change in the result of replacement. Even this feature indicates that they might be adjusted more often to the current load. Operating costs of replaced the transformer depend on peak load. The costs consist of: an amortization cost, costs of idle state losses, load costs, and cost of transformer replacement.

Considering that the economic losses caused by inappropriate use of MV/LV transformers can be significant, the proper selection of transformers becomes a major economic problem. Therefore, examine this issue theoretically as well as lay the foundations to develop practical guidelines of cost-effectiveness of transformer (with a low coefficient of peak power use) replacement can result in significant economic benefits.

2. Costs of Transformer Operating

Changes in the costs of energy transformation of one transformer, depending on the value of its peak load (S_p), are parabola. In diagram of changes in the costs of energy transformation of transformers with different nominal power rating, the parabolas intersect at the point that designates the so-called limit load S_g . Under that load, the annual costs of energy transformation of transformer with a lower power rating are lower than the annual costs of energy transformation of transformer with a higher power rating (Fig. 1.)

^{*} Assist. Prof. Daniel Perczyński, PhD.: Institute of Transport and Machine Operation, University of Technology and Life Sciences, Kaliskiego 7/2.3; 85 789, Bydgoszcz; Poland, daniel.perczynski@utp.edu.pl

^{**} Assist. Prof. Piotr Kolber, PhD.: Institute of Transport and Machine Operation, University of Technology and Life Sciences, Kaliskiego 7/2.3; 85 789, Bydgoszcz; Poland, piotr.kolber@utp.edu.pl

^{***} Assist. Prof. Sylwester Wawrzyniak, PhD.: Institute of Transport and Machine Operation, University of Technology and Life Sciences, Kaliskiego 7/2.3; 85 789, Bydgoszcz; Poland, sylwester.wawrzyniak@utp.edu.pl

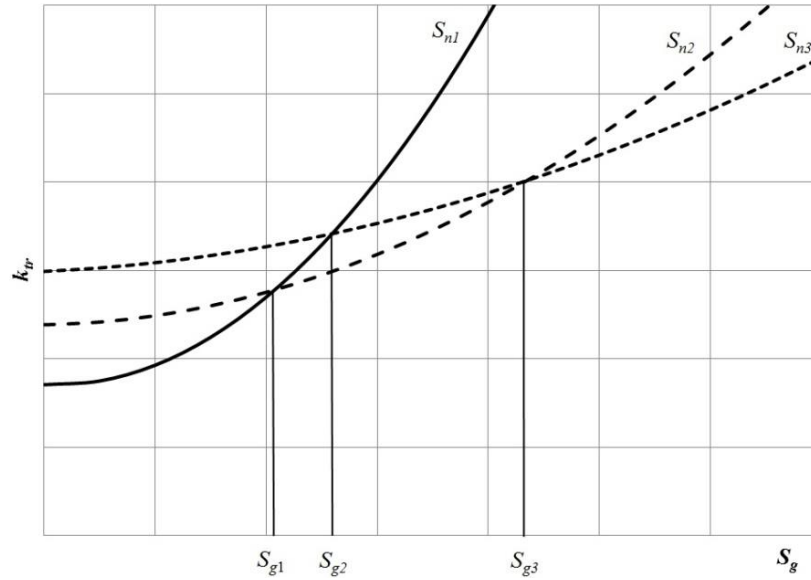


Fig. 1: The costs of energy transformation (k_{tr}) depending on peak load for transformers with power rating $S_{n1} < S_{n2} < S_{n3}$.

Total annual costs of transformation can be presented by the following formula (Niewiedział et al., 1998):

$$K_r = K_e^{st} + K_e^{zm}, \quad (1)$$

whereas annual fixed operating cost of transformer can be calculated from the following equation (Konstanciak, 2000):

$$K_e^{st} = K_n \cdot r_{et} \quad (2)$$

where:

r_{et} – coefficient of fixed operating costs:

$$r_{et} = r_{remt} + r_{ut} + r_{ost} \quad (3)$$

r_{remt} – share of renovation costs in total investment outlays,

r_{ut} – share of maintenance costs in total investment outlays,

r_{os} – share of personnel costs in total investment outlays.

Components of operating variable costs K_e^{zm} show the following equation (Marzecki, J., 1996):

$$K_e^{zm} = (\Delta P_j + k_e Q_o) T_p c_{\Delta A} + (\Delta P_{Cu} + k_e \cdot Q_{obc}) \tau \cdot c_{\Delta A} \left(\frac{S_s}{S_n} \right)^2 \quad (4)$$

where:

ΔP_j – nominal power rating losses in the idle state of transformer expressed in [kW],

ΔP_{Cu} – nominal load losses of transformer expressed in [kW],

Q_o – reactive power consumed by transformer at idling operation expressed in [kvar],

Q_{obc} – reactive power losses of transformer at nominal load expressed in [kvar],

k_e – the energy equivalent of reactive power expressed in [kW/kvar],

T_p – annual working time of transformer expressed in [h/year],

τ – annual calculated duration of the maximum loss expressed in [h/ year],

S_s – annual peak load of transformer expressed in [kV·A],

S_n – nominal power of transformer expressed in [kV·A],

$c_{\Delta A}$ – unit cost of energy to cover losses expressed in [PLN/kWh].

Power network should be considered, except in special cases, as an object of unlimited operating time that adapts to the load increment. The basic value of output for planning work of transformers in power stations is the value and increase in peak load as a function of time. With an adoption of exponential growth model of station peak load, the coefficient $k(t)$ takes the form:

$$k(t) = \left(1 + \frac{\alpha_w}{100}\right)^t = (1 + \alpha_w)^t \quad (5)$$

where:

- α_w – annual relative increase in transformer load expressed in [1/year],
- T – subsequent years of transformer operation.

For operating transformer, total annual costs amount in each year:

$$K_r(t) = K_n \cdot r_{et} + (\Delta P_j + k_e Q_o) I_p \cdot c_{\Delta A} + (\Delta P_{Cu} + k_e Q_{obc}) \cdot \tau \cdot c_{\Delta A} \left(\frac{k(t) S_{so}}{S_n}\right)^2 \quad (6)$$

where:

- S_{so} – peak load of transformer in the year of replacement to a different unit.

The equation (6) can be written as:

$$K_r(t) = K_n \cdot r_{et} + (\Delta P_j + k_e Q_o) I_p \cdot c_{\Delta A} + (\Delta P_{Cu} + k_e Q_{obc}) \cdot \tau \cdot c_{\Delta A} \cdot \beta_s^2 \cdot k^2(t) \quad (7)$$

where:

- β_s – load factor of currently operating transformer during peak load in the year of replacement.

Costs in the electrical power engineering are usually calculated as annual costs for one year which is a basic accounting period. When considering longer periods, the total costs are the sum of discounted costs for subsequent years of accounting period. Summing the costs depends only on two factors of the cost equation: the inverse of the discount rate and relation of squared coefficient of the load growth over the discount rate. Formulas containing these factors with an assumption of exponential model of peak load growth, take the form:

$$D = \sum_{t=1}^{t=T} \frac{1}{q^t} = \frac{q^T - 1}{q^T (q - 1)}, \quad E = \sum_{t=1}^{t=T} \frac{k^{2t}}{q^t} = \frac{k^2 (k^{2T} - q^T)}{q^T (k^2 - q)} \quad (8)$$

where:

- $q = 1 + p$ - discounting factor.

After considering the above data, the equation describing annual costs of transformer operation in the station takes the form:

$$K_r = K_n \cdot r_{et} + (\Delta P_j + k_e Q_o) I_p \cdot c_{\Delta A} \sum_{t=1}^{t=T} \frac{1}{q^t} + (\Delta P_{Cu} + k_e Q_{obc}) \cdot \tau \cdot c_{\Delta A} \cdot \beta_s^2 \cdot \sum_{t=1}^{t=T} \frac{k^{2t}}{q^t} \quad (9)$$

The period of transformer operation at the station (T) is determined by economic criteria while maintaining the technical condition. If for the condition for the maximum load factor of the transformer in the final year of operation at the station accept β_{sk} , then the period of operation T is a result of the following relation:

$$T \leq \frac{\ln(1 + \beta_{sk} - \beta_s)}{\ln(1 + \alpha_w)} \quad (10)$$

By entering to the equation (7) index 1 for currently operating transformer and index 2 for replaced transformer (smaller that replaces the existing one) and considering the relation (8), the following equation has been obtained:

$$K_{r1} = K_{n1} \cdot r_{et} + (\Delta P_{j1} + k_e Q_{o1}) I_p \cdot c_{\Delta A} \cdot D_1 + (\Delta P_{Cu1} + k_e Q_{obc1}) \cdot \tau \cdot c_{\Delta A} \cdot \beta_{s1}^2 \cdot E_1 \quad (11)$$

$$K_{r2} = K_{n2} \cdot r_{et} + (\Delta P_{j2} + k_e Q_{o2}) T_p \cdot c_{\Delta A} \cdot D_2 + (\Delta P_{Cu2} + k_e Q_{obc2}) \cdot \tau \cdot c_{\Delta A} \cdot \beta_{s2}^2 \cdot E_2 + K_w \quad (12)$$

where:

K_w – cost of transformer replacement.

Considering described values of equivalent annual costs of the transformer currently operating at the station and its replacement, the form of criterion functional is defined as:

$$F = K_{r1} - K_{r2} \quad (13)$$

The dependence of sample values of F functional of replacement transformer power rating on replaced the transformer data: $\beta_{s1} = 0.2$, $K_w = 1200$ PLN, $S_{so} = 50$ kVA ($S_{n1} = 250$ kVA), $\alpha_w = 0.03$, $\beta_{sk} = 1$, $\tau = 2500$ h is shown in Fig. 2.

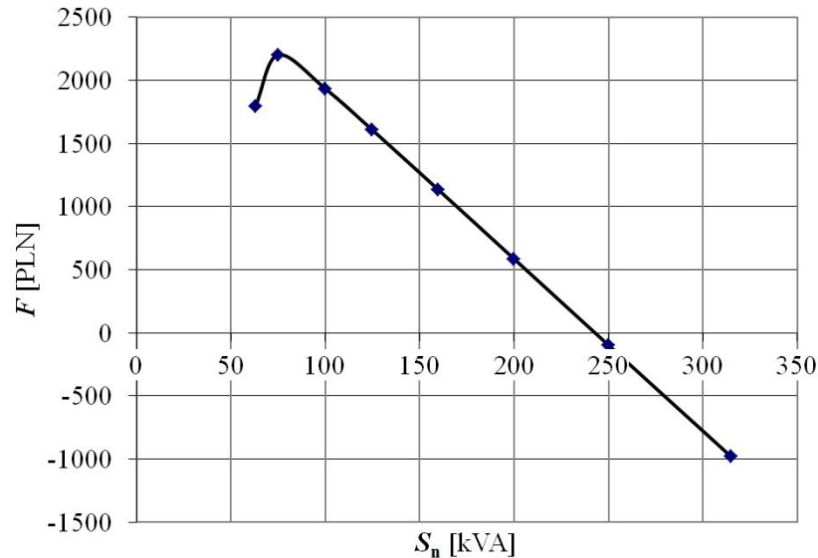


Fig. 2: The dependence of F functional values on transformer power rating.

3. Conclusions

Analysis of obtained results shows that significant number of power transformers operate with low coefficient of peak load. This situation affects the significant economic losses. Determination of the actual costs level of transformers MV/LV operating in the current method of accounting is very difficult. The existing statistics do not provide a precise registration cost components. In subject references (Konstanciak, 2000) there are very different values of constant operating costs coefficients r_c (from 7 to 4.9). Made an attempt to determine particular constant operating costs of Distribution Company shown that coefficient r_c is about 5% of the investment value for analyzed transformer.

The analysis shows that it is profitable to replace a transformer on a one with a lower power rating (in case of underload of currently operating transformer) and the optimum value of the peak load coefficient of replaced the transformer is a function of many variables and is in the range 0.8 – 0.92.

References

- Marzecki, J. (1996) Urban Power Networks. Oficyna Wydawnicza Politechniki Warszawskiej, Warszawa (in Polish).
- Konstanciak, M. (2000) Economic use if transformers – minimisation of transformation costs. Wydawnictwo Polskie Towarzystwo Przesyłu i Rozdziału Energii Elektrycznej, Poznań (in Polish).
- Niewiedział, E., Niewiedział, R. (1998) Analysis of effectiveness of the use of selected technical solutions distribution network MV and LV. Zeszyty Naukowe Politechniki Poznańskiej, Poznań, pp. 67-85 (in Polish).

SOLVING ANCHORAGE AREA PRESTRESSED AND NONPRESTRESSED COMPOSITES

L. Podolka*

Abstract: Paper present carry out experimental test for assessment behaviour composites in anchorage area because of element bond in cutting in beam or by rote anchorage. Will be make mathematical models in programm ATENA. Results experimental test and mathematical models will be comparing. Results are design method for determination anchorage length practice.

Keywords: Composites, Anchorage, Strengthening.

1. Introduction

Of mid-1990s use nonprestressed composites (FRP strips) for strengthening structures throughout world as well as Czech Republic. Experiences obtain on strengthening structures and practise experimental test make for result, that for utilize material property composites and for increasing effectiveness strengthening structures have to need use FRP strips, as that of prestressed reinforcement in the form of reinforcement noncohesion (loose cable). By reason of safety so that do need mechanical failure FRP strips, there are bond in the entire area.

2. Descripton Experimental Test Make to in Laboratory KÚ ČVUT

For verification new prestressed system firm STADO CZ, Ltd. will be make experimental test in laboratory KU ČVUT in Prague. System is construct of tensive apparatus made in firm “Chartered metrological centre K 103”, Čechova 20, Prague 7 (Mr. Josef Hajek), mechanical anchorage elements, two steel plates thickness 15 mm size 150*168 mm, six chemical anchorage M12 (inactive anchorage), so-called “tray” to which put upon active anchorage with drawing gun. Drawing gun it can be append to mechanical “hand” piston or press. The experimental element consisted of the reinforced concrete beam (250*350*1800mm) made of concrete B 30 according to the Czech Standard CSN 73 1201. Beam has to cutting size 170 x 350 mm depths 15 mm for inactive anchorage and cutting size 900*350 mm depths 20 mm for active anchorage with drawing gun. Tension strip have to take around step by step 7 kN so far maximum force 70 kN, that will be voted by standard strip from offer firm STADO CZ, Ltd. type S, size 50*1,4 mm with Young’s modulus $E = 150$ GPa and tensile strength $\sigma_t = 2000$ MPa. At tension strip will be monitoring strain strip, compression concrete and pressure into exit from mechanical press. Along expiry tension and anchorage FRP strip in active anchorage will be for eight week measuring slip strip in anchorage, change strain concrete (compression) and strain strip.

In laboratories KU ČVUT in Prague experimental tests were conducted with FRP reinforcement glued into the grooves. Experiments have shown that the fins affixed to the groove occurs approximately twofold increase in the anchoring force to anchor the same length compared to the slat affixed only on the lower face of the beam. Experimental tests were conducted on samples of three different classes of concrete (C 20/25, C 30/37 C 40/50) and three different anchor lengths (100 mm, 150 mm and 200 mm), a total of 27 samples were tested. The results were compared with similar results from 2001, when the samples were tested with slats glued to the surface.

The beam size 120*180 mm length 2000 mm of concrete C 20/25 XC1 reinforced bending 2*2 Ø R14, stirrups Ø R6/150 mm of length 2 m beam was amplified in the groove located FRP profile

* Assoc. Prof. Dr. Ing. Luboš Podolka: Institute Department of Civil Engineering, University of Technology and Economics in Czech Budejovice, Street Circular No. 517/30; 370 01, Czech Budejovice; CZ, podolka@mail.vstecb.cz

Ø 8 mm length 1700 mm. The beam before amplification was loaded at the moment of crack width of 0.2 mm and under this load then amplified beam and subsequently for about 24 hours, the load held on the same strength in the adhesive to harden. The beam was loaded until further violations.

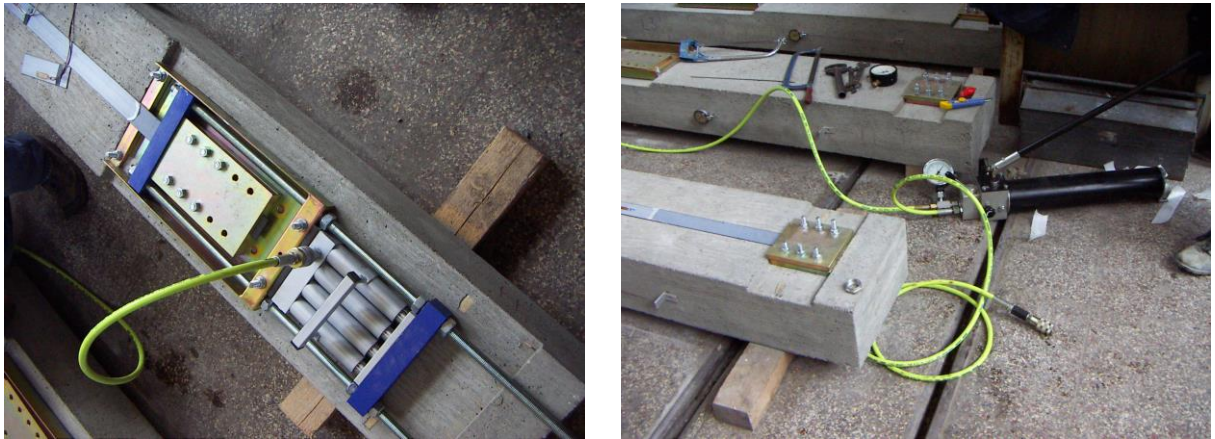


Fig. 1: Detail drawing gun, (four coupled piston all of piece) and mechanical piston.

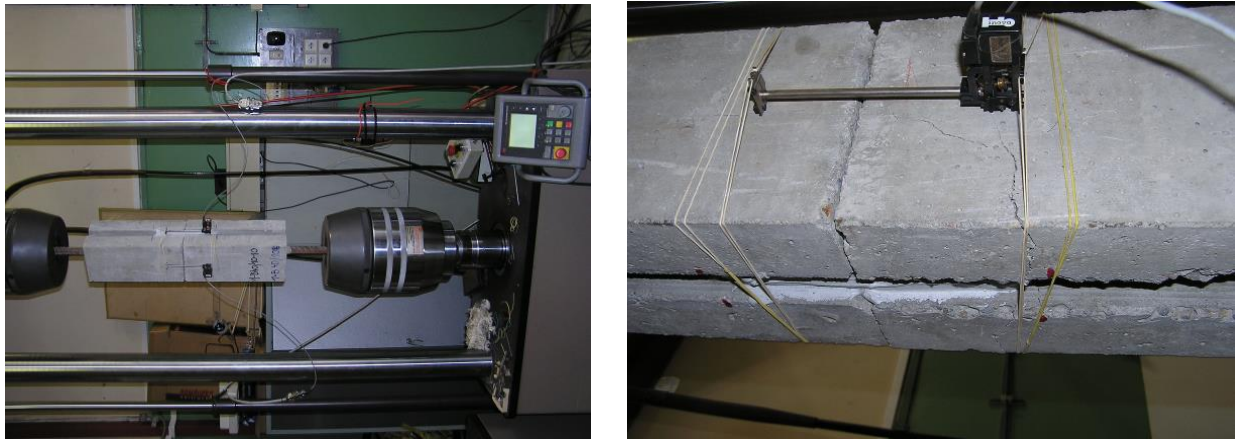


Fig. 2: Sight to experimental test, detail failure element.



Fig. 3: Pictures experimental element, respectively. Detail the damaged beam.

3. Check on Experimental Data Upon Model Make to Programm Atena

Above describe experimental element will be model in programm ATENA, that will be have to monitoring behaviour element at point active and inactive anchorage, i.e. transmission force from strengthening strip by mechanical anchorage to the concrete and propagation stress in concrete near anchorage. Flexion strain concrete beam gauge on experimental test in axis has been 0.005 - 0.007 mm by up to auxiliary aiming longitude 500 mm, e.i. $\varepsilon = 0.00001$.

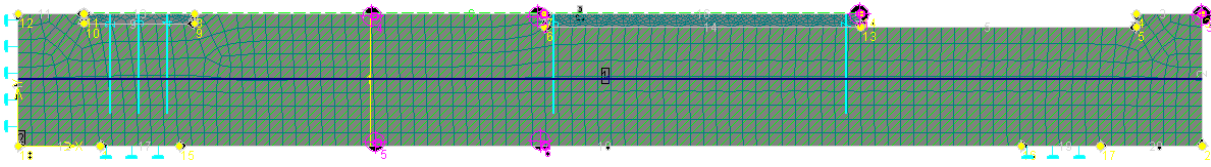


Fig. 4: Sight experimental model in program ATENA.

The above described experimental element was modeled program ATENA, so that it can monitor the behavior of the element in place anchorage reinforcing reinforcement, i.e., the force transmission from the glued reinforcing FRP reinforcing bars and concrete stress propagation in the groove.

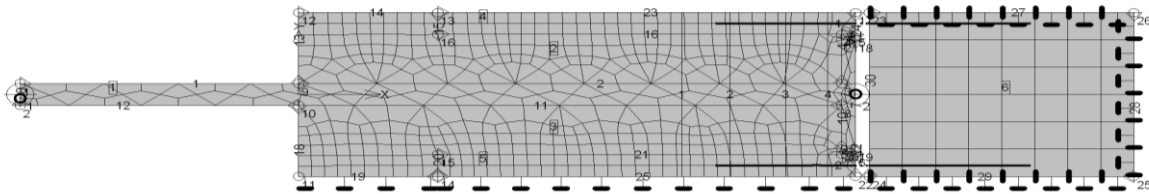


Fig. 5: Sight experimental model in program ATENA.

The above described experimental element was modeled in program ATENA, so that it can monitor the behavior of the element in place both active and passive anchors, i.e. power transfer from reinforcing bars through mechanical anchoring to the concrete and spread stresses in the concrete for anchors. Resp. the beam reinforced reinforcement glued in the groove spreading around enhancing tension reinforcement and transmission over the glued joints to crosslinking element.

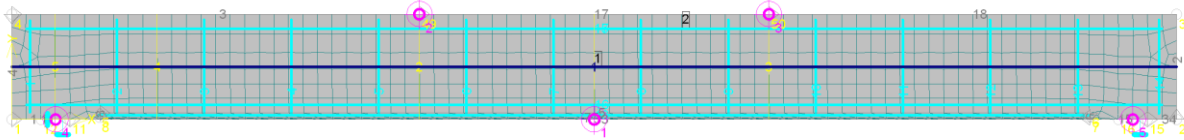


Fig. 6: View of the experimental model of program ATENA.

4. Power Transferred Anchorage:

a) for $l_v < 115$ mm

$$F_{v,k} = b_f \cdot \tau_{k,k} \cdot \sqrt[4]{a_r \cdot l_v} \cdot (0.4 - 0.0015l_v) \cdot \frac{E_f}{E_{f,prum}} \quad (1)$$

$$\tau_{k,k} = \sqrt{\left(2 \cdot f_{kt,k} - 2 \cdot \sqrt{(f_{kt,k}^2 + f_{kc,k} \cdot f_{kt,k})} + f_{kc,k}\right) f_{kt,k}} \quad (2)$$

- $f_{kt,k}$ - characteristic strength of the adhesive strength in N/mm^2 ,
- $f_{kc,k}$ - characteristic strength of the adhesive pressure in N/mm^2 ,
- a_r - spacing from the free edge of the workpiece in mm (max. 150 mm),
- l_v - anchor length,
- E_f - modulus slats guaranteed,
- $E_{f,prum}$ - average modulus of elasticity of the slats.

For experimentation can be considered:

$$f_{kt,k} = 16 N/mm^2, f_{ct,k} = 75 N/mm^2, \tau_{k,k} = 22.16 N/mm^2, a_r = 75 mm, b_f = 6 mm, t_f = 6 mm, \\ l_v = 100 mm, E_f = 150 GPa, E_{f,prum} = 180 GPa, \rightarrow F_{v,k} = 8143.8 N, \text{ for two rods } 16287.6 N,$$

Force measured in the experiment of $F_{exp} = 29.7$ kN, Force from the calculation $F_{vyp} = 16.3$ kN

$$s = \frac{F_{\text{exp}}}{F_{\text{vyp}}} = \frac{29.7}{16.3} = 1.82$$

Security design patterns :

b) for $l_v > 115$ mm

$$F_{v,k} = b_f \cdot \tau_{k,k} \cdot \sqrt[4]{a_r} \cdot \left(26.2 + 0.065 \cdot \tanh\left(\frac{a_r}{70}\right) (l_v - 115) \right) \cdot \frac{E_f}{E_{f,prum}} \quad (3)$$

$$T_k = T_{\text{max},k} \cdot \frac{l_t}{l_{t,\text{max}}} \cdot \left(2 - \frac{l_t}{l_{t,\text{max}}} \right) \quad (4)$$

$$T_{k,\text{max}} = 0.225 \cdot b_f \cdot \sqrt{E_f \cdot t_f} \cdot \sqrt{f_{ck} \cdot f_{ctm}} \quad (5)$$

$$l_{t,\text{max}} = 1.46 \cdot \sqrt{\frac{E_f \cdot t_f}{\sqrt{f_{ck} \cdot f_{ctm}}}} \quad (6)$$

$T_{k,\text{max}}$ - maximum power transferred in the anchorage,

$l_{t,\text{max}}$ - max corresponding bond length for power $T_{k,\text{max}}$,

l_t - of the proposed anchorage length,

b_f - slat width or diameter in mm rods,

t_f - segment thickness or diameter in mm rods,

E_f - guaranteed modulus slats or bars,

f_{ctm} - tensile strength of concrete, or strength value measured in the exhaust test of the concrete surface,

f_{ck} - characteristic value of the cylinder compressive strength of concrete.

5. Conclusions

For experiments with sealed rod showed the possibility of replacing the front discs glued laminated rod into the groove, the effectiveness of the same surface anchoring plates and rods is about 1.5 to 2 times.

Using prestressed FRP rods increases their utilization to 60 up to 70 %, while the rod is glued into the groove used to 35 up to 40 % of its strength when there is a sufficient reserve of pressure in the crosslinked section. While normally glued lamella on the surface of the beam is used to 15 up to 20 % of its strength. Using the prestressing tendon is also eliminate distortion amplified structure , while non-prestressed FRP reinforcement either on the surface or in a groove only contribute to the enhancement in terms I. Limit state (carrying capacity) minimum increase stiffness .

In cooperation with STADO CZ, Ltd. offers dimensioning software for amplification using FRP rods glued in the groove or on the surface of glued lamellas. The other vendor FRP technology for strengthening concrete structures offering similar dimensioning software as a tool for planners.

Acknowledgement

I would like to thank Stado CZ Ltd. for the experimental samples and laboratory KU ČVUT in Prague.

References

CSN ENV 1992-1-1 Desing of concrete structures, Part 1 :General rules and rules for buildings.

ATENA program, Červenka Consulting Ltd. Na Hřebenkach 55, 150 00 Praha 5, Czech Republic.

FRP materials, STADO CZ Ltd. Oldřichovská 194/16, 405 02 Děčín 7, Czech Republic.

THE EFFECT OF THRESHOLD VALUE ON THE RESIDUAL FATIGUE LIFETIME OF RAILWAY AXLES

P. Pokorný*, L. Náhlík**, P. Hutař***

Abstract: The fatigue failure of railway axles could have unaccepted consequences. Because of safe operation, it is important to determine the residual fatigue lifetime. The railway axle could contain some cracks either from manufacturing process or from previous service operation. Present defectoscopy can reliably detect only relatively long cracks (longer than 2 mm), see Zerbst et al. (2012). In other words, there is a risk that the existing crack is not detected by defectoscopy. For conservative establishment of the residual fatigue lifetime the crack, which could be not detected by defectoscopy, must be considered. This paper deals with an effect of the threshold value of fatigue crack propagation on the residual fatigue lifetime of railway axles. Two very commonly used materials for railway axles EA1N and EA4T steels are considered. The results of this paper could be used for safer operation of railway axles.

Keywords: Railway axle, Threshold value, Fatigue crack, Residual fatigue lifetime.

1. Introduction

The railway axle is one of the most loaded parts of the whole train. Therefore, the residual fatigue lifetime of railway axle is significant for safe operation of the train. The place of the possible crack is assumed in the T-notch where equivalent stress reaches the maximum value, see Fig. 1. Fatigue crack grows perpendicular to the principal stress (Schijve, 2008) and according to (Ševčík et al., 2012) the shape of the crack is assumed to be semi-elliptical with changing ratios between semi-axis during fatigue crack growth. The fatigue crack propagation description is based on the stress intensity factor K approach, which is commonly used approach for establishing of the residual fatigue lifetimes of railway axles (Zerbst et al., 2012); (Madia et al., 2011). Predominantly loading of railway axle is caused by rotary bending, therefore, for the simplification only mode I of loading is considered.

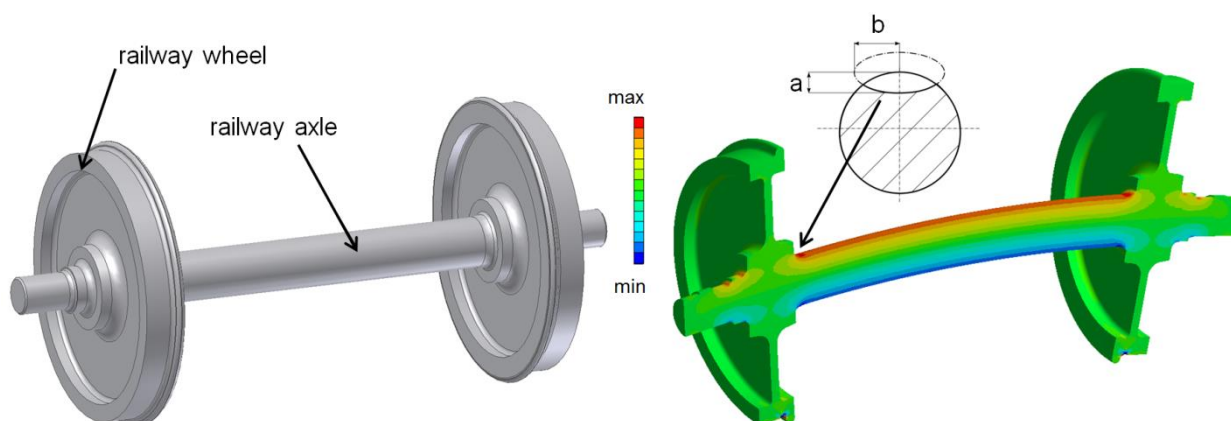


Fig. 1: The railway axle with considered crack (Pokorný et al., 2014).

* Ing. Pavel Pokorný.: Institute of Physics of Materials of the Academy of Sciences of the Czech Republic, v. v. i.; Žitkova 22; 616 62, Brno, CZ, Faculty of Mechanical Engineering, Brno University of Technology, Technická 2896/2, 616 69 Brno, CZ, pokorny@ipm.cz

** Assoc. Prof. Ing. Luboš Náhlík, PhD.: Institute of Physics of Materials, AS CR, Žitkova 513/22, 616 62, Brno, CZ, nahlik@ipm.cz

*** Assoc. Prof. Ing. Pavel Hutař, PhD.: Institute of Physics of Materials, AS CR, Žitkova 513/22, 616 62, Brno, CZ, hutar@ipm.cz

The stress intensity factor for mode I, K_I , is expressed as:

$$K_I = \sigma \sqrt{\pi a} Y_I(a), \quad (1)$$

where Y_I is function including the influence of railway axle and crack geometry. This function in polynomial form was obtained according to (Ševčík et al., 2012) by FEM modeling, a is crack length and σ is remote loading stress. The railway axles are subjected to variable amplitude loading. Predominantly loading is caused by weight of the vehicle, but there are additional forces acting during train movement. These forces arise when the train goes through curved track, over crossovers, switches etc. For accurate estimation of the residual fatigue lifetime the representative railway axle loading is necessary to know. The representative axle loading is often obtained by strain gage measurement. The typical load spectrum (sorted by Rain-flow method) is shown in Fig. 2.

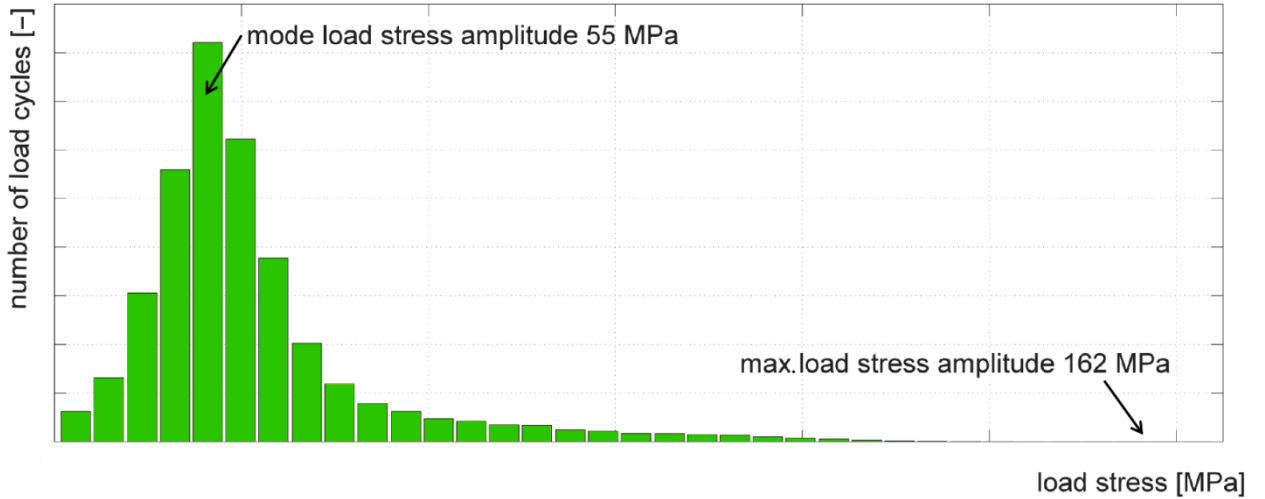


Fig. 2: Histogram of railway axle load spectrum (sorted into 35 classes of load amplitudes).

The place of considered crack is also influenced by press-fitted wheel, besides above mentioned railway axle load spectrum. The press-fit contributes to higher crack opening stress, so the total stress intensity factor K_{tot} is given as:

$$K_{tot} = K_I + K_{I,pressfit}, \quad (2)$$

where $K_{I,pressfit}$ is an additional stress intensity factor caused by presence of press-fit.

The additional stress intensity factor $K_{I,pressfit}$ can be expressed by polynomial function in the form:

$$K_{I,pressfit} = c_0 + c_1 a + c_2 a^2 + c_3 a^3 + c_4 a^4 + c_5 a^5 + c_6 a^6, \quad (3)$$

where determination of constants c_i is based on FEM modelling.

2. Estimation of the Residual Fatigue Lifetime

The residual fatigue lifetime is considered as number of cycles for crack growth from initial size to the critical one. For determination of number of cycles the Paris-Erdogan relationship is used:

$$\frac{da}{dN} = C(K_{tot})^m. \quad (4)$$

The crack increment is then obtained by integrating of Eq. 4. This equation is valid only for stress intensity factors greater than threshold value K_{th} . Otherwise, the increment of crack length is zero. Two very commonly used materials for railway axles, EA1N and EA4T steels, are assumed in this paper. Simplified v-K dependences of these materials are shown in Fig. 3.

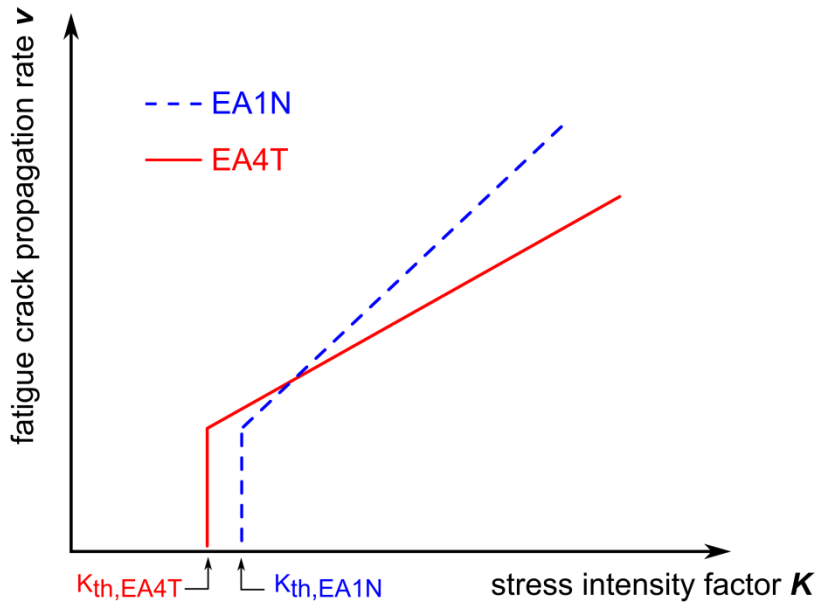


Fig. 3: Simplified v - K curves of considered materials (log-log representation).

2.1. Effect of different threshold values on the residual fatigue lifetime of railway axle

The threshold value is one of the most important inputs for establishing of the residual fatigue lifetimes of the railway axles. Although, the aim of manufactures is to produce material with the same chemical composition and mechanical properties, some scatter in material properties (e.g. threshold value K_{th}) between individual casts still exists. The next scatter is given by experimental establishment of threshold value K_{th} . Therefore, the determined residual fatigue lifetime could be different from the reality. Tab. 1 shows determined fatigue lifetimes for different threshold values K_{th} of EA4T steel. In case of initial crack length 1 mm the effect of different threshold value is greater than in case of initial crack length 2 mm. The EA1N is more sensitive on threshold value K_{th} than steel EA4T, see Tab. 2. For instance, the difference between $K_{th} = 6.8 \text{ MPa}\sqrt{\text{m}}$ and $K_{th} = 7.0 \text{ MPa}\sqrt{\text{m}}$ leads to residual fatigue lifetimes 1 481 000 km and 3 275 000 km, respectively. This implies that the incorrectly established threshold value by 3% leads to less than half of the original residual fatigue lifetime in this particular case.

Tab. 1: Residual fatigue lifetime in thousands of km for different considered threshold values (EA4T).

material EA4T							
considered K_{th} [$\text{MPa}\sqrt{\text{m}}$]	5	5.5	5.8	6*	6.2	6.5	7
thousands of km for fatigue crack growth from 1 mm to 55 mm	66	85	105	128	172	355	2 332
thousands of km for fatigue crack growth from 2 mm to 55 mm	46	50	54	58	63	71	93

Tab. 2: Residual fatigue lifetime in thousands of km for different considered threshold values (EA1N).

material EA1N							
considered K_{th} [$\text{MPa}\sqrt{\text{m}}$]	6	6.5	6.8	7*	7.2	7.5	8
thousands of km for fatigue crack growth from 1 mm to 55 mm	187	525	1 481	3 275	7 141	27 807	infinity
thousands of km for fatigue crack growth from 2 mm to 55 mm	68	82	94	104	116	142	240

* considered real mean threshold values

3. Discussion

The Fig. 4 shows evolution of threshold stress (stress expressed from Eq. 2 with substitution $K_{tot} = K_{th}$) in dependence on the crack length a . For initial crack lengths 1 mm and 2 mm respectively, many load stress amplitudes are under threshold value. According to Fig. 2 the mode load stress amplitude is 55 MPa. This stress corresponds to load by static weight of vehicle. However, stress amplitude 55 MPa gets over threshold value for cracks longer than 10 mm, see Fig. 4. Therefore, just only the several highest classes of load amplitudes (from histogram in Fig. 2) contribute to crack elongation for initial crack lengths 1 mm or 2 mm.

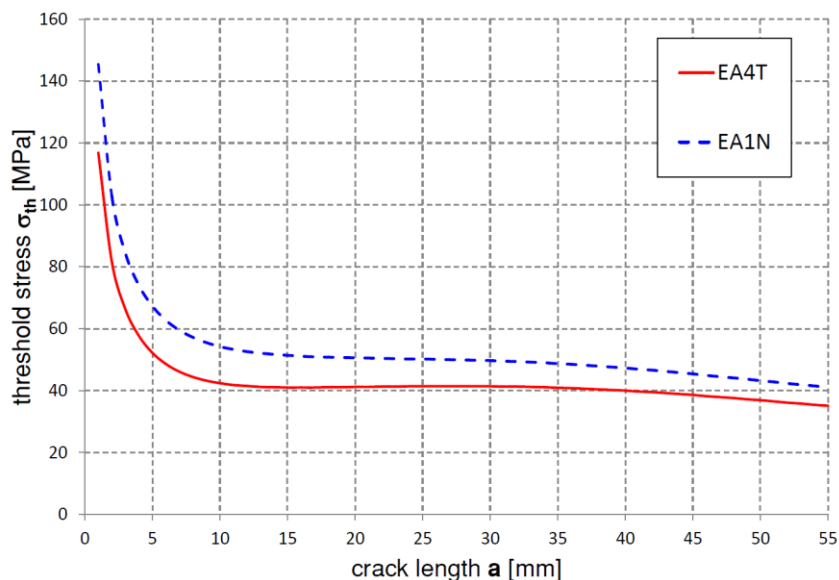


Fig. 4: Threshold stress σ_{th} in dependence on the crack length a .

4. Conclusions

This paper shows that threshold value is important input for estimation of the residual fatigue lifetime. Several computations with real and fictitious threshold values were carried out. The aim of this paper is to show difference between considered accurate threshold value and threshold values more or less deflecting of considered accurate one. The determined residual fatigue lifetimes exhibit relatively high sensitivity on accuracy of threshold values. This effect is more pronounced for material EA1N than for material EA4T. This sensitivity is smaller for longer cracks, see Tab.1 and Tab. 2. Therefore, the highest sensitivity is for railway axles made of EA1N steel with smaller initial crack. It follows that for accurate estimation of the residual fatigue lifetime the threshold value should be determined as precisely as it is possible.

Results obtained could be beneficial for better understanding of fatigue crack behavior in the railway axles.

Acknowledgement

This work was supported through the Specific academic research grant No. FSI-S-11-11/1190 provided to Brno University of Technology and grant No. CZ.1.07/2.3.00/20.0214 of the Ministry of Education, Youth and Sports of the Czech Republic.

References

- Zerbst, U. et al. (2012) Safe life and damage tolerance aspects of railway axles – A review. *Engng Fract Mech* 98, pp. 214-271.
- Schijve, J. (2008) *Fatigue of structures and materials*. New York: Springer
- Ševčík, M., Hutař, P., Zouhar, M., Náhlík, L. (2012) Numerical estimation of the fatigue crack front shape for a specimen with finite thickness, *International Journal of Fatigue* 39, pp. 75-80.
- Madia, M. et al. (2011) Stress intensity factor solutions for cracks in railway axles *Engng Fract Mech* 78, 5, pp. 764-792.
- Pokorný P., Náhlík L., Ševčík M., Hutař P. (2014) Effects of variable loading on residual fatigue life of the railway wheelset, *Key Engineering Materials Vols. 577-578*, pp. 121-124.

UTILIZING OF A WEIGHT-FIBRE-PULLEY-DRIVE MECHANICAL SYSTEM FOR THE INVESTIGATION OF A FIBRE BEHAVIOUR

P. Polach^{*}, M. Hajžman^{**}

Abstract: Experimental measurements focused on the investigation of a fibre behaviour are performed on an assembled weigh-fibre-pulley-drive mechanical system. The fibre is driven with one drive and it is led over a pulley. On its other end there is a prism-shaped steel weight, which moves in a prismatic linkage on an inclined plane. The position of the weight can be symmetric or asymmetric with respect to the vertical plane of drive-pulley symmetry. It is possible to add an extra mass to the weight. Drive exciting signals can be of a rectangular, a trapezoidal and a quasi-sinusoidal shape and there is a possibility of variation of a signal rate. Dynamic responses of the weight and the fibre are measured. The same system is numerically investigated by means of multibody models. The coincidence of results of experimental measurements and the simulations results is evaluated. The simulations aim is to create a phenomenological model of a fibre, which will be utilizable in fibre modelling in the case of more complicated mechanical or mechatronic systems.

Keywords: Fibre, Mechanical system, Dynamic response, Phenomenological model.

1. Introduction

The replacement of the chosen rigid elements of manipulators or mechanisms by fibres or cables (Chan, 2005) is advantageous due to the achievement of a lower moving inertia, which can lead to a higher machine speed, and lower production costs. Drawbacks of using the flexible elements like that can be associated with the fact that cables should be only in tension (e.g. Gosselin and Grenier, 2011) in the course of a motion.

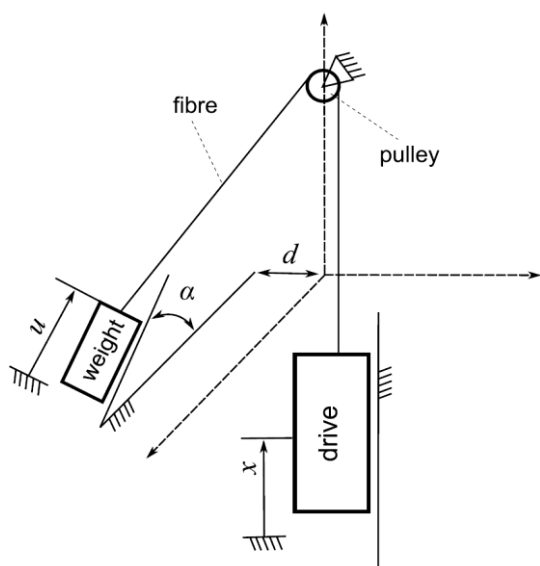


Fig. 1: Scheme and a real weight-fibre-pulley-drive mechanical system (asymmetric position of the weight).

^{*} Dr. Ing. Pavel Polach: Section of Materials and Mechanical Engineering Research, Výzkumný a zkušební ústav Plzeň s.r.o., Tylova 1581/46; 301 00, Plzeň; CZ, polach@vzuplzen.cz

^{**} Ing. Michal Hajžman, PhD.: Department of Computer-Aided Modelling, Výzkumný a zkušební ústav Plzeň s.r.o., Tylova 1581/46; 301 00, Plzeň; CZ, hajzman@vzuplzen.cz

Experimental measurements focused on the investigation of the fibre behaviour were performed on an assembled weigh-fibre-pulley-drive system (see Fig. 1). Its geometrical arrangement was changed several times on the basis of various pieces of knowledge. The fibre is driven with one drive, it is led over a pulley and on its other end there is a prism-shaped steel weight, which moves on an inclined plane. The angle of inclination of the inclined plane can be changed. The position of the weight can be symmetric or asymmetric with respect to the plane of a drive-pulley symmetry. It is possible to add an extra mass to the weight. Drive exciting signals can be of a rectangular, a trapezoidal and a quasi-sinusoidal shape and there is a possibility of variation of a signal rate. Time histories of the weight position, of the drive position and of the force acting in the fibre were recorded. The geometric dimensions and inertial characteristics of the weigh-fibre-pulley-drive mechanical system are given in Polach et al. (2013c), Polach et al. (2013d) and Polach et al. (2014).

The same system is numerically investigated using multibody models created in the **alaska** simulation tool. The multibody models of the weight-fibre-pulley-drive system in case of considering the symmetric and asymmetric position of the weight with respect to the plane of the drive-pulley symmetry slightly differ and are described in Polach et al. (2013c), Polach et al. (2013d) and Polach et al. (2014). The massless fibre model (e.g. Zi et al., 2008) is considered in this phase of investigation of the weight-fibre-pulley-drive system and comprise e.g. influences of fibre transversal vibration, “jumping” from pulley etc. The influence of the model parameters on the coincidence of the results of experimental measurements and the simulations results is evaluated. The simulation aim is to create a phenomenological model of a fibre, which will be utilizable in fibre modelling in the case of more complicated mechanical or mechatronic systems.

The paper summarizes investigating the weight-fibre-pulley-drive system given in Polach et al. (2013c), Polach et al. (2013d), Polach et al. (2013e) and Polach et al. (2014), where all combinations of the position of the weight with respect to the plane of the drive-pulley symmetry (symmetric or asymmetric) and of the mass of the weight (without or with added mass) were presented.

2. Simulation and Experimental Results

As it has already been stated the simulations aim was to create a phenomenological model of a fibre. When looking for compliance of the results of experimental measurement with the results of simulation influences of the following system parameters are considered: the fibre stiffness, the fibre damping coefficient and the friction force acting between the weight and the prismatic linkage in which the weight moves.

Investigation of the (carbon) fibre properties eliminating the influence of the drive and of the pulley was an intermediate stage before the measurement on the stand (Polach et al., 2013a; Polach et al., 2013b). A phenomenological model dependent on the fibre stiffness, on the fibre damping coefficient and on the friction force acting between the weight and the prismatic linkage was the result of this investigation. When looking for the fibre model (Polach et al., 2013b) that would ensure the similarity of time histories of the weight displacement and time histories of the dynamic force acting in a fibre as high as possible a fibre stiffness and a fibre damping coefficient were considered to be constant in this phase of the fibre behaviour research. The determined phenomenological model was not general, it is not suitable for the simulations of “quicker” tested situations (see Polach et al., 2013c; Polach et al., 2013d; Polach et al., 2013e; Polach et al., 2014) but general influences of individual parameters on the system behaviour, which are usable for all systems containing fibre-mass subsystem(s), were assessed.

“Starting” values at the phenomenological model creating are, identically with Polach et al. (2013a), fibre stiffness measured on a tensile testing machine ($94 \cdot 10^3$ N/m) and the fibre damping coefficient derived on the basis of experience (46.9 N·s/m). The “starting” friction force between the weight and the prismatic linkage is considered to be zero (Polach et al., 2013c).

Final values were calculated on the basis of the final values determined in Polach et al. (2013c) (stiffness = $34 \cdot 10^3$ N/m, damping coefficient = 27.5 N·s/m). The friction force course determined at investigating the weight-fibre mechanical system (Polach et al., 2013a) with the angle of inclination of the inclined plane 30 degrees was applied in the model of the weight-fibre-pulley-drive mechanical system.

Results of experimental measurements and simulations of 2 selected tested situations are presented (altogether 43 situations were tested). The influence of the fibre stiffness, the fibre damping coefficient

and the friction force acting between the weight and the prismatic linkage on time histories of the weight displacement and also on time histories of the dynamic force acting in the fibre was evaluated partly visually and partly on the basis of the value of the correlation coefficient between the records of the experimental measurements and the simulation results (Polach et al., 2013c; Polach et al., 2013d; Polach et al., 2013e; Polach et al., 2014).

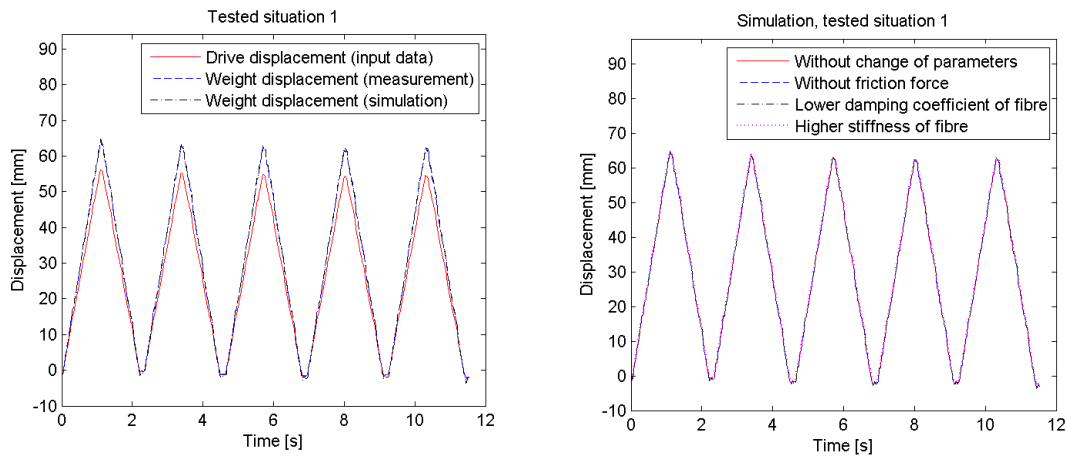


Fig. 2: Time histories of the weight displacement at “slower” tested situation 1 (symmetric position of the weight, the weight without added mass): left - Comparison of results of measurement and simulation; right - Influences of model parameters. (taken from Polach et al., 2013c).

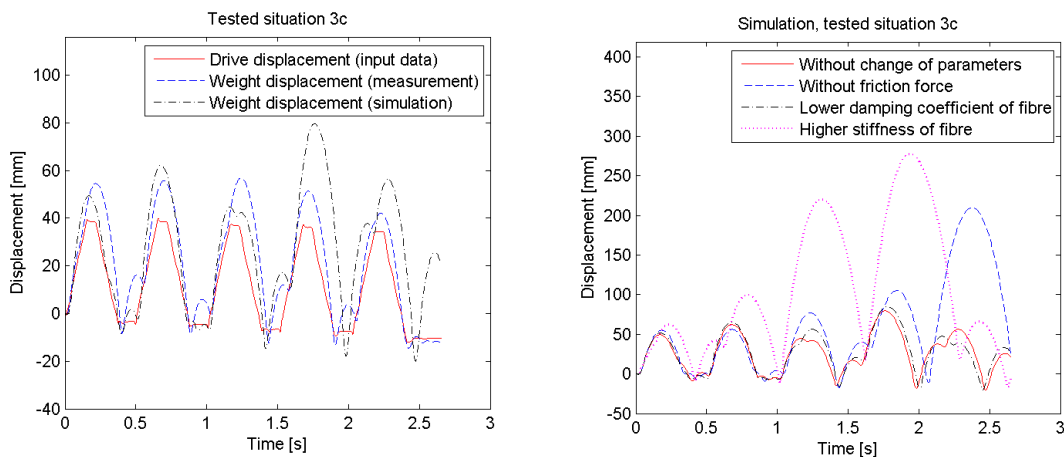


Fig. 3: Time histories of the weight displacement at “quicker” tested situation 3c (symmetric position of the weight, the weight without added mass): left - Comparison of results of measurement and simulation; right - Influences of model parameters. (taken from Polach et al., 2013c).

General pieces of knowledge from investigating the weight-fibre-pulley-drive system, independently of the combination of the position of the weight with respect to the plane of the drive-pulley symmetry (symmetric or asymmetric) and of the mass of the weight (without or with added mass), are similar (see Polach et al., 2013c; Polach et al., 2013d; Polach et al., 2013e; Polach et al., 2014).

Time histories of the weight displacement recorded at the experimental measurements and computed at the computer simulations at “slower” tested situations are approximately identical (see Fig. 2 left) and are identical independently of the fibre stiffness, the fibre damping coefficient and the friction force (see Fig. 2 right). At the “quicker” tested situations the measured and the computed time histories of the weight displacement are of the same character (see Fig. 3 left) and are dependent on all the phenomenological model parameters (see Fig. 3 right).

At all the simulations when changing the computational model the time histories of dynamic force acting in the fibre are different (more or less) but their character remains the same. From Polach et al. (2013c), Polach et al. (2013d), Polach et al. (2013e) and Polach et al. (2014) it is evident that time histories of dynamic force acting in the fibre are less suitable for searching for the parameters of the fibre phenomenological model.

From the obtained results it is evident that parameters of the fibre phenomenological model must be, in addition, considered dependent on the speed of the weight motion (i.e. on the input signal rate). For searching for the parameters of the fibre phenomenological model it is necessary to use the results of experimental measurements with the “quicker” drive motion. The possibility of performing experimental measurements with other time histories of drive motion or with a different geometrical arrangement of the experimental stand will be analysed.

3. Conclusions

The approach to the fibre modelling based on the force representations was utilised for the investigation of the motion of the weight in the weigh-fibre-pulley-drive mechanical system. The simulation aim is to create a phenomenological model of the fibre, which will be utilizable in fibre modelling in the case of more complicated mechanical or mechatronic systems. The created phenomenological model is assumed to be dependent on the fibre stiffness and on the fibre damping coefficient.

Development of the fibre phenomenological model will continue. From the obtained results it is evident that parameters of the fibre phenomenological model must be, in addition, considered dependent on the speed of the weight motion. The question is if it is possible to create the phenomenological model like that.

Acknowledgement

The paper has originated in the framework of solving No. P101/11/1627 project of the Czech Science Foundation entitled “Tilting Mechanisms Based on Fibre Parallel Kinematical Structure with Antibacklash Control” and institutional support for the long-time conception development of the research institution provided by the Ministry of Industry and Trade of the Czech Republic.

References

- Chan, E.H.M. (2005) Design and Implementation of a High-Speed Cable-Based Parallel Manipulator. PhD Thesis, University of Waterloo, Waterloo.
- Gosselin, C., Grenier, M. (2011) On the determination of the force distribution in overconstrained cable-driven parallel mechanisms. *Meccanica*, 2011, 46, 1, pp. 3-15.
- Polach, P., Hajžman, M., Václavík, J. (2013a) Simple fibre-mass model and experimental investigation, In: Proc. National Colloquium with International Participation Dynamics of Machines 2013 (L. Pešek ed.), Institute of Thermomechanics AS CR, v.v.i., Prague, 2013, pp. 79-84.
- Polach, P., Hajžman, M., Václavík, J. (2013b) Experimental and Computational Investigation of a Simple Fibre-mass System, In: Proc. 19th International Conference Engineering Mechanics 2013 (I. Zolotarev ed.), Institute of Thermomechanics AS CR, v.v.i., Svratka, 2013, CD-ROM.
- Polach, P., Hajžman, M., Václavík, J., Šika, Z., Svatoš, P. (2013c) Model parameters influence of a simple mechanical system with fibre and pulley with respect to experimental measurements, In: Proc. ECCOMAS Thematic Conference Multibody Dynamics 2013 (Z. Terze & M. Vrdoljak eds), University of Zagreb, Faculty of Mechanical Engineering and Naval Architecture, Zagreb, CD-ROM.
- Polach, P., Hajžman, M., Václavík, J., Šika, Z., Valášek, M. (2013d) Experimental and Computational Investigation of a Simple Mechanical System with Fibre and Pulley, In: Proc. 12th Conference on Dynamical Systems – Theory and Applications, Dynamical Systems – Applications (J. Awrejcewicz, M. Kaźmierczak, P. Olejnik & J. Mrozowski eds), Department of Automation, Biomechanics and Mechatronics, Łódź University of Technology, Łódź, pp. 717-728.
- Polach, P., Hajžman, M., Václavík, J., Šika, Z., Valášek, M. (2013e) Influence of the mass of the weight on the dynamic response of the simple mechanical system with fibre, In: Proc. 29th Conference with International Participation Computational Mechanics 2013 (V. Adámek, M. Zajíček & A. Jonášová eds), University of West Bohemia in Plzeň, Špičák, CD-ROM.
- Polach, P., Hajžman, M., Václavík, J., Červená, O. (2014) Dynamics of the Weight-fibre-pulley-drive Mechanical System: Influence of Mass of Weight at System Asymmetry, In: Proc. National Colloquium with International Participation Dynamics of Machines 2014 (L. Pešek ed.), Institute of Thermomechanics AS CR, v.v.i., Prague, 2013, pp. 115-124.
- Zi, B., Duan, B. Y., Du, J. L., Bao, H. (2008) Dynamic modeling and active control of a cable-suspended parallel robot. *Mechatronics*, 18, 1, pp. 1-12.

THE EXACT SOLUTION OF ELASTICITY MIXED PLAIN BOUNDARY VALUE PROBLEM IN A RECTANGULAR DOMAIN

G. Popov^{*}, N. Vaysfeld^{}, B. Zozulevich^{***}**

Abstract: *The plane mixed boundary value problem of elasticity on a rectangular domain is solved exactly. With the help of Fourier transformation the one-dimensional vector boundary problem in the transformation's domain is obtained. The components of the unknown vector are the displacement transformations. The problem is solved exactly with the methods of the matrix differential calculations. The constructed vector is inverted by the corresponding formulas of inverse Fourier transformation, so the displacement expressions are found in the form of Fourier series. The numerical investigation of the stress in dependence of the external loading value and domain's size is presented.*

Keywords: Rectangular domain, Mixed plain boundary value problem, Exact solution.

1. Introduction

Various engineering problems are reduced to the mixed plain boundary value problem in a rectangular domain. The history of this problem and its solution is very long and interesting (Sailendra N. Chatterjee and Shyam N. Prasad, 1973; Meleshko, 1998; Tokovyi and Vigak, 2002; Golovchan, 2006). The novelty of the presented paper is in the new approach (Popov and Vaysfeld, 2011) to the problem solution based on the reduction of the initial boundary value problem to the one-dimensional vector boundary value problem in the transformed domain. This new method of constructing the solution, with the help of the matrix differential calculations, allows to obtain the exact solution of the elasticity problem in a rectangular domain, when the smooth contact conditions are fulfilled on the domain faces.

2. Problem Statement

The elasticity plane deformation problem is assumed. The rectangular problem domain is defined as

$$0 < x < a, \quad 0 < y < b \quad (1)$$

The boundary conditions on the edges $x = 0$, $x = a$ are given by the following expressions

$$U(0, y) = 0, \quad \tau_{xy}(0, y) = 0, \quad 0 < y < b \quad (2)$$

$$U(a, y) = 0, \quad \tau_{xy}(a, y) = 0, \quad 0 < y < b \quad (3)$$

On the edge $y = b$ the normal stress are given

$$\sigma_y(x, b) = -p(x), \quad \tau_{yx}(x, b) = 0, \quad 0 < x < a \quad (4)$$

The face $y = 0$ is in the smooth contact with the solid base

* Prof. Gennadiy Popov, PhD., Doctor of Sc.: Institute of mathematics, economic and mechanics, Odessa Mechnikov University, Dvoryanskay Street, 2; 65026, Odessa; Ukraine, popov@onu.edu.ua

** Prof. Nataly Vaysfeld, PhD., Doctor of Sc.: Institute of mathematics, economic and mechanics, Odessa Mechnikov University, Dvoryanskay Street, 2; 65026, Odessa; Ukraine, vaysfeld@onu.edu.ua

*** Boris Zozulevich, Master: Institute of mathematics, economic and mechanics, Odessa Mechnikov University, Dvoryanskay Street, 2; 65026, Odessa; Ukraine, b.zozulevich@onu.edu.ua

$$V(x, 0) = 0, \quad \tau_{xy}(x, 0) = 0, \quad 0 < x < a \quad (5)$$

where $U(x, y) = u_x(x, y)$, $V(x, y) = u_y(x, y)$.

The displacements $U(x, y)$, $V(x, y)$ satisfy the equilibrium equations (Nowacki, 1970)

$$U''(x, y) + U''(x, y) + \mu_0(U''(x, y) + V' \cdot(x, y)) = 0 \quad (6)$$

$$V''(x, y) + V''(x, y) + \mu_0(U' \cdot(x, y) + V''(x, y)) = 0 \quad (7)$$

in the domain (1), where $\mu_0 = (1 - 2\mu)^{-1}$, μ is the Poisson's coefficient, and G is the shear modulus. The stroke denotes the derivative with respect to the variable r , the dot denotes the derivative with respect to the variable θ . The goal is to solve the boundary problem (2-7) in the domain (1).

3. The Solution of the Problem

Let's apply the sin- and cos- integral Fourier transformations (Sneddon, 1951) to the differential equations (6, 7)

$$U_n(y) = \int_0^a U(x, y) \sin(\alpha_n x) dx, \quad V_n(y) = \int_0^a V(x, y) \cos(\alpha_n x) dx, \quad \alpha_n = \frac{\pi n}{a} \quad (8)$$

In the transformations domain (8) system can be written in the following form (Nowacki, 1970)

$$U_n''(y) - \alpha_n^2(1 + \mu_0)U_n(y) - \mu_0\alpha_n V_n'(y) = 0 \quad (9)$$

$$(1 + \mu_0)V_n''(y) - \alpha_n^2 V_n(y) + \mu_0\alpha_n(1 + \mu_0)U_n'(y) = 0 \quad (10)$$

One should take into consideration that conditions of the smooth contact (2), (3) were satisfied during the transformation. The boundary conditions (4), (5) were reformulated in the terms of the displacements

$$V_n(0) = 0, \quad U_n'(0) = 0 \quad (11)$$

$$\alpha_n V_n(b) - U_n'(b) = 0, \quad \alpha_n \mu U_n(b) - (1 - \mu)V_n'(b) = 0 \quad (12)$$

The one-dimensional boundary problem (9-12) was formulated as the vector one. The following vector and matrix terms are introduced

$$\mathbf{E} = \begin{pmatrix} 1 & 0 \\ 0 & 1 + \mu_0 \end{pmatrix} \quad \mathbf{P} = \begin{pmatrix} 0 & -\mu_0\alpha_n \\ 0 & 1 + \mu_0 \end{pmatrix} \quad \mathbf{Q} = \begin{pmatrix} -\mu_0\alpha_n^2(1 + \mu_0) & 0 \\ 0 & \alpha_n^2 \end{pmatrix} \quad \mathbf{Z}(y) = \begin{pmatrix} U_n(y) \\ V_n(y) \end{pmatrix}$$

$$\mathbf{A}_1 = \begin{pmatrix} 1 & 0 \\ 0 & 0 \end{pmatrix} \quad \mathbf{B}_1 = \begin{pmatrix} 0 & 0 \\ 0 & 1 \end{pmatrix} \quad \mathbf{A}_2 = \begin{pmatrix} -1 & 0 \\ 0 & \mu - 1 \end{pmatrix} \quad \mathbf{B}_2 = \begin{pmatrix} 0 & \alpha_n \\ \alpha_n \mu & 0 \end{pmatrix} \quad (13)$$

Using this notation, the problem (9-12) is rewritten in the form

$$\begin{cases} L_2(\mathbf{Z}(y)) = 0, \\ U_i(\mathbf{Z}(y)) = 0, \quad i = 1, 2 \end{cases} \quad (14)$$

where $L_2(\mathbf{Z}(y)) = \mathbf{E}\mathbf{Z}''(y) + \mathbf{P}\mathbf{Z}'(y) + \mathbf{Q}\mathbf{Z}(y)$ is the differential operator, $U_i(\mathbf{Z}(y)) = \mathbf{A}_i\mathbf{Z}'(b_i) + \mathbf{B}_i\mathbf{Z}(b_i)$ are the boundary functionals, $i = 1$ corresponds to $b_1 = 0$, $i = 2$ corresponds to $b_2 = b$. For the solution of vector equation one needs to construct the homogenous

equation $L_2(\mathbf{Y}(y)) = 0$. One can assure that the correspondence $L_2(e^{sy}\mathbf{I}) = \mathbf{M}(s)e^{sy}$ is correct (\mathbf{I} is an unitary matrix). The construction of the fundamental matrix was done using the formula (Gantmakher, 1998)

$$\mathbf{Y}(y) = \frac{1}{2\pi i} \oint_C e^{sy} \mathbf{M}^{-1}(s) ds = \frac{1}{2\pi i} \oint_C \frac{e^{sy} \tilde{\mathbf{M}}(s)}{\det \mathbf{M}(s)} ds \quad (15)$$

where $\mathbf{M}^{-1}(s)$ is the inverse matrix to the matrix $\mathbf{M}(s) = \begin{pmatrix} s^2 - \alpha_n^2(1 + \mu_0) & -\mu_0 \alpha_n s \\ (1 + \mu_0)s^2 + \alpha_n s & -\alpha_n^2 \end{pmatrix}$, C is the contour including the poles of the under the integral function, $\det \mathbf{M}(s) = (s^2 - \alpha_n^2)^2$. After the calculation of integral (15) using the residual theorem, one obtains two linearly independent solutions of the matrix equation

$$\mathbf{Y}_0(y) = \frac{e^{\alpha_n y}}{4(1 + \mu_0)} \begin{pmatrix} \frac{\mu_0 \alpha_n y + \mu_0 + 2}{\alpha_n} & \mu_0 y \\ -\mu_0 y & -\frac{\mu_0 \alpha_n y - \mu_0 - 2}{\alpha_n} \end{pmatrix}$$

$$\mathbf{Y}_1(y) = \frac{e^{-\alpha_n y}}{4(1 + \mu_0)} \begin{pmatrix} \frac{\mu_0 \alpha_n y - \mu_0 - 2}{\alpha_n} & -\mu_0 y \\ -\mu_0 y & -\frac{\mu_0 \alpha_n y + \mu_0 + 2}{\alpha_n} \end{pmatrix} \quad (16)$$

The solution of the vector equation (14) was written in the form

$$\mathbf{Z}(y) = \mathbf{Y}_0(y) \begin{pmatrix} C_1 \\ C_2 \end{pmatrix} + \mathbf{Y}_1(y) \begin{pmatrix} C_3 \\ C_4 \end{pmatrix} \quad (17)$$

where $C_j, j = \overline{1, 4}$ are the unknown constants, which are found from the boundary conditions (14). Hence, the exact solution of the one-dimensional vector boundary problem (9-12) is constructed in the form

$$U_n(y) = \Delta_n (e^{\alpha_n(b+y)} (2\mu - \alpha_n(y-b) - 1) + e^{\alpha_n(-b+y)} (-2\mu + \alpha_n(y+b) + 1) + \quad (18)$$

$$+ e^{\alpha_n(b-y)} (2\mu + \alpha_n(y+b) - 1) - e^{\alpha_n(-b-y)} (2\mu + \alpha_n(y-b) - 1))$$

$$V_n(y) = \Delta_n (e^{\alpha_n(b+y)} (2\mu + \alpha_n(y+b) - 2) - e^{\alpha_n(-b+y)} (2\mu + \alpha_n(y+b) - 2) + \quad (19)$$

$$+ e^{\alpha_n(b-y)} (-2\mu + \alpha_n(y+b) + 2) + e^{\alpha_n(-b-y)} (2\mu - \alpha_n(y-b) - 2))$$

where $\Delta_n = P_n \left[2(4\alpha_n b + e^{2\alpha_n b} - e^{-2\alpha_n b}) G \alpha_n \right]^{-1}$, $P_n = \int_0^a p(x) \cos \alpha_n x dx$. The formulas (18, 19) are correct when $n = 1, 2, \dots$. The particular case is $n = 0$, when the equilibrium equations take the form

$$V_0''(y) = 0 \quad (20)$$

The solution of the equation (20), taking into consideration the boundary conditions, is obtained

$$V_0''(y) = -\frac{P_0(1-2\mu)}{2G(1-\mu)}y \quad (21)$$

The application of the inverse formulas of the integral transformations (8) to the expressions (18, 19) finishes the construction of the exact solution

$$U(x, y) = \frac{2}{a} \sum_{n=1}^{\infty} U_n(y) \sin(\alpha_n x), \quad V(x, y) = \frac{V_0(y)}{a} + \frac{2}{a} \sum_{n=1}^{\infty} V_n(y) \cos(\alpha_n x) \quad (22)$$

4. Numerical Results

With the help of the formulas (22), the stress is calculated exactly. The different forms of the loading $p(x) \equiv P$, $p(x) = Ax^2 + Bx + C$ in the rectangular domain $a = 2$, $b = 1$ were considered. The calculations were done on the face $x = 0$. The main interests are to estimate the values of the normal stress and to investigate the condition for the creation of stretching stress. The results of the calculations are shown in the Tab. 1 for different values of Poisson's coefficient (here the normal stress' values are multiplied by the 10).

Tab. 1: Values of normal stress on the face $x = 0$ for the different values of Poisson's coefficient.

μ	y										
	0	0.1	0.2	0.3	0.4	0.5	0.6	0.7	0.8	0.9	1.0
0.1	-5.99	-6.0	-6.1	-6.1	-6.1	-5.9	-5.2	-3.9	-0.96	5.11	22.76
0.2	-9.7	-9.7	-9.8	-9.8	-9.8	-9.6	-8.9	-7.6	-4.67	1.40	19.03
0.3	-14.5	-14.5	-14.5	-14.6	-14.5	-14.3	-13.7	-12.3	-9.43	-3.36	14.21
0.4	-20.8	-20.8	-20.9	-20.9	-20.9	-20.7	-20.1	-18.7	-15.8	-9.71	7.75

The results illustrate that the stretching stress appears as one approach to the upper face of the rectangle. The zones of its occurrence are investigated, depending on the geometrical parameters and elastic properties of the domain.

Acknowledgement

The research is supported by Ukrainian Department of Science and Education under Project No 0109U000920.

References

- Sailendra Chatterjee, N., Shyam Prasad, N. (1973) Some mixed boundary value problems of elasticity in a rectangular domain. *International Journal of Solids and Structures*, 9, 10, pp. 1193-1210.
- Meleshko, V. (1998) Byharmonic problem in the rectangle. *Applied Scientific Research*, 58, 1-4, pp. 217-249.
- Tokovyi, Yu., Vihak, V. (2002) Construction of elementary solutions to a plane elastic problem for a rectangular domain. *International Applied Mechanics*, 38, 7, pp. 829-836.
- Golovchan, V. (2006) On the solution of plane boundary-value problems of elasticity in a rectangle. *International Applied Mechanics*, 42, 1, pp. 84-93.
- Popov, G., Vaysfeld N. (2011) The steady-state oscillations of the elastic infinite cone loaded at a vertex by a concentrated force. *Acta Mechanica*. 221, Iss. 3-4, pp. 261-270.
- Nowacki, W. (1970) *The theory of elasticity*. Panstwowe Wydawnictwo Naukowe, Warszawa, (in Polish).
- Gantmakher, F. R. (1998) *The Theory of matrices*. AMS Chelsea Publishing, Providence, Rhode Island.
- Sneddon, I. N. (1951) *Fourier transforms*. McGraw-Hill, New York.

ADAPTIVE UPDATE OF SURROGATE MODELS FOR RELIABILITY-BASED DESIGN OPTIMIZATION: A REVIEW

A. Pospíšilová*, M. Lepš**

Abstract: *Meta-models (or surrogate models, formerly response surfaces) are getting popular in engineering designs. They are used to simulate the behaviour of structures with less computational demands than the original model (e.g. finite element models). It is still necessary to evaluate this expensive original model few times in some specified points called Design of Experiments (DoE). The first DoE is usually just space-filling to cover up the whole design space and the meta-model built with an initial DoE is therefore not very accurate everywhere. Other points are added to the meta-model to improve accuracy at important regions. In this paper, various updates of meta-models are reviewed from different points of view. Unfortunately, there is a distinction between updates even in reliability assessment and reliability-based design optimization research areas.*

Keywords: Surrogate models, Adaptive update, Reliability-based design optimization, Design of Experiments.

1. Introduction

Realistic simulations of a structural behaviour require usage of complex and very detailed models. If those models are used for an engineering design, it is inevitable to enumerate them several times. These so-called *true functions* or *performance functions* (based on e.g. a finite element method) can be quite expensive to evaluate several times consecutively. If even one evaluation of the true function is very time consuming, the optimization used for the engineering design can last for ages. To speed up the design process, the true model can be replaced by some model of the original model that has a very similar behaviour; however, it is less time consuming. Those models of models are called *meta-models* or *surrogate models* and require just few evaluations of the costly true function. Those evaluations are then used to create the meta-model. Proper locations where to evaluate the true function (called *support points*) have to be chosen properly usually by a *Design of experiments* with support points usually uniformly distributed in the whole design space. It is better to start with just a couple of support points and then find the correct positions where to add other support points to improve the meta-model mimicking the true model (called *updating*). Initial meta-models do not have the same accuracy as the true models particularly in locations that are most interesting for an engineering design such as the vicinity of the border between the safe and the failure domain called a *limit state*. Adaptive updating of meta-models can make the meta-model more accurate in those interesting locations.

2. Meta-Models and Updates

Meta-models can be divided into two fundamental parts: *non-interpolating* models minimizing sum of squares errors from some predetermined functional form (e.g. *polynomial surfaces*) and *interpolating* models intersecting all support points based on the idea of linear combination of some basis functions. Interpolating models can contain fixed basis functions (e.g. *thin-plate splines* or *multiquadrics*) or basis functions to be tuned, e.g. *Radial Basis Functions Networks* or *Kriging* (Jones, 2001). If the interpolating meta-model is trained only with few support points, it is too stiff to approximate the original behaviour of the true function and conversely, fitting the true function with plenty of points makes the model too

* Ing. Adéla Pospíšilová: Department of Mechanics, Faculty of Civil Engineering, Czech Technical University in Prague, Thákurova 7; 166 29, Prague; CZ, adela.pospisilova@fsv.cvut.cz

** Assoc. Prof. Ing. Matěj Lepš, PhD.: Department of Mechanics, Faculty of Civil Engineering, Czech Technical University in Prague, Thákurova 7; 166 29, Prague; CZ, leps@cml.fsv.cvut.cz

flexible and causes over-fitting (Forrester et al., 2008). In addition, Kriging allows computing the mean squared error (MSE) of any predicted outcome, which is frequently used for the meta-model updates. If any other meta-model type is more suitable for a specific problem, the generic updates have to be utilized.

2.1. Update for reliability assessment

The type of a meta-model update depends on a field of the model application. Despite appearing similar, a reliability assessment and a reliability optimization require a different updating approach. Consider the evaluation of the failure probability p_f in an n -dimensional space of random variables X_1, \dots, X_n as a multiple integral of a joint probability density function $f_X(x)$ over the failure domain $g(\mathbf{X}) \leq 0$. In the standard normal space, the Hasofer-Lind reliability index β is then defined as an inverse cumulative distribution function of the standard normal distribution $\beta = \Phi^{-1}(1-p_f)$. It can be geometrically understood as the shortest connecting line between the origin and the *most probable failure point* (MPFP). To improve the behaviour of the meta-model for the reliability assessment, the update is most essential around this MPFP, because this region contributes most to the total failure probability. Bucher & Bourgund (1990) came with the idea to update the response surface utilizing second-order polynomials.

2.2. Updates for reliability-based design optimization

One possible approach to define the reliability-based design optimization is

$$\min_{\mathbf{d} \in \mathbf{D}} c(\mathbf{v}, \mathbf{d}) \quad \text{s.t.} \quad \begin{cases} h_i(\mathbf{d}) \leq 0, & i = 1, \dots, n_e, \\ p_{f,j}(\mathbf{v}, \mathbf{d}) \leq p_{f,j}^{tol}, & j = 1, \dots, n_p. \end{cases} \quad (1)$$

The cost function $c(\mathbf{v}, \mathbf{d})$ is to be minimized with optimal values of design variables arranged in \mathbf{d} vector. Design variables are chosen from a design space \mathbf{D} . Uncertain parameters are arranged in vector \mathbf{v} . n_e is the total number of deterministic constraints defined by $h_i(\mathbf{d})$, $p_{f,j}(\mathbf{v}, \mathbf{d})$ stands for a probability of occurrence of j^{th} event and $p_{f,j}^{tol}$ is a prescribed tolerable threshold. n_p is the total number of probabilistic constraints. Design variables usually represent mean values of random variables and their optimal combination coincide with the minimum of the cost function under the fulfilled constraints.

Meta-models can replace both the cost function and the deterministic and probabilistic constraints. Nevertheless, there is a difference in their consecutive update. If the meta-model is used to compute the values of the objective function, an improvement of the meta-model is necessary in the vicinity of the best-so-far optimum found so as to allow for a convergence to the global optimum. Several strategies are used, namely *minimizing a response surface* (Jones, 2001), *maximizing the probability of improvement* (Kushner, 1964; Jones, 2001), *maximizing the expected improvement* (Jones et al., 1998) or *goal seeking* (Jones, 2001). On the other hand, if a meta-model is utilized for the constraint replacement, some contour (e.g. a limit state) has to be approximated. Algorithms as the *Efficient Global Reliability Analysis* (EGRA) (Bichon et al., 2008), modified *Active Kriging + Monte Carlo Simulation* (Echard et al., 2011) or *Meta-model-based importance sampling* (Dubourg, 2011) can be effectively employed. The latter algorithms utilize some special meta-models' features that are not available for all types of meta-models. The generic update can be carried out through placing new support points in a vicinity of the limit state still ensuring the uniform space-filling criterion e.g. by the MiniMax metric which leads to the multi-objective optimization (Myšáková et al., 2013). Although the replacement of probabilistic constraint seems to be the similar problem as in the reliability assessment, the layout is different due to its repeated evaluation for different designs. The limit state function can be understood as a collection of the MPFPs for different design variables combinations and thus the meta-model updating only in the one MPFP vicinity is not sufficient, but the vicinity of the whole contour needs to be updated.

2.2.1. Updates for meta-models replacing an objective function in RBDO

Minimizing a response surface approach (Jones, 2001) is independent of a used meta-model type. New support points are added sequentially into the best-so-far optimum found on the meta-model. In case of multi-modal problems, this method can converge prematurely in a local optimum or fail in the worst possible case. Additional points in DoE for the non-interpolating meta-models with fixed number of degrees of freedom need not help at all and this method can be misleading in finding any optima. The interpolating meta-models converge to the local optimum in most cases. To ensure that the local optimum is found the local search is carried out in its vicinity.

Maximizing the probability of improvement (Kushner, 1964; Jones et al., 1998) utilizes the ability of Kriging to compute MSE of a prediction. An uncertainty in the prediction is lesser (low MSE) in areas with higher concentration of support points and reversely. The output y^* at the point x^* not identical with any support point is not known, therefore y^* can be modelled as a random normal variable Y with a mean equal to the Kriging prediction $\hat{y}(x)$ and standard deviation s equal to the Kriging standard error. For more details about Kriging, see e.g. Jones et al. (1998). To find the global optimum, the minimum value y_{\min} of the true function evaluated on initial DoE is determined and the probability of improvement is maximized across the whole domain of x . The improvement is achieved when y_{\min} is greater than the uncertain output Y , thus $I = \max(y_{\min} - Y, 0)$ and the probability of improvement $P[I(x)]$ is according to Forrester et al. (2008)

$$P[I(x)] = \frac{1}{s\sqrt{2\pi}} \int_{-\infty}^0 \frac{(I - \hat{y}(x))^2}{2s^2} dI. \quad (2)$$

New support points are sequentially added into the maximum value of $P[I(x)]$ until the $P[I(x)]$ approximates zero. $P[I(x)]$ shows the location of the maximum improvement but not its amount. The better criterion is therefore the expected improvement function.

Maximizing the expected improvement function (EIF) (Jones et al., 1998) is based on the idea of the probability of improvement. EIF is an expected value of $P[I(x)]$ defined as

$$E[I(x)] = (y_{\min} - \hat{y})\Phi\left(\frac{y_{\min} - \hat{y}}{s}\right) + s\phi\left(\frac{y_{\min} - \hat{y}}{s}\right). \quad (3)$$

The maximum value of EIF localizes the next point that should be added into the surrogate model to make it more accurate. Proposed EIF makes a balance between a local and a global search. The local search is focused on an improvement of the local minimum vicinity and the global search concentrates primarily on unknown areas exploration where the standard error of the predictor has the maximum value. This approach is sequential and maximization of EIF is done repeatedly until the maximum of EIF is greater than some prescribed value. The Branch and Bound method used in Jones et al. (1998) for the maximization is however quite often too expensive to run to final convergence (Bichon et al., 2008). The complete global optimization algorithm is called Efficient Global Optimization (EGO).

Goal seeking searches for an input (a goal) that corresponds to a specific predefined function value. It is based on the maximization of the conditional log-likelihood function by varying inputs and Kriging model parameters; see Forrester et al. (2008) for more details.

2.2.2. Updates for meta-models replacing constraints functions in RBDO

Bichon et al. (2008) use an adaptive update of Kriging together with an adaptive importance sampling (AIS). An update of a meta-model is inspired by Jones et al. (1998). Instead of EIF, *Expected Feasibility function* (EFF) is utilized. Since an improvement of the meta-model is not used for global minimization but for the reliability assessment, the bound dividing the domain into the safe and the failure region has to be more accurate. An equality constraint for a reliability assessment is defined as $G(\mathbf{u}) = \bar{z}$ where \bar{z} is a threshold value. EFF is therefore integrated over a region $\bar{z} \pm \varepsilon$. Efficient Global Reliability Analysis (EGRA) first generates a small number of support points (at least to define the quadratic polynomial) and computes true function values in those support points for building the Gaussian process model. Those samples are recommended to cover the design space uniformly over the bounds $\pm 5\sigma$. The point that maximizes the EFF is located by DIRECT algorithm and the true function is calculated. EFF is maximized and support points are added into the meta-model repeatedly until the stopping criterion in the form of the prescribed maximum EFF value is not fulfilled.

Active Kriging + Monte Carlo Simulation (Echard et al., 2011) creates and updates a meta-model only on a generated Monte Carlo (MC) population and not on any other points. At the beginning, few support points are chosen from the whole MC population by e.g. k-means clustering. Subsequently, support points for an update are obtained by minimizing the so-called *Learning function* on whole MC population, which is the ratio of an absolute value of a predicted value by a meta-model to Kriging variance. Since the MC population is generated only for one combination of design variables, this method in its unmodified version works only for reliability assessment. Nevertheless, several options are available to extend it for RBDO. First, a new meta-model can be trained for each combination of design variables

proposed by RBD optimizer, however, this approach can be quite time consuming. Second, a meta-model is kept for all design variables combinations and just new points from new MC populations are added to make the meta-model more precise across the whole design space. Third, the MC population can be widened just for the meta-model improvement purposes.

Meta-model independent update for RBDO not utilizing the feature of the ability to forecast a predictor error is not very often used. Myšáková et al. (2013) use a multi-objective optimization for locating additional support points regardless of the meta-model type. There are two criteria: first, a new support point should be near the limit state that is carried out by minimizing the quadrate of the surrogate limit state function. Second, to bring the maximum new information, the point should be far from other points as quantified by MiniMax metric. The final Pareto-front is clustered and the best points are added to DoE to update the meta-model. This routine is run sequentially until the stopping criterion is fulfilled.

3. Conclusions

For a meta-model updating, it is necessary to distinguish what is a purpose of the meta-model. The reliability assessment requires an improvement mainly in the vicinity of the most probable point. In the reliability-based design optimization, the meta-model can replace an objective function or the constraints in the both forms of equality or inequality. In case of an objective function approximation, the global optimum should be located and updated. Constraints meta-models require an improvement in the defined contour dividing the space into the feasible (or safe) and non-feasible (or failure) domain. If Monte Carlo or variance reduction techniques (e.g. Importance sampling or Subset simulation) are utilized for a reliability assessment for each combination of design variables in the RBDO procedure, the meta-model replacing the true limit state function is more essential unless the objective function is very time consuming. A meta-model is one of very few options to solve the problem. However, the outcome is highly dependent on the meta-model ability to describe the given problem. Any time, an issue of over-fitting and/or over-simplification can occur and the quality of the used meta-model must be therefore continuously checked. For comparative studies of meta-models' performance under multiple modelling criteria, see e.g. Jin et al. (2001).

Acknowledgement

This work was supported by the Grant Agency of the Czech Technical University in Prague, grant No. SGS14/028/OHK1/1T/11, and the Czech Science Foundation, project No. 105/12/1146. Adéla Pospíšilová also would like to thank Prof. Christian Bucher from TU Vienna for his selfless help during her study visit at his department.

References

- Bichon, B. et al. (2008) Efficient global reliability analysis for nonlinear implicit performance functions. *AIAA journal*, 46, 10, pp. 2459-2468.
- Bucher, C., Bourgund, U. (1990) A fast and efficient response surface approach for structural reliability problems. *Structural safety*, 7, 1, pp. 57-66.
- Dubourg, V. (2011) Adaptive surrogate models for reliability analysis and reliability-based design optimization. PhD thesis, Université Blaise Pascal, Clermont-Ferrand, France.
- Echard, B., Gayton, N., Lemaire, M. (2011) AK-MCS: An active learning reliability method combining Kriging and Monte Carlo simulation. *Structural Safety*, 33, 2, pp. 145-154.
- Forrester, A., Sóbester, A., Keane, A. (2008) *Engineering design via surrogate modelling: a practical guide*. John Wiley & Sons.
- Jin, R., Chen, W., Simpson, T. W. (2001) Comparative studies of metamodelling techniques under multiple modelling criteria. *Structural and multidisciplinary optimization*, 23, pp. 1-13.
- Jones, D. R. (2001) A taxonomy of global optimization methods based on response surfaces. *Journal of global optimization*, 21, 4, pp. 345-383.
- Jones, D. R., Schonlau, M., Welch, W. J. (1998) Efficient global optimization of expensive black-box functions. *Journal of Global optimization*, 13, 4, pp. 455-492.
- Kushner, H. J. (1964) A new method of locating the maximum point of an arbitrary multipeak curve in the presence of noise. *Journal of Basic Engineering*, 86, 97, pp. 97-106.
- Myšáková, E., Pospíšilová, A., Lepš, M. (2013) Multiobjective adaptive updating of surrogate models, In: Proc. 19th Int. Conf. Engineering Mechanics, Inst. of Thermomechanics, Academy of Sciences of the Czech Republic.

FINITE ELEMENT ANALYSIS OF COMPRESSION OF LUMBAR SPINE WITH DYNAMIC IMPLANT

E. Prášilová*, Z. Florian*, P. Marcián*

Abstract: *The degenerative and traumatic injuries of a spine are very frequent. In those cases it is necessary to stabilize the corresponding spine segment using a spine implant. The spinal implants are rigid or flexible, the latter known as dynamic ones in medical practice. In this paper, the problems of the physiological spinal segment and the segment with implant were solved using the computational modelling (finite element method). Computational model consists of 4 lumbar vertebrae L2 – L5, intervertebral discs, joints and spinal implants. The spinal segment was loaded by the force 400N. The displacement of the whole system, contact pressure of cartilages, equivalent strain in cancellous bone and equivalent stress in the implant were analyzed. The deformation of the physiological model and the model with the implant are comparable, but the bone tissue of the model with the implant is dramatically more loaded in vicinity of the screws.*

Keywords: Spine, Implant, Intervertebral disc, Joints, Stress – strain analysis.

1. Introduction

Degenerative diseases and traumatic injuries of a spine afflict a great deal of the population of the Czech Republic. These injuries can lead to the oppression of blood vessels and nerves; besides, injuries of intervertebral discs (ID), joints and vertebrae occur frequently as well. In these cases, it is necessary to stabilize the damaged spinal segment with the implant.

The spinal implants are divided into rigid and flexible. The latter are known as dynamic ones in medical practice. The spinal implant has to stabilize the spinal segment for arbitrary (possible) load. It is clear, that the spinal segment with the flexible implant has to be stiffer than the physiological state of the spine. Moreover, the deformation of the segment in the physiological state is different for arbitrary load. The aim of this paper is stress – strain analysis of the flexible implant.

2. Materials and Methods

We can simulate a function of a spinal segment with the implant using the computational modeling. The computational modeling is suitable, because it allows us to change loads effectively, to simulate different states of the spinal segment and to analyze the results relatively easily. Besides, to perform an experiment in vivo is very demanding.

For a solution of the given problem by means of the finite element method, it is necessary to create a computational model which, in this case, consists of four independent parts: model of geometry, materials, loads and boundary conditions (Manek et al., 2012).

2.1. Geometry model

The geometry was created by using computer tomography (CT) data of a woman. The data were obtained from University of Iowa database (Visible Human Project CT Datasets 2012). The geometries of four lumbar vertebrae (L2 - L5) were modelled using the hybrid segmentation in software STL Model Creator (Marcián et al., 2011; Prášilová et al., 2012). Three models were created in this paper in order to compare the results of stress – strain analyses. The first one is a physiological model consisting of 4

* Bc. Eva Prášilová, Assoc. Prof. Ing. Zdeněk Florian, CSc., Ing. Petr Marcián, PhD.: Institute of Solid Mechanics, Mechatronics and Biomechanics, Faculty of Mechanical Engineering, Brno University of Technology, Technická 289/2, 616 69 Brno, CZ, eprasilova@seznam.cz, florian@fme.vutbr.cz, marcian@fme.vutbr.cz

vertebrae, 3 ID, 12 cartilages in joints. The second one is a spine model with a degraded ID. The last one is the model with a dynamic implant and with a degraded ID shown in Fig. 1 (the implant was inserted into vertebrae L2 and L3). The model with the implant consists of 39 parts and the physiological one consists of 19 parts that was modelled in software SolidWorks and ANSYS.

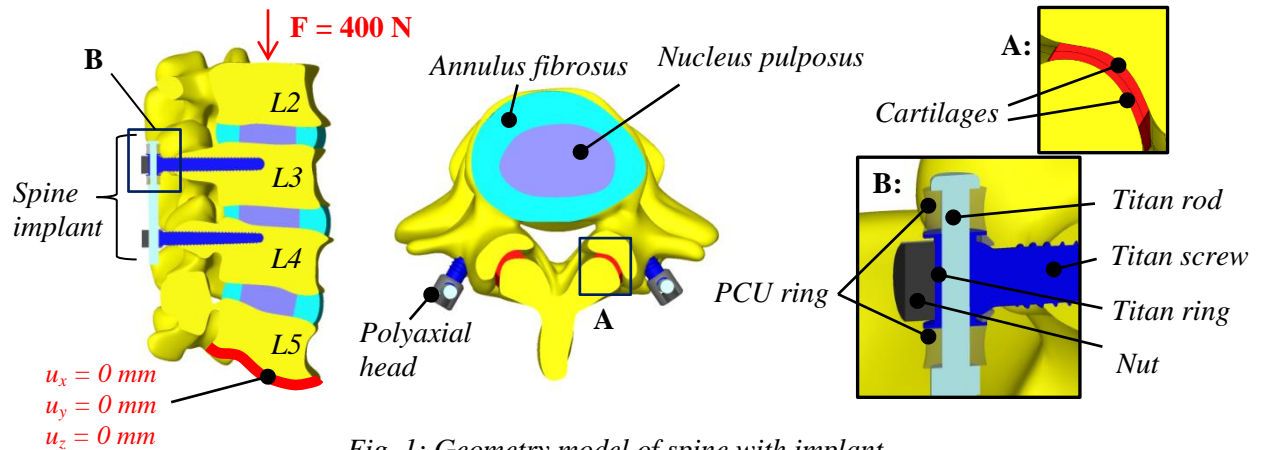


Fig. 1: Geometry model of spine with implant.

2.2. Models of materials

All components of the model was modelled by the linear elastic homogeneous isotropic model of material, which is specified by Young's modulus E and Possion's ratio μ on the basis of literature (Tab. 1), (Martinez et al., 1997; Goel et al., 1997).

Tab. 1: Material properties.

Material	Young's Modulus [MPa]	Poisson's ratio [-]
<i>Cortical bone</i>	<i>12 000</i>	<i>0.3</i>
<i>Cancellous bone</i>	<i>100</i>	<i>0.2</i>
<i>Cartilage</i>	<i>24</i>	<i>0.4</i>
<i>Nucleus pulposus/degraded</i>	<i>1/0.2</i>	<i>0.49</i>
<i>Annulus fibrosus/degraded</i>	<i>30/6</i>	<i>0.45</i>
<i>PCU (polycarbonate urethane)</i>	<i>31.8</i>	<i>0.3</i>
<i>Titanium alloy 100-Ti-6Al-7Nb</i>	<i>110 000</i>	<i>0.3</i>

2.3. Model of load and boundary conditions

On the bottom surface of vertebrae L5, all nodes were fixed. On the top surface of vertebrae L1, the compressive load $F = 400\text{ N}$ (Schrazi-Adl et al., 1987) was applied in all analyzed models.

2.4. Computational model

Finite elements SOLID186 and 187 were used for modeling of the vertebrae, cartilages, IDs and implant. SHELL181 was used for the cortical bone (thickness 1 mm). TARGET170 and CONTA174 were used for modeling of contact between cartilages (friction 0.001) and between titan alloys – PCU (friction 0.3). There were created six contact pairs between cartilages (Fig. 1, detail A) and then three contact pairs connected with the implant (titan ring with PCU rings, titan rod with titan ring and PCU rings, see detail B in the Fig. 1). The final number of degree of freedoms (DOF) for model with implant was 2.5 million and the physiological one had 1 million DOF. Due to the character of the problem and of the computational model, the solver was set to the large deflection mode.

3. Results

The total displacement results are shown in Fig. 2. The dominant displacement is in the direction of y axis (anterior – posterior direction). In the physiological model is $u_{y\max} = 3.09\text{ mm}$, the displacement of the

model with the degraded ID $u_{y_{max}} = 5.12 \text{ mm}$ and $u_{y_{max}} = 2.92 \text{ mm}$ when the implant and the degraded ID is used.

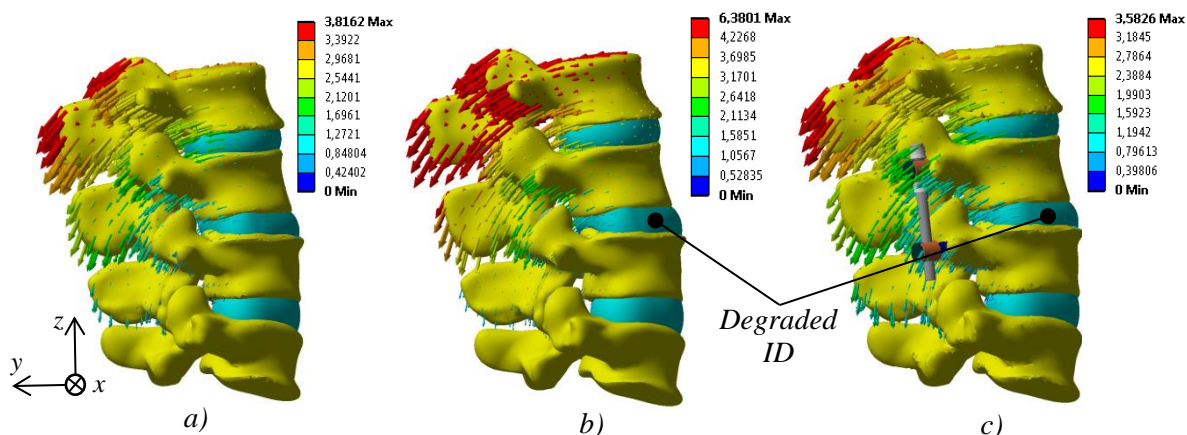


Fig. 2: Total displacement of: a) Physiological model; b) Model with degraded ID; c) Model with implant and degraded ID [mm].

The contact pressures in cartilages were analyzed in all three models. The maximum values of contact pressures are shown in the Fig. 3. The contact pressure distribution in the selected cartilages is shown as well. The greatest contact pressures occur in the model with degraded ID (specifically, in the cartilages of vertebrae L4/L5 (left)). The lowest pressures occur in the model with implant (specifically, in the cartilages of vertebrae L3/L4 (left)).

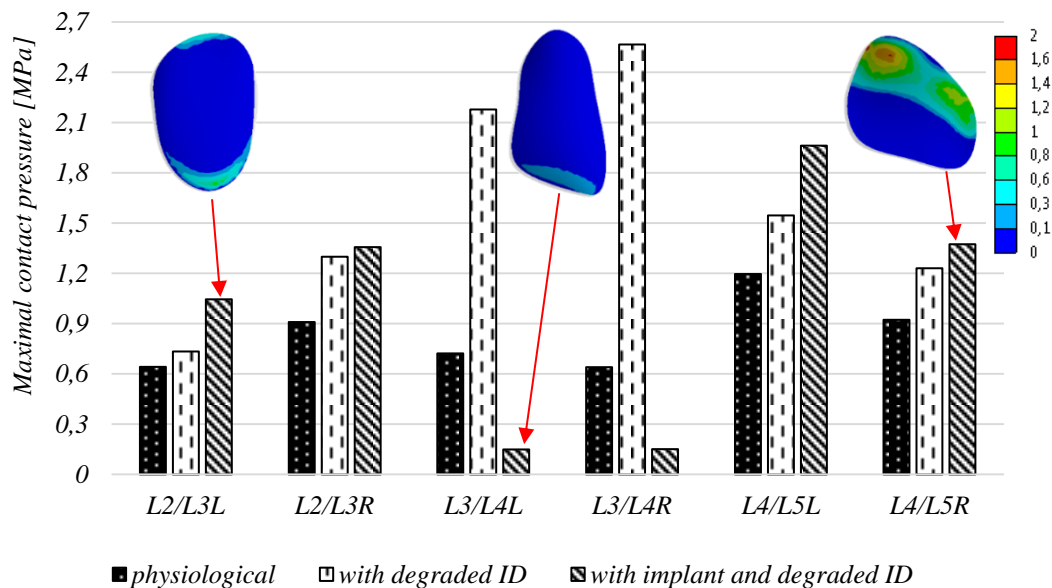


Fig. 3: Graph of contact pressures [MPa] of cartilages (note: Lxx/Lyy – contact between lumbar vertebrae number xx/yy, L – left side, R – right side).

The equivalent strain (strain intensity) was analysed in vertebrae L3 and L4 in the cancellous bone tissue (see Fig. 4a). For better understanding, the colour ranges were changed in order to correspond to intervals of strain intensity suggested by Frost theory (Martin et al., 1989). The Frost's theory says that the bone remodelling is limited by 2000 - 2500 $\mu\epsilon$ in the physiological statue and the bone overloading lies in the thresholds value 3500 and 4000 $\mu\epsilon$. From Fig. 4a, it can be seen that the cancellous bone tissue is overloaded in the places in the beginning and at the end of the screws.

To assess the limit state of elasticity, the equivalent stress was determined on the basis of the Von Mises yield criterion. The values of equivalent stress of implant are shown in Fig. 4b. The maximum value (177 MPa) is in the titan rod under the titan ring.

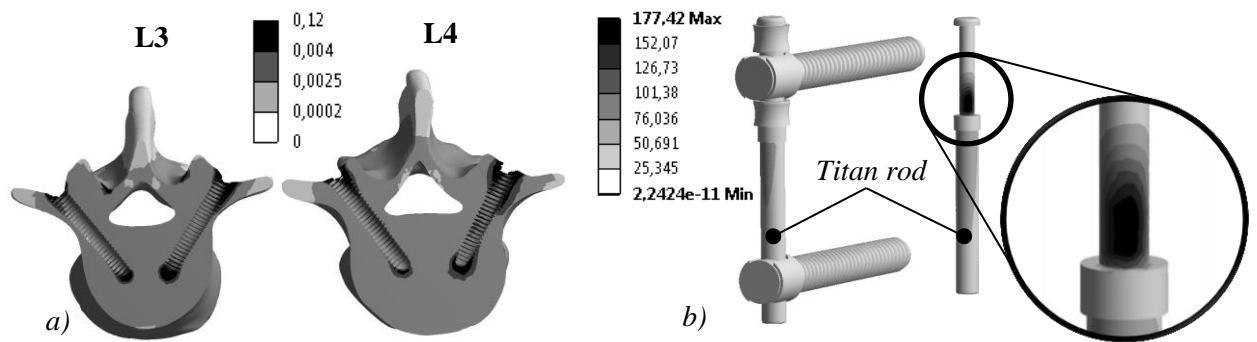


Fig. 4: a) Equivalent strain [-] of vertebrae L3 and L4; b) Equivalent stress [MPa] of implant.

4. Discussion

The results show that the deformations of the physiological model and model with dynamic implant are comparable. The largest u_y displacements occur in the spine model with degraded ID (40 % more than in case of the physiological model). As Fig. 2 and the results of u_y displacements show, the dynamic implant significantly decreases the deformations and the spine segment with degraded ID and implant approaches to the physiologic state (the difference is about 5.5 %).

The range of the calculated contact pressure is from 0.15 MPa to 2.57 MPa. The application of the implant decreases the contact pressure between L3/L4 approx. by 94 %. On the other hand, the pressure increase by 17% was occurred between L4/L5. Implant screws cause the stress redistribution in the vertebrae. The most loaded cancellous bone tissue was found in the part enclosing the screws in L3 and L4. Maximum Von Mises stress is 177 MPa in the titan rod which is subjected to bending. The value of maximum equivalent stress is under the yield stress.

5. Conclusion

This biomechanical study of the spine segment was focused on the stress-strain analysis of the physiological system and the system with the dynamic spine implant and the affected part of the degraded ID. It was shown that the dynamic spine implant has a positive influence on the deformation of the system with the degraded ID. Unfortunately, the bone tissue around screws is overloaded according to Frost theory.

Acknowledgement

The results of this project NETME CENTRE PLUS (LO1202) were co-funded by the Ministry of Education, Youth and Sports within the support program „National Sustainability Program I“. This work was supported by grant specific research FSI-S-14-2344.

References

- Manek, F., Marcián, P., Florian, Z., Valášek, J., Ebringerová, V. (2012) Biomechanical Study of Lumbar Spinal Fixation Device. *Applied Mechanics and Materials*, 232, pp. 142-146.
- Marcián, P., Konečný, O., Borák, L., Valášek, J., Řehák, K., Krpalek, D., Florian, Z. (2011) On the Level of Computational Models in Biomechanics Depending on Gained Data from CT/MRI and micro- Ct. In *MENDEL 2011. Mendel Journal series*, 1, pp. 255-267.
- Prášilová, E., Marcián, P., Krpalek, D., Řehák, K., Malina, R., Konečná, V. (2012) Comparative Study of Mechanical Properties of Bone Tissue Based on the CT and the micro-CT Slices. *Applied Mechanics and Materials*, 232, pp. 152-156.
- Martinez, J.B., Oloyede, V.O., Broom, N.D. (1997) Biomechanics of load-bearing of the intervertebral disc: an experimental and finite element model. *Medical Engineering Physics*, 19, pp. 145-156.
- Goel, V.K., Monroe, B.T., Gilbertson, L.G., Brinckmann, P. (1995) Interlaminar shear stresses and laminae separation in a disc. Finite element analysis of the L3-L4 motion segment subjected to axial compressive loads. *Spine* 20, pp. 689-698.
- Martin, R., Burr, D. (1989) *Structure, function and adaptation of compact bone*. New York: Raven Press, 1.
- Schrazi-Adl, A., Drouin, G. (1987) Load-bearing role of facets in a lumbar segment under sagittal plane loadings. *Journal of Biomechanics*, 20, pp. 601-613.

SINGLE CRACK BEHAVIOR OF FIBER REINFORCED LIME-BASED MORTAR

M. Přinosil^{*}, P. Kabele^{**}

Abstract: *The behavior of a single crack in a fiber composite strongly influences its macroscopic tensile behavior after initiation of the cracking. It affects whether the damage locates in one macro-crack or is represented by large amount of fine cracks and the composite retains the ability to carry the tensile stress in hardening response. As part of the research of fiber-reinforced lime-based mortar, the model of a single fiber-bridged crack response was developed, which allows prediction of the cohesive response for experimentally identified micromechanical parameters of individual components of the composite. Subsequently, the direct tensile test was performed with notched specimens of fiber-reinforced mortar to evaluate cohesive relation and also to verify the model. The notch ensures formation and further development of just one crack. The experiment was carried out for several different amounts of fibers in the composite. The results show that the maximum bridging stress is not only affected by strength of the fiber reinforcement, but also by shear strength of the matrix, which reduces the load carrying capacity.*

Keywords: Single crack behavior, Fiber composite, Lime-based mortar.

1. Introduction

Fiber composites are one of the modern trends of material engineering. Fibers in the composite are important not only with regard to shrinkage, but also to carrying capacity after initiation of the cracking. By systematic design of the composition, we can achieve that the composite exhibits hardening response and damages in the form of large amount of fine dispersed cracks during high tensile deformations. In the past, several criteria have been defined in order to attain such behavior (Marshall and Cox, 1988; Li and Wu, 1992). These criteria are related to the behavior of a single crack (either to strength of fiber reinforcement or to energy associated with crack propagation).

In our research we are developing a fiber composite, which shows strain-hardening response and multiple cracking under tensile loading. It consists of lime-based matrix reinforced with short synthetic fibers. The use of this composite is intended for maintenance and repair works of historic building and monuments. One of the tasks during the mixture design is to determine the appropriate amount of fibers in the composite to satisfy the specified mechanical criteria. It is necessary to take into account the workability of fresh mixture as well. Therefore, the direct tensile test on specimens with notch from designed mixture composition was performed. The main purpose of this work is to experimentally evaluate cohesive law of a single fiber-bridged crack (relation between bridging stress and crack opening displacement - COD) and to verify the proposed micromechanical model.

2. Numerical Simulations

In our previous work we proposed the model of a fiber bridged crack, which was able to predict relation between bridging stress and crack opening displacement (Přinosil and Kabele, 2012). It is based on behavior of individual fiber, whose response can be described by analytical relation between applied load and pullout displacement of the fiber (Li and Leung, 1992). Cohesive stress in the model is then calculated as the sum of forces in all fibers bridging the crack divided by area of the crack.

* Ing. Michal Přinosil: Czech Technical University in Prague, Faculty of Civil Engineering, Department of Mechanics, Thákurova 7; 166 29, Prague; CZ, michal.přinosil@fsv.cvut.cz

** Prof. Ing. Petr Kabele, PhD.: Czech Technical University in Prague, Faculty of Civil Engineering, Department of Mechanics, Thákurova 7; 166 29, Prague; CZ, petr.kabele@fsv.cvut.cz

Micromechanical parameters used in these relations were experimentally evaluated (Přinosil and Kabele, 2012; Přinosil and Kabele, 2013). Since the fibers are randomly generated in a volume of the specimen, results show some variance. Fig. 1 shows the results for several considered amounts of polyvinyl alcohol fibers (type REC 15×8, produced by Kuraray Company) in lime-based matrix.

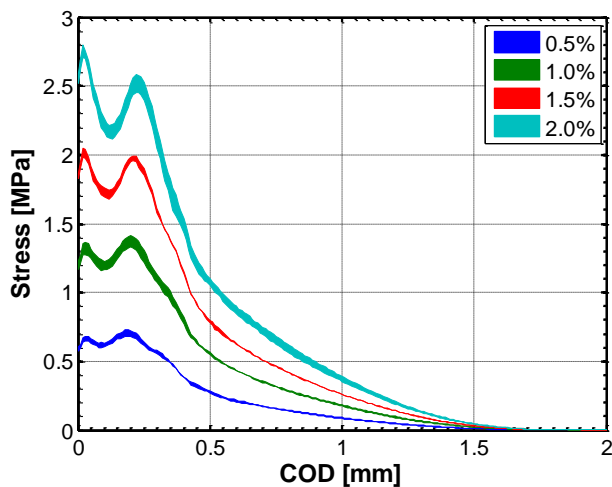


Fig. 1: Numerical tensile stress-crack opening displacement results.

3. Experimental Research

Experimental research was carried out in order to evaluate the single crack cohesive relation and also to validate the model. From fiber-reinforced lime mortar specimens with dimensions 16×55×80 mm were prepared with a thin notch around the whole cross-section at the middle of the specimen (Fig. 2, left). The notch was made in order to ensure formation and further opening of a single crack during tensile loading. Before the beginning of the test, the front surface of the specimen was covered by a contrasting color for the image analysis of displacements (Fig. 2, right).

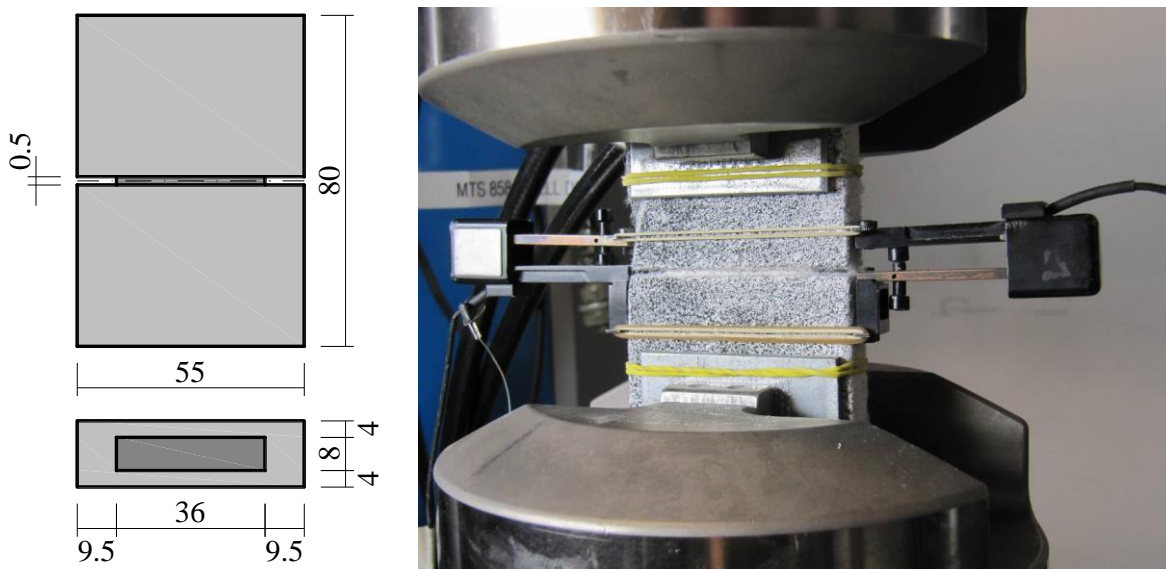


Fig. 2: Specimen geometry (left) and tensile test setup (right).

Direct tensile test was performed by means of the MTS 858 system with controlled crosshead displacement. During the experiment, the applied force in load-cell, crosshead displacement, deformation by two extensometers attached to the side surfaces were continuously recorded (Fig 2, right). Furthermore, the high resolution images of exposed part of the specimen were taken with frequency 1 Hz. Fig. 3 shows stress-crack opening displacement diagrams for mortar with four different fiber contents V_f (0.5%, 1.0%, 1.5%, 2.0%).

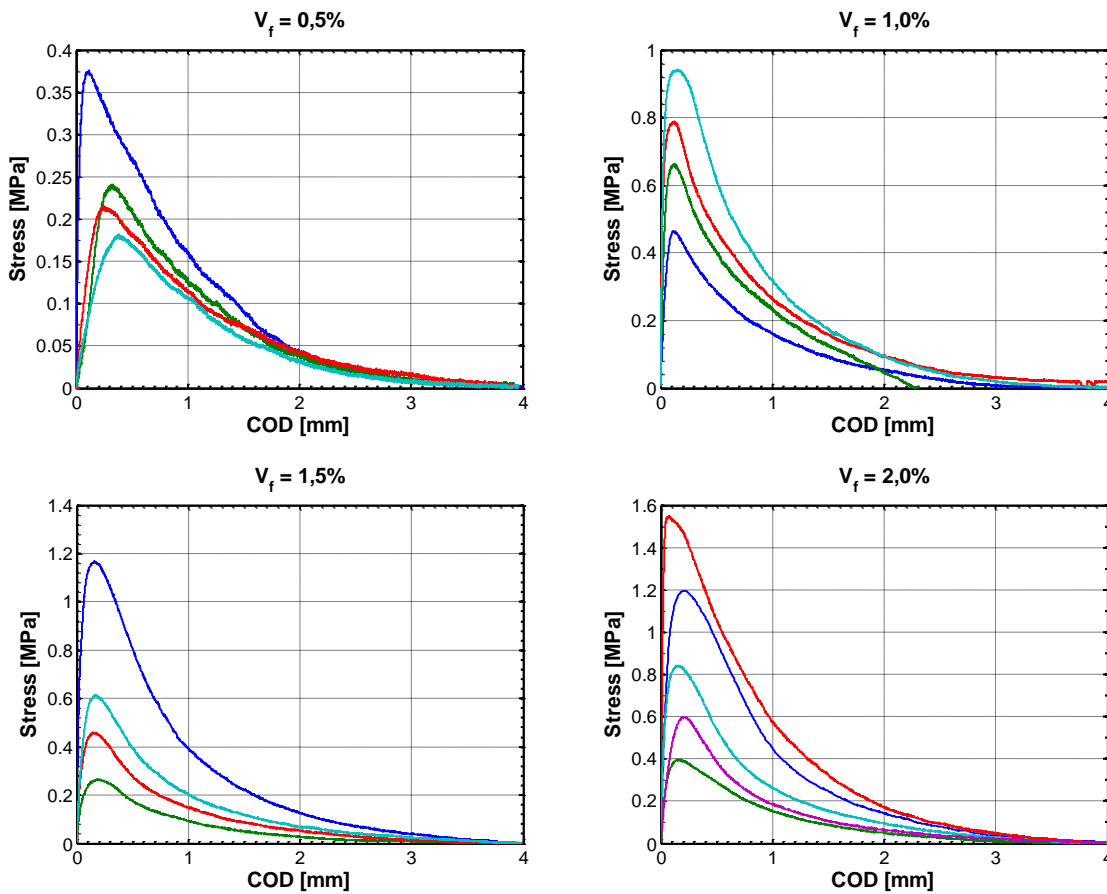


Fig. 3: Experimental tensile stress-crack opening displacement results.

4. Results and Discussion

In comparison with numerical simulations, experimental data show lower values of the maximum bridging stress and high variability. We consider that it is due to unusual mode of the failure. Instead of a typical flat crack, experimental specimens break in the shape of a shear cone (Fig. 4). For this failure mode it is expectable that the strength of fiber reinforcement is reduced because loading direction is not perpendicular to the crack surface. Thus the bridging fibers are more bent on crack surface and the concentration of the bending stress in a fiber reduces its load carrying capacity (Li and Leung, 1992). On the other hand, during breaking in this failure mode the frictional forces between both crack surfaces arises, but does not reach significant values. High scatter of the experimental results could be caused by variability of shear cone shape.



Fig. 4: Shear failure of the specimen.

5. Conclusions

The single crack response of fiber-reinforced lime based mortar has been investigated. Four sets of experimental specimens with different amounts of fibers were prepared and tested. Experimentally evaluated cohesive relations were compared with results of the proposed micromechanical model. In the case of experimental data, the value of maximum bridging stress was lower than the numerical results. It was caused by an unexpected mode of failure similar to a shear cone. This failure mode noticeably reduced the strength of the fiber reinforcement. Therefore, it is necessary to modify the proposed micromechanical model in the future work, so that it will be able to capture this phenomenon. Simultaneously it is necessary to perform detailed evaluation of results using image analysis.

Acknowledgement

The presented research has been carried out with the financial support of the Czech Technical University in Prague under project SGS14/OHK1-089/14.

References

- Li, V. C., Wu, H.-Ch. (1992) Conditions for pseudo strain-hardening in fiber reinforced brittle matrix composites. *Journal of Applied Mechanics Review*, 45, 8, pp. 390-398.
- Li, V. C., Leung C. K. Y. (1992) Steady state and multiple cracking of short random fiber composites. *Journal of Engineering Mechanics*, 118, 11, pp. 2246-2264.
- Li, V. C. (2003) On Engineered Cementitious Composites (ECC) – A review of the material and its applications. *Journal of Advanced Concrete Technology*, 1, 3, pp.215-230.
- Marshall, D. B., Cox, B. N. (1988) A J-integral method for calculating steady-state matrix cracking stresses in composites. *Mechanics of Materials*. 7, 2, pp. 127-133.
- Pereira, E. B., Fischer, G., Barros, J. A. O. (2012) Direct assessment of tensile stress-crack opening behavior of Strain Hardening Cementitious Composites (SHCC). *Cement and Concrete Research*, 42, 6, pp. 834-846.
- Přinosil, M., Kabele, P. (2012) Prediction of the behavior of lime mortar reinforced with fibers based on their micromechanical parameters, In: *Proc. International Conference on Structural Analysis of Historical Constructions, SAHC 2012* (Jasieńko, J. eds), Wrocław University of Technology, Faculty of Civil Engineering, Institute of Building Engineering, Wrocław, pp. 883-889.
- Přinosil, M., Kabele, P. (2013) Influence of composition on tensile and fracture properties of lime-based mortar, In: *Proc. 4th Conference Nano & Macro Mechanics 2013* (Padevět, P. eds), CTU in Prague, Faculty of Civil Engineering, Prague, pp. 163-170.

VIBRATIONS OF BLADES BUNCHES

L. Půst*, L. Pešek*

Abstract: Paper describes a mathematical model for analyzing the dynamic characteristics of five-blades bunch with different damping connections among individual blades. The connections of blades by means of special rubber elements either with the fixed contact with neighboring blades or with one-sided slip is presented. Systems with dry friction connections among blades by means of direct contacts or by inserted dry friction elements are described as well. As an example of analysis results, response curves of five-blades-bunch excited on first blade at different dry friction force in the first bending resonance is shown. Elaborated analysis create the basic theoretical background for evaluation of measurement on experimental bladed disk set in the laboratory of Institute of Thermomechanics of ASCR and it is also applied for evaluation of effectiveness of methods for suppression of forced vibration of blades.

Keywords: Damping, Dry friction, Five-blades-bunch, Harmonic excitation, Response curve.

1. Introduction

Introduction of additional damping elements or friction connection into blades' shroud can very effectively damps undesirable vibrations of turbine blades vibrations (Pesek and Pust, 2011a), (Pesek and Pust, 2011b). Many theoretical, numerical and experimental studies were done in Institute of Thermomechanics ASCR in this field. The previous investigation of dynamic properties of two-blades-model connected either by a rubber element, by direct friction contact or by inserted friction element showed very positive results. In the presented paper, the simple basic two-blades-model is enlarged on the study of five-blades-bunch provided again by means of different types of damping connections.

2. Mathematical Models of Five-Blades-Bunch

Because the experimental research is usually encumbered with a lot of marginal influences, the preliminary analytic-numerical solution of mathematical model has been done. This initial theoretical phase of research is very useful as it enables comparatively easy to complete knowledge of dynamic behaviour of studied system and optimise experimental procedures. Following types of mathematical models of five-blades-bunches were investigated.

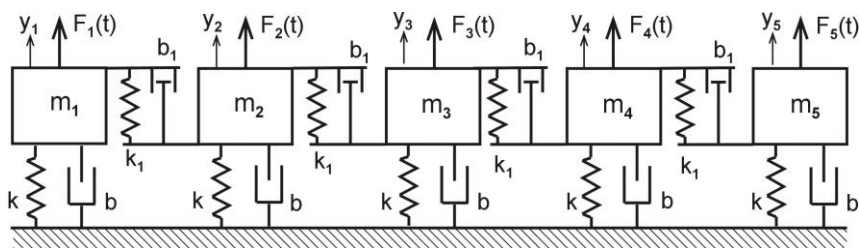


Fig. 1: Computational model of five-blades-bunch.

Five-blades-bunch can be modelled by a simple five masses system shown in Fig. 1, where the blades are replaced by 1 DOF systems, the eigenfrequencies of which correspond to the first bending eigenfrequencies of real blades. The torsion eigenfrequencies of these blades are supposed to be much higher than the bending ones (mass m , stiffness k , damping coefficient b) and therefore, in the first approximation, the torsion deformations and torsion vibrations of blades are not taken into account.

* Ing. Ladislav Půst, DrSc., Ing. Ludek Pešek, CSc.: Institute of Thermomechanics AS CR, v.v.i., Dolejškova 5, 18200 Prague, CZ, pust@it.cas.cz, pesek@it.cas.cz

The connections of blades are in Fig. 1 realized by special rubber elements (Jones, 2001), which are on their sides loaded by such sufficiently great friction forces in the contact areas with the neighbourhood masses that no slips occur in these connections during operation. The linear Voigt–Kelvin model describes deformation properties of rubber damping elements.

If the friction forces in the contact areas between rubber element and the neighbourhood masses are low, than a slip can occur at one side of rubber element. The rubber element is completely fix connected only to one model of blade, but it touches the other blade by the dry friction contact.

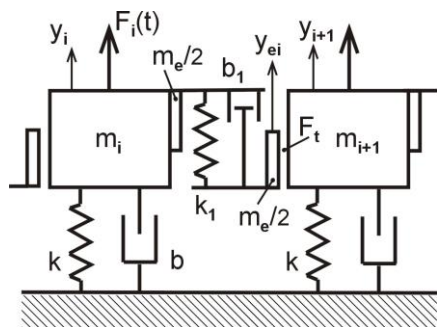


Fig. 2: Model of rubber damping element with one-side slip.

In such case, the dynamic computational model of the connection between two blades masses is shown in Fig. 2. One half of element's mass $m_e/2$ is fully connected with mass m_i , the second $m_e/2$ is connected with blade's mass m_{i+1} only by the sliding contact with the dry friction force F_t . Spring and damping element modelling the deformation properties of rubber link both half-element-masses together. Motion $y_{ei}(t)$ of the second half-element-mass $m_e/2$ is determined by the friction force and viscous elastic rubber forces and must be described by the individual differential equation.

Motion of such a whole system, in which the same slipping properties according to Fig. 2 is supposed, is described by nine nonlinear differential equations; five equations are for masses m_i ,

($i = 1 - 5$) and four ones for damping elements' masses $m_{ej} = m_e/2$, ($j = 1 - 4$).

The simplest damping connections among the blades heads are realized by direct contacts, where dry friction forces are described by Coulomb law (see Fig. 3a):

$$F_t = fF_N \operatorname{sgn}(v) = fF_N v/|v| = fF_N (H(v) - H(-v)) \quad \text{for } v \neq 0, \quad (1)$$

$$F_t \in \langle -fF_N, fF_N \rangle \quad \text{for } v = 0,$$

where f is coefficient of dry friction, F_N normal force, v relative velocity, F_t friction force, $H(v)$ Heaviside function: $H = 1$ for $v > 0$ and $H = 0$ for $v < 0$.

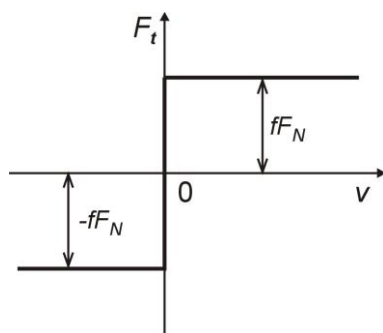


Fig. 3a: Coulomb dry friction characteristic.

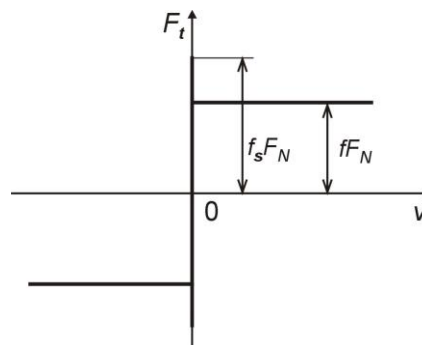


Fig. 3b: Different coefficients $f_s > f$.

A lot of friction couples made of various materials have friction coefficient f in motion ($v \neq 0$) different from the friction coefficient f_s without motion ($v = 0$, see Fig. 3b). Mathematical model of such a connection is similar to eqs. (1), where in the second equation f must be replaced by f_s .

The last investigated five-blades-bunch is a system with damping connections among the blades heads done by means of inserted stiff dry friction damping elements with masses m_e . These damping elements are held in the trapezoidal slot among heads by means of centrifugal force and saved against axial pushing out by means of stops (Fig. 4 left) or by weak springs (Fig. 4 right). Mathematical model in both cases contains several strongly nonlinear functions in nine differential motion equations.

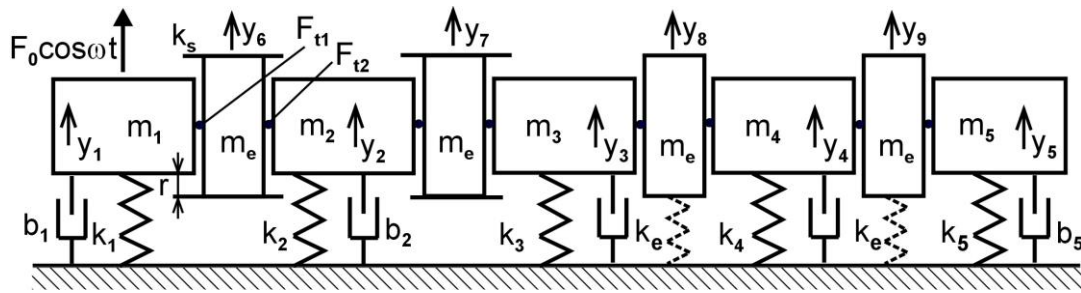


Fig. 4: Five-blades-bunch with inserted dry friction elements.

The harmonic excitation forces $F_{0i} \cos(\omega t)$ acting on blades, modelled here by masses m_i , can be generally of different magnitudes (Pesek and Pust, 2011a), (Pesek and Pust, 2011b). Sometimes we need to take into account also the coupling of blades due to the compliance of turbine disk. Effects of different forms of excitation force vector $F = [F_{01}, F_{02}, F_{03}, F_{04}, F_{05}]$, where $F_i(t) = F_{0i} \cos(\omega t)$, $i = 1, \dots, 5$ on the vibration of five-blades-bunches with different friction connections are analysed in the paper.

3. Free Vibration of Five-Blades-Bunch

The bunch of blades connected by viscous-elastic rubber elements are investigated both theoretically and experimentally and results of this work were presented on the last conference Engineering Mechanics 2013 and published in (Pust and Pesek, 2013a), (Pust and Pesek 2013b). It has been proved there, that due to the more complicated forms at higher eigen-modes the modes' damping increases with frequency even at the constant material viscous damping coefficient.

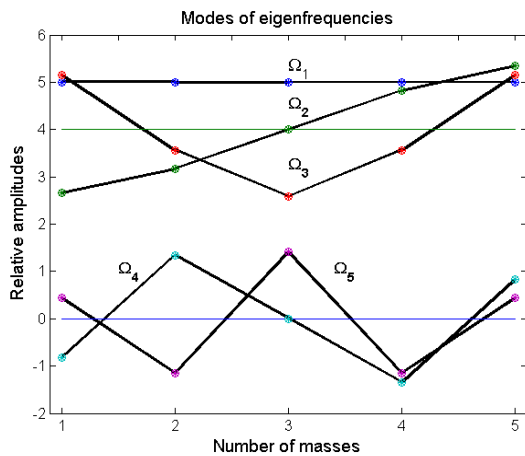


Fig. 5: Eigenmodes of five-blades-bunch.

The application of orthogonality of excitation forces distribution to the other eigenmodes of blades bundle was necessary for analysis and isolation of selected resonance.

The influence of friction connections in the contact surfaces between rubber and blades' heads was investigated as well. It was shown that the decrease of friction forces in contact surfaces increases the resonance amplitudes of excited mass and decreases amplitudes of other, non-excited masses. The first step at the beginning of investigation of nonlinear dry friction systems of blades bunches was the ascertaining of free vibration's modes (Fig. 5) and their exploitation for isolation of selected resonances.

4. Example of Response Curves of Five-Blades-Bunch

Let us show the influence of different coefficient of dry friction on the response curves of five-blades-bunch excited by a harmonic force acting on the first mass in the frequency range $f \in (120.5, 121.5)$ Hz containing the first resonance. Amplitude of excitation force is $F_0 = 10$ N. Response curves of five masses system connected by simple Coulomb dry friction forces in the contacts among masses are shown in Fig. 6. If the friction forces among blades are very low ($F_t = 0.2 F_0 = 2$ N) then the first, excited mass 1 vibrates with considerable higher amplitude than other four masses, which are fixed connected together due to the friction forces. However, in the resonance zone the increase of amplitudes causes separation of mass 2 from the coupled masses 3, 4, 5. All four masses connect together again in the over-resonance zone (Fig. 5, above left)

Twice higher friction ($F_t = 4$ N, Fig. 5, above right) connects masses nearer. Further increase of friction forces to $F_t = 5.5$ N (Fig. 5, bottom left) decreases again resonance peak of excited mass 1 and moderately increases amplitudes of rest of masses. The greatest friction force $F_t = 6.5$ N (Fig. 5, bottom right) results

in merging of all response curves into one line with exception of small part at 121 Hz, where small splitting of mass 1 from masses 2, 3, 4, 5 is recorded.

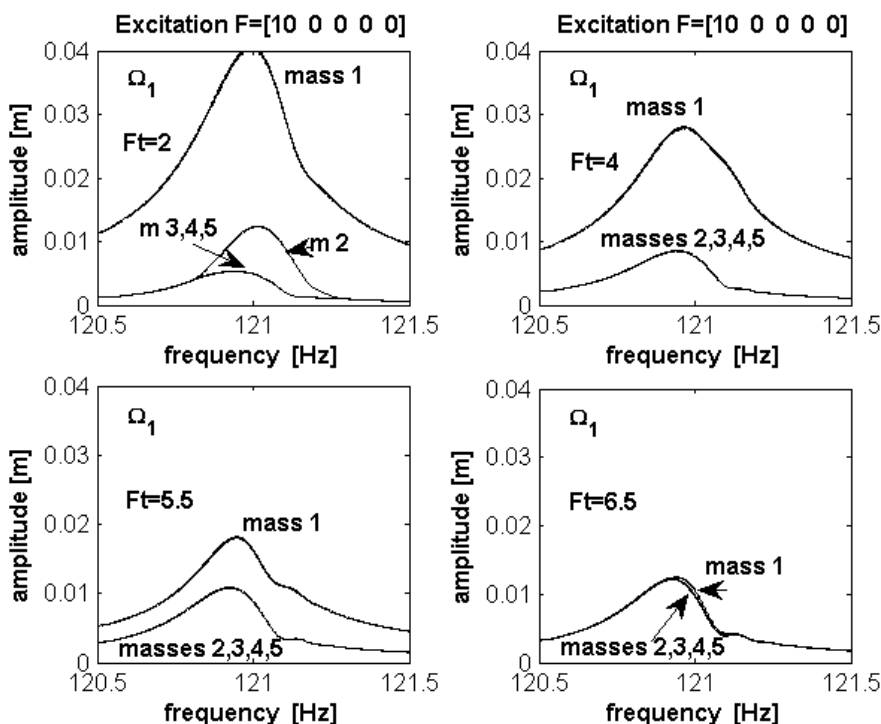


Fig. 6: Response curves of five-blades-bunch excited on first blade at different dry friction force $F_t = 2, 4, 5.5, 6.5$ N.

5. Conclusion

Analysis of dynamic behaviour of numerical models of five-blades-bundle with different types of damping elements is presented. The main attention was given to the response curves of individual blades. It was shown that the application of damping connections in blades shroud is advantageous for suppressing of resonance peaks.

Elaborated method of solution and obtained results create basic theoretical background for evaluation of measurement on laboratory experimental bladed disk set and for evaluation of effectiveness of the various types of damping elements on suppression of forced vibrations of blades.

Acknowledgements

This work was elaborated in Institute of Thermomechanics AS CR v.v.i. and supported by conceptual development of research organizations RVO: 61388998.

References

- Jones, D. G. (2001) Handbook of Viscoelastic Vibration Damping, John Wiley&Sons Ltd, New York.
- Pešek, L., Půst, L. (2011a) Mathematical model of a blade couple connected by damping element, In: Proc. 8th International Conference on Structural Dynamics, EURO DYN 2011, (Roeck G. De, ed.), Katolieke Universiteit, Leuven, pp. 2006-2011.
- Pešek, L., Půst, L. (2011b) Influence of dry friction damping on bladed disk vibration, In: Vibration Problems ICOVP 2011, (Petrikova I., ed.), Berlin, Springer, pp. 557-564.
- Půst, L., Pešek, L. (2011) Friction in blade system, In: Computational Mechanics 2011, (Zeman Vl. ed.), CD-ROM edition, 2 p.
- Půst, L., Pešek, L. (2013a) Mathematical Model of Blades Bundle with Damping Connections. Eastern European Journal of Enterprise Technologies, 2013, 10, pp. 43-46.
- Půst, L., Pešek, L. (2013b) Model of Turbine Blades Bundles, In: Engineering Mechanics 2013, (Zolotarev I., ed.) CD-ROM edition, pp. 467-477.

METHODS OF DETECTING THE UNDESIRABLE OBJECTS ON BELT CONVEYORS

A. Pustulka*

Abstract: *The paper presents the methods of detecting the undesirable objects (stones, not coal rocks) on belt conveyors. Among methods which can be applied are: a method utilizing the X-rays, an ultrasonic method, a sorting set and a thermal imaging method. A stone or another undesirable object which gets to belt conveyor can damage it. But if an undesirable object gets to the transporter, the system should detect and remove it.*

Keywords: Gangue, Conveyor belt, Defect detection, Separating, Lignite coal.

1. Introduction

Conveyor belts are important components for the opencast mining. Therefore, they should be modernized. Constant streamlining of their action supports the development of the mining, but thanks to modern technologies, a safety of work in the mine increases (<http://www.ppwb.org.pl/wb/79/10.php>). Extremely difficult conditions of the operation significantly influence on a durability of belt conveyors and on a belt of conveyor in particular.

The process is caused by (<http://www.ppwb.org.pl/wb/79/10.php>):

- non-axial structure of belt conveyors,
- insufficiently leveled structure of the transporter,
- exaggerated pollution of the space under the transporter,
- too big lumps of transported mining.

Waste, coming from a searched, recognized, stored ore deposit, is an extractive waste (Kotarska, 2012).

Waste rock can be:

- waste rock of the new mineshafts from currently conducted works connected with sinking,
- waste rock from the current mining,
- waste rock deposited in the objects of neutralizing (slag heaps).

Waste rock produced during the mining is mainly an unchanged natural element of the lithosphere built primarily of sandstones, dolomites, limestones, anhydrite, slates, marbles and gravels. An extract coming out of the waste rock contains the increased content of sulphates and dissolved substances.

Flotation waste rock is a mixture of coal dust, water, ash or sand of mineral resources. Material about the granularity from 0 to 0.5 mm and the content of ashes (non-inflammable permanent elements) is crossing 60 % (Kotarska, 2012).

* M.Sc. Eng. A. Pustulka: Chair of Fundamentals of Machinery Design and Tribology, Wroclaw University of Technology, ul. Lukasiewicza 7/9, 50 – 371 Wroclaw, Poland, agnieszka.pustulka@pwr.wroc.pl

2. Methods Used for the Detection of Waste Rocks on Belt Conveyors

The lignite has characteristic properties and because of that it is possible to identify it. It is presented in the Tabs. 1 – 3.

Tab. 1: Chemical composition and the value of the density of the lignite (Kaczmarczyk, 2009).

Chemical composition				Density [kg/m ³]
C [%]	H [%]	S+N [%]	O [%]	920 ÷ 950
58 ÷ 78	4.5 ÷ 7.5	10 ÷ 35	0.8 ÷ 4	

Tab. 2: Contribution of analytical elements in the lignite (Kaczmarczyk, 2009).

Contribution of analytical elements		
Moisture content [%]	Mineral matter [%]	Organic matter [%]
50	10	40

Tab. 3: Group elements in the organic matter of the lignite (Kaczmarczyk, 2009).

Group elements in the organic matter						
Humic acids [%]	Humins [%]	Bitumens [%]	Cellulose wadding [%]	Cellulose [%]	Residual vegetable matters [%]	Mineral charcoal [%]
13 ÷ 85	7 ÷ 81	80	70	40	2 ÷ 8	2 ÷ 80

In order to detect the waste rock on belt conveyors one should apply an appropriate method. Therefore such methods which enable detection of an undesirable object in mining product are discussed below. Comparison of these methods should help to choose the best one in terms of the detection of waste rocks.

2.1. Method utilizing the X-rays

X – ray scanner, which scan a mining product is installed on the initial stretch of belt conveyors. Next, the data from the scanner is controlled appropriately through the special program.

In the Fig. 1 is shown the structure system of the detection of waste rock. The program analyzes the image of a given part of mining products. The value of density of lignite is well-known and it amounts to 920 ÷ 965 kg/m³. A standard of the greyness scale is based on this value. If any undesirable object gets on the conveyors belt, it is automatically detected because it has parameters which are other than the standard. In case of detecting an undesirable object on belt conveyors, the program stops the conveyors belt, the object is removed and then the program resumes action.

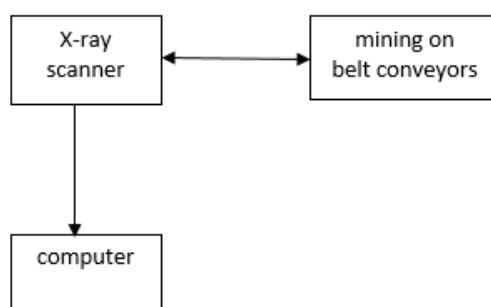


Fig. 1: Structure of the detection system of waste rocks (Pustulka, 2013).

A mobile X – ray scanner is designed to detect waste rocks on the belt conveyors. A mobile X – ray scanner of the AutoClear 150180 company is made as a model of the standard (Pustulka, 2013).

2.2. Sorting set

A classification of coal is based on account of the size of grains. Thanks to that, it is possible to design the system which separates the mining products.

The technological cycle of the sorting set starts when the material is found in the intake hopper, placed above the shaking screen. This intake hopper allows to point the stream of material for the shaking screen or to avoid that and slide it directly to the conveyor belt. By proper placing the intake hopper above the shaking screen, a classification of materials is held basing on the size of mesh of sieves. In the next step, products of classification are placed on appropriate belt conveyors. Each product is stored on the cones or it is directly given to the means of transport.

A possibility of classification on the basis of the size of coal grains of mining product is an advantage of this system. Thanks to such a system, there is a possibility of detecting an undesirable object, e.g. of waste rock.

This method isn't giving the 100% warranty on detecting undesirable objects (http://mifama.com.pl/files/resourcesmodule/@random4537640a142d9/1161934047_Glowne_produkty.pdf).

2.3. Thermal imaging method

The thermography consists of the measurement of the infrared radiation emitted by objects.

Thanks to applying the thermographic camera with IR and MSX resolution, different objects may be controlled. The thermal imaging method allows to detect undesirable objects on belt conveyors.

The values of thermographic camera radiations are registered in the infrared region of $0.9 \div 14 \mu\text{m}$. The dependence of value of the radiation intensity on the temperature is also well-known. The thermography allows to observe the differences of the temperature between various parts of working devices as well as between different objects. It is assumed that temperature of an undesirable object e.g. of a stone is different from the temperature of coal (<http://www.leren.pl/termowizja.html>).

2.4. Ultrasonic defectoscopy

Due to properties of ultrasound, one can distinguish (Andruszkiewicz, 2009), (Sliwinski, 2001):

- method of the echo,
- method of the shadow also the method of letting in,
- method of the resonance,
- TOFD method (time of flight diffraction).

Conduct of research with ultrasonic method relies on (Andruszkiewicz, 2009), (Sliwinski, 2001):

- entering ultrasonic waves into an object (of resilient waves), i.e. mechanical pulses about frequencies greater than 20 kHz; scanning the surface of the object is required;
- detection of signals, which were triggered by waves going through objects.

In case of detection of undesirable objects on belt conveyors the best method applied is a method of the echo which relies on: producing and entering impulses of ultrasonic waves into studied material and their receipt after straying from the material defect or limiting areas.

It is assumed that impulses of an ultrasonic wave are different in case of an undesirable object in mining product than when there is no such an object in mining product. It allows to detect and identifying this object (Andruszkiewicz, 2009), (Sliwinski, 2001).

3. Conclusions

Because of the characteristic properties of lignite, it is possible to identify the presence of undesirable objects in mining product basing on an analysis of these properties.

The paper presents methods enabling such identification. A proper application of these methods helps to detect the waste rock on a transporter. Among them are: method utilizing the X-rays, sorting set, thermal imaging method, ultrasonic defectoscopy.

Each of methods mentioned above can be used for detecting a stone in a mining product. The most accurate is an X-ray method to which utilization gives a higher probability of detecting an undesirable object.

Reference

- Andruszkiewicz, A. (2009) Ultrasonic pulse echo method in the study of two-phase flow liquid/gas, Wrocław University of Technology Publishing House, Wrocław (in Polish).
- Kaczmarczyk, J. (2009) Technical analysis of coal and biomass, Wrocław (in Polish).
- Kotarska, I. (2012) The waste of copper mining in Poland - the balance, the state of development and environmental aspects, Cuprum No. 4 (65) (in Polish).
- Pustulka, A. (2013) The Mechatronic system for Stones detection In the process of the Multi – bucket excavator mining, Master Thesis, Institute of Machinery Design and Operation, Wrocław University of Technology (in Polish).
- Sliwinski, A. (2001) Ultrasounds and their applications, WNT, Warszawa (in Polish).
- <http://www.leren.pl/termowizja.html>, downloaded: January 2014.
- <http://www.ppwb.org.pl/wb/79/10.php>, downloaded: January 2014.
- http://mifama.com.pl/files/resourcesmodule/@random4537640a142d9/1161934047_Glowne_produkty.pdf, downloaded: January 2014.

AIR-PRESSURE CHARACTERISTICS AND VISUALIZATION OF BUBBLING EFFECT IN WATER RESISTANCE THERAPY

V. Radolf*, J. Horáček*, V. Bula*, A. M. Laukkanen**

Abstract: *This study investigates the influence of a widely used method in voice training and therapy, phonation into a resonance tube with the outer end submerged in water ('water resistance therapy' with bubbling effect). Acoustic and electroglottographic (EGG) signals and air pressures in the mouth cavity were registered and the formation of bubbles was studied using high speed camera. Bubbling frequency dominates in the spectra of the pressure signal being about 15 dB higher than the amplitude of the first harmonic, which reflects the fundamental frequency of the vocal folds' vibration. Separation of the bubbles 10 cm under water surface starts when the buoyancy force acting on the bubble is approximately equal to the aerodynamic force in the tube.*

Keywords: Biomechanics of voice, Phonation into tubes, Voice therapy.

1. Introduction

Different variants of phonation into tubes and straws have become increasingly popular in voice training and therapy. In Scandinavia a resonance tube and water resistance therapy methods have been used (see Sovijärvi, 1964; Laukkanen, 1992; Simberg and Laine, 2007). Phonation into a resonance tube (25-28 cm in length, 8 mm inner diameter, made of glass) in air has been used for voice training of normal voiced subjects to improve loudness and voice quality in an effortless way. Phonation into resonance tube submerged into water has been used for voice patients with many types of voice disorders. Immersion depth of 1-2 cm is used to treat both hypofunctional and hyperfunctional voice disorders, while the depth 5-15 cm has been used for patients with incomplete vocal fold closure (Simberg and Laine, 2007).

The present study investigates the mechanism that causes formation of the bubbles and separates them from the tube end.

2. Methods

One female and one male volunteered as subjects. This study focused on ordinary (most comfortable) phonation of the female subject into glass resonance tube, 27 cm in length, 7 mm in inner diameter, where the target fundamental frequency, chosen by the subject and controlled throughout the experiment was 165 Hz.

The sound pressure level (*SPL*) inside the oral cavity was measured using the B&K 4182 special microphone probe designed for measurement of acoustic pressure in small cavities, and the mean oral pressure (P_{oral}) was measured by the digital manometer Greisinger Electronic GDH07AN connected with the oral cavity by a small compliant tube (inner diameter 1.5 mm, length 8 cm). The nose was closed with a clip to prevent any leakage of air through the nose. Electroglottographic signal (EGG) was registered using a dual channel device (Glottal Enterprises). The recording was made using 16.4 kHz sampling frequency by the PC controlled measurement system B&K PULSE 10 synchronized with a high speed camera that registered bubbling with the rate of 1000 frames per second.

Frequency range of the digital manometer started at 0 Hz but attenuated gradually frequencies above 80 Hz. The microphone probe was set to work in the range from 20 Hz to its upper limit 20 kHz. It means

* Institute of Thermomechanics, Academy of Sciences of the Czech Republic, Dolejškova 5, 182 00 Prague, CZ, radolf@it.cas.cz

** Speech and Voice Research Laboratory, School of Education, University of Tampere, FIN-33014, Tampere, Finland

that quite low frequency of bubbling F_B could not be detected by the microphone probe properly. Contrary to that, fundamental frequencies of the vibrating vocal folds F_0 , that were above 100 Hz, were correctly recorded by this probe.

3. Results

Example of simultaneously recorded time signals for the dynamic oral pressure, EGG signal, oral air pressure and images of formation of the bubbles are presented in Figs. 1 and 2.

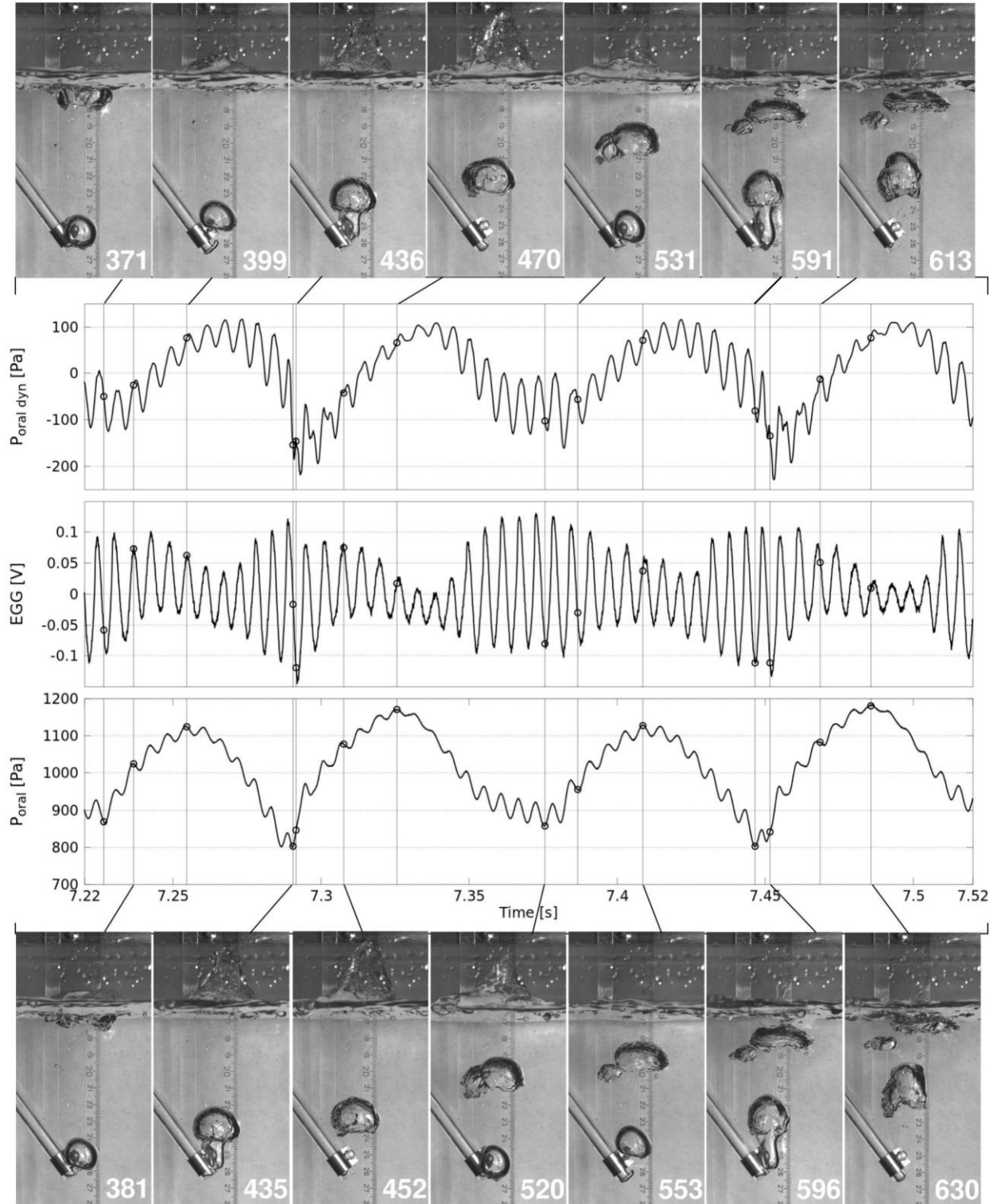


Fig. 1: Dynamic oral pressure, electroglottographic signal (EGG), oral air pressure (P_{oral}) and images taken by the high speed camera at the time instants marked by circles during a comfortable phonation into the resonance tube submerged 10 cm deep in water.

Comfortable phonation of the female subject into the tube submerged 10 cm deep in water is shown in Fig. 1. The time instants marked by small circles correspond to the images taken by the high speed camera. These images represent minimum of the oral pressure (see images 371, 435, 520, 591), maximum of the oral pressure (images 399, 470, 553, 630) and separation of a bubble from the tube end (381, 436, 531, 596). The other images (452, 613) represent the moments of maximum water level inside the tube measured from the outer end of the bottom tube.

The oral pressure multiplied by the cross-sectional area of the tube gives an airpressure force in the range from 31 mN to 45 mN. Buoyancy force acting on a bubble, when it is separated from the tube, was computed on the basis of volume of the bubble estimated from the corresponding image. This force was 41 mN and 46 mN for the frames 381 and 531, respectively, being slightly higher than the force in the tube at these time instants. Therefore we can conclude, that the bubble separation starts when the buoyancy force acting on the bubble is equal or a bit higher than the airpressure force in the tube.

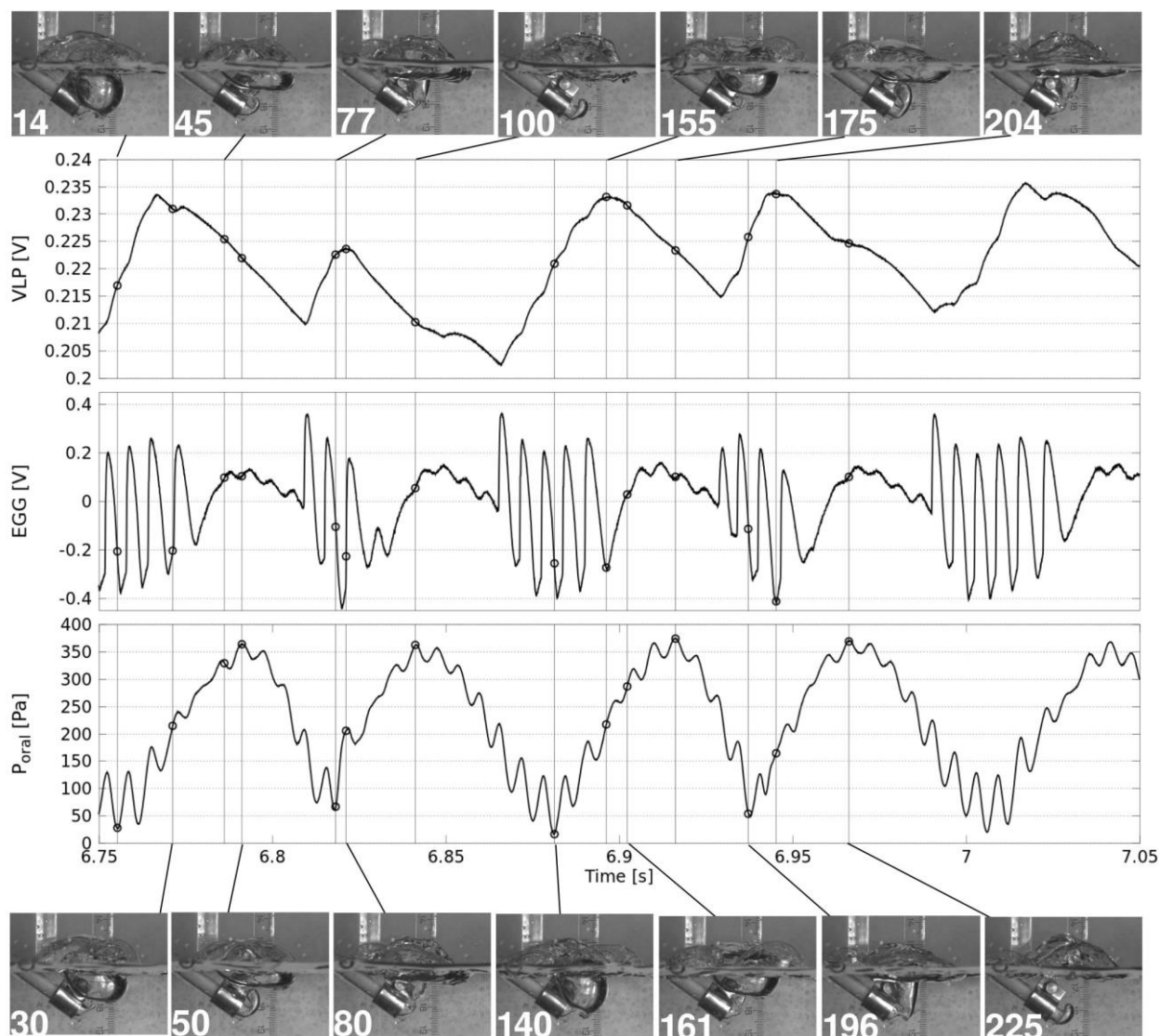


Fig. 2: Vertical larynx position (VLP), electroglottographic signal (EGG), oral air pressure (P_{oral}) and images taken by the high speed camera at the time instants marked by circles during a comfortable phonation into the resonance tube submerged 2 cm deep in water.

Comfortable phonation of the female subject into the tube 2 cm deep in water is presented in Fig. 2. The time instants marked by small circles correspond to the images from the high speed camera and represent minimum of the oral pressure (see images 14, 77, 140, 196), maximum of the oral pressure (images 50, 100, 175, 225) and separation of bubbles from the tube end (30, 45, 80, 155, 161, 204). The bubbles seem to be bigger in their volume because of lower hydrostatic pressure at the tube end submerged 2 cm in the water. However in this case the volume of the bubbles could not be properly estimated because the

bubbles reach the water level before separating from the tube end. The oral pressure multiplied by cross-sectional area of the tube gives the airpressure force in the range from 1 mN to 14 mN.

Oscillations caused by bubbling influence both the oral air pressure and vocal folds contact area as can be seen in EGG time signals. The bubbling frequency even affects vertical position of the larynx derived from amplitude difference between the two pairs of electrodes in EGG. See the upper graph in Fig. 2, where the maxima correspond to the time instants of separation the bubbles (images 30, 80, 155, 161, 204).

Frequency spectra of oral air pressure measured both by the digital manometer and by the microphone probe are displayed in Fig. 3 in the frequency range 0 – 200 Hz. The maximum peak of the intensity nearly 130 dB is located at the frequency of bubbling $F_B = 13$ Hz and $F_B = 16$ Hz for the tube end submerged 10 cm and 2 cm under water level, respectively. Lower peak at the frequency $F_B/2$ indicates a subharmonic effect in bubbling separation which can be recognized in the time signals as the lowest minima at 7.29 s and 7.45 s in Fig. 1 and 6.75 s, 6.88 s and 7.01 s in Fig. 2. Fundamental frequency of vibrating vocal folds around $F_0 = 165$ Hz is characterized by a peak of the level less than 120 dB (see the dashed lines in Fig. 3) surrounded by smaller peaks at frequency $F_0 \pm F_B$, that indicates amplitude modulation of F_0 by the bubbling frequency.

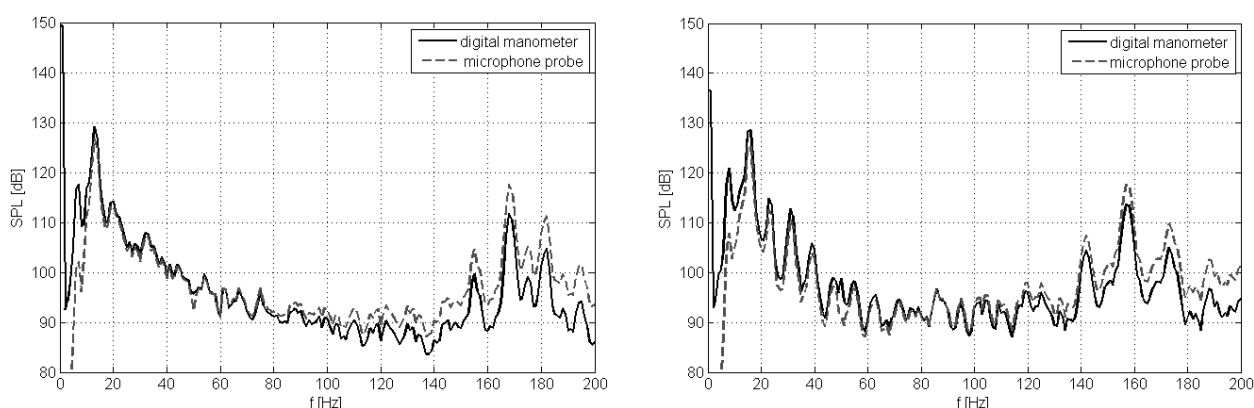


Fig. 3: Frequency spectra of oral air pressure signal registered by microphone probe (dashed line) and by digital manometer (full line) during comfortable phonation into the resonance tube submerged 10 cm (left) and 2 cm (right) deep in water.

4. Conclusions

Phonation into the resonance tube submerged under water surface substantially influences the oral-air pressure and vibration pattern of vocal folds by formation of the bubbles and their separation from the tube end. These changes show periodic character with the frequency 13 Hz and 16 Hz for 10 cm and 2 cm of water level, respectively. This bubbling frequency dominates in the spectra of the pressure signal being about 15 dB higher than the amplitude of the first harmonic, corresponding to vocal folds vibration at the fundamental frequency. Separation of the bubbles 10 cm under water starts when the buoyancy force acting on the bubble is approximately equal to the airpressure force inside the tube.

Acknowledgement

The study was supported under the grant of the Czech Science Foundation No P101/12/P579 and by the Academy of Finland (grants No. 1128095 and 134868).

References

- Laukkanen, A.-M. (1992) About the so called "resonance tubes" used in Finnish voice training practice. An electroglottographic and acoustic investigation on the effects of this method on the voice quality of subjects with normal voice. *Scandinavian Journal of Logopedics and Phoniatrics*, 17 (34), pp. 151-161.
- Simberg, S., Laine, A. (2007) The resonance tube method in voice therapy: description and practical implementations. *Logopedics Phoniatrics Vocology* 32, pp. 165-170.
- Sovijärvi, A. (1964) Die Bestimmung der Stimmkategorien mittels Resonanzröhren. *Verh. 5. Int Kongr Phon Wiss, Munster*. Basel/New York, S. Karger.

MODELING AND OPTIMIZATION OF SHAPES AND INTERFACES IN VIBROACOUSTIC

E. Rohan^{*}, V. Lukeš^{**}, Z. Novotný^{***}

Abstract: We consider acoustic wave propagation in waveguides which are equipped with perforated plates in a form of single or multi-plate panels. Recently we developed mathematical models of the acoustic or vibro-acoustic interaction on such perforated structures using the method of homogenization. These models describe transmission conditions imposed on flat interfaces representing the panels in the global acoustic problems. In view of vast application in the structural optimization, we developed the sensitivity analysis of the acoustic fields with respect to the perforation design. In this paper we report on methods of modeling and optimization of the waveguides designed by the shape, position of the panels and their design.

Keywords: Vibro-acoustic Transmission, Micro-perforated Panel, Homogenization, Optimization, Sensitivity Analysis.

1. Introduction

The paper deals with design sensitivity analysis and optimization of perforated plates or multi-plate panels which interact with acoustic waves. Transmission conditions for coupling the acoustic pressure fields on both sides of the interface were derived using the homogenization of vibroacoustic interactions in a fictitious layer in which the deforming plates are embedded, see (Rohan and Lukeš, 2010) and (Rohan and Lukeš, 2011, Rohan and Lukeš, 2013). This modeling approach allows one to reduce significantly complexity of finite element meshes needed for computing acoustic response in global domains (the waveguides), since the complicated geometries describing the perforated panels are handled when solving local problems in representative volumes. By virtue of the homogenization method, the “macroscopic” parameters involved in the non-local transmission conditions take into account specific shapes of the holes in the plate and the geometrical arrangement of the panels containing multiple plates.

The problem of minimization or maximization of transmission losses in a waveguide containing the plate can be solved to find piecewise periodic design of the plate perforation the shape of which is described with a few optimization parameters. Moreover we consider (simultaneously, or separately) optimization of the waveguide shape. The design sensitivity analysis of objective functions with respect to the design parameters is based on the shape derivatives and the adjoint equation technique.

2. Model of the Acoustic Waveguide with Homogenized Perforated Panels

We consider the global problem of the wave propagation in a waveguide $\Omega^G \subset R^3$ filled by the acoustic fluid. Ω^G is subdivided by perforated plate Γ_0 in two disjoint subdomains Ω^+ and Ω^- , so that $\Omega^G = \Omega^+ \cup \Omega^- \cup \Gamma_0$, see Fig. 1. The acoustic pressure field p is discontinuous in general along Γ_0 . Distribution of p in Ω^G is described by the following equations, where ω is the wave frequency (i.e. $\omega = \kappa \cdot c$ where c is the sound speed and κ is the wave number) and $g\kappa^2$ is the transversal acoustic velocity

* Prof. Dr. Ing. Eduard Rohan, DSc.: European Centre of Excellence, NTIS New Technologies for Information Society, Faculty of Applied Sciences, University of West Bohemia, Univerzitní 8, 30614, Pilsen, CZ, rohan@kme.zcu.cz

** Ing. Vladimr Lukeš, PhD.: Faculty of Applied Sciences, University of West Bohemia in Pilsen, Univerzitní 22, 306 14 Pilsen; CZ, vlukes@kme.zcu.cz

*** Bc. Zdeněk Novotný: Faculty of Applied Sciences, University of West Bohemia in Pilsen, Univerzitní 22, 306 14 Pilsen; CZ

$$\begin{aligned}
& c^2 \nabla^2 p + \omega^2 p = 0 \quad \text{in } \Omega^+ \cup \Omega^-, \\
& \left. \begin{aligned}
& \wp(\omega, [p]_{\Gamma_0}, g^0) = 0 \\
& c^2 \partial p / \partial n^\pm = \pm i \omega g
\end{aligned} \right\} \text{on } \Gamma_0, \\
& r i \omega p + c^2 \partial p / \partial n = s 2 i \omega \bar{p} \quad \text{on } \partial \Omega,
\end{aligned} \tag{1}$$

where \wp is an abstract function describing the homogenized transmission conditions, s, r and \bar{p} are given data, $[\cdot]_{\Gamma_0}$ is the jump across Γ_0 and $\partial p^\pm / \partial n^\pm$ is the normal derivative on Γ_0 computed using the traces of pressures p^\pm defined in domains Ω^+ and Ω^- , respectively. Boundary $\partial \Omega = \Gamma_w \cup \Gamma_{in} \cup \Gamma_{out}$ of the waveguide is split into walls and the input/output parts; by the constants r, s in (1) different conditions on $\partial \Omega$ are respected: $r = s = 0$ on the waveguide walls Γ_w , whereas $r = s = 1$ on Γ_{in} (waveguide input) and $r = 1, s = 0$ on Γ_{out} (waveguide output).

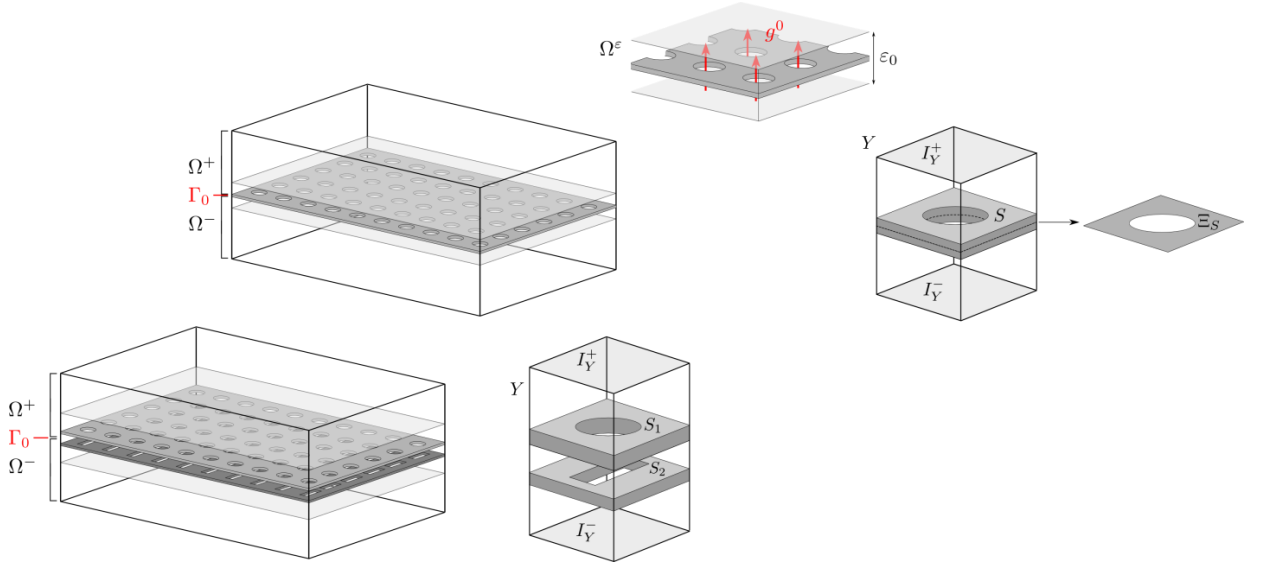


Fig. 1: Top: The global domain Ω^G and the transmission layer in which the plate is situated. The representative periodic cell (RPC) Y where the solid part S represents the perforated plate. Bottom: The double plate panel and its RPC.

The homogenized transmission conditions on Γ_0 , see (1), describe the vibro-acoustic transmission on the perforated plates and involve internal variables describing the plate displacements, deflection and rotations (in the case of the Reissner-Mindlin type models). There are two cases to follow:

Single plate panel. The homogenized Reissner-Mindlin thick plate is tailor-made for perforation by general cylindrical holes with axes orthogonal to the mid-plane of the plate (cf. (Rohan and Miara, 2011), an extension for the phononic plates), the transmission problem leads to two subproblems; the membrane “in-plane” modes of the plate vibrations coupled with surface tangent acoustic waves. The transmission condition involving g is related to the deflection-rotation modes of the plate vibrations coupled with the exterior acoustic fields.

Double-plate panel. Each of the plate is presented by thin plates. According to (Rohan and Lukeš, 2010), in general, there is coupling between transverse and surface acoustic waves, however, this phenomenon vanishes when the plate perforation preserves the transverse isotropy (e.g. the case of cylindrical holes). However, the coupling effect is retained also in a case of panels composed of parallel plates with “mutually shifted” cylindrical holes (possibly of different shapes) which, thus, break the transverse symmetry of the panel. We develop a homogenized vibro-acoustic transmission condition which is employed to couple two external acoustic fields on the both sides of the panel.

Here we describe the simpler of the two cases, involving only the simple plate model. For a given design (see below), the Galerkin formulation of (1) is to find $\mathbf{U} := (p, g, \omega, \boldsymbol{\theta}) \in \mathcal{U}$, such that

$$\Psi(\mathbf{U}, \mathbf{V}) = f(\mathbf{V}) \quad \forall \mathbf{V} = (q, \psi, z, \mathbf{v}) \in \mathcal{U}_0 = \mathcal{U}, \quad (2)$$

where (using the inner products $(\cdot, \cdot)_\Omega$ and $\langle \cdot, \cdot \rangle_{\Gamma_0}$)

$$\begin{aligned} \Psi(\mathbf{U}, \mathbf{V}) &:= c^2(\nabla p, \nabla q)_\Omega - \omega^2(p, q)_\Omega + c\langle p, q \rangle_{\Gamma_{in-out}} - i\omega c^2\langle g, q^+ - q^- \rangle_{\Gamma_0} \cdot \\ &+ \omega^2[C(w, \psi) + C(z, g) - F(g, \psi) - N(w, z) - M(\boldsymbol{\theta}, \mathbf{v})] \\ &+ E(\bar{\nabla}^s \boldsymbol{\theta}, \bar{\nabla}^s \boldsymbol{\vartheta}) + S(\bar{\nabla} w - \boldsymbol{\theta}, \bar{\nabla} z - \boldsymbol{\vartheta}) - i\omega \frac{1}{\varepsilon_0} \langle \psi, p^+ - p^- \rangle_{\Gamma_0}, \\ f(\mathbf{V}) &:= 2i\omega \langle \bar{p}, q \rangle_{\Gamma_{in}}, \end{aligned} \quad (3)$$

and \mathcal{U} is the set of admissible solutions. Above the bilinear forms C, F, N, M, E, S involve homogenized vibro-acoustic transmission coefficients depending on the perforation design which is given by distributed parameters \mathbf{d} . Recall the discontinuity of p and q (the test functions) on Γ_0 ; by $\varepsilon_0 > 0$ the real thickness of the plate is respected.

3. Optimal Design Problem

The design variables \mathbf{d} describe the shape of holes within the RPC, see Fig. 1. It is given by the design curve Γ_s which determines the simple cylindrical type of perforations. In a more general setting of “nearly-periodic” perforations, the geometry of holes can vary with the global coordinate $x \in \Gamma_0$. The second group of the design parameters \mathbf{a} describe the shape of waveguide $\partial\Omega_G$ in a standard way, see e.g. (Haslinger and Neittaanmäki, 1996). In our study both \mathbf{d} and \mathbf{a} are the selected control points of spline-boxes in which the microstructures (the RVE of the transmission layer), or the global domain Ω_G of the waveguide are embedded.

The optimal waveguide shape and perforation design problem can be defined as follows:

$$\begin{aligned} \min_{d \in D_{adm}, a \in A_{adm}} \Phi(\mathbf{U}), \quad \Phi(\mathbf{U}) &= \int_{\Omega_G} |p - \hat{p}|^2 \cdot \\ \text{subject to: } \mathbf{U} &\text{ solves (2)} \end{aligned} \quad (4)$$

Above \hat{p} is the desired acoustic field, D_{adm} is the set of admissible designs, constraining the shape regularity of the perforation and some other constraints (e.g. the area of the plate perforation); A_{adm} constraints shapes of Ω_G .

We report an example; the aim was to achieve a desired average acoustic pressure in the waveguide Ω_G . For simplicity, the plate is subdivided in 3 parts, each one is perforated by circular holes. Thus, only 3 optimization variables parameterize the design. The optimal designs are displayed in Fig. 2. The target average magnitude of the acoustic pressure was 317.14 m²/s.

4. Conclusions

The proposed modeling approach allows for an efficient treatment of the acoustic transmission on perforated plates. We considered various objective functions and optional constraints to optimize the

acoustic field in the waveguide. Recently we developed a model of the double-plate panels which can better influence the acoustic transmission.

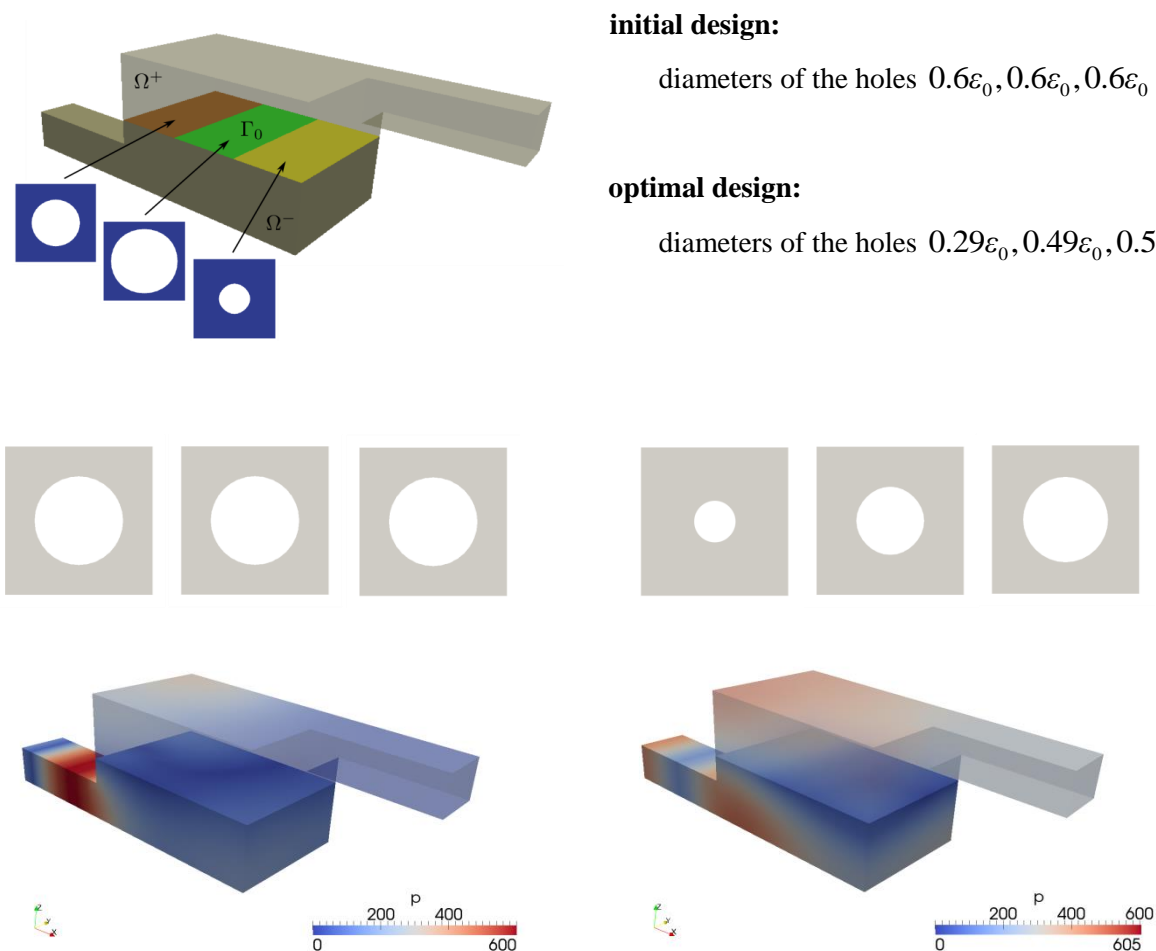


Fig. 2: Top-Right: The global domain Ω^G with a perforated plate, 3 sizes of holes in different parts are considered. Top-Left: Initial and optimized design of the three perforations. Bottom: The overall acoustic fields for the initial (left) and optimized (right) designs.

Acknowledgement

The research of was supported in part by the Czech Scientific Foundation project GACR P101/12/2315, and by the Technological Agency under the contract TACR Alfa, TA02010565.

References

Haslinger, J., Neittaanmäki, P. (1996) Finite Element Approximation for Optimal Shape, Material and Topology Design, 2nd ed. J. Wiley & Sons, Chichester, U.K..

Rohan, E., Lukeš, V. (2010) Homogenization of the acoustic transmission through perforated layer, J. of Comput. and Appl. Math., 234, pp. 1876-1885.

Rohan, E., Lukeš, V. (2011) Homogenized perforated interface in acoustic wave propagation – modeling and optimization, In: Proc. 10th International Conference on Vibration Problems, ICOVP 2011 (J. Náprstek et al, eds.), Springer Proceedings in Physics, 139, pp. 321-327.

Rohan, E., Lukeš, V. (2013) Optimal design in vibro-acoustic problems involving perforated plates. In: Proc. 11th International Conference on Vibration Problems (ICOVP-2013), Z. Dimitrovová et.al. (eds.) Lisbon, Portugal, AMPTAC, article, pp. 1-10, ISBN: 978-989-96264-4-7.

Rohan, E., Míara, B. (2011) Band gaps and vibration of strongly heterogeneous Reissner-Mindlin elastic plates, Comptes Rendus Mathématique, 349, pp. 777-781.

STRUCTURAL TECHNICAL INSPECTION AND PROJECT PREPARATION FOR RECONSTRUCTION OF REINFORCED CONCRETE RAILWAY VIADUCT IN KRNSKO

S. Řeháček*, V. Vacek*, J. Kolísko*, P. Huňka*, D. Čítek*, M. Brodňan**

Abstract: *This paper describes undertaking and results of structural technical inspection of reinforced concrete railway viaduct in the Krnsko municipality and subsequent project for preparation for its reconstruction as based on the findings of this inspection.*

Keywords: Railway Viaduct, Concrete, Technical inspection, Reconstruction.

1. History of the Viaduct

The Krnsko viaduct is a railway bridge located at 67.615 km on the line no. 070, i.e. line Praha – Turnov. The bridge is a valuable historical object and is national monument since 1958. The bridge has 3 arches and spans over the valley of Strenický brook and two roads I/16 and III/27223. When this railway was opened in 1865 a steel truss bridge of the Schiffkorn cascade was here. This bridge was replaced by welded steel continuous truss bridge in 1884. This bridge did not satisfy requirements of the traffic even before the WWI and its reconstruction was thus decided after 60 years of service. The tender was won by company Ing. Hlava and Dr. Kratochvíl. They designed 3 slender concrete arches with span of 28 m and height of 12 m between the existing pillars. There are vertical walls ended with smaller arches supporting 5m wide deck. The author of this design was Ing. Stanislav Bechyně. The bridge was built in 1924 and represented the first concrete railway bridge in Czechoslovakia. This bridge was remarkable not only for the construction material but also because the continuous trackbed was used. The overall construction time was approximately 5 and half months (finished on 18th Sep. 1924). The railway traffic was closed only for 40 days. There was 90 tons of steel used for the 4097 m³ of concrete. This makes 22.5 kg of steel per 1 m³ of concrete. The structure was designed as under-reinforced concrete whose strength is only a little bit greater than that of a regular concrete.

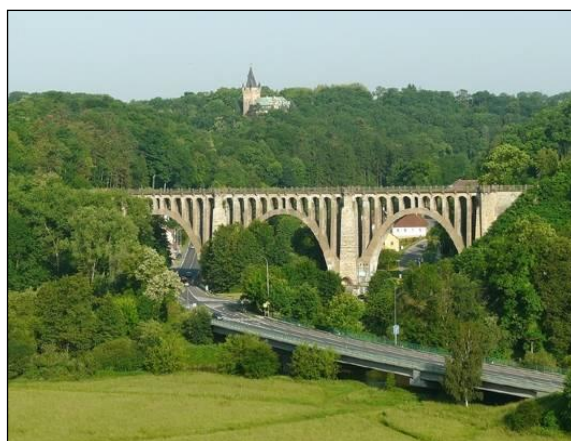


Fig. 1: General view of the Krnsko viaduct with castle Nový Stránov at the background.

* Ing. Stanislav Řeháček, Ing. Vítězslav Vacek, CSc, Assoc. Prof. Ing. Jiří Kolísko, PhD., Ing. Petr Huňka, Ing. David Čítek: Klokner Institute, Czech Technical University, Šolínova 7, 166 08 Prague; CZ, stanislav.rehacek@klok.cvut.cz, vitezslav.vacek@klok.cvut.cz, jiri.kolisko@klok.cvut.cz, petr.hunka@klok.cvut.cz, david.citek@klok.cvut.cz

** Ing. Miroslav Brodňan, PhD.: Žilinská univerzita, Univerzitná 8215/1010 26, Žilina; Slovakia, miroslav.brodnan@fstav.uniza.sk

2. Construction and Technical Inspection – Used Methods

According to the task definition of the developer (TOP CON SERVIS, s.r.o.) the inspection was to assess the condition of the load-carrying mainly reinforced concrete structure. The structure was damaged by long-term leakage due to damaged hydro-insulation of the deck. The main method was a visual inspection of the surface of the load-carrying structure including acoustic tracing of the reachable surfaces, inspection was based on classical foundations (Drochytka et al., 2012; Kolisko and Rehacek, 2007). In the next phase we carried out non-destructive and destructive tests of the concrete strength in compression, determined the thickness of carbonation layer, identified and localized the reinforcement and assessed its state of corrosion. During the in-site inspection tensile strength tests of surface layers concrete were carried out. Further the chemical analyses of the concrete was done to determine the content of aggressive agents such as chloride ions. The examination works have taken place in November and December 2011 and were led by Ing. Stanislav Řeháček and Assoc. Prof. Ing. Jiří Kolisko Ph.D.

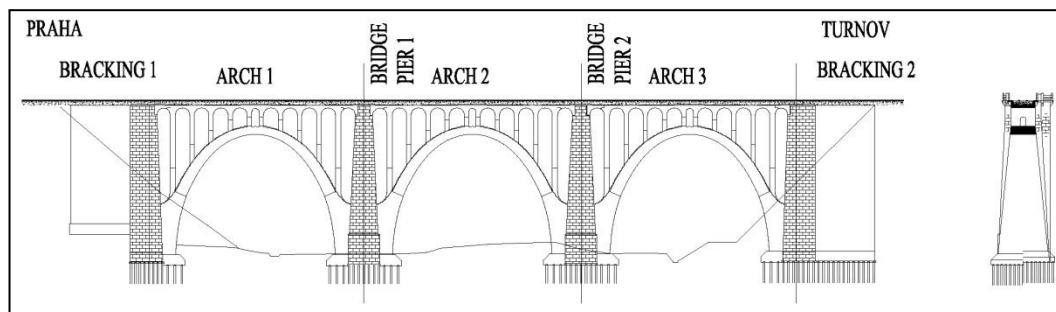


*Fig. 2: Longitudinal chart and cross section of the Krnsko viaduct.
The examination was carried out in indicated places.*

3. Results of the Construction and Technical Inspection

The inspection found out that visible parts of the bearing structure of the bridge do not show marks of significant defects as may be excessive deformations, remarkable cracks, crashed concrete parts etc., which would signal reduced loading capacity or even loss of the whole structure stability. Basic defect of inspected concrete, caused already during initial construction is its high patchiness (Fig. 4) found by almost half of core drills and visible in the form of gravel pockets even in large area of the visible surface. The structural concrete had been further damaged mainly due to intense leakage caused by non-functional hydro-insulation of the deck and impact of weather conditions. Its classification according to currently valid standard ČSN EN 206-1 was done individually for individual structural parts and varies in the marking range C16/20 to C 25/30. Found average tensile strength of surface layers reached about 2 MPa. Content of chloride ions in the surface layer up to 30 mm was assessed as low in accordance with ČSN EN 206-1. From the aspect of conditions for reinforcement corrosion the decisive parameter is depth of carbonation which is rather variable in the inspected structure. Good situation was found in main arches, the bearing reinforcement of which is located almost all in non-carbonated part of the concrete. Markedly worse situation is on the contrary in lateral walls of arcade system. Concrete columns and abutments have such a poor steel reinforcement that it has not been reached at all in the depth of 70 mm (measured from the surface). Corrosion of reinforcement found by probes was mostly surficial but locally also extreme, with the section thinner by more than 50 % (Fig. 3). On the surface of main wall arches is degraded the original water-insulation screed failing to fulfil its function long ago. The result are massive efflorescence with leaky cracks on the bottom face and sides of vaults, areal surficial degradation of upper face with local deterioration in bigger depths, in places reaching the steel reinforcement. In parts are visible gravel pockets, mainly by working joints, caused by mixtures and technologies of compacting used during construction of the bridge. Lightened vaults arranged in upper arcade are also damaged on the surface. Larger defects of the concrete are mainly on the edges of walls and in the area of in-built drainage downcomers. Locally can be found places with covering concrete layer ripped off which is caused by the corrosion – increased volume of profile of corroded steel reinforcing bars. Reinforcement corrosion is visible mainly in areas of thin coverage. Remarkable defects were found in the place of dilatation of inserted deck fields, through which is water strongly leaking to the structures of lightening arcades. Reinforced nibs are markedly damaged, on which are set the inserted field and related stonework of columns. Damage of concrete in this area is reaching deepest. Stone parts of columns and abutments are

deteriorated only superficially in very thin layer. Abutments are damaged more than columns in connection with more extensive accumulation of water behind the reverse side and also due to impact of roots of spreading vegetation including woods. Concrete parts of columns and abutments are damaged similarly to the main vault arches.



Fig. 3: Deep corrosion of the reinforcement.



Fig. 4: Detail of the drillhole – patchy concrete.

4. Concept of Solution of the Bridge Maintenance

4.1. Reconstruction of inserted fields setting

Part of the bearing structure are six inserted fields 2.8 m – 3.2 m with semicircular suspended soffit separated with dilatation joints from abutments, columns and arched parts of NK. Inserted fields will be lifted and maintained with the same procedures as other parts of reinforced bearing structures. Weight of each inserted field is about 43 t. Lifting will be done with use of pre-designed assembly tools.

Masonry of abutments and columns will be unpieced in the place of setting of inserted fields up to the height of 0.5 m and replaced with new reinforced bearing sills made from concrete C30/37 - XF3. Couple of bearing sills on the columns will be fastened together with steel bars set in the drills in original pier cap. Anchoring of bars will be hidden in the bearing sill. New reinforced bearing sills will connect the upper part of the column in the area of setting of inserted fields thus allowing fitting of Teflon ledgement bearing and would improve distribution of horizontal forces caused by the transportation to stone parts of the substructures and exclude transmission of horizontal forces originated in temperatures caused by non-functional sliding bearing and causing degradation of upper parts of stone abutments and columns. Degraded concrete of nibs of bearing structures will be demolished, remaining parts will be cleaned and possible damaged reinforcement will be completed and nibs will be re-profiled or completed with concrete into the original shape. Refurbished original inserted fields will be set on Teflon ledgements.

4.2. Refurbishment of reinforced bearing structure

The whole original reinforced structure will be refurbished including inserted fields, which will be refurbished after their getting down. With exception of inserted fields all works will be performed under operation on the bridge after setting up of new waterproof insulation.

Proposed procedure of refurbishment works includes the following:

- preparation of the base with silica sand blasting,
- removal of damaged covering layers in parts of corroded reinforcement, stripping, cleaning and passivation of corroding reinforcement or its completion, if necessary,
- grouting of the whole structure with micro-fine-cement (MFC),
- filling of gravel pockets and caverns,
- re-profiling,
- allover consolidation screed,
- protective paint.

4.3. Refurbishment of functional layers of ledges

In areas where the functional layer is not cohesive with the base, mainly in wall niches on abutments or where it is damaged, it will be removed. Subsequently the functional layers of ledges, depending on the grade of damage in individual areas will be concreted with the layer reinforced with mesh or re-profiled. Dilatation joints in parts of ends of inserted fields will be sealed or covered.

4.4. Refurbishment of stone walls of the substructure

Walling of the substructure will be rid of remains of vegetation, cleaned by jet water, deeply re-jointed and based on results of water pressure tests it will be grouted with cement mixture. Individual weathered stones will be replaced, faces of abutments will be locally re-masoned.

4.5. Waterproof insulation

Bearing structure of the bridge will be insulated with system of waterproof insulation (SVI) against descending water with asphalt double-strip waterproof layer, fully connected with the base, on horizontal areas with hard protective layer from cast asphalt 30 mm thick, on vertical areas with soft protective layer.

Functional area of ledges will be insulated with directly-functional screed with coarsening pour pulled over the strip of anchoring of the insulation on the side of rail bed.

4.6. Drainage

Current concept of bridge drainage will be kept, only cross drains will be added in the place of termination of the insulation behind ends of wing walls.

Original layer of cambered concrete thickness of 0 to 170 mm in the bridge axis will be demolished and replaced with new cambered concrete layer C30/37 - XF3 reinforced with mesh, thickness 50 - 220 mm in the bridge axis. Original drains of the insulation surface will be replaced. Original downtakes of drainage will have replaced the pipes from rustproof steel. In the area of entries of revision staircases through walls will be connected downcomers made from HDPE pipes running on internal side of walls, except concrete section, from the top directly to original concrete drains, running along revision staircases on the upper surfaces of vaults.

4.7. Handrailing

With regards to national heritage protection the original reinforced handrailing columns will be preserved on the bridge. Original couple of pipe rails will be replaced with triplet of rails on the elevations of pipe rails axis 150 mm, 650 mm and 1150 mm above functional layer of the ledge. Concrete columns will be redeveloped.

5. Conclusion

Reconstruction of the bridge showing constant defects has in majority two steps. First is to stop degradation of concrete and second is to reinforce the concrete. Taking into consideration that this bridge has necessary ability of passage, all financial means will be used for complete redevelopment and water insulation of the whole building thus extending its life for another decades.

Acknowledgements

The article was made with contribution of the grant GAČR P105/12/G059.

References

- Kolisko, J., Rehacek, S. (2007) Pavel Wonka Bridge in Pardubice - Diagnostics of the State of Corrosion of Freely Prestressed Cables and Use of Special Materials in Designing Remedial Measures. In Sanace 2007. Brno: Sdružení pro sanace betonových konstrukcí, 2007, pp. 72-78, ISSN 1211-3700, (in Czech).
- Drochytka, R., Dohnalek, J., Bydzovsky, J., Pumpr, V., Dufka, A., Dohnalek, P. (2012) Technical specifications for concrete construction TP SSBK III., Brno: Sdruzeni pro sanace betonovych konstrukci, 265 p. ISBN: 978-80-260-2210-7, (in Czech).

STRAIN ANALYSIS OF BONE HEALING

K. Řehák^{*}, B. Skallerud^{**}

Abstract: *The distraction osteogenesis has an important position in orthopedic surgery, and it is still object of research to get better understanding of bone healing. The response of callus bone to mechanical loading can be used for assessment of treatment progress. The mechanical strain distribution is often used for assessment in case of bone remodeling (Frost, 1994), thus it could provide additional information of fracture healing progress as well. The strength of the whole callus bone is significantly affected by architecture and tissue properties, which are very difficult to obtain. This article presents finite element analysis of bone fracture healing based on input information obtained from micro-CT scans. The objective of this study is to find which part of callus determines the maximal appropriate loading of whole callus. The four pieces of rabbit tibia fracture callus were micro-CT scanned 30 days after osteotomy using an isotropic voxel size of 20 μm. All finite element models were axially loaded to investigate the reaction force value for different segments of the callus. The mechanical strain distribution and reaction forces of callus were evaluated to compare the differences between each part of models. The results show that the present approach by using finite element method (FEM) is a useful tool in understanding and assessment of fracture healing process.*

Keywords: Micro-CT, Fracture callus, Microstructure, Tissue properties, Finite element method.

1. Introduction

Many people suffer from unequal length of extremities or dwarfism. One treatment procedure is offered in orthopaedics by means of distraction osteogenesis (bone lengthening). The whole process of distraction osteogenesis could be separated into two phases, bone lengthening and consolidation (fixed length, bone maturation). In this second phase of fracture healing, the callus consists of several tissue types. The bone reacts to the mechanical loading by remodeling if it is loaded optimally. The mechanostat hypothesis describes the process of how bone responds to loading (Frost, 1994). This approach can be used for bone healing process at the end of the second phase of bone lengthening.

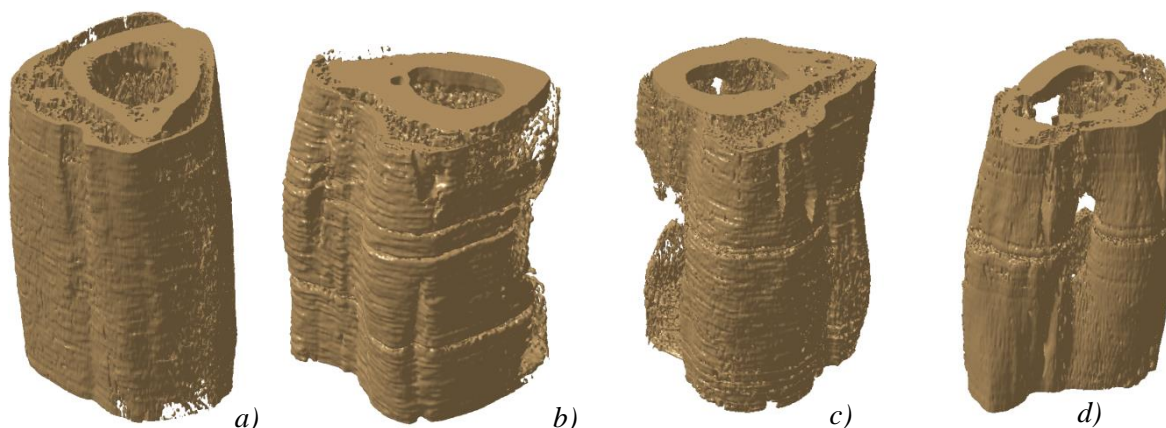


Fig. 1: Shape of all callus a), b), c), d).

^{*} Ing. Kamil Řehák: Brno University of Technology, Faculty of Mechanical Engineering, Institute of Solid Mechanics, Mechatronics and Biomechanics, Technická 2896/2, 616 69 Brno, CZ, kamil.rehak@gmail.com

^{**} Prof. dr. Ing. Bjorn Helge Skallerud: Norwegian University of Science and Technology, Department of Structural Engineering, Richard Birkelands vei 1a, 7491 Trondheim, Norway, bjorn.skallerud@ntnu.no

This study of callus bone response was performed on four rabbit tibia subjected to mid-diaphyseal osteotomy and distraction osteogenesis. The geometry of all callus is shown in Fig. 1. After 30 days (10 days distraction and 20 days consolidation) each callus was scanned using a high resolution micro-CT system [SCANCO Medical AG]. The length of each callus was in range of 10-12 mm, the cross-section diameter is approximately 8 mm. The specimen was scanned at 20 μm resolution. More details can be found in (Aleksyniene et al., 2009).

If a voxel based finite element mesh of the whole rabbit callus is created, using the 20 micrometer scanning resolution, one ends up with approximately 150 million finite elements. This is not computationally feasible without supercomputers and parallelized numerical schemes, thus some simplifications are necessary.

The overall goal of this study was to determine which part of the callus provides the most important stiffness. The FEM software ANSYS was used for this purpose. The detailed finite element models are created from microCT files (Marcian et al., 2012; Marcian et al., 2012).

2. Methods

The scans obtained from micro-CT were segmented in STL Model Creator (Marcian et al., 2011), where saving of pixel intensities is enabled. The pixel intensity can be recalculated to Young's modulus, thus the material properties can be read into finite element software according to element position (Fujiki et al., 2013; Valasek et al., 2010). The dependence of pixel intensity in microCT scans and Young's modulus value is shown in Fig. 2, which is similar to other work (Fujiki et al., 2013; Shefelbine et al., 2005). The range of pixel intensity is 0-4095. The maximum value of Young's modulus was determined based on La Russa (2012), where experiments and numerical models were compared in three point bending. The computational model of each callus is created accounting only for voxels with pixel intensity above 1250. The computational model of callus A with nonhomogeneous linear elastic material properties is shown in Fig. 3. In order to have feasible FE models, instead of using solid elements with 20 micrometer edge, the size was set to 60 micrometer. This led up to 4 millions elements for each segment of callus. The discretization was created using the tetrahedral 10-node element SOLID187, which has a quadratic displacement interpolation and is convenient in capturing details and avoiding bad element shapes. Each callus was divided into five segments. Each segment was axially loaded by 0.1% elongation by prescribing displacement at the bounding sections of the segment. Afterwards the corresponding reaction force was calculated. This provides information about how the stiffness is distributed along the callus.

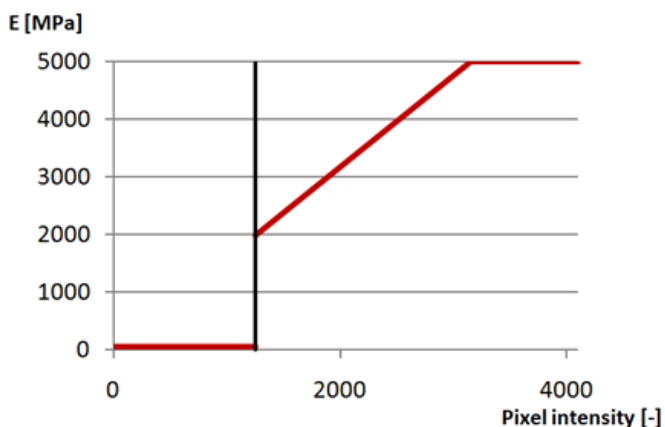


Fig. 2: Young's modulus dependence on pixel intensity.

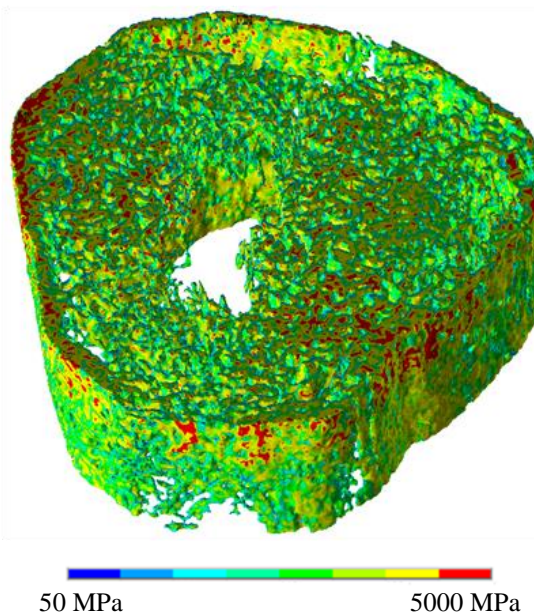


Fig. 3: Young's modulus of callus A second segment.

3. Results

The reaction force due to the displacement loading was calculated for each segment and compared to the highest value of each callus. The distribution of the reaction force along callus is shown in Fig. 4. The highest value of force, which corresponds to 0.1% segment strain, is dominantly in middle segment in case of callus B, C, D; and in the second segment in callus A. On the other hand the force difference between second and third segment of callus A is not so significant. The lowest value of force is 46%, but the reaction force of third segment of callus D is significantly higher than in other segments. The highest value in the middle part could be due to the callus cross section, which is largest in the middle part of the callus and smaller at the ends. Also the material properties are important in this regard. The quantity of mineralized tissue is significantly changing through whole process of healing (Morgan et al., 2009). The time of scanning callus corresponds to end of second phase (consolidation). At the callus ends the old cortical bone is present and new bone must be connected to them, which is more difficult than creation of new bone in the whole volume, like in the middle.

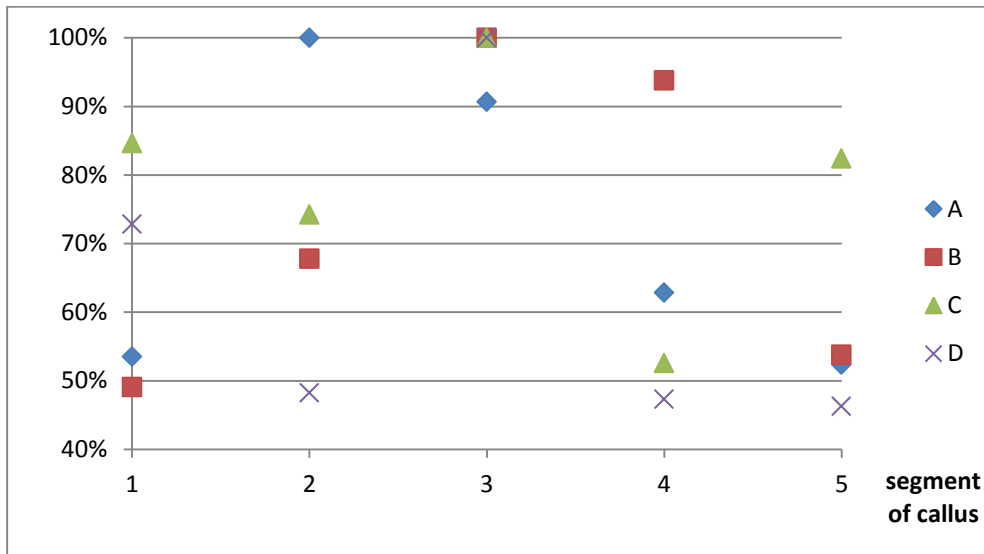


Fig. 4: Reaction force due to 0.1% nominal strain in percent of highest value of each callus.

The mechanical strain distribution of four calluses was investigated to see if the response to mechanical loading is physiological or pathological overloading. In the present study we use microstrain to assess callus model response. A closer study of strain distributions shows that the whole callus is in physiological loading, thus the remodelling of callus can be expected. Physiological loading is defined for strain 0.0002-0.002. (Frost, 1994) The strain distribution of callus A is shown in Fig. 5.

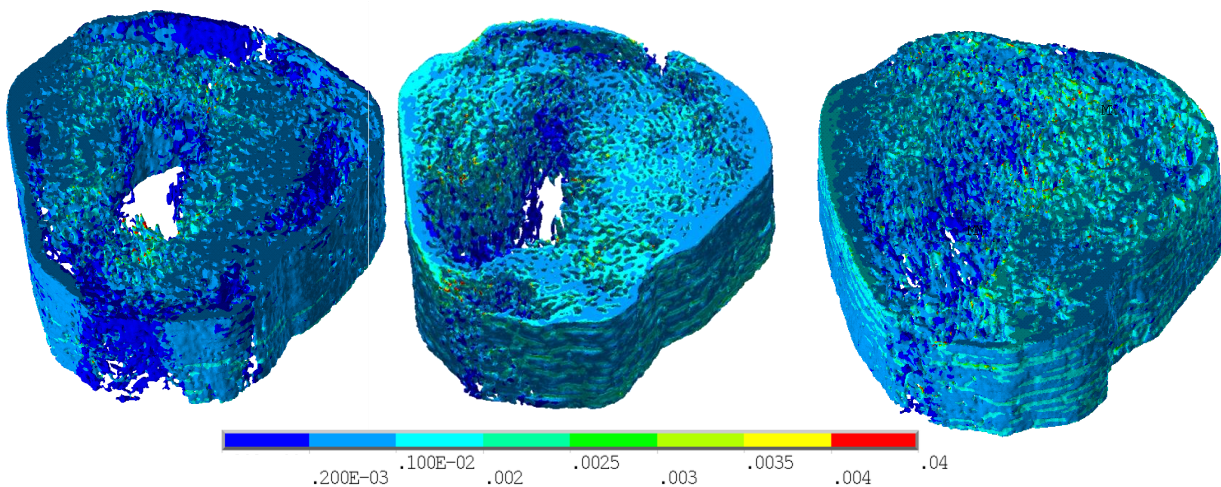


Fig. 5: Strain distribution of callus A, first, second and third part.

4. Conclusions

The present study focused on determination of which part of callus has lower stiffness and governs the optimal loading to support bone healing. To find the lowest stiffness part the four calluses were divided into five parts, which were loaded by elongation 0.1%. The reaction forces were evaluated and compared to the highest value of each callus. The analysis of the callus shows that the end parts were the low stiffness segment, thus the optimal loading should be determined based on them. The middle part seems to be stiffer due to larger cross-section, moreover the material properties of this part at this healing phase are getting closer to mature bone mechanical properties.

The results of finite element analysis show that the callus reaction to loading can be evaluated by mechanical strain distribution, which is dominantly below the bone pathological overloading value.

Further work should deal with better determination of critical callus location, and time dependent analysis is necessary to perform (Vetter et al., 2011). The micro-CT should be done through whole phase of healing and the new experiments should be done to get more accurate estimates of Young's modulus.

Acknowledgement

This work was supported by specific research FSI-J-12-5 and specific research FSI-S-14-2344. The authors are grateful for input from Drs. R. Aleksyniene and V. Russa.

References

- Aleksyniene, R., Thomsen, J. S., Eckhardt, H., Bundgaard, K. G., Lind, M., Hvid, I. (2009) Three-dimensional microstructural properties of regenerated mineralizing tissue after OTH treatment in a rabbit tibial lengthening model, *J Musculoskelet. Neuronal Interact.* 9, pp. 268-277.
- Frost, H. M. (1994) Wolff's law and bone's structural adaptations to mechanical usage: an overview for clinicians, *The Angle Orthodontist*, Vol. 64, No. 3, pp 175-188.
- Fujiki, K., Aoki, K., Marcián, P., Borák, L., Hudieb, M., Ohya, K., Igarashi, Y., Wakabayashi, N. (2013) The influence of mechanical stimulation on osteoclast localization in the mouse maxilla: bone histomorphometry and finite element analysis, *Biomech and Mod in Mechanobio*, pp. 325-333.
- LaRussa, V. (2012) Biomechanical aspects of distraction osteogenesis, PhD Thesis, Dep Structural Engineering, Norwegian Univ Science and Techn.
- Marcian, P., Konecny, O., Borak, L., Valasek, J., Rehak, K., Krpalek, D., Florian, Z. (2011) On the Level of Computational Models in Biomechanics Depending on Gained Data from CT/MRI and Micro-CT, *Mendel*, pp. 255-267.
- Marcian, P., Majer, Z., Dlouhy, I., Florian Z. (2012) Estimation of Local Mechanical Properties of Highly Porous Ceramic Materials, *Chemicke listy*, pp. 476-477.
- Marcian, P., Majer, Z., Florian Z., Dlouhy, I. (2012) Stress Strain Analysis of High Porous Ceramics, *Advanced Materials Research*, pp. 1330-1333.
- Morgan, E. F., Mason, Z. D., Chien, K. B., Pfeiffer, A. J., Barners, G.L., Einhorn, T. A., Gerstenfeld, L. C. (2009) Micro-computed tomography assessment of fracture healing: Relationships among callus structure, composition and mechanical function, *Bone* 44, pp. 335-344.
- Shelfelbine, S. J., Simon, U., Claes, L., Gold, A., Gabet, Y., Bab, I., Muller, R., Augat, P., (2005) Prediction of fracture callus mechanical properties using micro-CT images and voxel-based finite element analysis, *Bone* 36 480-488.
- Valasek, J., Marcian, P., Krpalek, D., Borak, L., Florian, Z., Konecny, O. (2010) Material Properties of Bone Tissue Obtained from CT for Biomechanics Purposes, *Mendel Journal series*, pp. 483-490.
- Vetter, A., Liu, Y., Witt, F., Manjubala, I., Sander, O., Epari, D.R., Fratzl, P., Duda, G.N., Weinkamer, R. (2011) The mechanical heterogeneity of hard callus influences local tissue strains during bone healing: A finite element study based on sheep experiments, *Journal of Biomechanics* 44, pp 517-523.

NUMERICAL EXPLICIT ANALYSIS OF ABSORBING MATERIALS USED IN MULTILAYER MINE PROTECTION

R. Řídký*, J. Buchar**, S. Rolc***, M. Drdlová****, J. Krátký*****

Abstract: An interaction of the blast pressure wave after detonation of a blast mine under the multilayer mine protection mounted on a military vehicle is described in this project. The main focus was applied to absorbing capability of the multilayer sandwich. Results from numerical simulations were compared with experimental tests. The test procedure is provided according to STANAG 4569/AEP-55 standard with threat level 3B. The main armor material, aluminum, enables high local plastic deformation and high global deflection of the plate. The aluminum foam layer increase an absorption capacity of the armor assembly against a surface attacks. The material crushable foam was used for the aluminum foam layer modeling. Soil, air and explosive were modeled using Euler type FEM grids. Not only deflection, but also stress and strain values were evaluated over all multilayer plates. The residual deflection presents good correlation between the simulation and test. The main goal of this project was to develop a multilayer armor that is able to protect a typical military vehicle against the 8 kg TNT blast mine. It was achieved by a combination of an aluminum base armor, aluminum foam, a glass fiber laminate and ballistic steel sheet.

Keywords: ANSYS, Explicit Analysis, Mine protection, Blast load, LS-Dyna.

1. Introduction

The present time is bringing wide range of terrorist attack forms. One of them, mine explosion under a military vehicle, was a subject of investigation in this project. The numerical simulations described in this paper investigate an interaction of the blast pressure wave after detonation surrogate charge under the multilayer mine protection mounted on that vehicle. Especially the absorbing capability of the protection was investigated. An influence of the aluminum foams was gratefully noticed. The results from numerical simulations were compared with results from experimental tests. One of objectives of this work was to validate material parameters and numerical simulation setup that is able to describe mentioned mine test. In future this procedure will be applied in the next step of analysis, design of a military vehicle protection.

2. Problem Description

This test represents an attack of the blast mine to the sandwich armor plate (Rolc, 2007 and 2008). The sandwich is mounted on the vehicle from a bottom side. The mine is placed in the soil ground. The test is provided according AEP-55 standard with threat level 3B. Whole experimental equipment (stand) was modeled with regards to correct loading and boundary conditions application.

The related standard AEP-55 level 3B prescribes for an armor testing a blast effect of a surrogate charge placed under the center of tested armor. The reference mass of explosive was to be adjusted to 8 kg of TNT. The mine was placed in sand ground 100 mm under surface of the soil (dimension was measured from the top of the mine casing). Dimension between ground and bottom area of the armor (ground clearance) was prescribed about 450 mm.

* Ing. Radek Řídký: SVSFEM s.r.o., Škrochova 42; 615 00, Brno; CZ, rridky@svsfem.cz

** Prof. Ing. Jaroslav Buchar, DSc.: SVSFEM s.r.o., Škrochova 42; 615 00, Brno; CZ, buchar@svsfem.cz

*** Assoc. Prof. Ing. Stanislav Rolc, CSc.: Vojenský výzkumný ústav. s. p., Veslařská 230, 637 00 Brno, CZ, rolc@vvubrno.cz

**** Ing. Martina Drdlová: Výzkumný ústav stavebních hmot, a. s., Hněvkovského 65, 617 00 Brno, CZ, drdlova@vustah.cz

***** Ing. Josef Krátký, PhD.: BOGGES spol. s.r.o., Rudice 1, 679 06 Rudice, CZ, josef.kratky@boggess.cz

The experimental equipment (stand) in Fig. 1 represents a mass of the protected vehicle. The analyzed assembly consists of four plates: ballistic aluminum, aluminum foam, glass fiber composite and ballistic steel.



Fig. 1: Experimental equipment – stand and testing plate.

The geometry of the stand and testing armor were modeled in complete 3D space with two planes of symmetry (only one quarter of the system has been modeled). The FE model in Fig. 2 was created according related 3D CAD drawing. Analyzed armor was modeled as a sandwich plate.

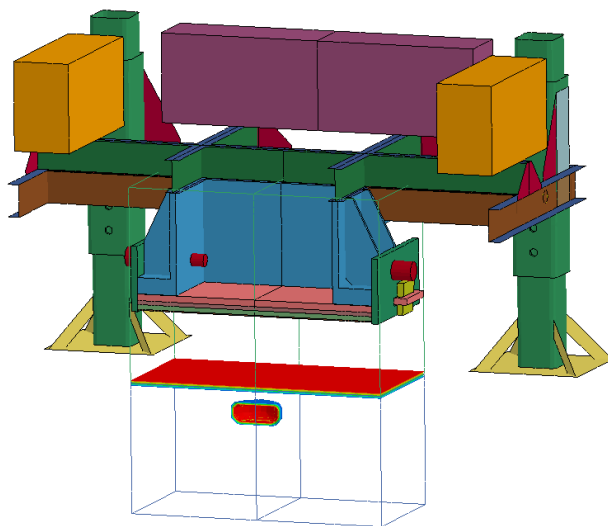


Fig. 2: Numerical model of the equipment.

All of the components in the experimental device were modeled using Lagrange type FEM grids. Also all of the stand components were modeled using material equation Johnson-Cook. Johnson and Cook (Buchar, 2003) express the flow in material model as

$$\sigma_y = (A + B\epsilon_p^n)(1 + C \ln \epsilon^*)(1 - T^{*m}) \quad (1)$$

where **A**, **B**, **C**, **n** and **m** is input constants, ϵ_p is effective plastic strain,

$$T^* \text{ is homologous temperature} = (T - T_{\text{room}})/(T_{\text{melt}} - T_{\text{room}}).$$

The material crushable foam from LS-DYNA database was used for the Aluminum foam layer modeling. This material is dedicated to modeling crushable foam with optional damping and tension cut-off. Unloading is fully elastic. Tension is treated as elastic-perfectly-plastic at the tension cut-off value. The volumetric strain is defined in terms of the relative volume, **V**, as:

$$\gamma = 1 - V \quad (2)$$

The relative volume is defined as the ratio of the current to the initial volume.

Soil, air and explosive in this numerical analysis were modeled using Euler type FEM grids.

3. Mine Protection Results

The initial models supposed a plastic deformation of the armor sandwich with high deflection but without any significant rupture of plates. However this assumption had to be revoked. The front cover plate in simulations was damaged in whole thickness in many armor simulation variants, see Fig. 3. Moreover the main aluminum armor presented some partial crack too. The failure model and elements eroding were added to the material properties.

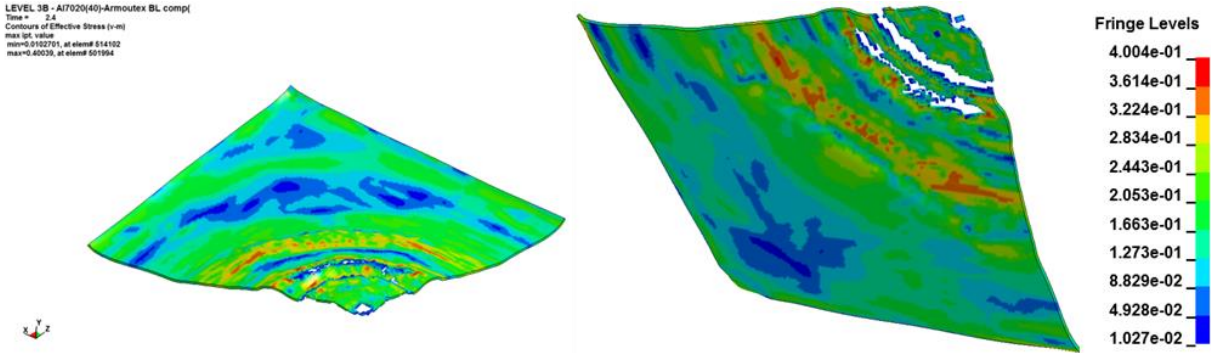


Fig. 3: Effective Stress on the front aluminum cover plate.

The main result from a simulation, residual armor deflection, was decreased in a few simulation steps about 35% to 78 mm in the plate center.

Apart from that also stress and strain values were evaluated over all multilayer plates. The main armor material, aluminum, enables high local plastic deformation and high global deflection of the plate as well.

The aluminum foam layer increase an absorption capacity of the armor assembly against a surface attacks.

Some local areas on the base armor exceed a limit strain 8%. It can cause a failure on the base armor around the stand fixing edge. This was confirmed in a real test.

4. Verification of the Numerical Simulation in Real Tests

The real tests of the armor assembly were performed in two parts. The first test was done after some first simulation in order to agree a numerical model and all his parameters. The second test round was done after a few steps of numerical simulations due to verify the final optimized multilayer armor configuration.

The first comparison between the real test and numerical simulation presented next difference in the residual deflection – Tab. 1.

Tab. 1: Measurement versus simulation comparison.

	Measurement	FE simulation	Difference [%]
<i>Residual deflection</i>			
Armor type I	80.0	90.0	+13%

The material properties used in material models were correlated according to the test results. The optimized multilayer armor variant was checked in a real test with next result.

Next table presents a typical result from a comparison between the final simulation and real test.

Tab. 2: Measurement versus improved simulation comparison.

	Measurement	FE simulation	Difference [%]
<i>Residual deflection</i>			
Armor type II	76.1	78.0	+2%

The residual deflection presents good correlation between the simulation and test, as show Fig. 4 and Tab. 2.

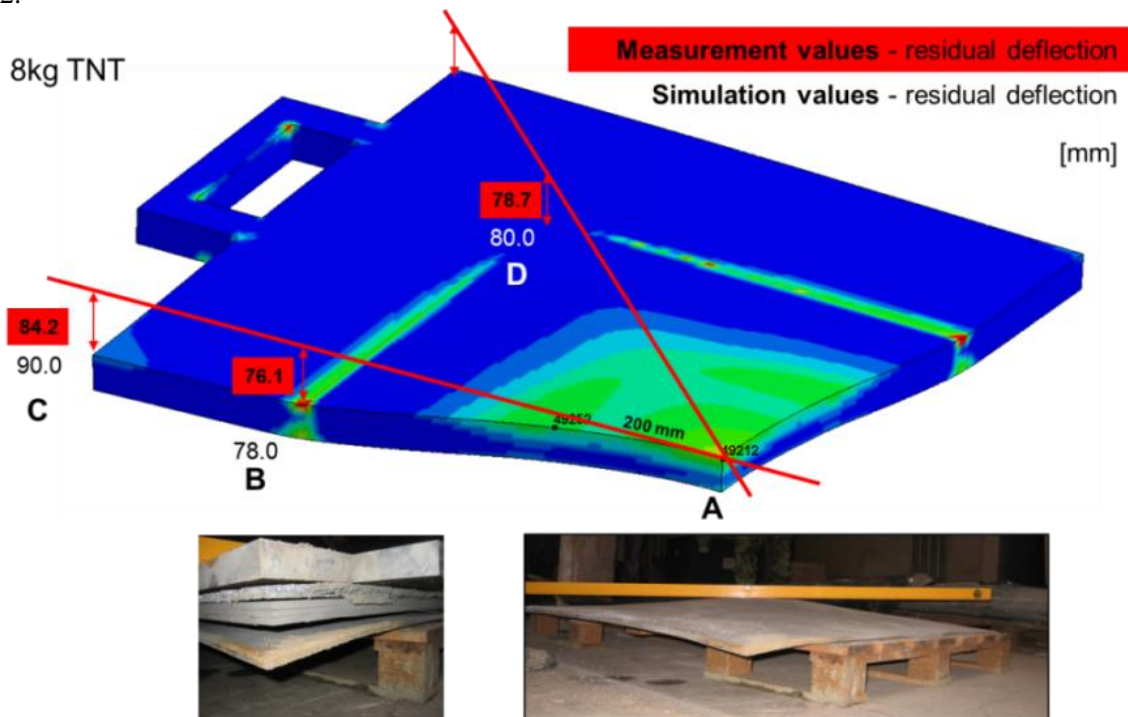


Fig. 4: Verification test of the numerical model.

5. Conclusion

One of the goals of this project was to develop a multilayer armor that is able to protect a typical military vehicle against the 8 kg TNT blast mine. It was achieved by a combination of the aluminum base armor, aluminum foam, a glass fiber laminate and ballistic steel sheet. The dynamic and residual displacements of the armor assembly were decreased during an optimization process applied in sets of numerical simulations.

The benefit from the absorbing material – aluminum foam – was confirmed during numerical simulations and real tests as well. Those studies allow a detailed investigation of a behavior of the absorbing materials that will be implemented in next steps of the project.

The result absorbing multilayer armor is planned to be used in next industry application, mine protection of the military vehicle.

Acknowledgement

The authors gratefully acknowledge the financial support from the Grant Agency of the Czech Republic through the project GAČR GA13-22945S.

References

- Rolc, S., Adamík, V., Buchar, J., Severa L. (2007) Plate response to buried charge explosion. Shock Wave and Hypervelocity Phenomena - Material Science Forum. vol. 566, No. 1, pp. 83-88. ISSN 0255-5476.
- Rolc, S., Buchar, J., Krátký, J., Graeber, S., Havlíček, M., Pecháček, J. (2008) Response of the plate to the buried blast mine explosion. In 24th International Symposium on Ballistics. 1. ed. Pennsylvania: DEStech Publications, pp. 512-518. ISBN 978-1-932078-93-0.
- Buchar, J., Voldřich, J. (2003) Terminal Ballistics. Academia, ISBN 80-200-1222-2 (in Czech).
- STANAG 4569, (Edition 1) Protection levels for occupants of logistic and light armoured vehicles. May 2004, NSA/0533-LAND/4569, Brussels.
- AEP-55, Volume 2, (Edition 1). Procedures for evaluating the protection level of logistic and light armoured vehicles – Mine threat. Allied engineering publication, September 2006, NSA, Brussels.

PARALLEL NUMERICAL COMPUTATION OF DISTRIBUTION OF PRESURE PAST AN OSCILATING AIRFOIL NACA0015

V. Řídký*, P. Šidlof**

Abstract: *The article is devoted to 2D parallel numerical computation of pressure on the surface of an elastically supported airfoil self-oscillating due to interaction with the airflow. Movement of airfoil is described by translation and rotation, identified from experimental data. A new boundary condition for the 2DOF motion of the airfoil was implemented in OpenFoam, an open-source software package based on finite volume method. The results of numerical simulation (distribution of pressure on the surface of airfoil) are compared with experimental data measured in a wind tunnel, where a physical model of NACA0015 airfoil was mounted and tuned to exhibit the flutter instability. The experimental results were obtained previously in the Institute of Thermomechanics by interferographic measurement in a subsonic wind tunnel.*

Keywords: OpenFOAM, Airfoil, Parallel computing and dynamic mesh.

1. Introduction

Numerical simulation of flow around an oscillating NACA0015 airfoil is a very complex problem. In this case is coupled a problematic of numerical solution of a flow and the interaction of fluids and elastic structures. The airfoil can be approximated as a two-degree-of-freedom system, with vertical translation and rotation modes. Movement is harmonic with constant amplitude (flutter instability). This movement is described below.

The numerical solution of interaction of fluids and elastic structures are very often time consuming. Flow around an oscillating airfoil is complex and during large angles of -attack massive flow separation may occur. In aerospace engineering applications, flow is almost always turbulent. Two-dimensional models are still applied from practical reasons, mainly because the computational cost is drastically lower. For the numerical simulation of laminar and turbulent flow is possible to use the following approaches. The most frequent in CFD are RANS model (Reynolds Averaged Navier-Stokes equations). Because the Navier Stokes equations are nonlinear after averaging arises a new term the Reynolds stress. This term is modelled. In this case a two equations model $k-\omega$ SST (Menter, 1994) is used. This model gives good results in adverse pressure gradients and separating flows. Next possibility how model the turbulent flow is used LES (Large Eddy Simulations). The solutions of the Navier-Stokes equations are divided into two parts. Large coherent turbulent structures are solved directly and the small-scale isotropic turbulence is modelled. The third possibility is the Direct Numerical Simulations (DNS), which solve directly the Navier-Stokes equations. Element size corresponds to the smallest scales of turbulence, this is the reason why the mesh must be fine enough. The number of elements scales with $Re^{9/4}$.

This paper is focused on 2D numerical solution of incompressible and compressible airflow past the airfoil. The distribution of p/p_0 on the surface of the airfoil when using incompressible model of flow (without turbulence model and SST $k-\omega$ model turbulence) and compressible model of flow (without turbulence model) is compared. The results of numerical simulations are compared with experimental data measured in aerodynamic tunnel of the Institute of Thermomechanics in Nový Knín. In the experiment, the pressures are evaluated from interferograms obtained using Mach-Zehnder interferometer, as described in (Vlček, 2010).

* Ing. Václav Řídký: Technical University of Liberec, Studentská 2, Liberec 461 17; CZ, vaclav.ridky@tul.cz

** Ing. Petr Šidlof, PhD.: Technical University of Liberec, Studentská 2, Liberec 461 17; CZ, sidlof@it.cas.cz

2. Methods

Numerical simulation is solved in software package OpenFoam (finite volume method) and the meshes are created in mesh generator GridPro. For the mathematical description of flow around the airfoil are used incompressible (1), (2) and compressible (3), (4) Navier-Stokes equations.

$$\nabla \cdot \mathbf{u} = 0 \quad (1)$$

$$\frac{\partial \mathbf{u}}{\partial t} + \nabla \cdot (\mathbf{u}\mathbf{u}) - \nabla \cdot \nu \nabla \mathbf{u} + \frac{1}{\rho} \nabla p = 0 \quad (2)$$

$$\frac{\partial \rho}{\partial t} + \nabla \cdot (\rho \mathbf{u}) = 0 \quad (3)$$

$$\frac{\partial \rho \mathbf{u}}{\partial t} + \nabla \cdot (\rho \mathbf{u}\mathbf{u}) - \nabla \cdot \mu \nabla \mathbf{u} + \nabla p = 0 \quad (4)$$

Here \mathbf{u} , p and ρ are fluid velocity, pressure, and density, ν is kinematic viscosity and μ is dynamic viscosity. For the compressible flow is needed also equation for heat transfer. When the k - ω SST turbulence model is used, the equation for k (turbulence kinetic energy) and ω (specific dissipation rate) is necessary:

$$\frac{\partial k}{\partial t} + U_j \frac{\partial k}{\partial x_j} = P_k - \beta^* k \omega + \frac{\partial}{\partial x_j} \left[(\nu + \sigma_k \nu_T) \frac{\partial k}{\partial x_j} \right] \quad (5)$$

$$\frac{\partial \omega}{\partial t} + U_j \frac{\partial \omega}{\partial x_j} = \alpha S^2 - \beta^* \omega^2 + \frac{\partial}{\partial x_j} \left[(\nu + \sigma_k \nu_T) \frac{\partial \omega}{\partial x_j} \right] + 2(1 - F_1) \sigma_{\omega 2} \frac{1}{\omega} \frac{\partial k}{\partial x_i} \frac{\partial \omega}{\partial x_i} \quad (6)$$

$$\mu_t = \frac{\rho a_1 k}{\max(a_1 \omega, \Omega F_2)}; F_2 = \tanh \left(\left(\max \left[\frac{2\sqrt{k}}{\beta^* \omega y}, \frac{500\nu}{y^2 \omega} \right] \right)^2 \right); P_k = \min \left(\tau_{ij} \frac{\partial U_i}{\partial x_j} k \omega 10 \beta^* \right) \quad (7)$$

$$F_1 = \tanh \left\{ \left(\min \left(\max \left[\frac{\sqrt{k}}{\omega y \beta^*}, \frac{500\nu}{y^2 \omega}, \frac{4\sigma_{\omega 2} k}{CD_{k\omega} y^2} \right] \right) \right)^4 \right\}; CD_{k\omega} = \max \left(2\rho \sigma_{\omega 2} \frac{1}{\omega} \frac{\partial k}{\partial x_i} \frac{\partial \omega}{\partial x_i}, 10^{-10} \right) \quad (8)$$

$$\alpha_1 = \frac{5}{9}, \alpha_2 = 0.44, \beta_1 = \frac{3}{40}, \beta_2 = 0.0828, \beta^* = \frac{9}{100}, \sigma_{k1} = 0.85, \sigma_{k2} = 1, \sigma_{\omega 1} = 0.5, \sigma_{\omega 2} = 0.856$$

The 2D Geometry corresponds to the experimental setup. OpenFoam. Mesh used for numerical simulation is a c -type mesh and number of element is 80000. Boundary condition for velocity, pressure and movement are same for all cases. Movement of the airfoil is prescribed as boundary condition on boundary (Γ_{wing}). This boundary was implement to OpenFoam and the movement with two degrees of freedom has several parameters. Parameters are frequency 19.5 Hz, the amplitude of the plunging movement was ± 7 mm, the amplitude of the rotational movement is $\pm 17^\circ$ and phase shift between translation and rotation is 8° (Vlček, 2011).

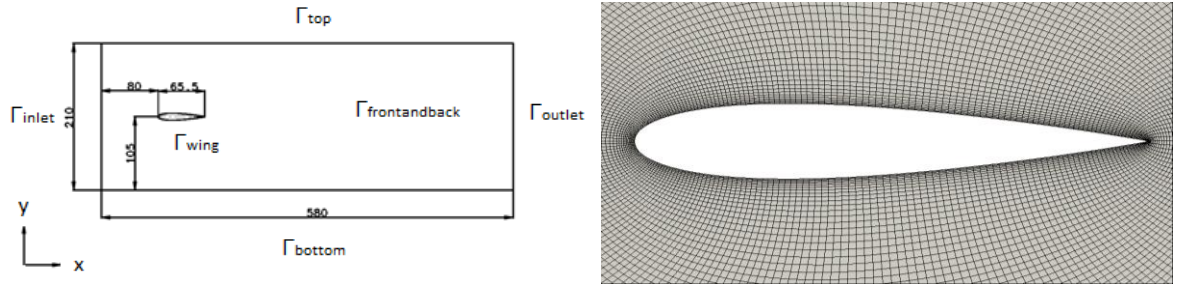


Fig. 1: Computational domain with boundary condition (left) and c -mesh around the airfoil (right).

Following boundary conditions for velocity were prescribed: on input (Γ_{inlet}) is prescribed velocity $u = 147$ m/s. On the walls of channel (Γ_{top} and Γ_{bottom}) is prescribed velocity $u = 0$ m/s. On the surface of the wing (Γ_{wing}) is prescribed velocity which corresponds to local velocity of the airfoil movement. Due to large intensity of vorticity resulting from flow separation downstream of the wing surface a stabilized boundary condition is prescribed at outlet Γ_{out} : condition $\partial u / \partial n = 0$ when velocity direction points outward of the domain, $u = 0$ m/s otherwise. Boundary conditions for the pressure at the inlet (Γ_{out}) prescribe $p = 98925$ Pa. All walls (Γ_{outlet} , Γ_{top} , and Γ_{bottom}) have the Neumann boundary condition $\partial p / \partial n = 0$.

For compressible flow without turbulence model is added boundary condition for temperature. On all surfaces is prescribed temperature measured during the experiment (293 °K). For turbulent variable is on the input (Γ_{inlet}) and output (Γ_{out}) value for $k = 85 \text{ m}^2/\text{s}^2$ and for $\omega = 940 \text{ 1/s}$. On the other wall (Γ_{wing} , Γ_{top} and Γ_{bottom}) are wall functions because thickness first element on the surface of the airfoil is $y^+ = 20$.

3. Results

Results from numerical simulations (pressure) is normalized using reference pressure, because experimental data are also normalized. Value of the pressure is averaged over five periods of vibration. On the graphs (Figs. 2-6) are results in the phases. The zero pitch of the airfoil occurs near phase 013, the time interval between the phases is 2 ms and between phase 006 and phase 010 is 4 ms (index of phase is number of milliseconds from the top position of rotation). The graphs show the normalized pressure field around the airfoil in four specific phases of one vibration period $T = 51.3 \text{ ms}$. On the graphs are compared normalized pressure distribution p/p_0 on the surface of the airfoil on the left side are results from top surface of the airfoil and on the right side are results from bottom surface of the airfoil.

All models indicate the same position of the stagnation point and are conforming to the experiment. In the current numerical simulations, the best agreement with the experimental data is obtained using the incompressible simulation with the $k-\omega$ SST turbulence model.

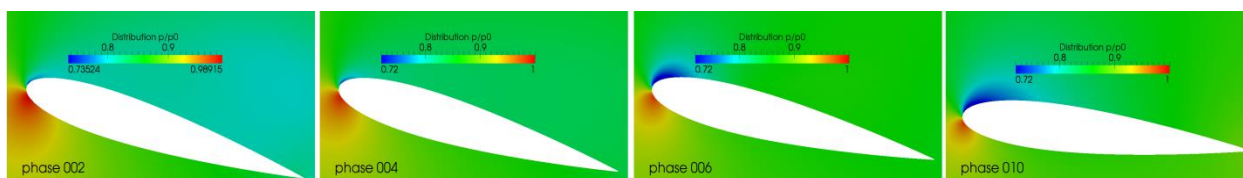


Fig. 2: Normalized pressure distribution p/p_0 for incompressible flow with turbulence model on the surface of the airfoil from numerical simulation and demonstration phase of rotation.

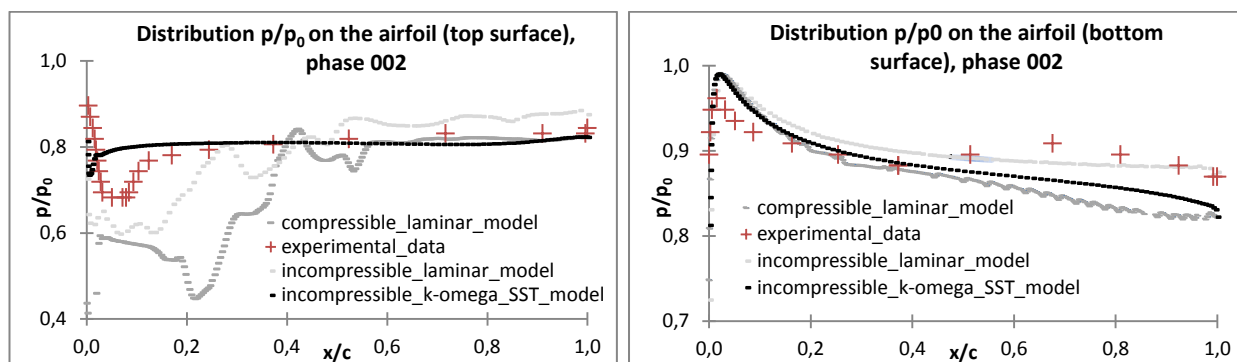


Fig. 3: Normalized pressure distribution p/p_0 on the surface of the airfoil from experiment and numerical simulation, on the left is result on the top surface, on the right is result on the bottom surface, phase 002.

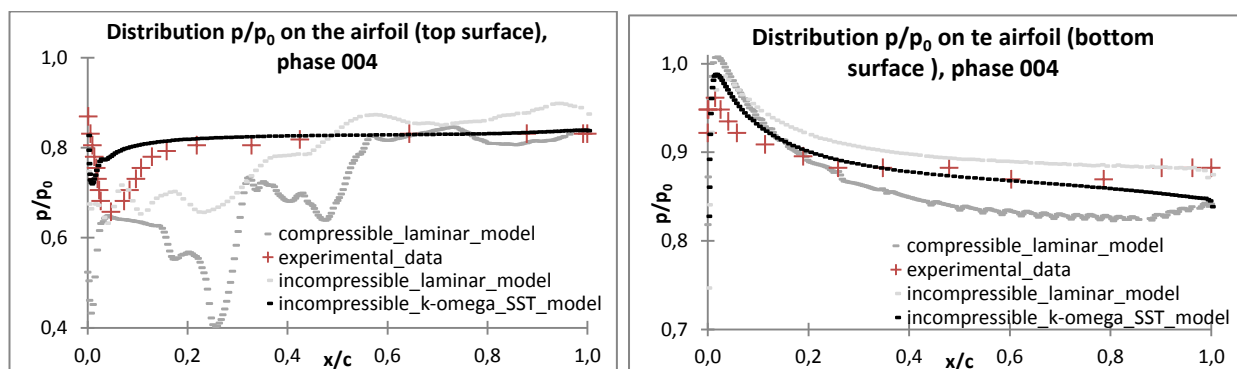


Fig. 4: Normalized pressure distribution p/p_0 on the surface of the airfoil from experiment and numerical simulation, on the left is result on the top surface, on the right is result on the bottom surface, phase 004.

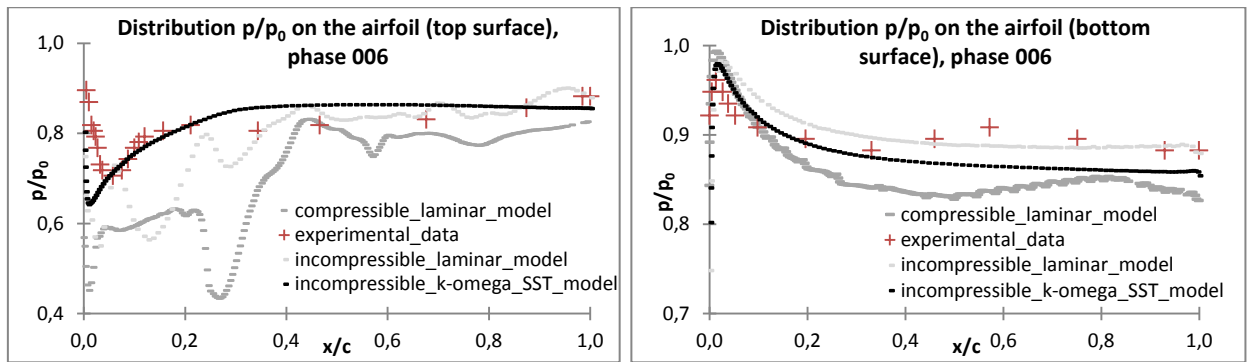


Fig. 5: Normalized pressure distribution p/p_0 on the surface of the airfoil from experiment and numerical simulation, on the left is result on the top surface, on the right is result on the bottom surface, phase 006.

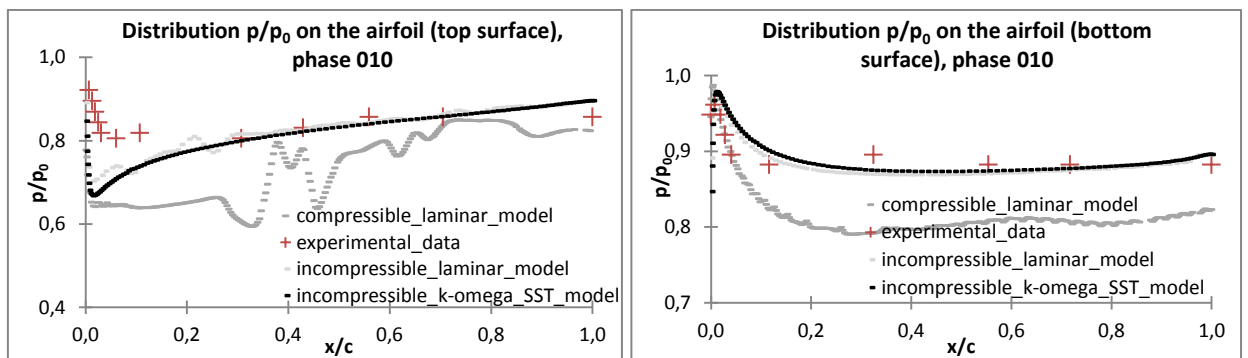


Fig. 6: Normalized pressure distribution p/p_0 on the surface of the airfoil from experiment and numerical simulation, on the left is result on the top surface on the right is result on the bottom surface, phase 010.

4. Conclusions

Numerical simulations of airflow past a vibrating airfoil were performed and compared with experimental data. Model without model of turbulence provides good match with the experimental data only in the regions, where there is no flow separation. In the separated regions, the results of numerical simulations without turbulence model and experiments are very different. The evaluation of the interferographic images, on the other hand, is also problematic, especially in the regions of high density gradients. But SST $k-\omega$ model turbulence gives satisfactory results in the separated region. Problem is here placed where the flow separates. In numerical solution the flow separation point is close to the leading edge. In the experiment the flow separates at approximately 0.07 of the chord length. The difference may be caused by the surface roughness of the physical model.

Acknowledgement

The research has been supported by the Czech Science Foundation, project 13-10527S "Subsonic flutter analysis of elastically supported airfoils using interferometry and CFD". We also wish to acknowledge the help of Dr. Václav Vlček, who provided the data from previous measurements in the wind tunnel.

References

- Menter, F. R. (1994) Two-Equation Eddy-Viscosity Turbulence Models for Engineering Applications, AIAA Journal, 32, 8, pp. 1598-1605.
- Vlček, V., Kozánek, J., Zolotarev, I. (2011) Forces acting on the fluttering profile in the wind tunnel. Vibration problems ICOVP 2011 - Supplement, 10, pp. 516-522.
- Vlček, V., Kozánek, J. (2010) Preliminary interferometry measurements of flow field around a fluttering NACA0015 profile. Engineering Mechanics 2010, 12, pp. 540-550.

MICROMECHANICS APPLIED TO MACRO-MODEL OF A SPINAL SEGMENT

Z. Sant^{*}, A. Vella^{**}, R. Blanchard^{***}, Ch. Hellmich^{****}

Abstract: *Spinal segments, with the complexity of spinal activities, call for a better understanding of 3D-biomechanical behaviour to improve the design of spinal implants. The biomechanics of endplates is one of the many areas that are still not fully understood. There are number of factors that might play a role in the biomechanical response of the endplates when the load is transferred from the superior vertebra via endplate and adjacent intervertebral disc to the inferior vertebra. Studies using finite element (FE) models usually present a simplified idealistic isotropic continuum as a bone tissue and cartilage model. This simplification might hinder the real stress-strain distribution at the region of prime interest – the endplate. Multiscale FEM provides the tool to overcome difficulties in simulation of macro model behaviour while considering the micromechanics of bone tissue. The specific patient model, evaluated from CT scans and applied to the existing FE model, gave promising results with the highest stress of 3.1 MPa at the central part of endplate while the model with isotropic continuum presented the highest stress of 1.3 MPa at the lateral side of annulus fibrosus. Results obtained from the patient specific model correspond to known clinical observations of the endplate damage.*

Keywords: Spinal Segment, Finite Element Method, Micromechanics.

1. Introduction

Finite element analysis (FEA) became a common tool in biomedical engineering mainly for the analysis and design of medical devices. With the new imaging technology introduced into the modelling process, usually based on CT scans, the possibility and in a sense the necessity to characterize tissue properties on micro and nano scale level emerged. Bridging the two different hierarchical levels, geometry macro-model and micro-, nano- properties of tissue, was possible due to newly developed mathematical tools. There are few recent studies, which assign heterogeneous tissue properties derived from CT scan images to the voxel while directly creating an FE model. This approach has two major drawbacks; given that the FE model is built from a large number of voxels, running the computation requires powerful computers and considerable computational time. The second shortcoming arises from the method leading directly to the FE model without geometry. Any alteration to the model means a modification to the FE model itself, which is a tedious task. This paper will present a different approach and provides comparisons between classical isotropic material models and specific patient orthotropic material defined with a novel approach developed at the Vienna University of Technology, Austria.

1.1. Problem description

Understanding the mechanics of a load transfer between two adjacent vertebrae requires analysis of large amount of clinical data. Such an approach would require, in a small hospital, a lengthy process of gathering a sufficient amount of data for meaningful statistical analysis. Thus when the request, to bring more information about the behaviour of endplates representing a specialized tissue connecting two

* Dr. Ing. Zdenka Sant: Mechanical Engineering Department, University of Malta, Tal Qroqq; MSD2080, Msida; Malta, zdenka.sant@um.edu.mt

** Alain Vella: Mechanical Engineering Department, University of Malta, Tal Qroqq; MSD2080, Msida; Malta, (Imperial College London, GB), carmel.v86@gmail.com

*** Romane Blanchard: Vienna University of Technology, Institute for Mechanics of Materials and Structures, Karlsplatz 13/202, A-1040, Vienna, Austria, Romane.Blanchard@tuwien.ac.at

**** Prof. Christian Hellmich: Vienna University of Technology, Institute for Mechanics of Materials and Structures, Karlsplatz 13/202, A-1040, Vienna, Austria, christian.hellmich@tuwien.ac.at

vertebrae and the adjacent intervertebral disc (IVD) came, it was agreed to run a test “in silico” by means of FEA simulation.

1.2. Spinal segment model

The geometrical model of a virtual segment consisting of an IVD and two adjacent vertebrae was manually segmented by means of NURBS drawing software and CT scans. The bone tissue densities were represented by two material models. These were assigned the properties of isotropic homogeneous continuum, which was defined by a single value of Poisson’s ratio, and Young’s modulus of 16 GPa and 120 MPa for cortical and cancellous bone respectively. The surface of both vertebrae was coated by shell elements and material properties associated with cortical bone tissue. An average thickness of 1 mm was assumed over the entire outer surface. The endplate areas were discretized using shell elements and associated with the corresponding material model defining Young’s modulus of 500 MPa as stated by literature. All solid elements enclosed in the vertebrae volumes were assigned properties that corresponded to material models commonly used to simulate the behaviour of cancellous bone. The simulation of posture with different load conditions was adopted from (Arjmand, 2006). Due to a lack

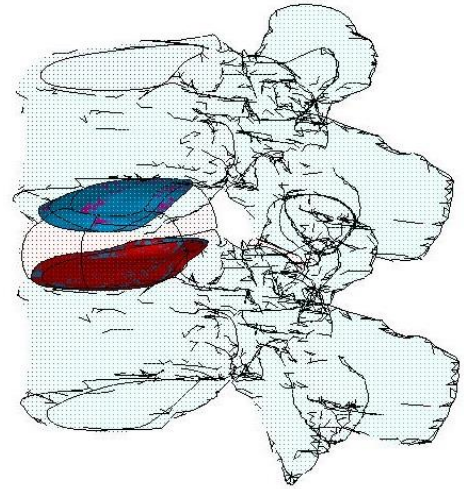


Fig. 1: Spinal segment L3-L4 with IVD endplates marked by colour.

of specialized experimental devices, the validation of results was then in hands of medical specialists. It was concluded that the endplate behaviour corresponds to basic clinical observation but the results could not answer the major question about strains and stresses at the location of interest due to the simplistic model of tissue properties. The results, based on isotropic materials as the only available resource and knowledge at that time, were published (Sant, 2012). This model is used in the work with label M_{iso} to compare the influence of micromechanics on the biomechanical response of the endplate.

2. Implementation of Micromechanics

In the presented work, a different strategy was used to assign the specific material properties from the subject’s CT scan to the existing FE model. This novel method, developed at the Vienna University of Technology, Austria, by the team lead by Prof. Hellmich and described in (Blanchard, 2013), is based on the application of micromechanics. Each pixel/voxel recorded from the CT scan, represented by its voxel-specific grey value (GV), is associated with the density of the material documented in the respective voxel, which is composed of fluid filled vascular pores and extravascular bone tissue, the latter consisting of bone’s elementary constituents: hydroxyapatite, collagen, and water. Corresponding voxel-specific vascular porosities constitute the key input data to multiscale micromechanics of bone tissue, delivering the voxel-specific elastic properties. The newly developed material model was then mapped onto representative volumes elements of the existing FE model. Fig. 2 depicts the distribution of patient’s specific orthotropic elastic model of bone tissue that corresponds to the bone tissue density distribution. The map of

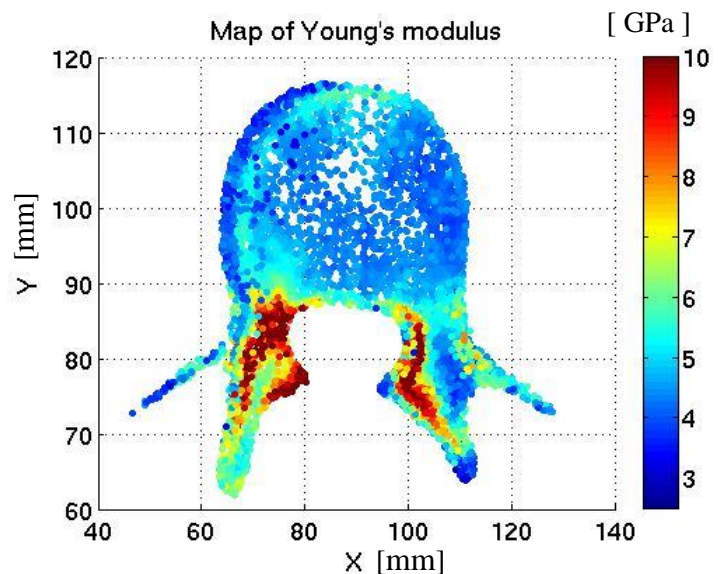


Fig. 2: Map of Young's modulus on the transverse cross-section at z-level of GCS.

Young's modulus on a transverse cross-section through the vertebral body and pedicle region reveals the variation of material properties.

Adjusting the material properties in the corresponding database provides the possibility to change the isotropic material properties in the existing FE model. Assigning orthotropic material properties in this case would require using GV as a variable controlling the selection of the corresponding mechanical properties according to the element representative volume position in the general coordinate system (GCS). The coordinates of the centroid and nodes for each existing element of the FE vertebra model were exported into a program, which selected voxels within the corresponding element volume for further processing. Then the selected number of voxels each with explicit density of tissue material were processed to obtain a homogenized property enclosed within the element volume and defined by a single GV. In this manner the material properties assigned to the GV were associated with the existing elements and for each GV, starting at 70 up to 225, a specific material model defined by Young's modulus E_x , E_y , E_z , shear modulus G_{xy} , G_{yz} , G_{xz} , and Poisson's ratio ν_{xy} , ν_{xz} , ν_{yz} was created. The coordinate system of elements was tilted to the directions that correspond to an orientation of the trabeculae alignment within bone tissue.

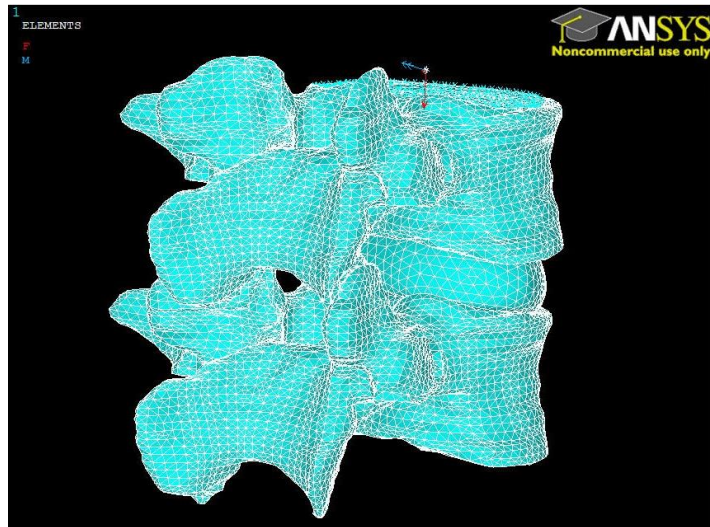


Fig. 3: FE model with applied load at the CP node from where is the normal and shear force, accompanied by sagittal moment transferred on the L3 superior endplate.

The boundary conditions (BC) were set to correspond to the same BC as implemented on the M_{iso} model. This assumed a stationary sacrum, thus the inferior endplate of the L4 vertebra was fully constrained. The load transfer between the vertebrae and the IVD was possible by means of two contact pairs between the vertebrae and adjacent IVD, set to a "bonded" condition. The applied load at the mid-point of IVD, as shown in Fig. 3, corresponds to the subject's upright position while carrying load of 180 N (Arjmand, 2006). The normal force orthogonal to the L3 superior endplate of 688 N, shear force in plane of the superior endplate of 90 N, and sagittal moment of 3.1 Nm were redistributed from the control node via an associated contact pair.

3. Results

All three models with identical geometry were assigned a different material properties. Model M_{iso} remained with initial isotropic continuum material model while the second model, M2, preserved the idealized continuum material of cortical and cancellous bone for the L4 vertebra only, and the GVs were mapped on the volume of elements of the superior vertebra L3 as described earlier. In the third model, M3, both vertebrae had bone tissue properties assigned based on the GV evaluated from the CT scan. In all three cases it was assumed that the IVD retains mechanical properties varying in radial and circumferential direction. These were extrapolated from (Acaroglu, 1995) assuming a linear variation in sagittal and transverse direction (Sant, 2012). The same loading

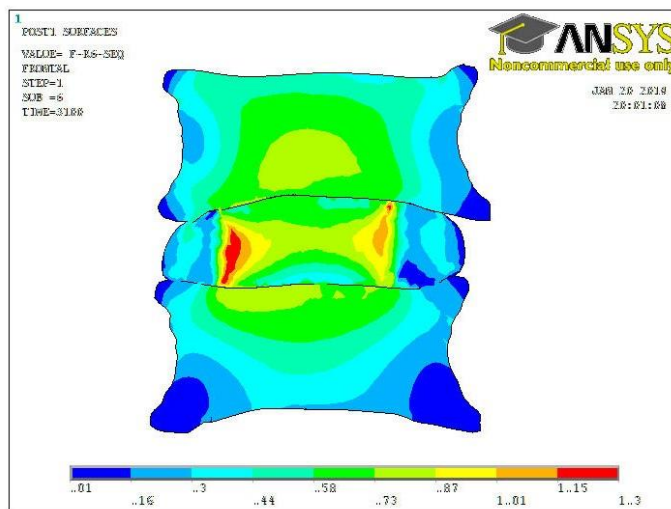


Fig. 4: von Mises stress distribution within the frontal cut through the segment - model M_{iso} .

condition and BC were applied to all models.

Analysis of the results obtained for the M_{iso} model revealed the highest stress developed at the lateral side of the IVD with equivalent stress reaching 1.3 MPa as shown in Fig. 4. The highest stress occurring within the annulus fibrosus at the anterior part of the median plane reached 1.05 MPa. The stress in the region of the endplates did not exceed 1 MPa while the highest strain intensity occurred at the left lateral side of the IVD. The results of the simulation run on the model M3 resulted in the highest equivalent stress at the central part of endplates as shown in Fig. 5. The maximum stress reached above 3 MPa somewhat posteriorly as shown in Fig.6 in the cut through the median plane.

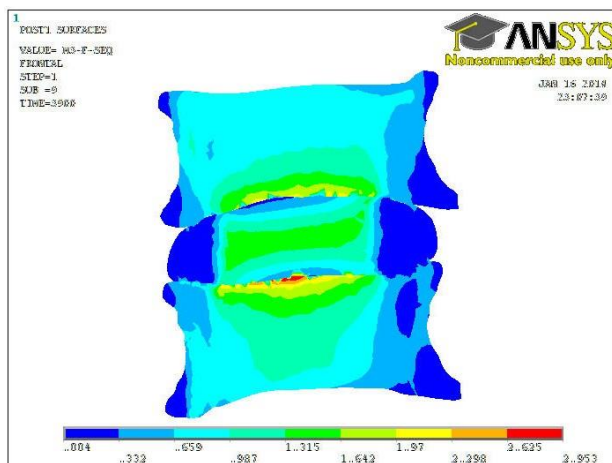


Fig. 5: von Mises stress distribution within the frontal cut through the segment - model M3.

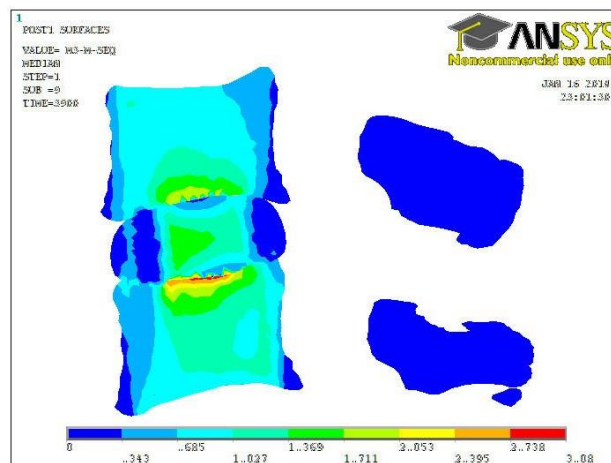


Fig. 6: von Mises stress distribution within the median cut through the segment - model M3.

4. Conclusion

The behaviour of the interface between the two vertebrae is highly dependent on the state of the IVD, the endplate condition, and the bone tissue quality. There is a difference in the stress and strain magnitude as well as in the distribution patterns within the models M_{iso} and M3. Whereas for the model M_{iso} the overall stress within the vertebra did not exceed 0.8 MPa, within model M3 the stress away from the endplates reached around 1 MPa with an increase in the caudal/cranial direction to its maximum slightly above 3 MPa at the endplates. The voxel-specific elastic properties, corresponding to the continually changing tissue density that respect the micromechanics of the composition, eliminated the unnatural stress concentration at the boundaries of two different materials as observed in M_{iso} model results. The stress of 1 MPa developed within the cancellous bone tissue corresponds to known measured values. The results obtained from M3 model are in agreement with clinical observation. These results should be verified experimentally, if possible.

Acknowledgement

The authors are grateful to the Research Ethics Committee for their kind permission to use CT scans, the Radiology Department, Mater Dei hospital for use of CT scans and their invaluable help without which the work would be impossible. Further gratitude goes to all collaborators from the COST Action MP1005: NAMABIO for support of this project, in particular through a Short Term Scientific Mission.

References

- Acaroglu, E. R., Latridis, J. C., Setton, L. A., Foster, R. J., Mow, V. C., Weidenbaum, M. (1995) Degeneration and aging affect the tensile behaviour of human lumbar annulus fibrosus, *Spine*, 20, 24, pp. 2690-2701.
- Arjmand, N., Shirazi-Adl, A. (2006) Model and in vivo studies on human trunk load partitioning and stability in isometric forward flexion. *Journal of Biomechanics*, 39, 3, pp. 510-521.
- Blanchard, R., Dejacq, A., Bongaers, E., Hellmich, Ch. (2013) Intravoxel bone micromechanics for micro CT-based finite element simulations. *Journal of Biomechanics*, 46, 15, pp. 2710-2721.
- Sant, Z., Cauchi, M., Spiteri, M. (2012) Analysis of stress-strain distribution within a spinal segment. *Journal of Mechanics of Materials and Structures*, 7, 3, pp. 255-263.

BSFC PREDICTION OF A DIESEL ENGINE FUELLED WITH BIODIESEL BY RSM

A. Shirneshan*

Abstract: *The effects of biodiesel (from waste cooking oil) in fuel mixture (biodiesel and diesel fuel No. 2) on brake specific fuel consumption (BSFC) of a diesel engine were investigated by response surface methodology (RSM) in this study. The experiments were conducted on a four cylinder direct-injection diesel engine. The developed mathematical models by RSM were helpful to predict the response parameters and further to identify the significant interactions between the input factors on the response. Results showed that the use of biodiesel BSFC increases 18 to 24% by the using net biodiesel. Also results showed that the reduction in engine load appeared to cause an increase in BSFC which increase up to 15% by reducing the engine load.*

Keywords: BSFC, Biodiesel, Diesel engine, RSM, Engine speed.

1. Introduction

Biodiesel has received wide attention as a replacement for diesel fuel because it is biodegradable, nontoxic and can significantly reduce toxic emissions and overall life cycle emission of CO₂ from the engine when burned as a fuel (Xue et al., 2011). If the fuel properties of biodiesel are compared to petroleum diesel fuel, it can be seen that biodiesel has higher viscosity, density, pour point, flash point and cetane number and no sulphur link (Canakci et al., 2009). Many researches compared the blends with different content biodiesel For BSFC. Most of them (Aydin and Bayindir, 2010; Meng et al., 2008; Godiganur et al., 2010; Qi et al., 2010) agreed that the fuel consumption of an engine fueled with biodiesel becomes higher. Some of them (Armas et al., 2010; Zhu et al., 2010; Godiganur et al., 2010; Labeckas and Slavinskas, 2006) believed that, with increasing the content of biodiesel, engine fuel consumption will increase. On the contrary, it was reported in (Ozgünay et al., 2007; Song and Zhang, 2008; Pal et al., 2010) that fuel consumption was decreased for biodiesel compared to diesel. The objective of this research work is to investigate the effects of biodiesel percentage of in fuel mixture (biodiesel and diesel fuel No. 2), engine speed and engine load on changes in brake specific fuel consumption (BSFC) by response surface methodology (RSM).

2. Methods

2.1. Biodiesel preparation, Test engine experimental procedure

Biodiesel from waste vegetable cooking oil is a more economical source of the fuel, so in the present investigation biodiesel was produced from this source.

The engine tests were carried out on a 4-cylinder, four-stroke, turbocharged, water cooled and DI diesel engine (110 hp at 2800 rpm). The engine speed was measured by a digital tachometer with a resolution of 1 rpm. The engine was coupled to an E400 ferromagnetism dynamometer to provide brake load and a system with scale method was used to for determination of consumed fuel. The engine was allowed to run for a few times until the exhaust gas temperature, the cooling water temperature, the lubricating oil temperature, have attained steady-state values and then the data were recorded.

* Assistant Prof. Alireza Shirneshan, PhD.: Department of Mechanical Engineering, Najafabad Branch, Islamic Azad University, Isfahan, Iran, arshirneshan@yahoo.com

2.2. Experimental design and statistical analysis

The standard RSM design using central composite design (CCD) was employed to examine the relationship between the response variables and set of quantitative experimental factors. The independent variables were percentage of biodiesel in fuel mixture in fuel mixture (x_1), engine speed (x_2) and engine load (x_3). The response (y) was BSFC. The coefficients of the polynomial were represented according equation (1) by b_0 (constant term); b_1 , b_2 and b_3 (linear effects); b_{11} , b_{22} and b_{33} (quadratic effects); and b_{12} , b_{13} and b_{23} (interaction effects):

$$y = b_0 + b_1x_1 + b_2x_2 + b_3x_3 + b_{11}x_1^2 + b_{22}x_2^2 + b_{33}x_3^2 + b_{12}x_1x_2 + b_{13}x_1x_3 + b_{23}x_2x_3 \quad (1)$$

Minitab software version 15.0 was used to develop the mathematical models and to evaluate the subsequent regression analyses and analyses of variance (ANOVA). Based on these models, the main and interaction effects of the process parameters on BSFC characteristics were computed and plotted in contour plots as shown in Fig. 1.

3. Analysis and Results

3.1. Statistical analysis

The complete 20 numbers of experiments were performed and the experimental data for BSFC of the diesel engine are shown in Tab. 1. The statistical analysis indicates that the proposed model (Eq. (2)) was adequate, possessing no significant lack of fit and with very satisfactory value of the R^2 (96.4%) for the response. Fig. 1 shows the interactions between the engine speed and responses in contour plot form. The graphical form plots were obtained by holding the value of engine load at 25%, 50%, 75% and 100% constant level in the related mathematical model.

Tab. 1: The experimental and predicted data for the response.

Experiment number		1	2	3	4	5	6	7	8	9	10
BSFC (gr/(kW.hr))	Experimental data	234	258.6	245.8	288.3	219.5	241.6	238.7	265.9	210.5	261
	Predicted data	230.6	258.7	248.8	288.5	217	236.3	235.2	266	213.1	262.7
Experiment number		11	12	13	14	15	16	17	18	19	20
BSFC (gr/(kW.hr))	Experimental data	237.4	284.3	257	220	238.6	242.8	250.8	236.4	241.2	239.6
	Predicted data	242.7	283	256.4	226	241.2	241.2	241.2	241.2	241.2	241.2

$$BSFC(\text{gr}/(\text{kW}/\text{hr})) = 298.74 + (0.5)x_1 + (-0.088)x_2 + (-0.236)x_3 + (0.0014)x_1^2 + (2.67 \times 10^{-5})x_2^2 + (-0.00018)x_1x_2 + (-0.00336)x_1x_3 \quad (2)$$

3.2. Brake specific fuel consumption (BSFC)

Fig. 1 shows the effects of biodiesel percentage and engine speed on the predicted BSFC of the engine at various load condition. As the Fig. 1 show, the maximum BSFC is more than 330 (gr/Kw.hr) for fuel blends included more than 95% biodiesel at 25% engine load and engine speed between 2700 to 2800 rpm. Also the minimum BSFC (less than 208 (gr/Kw.hr)) happens at full engine load and engine speed between 1500 to 1700 rpm for fuel blends included less than 10% biodiesel. According to the results, the BSFC initially decreased with increase in speed up to 1300 rpm and then BSFC remains approximately constant between 1300 rpm and 1900 rpm. For the range more than 1900 rpm, the BSFC increased sharply with speed. The predicted values for BSFC increase with the increasing amount of biodiesel in the fuel blend. The heating value of the biodiesel is lower than that of diesel fuel No. 2. Therefore, if the engine was fueled with biodiesel or its blends, the BSFC will increase due to the produced lower brake power caused by the lower energy content of the biodiesel (Aydin and Bayindir, 2010; Ozsezen et al., 2009; Adaileh and AlQdah, 2012; Hossain et al., 2013). At the same time, for the same volume, more

biodiesel fuel based on the mass flow was injected into the combustion chamber than diesel fuel No. 2 due to its higher density. In addition to these parameters, viscosity, the atomization ratio and injection pressure should be considered since they have some effects on the BSFC values (Lin et al., 2009; Song and Zhang, 2008). As the Fig. 1 show with increase in load, the BSFC of biodiesel decreases. One possible explanation for this trend could be the higher percentage of increase in brake power with load as compared to fuel consumption (Godiganur et al., 2010; Qi et al., 2010).

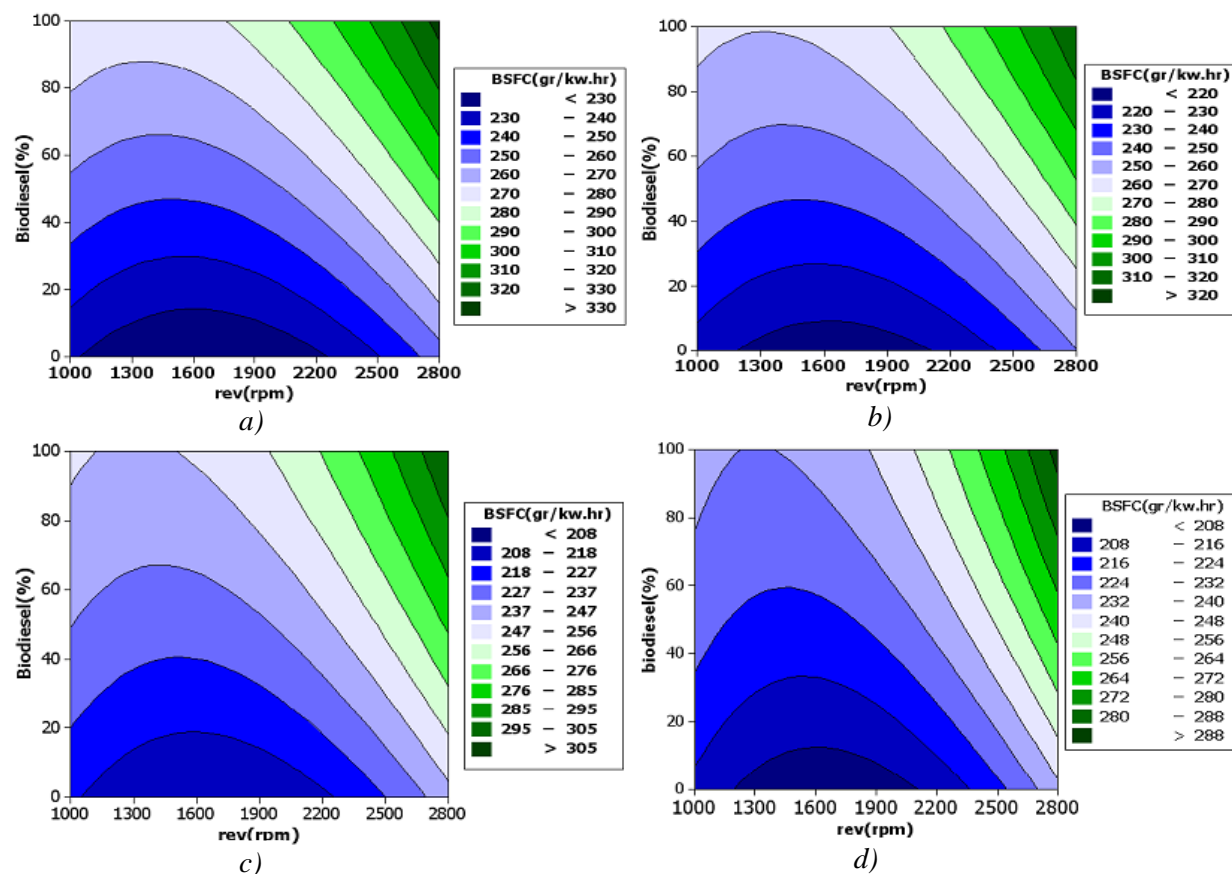


Fig. 1: Effect of percentage of biodiesel in fuel mixture and engine speed on BSFC at: a) 25%; b) 50%; c) 75%; d) 100% (full) engine load.

4. Conclusions

- The statistical models as fitted can be effectively used to predict the engine performance. Also the effect of biodiesel produced from waste cooking oil blends and diesel No. 2 fuel on engine performance was investigated.
- The brake specific fuel consumption increases with the increase of biodiesel in the blends, due to the lower heating value of biodiesel. Results showed that the brake specific fuel consumption of diesel No. 2 fuel is 18 to 24% more than the brake specific fuel consumption of net biodiesel at various engine loads.
- The brake specific fuel consumption at 25% engine load was around 15% more than this characteristic at full engine load for all fuel blends.
- These results are similar to those found in the literature and support that waste cooking oil methyl esters have similar properties with diesel fuel.
- Also the results of the study show that use of biodiesel blends with diesel had not significant change on performance of the diesel engine.

References

Adaileh, W. M., AlQdah, K. S. (2012) Performance of Diesel Engine Fuelled by a Biodiesel Extracted From A Waste Coking Oil. Energy Procedia, 18, pp. 1317-1334.

- Armas O., Yehliu K., Boehman A. L. (2010) Effect of alternative fuels on exhaust emissions during diesel engine operation with matched combustion phasing. *Fuel*, 89, pp. 438-456.
- Aydin, H., Bayindir, H. (2010) Performance and emission analysis of cottonseed oil methyl ester in a diesel engine. *Renew Energy*, 35, pp. 588-592.
- Canakci, M., Ozsezen, A. N., Arcaklioglu, E., Erdil, A. (2009) Prediction of performance and exhaust emissions of a diesel engine fueled with biodiesel produced from waste frying palm oil. *Expert Syst Appl*, 36, 5, pp. 9268-9280.
- Godiganur, S., Murthy, CH.S., Reddy, R. P. (2010) Performance and emission characteristics of a Kirloskar HA394 diesel engine operated on fish oil methyl esters. *Renew Energ*, 35, pp. 355-359.
- Hossain, A. K., Ouadi, M., Siddiqui, S. U., Yang, Y., Brammer, J., Hornung, A., Kay, M., Davies, P. A. (2013) Experimental investigation of performance, emission and combustion characteristics of an indirect injection multi-cylinder CI engine fuelled by blends of de-inking sludge pyrolysis oil with biodiesel. *Fuel*, 105, pp. 135-142.
- Labeckas, G., Slavinskas, S. (2006) The effect of rapeseed oil methyl ester on direct injection diesel engine performance and exhaust emissions. *Energ Convers Manage*, 47, pp. 1954-1967.
- Lin, B., Huang, J., Huang, D. (2009) Experimental study of the effects of vegetable oil methyl ester on DI diesel engine performance characteristics and pollutant emissions. *Fuel*, 88, pp. 1779-1785.
- Meng, X., Chen, G., Wang, Y. (2008) Biodiesel production from waste cooking oil via alkali catalyst and its engine test. *Fuel Process Technol*, 2008, pp. 89:851-857.
- Ozgünay, H., Colak, S., Zengin, G., Sari, O., Sarikahya, H., Yüceer, L. (2007) Performance and emission study of biodiesel from leather industry pre-fleshings. *Waste Manage*, 27, pp. 1897-1901.
- Ozsezen, A. N., Canakci, M., Turkcan, A., Sayin, C. (2009) Performance and combustion characteristics of a DI diesel engine fueled with waste palm oil and canola oil methyl esters. *Fuel*; 88:629-636.
- Pal, A., Verma, A., Kachhwaha, S. S., Maji, S. (2010) Biodiesel production through hydrodynamic cavitation and performance testing. *Renew Energ*, 35, pp. 619-624.
- Qi, D. H., Chen, H., Geng, L. M., Bian, Y. Z. H. (2010) Experimental studies on the combustion characteristics and performance of a direct injection engine fueled with biodiesel/diesel blends. *Energ Convers Manage*, 51, pp. 2985-2992.
- Ribeiro, N. M., Pinto, A. C., Quintella, C. M., Rocha, G. O. D., Teixeira, L. S. G., Guarieiro, L. L. N., et al. (2007) The role of additives for diesel and diesel blended (ethanol or biodiesel) fuels: a review. *Energ Fuel*, 21, pp. 2433-2445.
- Song, J. T., Zhang, C. H. (2008) An experimental study on the performance and exhaust emissions of a diesel engine fuelled with soybean oil methyl ester. *P I Mech Eng D-J Aut*, 222, pp. 2487-2496.
- Xue, J., Grift, T. E., Hansen, A. C. (2011) Effect of biodiesel on engine performances and emissions. *Renewable and Sustainable Energy Reviews Journal*, 15, pp. 1098-1116.
- Zhu, L., Zhang, W., Liu, W., Huang, Z. (2010) Experimental study on particulate and NOx emissions of a diesel engine fueled with ultra low sulfur diesel, RME-diesel blends and PME-diesel blends. *Sci Total Environ*, 408, pp. 1050-1058.

EXPERIMENTAL MODAL ANALYSIS OF WASHING MACHINE PULLEY

M. Schrötter^{*}, M. Hagara^{**}, P. Lengvarský^{***}

Abstract: *The aim of the experiment was to perform experimental modal analysis of the pulley, which serves for propulsion of washing machine, and consequently to estimate its modal parameters. There are presented results of the experimental measurement in this article, verified by finite element method. Also there is showed several problems which occurred during the measurement. The end of the article is devoted to result discussion.*

Keywords: Pulley, Modal analysis, Natural frequencies.

1. Introduction

Nowadays the big emphasis is devoted to the ecology of domestic appliances and energy losses related with them, which emerge with their running. From this aspect our attention was focused on investigation of washing machine's pulley modal parameters – natural frequencies and mode shapes. The measurement was performed on the pulley attached to a drum of a washing machine. This method can be considered as clamped, owing to mechanical blocking of the drum rotation.

2. Modal Analysis of the Pulley

2.1. Experimental modal analysis

Experimental modal analysis was performed by Bruel and Kjaer's PULSE system. As an exciter Bruel and Kjaer's modal hammer was used, type 8206. Owing to the frequency band of interest, 3200 Hz, the plastic tip of hammer was used. To not influence the natural frequencies the contactless transducer had to be used because of low pulley weight. Also the shape of the pulley was not suitable for using of conventional accelerometer so as a transducer the laser vibrometer Polytec PDV 100 was used. It measures the velocity of vibration by Doppler effect (Randall).

Before the measurement the sufficient number of measuring point (DOF's) had to be created on the pulley to sufficiently render the mode shapes. From that reason the pulley was theoretically divided into three parts: the middle, the rim and the three arms. There were created twelve points in the middle of pulley, five points on each arm and 24 points on the rim.

With respect to fact that the response of both the pulley middle and the ring was significantly different also by free support, the middle was significantly stiffer than the rim, the reference point was chosen on the pulley arm.

The measurement was performed in two stages. The first one, the exciter and transducer were oriented axially (front side) and second one when the transducer and exciter were oriented in radial direction.

* Ing. Martin Schrötter: Department of Applied Mechanics and Mechatronics, Technical University of Košice, Letná 9; 042 00, Košice; Slovakia, martin.schrotter@tuke.sk

** Ing. Martin Hagara, PhD.: Department of Applied Mechanics and Mechatronics, Technical University of Košice, Letná 9; 042 00, Košice; Slovakia, martin.hagara@tuke.sk

*** Ing. Pavol Lengvarský: Department of Applied Mechanics and Mechatronics, Technical University of Košice, Letná 9; 042 00, Košice; Slovakia, pavol.lengvarsky@tuke.sk

After the measurement the particular frequency response functions were converted to the Pulse Reflex and modal parameter extraction was performed by rational fraction polynomial method with maximum iteration of 40. Upon the stability diagram and phase shift diagram the natural frequencies were obtained (Bilošová, 2011).

The rational fraction polynomial method (frequency domain - single input single output - multi degree of freedom) was used owing to its suitability for investigation of close modes of vibration with respect to the effect of residuals outside the frequency range of interest. The close modes of the pulley were expected by the reason of symmetric pulley shape.

2.2. Numerical modal analysis

Numerical modal analysis is performed in the simulation program SolidWorks. The geometry of washing machine pulley with maximal diameter 300 mm is created in 3D background. Then frequency study is selected and the material AL 46000 is defined. Material properties of AL 46000 are presented in Tab. 1 (SolidWorks).

The mesh on the washing machine pulley is generated automatically by SolidWorks, while the spatial element SOLID187 is used. The element is defined by 10 nodes while each node has three degrees of freedom. The SOLID187 has a quadratic shifting behavior and is suitable for modeling of the finite element irregular mesh. The size of the element is 3.6 mm with tolerance 0.18 mm. The mesh in Fig. 1 is created of 38362 elements and of 77421 nodes (SolidWorks).



Fig. 1: Mesh of finite elements on the washing machine pulley.

Tab. 1: Material properties of AL 46000.

Property	Value with units
Elastic modulus	75 000 MPa
Tensile Strength	140 MPa
Yield Strength	250 MPa
Mass density	2000 kg/m ³
Poisson's ratio	0.3

In SolidWorks the axial, radial and circumferential movements are constrained. These fixtures are applied in middle of the pulley.

3. Obtained Results and their Comparison

The obtained natural frequencies are presented in Tab. 2 and the obtained mode shapes are depicted in Figs. 2 to 7. The mode shapes presented below are for Pulse and SolidWorks respectively.

Tab. 2: The comparison of pulley natural frequencies.

Frequency number	PULSE	SolidWorks
1.	80 Hz	84 Hz
2.	120 Hz	129 Hz
3.	182 Hz	194 Hz
4.	262 Hz	281 Hz
5.	594 Hz	618 Hz
6.	784 Hz	800 Hz
7.	930 Hz	951 Hz
8.	1176 Hz	1204 Hz
9.	1848 Hz	1885 Hz
10.	2622 Hz	2683 Hz
11.	3146 Hz	3227 Hz

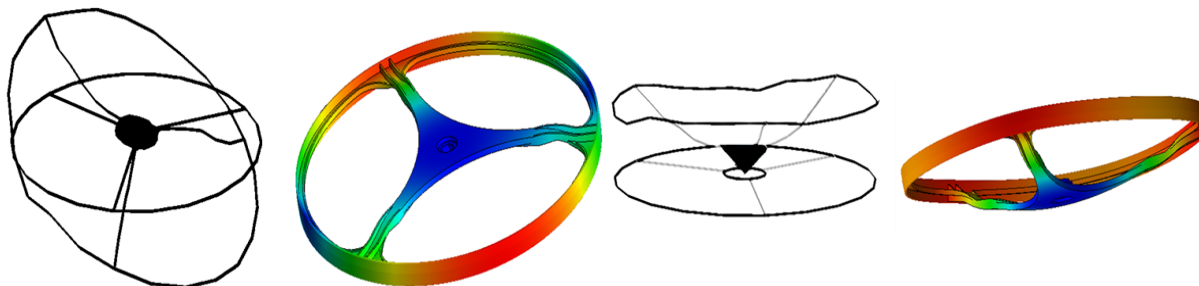


Fig. 2: The first and the second mode shape.

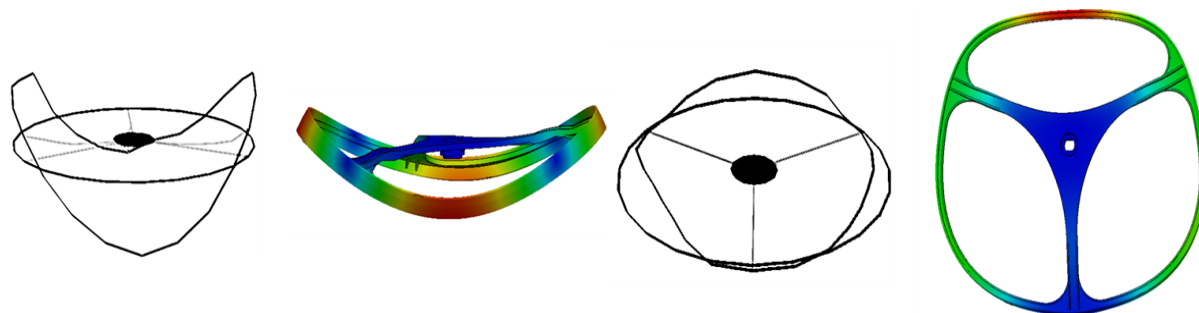


Fig. 3: The third and the fourth mode shape.

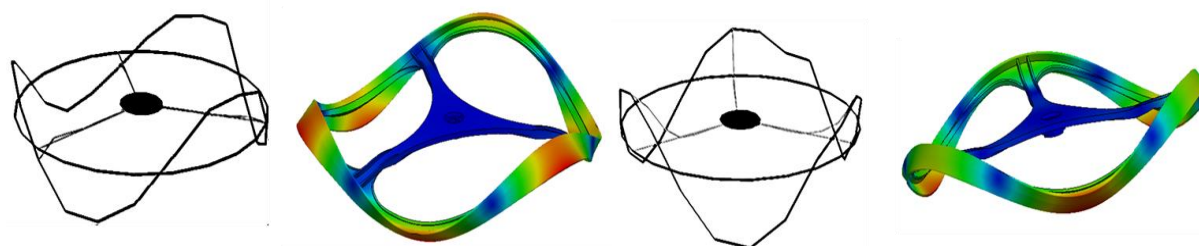


Fig. 4: The fifth mode shape and the sixth mode shape.

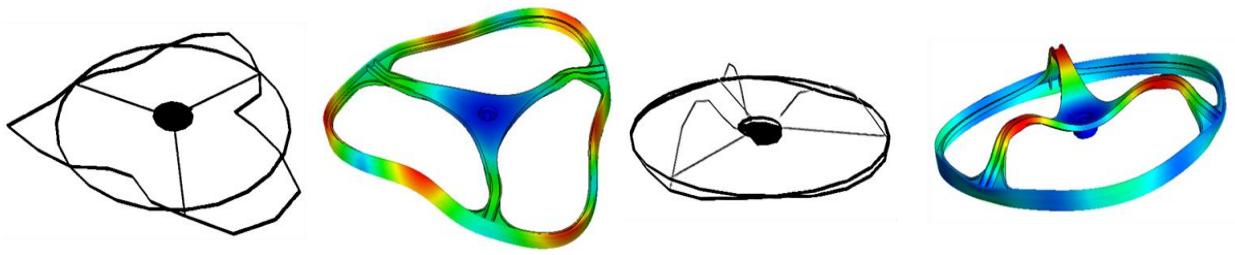


Fig. 5: The seventh mode shape and the eighth mode shape.

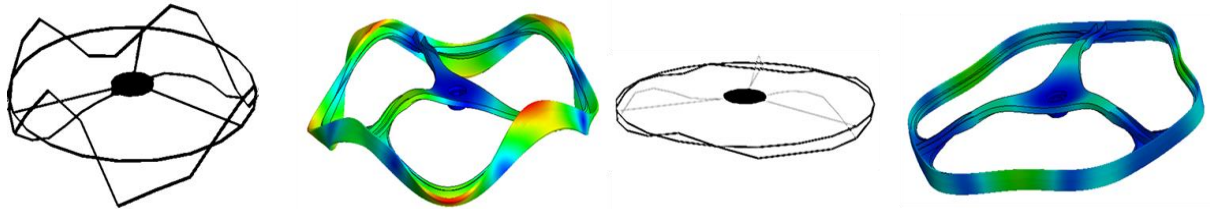


Fig. 6: The ninth mode shape and the tenth mode shape.

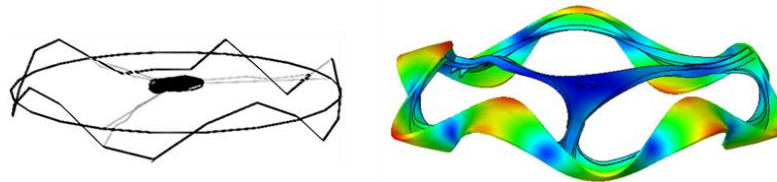


Fig. 7: The eleventh mode shape.

4. Conclusions

The usual washing machine revs are in the range from 0 to 1200 rpm. The drum and the pulley are connected rigidly so their revs are same. From the upper table we can see that there are 8 natural frequencies in this range. All of these natural frequencies but one are measured from the first measurement stage – the axial measurement. Their particular mode shapes, as it is possible to see from Figs. 2-7, are mostly presented in the axial direction. It is worth to point out the fifth frequency – 594.Hz. This frequency is acquired from the second measurement stage – the radial measurement. Its mode shape (deformation) is in radial direction, so the washing process at this frequency (rpm) can create creeping of the pulley belt, what lead to the unwanted energy losses.

Acknowledgement

This article was created with support of VEGA grant projects: VEGA 1/1205/12 Numerical modeling of mechatronic systems and VEGA 1/0937/12: The development of non-traditional experimental methods for mechanical and mechatronic systems.

References

- Ewins, D. J. (2000) Modal Testing: Theory, Practice and Application. Journal of Sound and Vibration, Second Edition, Wiley, England.
- Bilošová, A. (2011) Experimental modal analysis. Ostrava, CZ (in Czech).
- Randall, R. B. Frequency Analysis, Brüel&Kjær, Denmark.
- SolidWorks: Products, [online], <http://www.solidworks.com/-sw/products/10141_ENU_HTML.htm>.
- SolidWorks Simulation, [online], <http://www.solidworks.com/-sw/products/10169_ENU_HTML.htm>.
- Trebuňa, F., Šimčák, F. (2007) Manual Experimental Mechanics, Sjf TU, Košice, ISBN 978-80-8073-816-7, (in Slovak).

ANALYSIS OF DYNAMIC LOADING OF BAR STRAIGHTENING MACHINE COMPONENTS

P. Skalka *, J. Sobotka **

Abstract: *The oblique bar straighteners are rotary forming machines, which are used for straightening of round bars designed for further processing. During straightening the bars are rotating among hyperbolic rollers, which are held by holders. The bottom rollers are driven by electric motor connected with a gearbox and cardan shafts. During the straightening the machine is loaded with enormous forces and torque moments. This paper is focused on determining torque moments, which are required for design of straightening machine. The straightening machine described below has 7 rollers and it is designed for bars with a 200 mm diameter.*

Keywords: Oblique straightening machine, Finite element method, Plasticity.

1. Introduction

The bar straightening is based on their bending among the straightening rollers. The bending moment, which evokes in the bar during the straightening, must be large enough for plastic strain initialization in the bar. The bending moment is created by adjusting of three rollers (number 3, 6 and 7 Fig. 3) towards the straightening bar (Fig. 2). In the case of the oblique straightening the translation motion of the bar is dependent on the rotation of straightened bar. Plastic strain is initialized on the bar surface by bar rotating. Plastic strain is necessary for bar straightening. The rollers have the shape of rotational hyperboloid. For bar straightening it is necessary to know the values of torque moments, which are evoked in the holders and torque moments needed for the driving of rollers. Required values were obtained by numerical simulations (Finite Element Method). Before their use the experimental verification needs to be done.



Fig. 1: Bars before straightening.

2. Oblique Straightening Machine

The structure of straightening machine (Fig. 3) consists of two driven and five not driven working rollers, straightened bar and input-output trough. The input dates: Working rollers can rotate around axis of their rotation and they are set at the angle 26° and 30° to the axis of straightened bar (Fig. 2). The working rollers are modelled as rigid and they are positioned in fixed holders. The diameter of straightened bar is 200 mm, curve radius - 180 m and length - 6 m. The material of straightened bar is named 30CrNiMo8+QT. The yield stress

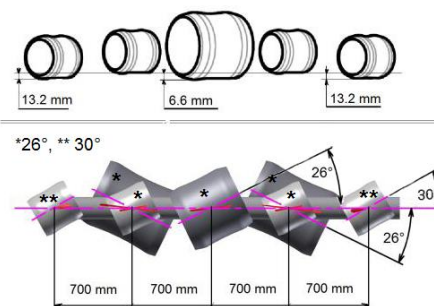


Fig. 2: Setting of rollers.

* Ing. Petr Skalka, PhD.: Faculty of Mechanical Engineering, Brno University of Technology; Technická 2896/2; 616 69, Brno; CZ, skalka@fme.vutbr.cz

** Bc. Jiří Sobotka: Faculty of Mechanical Engineering, Brno University of Technology; Technická 2896/2; 616 69, Brno; CZ, y126357@stud.fme.vutbr.cz

of this material is approximately 1000 MPa. The model of plasticity was used with isotropic hardening. The rotation of driven working rollers was 40 rpm, friction between the rollers and the bar - $f = 0.2$ (var. a), $f = 0.1$ (var. b), and the gravity acceleration - $g = 9.81 \text{ m/s}^2$.

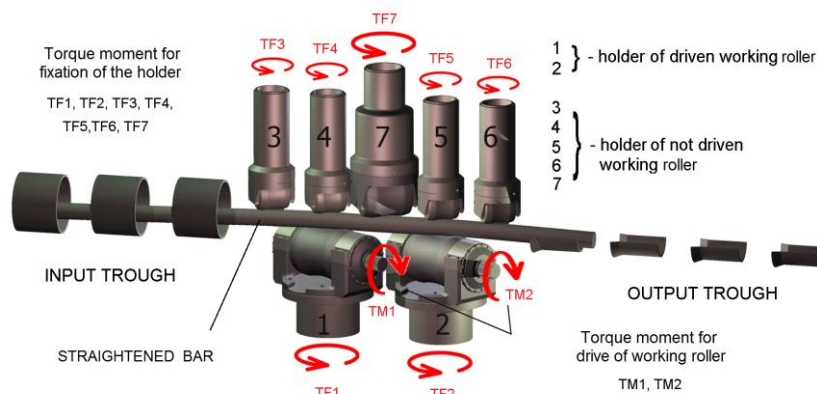


Fig. 3: Structure of oblique straightening machine.

The processes: Input and output troughs are used for a transport of the straightened bar. The bar is driven by trough rollers. When the bar is among working rollers (number 1, 3, 4 and 7), the rollers of the trough are diverted. Then the straightened bar is driven by working rollers of straightening machine. When the bar straightening is finished, rollers of output trough move the bar into the feeder.

Detail analyses of dynamics and vibrations in the process of bar straightening are covered by the article (Lošák, 2014). The analysis of the shape deviations of the aligned bar is in (Fuis, 2014), which is based on (Fuis et al., 2009 and 2011).

3. Numerical Simulations

Numerical simulations were focused on:

- a) determining stress-strain state during the straightening process,
- b) determining torque moments for fixation of holders (1-7),
- c) determining torque moments for drive of rollers (1 and 2).

4. Results

Stress-strain state of straightened bar (in the fifth seconds of the straightening process) is shown in Fig. 4.

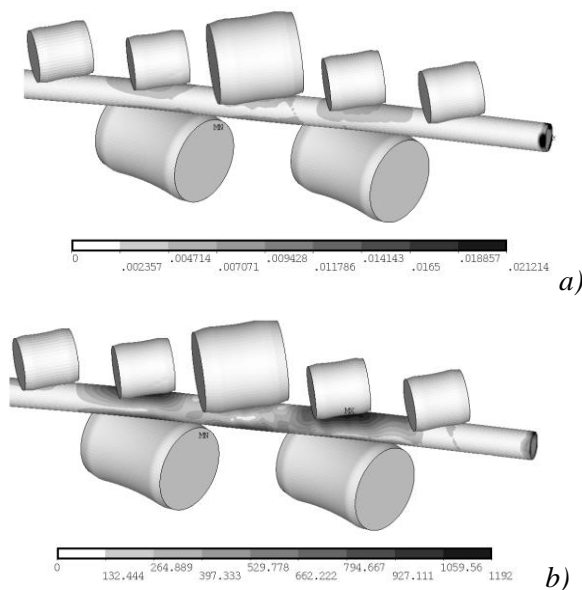


Fig. 4: Contours of: a) equivalent plastic strain [-], b) equivalent stress [MPa].

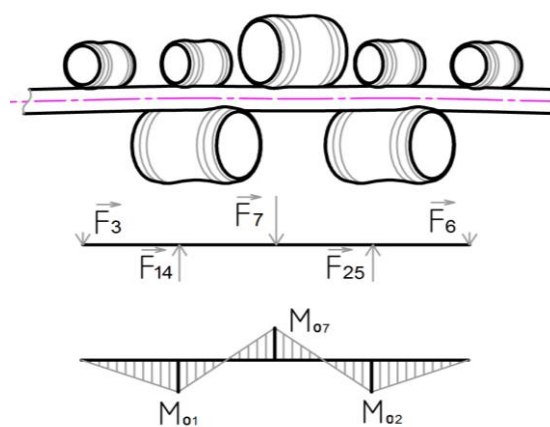


Fig. 5: Forces and bending moments acting on a bar.

The highest value of equivalent stress is approximately 1192 MPa (Fig. 4) in the place with largest bending moment (Fig. 5) during the straightening. The highest value of equivalent plastic strain (approximately 0.007 [-]) is in the same place (Fig. 4). The value of equivalent stress and equivalent plastic strain is the same for both solved variants of friction ($f = 0.2, f = 0.1$). The highest value of torque moments for holder fixation is on the roller 1. The second highest value is on the roller 7 (see Fig. 6 - top). These values are approximately 125000 Nm (roller 1) and 80000 Nm (roller 7). These rollers are most loaded. The gradual inclusion of rollers in the straightening process is shown in Fig. 6. The torque moment for drive of working roller 1 and working roller 2 is approximately 85000 Nm (roller 1) and 60000 Nm (roller 2) - see Fig. 6 - bottom.

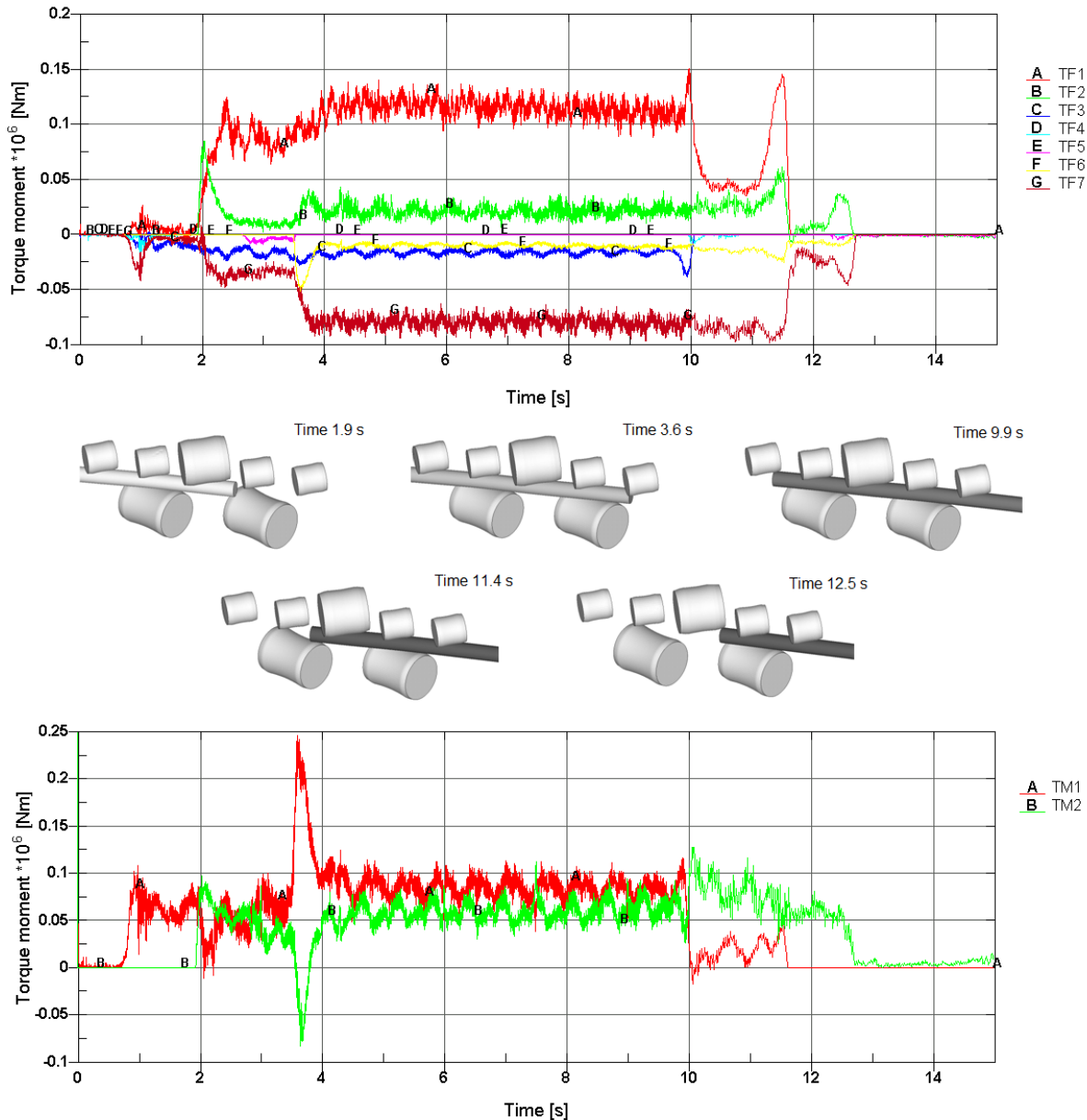


Fig. 6: Torque moments for fixation of holders (top) and for drive of rollers (bottom), $f = 0.2$.

When the friction coefficient is equal to 0.1, we can say: the highest value of torque moments for fixation of holders is on the roller 1. This value is approximately 100000 Nm (roller 1) - see Fig. 7 - top. The second highest value of torque moments for fixation of holders is on the roller 7. This value is approximately 80000 Nm (roller 7) - see Fig. 7 - top. The torque moment for drive of working rollers (1, 2) is approximately 70000 Nm - see Fig. 7 - bottom.

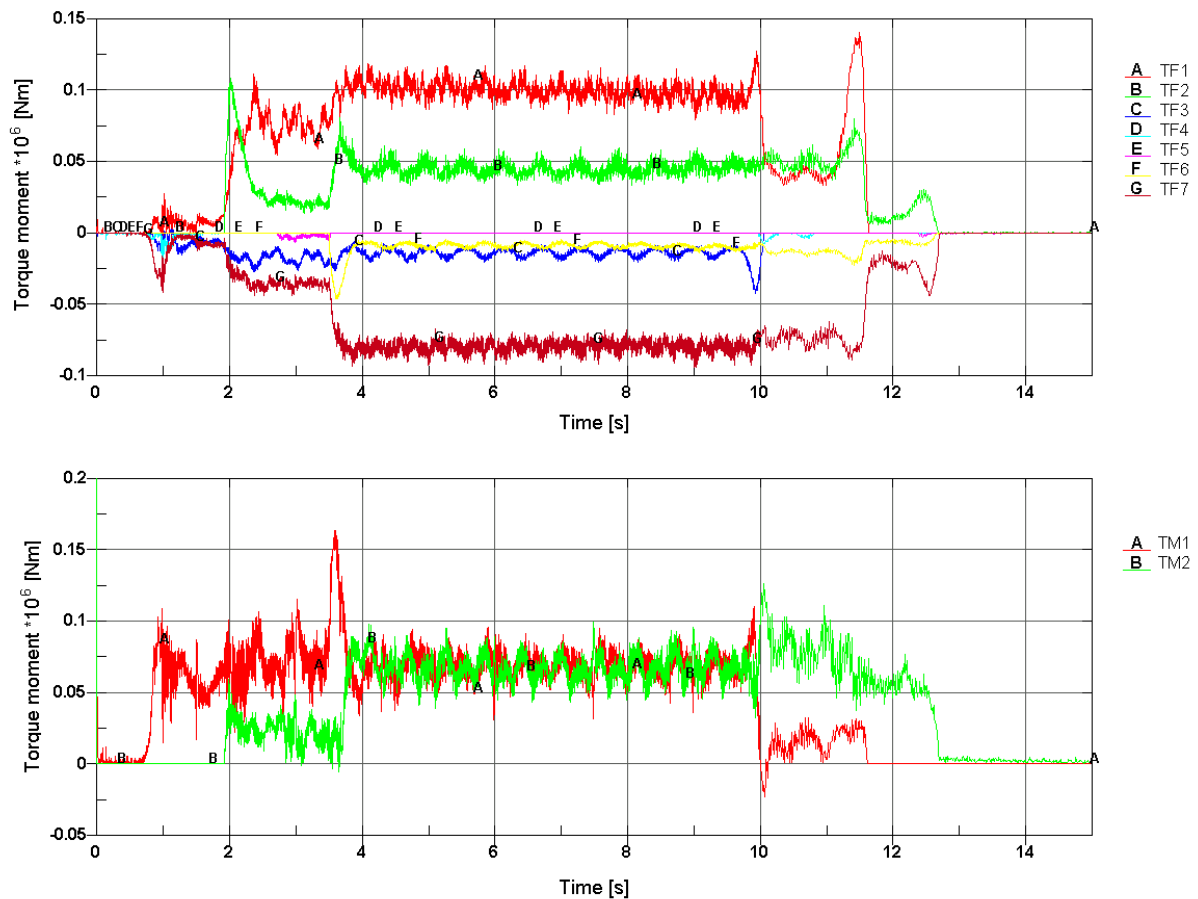


Fig. 7: Torque moments for fixation of holders (top) and for drive of rollers (bottom), $f = 0.1$.

4. Conclusions

By comparing two variants of friction (that we have solved), we can say, that the lower friction reduces torque moments for drive of rollers and for fixation of holders. During the bar straightening torque moments for drive of working rollers will increase to the value of 250000 Nm ($f = 0.2$, see Fig. 6 - bottom) and to the value of 165000 Nm ($f = 0.1$, see Fig. 7 - bottom). This increase of torque moments occurs when the straightening bar comes into the contact with the roller number 6 (see Fig. 6, Fig. 7 – time 3.6 s). The further increase of torque moments is connected with the loosing contact of the bar with the roller number 3 (see Fig. 6, Fig. 7 – time 9.9 s).

Acknowledgement

This work was supported by Grant Specific Research FSI-S-14-2311.

References

www.zdas.cz

- Lošák P. (2014) Identification of vibration causes based on spectrograms during the straightening process. In: Proc. 20th Inter. Conference Engineering Mechanics, (V. Fuis, ed.), Svratka, Czech Republic, pp. 368-371.
- Fuis V. (2014) Shape deviations analysis of the aligned bars. In: Proc. 20th Inter. Conference Engineering Mechanics, (V. Fuis, ed.), Svratka, Czech Republic, pp. 184-187.
- Fuis, V., Koukal, M., Florian, Z. (2011) Shape Deviations of the Contact Areas of the Total Hip Replacement. In: Proc. 9th Inter. Conference on Mechatronics Location: Warsaw, Poland. Mechatronics: Recent Technological and Scientific Advances, pp. 203-212.
- Fuis, V. (2009) Tensile Stress Analysis of the Ceramic Head with Micro and Macro Shape Deviations of the Contact Areas. In: Proc. 8th Inter. Conference on Mechatronics, Luhacovice, Czech Republic, Recent Advances in Mechatronics: 2008-2009, pp. 425-430.

FREE VIBRATION ANALYSIS OF TIMOSHENKO BEAM WITH DISCONTINUITIES USING DISTRIBUTIONS

J. Sobotka *

Abstract: *The general equations for the transverse vibration of Timoshenko beam have been used since they were derived by means of classical derivatives of the shear force, the bending moment, the rotation of a cross section and the deflection of the beam. However these derivatives are not defined at such points of a center-line between ends of the beam in which there is a concentrated support or a concentrated mass or a concentrated mass moment of inertia or an internal hinge connecting beam segments, which are discontinuities that can be met with in practice. We have applied distributional derivative for discontinuous shear force, discontinuous bending moment, and discontinuous rotation of a cross section of the beam in order to derive a generalized mathematical model for free transverse vibration as a system of partial differential equations. We have computed general solution to the generalized mathematical model for prismatic beam by means of symbolic programming approach via MAPLE. As a result of this approach, computing natural frequencies and modal shapes of the beam, we do not have to put together any continuity conditions at discontinuity points mentioned.*

Keywords: Timoshenko beam, Transverse vibration, Discontinuities, Dirac distribution.

1. Introduction

Classical analytical method of calculating natural frequencies of a beam with discontinuities is based on the following main steps (Timoshenko, 1937). Firstly we divide the beam into segments without discontinuities. Secondly we find continuous solution to a differential equation of motion for each segment separately. Thirdly we express boundary conditions for each segment, and continuity conditions among adjoining segments leading to a homogeneous system of linear algebraic equations. Finally we derive a frequency equation as a condition of nontrivial solution to the homogeneous system of linear equations.

Applying distributional derivative definition for discontinuous shear force, discontinuous bending moment, and discontinuous rotation of a cross section of a beam, we can derive a mathematical model for free transverse vibration of Timoshenko beam with discontinuities caused by concentrated supports or concentrated masses or concentrated mass moments of inertia situated between ends of the beam, or hinges connecting beam segments. This mathematical model can be solved like only one differential task without dividing the beam into segments where all the continuity conditions among adjoining segments are fulfilled automatically. Using this approach, we have only four integration constants irrespective of the number of the discontinuities.

2. Classical Equations of Motion for Free Transverse Vibration of Timoshenko Beam

According to Timoshenko's theory, we can express simultaneous differential equations of motion for free transverse vibration of the beam without discontinuities in the shear force, in the bending moment, in the rotation of the cross section or in the transverse displacement of the centerline of the beam (Rao, 2007) as

$$\rho A(x) \left(\frac{\partial^2}{\partial t^2} w(x, t) \right) = k G \left(\frac{\partial}{\partial x} \left(A(x) \left(\left(\frac{\partial}{\partial x} w(x, t) \right) - \phi(x, t) \right) \right) \right), \quad (1)$$

* Ing. Jiří Sobotka, PhD.: ČEZ, a.s., 67550 Dukovany; CZ, jiri.sobotka@cez.cz; jiri.sobotka@iol.cz

$$\rho J(x) \left(\frac{\partial^2}{\partial t^2} \phi(x, t) \right) = k G A(x) \left(\left(\frac{\partial}{\partial x} w(x, t) \right) - \phi(x, t) \right) + E \left(\frac{\partial}{\partial x} \left(J(x) \left(\frac{\partial}{\partial x} \phi(x, t) \right) \right) \right), \quad (2)$$

where $w(x, t)$ is the total transverse displacement of the beam centerline, $\phi(x, t)$ the rotation of the cross section assumed without warping, $A(x)$ the cross-sectional area, $J(x)$ the area moment of inertia, k the dynamic shear correction factor (Mindlin and Deresiewicz, 1953; Dong et al., 2010), E the modulus of elasticity (Young's modulus), G the shear modulus of elasticity, ρ the density.

3. Mathematical Model for Free Transverse Vibration of Timoshenko Beam with Discontinuities

In order to be able to express possible discontinuities in shear force, bending moment or in rotation of cross section along a centerline of a beam mathematically without cutting the beam into segments that would be without discontinuities in support, loading or without internal hinges, we use distributional derivative (Schwartz, 1966; Štěpánek, 2001; Kanwal, 2004), which consists of two main parts. Its first part is a classical derivative, while the second one is distributional as a sum of products of the Dirac singular distribution moved into the point of the discontinuity and a magnitude of the jump discontinuity of the quantity being differentiated.

When a beam supported at concentrated supports or carrying concentrated inertia masses between its ends is vibrating, jump discontinuities in shear force can occur at corresponding points of centerline of the beam. Expressing the first classical partial derivative of the shear force with respect to x from the force equation of motion for an element cut out of the beam, and adding distributional parts in the form of the product, we can derive Eq. (3), where $r_i(t)$ is a reaction force at i th concentrated support at a point $x = a_i$ ($0 < a_i < l$), l is the length of the beam, m_i is a concentrated inertia mass at a point $x = b_i$ ($0 < b_i < l$), $\text{Dirac}(x-a_i)$ denotes the Dirac distribution moved into the point of the discontinuity, n_1 is a number of point supports, and n_2 is a number of concentrated inertia masses.

When a beam carrying concentrated masses with moments of inertia of J_i at points $x=c_i$ ($0 < c_i < l$) is vibrating, jump discontinuities in bending moment can occur at these points. Expressing the first classical partial derivative of the bending moment with respect to x from the moment equation of motion for an infinitesimal element of the beam, and adding products of a magnitude of the jumps and the Dirac distribution situated at the point of the discontinuity, we can acquire Eq. (4), the right hand side of which is the distributional derivative of the bending moment covering n_3 jump discontinuities.

If a beam containing hinges connecting segments of the beam at points $x=d_i$ ($0 < d_i < l$) is vibrating, jump discontinuities in rotation of the cross section of a magnitude $\psi_i(t)$ may be found at these points. Expressing the first classical partial derivative of the rotation of the cross section with the respect to x from the deformation relation of the beam centerline curvature, and adding corresponding distributional parts, we can obtain Eq. (5), where n_4 is a number of internal hinges.

$$\frac{\partial}{\partial x} Q(x, t) = \rho A(x) \left(\frac{\partial^2}{\partial t^2} w(x, t) \right) + \left(\sum_{i=1}^{n_1} r_i(t) \text{Dirac}(x-a_i) \right) + \left(\sum_{i=1}^{n_2} m_i \left(\frac{\partial^2}{\partial t^2} w(x, t) \right) \Big|_{x=b_i} \text{Dirac}(x-b_i) \right), \quad (3)$$

$$\frac{\partial}{\partial x} M(x, t) = Q(x, t) - \rho J(x) \left(\frac{\partial^2}{\partial t^2} \phi(x, t) \right) - \left(\sum_{i=1}^{n_3} J_i \left(\frac{\partial^2}{\partial t^2} \phi(x, t) \right) \Big|_{x=c_i} \text{Dirac}(x-c_i) \right), \quad (4)$$

$$\frac{\partial}{\partial x} \phi(x, t) = -\frac{M(x, t)}{E J(x)} + \left(\sum_{i=1}^{n_4} \psi_i(t) \text{Dirac}(x-d_i) \right), \quad (5)$$

$$\frac{\partial}{\partial x} w(x, t) = \phi(x, t) + \frac{Q(x, t)}{k G A(x)}. \quad (6)$$

4. Free Vibration Solution

Supposing a harmonic time variation of solution to equations (3) to (6) as

$$Q(x, t) = Q_s(x) \cos(\Omega t), \quad M(x, t) = M_s(x) \cos(\Omega t), \quad \phi(x, t) = \phi_s(x) \cos(\Omega t),$$

$$w(x, t) = w_s(x) \cos(\Omega t), \quad r_i(t) = R_i \cos(\Omega t), \quad \psi_i(t) = \Psi_i \cos(\Omega t),$$

where Ω is a circular frequency of vibration, and denoting amplitudes of vibration at points with concentrated transverse inertia forces and bending moments as

$$W_i = \lim_{x \rightarrow b_i} w_s(x), \quad \Phi_i = \lim_{x \rightarrow c_i} \phi_s(x), \quad (7)$$

we can derive a system of ordinary differential equations (8) to (11) for unknown general shapes of the deflection (w_s), the rotation of the cross section (ϕ_s), the bending moment (M_s), and the shear force (Q_s) for a uniform beam as

$$\frac{d}{dx} Q_s(x) = -\rho A w_s(x) \Omega^2 + \left(\sum_{i=1}^{n_1} R_i \text{Dirac}(x - a_i) \right) - \left(\sum_{i=1}^{n_2} m_i W_i \Omega^2 \text{Dirac}(x - b_i) \right), \quad (8)$$

$$\frac{d}{dx} M_s(x) = Q_s(x) + \rho J \phi_s(x) \Omega^2 + \left(\sum_{i=1}^{n_3} J_i \Phi_i \Omega^2 \text{Dirac}(x - c_i) \right), \quad (9)$$

$$\frac{d}{dx} \phi_s(x) = -\frac{M_s(x)}{EJ} + \left(\sum_{i=1}^{n_4} \Psi_i \text{Dirac}(x - d_i) \right), \quad (10)$$

$$\frac{d}{dx} w_s(x) = \phi_s(x) + \frac{Q_s(x)}{kGA}. \quad (11)$$

Characteristic functions of uniform Timoshenko beam with discontinuities

We have used the Laplace transform method so as to compute general solution to the system of Eqs. (8) to (11), i.e. characteristic functions of the beam, with integration constants in the form of initial parameters. Laplace transforms of unknown quantities are rational functions with a denominator which has a form of a quartic polynomial. Performing partial fraction decompositions of these rational functions, we must distinguish among three different cases:

$$\text{i) } \Omega < \frac{\sqrt{J\rho A k G}}{J\rho},$$

$$\text{ii) } \Omega > \frac{\sqrt{J\rho A k G}}{J\rho},$$

$$\text{iii) } \Omega = \frac{\sqrt{J\rho A k G}}{J\rho}.$$

In order to simplify expressions of the general solution, we introduce denotation:

$$\alpha = \frac{\sqrt{-2J E k G (\Omega J \rho k G + \Omega J E \rho - \sqrt{\Omega^2 J^2 \rho^2 k^2 G^2 - 2\Omega^2 J^2 \rho^2 k G E + \Omega^2 J^2 E^2 \rho^2 + 4J E k^2 G^2 A \rho}) \Omega}}{2 E J G k},$$

$$\beta = \frac{\sqrt{2J E k G (\Omega J \rho k G + \Omega J E \rho + \sqrt{\Omega^2 J^2 \rho^2 k^2 G^2 - 2\Omega^2 J^2 \rho^2 k G E + \Omega^2 J^2 E^2 \rho^2 + 4J E k^2 G^2 A \rho}) \Omega}}{2 E J G k}.$$

For example, when $\Omega < \frac{\sqrt{J\rho A k G}}{J\rho}$, the general shape of the rotation of the cross section may be expressed as follows:

$$\begin{aligned} \phi_s(x) = & \frac{(-\cosh(\alpha x) + \cos(\beta x)) Q_s(0)}{EJ(\alpha^2 + \beta^2)} + \frac{((\rho \Omega^2 - kG\beta^2) \sin(\beta x) \alpha - (\alpha^2 Gk + \rho \Omega^2) \sinh(\alpha x) \beta) M_s(0)}{(\alpha^2 + \beta^2) \alpha \beta G k J E} \\ & + \frac{(\cosh(\alpha x) (\alpha^2 Gk + \rho \Omega^2) + \cos(\beta x) (kG\beta^2 - \rho \Omega^2)) \phi_s(0)}{(\alpha^2 + \beta^2) k G} \\ & + \frac{A \rho \Omega^2 (\beta \sinh(\alpha x) - \sin(\beta x) \alpha) w_s(0)}{(\alpha^2 + \beta^2) E J \beta \alpha} \\ & + \left(\sum_{i=1}^{n_1} \frac{\text{Heavisid}\delta(x - a_i) R_i (-\cosh(\alpha(x - a_i)) + \cos(\beta(x - a_i)))}{J E (\alpha^2 + \beta^2)} \right) \end{aligned}$$

$$\begin{aligned}
& + \left(\sum_{i=1}^{n_2} \frac{\text{Heaviside}(x-b_i) m_i W_i \Omega^2 (\cosh(\alpha(x-b_i)) - \cos(\beta(x-b_i)))}{E J (\alpha^2 + \beta^2)} \right) + \left(\right. \\
& \sum_{i=1}^{n_3} \frac{\text{Heaviside}(x-c_i) (-\alpha^2 G k + \rho \Omega^2) \sinh(\alpha(x-c_i)) \beta + (\rho \Omega^2 - k G \beta^2) \sin(\beta(x-c_i)) \alpha \Omega^2 \Phi_i J_i}{(\alpha^2 + \beta^2) \alpha \beta G k E J} \left. \right) \\
& + \left(\sum_{i=1}^{n_4} \frac{\text{Heaviside}(x-d_i) \Psi_i (\cos(\beta(x-d_i)) (k G \beta^2 - \rho \Omega^2) + \cosh(\alpha(x-d_i)) (\alpha^2 G k + \rho \Omega^2))}{(\alpha^2 + \beta^2) k G} \right)
\end{aligned}$$

where $\text{Heaviside}(x-a)$ is the denotation used in MAPLE for Heaviside's unit step function moved into the point $x = a$.

5. Conclusions

Contribution of this paper to modal analysis of Timoshenko beam is that the mathematical model for free transverse vibration, i.e. Eqs. (3) to (6), holds true also for the discontinuous shear force, the discontinuous bending moment and the discontinuous rotation of the cross section.

Discontinuities in shear force are supposed to be owing to idealized concentrated supports or inertia masses situated between ends of the beam. Likewise, discontinuities in bending moment are assumed to be due to idealized concentrated moments of inertia situated between ends of the beam. On the contrary, discontinuities in rotation of the cross section are caused by real hinges connecting beam segments. Jump discontinuities in unknown dependently variable quantities have been expressed in corresponding distributional derivatives (3)-(5), where the singular distribution $\text{Dirac}(x)$, which is usually denoted as $\delta(x)$, is always moved into the point with the discontinuity mentioned, and multiplied by a magnitude of the discontinuity.

To be able to find natural frequencies and modal shapes of Timoshenko beam analytically with discontinuities mentioned, we have derived Eqs. (8) to (11) for shapes of the shear force, the bending moment, the rotation of the cross section and the deflection. Using the Laplace transform method with MAPLE software system, we have computed general solution to the system containing integration constants in the form of initial parameters. Computing limits (7), we can express the unknown amplitudes of the deflection, W_i , and rotation of the cross section, Φ_i , as functions of initial parameters. In order to determine the unknown initial parameters, we must establish four boundary conditions. So as to determine the unknown reactions at concentrated supports between ends of the beam, and amplitudes of discontinuities in the rotation of the cross section at hinges connecting beam segments, we must establish corresponding deformation conditions at these points. These deformation and boundary conditions create all together a homogeneous system of linear equations. The condition of the nontrivial solution to this system is the frequency equation of the beam with discontinuities assumed.

References

- Dong, S. B., Alpdogan, C., Taciroglu, E. (2010). Much ado about shear correction factors in Timoshenko beam theory. *International Journal of Solids and Structures*, 47(13), 1651-1665.
- Kanwal, R. P. (2004) *Generalized Functions*. Birkhäuser, Boston.
- Mindlin, R. D., Deresiewicz, H. (1953). Timoshenko's shear coefficient for flexural vibrations of beams (No. TR-10). Columbia Univ New York.
- Rao, S. S. (2007) *Vibration of Continuous Systems*. Wiley, New Jersey.
- Schwartz, L. (1966) *Theorie des Distributions*, Hermann, Paris.
- Štěpánek, J. (2001) *Distribution and differential equations*. Karolinum, Praha (in Czech).
- Timoshenko, S. P. (1937) *Vibration problems in engineering*. Van Nostrand, New York.

INFLUENCE OF THE BENDING RIGIDITY FACTOR ON VIBRATION AND INSTABILITY OF A COLUMN WITH INTERNAL CRACK

K. Sokół*

Abstract: *In this paper, the results of studies on transverse vibrations and instability of a geometrically nonlinear column with internal crack subjected to Euler's load are presented. The investigated column is composed of two members. The bending rigidity stiffness between members is described by the bending rigidity ratio. The internal member consists of two elements, connected by a pin and a rotational spring of stiffness C . The rotational spring stiffness C shows the size of crack. The boundary problem has been formulated on the basis of the Hamilton's principle. Due to the geometrical nonlinearity of the system, the solution of the problem was performed by means of the perturbation method. The natural vibration frequencies were computed after obtaining the equations from the first power of the small parameter ϵ . The results of numerical calculation illustrate the influence of the bending rigidity factor and crack size on vibration frequency and critical loading of the system.*

Keywords: Crack, Column, Vibration, Non-linear system, Instability.

1. Introduction

The types of connection between elements of the structure as well as physical and geometrical features have great influence on dynamic behavior of the system. The failure of the structure may be caused by the crack propagation. The vibration monitoring and crack detection are needed to prevent system failure. The knowledge of crack effect on static and dynamic behavior is important issue in practical applications.

The problems of analysis of the structures with cracks (cracks can be divided into always open and breathing ones), dynamic characteristics of systems and mathematical models have been discussed in past years by Anifantis (1981), Chondros and Dimarogonas (1989), Lee and Bergman (1994), Chondros (2001), Binici (2005).

In this paper the massless rotational spring represents the crack. The spring stiffness coefficient depends on the crack depth. The natural boundary conditions satisfy the continuity of transversal and longitudinal displacements, bending moments and shear forces in the point of location of rotational spring (Uzny, 2011). In many scientific papers authors are focused only on vibration analysis of cracked single columns (Arif Gurel, 2007). In this paper the two member column with internal crack has been investigated. Additionally, the influence of the different magnitudes of bending rigidity factor between the elements of the system on dynamic behavior is also taken into the account.

The investigated system due to its geometrical features is treated as a slender one. Main objective of this work is monitoring of the structure's dynamic behavior. The monitoring is based on vibration frequency and shape mode analysis. The critical force magnitude as a function of a cracked system is also presented. The obtained magnitudes are compared to the uncracked system. The results of numerical calculations allow to predict the possible crack initiation in the cantilever two member column loaded by axially applied external force with constant line of action. Furthermore, the investigated wide range of magnitudes of bending rigidity factor gives a scope on dynamic behavior of the system in different configurations.

* Krzysztof Sokół, PhD.: Institute of Mechanics and Machine Design Foundation, Częstochowa University of Technology, Dąbrowskiego 73, 42-200 Częstochowa, Poland, sokol@imipkm.pcz.pl

2. Problem Formulation

In the Fig. 1 the investigated cantilever column is presented. Rods (2) and (3) are connected by the pin and rotational spring of stiffness C (the smaller magnitude of C the greater crack size). The system is loaded by the external force P applied in the point of connection of rods (1) and (3). Rods have the lengths l_1, l_2, l_3 respectively. The physical model of the investigated system may be composed of two coaxial tubes, tube and rod or be a flat frame.

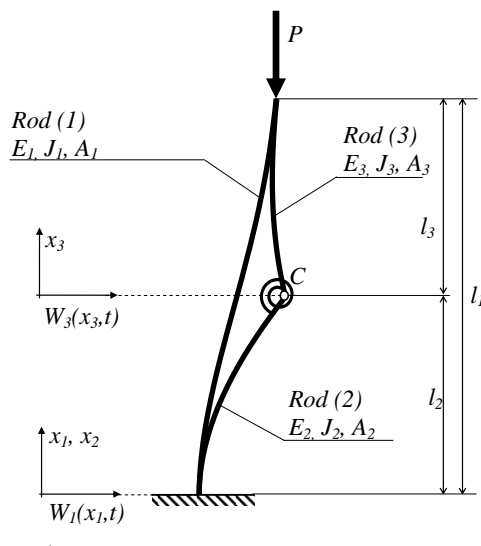


Fig. 1: Bent axes diagram of the investigated system.

The boundary problem has been formulated on the basis of the Hamilton's principle:

$$\delta \int_{t_1}^{t_2} (E^k - E^p) dt = 0 \quad (1)$$

where the kinetic E^k and potential E^p energies are expressed as follows:

$$E^k = \frac{1}{2} \sum_{i=1}^3 \int_0^{l_i} \rho_i A_i \left(\frac{\partial W_i(x_i, t)}{\partial t} \right)^2 dx \quad (2)$$

$$E^p = \frac{1}{2} \left\{ \sum_{i=1}^3 \int_0^{l_i} E_i J_i \left[\frac{\partial^2 W_i(x_i, t)}{\partial x_i^2} \right]^2 dx + \int_0^{l_i} E_i A_i \left[\frac{\partial U_i(x_i, t)}{\partial x_i} + \frac{1}{2} \left(\frac{\partial W_i(x_i, t)}{\partial x_i} \right)^2 \right]^2 dx + \frac{1}{2} C \left(\frac{\partial W_3(x_3, t)}{\partial x_3} \Big|_{x_3=0} - \frac{\partial W_2(x_2, t)}{\partial x_2} \Big|_{x_2=l_2} \right)^2 \right\} + P U_1(l_1, t), \quad (3)$$

where the following notation is used: E_i – Young modulus, J_i – moment of inertia, A_i – cross section area ρ_i – material density C – rotational spring stiffness, P – external load. Substitution of equations (2) and (3) into (1) leads to among alia the equations of motion (4)

$$E_i J_i \frac{\partial^4 W_i(x_i, t)}{\partial x_i^4} - S_i(t) \frac{\partial^2 W_i(x_i, t)}{\partial x_i^2} + \rho_i A_i \frac{\partial^2 W_i(x_i, t)}{\partial t^2} = 0 \quad i = 1, 2, 3 \quad (4)$$

and natural boundary conditions. The geometrical and natural boundary conditions are as follows:

$$\begin{aligned}
W_2(l_2, t) = W_3(0, t) \quad W_1(l_1, t) = W_3(l_3, t), \quad E_1 J_1 \frac{\partial^2 W_1(x_1, t)}{\partial x_1^2} \Big|_{x_1=l_1} + E_3 J_3 \frac{\partial^2 W_3(x_3, t)}{\partial x_3^2} \Big|_{x_3=l_3} = 0, \quad S_1 + S_2 = P \\
E_1 J_1 \frac{\partial^3 W_1(x_1, t)}{\partial x_1^3} \Big|_{x_1=l_1} + P \frac{\partial W_1(x_1, t)}{\partial x_1} \Big|_{x_1=l_1} + E_3 J_3 \frac{\partial^3 W_3(x_3, t)}{\partial x_3^3} \Big|_{x_3=l_3} = 0, \quad W_2(0, t) = \frac{\partial W_2(x_2, t)}{\partial x_2} \Big|_{x_2=0} = 0 \\
E_2 J_2 \frac{\partial^3 W_2(x_2, t)}{\partial x_2^3} \Big|_{x_2=l_2} + S_2 \frac{\partial W_2(x_2, t)}{\partial x_2} \Big|_{x_2=l_2} - E_3 J_3 \frac{\partial^3 W_3(x_3, t)}{\partial x_3^3} \Big|_{x_3=0} - S_3 \frac{\partial W_3(x_3, t)}{\partial x_3} \Big|_{x_3=0} = 0, \quad S_2 = S_3 \quad (5a-n) \\
-E_3 J_3 \frac{\partial^2 W_3(x_3, t)}{\partial x_3^2} \Big|_{x_3=0} + C \left[\frac{\partial W_3(x_3, t)}{\partial x_3} \Big|_{x_3=0} - \frac{\partial W_2(x_2, t)}{\partial x_2} \Big|_{x_2=l_2} \right] = 0, \quad W_1(0, t) = \frac{\partial W_1(x_1, t)}{\partial x_1} \Big|_{x_1=0} = 0 \\
E_2 J_2 \frac{\partial^2 W_2(x_2, t)}{\partial x_2^2} \Big|_{x_2=l_2} - C \left[\frac{\partial W_3(x_3, t)}{\partial x_3} \Big|_{x_3=0} - \frac{\partial W_2(x_2, t)}{\partial x_2} \Big|_{x_2=l_2} \right] = 0, \quad \frac{\partial W_1(x_1, t)}{\partial x_1} \Big|_{x_1=l_1} = \frac{\partial W_3(x_3, t)}{\partial x_3} \Big|_{x_3=l_3}
\end{aligned}$$

3. Results of Numerical Calculations

The results of numerical calculations shown in Figs. 2 and 3 are presented in the non-dimensional form, where

$$p = \frac{Pl^2}{E_1 J_1 + E_2 J_2}, \quad c = \frac{Cl}{E_1 J_1 + E_2 J_2}, \quad \omega = \sqrt{\Omega^2 \frac{(\rho_1 A_1 + \rho_2 A_2) l^4}{E_1 J_1 + E_2 J_2}}, \quad r_m = \frac{E_2 J_2}{E_1 J_1}, \quad r_w = \frac{E_3 J_3}{E_2 J_2}, \quad d_i = \frac{l_i}{l}.$$

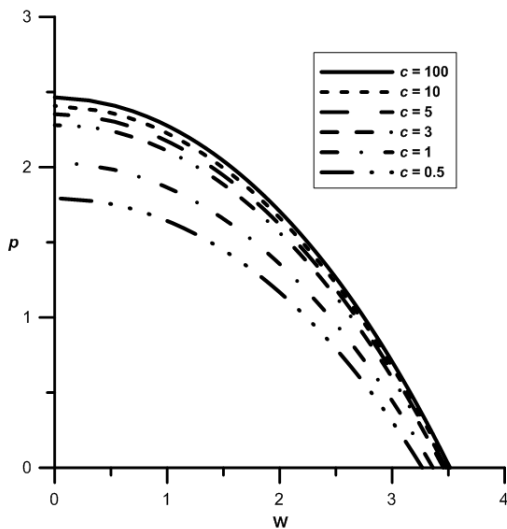


Fig. 2: External load vs. vibration frequency for different crack size ($d_2 = 0.5$, $r_m = r_w = 1$).

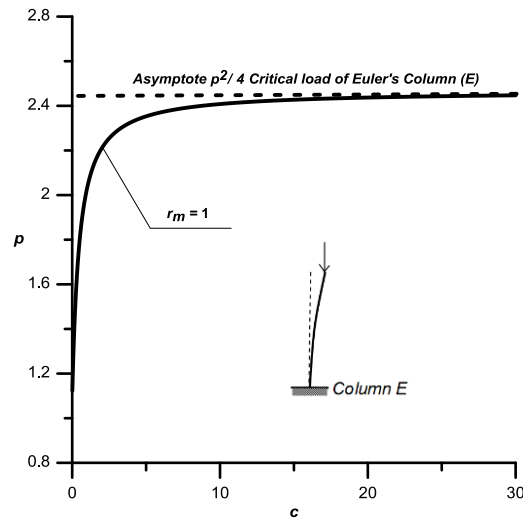


Fig. 3: Influence of crack size on maximum load magnitude ($d_2 = 0.5$, $r_w = 1$).

In the Fig. 2 an influence of crack size localized in the middle of the column is presented. When the crack is small ($c = 10, 100$) the magnitudes of maximum load are comparable. With the reduction of the rotational spring stiffness ($c = 5, 3, 1, 0.5$) the decrease of natural vibration frequency and critical loading occurs. It can be concluded that the critical force strongly depends on crack size, as illustrated on – Fig. 3. The critical force of the system without crack (the investigated system with great magnitude of c can be treated as a particular case which corresponds to Euler's column) is

$$p_{cr} = \frac{\pi^2}{4}.$$

In the case when the bending rigidity factor ratio between rods (1) and (2) is changing regardless to crack size the natural vibration frequency and maximum loading are varying. If r_m parameter is greater than 1

($E_2J_2 > E_1J_1$), then with the growing crack size the reduction of vibration frequency and maximum loading appears (Fig. 4). When $r_m < 1$ the opposite situation takes place. In the Fig. 5 the curves on the plane $p - r_m$ for different crack size have been plotted.

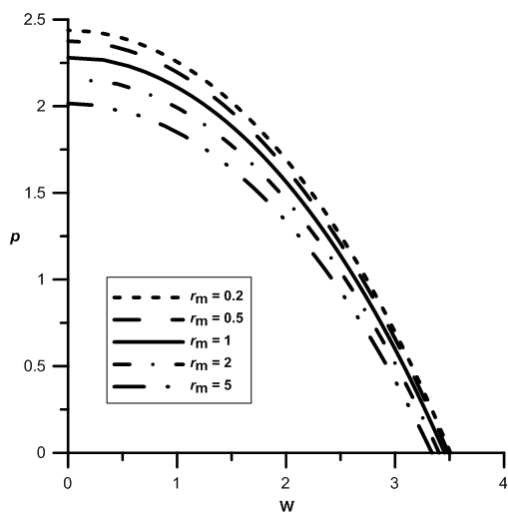


Fig. 4: External load vs. vibration frequency for different rigidity factors ($d_2 = 0.5$, $c = 3$, $r_w = 1$).

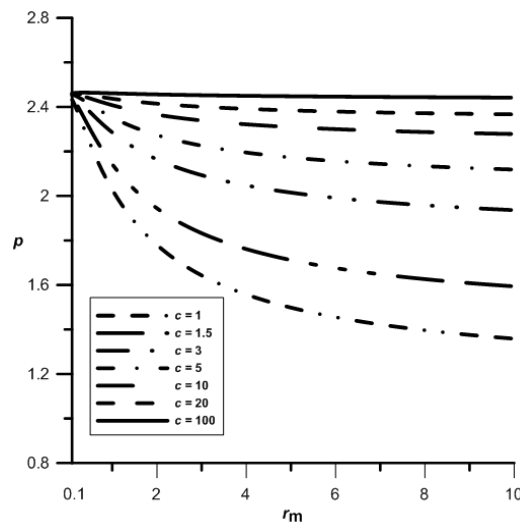


Fig. 5: Rigidity factor as a function of external load for different crack size ($d_2 = 0.5$, $r_w = 1$).

The reduction of r_m regardless to crack size causes an increase of maximum loading capacity of the column. With the $r_m > 1$, the growing crack size corresponds to rapid decrease of p magnitude. The change of maximum force magnitude results in vibration frequency change.

4. Conclusions

In this paper the influence of the bending rigidity factor ratio between rods (1) and (2) on the dynamic behavior of the cantilever column with internal crack have been investigated. The results of numerical calculations can be used to identify crack size on the basis of natural vibration frequency analysis. It can be concluded that crack size has significant influence on vibration frequency and maximum load magnitude. For larger crack size the lower critical load was obtained. For $r_m > 1$ the influence of the crack size on investigated parameters is significant. There exists crack size above which the change in r_m parameter on maximum load and vibration frequency is very small. The deviation in the dynamic behavior of the investigated system might be considered as a possible indicator of crack initiation.

Acknowledgement

This work was funded by Czestochowa University of Technology BS/PB1-101-3020/11/P.

References

- Anifantis, N., A. Dimarogonas, A. (1981) Stability of columns with a single crack subjected to follower and axial loads. *International Journal of Solids and Structures*, 19, pp. 281-291.
- Arif Gurel, M. (2007) Buckling of slender prismatic circular columns weakened by multiple edge cracks. *Acta Mechanica*, 188, pp. 1-19.
- Binici, B. (2005) Vibration of beams with multiple open cracks subjected to axial force, *Journal of Sound and Vibration*, 287, pp. 277-295.
- Chondros, T. G., Dimarogonas, T. G. (1989) Dynamic sensivity of structures to cracks. *Journal of Vibration, Acoustics, Stress and Reliability in Design*, 111, pp. 251-256.
- Chondros. T. G. (2001) The continuous crack flexibility model for crack identification. *Fatigue & Fracture of Engineering Materials & Structures*, 24, pp. 643-650.
- Lee, J., Bergman, L. A. (1994) The vibration of stepped beams and rectangular plates by an elemental dynamic flexibility method. *Journal of Sound and Vibration*, 171, pp. 617-640.
- Uzny S. (2011) Local and global instability and vibrations of a slender system consisting of two coaxial elements. *Thin-Walled Structures*, 49 (2011) pp. 618-626.

ON POSSIBILITIES OF DIAGNOSING OF CATERPILLAR UNDERCARRIAGES IN LARGE-SIZE WORKING MACHINES

P. Sokolski*

Abstract: *The paper concerns issues of diagnosing a technical state of caterpillar undercarriages of large-size working machines. Exemplary failures of their parts are presented. Different possibilities of performing diagnostic process basing on criterion of location of sensors are discussed. Each of the presented methods is supported by various examples of possible implementation in real operating conditions in an open-pit mine.*

Keywords: Surface mining, Large-size working machines, Caterpillar chain links, Diagnostic signals.

1. Introduction

In basic open-pit machines operated in brown coal mines 3 types of undercarriages are usually applied: walking, rail and caterpillar ones (Durst, 1986; Wong, 1989). The latter are the most common because of number of fundamental advantages, including high mobility in extreme working conditions, high value of thrust and low base compression. Such undercarriages are presented in the Fig. 1.



Fig. 1: A set of 2 caterpillar undercarriages. Source: author's archive.

Durability of driving units plays a key role in terms of reliability of the entire machine (an excavator or a damping conveyor). The character of degradation of subassemblies and parts of large-size working machines' undercarriages strictly depends on loading acting on them. Because of that, to assess the durability of these elements it is needed to evaluate values of the forces generated during the work of such a machine. An empirical method enabling this analysis is presented in work (Smolnicki and Maslak, 2012).

Degradation and damages of different parts of caterpillar undercarriages in large-size working machines is described in details in works (Bosnjak et al., 2010; Bosnjak et al., 2011). A comprehensive attitude to this problem can include both experiments on real elements and numerical simulations based e.g. on FEM.

* Piotr Sokolski, PhD.: Chair of Fundamentals of Machinery Design, Wrocław University of Technology, ul. Łukasiewicza 7/9; 50-371 Wrocław; Poland, piotr.sokolski@pwr.wroc.pl

Among all elements of caterpillar undercarriages chain links are one of the most important as even insignificant degradation of their technical state can have a negative impact on the mobility of the driving unit (Sokolski, 2012).

Ovalization of a pin-joint hole or plastic deformation of only one link's lug can make the whole machine unfit for use or at least decrease its serviceability. In case of a tear-off of a link's lug, the caterpillar chain is damaged disabling further movement of this undercarriage. It also can negatively influence the stability of the machine. A caterpillar link in good technical state and links with exemplary failures are shown in the Fig. 2. More detailed description of typical failures of the chain links, including information about their areas especially endangered to damages is presented in work (Sokolski and Sokolski, 2014).



Fig. 2: Caterpillar chain links: a) Bottom view of a part in a good technical state; parts with typical failures; b) Torn-off lug; c) Plastically strained lugs. Source: author's archive.

2. Diagnosing of Caterpillar Undercarriages

In recent years diagnostics have become more and more important in the field of operation of large-size working machines in Polish open-pit mines. Different techniques and procedures are used for evaluation of technical state of parts and assemblies of basic mining machinery (Sobczykiewicz and Kowalczyk, 2009). Thermal and vibroacoustic signals are used most of all. However there are no such procedures applied for monitoring of undercarriages. Because of that there is a particular need for formulation of theoretical principles and practical implementation of monitoring and diagnosing of undercarriage

assemblies. It refers to evaluation of technical state of links, plates, supporting wheels and balance lever's units.

In this context, the diagnostic task should meet the following basic requirements (Sokolski, 2012):

- To be achievable in the process of normal functioning of the undercarriage (the working process of the machine), because then the obtained data reflect the real state of the examined parts.
- To provide the necessary information about both the technical state and the wear processes occurring in these parts.
- To ensure acquiring the required information at an acceptable level of running expenses (taking into account economic criteria).

In order to develop effective diagnostic procedures applied for monitoring of undercarriages of large-size working machinery, appropriate observation tools must be selected. The main factor in the applicability of such a system is the character of operating conditions of the undercarriages. In particular one can list extremely high loading and constant adverse environmental influence (mud, dust, rain, snow, etc.). For these reasons, many commonly used diagnostic tools can not be applied for evaluation of technical state of driving mechanisms of excavators or damping conveyors.

To put in order all of the possible monitoring methods, as a criterion of classification one can select the location of the components of the measuring system. If so, then the diagnostic process using sensors placed on the assessed object or sensors located outside it can be distinguished (Sokolski, 2012).

Technical condition of an undercarriage can be evaluated using invasive methods with sensors installed on both stationary and movable elements. In the first case a diagnostic test can be based for example on monitoring interactions between components cooperating directly with the part on which the data is registered. In this variant, it is also possible to measure and evaluate geometric relationships with selected moving parts.

For instance: for a pair of "balance lever - caterpillar plate" an indicator for an assessment of degradation processes may be the distance between the balance lever (a reference element) and selected plates. When this value exceeds limiting ones from the acceptable range, one can make a conclusion that e.g. deterioration of the tensioning system is advanced. Such degradation may result in an increase in so-called overhang of the upper side of the caterpillar chain.

Another example of diagnosing of the technical state of caterpillar driving units using sensors on stationary parts is an acquisition and analysis of vibroacoustic signal registered on the system of balance levers.

For the case of a sensor placed on a moving part, measurements of the caterpillar chain's pitch can be proposed. Such a test may rely on determining the distance between adjacent plates. Mutual wear of links and pins may result in the formation of clearances in this tribological pairs, which directly effect in a change of the chain's pitch.

Another possibility of implementing an assessment of caterpillar chain's technical state using a sensor on a movable part can be a strategy analogous to the one described previously. This method bases on the measurement of the distance between a fixed and a movable element. In such a case a sensor can be placed on a plate and as the reference object one of stationary parts of the undercarriage such as a balance lever can be selected.

To get a diagnostic data in terms of evaluation of the technical state of caterpillar driving units with an outside sensor one of non-invasive methods can be carried out. Recording of diagnostic signals through sensors located outside the tested elements can be implemented using a suitable wireless technology. In this situation there is no need for direct access to the machine what should be considered as one of the main advantages of such a monitoring strategy. Intensive development of wireless signal transmission techniques creates a relatively large choice. Often the decisive criterion is the cost of an implementation of this system.

In the author's opinion the most reasonable among wireless methods can be: analyses based on acoustic signals generated during a movement of a basic mining machine and assessment upon base compression under the caterpillar as well.

In the first case through the evaluation of an acoustic spectrum and determination of basic parameters characterizing this signal, it is possible to assess the progress of degradation processes. Additionally, analyzing such a signal it is possible to identify failures occurred in undercarriages' parts.

Base compression under a moving undercarriage enables evaluation of the distribution of loads transferred from machine to subsoil. It is highly dependent on the state of the chassis' components.

Both of the described methods (the acoustic one and the analysis of base compression) were positively verified by the author. The results of analyses and methods of assessment are described in details in (Sokolski, 2012).

3. Conclusions

The process of diagnosing of the technical state of large-size caterpillar undercarriages is a significant factor increasing the operational reliability of their assemblies. Therefore it is a key issue and comprises a part of a development trend of monitoring of open-pit basic machines.

A typical phenomenon during diagnosing is an unequal influence of changes in the technical state of observed parts on different diagnostic signals. For this reason, a selection of redundant signals is well-founded. It allows reducing the number of failures that could not be registered. In addition, this way of monitoring reduces the possibility of an error in the assessment of the technical state of the tested parts. These factors increase the likelihood of formulating the correct diagnosis.

The monitoring strategies described in the paper allow to conduct differently the diagnostic process. Because of that one can adapt a research method to possessed measuring devices. Another advantage of such a situation is as well a possibility of building a comprehensive diagnostic procedure based on an utilization of complementary and redundant signals.

In most cases because of the real operating conditions of large-size caterpillar undercarriages, the usage of a diagnostic system with sensors installed directly on a tested object can not be performed. It is mainly because of the possibility of a mechanical damage to these devices. For this reason the best (if not only) empirically sensible solution is a usage of sensors placed outside elements of caterpillar undercarriages.

Acknowledgement

This work was realized within a framework of Fellowship co-financed by European Union within European Social Fund (Research project MK/SN/340/VI/2012/U).

References

- Bosnjak, S., Petkovic, Z., Zrnic, N., Pantelic, M., Obradovic, A. (2010) Failure analysis and redesign of the bucket wheel excavator two-wheel bogie. *Engineering Failure Analysis*, No. 17, pp. 473-485.
- Bosnjak, S. M., Arsic, M. A., Zrnic, N. D., Odanovic, Z. D., Djordevic, M. D. (2011) Failure Analysis of the Stacker Crawler Chain Link. *Procedia Engineering*, No. 10, pp. 2244-2249.
- Durst, W., Vogt, W. (1986) *Schaufelradbagger*. Trans. Tech. Publications, Clausthal – Zellerfeld (in German).
- Smolnicki, T., Maslak, P. (2012) Multicaterpillar track chassis of big machines – identification of loads. *Key Engineering Materials*, Vol. 490, pp. 187-194.
- Sobczykiewicz, W., Kowalczyk, M. (2009) Accomplishing the required fatigue life of load-carrying machine structures. Integrated approach. *Surface Mining*, No. 4-5, pp. 109-114 (in Polish).
- Sokolski, P. (2012) A diagnosing method of crawler chain links in large-size working machines (PhD Thesis). Institute of Machinery Design and Operation, Wrocław University of Technology, Wrocław (in Polish).
- Sokolski, P., Sokolski, M. (2014) Evaluation of resistance to catastrophic failures of large-size caterpillar chain links of open-pit mining machinery. *Eksploracja i Niezawodność – Maintenance and Reliability*, Vol. 16, No. 1, pp. 80-84.
- Wong, J. Y. (1989) *Terramechanics and off-road vehicles*. Elsevier, Amsterdam.

CALCULATING THE AIR FLOW VELOCITY IN AIR CAVITIES IN WALLS

J. Solar^{*}

Abstract: *Moisture from walling masonry, in particular in historic and protected buildings, is often removed by means of air cavities located in walls under the ground level. The air flow should be, if possible, almost uninterrupted so that this method could be efficient. This paper discusses the calculation of the air flow velocity inside the wall cavities.*

Keywords: Wet masonry, Remediation of wet masonry, Air cavities, Air flow in air cavities.

1. Introduction

Air insulation methods have ranked among frequent methods used for removal of moisture from walling masonry. This is, in particular, the case of historic buildings. When designing, an empiric approach is often used for air cavities. The air flow should be, if possible, almost uninterrupted so that this method could be efficient in the air cavities. The calculation below is for an air cavity (see Fig. 1) with natural flow of air where both the suction and exhaust holes are located at the outside.

2. Calculating an Open Air Cavity

In order to calculate performance of an air cavity in a wall it is necessary to determine the velocity of air in the air cavity – w_x [$\text{m}\cdot\text{s}^{-1}$], the temperature of the air which flows in the air cavity – t_x [$^{\circ}\text{C}$], the partial pressure of water vapours in the air cavity – p_{dx} [Pa], the partial pressure of water vapours in the air cavity upon saturation – p_{dx}^* [Pa], condensation of water vapours in the air cavity and a pressure drop of the air flow – Δp [Pa], the pressure loss – Δp_z [Pa], and to decide whether the air cavity works properly. This paper discusses only the calculation of the air flow velocity and the related development of temperature of the air flow in the air cavity.

3. Velocity of the Air Flow in the Air Cavity

In past, the relation for calculation of the air flow velocity in an open air layer (for instance, in calculation of two-layer roofs) was developed on the basis of generally known equations which are valid for the pressure drop of the air flow in the air cavity and the equations which describe the friction losses and resistance integrated into the air cavity. By analogy, this relation can be used in calculations of air cavities through which the air flows naturally. This relation is specified in (Řehánek, 1982). The equation for the air cavity is as follows:

$$w_x = \sqrt{\frac{2 \cdot h \cdot (\rho_v - \rho_x) + (A_n - A_z) \cdot w_v^2 \cdot \rho_v}{\lambda \cdot \frac{l_x}{d_r} \cdot \rho_x + \sum \xi \cdot \rho_x}} \quad [\text{m}\cdot\text{s}^{-1}] \quad (1)$$

where: h [m] – is the difference in heights between the axis of the suction and exhaust holes.
 ρ_v [$\text{kg}\cdot\text{m}^{-3}$] – is the volumetric weight of the outdoor air.

^{*} Assoc. Prof. Jaroslav Solar, PhD.: VŠB-TU Ostrava, Faculty of Civil Engineering, Ludvíka Podéště 1875, 708 33 Ostrava-Poruba, CZ, jaroslav.solar@vsb.cz

ρ_x [kg.m⁻³] – is the volumetric weight of the air in the air cavity located in the x distance from the suction hole.

w_v [m.s⁻¹] – is the wind velocity which is determined either pursuant to ČSN 73 0540-3, (Řehánek, 1982) or on the basis of local meteorological data.

A_n [-] – is the aerodynamic coefficient on the wind side ($A_a = 0.6$).

A_z [-] – is the aerodynamic coefficient on the lee side ($A_a = -0.3$).

The aerodynamic coefficients A_a and A_z are used only if the air cavity is connected to the outdoor air.

l_x [m] – is the length of the section in the air cavity.

ξ [-] – is the coefficient of integrated resistance (see ČSN 73 0540-3 and (Řehánek, 1982)).

d_r [m] – is the equivalent diameter of the air cavity located in the x distance from the suction hole:

$$d_r = \frac{2 \cdot v \cdot s}{v + s} \quad [\text{m}] \quad (2)$$

where: v [m] – is the internal ground clearance of the air cavity.

s [m] – is the internal free width of the air cavity.

λ [-] – is the resistance coefficient which depends on the Reynolds number Re and is as follows:

$$\text{a) for the laminar flow (Re} \leq 2320\text{): } \lambda = \frac{64}{Re} \quad [-] \quad (3)$$

$$\text{b) for the turbulent flow (Re} > 2320\text{): } \lambda = 0.0032 + \frac{0.221}{Re^{0.237}} \quad [-] \quad (4)$$

$$\text{where: } Re \text{ [-] is the Reynolds' number : } Re = \frac{w_x \cdot d_r}{\nu} \quad [-] \quad (5)$$

where: d_r [m] – is the equivalent diameter of the air cavity.

w_x [m.s⁻¹] – is the air flow velocity in the air cavity.

ν [m².s⁻¹] – is the kinematic air viscosity which can be determined as follows:

$$\nu = \frac{\eta}{\rho_x} \quad [\text{m}^2 \cdot \text{s}^{-1}] \quad (6)$$

where: ρ_x [kg.m⁻³] – is the volumetric weight of the air in the air cavity in the x point located out of the suction.

η [Pa.s] – is the dynamic air viscosity which can be determined as follows:

$$\eta = (17.2 + 0.047 \cdot t_x) \cdot 10^{-6} \quad [\text{Pa.s}] \quad (7)$$

where: t_x [°C] – is the temperature of the air in the air cavity located in the x distance from the suction hole.

The most complicated part of the calculation is, however, the calculation of the velocity of the air which flows through the air cavity with natural air flow - w_x [m.s⁻¹]. The reason is that the velocity depends on two parameters:

- 1) on the resistance coefficient λ [-] which depends, in turn, on the air flow velocity w_x [m.s⁻¹] and on the Reynolds' number Re [-],
- 2) on the volumetric weight of the air in the air cavity in the distance x from the suction, ρ_x [kg.m⁻³], which, in turns, depends on the temperature of the air t_x [°C] in the air cavity in the distance x.

This means, no explicit solution is possible for the velocity of the air flow in the air cavity - w_x [m.s⁻¹]. A numerical approach only can be used. It is advisable to use a software application.

4. Calculating the Temperature in the Air Cavity

The temperature in the air cavity is calculated using the balance equation:

$$Q = Q_1 + Q_2 + Q_3 + Q_4 \quad [\text{W}] \quad (8)$$

where: Q [W] is the total heat transfer rate of the air which enters the air cavity.

Q_1 through Q_4 [W] is the quantity of the air which enters the air cavity through the structures No. 1 to No. 4.

$$Q_1 = v \cdot U_1 \cdot (t_1 - t_x) \cdot dx \quad [\text{W}] \quad (9)$$

$$Q_2 = s \cdot U_2 \cdot (t_2 - t_x) \cdot dx \quad [\text{W}] \quad (10)$$

$$Q_3 = v \cdot U_3 \cdot (t_3 - t_x) \cdot dx \quad [\text{W}] \quad (11)$$

$$Q_4 = s \cdot U_4 \cdot (t_4 - t_x) \cdot dx \quad [\text{W}] \quad (12)$$

where: v [m] is the internal ground clearance of the air cavity.

s [m] is the internal free width of the air cavity.

U_1 through U_4 [$\text{W} \cdot \text{m}^{-2} \cdot \text{K}^{-1}$] are the heat transfer coefficients No. 1 through 4 for the structure

t_1 through t_4 [$^{\circ}\text{C}$] are the ambient air temperatures No. 1 through 4 for the structure outside

t_x [$^{\circ}\text{C}$] – is the temperature of the air inside the air cavity located in the x distance from the suction hole.

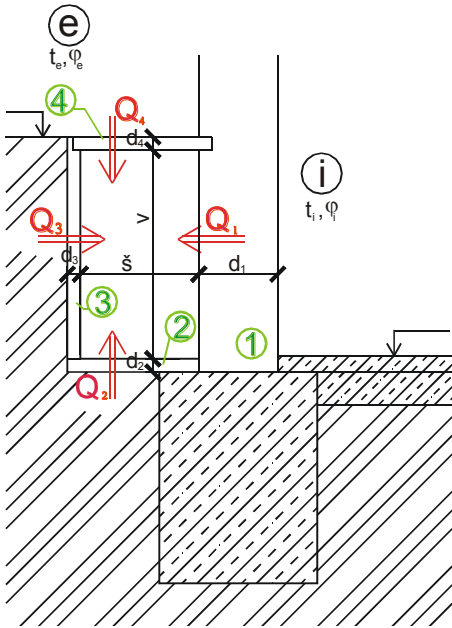


Fig. 1: Scheme of air cavity in wall.

The equation is as follows:

$$Q = Q_t \quad [\text{W}] \quad (13)$$

where: Q_t [W] – is heat transfer rate which increases the temperature of the air in the air cavity by dt_x

$$Q_t = c \cdot M \cdot dt_x \quad [\text{W}] \quad (14)$$

$$M = \rho_x \cdot s \cdot v \cdot w \quad [\text{kg} \cdot \text{s}^{-1}] \quad (15)$$

where: w [$\text{m} \cdot \text{s}^{-1}$] – is the air flow velocity in the air cavity.

ρ_x [$\text{kg} \cdot \text{m}^{-3}$] – is the volumetric weight of the air in the air cavity located in the distance x from the suction hole.

v [m] – is the internal ground clearance of the air cavity.

s [m] – is the internal free width of the air cavity.

c [$\text{J} \cdot \text{kg}^{-1} \cdot \text{K}^{-1}$] – is the specific thermal capacity which results from the formula below:

$$c = 1010 + 0.12t_x \quad [\text{J} \cdot \text{kg}^{-1} \cdot \text{K}^{-1}] \quad (16)$$

where: t_x [$^{\circ}\text{C}$] – is the temperature of the air inside the air cavity located in the x distance from the suction hole.

Because this equation can be used for calculation of the specific thermal capacity only if the air is dry, it is possible to use directly $c = 1010 \text{ J} \cdot \text{kg}^{-1} \cdot \text{K}^{-1}$ in the calculation.

Having substituted Q , Q_1 , Q_2 , Q_3 and Q_4 in (8) one obtains:

$$c \cdot M \cdot dt_x = v \cdot U_1 \cdot (t_1 - t_x) \cdot dx + s \cdot U_2 \cdot (t_2 - t_x) \cdot dx + v \cdot U_3 \cdot (t_3 - t_x) \cdot dx + s \cdot U_4 \cdot (t_4 - t_x) \cdot dx$$

$$c \cdot M \cdot dt_x = v \cdot U_1 \cdot t_1 \cdot dx - v \cdot U_1 \cdot t_x \cdot dx + s \cdot U_2 \cdot t_2 \cdot dx - s \cdot U_2 \cdot t_x \cdot dx + v \cdot U_3 \cdot t_3 \cdot dx - v \cdot U_3 \cdot t_x \cdot dx + s \cdot U_4 \cdot t_4 \cdot dx - s \cdot U_4 \cdot t_x \cdot dx$$

$$c \cdot M \cdot dt_x = v \cdot U_1 \cdot t_1 \cdot dx + s \cdot U_2 \cdot t_2 \cdot dx + v \cdot U_3 \cdot t_3 \cdot dx + s \cdot U_4 \cdot t_4 \cdot dx - v \cdot U_1 \cdot t_x \cdot dx - s \cdot U_2 \cdot t_x \cdot dx - v \cdot U_3 \cdot t_x \cdot dx - s \cdot U_4 \cdot t_x \cdot dx$$

$$c \cdot M \cdot dt_x = (v \cdot U_1 \cdot t_1 + s \cdot U_2 \cdot t_2 + v \cdot U_3 \cdot t_3 + s \cdot U_4 \cdot t_4) \cdot dx - (v \cdot U_1 + s \cdot U_2 + v \cdot U_3 + s \cdot U_4) \cdot t_x \cdot dx$$

The terms in the brackets can be expressed as the constants A and B:

$$A = v \cdot U_1 \cdot t_1 + s \cdot U_2 \cdot t_2 + v \cdot U_3 \cdot t_3 + s \cdot U_4 \cdot t_4$$

$$B = v \cdot U_1 + s \cdot U_2 + v \cdot U_3 + s \cdot U_4$$

Then, one obtains:

$$\begin{aligned} c \cdot M \cdot dt_x &= A \cdot dx - B \cdot t_x \cdot dx \\ c \cdot M \cdot dt_x &= (A - B \cdot t_x) \cdot dx \end{aligned}$$

After modification:

$$\frac{dt_x}{A - B \cdot t_x} = \frac{dx}{c \cdot M}$$

After substitution:

$$\begin{aligned} A - B \cdot t_x &= Z \\ dZ &= -B \cdot dt_x \\ dt_x &= -\frac{dZ}{B} \end{aligned}$$

Then:

$$-\frac{dZ}{B \cdot Z} = \frac{dx}{c \cdot M}$$

or:

$$\frac{B}{c \cdot M} \cdot dx + \frac{dZ}{Z} = C$$

Equation integral:

$$\begin{aligned} \frac{B}{c \cdot M} \cdot \int dx + \int \frac{dZ}{Z} &= C \\ \frac{B}{c \cdot M} \cdot x + \ln Z &= C \end{aligned}$$

The integration constant is derived from a general boundary condition: $x = 0$, then $t_x = t_0$.

This means, the temperature of the air at the beginning of the air cavity is same as the temperature of the air at the exit, t_0 . If $x = 0$ and the boundary condition above is fulfilled, the equation is as follows:
 $\ln Z = \ln(A - B \cdot t_0) = C$

so:

$$\ln(A - B \cdot t_x) = \ln(A - B \cdot t_0) - \frac{B}{c \cdot M} \cdot x$$

After modification:

$$A - B \cdot t_x = (A - B \cdot t_0) \cdot e^{\left(\frac{-B}{c \cdot M} \cdot x\right)}$$

then:

$$-B \cdot t_x = (A - B \cdot t_0) \cdot e^{\left(\frac{-B}{c \cdot M} \cdot x\right)} - A$$

$$-B \cdot t_x = -(A - B \cdot t_0) \cdot e^{\left(\frac{-B}{c \cdot M} \cdot x\right)} + A$$

Resulting formula:

$$t_x = \frac{A - (A - B \cdot t_0) \cdot e^{\left(\frac{-B}{c \cdot M} \cdot x\right)}}{B} \quad [^\circ\text{C}], \quad (17)$$

where: x [m] is the distance from the point from the start of the air cavity.

t_x [°C] is the temperature in x in the air cavity.

References

- Řehánek, J. et al. (1982) Thermal and technical standards. Comments to ČSN 73 0540, ČSN 73 0542, ČSN 73 0549, ČSN 73 0560 a ČSN 73 0565. Vydavatelství Úřadu pro normalizaci a měření. Prague, (in Czech).
 ČSN 73 0540-3 (2005) Thermal protection of buildings-Part 3: Design values of variables. (in Czech).

INFLUENCE OF AIRFLOW-RIVULET INTERACTION ON CIRCULAR CYLINDER IN UNIFORM FLOW

R. Soltys^{*}, M. Tomko^{**}

Abstract: *Vibrations of cables subjected to rain-wind interaction was several times observed on existing structures. This paper deals with numerical simulation of airflow-rivulet interaction using fluid-structure interaction (FSI). Computational fluid dynamics (CFD) model involves uniform flow which represents air with constant speed at inlet. An incompressible fluid flow with Navier-Stokes equations has been applied. Computational structure dynamics (CSD) model involves cylinder and rigid water rivulet which is allowed to move on cylinder's surface. Periodic movement of rivulet has been observed which vibration frequency has been lower than vortex shedding frequency. The frequency of periodically moving rivulet also has appeared in estimated cylinder aerodynamic characteristics.*

Keywords: Aerodynamic characteristics, Flow past cylinder, Fluid-structure interaction, Water rivulet.

1. Introduction

Significant part of cable-stayed bridges are inclined cables which are sensible to dynamic loading due to their low structural damping. In special weather conditions cables may vibrate with large amplitudes as was observed on several bridges (Meikonishi Bridge, Hikami and Shiraishi, 1988; Fred Hartman Bridge, Zuo et al., 2007). This aeroelastic phenomenon is known as rain-wind induced vibration (RWIV). During last decades numerous wind-tunnel experiments have been realized focused on formation of rivulets and aerodynamic influence on vibration of cables (Matsumoto et al., 2003; Zhang et al., 2008). Fluid mechanical interpretation has been deduced on mechanical models (Yamaguchi, 1990; Peil and Nahrath, 2003; Seidel and Dinkler, 2006) and analytical solutions of airflow-rivulet has also been presented (Seidel and Dinkler, 2006). Using numerical simulations two different approaches has been presented. First, rivulet has been considered as a rigid protuberance and the flow (Li and Gu, 2006). In second approach, the thin-film model has been used to investigate formation of rivulets which modifies effective shape of the body.

According to the complexity and three-dimensionality of the RWIV problem fluid-structure interaction (FSI) approach has been used for investigation airflow-induced rivulet movement, related influence on the airflow and changes of cylinder aerodynamic characteristics.

2. Applied Physical and Boundary Conditions to Numerical Model

Conditions in which the rivulets can be formed have been investigated by several studies (Lemaitre et al., 2010; Consentino et al. 2003). Such as wind velocity when cable vibrations occurs ($5 - 17$ m/s), cable diameter ($0.1 - 0.25$ m), Reynolds number ($0.5 \cdot 10^5 - 1.5 \cdot 10^5$), cable orientation considering wind direction and angle of inclination.

In this study horizontally positioned circular cylinder with diameter $d = 0.12$ m using two-dimensional coupled airflow-rivulet interaction model using fluid-structure interaction (FSI) has been investigated. Air with uniform speed of $u = 13$ m/s has been considered with corresponding Reynolds number $Re = 10^5$ and the air has been represented by incompressible viscous fluid flow in Computational fluid dynamics

* Ing. Robert Soltys, PhD.: Institute of Structural Engineering, Faculty of Civil Engineering, Technical University of Kosice, Vysokoskolska 4; 042 00, Kosice; Slovakia, robert.soltys@tuke.sk

** Assoc. Prof. Ing. Michal Tomko, PhD.: Institute of Structural Engineering, Faculty of Civil Engineering, Technical University of Kosice, Vysokoskolska 4; 042 00, Kosice; Slovakia, michal.tomko@tuke.sk

(CFD) model with applied Navier-Stokes equations in turbulent regime with Spalart-Allmaras Detached Eddy Simulation model (SA-DES). Dimensions of rivulet has been adopted according to Matsumoto et al. (2003) as shown in Fig. 1. Initial position of rivulet has been considered at the bottom of the horizontally mounted cylinder with angle related to flow direction of $\theta = 270^\circ$. It has been considered, the initial position of rivulet has been affected by gravitational force. Mesh of coupled computational model and applied boundary conditions are shown in Fig. 2. Cutting-out circularly-shaped water rivulet has been considered with density of 1000 kg/m^3 and nearly infinitesimally rigid, therefore, no surface tension forces have been applied. Rivulet mesh has been fixed to cylinder mesh via shared nodes. In cylinder model nearly infinitesimally small mass and infinitesimal rigidity has been considered. As FSI interaction has been applied and cylinder mesh has been fixed rigidly through its center node, the aerodynamic characteristics have been effectively calculated from resulting forces in this node. Flow model mesh density has been decreasing as the distance from cylinder surface has been increasing. Therefore, high mesh density has been achieved in boundary layer and less time consuming model has been acquired, observing sufficient accuracy (according to experimental measurements) as can be seen in Tab. 1.

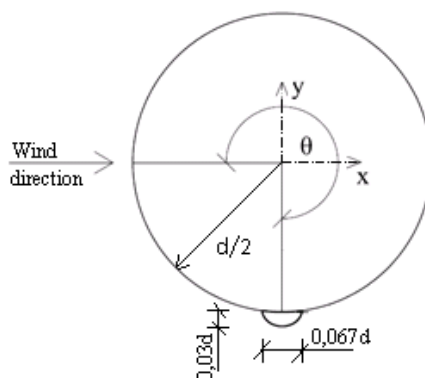


Fig. 1: Cylinder and rivulet relative position and dimensions.

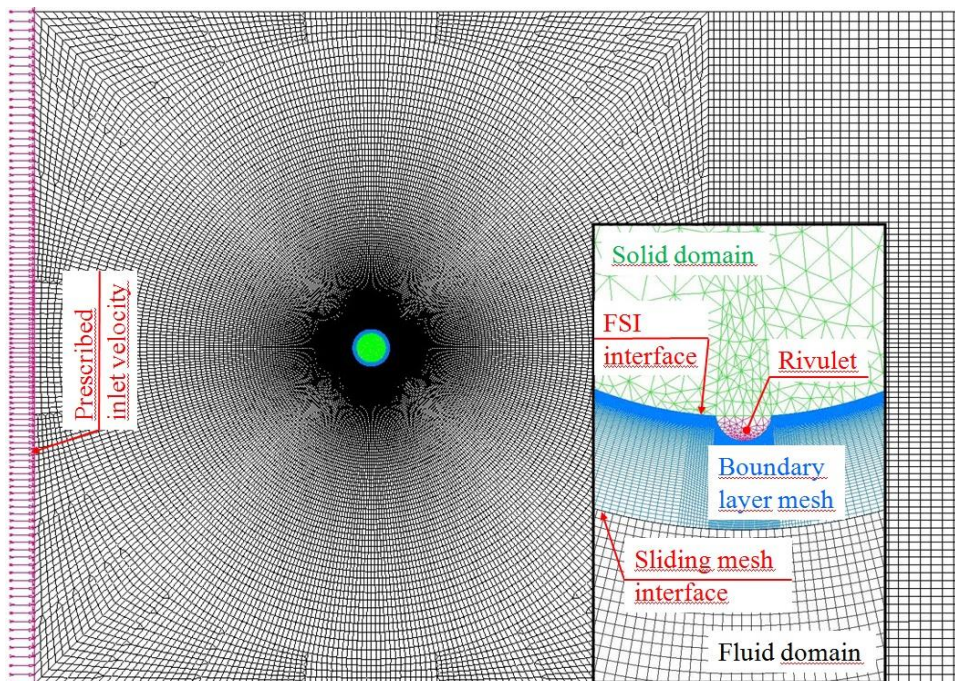


Fig. 2: CFD, CSD and rivulet model meshes and applied boundary conditions.

Tab. 1 summarizes computed aerodynamic characteristics (c_d is drag coefficient, S_t is Strouhal number and f_{sh} is vortex shedding frequency), compared with numerically and experimentally obtained results by Breuer (2000), Wieselsberger (1921) and Roshko (1961). Boundary layer mesh has been fixed to rivulet mesh, therefore the movements have been coupled and sliding mesh interface between two fluid meshes was necessary.

Tab. 1: Aerodynamic characteristics of flow past circular cylinder with and without rivulet.

Method (Re = 10 ⁵)	Mesh size	c_d (-)	S_t (-)	f_{sh} (Hz)
Without rivulet, simulation - SA-DES	200 x 400	1.224	0.201	21.74
With rivulet, simulation - SA-DES	200 x 400	1.385	0.203	22.0
Breuer (2000), LES turbulent model, 3D, (Re = 1.4.10 ⁵)	165 x 165	1.218	0.217	-
	325 x 325	1.286	0.203	-
Wieselsberger (1921), experiment	-	≐1.2	≐0.2	-
Roshko (1961), experiment	-	-	≐0.19	-

3. Equation of Motion for Rivulet

Rivulet motion can be described according to Seider and Dinker (2006) in polar coordinates using equations of motion

$$m(\ddot{\theta}d + \ddot{x} \sin \theta + \ddot{y} \cos \theta) = T, \quad (1)$$

$$m(-\dot{\theta}^2 d - \ddot{x} \cos \theta + \ddot{y} \sin \theta) = N, \quad (2)$$

where m , T , N are rivulet mass, tangential and normal force.

4. Results

Fig. 3 displays the temporal evolution of rivulet position on cylinder surface and corresponding power spectral density. As can be seen, the rivulet hasn't shifted in downwind location, but it has been moving periodically with frequency 3 Hz at the bottom region of the cylinder. It has been assumed, this periodical movement has been particularly coordinated by gravitational force.

Time course of drag and lift coefficients is shown in Fig. 4, also power spectral density of drag coefficient has been calculated. Periodicity with frequency 3 Hz in drag coefficient has been observed which is in coincidence with periodical movement of rivulet. Consequently, the rivulet occurrence directly influences aerodynamic behavior of cylinder. Therefore, aerodynamic force direction and intensity is changing time-dependently.

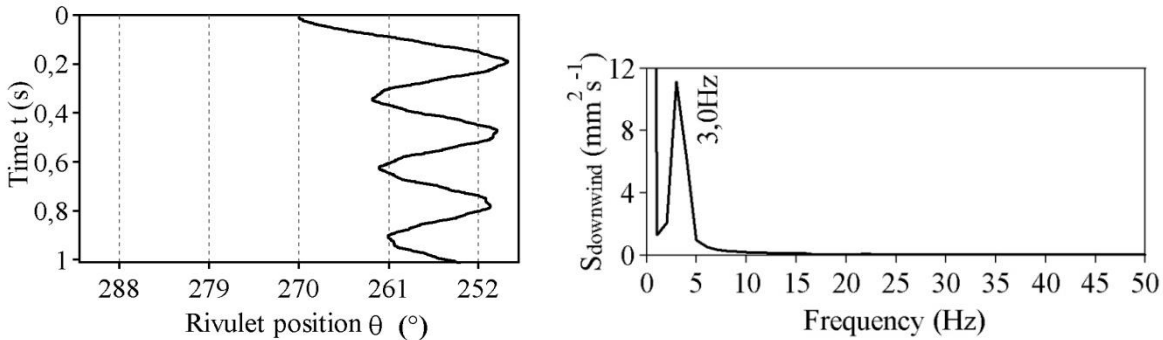


Fig. 3: Rivulet position in time domain (left) and power spectral density (right).

When comparing the values of drag coefficients when rivulet occurred and without rivulet (Tab. 1), significantly increased value has been observed, despite of very small rivulet dimensions. Rivulet occurrence hasn't changed the vortex shedding frequency significantly.

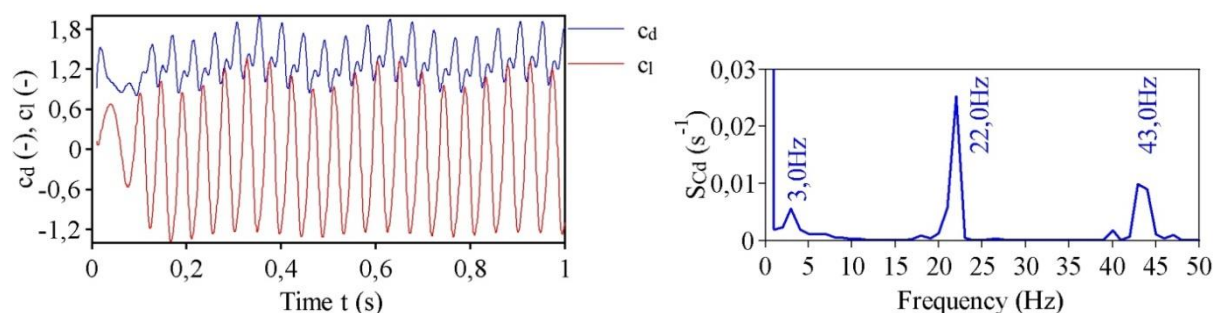


Fig. 4: Drag and lift coefficients (left) and drag coefficient power spectral density (right).

5. Conclusions

Numerical simulation based on coupled model of airflow-rivulet interaction, using commercial software Adina 8.7, has been created. Simulations without and with water rivulet occurrence on circular cylinder surface has been investigated. As the horizontally mounted cylinder has been considered, the gravitational force has been included. It has been assumed, the gravitational force has the influence on periodical rivulet movement. Periodicity of the occurred movement has been 1/7 of vortex shedding frequency. As the frequency of aerodynamic forces on cylinder with formatted rivulet are smaller than vortex shedding frequency and if this phenomenon occurred on cables, resonance of galloping could be arisen. If rivulet was formatted an cylinder section of cable which eigenfrequency was nearby the rivulet-motion frequency, resonance may occur. This resonant effect is called galloping.

Acknowledgement

The present work has been carried out within the project “Supporting of the Centre of excellent integrated research of advanced building structures, materials and technologies”, based on the Operational program Research and development, financed by the European Regional Development Fund of the European Union. The paper is carried out within the project No. 1/0321/12, partially founded by the Science Grant Agency of the Ministry of Education of Slovak Republic and the Slovak Academy of Sciences.

References

- Breuer, M. (2000) A challenging test case for large eddy simulation: high Reynolds number circular cylinder flow., *International Journal of Heat and Fluid Flow*, 21, pp. 648-654.
- Cosentino, N., Flamand, O., Ceccoli, C. (2003) Rain-wind induced vibration of inclined stay cables. Part II: mechanical modeling and parameter characterisation., *Wind Struct.*, pp. 485-498.
- Hikami, Y., Shiraishi, N. (1988) Rain-wind induced vibrations of cables in cable stayed bridges., *J. Wind Eng. Ind. Aerodyn.*, 29 (1-3), pp. 409-418.
- Lemaitre, C., de Langre, E., Hémon, P. (2010), Rainwater rivulets running on a stay cable subject to wind., *European Journal of Mechanics B/Fluids*, 29, pp. 251-258.
- Li, S. Y., Gu, M. (2006) Numerical simulations of flow around stay cables with and without fixed artificial rivulets., In: *Proc. 4th Int. Symp. Comp. Wind Eng. (CWE2006)*, Yokohama, Japan, pp. 307-310.
- Matsumoto, M., Yagi, T., Goto, M., Sakai, S. (2003) Rain-wind-induced vibrations of inclined cables at limited high reduced wind velocity region., *J. Wind Eng. Ind. Aerodyn.*, 92, pp. 1-12.
- Peil, U., Nahrath, N. (2003) Modeling of rain-wind induced vibrations., *Wind Struct.*, 6 (1), pp. 41-52.
- Roshko, A. (1961), Experiments on the past a circular cylinder at very high Reynolds number., *Journal of Fluid Mechanics*, 10, pp. 345-356.
- Seidel, C., Dinkler, D. (2006) Rain-wind induced vibrations - phenomenology, mechanical modelling and numerical analysis., *Computer and Structures*, 84, pp. 1584-1595.
- Wieselsberger, C. (1921) Recent findings on the laws of the liquid and air resistance. *Phys. Z.*, 22, pp. 321-328, (in German).
- Yamaguchi, H. (1990) Analytical study on growth mechanism of rain vibration of cables, *J. Wind Eng. Ind. Aerodyn.*, (33), pp. 73-80.
- Zhan, S., Xu, Y. L., Zhou, H. J., Shum, K.M. (2008) Experimental study of wind-rain-induced cable vibration using a new model setup scheme., *J. Wind Eng. Ind. Aerodyn.*, 96, pp. 2438-2451.
- Zuo, D. Jones, N. P., Main, J. A. (2008) Field observation of vortex and rain-wind-induced stay-cable vibrations in a three-dimensional environment. *J. Wind Eng. Ind. Aerodyn.*, 96 (6-7), pp. 1124-1133.

THEORETICAL AND NUMERICAL SOLUTION OF A NEAR SONIC FLOW CONSIDERING THE OFF-DESIGN CONDITIONS

J. Stodulka^{*}, H. Sobieczky^{**}

Abstract: *The work deals with comparison of analytical design methods for transonic flows with modern computational fluid dynamics codes. The theory based on potential flow transformed into modified hodograph plane and simplified by near sonic flow conditions gives an exact solution of a cusped airfoil pointed into the sonic free stream. Results obtained from corresponding commercial ANSYS Fluent inviscid CFD code are compared with this theory on such profile. Because of considerable sensitivity of transonic flows, some off-design conditions in means of different free stream velocities are mentioned and analyzed to see the influence of small changes in boundary conditions on developed flow field.*

Keywords: Transonic flow, Hodograph, Airfoil, CFD, Simulation, Off-design conditions.

1. Introduction

Mathematical solution of transonic flows brings together classical hydraulic methods together with the wave propagation solutions to resolve the co-existence of both elliptic and hyperbolic differential equations. The subsonic field can be solved with methods related to conformal mapping and supersonic field then using method of characteristics. This theory allows us to design airfoil shapes with predicted flow behavior around them which can be easily compared with numerical simulations. Modern CFD codes can be used as an extension to this theory and provide fast response to theoretical results or confirm the influence of possible off-design conditions.

2. Theoretical Model

The mathematical model stands on the basis of potential flow. To avoid the non-linearity of basic system of equations we can transform the solution to modified hodograph plane replacing physical coordinates x, y with new, flow angle ϑ and Prandtl-Mayer angle ν . The fact that we are assuming only the near sonic flow, that means flow with only small perturbations to sonic flow, simplifies the equations enough to solve exactly the conformal subsonic zone and also characteristic supersonic zone.

This solution, deeply described in Stodulka and Sobieczky (2014), can lead us to design of cusped airfoil pointed into the sonic free stream, see Fig. 1. This airfoil with sharp leading and trailing edge cuts the incoming flow which is then accelerated smoothly from sub to supersonic velocities past the airfoil forming oblique shocks at the trailing edge. Its shape is defined by thickness parameter τ and camber parameter ω .

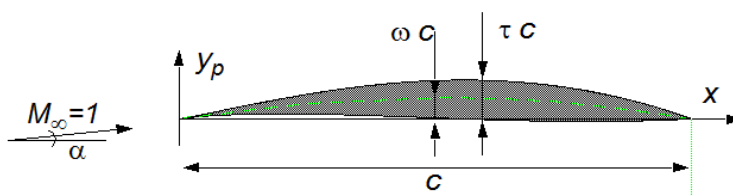


Fig. 1: Cusped airfoil parameters.

^{*} Ing. Jiří Stodulka: Department of Fluid Mechanics and Thermodynamics; Czech Technical University in Prague; Technická 4; 166 07, Prague; CZ, jiri.stodulka@fs.cvut.cz

^{**} Hon Prof. Helmut Sobieczky, DrTechn.: Institute of technology; Technical University Vienna; Resselgasse 3; 1040, Vienna; Austria, helmut@sobieczky.at

Finding analytical solutions to above hodograph relations allows us to derive the formulae defining the shape, flow conditions and pressure coefficient for cusped airfoils in a uniform sonic flow $M_\infty = 1$ (Sobieczky, 1975). The camber/thickness parameter is given by:

$$P\left(\frac{\omega}{\tau}\right) = 2^{13/2} \cdot 3^{3/2} \cdot 5^{-7/2} \cdot \frac{\omega}{\tau} \left[1 + 2^{12} \cdot 3 \cdot 5^{-6} \left(\frac{\omega}{\tau}\right)^2 \right]^{-1/2} \quad (1)$$

and using this parameter we can describe the angle of attack:

$$\alpha = \tau \cdot 2^{-9/2} \cdot 3^{-1/2} \cdot 5^{5/2} \cdot P \frac{1 - 2^{-1} \cdot 3^{-4} \cdot 5 \cdot 13 P^2}{(1 - 2^{-1} \cdot 3^{-2} \cdot 5 P^2)^{3/2}} \quad (2)$$

geometry data:

$$y_p(X) = \tau \cdot X(1-X) \left(2^2 \cdot \frac{\omega}{\tau} \pm 2^{-2} \cdot 3^{-3/2} \cdot 5^{5/2} \cdot X^{1/2} \right) \quad (3)$$

and finally the pressure coefficient:

$$c_p = \frac{(5^2 \cdot \tau)^{2/3}}{\left[2^2 \cdot 3 \cdot (\gamma + 1) \right]^{1/3}} \left[\frac{(1 - 2^{-2} \cdot 3^{-2} \cdot 5 P^2)}{(1 - 2^{-1} \cdot 3^{-2} \cdot 5 P^2)} - 2^{-1} \cdot 5 X \mp \frac{2^{-1/2} \cdot 3^{-1} \cdot 5 P \cdot X^{1/2}}{(1 - 2^{-1} \cdot 3^{-2} \cdot 5 P^2)^{1/2}} \right] \quad (4)$$

where γ is the specific heat capacity ratio.

Knowing these, we have a complete analytical solution of this problem of specified sharp cusped airfoil pointed into the sonic free stream.

3. Numerical Model

For numerical simulation a thin, lightly cambered airfoil was chosen with parameters $\tau = 0.05$ and $\omega/\tau = 0.02$. The simulation was performed using inviscid ANSYS Fluent CFD model on quad mapped mesh with approx. 100000 elements with implemented AUSM numerical flux scheme with second order upwind. The only boundary condition was set as a pressure far field (ANSYS Inc. 2013).

Results in form of Mach number contours are shown on Fig. 2. It shows clearly shock free transonic character of the flow past airfoil ended by oblique shocks. The whole flow behavior corresponds also perfectly with the predicted flow field form theoretical analysis.

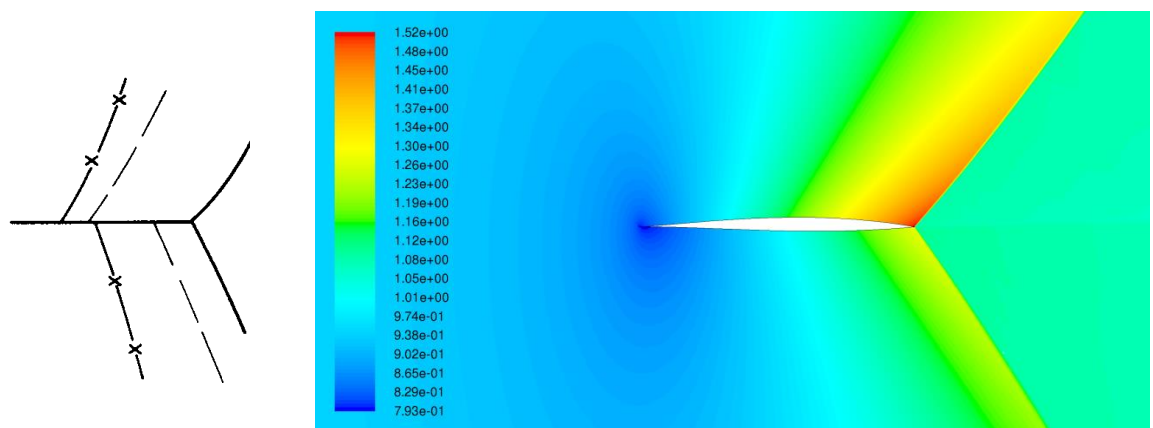


Fig. 2: Contours of Mach number.

Pressure coefficient distribution along the profile surface is compared on Fig. 3, with solid line representing numerical results and dashed the theoretical. Both lines are corresponding well in displayed range, but for thicker and more cambered airfoils reached Mach numbers rise and deviations start to appear in these regions, what is probably caused by deviation from near sonic flow theory assumptions. More about the numerical simulations can be found also in Stodulka and Sobieczky (2014).

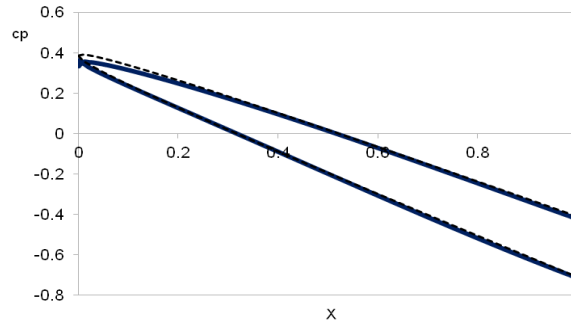


Fig. 3: Pressure coefficient distribution.

4. Off-Design Conditions

Previous chapter confirmed well the correspondence between theoretical and numerical results and ability of the CFD code to describe expected flow field. But such sensitive boundary condition as a sonic free stream holds this case strictly in an academic field. To get closer to real problems it is easy to imagine some off-design modifications with incoming speed oscillating around sonic value. For upcoming simulations was used the symmetrical cusp with thickness parameter $\tau = 0.05$. The numeric setup remained same as in previous models and the only difference was in domain dimensions and computational mesh. Due to larger domain and size savings was used the unstructured adapted tri mesh.

If we will assume only small perturbations to sonic flow we can expect a creation of detached bow wave in front of the airfoil for slightly supersonic velocities. The location of the wave depends on free stream Mach number, the higher the velocity is, the closer is the distance between the leading edge and shock until it attaches. Behind the bow wave is the flow field similar to the sonic case with smooth acceleration and oblique shocks. Expected result and simulation is shown on Fig. 4.

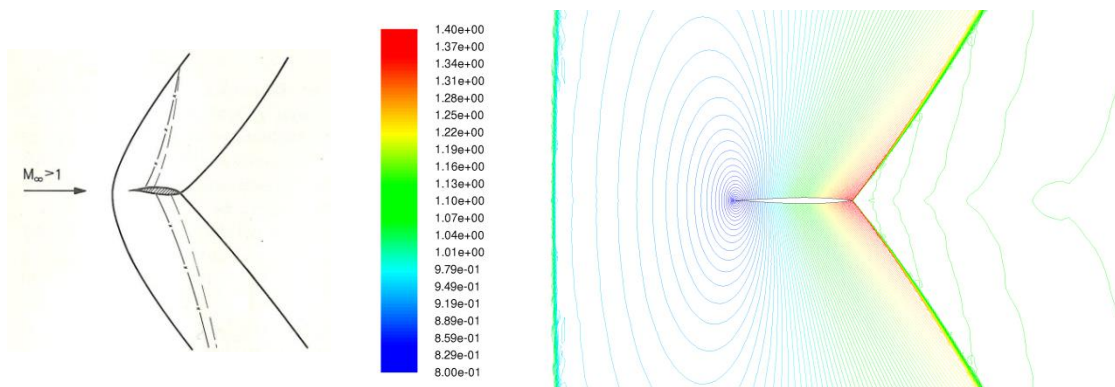


Fig. 4: Cusped airfoil in supersonic free stream, $M_\infty = 1.05$.

There are also some results explaining shape, strength and location of detached shock depending on the free stream Mach number (Sobieczky, 1974). Dependence of wave location and free stream velocity is shown on Fig. 5. Solid points are simulation data, crosses are data from DLR- τ code (Trenker and Sobieczky, 2001) and dashed line is theoretically exact asymptote.

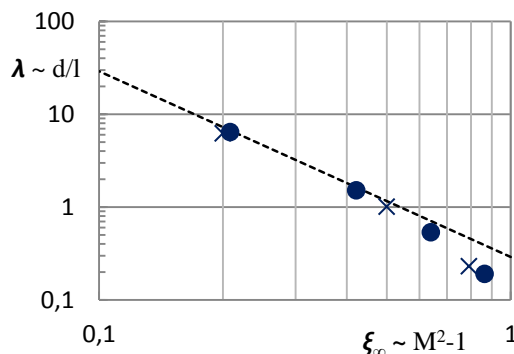


Fig. 5: Bow wave location for different Mach numbers.

The opposite problem appears when the free stream velocity will be subsonic. This case leads to creation of so called fish tail wave formed behind the cusp separating the local supersonic domain from the rest of the flow field. This configuration is showed on Fig. 6.

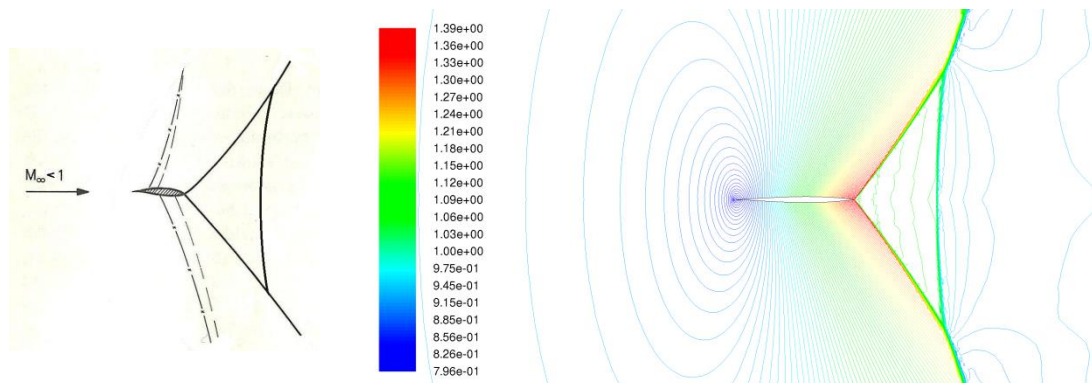


Fig. 6: Cusped airfoil in subsonic free stream, $M_\infty = 0.95$.

These two cases extend the problematic of developed sonic flow past sharp profile and describe the sensitivity of transonic problems as a whole. It is clear that the results from CFD code correspond well with expected flow field for both off-design cases and even here proved itself as fast and reliable tool for design and verification.

5. Conclusions

The near sonic flow theory using conformal together with characteristic mapping for both velocity regions gives a precise modified hodograph solution of the whole flow field past cusped airfoil in a sonic free stream. Due to availability of modern computational fluid dynamics codes, the numerical experiment enables to receive data on parameters and flow structures past these airfoils very fast and effectively to be compared with the theory. And obtained results confirmed well the accordance between numerical and exact analytical data by means of described near sonic flow theory. CFD results showed the described problem in a new light and turned out to be a powerful tool for fast verifications or sensitivity analysis giving new objects for theory solutions. Off-design condition setups added a bit more practical view on the problematic and proved that even here we are still able to predict and simulate the flow behavior correctly. Especially for cases described above is the numerical simulation the only way how to compare and discuss obtained results and theories. Posted results also confirmed significant sensitivity of transonic flows, especially when talking about sonic and near sonic problems. At the end it is necessary to say that more than any concrete practical value this work is aimed to show the possibility of using the already developed theories for creating first systematic designs that can be initial cases for optimized shapes for real prototypes and these cases in transonic regime are now easily comparable with results obtained from modern CFD codes.

Acknowledgement

This work has been supported by the Grant Agency of Czech Technical University in Prague, grant no. SGS13/180/OHK2/3T/12

References

- Stodulka, J., Sobieczky, H. (2014) On transonic flow models for optimized design and experiment, submitted to European Physical Journal Web of Conferences.
- Sobieczky, H. (1975) Tragende Schnabelprofile in stossfreier Schallanstoerung, ZAMP 26.
- ANSYS Fluent 14.5 Users Guide (2013), ANSYS, Inc.
- Sobieczky, H. (1974) Die abgeloeeste transsonische Kopfwelle, Z. Flugwiss. 22.
- Trenker, M., Sobieczky, H. (2001) Using the gasdynamic knowledge base for aerodynamic design and optimization in the sonic speed, In: Proc. Int. Symp on Inverse problems in Engineering Mechanics, Nagano.

COMBINATION OF FEM AND DEM WITH APPLICATION TO RAILWAY BALLAST-SLEEPER INTERACTION

J. Stránský*

Abstract: *Combination of two numerical methods - continuum based finite element method (FEM) and discrete based discrete element method (DEM) is presented in this contribution. The method is applicable to explicit dynamic problems and specifically will be applied to modeling of interaction between railway ballast (modeled by polyhedral discrete elements) and railway sleeper (modeled with standard finite elements). The problem is addressed from both theoretical and implementation point of view.*

Keywords: DEF, FEM, Surface coupling, Explicit dynamics, Multi-method.

1. Introduction

Numerical simulations are an indispensable part of current engineering and science development. For different engineering areas there are different numerical methods used. In solid phase mechanics, the leading methods are the finite element method (FEM) and the discrete element method (DEM). FEM is rigorously derived from the continuum theory and is being used for the description of deformable continuous bodies, while DEM describes particulate materials, usually modeled by perfectly rigid particles and their interactions determined from fictitious overlaps of these rigid particles.

Often an engineering problem can be modeled using only one of the aforementioned methods. A railway sleeper would be simulated by FEM, an assembly of ballast particles by DEM. One possible approach how to model an interaction between sleeper and ballast would be to split the problem into two domains (the sleeper part modeled by FEM and the ballast part modeled by DEM) and appropriately couple them. This approach is described in this contribution.

There are countless software programs for both FEM and DEM. Some of them are commercial (usually without possibility to change the code and adjust the behavior to our requirements (combination with another software for instance). However, there exist programs with open source code, which the user can modify, possibly for coupling with other programs. In the present article, coupling of FEM code OOFEM (Patzák and Bittnar, 2001) and DEM code YADE (Šmilauer et al., 2010) is presented. Both programs have the core written in C++ (providing efficient execution of time consuming routines), user interface written in Python (modern dynamic object oriented scripting language, providing easy to use scripting while preserving the C++ efficiency) and extensible object oriented architecture allowing independent implementation of new features - new material model or new particle shapes for instance.

Theoretical aspects of the combination are described in section 2 and the implementation in section 3.

2. Theory

2.1. Discrete element method

In the discrete element method, the particles are represented as a set of perfectly rigid particles. In this contribution, the particles have a shape of convex polyhedrons (Eliáš, 2013). The convex polyhedrons are defined as an intersection of several half-spaces. Each half-space is defined by oriented plane, see Fig. 1.

* Ing. Jan Stránský: Faculty of Civil Engineering, Czech Technical University in Prague, Thákurova 7/2077; 166 29, Prague; CZ, jan.stransky@fsv.cvut.cz

DEM solves numerically equations of motion, which are according to the perfect rigidity assumption idealized as a mass point with 6 degrees of freedom (3 displacements and 3 rotations). Forces and moments in equations of motion can be prescribed (gravity for instance) or are computed according to constitutive laws from mutual displacements and rotations of individual particles. In the current work, the normal force between two particles is directly proportional to the volume of intersection of two particles or is zero if there is no intersection. The point of action is placed to the center of mass of intersecting polyhedron and its direction is determined as a normal to the plane approximating in the sense of least squares "visible" edges of the intersection (edges of the intersection belonging to both intersecting particles). Also the shear force is incrementally computed from mutual displacement and rotation of both particles. The algorithm is described by Eliáš (2013) in detail and illustrated in Fig. 1.

Analogical algorithm may be applied to the case, when one of the particles is a planar triangle. For interaction evaluation, the triangle is "extruded" to form a wedge, represented as a polyhedron, and the algorithm described above is applied. After the contact force acting on the triangular particle is known (its direction, magnitude and point of action), it can be approximated with the help of FEM-like linear approximation to triangle vertices. This concept is used in the next section.

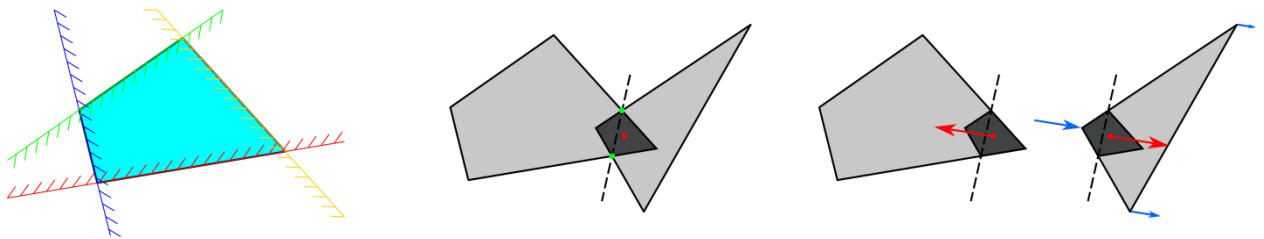


Fig. 1: 2D illustration: polyhedron as an intersection of half-spaces (left), intersection of two polyhedrons (middle) and contact force (right) applied to the centroid of intersection (red) and its interpolation to vertices (blue).

2.2. Combination with finite element method

The method according to Stránský (2013) for combination of DEM and FEM is used. As was already mentioned, each domain of the problem is solved separately. Ballast particles are solved by polyhedral DEM, while the sleeper is solved by FEM with linear tetrahedrons. The problem is solved as explicit dynamics.

Firstly, the surface of tetrahedral FEM mesh is extracted, forming a set of triangles. These triangles are then copied into DEM solution. In this work they are called "FEM particles".

In each time step of the problem, DEM domain is solved at first. In this stage, the FEM particles are not allowed to move playing a role of fixed boundary. The results of DEM part of the solution are new positions of polyhedral particles and also forces applied to triangular FEM particles. These forces are approximated to triangle vertices (corresponding to nodes of FEM mesh) and the resulting vertex force is computed as a sum of contribution of all triangles sharing the vertex.

These vertex forces are then passed to the FEM domain as external load (nodal forces). New time step of the FEM domain is solved according to these forces, resulting in new nodal positions. Values of new nodal positions are passed back to DEM domain. The position and shape of FEM particles are updated according to this information.

Then a new time step is solved following the same algorithm.

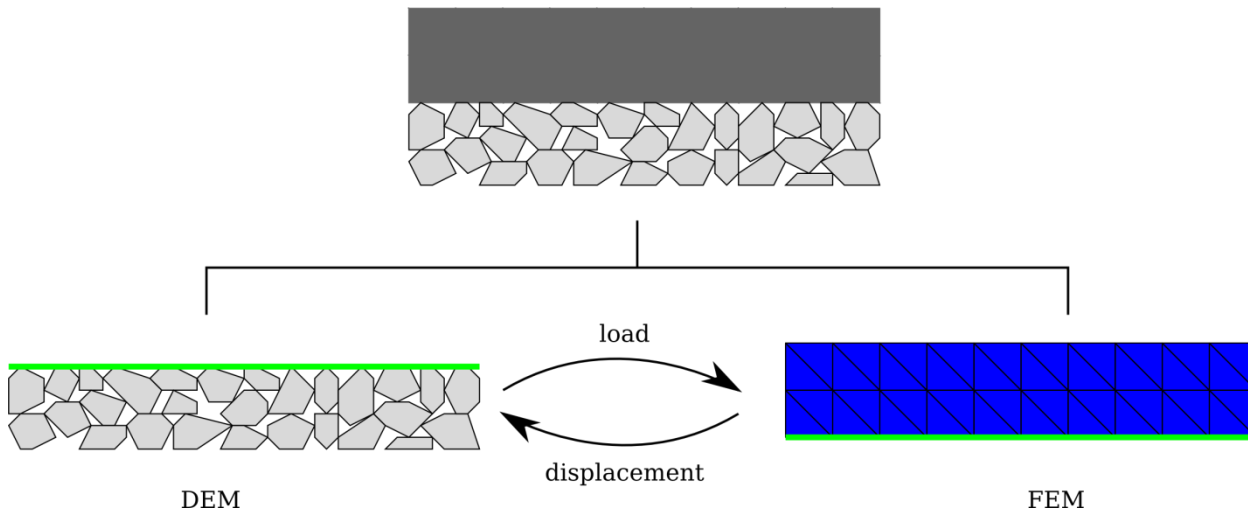


Fig. 2: Illustration of DEM and FEM combination.

3. Implementation

The implementation of polyhedral particles in YADE software, including contact detection, contact forces evaluation etc., is described in Eliáš (2013). The described implementation also involves polyhedron-triangle interactions, therefore no new implementation is needed.

Both chosen programs OOFEM and YADE work based on input files (YADE uses Python controlling scripts and OOFEM has its own format of text input files). For each domain, the input file is created at first, containing information about geometry, discretization, boundary and initial conditions, materials etc. OOFEM input file contains information only about finite element mesh, YADE input file only about polyhedral particles.

Both programs use Python scripting language as a user interface. Firstly, from one master controlling Python script both FEM and DEM domains are initialized according to prearranged input files. To the DEM domain (containing only polyhedrons so far), the FEM particles (extracted as a boundary of FEM domain) are copied as triangular particles.

From the master script it is possible to access and dynamically modify variables in both programs.

The master script in the beginning:

- initializes OOFEM, which reads its input file;
- initializes YADE, which reads its input file;
- gets information from OOFEM about FEM boundary, passes this information to YADE, which creates copies of these triangles.

The master script then follows algorithm described in section 2.2:

- YADE computes one time step;
- DEM contact forces are transferred to nodal forces and are passed to OOFEM;
- OOFEM computes one time step and the displacements are passed to YADE;
- YADE updates positions of FEM particles
- proceeds to the next time step

The implementation and the source code are intended to be open source with the possibility of free download. Also integration into a wider framework, specifically MuPIF (Multi-Physics Integration Framework) by Patzák et al. (2013) would be a natural direction of further development. In such case, also other programs than OOFEM and YADE might be used in the same context.

4. Summary

A method for combination of FEM and DEM applicable for explicit dynamic problems was presented in this contribution.

The application of the method will be modeling of interaction of railway ballast and sleeper interaction.

Despite the effort of the author, the implementation, documentation, code publication and examples have not been fully completed before this paper deadline. However, they will be presented during the conference and on web pages of related projects as soon as they are finished.

A future work on the topic may address more efficient implementation or using the method on other application topics.

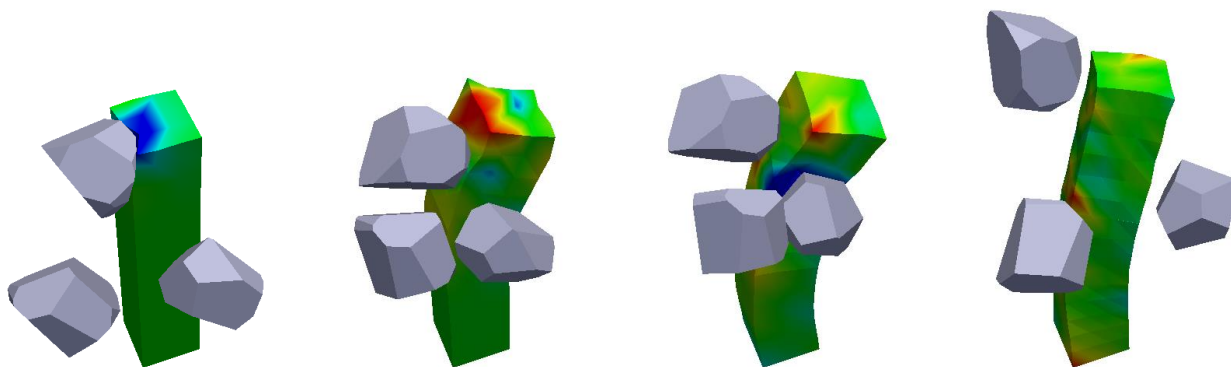


Fig. 3: Example of simple simulation.

Acknowledgement

Financial support of the Czech Technical University in Prague under project SGS no. OHK1-089/14 is gratefully acknowledged.

References

<http://mech.fsv.cvut.cz/mupif>

<http://www.oofem.org>

<http://yade-dem.org>

Eliáš, J. (2013) DEM simulation of railway ballast using polyhedral elemental shape, in: Particle-Based Methods III. Fundamentals and Applications (M. Bischoff et al. eds.), CIMNE, Barcelona, Spain, pp. 247-256.

Patzák, B., Bittnar, Z. (2001) Design of object oriented finite element code. *Advances in Engineering Software*, 32, pp. 759-767.

Patzák, B., Rypl, D., Kruis, J. (2012) MuPIF - A distributed multi-physics integration tool. *Advances in Engineering Software*, 60-61, pp. 89-97.

Stránský, J. (2013) Open source DEM-FEM coupling, In: Particle-Based Methods III. Fundamentals and Applications (M. Bischoff et al. eds.), CIMNE, Barcelona, Spain, pp. 46-57.

Šmilauer, V., Catalano, E., Chareyre, B., Dorofeenko, S., Duriez, J., Gladky, A., Kozicki, J., Modenese, C., Scholtès, L., Sibille, L., Stránský, J., Thoeni, K. (2010) *Yade Documentation* (V. Šmilauer ed.), The Yade Project, 1st ed. <http://yade-dem.org/doc/>.

APPLICATION OF SIMPLIFIED MECHANICAL MODEL FOR DESCRIPTION OF SPECIMEN SIZE EFFECT ON RESISTANCE AGAINST STABLE TEARING

L. Stratil*, F. Šiška**, H. Hadraba***, I. Dlouhý****

Abstract: *This contribution deals with a size effect on J-R curve of three points bend specimens made from Eurofer97 steel and with possibilities to predict the specimen behaviour between various specimen sizes. To do it, a simplified mechanical model proposed by Schindler is applied to obtained tests results in order to predict observed size effect on J-R curve.*

Keywords: Size effect, Three point bend, Scaling laws, Eurofer97, J-R curve.

1. Introduction

The fracture toughness standards specify the size requirements on tested specimens in order to maintain a validity of fracture parameters describing the conditions at the crack tip in relation to measured toughness values (ISO 12135, 2002). These size requirements are in cases of materials with high toughness very demanding concerning the size of tested specimens. Moreover there are certain cases where is available only limited amount of test material and only miniature specimens offer possibilities of direct fracture toughness estimation. In both cases an interpretation of measured values in relation to valid values of fracture parameters or for application to structural components is needed (Dlouhý et al., 2006). The studied material Eurofer97 steel was developed for applications in nuclear industry. The specimen size effect in these applications is very relevant especially when miniature specimens demonstrate significant decreasing of resistance against stable tearing for high toughness alloys (Ono et al., 2006). In following, the Schindler's model (Schindler and Veidt, 1998) is briefly introduced and it is applied to the experimentally determined results to predict specimen size effect on J-R curve of the Eurofer97 steel.

2. Schindler's Model

As shown by the Schindler et al. (Schindler and Veidt, 1998; Schindler and Bertschinger, 2002) the J-R curve (Fig. 1) can be estimated from the continuous force-displacement diagram of a single, uninterrupted, static or dynamic bending test (Fig. 2) by:

$$J(\Delta a) = C \cdot \Delta a^p \text{ for } \Delta a = \Delta a_m, \quad (1)$$

where

$$C = \left(\frac{2}{p}\right)^p \cdot \frac{\eta(a_0)}{B (W - a_0)^{1+p}} \cdot W_t^p \cdot W_{mp}^{1-p}, \quad (2)$$

* Ing. Luděk Stratil: CEITEC IPM, Institute of Physics of Materials, v.v.i., Academy of Sciences of the Czech Republic; Zizkova 22; 616 62, Brno; CZ, stratil@ipm.cz

** Dr. Ing. Filip Šiška, PhD.: CEITEC IPM, Institute of Physics of Materials, v.v.i., Academy of Sciences of the Czech Republic; Zizkova 22; 616 62, Brno; CZ, siska@ipm.cz

*** Ing. Hynek Hadraba, PhD.: CEITEC IPM, Institute of Physics of Materials, v.v.i., Academy of Sciences of the Czech Republic; Zizkova 22; 616 62, Brno; CZ, hadraba@ipm.cz

**** Prof. Ing. Ivo Dlouhý: CEITEC IPM, Institute of Physics of Materials, v.v.i., Academy of Sciences of the Czech Republic; Zizkova 22; 616 62, Brno; CZ, idlouhy@ipm.cz and Institute of Material Science and Engineering, Faculty of Mech. Engineering, Brno University of Technology; Technicka 2; 616 69, Brno; CZ, dlouhy@fme.vutbr.cz

$$p = \left(1 + \frac{W_{mp}}{2W_t} \right)^{-1} \quad (3)$$

B and $b_0 = W - a_0$ are the specimen thickness, and ligament length, respectively. Δa_m is a crack length at maximum force (F_m), Fig. 1. W_{mp} and W_t are dissipated energy at maximum force and the total fracture energy, respectively. These values of energies can be obtained from the load-displacement diagram (Fig. 2). W_{mt} is a remaining part of the total fracture energy consumed for a breaking of specimen. Mutual relation between mentioned characteristic energies is given in (4).

$$W_t = W_{mp} + W_{mt} \quad (4)$$

According to eqs. (1-3) the J-R curve is determined by only two experimental parameters, W_{mp} and W_t , which can be determined from the force-displacement diagram.

The scaling laws for parameters, W_{mp} and W_t , were derived based on the same mechanical models and the same assumptions as used for derivation of eqs. (1-3) (Schindler and Veidt, 1998). In the following, data corresponding to the sub-size specimens or their dimensions are denoted by a prime, i.e. F_m' , W_{mp}' or B' .

The energy at the maximum force was derived as:

$$W_{mp} = \frac{B}{B'} \cdot \frac{\eta'}{\eta} \cdot \left(\frac{b_0'}{b_0} \right)^{1+p} \cdot W_{mp}' \quad (5a)$$

where

$$p = \left(1 + \frac{W_{mp}'}{2W_t'} \right)^{-1} \quad (5b)$$

The total fracture energy is given by Eq. (4). Scaling laws for the first term is given in Eq. (5). The second term was obtained in the form:

$$W_{mt} = \frac{B}{B'} \cdot \frac{\eta'}{\eta} \cdot \left(\frac{b_0'}{b_0} \right)^2 \cdot W_{mt}' \quad (6)$$

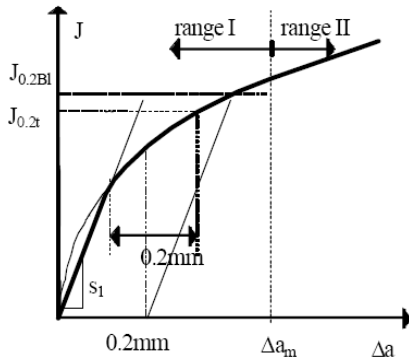


Fig. 1: Schematic description of J-R curve.

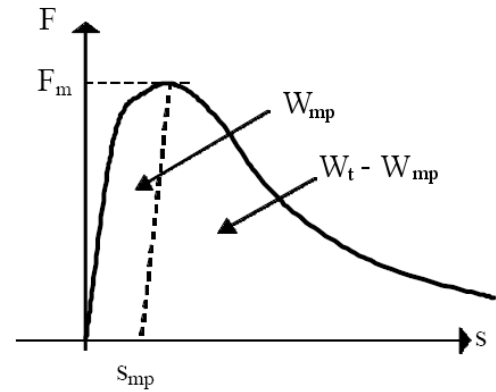


Fig. 2: Load vs. displacement diagram.

3. Description of Realized Experiments

Crack resistance curves were measured to describe specimen size effect in ductile regime of the Eurofer97 steel. The specimens were manufactured from the plate of thickness 25 mm (heat nr. 993393) with crack orientation in transversal direction of the plate. J-R curve were measured on three sizes of pre-cracked three-point-bend specimens (Tab. 1) by multi-specimen technique by test rate 1 mm/min at room temperature. The construction of curves was done in accordance with standard ISO 12135 (ISO 12135, 2002).

The input values to the Schindler's model require description load vs. deflection of specimen loaded up to total fracture. However, results of appropriate experiments have not been available yet. In order to verify the possibilities of prediction of Schindler's model the calibrated damage model of ductile fracture Gurson-Tvergaard-Needleman (Tvergaard and Needleman, 1984) was used to obtain load vs. deflection diagram of selected specimens PKLST and PCC. In previous work this damage model was calibrated for studied steel (Stratil et al., 2013) and the J-R curves of tested specimens were successfully simulated provided an appropriate element size is chosen (Stratil, 2014). Due to good description of J-R curves, see Fig. 3, it is assumed that GTN model provides a reliable simulation of the total fracture of the specimens. The outputs from performed three dimensional simulations of the tests of PKLST and PCC specimens with the element size from Fig. 3 are in Fig. 4 and the obtained key parameters are in Tab. 1.

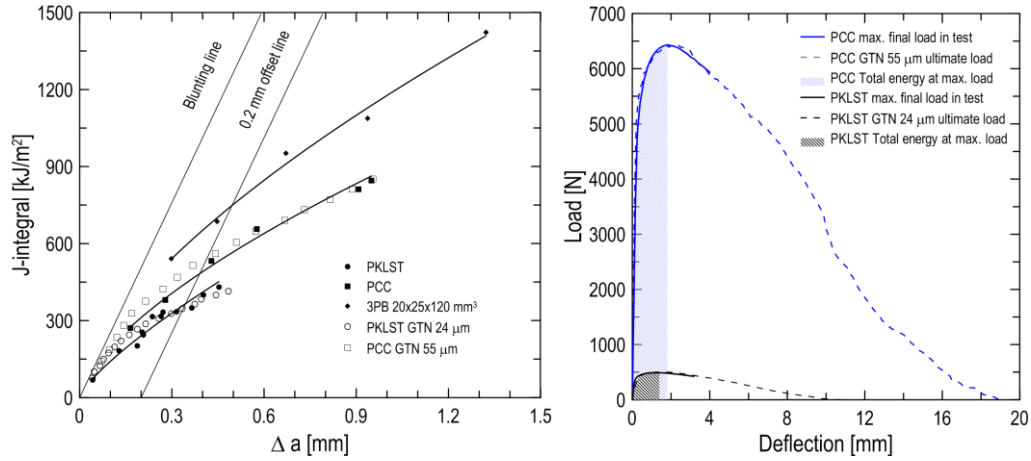


Fig. 3: Experimentally measured J-R curves and results of GTN model simulation (left).

Fig. 4: Load vs. displacement diagram obtained from simulations of PCC and PKLST (right).

Tab. 1: Parameters from simulation of tests by GTN model and specimen characteristics.

Key parameter	PKLST	PCC	Dimensions	PKLST	PCC	3PB 20×25
W_{mp} [J]	0.508	9.506	B [mm]	3	10	20
W_t [J]	2.945	26.726	W [mm]	4	10	25
F_m [kN]	0.502	6.449	b_0 [mm]	2	5	11.9
			S [mm]	24	40	100

4. Application and Discussion of Schindler's Model

The experimental results of J-R curve measurement showed a very strong size effects. Decreasing of specimen size leads to decrease both initiation and propagation values of J-integral. In case of pre-cracked specimens Schindler recommends using a modified definition of power law exponent p for suitable approximation of real shape of J-R curve (Schindler and Veidt, 1998):

$$p = \frac{3}{4} \cdot \left(1 + \frac{W_{mp}}{W_t} \right)^{-1} \quad (7)$$

A optimised procedure for prediction of J-R curve of specimen of different size is hence following. First, the key test parameters of the measured specimen are scaled-up/down to a desirable specimen size and then construction of J-R curve of desirable specimen size is carried out using a modified definition of power law exponent. Predicted J-R curve both from key test parameters of PKLST and PCC specimens are in Fig. 5 and 6. With regard to the simplification of the model, natural scatter of measured data and

the use of input data from simulations of GTN model are predicted curves in close agreement with experimental data.

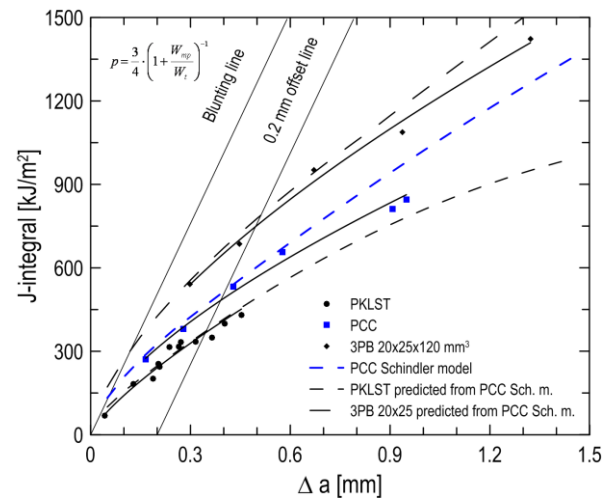
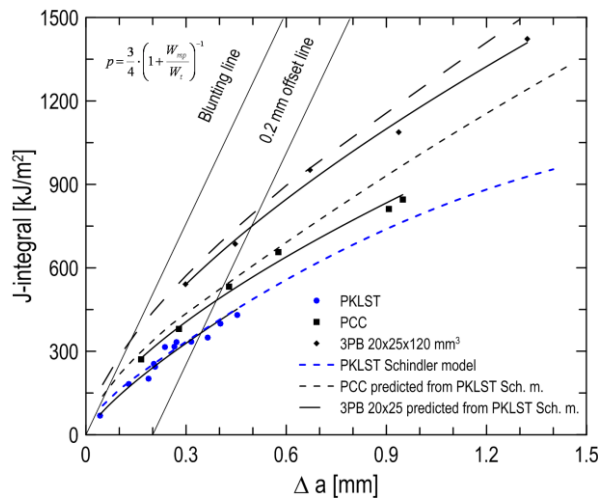


Fig. 5: Experimental J-R curves and their prediction by Schindler's model based on data of PKLST (left).

Fig. 6: Experimental J-R curves and their prediction by Schindler's model based on data of PCC (right).

5. Conclusions

The performance of Schindler's model seems to be very promising for prediction of specimen size effect on J-R curves or potentially for other fracture characteristics. For suitable application of the model to a pre-cracked specimen a modified definition of power law exponent is needed. The results of this study were based on the outputs from FE simulations of total specimens' fracture using calibrated GTN model. It is necessarily to verify obtained findings using real experimental data, what will be done in future.

Acknowledgement

Work on this project has been supported by the Education for Competitiveness Operational Programme, project CZ.1.07./2.3.00/20.0197 Multidisciplinary research team in design of materials and its involvement in international cooperation. The authors also acknowledge support of a project CEITEC – Central European Institute of Technology with research infrastructure supported by the project CZ.1.05/1.1.00/02.0068.

References

- Dlouhy, I., Chlup, Z., Kozák, V. (2006) Constraint effects at brittle fracture initiation in a cast ferritic steel. *Engineering Fracture Mechanics*, 71, 4-6, pp. 873-883.
- ISO 12135:2002(E) – Metallic Materials – Unified Method of Test for the Determination of Quasistatic Fracture Toughness.
- Ono, H., Kasada, R., H., Kimura, A. (2006) Small Specimen Test Technique for Evaluating Fracture Toughness of Blanket Structural Materials. *Journal of Nuclear Materials*, 81, 8-14, pp. 981-986.
- Schindler, H. J., Veidt, M. (1998) Fracture toughness evaluation from instrumented sub-size Charpy-type tests, in: *Small Specimen Test Techniques: ASTM STP 1329*, Philadelphia, PA: ASTM International, pp. 48-62.
- Schindler, H. J., Bertschinger, P. (2002) Relation of fracture energy of sub-sized Charpy specimens to standard Charpy energy and fracture toughness. *Transferability of fracture Mechanical Characteristics*, NATO Science Series, 78, 2002, pp. 213-224.
- Stratil, L., Hadraba, H., Šiška, F., Dlouhý, I. (2013) A calibration of Gurson-Tvergaard-Needleman micromechanical model of ductile fracture, in: *19th Int. Conf. Engineering Mechanics*, Svratka, pp. 560-566.
- Stratil, L. (2014) Determination of fracture mechanical characteristics of small test specimens. *Doctoral Thesis*, Faculty of Mechanical Engineering, Brno University of Technology (in Czech).
- Tvergaard, V., Needleman, A. (1984) Analysis of the cup-cone fracture in a round tensile bar. *Acta Metallurgica*, 32, pp. 157-196.

EXPERIMENTAL EVALUATION OF MR DAMPER TIME RESPONSE ON MODIFIED GROUNDHOOK ALGORITHM EFFICIENCY

Z. Strecker^{*}, J. Roupec^{*}, M. Kubík^{*}, D. Friedel^{*}

Abstract: *Semiactive algorithms have great potential in improving car suspension. One of the damper types with adjustable characteristics, which seems to be suitable for semi-active car suspension, is the magnetorheological damper. Such control algorithms require the ability to switch damping characteristics within one stroke. Time response of car MR dampers is in the range of tens of milliseconds. Although the time response is often ignored in semiactive algorithm simulations, it can influence the suspension efficiency in real systems. The influence of MR damper time response on the modified groundhook algorithm was simulated on quarter-car suspension model and verified on an experimental trolley. Results show that ignoring time response of MR damper during design of the semiactive suspension can reduce overall suspension quality of a real system.*

Keywords: MR damper, Modified groundhook, Response time, Suspension, Semi-active.

1. Introduction

The aim of the car suspension is minimization of sprung mass vibrations (comfort function) and ensuring as stable grip as possible (safety function). Recently, only passive systems have been used in most of the cases. Better suspension quality can be achieved when a fast semi-active suspension system is used. In this case, the damper characteristic is changed several times within one stroke.

Many semiactive control algorithms have been designed in theory. These algorithms can be generally divided into two groups. The First group consists of algorithms improving ride comfort. This group includes the skyhook algorithm which was originally designed by Karnopp et al. (1974) and further optimized by Ahmadian et al. (2005). The Second group consists of algorithms improving wheel grip. The most famous algorithm belonging to this group – groundhook was described by Valášek et al. (1998). Yao et al. (2002), Koo et al. (2004) and Kim et al. (2007) compared suspension quality with MR dampers using semiactive algorithms and showed their considerable potential. Authors, however, ignored time response of the MR damper (time needed for reaching 63% of final steady-state value after a step of the control signal).

Maas et al. (2011) designed a MR clutch with very fast time response. The time response (dependent on ferrite particles to oil ratio in the MR fluid) was measured in the range of 0.76 – 1.26 ms. Goncalves et al. (2006) measured time response of the MR fluid itself. Again, the time response was dependent on ferrite particles to oil ratio and was in the range of 0.45 – 0.6 ms. Although authors Koo et al. (2006) and Yang et al. (2004) measured time responses of usual MR dampers in the range of tens of milliseconds, time response shorter than 1.5 ms can be expected from MR damper if designing methods from fast MR clutch construction are used.

2. Materials and Methods

The impact of time response on semiactive algorithm efficiency was tested on a quarter car suspension model (Fig. 1), where MR damper is used. Its damping characteristics can be changed by the current in the coil.

^{*} Ing. Zbyněk Strecker, PhD., Ing. Jakub Roupec, PhD., Ing. Michal Kubík, Ing. Daniel Friedel: Institute of Machine and Industrial Design, Brno Technical University, Technická 2896/2; 616 69, Brno; CZ, y83216@stud.fme.vutbr.cz, roupec.j@fme.vutbr.cz, y115760@stud.fme.vutbr.cz, y106436@stud.fme.vutbr.cz

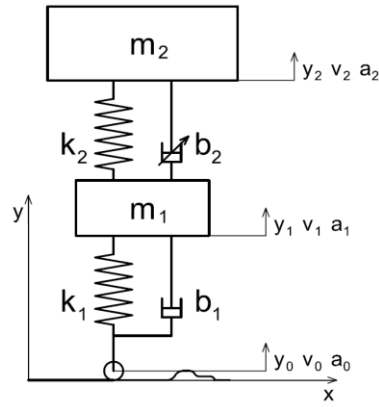


Fig. 1: Quarter suspension model used for simulation.

2.1. Algorithm principle

For evaluation, an algorithm which improves grip was chosen. The groundhook algorithm however needs, as one of the input signals, relative speed of the wheel to the road. This signal is very difficult to obtain in real conditions. Therefore, modified groundhook algorithm was designed. This algorithm needs only unsprung mass acceleration and relative velocity of sprung and unsprung mass signals. The rule for switching the damper to high damping state b_{2h} , respectively low damping state b_{2l} , is according to equation (1):

$$\begin{aligned} a_1 \cdot (v_2 - v_1) \geq 0 &\Rightarrow F_{GHMOD} = b_{2h} \cdot (v_2 - v_1) \\ a_1 \cdot (v_2 - v_1) < 0 &\Rightarrow F_{GHMOD} = b_{2l} \cdot (v_2 - v_1) \end{aligned} \quad (1)$$

2.2. Experiment

The suspension quality was measured on a Pioneer experimental trolley which was riding over a speed bump on a Dynotec road simulator (Fig. 2). Modal parameters of the trolley were tuned to the similar characteristics like rear suspension of Škoda Fabia car. Two options were compared – passive setting of the MR damper and damper controlled with semiactive algorithm modified groundhook. The control range of the MR damper was chosen in order to reach best possible comfort and best possible grip in passive mode. It was possible to change the response time in the range of 8.4 – 22 ms. On the trolley, there was an unsprung mass acceleration sensor, stroke position sensor (needed for algorithm) and sprung mass acceleration sensor (used for suspension quality evaluation). The road simulator was equipped with a sensor measuring force of the wheel on the road (used for suspension quality evaluation) and with a hall sensor for measuring the speed of the road.

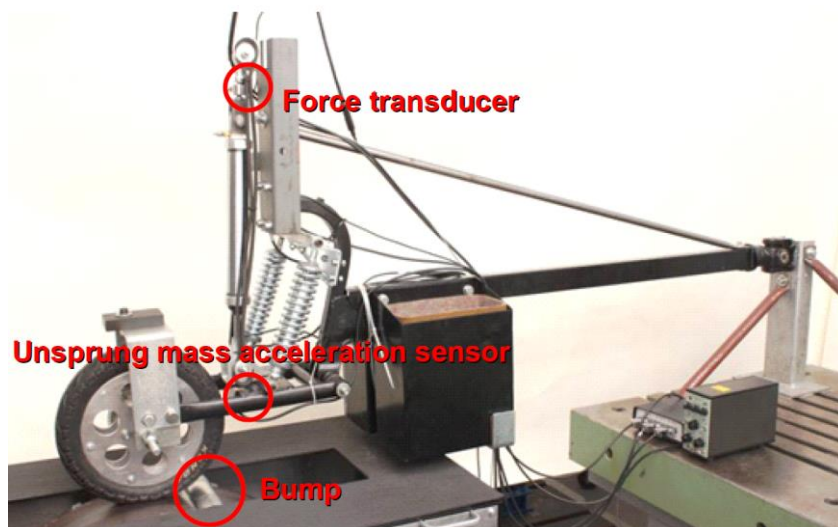


Fig. 2: Experimental trolley on the road simulator.

The suspension quality was evaluated with the help of deviation of the sprung mass acceleration – eq. (2) (the lower value, the better comfort) and deviation of wheel on the road force – eq. (3) (the lower value, the better grip):

$$\sigma(a_2) = \sqrt{\frac{1}{N} \sum_{i=1}^N a_{2i}^2}, \quad (2)$$

$$\sigma_F = \sqrt{\frac{1}{N} \sum_{i=1}^N (F_i - F_{stat})^2} \quad (3)$$

3. Results

In Fig.3 the suspension quality in passive mode is compared to suspension quality using semiactive algorithm modified groundhook. Solid line shows dependency of grip and comfort on electrical current (damping respectively) of the suspension in passive mode. The best comfort was achieved for zero current, but the grip was the worst. With growing current (higher damping) the comfort drops, but the grip grows. When the current is 1.6 A, the best possible grip is reached and further current grow (higher damping) causes decrease of both grip and comfort.

Dash-dot line shows the result of suspension controlled with modified groundhook algorithm with MR damper with usual response time (20 ms), dotted line is for MR damper with 8 ms (shortest possible for used MR damper) and dashed line is for MR damper with very short response time (1.5 ms). When the suspension is in semiactive mode, MR damper can be switched into two states – with high current I_{max} (large damping) and with low (or without) current I_{min} (small damping). In the modified groundhook mode with MR damper response time 1.5 ms, a current smaller than 1.4 A is not expedient, because in comparison with passive mode, both comfort and grip are worse. When the damper is switched between states with 0 A and 2.5 A, much higher grip can be achieved in comparison with any setting in passive mode. This applies, however, only for suspension with MR damper with short response time. When the response time is 20 ms, comfort is slightly improved, but it is impossible to reach higher grip in comparison with passive mode even when the largest possible range of the damper is used.

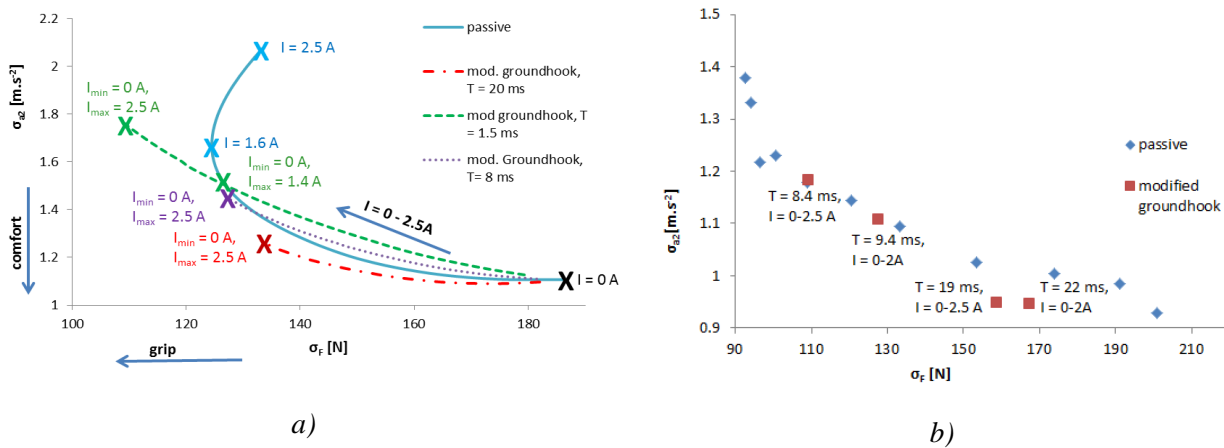


Fig. 3: Comparison of suspension quality in passive and semi-active mode: a) Simulation; b) Experiment.

In Fig. 3b there are experimental results with suspension in passive and “slow” semiactive mode. Measurements show that when the response time of the MR damper was between 19 - 22 ms, comfort was slightly improved. When the MR damper response time was reduced to 8.4 - 9.4 ms, no improvement compared to passive mode was achieved (in accordance with simulation). It can be assumed that suspension quality of a real system can be improved by using modified groundhook algorithm only in case when the response time of the damper is < 1.5 ms.

The explanation is in Fig. 4. When the response time of the damper is 20 ms, the violet line shows the force growth, respectively drop, after switching the electrical current on and off.

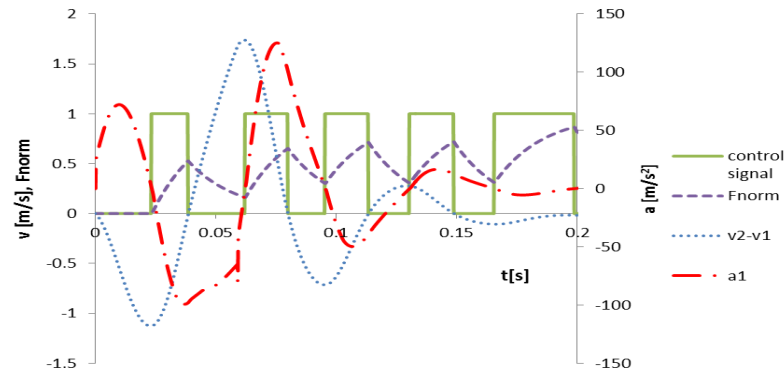


Fig. 4: Time course of generated force of MR damper with 20 ms time response.

4. Conclusions

New semiactive algorithm - modified groundhook was designed. This algorithm can in comparison with passive suspension improve grip, but it does not need the signal with relative speed between the wheel and road like conventional groundhook. Simulations show that if the response time of the MR damper is long, the quality of suspension controlled with modified groundhook algorithm can not bring improvement to passive mode. The results from simulations were confirmed by measurements with MR damper with time response 8 ms and 20 ms. Significant improvement of the grip is expected in case when the MR damper with time response < 1.5 ms is used in semiactive suspension. These conclusions are however based only on the results from simulations. Experimental verification was not conducted, while a MR damper with such short response time is not available. Considering existence of MR devices with time < 1.5 ms, possibility of development of MR damper with short response time is high. At the same time it is necessary to change significantly the conventional construction of MR dampers.

Acknowledgements

This work is an output of cooperation between GAČR13-31834P, FSI-S-14-2329 and NETME Centre, regional R&D centre built with the financial support from the Operational Programme Research and Development for Innovations within the project NETME Centre (New Technologies for Mechanical Engineering), Reg. No. CZ.1.05/2.1.00/01.0002 and, in the follow-up sustainability stage, supported through NETME CENTRE PLUS (LO1202) by financial means from the Ministry of Education, Youth and Sports under the "National Sustainability Programme I".

References

- Ahmadian, M., Goncalves, F. D., Sandu, C. (2005) An experimental analysis of suitability of various semiactive control methods for magneto-rheological vehicle suspensions. In *Smart Struct. and Mat.* pp. 208-216.
- Goncalves, F. D., Ahmadian, M., Carlson, J. (2006) Investigating the magnetorheological effect at high flow velocities. *SMAS*, 15, 1, pp. 75.
- Karnopp, D., Crosby, M. J., Harwood, R. A. (1974) Vibration control using semi-active force generators. *ASME Journal of Engineering for Industry*, 96, 2, pp. 619-626.
- Kim, R. K., Hong, K. S. (2007) Skyhook control using a full-vehicle model and four relative displacement sensors. In: *Control, Automation and Systems, 2007. ICCAS'07. International Conference on.* IEEE, pp. 268-272.
- Koo, J. H., Ahmadian, M., Setareh, M. (2003) Experimental evaluation of magnetorheological dampers for semi-active tuned vibration absorbers. In *Smart Struct. and Mat. Int. Soc. for Optics and Photonics*, pp. 83-91.
- Koo, J. H., Goncalves, F. D., Ahmadian, M. (2006) A comprehensive analysis of the response time of mr dampers. *Smart materials and structures*, 15, 2, pp. 351.
- Maas, J., Guth, D. (2011) Experimental investigation of the transient behavior of mr fluids. *ASME*.
- Valášek, M., Kortům, W., Šika, Z., Magdolen, L., Vaculín, O. (1998) Development of semi-active road-friendly truck suspensions. *Control Engineering Practice*, 6, 6, pp. 735-744.
- Yang, G., Spencer Jr, B. F., Jung, H. J., Carlson, J. D. (2004) Dynamic modeling of large-scale magnetorheological damper systems for civil engineering applications. *Jour. of Eng. Mech.*, 130, 9, pp. 1107-1114.
- Yao, G., Yap, F., Chen, G., Li, W., Yeo, S. (2002) Mr damper and its application for semi-active control of vehicle suspension system. *Mechatronics*, 12, 7, pp. 963 - 973.

AN APPLICATION OF ULTRASOUNDS TO ASSESSMENT OF HARMFUL SALTS ACCUMULATION IN THE BODY OF TRADITIONAL CERAMICS

T. Stryszewska^{*}, S. Kańka^{**}

Abstract: *The long-term utilisation of the ceramic bricks in different conditions, particularly in the presence of moisture, induces the progressive changes, which over time can initiate a gradual loss of performance. This process is related to, inter alia, the collection in the texture of ceramic bricks the salts, derived from the external environment, which may crystallize in the pores of the material. Furthermore, they can form corrosion products in the reaction with the components of the shard. The presence of both enables the loss of performance of the material. Therefore, the studies were undertaken aimed at determining the ability of the various salts to accumulate in the shard of an ordinary ceramic bricks. The accumulation was evaluated on the basis of the mass change and measurements of the ultrasonic pulse velocity.*

Keywords: Ceramic brick, Accumulation of salts, Ultrasound.

1. Introduction

As a result of capillary of water, a porous texture of the ceramic brick is subjected to full saturation. This process often occurs in the walls of old buildings. Along the water, salts dissolved in it penetrate into the material (Hall and Hoff, 2009). Many of them, including salts of sulphate and chloride are not neutral to the sustainability of the brick body. The presence of salts in the ceramic brick changes its physical and mechanical properties. The porous texture promotes accumulation of corrosion products, and the crystallized salts with time of operation (Stryszewska and Wodnicka, 2013). Obviously, the intensity and speed of this process depends on the type and aggressiveness of the external environment and the output characteristics of the ceramic body (phase composition and pore structure).

The article presents the results of laboratory tests, which concerned the ability of accumulation of chloride and sulphate salts in the body of an ordinary brick. This process was monitored by measuring the mass change of tested samples and the determination of changes in the ultrasonic pulse velocity in the ceramic body, in which the porous texture gradually increases the amount of crystallized salts (Runkiewicz and Rodzik, 1990; Lewińska-Romicka, 2001; Hager, 2011).

2. Tested Materials

To the study, ceramic samples, cut out of a brick sized 235 x 115 x 70 mm, were selected. The tested ceramic material was characterized by the following properties (Kańka & Stryszewska, 2013):

- compressive strength	69.5 [MPa],
- actual density	2.68 [g/cm ³],
- bulk density	1.83 [g/cm ³],
- total porosity	31.6 [%],
- open porosity	26.2 [%],
- closed porosity	5.4 [%],
- mass absorption	14.3 [%].

* Teresa Stryszewska, PhD ing.: Institute of Building Materials and Structures, Cracow University of Technology, Warszawska Street 24; 31-155 Cracow; Poland, tstryszewska@pk.edu.pl

** Stanisław Kańka PhD ing.: Institute of Building Materials and Structures, Cracow University of Technology, Warszawska Street 24; 31-155 Cracow; Poland, skanka@pk.edu.pl

The mass variation and measurements of ultrasonic pulse velocity in the material were performed on cylindrical samples with a diameter of 75 mm and a height of 70 mm (thickness of the brick).

3. Research Methods

From a batch of manufactured products, undamaged bricks were chosen, from which adequate, cylindrical samples were cutout. After drying to a constant mass, the prepared samples were exposed to corrosion in solutions:

- magnesium sulphate, wherein the concentration of SO_4^{2-} ions was 50 g/dm^3 ,
- sodium chloride, a concentration of Cl^- was 50 g/dm^3 ,
- magnesium sulphate and sodium chloride, wherein the concentration of SO_4^{2-} ions was 25 g/dm^3 and Cl^- ions concentration reached 25 g/dm^3 .

The corrosive exposure was carried out periodically. For two days, the tested pieces were immersed in corrosive solutions to $\frac{1}{2}$ of the amount of the sample. At this time, as a result of the capillary action, the samples underwent saturation throughout their whole height. Then, the samples saturated with the corrosive solutions, were dried for two consecutive days at a temperature of 115°C . The article presents the results of a study involving 36 cycles of corrosive exposure performed on 5 samples in each environment.

As diagnostic features for determining the ability of accumulation of particular salts and corrosion products, formed in the ceramic body. The mass of corroded elements and the change of ultrasonic pulse velocity, measured a height of the cylinder, were tested. This method is based on the physical relationship between propagation of ultrasonic pulse velocity in the material and this material properties. In this case, the relationship between the ultrasonic pulse velocity and the density of material, that is a ceramic body. Tests were performed with a defectoscope Pundit Plus equipped with cylindrical probes with a frequency of 54 kHz. During the measurement, the probes (emitter and receiver) were placed opposite each other. To ensure the proper transmission of ultrasonic waves between the heads and the audited samples a coupling agent in was used.

The aim of the study was to determine the characteristic of changes in ultrasonic pulse velocity through the ceramic material, as a result of successive variations in the texture, during the cyclic exposure to corrosion. The particles of the medium begin to vibrate and transmit the part of their energy to the neighboring ones. Transferring of this energy is the essence of elastic wave motion and the speed of the transfer is the essence of the measurement. The potential impact of the geometry of the tested piece on the speed of propagation of the wave was eliminated by testing samples of the same shape.

4. Results and Analysis

Measurements of the mass and velocity of propagation of the ultrasonic pulse were performed after each full cycle that is after two days of saturation and two days of drying at 115°C . The obtained results are the average values of 5 samples and they are shown in Figs. 1-3.

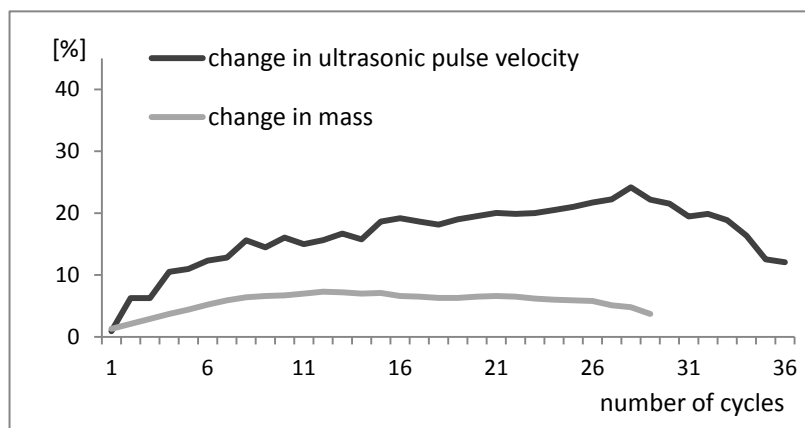


Fig. 1: Changes in mass and ultrasonic pulse velocity of body of the ceramic brick exposed to the of MgSO_4 environment.

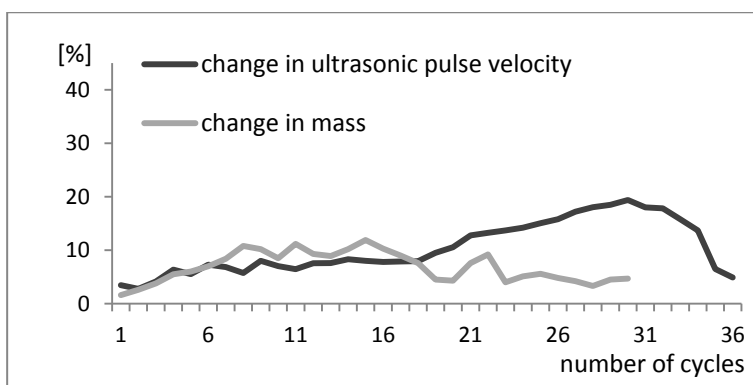


Fig. 2: Changes in mass and ultrasonic pulse velocity of body of the ceramic brick exposed to the of NaCl environment.

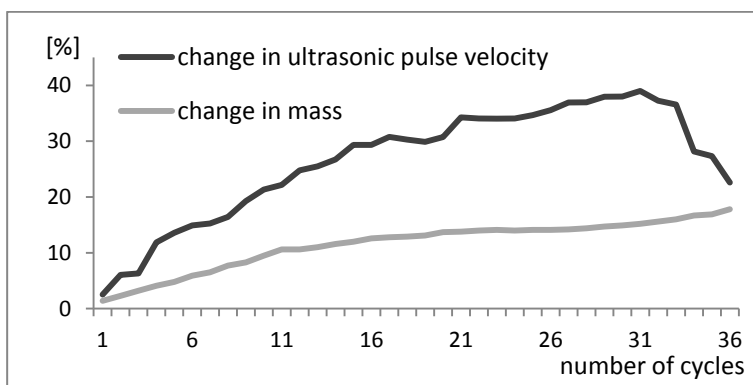


Fig. 3: Changes in mass and ultrasonic pulse velocity of body of the ceramic brick exposed to the of MgSO4 + NaCl environment.

In the initial period of corrosive exposure in all environments, obtained results reflect directly the weight of the salt, which crystallized in the material. However, in the long term, mass result was the outcome of two processes, the weight increase associated with the salts crystallization and the loss, as a effect of destruction of the tested piece. The corossive exposure has caused exfoliation, delamination of materials and formation of cracks.

In contrast, ultrasonic pulse velocity has proved the caulking process of the ceramic body, with increasing number of cycles, regardless of the corrosive environment. Despite of the weight decrease of the tested pieces, as a result of flaking or crumbling of the material, the body was undergoing of continuous sealing which was reflected in the recorded increase in ultrasonic pulse velocity. After obtaining the maximum of wave flow velocity, sharp decline was noticed, associated with waves attenuation on the verge of continous medium that was caulked by salts crystallized of the ceramic body, and medium devoided of discontinuity i.e. air-filled crack.

In the environment of magnesium sulphate, the mass measuring change of the samples and measuring of wave velocity, in the initial period of the exposure, i.e. up to the 10th cycle, points to the sealing of the brick body. The continued exposure was connected with a decrease in mass while an increase in the ultrasonic pulse velocity was still observed. The mass loss was due to mechanism of intensive degradation of the upper and outer layers of the tested pieces. On the other hand, the core of samples has been undergone a constant caulking. The maximal increase of the velocity was recorded after 28 cycles and reached 25%.

Characteristics of changes in mass and the velocity of the wave flow for samples exposed in a solution containing only the chloride ions indicates the intensive weight gain during the initial study period, i.e. up to the 10th of cycle. Maximum weight gain of samples reached 12%. The further process of exposure caused a rapid destruction of the material being tested. The characteristic of changes in the mass of samples after the 11th cycle, illustrates the intense process of crushing and flaking of the material, accompanied by a process of accumulation of sodium chloride. In the next cycles of corrosion, the appearance of cracks and subsequent growth of those that had appeared previously, were observed. In this environment, the best results correlation of mass changes and changes in the wave velocity, was detected

around the 17th cycle. The sudden increases of weight and velocity changes during this period of the exposure resulted from the intense process of peeling of the surface layers and the formation of small cracks in the deeper layers of the material. This resulted in a loss of continuity of the material at an early stage of the exposure. The maximum pulse velocity reached 20%, and was already registered after the 27th cycle. The further exposure was accompanied by the formation of distinct cleavage planes, the presence of which resulted in a sharp decline in ultrasonic wave velocity and the destruction of corroded elements.

In the environment containing both the chloride and sulphate ions, tested samples of the material in the entire study period were characterized by mass increase. Maximum mass gain reached nearly 20%. The measuring of the wave velocity was carried out simultaneously and it indicated that the sample of material corroded in this environment underwent the greatest caulking. Maximal increase of the pulse velocity was recorded after 30 cycles and reached the level of 40%. After this time, there was a decrease associated with the appearance of cracks in the material. In the final step of the exposure, the cracks appeared accompanied by decrease in the wave velocity. However, the material did not crumble and peel. Thus, both the mass gain and changes in velocity reflected the ability of salts accumulation in the material texture.

5. Conclusions

On the basis of the study it was concluded that:

1. The ability to accumulate the salt in the body, as measured by mass change and the change of an ultrasonic pulse velocity, is clearly dependent on the type of salt.
2. No clear correlation between the results of mass measurement and measure of ultrasonic pulse velocity propagation, in relation to the number of cycles, after which maximum changes of the measured values was noted, is associated with a different mechanism of destruction of the corroded materials. In the case of destruction, which begins at the surface and progresses into the material, initially mass loss is primarily observed. In contrast, no effect on the change in the ultrasonic pulse velocity is noticed. Opposite to the issue, when the destruction depends on the formation of cracks in the entire volume of the material. This results in a decrease in both the mass and wave velocity of a comparable number of cycles of corrosion.
3. Characteristics of ultrasonic pulse velocity through the ceramic body with the passage of the number of cycles can be a basis for the assessment of changes occurring in the material under the influence of the external environment containing the sulphate and chloride ions.
4. Measurements of the ultrasonic pulse velocity is a non-destructive testing, therefore, to know the relationship between the speed of the wave passing through a ceramic brick and its texture can be a valuable source of information on the physical and chemical processes occurring in the material. This is of particular importance for the assessment of the technical condition of historic buildings.

References

- Hager, I. (2011) The compressive strength and the speed of the ultrasonic wave propagation in the concrete standard and high-heat-treated. *Zeszyty Naukowe Politechniki Rzeszowskiej. Budownictwo i Inżynieria Środowiska*, 276, pp. 307-312 (in Polish).
- Hall, C., Hoff, W. D. (2009) *Water transport in brick, stone and concrete*. 2nd edition. Taylor and Francis Group.
- Kańska, S., Stryszewska, T. (2013) Influence of full water permeating of ceramic body on its selected physico-mechanical properties. IX Conference PTCer, Zakopane, pp. 75.
- Lewińska-Romicka, A. (1990) *Non-destructive testing. Podstawy defektoskopii*. WNT, Warszawa (in Polish).
- Runkiewicz, L., Rodzik, W. (1990) Non-destructive testing strength of masonry historic buildings. *Inżynieria i Budownictwo*, 2, pp. 50-52, (in Polish).
- Stryszewska, T., Wodnicka, K. (2013) The texture and microstructure of ceramic brick contaminated by chloride and sulfate ions. *Ceramic Materials*, 1, pp. 87-91.

HYBRID METHOD FOR DETERMINING FATIGUE CHARACTERISTIC IN HIGH CYCLE LIFE

P. Strzelecki^{*}, J. Sempruch^{**}

Abstract: The paper presents hybrid method for determine fatigue S-N curve in limited life region. To invent this method, gamma distribution of slope coefficient fatigue characteristics has been estimated. From this distribution was proposed value of slope S-N curve as mode of distribution m slope for smooth and notched specimen. To verify this approach, fatigue test of smooth and notched specimen of 42CrMo4 and C45+C steel has been carried out. Qualitative verification has occurred that proposed method get better results for notched specimen and worse for smooth specimen.

Keywords: High-cycle fatigue, Fatigue design, Accelerated methods, Hybrid methods, S-N curve.

1. Introduction

To dimensioning the new element of machine, constructor must have fatigue characteristic of material which will be used. To obtain such diagram, it should be carry out fatigue tests e.g. by standard PN H 04325:1976. These tests are expensive, long and conservative. From these reasons, analytical methods has been invented. These methods can be found e.g. in publications by Neimitz A. et al. (2008), Lee Yung-Li et al. (2005) and Strzelecki and Sempruch (2011).

In papers Strzelecki and Sempruch (2012) and Strzelecki and Sempruch (2014) have been made verification of analytical methods. In these papers have been proved that analytical methods can provide to big mistake. For this reason, hybrid (analytical-experimental) method will be presented.

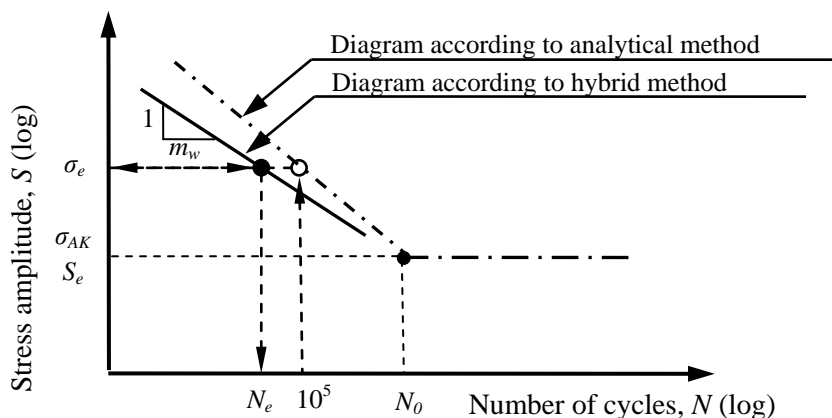


Fig. 1: Hybrid (analytical-experimental) approach to determine line of S-N curve for limited fatigue life.

2. Description of Hybrid Method

Hybrid method is based on determine fatigue curve by analytical method e.g. FITNET method. First, it must be determine characteristic by analytical method. Then it is calculate value of stress amplitude (σ_e)

^{*} M.Sc. Ing. Przemysław Strzelecki, PhD. Student: Institute of Mechanical Engineering, University of Technology and Life Sciences, 85-789 Bydgoszcz, Poland; p.strzelecki@utp.edu.pl

^{**} Prof. Ing. Janusz Sempruch: Institute of Mechanical Engineering, University of Technology and Life Sciences, 85-789 Bydgoszcz, Poland; semjan@utp.edu.pl

for 10^5 cycles according determined characteristic. Next step is carrying out fatigue test for load equal σ_e for three specimen. After that, it is calculated mean value of got results – N_e . Now, through point with coordinate (N_e, σ_e) it is drawing line with slope m_w . On Fig. 1, the above schematic procedure was presented. Coefficient m_w is equal 10.9 for smooth specimen and 5.3 for notched specimen (structural element). These value for m_w has been obtained from gamma distribution estimated from coefficient m_a for fatigue characteristic for normal stress for smooth (91 characteristics) and notched (41 characteristics) specimen - Fig. 2. Data has taken from literature. On Fig. 2 by green point has been marked mode which equal 10.9 for smooth specimen and 5.3 for notched specimen.

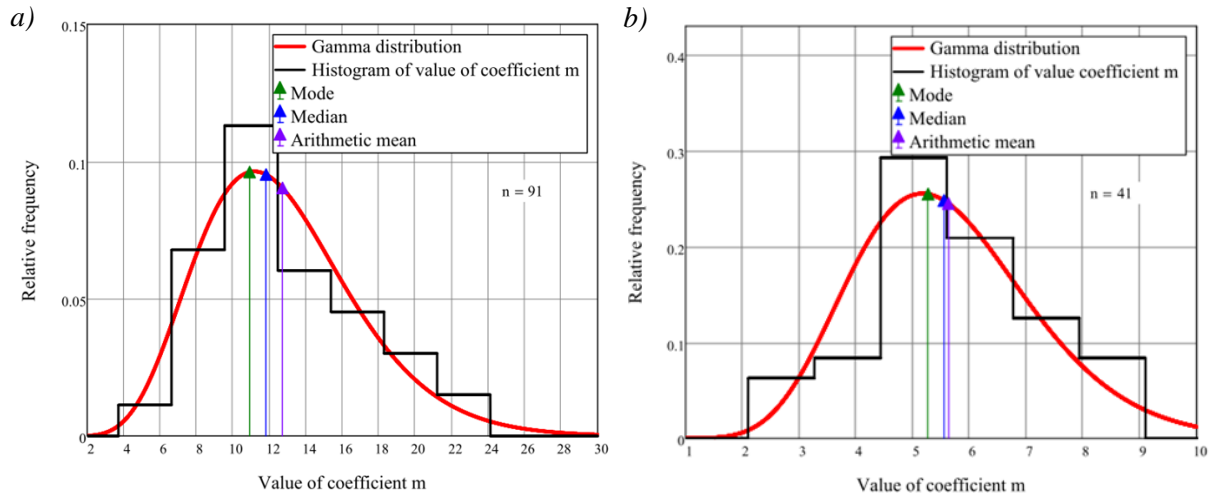


Fig. 2: Distribution of coefficient m_a for construction steel materials for: a) Unnotched specimen; b) Notched specimen.

3. Methodology of the Experiment

To verify above method, fatigue tests of material 42CrMo4 and C45+C, were carried out. In papers Strzelecki and Sempruch (2012) and Strzelecki and Sempruch (2014) was presented the geometry of smooth and notched specimen. Machine for rotating bending was being used. In paper Strzelecki and Sempruch (2012) has been made and presented verification of this device.

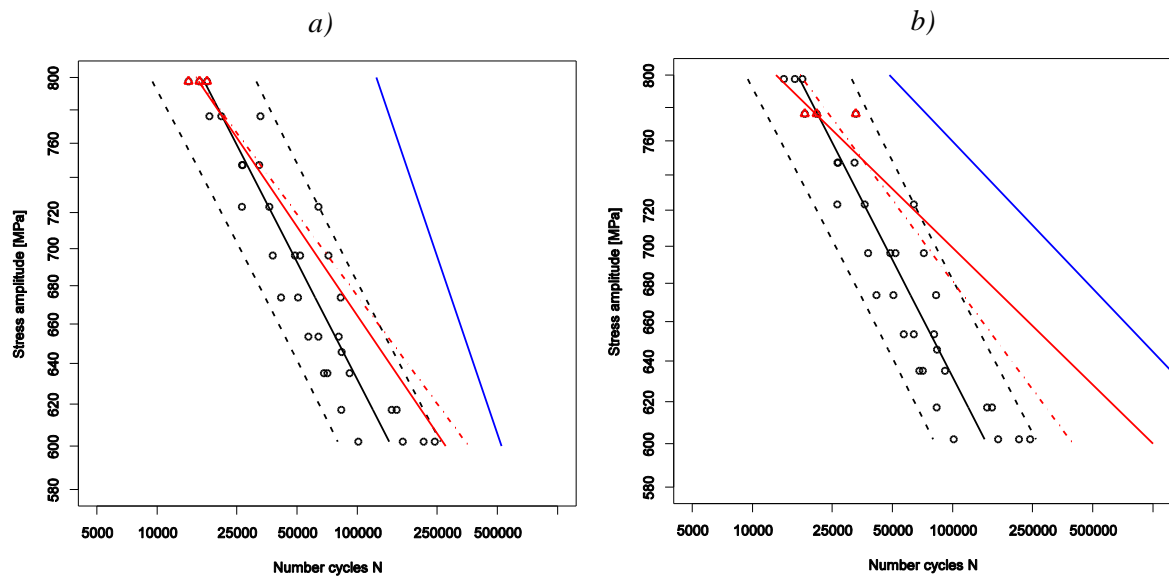


Fig. 3: S-N curve for 42CrMo4 steel for smooth specimen and characteristic according: a) FITNET method; b) Lee & Taylor method. Black line – curve estimated from experiment, blue line – according analytical method, red dot and dash line – according hybrid method, red line – through points N_e, σ_e and $\sigma_{AK}/S_e, N_0$, black dashed line – scatter band for confidence level 5%, points – results from experiment.

4. Results of Experiment and Determined Characteristics

Results of fatigue test are present on Fig. 3 to Fig. 6. Characteristics determine by analytical and hybrid method has been marked on Fig. 3 to Fig. 6. FITNET method and Lee and Taylor method has been taken to make comparison of analytical and hybrid approach.

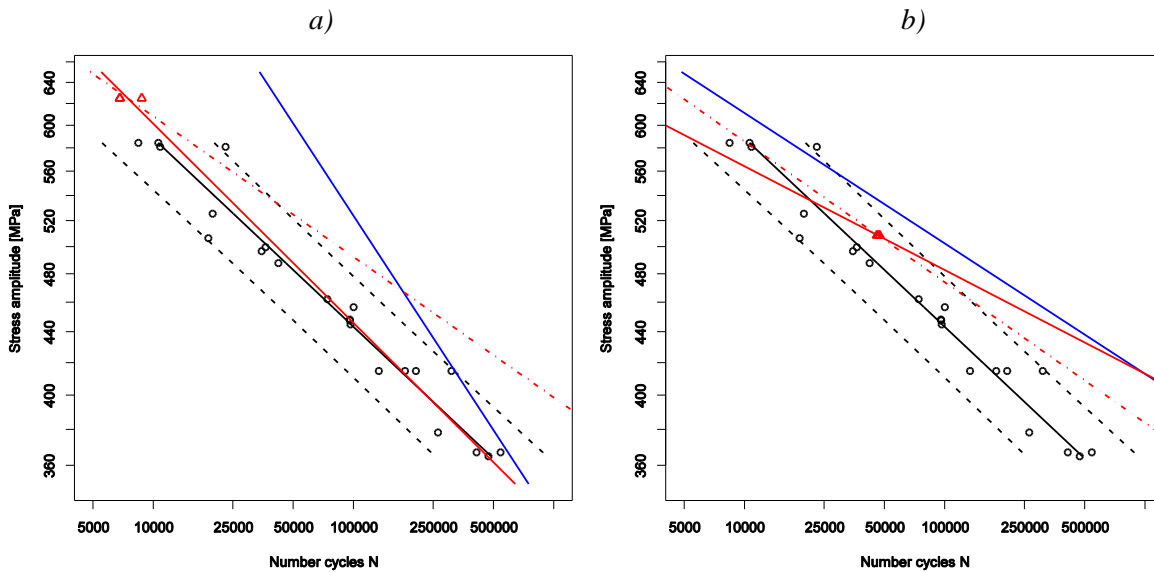


Fig. 4: S-N curve for C45+C steel for smooth specimen and characteristic according: a) FITNET method; b) Lee & Taylor method. Black line – curve estimated from experiment, blue line – according analytical method, red dot and dash line – according hybrid method, red line – through points N_e, σ_e and $\sigma_{AK}/S_e, N_0$, black dashed line – scatter band for confidence level 5%, points – results from experiment.

It must be explain that red line has been drawn through point (N_e, σ_e) and $(\sigma_{AK}/S_e, N_0)$. This approach is present to show influence of determine fatigue limit and knee point on error of getting characteristic. This error will always occur went fatigue properties are determining on monotonic properties of material – ultimate strength in this case. For example, N_0 has different proposition for value presented by Sonsino (2007) and Ligaj and Szala (2013).

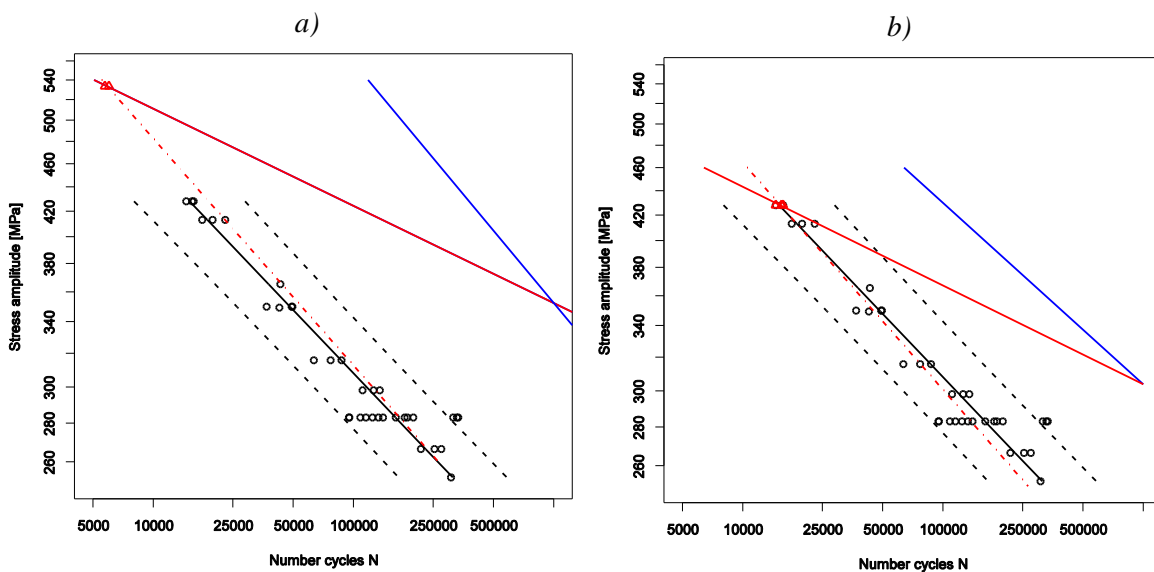


Fig. 5: S-N curve for 42CrMo4 steel for notched specimen $K_t = 1.99$ and characteristic according: a) FITNET method; b) Lee & Taylor method. Black line – curve estimated from experiment, blue line – according analytical method, red dot and dash line – according hybrid method, red line – through points N_e, σ_e and $\sigma_{AK}/S_e, N_0$, black dashed line – scatter band for confidence level 5%, points – results from experiment.

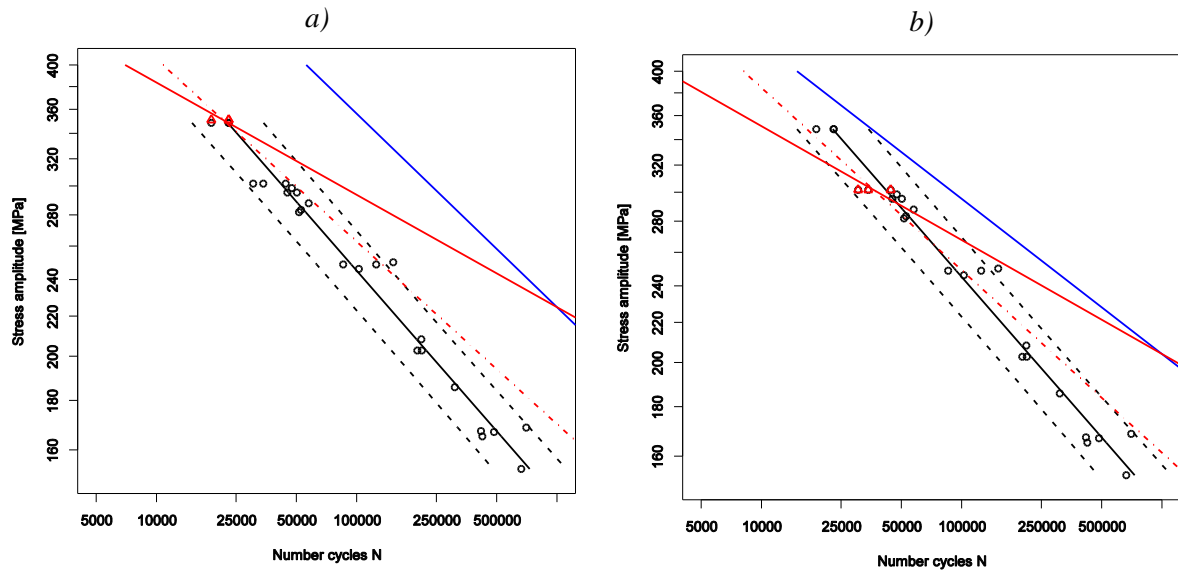


Fig. 6: S-N curve for C45+C steel for notched specimen $K_t = 1.99$ and characteristic according: a) FITNET method; b) Lee & Taylor method. Black line – curve estimated from experiment, blue line – according analytical method, red dot and dash line – according hybrid method, red line – through points N_e, σ_e and $\sigma_{AK}/S_e, N_0$, black dashed line – scatter band for confidence level 5%, points – results from experiment.

5. Summary

Proposed hybrid method has been obtained better results than analytical method. On Fig. 3 to Fig. 6 was presented hybrid method with fixed slope coefficient and hybrid method for determining by two points. It is visible, that better fitting to curve estimated from experiment have hybrid method with constant coefficient. Only for smooth specimen and using FITNET method is converse.

Reference

- Lee, Y.-L., Pan, J., Hathaway, R. B., Barkey, M. E. (2005) Fatigue testing and analysis, University of Alabama, Elsevier.
- Ligaj, B., Szala, G. (2013) Hybrid method for calculating fatigue life (in Polish). edited by J. Szali, Bydgoszcz ITE.
- Neimitz, A., Dzioba, I., Graba, M., Okrajni, J. (2008) Evaluation of strength, life and safety of structural components contain defects. Politechnika Świętokrzyska, Kielce.
- PN-H-04325:1976, Test of metal fatigue - Basic terms and general guidelines for preparing of samples and carry out tests.
- Sempruch, J., Strzelecki, P. (2011) Error of fatigue life determination according to the FITNET method. In: Proc. 17th International Conference Engineering Mechanics, (V. Fuis, ed.), Svratka, Czech Republic, pp. 531-534.
- Sonsino, S. M. (2007) Course of SN-curves especially in the high-cycle fatigue regime with regard to component design and safety. International Journal of Fatigue, Vol. 29, No. 12, pp. 2246-2258.
- Strzelecki, P., Sempruch, J. (2012) Experimental Verification of the Analytical Method for Estimated S-N Curve in Limited Fatigue Life, Materials Science Forum, Vol. 726, pp. 11-16.
- Strzelecki, P., Sempruch, J. (2011) Modification of selected methods of rapid determination of fatigue characteristics in the range of limited fatigue life, Journal of Polish Cimac Selected problems of designing and operating technical systems Vol. 6, No. 3; pp. 289.
- Strzelecki, P., Sempruch, J. (2014) Experimental Verification of Analytical Method for Determining the S-N Curve Alloy Steel, Key Engineering Materials, Vol. 598, pp. 219-224.

EVALUATION OF THE AREAL TEXTILE THINNING

B. Stríž^{*}, M. Vyšanská^{**}

Abstract: *The areal textile with outstanding structure is approximated by the areal continuum with the same mechanical properties. This allows to use the equations of the continuum mechanics and to define the basic mechanical properties of the textile. Till this time no suitable experimental method for continuous measurement of textile fabric thinning during straining exists. This is the reason, why the mechanical properties of the textiles are expressed through the force per unit length in N/m. The main aim of the presented paper is to theoretically define the areal textile thinning during its straining through the continuum mechanics.*

Keywords: Mechanics of continuum, Conjugate pairs, Specific forces, Cauchy conjugate pair, Thinning of areal textile.

1. Mechanics of the areal textiles

The identification of the mechanical properties of the areal textiles under the uniaxial and biaxial straining is physical problem, which leads to a task with seven unknowns. The textile fabric is very specific formation; therefore it is necessary to describe its mechanical properties (in contrast to solids) for particular state of stress and strain.

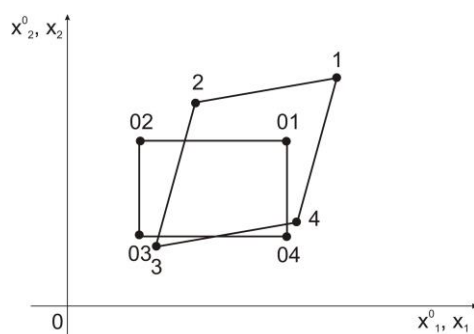


Fig. 1: The geometry of original and deformed sample.

The dependence between Euler's and Lagrange's point coordinates (according to Striz (2001) (Part I)) can be evaluated by measuring the movements of observed points of areal fabric, Fig. 1:

$$x_i^p = x_i^{op} + w_i^p, \quad i = 1, 2, \quad (1)$$

where p is point number, the circle denotes the Lagrange coordinate. The work by Striz and Vysanska (2011) describes the deformation process of the material using deformation gradient F and the jacobian J . Tensor F is expressed as

$$F = \begin{pmatrix} 1 + v_{11} & v_{12} & 0 \\ v_{21} & 1 + v_{22} & 0 \\ 0 & 0 & 1 + v_{33} \end{pmatrix} \quad (2)$$

^{*} Prof. RNDr. Bohuslav Stríž, DSc.: Technical University of Liberec, Faculty of Textile Engineering, Department of Textile Technologies, Studentska 2; Liberec; 461 17, CZ; bohuslav.striz@tul.cz

^{**} Ing. Monika Vyšanská, PhD.: Technical University of Liberec, Faculty of Textile Engineering, Department of Textile Technologies, Studentska 2; Liberec; 461 17, CZ; monika.vysanska@tul.cz

and jacobian J

$$J = (1 + v_{33})[(1 + v_{11})(1 + v_{22}) - v_{12}v_{21}] \quad (3)$$

The parameters v_{ij} are the differential movements of the vertices of areal fabric on Fig. 1. Let's define tensor of extension U and tensor of rotation R using of the material deformational gradient F .

$$\begin{aligned} U^2 &= F^T F, \\ F &= R U. \end{aligned} \quad (4)$$

Tensor of extension U can be determined, for example, by so called method of the projectors according to Striz (2001) (Part I). Till this time, the unpublished method for determination of tensors U and R is presented below. The tensors U , R have following structure

$$U = \begin{pmatrix} u_{11} & u_{12} & 0 \\ u_{12} & u_{22} & 0 \\ 0 & 0 & 1 + v_{33} \end{pmatrix}, \quad (5)$$

$$R = \begin{pmatrix} r_{11} & r_{12} & 0 \\ -r_{12} & r_{11} & 0 \\ 0 & 0 & 1 \end{pmatrix}. \quad (6)$$

The individual components can be expressed as

$$\begin{aligned} u_{11} &= \frac{(1 + v_{11})(2 + v_{11} + v_{22}) + v_{21}(v_{21} - v_{12})}{\sqrt{4(1 + v_{11} + v_{22}) + (v_{11} + v_{22})^2 + (v_{12} - v_{21})^2}}, \\ u_{22} &= \frac{(1 + v_{22})(2 + v_{11} + v_{22}) + v_{12}(v_{12} - v_{21})}{\sqrt{4(1 + v_{11} + v_{22}) + (v_{11} + v_{22})^2 + (v_{12} - v_{21})^2}}, \\ u_{12} &= \frac{(1 + v_{11})v_{12} + (1 + v_{22})v_{21}}{\sqrt{4(1 + v_{11} + v_{22}) + (v_{11} + v_{22})^2 + (v_{12} - v_{21})^2}}. \end{aligned} \quad (7)$$

$$\begin{aligned} r_{11} &= \frac{2 + v_{11} + v_{22}}{\sqrt{4(1 + v_{11} + v_{22}) + (v_{11} + v_{22})^2 + (v_{12} - v_{21})^2}}, \\ r_{12} &= \frac{v_{12} - v_{21}}{\sqrt{4(1 + v_{11} + v_{22}) + (v_{11} + v_{22})^2 + (v_{12} - v_{21})^2}}. \end{aligned} \quad (8)$$

It is easy to find, that equation (2) is satisfied.

The definition of the unit-less quantity v_{33} is based on the Cauchy's relative force Σ :

$$\Sigma = \begin{pmatrix} S_{11} & S_{12} & 0 \\ S_{12} & S_{22} & 0 \\ 0 & 0 & 0 \end{pmatrix} \quad (9)$$

and corresponding deformation $\varepsilon_{ij}(m)$, which is work-conjugate to Σ . The components of the tensor Σ are determined from the static balance equations of forces $Q_1(x)$, $Q_2(x)$ in the fabric axes 11 and 22 according to Striz (2001) (Part II).

The deformation tensor $\varepsilon_{ij}(m)$ is defined using the tensor of extension U and meanwhile unknown parameter "m":

$$\varepsilon_{ij}(m) = \frac{1}{m} [U^m - I] \quad (10)$$

The exponent “ m ” characterizes the conjugate pair. The presented work is looking for the particular value of “ m ” for the textile fabric. The conjugate pair has to fulfill condition of equality of mechanical work (energy), obtained from known conjugate pairs with parameters of: 2, 1, 0, -1, -2.

$$I(m) = \int_0^{x_{\max}} \left[s_{11} \frac{d\varepsilon_{11}}{dx} + s_{22} \frac{d\varepsilon_{22}}{dx} + 2s_{12} \frac{d\varepsilon_{12}}{dx} \right] dx = D, \quad (11)$$

where $x = \frac{Q_1(x)}{Q_{1\max}}$, and Q_1 is outer force along axis 1.

To determine the quantity D it is necessary to use two conjugate pairs at minimum. The method presented in Striz and Vysanska (2011) defines the relative forces and deformations in equation (11). Parameter “ m ” in Cauchy conjugate pair is assessed from equation (11). Then the conjugate pair is set for given fabric.

2. Evaluation of the Fabric Thinning

The method described in Striz and Vysanska, (2011) together with parameter “ m ” from equation (11) can be used to express the values of six mechanical modules \bar{E}_{ij} . One can express the invariant shear modulus using \bar{E}_{ij} modules according to

$$\tilde{E}_4 = \frac{1}{2} \left[\frac{1}{4} (\bar{E}_{11} + \bar{E}_{22} - 2\bar{E}_{12}) + \bar{E}_4 \right]. \quad (12)$$

Further we have determined τ_i and γ_i , which are also invariant:

$$\begin{aligned} \tau_i &= \frac{1}{\sqrt{6}} \sqrt{(s_{11} - s_{22})^2 + s_{11}^2 + s_{22}^2 + 6s_{12}^2}, \\ \gamma_i &= \sqrt{\frac{2}{3}} \sqrt{(\varepsilon_{11} - \varepsilon_{22})^2 + (\varepsilon_{22} - \varepsilon_{33})^2 + (\varepsilon_{33} - \varepsilon_{11})^2 + 6\varepsilon_{12}^2}. \end{aligned} \quad (13)$$

In linear mechanics this relation is valid:

$$G = \frac{\tau_i}{\gamma_i},$$

where G is shear modulus. We determine similar equation for non-linear mechanics:

$$\tilde{E}_4 = \frac{\tau_i}{\gamma_i}. \quad (14)$$

After substitution of the equations (14), (13) in (12) and adjustment we get

$$\frac{1}{4} (\bar{E}_{11} + \bar{E}_{22} - 2\bar{E}_{12}) + \bar{E}_4 = \frac{\sqrt{(s_{11} - s_{22})^2 + s_{11}^2 + s_{22}^2 + 6s_{12}^2}}{\sqrt{(\varepsilon_{11} - \varepsilon_{22})^2 + (\varepsilon_{22} - \varepsilon_{33})^2 + (\varepsilon_{33} - \varepsilon_{11})^2 + 6\varepsilon_{12}^2}}. \quad (15)$$

We define unknown ε_{33} from equation (11) and on the basis of the equations (4) and (9) we can express it like

$$\varepsilon_{33} = \frac{1}{m} \left[(1 + \nu_{33})^m - 1 \right] \quad (16)$$

Unit-less quantity ν_{33} can be expressed in the following form

$$h = h_0(1 + v_{33}), \quad (17)$$

where h_0 is initial measured thickness of the areal fabric and h is running thickness of fabric and together with the quantity v_{33} is dependent on established coordinate x in a relation (11). Then the problem of fabric thinning is solved.

The components of conjugate pairs s_{ij} and ε_{ij} are stated from equations in Striz and Vysanska (2011):

$$\begin{aligned} S_B &= \frac{J}{2} \left(F^{-1} \Sigma R + R^T \Sigma (F^{-1})^T \right), \\ s_{ij} &= \frac{1}{2} \left(S_B U^{1-n} + U^{1-n} S_B \right), \\ \varepsilon_{ij} &= \frac{1}{n} \left(U^n - I \right), \end{aligned} \quad (18)$$

where S_B is Biott tensor of variable forces ($n = 1$). By solving the problem for various exponents ($n = 2, 1, 0, -1, -2, m$) one can determine the thickness of the fabric $h(x, n)$ from the equations mentioned above. For different areal textiles and different conjugate pairs we get unsuitable values of h (e.g. $h > h_0$). If we substitute exponent $n = m$ in equations (18), we can gain for value s_{ij} the quantity Σ , and so verify calculated value of „ m “.

3. Conclusions

Till this time no experimental method for running measurement of textile thinning during fabric loading exists. The present work allows validating calculated values of (m, h) and excluding unsuitable conjugate pairs, when such method will be available.

References

- Striz, B. (2001) Mechanics of Textiles, Part 1: Basis of Continuum Mechanics, TU Liberec, (in Czech).
- Striz, B., Vysanska, M. (2011) Mechanics of flat textile fabrice – theory, In: Proc. 17th Inter. Conf. Engineering Mechanics (V. Fuis, ed.), Svratka, Czech Republic, pp. 575-579.
- Striz, B. (2001) Mechanics of Textiles, Part 2: Basis of Continuum Mechanics, TU Liberec, (in Czech).

RHIZARTHROSIS AND ITS TREATMENT, STRESS AND DEFORMATION ANALYSIS OF THE TOTAL JOINT REPLACEMENT

T. Svojanovský*, L. Trtík**

Abstract: *The first part of this paper deals with consequences and treatment of trapeziometacarpal joint disease called rhizarthrosis. Rhizarthrosis consists of some different phases. Initial phase can be asymptomatic, but in next phases bad mobility and unpleasant pain can occur. There are many ways how to reduce the pain and improve the mobility caused by rhizarthrosis. However, in serious cases the problem can be solved completely only by the total joint replacement. There have been many surgeries carried out since 2008 in the Czech Republic. Development of such total joint replacement is still current thanks to its optimization. There are some advantages resulting from the development, e.g. longer lifespan of the implant, better biocompatibility etc. Therefore the second part of the paper aims at stress and deformation analysis of simplified model of the joint replacement. An equivalent stress and a contact pressure are investigated.*

Keywords: Rhizarthrosis, Trapeziometacarpal joint, Total joint replacement, Stress and deformation analysis, Finite element method.

1. Introduction

Many people suffer from painful diseases of joints. However, similar diseases affect not only people of an old age and it is necessary to eliminate the problems. Fortunately, a specific scientific branch called biomechanics has been developed for last decades. Biomechanics gathers important knowledge of an engineering mechanics and a medicine applying them on a development of various types of replacements. Treatment of joint diseases includes a lot of methods, but the most efficient are partial and total joint replacements. The similar situation is in the hip joint (Fuis et al., 2001, 2002, 2004, 2009, 2009a, 2011 and 2011a).

2. Rhizarthrosis

Rhizarthrosis is a kind of an arthrosis, i.e. painful degenerative joint disease, namely disease of trapeziometacarpal joint connecting thumb bones with wrist bones. Rhizarthrosis is one of the most frequent arthrosis of hand. Compared to men, there are 80-90% of women over age of 50 suffering from it (Trtik, 2011). Occasionally, it is a result of partial luxation – subluxation. Rarely, a fracture in the joint surrounding can be the reason of disease.

2.1. Consequences of rhizarthrosis

Many studies discovered rhizarthrosis occurs related to disability of neighboring joints. The characteristic feature is a presence of bony projections – osteophytes. Increasing of the osteophytes causes reduction of a joint space, damage of an intermetacarpal ligament and following evolution of a subluxation. Growth of osteophytes can bring a lot of other unpleasant problems.

The first phase of rhizarthrosis is asymptomatic. As time goes by, particularly hard work and movement result in a pain located in the first metacarpus basis. Swellings, immobility and low strength of the thumb are typical symptoms of an advanced stage. For the correct identification of the location of pain origin, medical examination by touching (palpating) an area of the hand have to be done necessarily. Commonly,

* Bc. Tomáš Svojanovský: Institute of Solid Mechanics, Mechatronics and Biomechanics, Brno University of Technology, Technická 2896/2; 616 69, Brno; CZ, svojanovsky.t@seznam.cz

** MUDr. Lubomír Trtík: Department of Orthopedic Surgery, Husova 2624; 580 01 Havlíčkův Brod; CZ, lubomir.trtik@klikni.cz

mobility of the thumb in accordance with a flexion, extension, abduction and adduction is medically examined. Generally, evaluation of thumb opposition according to Kapandji is carried out. This simple evaluation consists in pressing the thumb against other fingers. There are many classifications of determination of the joint disability level, e.g. according to Dell, Eaton-Littler, etc. Let's introduce classification according to Dell:

- **1st stage** - The joint space is smaller and smaller, but there haven't been any osteophytes and subluxation yet.
- **2nd stage** - The first osteophytes and slight subluxation can be noticed.
- **3rd stage** - The osteophytes are big and subluxation is extensive. The thumb is irreversibly deflected from initial position.
- **4th stage** - The joint line fades away, pain is manifested moderately. On the other hand, mobility of the thumb is nearly impossible.

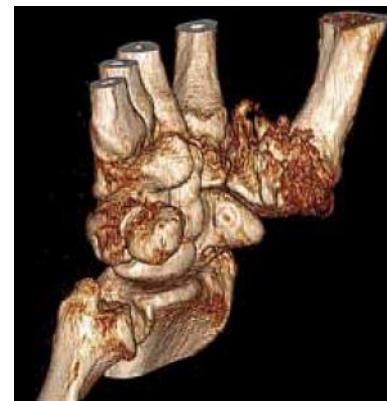


Fig. 1: Advanced stage of rhizarthrosis.

2.2. Treatment of rhizarthrosis

There are many ways how to reduce or entirely eliminate symptoms of rhizarthrosis. Basically, conservative and surgical medical treatments of the disease are distinguished. Conservative treatment is carried out in case of less serious problems when doctors strive for reduction of a pain manifestation. Usually, pain stage has persisted for 2-3 years, sometimes longer. Conservative treatment requires use of orthoses and medicaments, for instance analgesics (non-steroidal anti-inflammatory drugs etc.).

2.2.1. Trapeziectomy and arthrodesis

Surgical solution includes three different ways of treatment, namely trapeziectomy, arthrodesis and trapezium prosthesis. Trapeziectomy is a surgery to remove the trapezium bone. Arthrodesis is the artificial induction of joint ossification between two bones. The joints are immobilized at the level of fusion. This surgery is done to relieve pain at the expense of mobility. The plaster fixation has been required for three months at most. Among others, there is a problem of loss of the thumb dexterity.

2.2.2. Partial and total trapezium replacements

If there is the only partial arthrosis of the joint, the partial prosthesis of the first metacarpus basis suffices. In the present these replacements are made of pyrolytic carbon. Well-known types are Asword-Blatt and Kessler. The total trapezium replacement replaces all the trapezium bone, but the metacarpus bone remains. The most famous is Swanson's silastic implant.

2.2.3. Total trapeziometacarpal replacements

On the development of replacements Jacques Duparc and Jean-Yves de La Caffinière have participated since 1970s. The goal was an anatomic adaptation, acceptable mobility, sufficient stability and high service life. Whereas the first generation was disappointing, the contemporary second generation is much more successful. Some names of the second generation models are Elektra, Roseland, Arpe, Carat, Maïa, Rubis2, Ivory etc. Improvement of the replacements was caused by the progress of mechanical engineering and medicine. In the technical sphere, anchoring into a bone and surface finishing of matter was improved. In the medical science the process of surgery became better.

In the Czech Republic are frequently used these types of total joint replacements – Maïa and Rubis2. Individual types differ in a use of material and center of rotation mainly. The metal stem of Maïa type is pressed in the polyethylene cup and the center of thumb rotation is in trapezium. On the other hand, both the stem and the cup of Rubis2 type are metal and the center of rotation is in the first metacarpus basis.

There are advantages of the second generation replacements like preserving anatomy and mainly invariability of the physiological center of rotation. In contrast, disadvantages are luxation (6-8% of patients) and release of a connection between prosthesis and bone (10% of patients).



Fig. 2: Total replacement Maia.



Fig. 3: Total replacement Rubis2.

3. Stress and Deformation Analysis

Thanks to need of development of partial and total joint replacements, experimental and computational modelings are done. For this particular prosthesis, stress and deformational analysis was carried out by numerical computational modeling by finite element method software (ANSYS).

The simplified model of geometry corresponding approximately with real used implants was made. Diameters of contact surfaces of the cup and the stem are 7 and 7.05 mm. For both parts of model the only material was chosen, namely frequently used Cr-Co-Mo alloy with Young's modulus 208 GPa and Poisson's ratio 0.3. Axial symmetry loading by pressing the stem to the cup by force of maximum magnitude of 1200 N was preferred.

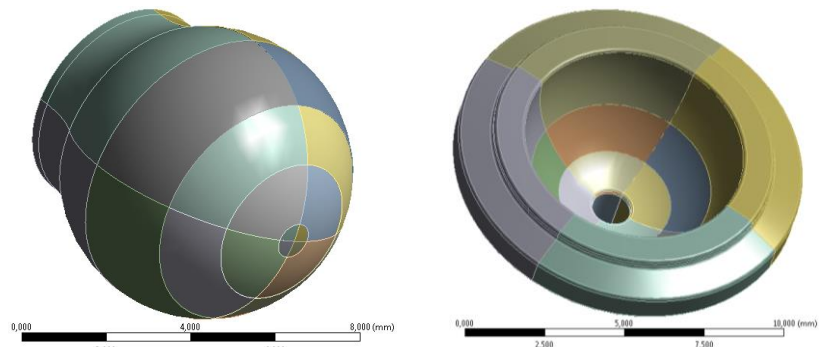


Fig. 4: Simplified model of geometry of joint replacement.

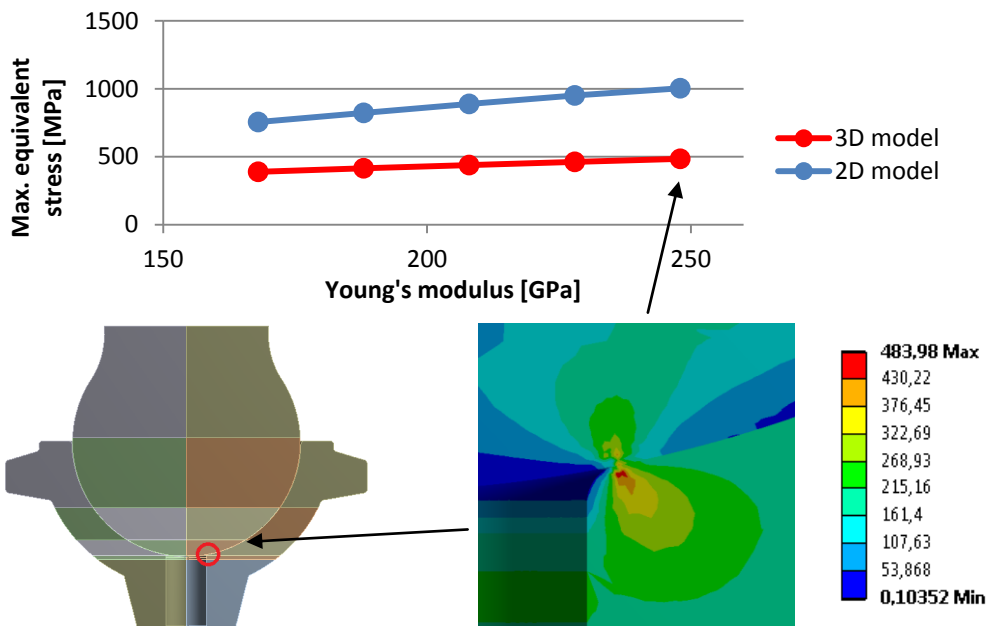


Fig. 5: Dependence between maximal Tresca equivalent stress and Young's modulus.

Contact between the stem and the cup was defined with frictional coefficient 0.3. Just because of the frictional contact, analysis is nonlinear and therefore much more complicated. Discretization of the model

was created with use of axial symmetry. Whereas in the contact area very small elements were created, farther, the elements remained bigger in order to efficient calculation. It is very important to know that quality of mesh determines exactness of results. For comparison, three dimensional and two dimensional axial symmetrical analyses were performed. A use of an axial symmetrical analysis is limited but very useful if possible. Although the results of two and three dimensional models are different, trend situation is evident.

Whereas an influence of frictional coefficient (not mentioned here) is relatively negligible, in contrast, Young's modulus influences studied quantities substantially. It is evident that increasing Young's modulus causes increasing of maximal Tresca equivalent stress as well as maximal contact pressure. In conformity with contact pressure, contact area decreases (Svojanovský, 2013).

4. Conclusions

The overview of treatment of rhizarthrosis tries to highlight an importance of biomechanics. Development of biomechanics is caused thanks to very significant progress of medicine and engineering mechanics in last decades. In the engineering mechanics finite element method is one of the most important computational methods. Nevertheless, it is suitable to combine this method with experiments and essential knowledge of an engineer to achieve credible results.

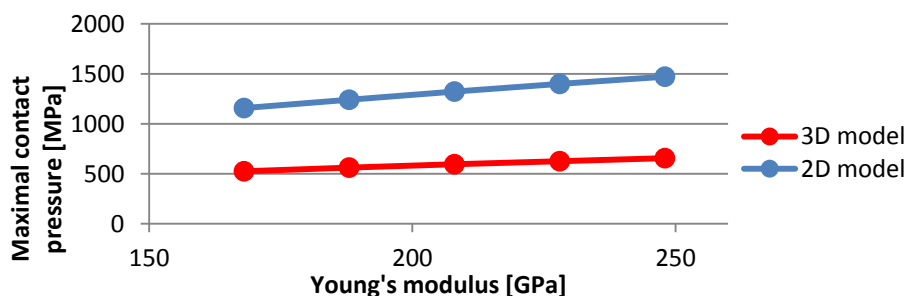


Fig. 6: Dependence between maximal contact pressure and Young's modulus.

Acknowledgement

This work was supported by specific research FSI-S-14-2344.

References

- Trtík, L. (2011) Rhizarthrosis, current possibilities of treatment. *Ortopedie* 1: 30-35, 2011 Available on: http://fvconsult.krivanekludek.cz/prednasky/Trtik_Rizartroza.pdf, pp. 28-33.
- Fuis, V., Janicek, P. (2002) Stress and reliability analyses of damaged ceramic femoral heads, Conference on Damage and Fracture Mechanics, Maui Hawaii, Structures and Materials Vol. 12, pp. 475-485.
- Fuis, V., Koukal, M., Florian, Z. (2011) Shape Deviations of the Contact Areas of the Total Hip Replacement, In: 9th International Conference on Mechatronics, Warsaw, Poland pp. 203-212.
- Fuis, V., Malek, M., Janicek, P. (2011a) Probability of destruction of Ceramics using Weibull's Theory, In: Proc. 17th International Conference on Engineering Mechanics, Svratka, Czech Republic, pp. 155-158.
- Fuis, V. (2004) Stress and reliability analyses of ceramic femoral heads with 3D manufacturing inaccuracies, In: Proc. 11th World Congress in Mechanism and Machine Science, Tianjin, China pp. 2197-2201.
- Fuis, V. (2009) Tensile Stress Analysis of the Ceramic Head with Micro and Macro Shape Deviations of the Contact Areas, Recent Advances in Mechatronics: 2008-2009, In: Proc. International Conference on Mechatronics, Brno, Czech Republic, pp. 425-430.
- Fuis, V., Varga, J. (2009a) Stress Analyses of the Hip Joint Endoprosthesis Ceramic Head with Different Shapes of the Cone Opening. In: Proc. 13th International Conference on Biomedical Engineering, IFMBE Proceedings Vol. 23, Iss. 1-3, pp. 2012-2015.
- Fuis, V., Janicek, P. (2001) Stress and reliability analyses of ceramic femoral heads with axisymmetric production inaccuracies. In: Proc. 9th Mediterranean Conference on Medical and Biological Engineering and Computing, Pula, Croatia, IFMBE Proceedings Pts. 1 and 2, pp. 632-635.
- Svojanovský, T. (2013) Stress and deformation analysis of the stem and cup of the total replacement of the trapeziometacarpal joint. Thesis Brno University of Technology, Brno, 71 p. (in Czech).

NUMERICAL MODEL FOR HISTORICAL MORTARS EXPOSED TO FREEZING TEMPERATURES

J. Sýkora*

Abstract: *The present contribution is devoted to modeling of degradation processes in historical mortars exposed to moisture impact during freezing. Internal damage caused by ice crystallization in pores is one of the most important factors limiting the service life of historical structures. Coupling the transport processes with the mechanical part will allow us to address the impact of moisture on the durability, strength and stiffness of mortars. This should be accomplished with the help of a complex thermo-hygro-mechanical model representing one of the prime objectives of this work. The proposed formulation is based on the extension of the classical poroelasticity models with the damage mechanics. The whole concept is demonstrated on a two-dimensional moisture transport in the environment with temperature below freezing point.*

Keywords: Coupled heat and moisture transport, Ice crystallization process, Damage, Historical mortar.

1. Introduction

In the literature, the above described problem is addressed from several perspectives. The first group of publications is focused on the description of the coupled heat and moisture transport reflecting the moisture migration under the conditions of the ice crystal formation in the pores, 2-D and 3-D aspects and different moisture/heat sources, such as wind driven rain, solar short and long wave radiation etc., see (Kong and Wang, 2011; Künzle and Kiessl, 1996; Tan et al., 2011). While models for transport processes have been developed during several decades, the theory of ice crystallization in the pores has emerged only recently, (Scherer, 1993; Scherer 1999; Sun and Scherer, 2010). The authors established relations between physical state of porous system and pore pressures. The physical conditions of ice formation process are described by thermodynamic balance equation between ice, liquid water and solid matrix. Finally, the mechanical response of porous media subjected to the frost action was studied by several authors (Coussy and Monteiro, 2008; Wardeh and Perrin, 2008; Zuber and Marchand, 2000). On the one hand, the poroelasticity formulation based on Biot's continuum model was adopted. It is an efficient method for elastic modeling of porous system, which is subjected to the pressure of the fluid. On the other hand, a novel micromechanics approach was introduced to analyze the creation of micro-cracks in the microstructure during freezing process (Liu et al., 2011). These results predict effective mechanical and transport properties at microscopic level and can be utilized as an input for multi-scale analysis of porous media.

Our goal is to quantify the internal damage caused by the ice crystallization pressure in historical mortars. In particular, a critical point in a restoration works is frequent applications of lime mortars for preserving compatibility with the historical materials. However, lime mortars are very porous, their mechanical strength and durability are mostly very low, thus the development of a lime mortar with improved internal hydrophobicity and associated improved resistance against damage due to the effects of ice crystallization is inevitable. To address this issue with respect to its complexity, an analysis combining both experimental work and numerical simulations has to be done. Nevertheless, the numerical methodology developed within this work can be utilized to simulate the response of any porous material subjected to the frost action.

* Ing. Jan Sýkora, PhD.: Czech Technical University in Prague, Faculty of Civil Engineering, Thákurova 7, 166 29, Prague, CZ, jan.sykora.1@fsv.cvut.cz

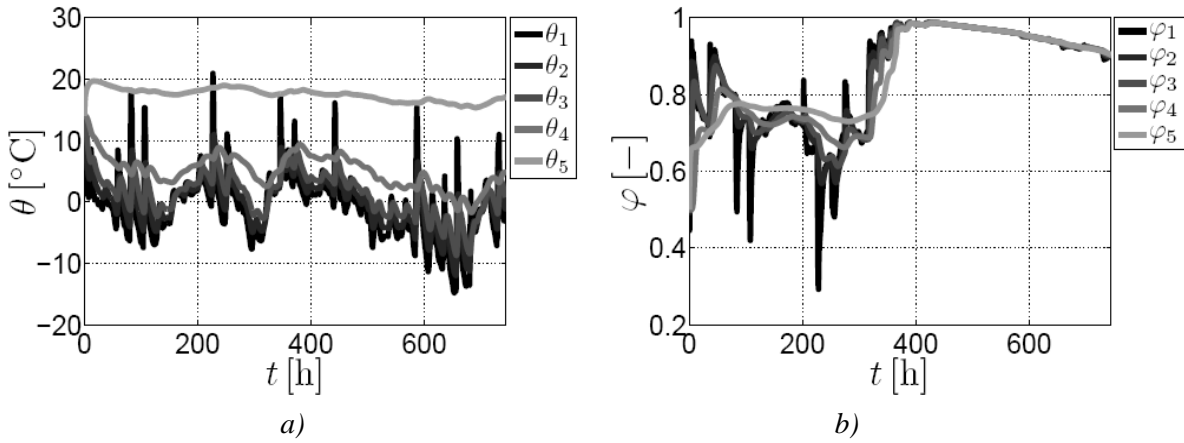


Fig. 2: a) Resulting temperature at selected nodes; b) Resulting moisture at selected nodes.

The results are presented in Fig. 2 showing variation of the temperature and moisture at selected nodes labeled in Fig. 1. The obtained results clearly manifesting the influence of exterior boundary conditions on the temperature and moisture fields, especially near the exterior surface of the two-dimensional domain.

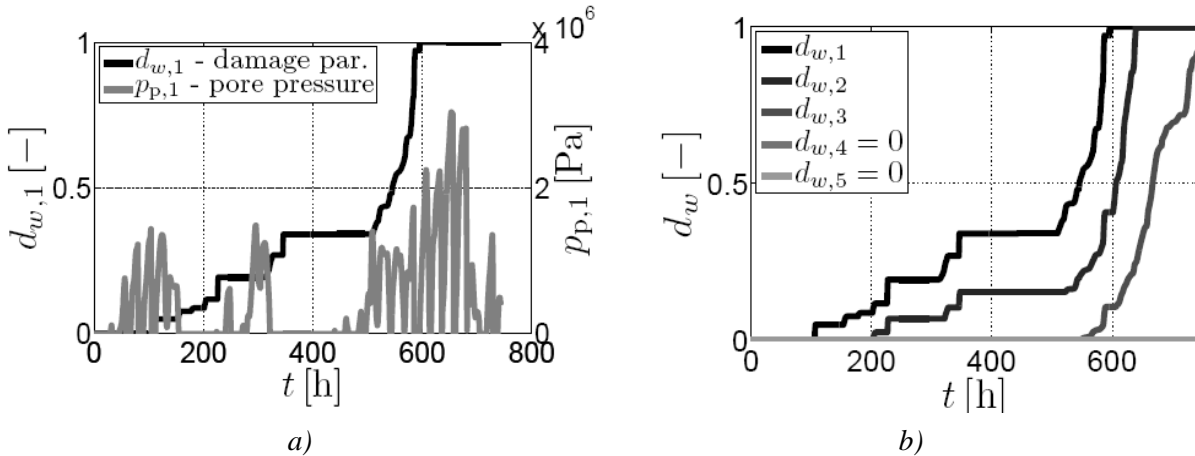


Fig. 3: a) Evolution of damage parameter $d_{w,1}$ [-] and pore pressure $p_{p,1}$ [Pa] at node 1; b) Evolution of damage parameters d_w [-] at selected nodes.

Several interesting results have been derived within the scope of the calculation of internal damage. Fig. 3a, b display the evolution of damage parameter and its dependence on the average pore pressure. Beside the comparison of the evolution of damage parameter in the time, we also compare growth of damage parameter in the domain, see Fig. 4. Analysis of these results allows better understanding of physical phenomena in porous media subjected to the frost action. A fast moisture increase in the zone close to the exterior surface (Fig. 2b) leads also to the similar trend of the damage parameter, see Fig. 3a. This can be attributed to the lower exterior temperature and higher moisture content in the surface layer caused by the driving-rain flux. The calculated results promote the capability of proposed governing equations to simulate a degradation processes in the building materials exposed to real weather conditions.

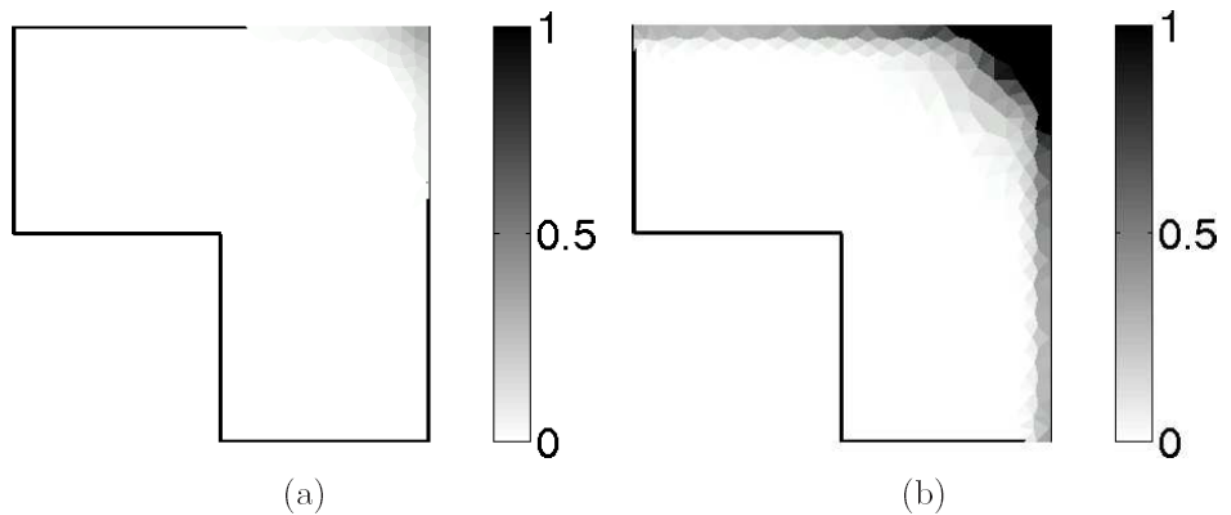


Fig. 3: Evolution of damage parameter d_w [-] after $t = 372$ [h], (b) evolution of damage parameter d_w [-] at the end of analyzed time period ($t = 744$ [h]).

4. Conclusions

This paper presents the numerical modeling of damage caused by ice crystallization process in historical mortars. Attention is focused on the thermo-hydro-mechanical model developed here in the framework of uncoupled algorithmic scheme. In particular, we employed coupled heat and moisture model, which is sufficiently robust to describe real-world materials, but which is also highly nonlinear, time-dependent material model. Supported by several successful applications in civil engineering we adopted Biot's model and the nonlocal isotropic damage model in the framework to simulate the frost action on porous media.

Acknowledgement

This outcome has been achieved with the financial support of project NAKI - DF11P01OVV0080.

References

- Coussy, O., Monteiro, P. (2008) Poroelastic model for concrete exposed to freezing temperatures. *Cement and Concrete Research*, 38, 1, pp. 40-48.
- Kong, F., Wang, H. (2011) Heat and mass coupled transfer combined with freezing process in building materials: Modeling and experimental verification. *Energy and Building*, 43, 10, pp. 2850-2859.
- Künzel, H. M., Kiessl, K. (1996) Calculation of heat and moisture transfer in exposed building components. *International Journal of Heat and Mass Transfer*, 40, 1, pp. 159-167.
- Liu, L., Ye, G., Schlagen, E. Chen, H., Qian, Z. Sun, W., van Breugel, K. (2011) Modeling of the internal damage of saturated cement paste due to ice crystallization pressure during freezing. *Cement and Concrete Research*, 33, 5, pp. 562-571.
- Scherer, G. W. (1993) Freezing gels. *Journal of Non-Crystalline Solids*, 155, 1, pp. 1-25.
- Scherer, G. W. (1999) Crystallization in pores. *Cement and Concrete Research*, 29, 8, pp. 1347-1358.
- Sun, Z., Scherer, G. W. (2010) Effect of air voids on salt scaling and internal freezing. *Cement and Concrete Research*, 40, 2, pp. 260-270.
- Sýkora, J., Šejnoha, M., Šejnoha, J. (2013) Homogenization of coupled heat and moisture transport in masonry structures including interfaces. *Applied Mathematics and Computation*, 219, 13, pp. 7275-7285.
- Sýkora, J. (2014) Modeling of Degradation Processes in Historical Mortars. *Advances in Engineering Software*, accepted for publication.
- Tan, X., Chen, W., Tian, H., Cao, J. (2011) Water flow and heat transport including ice/water phase change in porous media: Numerical simulation and application. *Cold Regions and Technology*, 68, 1-2, pp. 74-84.
- Wardeh, G., Perrin, B. (2008) Numerical modelling of the behaviour of consolidated porous media exposed to frost action. *Construction and Building Materials*, 22, 4, pp. 600-608.
- Zuber, B., Marchand, J. (2000) Modeling the deterioration of hydrated cement systems exposed to frost action - Part 1: Description of the mathematical model. *Cement and Concrete Research*, 30, 12, pp. 1929-1939.

HUMAN SAFETY CRITERIA FOR EXISTING BRIDGES CONSIDERING EMERGENCY AND CRISIS SITUATIONS

M. Sykora, M. Holicky^{*}, R. Lenner^{**}, P. Manas^{***}

Abstract: Specification of the target reliability levels is a key issue of the assessment of existing bridges in emergency and crisis situations. ISO 2394 indicates procedures for specification of the target reliability by the total cost optimisation in conjunction with human safety criteria. Since the latter criteria often dominate the target reliability for existing structures, their application is discussed in detail focusing on conditions specific to emergency and crisis situations. For a reference period of one week the target reliability indices range mostly from 3.1 to 3.6, thus significantly lower than those applied in the design of new structures.

Keywords: Target Reliability, Human Safety, Existing Bridges, Emergency Situations.

1. Introduction

The target reliability levels in national and international documents for new and existing structures are inconsistent in terms of the recommended values and the criteria according to which appropriate values are to be selected. Almost no recommendations are available for temporary structures (Holicky, 2013) and for structures under temporary conditions including emergency and crisis situations.

In this study a general procedure for the assessment of target reliabilities of structures during emergency or crisis situations is developed. An emergency or crisis situation is assumed to last only few days or weeks. Target reliabilities discussed in the study are to be applied in the assessment of existing bridges in ultimate limit states when immediate decisions on permissions for crossing of heavy freights due to military and civilian traffic are needed and a bridge resistance cannot be readily increased.

Specification of the target reliability levels is required for the probabilistic assessment of existing bridges as well as modifications of partial factors used in a deterministic assessment. The reliability assessment in emergency or crisis situations is generally associated with a short duration and it should be considered that it may be difficult or even impossible to strengthen a bridge during such a limited period.

The target reliability levels recommended in *EN 1990:2002* for the basis of structural design are primarily intended for new structures; different reliability classes are associated with different consequences of failure. More detailed classification is given in *ISO 2394:1998* for the general principles on structural reliability where relative costs of safety measures are also taken into account. *ISO 13822:2010* for the assessment of existing structures indicates four target reliability levels for different consequences of failure. For instance moderate consequences are associated with the target reliability index (see *EN 1990*) $\beta = 3.8$, high consequences with $\beta = 4.3$. These values are related to “a minimum standard period for safety (e.g. 50 years)”. In addition *ISO 13822* indicates a possibility to specify the target reliability levels for existing structures by optimisation of the total cost in conjunction with the criteria for safety of people. Sykora and Holicky (2012) recognised that upgrades of existing structures are expensive and economic criteria yield lower optimum reliabilities than those required for human safety. Therefore, the present study is focused entirely on human safety criteria; cost optimisation for existing bridges in emergency and crisis situations is discussed by Sykora et al. (2014).

* Ing. Miroslav Sykora, PhD., Prof. Ing. Milan Holicky, PhD., DSc.: Klokner Institute, Czech Technical University in Prague, Solinova 7; 166 08, Prague; CZ, miroslav.sykora@klok.cvut.cz; milan.holicky@klok.cvut.cz

** Roman Lenner, MSc, PE.: Institute of Structural Engineering, University of Bundeswehr, 85577 Neubiberg, Germany; roman.lenner@unibw.de

*** Assoc. Prof. Pavel Mañas, PhD.: Faculty of Military Technology, University of Defence, Kounicova 65, 612 00 Brno, CZ, pavel.manas@unob.cz

2. Requirements on Individual Human Risk

General guidelines for the assessment of target reliabilities with respect to human safety are provided in *ISO 2394*. In principle, structural design and assessment of existing bridges are not distinguished. It is noted that a recent draft of this standard introduces new procedures to establish appropriate target reliabilities considering human safety on the basis of the Life Quality Index, Nathwani et al. (2009). Since further developments seem to be needed to facilitate practical applications of this approach, the present study deals with the principles provided in *ISO 2394:1998*.

ISO 2394 states that structural reliability is important first and foremost if people may be killed or sustain injuries as a result of the collapse. An acceptable maximum value for the failure probability might be found from a comparison of risks resulting from other activities. Individual lethal accident rates ranging between 10^{-6} and 10^{-5} per year (as accepted by Steenbergen and Vrouwenvelder (2010) and Sykora and Holicky (2012)), seem to be reasonable for structures in persistent design situations, when compared to the typical rates in industries, e.g.:

- 10^{-4} per year for work in all industries (2×10^{-4} for users of motor vehicles),
- 10^{-5} per year for third parties in ship industry (passengers or public ashore).

The overall individual lethal accident rate of 10^{-4} per year is a common value of reference; rates over 10^{-3} are deemed unacceptably high, Stewart (2011). For military situations Goldberg (2010) derived an individual lethal rate of 4×10^{-3} per year. Hostile actions, accidents, illnesses or self-inflicted actions for the Operation Iraqi Freedom in 2003-2006 were considered. In emergency and crisis situations higher risks may be acceptable since they may be compensated by a mitigation of consequences in endangered areas. Therefore, a tentative value of 10^{-3} per year is considered hereafter as associated with uncommon accidents, Melchers (2001). It is tacitly assumed that the safety of rescue corps members is endangered.

The concept of individual risk provided in *ISO 2394* then yields the following relationship between the target failure probability p_f and the conditional probability of occupant fatality p_1 , given the structural failure in emergency or crisis situation:

$$p_f \text{ (per year)} \leq 10^{-3} \text{ per year} / p_1 \quad (1)$$

With respect to the loss of human life, *EN 1990* distinguishes among low, medium, or high consequences (CC1-CC3, respectively). The conditional probabilities p_1 indicated in Fig. 1 for assessment of bridges classified in various CCs are based on a literature review and recommendations by Steenbergen and Vrouwenvelder (2010). For emergency and crisis situations, the target failure probabilities of a structural member, related to a reference period t_{ref} in years become:

$$p_f \leq 10^{-3} \text{ per year} / p_1 \times t_{ref} \quad (2)$$

Corresponding target reliability index is derived using the cumulative distribution function of the standardized normal distribution, $\beta = -\Phi(p_f)$. Fig. 1 shows the variation of target reliability index β with the conditional probability p_1 for different reference periods. It appears that the target reliabilities are affected by the conditional probability p_1 and more significantly by the reference period. Considering middle values of p_1 , the following target reliability indices may be considered:

- CC2 ($p_1 = 0.02$): $\beta = 3.1-2.6$,
- CC3 ($p_1 = 0.1$): $\beta = 3.6-3.1$

for reference periods from one week to one month, respectively. CC1 is not discussed hereafter as it is deemed irrelevant for most bridges. Regarding selection of an appropriate consequence class, background document to EN 1990 by CEN/TC250 (1996) indicates that a higher reliability level should be required for:

- a structure which is likely to collapse suddenly without a warning that would allow implementation of measures to avoid severe consequences,
- non-robust structural systems where a local failure may lead to a rapid progressive collapse.

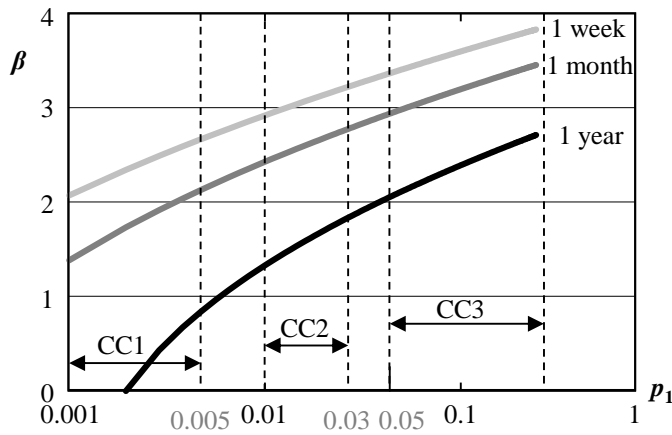


Fig. 1: Variation of β with the conditional probability p_1 for different reference periods.

3. Limitations of the Concept of Individual Risk

The aforementioned concept should be applied with uttermost caution. The target levels in Fig. 1 regard only safety of users of a bridge and fail to consider additional costs including life losses related to temporary bridge closure if the criterion is not fulfilled. The decision regarding the permission of heavy freight crossing depends on the case-specific conditions. In general, it should aim at balancing risks of users and risks of individuals endangered when the crossing is not permitted (see the example below).

Besides the individual risk concept, *ISO 2394* indicates that in many cases authorities explicitly intend to avoid accidents with a large number of fatalities and proposes an additional societal risk criterion based on an *F-N* curve. However, application of this criterion requires a case-specific approach and it is out of the scope of this paper to provide a general guidance in this regard. Moreover, Sykora and Holicky (2012) showed that the individual risk criterion is dominating over the societal criterion except for failures with vast collapsed areas.

4. Examples

4.1. Human safety not endangered when transport is not permitted

The application of the derived target reliabilities in conjunction with the partial factor method (*EN 1990*) is illustrated by a simple example. An excessively heavy freight is to be transported over a reinforced concrete bridge. It is assumed that the duration of an emergency situation is two weeks and the crossing is to be allowed at any time during this period, $t_{\text{ref}} = 0.038$ y. The bridge is classified in CC3 (high consequence for the loss of human life in the case of failure, failure occurring without previous warning as may be relevant for shear failure of reinforced concrete beam or buckling of bridge piers) and thus $p_1 \approx 0.1$. Human safety is not endangered when the transport is not permitted. However, the driver's safety is to be considered.

Equation (2) then leads to $p_f \leq 3.8 \times 10^{-4}$ and $\beta = 3.4$. Adjustment of partial factors using the β -value is straightforward; see Caspeele et al. (2013) and Sykora et al. (2013). For instance the partial factor for concrete compressive strength reduces from $\gamma_c = 1.5$ for structural design to about 1.3 in this case.

4.2. Human safety endangered when the transport is not permitted

Now it is assumed that the human safety is endangered when the transport is not allowed. This can be represented by the transportation of decontamination units in immediate response to an industrial or chemical explosion, or the transport of portable flood barriers. Two hazard scenarios are considered in the case when the transport is not permitted - an expert judgement suggests that:

- Scenario 1: it is "impossible" that there are ten fatalities in the endangered area (associated with probability of about 0.02, Budescu and Wallsten (1985)), related risk in terms of the expected number of fatalities is a product of the consequences and probability of unfavourable event, $R(\text{scenario 1}) = 10 \times 0.02 = 0.2$ (fatalities).

- Scenario 2: Provided that the event Scenario 1 does not occur (probability 1-0.02), it is “very unlikely” that there is a single fatality in the endangered area; the qualitative term “very unlikely” may be associated with probability of having a single fatality of about 0.15, Budescu and Wallsten (1985). The related risk is $R(\text{scenario 2}) = 1 \times 0.15 (1 - 0.02) = 0.15$ (fatalities).

The decision “not to permit the transport” thus relates to the total risk $R = R(\text{scenario 1}) + R(\text{scenario 2}) = 0.35$ (fatalities). When the transport is permitted, related risk should be lower than in the previous case:

$$p_f(1 \times p_1 + R) \leq R \quad (3)$$

where p_f = failure probability given the crossing. The term in brackets in equation (3) represents risks given failure of the bridge. Only a driver is assumed to be present on the bridge during the crossing. For $p_1 = 0.1$ (CC3) and $R = 0.35$, equation (3) yields an excessively high failure probability, $p_f \leq 0.78$ ($\beta < 0$). In this case the target reliability should be established on the basis of risk optimisation considering both economic and societal consequences of the bridge closure and potential bridge failure due to the transport.

5. Concluding Remarks

The target reliability levels recommended in various standards for new and existing structures are inconsistent; almost no recommendations are available for structures under temporary conditions including emergency and crisis situations. Target reliabilities related to these situations can be required for the assessment of existing bridges when immediate decisions on permissions for the crossings of heavy freights are needed. It may be appropriate to require lower target reliabilities for existing bridges than for new structures. In particular situations it needs to be clarified whether and what minimum levels of human safety should be considered. Human safety criterion leads to target reliability indices within the range from 3.1 to 3.6 for a reference period of one week.

Acknowledgements

This contribution is based on outcomes of the research projects VG20122015089 supported by the Ministry of the Interior of the Czech Republic and P105/12/0589 supported by the Czech Science Foundation. The study is partly based on a Ph.D. thesis by Lenner (2014).

References

- Budescu, D. V., Wallsten, T. S. (1985) Consistency in interpretation of probabilistic phrases. *Organ Behav Hum Decis Process*, 36, 3, pp. 391-405.
- Caspeele, R., Sykora, M., Allaix, D. L., Steenbergen, R. (2013) The Design Value Method and Adjusted Partial Factor Approach for Existing Structures. *Struct.Eng.Int.*, 23, 4, pp. 386-393.
- CEN/TC250 (1996) Background Document EC1: Part1: Basis of Design, 2nd draft. ECCS.
- Goldberg, M. S. (2010) Death and injury rates of U.S. military personnel in Iraq. *Mil.Med.*, 175, 4, pp. 220-226.
- Holicky, M. (2013) Optimisation of the target reliability for temporary structures. *Civ Eng Environ Syst*, 30, 2, pp. 87-96.
- Lenner, R. (2014) Safety Concept and Partial Factors for Military Assessment of Existing Concrete Bridges (PhD. Thesis). Neubiberg, Germany, Universität der Bundeswehr.
- Melchers, R. E. (2001) *Structural Reliability Analysis and Prediction*. Chichester, England, John Wiley & Sons Ltd.
- Nathwani, J. S., Pandey, M. D., Lind, N.C. (2009) *Engineering Decisions for Life Quality: How Safe is Safe Enough?* London, Springer-Verlag.
- Steenbergen, R. D. J. M., Vrouwenvelder, A.C.W.M. (2010) Safety philosophy for existing structures and partial factors for traffic loads on bridges. *Heron*, 55, 2, pp. 123-139.
- Stewart, M. G. (2011) Life-safety risks and optimisation of protective measures against terrorist threats to infrastructure. *Structure and Infrastructure Engineering*, 7, 6, pp. 431-440.
- Sykora, M., Holicky, M., Lenner, R., Manas, P. (2014) Target Reliability Levels for Existing Bridges Considering Emergency and Crisis Situations (accepted for publication). *AiMT*, 8, 1, pp. 14.
- Sykora, M., Holicky, M. (2012) Target reliability levels for the assessment of existing structures - case study, In: *Proc. IALCCE 2012* (A. Strauss, K. Bergmeister & D.M. Frangopol eds.), Vienna, CRC Press/Balkema, pp. 813-820.
- Sykora, M., Holicky, M., Markova, J. (2013) Verification of existing reinforced concrete bridges using the semi-probabilistic approach. *Eng.Struct.*, 56, 0, pp. 1419-1426.

MATHEMATICAL DESCRIPTION OF BEHAVIOUR OF A HUMAN BODY DURING WALKING – STANCE PHASE

V. Šána^{*}, M. Polák^{**}

Abstract: *The presented paper deals with a mathematical description of behaviour of a human body during walking. Especially the work is aimed at the stance phase of walking process, where the pedestrian's foot is in permanent contact with the ground. If we simplify the human body as a mass point, which is placed in the CoM (center of mass), we are able to state that the pedestrian is acting as an inverted mathematical pendulum, which means that mass of the pendulum hinge is neglected. Thus the vertical force component in the hinge of inverted pendulum corresponds to the time behaviour of the contact force experimentally observed. The simplified pedestrian model was considered as two dimensional, defined in the plane of walking. The solution of this problem was executed in the central gravity field.*

Keywords: Stance Phase of Walking, Inverted Pendulum Model, Runge – Kutta fifth-order method, Ground Reaction Force.

1. Introduction

The human walking is quite complex type of motion, therefore there were introduced some simple models, which allows the mathematical description of this problem by a system of the second-order differential equations. These models of passive walkers are the Rimless wheel model (Margaria, 1976) and the Bipedal walking model (Goswami et. al., 1997). Both of these models (or some of the other models) are based on the behaviour of the mathematical pendulum or inverted mathematical pendulum. This is the reason why the goal of this paper is the numerical study of behaviour of the inverted mathematical pendulum. Respectively it is aimed at the mathematical description of behaviour of a contact force during a stance phase of human gait cycle. The gait cycle is the periodical process, which could be divided into next phases, the stance phase and the swing phase. Detailed description of the human gait cycle was determined by (Vaughan, 1992).

2. Mathematical Modeling

Firstly the equations of motion of the inverted pendulum had to be deduced (see Fig. 1). These equations could be determined by a different approaches e.g. Newton's or D'Alambert approach. Note that the difference between these two assumptions is only in a process of assembling the equations of motion. The Newton's principle uses the principle of equivalence, where the acting force is proportional to the acting acceleration. On the other hand, the D'Alambert's principle takes into account a force of inertia and uses an equilibrium conditions. These procedures are appropriate for the simple or unconstrained dynamical systems. For more complex or constrained systems the Lagrange's analytical approach is more suitable. The equations of motion are derived from the Lagrange-Euler's equations

$$\frac{d}{dt} \left(\frac{\partial L}{\partial \dot{q}_i} \right) - \frac{\partial L}{\partial q_i} = 0 \quad i = 1, 2, \dots, n \quad (1)$$

^{*} Ing. Vladimír Šána : Faculty of Civil Engineering, Department of Mechanics, Czech Technical University in Prague, Thákurova 559/7; 140 00, Prague; CZ, vladimir.sana@fsv.cvut.cz

^{**} Prof. Ing. Michal Polák, CSc: Faculty of Civil Engineering, Department of Mechanics, Czech Technical University in Prague, Thákurova 778/9; 140 00, Prague; CZ, polak@fsv.cvut.cz

where L is the Lagrange's functional (Lagrangian), defined by the equation (3), \dot{q}_i and q_i are unknown generalized velocities and generalized spatial coordinates

$$L(t, q_i, \dot{q}_i) = T - U \quad (2)$$

where T is the kinetic energy of the whole system and U is the potential energy. The Lagrangian depends on generalized coordinates and its velocities and implicitly dependent on the time.

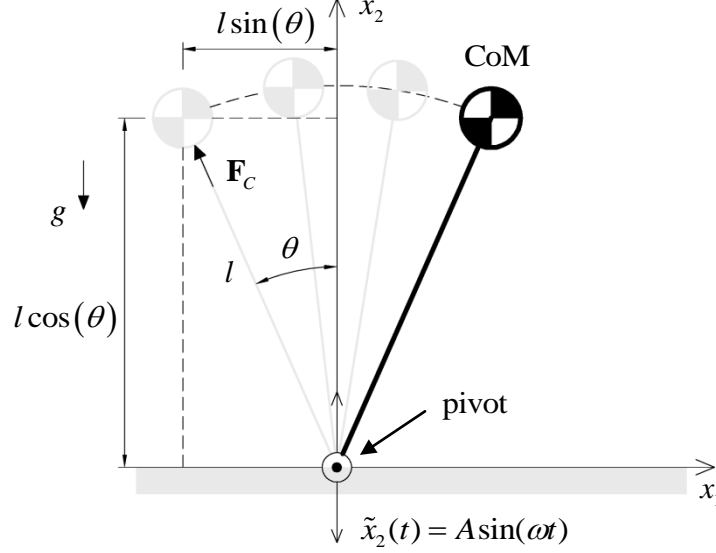


Fig. 1: The scheme of the inverted pendulum model with shaking pivot.

3. Derivation of the Equations of Motion of Inverted Pendulum Model

The well-known simple equation of motion of the inverted 2D pendulum with massless hinge is defined by the equation

$$\ddot{\theta}(t) - g/l \sin(\theta(t)) = 0 \quad (3)$$

where $\ddot{\theta}(t)$ is the angular acceleration, g is the gravitational acceleration, l is the length of the pendulum hinge and $\theta(t)$ is the angle. This second-order ODE could be linearized, with assumption that $\theta(t)$ is small, according to the Taylor-Mc Laurin's Series, thus $\sin \theta(t) \approx \theta(t)$. The system, described by the equation (3), is stabilized by the vertical harmonic motion of the pivot (see Fig. 1). This motion was considered as harmonic function, which is described by the formula

$$\tilde{x}_2(t) = A \sin(\omega t) \quad (4)$$

where A is the constant amplitude, ω is the circular frequency. If the shaking pivot is considered and appropriate time derivatives are executed (see equation (1)), the kinetic energy of the system could be written in the form

$$T = \frac{1}{2} ml^2 \dot{\theta}^2 + \frac{1}{2} m (\omega^2 A^2 \cos^2(\omega t) - 2\omega A \dot{\theta} l \cos(\omega t) \sin(\theta)) \quad (5)$$

And the potential energy of system as

$$U = mgl \cos(\theta) \quad (6)$$

After assembling the Lagrange's functional (2) and executing the appropriate partial and total derivatives (1) the equation of motion of the inverted pendulum stabilized by shaking pivot could be obtained as

$$\ddot{\theta}(t) - \sin(\theta(t)) (g/l - \omega^2 A/l \sin(\omega t)) = 0 \quad (7)$$

The range of stability was expressed via the Mathieu's equation which is described by relation

$$\frac{d^2\theta}{d\tau^2} + [\delta + \varepsilon \cos(\tau)]\theta = 0 \quad (8)$$

This equation was derived with assumption that θ is small and by using the substitution $\tau = \omega t$, $\delta = -\left(\frac{\omega_0}{\omega}\right)^2$ where $\omega_0^2 = g/l$ and $\varepsilon = \frac{A}{l}$. The stability is ensured if $\varepsilon/\sqrt{\delta} < \sqrt{2}$ (Smith, Blackburn et. al. 1992), note that the amplitude $A \ll L$.

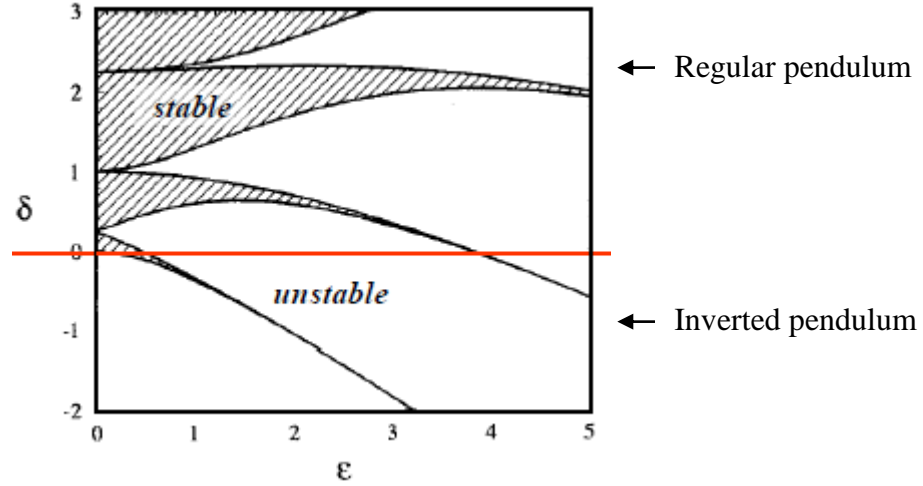


Fig. 2: The region of stability of regular and inverted pendulum (Smith, Blackburn et. al., 1992).

4. Numerical Solution

The numerical solution of the equation (7) was executed via the Runge-Kutta fifth order method with initial conditions $\theta(t) = -\pi/8$ rad and $\dot{\theta}(t) = 1.8$ rad \cdot s⁻¹. The relation between the angular and translational velocity is expressed as

$$v(t) = \dot{\theta}(t)l \quad (9)$$

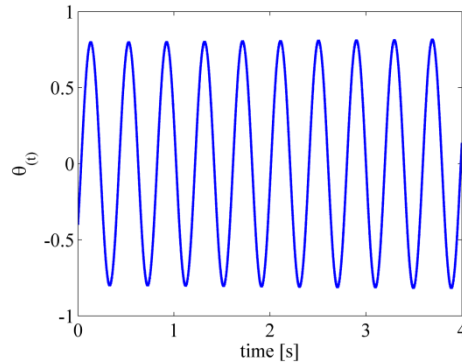


Fig. 3: Time behaviour of the angle $\theta(t)$ of stabilized inverted pendulum.

The vertical component of the ground reaction force (GRF) could be defined simply as

$$F_{x_2}^C = m\ddot{x}_{2CoM} + mg \quad (10)$$

where \ddot{x}_{2CoM} is the acceleration of the Center of the Mass (CoM) in vertical direction and mg is the force due to gravity. The vertical acceleration of the point mass was transformed into the polar coordinates by differentiation the relation $x_2 = l \cos(\theta)$ with respect to the time. Thus the GRF was obtained in the form

$$F_{x_2}^C = mg - ml(\ddot{\theta} \sin(\theta) + \dot{\theta}^2 \cos(\theta)) \quad (11)$$

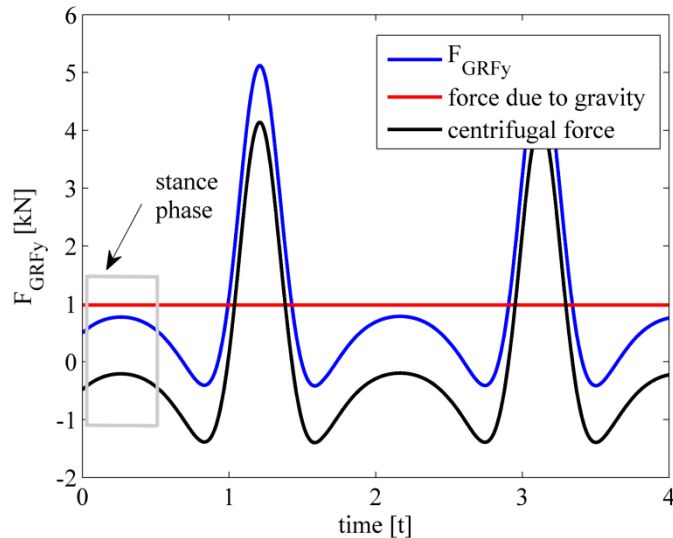


Fig. 4: Time behaviour of the vertical component of the GRF computed on model of inverted pendulum.

5. Conclusion

The mathematical description of the stance phase of human gait cycle was presented in this paper. Human body locomotion should be simplified and described by the movement of the inverted pendulum during a stance phase, which has been stabilized by the vertically vibrating pivot. The obtained time behaviour of the stabilized inverted pendulum is shown in the Fig. 3. As it is obvious from the Fig. 3 a stable periodic motion is obtained due to the stabilization process of the system described by the equation (7).

The numerical study of the inverted mathematical pendulum showed a good accordance with the assumption that the decrease of the contact force during a stance phase of walking occurs. The decrease of the GRF is caused by the transmission of the body weight of a pedestrian. Thus the model of the inverted pendulum provides a good mathematical description of behaviour of the human body during stance phase.

Acknowledgement

This paper has been created thanks to the project SGS OHK1-023/14 supported by the Czech Technical University in the Prague, which is gratefully acknowledged.

References

- Alexander, R. McN. (1992) Simple models of walking and jumping. *Human Movt Sci.* 11: 3-9.
- Smith, Blackburn, et. al. (1992) Stability and Hopf bifurcations in an inverted pendulum. *Am J. Phys.* 60(10).
- Brdička, M., Samek L., Sopko, B. (2005) *Continuum Mechanics*. ACADEMIA, ISBN 80-200-1344-X, Prague, (in Czech).
- Fangde, L. *Adaptive Motion Synthesis and Motor Invariant Theory*. Bournemouth University, United Kingdom. PhD. Thesis.
- Macur, M. (2010) *Introduction to analytical mechanics and continuum mechanics*. VUTIUM, ISBN 978-80-214-3944-3, Brno (in Czech).
- Anderson, F. C., Pandy, M. G. (2003) Individual muscle contributions to support in normal walking. *Gait and Posture*. 159-169.
- Pratt, E. J. *Exploiting Inherent Robustness and Natural Dynamics in the Control of Bipedal Walking Robots*. Massachusetts Institute of Technology, USA. PhD. Thesis.

LOCALIZATION PROBLEM OF COUPLED DUCTILE FAILURE MODELS COMPARED TO UNCOUPLED ONES

F. Šebek^{*}, P. Kubík^{**}, J. Petruška^{***}

Abstract: Comparison of accumulated damage field of coupled and uncoupled ductile damage models together with history of variables used in calibration process is presented in this paper. Using a non-linear damage accumulation in a local point of view, ductile failure criterion proposed by Xue is adopted and implemented into the Abaqus/Explicit via the user subroutine VUMAT for both types of models. Significant difference in localization between the coupled and uncoupled model is shown. The localization effect generally occurs when coupled models are used. One of the widespread practices to handle it is to use the non-local approach. In the other hand, we would not be able to predict a slant fracture without a certain degree of localization as shown in presented paper. Finally, the aluminum alloy 2024-T351 was examined.

Keywords: Localization, Ductile, Failure, Damage, Explicit.

1. Introduction

The ductile fracture has been observed and less or more appropriate failure models have been developed since the second half of the last century. Several different approaches have been evolved, as the Continuum Damage Mechanics (CDM), porosity based models, decohering zone models, empirical models, void nucleation, growth and linkage models and forming limit diagrams.

The basics of CDM were laid by Kachanov (1958) in the sense of creep. Coupled ductile model represents model where the plasticity is influenced by damage process and vice versa. On the contrary, uncoupled ductile models do not couple the plastic flow with damage accumulation, so only the damage process is affected by plasticity. These models are empirical and can be also called as phenomenological.

2. Outline of Applied Approach

The non-linear damage accumulation in a local point of view is adopted for comparison purposes. Next presumption is using von Mises yield condition for the plastic flow and assuming the material to be isotropic.

Xue (2007) developed new ductile failure criterion based on CDM in his doctoral thesis. At first, it is necessary to identify the flow curve and then six material constants through various experimental tests.

Here follows short outline of criterion proposed by Xue (2007) which we adopted. Equation describing the stress-strain relationship of matrix material is:

$$\sigma_M = \sigma_{y0} \left(1 + \frac{\bar{\varepsilon}_p}{\bar{\varepsilon}_k} \right)^n \quad (1)$$

where σ_M is the matrix stress, σ_{y0} is the initial yield stress, $\bar{\varepsilon}_p$ is the equivalent plastic strain, $\bar{\varepsilon}_k$ is the reference strain and n is the strain hardening exponent.

* Ing. František Šebek: Institute of Solid Mechanics, Mechatronics and Biomechanics, Faculty of Mechanical Engineering, Brno University of Technology, Technická 2896/2; 616 69, Brno; CZ, y107598@stud.fme.vutbr.cz

** Ing. Petr Kubík: Institute of Solid Mechanics, Mechatronics and Biomechanics, Faculty of Mechanical Engineering, Brno University of Technology, Technická 2896/2; 616 69, Brno; CZ, m3petr@gmail.com

*** Prof. Ing. Jindřich Petruška, CSc.: Institute of Solid Mechanics, Mechatronics and Biomechanics, Faculty of Mechanical Engineering, Brno University of Technology, Technická 2896/2; 616 69, Brno; CZ, petruska@fme.vutbr.cz

The yield condition is given as:

$$\bar{\sigma} - w\sigma_M \leq 0 \quad (2)$$

where w is a weakening factor dependent on the damage parameter D through:

$$w = 1 - D^\beta \quad (3)$$

where β is a material constant. Then, the damage evolution law for complex loading paths can be written as:

$$D = \int_0^{\bar{\varepsilon}_f} m \left(\frac{\bar{\varepsilon}_p}{\bar{\varepsilon}_f} \right)^{m-1} \frac{d\bar{\varepsilon}_p}{\bar{\varepsilon}_f} \quad (4)$$

where m is the damage exponent and $\bar{\varepsilon}_f$ is the fracture strain. The fracture depends on current stress state, thus, it is a function of pressure and Lode dependence:

$$\bar{\varepsilon}_f = \bar{\varepsilon}_{f0} \mu_p \mu_L \quad (5)$$

where $\bar{\varepsilon}_{f0}$ is the uniaxial tensile failure strain without confining pressure. Above functions of pressure and Lode dependence can be expressed through:

$$\mu_p = 1 - q \log \left(1 - \frac{p}{p_l} \right) \quad \text{and} \quad \mu_L = 1 + (1 - \gamma) |\bar{\theta}| \quad (6)$$

where q is the shape parameter, p is the pressure, p_l is the limiting pressure governing the cut-off value, γ is the fracture strain ratio and $\bar{\theta}$ is the normalized Lode angle.

3. Material Data

The aluminum alloy 2024-T351 was used and ductile failure criterion proposed by Xue (2007) were taken over with following material constants, $\bar{\varepsilon}_{f0} = 0.8$, $p_l = 800$ MPa, $q = 1.5$, $\gamma = 0.4$, $m = 2$, $\beta = 2$ (Xue, 2007).

We also took over the flow curve of matrix material fitted from tensile tests of smooth cylindrical specimens with 9 mm diameters. Material constants defining the stress-strain relationship follows here, $\sigma_{y0} = 300$ MPa, $\bar{\varepsilon}_k = 0.00769$ and $n = 0.185$ (Xue, 2007).

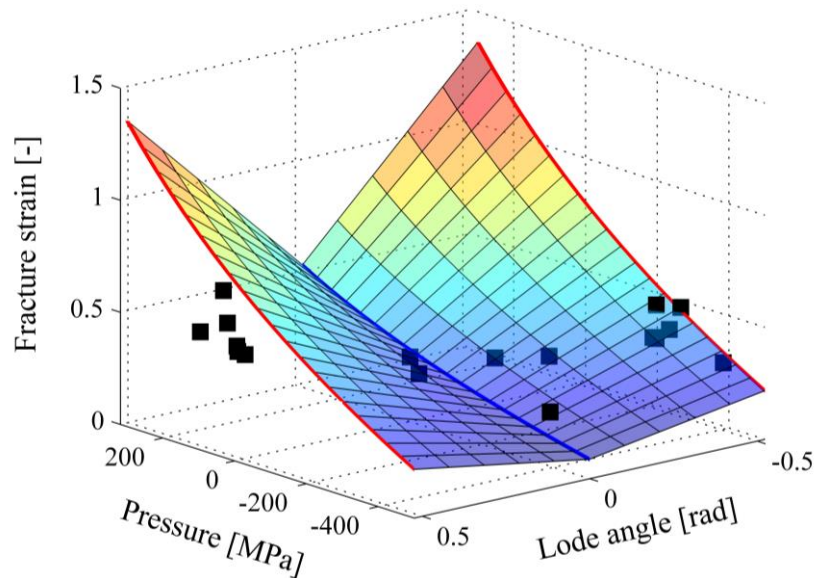


Fig. 1: Fracture envelope of criterion proposed by Xue (2007) for set of material constants taken over after Xue (2007).

The set of material constants listed above gives the fracture envelope shown in Fig. 1. Lou et al. (2013) reviewed experimental results of Bao and Wierzbicki (2004), Bai and Wierzbicki (2010) and Khan and Liu (2012). All these experimental results are placed in Fig. 1 as black squares. As one can see, the fracture strain of criterion proposed by Xue (2007) at axisymmetric compression is much higher than results reviewed by Lou et al. (2013).

4. Numerical Simulations

In this chapter, the numerical simulations of smooth and notched cylindrical specimens and double grooved specimen (Bao and Wierzbicki, 2004) are presented. First set of simulations was done using the criterion proposed by Xue (2007) and the second set for the same criterion but without weakening. The weakening factor was held unity in whole simulation, so the model was uncoupled.

Fields of damage parameter for coupled and uncoupled models immediately before and after the crack initiation are depicted in following Figs. 2-5.

In Fig. 6, the history of the pressure and the stress triaxiality is depicted because these variables influence the most the ductile fracture initiation and propagation.

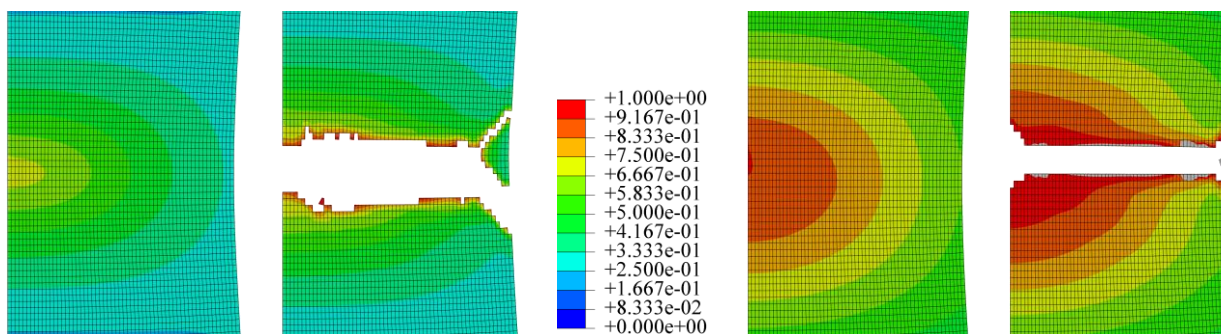


Fig. 2: Fields of damage parameter before and after initiation for smooth cylindrical specimen. At left due to coupled model and at right due to uncoupled one.

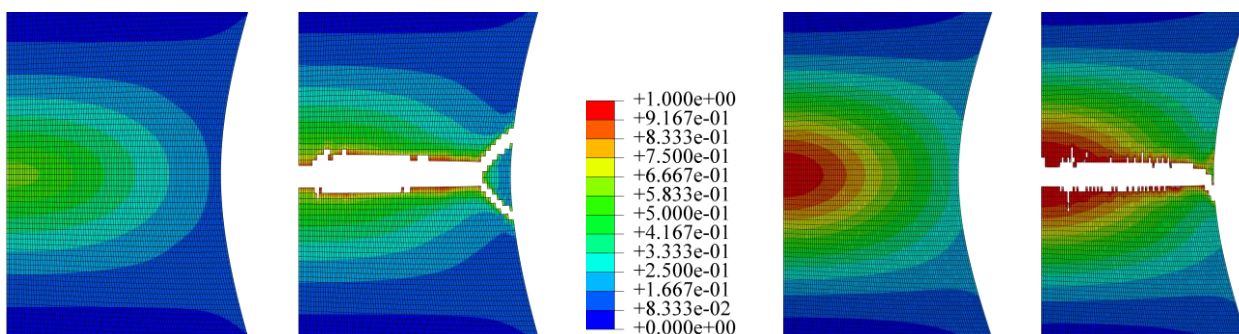


Fig. 3: Fields of damage parameter before and after initiation for notched cylindrical specimen with radius 12 mm. At left due to coupled model and at right due to uncoupled one.

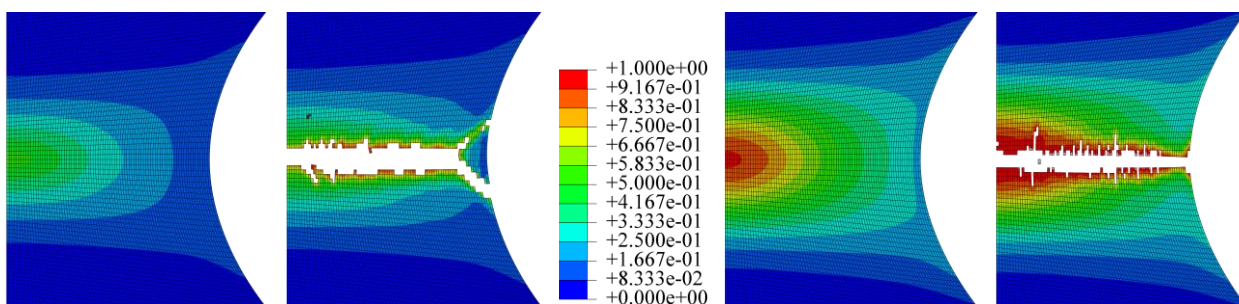


Fig. 4: Fields of damage parameter before and after initiation for notched cylindrical specimen with radius 4 mm. At left due to coupled model and at right due to uncoupled one.

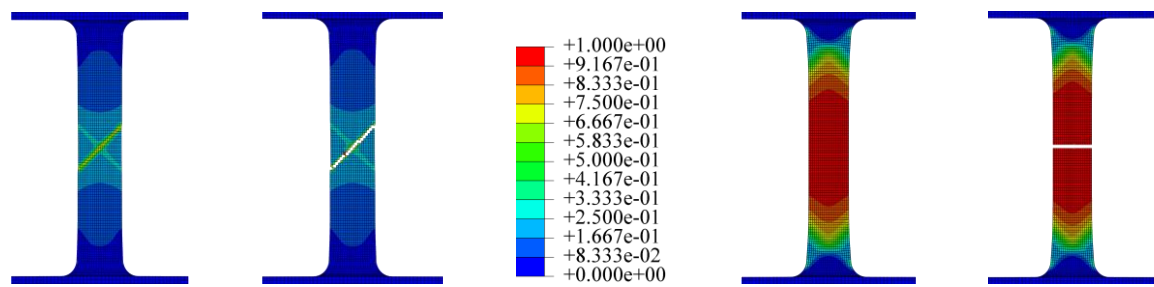


Fig. 5: Fields of damage parameter before and after initiation for double grooved specimen inducing plane strain. At left due to coupled model and at right due to uncoupled one.

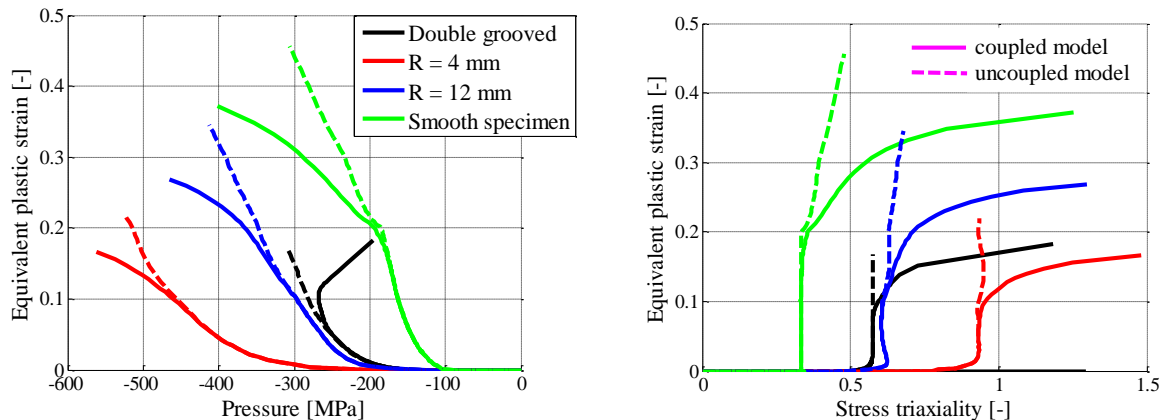


Fig. 6: History of the pressure and the stress triaxiality during straining.

5. Conclusions

Localization effect of coupled model in comparison to uncoupled one was presented. There is a strong localization in the case of coupled model due to coupling the fracture criterion with the flow rule. As shown, in the case of uncoupled model the localization effect did not occur. Therefore, such model is not able to predict the slant fracture, especially in the case of plane strain. It was also shown there is a significant difference in the loading history of the stress triaxiality between the coupled and uncoupled model. The coupled model shows considerable change in progress in the final part of the straining.

Acknowledgement

This work is an output of cooperation between grant project FSI-S-14-2311 and NETME Centre, regional R&D centre built with the financial support from the Operational Programme Research and Development for Innovations within the project NETME Centre (New Technologies for Mechanical Engineering), Reg. No. CZ.1.05/2.1.00/01.0002 and, in the follow-up sustainability stage, supported through NETME CENTRE PLUS (LO1202) by financial means from the Ministry of Education, Youth and Sports under the „National Sustainability Programme I“.

References

- Bai Y., Wierzbicki T. (2010) Application of extended Mohr–Coulomb criterion to ductile fracture. *International Journal of Fracture*, vol. 161, issue 1, pp. 1-20.
- Bao Y., Wierzbicki T. (2004) On fracture locus in the equivalent strain and stress triaxiality space. *International Journal of Mechanical Sciences*, vol. 46, issue 1, pp. 81-98.
- Kachanov L. M. (1958) Rupture time under creep conditions. *Izvestia Akademii Nauk SSSR, Otdelenie tekhnicheskich nauk*, vol. 8, pp. 26-31 (in Russian).
- Khan A. S., Liu H. (2012) A new approach for ductile fracture prediction on Al 2024-T351 alloy. *International Journal of Plasticity*, vol. 35, pp. 1-12.
- Lou Y., Yoon W. J., Huh H. (2013) Modeling of shear ductile fracture considering a changeable cut-off value for stress triaxiality, *International Journal of Plasticity*, in press.
- Xue L. (2007) *Ductile Fracture Modeling - Theory, Experimental Investigation and Numerical Verification*. PhD. thesis, Massachusetts Institute of Technology.

FRACTURE TOUGHNESS OF KAOLIN FIRED AT DIFFERENT TEMPERATURES

P. Šín^{*}, F. Sergejev^{**}, I. Štubňa^{***}

Abstract: The fracture toughness (FT) test was performed at room temperature on ceramic samples made from kaolin at temperatures of 400–1250 °C at a heating and cooling rate of 5 °C/min. The precrack was made by indentation under the loads 10–200 N, the dwell time was 45 s and the loading rate was 10 N/s. Results of the FT tests were in accordance with the changes in structure of the samples after the partial firings. The FT from 20 °C to 500 °C is almost constant and it varies between 0.1 MPa·m^{0.5} and 0.2 MPa·m^{0.5}. Dehydroxylation (420–600 °C) and solid state sintering (700–950 °C) does not influence the value of FT. At temperature interval where we assume liquid state sintering (1000–1250 °C) we observe an exponential increase of FT up to 0.6 MPa·m^{0.5}. From comparison of FT, Young modulus and flexural strength, a correlation and proportionality of these mechanical properties follows.

Keywords: Fracture toughness, Mechanical strength, Sintering, Dehydroxylation.

1. Introduction

Mechanical parameters are important characteristics of ceramic materials. Each ceramic product is mechanically stressed during technological processes as drying and firing as well as in actual service. For example it is known that increasing the temperature during a firing is only possible until the limit, when the thermomechanical stress is lower than the mechanical strength (Norton, 1970; Hanykýř, 2000).

Mechanical strength during firing was investigated in (Štubňa, 1992; Štubňa, 2011). Classical ceramics based on kaolinite and illite are presented in many fields of industry. Significant progress was made during the last few decades in increasing the mechanical strength of ceramic material.

Mechanical strength after firing at different temperatures was measured in (Štubňa, 2011). However, we did not find the results for fracture toughness (K_{Ic}) for kaolin in the literature in spite of the fact that kaolin plays a crucial role in such ceramics, e.g. in porcelain.

Ceramic materials are brittle. A lot of research is conducted to decrease the brittleness of advanced ceramics (Guo, 1996; Okabe, 2001). This brittleness may be judged indirectly by K_{Ic} which denotes material resistance to brittle fracture when a crack of critical size is present. The subscript Ic denotes the mode I crack opening under normal tensile stress perpendicular to the crack path. Brittle fracture is very characteristic for materials with low fracture toughness (Hertzberg, 1995). A related concept is the work of fracture (γ_{wof}), which is directly proportional to K_{Ic}^2 / E , where E is the Young's modulus of material (Dos Santos, 2003).

The aim of this contribution is to find out how K_{Ic} of the fired kaolin depends on the firing temperature.

* RNDr. Peter Šín, PhD.: Department of Physics, Faculty of Civil Engineering, Slovak University of Technology, Radlinskeho 11, 81368 Bratislava, Slovakia, peter.sin@stuba.sk

** Assoc. Prof. Ing. Fjodor Sergejev, PhD.: Department of Materials Engineering, Faculty of Mechanical Engineering, Tallinn University of Technology, Ehitajate tee 5, 12618 Tallinn, Estonia, fjodor.sergejev@ttu.ee

*** Assoc. Prof. Ing. Igor Štubňa, CSc.: Department of Physics, Faculty of Natural Sciences, Constantine the Philosopher University, A. Hlinku 1, 94974 Nitra, Slovakia, istubna@ukf.sk

2. Theoretical Background

For the surface crack method and the three-point-bending, we calculate the fracture toughness K_{Isc} from the following equation:

$$K_{Isc} = Y \left(\frac{3P_{max}S_0}{2BW^2} \right) \sqrt{a} 10^{-6} \quad (1)$$

where K_{Isc} = fracture toughness [$\text{MPa} \cdot \text{m}^{0.5}$], Y = stress intensity factor coefficient, P_{max} = breaking force [N], S_0 = outer span [m], B = side-to-side dimension of the test specimen perpendicular to the crack length (depth) [m], W = top to bottom dimension of the tested specimen parallel to crack length (depth) [m], a = crack depth [m], c = crack half width [m].

A precrack is a Vickers indentation at the load 10–200 N and dwell time 45 s. Therefore, the stress intensity factor coefficient is

$$Y_s = \frac{\sqrt{\pi}MH_1S}{\sqrt{Q}} \quad (2)$$

where $H_1 = 1 - (0.34 + 0.11a/c)(a/W)$ and $S = (1.1 + 0.35(a/W)^2)\sqrt{a/c}$, [ASTM C1421-10].

3. Experimental

Samples were made from kaolin, its chemical composition is in Tab. 1.

Tab. 1: Composition of Sedlec kaolin.

Component name	LOI	SiO ₂	Al ₂ O ₃	Fe ₂ O ₃	TiO ₂	CaO	MgO	K ₂ O	Na ₂ O
Weight %	12.95	45.80	37.31	0.98	0.17	0.58	0.46	1.17	0.58

Kaolin was crushed and sieved and a powder was mixed with water to obtain a plastic mass with 20 wt.% of water. Prismatic samples of the dimensions 5×5×20 mm were cut from the wet mass, dried in the open air for 5 days and then grinded and polished. The sets of 5 samples were fired at temperatures 400, 425, 450, 475, 500, 550, 600, 650, 700, 730, 760, 790, 820, 850, 880, 910, 950, 1000, 1050, 1100, 1150, 1200 and 1250 °C. The heating and cooling rate was 5 °C/min without soaking at the highest temperature.

After firing, the samples were polished with sandpaper No. 800 using a rotating machine. The final dimensions of the samples were close to 3×4×20 mm. The structure of material is highly porous with a net of open pores. The porosity varies from 32 % for green ceramics to 37 % at 500 °C and decreases to 5 % within an interval of 1000–1200 °C (Štubňa, 1997).

To make a precrack, an indentation was performed by hardness tester Zwick-Indtenc 5030 SKV in the middle of the 4×20 mm face using a load of 10–200 N and dwell time of 45 s. The diagonals of indentation were parallel with the sample sides. After that, the indentations were coloured with red dye penetrant ARDROX F6R for 10–60 min.

A fracture toughness test was performed on the Instron dynamic testing system 8516 under the loading rate of 10 N/s according to standard (ASTM C1421-10).

4. Results and Discussion

The dependence of the fracture toughness on the firing temperature is shown in Fig. 1. The standard deviation of K_{Ic} varies from 2 % to 18 %.

Similar graphs, as pictured in Fig. 2, were obtained for flexural strength and Young's modulus on samples made from a quartz porcelain mixture (50 wt. % of kaolin, 25 wt. % of feldspar, 25 wt. % of quartz) measured at the same conditions (Štubňa, 2010; Štubňa, 2011), see Fig. 2. Although the material composition of these samples is different, the processes in them and their consequences during heating are mainly determined by the reactions and structural changes in kaolinite (Norton, 1970; Hanykýř,

2000). Therefore, we can use the results presented in Fig. 2 for a qualitative explanation of the fracture toughness results pictured in Fig. 3. The fracture toughness, Young's modulus, and flexural strength have similar temperature dependences, as follows from Fig. 1 and Fig. 2, so they correlate together.

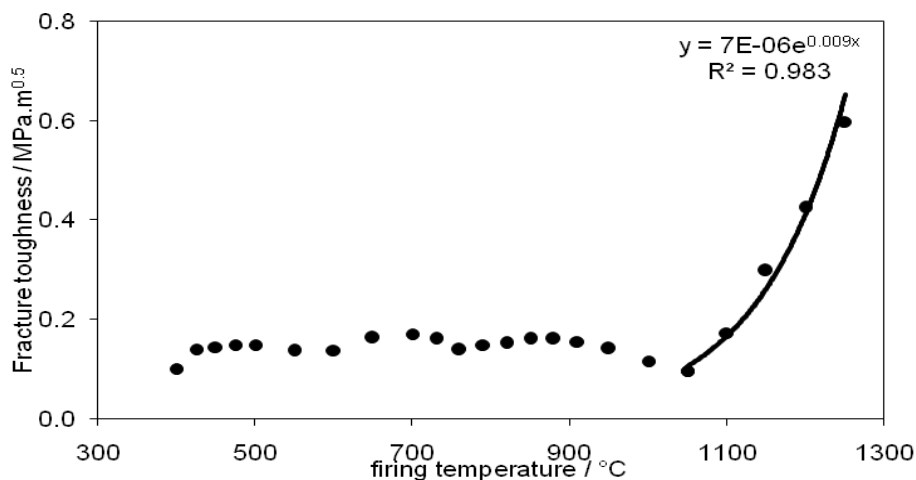


Fig. 1: The dependence of fracture toughness on firing temperature.

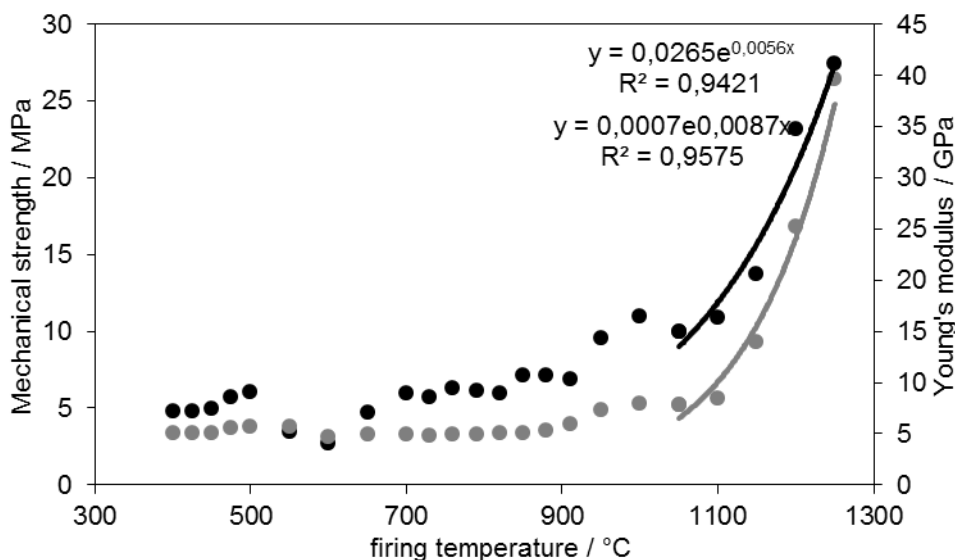


Fig. 2: The dependence of flexural strength (●) and Young's modulus (●) on firing temperature.

For the samples fired at 20–500 °C no changes in structure occurred at these low temperatures (Norton, 1970; Hanykýř, 2000), therefore the mechanical strength and Young's modulus, Fig. 2, are nearly constant in this range. The same is valid for the fracture toughness, as can be seen in Fig. 1.

For the samples fired at 500–700 °C, dehydroxylation, which weakens the kaolinite crystals, takes place. Metakaolinite created during dehydroxylation is a very porous material with internal vacancies (Freund, 1967) and lowers the mechanical properties of the samples. We observe a significant decrease of the mechanical properties within the temperature region of 500–700 °C, see Fig. 1, Fig. 2. We can assume that the kaolinite crystals are being rebuilt, so they become very defective during the dehydroxylation and this property remains even after cooling up to room temperature.

For samples fired at 1050–1250 °C, there is an exponential increase in the fracture toughness as well as the mechanical strength and Young's modulus increase dramatically. The solid-state sintering continues up to 1150 °C where feldspar begins to melt and a liquid-phase sintering starts. The samples contain a glassy phase, their density is higher, and this corresponds to higher values of the flexural strength measured at room temperature.

5. Conclusions

A development of the mechanical properties (fracture toughness, Young's modulus and flexural strength) of kaolin after the firing was experimentally studied at room temperature. It was found that:

1. Fracture toughness from 20 to 500 °C is almost constant and it varies between 0.1 and 0.2 MPa·m^{0.5}.
2. Dehydroxylation has a small influence on the value of the fracture toughness.
3. In the temperature interval 1000–1250 °C, where intensive sintering takes place, we observe an exponential increase of fracture toughness.
4. From a comparison of the fracture toughness, Young's modulus and flexural strength follows a correlation and proportionality.

Acknowledgement

This work has been supported by the grants VEGA 1/0464/12 Temperature influence on mechanical and thermophysical properties of building ceramic on the power plant ash basis and VEGA 1/0689/13 Hygric Deformation of Building Materials as well as by the Estonian target financed grant SF0140091s08. European Social Fund's Doctoral Studies and Internationalization Program DoRa also supported this research.

References

- ASTM C1421-10. Standard Test Method for Determination of Fracture Toughness of Advanced Ceramics at Ambient Temperature.
- Dos Santos, S. F., De Anchieta, R. J. (2003) Correlation between Fracture Toughness, Work of Fracture, and Fractal Dimensions of Alumina-Mullite-Zirconia Composites. *Materials Research*, 6, pp. 219-226.
- Freund, F. (1967) Kaolinite-metakaolinite, a Model of a Solid with Extremely High Lattice Defect Concentration. *Berichte Deutsche Keramische Gesellschaft*, 44, pp. 5-13.
- Guo, J. K. (1966) Stress Design of the Ceramic Grain Boundary. *Materials Chemistry and Physics*, 43, pp. 99-102.
- Hankýř, V., Kutzendorfer, J. (2000) Ceramic technology. Silis Praha a Vega, Hradec Králové, Praha, (in Czech).
- Hertzberg, R. W. (1995) Deformation and Fracture Mechanics of Engineering Materials (4th Edition). Wiley, New York.
- Norton, F. H. (1970) Fine Ceramics – Technology and Application. McGraw-Hill Book Co., New York.
- Okabe, N. (2001) Application Technique and Evaluation for Functional and Structural Design of Ceramics. *Journal of the Ceramic Society of Japan*, 109, 12, pp. S135-S143.
- Štubňa, I., Kozík, T., Hanic F. (1992) Young's Modulus and Mechanical Strength of Porcelain at the Firing Cooling Stage. *Ceramics International*, 18, pp. 353-354.
- Štubňa, I., Kozík, T. (1997) Permeability of the Electroceramics to Gas and Its Dependence on the Firing Temperature. *Ceramics International*, 23, pp. 247-249.
- Štubňa, I., Trník, A., Chmelík, F., Vozár L. (2011) Mechanical Properties of Kaolin-base Ceramics during Firing. *Materiali in Tehnologie*. InTech Open Access Publisher, Rijeka, pp. 229-244.
- Štubňa, I., Trník, A., Šin, P., Sokolář, R. (2011) Relationship between Mechanical Strength and Young's Modulus in Traditional Ceramics. *Materiali in Tehnologie*, 45, 4, pp. 375-378.
- Štubňa, I., Šin, P., Trník, A., Vozár, L. (2010) Relationship between Mechanical Strength and Young's Modulus in Traditional Ceramics. *Proc. Material-Acoustics-Place*, Slovak University of Technology, Zvolen, pp. 121-126.

NUMERICAL SIMULATION OF VIDEOKYMOGRAPHIC IMAGES FROM THE RESULTS OF THE FINITE ELEMENT MODEL

P. Švancara^{*}, J. Horáček^{**}, T. Martínek^{***}, J. G. Švec^{****}

Abstract: *The study presents a two-dimensional (2D) finite element (FE) model of the fluid-structure-acoustic interaction during flow induced self-oscillation of the human vocal folds. The FE model combines the FE models of the vocal folds, the trachea and the simplified human vocal tract shaped for phonation of vowel [a:]. The fluid-structure interaction is solved using explicit coupling scheme with separated solvers for structure and fluid domain. The developed FE model comprises large deformations of the vocal-fold tissue, vocal-fold contact, fluid-structure interaction, morphing the fluid mesh according to the vocal-fold motion (Arbitrary Lagrangian-Eulerian approach), solution of unsteady viscous compressible airflow described by the Navier-Stokes equations and airflow separation during the glottis closure. The effect of lamina propria thickness and material properties on simulated videokymographic (VKG) images of vocal-fold vibrations are analyzed. Such variation of the lamina propria properties can be caused by certain vocal-fold pathologies such as Reinke's edema. The developed FE model can be used to study relations among pathological changes in vocal folds tissue, the resulting VKG images and the produced sound spectra.*

Keywords: Biomechanics of voice, Videokymography, Simulation of phonation, Fluid-structure-acoustic interaction, Finite element method.

1. Introduction

Human voice production should be considered as a fluid-structure-acoustic interaction problem, where acoustic waves propagating through the vocal tract are generated by the flow-induced vibrations of the vocal folds. In literature some experimental models of this problem have been published (Titze, 2006). Published computational models include reduced-order models (Horáček et al., 2005), models of flow (Zhao et al., 2002) and finite element (FE) models (Zheng, et al., 2011). Advantage of FE models is their ability to deal with complex geometry of the vocal folds and vocal tract and ability to solve fluid-structure-acoustic interaction.

In recent works of the authors (Švancara et al., 2011; Švancara et al., 2012) a three-dimensional (3D) FE model of flow-induced oscillations of the vocal folds in interaction with acoustic spaces of the vocal tract was developed. This paper presents newly developed 2D FE model of phonation using in literature widely used M5 geometry of the vocal folds (Scherer et al., 2001), four-layers vocal fold structure, much finer FE mesh for the airflow modelling and construction of VKG images resulting from this 2D FE model. Videokymography is a high-speed imaging technique for investigation of vocal folds vibrations, which is widely used in clinical practise (Švec and Schutte, 1996).

2. Method

The 2D FE model was developed using the program system ANSYS 14.5. The geometry of the left vocal fold according Scherer's M5 geometry is shown in Fig. 1a. Model allows variation of lamina propria

* Ing. Pavel Švancara, PhD.: Institute of Solid Mechanics, Mechatronics and Biomechanics; Brno University of Technology; Technická 2896/2; 616 69, Brno; CZ, svancara@fme.vutbr.cz

** Ing. Jaromír Horáček, DSc.: Institute of Thermomechanics; Academy of Sciences of the Czech Republic; Dolejškova 1402/5; 182 00, Prague; CZ, jaromirh@it.cas.cz

*** Ing. Tomáš Martínek: Institute of Solid Mechanics, Mechatronics and Biomechanics; Brno University of Technology; Technická 2896/2; 616 69, Brno; CZ, y107940@stud.fme.vutbr.cz

**** RNDr. Jan G. Švec, PhD.: Department of Biophysics; Palacky University Olomouc; 17. listopadu 12; 771 46, Olomouc, CZ, svecjang@gmail.com.cz

thickness (parameter T_{SLP}) in range 0.15-1.8 mm. Fig. 1b shows the FE model of the four layered tissue of the vocal folds. The FE model of the trachea and the simplified acoustic spaces of the human vocal tract shaped for simulation of phonation of vowel [a:] is shown in Fig. 1c. The model of the vocal tract for the Czech vowel [a:] was created by converting data from magnetic resonance images (MRI) (Radolf, 2010). The vocal folds are modelled by a four layered tissue – epithelium, lamina propria, ligament and muscle with homogenous and isotropic material of each layer.

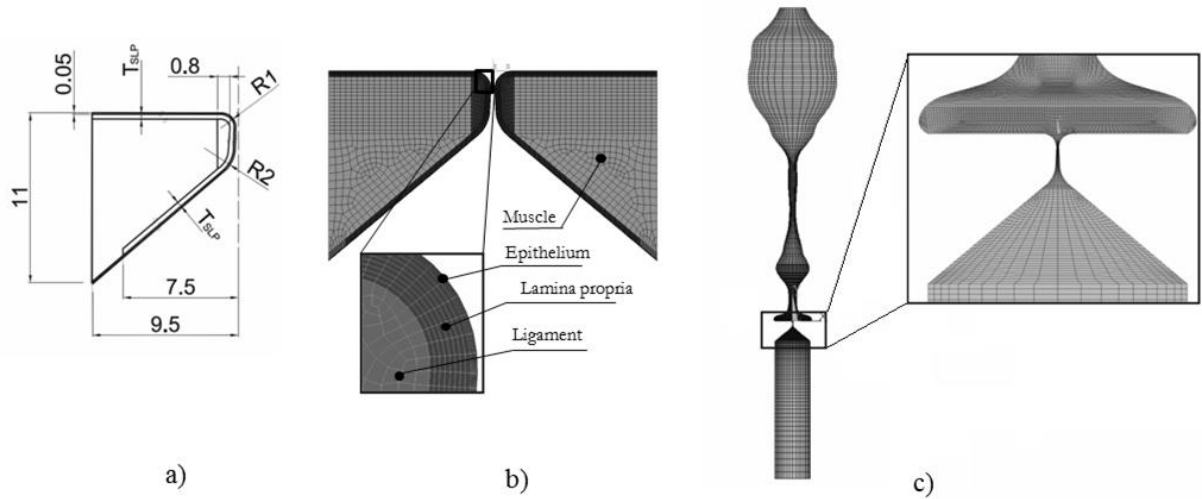


Fig. 1: a) Geometry of the left vocal fold; b) FE model of the four layered tissue of the vocal folds; c) FE model of the acoustic spaces of the trachea and the vocal tract for Czech vowel [a:].

FE model consists of 4014 linear 3-node and 4-node structural elements and 11206 linear 4-node fluid elements. Before the fluid-structure interaction simulation starts the vocal folds are pushed slightly into the contact. Contact of the vocal folds was modelled by the symmetric surface to surface contact pair elements on faces of the vocal folds. Proportional (Rayleigh) structural damping with dimensionless coefficients $\alpha = 110$ and $\beta = 3 \times 10^{-4}$ was used for all layers.

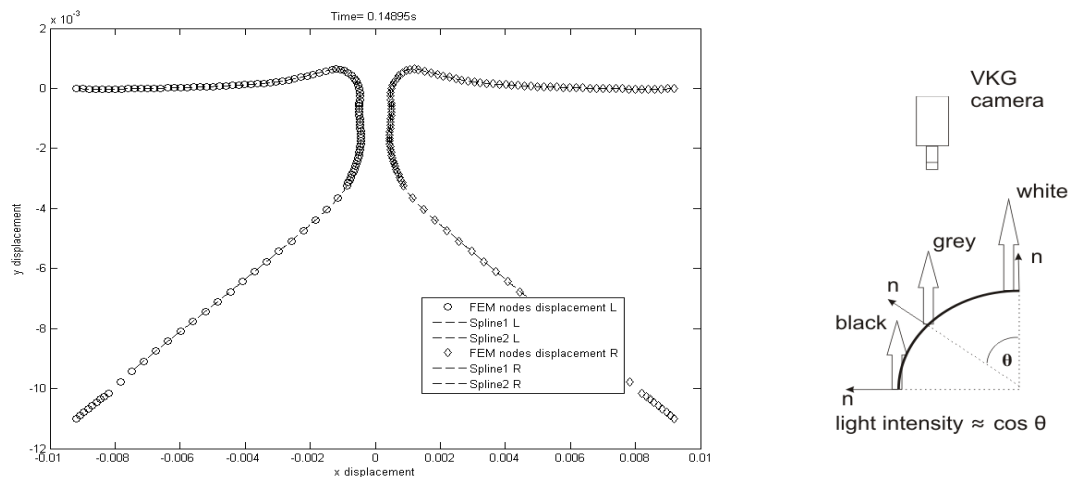


Fig. 2: Interpolation of computed positions of FE nodes by splines (left) and a schematic of the reflected light intensity using a cosine emission law (right- according to Horáček et al., 2009).

The fluid-structure interaction is solved using explicit coupling scheme with separated solvers for structure and fluid domain. The results of the airflow solution are transferred as loads on the vocal folds surface, then the vocal folds motion is computed, then the fluid mesh is morphed according to the vocal fold movement and then again the fluid flow is solved. For solving the moving boundaries of the fluid domain the Arbitrary Lagrangian-Eulerian (ALE) approach is used. The vibrations of the vocal folds was computed by a transient analysis with a time step $\Delta t = 1.5 \times 10^{-4} s$, taking into account the large deformations of the vocal fold tissue and vocal fold collisions. The airflow was solved as unsteady viscous compressible and laminar flow using transient analysis with the same time step as vocal folds

movement solution. For modelling the acoustic wave propagation in fluid domain, the compressible Navier-Stokes equations were utilized. A constant airflow velocity at the entrance to the subglottal space was prescribed as driving parameter and zero acoustic pressure was prescribed on the upper end of the vocal tract in order to simulate radiation into the open space.

For simulation of VKG images from the results of the FE model, a special program was developed in Matlab. The program first interpolates computed positions of FE nodes on vocal folds surface by splines to achieve better spatial resolution (see Fig. 2). A shape-preserving piecewise cubic interpolation is used with spatial resolution $1 \times 10^{-5} m$. And then the emission cosine law is used for computation of light intensity reflected from the visible vocal-fold surface depending on the surface angle.

3. Results and Discussion

Fig. 3 shows an example of computed displacements in x and y directions of selected nodes on the face of the left and right vocal fold for the model with thickness of lamina propria $T_{SLP}=1.35 mm$. The first nodes were located on the top margin of the vocal folds and the second ones on the bottom margin. From the results we can see that oscillations of the vocal folds are symmetric and are stabilized after first few periods of the transient regime. We could also see a phase delay in displacement in x direction between the nodes on the top and bottom margins of the vocal folds. It is a result of upward-propagating mucosal wave (Titze, 2006). Displacements in y direction for nodes on top margin for the left and right vocal fold are exactly the same so curves in graph lying on each other. Same situation is for the displacements in y direction of the nodes on bottom margin.

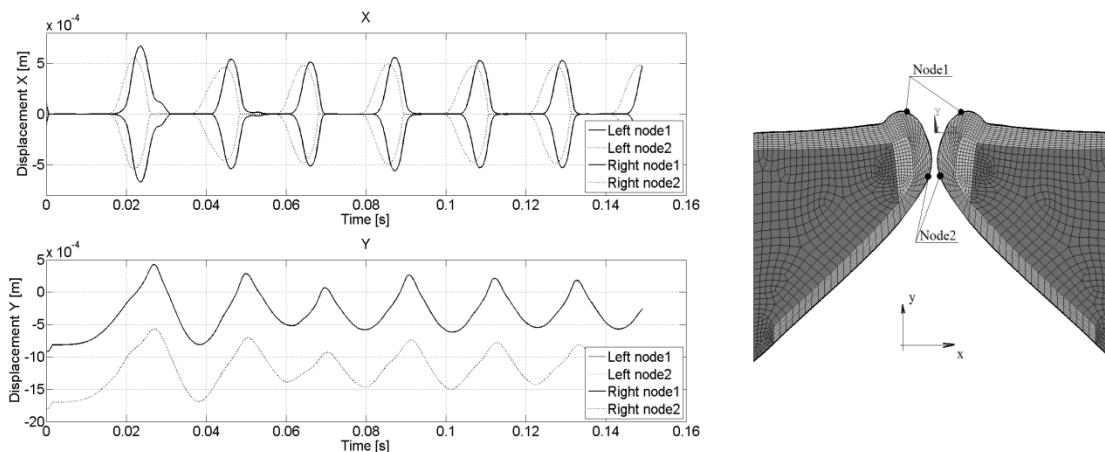


Fig. 3: Computed displacements in x and y directions of selected nodes on the face of the left and right vocal fold.

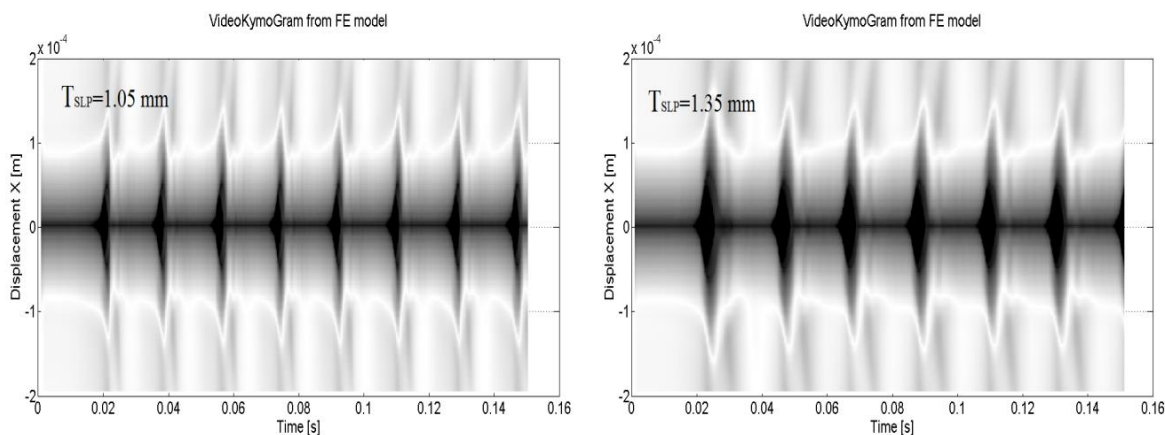


Fig. 4: VKG images created from the FE modelling results for model with thickness of lamina propria 1.05 mm (left) and 1.35 mm (right).

Example of a VKG images created from the results of FE modelling for the model with thickness of lamina propria TSLP = 1.05 mm and TSLP = 1.35 mm is shown in Fig. 4. The results show that with increasing thickness of lamina propria maximum gap between open vocal folds is increasing, time when vocal folds are open (open quotient) is increasing, there is more rounded transition from opening to closing phase and the vocal folds change more clearly their shape from convergent to divergent during one oscillation period. When the Young modulus of the lamina propria and their damping is decreased then more prominent mucosal wave can be observed.

4. Conclusions

A two-dimensional FE model of the vocal fold self-oscillations in interaction with the vocal tract acoustics was created. Computed results showed that prescribed constant airflow velocity at the entrance to the subglottal space produce vocal folds self-oscillations that are symmetric and stabilized after first few periods of the transient regime. The used compressible Navier-Stokes equations capture acoustic wave propagation phenomena in fluid and therefore a complete fluid-structure-acoustic interaction is modelled. Numerically simulated results show very close similarities with real human voice production, i.e. fundamental oscillation frequency, mean subglottal pressure and acoustic resonances corresponding to the formants of the vocal tract cavities. Also VKG images created from the results of FE modelling shows close similarities to those observed laryngoscopically in real human vocal folds.

Acknowledgement

This research is supported by the Grant Agency of the Czech Republic by the project No P101/12/1306 and by the European Social Fund Projects OP VK CZ.1.07/2.4.00/17.0009.

References

- Titze, I. R. (2006) *The Myoelastic Aerodynamic Theory of Phonation*, National Centre for Voice and Speech, Denver and Iowa City.
- Horáček, J., Šidlof, P., Švec, J. G. (2005) Numerical simulation of self-oscillations of human vocal folds with Hertz model of impact forces. *Journal of Fluids and Structures*, 20, pp. 853-869.
- Zhao, W., Zhang, C., Frankel, S. H., Mongeau, L. (2002) Computational aeroacoustic of phonation, part I: Numerical methods, acoustic analogy validation, and effects of glottal geometry, *Journal of the Acoustical Society of America*, 112, pp. 2134-2146.
- Zheng, X., Mittal, R., Xue, Q., Bielamowicz, S. (2011) Direct-numerical simulation of the glottal jet and vocal-fold dynamics in a three-dimensional laryngeal model. *Journal of the Acoustical Society of America*, 130, 1, pp. 404-4015.
- Švancara, P., Horáček, J., Hrůza, V. (2011) FE modelling of the fluid-structure-acoustic interaction for the vocal folds self-oscillation. In: *Vibration Problems ICOVP 2011* (Náprstek, J., Horáček, J., Okrouhlík, M., Marvalová, B., Verhulst, F., Sawicki, J., eds.), Springer, Berlin, pp. 801-807.
- Švancara, P., Horáček, J., Švec, J. G. (2012) Numerical Simulation of the self-oscillations of the vocal folds and of the resulting acoustic phenomena in the vocal tract. In: *Advances in Mechanisms Design* (Beran, J., Bílek, M., Hejnová, M., Žabka, P., eds.), Springer, Dordrecht, pp. 357-363.
- Scherer, R. C., Shinwari, D., De Witt, K. J., Zhang, C., Kucinski, B. R., Afjeh, A. A. (2001). Intraglottal pressure profiles for a symmetric and oblique glottis with a divergence angle of 10 degrees. *Journal of the Acoustical Society of America*, 109, 4, pp. 1616-1630.
- Švec, J. G., Schutte H. K. (1996) Videokymography: high-speed line scanning of vocal fold vibration. *Journal of Voice*, 10, pp. 201-205.
- Radolf, V. (2010) Direct and inverse task in acoustics of the human vocal tract. PhD. Thesis, Faculty of Mechanical Engineering, Czech Technical University, Prague, 95 p.
- Horáček, J., Švec, J. G., Šidlof, P. (2009) Numerical simulation of videokymographic images of self-oscillating vocal folds. In: *Proc. 3rd Advanced Voice Function Assessment International Workshop*, EUIT Telecomunicación, Madrid, pp. 13-16.

INNOVATIVE MODULAR PNEUMATIC VALVE TERMINAL WITH SELF-DIAGNOSIS, CONTROL AND NETWORK COMMUNICATIONS

J. E. Takosoglu^{*}, P. A. Laski^{**}, S. Blasiak^{***}

Abstract: *The main objective of our research project was to design an innovative modular pneumatic valve terminal with self-diagnosis, control system and industrial network communications for process control, in which for safety or sensitivity reasons of the process is required to confirm switching the valves. Valve terminal with an integrated electronic system allows, depending on the type of device confirmation of function of the valves, control of the valves, control of the logic states, pressure measurement, valves diagnostics. Depending on demand will be available three types of the valve terminal: basic, control and diagnostic. Diagnostic type of valve terminal integrates the functions of two previous types valve terminal and expands the functions about self-diagnosis and troubleshooting.*

Keywords: Pneumatic valve terminal, Self-diagnosis, Directional pneumatic valve, Energy saving systems.

1. Introduction

Currently, there is Directive of the European Parliament and Council called machinery directive and safety standards harmonized with the Machinery Directive type A, B, B2, C for companies involved the design and / or producing and / or marketing of commercial machines. Adapting to these requirements is now an integral part of the activity of each legal entity engaged in the machines within the European Economic Area (EU Member States plus Norway, Iceland, Liechtenstein and Switzerland). There are requirements that must be met by the machine, their failure is associated with the possibility to hold accountable (Directive on the liability for defective products 85/374/EEC and Directive 1999/34/EC amending it). The reason why the market partners (employers, insurance companies, administration, technical supervision) are interested in applying the provisions of the Directives, is the expectation to meet the requirements for products, enabling fair competition when placing products to trading on the single European market (which is an essential part of enabling free movement of goods) and the safety of users.

The development of automation and robotics has contributed to an increased interest in electro-pneumatic servo-drives, which are highly dynamic, reliable, and cheap to manufacture. However, their application to industrial robots and manipulators is limited due to unsatisfactory positioning accuracy, with this problem being difficult to solve in the case of pneumatic systems (Takosoglu et al., 2009; Takosoglu and Laski, 2011; Takosoglu et al., 2012). Therefore pneumatic directional control valves are widely and commonly used on production lines in simple automation systems. Function of pneumatic directional control valves is separation the compressed air stream between the flow surfaces of the outputs (Gerc, 1973; Szenajch, 1997). Such constructions do not return information specifying the position of the piston in the valve, and thus does not possibility of diagnosis failure of the valve and drive. The systems used to control the fluid drives do not have direct safety circuits confirming switching the valve. In the fluid systems should be the following safety features: off under pressure, reducing pressure and force, venting, speed limit, movement

* Dr Jakub Takosoglu, PhD.: Kielce University of Technology, Faculty of Mechatronics and Machine Design, Department of Mechatronics Devices, Aleja Tysiąclecia Państwa Polskiego 7, 25- 314 Kielce, Poland, qba@tu.kielce.pl

** Dr Paweł Łaski, PhD.: Kielce University of Technology, Faculty of Mechatronics and Machine Design, Department of Automation and Robotics, Aleja Tysiąclecia Państwa Polskiego 7, 25- 314 Kielce, Poland, pawell@tu.kielce.pl

*** Dr Sławomir Błasiak, PhD.: Kielce University of Technology, Faculty of Mechatronics and Machine Design, Department of Mechanical Technology and Metrology, Aleja Tysiąclecia Państwa Polskiego 7, 25- 314 Kielce, Poland, sblasiak@tu.kielce.pl

without danger, stopping, holding and blocking the action, reversing the direction of movement, protection against unexpected starting.

2. Design of Pneumatic Valve Terminal

Designed valve terminals will be equipped with components which provide:

Status checks of controls elements:

- confirmation of switching the valves,
- reading logic states of IO modules,
- parameters measurement of controlled elements.

Control of driving systems:

- switching the valves
- change the logic states.

Diagnostics of processes and valves:

- parameters checking,
- errors indication,
- valve diagnostics,
- diagnostics of selected states of the process.

All available functions of pneumatic valve terminal operate in real time (Blasiak et al., 2013). Fig. 1 shows the module of pneumatic control valve in cross section.

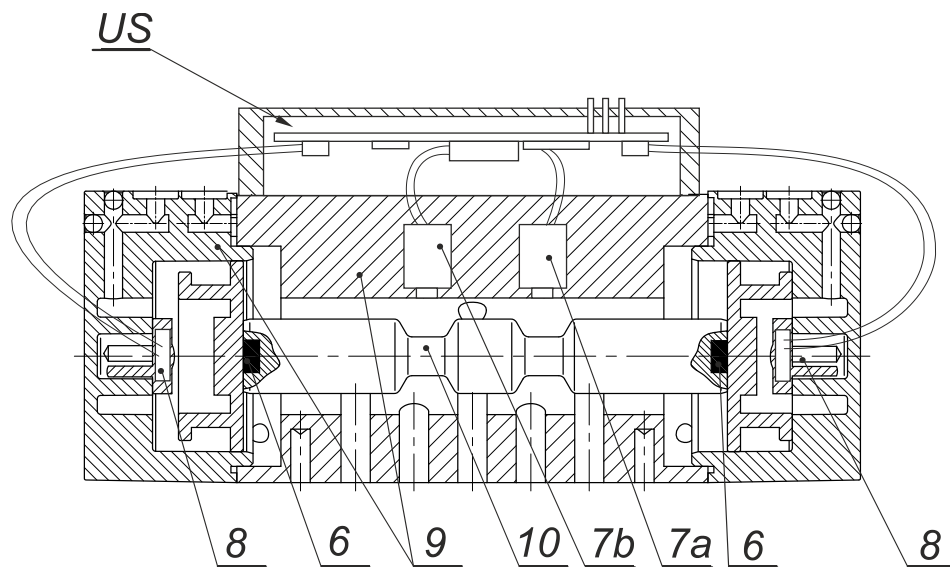


Fig. 1: Cross section of pneumatic control valve: US – control system, 6 – permanent magnets, 8 – magnetic sensors, 9 – valve body, 10 – valve piston.

Due to industrial demand, valve terminals will be characterized by a modular structure. This allows to apply the device to the proper process. The designed device will consist of the following electronic modules:

- main controller module,
- communication module,
- dedicated modules of pneumatic valves,
- universal IO modules,
- universal AI AO modules,
- DC motors modules and servo drives modules.

Fig. 2 shows a schematic diagram of the control system of the double acting pneumatic cylinder by using of the proposed innovative modular pneumatic valve terminals with self-diagnosis, control and communications network.

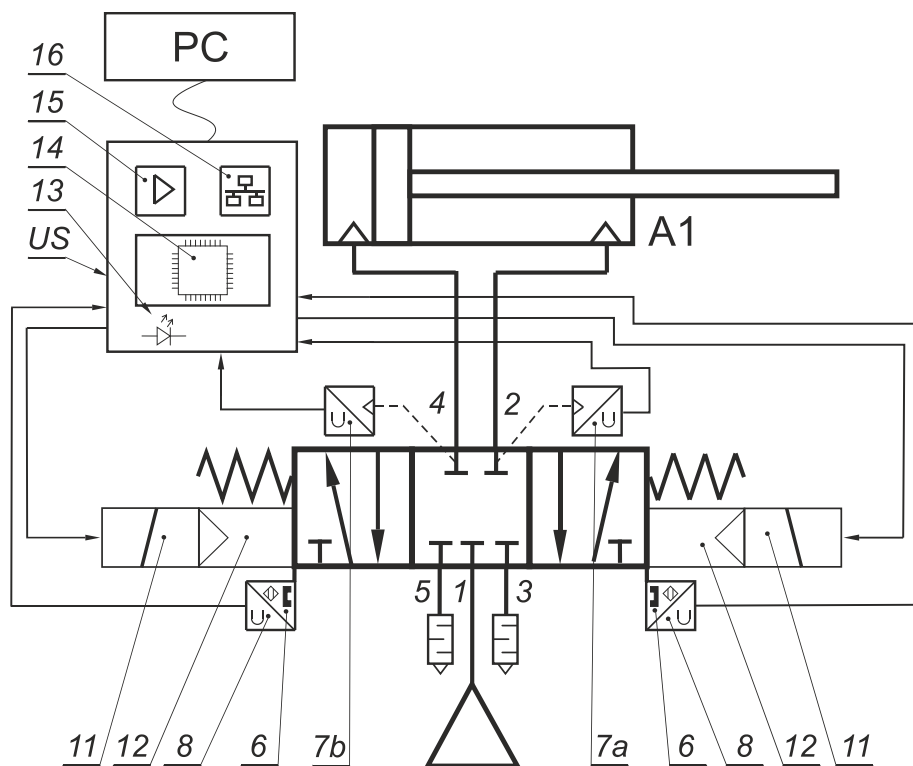


Fig. 2: Schematic diagram of the control system of pneumatic cylinder.

In the body 9 of the valve are flow ways 1, 2, 3, 4, 5, and a piston 10, where on ends, are mounted permanent magnets 6. In the body 9 are a pressure sensors 7a, 7b placed in the chamber, which space is connected to the outputs 2 and 4 of the valve. The pressure sensors are connected to the AD transducer of the US control system. The coil 11 controls the pre-valve 12. After applying the voltage to the coil 11, the pre-valve is switched and compressed air moves the piston valve 10 to one of the end positions. Moving the piston causing opening the flow surface and air flow to the one of the two outputs (2 or 4), depending on the position (left or right) of the piston 10. The magnetic sensors 8 detect the position of the permanent magnets 6 installed on the ends of the piston 10. This is confirmed the position of the piston valve, and is the equivalent to total valve switching. In outputs 2 and 4 by means of sensors 7a and 7b is measured pressure. The pressure measurement and confirmation of the end positions of the piston 10 carries out self-diagnostics, safety features, and self-monitoring of the control valve. The control system US contains a microcontroller equipped with AD transducers and connected to amplifiers. To the AD transducers are connected magnetic sensors 8, and pressure sensors 7a, 7b. Amplifiers 15 are connected to the coils 11 of the pre-valve 12. The microcontroller 14 is connected to the network communication module 16, and optical indicator LED 13. The program code of the microcontroller can be written in the Matlab-Simulink (Gapinski et al., 2013). US control system with microcontroller 14 is used to control, pressure monitoring, monitoring end positions of the piston valve, safety features, save to SD card, monitoring process states and performs the functions of self-diagnosis. By means of diagnostics can be detected errors and failures in the operation of the valves.

In addition, diagnosis can be done also for driving systems by installing the position sensors on actuators. The control system has a network communication module 16 and a web server that allows monitoring, remote diagnostics, viewing, logging errors and failures using the Web site. Network communication module 16 also allows to communicate with master slave devices such as a PC, PLC, input and output modules. The US control system shows some prompts on LED 13. All elements connected together (electronic modules and pneumatic valve modules) form the pneumatic valve terminal. Fig. 3 shows the general view of the designed pneumatic valve terminal built with five control valves 5/2 (five ways and two positions).

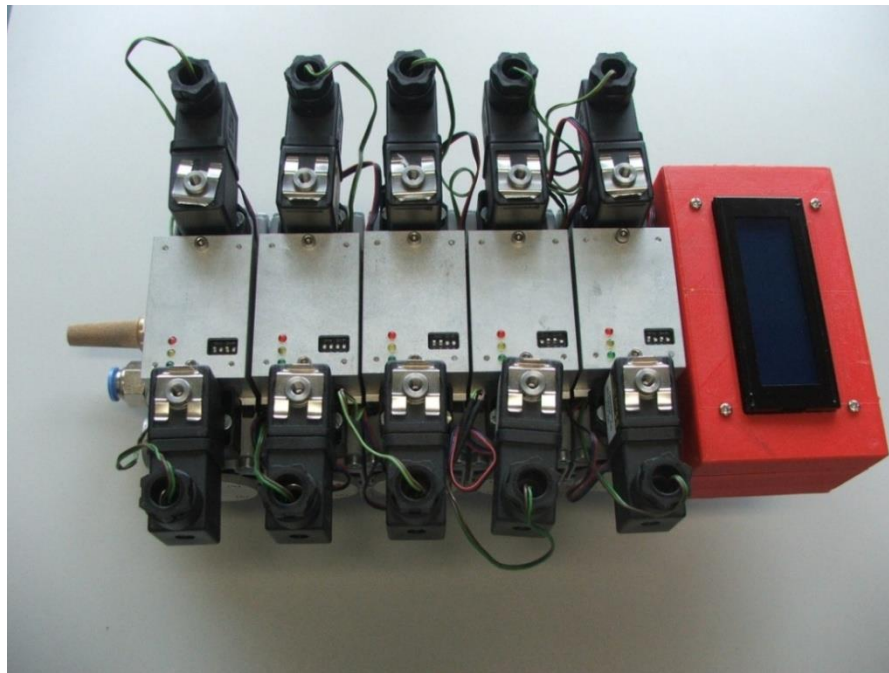


Fig. 3: The general view of the designed pneumatic valve terminal.

3. Conclusions

The authors conducted a market analysis of existing solutions manufacturers of pneumatic Bosch Rexroth, Festo, Asco Numatic, Parker, Hoerbiger Origa, Prema. Only Festo and Asco Numatic have equipped the valve terminals in a simplified diagnostic system. Designed pneumatic valve terminal has many features that set it apart from of competitive in the field of diagnostic activities: confirmation of the position of the piston valve in all positions, pressure measurement in 2 and 4 outputs, archiving of measurement data, possibility of control, remote control and monitoring. The last feature is ensured by the external communication with the device via the Internet. The communication system will operate on PROFINET or PROFIBUS allowing connection of ICT networks with distributed intelligent automation systems. Designed innovative modular pneumatic valve terminal with self-diagnosis, control system and industrial network communications meets all the assumptions. The pneumatic valve was presented at Poznan International Fair ITM 2013 and VI Fair of Pneumatics, Hydraulics, Drives and Controls PNEUMATICON 2013 in Kielce, where was recognized by the industry and won the gold medal. Pneumatic valve terminal can be used in the control, diagnosis and control of technological processes in which for safety or sensitivity reasons of the process is required to develop a specific states of actuators, confirmation switching the valves and monitoring the control system.

References

- Takosoglu, J. E., Dindorf, R. F., Laski, P. A. (2009) Rapid prototyping of fuzzy controller pneumatic servo-system. *International Journal of Advanced Manufacturing Technology* Vol. 40, No. (3-4), pp. 349-361.
- Takosoglu, J. E., Laski, P. A., Blasiak, S. (2012) A fuzzy controller for the positioning control of an electro-pneumatic servo-drive. In: *Proc. Institution of Mechanical Engineers Part I-Journal of Systems and Control Engineering*, Vol. 226, No. 10, 2012, pp. 1335-1343.
- Takosoglu, J. E., Laski, P. A. (2011) Intelligent positioning system of electro-pneumatic servo-drive. *Annals of DAAAM & Proceedings* 22 (1), pp. 1641-1642.
- Gerc, E. (1973) *Pneumatic actuators: theory and calculation*. WNT, Warszawa (in Polish).
- Szenajch, W. (1997) *Drive and control of air*. WNT, Warszawa (in Polish).
- Blasiak, S., Laski, P., Takosoglu, J. (2013) Parametric analysis of heat transfer in non-contacting face seals, *International Journal of Heat and Mass Transfer*, Vol. 57, No. 1, 2013, pp. 22-31.
- Gapinski, D., Koruba, Z., Krzysztofik, I. (2013) The model of dynamics and control of modified optical scanning seeker in anti-aircraft rocket missile, *Mechanical Systems and Signal Processing*, Vol. 45, Iss. 2, pp. 433-447.

COMPUTER NONLINEAR ANALYSIS OF THE INFLUENCE OF MATERIAL CHARACTERISTICS ON THE RESPONSE OF A BASEMENT STRUCTURE LOADED BY GROUND WATER BUOYANCY

P. Tej^{*}, V. Vacek^{**}, J. Kolisko^{***}, J. Čech^{****} F. Lo Monte^{*****}

Abstract: *The paper focuses on a computer nonlinear analysis of the formation and development of cracks in a concrete slab exposed to a uniform continuous load on the lower surface. The analysis is based on an actual example of the formation and development of cracks of the width of approx. 0.3 mm in a basement slab exposed to ground water buoyancy. The paper illustrates the setting of the material model of the reinforced concrete slab according to the actual material properties and the similarity of the computer results to an incident of real damage to the basement structure. On the basis of the same cracks on the model and on the real structure, a load value that caused this damage was estimated. The aim of this article was to find such material characteristics of a basement structure of the same size and shape and under the same extreme load that shows cracks with a maximum width of 0.1 mm to ensure the waterproofing safety.*

Keywords: Concrete, Cracks, Computer analysis, Ground water buoyancy, Material characteristics.

1. Introduction

This paper deals with the analysis of the development of cracks in a basement reinforced concrete slab of a residential building. The thickness of the slab is predominantly 300 mm, the thicker parts being 600, 800, 900 and 1000 mm. The variations in thickness between the different parts are solved by bevels. Due to the expected groundwater buoyancy (1.5 m), the building foundation is still supplemented by 9 tension micropiles holding the slab in the middle of the span, in the place with the maximum anticipated effect of buoyancy. The thickness of the perimeter walls is 300 mm.

2. Computer Analysis

The basement slab contains significant cracks and water leaks up to the upper surface of the slab. To determine the causes of the damage, a detailed computer analysis of internal forces, stress, strain and the crack width was carried out. The static model was created in ATENA software 4.3.1, ATENA 3D ENGINEERING (Červenka et al., 2002, 2013).

The program is based on the finite element method. The model of the structure was loaded by the structure's own weight, by the forces from the upper structure, and by the hydrostatic pressure of the water column, corresponding to the ground water level 1.5 m over the basement slab (as it was designed).

The static model comprises plate macro-elements reinforced by the specified degree of reinforcement. The plate elements are quadrangular, to be meshed by finite elements - quadratic bricks. Concrete C 30/37, with mean values of the material properties, is used as the construction material of the slab. The

* Ing. Petr Tej, PhD.: Klokner Institute, CTU in Prague, Šolínova 7, 166 08 Prague; CZ, petr.tej@klok.cvut.cz

** Ing. Vítězslav Vacek, CSc.: Klokner Institute, CTU in Prague, Šolínova 7, 166 08 Prague; CZ, vitezslav.vacek@klok.cvut.cz

*** Assoc. Prof. Ing. Jiří Kolisko, PhD.: Klokner Institute, CTU in Prague, Šolínova 7, 166 08 Prague; CZ, jiri.kolisko@klok.cvut.cz

**** Ing. Jindřich Čech: Klokner Institute, CTU in Prague, Šolínova 7, 166 08 Prague; CZ, jindrich.cech@klok.cvut.cz

***** MSc. Francesco Lo Monte: Politecnico di Milano, Piazza Leonardo da Vinci, 32 20133 Milano; Italy, lomonte@stru.polimi.it

steel reinforcement B 500B is specified, inputted also with the mean values. Bevels under the columns are modeled using standard macro-elements. The walls and pillars are replaced by the load distribution elements, which are modeled as plates with a height of 300 mm. For these units, 3D Elastic material is specified. The underlying bedrock is modeled using springs for areas with a compression stiffness of 45 MPa. The length of the spring corresponds to the gravel layer thickness of 200 mm. Extra horizontal supports are attached to the slab and its bevels, because the springs support the slab only in the vertical direction. Additional vertical supports are represented by piles modeled by a load distribution plate of 400 x 400 mm. The upper face of the plate is propped against the slab in a vertical direction. This support is put in action only when the model is loaded by increasing the ground water level. Thus, the value of the pressure from the water level of 1.5 m corresponds to the value of the vertical reaction 0 kN. The model is loaded by the slab's own weight (step 1), by the upper structure (values of forces and loads according to the static calculation - 5 steps), by the basic ground water level 1.5 m over the basement slab (in five steps, each 20 % of the total value), and by the rising ground water level, when at each step the load increases by the equivalent of 0.1 m of the ground water level up to the level of 3.5 m (the level rises by 2 m in 20 steps). The water level then falls to 1.2 m, before rising again to the original level of 1.5 meters, again in steps of 0.1 m.

The aim of this procedure was to determine whether the significant cracks in the slab could have been caused by the effect of groundwater buoyancy, and what the approximate critical value was.

During the decrease from the water column height of 1.663 m to the height of 1.54 m, the numerical model showed an average crack width decrease of 0.0133 mm. During the further water column decrease down to a height of 1.267 m, an average crack width decrease of 0.02 mm was calculated, and in a further decrease down to the water column height of 1.238 m, an average crack width of 0.008 mm was determined. In a subsequent increase up to a level of 1.485 m, the average crack width increased up to 0.018 mm. These results agree very well with the measured values.

The computer analysis shows that the cracks in the slab are caused by water buoyancy on the lower surface of the slab. The static load, according to which the slab was designed, took into consideration water pressure corresponding to the height of the water column of 1.5 m over the basement slab. The results of the computer analysis of loading the basement slab by the upper construction and the pressure of the water column of 1.5 m showed cracks with a width of 0.072 mm. More cracks started to appear with the increase in water level (and therefore the pressure). The cracks of the width exceeding 0.1 mm are critical for the impermeability of the structure. In some places of the tested slab a crack width of 0.1 mm was already exceeded by a water column height of 1.8 m. The next increase in the water level up to 3.5 m induces the development of a network of cracks, some of them reaching a width of 0.295 mm. In the following simulation of the decrease of the water column height back to the value of 1.5 m, the maximum crack width falls to 0.172 mm (refer with: Fig. 1.).



Fig. 1: Formation and development of cracks in a reinforced concrete slab - equivalent height of water column 3.5 m, max. crack width 0.295 mm.

Tab. 1: Table of crack widths depending on the height of water column.

Load direction	Height of water column [m]	Max. crack width [m]	Load direction	Height of water column [m]	Max. crack width [m]
increasing	1,5	$7,15 \cdot 10^{-5}$	decreasing	3,1	$2,76 \cdot 10^{-4}$
	1,6	$8,6 \cdot 10^{-5}$		3	$2,67 \cdot 10^{-4}$
	1,7	$9,37 \cdot 10^{-5}$		2,9	$2,59 \cdot 10^{-4}$
	1,8	$1,03 \cdot 10^{-4}$		2,8	$2,52 \cdot 10^{-4}$
	1,9	$1,11 \cdot 10^{-4}$		2,7	$2,45 \cdot 10^{-4}$
	2	$1,19 \cdot 10^{-4}$		2,6	$2,39 \cdot 10^{-4}$
	2,1	$1,31 \cdot 10^{-4}$		2,5	$2,32 \cdot 10^{-4}$
	2,2	$1,47 \cdot 10^{-4}$		2,4	$2,25 \cdot 10^{-4}$
	2,3	$1,56 \cdot 10^{-4}$		2,3	$2,18 \cdot 10^{-4}$
	2,4	$1,67 \cdot 10^{-4}$		2,2	$2,11 \cdot 10^{-4}$
	2,5	$1,63 \cdot 10^{-4}$		2,1	$2,05 \cdot 10^{-4}$
	2,6	$1,84 \cdot 10^{-4}$		2	$2,01 \cdot 10^{-4}$
	2,7	$1,98 \cdot 10^{-4}$		1,9	$1,97 \cdot 10^{-4}$
	2,8	$2,05 \cdot 10^{-4}$		1,8	$1,90 \cdot 10^{-4}$
	2,9	$2,17 \cdot 10^{-4}$		1,7	$1,84 \cdot 10^{-4}$
	3	$2,32 \cdot 10^{-4}$		1,6	$1,77 \cdot 10^{-4}$
	3,1	$2,43 \cdot 10^{-4}$		1,5	$1,72 \cdot 10^{-4}$
	3,2	$2,47 \cdot 10^{-4}$		1,4	$1,66 \cdot 10^{-4}$
	3,3	$2,62 \cdot 10^{-4}$		1,3	$1,61 \cdot 10^{-4}$
	3,4	$2,84 \cdot 10^{-4}$		1,2	$1,55 \cdot 10^{-4}$
3,5	$2,95 \cdot 10^{-4}$	1,3	$1,61 \cdot 10^{-4}$		
decreasing	3,4	$2,87 \cdot 10^{-4}$	increasing	1,4	$1,66 \cdot 10^{-4}$
	3,3	$2,92 \cdot 10^{-4}$		1,5	$1,72 \cdot 10^{-4}$
	3,2	$2,84 \cdot 10^{-4}$		1,6	$1,77 \cdot 10^{-4}$

In the next step, by successive iterations, the combination of material properties which gave a maximum crack width of 0.1 mm in a structure of the same dimensions and shape were found. Concrete C50/60 was used, and the reinforcement area was proposed as being double the area of the original proposal. So that along the upper surface bars of 25 mm were used at a distance of 50 mm in both directions, and along the lower surface of the profile bars of 12 mm were used at a distance of 125 mm. Thus, the remodeled structure carried a groundwater pressure of the equivalent water column height of 3.5 m with a maximal crack width of 0.1 mm (refer with: Fig. 2).



Fig. 2: Formation and development of cracks in a reinforced concrete slab with adapted material characteristics - equivalent height of water column 3.5 m, max. crack width 0.1 mm.

3. Conclusions

Cracks represent a typical failure mode of reinforced concrete slabs used as foundation plates. Considering the durability and serviceability of a structure, the most crucial cracks are those which lead to water penetration. Water generally leaks into cracks wider than 0.1 mm.

The cracks can originate in the process of chemical shrinkage during the setting and hardening of concrete, respectively in the process of bound contraction during the building of individual parts of the structure. The other cause of the crack development can be water buoyancy exceeding the design value.

It is therefore necessary to design the structure base plates so as to prevent water leakage. The structure should be designed using quality class of concrete and adequate reinforcement that can withstand water pressure.

Due to the frequent failures of the base plates caused by groundwater pressure is extremely important to perform preliminary surveys of groundwater layers and design the structure to the value of the maximum water pressure acting the structure.

Acknowledgement

The study is based on the outcomes of research projects VG20122015089 supported by the Ministry of the Interior of the Czech Republic.

References

- Vacek, V., Tej, P., Kolísko, J., Čech, J. (2013) Expert report NO. 130083J, Klokner Institute CTU in Prague.
- Červenka, J., Pukl, R., Červenka, V. (2013) Design of Sustainable Reinforced Concrete Structures Assisted by Numerical Simulations, In: Proc. 3rd Int. Conf. on Sustainable Materials and Technologies, SCMT 3, Kyoto, paper 332.
- Červenka, J. (2013) Design of Reinforced Concrete Structures by Numerical Simulation, A XXIII-a Conferinta Nationala A.I.C.P.S., May 30, Bucharest, pp. 150-153.
- ČSN EN 1992-1-1 Eurocode 2: Design of concrete structures.

AEROELASTICITY OF SLENDER FACADE SHEETS

A. Tesár*

Abstract: *The analysis of linear and nonlinear aeroelastic behavior of slender façade sheets is the focus of intense efforts because of pressing problems of disaster prevention of such structures. Theoretical analysis is interesting but the brain washing in the wind engineering is inevitable. Due to irregularities and inhomogenities in the facade as well as in the wind forcing the item „garbage in, garbage out“ appears there as significant option in modeling. Calculations are to be based on theoretical approach and be confronted with experimental results in order to satisfy the model similarity with reality and to develop suitable virtual models for the assessment of the problem.*

Keywords: Aeroelasticity, Boundary layer, Database, Façade, Virtual model, Wind tunnel.

1. Introduction

The development of suitable techniques for assessment of wind turbulences in ultimate aeroelastic behavior of slender facade walls equipped with thin glass or plexiglass sheets is the focus of efforts in this paper. Theoretical and experimental analysis of ultimate dynamic behavior of such slender facades is studied because of pressing problems of sound insulation and disaster prevention of such structures. In order to avoid the general problem „garbage in, garbage out“ in the analysis, the treatment uses the database of input data obtained by experimental tests in the wind canal.



Fig. 1: Cheese House in Nitra, Slovakia.

* Alexander Tesár, Ing., Phd., DSc., Assoc. Prof., FEng., Institute of Construction and Architecture, Slovak Academy of Sciences, Dubravská cesta 9, 845 03 Bratislava, Slovakia, alexander.tesar@gmail.com

2. Tests in Wind Canal

The application of the problem studied was made on the plexiglass facade of the building „Cheese House“, erected in Nitra, Slovakia (Fig. 1). The facade is made of yellow plexiglass sheets and is modeling architectural configuration of the Emmenthaler Cheese. The research was made in the wind tunnel of the Institute of Construction and Architecture, Slovak Academy of Sciences, Bratislava.

Studied was the facade panel in scale 1:1, made of plexiglass sheet and attached by joints into supporting steel frame. The width of the plexiglass sheet is 15 mm. Its maximal dimensions are 1100 x 812 mm. The views of the model are in Figs. 2 and 3. The panel is a part of actual facade sheet and therefore no treatment of the model similarity was required. Due to the wind forcing the sheet acts with quasi-static displacements combined with horizontal vibrations of supporting steel structure. The tests were made via strains and accelerations measured in the sheet in the wind tunnel.



Fig. 2: View of the model.



Fig. 3: View of the model in wind canal.

The sheet was subjected to laminar and turbulent wind forcing until velocity 40 m/sec. Measured were three accelerations (A1, A2 and A3) and four relative displacements (T1, T2, T3 and T4), respecting the air velocity (Vel) in the wind canal.

Used was the modul of the canal with cross-section 1200 x 1200 mm. The testing was made in accordance with the wind forcing on actual facade in situ with plexiglass sheets distanced 400 mm from the surface brick wall of the building. In scope of testing the brick wall was modeled by the floor of the wind canal and the plexiglass sheet was located in the height 400 mm above it.

The tests in wind canal were made for three experimental configurations:

- a) plexiglass panel in horizontal level 0° – shear wind acting parallel along the facade,
- b) plexiglass panel in skew level -15° – suction due to fall down wind,
- c) plexiglass panel in skew level $+15^\circ$ – pressure due to skew wind and face uplift wind.

Some results obtained are illustrated in Figs. 4, 5 and 6.

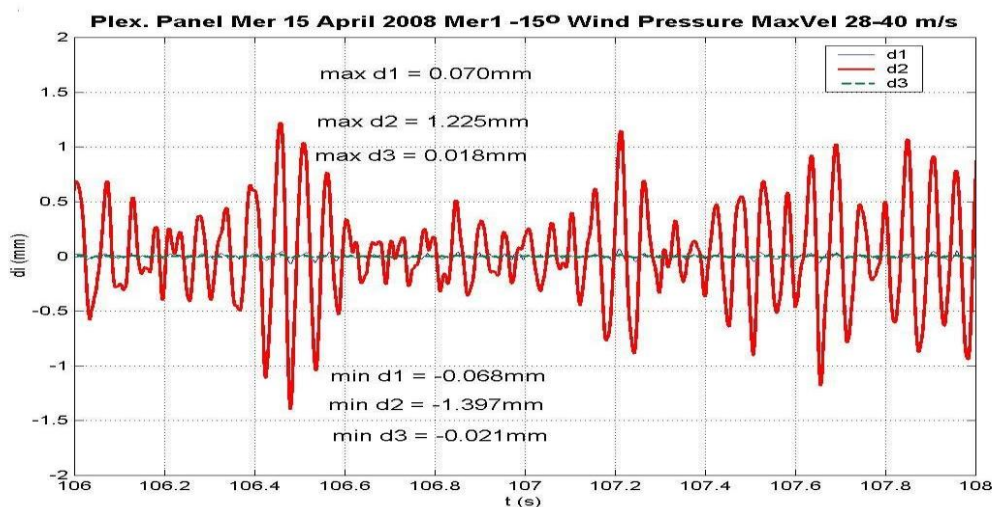


Fig. 4: Horizontal ($d1$), vertical ($d2$) and shear ($d3$) deformation amplitudes in configuration 0° .

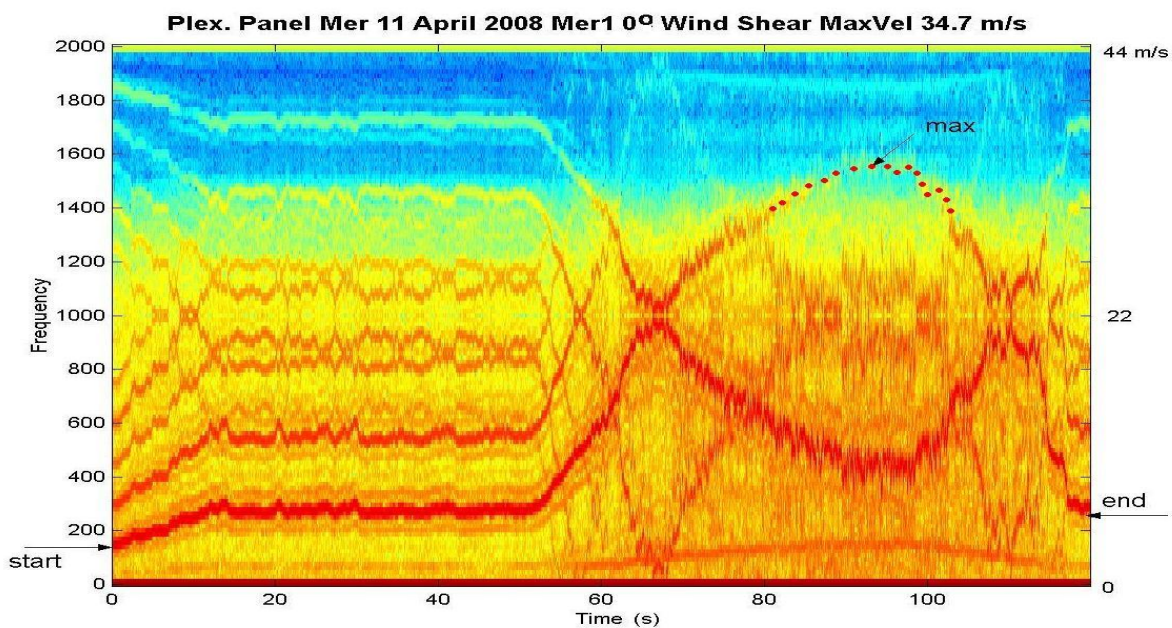
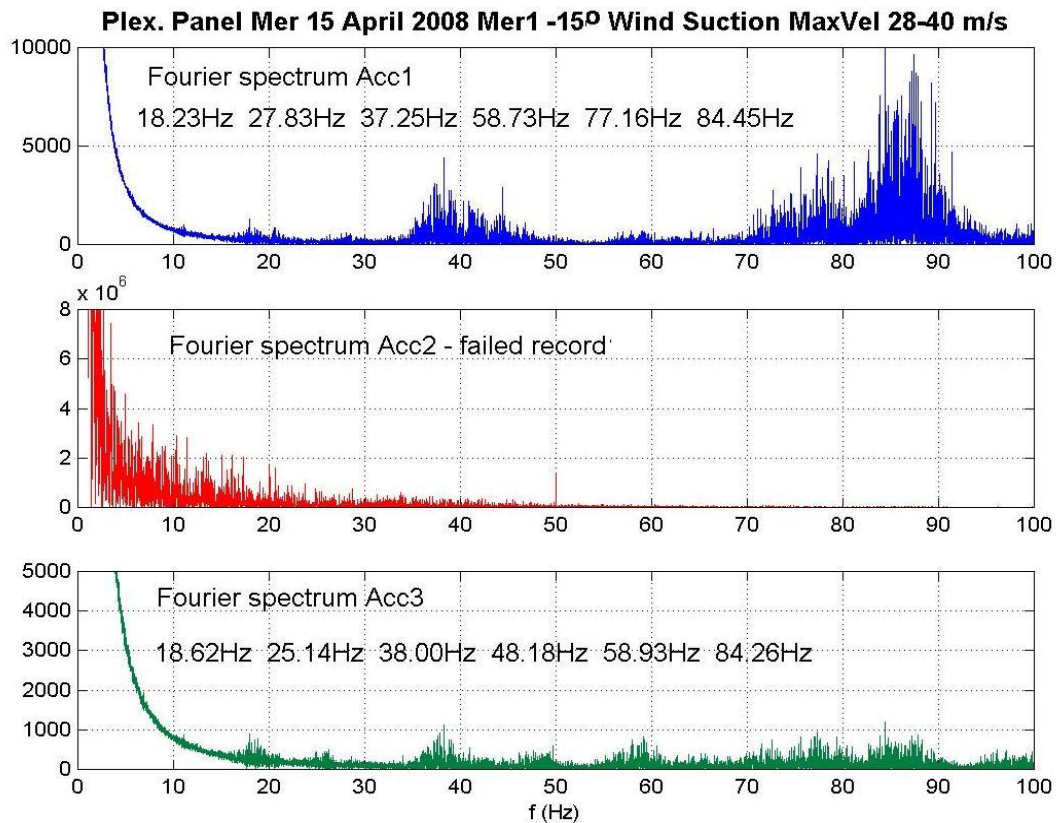


Fig. 5: Configuration 0° - wind velocity Vel (m/s).



3. Conclusions

The evaluation of time response and of extreme values of the data summed up has brought the conclusion that resulting response of the plexiglass sheet is dominated by dynamic displacements with pressure and sucking of the wind. The displacements have irregular distribution along the surface of the sheet. The turbulences of the air flow influence deformations and vibrations of the plexiglass sheet and of supporting members (see Tesar, 2006, 2011, 2012, 2012a). All results evaluated were summed up in the database of input data for tuning and creation of virtual models with numerical analysis made in advance. The confrontation of numerical and experimental data resulted in satisfactory agreement of both approaches. In order to avoid the discrepancy of numerical results and in situ measurements (garbage in, garbage out) there was established the database of the results obtained. Such database contains all significant input data for virtual testing and assessment of the problem. On the basis of evaluation of the results obtained was specified the reliability of the plexiglass facade sheet, its supporting steel structures and joints for in situ implementation.

References

- Tesar, A. (2006) Aeroelastic assessment of ultimate aeroelastic behaviour of the long-span bridge in Svrčinovec, North Slovakia. Technical Report, Institute of Construction and Architecture, Slovak Academy of Sciences, Bratislava.
- Tesar, A. (2011) Aeroelastic assessment of elements of photovoltaic power plants. Technical report for RAAB VILLANZSZERELŐ KFT., Győr.
- Tesar, A. (2012) Multi-functioning in virtual monitoring of thin-walled bridges. Journal of Mechanics Engineering and Automation, David Publishing Company, Vol. 2, No. 11, Serial Number 17, pp. 701-708.
- Tesar, A. (2012a) Tuned vibration control in aeroelasticity of slender wood bridges. Coupled Systems Mechanics, Vol. 1, No. 3, pp. 219-234.

ATOMISER WITH EXCITATION BY A FLUIDIC OSCILLATOR

V. Tesař*, J. Hykl*

Abstract: Paper summarises results obtained in feasibility study of a novel pneumatic atomiser for generation of fine spray of water droplets. The novel feature, leading to smaller size of the droplets, is pulsating the air supply by means of a no-moving-part fluidic oscillator. Tests involved taking images of the spray by a high-speed camera and measurements of the droplet size spectra by laser light scattering. Conclusions suggest that the concept is promising, though it necessitates further development and optimisation.

Keywords: Atomiser, Droplet spray, Fluidic oscillator.

1. Introduction

Described as atomisers are usually devices generating fine spray by action of very high pressure differences in the percolation regime, i.e. using narrow exit passages for producing very narrow liquid jets which decompose into the spray of fine droplets by the Plateau-Rayleigh surface instability. There is, however, a wide range of exiting or potential applications for devices the two-fluid (mainly, of course, gas/liquid) designs with the fragmentation of liquid small operating with much lower pressure difference levels – but with the simple passive orifice-type passages it is not easy to achieve the desirable small droplet size. A solution of the problem offer volumes by means of the strong pulsation caused by the large (up to three decimal orders of magnitude) difference in specific volumes of the two fluids. Recently became known another alternative in which the pulsation is input from a separate (though located inside the same device) oscillator. Particularly attractive is pulsating the air flow into the atomiser by a no-moving-part fluidic self-excited oscillator, characterised by robustness, low cost, long life and maintenance-free operation.

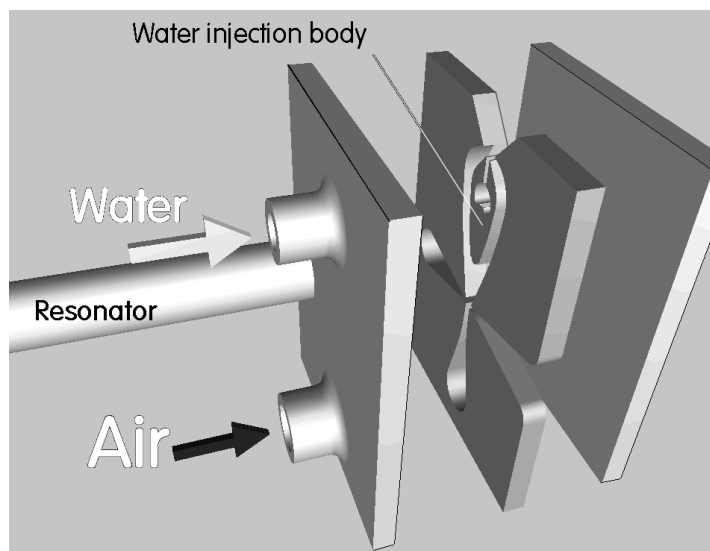


Fig. 1: Expanded view of the atomiser with feedback effect based on the propagation of compression and rarefaction waves in the resonator channel – a recently introduced method of securing the negative feedback action.

* Prof. Ing. Václav Tesař, RNDr. Jiří Hykl, PhD.: Institute of Thermomechanics AS CR v.v.i., Dolejškova 5; 182 00, Prague; CZ, tesar@it.cas.cz

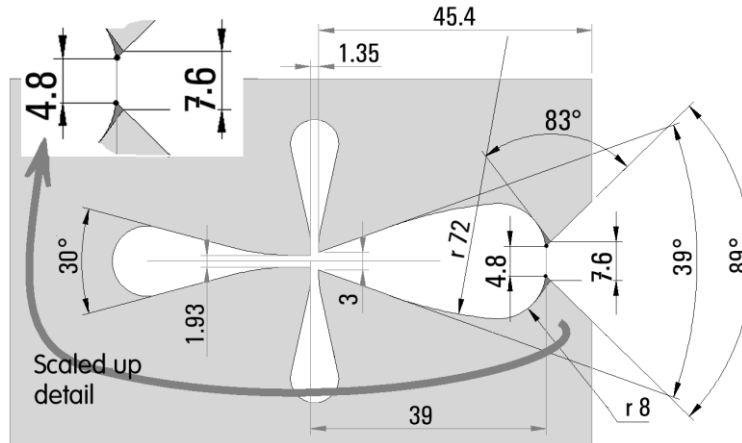


Fig. 2: Geometry and dimensioning of the main plate - with laser-cut cavities for air flow – of the model used in laboratory tests. The expanded detail is the part where it became necessary in one test series to make changes eliminating the unwanted strong positive feedback effect.

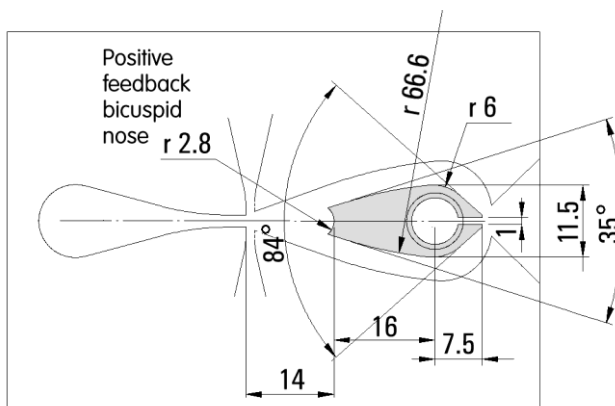


Fig. 3: Photograph of the assembled atomiser. Two identical central plates may be recognised; in the actual tests only one of these plates was used.

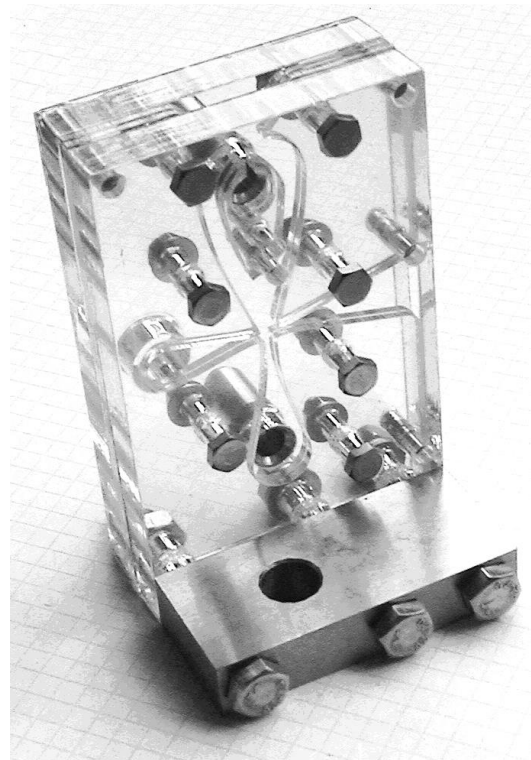


Fig. 4: Shape, positioning and dimensions of the small water-injection body. Early tests were made with this body removed – just to obtain more experimental data without the expenses of making alternative configurations.

Authors performed a feasibility study of such a fluidic device, legally protected by a recently submitted Czech Republic Patent Application. As shown in Fig. 1, the device operates in the self-excited oscillation regime because it is directly derived from known designs of jet-deflection diverter-type fluidic oscillators. It retains the usual geometry of the supply nozzle, a pair of control nozzles, and the interaction cavity with a pair of Coanda-effect attachment walls. Also the common bi-cuspid shape of the splitter nose opposite to the supply nozzle is retained. The diffusers which in fluidic amplifiers and oscillators secures pressure recovery for good effectiveness are, however, replaced by the pair of practically constant cross section channels, usually curved so as to reach to the exit of water-jet generating injection body.

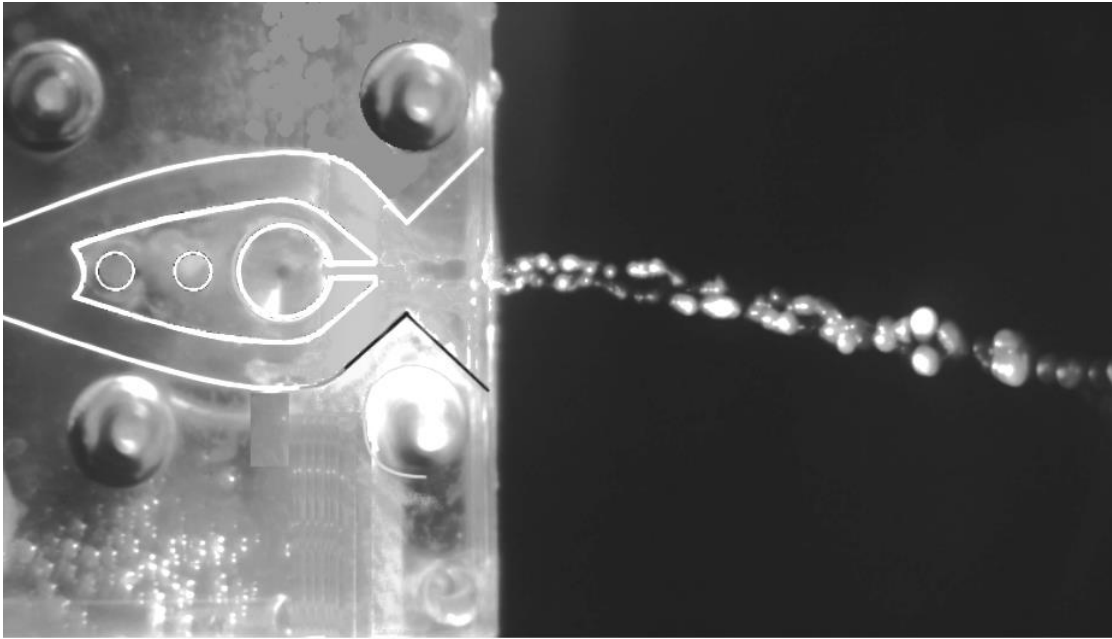


Fig. 5: A frame from the high-speed camera record obtained in preliminary tests with water flow alone (no fluidic oscillation). Note the large size of the drops. Also the changed geometry of the exit (cf. Fig. 2) may be here recognised.

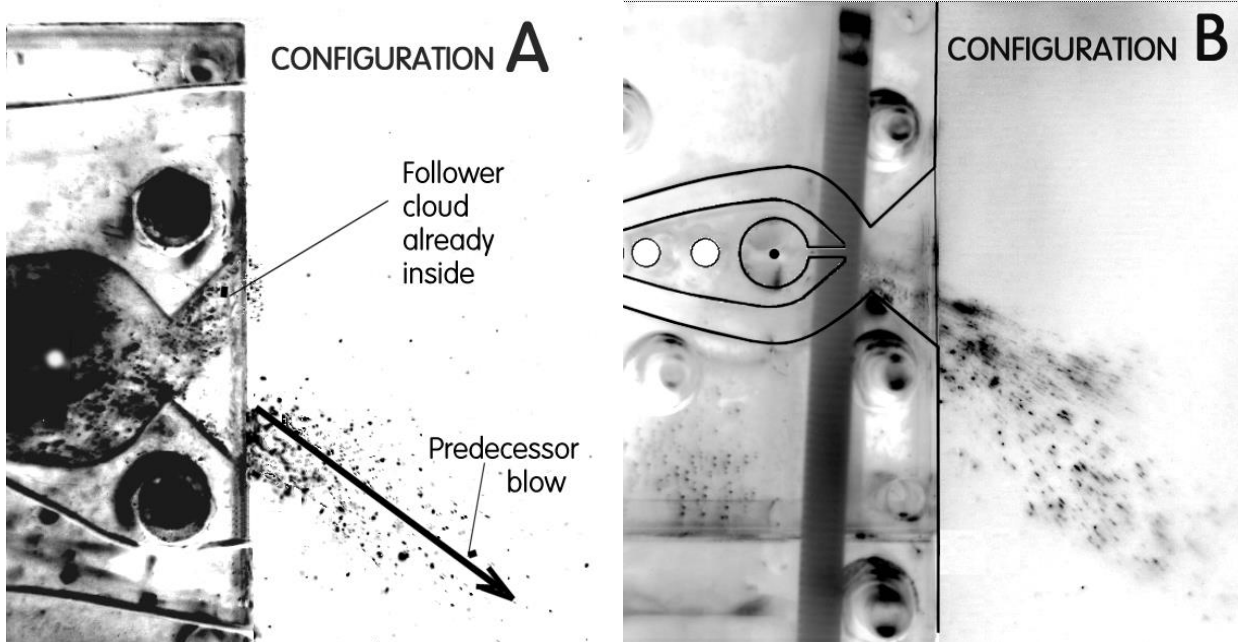


Fig. 6: (Left) Negative colour photograph of the spray generated without the water-injector body in the atomiser with fluidic oscillation. The water volumes fragmenting action depends here on the violent flow direction changes and in comparison with Fig.5 is seen to be quite effective.

Fig. 7: (Right) Photograph (again in the inverse grayscale) of the spray generated with the water-injection body in place. Without the substantial kinetic energy loss of the air flow inside the interaction cavity, typical for the version from Fig. 6, here the velocities of generated spray are high. (high speed is recognisable from the visible motion-smearing of the droplet images despite the very short exposure time mere $39 \mu\text{s}$).

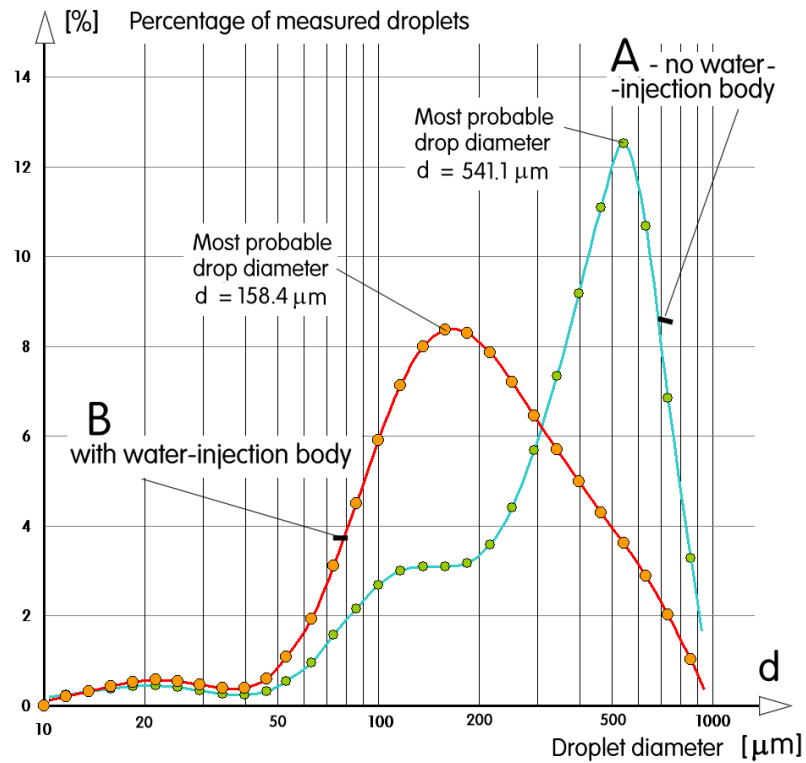


Fig. 8: Example of results obtained in measurements of generated droplet size spectra. Considering the rather small applied pressure, the size of the droplets is quite small – especially with the version B (Fig. 7) containing the internal water-injection body.

Performed testing included recording the spray development images by high-speed camera and scattered-light optical measurements of droplet size spectra. Because of the limited means and time, investigated were only two alternative configurations – A without the water-injector body, relying with the water fragmentation on violent velocity magnitude and direction inside the enlarged interaction cavity, and B near to the original design with the water injection body in its place (but with the cavity exits adapted to suit also the other role, which perhaps influenced negatively the performance), relying on higher-velocity impact blows on the water jet. Considering the relatively small pressure levels applied and the quite small size of the droplets presented in Fig. 8, the configuration B may be an interesting starting point for a more extensive research and optimisation.

Acknowledgements

Authors' research was supported by grant 13-2304S obtained from GAČR. They were also recipients of institutional support RVO: 61388998. Gratefully acknowledged is the help of Dr. Jiří Šonský who kindly made available his high-speed camera and also software for image processing. In the experimental effort authors were helped by Assoc. Prof. M. Jilek.

ROBUST CONTROL ALGORITHM FOR PMSM MOTOR WITH HALL POSITION SENSORS

J. Toman^{*}, I. Szabo^{**}, V. Singule^{***}

Abstract: *The paper deals with a development of robust control algorithm for electro-mechanical actuator, which is intended to delivery of fuel to Auxiliary Power Unit APU in an aircraft. Contemporary technological developments within the all-electric aircraft concept lead to replacement of existing hydraulic-mechanical circuits by intelligent actuators based on electrical servo drives which increase overall reliability and utility value, decrease operating costs, dimensions and weight. The aims of the development were to design a model of control algorithm for Electrically Driven Fuel Pump EDFP in accordance with rigid aviation standards and to verify this algorithm on a test bench that simulates a real fuel circuit. A Permanent Magnet Synchronous Motor PMSM is used as actuator and low-cost Hall position sensors are selected for sensing rotor position.*

Keywords: PMSM, EDFP, APU, Hall sensors, PWM.

1. Introduction

The EDFP is a part of APU and is composed of a fuel pump, Stop Valve (SV), PMSM with Hall sensors and Control System CS. The APU is a bleed-less turbine essentially supplying mechanical and/or electrical power to the A/C. The system architecture block diagram is depicted in the Fig. 1. The aim of this paper is focused only on design and verification of model of a complex control algorithm for the EDFP. The models of the other parts of this system were detailed described in papers (J. Toman et al., 2012; V. Hubík et al., 2008).

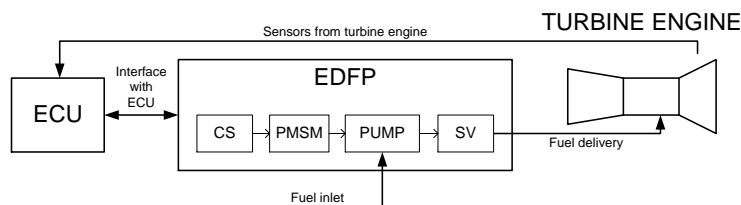


Fig. 1: EDFP system architecture.

The main problem of the control algorithms is to determine the position of the rotor with the accuracy needed for effective and safe operation. There are two well-known ways to determine the rotor position: a usage of common sensors like incremental encoder and resolver or a usage of Hall sensors. The usage of Hall sensors is advantageous because it does not require a mechanical coupling and the cost is low. The speed measurement and prediction algorithms can be used to solve the problem of a lack of information obtained from the sensors. This solution is effective when the speed changes of the rotor are negligible or at least are slow. If significant dynamic changes are present in the system, more complex control algorithms are needed to handle the obstacles caused by these changes. In addition, the reliability of algorithms will be guaranteed even if the sensor is faulty. This control strategy approach was inspired by papers (S. B. Ozturk et al., 2006; A. Lidozzi et al., 2007)

^{*} Ing. Jiri Toman: UNIS, a.s., Division Aerospace and Advanced Control, Jundrovská 33, Brno, CZ, jtoman@unis.cz

^{**} Ing. Istvan Szabo PhD.: UNIS, a.s., Division Aerospace and Advanced Control, Jundrovská 33, Brno, CZ, iszabo@unis.cz

^{***} Assoc. Prof. Ing. Vladislav Singule, CSc.: Faculty of Mechanical Engineering, Brno University of Technology, Technická 2, Brno, CZ, singule@fme.vutbr.cz

The designed control algorithm shall ensure safe and reliable control of the PMSM motor that drives the EDFP. EDFP operation shall be ensured under various external conditions, including harsh environments and unknown initial states such as fuel pressure in the system, position of the rotor or necessary starting torque of the PMSM motor.

Requirements for the control system were defined during the early stage of the project by consultation with external aviation specialists. These requirements include electrical characteristics, reaction of the control system to defined incidents, start-up characteristics, control commands, environmental etc. From the control algorithm design point of view, the following main requirements shall be taken into account:

- The maximum underflow should be less than 2% at $\Delta\omega > 40\%$ and the fuel flow should stabilize in 240 ms.
- In case of stop command the EDFP shall stop in less than 100 ms

2. Control System Modeling and Simulations

The control algorithm was designed to improve the performance of a standard low-cost sensor control solution with three Hall sensors, without adding other demands on computational power. The main idea is to estimate the actual rotor position between sensed changes of the Hall sensors outputs by measuring the time period of a full electrical revolution and assuming that the next period has approximately the same length. This enables the estimation of the rotor position within one electrical revolution.

The whole control is realized by the Commutation&Control module inside the Control Electronics model. This model is shown in Fig. 2 with several external modules which give the necessary data, such as a timer, speed calculation and interrupt requests IRQA.

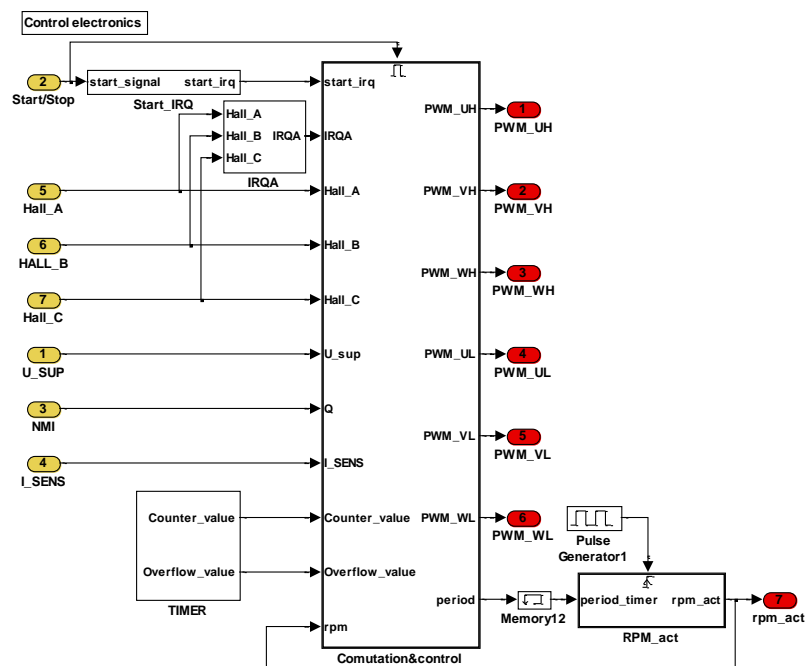


Fig. 2: Overall view of control electronics module with external speed estimation module, timer and interrupt generators.

Commutation&Control is the main module, which includes most of motor control procedures. Its operation is enabled by receiving the start signal. This subsystem and its modules are responsible for the following tasks: *IRQA_USR* - determining actual rotor position, computing revolution period, *Control_system* - speed and current control, generating PWM duty signal, *Period_correction* - correcting revolution period in case of sudden rotor stop, *TimerA* - generating interrupts to trigger function of *Sin_commutation* block, *Sin_commutation* - creating sinusoidal waveforms from PWM duty, *PWM* - generating pulse width modulated signal to drive power transistors, *Startup_timer* - aligning rotor into desired starting position, *Hall_interrupt* - generating interrupts based on Hall sensors output change. The model structure of this module is shown in Fig. 3.

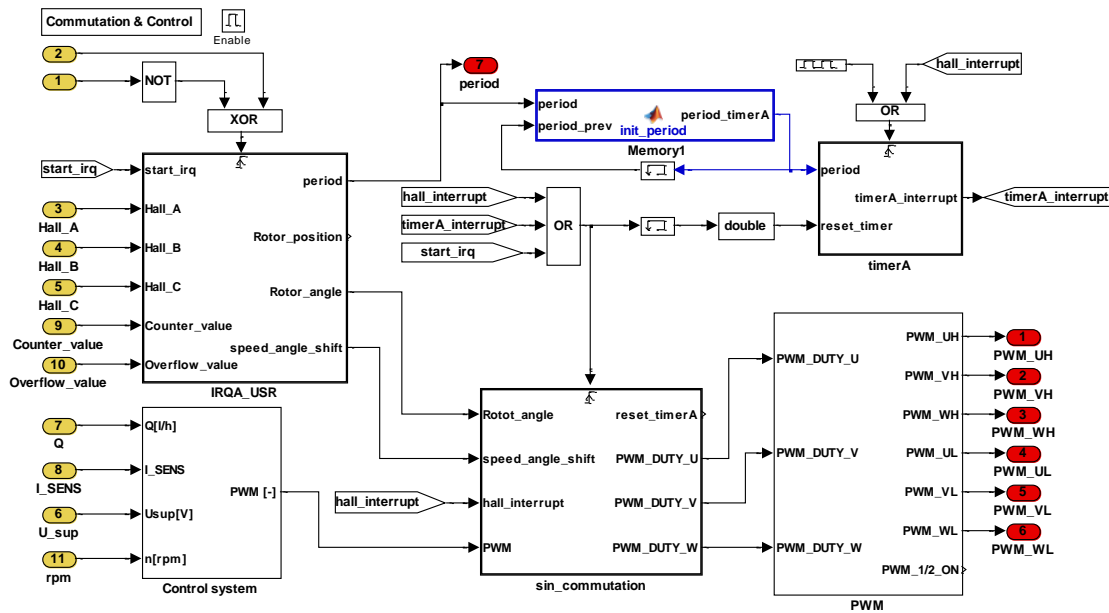


Fig. 3: Commutation & Control module.

2.1. Control system

Current and speed control system consists of two regulators, connected into the cascade. The difference is in the integrator limiting, which sets not only the limit for the maximum regulator output but also for the maximum increment in one computing step. The regulators are preceded by a switch disabling their function (and thus preventing them from integrating the regulation error) during the initial rotor positioning phase. PWM signal is connected to the Sin_commutation subsystem, its magnitude is corrected to cover a potential supply voltage drop. The anti-windup block and output saturation is implemented in the classic digital proportional-integral-derivative controller.

3. Verification of the Design Control Algorithm on Real Target

The control algorithm was implemented to control unit and then mounted on the EDFP and performance tests were carried out on an evaluation mock-up platform that simulates a real fuel circuit. These tests were performed with particular emphasis on start and stop sequences of the EDFP.

The start sequence of the fuel pump, shown in Fig. 4, was verified for a step change request from 50 percent of the fuel flow. This means that the starting flow level was 43 l/h (3250 rpm of the BLDC motor) at 2 MPa of back pressure. The required flow after step change should be 92 l/h (7300 rpm of the BLDC motor) at 3.9 MPa of back pressure. Fig. 4 compares the optimized pump characteristic with the original values. With a precisely tuned motor controller it is possible to achieve a start time of less than 200 ms and to fulfill the requirements.

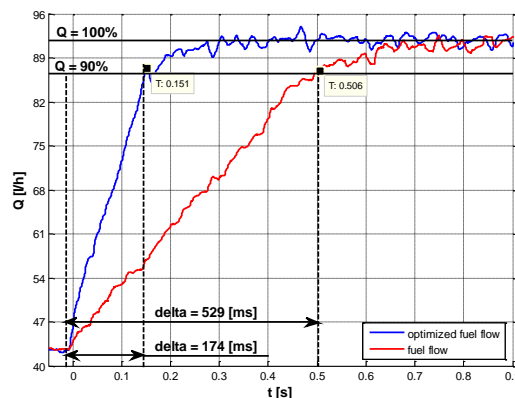


Fig. 4: The EDFP start sequence measurement.

The next important feature of the fuel pump is the stop time performance. This behavior is crucial for the turbine control system and dynamic of the whole hydraulic chain. According to the technical specification, the requirement is a stop time shorter than 100 ms when stop command received.

The stop time characteristic was much more difficult to measure. The directly connected speed or flow sensor to the fuel pump influences the stop time characteristic. The only way was to measure the speed from the motor's internal Hall sensors. There are two graphs in Fig. 6 that represent the output signal from the position sensors. After a simple MATLAB post-process it is possible to evaluate the actual rotor speed.

The graph on the left side in Fig. 5 shows the stop time characteristic when the system is not perfectly optimized. The fuel pump should stop in this case from the nominal fuel flow of 92 l/h (7300 rpm of the BLDC motor) at 3.9 MPa of back pressure. It is obvious that the technical specification requirement has not been fulfilled. The stop time is more than 200 ms.

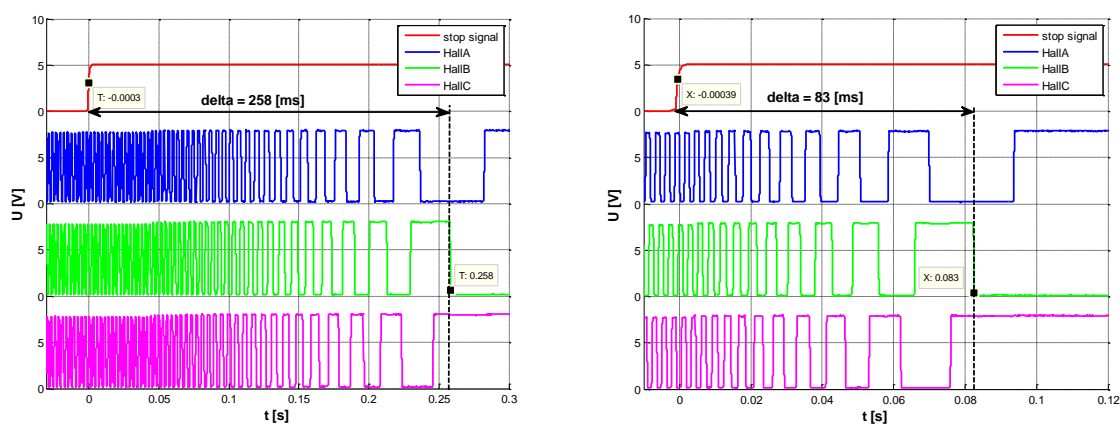


Fig. 5: The stop time characteristic with not optimized and optimized controller.

The second graph in Fig. 5 shows the stop time characteristic of the optimized controller. The same measurement method has been used in this case. The stop time has reduced to 83 ms which is acceptable.

4. Conclusions

Development and certification of any device in the aerospace industry requires a thorough approach, including definition of requirements, design of electronics, software coding and testing. In addition, very complex documentation must be maintained for the whole development and lifetime cycle.

The article describes the development of control algorithms to improve run-up performance and reliability of the EDFP with PMSM motor in actuating devices for safety critical applications. The development procedures described in this article indicate that they can bring about significant improvements in performance, safety and reliability of the control system along with reduction of development time and costs.

Acknowledgement

This work has been funded by the European Commission within the FP7 project "Efficient Systems and Propulsion for Small Aircraft ESPOSA", grant agreement No. ACP1-GA-2011-284859-ESPOSA.

References

- Ozturk, S. B., Akin, B., Toliyat, H. A., Ashrafzadeh, F. (2006) Low-cost direct torque control of permanent magnet synchronous motor using Halleffect sensors, in Proc. IEEE Appl. Power Electron. Conf., pp. 19-23.
- Lidozzi, A., Solero, L., Crescimbin, F., Di Napoli, A. (2007) SVM PMSM drive with low resolution Hall-effect sensors, IEEE Trans. Power Electron., Vol. 22, No. 1, pp. 282-290.
- Hubík, V., Švéda, M., Singule, V. (2008) Mathematical model of a sensorless BLDC motor for aerospace actuators, In Modelling and Simulation MS 2008. Quebec City, Quebec, Canada, pp. 165-169.
- Toman, J., Hubík, V., Singule, V. (2012) Development of the Control System for Electric Actuator with BLDC Motor, Engineering Mechanics, Vol. 18, pp. 289-296.

PRACTICAL IMPLEMENTATION OF SELECTED MEAN STRESS MODELS FOR RESULTS OF FATIGUE TESTS REALIZED FOR MINI SPECIMEN

T. Tomaszewski^{*}, J. Sempruch^{**}

Abstract: *The cyclic properties of structural materials may be identified by means of mini specimens only. The method is limited by specimen geometry and test conditions. The mini specimens are characterised by low rigidity with a tendency to buckling. Within the range of stresses used, the tests may be based on a one-sided cycle only, which eliminates compressive stress. It requires determination of symmetric stress cycles ($R = -1$) characteristics. An experimental σ_a - N curve for cycle with stress ratio $R = 0.1$ was determined based on mini specimen testing. The curve was further used to determine a curve for symmetric stress cycles $R = -1$ using selected mean stress models.*

Keywords: Mini specimen, Mean stress, High-cycle fatigue, Aluminum alloy, Schütz curve.

1. Introduction

Time-variable stresses result in the fatigue cracks and damage to machine components. A fatigue is described as a phenomenological process where known relations have narrow and strictly determined ranges of application. The process is complex and cannot be described by a single general model. The development of new production technologies, e.g. thin-walled structures, results in a lack of reliable procedures for the assessment of material and product (structural component) fatigue properties. It is thus advisable to develop new test methods which will expand on the currently utilised procedures (normative requirements).

The tests to identify cyclic properties of materials using mini specimens have been developed to verify new test methods. Specimen geometry is defined below standard dimensions (PN-74/H-04327). A small size of the specimen allows to extend the scope of material fatigue tests to the products where taking normative samples is not feasible. Its low volume also facilitates comprehensive fatigue test in case of limited availability of the tested material. It applies to the assessment of a damage extent of components in use compared to new components (Lord et al., 2002). It also seems that the use of the mini specimens may reduce the high costs of fatigue tests resulting mostly from the availability of the testing machines, through the reduced range of forces used (lower specimen cross-section) and use of less expensive loading systems.

The mini specimen geometry is characterised by a low cross-section and a low rigidity thus resulting in a low buckling resistance, which requires use of tensile stress only (stress ratio ($R = \sigma_{min}/\sigma_{max}$) higher than zero). The data for symmetric stress cycles ($R = -1$) or cycles pulsating from zero ($R = 0$) are used in the fatigue strength engineering calculations. The test results (fatigue strength) obtained for the mini specimen based on the resulting equations (R – actual) must be estimated to the equations for $R = -1$ or $R = 0$.

The aim of the study is to determine the fatigue strength for $R = -1$ cycles based on the σ_a - N characteristics empirically determined for $R = 0.1$ (for a mini specimen) and to analyse selected analytical mean stress models. The tests are performed on the aluminum alloy specimens.

^{*} Mgr inż. Tomasz Tomaszewski: Faculty of Mechanical Engineering, University of Technology and Life Sciences, al. Prof. S. Kaliskiego 7, 85-789 Bydgoszcz; Poland, tomaszewski@utp.edu.pl

^{**} Prof. dr hab. inż. Janusz Sempruch: Faculty of Mechanical Engineering, University of Technology and Life Sciences al. Prof. S. Kaliskiego 7, 85-789 Bydgoszcz; Poland, semjan@utp.edu.pl

2. Stress Cycle Asymmetry

A fatigue life depends on stress amplitude (σ_a) and a mean stress (σ_m). The ratio varies for different metals and determines material sensitivity to the stress cycle asymmetry (ψ_σ). Its value within the fatigue limit is expressed as the following equation:

$$\psi_\sigma = \frac{2\sigma_{(-1)} - \sigma_{(0)}}{\sigma_{(0)}} \quad (1)$$

where:

$\sigma_{(-1)}$ – fatigue life for $R = -1$,

$\sigma_{(0)}$ – fatigue life for $R = 0$.

The increase in coefficient ψ_σ indicates higher sensitivity of material to the stress cycle asymmetry. The aluminum alloys does not feature a sharply outlined fatigue limit (Sonsino, 2007). The coefficient ψ_σ was verified at a fatigue strength corresponding to the fatigue life of 2×10^6 (σ_a-N curve break).

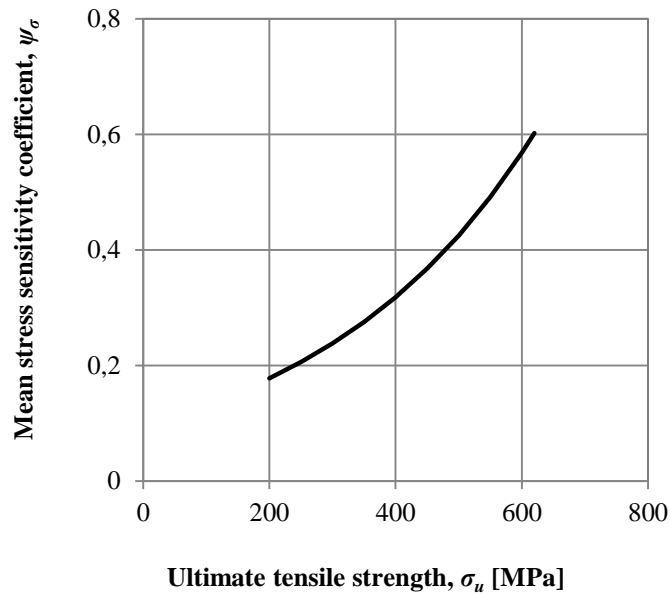


Fig. 1: Relation between the mean stress sensitivity coefficient and the ultimate tensile strength (Schütz curve (Schijve, 2004)).

Tab. 1: Models of mean stress effects (Ligaj et al., 2011; Sekercioglu et al., 2013).

Author	Form	Author	Form
Gerber	$\sigma_a = \sigma_{(-1)} \left[1 - \left(\frac{\sigma_m}{\sigma_u} \right)^2 \right]$	Goodman	$\sigma_a = \sigma_{(-1)} \left[1 - \left(\frac{\sigma_m}{\sigma_u} \right) \right]$
Haigh	$\sigma_a = \sigma_{(-1)} \left[1 - \left(\frac{\sigma_m}{\sigma_u} \right)^2 \right]^{1/2}$	Soderberg	$\sigma_a = \sigma_{(-1)} \left[1 - \left(\frac{\sigma_m}{\sigma_y} \right) \right]$
Morrow	$\sigma_a = \sigma_{(-1)} \left[1 - \left(\frac{\sigma_m}{\sigma_f} \right) \right]$	Smith-Watson-Topper	$\sigma_a = \frac{\sigma_{(-1)}}{\sqrt{\frac{2}{1-R}}}$
Bagci	$\sigma_a = \sigma_{(-1)} \left[1 - \left(\frac{\sigma_m}{\sigma_y} \right)^4 \right]$	ASME-elliptic	$\sigma_a = \sigma_{(-1)} \left[1 - \left(\frac{\sigma_m}{\sigma_y} \right)^2 \right]^{1/2}$
Clemson	$\sigma_a = \sigma_{(-1)} \left[1 - \left(\frac{\sigma_m}{\sigma_y} \right)^{\sigma_y / \sigma_{(-1)}} \right]$	Sekercioglu	$\sigma_a = \sigma_{(-1)} \left[1 - \left(\frac{\sigma_m}{\sigma_y} \right)^2 \right]^k$

The strength and fatigue properties of aluminum alloys were used to analyse the mean stress effect (literature: 24S-T3 (Grover et al., 1954), 75S-T6 (Grover et al., 1954), 6061-T6 (Sekercioglu et al., 2013), D16CzATW (Szala et al., 2005), own studies: AW-6063-T6). The coefficient ψ_σ is related to a tensile strength. The relation is shown as a curve in Fig. 1. The mean stress effect increases in materials with a higher tensile strength.

A model of the mean stress effect is also used to describe the relation between the stress amplitude (σ_a) and the mean stress (σ_m) (see Tab. 1). It determines fatigue strength for cycles at different stress ratio (R). Goodman, Morrow and Sederberg model are used for the linear relation between σ_a and σ_m . Other models describe the relation as a parabola. A material strength property ($\sigma_u, \sigma_y, \sigma_f$) and the equation are variable model parameters.

3. Verification of the Effect of Mean Stress on Aluminum Alloys

Mini specimen test results may create problems with the effect of scale and mean stress. The analyses including the identification of the effect of scale were discussed in relevant studies (Tomaszewski et al., 2012; Tomaszewski et al., 2014). This article focuses on the effect of mean stress. The curve σ_a-N ($R = -1$) was determined based on the characteristics of determined experimentally for $R = 0.1$ cycles with selected models of the effect of mean stress.

The model analysis was performed for EN AW-6063 aluminum alloy (see Fig. 2). The characteristics were determined experimentally for a mini specimen with a cross-section of 3.5 mm^2 . The tests of high-cycle fatigue with controlled stress were performed. The detailed test conditions are detailed in the relevant study (Tomaszewski et al., 2012).

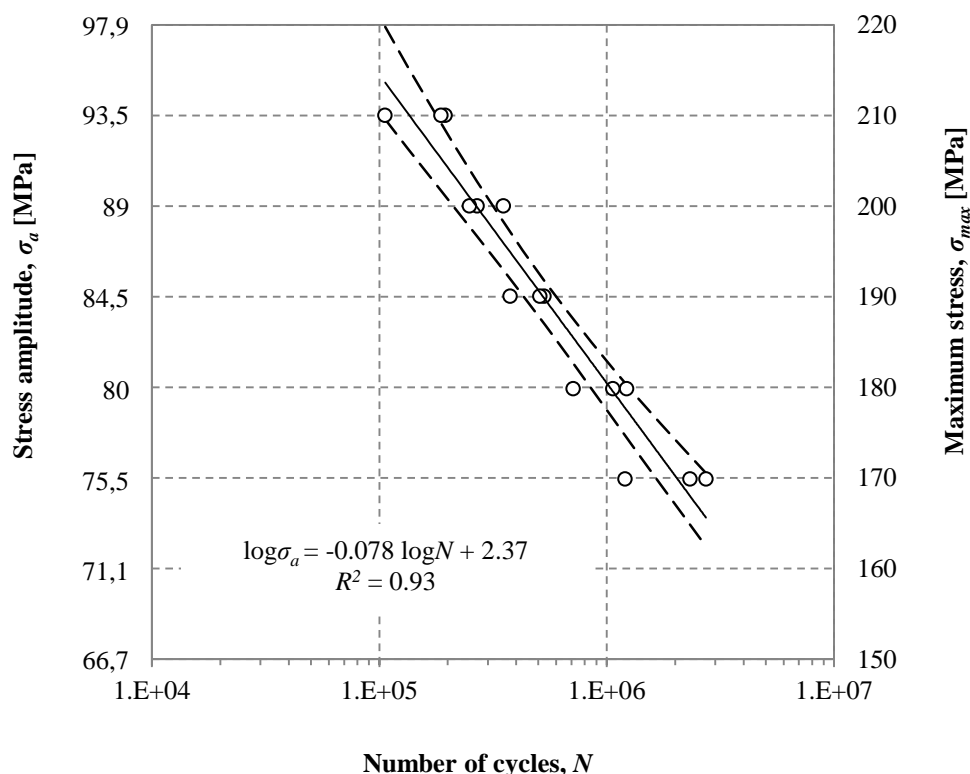


Fig. 2: Curve σ_a-N for a mini specimen made of EN AW-6063 aluminum alloy.

Fatigue strength was estimated within the lower (1.3×10^5 cycles) and the upper (2×10^6 cycles) high-cycle fatigue limits. The curves σ_a-N for $R = -1$ are shown in Fig. 3. The results were compared with a fatigue strength determined based on the coefficient ψ_σ as read from a Schütz curve (Fig. 3b) for EN AW-6063 ($\sigma_u = 230 \text{ MPa}$, $\psi_\sigma = 0.19$).

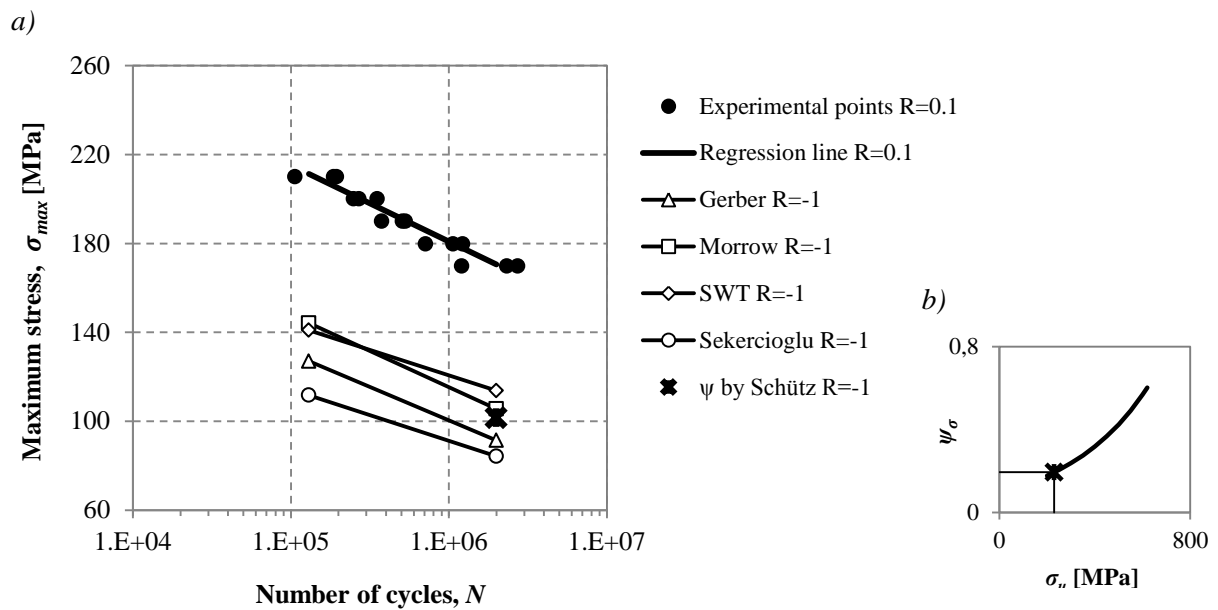


Fig. 3: Mean stress effect analysis: a) σ_a - N curve position; b) Schütz curve for EN AW-6063 aluminum alloy.

4. Summary

One of the most significant limitations of using the mini specimens to determine the σ_a - N fatigue characteristics is the use of loads with a tensile component only (i.e. one-sided at $R > 0$). The analysis of selected analytical models of the effect of mean stress on fatigue strength was performed. The scope of analysis included a verification of errors in estimation of the fatigue strength of aluminum alloys. The models used allowed the assessment of characteristics ($R = -1$) other than experimental ($R = 0.1$).

References

- Grover, H. J., Hyler, W. S., Kuhn, P., Landers, C. B., Howell, F. M. (1954) Axial-load fatigue properties of 24S-T and 75S-T aluminum alloy as determined in several laboratories, National Advisory Committee for Aeronautics Collection, 1190.
- Ligaj, B., Szala, G. (2011) Two-parameter fatigue characteristics of structural steels and their experimental verification, Wydawnictwo Instytutu Technologii Eksploatacji – Państwowego Instytutu Badawczego (in Polish).
- Lord, J., Orkney, L., Roebuck, B. (2002) Validation of a miniature tensile strength measurement system, Small Specimen Test Techniques: Fourth Volume, Journal of ASTM International, pp. 234-250.
- PN-74/H-04327 The study of metal fatigue. Trying to axial tension - compression at constant cycle of external loads (in Polish).
- Schijve, J. (2004) Fatigue of Structures and Materials, Kluwer Academic Publishers.
- Sekercioglu, T., Canyurt, O. E. (2013) Development of the positive mean stress diagrams using genetic algorithm approach, Fatigue & Fracture of Engineering Materials & Structures, pp. 1-8.
- Sonsino, C. M. (2007) Course of SN-curves especially in the high-cycle fatigue regime with regard to component design and safety, International Journal of Fatigue, 29, pp. 2246-2258.
- Szala, J., Lipski, A. (2005) Concept descriptions of the fatigue properties of materials in the calculation of the fatigue life of components, Zagadnienia Eksploatacji Maszyn, Vol. 40, Nr. 2, pp. 71-90 (in Polish).
- Tomaszewski, T., Sempruch, J. (2012) Determination of the fatigue properties of aluminum alloy using mini specimen, Materials Science Forum, 726, pp. 63-68.
- Tomaszewski, T., Sempruch, J. (2014) Verification of the fatigue test method applied with the use of mini specimen, Key Engineering Materials, 598, pp. 243-248.

HOMOGENIZATION OF THE ELECTRO-OSMOSIS PHENOMENA IN THE CORTICAL BONE POROUS STRUCTURE

J. Turjanicová^{*}, E. Rohan^{**}

Abstract: *This note deals with the electro-osmosis phenomena in the cortical bone micro-structure considered as porous medium with one porosity level. The microscopic model is given by the system of equations describing the ionic transport in a canalicular network saturated with a bone ionized fluid. Unfolding homogenization method is used to derive effective equations for the ion concentrations and electric field potentials.*

Keywords: Homogenization, Electro-osmosis, Porous medium, Biomechanics.

1. Introduction

The electro-osmosis in the porous medium is a multiscale phenomenon with numerous applications in geophysics or tissue biomechanics. In particular, the electro-osmosis is responsible for important physiological processes in the cortical bone tissue. Cortical bone is seen as a highly hierarchical structure with multiple porosities on different scale levels of the osteon; usually the following three main levels are distinguished (Moyné and Murad, 2002). The vascular porosity level is the largest one, represented by the Haversian (or osteonal) and the Volkmann canals distributed in the collagen-apatite matrix. This matrix is porous; it incorporates lacunae and canaliculi which form the lacuno-canalicular porosity. Its matrix is formed by porosity associated with the space between collagen and the crystallites of the mineral apatite.

The present work is focused on electro-osmosis phenomena at the lacuno-canalicular porosity level, further referred to as the microscopic level. At this scale the mechanotransduction is an important phenomenon responsible for the bone tissue resorption and deposition (Rohan et al., 2012). Both these processes are related to the strain generated electric potentials which are associated with the electrolyte flows in the pores.

The lacuno-canalicular porosity (characteristic scale $l \approx 10 \text{ nm}$) can be modeled as a porous medium with fluid filled pores in the solid matrix. The fluid is a solution with two types of monovalent ions of opposite polarizations (cations Na^+ and anions Cl^-). Further, we consider the solid phase and the solid-fluid interface, both featured by negative electric charges.

In this short text, in Section 2, we present a mathematical model of electro-diffusion relevant to the porosity level and report on the homogenization result in Section 3, to provide an effective model relevant to the macroscopic scale, i.e. the osteon level. The numerical implementation of the two-scale modeling has been made and is illustrated in Section 3.

2. Mathematical Model

This section provides a brief description of mathematical relations describing the electro-osmosis at the microscopic level. The model describing macroscopic behaviour was obtained by homogenization.

^{*} Ing. Jana Turjanicová: Department of Mechanics, University of West Bohemia in Pilsen, Univerzitní 8; 301 00, Pilsen; CZ, turjani@kme.zcu.cz

^{**} Prof. Dr. Ing. Eduard Rohan, DSc.: Dept. of Mechanics, New Technologies for Information Society – The Center of Excellence, Univerzitní 8; 301 00, Pilsen; CZ, rohan@kme.zcu.cz

2.1. Model of electro-osmosis

The porous medium occupies the domain Ω with coordinations $x \in R^n$, which is decomposed into solid and fluid parts denoted as Ω_s and Ω_f , respectively. The solid-fluid interface Γ is defined as $\Gamma = \partial\Omega_f \cap \partial\Omega_s$ with the outward normal unit vector, \mathbf{n} in general, thus $\mathbf{n}^s = -\mathbf{n}^f$. Through the text the symbol ∂ denotes a boundary of a domain and subscripts s and f refer to quantities belonging to the solid and fluid parts, respectively. Further, the mathematical model of electro-diffusion is introduced.

$$-\nabla \cdot \alpha_s \epsilon_0 \nabla \Phi = \hat{\pi}_s \quad \text{in } \Omega_s \quad (1)$$

$$-\nabla \cdot \alpha_f \epsilon_0 \nabla \Phi = \pi_f \quad \text{in } \Omega_f \quad (2)$$

$$\mathbf{n} \cdot \alpha \nabla \Phi = 0 \quad \text{on } \partial\Omega \quad (3)$$

$$\mathbf{n}^f \cdot \alpha_f \nabla \Phi|_f = -\alpha_f / e_f [\Phi]_\Gamma + \rho/2 \quad \text{on } \Gamma_f \quad (4)$$

$$\mathbf{n}^s \cdot \alpha_s \nabla \Phi|_s = -\alpha_s / e_s [\Phi]_\Gamma - \rho/2 \quad \text{on } \Gamma_s \quad (5)$$

$$\partial Q^\pm / \partial t + \mathbf{w}_f \cdot \nabla Q^\pm - \nabla \cdot \mathbf{D} \cdot (\nabla Q^\pm \pm (z^\pm F / RT) Q^\pm \nabla \Phi) = 0 \quad \text{in } \Omega_f \quad (6)$$

$$\mathbf{n} \cdot \mathbf{D}^\pm \cdot (\nabla Q^\pm \pm (z^\pm F / RT) Q^\pm \nabla \Phi) = 0 \quad \text{on } \Gamma \quad (7)$$

$$Q^\pm = Q_0^\pm \quad \text{on } \partial\Omega \setminus \Gamma \quad (8)$$

Eqs. (1) and (2) are the Gauss-Poisson equations of electrostatics in the solid and fluid, where $\alpha_d, d = f, s$ is relative permittivity, ϵ_0 is permittivity of the void space, π_d is a volume electric charge and by Φ is the electric potential. Using Faraday constant F and the valence of ion particles $z^+ = 1, z^- = -1$, the volume electric charge in the fluid can be expressed, by the definition, as the product between the molar charges and the difference of concentration of cations Q^+ and anions Q^- , thus $\pi_f = F(z^+ Q^+ - z^- Q^-)$.

The two boundary conditions (4) and (5) result from one-dimensional electrostatics Dirichlet problem describing charge distribution in a thin layer of thickness e on the solid-fluid interface, where represent modified charge. The condition (3) means that the medium is isolated from outer space.

The movement of ions is described by the Nernst-Planck equation (6), for Newtonian incompressible fluid with vector of convection velocity \mathbf{w}_f and absolute temperature T . Water-ion diffusion coefficients for cations and anions are in form of second-order tensors \mathbf{D}^\pm and R is constant of ideal gas. By condition (8) the electroneutrality is preserved, while (7) expresses the flux of ions through Γ .

2.2. Microscopic model

Following the approach introduced in the report Rohan (2012), the upscaling of linearized system (1)-(8) in its dimensionless weak form was performed using the periodic homogenization using the assumption of material periodicity; Ω is assumed to be generated as a periodic lattice based on the so-called representative periodic cell (RPC) Y with coordinates $y = x/\epsilon$, where ϵ_0 is the small parameter of the asymptotic analysis, describing the scale between macro- and microscopic coordinates. The dimensionless potentials φ_d^ϵ and concentrations $v^{\pm\epsilon}$ are decomposed into their macro- (denoted by superscript 0) and microscopic (superscript 1) parts as

$$v^\epsilon(x) = v^{\epsilon,0}(x, x/\epsilon) + \epsilon v^{\epsilon,1}(x, x/\epsilon) \quad \varphi^\epsilon(x) = \varphi^{\epsilon,0}(x, x/\epsilon) + \epsilon \varphi^{\epsilon,1}(x, x/\epsilon)$$

Knowing osteon micro-structure, namely the canalicular network geometry, the RPC Y is decomposed accordingly to domain $\Omega, Y = Y_s \cup Y_f \cup \Gamma_Y, Y_f = Y \setminus \bar{Y}_f, \Gamma_Y = \bar{Y}_s \cap \bar{Y}_f$. By the homogenization, the local problems on the RPC Y are obtained, as follows: Find $(\varphi_f^1, \varphi_s^1, v^{\pm 1})$ such that for $x \in \Omega$

$$\int_{\Omega \times Y_f} \mathbb{D}^\pm \cdot (\nabla_x \vartheta^{0\pm} + \nabla_y \vartheta^{1\pm}) \cdot \nabla_y \theta^{1\pm} + \int_{\Omega \times Y_f} \bar{\beta}(\pm c^\pm) \mathbb{D}^\pm \cdot (\nabla_x \varphi_f^0 + \nabla_y \varphi_f^1) \cdot \nabla_y \theta^{1\pm} = 0, \quad (9)$$

$$\int_{Y_d} \alpha_d (\nabla_x \varphi_d^0 + \nabla_y \varphi_d^1) \cdot \nabla_y \psi_d^1 = 0, \quad d = f, s, \quad (10)$$

for all test function θ^\pm, ψ_d^j in Sobolev space of admissible Y-periodic functions $H^1_\#(Y_d)$. By virtue of the problem linearization, c^\pm are given ionic concentrations and $\bar{\beta} = \Phi_Z F/RT$. Symbol \int refers to $1/|Y| \int$.

2.3. Homogenized model

Following steps from the report Rohan (2012), the microscopic parts of variables $(\varphi_f^j, \varphi_s^j, \nu^{j\pm})$ can be express as a linear combinations of so-called corrector basis functions. Those functions represent characteristic response on the RPC Y and are necessary for expressions of effective coefficients $\mathbf{D}_H^\pm, \mathbf{B}_H^\pm, \mathbf{A}_H^d, \mathbf{C}_H^\pm, \mathbf{S}_H^\pm$ approximating characteristics of the macroscopic medium. The homogenized macroscopic form of the electrostatic equation for the potential φ_f^0, φ_s^0 in the solid and the fluid yields

$$\begin{aligned} & \sum_{d=f,s} \int_{\Omega} \nabla \psi_d^0 \cdot \mathbb{A}_H^d \cdot \nabla \varphi_d^0 + \int_{\Omega} \mathcal{M}_{\Gamma_Y}(\bar{\alpha})(\varphi_f^0 - \varphi_s^0)(\psi_f^0 - \psi_s^0) - \\ & - \frac{|Y_f|}{\lambda_D^2 |Y|} \int_{\Omega} \psi_f^0 (\vartheta^{0+} - \vartheta^{0-}) = \int_{\Omega} \mathcal{M}_{\Gamma_Y}(\bar{\pi}_s) \psi_s^0 + \int_{\Omega} \frac{\psi_f^0 + \psi_s^0}{2} \mathcal{M}_{\Gamma_Y}(\bar{\varrho}), \end{aligned} \quad (11)$$

for all $\psi_d^0 \in H^1(\Omega)$. Note, that \mathcal{M} is an operator of a mean value of a variable over the interface. By overline the dimensionless variables are denoted.

The electro-diffusion on the macroscopic scale is described by two equations for concentrations $(\nu^{0\pm})$

$$\begin{aligned} & \frac{|Y_f|}{|Y|} \int_{\Omega} \partial_t \vartheta^{0\pm} \theta^{0\pm} + \int_{\Omega} \mathbf{C}_H^\pm(\mathbf{w}_f) \cdot \nabla (\vartheta^{0+} + \vartheta^{0-}) \theta^{0\pm} + \int_{\Omega} \mathbf{S}_H^\pm(\mathbf{w}_f) \cdot (\nabla \varphi_f^0) \theta^{0\pm} + \\ & + \sum_{z=+,-} \int_{\Omega} \nabla \theta^{0z} \cdot \mathbb{D}_H^\pm \cdot \nabla (\vartheta^{0+} + \vartheta^{0-}) + \int_{\Omega} \nabla \theta^{0z} \cdot \mathbb{B}_H^\pm \cdot \nabla \varphi_f^0 = 0 \end{aligned} \quad (12)$$

for all $\theta^{0z} \in H^1(\Omega)$. If we consider symmetric electrolyte, Eq. (11) becomes independent on the concentration and, thus, can be solved separately from Eqs. (12), now reduced to only one equation for variable ν^0 , see (Turjanicová, 2013).

3. Results

The homogenization procedure and homogenized problem on macroscale was implemented in the software *SfePy*. The canalicular level was represented by cubic RPC with three connected channels in directions of main axes. The homogenized problem given by Eqs. (11) and (12) was solved on the simple prismatic geometry, representing small part of osteonal wall. The left side of Fig. 1 illustrates the macroscopic solutions $(\varphi_f^0, \varphi_s^0, \nu^0)$ alongside the y-coordinate of test problem with boundary and initial conditions $\varphi_s^0(x, l, z) = 100, \varphi_f^0(x, l, z) = 0, \nu_f^0(x, l, z, t) = 10, \nu^0(x, y, z, 0) = 10$. On the right in the Fig. 1 is shown recovered microscopic diffusion flux on the RPC Y representing microstructure.

4. Conclusions

This work reports on the two-scale modeling of electro-osmosis phenomenon in the cortical bone osteon. The microscopic model with only one porosity level was introduced, whereby the flow problem was treated as decoupled. The homogenized model enables to describe distribution of voltage in both solid and fluid phases and the ionic concentrations at the macroscopic level of bone osteon. By virtue of the corrector results, the microscopic distribution of electric fields and concentration fluxes can be recovered.

It is possible to assess influence of the geometrical arrangement of the fluid channels in the microstructure on the effective material properties and the local electro-osmosis processes. In the further research an extension of the model for coupled fluid-solid interaction will be pursued and the role of the solid piezoelectricity will be reviewed in the context of the recent work (Lemaire et al., 2011), where an alternative upscaling approach was used.

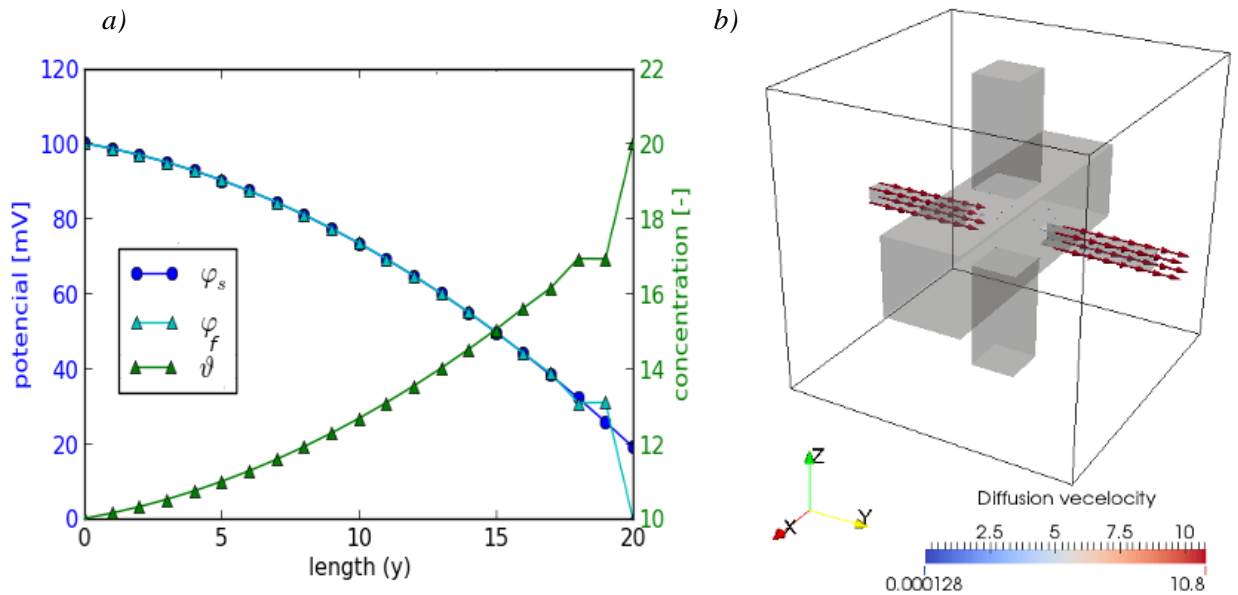


Fig. 1: a) Solutions (φ_f^0 , φ_s^0 , ψ^0) of homogenized problem; b) Recovered microscopic diffusion velocity on the RPC Y.

Acknowledgement

The research of was supported in part by project NT 13326 of the Ministry of Health of the Czech Republic and by the European Regional Development Fund (ERDF), project “NTIS - New Technologies for Information Society”, European Centre of Excellence, CZ.1.05/1.1.00/02.0090. Jana Turjanicová is also grateful for the support of her work by project SGS-2013-026.

References

- Moyne, C., Murad, M. A. (2002) Electro-chemo-mechanical couplings in swelling clays derived from a micro/macro-homogenization procedure, *Int. J. of Sol. and Struc.*, Inst. for Research, 39, 25, pp. 6159-6190.
- Lemaire, T., et al. (2011) A multiscale theoretical investigation of electric measurements in living bone – Piezoelectricity and electrokinetics, *Bull. Math. Biol.*, 73, pp. 2649-2677.
- Rohan, E. (2012) Homogenization of electro-osmosis in porous solid saturated by ionized fluid. Report - preprint.
- Rohan, E., et al. (2012) Multiscale modeling of a fluid saturated medium with double porosity: Relevance to the compact bone, *Journal of the Mechanics and Physics of Solids*, 60, 5, pp. 857-881.
- Turjanicová, J. (2013) Electro-mechanical coupling in porous bone structure - homogenization method application, Diploma thesis, University of West Bohemia, Pilsen.

THE INFLUENCE OF DIFFERENT IMPLEMENTATION OF PERIODIC BOUNDARY CONDITIONS INTO FEM SOFTWARE

S. Urbanová^{*}, J. Vorel^{**}, M. Šejnoha^{***}

Abstract: *This paper deals with the implementation of periodic boundary conditions in homogenization to determine effective elastic properties of arbitrary composite systems assuming two specific implementation schemes. As an example, the homogenization procedure applied to a composite system with plain weave textile basalt reinforcement was examined. The geometry of the analyzed sample was idealized with the help of statistically equivalent periodic unit cell. The comparison of the effective properties shows consistency of both implementations.*

Keywords: Periodic boundary conditions, Homogenization, Finite element method, Stress control, Strain control.

1. Introduction

Even with a large number of various numerical techniques at hand, the finite element method (FEM) is still considered to be the most universal method for solving variation formulated problems of physics connected to problems of field theory. One of the significant advantages of FEM in the field of continuum mechanics is particularly the possibility of solving tasks for universal geometric shapes of the analysis domain, universal load and support and also for complex constitutive relations of a material. Herein, FEM is adopted to solve the homogenization problem at the level of statistically equivalent periodic unit cell (SEPUC) of a textile reinforced composite formulated at the level of yarns, meso-scale.

In particular, we are concerned with a representative volume element (RVE) having well defined geometry and boundary conditions. Since this RVE is assumed periodic, often termed a periodic unit cell (PUC), the formulation has to be accompanied by so called periodic boundary conditions. In terms of loading, two different approaches can be adopted, stress or strain control loading conditions, to arrive at the estimates of effective properties. In terms of numerical implementation, we compare two specific ways of implementing periodic boundary conditions here linked to FEIn and OOFEM software products, respectively (Patzák and Bittnar).

2. Solution in Terms of Fluctuation Fields - FEIn

First, we consider the FEIn software product that allows for a direct application of the load in the form of macroscopically constant strain \mathbf{E} , or stress $\boldsymbol{\Sigma}$. Unlike most commercial software, here the primary unknown is the fluctuation part of the displacement field \mathbf{u}^* , which enables rather straightforward implementation of the periodic boundary conditions. This step will be explained as one particular point of a general 1st order homogenization scheme discussed next.

To that end, suppose that the local strain field can be decomposed into the homogeneous, macroscopically linear part $\mathbf{U} = \mathbf{E} \cdot \mathbf{x}$ and the fluctuation part \mathbf{u}^* such that

$$\mathbf{u}(\mathbf{x}) = \mathbf{E} \cdot \mathbf{x} + \mathbf{u}^*(\mathbf{x}). \quad (1)$$

* Ing. Soňa Urbanová: Faculty of Civil Engineering, CTU in Prague, Thákurova 7, 166 29, Prague; CZ, sona.urbanova@fsv.cvut.cz

** Ing. Jan Vorel, PhD.: Faculty of Civil Engineering, CTU in Prague, Thákurova 7, 166 29, Prague; CZ, jan.vorel@fsv.cvut.cz

*** Prof. Ing. Michal Šejnoha, PhD., DSc.: Faculty of Civil Engineering, CTU in Prague, Thákurova 7, 166 29, Prague; CZ, sejnomo@fsv.cvut.cz

Local strain thus becomes

$$\boldsymbol{\varepsilon}(x) = \mathbf{E} + \boldsymbol{\varepsilon}^*(x). \quad (2)$$

The displacements \mathbf{u}^* are assumed periodic, the same displacements \mathbf{u}^* on opposite sides of the unit cell, to ensure that the fluctuation part of strain disappears up on volume averaging, i.e. $\langle \boldsymbol{\varepsilon}^* \rangle = \mathbf{0}$, $\langle \boldsymbol{\varepsilon} \rangle = \mathbf{E}$.

Introduction of local $\boldsymbol{\sigma}(x)$ and macroscopic $\boldsymbol{\Sigma} = \langle \boldsymbol{\sigma} \rangle$ stress fields allows us to express the virtual format of Hill's Lemma as

$$\langle \delta \boldsymbol{\varepsilon}(x)^\top \boldsymbol{\sigma}(x) \rangle = \delta \mathbf{E}^\top \boldsymbol{\Sigma}. \quad (3)$$

The local constitutive law reads

$$\boldsymbol{\sigma}(x) = \mathbf{L}(x) \boldsymbol{\varepsilon}(x). \quad (4)$$

Substituting Eq. (4) into Eq. (3) gives

$$\delta \mathbf{E}^\top \langle \mathbf{L}(x) (\mathbf{E} + \boldsymbol{\varepsilon}^*(x)) \rangle + \langle \delta \boldsymbol{\varepsilon}^*(x)^\top \mathbf{L}(x) \mathbf{E} \rangle + \langle \delta \boldsymbol{\varepsilon}^*(x)^\top \mathbf{L}(x) \boldsymbol{\varepsilon}^*(x) \rangle = \delta \mathbf{E}^\top \boldsymbol{\Sigma}. \quad (5)$$

Since $\delta \mathbf{E}$ and $\delta \boldsymbol{\varepsilon}^*(x)$ are independent, we can split Eq. (5) into two equations

$$\delta \mathbf{E}^\top \boldsymbol{\Sigma} = \delta \mathbf{E}^\top \left[\langle \mathbf{L}(x) \rangle \mathbf{E} + \langle \mathbf{L}(x) \boldsymbol{\varepsilon}^*(x) \rangle \right], \quad (6)$$

$$0 = \langle \delta \boldsymbol{\varepsilon}^*(x)^\top \mathbf{L}(x) \rangle \mathbf{E} + \langle \delta \boldsymbol{\varepsilon}^*(x)^\top \mathbf{L}(x) \boldsymbol{\varepsilon}^*(x) \rangle. \quad (7)$$

Referring to (Šejnoha and Zeman, 2013) it can be shown that Eq. (6) and (7) are directly applicable when prescribing the overall stress $\boldsymbol{\Sigma}$. In case of prescribed overall strain \mathbf{E} , Eq. (7) reduces to

$$\Omega \langle \mathbf{L}(x) (\mathbf{E} + \boldsymbol{\varepsilon}^*(x)) \delta \boldsymbol{\varepsilon}^*(x) \rangle = 0. \quad (8)$$

There are two options how to account for the periodic boundary conditions. If starting directly from Eq. (6) and (7) or Eq. (8), the solution is searched in terms of unknown \mathbf{u}^* . In such a case the periodicity of \mathbf{u}^* is enforced simply by assigning the same code numbers to the associated degrees of freedom of \mathbf{u}^* . However, when using commercial codes implementation of periodic boundary conditions is not that straightforward and will be explained in more detail in the next section.

3. Solution in Terms of Total Fields - OOFEM

To begin with, assume a three-dimensional rectangular SEPUC with dimensions l (x-direction), b (y-direction) and h (z-direction), see Fig. 1.

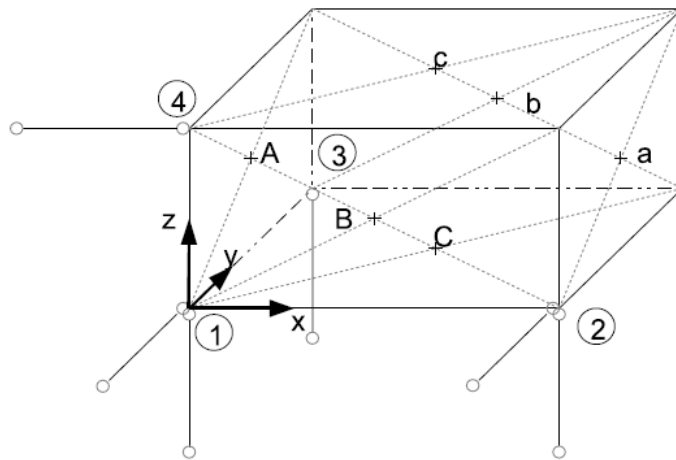


Fig. 1: Scheme of SEPUC.

The macroscopic linear displacements attain the form

$$\begin{Bmatrix} U_{(x,y,z)} \\ V_{(x,y,z)} \\ W_{(x,y,z)} \end{Bmatrix} = \underbrace{\begin{bmatrix} 1 - \frac{x}{l} - \frac{y}{b} - \frac{z}{h} & \frac{x}{l} & \frac{y}{b} & 0 & 0 & 0 \\ 0 & 0 & 0 & \frac{y}{b} & \frac{z}{h} & 0 \\ 0 & 0 & 0 & 0 & 0 & \frac{z}{h} \end{bmatrix}}_{\mathbf{A}} \underbrace{\begin{Bmatrix} u_1 \\ u_2 \\ u_3 \\ v_3 \\ v_4 \\ w_4 \end{Bmatrix}}_{\mathbf{d}}, \quad (9)$$

u_1 - w_4 corresponds to free nodal displacements of the supported nodes, see Fig. 1. The associated strain field is then provided by

$$\underbrace{\begin{Bmatrix} E_{xx} \\ E_{yy} \\ E_{zz} \\ 2E_{xy} \\ 2E_{yz} \\ 2E_{xz} \end{Bmatrix}}_{\mathbf{E}} = \underbrace{\begin{bmatrix} -\frac{1}{l} & \frac{1}{l} & 0 & 0 & 0 & 0 \\ 0 & 0 & 0 & \frac{1}{b} & 0 & 0 \\ 0 & 0 & 0 & 0 & \frac{1}{h} & 0 \\ -\frac{1}{b} & 0 & \frac{1}{b} & 0 & 0 & 0 \\ 0 & 0 & 0 & 0 & \frac{1}{h} & 0 \\ -\frac{1}{h} & 0 & 0 & 0 & 0 & 0 \end{bmatrix}}_{\mathbf{B}} \underbrace{\begin{Bmatrix} u_1 \\ u_2 \\ u_3 \\ v_3 \\ v_4 \\ w_4 \end{Bmatrix}}_{\mathbf{d}} \Rightarrow \mathbf{E} = \mathbf{B}\mathbf{d} \quad (10)$$

Combining Eqs. (10) and (9) gives

$$U_{(x,y,z)} = E_{xx}x + 2E_{xy}y + 2E_{xz}(z - H) + u^*_{(x,y,z)}, \quad (11)$$

$$V_{(x,y,z)} = E_{yy}y + 2E_{yz}z + v^*_{(x,y,z)}, \quad (12)$$

$$W_{(x,y,z)} = E_{zz}z + w^*_{(x,y,z)}. \quad (13)$$

The assumption of periodic boundary condition leads to

$$u_a = -u_1 + u_2 + u_A, \quad (14)$$

$$v_b = v_3 + v_B, \quad (15)$$

$$w_c = w_4 + w_C. \quad (16)$$

When macroscopic constant strain is prescribed, the control displacements in the form (11) - (13) need to be prescribed while for the stress control conditions, the appropriate averages of stress components can be ensured by applying appropriate concentrated forces according to the next equations

$$\mathbf{F} = \mathbf{B}^T \boldsymbol{\Sigma} lhb. \quad (17)$$

4. Evaluation of Effective Properties Using Periodic Boundary Conditions

As an example, we consider the composite reinforced by plain weave basalt reinforcement, see Fig. 2.

The actual analysis was performed exploiting the SEPUC in Fig. 1, see (Šejnoha and Zeman, 2013, Vorel et al., 2013) for more details.

The analyzed composite consists of three materials – pores, matrix and basalt reinforcements. At the level of SEPUC (meso-scale), the reinforcements are introduced through the homogenized properties of yarns. These in turn are found from an independent homogenization procedure carried out first at the level of fibers (micro-scale) here employing the Mori-Tanaka averaging scheme (Šejnoha and Zeman, 2013). This method builds upon the knowledge of the shape and orientation of the reinforcements, their material properties and volume fractions. The resulting homogenized properties of the basalt yarn together with

the assumed matrix properties are listed in Tab.1. Tab. 2 then summarizes the effective stiffnesses of the entire system obtained for the two loading conditions and the used software products.

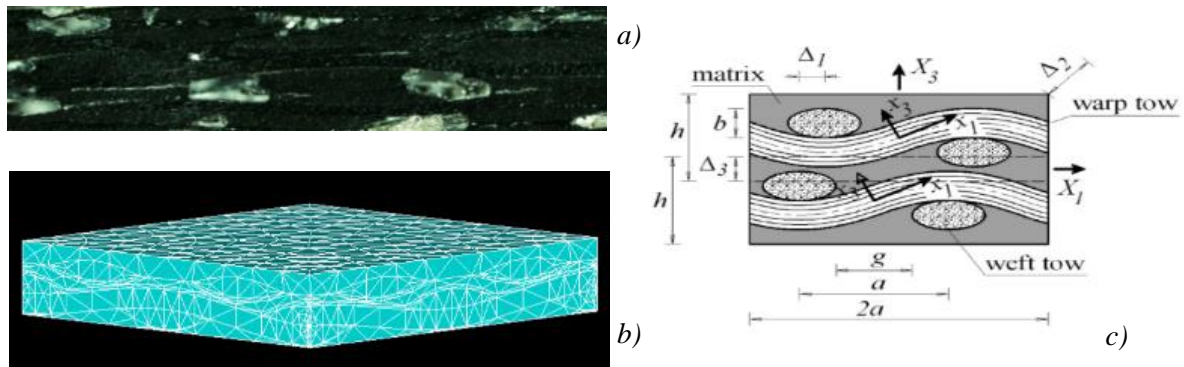


Fig. 2: a) Real microstructure; b) Discretization to finite elements; c) Two-layer SEPUC.

Tab. 1: Considered material properties.

Type of material	Material property								
	E_{xx}	E_{yy}	E_{zz}	G_{yz}	G_{xz}	G_{xy}	ν_{yz}	ν_{xz}	ν_{xy}
	[GPa]			[GPa]			[-]		
Basalt yarns	53	6.1	6.2	2.6	3.6	3.6	0.3	0.23	0.23
Matrix	2.12			0.85			0.24		

Tab. 2: Elements of stiffness tensor of composite system.

Homogenization procedure	Composite with basalt reinforcement					
	Stiffness tensor elements [GPa]					
	C_{11}	C_{22}	C_{33}	C_{44}	C_{55}	C_{66}
Feln - strain control	13.162	13.168	0.542	0.328	0.329	1.758
Feln - stress control	13.162	13.168	0.542	0.328	0.329	1.758
OOFEM - strain control	13.540	13.539	0.704	0.372	0.372	1.756
OOFEM - stress control	13.339	13.342	0.695	0.371	0.371	1.753

5. Conclusions

Four particular approaches were considered in this paper to estimate the effective elastic properties of a multi-layered textile composite reinforced with basalt fabric. The solutions performed in terms of the fluctuation (Feln) as well as total (OOFEM) displacements were examined. It is evident that both formulations deliver almost the same results regardless of the assumed loading conditions. Thus both procedures to implement the periodic boundary conditions are equally applicable.

Acknowledgement

The research project by the Grant Agency of the Czech Technical University in Prague grant no. SGS OHK1-089/14 is gratefully acknowledged.

References

- Patzák, B., Bittnar, Z. (2001) Design of object oriented finite element code. *Advances in Engineering Software*, 32 (10-11):759-767, OOFEM project home page, <http://www.oofem.org>, 2000.
- Šejnoha, M., Zeman, J. (2013) *Micromechanics in practice*. WIT Press, Southampton, Boston.
- Vorel, J., Zeman, J., Šejnoha, M. (2013) Homogenization of plain weave composites with imperfect microstructure: Part II - Analysis of real-world materials. *International Journal for Multiscale Computational Engineering*, 11, 5, pp. 443-462.

BIFURCATION LOAD OF A COLUMN COMPOSED OF PIPE AND ROD WITH TWO-PARAMETRIC ELASTIC ELEMENT

S. Uzny*

Abstract: *In this paper the slender system subjected to Euler's load has been presented. Considered system is composed of two elements: pipe and rod. The rod is mounted concentrically with the pipe; in such way that the deflection and angle of deflection of pipe and rod are identical. The investigated system is hinged on both ends. In the column between pipe and rod the two-parametric elastic element has been placed. Both transversal and rotational displacements are being limited by means of this element. In the work static problem of considered column was formulated on the basis of minimum total potential energy principle (static criterion of instability). Rectilinear form of static equilibrium is only considered in this paper. On the basis of static criterion of instability the bifurcation load (the biggest load at which system is still in the rectilinear equilibrium) has been determined in relation to system's parameters. The parameters of the system are as follows: stiffness of translational and rotational springs (elastic layer), flexural rigidity asymmetry factor (pipe and rod), parameter of location of elastic layer.*

Keywords: Column, Divergence system, Euler's load, Two-parametric elastic layer.

1. Introduction

Slender systems subjected to both conservative and non-conservative type of loads were the subject of many investigations. Euler's load (Euler, 1744; Uzny, 2011; Sokół, 2014), at which external force does not change the direction of action is the most popular one in slender systems. In literature the others types of external load of columns loads can be found. Generalized load (Bochenek and Życzkowski, 2004), a load with force directed towards the positive or negative pole (Gajewski and Życzkowski, 1969), characteristic load (Tomski's load) (Tomski and Uzny, 2008, 2013a) can be considered as a conservative ones. Generalized Beck's load (Beck, 1952; Tomski and Uzny, 2013b; Langthjem and Sugiyama, 2000) and generalized Reut's (Langthjem and Sugiyama, 2000; Nemat-Nasser and Herrmann, 1966) load can be qualified as a non-conservative loads.

Slender systems can be divided into constructions composed of the identical elements or elements with different bending and compression stiffness (Uzny, 2011; Tomski and Uzny, 2008). The second group can be characterized by two forms of static equilibrium: rectilinear and curvilinear. The magnitude of external load, at which rectilinear form occurs, is changing from zero up to value of bifurcation load. Curvilinear form of static equilibrium occurs between bifurcation and critical force. In this type the local and global instability phenomenon occurs (Uzny, 2011; Tomski and Uzny, 2008). The regions of local and global instability depend on flexural rigidity asymmetry factor. Slender system composed of two elements: pipe and rod with different stiffness was researched in work (Uzny, 2011), where a single-parametric elastic layer was placed between pipe and rod. By means of this element an increase in bifurcation load has been achieved (especially in the area of local instability). Additionally in this system the change of buckling form; region of local instability is decreasing at greater stiffness of single-parametric elastic layer.

The main purpose of this work is to study an influence of two-parametric elastic layer on stability of system composed of pipe and concentrically installed rod.

* Prof. Sebastian Uzny, PhD.: Institute of Mechanics and Machine Design Foundation, Częstochowa University of Technology, Dąbrowskiego 73, 42-200 Częstochowa, Poland, uzny@imipkm.pcz.pl

2. Problem Formulation and Solution

Considered column composed of pipe and rod is presented in Fig. 1b (column C2E). The rod is mounted concentrically with the pipe; in such way that the deflection and angle of deflection of pipe and rod are identical. System is loaded by compressive external force with constant line of action (Euler's force). The investigated system is hinged on both ends as shown in Fig. 1a. In the column between pipe and rod the two-parametric elastic element has been placed. Elastic layer was modeled by means of spring system which consist of transversal spring (with rigidity C_T) and rotational one (with rigidity C_R). Location of elastic layer is defined by the parameter ζ . In this study, it is assumed that total flexural rigidity of system is constant ($(EJ)_1 + (EJ)_2 = (EJ) = idem$). Flexural rigidity asymmetry factor is a variable parameter, which is defined as follows:

$$\mu_a = \frac{(EJ)_2}{(EJ)_1} \quad (1)$$

Bifurcation force of complex system will be compared to critical load of the system composed from the pipe only (column C1E) – Fig. 1c. Mathematical model of the investigated complex system (C2E) is presented in Fig. 1a. This model consists of four elements. Elements marked with subscripts 11 and 12 correspond to pipe whereas subscripts 21 and 22 model the rod. Bending rigidities in the mathematical model are marked as follows: $(EJ)_{11} = (EJ)_{12} = (EJ)_1$ and $(EJ)_{21} = (EJ)_{22} = (EJ)_2$.

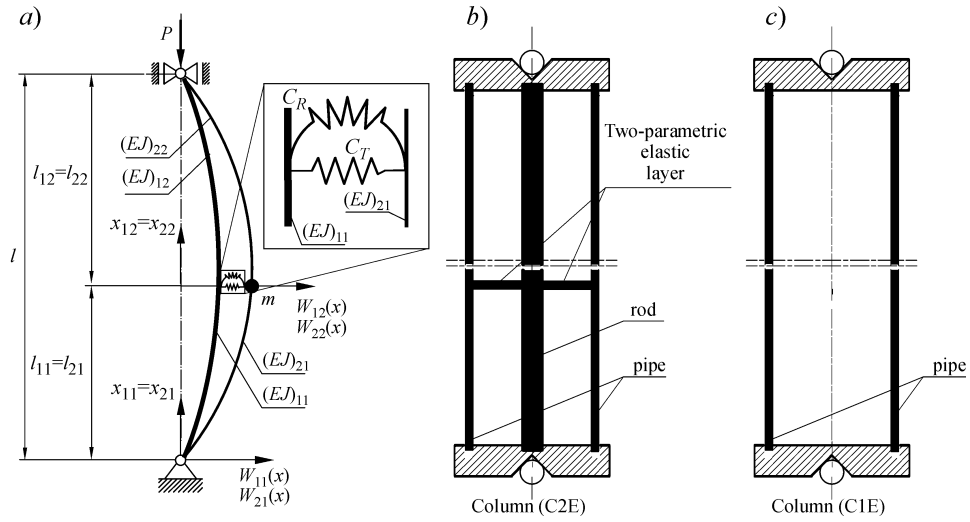


Fig. 1: Considered systems.

The problem has been formulated on the basis of the minimum total potential energy principle.

$$\delta V = 0 \quad (2)$$

Potential energy of considered system is as follows:

$$V = \frac{1}{2} \sum_i \sum_j (EJ)_{ij} \int_0^{l_{ij}} (W_{ij}''(x_{ij}))^2 dx_{ij} - \frac{1}{2} \sum_i \sum_j S_{ij} \int_0^{l_{ij}} (W_{ij}'(x_{ij}))^2 dx_{ij} + \frac{1}{2} C_T (W_{11}(l_{11}) - W_{21}(l_{21}))^2 + \frac{1}{2} C_R \left(W_{11}'(x_{11}) \Big|_{x_{11}=l_{11}} - W_{21}'(x_{21}) \Big|_{x_{21}=l_{21}} \right)^2 \quad (3)$$

Internal forces in individual elements of mathematical model are determined as (Uzny, 2011):

$$S_{11} = S_{12} = P \frac{(EA)_{11}}{(EA)_{11} + (EA)_{21}}, \quad S_{21} = S_{22} = P - S_{11} \quad (4)$$

In equations (4) longitudinal rigidities of individual units are marked as $(EA)_{ij}$. Geometrical boundary conditions of considered column are present below:

$$W_{11}(0) = W_{21}(0) = W_{12}(l_{12}) = W_{22}(l_{22}) = 0, \quad W_{11}(l_{11}) = W_{12}(0), \quad W_{21}(l_{21}) = W_{22}(0) \quad (5a-h)$$

$$W_{11}'(x_{11}) \Big|_{x_{11}=0} = W_{21}'(x_{21}) \Big|_{x_{21}=0}, \quad W_{12}'(x_{12}) \Big|_{x_{12}=l_{12}} = W_{22}'(x_{22}) \Big|_{x_{22}=l_{22}} \quad (5i, j)$$

$$W_{11}^I(x_{11}) \Big|_{x_{11}=l_{11}} = W_{12}^I(x_{12}) \Big|_{x_{12}=0}, W_{21}^I(x_{21}) \Big|_{x_{21}=l_{21}} = W_{22}^I(x_{22}) \Big|_{x_{22}=0} = 0 \quad (5k, l)$$

After substitution of (3) into minimum potential energy principle (2) and taking into account geometrical boundary conditions (5), the differential equation for unknown static displacement (6) and natural boundary conditions (7) were obtained:

$$(EJ)_{ij} W_{ij}^{IV}(x_{ij}) + S_{ij} W_{ij}^{II}(x_{ij}) = 0 \quad (6)$$

$$\sum_i (EJ)_{i1} W_{i1}^{II}(x_{i1}) \Big|_{x_{i1}=0} = 0, \sum_i (EJ)_{i2} W_{i2}^{II}(x_{i2}) \Big|_{x_{i2}=l_{i2}} = 0 \quad (7a, b)$$

$$(EJ)_{11} W_{11}^{III}(x_{11}) \Big|_{x_{11}=l_{11}} - (EJ)_{12} W_{12}^{III}(x_{12}) \Big|_{x_{12}=0} - C_T (W_{11}(l_{11}) - W_{21}(l_{21})) = 0 \quad (7c)$$

$$(EJ)_{21} W_{21}^{III}(x_{21}) \Big|_{x_{21}=l_{21}} - (EJ)_{22} W_{22}^{III}(x_{22}) \Big|_{x_{22}=0} + C_T (W_{11}(l_{11}) - W_{21}(l_{21})) = 0 \quad (7d)$$

$$-(EJ)_{11} W_{11}^{II}(x_{11}) \Big|_{x_{11}=l_{11}} + (EJ)_{12} W_{12}^{II}(x_{12}) \Big|_{x_{12}=0} - C_R (W_{11}^I(x_{11}) \Big|_{x_{11}=l_{11}} - W_{21}^I(x_{21}) \Big|_{x_{21}=l_{21}}) = 0 \quad (7e)$$

$$-(EJ)_{21} W_{21}^{II}(x_{21}) \Big|_{x_{21}=l_{21}} + (EJ)_{22} W_{22}^{II}(x_{22}) \Big|_{x_{22}=0} + C_R (W_{11}^I(x_{11}) \Big|_{x_{11}=l_{11}} - W_{21}^I(x_{21}) \Big|_{x_{21}=l_{21}}) = 0 \quad (7f)$$

The solutions of (6) can be presented in the following form:

$$W_{ij}(x_{ij}) = A_{ij} \cos\left(\sqrt{\frac{S_{ij}}{(EJ)_{ij}}} x_{ij}\right) + B_{ij} \sin\left(\sqrt{\frac{S_{ij}}{(EJ)_{ij}}} x_{ij}\right) + C_{ij} x_{ij} + D_{ij} \quad (8)$$

Substitution of solutions (8) into boundary conditions (5), (7) one obtains the system of equations for which the matrix determinant is equated to zero; a transcendental equation for bifurcation force P_b .

3. Results of Numerical Calculations

The sample of results of numerical calculations is presented in Fig. 2.

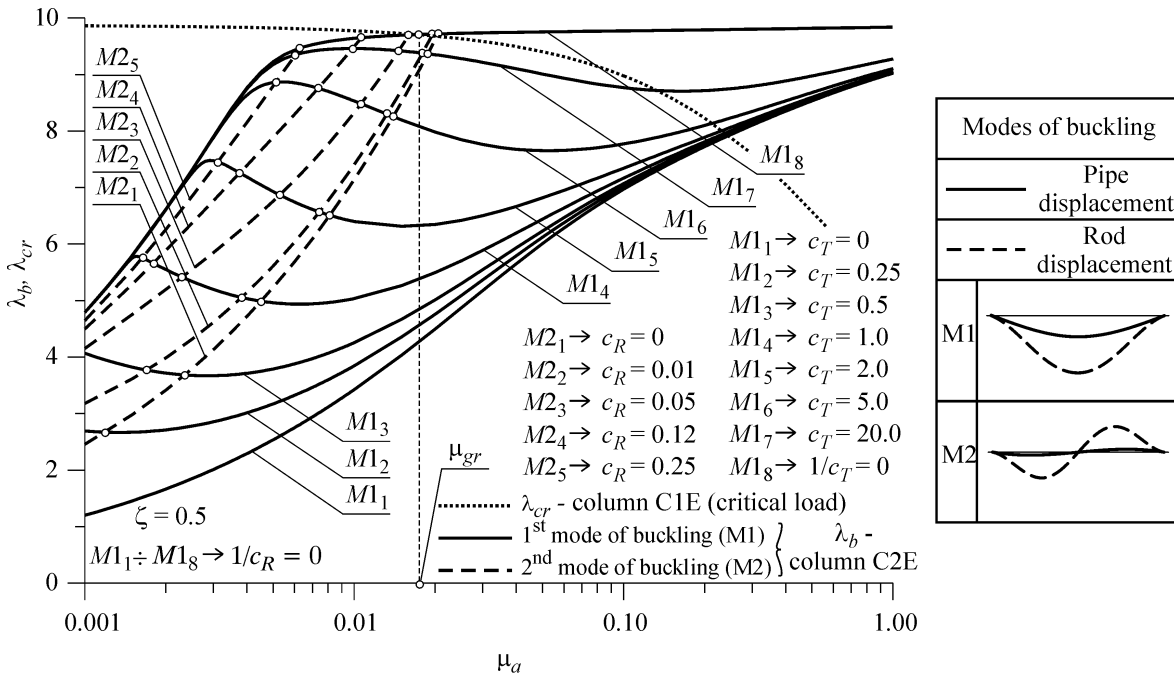


Fig. 2: Bifurcation load in relationship to the factor μ_a .

Bifurcation load was determined as dependent on flexural rigidity asymmetry factor μ_a . Calculations were performed for different values of transversal C_T and rotational C_R rigidities with $\zeta = 0.5$ (elastic layer is placed on the half of system's length). Non-dimensional parameters, used for more general presentation of results of numerical calculations (Fig. 2), are defined as follows:

$$c_T = \frac{C_T(l)^3}{(EJ)}; \quad c_R = \frac{C_R l}{(EJ)}; \quad \lambda_b = \frac{P_b(l)^2}{(EJ)}; \quad \lambda_{cr} = \frac{P_{cr}(l)^2}{(EJ)}, \quad \zeta_A = \frac{l_{11}}{l} \quad (9a-e)$$

The bifurcation load of column C2E and critical load of C1E system are plotted in Fig. 2. The different types of lines were used in order to distinguish buckling modes. The magnitude of flexural rigidity asymmetry factor, at which critical force of column C1E is higher than bifurcation force of column C2E, corresponds to local instability of considered system.

4. Conclusions

In this paper an influence of two-parametric elastic layer on bifurcation load of a slender system composed of pipe and rod is presented. It was demonstrated that the increase of transversal rigidity as well as rotational one causes an increase of the bifurcation load. Influence of rotational rigidity on bifurcation load is noticeable even at smaller value of the flexural rigidity asymmetry factor. Parameters of rigidity of the elastic layer have also an influence on buckling mode (curves for column C2E – Fig. 2). In the future considered system can be further researched and developed (especially an influence of two-parametric layer on vibration frequency).

Acknowledgements

The study has been carried out within the statutory funds of the Czestochowa University of Technology (BS/PB-1-101-3020/11/P).

References

- Beck, M. (1952) Die knicklast des einseitig eingespannten tangential gedruckten stabes. *Z. Angew. Math. Phys.*, 3, 3, pp. 225-228.
- Bochenek, B., Życzkowski M. (2004) Analytical approach to optimization of columns for postbuckling behaviour. *Structural and Multidisciplinary Optimization*, 28, 4, pp. 252-261.
- Bogacz, R., Irretier, H., Mahrenholtz, O. (1980) Optimal design of structures subjected to follower forces. *Ingenieur Archive*, 49, pp. 63-71.
- Euler, L. (1744) *Methodus inveniendi lineas curvas maximi minime proprietate gaudentes*, Appendix: De curvis elasticis. Lausanne and Geneva.
- Gajewski, A., Życzkowski, M. (1969) Optima shaping of an Elastic Homogeneous Bar Compressed by Polar Force. *Biuletyn de L'Academie Polonaise des Sciences*, 17, 10, pp. 479-488.
- Gajewski, A., Życzkowski, M. (1970) Optimal Design of Elastic Columns Subject to the General Conservative Behaviour of Loading. *Z. Angew. Math. Phys.*, 21, 1970, 806-818.
- Langthjem, M. A., Sugiyama, Y. (2000) Dynamic stability of columns subjected to follower loads: a survey. *Journal of Sound and Vibration*, 238, 5, pp. 809-851.
- Nemat-Nasser, S., Herrmann, G. (1966) Adjoint Systems in Nonconservative Problems of Elastic Stability. *AIAA Journal*, 4, 12, pp. 2221-2222.
- Sokół, K. (2014). Linear and Nonlinear Vibrations of a Column with an Internal Crack. *J. Eng. Mech.* 10.1061/(ASCE)EM.1943-7889.0000719, 04014021.
- Tomski, L., Uzny, S. (2008) Free vibration and the stability of a geometrically non-linear column loaded by a follower force directed towards the positive pole. *International Journal of Solids and Structures*, 45, 1, pp. 87-112.
- Tomski, L., Uzny, S. (2013a) The stability and free vibrations of a column subjected to a conservative load generated by a head with a parabolic contour. *International Journal of Structural Stability and Dynamics*, 13(7), (doi: 10.1142/S0219455413400129).
- Tomski, L., Uzny, S. (2013b) Free Vibrations and Stability of a New Slender System Subjected to a Conservative or Non-Conservative Load. *Journal of Engineering Mechanics-ASCE*, 139, 8, pp. 1133-1148.
- Uzny, S. (2011) Local and global instability and vibrations of a slender system consisting of two coaxial elements. *Thin-Walled Structures*, 49, pp. 618-626.

NUMERICAL SIMULATION OF VIDEO-KYMOGRAPHIC RECORDS OF THE VOCAL FOLD VIBRATION

T. Vampola^{*}, J. Horáček^{**}

Abstract: *The reconstruction of the video-kymographic records from the numerical simulation of the vocal fold vibration is used for prediction of the type of vocal fold damaged. Three-dimensional (3D) finite element (FE) fully parametric model of the human larynx was developed and used for numerical simulation of stresses during vibrating vocal folds with collisions. The complex model consists of the vocal folds, arytenoids, thyroid and cricoid cartilages. The vocal fold tissue is modeled as a three layered transversal isotropic material. The results of numerical simulation of the vocal folds oscillations excited by a prescribed intraglottal aerodynamic pressure are presented. The FE contact elements are used for modelling the vocal folds collisions and the stresses in the vocal fold tissue are computed in time domain. The damaged of the ligament tissue is simulated by the modification of the modulus of elasticity. The video-kymographic records are reconstructed for health and damaged vocal folds. The results show significant dynamic stresses in all there directions (horizontal, vertical and anterior-posterior).*

Keywords: Biomechanics of human voice, 3D FE model of human larynx, Vocal fold vibration, Video-kymographic record.

1. Introduction

With regard to the clinical practice, when basic investigative techniques include video-kymographic, the question arises of whether the character of vibration recorded by the high-speed camera can be used for prediction of the damage to the vocal cords. Therefore, the computer model of the human vocal folds was designed enabling to model some pathological situations and voice disorders. Some simplified lumped mass dynamic models of phonation can be used for a rough estimate of the impact stress or acceleration level depending on various phonation parameters like e.g. prephonatory glottal gap, subglottal pressure and fundamental frequency (Horáček et al., 2005). Because the mechanical loading of vocal fold self-oscillations with collisions is caused by a combination of the aerodynamic, inertial and impact forces and moreover, regarding the complicated three-dimensional (3D) structure and material properties of the living tissue, is necessary assembled more sophisticated models based on Finite Element (FE) modelling enable us to estimate all main normal and shear stresses in the different vocal fold tissue layers in all three directions, even if the computational demands on computers and computer time needed are much higher and still limited. These models can be used for the evaluation of the correlation between the deformation and stresses fields of the vocal fold tissues with the video-kymographic records of the vocal folds vibrations.

2. Methods

The 3D complex dynamic FE model of the human larynx was developed by transferring the CT image data from the DICOM format to the FE mesh. The geometrical configuration of the cross-section of the vocal fold was taken according to Hirano (1975). Three layers of vocal fold tissue are considered (Titze, 2006): epithelium, vocal ligament and muscle with different physical and material properties - see Fig. 1.

* Assoc. Prof. Dr. Ing. Tomáš Vampola: Dept. of Mechanics, Biomechanics and Mechatronics, CTU in Prague, Karlovo nám. 13, 121 35 Prague, CZ, tomas.vampola@fs.cvut.cz

** Ing. Jaromír Horáček, DrSc.: Institute of Thermomechanics, Academy of Sciences of the Czech Republic, Dolejškova 5, 182 00 Prague, CZ, jaromirh@it.cas.cz

The developed fully parameterized 3D FE model enables to vary the thickness and material properties of the individual layers and to take into account longitudinal pretension and adduction of the vocal folds by positioning of the arytenoids and thyroid cartilages – see Fig. 1.

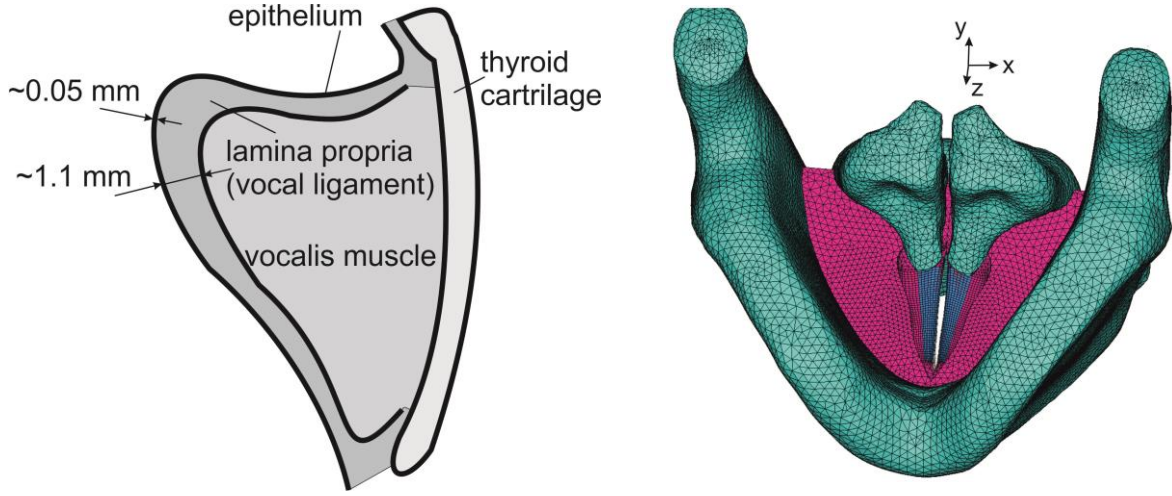


Fig. 1. Schema of the vocal fold with three tissue layers (left), FE model of the human larynx with the vocal folds between the arytenoids and thyroid cartilages (right).

The nonlinear elasticity theory for large-strain deformations with the linear transversal isotropic material model was used for the vocal fold tissue, where the matrix of the elastic constants in strain-stress relations is defined as follows:

$$\begin{bmatrix} \varepsilon_{xx} \\ \varepsilon_{yy} \\ \varepsilon_{zz} \\ \varepsilon_{xy} \\ \varepsilon_{xz} \\ \varepsilon_{yz} \end{bmatrix} = \begin{bmatrix} E_p^{-1} & -\mu_p E_p^{-1} & -\mu_{pl} E_p^{-1} & 0 & 0 & 0 \\ -\mu_p E_p^{-1} & E_p^{-1} & -\mu_{pl} E_p^{-1} & 0 & 0 & 0 \\ -\mu_{lp} E_l^{-1} & -\mu_{lp} E_l^{-1} & E_l^{-1} & 0 & 0 & 0 \\ 0 & 0 & 0 & G_p^{-1} & 0 & 0 \\ 0 & 0 & 0 & 0 & G_l^{-1} & 0 \\ 0 & 0 & 0 & 0 & 0 & G_l^{-1} \end{bmatrix} \begin{bmatrix} \sigma_{xx} \\ \sigma_{yy} \\ \sigma_{zz} \\ \sigma_{xy} \\ \sigma_{xz} \\ \sigma_{yz} \end{bmatrix} \quad (1)$$

where $E_p = 2 G_p (1 + \mu_p)$ is the Young modulus, μ_p is the Poisson number and G_p is the shear modulus in perpendicular plane xy to the ligament fibers, and analogical constants are denoted by the index l for the longitudinal direction z . The tissues material constants considered are summarized in Tab. 1.

Tab. 1: Nominal values of material constants of individual tissue layers according to Mital (2008) – E = Epithelium, L = Ligament, M = Muscle, C = Cartilage, LT = Loose connective Tissue.

	E	L	M	C	LT
G_p [kPa]	0.530	0.870	1.050	-	-
G_l [kPa]	10	40	12	-	-
μ_p	0.3	0.3	0.3	0.47	0.4999
$E_l(\varepsilon)$ [kPa]	26	104	31	-	-
ρ [kgm ⁻³]	1020	1020	1020	1020	1020
μ_{lp}	0.3	0.3	0.3	-	-

2.1. Numerical simulation of vocal folds vibration

The motion of the vocal folds was numerically simulated for a prescribed intraglottal pressure given by a periodic function in the time domain. The intraglottal pressure signal loading the vocal fold surface was generated by the 2D aero elastic model (see Horáček et al., 2005) of the vocal folds during the vocal folds self-sustained vibrations for the airflow rate $Q = 0.179$ l/s the prephonatory glottal half-gap $g_0 = 0.2$ mm

and the fundamental frequency $F_0=100.766$ Hz, that corresponded to the subglottal pressure $P_{\text{sub}}=378.4$ Pa, and the resulted vocal folds vibration were characterized by the open quotient $OQ=0.725$, defined as the open time of the glottis divided by the period length of the vocal folds vibrations, by the maximum glottis opening $GO=1.27$ mm and the maximum impact stress estimated by the Hertz theory $IS=1328$ Pa.

2.2. Computed displacement

The limits of the computed trajectories of the middle cross-section are presented in Fig. 2. These deformations can be used for reconstruction of the video-kymograph records of the human vocal fold vibration see Fig. 3. The damaged of the vocal fold was simulated by the decreasing of the modulus of elasticity of the ligament tissue about 20%.

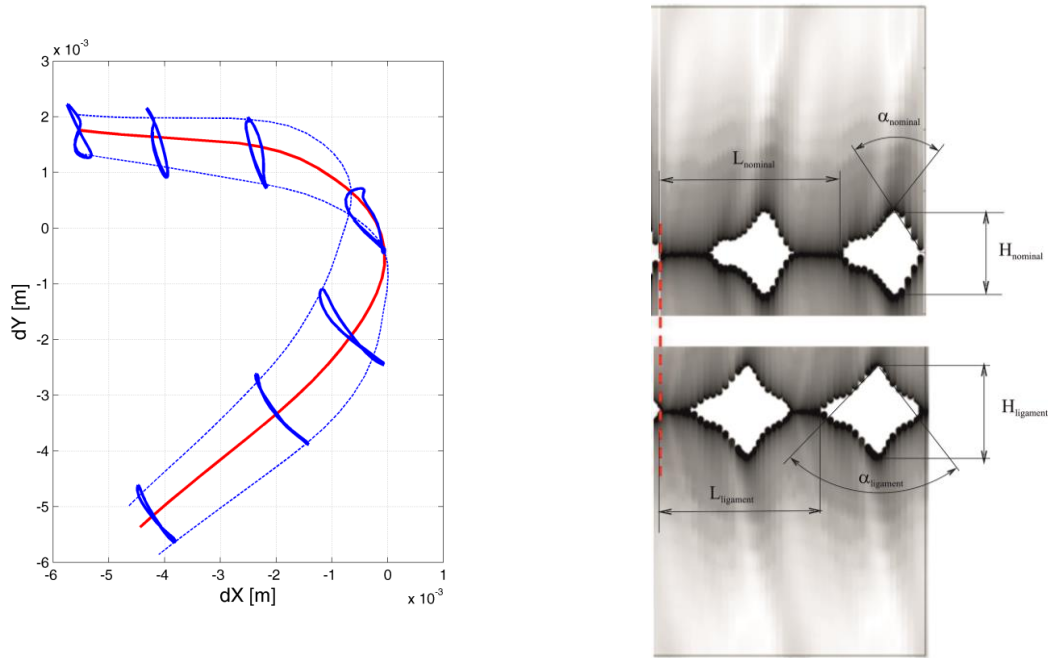


Fig. 2: Nominal shape (red full curve) and maximal deformation (blue dotted curves) in the middle cross-section of the health vocal fold (right), comparison of the reconstructed video-kymograph records for the health and damaged vocal fold (right).

The computed trajectories $u_x(t)$, $u_y(t)$, $u_z(t)$ in the selected nodes of the vocal fold tissue during stabilized oscillation cycles are shown in Fig. 2. A very complicated motion is evident. The mucous Rayleigh type waves are propagating near the vocal fold surface, especially in the upper part of the vocal fold. The maximum value of the peak to peak displacement in the medial (x) direction is about 0.8 mm from and inferior-superior (y) direction is about 1.5 mm. The medial displacement in x direction is limited by the vocal fold collisions. The anterior–posterior vibration amplitude in z direction is negligible. The maximum vibration amplitudes are on the vocal fold surface, the vibration amplitudes are decreasing in the deeper tissue layers.

Tab. 2: Characteristics of vibration for health and damaged vocal fold. OQ =Open Quotient, CQ =Close Quotient, CIQ =Closing Quotient, SQ =Speed Quotient, SI = Speed Index and frequency of vibration for health and damaged vocal fold

	OQ	CQ	CIQ	SQ	SI	f [Hz]
	t_2/t_1	$1-t_2/t_1$	t_2/t_1-1	$t_3/(t_2-t_1)$	$(SQ-1)/(SQ+1)$	$1/t_1$
health	0.633	0.367	0.212	1.990	0.0828	95.24
damaged	0.724	0.275	0.312	1.319	0.0344	96.9

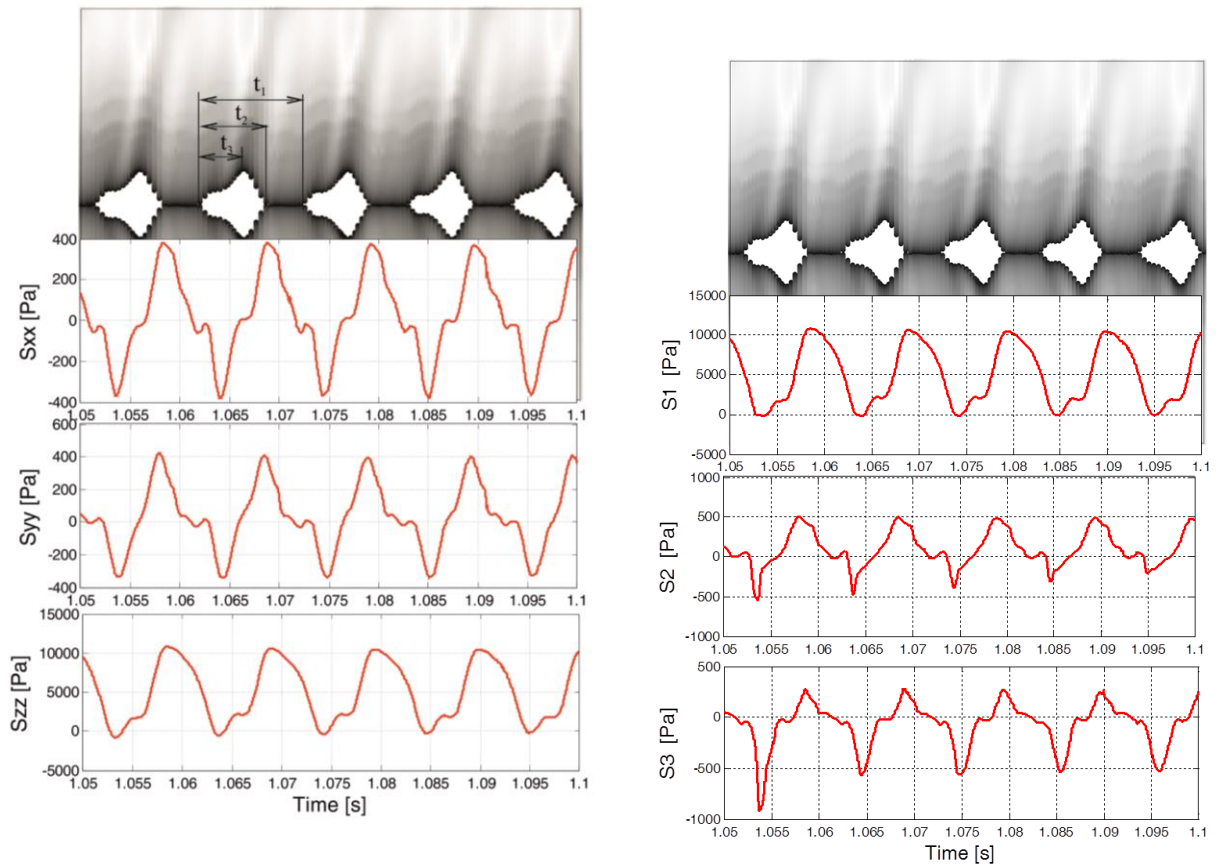


Fig. 3: Reconstruction of the video-kymographic records (top) and the normal stresses and principal stresses (bottom) of the health vocal folds.

3. Conclusions

The geometry of the parametric 3D FE model of the vocal folds developed as a part of the complex larynx model can be easily modified, enabling tuning and optimization procedures for finding proper model geometric and material parameters related to the vocal fold vibration characteristics. The results suggest that the model enables to predict stresses in the layered vocal fold tissue due to the vibration of the vocal folds in phonation regimes with collisions. The motion of the vocal folds excited by periodic intraglottal pressure pulses seems to be qualitatively similar to the vibration patterns known from clinical observations. From the preliminary results can be concluded that the reconstructed video-kymographic records are sensitive enough to the material parameters and geometric reconfiguration of the vocal fold and can be used for prediction of the vocal fold damaged.

Acknowledgement

The research is supported by the Grant Agency of the Czech Republic by project No P101/12/1306 “Biomechanical modelling of human voice production - way to artificial vocal folds”.

References

- Mittal, R., Zheng, X., Bhardwaj, R., Seo, J. H., Xue, Q., Bielamowicz, S. (2011) Toward a simulation-based tool for the treatment of vocal fold paralysis, *Frontiers in Computational Physiology and Medicine*, 2, article 19, pp. 1-15.
- Hirano, M. (1975) Phonosurgery, basic and clinical investigations, *Otologia Fukuoka* 21 (Supl. 1), pp. 239-262.
- Horáček, J., Šidlof, P., Švec, J. G. (2005) Numerical simulation of self-oscillations of human vocal folds with Hertz model of impact forces, *J. Fluids and Structures* 20, pp. 853-869.
- Titze, I. R. (2006) *The Myoelastic Aerodynamic Theory of Phonation*. National Centre for Voice and Speech, Denver and Iowa City, USA. (ISBN-13: 978-0-87414-156-6).

CONCENTRATION DISTRIBUTION OF COARSE-GRAINED PARTICLE-WATER MIXTURE IN HORIZONTAL PIPE

P. Vlasak^{*}, Z. Chara^{**}, J. Konfršt^{***}, J. Krupička^{****}

Abstract: *The paper describes the results of coarse-grained particle-water mixture measurements in an experimental pipeline loop of inner diameter 100 mm. Graded basalt pebbles of mean diameter 11 mm, conveyed by water, were investigated. The concentration distribution measurements were carried out with application of gamma-ray based device. Presented results refer to the effect of mixture velocity and overall concentration on chord-averaged concentration and local concentration distribution in the horizontal pipe. The study revealed that the coarse-grained particle-water mixtures were significantly stratified, solid particles moved principally close to the pipe invert, for higher and moderate flow velocities saltation becomes dominant mode of the sediment transport.*

Keywords: Particle-water mixture, Horizontal conveying, Coarse-grained slurry, Gamma-ray radiometry, Concentration distribution.

1. Introduction

Pipeline transport of coarse-grained material is not very frequently used due to the problems of severe wear, material degradation, high deposition velocity limit and consequently also operational velocities and energy requirement. However, pipeline transport of coarse particles is of potential importance in, e.g. mining industry, the Alberta sands petroleum extraction, or for poly-metallic nodules transport from the ocean bottom to the surface (Vlasak et al., 2012). The understanding of the slurry flow behaviour makes it possible to optimize transport parameters and energy requirements, to improve quality, safety, economy and reliability of transport and/or processing of the transported material. The flow of heterogeneous slurries in a horizontal pipe may be defined as the flow with an asymmetrical concentration and velocity distribution, where a Coulomb friction contributes significantly to the friction losses. A flow pattern with a bed layer and a skewed concentration distribution generally exist for these slurries. The first mechanistic approach for coarse-grained particle slurry flow was probably that of Newitt et al., (1955), who distinguished between velocity dependent fluid friction and velocity independent particle-wall friction of the Coulomb type, and defined coarse particle conveyance as flow with a sliding bed and particle saltation.

Wilson (1976) proposed a two-layer model for settling slurries with fully stratified flow pattern, where all particles are supposed to be concentrated in the lower portion of the pipe, where concentration approaches the loose-packed value, and the Coulombic contribution to particle-wall friction is dominant. In the upper layer, only the carrier liquid is presented. Based on experimental data from the large test pipelines of the Saskatchewan Research Council (Gillies et al., 1991) the two-layer model was extended for finer particles. Because the layers differ in the solids concentration and velocity, there is a difference in the mean velocities of the particles and the liquid. Slip between the particles and the liquid results in a continuous transfer of energy from the fluid to the particle and from the particle to the pipe wall.

* Prof. Ing. Pavel Vlasák, DSc.: Institute of Hydrodynamics ASCR, v. v. i., Pod Patankou 30/5; 166 12, Prague; CZ, vlasak@ih.cas.cz

** Assoc. Prof. Ing. Zdeněk Chára, CSc.: Institute of Hydrodynamics ASCR, v. v. i., Pod Patankou 30/5; Prague; CZ, chara@ih.cas.cz

*** Ing. Jiří Konfršt, PhD.: Institute of Hydrodynamics ASCR, v. v. i., Pod Patankou 30/5; Prague; CZ, konfrst@ih.cas.cz

**** Ing. Jan Krupička: Institute of Hydrodynamics ASCR, v. v. i., Pod Patankou 30/5; Prague; CZ, krupicka@ih.cas.cz

A progress in the theoretical description of heterogeneous slurry flow is limited due to the lack of experimental data describing the flow behaviour and an inner structure of slurry flow. The study of the inner structure of such flow is very difficult, since many well-known techniques suitable to determine the inner structure of fluid flow (e.g. LDV, PIV, UVP) can be used in solid-liquid mixtures with strong limitations. Description of the slurry flow behaviour and the inner structure are much more complex than measurements of overall flow parameters, e.g. the flow rate, pressure drops, mean concentration.

2. Experimental Equipment and Material

The experimental pipe loop (see Fig. 1) is suitable for study the effect of mixture velocity and concentration on pressure drops in horizontal (A), inclined and vertical (B) pipe sections, which consist of smooth stainless steel pipes of inner diameter $D = 100$ mm. Slurry was prepared in a mixing tank (1) and pumped into the test loop by a centrifugal slurry pump GIW LCC-M 80-300 (2) with variable speed drive (3). The pressure drops were measured by the Rosemount DP transmitters 1151DP (8) over a broad range of mean mixture velocities, from values close to deposition limit velocity about 1 m/s to maximum values about 5.5 m/s. The mean velocities were measured by a Krohne magnetic flow meter OPTIFLUX 5000 (9), mounted in the short vertical section (C) at the end of the loop. The vertical U-tube enables evaluation of the delivered concentration of solids. To measure the local concentration the loop is equipped with radiometric density meters (10) and a special support controlled by the computer, which serves for positioning of both the source and the detector (Krupicka and Matousek, 2012). Transparent viewing pipe sections (7) for visual observation were situated just behind the measuring sections in both the horizontal and also in inclinable sections. The flow divider (11) allows collection of slurry samples in the calibrated sampling tank (5) and measuring of the delivered concentration and flow rate.

The studied mixtures consist of a narrow particle size distribution graded basalt pebbles (particle diameter, d , ranged from 8 to 16 mm, $d_{50} = 11.0$ mm, density $\rho_p = 2787$ kg/m³), see Fig. 2. Water was used as a carrier liquid and the overall concentration, c_v , ranged from 3 to 15% (Vlasak et al., 2013).

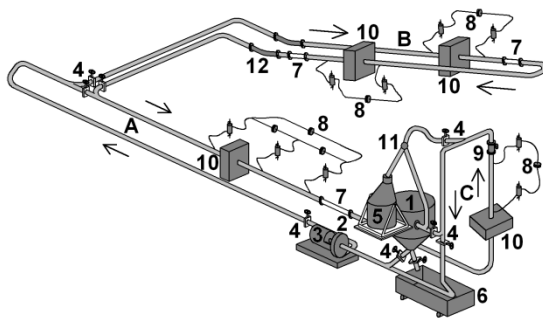


Fig. 1: Experimental test loop.



Fig. 2: The used material, graded basalt pebbles.

3. Concentration Distribution

Distribution of the local concentration in the pipe cross-section is one of important parameters for understanding the physical mechanism of the heterogeneous mixture flow. It has a great effect on both the mixture's flow behaviour and pressure drops, too. Various methods have been used for measurement of the local concentration, e.g. isokinetic sampling, visualisation techniques, electrical resistance or radiometric methods.

From visualization of the coarse-grained mixtures flow we found, that particles slide and rolled along the pipe invert for the low mixture velocities. With the increasing mixture velocity individual particles passed to the saltation mode and for higher slurry velocities most of particles lifted off the pipe bottom, moved in saltation or even suspended mode over the whole pipe cross-section. The particle velocities increased with increasing distance from pipe invert; the, velocities of the saltating particles were significantly higher than those of the particles sliding or rolling particles moving in contact with the pipe wall. For high and moderate flow velocities the saltation becomes very important mode of the particle movement (Vlasak et al., 2014). However, most of the particles were concentrated in the lower portion of the pipe and moved in saltation mode with intensive rotation and contact with the pipe bottom and walls (Lukerchenko et al., 2006).

The concentration distribution in the vertical profile of a horizontal pipe section was measured using of a radiometric device and the effects of mixture velocity and concentration on the chord-averaged concentration in the vertical concentration profile were analysed, see Fig. 3. The concentration profile can be divided into two parts. The local concentration tends to approach zero (i.e. practically only the carrier liquid) in the upper portion of the pipe, which occupied from about 35 to 65% of the pipe cross-section; this area increased with decreasing overall mixture concentration. A nearly linear concentration distribution can be recognized in the lower portion of the pipe. A local maximum concentration could be observed at height about 10 mm from the pipe invert for higher flow velocities. The concentration in the bed layer increased with increasing mean concentration from about 30% to 60%. It was observed that for lower velocities and/or higher means concentrations the bed concentration reached about 60% (value close to the loose-packed value), what demonstrate formation of movable or stationary bed layer. The observed concentration profiles are in good agreement with the profiles measured by Pugh and Wilson (1999), Matousek (2009), and Sobota et al., (2009) for mixtures of different solid materials with smaller particle diameters. Based on the conducted measurement it is evident that coarse particles tend to occupy the bottom part of the pipe, but when mixture velocities extended enough the depositions limit, the solid particles moved commonly in the area around the central part of the pipe cross-section.

To determine the local concentration distribution through the pipe cross-section the parallel projections of gamma-ray beams were provided at several angles around the pipe axis (i.e. from 0 to 175° at interval of 15°), and the collected data were processed by the computer tomography method. Measurement of the

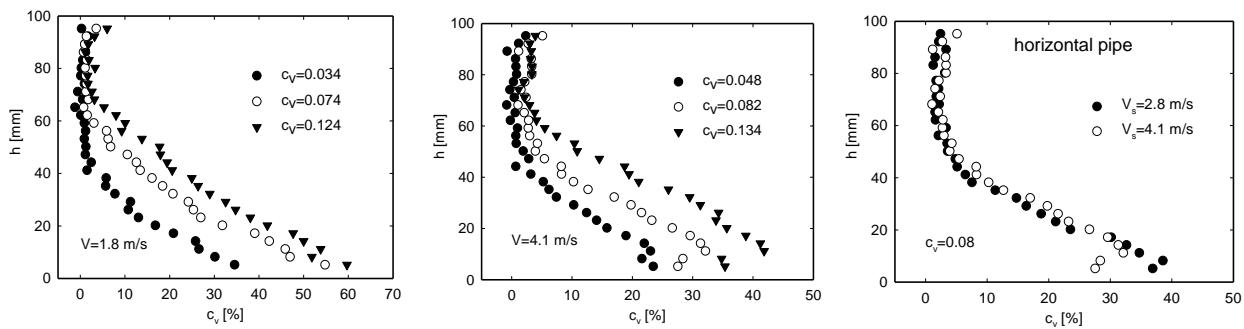


Fig. 3: Vertical profiles of chord-averaged concentration in horizontal pipe.

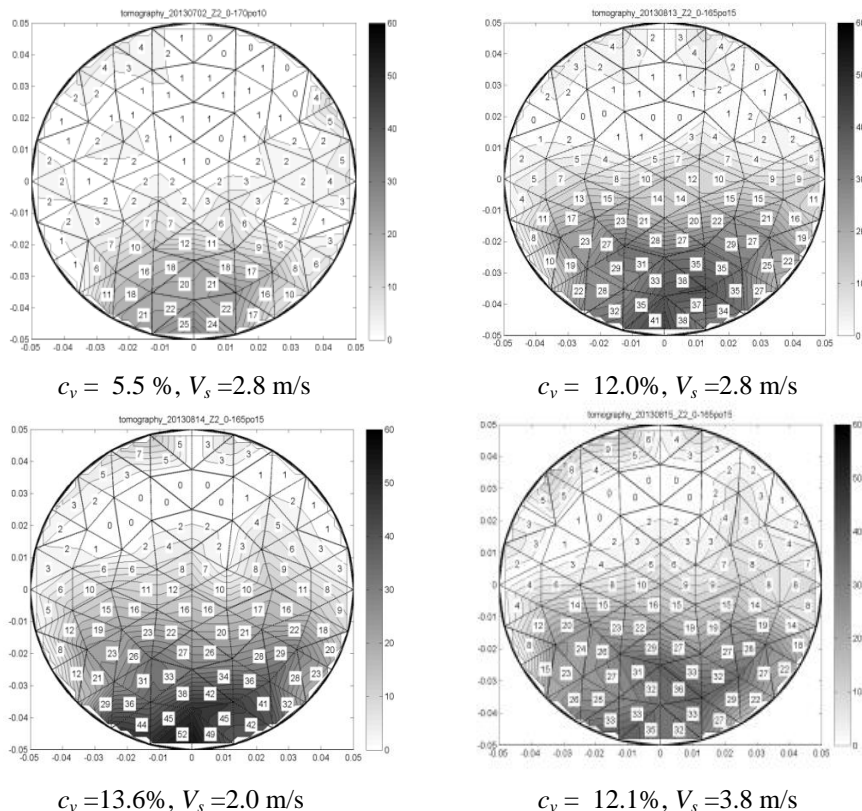


Fig. 4: Local volumetric concentration distribution in horizontal pipe section.

local concentration maps is rather time consuming; however it made it possible to evaluate the effect of the slurry velocity, V_s , and mean concentration, c_v , on the solids distribution in the pipe cross-section. From the observed local concentration maps, see Fig. 4, it is evident that conveyed particles tend to occupy the bottom part of the pipe, and their distribution is practically symmetrical to the vertical plane of symmetry. With increasing mixture velocity and concentration values, the measured coarse-grained particles moved commonly in the area above the pipe invert, up to central portion of the pipe cross-section. The observed particle concentration near both lateral walls of the pipe was slightly less than that in the central portion of the pipe cross-section. The observed concentration maps are in good agreement with the concentration profiles measured for mixtures of different solid materials with smaller particles (Sobota et al., 2009). Some errors were detected in regions close to the pipe wall, and especially near the pipe top, where probably due to the strong effect of the pipe material on gamma-ray absorption, a higher range of errors was detected (there are no reason for increasing concentration near top of the pipe, especially for lower flow velocities).

4. Conclusions

The effect of slurry velocity and concentration on the flow behaviour of coarse-grained particle – water mixtures' in turbulent regime was studied in horizontal smooth pipe of inner diameter $D = 100$ mm. The visualisation and local concentration measurements revealed that the coarse-grained particle-water mixtures in the horizontal pipe section were significantly stratified and sliding or even stationary bed layers were formed. The particles moved principally in a layer close to the pipe invert, for higher and moderate flow velocities particle saltation became the dominant mode of particle movement. Particles were also observed in the central portion of the pipe cross-section. Measurement of the local concentration distribution in the horizontal pipe confirmed that for coarse-grained mixtures the local concentration tends to approach zero in the upper portion of the pipe (from 35 to 65% of the pipe cross-section). A nearly linear concentration distribution can be recognized in the lower portion of the pipe. The concentration in the bed layer increased with increasing mean concentration, from about 40% to 60%, which is close to the loose-packed value, and it demonstrate flow with sliding bed.

Acknowledgement:

Supports under the project P105/10/1574 of the Grant Agency of the Czech Republic, and RVO: 67985874 of the A S C R are gratefully acknowledged.

References

- Gillies, R.G., Shook, C. A., Wilson, K. C. (1991) An improved two layer model for slurry flow, *Can. J. Chem. Eng.*, 69, pp. 173-178.
- Krupicka, J., Matousek, V. (2012) Gamma-ray-based method for density sensing in pipes-evaluation of measurement and data processing, In: *Proc. 2nd IAHR Europe Congress, Munich, Germany.*
- Lukerchenko, N., Chara, Z., Vlasak, P. (2006) 2D numerical model of particle-bed collision in fluid-particle flows over bed. *J. Hydraulic Research* 44(1), pp. 70-78.
- Matousek, V. (2009) Concentration profiles and solids transport above stationary deposit in enclosed conduit. *J. Hydraul. Eng. ASCE* 135 (12), pp. 1101-1106.
- Newitt, D. M., Richardson, J. F., Abbott, M., Turtle, R. B. (1955) Hydraulic conveying of solids in horizontal pipes, *Transaction Institute Chemical Engineers*, 33(2), pp. 93-113.
- Pugh, F. J., Wilson, K. C. (1999) Role of the interface in stratified slurry flow, *Powder Technol.*, 104, pp. 221-226.
- Sobota, J., Vlasak, P., Stozik, G., Plewa, F. (2009) Vertical distribution of concentration in horizontal pipeline – density and particle size influence, In: *Proc. Eighth (8) ISOPE Ocean Mining & Gas Hydrates, Symposium (J. S. Chung ed)*, Chennai, India, pp. 220-224.
- Vlasak, P., Kysela, B., Chara, Z. (2012) Flow Structure of Coarse-Grained Slurry in Horizontal Pipe. *J. Hydrol. Hydromech.* 60(2), pp. 115-124.
- Vlasak P., Kysela B., Chara Z. (2014) Fully stratified particle-laden flow in horizontal circular pipe, *Particulate Science and Technology*, 32(2), pp. 179-185.
- Vlasak P., Chara Z., Konfrst J., Kysela B. (2013) Experimental Investigation of Coarse-Grained Particles in Pipes, In: *Proc. 16th Int. Conf. on Transport & Sedimentation of Solid Particles (J. Sobota & H. Eckstadt eds)*, Rostock, Germany, pp. 265-273.
- Wilson, K. C. (1976) A unified physically based analysis of solid-liquid pipeline flow, In: *Proc of Hydrotransport 4, Banff (Canada), BHRA (U.K.)*, Paper A1, pp. 1-16.

FLUTTER AT A LOW VELOCITY

V. Vlček^{*}, J. Kozánek^{**}, I. Zolotarev^{***}

Abstract: Aeroelastic experiments with the profile NACA0015 were realized in the suction type aerodynamic tunnel of the Institute of Thermomechanics, Czech Academy of Sciences, Prague. The profile had two degrees of freedom realized in translation and rotation motion and flow velocity was just up its critical value. The flow field was measured with interferometry method and the results obtained at the velocity $M = 0.23$ in the flutter regime are presented. The evaluation of interferograms enabled to determine the components of the drag and lift forces.

Keywords: Aeroelasticity, Flutter, Interferometry, Subsonic flow.

1. Introduction

The experimental stand was newly constructed with regard to requirements of optical methods. The profile was therefore installed on the plug in the shiftable frame. The chord was 64.5 mm, the center of rotation was in 1/3 of the chord length behind the leading edge of the profile. For optical measurement the Mach-Zehnder interferometer with the diameter of the visual field 160 mm was used, interferograms were recorded with frequency 1000 frames/s (Hodges et al., 2002; Bernal et al., 2009; Vlček et al., 2013).

As example, the flutter at $M = 0.23$ (at $M = 0.21$ the flutter not occurred) was visualized with interferometer using the infinite fringe width. One of these interferograms is presented in Fig. 1. Forces acting on the profile surface and their decompositions into the test section axes are shown.

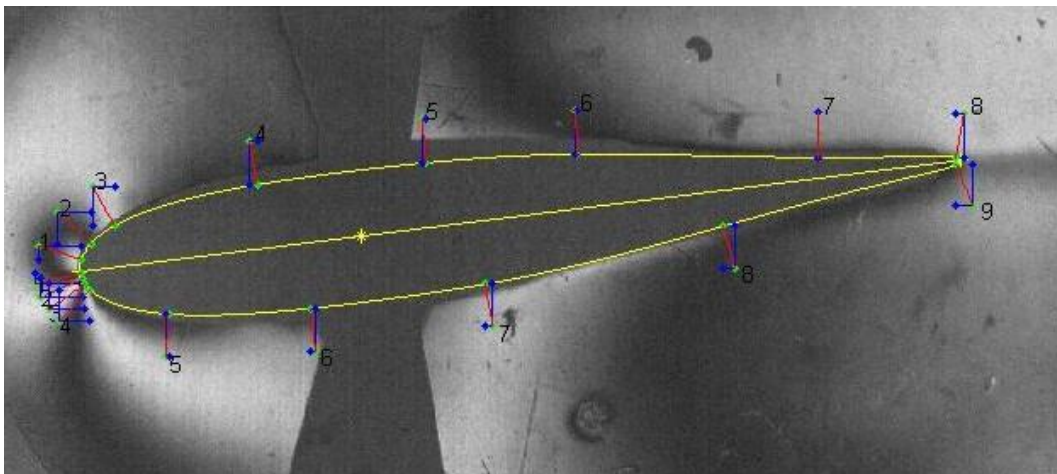


Fig. 1: Interferogramm of the flow at $M = 0.23$.

2. Kinematics of the Profile Motion

The translation of the profile was registered with mechanical sensors, the angle of attack was evaluated

^{*} Ing. Václav Vlček, CSc.: Institute of Thermomechanics, v.v.i., Academy of Sciences of the Czech Republic, Dolejškova 5, 182 00, Prague; CZ, vlcek@it.cas.cz

^{**} Ing. Jan Kozánek, CSc.: Institute of Thermomechanics, v.v.i., Academy of Sciences of the Czech Republic, Dolejškova 5, 182 00, Prague; CZ, kozanek@it.cas.cz

^{***} Ing. Igor Zolotarev, CSc.: Institute of Thermomechanics, v.v.i., Academy of Sciences of the Czech Republic, Dolejškova 5, 182 00, Prague; CZ, igor@it.cas.cz

from interferograms. The profile positions during flutter are in Fig. 2. As in experiments realized before, where the flow separation not occurred, the positions parallel to the flow direction in bottom and top dead translation positions are close one to other (thick lines).

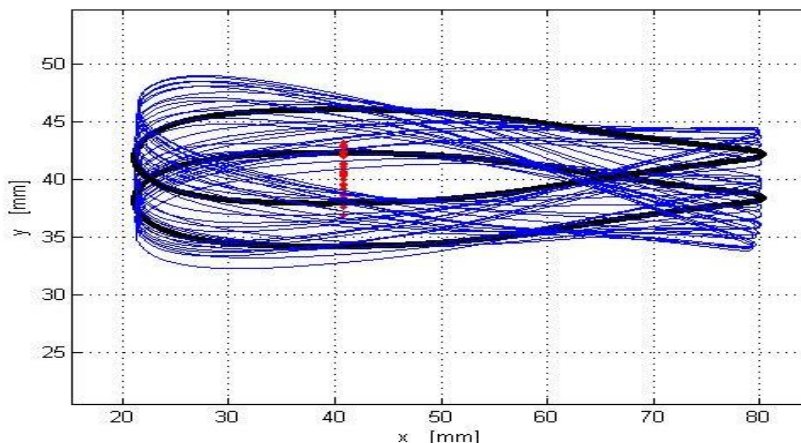


Fig. 2: Positions of the profile during one period of the flutter.

The time changes of the translation and angle of attack of the profile are depicted in Fig. 3. The positive direction of translation is upwards and the positive direction of the angle is clockwise. The phase shift between these quantities is almost half of the period.

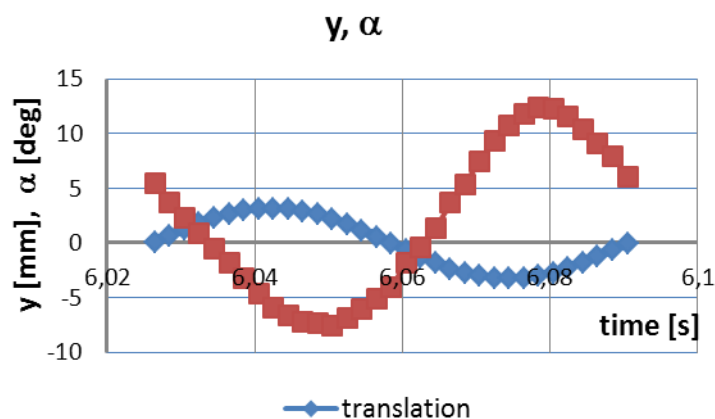


Fig. 3: Translation and angle of attack in one period of flutter.

The relation between the translation and angle of attack of the profile is visible in Fig. 4, where the direction of the movement is anticlockwise. The excentricity of the loop position is due to the nonzero angle of attack in the profile motionless position. The adjustment of the initial position was possible to arrange only after some group of experiments, because it requires also disassembly of optical glasses and subsequent adjustment of the optical system.

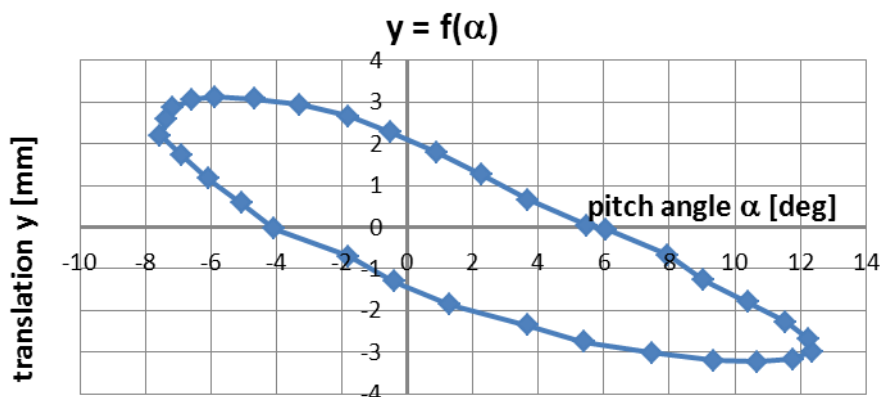


Fig. 4: Loop generated by the phase shift of translation and rotation.

3. Results of Interferogramms Evaluation

Optical measurement enabled to evaluate the force action of the flow field on the separate parts of the body. Here we used the calculation of lift forces acting on lower and upper surface separately and results are depicted in Figs. 5 and 7. Upper and lower surface are defined by their position in relation to the chord. The force is denoted by F [N], indexes x and y denotes the direction of the force action in the direction on of axes x and y ; indexes l and u denotes the force action on lower or upper surface of the profile.

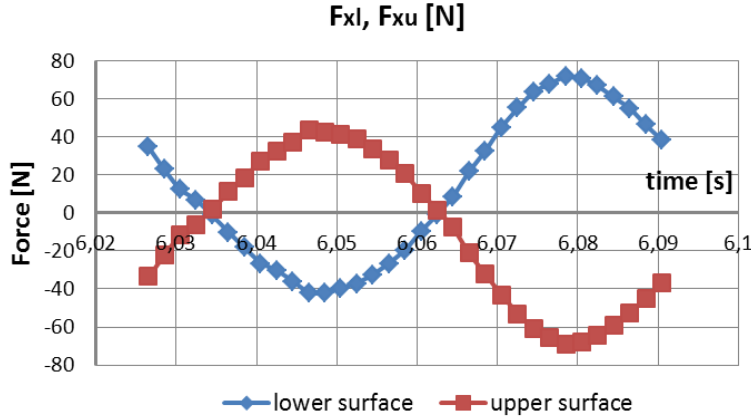


Fig. 5: Drag components of the profile.

Drag components acting on the lower and upper surface are in almost opposite phase, therefore the force resulting from their summation in Fig. 5 has a bad arranged shape.

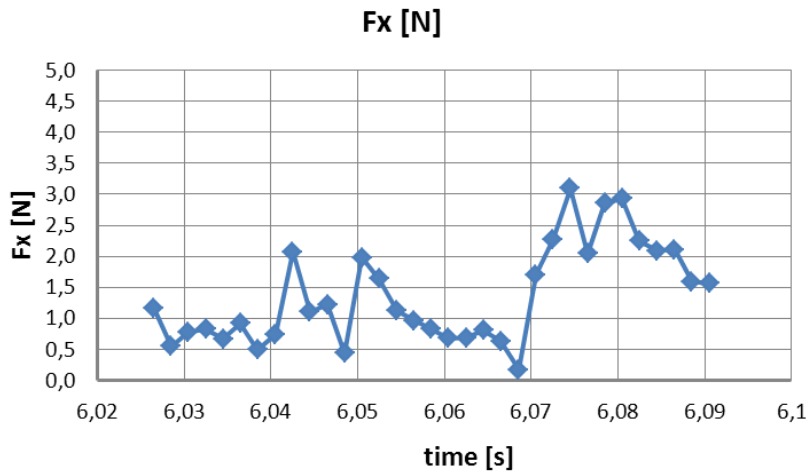


Fig. 6: The total drag of the profile determined from the interferogramms.

Lift components acting on the lower surface F_{yl} and on the upper surface F_{yu} and total lift during one period and determined from interferogramms are in Fig. 6.

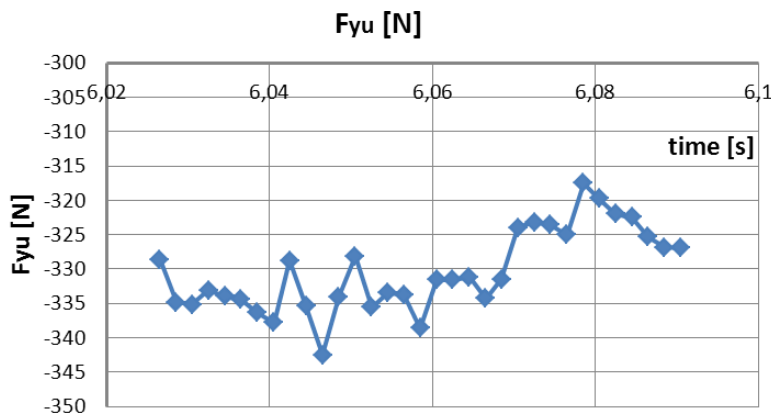


Fig. 7: Lift component acting on the upper surface.

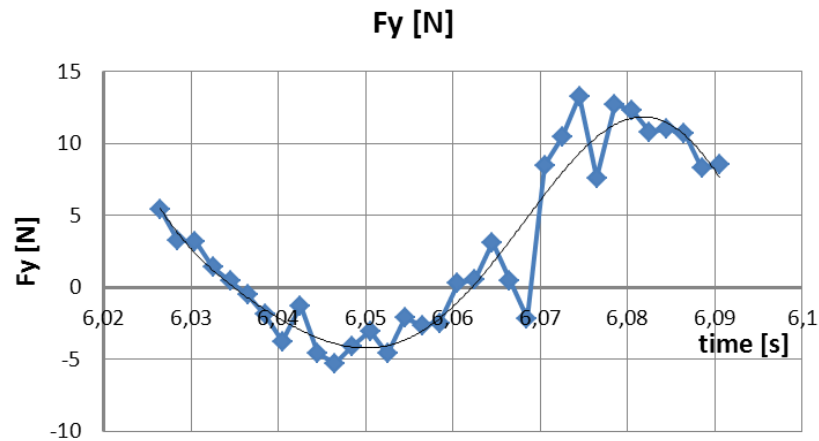


Fig. 8: Total lift of the profile during one flutter period.

The lift unlike the drag has worse arranged components and better arranged total lift.

4. Conclusion

The accuracy of the interferometric method is basically limited by the assumption of isentropic flow changes, and inside this limitation its accuracy increases with the number of visible fringes. The number of fringes increases with flow velocity and with the width of the flow section. The ability of interferometric method to measure flutter flow parameters in the same test section in the range of velocities $M = 0.3 - 0.45$ was verified formerly (see also Vlček et al., 2013; Zolotarev et al., 2012, Zolotarev 1987). The described experiment was an attempt to check out this method using lower Mach numbers in the same, relatively narrow test section. It is shown, that this method is useful for measuring flutter flow field in a wide region of flutter parameters.

Acknowledgement

The authors gratefully acknowledge the Grant Agency of the Czech Republic for supporting this work under Grant No. 13-10527S „Subsonic flutter analysis of elastically supported airfoils using interferometry and CFD“. We are also grateful to Ing. Jaromír Horáček, DrSc. from the Institute of Thermomechanics AS CR for valuable comments and suggestions. We are also grateful to Ing. Martin Luxa, PhD., Ing. David Šimurda, PhD. from the Institute of Thermomechanics AS CR and to visiting students Ondřej Kachel and Jan Česal for the participation during experiments and their evaluation.

References

- Hodges, D. H., Pierce, G. A. (2002) Introduction to structural dynamics and aeroelasticity, Cambridge University Press, 2002.
- Bernal, L. P., Ol, M. V., Szcublewski, D. P., Cox, C. A. (2009) Unsteady force measurements in pitching-plunging airfoils. AIAA Paper 2009-4031, 2009.
- Vlček, V., Kozánek, J., Zolotarev, I. (2013) Optical measurement of the flow field around the aerodynamic profile in flutter regime. In: Proc. Colloquium Dynamics of Machines 2013, Prague, Czech Republic, pp. 131-138, (in Czech).
- Zolotarev, I., Vlček, V., Kozánek, J. (2012) Experimental results of a fluttering profile in the wind tunnel. Proc. Flow-Induced Vibration. Dublin: School of Engineering Trinity College, Dublin, 2012, pp. 677-680.
- Zolotarev, I. (1987) Optimisation of the aerodynamic damping of a cylindrical shell conveying fluid with the aid of boundary conditions, Soviet Machine Science, 1987, No 1, pp. 49-55.

FLAME FRONT TRACKING IN IMPINGING JET FLAMES

J. Vondál^{*}, M. van der Steen^{**}, M. J. Tummers^{***}

Abstract: Flame tracking is important in the study of flame-wall interaction. Based on flame area, stretch angle and flame thickness the wall effect on the flame can be evaluated. The proposed tracking method is based on differences in seeding particle density in unburnt and burnt gases. Particle images are recorded with a high-speed Particle Image Velocimetry (PIV) system that consists of a high speed CMOS camera and high-repetition rate, diode-pumped Nd:YLF laser. The instantaneous flame front is recognizable in the raw PIV images and the key task is to detect it automatically with image processing tools. Interaction with the wall and an unexpected shift of the wall position during the measurements (due to heating) makes this task very challenging. This paper presents a procedure for entire flame front tracking which utilizes generally available image processing tools. Several issues in the measurement of the flame front are highlighted and their solution or elimination is proposed.

Keywords: Flame Tracking, Impinging Jet, PIV, Image Processing.

1. Introduction

Flame-wall interaction is important topic for process industry. Its effect is utilized e.g. in impinging jet flames for enhancing wall heat flux (Chander and Ray, 2005). It is used for rapid increase in heat flux when compared to conventional heating separated to radiant and convective sections. Proper understanding can improve design of combustion devices and improve prediction of wall lifetime. The flame front itself does not usually reach the wall due to the loss of energy. The wall temperature tends to be significantly lower than the ignition temperature of the gas mixture. Therefore, the reaction zone cannot reach the wall and the flame is quenched in the thin layer near the wall. Quenching has significant influence on the pollutant formation (Li et al, 2010). Effects of quenching can be investigated by varying the wall temperature which influences the layer thickness.

1.1. Flame tracking

Flame analysis can be performed in several ways. One is to track the flame front via image processing algorithms. The flame front tracking is based on differences in seeding particle density in unburnt and burnt gases. This difference in density can be clearly seen in Fig. 1. Some authors have suggested to use seeding particles, such as oil or incense smoke, (Jeanne et al., 2000) that are visible only in unburnt region of the flame or using threshold value with no further details on their procedure (Tachibana et al., 2004; Hartung et al., 2009). Some advanced methods for flame front tracking based on Canny filter edge detector were developed (Coron et al., 2004), but did not show convincing improvements. Our procedure proposes using

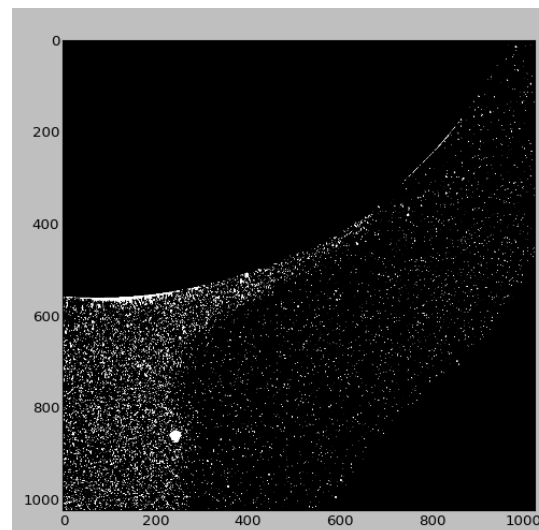


Fig. 1: PIV image of an impinging jet flame.

^{*} Ing. Jiří Vondál, PhD.: Institute of Process and Environmental Engineering, Faculty of Mechanical Engineering, Brno University of Technology, Technická 2, Brno, CZ, vondal@fme.vutbr.cz

^{**} Maikel van der Steen: Department of Process and Energy, Delft University of Technology, Mekelweg 2, 2628CD, Delft, The Netherlands, M.vanderSteen@student.tudelft.nl

^{***} Dr. Mark J. Tummers, Department of Process and Energy, Delft University of Technology, Mekelweg 2, 2628CD, Delft, The Netherlands, M.J.Tummers@tudelft.nl

general filters available in many libraries for image processing and therefore is easy to implement.

2. Experimental Facility

The experimental setup consists of a horizontal cylindrical stainless steel pipe with an outside diameter of 88.9 mm which is convectively cooled by air on the pipes' inner surface. The pipe axis is oriented perpendicular to the vertical jet axis. The burner fires natural gas premixed with air from a copper pipe with an inner diameter of 26 mm with open end – see Fig. 2. Seeding particles (aluminum oxide) are injected into the mixture by using a cyclone seeder.



Fig. 2: Experimental set-up.

The particle image velocimetry system consists of a high-speed CMOS camera (LaVision High Speed Star) with 1024×1024 pixels and 12-bit resolution. The laser is a dual oscillator/single head diode pumped Nd:YLF Darwin Duo 527-80-M emitting green light with a wavelength of 527 nm. The duration of a laser pulse is about 150 ns. The PIV system collected double frame images at a frequency of 1500 Hz. The laser sheet is perpendicular to the cooled cylindrical pipe axis and stretches in vertical direction from the cooled impingement pipe to the jet exit.

3. Measurement

Two different cases were considered in this study. The first is a “cold” case with full (internal) cooling of the horizontal pipe which is heated by the impinging flame. The second is a “hot” case without cooling of the horizontal pipe. The highest wall temperature as measured by a thermocouple mounted just below the inner surface of the pipe is 580 °C for the “hot” case and 178 °C for the “cold” case. For each case several data sets were obtained to ensure repeatability and to allow evaluation of statistical quantities.

Several problems had to be solved to capture satisfying images. One problem was the apparent shift in the wall position observed in the images for the cold and hot wall temperature. Even when the camera remains in a fixed position the wall highlighted by laser sheet appears to have increased in diameter by 1.6 mm (36 px). This effect can be clearly seen when cold and hot sets of images are compared. The shift is not large, but it significantly disturbs the image processing and pipe edge detection. This shift might be caused by two physical effects, i.e. thermal expansion of steel and optical distortion of light rays due to different air temperatures. Another difficulty for image processing is the masking of wall reflections prior to application of filters. Masking is performed by using circles with slightly larger diameter than the pipe itself to hide all reflections. Among hot and cold wall cases the circle diameter may differ by up to 142 px (6.5 mm). It is not only due to wall shift, but also due to differences in deposition of the seeding particles on the walls which scatters more light towards camera.

Limiting the amount of laser light reflected by the wall of the horizontal pipe was also the key issue. It was solved by decreasing the angle between the camera axis and horizontal pipe axis. The final setup can be seen in Fig. 2. The thickness of the overexposed reflection from wall on captured image was reduced to 10 px (0.46 mm). This allowed more accurate imaging of seeding particles in the near wall region.

A limiting factor of the proposed image processing method

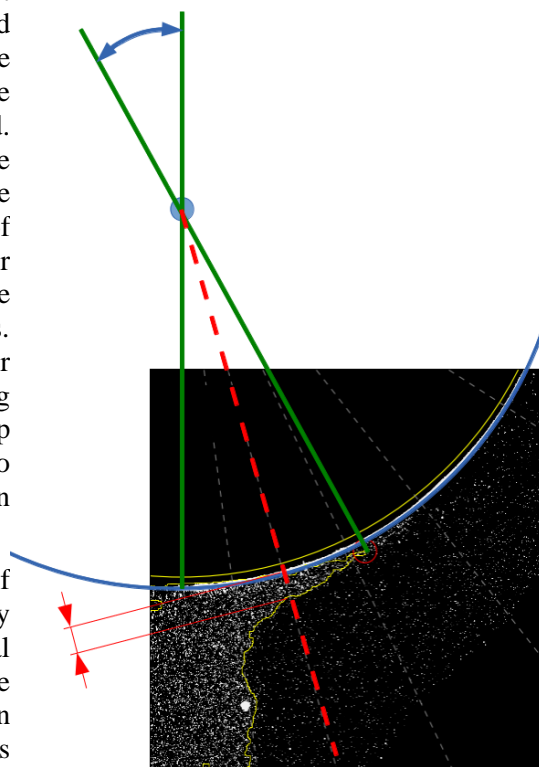


Fig. 3: Properties of the stretched flame.

is the variation in time of the seeding particle density. Ideally, the same seeding density should be used for all cases to achieve comparable tracking of flame. The most challenging region for accurate tracking is the far side of the flame stretching around the horizontal pipe where the stretch angle is measured (see red circle in Fig. 3).

4. Image Processing

The aim of image processing is tracking of the flame front and extracting characteristics of the flame such as: flame area, stretch angle, thickness of the stretching flame, distance of the flame from the cooled wall (quenching layer) as indicated in Fig. 3. We aim at assembling the set of generally available methods which provide the best results. The suggested procedure of the image processing method is illustrated in Fig. 4. It can be implemented with e.g. Python SciPy library (Jones et al., 2001) and its extension for image processing Scikit-image (Walt, 2013).

The first step is to remove the background by creating an average image from a set of 1000 images followed by its subtraction from each individual image. In the second step the overexposed region (caused by reflections from the horizontal pipe) and unimportant areas (such as area inside the horizontal pipe) of the images are masked (erased). Adaptive threshold follows with the lower threshold value obtained from an averaged intensity value from rows 500 to 1024 (in bottom part of the image). Threshold value is then calculated as:

$$T_h = \bar{I} \cdot 2.87 - 7.67 \quad (1)$$

where \bar{I} is average intensity.

Equation 1 was obtained by experimental fitting the threshold value to the average intensity value in several data sets. All pixels with an intensity lower than T_h are set to 0 and all pixels with intensity higher than 20 are set to 20. This narrows the range of intensity values and improves behavior of uniform filtering.

The uniform filter is a two-dimensional filter implemented as a sequence of one-dimensional uniform filters with size 30 px in each axis. This blurred image is then further smoothed by a Gaussian filter with standard deviation set to 3.

A binary threshold produces a single solid area of the flame with intensity 1, while rest of image has intensity 0. Smaller artifacts, not

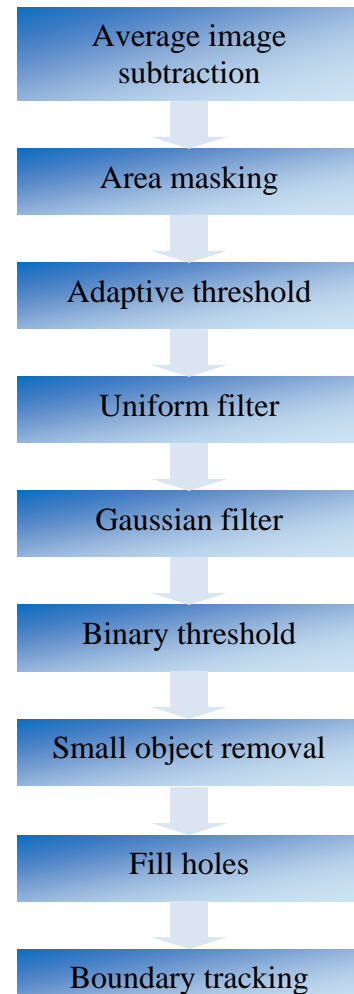


Fig. 4: Procedure of the flame front tracking.

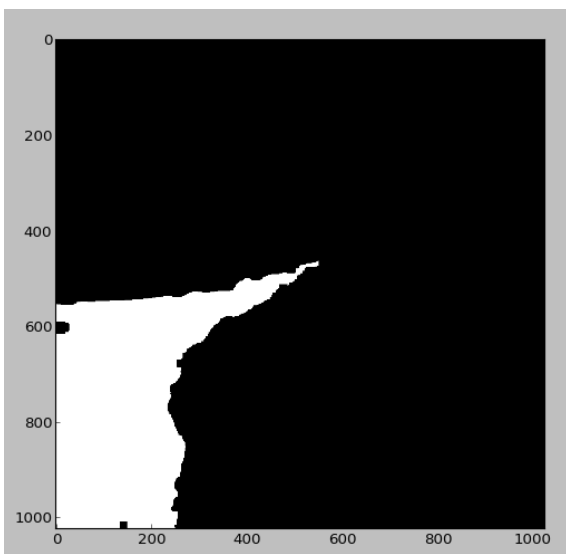


Fig. 5: Binary image of the flame.

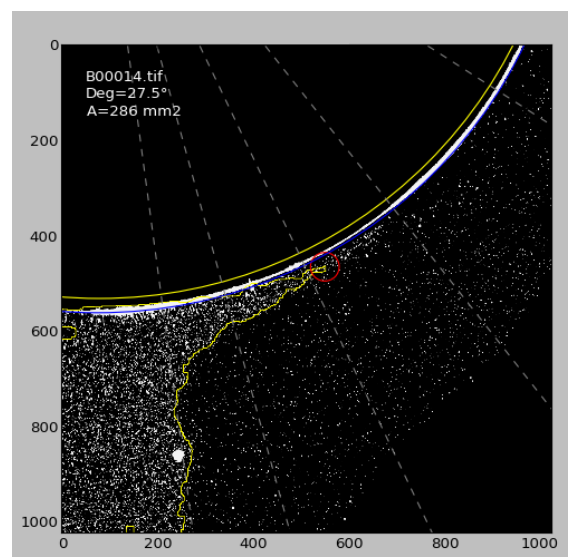


Fig. 6: PIV image with highlighted flame boundary.

connected to the core of the flame, are removed by small object removal method. The maximum size of the object to remove is 15000 px. Only the flame itself remains in the image. However, there may be small holes inside the flame due to disturbances in seeding density. Those are removed by fill holes method based on binary dilation. The final binary image is shown in Fig. 5. The last step is boundary tracking performed on the cleaned binary image. This step highlights the boundary (see final image in Fig. 6) and allows us to label the flame with appropriate properties.

The core body of the flame is tracked well, however, in the stretched part of the flame there are separated areas of unburnt gases travelling away from the flame. Those structures influence the detection of the stretch angle and may cause a significant overestimation of its value.

5. Conclusions

A method is proposed to derive instantaneous flame fronts from raw PIV images. The method enables the extraction of valuable data on impinging flames such as: flame area, stretch angle, thickness of the stretching flame, distance between the flame and the cooled wall (quenching layer). The method is based on the variation of the particle seeding density between (cold) unburnt gases and (hot) combustion products. The data processing method was applied to sets of raw PIV images and flame front could be detected accurately in both cases.

Acknowledgement

The authors gratefully acknowledge financial support within the framework of Operational Programme “Investment in education development” CZ.1.07/2.3.00/20.0020 and within the framework of Operational Programme “Research and Development for Innovations” – “NETME Centre – New Technologies for Mechanical Engineering”. This work was also supported by the project CZ.1.07/2.3.00/30.0039 of Brno University of Technology.

References

- Chander, S., Ray, A. (2005) Flame impingement heat transfer: A review. *Energy Conversion and Management*. 46 (18–19), 2803–2837. Available from: doi:10.1016/j.enconman.2005.01.011.
- Coron, X., Champion, J., Champion, M. (2004) Simultaneous measurements of velocity field and flame front contour in stagnating turbulent premixed flames by mean of PIV. In: Twelfth International Symposium on Applications of Laser Techniques to Fluid Mechanics, Lisbon, Portugal. Available from: in3.dem.ist.utl.pt/LXLASER2004/pdf/paper_04_3.pdf.
- Hartung, G., Hult, J., Balachandran, R., Mackley, M. R., et al. (2009) Flame front tracking in turbulent lean premixed flames using stereo PIV and time-sequenced planar LIF of OH. *Applied Physics B*. 96 (4), 843–862. Available from: doi:10.1007/s00340-009-3647-0.
- Jeanne, B., Samson, E., Renou, B., Boukhalfa, A. (2000) Bunsen flame analysis using simultaneous tomographic images and PIV in the fresh and burnt gases. In: 2000 Available from: ltces.dem.ist.utl.pt/lxaser/lxaser2000/papers/pdf/30_2.pdf.
- Jones, E., Oliphant, T., Peterson, P., et al. (2001) SciPy: Open source scientific tools for Python. Available from: www.scipy.org.
- Li, H. B., Zhen, H. S., Leung, C. W., Cheung, C. S. (2010) Effects of plate temperature on heat transfer and emissions of impinging flames. *International Journal of Heat and Mass Transfer*. 53 (19–20), 4176–4184. Available from: doi:10.1016/j.ijheatmasstransfer.2010.05.040.
- Tachibana, S., Zimmer, L., Suzuki, K. (2004) Flame front detection and dynamics using PIV in a turbulent premixed flame. In: Lisbon, Portugal. Available from: in3.dem.ist.utl.pt/LXLASER2004/pdf/paper_04_4.pdf.
- Walt, S. van der (2013) Scikit-image: Image processing in Python. Available from: scikit-image.org/.

NUMERICAL INVESTIGATION OF SHEAR BEHAVIOR SHCC STRUCTURAL ELEMENTS

J. Vorel^{*}, W. P. Boshoff^{**}

Abstract: *Fiber reinforced cement-based composites is a large group of composites with variety of properties. The purpose of adding fibers is to overcome the brittleness of the concrete by improving the post-cracking behavior and enhancing ductility. This paper deals with the group Strain Hardening Cement based Composites (SHCC) which exhibits excellent mechanical behavior showing tensile strain hardening and multiple fine cracks. The primary objective of the presented research is to verify a developed constitutive model. The constitutive model is intended to be utilized for large-scale simulations and thus it must be robust and efficient. Therefore, it is necessary to compare the numerical simulations against the experimental data. The paper summarizes the studies performed on the shear behavior of reinforced SHCC elements tested on beam specimens monotonically loaded by an anti-symmetrical moment.*

Keywords: Strain Hardening Cement-based Composite (SHCC), Rotating crack model, Damage, Shear behavior.

1. Introduction

Concrete has been used for many centuries as a safe and durable building material. Two of the main advantages of concrete are its high compressive strength and that it can be cast on the construction site into a variety of shapes and sizes. The most prominent disadvantages of concrete and other cementitious materials are their brittle failure behavior in tension and low tensile strength. The low tensile strength is usually compensated for with steel reinforcement, but wide cracks leading to the corrosion of the steel reinforcement still occur during the normal use of concrete (Otieno et al., 2010). These cracks lead to durability problems and cause structural degradation to occur more rapidly.

Fiber reinforced cement-based composites is a large group of composites with variety of properties. The purpose of adding fibers is to overcome the brittleness of the concrete by improving the post-cracking behavior and enhancing ductility. This paper deals with the group Strain Hardening Cement based Composites (SHCC) which exhibits excellent mechanical behavior showing tensile strain hardening and multiple fine cracks (Li and Wang, 2001; Boshoff and van Zijl, 2007). The primary objective of the presented research is to verify a developed constitutive model described in (Vorel and Boshoff, 2012; Vorel and Boshoff, 2013). The constitutive model is intended to be utilized for large-scale simulations and thus it must be robust and efficient. Therefore, it is necessary to compare the numerical simulations against the experimental data. The paper summarizes the studies performed on the shear behavior of R/ECC elements tested on beam specimens monotonically loaded by an anti-symmetrical moment (so-called Ohno method). Two different specimens, with and without stirrups, are assumed (Kabele and Kanakubo, 2007; Kabele, 2009).

2. Computational Model

In this section the main features of the utilized numerical model are briefly described. The complete description and definition of the model can be found in (Vorel and Boshoff, 2012; Vorel and Boshoff, 2013). The model is implemented in the open source finite element code OOFEM (Patzák and Bittnar,

* Ing. Jan Vorel, PhD.: Department of Mechanics, Faculty of Civil Engineering, CTU in Prague; Thákurova 7; 166 29, Prague; CZ, jan.vorel@fsv.cvut.cz

** Prof. William P. Boshoff, PhD.: Department of Civil Engineering, Stellenbosch University; Private Bag X1 Matieland 7602; Stellenbosch; South Africa, bboshoff@sun.ac.za

2001) for plane stress elements using a coaxial rotating crack method (RCM) with two orthogonal cracks as described in (Han et al., 2003). This numerical approach is classified as the smeared crack model with the softening defined by means of the cohesive crack and overlapping crack model (Carpinteri et al., 2007).

To model the specific behavior of SHCC in tension, the application of classical constitutive material models used for quasi-brittle materials is not straightforward. The employed numerical model is based on a rotating crack assumption to capture the strain hardening and softening, the multiple cracking, the crack localization and multiple orthogonal crack patterns (Suryanto et al., 2008). In heterogeneous materials where micro-cracking occurs prior to the formation of a macro-crack, the rotating crack model may be more realistic than the fixed crack model. Micro-cracks are formed orthogonally to the major principal stress when the tensile strength is first violated. However, upon rotation of the principal stress axes new micro-cracks arise in the “rotated” direction and it is most likely that upon termination of the stress rotation, the latter micro-cracks will grow into macro-cracks. This justifies the choice of a rotating crack model from a physical perspective. A complete description of the rotating crack model can be found, e.g., in (Rots, 1998). Note that the rotating crack model evaluates a given strain state and generates the inelastic strain in the principal directions of the strain and does not automatically include the effect of Poisson's ratio, as the stress is evaluated on the basis of individual principal strains.

To allow the residual deformations and to account for the Poisson ratio effect, a new approach is employed where the effective principal strain is used to determine the equivalent stress from the simplified uniaxial stress-strain diagram. The effective principal strain is based on the principal strain, which is free of inelastic deformations caused during the stress state change. The evolution of inelastic strain is assumed to be linearly dependent on the previously reached maximum strain for the elastic and hardening part and linearly dependent on the crack opening for the softening branch. This simplification corresponds well with experimental results (Vorel and Boshoff, 2012).

3. Numerical Study

The open source finite element program OOFEM is utilized to perform numerical simulations of selected experiments on Ohno beams. The specimens labeled PVA20-00 and PVA20-30 in (Kabele and Kanakubo, 2007) with shear reinforcement ratios of 0.0 and 0.3%, respectively, are exploited. Plane stress idealization of the problem was adopted. The finite element mesh typically consisted of about 3300 isoparametric four-node quadrilateral plane-stress finite elements of size around 25 mm. The SHCC material is represented by the constitutive model briefly described in the previous section. The material parameters summarized in Tab. 1 are obtained by fitting the uniaxial stress-strain diagrams presented in (Kanakubo, 2006; Kabele and Kanakubo, 2007; Kanakubo et al., 2007). The main steel bars and stirrups are represented by two-node truss elements with the cross-sectional area and position presented in (Kanakubo et al., 2007). The Mises plasticity condition with no hardening is assumed for the steel (Kanakubo et al., 2007) and an isotropic damage model with exponential softening is assumed for the

Tab. 1: SHCC model parameters.

General		Tension		Compression	
<i>Param.</i>	<i>Value</i>	<i>Param.</i>	<i>Value</i>	<i>Param.</i>	<i>Value</i>
E	18.41 GPa	σ_{t0}	3.4 MPa	$ \sigma_{c0} $	1.0 MPa
ν	0.35	ε_{tp}	0.0167	$ \varepsilon_{cp} $	0.0035
		σ_{tp}	4.1	$ \sigma_{cp} $	39.3 MPa
		$w_{t,cr}$	4.37 mm	$ w_{c,cr} $	0.23
		a_t	3.0	a_c	3.0
		b_t	0.8	b_c	0.8
		b_t^{cl}	0.9	b_c^{cl}	0.98
				β_c	2.2

steel-concrete contact, see (Patzák, 2013) for more details. The strength limit for the interface elements is setup to approx. 5 MPa.

Fig. 1 depicts the overall response of the beams, i.e., the shear load (one third of applied force) vs. translational angle (rotation of the side stubs about support pins). The peak load and the pre-peak loading part is captured satisfactorily for the beam without shear reinforcement (PVA20-00). However, the beam with the shear reinforcement shows a softer response and underpredicts the peak load by 15% when compared to the experimental data. This deficiency is attributed to the insufficient description of the steel-concrete interface due to the utilized interface model.

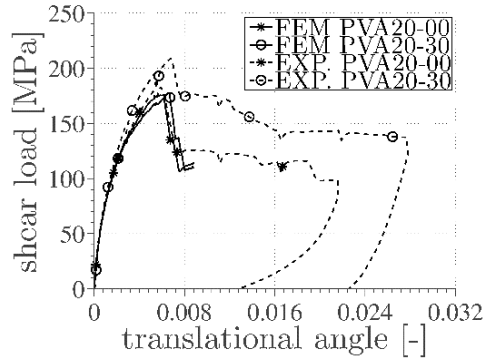


Fig. 1: Comparison of numerical simulations and experimental data.

To demonstrate the behavior of the beams at the peak load, Fig. 2 shows the damage magnitude of the individual beams.

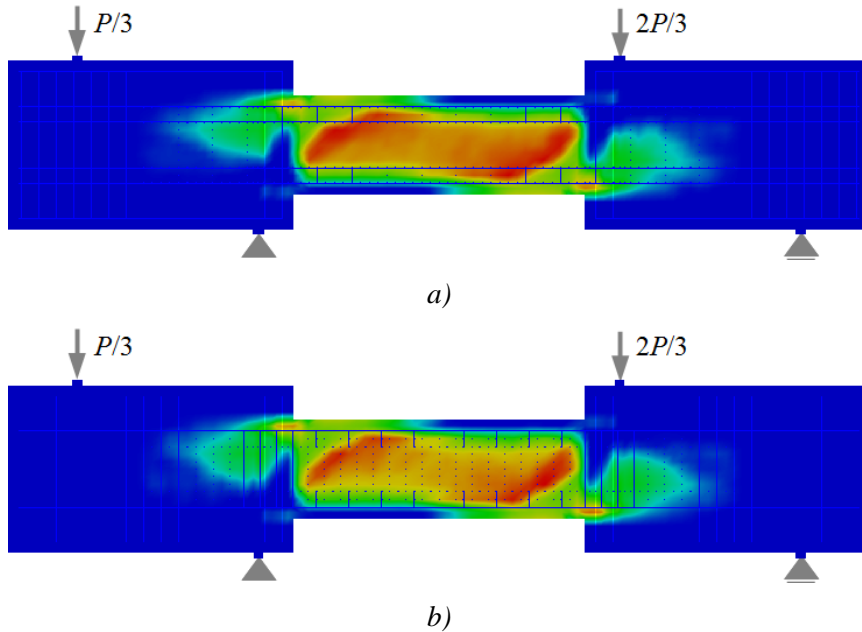


Fig. 2: Damage at the peak load for beams: a) PVA20-00, b) PVA20-30.

4. Conclusions

Based on the comparison of experiments and numerical analyses, the following conclusions related to the shear behavior of utilized numerical model can be drawn. The material model based on the rotating cracks appears to be sufficient for the simulation of the shear loaded structural members, as can be seen in Fig. 1. However, if the higher shear reinforcement ratio is assumed, the outlined numerical approach underpredicts the peak load. This behavior is attributed to the utilized interface model and will be the subject of future research.

Acknowledgement

The financial support provided by the GAČR grant No. P105/12/P353 is gratefully acknowledged.

References

- Boshoff, W. P., van Zijl, G. (2007) Time-dependant response of ECC: Characterisation of creep and rate dependence. *Cement and Concrete Research*, 37, pp. 725-734.
- Carpinteri, A., Corrado, M., Paggi, M., Mancini, G. (2007) Cohesive versus overlapping crack model for a size effect analysis of RC elements in bending, In: Proc. 6th International FraMCoS, Catania, Italy, pp. 655-663.
- Han, T.-S., Feenstra, P., Billington, S. (2003) Simulation of highly ductile fiberreinforced cement-based composite components under cyclic loading. *ACI Structural Journal*, 100, 6, pp. 749-757.
- Li, V., Wang, S. (2001) Tensile strain-hardening behavior of PVA-ECC. *ACI Materials Journal*, 98, 6, pp. 483-492.
- Kabele, P. (2009) Finite element fracture analysis of reinforced SHCC members, in: Proc. of the International Conference on Advanced Concrete Materials, Stellenbosch, South Africa, pp. 237-244.
- Kabele, P., Kanakubo, T. (2007) Experimental and Numerical Investigation of Shear Behavior of PVA-ECC in Structural Elements, In: Proc. 5th International Workshop on High Performance Fiber Reinforced Cementitious Composites (HPFRCC5), Maniz, Germany, pp. 137-145.
- Kanakubo, T. (2006) Tensile Characteristics Evaluation Method for Ductile Fiber-Reinforced Cementitious Composites. *Journal of Advanced Concrete Technology*, 4, 1, pp. 3-17.
- Kanakubo, T., Shimizu, K., Kanda, T., Nagai, S. (2007) Evaluation of bending and shear capacities of HPFRCC members toward the structural application, in: Proc. of the Hokkaido University COE Workshop on High Performance Fiber Reinforced Composites for Sustainable Infrastructure System, Sapporo, Japan, pp. 35-44.
- Otieno, M. B., Alexander, M. G., Beushausen, H. -D. (2010) Corrosion in cracked and uncracked concrete - influence of crack width, concrete quality and crack reopening. *Magazine of Concrete Research*, 62, 6, pp. 393-404.
- Patzák, B. (2013) Material Model Library Manual. Oofem manual, CTU in Prague, Prague, Czech Republic.
- Patzák, B., Bittnar, Z. (2001) Design of object oriented finite element code. *Advances in Engineering Software*, 32, 10-11, pp. 759-767.
- Rots, J. (1998) Computational modeling of concrete fracture, Ph.D. Thesis, Delft University of Technology.
- Suryanto, B., Nagai, K., Maekawa, K. (2008) Influence of damage on cracking behavior of ductile fibre-reinforced cementitious composite, In: Proc. 8th International Conference on Creep, Shrinkage and Durability of Concrete and Concrete Structures, Ise-Shima, Japan, pp. 495-500.
- Vorel, J., Boshoff, W. P. (2012) Numerical modelling of engineered cement-based composites, In: Proc. 18th Engineering Mechanics 2012, Svratka, Czech Republic, pp. 1-10.
- Vorel, J., Boshoff, W. P. (2013) Numerical simulation of ductile fiber-reinforced cement-based composite. *Journal of Computational and Applied Mathematics*. Accepted, available online.

MODELING AND SIMULATION OF THE RECUPERATIVE HEAT EXCHANGER

S. Wawrzyniak^{*}, K. Peszyński^{**}

Abstract: *The paper demonstrates mathematic model of the recuperative heat exchanger. System response in analytical form was designated by solving differential equations system. Transfer function of analysing exchanger was also designated. Based on transfer function, there was performed a simulation of tank treated as controlled plant.*

Keywords: Modelling, Dynamic characteristic, Heat exchanger, Simulation, SCILAB.

1. Introduction

The main issue in control system design is an identification of controlled plant. Only for well-recognised controlled plant, settable time constants of the control system can be selected in the way that the constants will be close to optimum from a specific quality control criteria point of view (e.g. minimum time, aperiodic order etc.). The paper demonstrates an example of mathematical modelling of shell tank heat exchanger used in Spirits Factories for heat recovery for domestic purposes from produced alcohol.

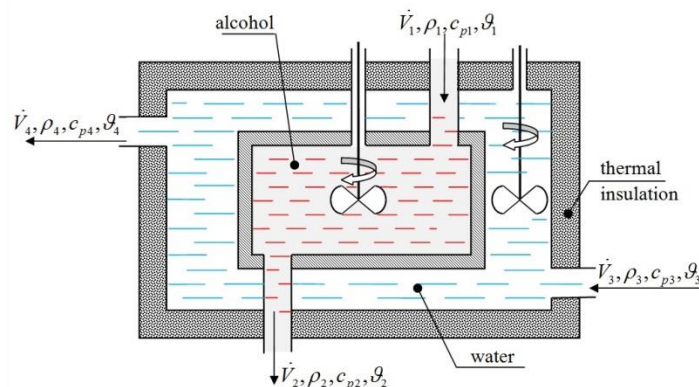


Fig. 1: Schematic representation of analysing shell tank heat exchanger.

2. Mathematical Modelling

2.1. Simplifying assumptions

Below are presented the basic simplifying assumptions which have to be supplemented in the next stage of the modelling process (Cengel et al., 2001):

- uniform temperature distribution in chambers (lumped parameter), the assumption is made possible by using the stirrers (Fig. 1),
- negligibly small changes in ρ_i mass density (dealing with liquids),
- negligibly small heat capacity of the wall of inner and outer tank,
- system is perfectly isolated from the environment (negligible heat losses).

^{*} Assist. Prof. Sylwester Wawrzyniak, PhD.: Control Group, Institute of Transport and Machine Operation, University of Technology and Life Sciences, Kaliskiego 7/2.3; 85 789, Bydgoszcz; Poland, sylwester.wawrzyniak@utp.edu.pl

^{**} Assoc. Prof. Kazimierz Peszyński, PhD.: Control Group, Institute of Transport and Machine Operation, University of Technology and Life Sciences, Kaliskiego 7/2.3; 85 789, Bydgoszcz; Poland, kazimierz.peszynski@utp.edu.pl

2.2. Initial mathematical description

The coolant (water) flows through outer tank and the cooled liquid (alcohol) flows through inner tank. For each tank the motion equations can be determined. Based on above simplifying assumptions, the equations can be written as:

$$V_1 \rho_2 c_{p2} \frac{d\mathcal{G}_2}{dt} = \dot{V}_1 \rho_1 c_{p1} \mathcal{G}_1 - \dot{V}_2 \rho_2 c_{p2} \mathcal{G}_2 - kA(\mathcal{G}_2 - \mathcal{G}_4) \quad (1)$$

$$V_3 \rho_4 c_{p4} \frac{d\mathcal{G}_4}{dt} = \dot{V}_3 \rho_3 c_{p3} \mathcal{G}_3 - \dot{V}_4 \rho_4 c_{p4} \mathcal{G}_4 - kA(\mathcal{G}_2 - \mathcal{G}_4) \quad (2)$$

where: A – cooling surface – inner tank surface (m^2), k – heat transfer coefficient ($\frac{\text{W}}{\text{m}^2 \cdot \text{K}}$), $\mathcal{G}_1, \mathcal{G}_2, \mathcal{G}_3, \mathcal{G}_4$ – temperature ($^{\circ}\text{C}$) in accordance with Fig. 1, V_1, V_2 – liquid volume in each tank (m^3).

During the following calculations it is assumed that $\dot{V}_1 = \dot{V}_2 = \text{const}$, $\dot{V}_3 = \dot{V}_4 = \text{const}$. V_1 and V_3 are also constant. Then $k = k(\dot{V}) = \text{const}$, $\rho_1 = \rho_2$, $\rho_3 = \rho_4$. Therefore, it can be written:

$$m_1 c_{p2} \frac{d\mathcal{G}_2}{dt} = \dot{m}_1 c_{p1} \mathcal{G}_1 - \dot{m}_1 c_{p2} \mathcal{G}_2 - kA(\mathcal{G}_2 - \mathcal{G}_4) \quad (3)$$

$$m_3 c_{p4} \frac{d\mathcal{G}_4}{dt} = \dot{m}_3 c_{p3} \mathcal{G}_3 - \dot{m}_3 c_{p4} \mathcal{G}_4 + kA(\mathcal{G}_2 - \mathcal{G}_4) \quad (4)$$

where: $m_1 = V_1 \rho_2$ – mass of cooled alcohol (kg), $\dot{m}_1 = \dot{V}_1 \rho_2$ – mass flow of cooled factor by the exchanger ($\text{kg} \cdot \text{s}^{-1}$).

The result is a system of two simplified differential equations that describe the dynamic properties of shell tank heat exchanger. To obtain one differential equation that is used for describing the impact of changes in the disturbance variables \mathcal{G}_1 and \mathcal{G}_3 on the output temperature \mathcal{G}_2 , first there must be determined the temperature \mathcal{G}_4 from the equation (3) and then this equation must be differentiated in terms of time and substituted into equation (4) instead of \mathcal{G}_4 and $\dot{\mathcal{G}}_4$. Thus after appropriate transformations, the second-order differential equation was obtained in the form of:

$$\begin{aligned} & \frac{m_1 m_2 c_{p2} c_{p4}}{kA} \ddot{\mathcal{G}}_2 + \left[m_2 c_{p4} \left(1 + \frac{\dot{m}_1 c_{p2}}{kA} \right) + m_1 c_{p2} \left(1 + \frac{\dot{m}_3 c_{p4}}{kA} \right) \right] \dot{\mathcal{G}}_2 + \\ & + \left[\dot{m}_1 c_{p2} + \dot{m}_3 c_{p4} \left(1 + \frac{\dot{m}_1 c_{p2}}{kA} \right) \right] \mathcal{G}_2 = \dot{m}_1 c_{p1} \left(1 + \frac{\dot{m}_3 c_{p4}}{kA} \right) \mathcal{G}_1 + \frac{\dot{m}_1 c_{p1} m_2 c_{p4}}{kA} \dot{\mathcal{G}}_1 + \dot{m}_3 c_{p3} \mathcal{G}_3 \end{aligned} \quad (5)$$

Initial conditions for $t=0$ are $\mathcal{G}_2 = \mathcal{G}_{2o}$, $\dot{\mathcal{G}}_2(0) = 0$.

2.3. Analytical solution

Analysed recuperative heat exchanger (Peszyński et al., 2011) is a very good example of device for energy recovery. Into exchanger flows $\dot{m}_1 = 10 \text{kg} \cdot \text{s}^{-1}$ of warm ethyl alcohol and $\dot{m}_3 = 15 \text{kg} \cdot \text{s}^{-1}$ of cold water. The mass of cooled liquid equals $m_1 = 564 \text{kg}$ and the mass of coolant is $m_2 = 200 \text{kg}$. Mean specific heat of cooled liquid is $c_{p2} = 2.85 \text{kJ} \cdot \text{kg}^{-1} \cdot \text{K}^{-1}$ while flowing $\text{C}_2\text{H}_5\text{OH}$ equals $c_{p1} = 2.97 \text{kJ} \cdot \text{kg}^{-1} \cdot \text{K}^{-1}$ and cooling water is $c_{p3} = c_{p4} = 4.19 \text{kJ} \cdot \text{kg}^{-1} \cdot \text{K}^{-1}$. Temperature of cooling water is 5°C while heat transfer coefficient equals $k = 5.02 \text{kW} \cdot \text{m}^{-2} \cdot \text{K}^{-1}$. The size of humidified surface is $A = 3 \text{m}^2$. Based on these data the transient function was designated. The function determines the temperature of cooled ethyl alcohol if the temperature of the flowing medium increases to 60°C .

To speed up the calculations, in the first place the constants of differential equation (5) were determined and the initial conditions in a steady state were assumed. After substituting the appropriate values, the equation was obtained:

$$92547.25 \ddot{\vartheta}_2 + 10680.45 \dot{\vartheta}_2 + 210.29 \vartheta_2 = 153.65 \vartheta_1 + 1652.63 \dot{\vartheta}_1 + 62.85 \vartheta_3 \text{ kJ} \cdot \text{s}^{-1} \quad (6)$$

where: $t=0$, $\vartheta_2 = \vartheta_{2o}$, $\dot{\vartheta}_2(0) = 0$.

To determine the steady state temperature $\vartheta_2(0)$ the equation (6) has been used wherein it is assumed that the derivatives occurring in the differential equation are zero, therefore:

$$210.29 \vartheta_{2o} = 153.65 \vartheta_{1o} + 62.85 \vartheta_{3o} \text{ hence } \vartheta_{2o} = \frac{153.65 \cdot 50 + 62.85 \cdot 5}{210.29} = 38^\circ\text{C}.$$

Because of the differential equation (6) contains derivative $\dot{\vartheta}_1$ on the right side, therefore the derivative has to be eliminated and a new forced initial condition has to be designated

$$\dot{\vartheta}_2(0_t), \dot{\vartheta}_2(0_+) = \frac{1652.63}{92547.25} [\vartheta_1(0_+) - \vartheta_1(0_-)] = 0.018 \cdot (60 - 50) = 0.18^\circ\text{C} \cdot \text{s}^{-1}.$$

The equation (6) can be written as:

$$92547.25 \ddot{\vartheta}_2 + 10680.45 \dot{\vartheta}_2 + 210.29 \vartheta_2 = 153.65 \vartheta_1 + 62.85 \vartheta_3 \quad (7)$$

assumed initial conditions: $t=0$, $\vartheta_2(0) = 38^\circ\text{C}$, $\dot{\vartheta}_2(0_+) = 0.18^\circ\text{C} \cdot \text{s}^{-1}$.

After solving the characteristic equation $92547.25 \lambda^2 + 10680.45 \lambda + 210.29 = 0$, two roots were obtained:

$$\lambda_1 = -0.025, \lambda_2 = -0.090.$$

Particular solution of the differential equation in constant form of X for $\vartheta_1 = 60^\circ\text{C}$, $\vartheta_3 = 5^\circ\text{C}$ equals: $210.29 X = 153.65 \cdot 60 + 62.85 \cdot 5$, $X = 45.3$. The general integral of the differential equation (7) is:

$$\vartheta_2 = C_1 e^{-0.025t} + C_2 e^{-0.090t} + 45.3$$

C_1 and C_2 constants have been determined from the initial conditions of the equation (7):

$$\vartheta_2(0) = 38 = C_1 + C_2 + 45.3; \dot{\vartheta}_2(0_+) = 0.18 = -0.025C_1 - 0.090C_2$$

Solving this system of algebraic equations allows to calculate constants: $C_1 = -7.34$, $C_2 = 0.038$.

Function that determines variations of temperature ϑ_2 of time was obtained, i.e. motion equation (dynamic characteristic of analysing plant).

$$\vartheta_2(t) = 45.3 - 7.34 e^{-0.025t} + 0.038 e^{-0.090t} \quad (8)$$

The value of the temperature in the new steady state was achieved through the calculation of equation limit (8) for $t \rightarrow \infty$.

$$\lim_{t \rightarrow \infty} \vartheta_2(t) = 45.3 = \overline{\vartheta_{2o}}$$

3. Simulation

Simulation of heating processes in exchanger was carried out in SCILAB environment, exactly in Xcos graphical editor (Bartoszak, 2012). For this purpose, the mathematical model described above was converted to differential form. The initial steady state before the disturbance has been adopted as a working point. It is the most common way of properties description used in automatics because it allows to create a transfer function of an object. The initial values for the working point are as follows: $\vartheta_{1o} = 50^\circ\text{C}$, $\vartheta_{2o} = 38^\circ\text{C}$, $\vartheta_{3o} = 5^\circ\text{C}$, $\vartheta_{4o} = 11.6^\circ\text{C}$.

The differential equation (7) takes the form:

$$92547.3 \Delta \ddot{\vartheta}_2 + 10680.45 \Delta \dot{\vartheta}_2 + 210.3 \Delta \vartheta_2 = 153.65 \Delta \vartheta_1 \quad (9)$$

where initial conditions for $t=0$ are: $\Delta \vartheta_2(0) = 0$ and $\Delta \dot{\vartheta}_2(0_+) = 0.18^\circ\text{C} \cdot \text{s}^{-1}$.

In order to solve a task in differential form, the Laplace transform was used. By applying the principles of the transform, equation was obtained in the Laplace transform form

$$92547,3[s^2\Delta\vartheta_2(s) - \Delta\dot{\vartheta}_2(0_+)] + 10680,45s\Delta\vartheta_2(s) + 210,3\Delta\vartheta_2(s) = 153,65\Delta\vartheta_1(s) \quad (10)$$

From equation (10) the image of output function $\Delta\vartheta_2(s)$ was obtained

$$\Delta\vartheta_2(s) = \frac{153,65\Delta\vartheta_1(s) + 92547,3\Delta\dot{\vartheta}_2(0_+)}{92547,3s^2 + 10680,45s + 210,3} \quad (11)$$

After substituting numerical value for $\Delta\dot{\vartheta}_2(0_+)$ and taking into account that the size of input changes in step form, transfer function was obtained

$$\frac{\Delta\vartheta_2(s)}{\Delta\vartheta_1(s)} = \frac{1665,85s + 153,65}{92547,35s^2 + 10680,45s + 210,3} \quad (12)$$

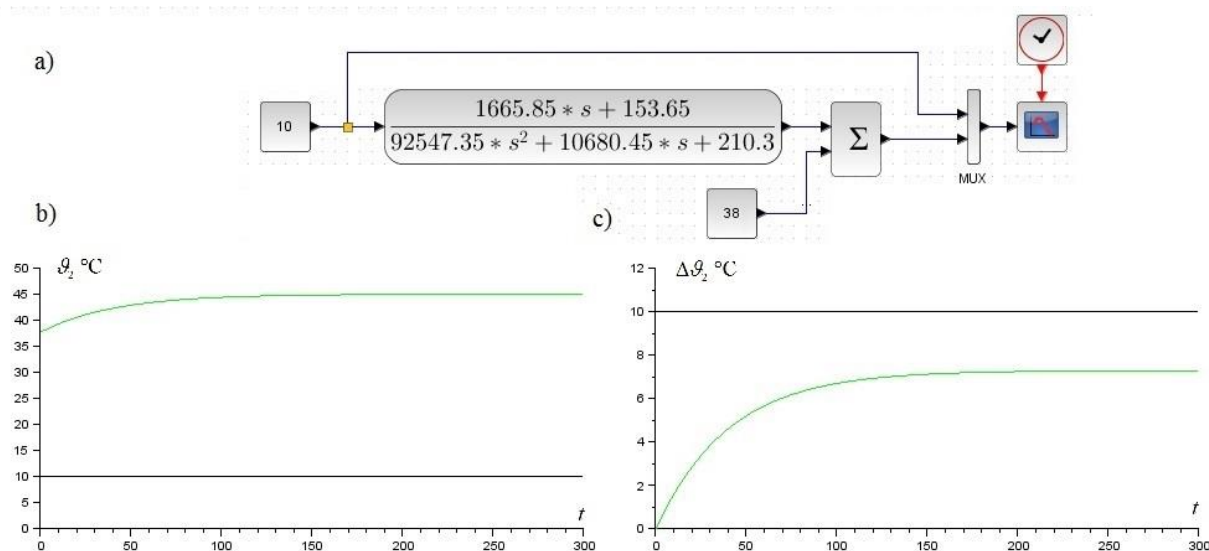


Fig. 2: SCILAB simulation: a) flowchart; b) ϑ_2 system response; c) differential response of $\Delta\vartheta_2$ system.

The equation (12) was moved to SCILAB numerical environment (Fig. 2a). Because of abrupt change of alcohol temperature was $\Delta\vartheta_1(s)=10^\circ\text{C}$, at the input of system it was applied the conversion block $\text{CONST}_m = 10$. The value defined as the working point was also added to the output value using block $\text{CONST}_m = 38.0$. The time course of output changes in the output is shown in Fig. 2b.

4. Conclusions

Obtained mathematical model of recuperative heat exchanger was very useful to determine the time constants of designed control system. Designation of mathematical model was necessary because ordering party, in the view of type and continuity of production, did not allow its determination by using experimental methods. Diagram shown on Fig. 2b was used to determine the time constants by Ziegler method. The only verification form of the mathematical model was PID controller tuning. The PID controller tuning provided based on the mathematical model created established the assumed quality control.

References

- Bartoszak, B. (2012) Analysis of the selected control system with disturbance measurement in the MATLAB environment. Diploma thesis. FME University of Technology and Life Sciences Bydgoszcz, Poland. (in Polish).
- Cengel, Y. A., Boles, M. A. (2001) Thermodynamics: An Engineering Approach, ISBN-10: 0072383321, ISBN-13: 978-0072383324, Edition: 4th.
- Peszyński, K., Wawrzyniak, W. (2011) Identification of the Recuperative Heat Exchanger. Statute Research no 19/2011 Modeling and Control of Thermal and Energy Systems (internal report Faculty of Mechanical Engineering – not published).

THEORETICAL ALGORITHM TO ASSESS THE VALUES OF THE BREAKING LOAD OF BARS SITUATED IN THE SUPPORTING ZONE OF THE SLAB-COLUMN CONNECTION

B. Wieczorek*

Abstract: *Catastrophes of reinforced concrete building structures, particularly slab-column structures, which happened so far, indicate the necessity of analyzing the behaviour of this type of structures exerted by additional loads. The destruction of the supporting zone due to punching and the lack of adequately constructed reinforcement may result in a progressive catastrophe. Instructions concerning the prevention of such situations are to be found only in CSA A23.3 (2011) and ACI 318 (2004). The present paper deals with a model of calculations which permits to assess the values of reserves of the load-bearing capacity of the supporting zone after its destruction by punching. The presented considerations are based on results of experimental investigations carried out on reinforced concrete models of slab-column connections in the scale 1:1. The model of calculations permits to assess the values of the forces of the load, at which the bars situated immediately in the supporting zone fail. This model was verified basing on the results of experimental investigations, performed on simplified tested models.*

Keywords: Reinforced concrete structure, Progressive collapse, Punching, Slab-column connections, Two-way slabs structural integrity reinforcement, Experimental research.

1. Introduction

Slab-column structures are very common and provide an economical structural system. Investigative analyses of the behaviour of the supporting zone of slab-column structures within the range of their destruction due to punching permitted to develop various methods of calculations in this respect. But over the past years several failures of buildings have occurred, resulting in progressive collapses. The catastrophes in Boston, in Bailey Crossroads, in Cocoa Beach Florida, in Warsaw, in Mexico City and in Switzerland indicate the need of careful designing the reinforced concrete slab-column connections in order to prevent a progressive collapse. An inadequately constructed supporting reinforcement may result in a complete destruction of the whole structure.

Some research programs have been carried out to investigate the post-failure behaviour of slab-column structures. Research results, and also the technical and engineering procedure of modelling a flat slab of reinforced concrete slab-column structures were presented in literature (Wieczorek M, 2013, 2014). The application of continuous bottom reinforcement was recommended (Mitchell et al., 1979, 1984, 2012) as a practical and economical solution. Melo and Regan (1998) reported tests of slabs which were aimed at identifying the type of failure and predicting the post-punching resistance. The influence of the top and bottom reinforcement, the size of the reinforcing bars, the layout of the reinforcement and the stress-strain characteristics of the reinforcement were investigated by Mirzaei (2010). In order to assess accurately the reserve of the load capacity of the supporting zone after its destruction due to punching, reinforced concrete models of slab-column connections have been investigated in the scale 1:1 (Wieczorek B., 2013, 2014).

2. Description of the Problem

In order to assess accurately the reserve of the load capacity of the supporting zone after its destruction due to punching, reinforced concrete models of slab-column connections have been investigated

* Barbara Wieczorek, PhD. Eng.: Department of Theory of Building Structures, Faculty of Civil Engineering, Silesian University of Technology, Akademicka 5 st., 44-100 Gliwice, Poland, barbara.wieczorek@polsl.pl

in the scale 1:1 (Wieczorek B., 2013, 2014). The column was placed in three different positions in relation to the centre of the slab, viz. axially, on the unidirectional and the bidirectional eccentricity. Moreover, investigations concerning the load-bearing capacity of bars crossing each other above the column were carried out on a simplified model. Similarly as in the case of basic models, the column was situated in three different positions. The investigations were performed basing on basic and simplified models, which permitted to verify the assumption of possible simplifications of the tested models. The conformity of the obtained results on the level up to 5% justifies the statement that the results of investigations concerning the load-bearing capacity of slab-column connections based on simplified models provides a rather exact approximation. Basing on these investigations of simplified models, a numerical model was developed.

Due to practical reasons it proved to be expedient for the designers to elaborate a model of calculations which would make it possible to assess the load-bearing capacity of a slab-column connection, depending on the applied reinforcement.

These considerations were based on the results of investigations performed on a simplified model of a slab-column connection (Wieczorek B., 2013). This model consisted of the column element, through which passed two bars with a diameter of 16 mm. The test was carried out on a test stand in accordance with the diagram presented in Fig. 1. The reinforcing bars were fastened permanently on the test stand (Fig. 2), and the load was exerted on the base of the column. The aim of this test was to determine the relation between the vertical displacement of the column and the exerted load, and also to determine the value of the force of the load, at which the bars passing above the column fail.

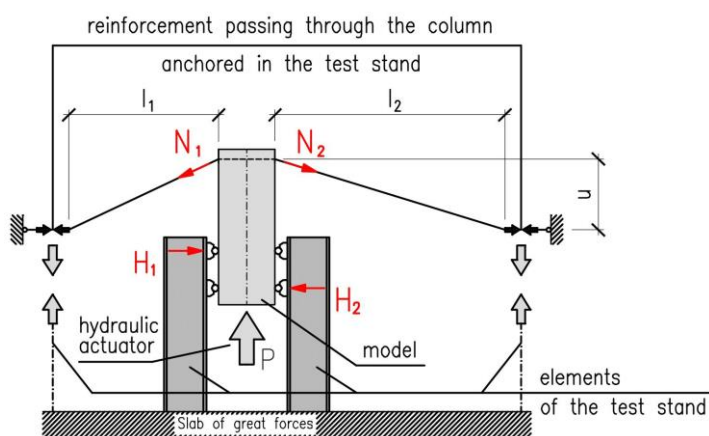


Fig. 1: Diagram of the load exerted on the model with the arrangement of forces taken into account in the model of calculations.

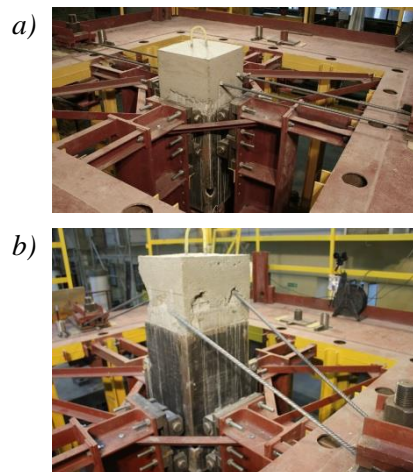


Fig. 2: Model situated on the test stand: a) Before the test; b) After the rupture of the bar.

The experimental investigations were carried out on reinforcing bars of class C in compliance with the Eurocode 2 (2010) with a diameter of 16 mm and an entire length of 2800 mm, the width of the column zone amounting to 400 mm. Two different situations of the column versus the test stand were considered, viz. axial ($l_1 = l_2 = 1200$ mm) and eccentrically equal to 285 mm ($l_1 = 915$ mm and $l_2 = 1485$ mm).

The model of calculations was constructed basing on the diagram corresponding to the performed tests, as shown in Fig. 1. Due to the forced vertical displacement of the column, caused by the load P exerted on its base, in the bars crossing the column above there occur, respectively, axial forces N_1 and N_2 , resulting from the lengthening of the bars on the left and right-hand side of the column in relation to their initial length l_1 and l_2 , measured from the point where the reinforcing bars are fastened to the test stand to the point at the edge of the column.

Basing on the diagram in Fig. 1, an algorithm was derived which permits to determine the values of the forces N_1 and N_2 occurring in the bars. The values of these forces depend directly on the value of the vertical displacement of the column and the initial length of the bars, as well as on the physical parameters of the reinforcing steel and the diameter of the bars. Besides that, also the horizontal interaction of H_1 and H_2 upon the column were taken into consideration. These forces result from the construction of the test stand, ensuring the vertical displacement of the column in the course of testing.

3. Synthesis of the Results

The results of calculations carried out basing on the derived algorithm were compared with the results of experimental investigations. The values of the force F obtained in tests were compared with the values of the forces N_1 and N_2 . These values and their resultant in the vertical direction $W_y = N_{1y} + N_{2y}$ depending on the displacement of the column u have been presented in Fig. 3. The compatibility of the force W_y with the force P amounts to 3%. Larger differences in the initial range of displacements up to 170 mm are due to matching of the elements of the model with the test stand at the beginning of the tests.

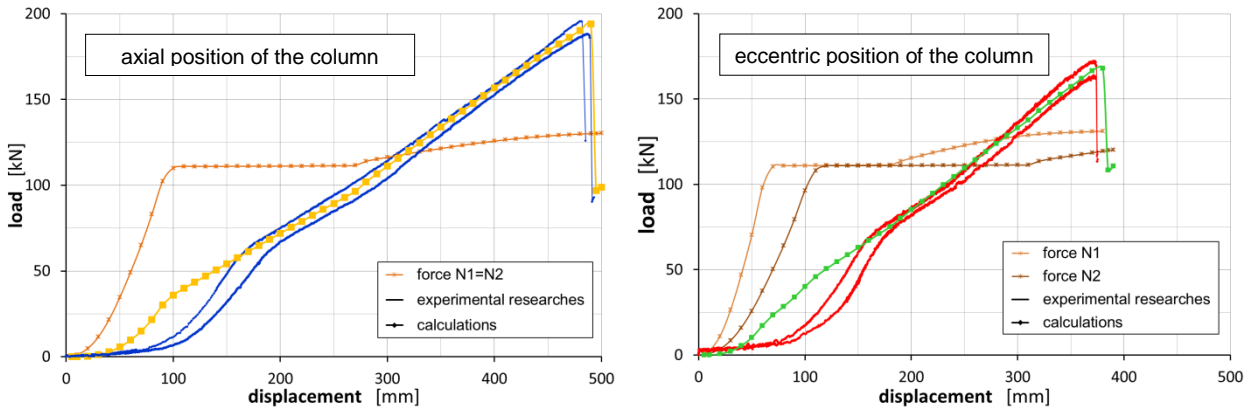


Fig. 3: Graph of changes of the loads as a function of the displacement of the column.

When investigating the strength of reinforcement steel in order to determine the relation between the stresses and deformations, the mean value of the force N_{max} was found, at which the bar ruptures. In the case of the applied reinforcing bars of the class C with a diameter of 16 mm the value of the force N_{max} amounted to 130.3 kN. It has been observed that the moment when the highest value of the force of the load P_{max} occurs, corresponds exactly with the moment when in one of the bars the value of the longitudinal force is equal to the value of the force of breaking N_{max} , whereas the force in one of the other bars is close to the value N_{max} . The difference between the forces N_1 and N_2 amounts then to about 5%. Such a compatibility was attained both in the case of an axial and eccentric position of the column.

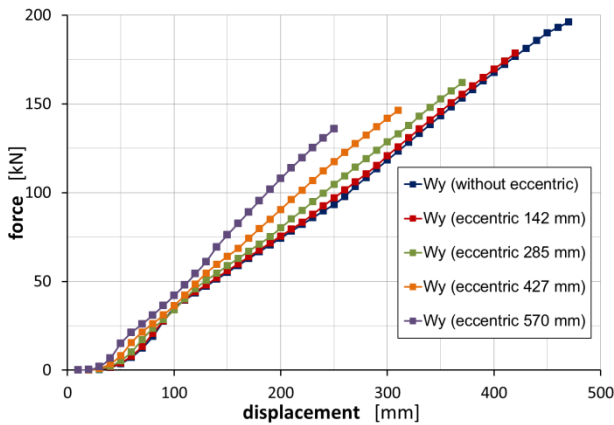


Fig. 4: Graph of changes of the forces W_y at different positions of the column.

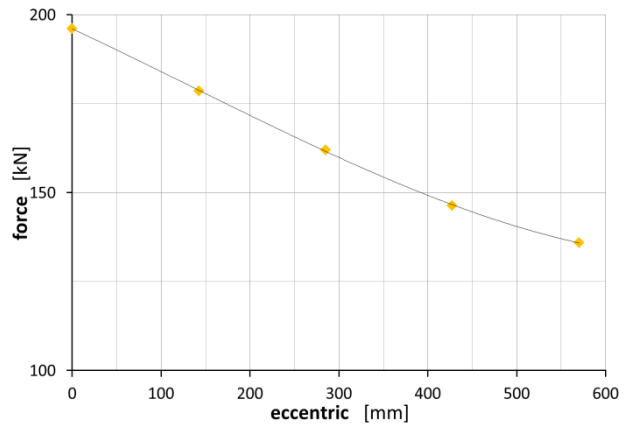


Fig. 5: Dependence of the force $W_{y,max}$ on the eccentric position of the column.

Making use of the elaborated algorithm, the influence of the eccentric position of the column on the value of the destructive force $W_{y,max}$ was analyzed, corresponding to the force of the load P_{max} . The position of the column was considered, respectively in the eccentric equal to 142.5 mm, 285 mm, 427.5 mm and 570 mm. The obtained results have been presented in Fig. 4. A linear decrease of the value of the force $W_{y,max}$ was observed when the column was shifted in relation to its axial position (Fig. 5). The relation between the value of the force $W_{y,max}$ and the shift of the axis of the column is denoted by the function $W_{y,max}(e) = 10^{-7}e^3 - 5^{-5}e^2 - 0.1168e + 196.05$.

4. Conclusions

The elaborated model of calculations permits to assess the value, of the destructive force $W_{y,max}$, at which the bars of the reinforcement passing just above the column in its connecting with the slab rupture. The value of this force depends on the amount of the applied reinforcement and the length of anchoring the reinforcing bars, taking also into account the possibility of an eccentric position of the column with regard to the surface of the slab. The application of this model requires, however, very exact information about the relation $\sigma-\varepsilon$ concerning the applied reinforcing steel. In spite of the assumed simplifications in relation to actual slab-column structures, this model provides results rather close to those obtained experimentally.

Basing on already published results of investigations and the performed analyses, as well as the results of numerical calculations (Wieczorek B., 2013, 2014), this suggested model of calculations may be used to assess preliminarily the reserve of the load-bearing capacity of a slab-column connection after its destruction by punching.

References

- ACI Committee 318 (2011) Building code requirements for structural concrete and commentary, American Concrete Institute, United State America.
- CSA Standard A23.3-04 (2004) Design of concrete structures, Canadian Standard Association.
- PN-EN 1992-1-1: 2004/AC (2010) Eurocode 2, Design of concrete structures - Part 1-1: General rules and rules for buildings, European Standard.
- Habibi, F., Redi, E., Cook, W.D., Mitchell, D. (2012) Assessment of CSA A23.3 structural integrity requirements for two-way slabs. Canadian Journal of Civil Engineering, 39.
- Hawkins, N.M., Mitchell, D. (1979) Progressive collapse of flat plate structures. Journal of the American Concrete Institute, 76(7).
- Melo, G. S. S. A., Regan, P. E. (1998) Post-punching resistance of connections between flat slabs and interior columns. Magazine of Concrete Research, 50(4).
- Mirzaei, Y. (2010) Post-punching behavior of reinforced concrete slabs. Ph.D. thesis, School of Architecture, Civil and Environmental Engineering, Ecole polytechnique fédérale de Lausanne (EPFL), Switzerland.
- Mitchell, D., Cook, W. D. (1984) Preventing Progressive Collapse of Slabs Structures. Journal of Structural Engineering, 110(7).
- Wieczorek, B. (2013) Influence of the location of the column on the load capacity of a slab-column connection for the inner column after punching, Procedia Engineering, Vol. 57.
- Wieczorek, B. (2013) Idea of a simplified model to determination of the load capacity of and inner slab-column connection after its punching, Procedia Engineering, Vol. 65.
- Wieczorek, B. (2013) Load-bearing capacity of reinforcing bars in the zone of the slab-column connection determined experimentally and in the result of numerical calculations, Procedia Engineering, Vol. 65.
- Wieczorek B. (2014) Experimental tests for the analysis of a load-bearing capacity of an internal slab-column connection after its punching at various positions of the column, Advanced Materials Research „Structural and physical aspects of civil engineering”.
- Wieczorek B. (2014) Load capacity of an internal slab-column connection depending on the geometric parameters of the reinforcement, Advanced Materials Research „Structural and physical aspects of civil engineering”.
- Wieczorek, M. (2013) Influence of amount and arrangement of reinforcement on the mechanism of destruction of the corner part of a slab-column structure, Procedia Engineering, Vol. 57.
- Wieczorek, M. (2013) Investigations concerning the corner part of the reinforced concrete structure in the emergency of removing the corner support, Procedia Engineering, Vol. 65.
- Wieczorek, M. (2013) Concept of shell-beam model of slab-column connection based on analysis of the 3D model, Procedia Engineering, Vol. 65.
- Wieczorek M. (2014) Comparison experimental tests of behavior of the slab-column structure after removal of the corner support with the simplified models describing the mechanism of destruction, Advanced Materials Research „Structural and physical aspects of civil engineering”.
- Wieczorek M. (2014) Narrow reinforced concrete slabs after their flexural destruction, Advanced Materials Research „Structural and physical aspects of civil engineering”.

NUMERICAL MODELLING OF THE DESTRUCTION OF REINFORCEMENT BARS IN THE SUPPORTING ZONE OF THE COLUMN

B. Wieczorek*

Abstract: *The destruction of the supporting zone of slab-column structures caused by a breakdown, pulls the upper reinforcement in the course of the dropping down of the roof upwards. The only element which can deter a further catastrophe is the reinforcement at the bottom, which is not torn off, but even pressed against the concrete of the column and the slab. The paper presents the results of laboratory tests performed on a simplified model of a slab-column connection. The aim of investigations was to find out at which value of the load the destruction of such a connection occurs due to the rupture of the bars above the column. Basing on these investigations a numerical model was developed in the ANSYS program. In order to render the conditions of connecting the reinforced concrete element with the reinforcement bars in the case of considerable deformations, the model was divided into finite elements. In modelling the fragment of the connection of reinforcement bars with the concrete and anchoring, the contacting elements were used. The obtained results of laboratory tests and the results of numerical calculations permitted to determine the relations between the exerted load and the displacement of the column in time and also to determine the values of the force at which the breakdown of the bars above the column had taken place.*

Keywords: Reinforced concrete structure, Slab-column connections, Two-way slabs structural integrity reinforcement, Experimental research, Numerical model.

1. Introduction

In the light of investigations carried out so far, the mechanical properties and static behaviour of the concrete and reinforcement in the zone adjacent to the support of slab-column structures are rather well known. The methods of calculations and the principles of design have been elaborated. For the sake of safety precise understanding of the behaviour of this type of these zones of structures in the range of destructive loads is very important. Instructions concerning the prevention of such situations are to be found only in standards: ACI 318 (2004) and CSA A23.3 (2011).

An inadequately constructed supporting reinforcement may result in a complete destruction of the whole structure. Researches have been carried out to investigate the post-failure behaviour of slab-column structures. The results of these tests, and also the technical and engineering procedure of modelling a flat slab of reinforced concrete slab-column structures were presented in literature (Wieczorek M, 2013, 2014). The application of continuous bottom reinforcement was recommended (Mitchell et al., 1979, 1984, 2012) as a practical and economical solution in order to prevent a progressive collapse. The reinforced concrete models of slab-column connections with bottom bars passing through the column have been investigated (Wieczorek B., 2013, 2014). Based on these investigations the reserve of the load capacity of the supporting zone after its destruction due to punching has been accurately estimated.

2. Description of the Problem

In investigations (Wieczorek B., 2013, 2014) a model corresponding to the actual behaviour of a slab-column connection has been applied. Within the frame of these investigations and basing on the obtained results, a simplified model of a slab-column connection could be developed, which can be used to determine the value of the load at which the reinforcement bars will rupture.

* Barbara Wieczorek, PhD. Eng.: Department of Theory of Building Structures, Faculty of Civil Engineering, Silesian University of Technology, Akademicka 5 st.,44-100 Gliwice, Poland, barbara.wieczorek@polsl.pl

The paper presents the results of laboratory tests performed on a simplified model of a slab-column connection (Fig. 1). The aim of investigations was to find out at which value of the load the destruction of such a connection occurs due to rupture of the bars above the column. The simplified model consisted of a column with a cross-section of 400 x 400 mm and a height of 500 mm (Fig. 1), by which passed four bars. In each model a bottom reinforcement crossing above the column was constructed of reinforcing steel class C ($\epsilon_{uk} = 11.8\%$, $f_{tk}/f_{yk} = 1.196$ and $f_{yk} = 547.1$ MPa) (Eurocode 2, 2010). The column was situated axially in relation to the centre of the test stand (Fig. 2).

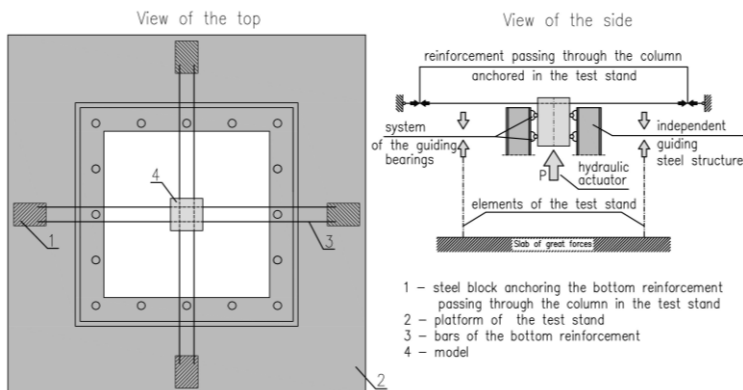


Fig. 1: Diagram of the load exerted on the model.



Fig. 2: Model situated on the test stand during the tests.

3. Numerical Model

Basing on these investigations a numerical model was developed in the ANSYS program (Fig. 3). In order to simulate the connection of the reinforced concrete element with the reinforcement bars in the case of considerable deformations, at the edges of the model bevels were cut in the shape of quarter rounds. In the course of testing, parts of the concrete were loosened and the bars were supported on curved arches.

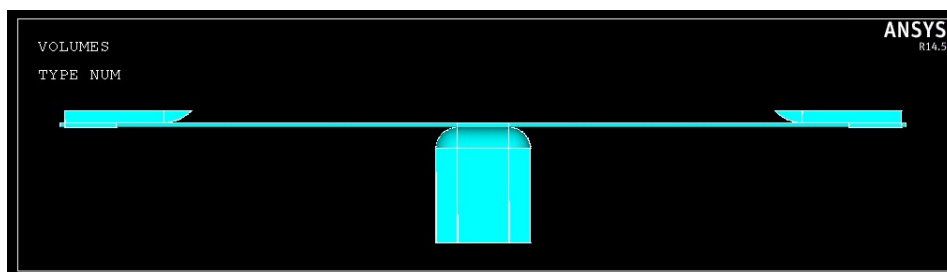


Fig. 3: Numerical model of the analyzed problem.

While constructing the model, great care was paid to an accurate representation of three kinds of the material applied in the investigations, complying with the ANSYS program:

- anchoring - steel - linearly elastic material,
- reinforcement bars - steel - ϵ - σ characteristics in compliance with the diagram,
- column - concrete - linearly elastic material $E = 30$ GPa complying with the tests.

In order to meet the conditions of connecting the reinforced concrete element with the reinforcement bars in the case of considerable deformations, the modal was divided into finite elements, applying the 20-node element SOLID86. In modelling the fragment of the connection of reinforcement bars with the concrete and anchoring, the contacting elements TARGET170 and COUNA174 were used.

Similarly as in the investigations, the load was in the model exerted on the bottom part of the column in one step, divided into substeps, thus obtaining the values of stresses and strains in the nodes of the final elements. Thanks to this, similarly as in the case of the tested model, it was possible to get a diagram of displacements of the column as a function of the load. The range of the resulting maximum displacement in the numerical model is to be seen in Fig. 4.

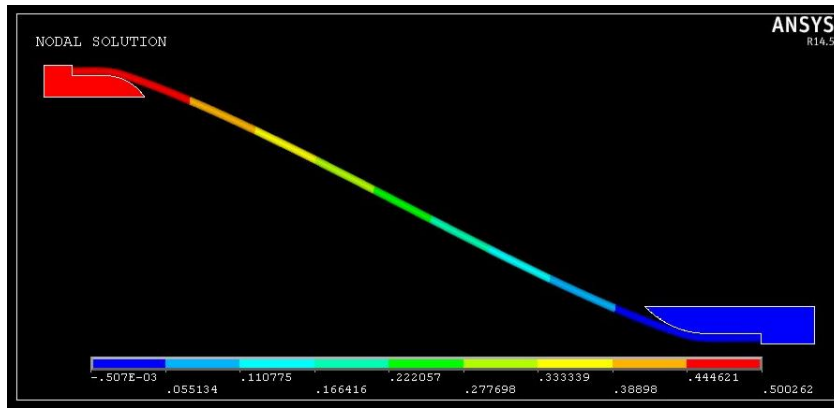


Fig. 4: The range of displacements of the column.

Below there are maps of the distribution of stresses obtained in the last substep of loading preceding the destruction. An exemplary distribution of normal stresses along the axis of the bars in the vicinity of the construction of the bar over the column and at the place the anchoring of the bar have been shown in Fig. 5.

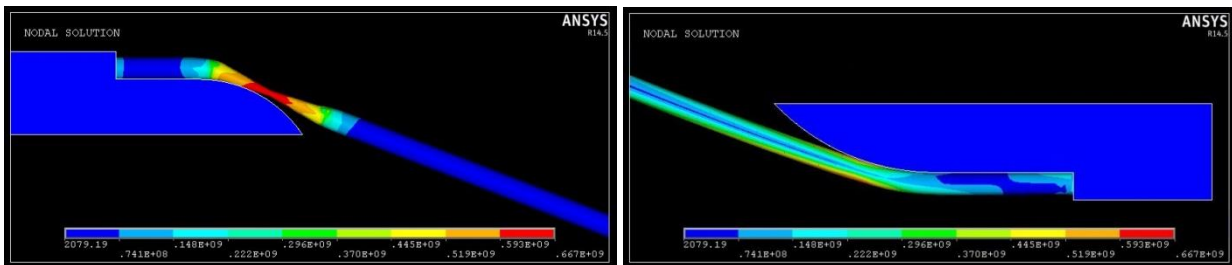


Fig. 5: Map of the stresses: column and anchoring.

4. Synthesis of the Results

The results of laboratory tests and numerical calculations have been compared, permitting to determine the dependence of the displacement of the column on the exerted load (Fig. 6). The values of the forces due to which the corresponding bars above the columns ruptured have been gathered in Tab. 1.

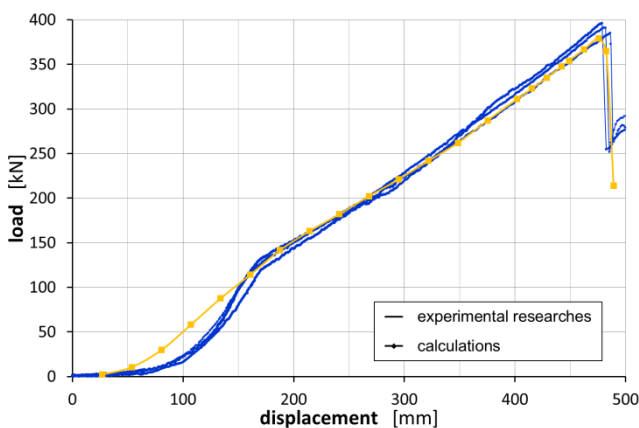


Fig. 6: Graph of changes in the displacement of the column as a function of the load.

Tab. 1: The values of forces and displacements obtained in the tests and the numerical model.

	Tested model	Numerical model
Maximum load obtained in tests	394.96 kN	
	391.17 kN	379.09 kN
	383.91 kN	
Displacement of the column	476 mm	
	481 mm	477 mm
	485 mm	

The difference in the percentage of numerical calculations in relation to the tests is less than 5%. The value of the load causing the rupture of the first bar, calculated numerically, amounts to 95.9%-98.7% of the value of the force obtained by testing the model.

Basing on numerical calculations, the stresses were analyzed which occurred in the bars passing through the column. The values of the stress in the cross-section of the bar at the spot of its considerable constriction (where the bar later ruptured) and in the centre of the span between the column and the anchoring was determined at the moment of reading the highest value of the charging force.

An analysis of the obtained results indicates a considerable effect of bending on the load-bearing capacity of the bars passing through the column. The load-bearing capacity of these bars is additionally affected by their bending by about 9%. Simultaneously, also the values of stresses occurring in the cross-section of the bar have been compared with the tensile strength of the steel. These stresses amounted to 98.78% of the tensile strength f_{tk} .

The values of stresses permitted to determine the degree of the boundary degradation of the axial force in the bar, resulting from the bending of the bar at the point of its contact with the anchoring element of the reinforcement or concrete column. This is of essential importance, because in the solution quoted in the standard (ACI, 2011, CSA, 2004) this phenomenon has been left out of account, and in calculations only the value of the axial force is taken into consideration. The values of the load-carrying capacity $F_{cal} = 439.79$ kN calculated according to standards is higher than the value obtained by testing.

5. Conclusions

Attempts to represent investigative models, the procedure of investigations and the obtained results in computer programs are a rather difficult task, due to the lack of information concerning all the processes encountered in the course of laboratory tests. The comparison quoted above indicates the possibility of constructing a rather good numerical model, which can simulate the aforesaid laboratory tests. The obtained numerical model permits to determine exactly the degree of degradation of the load capacity in reinforcement bars.

References

- ACI Committee 318 (2011) Building code requirements for structural concrete and commentary, American Concrete Institute, United State America.
- CSA Standard A23.3-04 (2004) Design of concrete structures, Canadian Standard Association.
- PN-EN 1992-1-1: 2004/AC (2010) Eurocode 2, Design of concrete structures - Part 1-1: General rules and rules for buildings, European Standard.
- Habibi, F., Redi, E., Cook, W. D., Mitchell, D. (2012) Assessment of CSA A23.3 structural integrity requirements for two-way slabs. Canadian Journal of Civil Engineering, 39.
- Hawkins, N. M., Mitchell, D. (1979) Progressive collapse of flat plate structures. Journal of the American Concrete Institute, 76(7).
- Mitchell, D., Cook, W. D. (1984) Preventing Progressive Collapse of Slabs Structures. Journal of Structural Engineering, 110(7).
- Wieczorek, B. (2013) Influence of the location of the column on the load capacity of a slab-column connection for the inner column after punching, Procedia Engineering, Vol. 57.
- Wieczorek, B. (2013) Idea of a simplified model to determination of the load capacity of and inner slab-column connection after its punching, Procedia Engineering, Vol. 65.
- Wieczorek, B. (2013) Load-bearing capacity of reinforcing bars in the zone of the slab-column connection determined experimentally and in the result of numerical calculations, Procedia Engineering, Vol. 65.
- Wieczorek B. (2014) Experimental tests for the analysis of a load-bearing capacity of an internal slab-column connection after its punching at various positions of the column, Advanced Materials Research „Structural and physical aspects of civil engineering”.
- Wieczorek B. (2014) Load capacity of an internal slab-column connection depending on the geometric parameters of the reinforcement, Advanced Materials Research „Structural and physical aspects of civil engineering”.
- Wieczorek, M. (2013) Influence of amount and arrangement of reinforcement on the mechanism of destruction of the corner part of a slab-column structure, Procedia Engineering, Vol. 57.
- Wieczorek, M. (2013) Investigations concerning the corner part of the reinforced concrete structure in the emergency of removing the corner support, Procedia Engineering, Vol. 65.
- Wieczorek, M. (2013) Concept of shell-beam model of slab-column connection based on analysis of the 3D model, Procedia Engineering, Vol. 65.
- Wieczorek M. (2014) Comparison experimental tests of behavior of the slab-column structure after removal of the corner support with the simplified models describing the mechanism of destruction, Advanced Materials Research „Structural and physical aspects of civil engineering”.
- Wieczorek M. (2014) Narrow reinforced concrete slabs after their flexural destruction, Advanced Materials Research „Structural and physical aspects of civil engineering”.

NUMERICAL ANALYSIS OF THE DEFORMATION OF THE CORNER PART OF SLAB-COLUMN STRUCTURES

M. Wieczorek*

Abstract: *The paper presents the results of a numerical analysis of the corner part of a slab-column structure performed on the scale 1:2. The analysis is based on laboratory tests of a reinforced concrete slab with dimensions of 4000 × 4000 × 100 mm. The aim of the performed calculations was to illustrate the observed phenomena and to provide more detailed information concerning them. The results of calculations have been compared with the results obtained in the course of laboratory investigations.*

Keywords: Reinforced concrete, Progressive collapse, Failure stage, Numerical analyzes.

1. Introduction

One of the types of structural systems applied in the construction of buildings are slab-column structures. The resistance of such structures to exceptional loads is, however, less than that of other structural systems. Therefore, every unusual effect (impacts of vehicles, internal explosions of gas or assassinations) may lead to a progressive catastrophe. This phenomenon is characterized by the appearance of damages which are unproportional to the incident by which it has been caused. Therefore, it is so important to counteract them. From the economical point of view, an optimal solution is to secure protect the structure already while it is being designed, either by increasing its reinforcement or by changing its arrangement. The aim of the present investigations was to construct a numerical model of the corner part of such a slab-column structure. The developed numerical models permitted to determine the values of displacements, the deformation of the reinforcement and the reaction of the supports. These values were then compared with the results of tests in the laboratory.

2. Description of the Tested Model and the Test Stand

The model for these investigations was designed in such a way that it would illustrate in the course of testing the behaviour of the corner part of an actual slab-column structure in the scale 1:2. Taking into account the axial dimensions of the supports - 3000×3000 mm - a flat reinforced concrete slab was used with the dimensions 4000×4000×100 mm (Fig. 1). The reinforcement of the model was determined in compliance with the recommendations given in the standard EC2 (2010), taking into account the loads quoted in EC1 (2010). The statistically calculated values of the bending moments permitted to determine the number and diameter of the reinforcement, which was then constructed in the form of two parallel grids. In accordance with the recommendations suggested in standards (CSA, 2004, EC, 2010, GSA, 2003) and papers (Wieczorek B., 2013, 2014), in the axes of the columns an additional reinforcement was provided in order to prevent a development of damages typical for a progressive collapse. The model, the distribution of reinforcement and the strength parameters of the applied materials have been described in detail in some papers (Wieczorek M., 2013). The test stand consisted of four prefabricated supports with a height of 2400 mm, which were fixed to the slab on the floor of the laboratory. On these supports the dynamometers measuring the reactions of the support were imbedded in a specially prepared clamping. In the place where the loss of support was simulated, instead of prefabricated reinforced concrete a hydraulic cylinder with a large extension was applied.

* Mirosław Wieczorek, Ph.D.: Department of Building Structures, Faculty of Civil Engineering, Silesian University of Technology, Akademicka Street 5; 44-100, Gliwice; Poland, miroslaw.wieczorek@polsl.pl

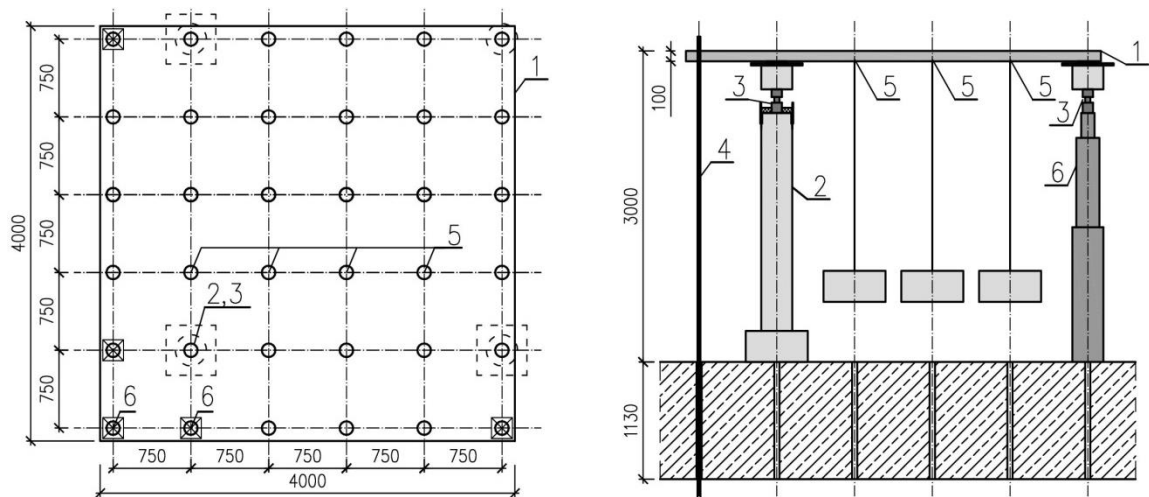


Fig. 1: View of the test stand and the model (Wieczorek M., 2013) (1 – tested model, 2 – prefabricated column, 3 – dynamometers measuring the reactions of the supports, 4 – steel rod used to stabilize the model vertically, 5 – points of the load application (concrete weights), 6 – hydraulic cylinder).

3. Description of the Numerical Model

The phenomenon of destruction of the investigated model presented by M. Wieczorek (2013) is a rather complex problem. In every cross-section the element is affected simultaneously by axial forces, bending moments and shear forces. Moreover, due to the considerable redistribution of the internal forces (large displacements, plastification of the reinforcement, scratching and cracks in the concrete) classic methods of calculations cannot be applied. In the numerical analysis dealt with further on two calculation models have been taken into account, independently of each other. The geometrical parameters and the parameters of strength of the used material were in each of these models the same. Precise data may be found in the paper (Wieczorek M., 2013).

3.1. Description of Model 1

The Model 1 was developed in compliance with the programme ABC-Slab. This programme permits to determine vertical displacements and internal forces in accordance with the assumptions EC2 (both concerning the elastic behaviour of the element and after its scratching). In compliance with the assumptions EC2 the programme assumes in the calculations characteristics of the strength of materials, neglecting in the calculations the effect of axial forces. Calculations of reinforced concrete elements in the elastic state are completed when in anyone of the finite elements the value of the tensile strength of the concrete is exceeded. Next, the rigidity of each finite element is determined by means of the iterative method. The rigidity of scratched elements is determined basing on deformations of the reinforcement.

3.2. Description of Model 2

The Model 2 constitutes the author's own suggestion concerning the modelling of strongly deformed reinforced concrete structures. Similarly as Model 1 this model was constructed applying the software ABC-Slab. In the first stage of the analysis, based on results (Wieczorek M., 2014), the ultimate values of the bending moments were determined basing on calculations of the strength according to EC2. In the second stage the load was gradually increased by 50 kg (0.5 kN). Then at each increase of the load (in each finite element) the obtained values of the bending moments (calculated statically) were compared with the ultimate values of the bending moment resulting from calculations of the strength. If the moment resulting from statical calculations exceeded the value of the ultimate moment, the rigidity of the given finite element was manually changed by reducing its thickness, after which again statical calculations were carried out. When the value of the statical moment was less than or equal to the ultimate value, its value was increased to the next step of loading. In the case of a higher value of the load, the comparison of the values of the moments was repeated and the rigidity of the selected finite elements was reduced.

4. Results of Laboratory Tests and Numerical Calculations

The main aim of laboratory tests was to observe the behaviour of the investigated model and to describe the mechanism of the damage (Wieczorek M., 2014). Besides that, the reaction of the supports and the vertical displacements of the upper surface of the model were automatically measured. Basing on observations it has been found that the most reliable points describing the deformation of the whole model are the points situated at the corner and in the centre of the investigated field. Fig. 2a (taken over from Wieczorek M., 2013) presents diagrams of the vertical displacement of the characteristic points in the load function. As the investigations of the model required 60 days and were divided into several stages of loading and releasing, Fig. 2a displays perturbations, denoted by the numbers 1÷7. In the following stage the values of displacements attained in the course of investigations and numerical calculations have been gathered in Fig. 2b. As the next stage, the values of displacements attained in the tests and numerical calculations have been gathered in Fig. 2b,c. The reaction of the supports was measured at eight points (Fig. 3a) by means of dynamometers (reaction R1, R2 and R3) and electric resistance wire strain gauges which had been glued on the steel rod used to stabilize the model vertically (reactions R4, R5, R6, R7 and R8). The obtained results are shown in Fig. 3b, c.

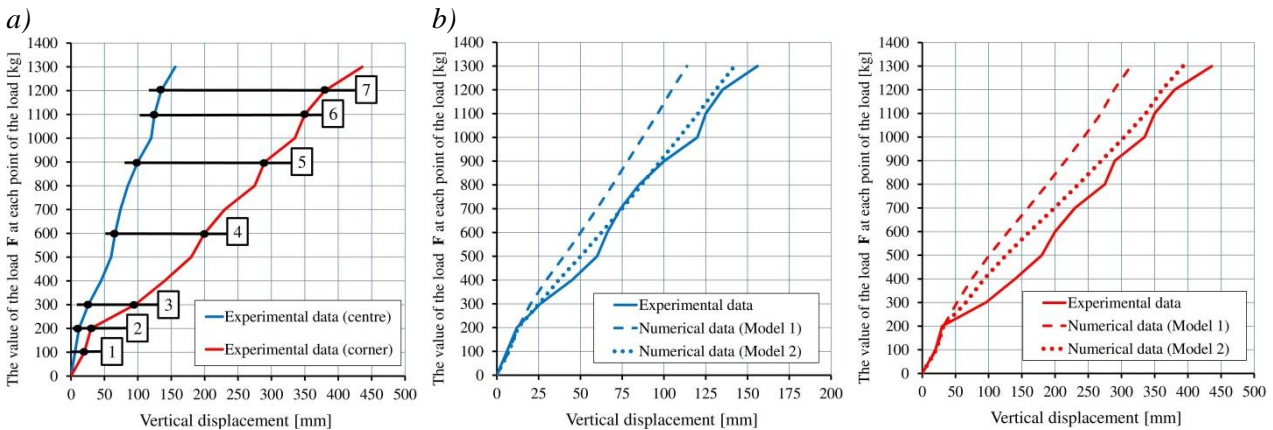


Fig. 2: Results - displacement of the corners and the centre of the slab as a function of the load:
 a) Experimental data (1 ÷ 7 - points of changes in the graph resulting from the disruption of investigation);
 b) Experimental and numerical data of the centre of the slab;
 c) Experimental and numerical data concerning the corner of the slab.

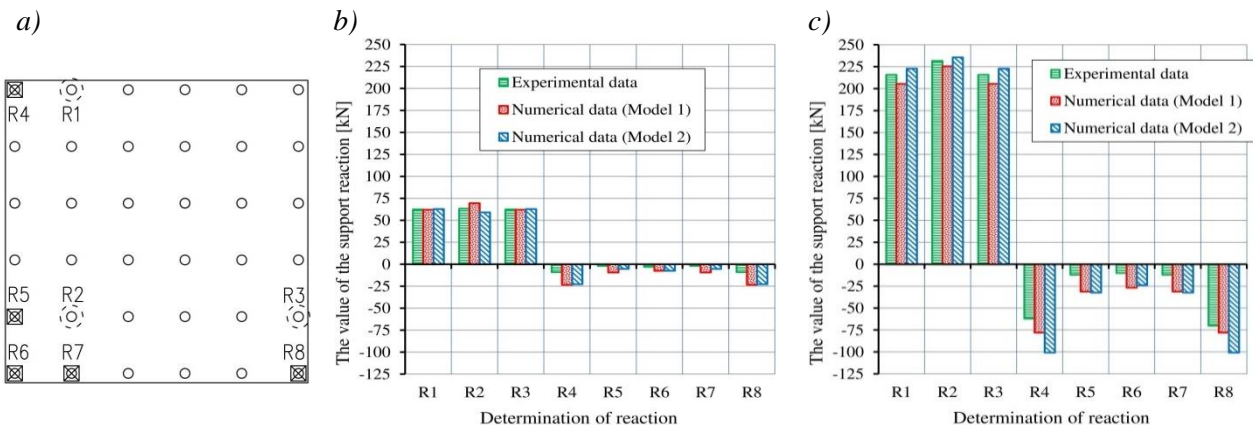


Fig. 3: Results - support reactions: a) Determining support reactions;
 b) Experimental and numerical values of support reactions under load $F = 300$ kg (3 kN);
 c) Experimental and numerical values of support reactions under load $F = 1300$ kg (13 kN).

5. Summary and Conclusions

The aim of the analysis dealt with in this paper was to represent the mechanism of destruction of the corner part of a slab-column structure in its state of a possible break-down, caused by the removal of the support at its corner. This problem is extremely complex due to the material heterogeneity of the model (the joining of steel and concrete), the application of nonlinear material models (the definition of steel as elastic-plastic material and concrete as elastic-brittle material)

and the occurrence of internal forces (axial force, bending moment and shear force) in two directions perpendicular to each other. The application of two approaches in the analysis (two different models) has made it possible to determine approximately the range in which a satisfying approximation to the investigated model could be achieved. The performed analysis leads to the following conclusions:

- The assumptions governing the calculations of procedures determining the rigidity of reinforced concrete elements quote in EC2 permit to attain good results in the elastic range. The non-elastic range revealed considerably differing results, decreasing with the growing value of the load. The obtained results prove that the algorithm of calculations suggested in EC2, based on a regular distribution of the scratches, is correct. In the experimental model the formation of scratches depended mainly on local parameters. Just preceding the destruction regular (symmetrical) scratches turned up. A drawback of the applied model is the impossibility of reading off the values of stresses in the reinforcing bars, which can be calculated basing only on the values of the bending moments.
- The proposed model of calculations (Model 2) has made it possible to get the values of displacements much more approximated to the experimental ones than in the case of Model 1. A particularly adequate mapping of the results was achieved in the first part of the non-elastic range. In the break-down situation the obtained values of displacement were almost the same as in Model 1.
- Each one of all these models permitted to get a very good approximation of the values of the reaction of the supports; these latter ones were measured on the supports. The values of reactions measured on steel bars with a diameter of 28 mm (stabilizing the model) differ considerably from the values resulting from numerical calculations. The reason of these differences is the application of the method of measuring the force in a steel bar. This measurement was accomplished by the electric resistance wire strain gauges glued on to the bar, and then measuring its deformation and determining the force in the bar.

Acknowledgement

These investigations were sponsored by the grant N506 244338 of the Ministry of Science and High-School Education in Poland from the means assigned for education in the years 2010-2012.

References

- CSA Standard A23.3-04 (2004) Design of concrete structures, Canadian Standard Association.
- EN 1991-1-1:2006/AC, Eurocode 1 (2010) Actions on structures - Part 1-1: General actions -Densities, self-weight, imposed loads for buildings.
- EN 1991-1-7:2006/AC, Eurocode 1 (2010) Actions on structures - Part 1-7: General actions – Accidental actions.
- EN 1992-1-1:2004/AC, Eurocode 2 (2010) Design of concrete structures – Part 1-1: General rules and rules for buildings.
- GSA General Services Administration (2003) Progressive collapse analysis and design guidelines for new federal office buildings and major modernization projects. Washington, D.C.
- Wieczorek, B. (2013) Influence of the location of the column on the load capacity of a slab-column connection for the inner column after punching, *Procedia Engineering*, Vol. 57.
- Wieczorek, B. (2013) Idea of a simplified model to determination of the load capacity of and inner slab-column connection after its punching, *Procedia Engineering*, Vol. 65.
- Wieczorek, B. (2013) Load-bearing capacity of reinforcing bars in the zone of the slab-column connection determined experimentally and in the result of numerical calculations, *Procedia Engineering*, Vol. 65.
- Wieczorek B. (2014) Experimental tests for the analysis of a load-bearing capacity of an internal slab-column connection after its punching at various positions of the column, *Advanced Materials Research „Structural and physical aspects of civil engineering”*.
- Wieczorek B. (2014) Load capacity of an internal slab-column connection depending on the geometric parameters of the reinforcement, *Advanced Materials Research „Structural and physical aspects of civil engineering”*.
- Wieczorek, M. (2013) Investigations concerning the corner part of the reinforced concrete structure in the emergency of removing the corner support, *Procedia Engineering*, Vol. 65.
- Wieczorek M. (2014) Comparison experimental tests of behavior of the slab-column structure after removal of the corner support with the simplified models describing the mechanism of destruction, *Advanced Materials Research „Structural and physical aspects of civil engineering”*.
- Wieczorek M. (2014) Narrow reinforced concrete slabs after their flexural destruction, *Advanced Materials Research „Structural and physical aspects of civil engineering”*.

NUMERICAL ANALYSIS OF NARROW SINGLE-SPAN, GRAVITATIONALLY LOADED CONCRETE SLABS REINFORCED BY STEEL WITH A MEAN DUCTILITY

M. Wieczorek*

Abstract: *In the course of the exploitation of building structures frequently situations turn up, when the structure is not adequately used (it may, for instance, be exposed to considerably greater loads than had previously been intended). In the state of an emergency the overload of the structure, essential reserves of their load-bearing capacity may turn up in the case of the self-acting work as a flexible strand. The aim of calculations was to illustrate and obtain more detailed information concerning the phenomena occurring in the course of laboratory tests. The paper presents the results of these calculations, comparing them with those obtained by laboratory tests.*

Keywords: Reinforced concrete, Progressive collapse, Failure stage, Numerical analyzes.

1. Introduction

The models applied in these investigations were designed as a cut band of a monolithic floor reinforced only in one direction. Taking into consideration the distance of the points of supporting equal to 3740 mm, four identical flat reinforced concrete slabs were made with the dimensions 3860×480×100 mm. The models were reinforced by bars with a diameter $\varnothing 8$ mm. The transverse reinforcement consisted of bars with a diameter of $\varnothing 8$ mm and a spacing of 200 mm. After 210 days these models were placed on steel supports (2 in Fig. 1). After the rectification of the models on the supports, the main reinforcement was welded onto the steel tension members (3 in Fig. 1). As the last stage of preparatory operations the steel tension members were anchored in the floor of the laboratory. The test stand and the model, the distribution of reinforcement and the strength parameters of the applied materials have been described comprehensively by Wieczorek M. (2014).

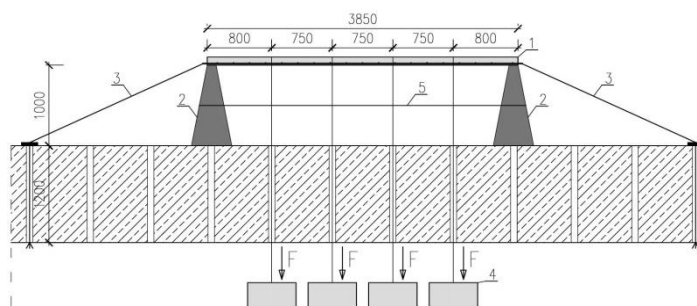


Fig. 1: Test stand (Wieczorek M., 2013): 1 - tested element, 2 - steel support, 3 - steel tension members, 4 - load, 5 - baseline for measuring the displacements.

2. Description of the Numerical Model

The phenomenon of destruction of the investigated model presented in the paper (Wieczorek M., 2013) can, due to its dimensions, be considered as a two-dimensional problem. In the first stage of investigations the tested element there occurs only a bending moment. Due to a horizontal blocking in the cross-section besides the bending moment additional longitudinal tensile forces turn up. The value

* Mirosław Wieczorek, PhD.: Department of Building Structures, Faculty of Civil Engineering, Silesian University of Technology, Akademicka Street 5; 44-100, Gliwice; Poland, miroslaw.wieczorek@polsl.pl

of these forces depends mainly on the mechanical parameters of the applied reinforcing steel (the decisive parameter is the ductility of the reinforcing steel). In the numerical analysis, dealt with further on, for each investigated model two independent models of calculations were developed, viz.:

- Models of the type A. These were developed in compliance with the programme ABC-Slab, which permits to determine the vertical displacements and internal forces according to the assumptions EC2 (2010) (both in the range of elastic behaviour of the element and after its cracking). In compliance with the assumptions of EC2 the programme applied in the calculations the characteristic strength of the materials. Moreover, the programme takes into account in the calculations the effect of axial forces. The calculations concerning reinforced concrete elements are completed when the value of the tensile strength of the concrete in any finite element is exceeded. Then the rigidity of each finite element is determined separately by means of the iterative method. The rigidity of scratched elements is determined basing on the deformation of the reinforcement. An exemplary view of the numerical model is given on Fig. 3.
- Models of the type B. These models were developed in the programme ANSYS (Fig. 4). Similarly as in the investigations (Barbosa, 1997; Mahmood and Ibrahim, 2009; Anthony and Wolanski, 2004; Willam and Tanabe, 2001, Wieczorek B., 2013), two kinds of finite elements were applied, viz. a solid element Solid65 and a rod element Link8. Both of them were assigned with parameters according to (Wieczorek M., 2014). The element Solid65 was used to model the concrete (SAS, 2003). This element has eight nodes with three degrees of freedom at each: node translations in the nodal x, y, and z directions. The element is capable of plastic deformation, cracking in three orthogonal directions, and crushing. The element Link8 was used to model steel reinforcement (SAS, 2003). This element is a 3D spar element and has two nodes with three degrees of freedom at each node: translations in the nodal x, y, and z directions. This element is capable of plastic deformation. During the preparation of the numerical model, the suggestions and the guidelines contained in the scientific works (Wieczorek, B., 2014) were used. Also, the methodology of numerical modeling the reinforcement bars in concrete which takes into account a plastic state of the destruction of the reinforcing steel with high ductility had been applied.

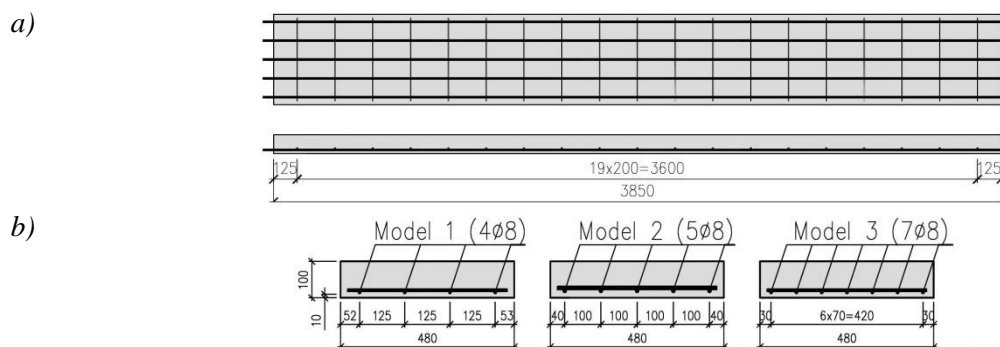


Fig. 2: Model of testing - arrangement of the reinforcement (Wieczorek M., 2013):
a) Horizontal projection and longitudinal cross-section; b) Cross-section of the models.

3. Results of Laboratory Tests and Numerical Calculations

The main aim of laboratory tests was to observe the behaviour of the investigated models after their flexural destruction and to determine the value of the boundary load. After every increase of the load the values of vertical displacements of the upper surface of the tested models were read off and also the value of deformation of the reinforcing bars. The deformations were measured by means of electric resistance wire strain gauges. Fig. 3 and Fig. 4 present examples of views of the constructed numerical models previous to and after their being loaded. For each model, diagrams of vertical displacements of the upper surface in the function of loading were obtained, which were compared with the results of experimental investigations (Fig. 5). The values of the deformation of the reinforcing bars could be directly compared only with the results of numerical calculations concerning models of the type B, accomplished in the programme ANSYS. Also the values of deformations in models of the type A were determined in a simplified way. The deflection of the numerical model was determined at each step of calculations based on the assumptions EC2. In the case of a known curvature of the deflection, the approximate value of the axial force was determined based on a "chain curve". As the next step,

the values of stresses occurring in the reinforcement were calculated, and basing on material tests the corresponding values of deformations were assigned to them. The results of this comparison of the numerical values with experimental ones have been presented in Fig. 6.

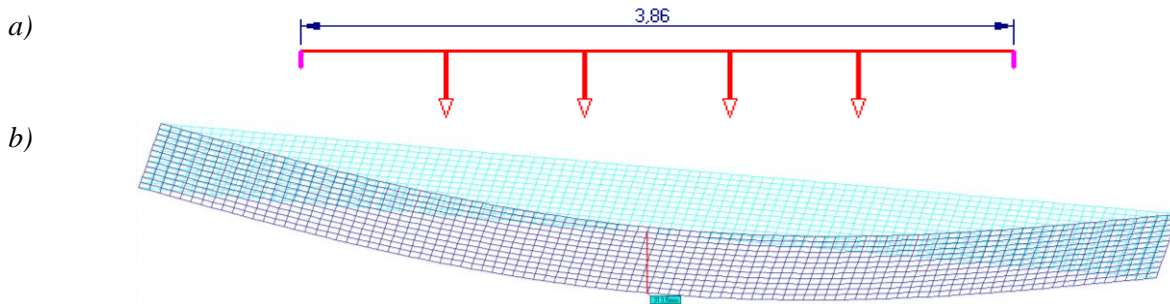


Fig. 3: Example of Model type A: a) Supporting manner; b) View of the model previous to its deformation and after to its deformation.

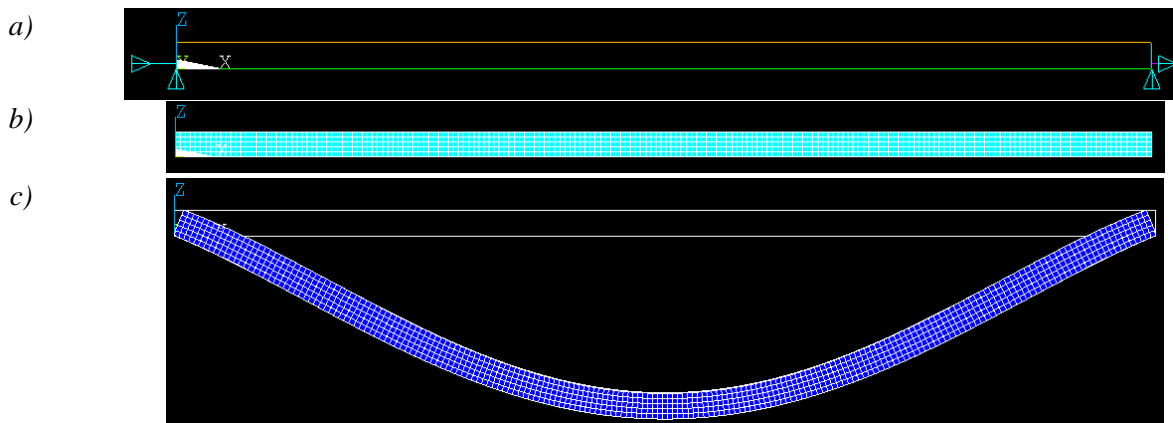


Fig. 4: Example of Model type B: a) Supporting manner; b) View of the model previous to its deformation; c) Deformed model.

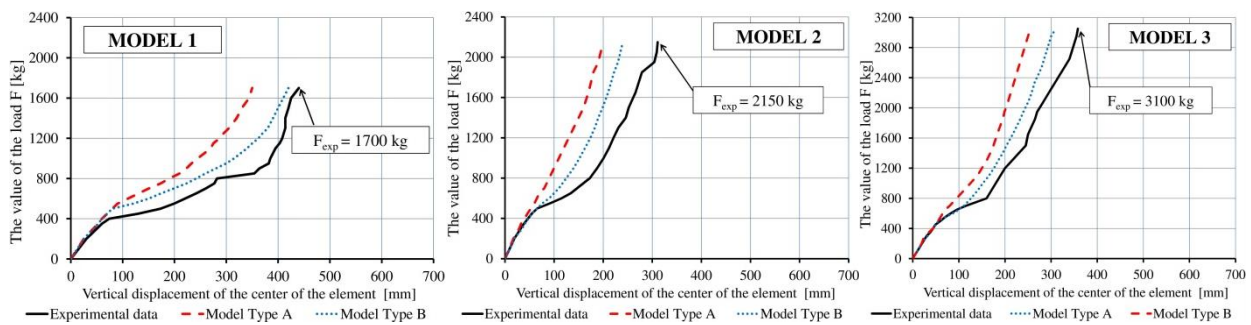


Fig. 5: Results - displacement of the center of the models as a function of the load.

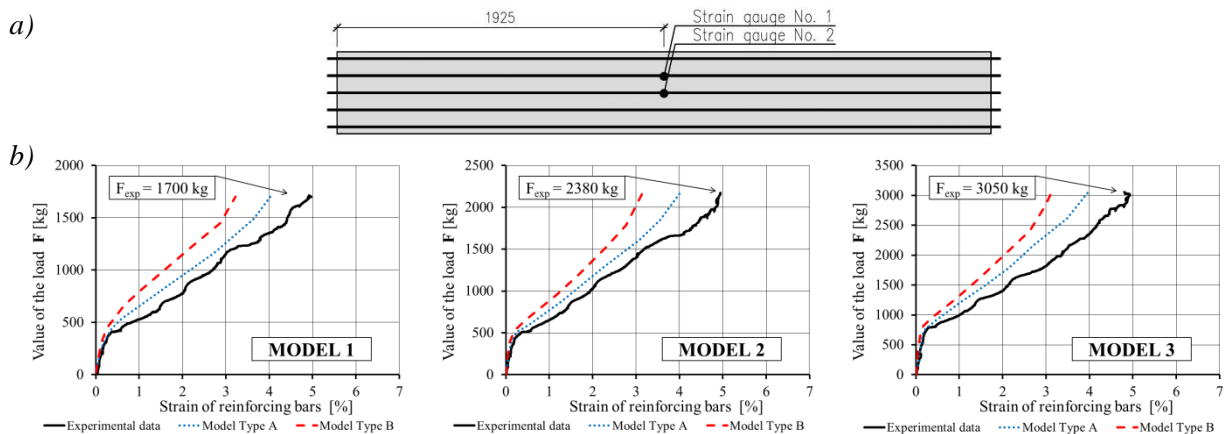


Fig. 6: Results - strain of the reinforcing bars: a) Arrangement of the strain gauges; b) Experimental and numerical data.

4. Summary and Conclusions

The aim of the presented analysis was to attempt a numerical mapping of the behavior of narrow reinforced concrete slabs in the state of a break-down, brought about by overloading the structure. The performed tests, as well as the numerical analysis, confirmed the substance and role of the ductility of steel, permitting in some kinds of structures to make use of the reserve of load-bearing capacity, resulting from the possible self-realization of behaviour of the tension member in the structural element. In the course of performing the numerical analysis it has been found that:

- The applied procedure of determining the deformation of the bars of the reinforcement, consisting in converting the values of the bending moment and axial force into stresses followed by reading off the proper value of deformations in the diagram σ - ϵ . The calculated values obtained were lower deformation by 35.12%, 35.93% and 36.52% (respectively in Model 1, Model 2, Model 3 type A) from the strains obtained during experimental research. In models type B the differences amounted to 18.63%, 18.38% and 19.61%. Such large differences may result from the lack of an adequate level of the redistribution of the internal forces occurring in the experimental models, which had not been mapped fully in the numerical calculations. Thus, the values of the bending moments are considerably larger than those in numerical models of the type A.
- The values of deformations of the reinforcing bars obtained in the case of the models of type B are decidedly closer to the experimental values than those concerning models of the type A. Similarly as in the case of models of the type A, it may be assumed that the internal forces in the experimental models had undergone a considerable redistribution in comparison with numerical models, where such a redistribution did not occur.
- The differences between the values of displacements encountered in the course of laboratory testing and those obtained in numerical calculations may also be due to the applied parameters of the strength of concrete. The mechanical parameters of concrete (shear strength, tensile strength, coefficient of elasticity, Poisson's ratio), obtained basing on standard tests of the materials, may differ from the parameters of the strength of concrete in the models. One of many factors affecting the values of the parameters of the strength of concrete in the samples and the investigated models is the way of curing of fresh concrete.

References

- Anthony, J., Wolanski, B. S. (2004) Flexural behavior of reinforced and prestressed concrete beams using finite element analysis, A Thesis submitted to the Faculty of the Graduate School, Marquette University, in Partial Fulfillment of the Requirements for the Degree of Master of Science Milwaukee, Wisconsin May.
- Barbosa, A. F. (1997) A study of models for nonlinear finite element analysis of concrete structures (Dissertation for attainment of Master Degree), Federal University of Minas Gerais.
- PN-EN 1992-1-1: 2004/AC (2010) Eurocode 2, Design of concrete structures - Part 1-1: General rules and rules for buildings, European Standard.
- Mahmood, M. Sh., Ibrahim, A. M. (2009) Finite element modeling of reinforced concrete beams strengthened with FRP laminates, European Journal of Scientific Research, Vol. 30, No. 4.
- SAS (2003) ANSYS 7.1 Finite Element Analysis System, SAS IP, Inc.
- Wieczorek, B. (2013) Idea of a simplified model to determination of the load capacity of and inner slab-column connection after its punching, Procedia Engineering, Vol. 65.
- Wieczorek, B. (2013) Load-bearing capacity of reinforcing bars in the zone of the slab-column connection determined experimentally and in the result of numerical calculations, Procedia Engineering, Vol. 65.
- Wieczorek B. (2014) Experimental tests for the analysis of a load-bearing capacity of an internal slab-column connection after its punching at various positions of the column, Advanced Materials Research „Structural and physical aspects of civil engineering”.
- Wieczorek B. (2014) Load capacity of an internal slab-column connection depending on the geometric parameters of the reinforcement, Advanced Materials Research „Structural and physical aspects of civil engineering”.
- Wieczorek M. (2014) Narrow reinforced concrete slabs after their flexural destruction, Advanced Materials Research „Structural and physical aspects of civil engineering”.
- Willam, K., Tanabe, T.A., Ed. (2001), Finite element analysis of reinforced concrete structures, American Concrete Institute, Farmington Hills, MI.

ON THE STRAIN-HARDENING PARAMETERS OF S355J2H STEEL CONSIDERING THE INFLUENCE OF TEMPERATURE

J. Winczek^{*}, P. Ziobrowski^{**}

Abstract: Calculation of stresses in the steel elements subjected to the influence of thermo-mechanical loads requires taking into account the influence of temperature on material mechanical properties, including stress-strain curve. In this paper, on the basis of Ludwik, Hollomon, Swift and Voce equations, the modelling of strain-hardening curves of S355J2H steel considering the influence of temperature is discussed. The consideration were made on the basis of experimental results published in the literature as stress-strain curves S355J2H steel for selected temperatures. The values of the parameters in the equations of the individual models were determined, which allowed to analytical description of the material strain-hardening curves.

Keywords: Mechanics, Thermomechanics, Modelling.

1. Introduction

The modelling of thermo-mechanical states of metals and their alloys requires defining stress-strain dependence as the function of temperature. The mathematical modelling of the tensile curves, including strain-hardening curves, has been the subject of research and analysis from the beginning of the last century. With the development of computer methods and simulation tests, the interest in this problem has increased, especially when it comes to modeling of thermo-mechanical states in technological processes of metals and their alloys. Then, different models of material strengthening are used and functions are sought which combine the temperature with stress-strain curve parameters such as yield stress, longitudinal modulus of elasticity or reinforcement modulus.

2. Mathematical Models of Strain-Hardening Curves

Ludwik (1909) began modelling of the stress-strain curve and described it with this function:

$$\sigma = \sigma_0 + K_L \varepsilon^{n_L} \quad (1)$$

where σ represents stress, σ_0 yield stress, ε plastic strain, K_L and n_L are the experimentally determined parameters. In turn, Hollomon (1945) suggested a function:

$$\sigma = K_H \varepsilon^{n_H} \quad (2)$$

Swift (1952) regarding the Hollomon's law introduced the constant into the strain term:

$$\varepsilon = \varepsilon_0 + K_S \sigma^{n_S} \quad \text{or} \quad \sigma = K'_S (\varepsilon + \varepsilon_0)^{n'_S} \quad (3)$$

where ε_0 , K_S , K'_S , n_S i n'_S are the parameters.

During the tests of AISI 304 austenitic steel Ludwik's equation for plastic strains smaller then 0.1 showed differences in the experimentally obtained stress-strain curve, Ludwigson (1971) proposed a modified form of the Ludwik's equation:

* Prof. Jerzy Winczek, PhD.: Institute of Mechanics and Machine Design Foundations, Czestochowa University of Technology, Dabrowski str. 73 r.52; 42-201 Czestochowa; Poland, winczek@imipkm.pcz.czyst.pl

** Ing. Pawel Ziobrowski: Institute of Mechanics and Machine Design Foundations, Czestochowa University of Technology, Dabrowski str. 73 r.52; 42-201 Czestochowa; Poland, pawel_ziobrowski@o2.pl

$$\sigma = K_{1L}\varepsilon^{n_{1L}} + K_{2L}\exp(n_{2L}\varepsilon) \quad (4)$$

In modelling the strain-hardening curve at elevated temperatures based on the relationship between stress and strain defined by Voce (1948), the following function is used (Sivaprasad et al.,1997):

$$\sigma = \sigma_1 + (\sigma_s - \sigma_1) \left[1 - \exp\left(-\frac{\varepsilon - \varepsilon_1}{\varepsilon_c}\right) \right] \quad (5)$$

where ε is a plastic strain, σ_1 and ε_1 represent first measurement of the stress and the strain respectively, σ_s saturation stress, ε_c strain constant. If $\varepsilon_1 = 0$ (limit of applicability of Hook's law or yield point), then:

$$\sigma = \sigma_s - K_V \exp(n_V \varepsilon) \quad (6)$$

where $n_V = -1 / \varepsilon_c$.

Tab. 1: The values of the parameters in the Hollomon, Ludwik, Swift and Voce equations.

T [K]	Hollomon		Ludwik		Swift			Voce	
	K_H [MPa]	n_H	K_L [MPa]	n_L	K'_s [MPa]	n'_s	ε_0	K_V [MPa]	n_V
373	595.623	0.025	1091.586	0.686	629.030	0.038	0.000552	67.010	-320.757
473	598.873	0.033	1364.178	0.676	640.770	0.050	0.000470	86.900	-324.231
573	640.525	0.055	2200.745	0.684	711.770	0.081	0.000405	133.550	-330.040
673	588.637	0.061	2223.998	0.689	661.720	0.090	0.000393	131.660	-331.900
773	520.860	0.097	2588.759	0.699	604.110	0.133	0.000281	147.410	-332.185
873	289.489	0.127	1413.884	0.676	326.120	0.156	0.000156	89.690	-329.945
973	144.013	0.125	559.759	0.612	156.100	0.145	0.000091	45.900	-337.570
1023	93.107	0.111	411.527	0.661	103.820	0.138	0.000169	28.020	-325.894
1073	50.166	0.112	208.059	0.653	54.542	0.134	0.000150	15.130	-311.631
1123	62.539	0.186	149.298	0.485	56.673	0.162	0.000007	21.380	-325.011
1173	29.028	0.147	105.904	0.612	29.477	0.151	0.000066	9.300	-310.,561

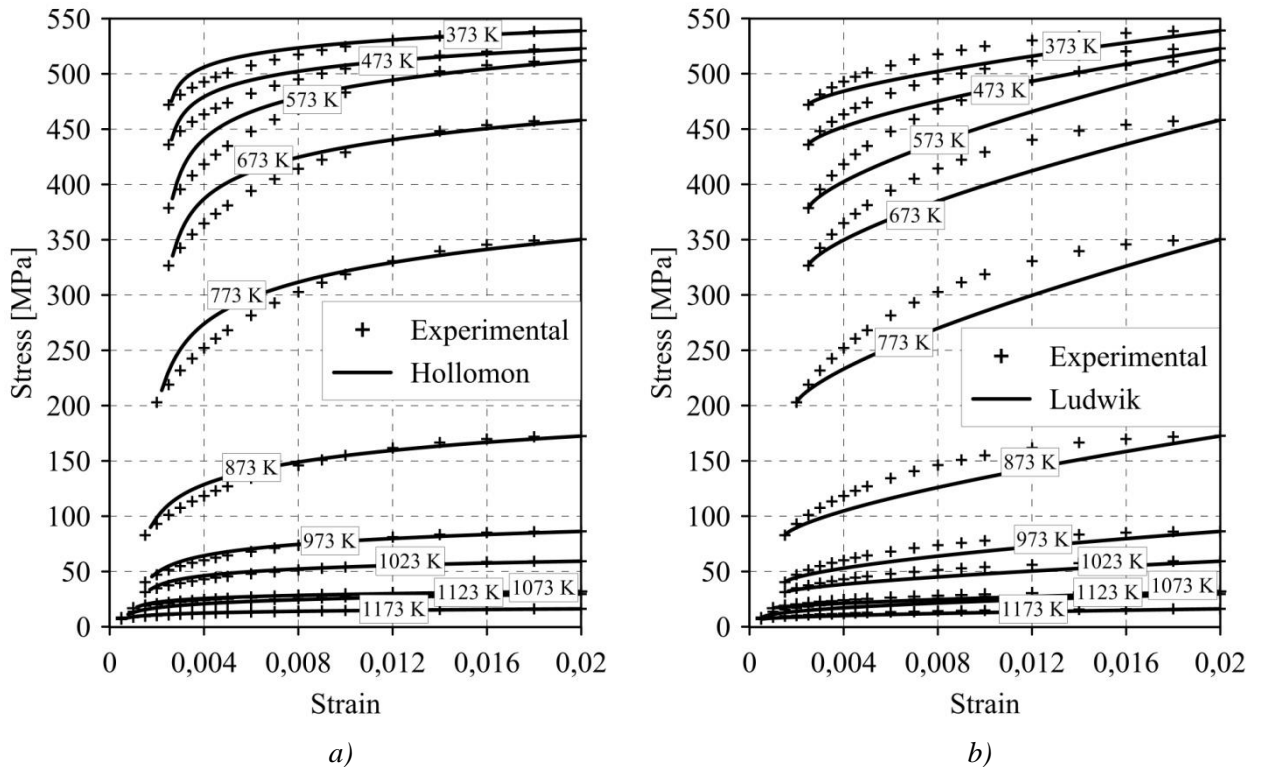


Fig. 1: Strain-hardening curves of structural steel S355J2H at temperatures 373 – 1173 K modelled by the equations: a) Hollomon; b) Ludwik.

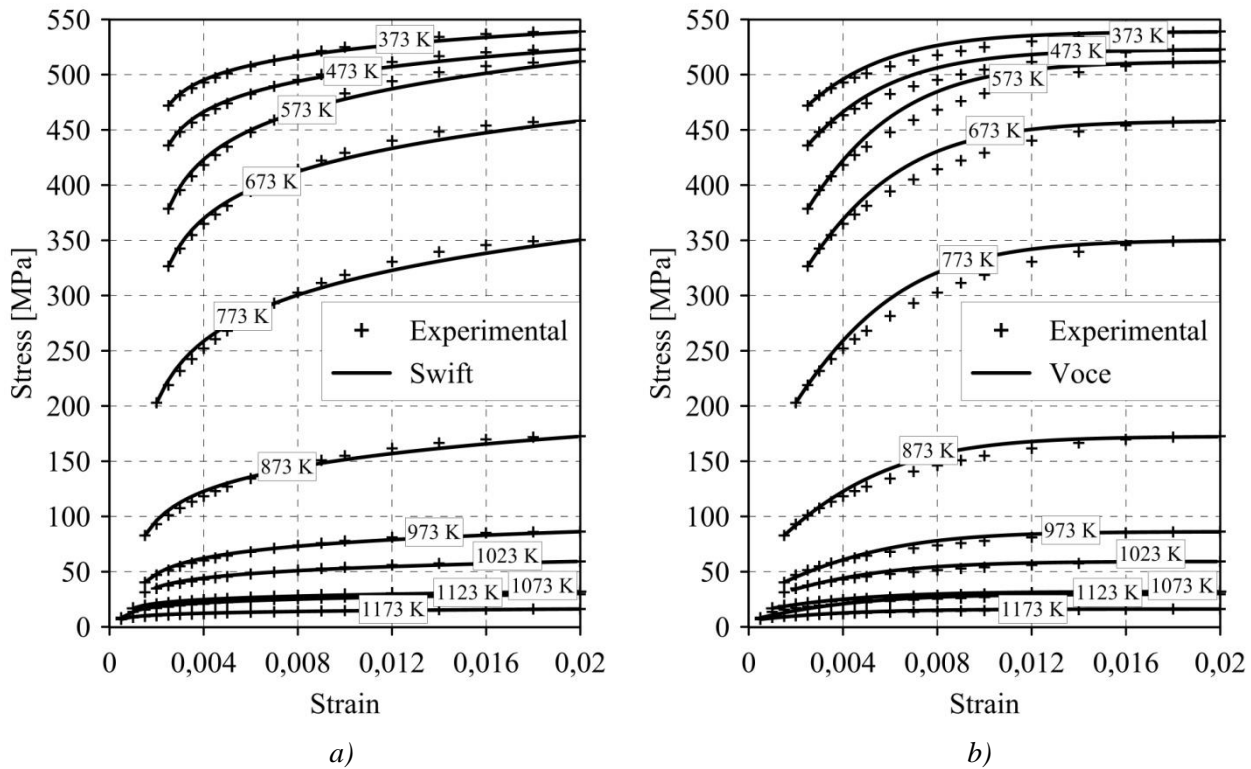


Fig. 2: Strain-hardening curves of structural steel S3 55J2H at temperatures 373 – 1173 K modelled by the equations: a) Swift; d) Voce.

This paper presents an analysis of models of strain-hardening curves of the material as a function of temperature for the steel S355J2H based on the results of experimental studies contained in the research report Outinen et al. (2001). The parameters of the Hollomon's, Ludwik's, Swift's and Voce's equations for different temperatures were determined (Tab. 1, Figs. 1 and 2). Then the functions of these parameters depending on the temperature were determined, which for Swift's and Hollomon's present equations (7) – (11) and Figs. 3 and 4. The comparison of the stress-strain curves described by Swift and Hollomon laws for the temperature 775K with the experimental results and the curves obtained by interpolation from 875K and 675K in Fig. 5 is presented.

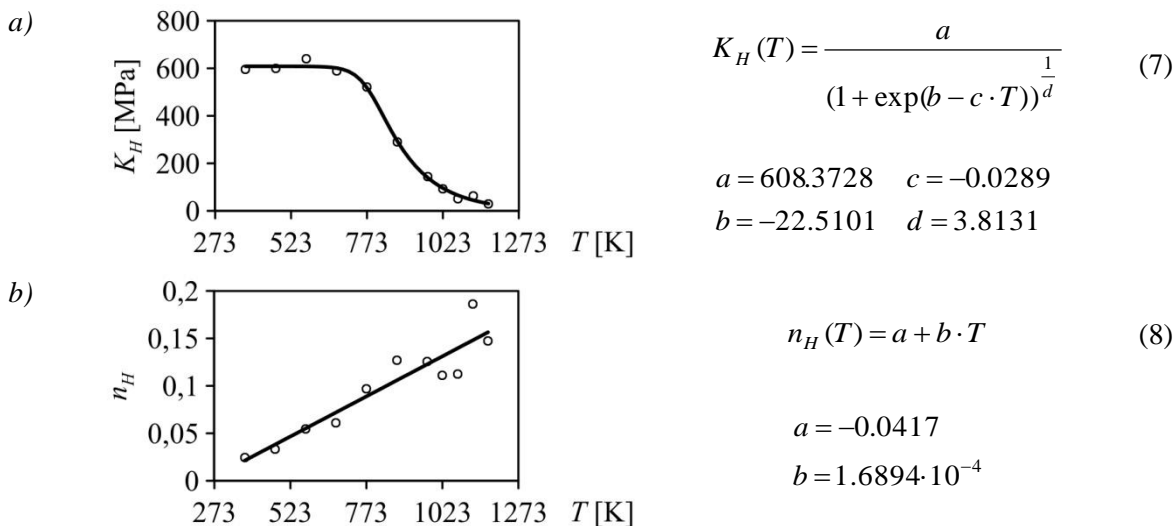


Fig. 3: Parameters in the Hollomon equation as a function of temperature and suggested models.

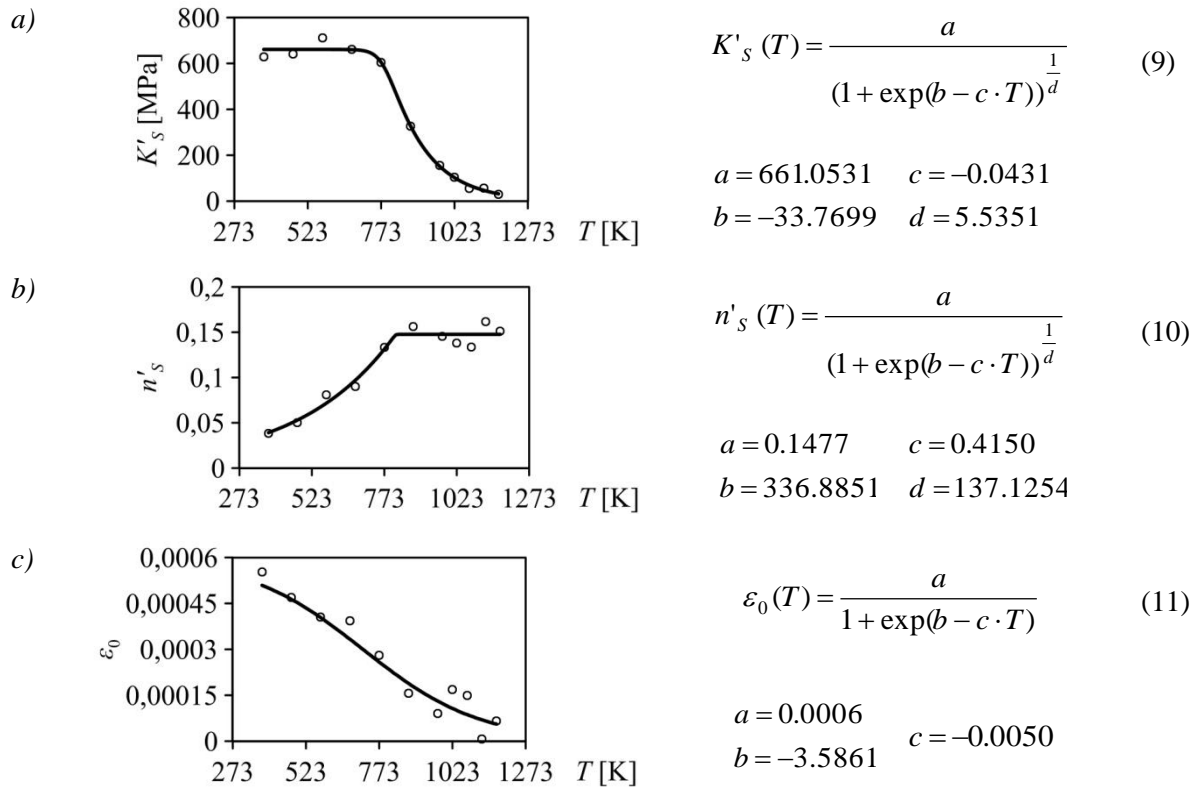


Fig. 4: Parameters in the Swift equation as a function of temperature and suggested models.

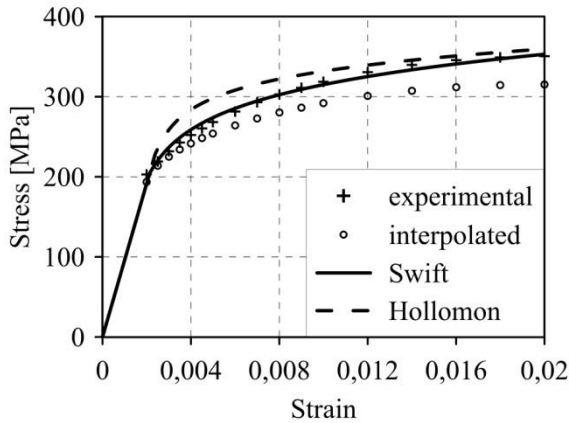


Fig. 5: The comparison of the stress-strain curves described by Swift and Hollomon laws for the temperature 775K with the experimental results and the curves obtained by interpolation.

3. Conclusions

The closest approximation of modelled stress-strain curves to the experimental results was achieved through using the Swift's law, then the Hollomon's and the Voce's law. Application of the Ludwik's law gives the greatest divergence from the experimental stress-strain curves.

The determined values of parameters for individual equations (laws) as a temperature function allow to define a stress-strain curve for any temperature and represent an alternative solution to the interpolation method.

References

- Hollomon, J. H. (1945) Tensile deformation, Trans. Metall. Soc. AIME, 162, pp. 268-290.
- Ludwigson, D. C. (1971) Modified stress-strain relation for FCC metals and alloys, Metall. Trans. 2, pp. 2825-2828.
- Ludwik, P. (1909) Elemente der Technologischen mechanik, Verlag von Julius Springer, Berlin.
- Outinen, J., Kaitila, O., Mäkeläinen, P. (2001) High-temperature testing of structural steel and modelling structure at fire temperatures. Research report. Helsinki University of Technology, Laboratory of Steel Structures, Publications 23, Espoo.
- Sivaprasad, P. V., Venugopal, S., Venkadesan, S. (1997) Tensile flow and work-hardening behavior of a Ti-Modified austenitic stainless steel, Metallurgical and Materials Transactions 28A, pp. 171-178.
- Swift, H. W. (1952) Plastic instability under plane stress, Journal of the Mechanics and Physics of Solids 1, pp. 1-18.
- Voce E. (1948) The relationship between stress and strain for homogeneous deformation, Journal of the Institute of Metals, pp. 537-562.

ZIRCONIUM DIOXIDE – STATIC TEST ON GLUED CONNECTIONS

M. Wirwicki*, T. Topoliński**

Abstract: *The popularity of zirconium dioxide has increased among dentists and dental technicians in the recent years. Due to its chemical content and mechanical properties, it may successfully replace non-aesthetic substructures or metal crowns. The article presents the geometry with the dimension of zirconium dioxide bars. Two of the most popular glues on the dental care market are presented, as well as a diagram of the tested joint. The results acquired are quite scattered, which may have resulted from, among other things, the amount of flash, the method of surface preparation or the thickness of the glue joint. Photographs of samples with small and large amounts of flash were presented and compared with the resistance of the glued joints.*

Keywords: Zirconium dioxide, Static stretching tests, Glue, Dentistry.

1. Introduction

Zirconium dioxide is a ceramic material which has been gaining the attention of dentists since the 90th. This is thanks to the fact that its processing is very simple with the use of CAD/CAM systems and 3D scanners which allow to create a digital reproduction of the patient's cavities. The method involves processing in soft, pre-sintered material, and then full sintering – curing the material in 1400°C for 8 hours. The crown is then covered with artificial glaze – a ceramic material that imitates the colour of the patient's teeth. There are 3 types of dental crowns: ones with metal, galvanic-ceramic or fully ceramic substructure. In order to place a dental crown in a patient's mouth, a dentist must first prepare the natural tooth - grind the crown. After processing the tooth, the zirconium crown is glued to the tooth. There are two types of dental glues - cements: adhesive and self-adhesive. Their difference is in the gluing and preparation procedures: in the adhesive type, all ingredients of the glue have to be applied separately, which gives the dentist higher control over the glue joint. In the self-adhesive type, two ingredients are mixed using a special pad, and then, after mixing, the dentist can proceed to the gluing stage.

The purpose of this work is to analyse static stretching test results of the glue joint between zirconium and stainless steel, for the proposed geometry of samples, in a comparison to the two most frequently used glues on the market.

2. Material and Method

3M's Cyrkon Lava material, intended for the creation of crowns and bridges in CAD/CAM technology, was used for the test. The material supplied by the manufacturer was cut with a Buehler ISOMET 5000 [POLAND] saw into smaller blocks of 25 mm x 16 mm x 1.87 mm. The elements were then laser cut using an Alfalas WS [POLAND] device, with laser settings preventing the overheating of zirconium. Such cutting provided 8 1.87 mm x 1.87 mm x 10 mm samples. The samples were then sent to a laboratory certified by the manufacturer, where sintering took place. The process involved 8-hour treatment in a special furnace in 1400°C. During that time, technological shrinkage of the whole crown took place, amounting to about 20% of its volume. After the treatment, the material was show-white and exhibited a significant improvement in terms of mechanical properties. Fig. 1 below presents the

* M.Sc. Eng. Mateusz Wirwicki: Institute of Mechanics and Machine Design, University of Technology and Life Sciences, Ks. Kordeckiego 20; 85-225, Bydgoszcz; Poland, wirwicki@utp.edu.pl

** Prof. Tomasz Topoliński: Institute of Mechanics and Machinery Construction, University of Technology and Life Sciences, Ks. Kordeckiego 20; 85-225, Bydgoszcz; Poland, topol@utp.edu.pl

geometry of the tested samples after sintering. The dimensions of the samples after treatment were 1.5 mm x 1.5 mm x 8 mm.

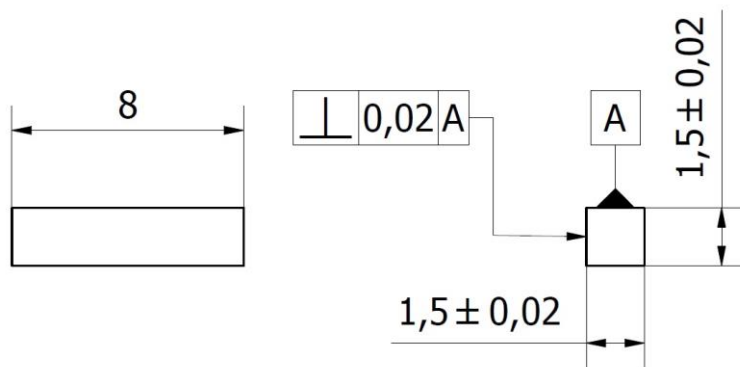


Fig. 1: Geometry with the dimensions of the zirconium dioxide bars.

3. Static Test for Resistance to Extension

The tested material was 3M ESPE's Cyrkon Lava, which is used in dental clinics to make single crowns, 3 and 4-point bridges or implant joints. This type of zirconium oxide features high resistance as well as perfect and natural look. The material is transparent and biocompatible. Its structure is metal-free. In recent years, dental ceramic materials have developed significantly in terms of mechanical properties. Glued joints play an important role in the treatment of a patient's mouth. Therefore, the selection of an appropriate glue for a given clinical case is of utmost importance. There are many types of cements on the dental care market, however their product description is usually insufficient. In order to select a correct adhesive it is thus particularly vital to learn the mechanical properties of the given joint.

The static stretching test was conducted using an Instron 8874 instrument with a tension meter with the range of ± 5 kN. The speed of relocation of the upper arm (machine actuator) was 0.5 mm/min. The 30 test samples were made in the form of cuboid 1.5 mm x 1.5 mm x 8 mm bars, as described earlier, and were glued to stainless steel with the 3M ESPE RelyX U200 Automix glue and the Kerr Maxcem Elite glue. The glues were selected with the aid of dentists and are the most popular products of this type used by dental clinics.

Fig. 2 below presents the diagram of gluing samples, with the joint area marked.

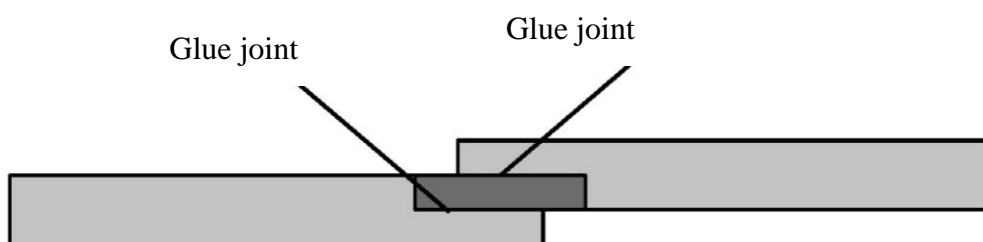


Fig. 2: Test sample diagram.

For the aforementioned glues, the gluing process (curing of the glue between two surfaces) requires a UV lamp. The joint was cured with a Satelec Mini Led Black UV lamp with the following parameters: power – 1250 mW/cm², wavelength 420 – 480 nm, exposure time 10 sec.

4. Results and Summary

The purpose of the study was to conduct a static resistance test of the glue joint. The samples were divided into two groups, 15 pcs for each of the two glue types: 3M ESPE RelyX U200 Automix and Kerr Maxcem Elite. Before the test, each of the samples was checked with a stereoscopic microscope in order to determine whether the joint was satisfactory. Test results for the 3M ESPE RelyX U 200 Automix

cement are presented in Tab. 1, and for Kerr Maxcem Elite - in Tab. 2. Average force values are 63.5 N for RelyX and 65.8 N for Maxcem, average tension values were approx. 7 MPa for both materials. The high scatter of the results (16% and 14%) may have resulted from various factors influencing the resistance of the glued joints.

Tab. 1: Test results for joint glued with 3M ESPE RelyX U200.

Average force value	Average tension value	Standard deviation	Relative standard deviation
63.5 N	7 MPa	10	16%

Tab. 2: Test results for joint glued with Kerr Maxcem Elite.

Average force value	Average tension value	Standard deviation	Relative standard deviation
65.8	7 MPa	7	14%

One of the main components of the glued joint resistance is the size of flash. The effect is related to the amount of glue outflow to the edges of the joint, which increases the joint surface. Another factor is the method of surface preparation. The glued surfaces must be clean, degreased and oxide-free. Fig. 3a presents images of tested samples with small flash, for which stretching resistance was decreased; Fig. 3b with large flash, where the resistance was much higher.

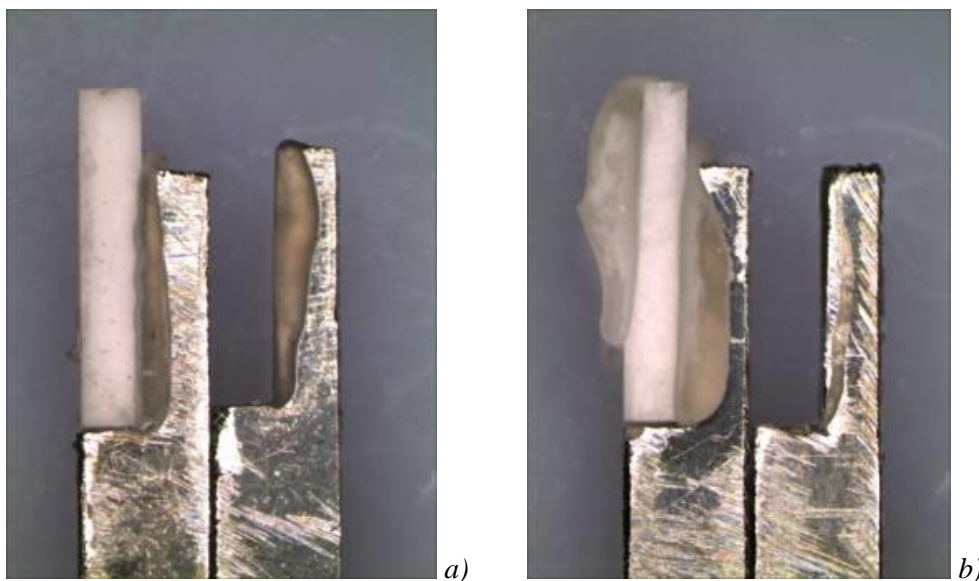


Fig. 3: Photographs of the tested samples a) with small flash and b) with large flash.

The analysis conducted did not fully determine the final resistance of glue joints. It is important to select suitable glue thickness for the given joint, and the gluing process should be performed in appropriate conditions. The large number of parameters related to quality and resistance means that for a joint with specific geometric and material features a suitable joining technique must be applied. In future studies, the authors intend to perform static tests for glued joints with flash removed.

References

Ashcroft, I. A., Abdel Wahab, M. M., Crocombe, A. D., Hughes, D. J., Shaw, S. J. (2001) The effect of environment on the fatigue of bonded composite joints. Part 1: testing and fractography. Composites: Part A, 34, pp. 45-58.

- Ashcroft, I. A., Abdel Wahab, M. M., Crocombe, A. D., Hughes, D. J., Shaw, S. J. (2001) The effect of environment on the fatigue of bonded composite joints. Part 2: fatigue threshold prediction. *Composites: Part A*, 34, pp. 59-69.
- Domińczuk, J. (2011) Influence of selected factors on the structural and technological strength bonding. *Postępy Nauki i Techniki*, 10, pp. 14-26 (in Polish).
- Hagge, M., Lindemuth, J. (2001) Shear bond strength of an autopolymerizing core buildup composite bonded to dentin with 9 dentin adhesive systems. *The journal of prosthetic dentistry*, 86, 6, pp. 620-623.
- Khoramishad, H., Crocombe, A. D., Katnam, K. B., Ashcroft, I. A. (2010) Predicting fatigue damage in adhesively bonded joints using a cohesive zone model. *International Journal of Fatigue*, 32, pp. 1146-1158.
- Melogranaa, J. D., Grenestedt, J. L., Maroun, W. J. (2002) Adhesive tongue and groove joints between thin carbon fiber laminates and steel. *Composites: Part A*, 34, pp. 119-124.
- Minori, H., Akkikazu, S., Daiichiro, Y., Harunori, G., Pekka, K. V., Akiyoshi, S. (2010) The effect of surface treatment on bond strength of layering porcelain and hybrid composite bonded to zirconium dioxide ceramics. *The journal of prosthodontic reaserch*, 55, pp. 146-153.
- Pashley, D., Sano, H., Ciucchi, B., Yoshiyama, M., Carvalho, R. (1995) Adhesion testing of dentin bonding agents: A review. *Dental Materials*, 11, pp. 117-125.
- Rudawska, A., Dębski, H. (2010) Modeling the process of destruction of the adhesive bond in a single lap adhesive joint aluminum sheets. *Mechanik*, 2/2010, pp. 118-121 (in Polish).
- Wirwicki, M., Topoliński, T. (2011) Methodology of fatigue tests for glued dental samples, *Journal of Polish CIMAC*, Vol. 6 No. 3: 355-364.
- Wirwicki, M., Topoliński, T. (2014) Determining the S-N fatigue curve for lava zirconium dioxide, *Advanced Materials Research*, Vol. 845: 153-157.

A NUMERICAL ANALYSIS OF THE FLOW THROUGH THE ELBOW IN THE BOILER PULVERIZED COAL SYSTEM

J. Wydrych^{*}, G. Borsuk^{*}, B. Dobrowolski^{*}

Abstract: *Use of large power boilers requires appropriate distribution of the air - coal particle mixture to particular burners. The tests of gas and coal distribution show the problem of their non-uniformity under different working conditions of the system. In the paper multi-phase flow models were presented in the installation with elbow. In the work three methods: Euler-Euler, Euler-Lagrange and E-L with modification were compared with results of experiment. This work shows that the Euler-Euler model seems to be more useful for the considered flows.*

Keywords: CFD, Pneumatic conveying systems.

1. Introduction

In the pneumatic conveying systems in power boilers, the solid particle separation in some areas is a significant problem. Diversification of concentration and uncontrolled segregation of particles of such systems take place in many cases. As a consequence, diversification of propagation, disturbances of the combustion process and accelerated erosion of the installation elements may occur (Dobrowolski et al., 2007, El-Behery et al., 2009, Miller et al., 2009). Moreover in the large power boilers, the required distribution of the air-coal mixture to particular burners must be obtained. This problem is very significant because of limitation of incomplete combustion losses, furnace elements durability and NO_x emission. This paper presents numerical calculations of the air-coal dust mixture flow through the pipeline with the built-in elbow. The results of calculations for gas and particle separation show the problem of non-uniformity of their distribution. It follows that particle distributions to particular outlets are non-uniform and vary under different working conditions of the installation (Rajniak et al., 2008, Spedding et al., 2007, Woods et al., 2008). The calculations were performed in order to qualitative and quantitative comparison of the results for two methods of simulation: the Euler-Lagrange and the Euler-Euler. The Euler-Lagrange model is usually applied for tests of the multiphase gas-solid particle mixture flow. It provides good quality of the results for volume fractions of solid particles not exceeding 12%. From the analyzes of elements as elbows, distributors or cyclone separators it appears that in some of theirs area the limit value 12% is exceeded (Jaworski et al., 2002). This work shows that the Euler-Euler model seems to be more useful for the considered flows (Wydrych, 2010).

2. Methods

Presence of the particles in the gas stream influences the gas motion, and this influence depends on the particle diameters and concentration. In the simplest case, the mixture motion can be described by introduction of the substitute density to the equations of motion. In simulation of motion of the gas-particles mixture, two approaches are applied (Fokeer et al., 2004):

- particles are treated as the material points displacing in the space, and their interactions with gas and the walls are taken into account (the Lagrange method) (Lain et al., 2012),
- the particle phase is replaced by the fictitious fluid with suitably defined physical properties (the Euler method).

^{*} Jacek Wydrych, PhD., Grzegorz Borsuk, PhD., Bolesław Dobrowolski, PhD./DSc: Department of Thermal Engineering and Industrial Facilities, Opole University of Technology, Opole, Poland, j.wydrych@po.opole.pl, g.borsuk@po.opole.pl, b.dobrowolski@po.opole.pl

Neglecting the phase changes and assuming that both phases are incompressible, and the flow is isothermal and stationary, the gas motion can be described in the uniform, generalized conservative form (Dobrowolski et al., 2007), containing convection, diffusion and source components. In a consequence we obtain:

$$\frac{\partial(\rho\phi)}{\partial t} + \frac{\partial(\rho U_i \phi)}{\partial x_i} = \frac{\partial}{\partial x_i} \left(\Gamma_\phi \frac{\partial \phi}{\partial x_i} \right) + S_\phi + S_{\phi p} \quad (1)$$

where ϕ is a generalized dependent variable, Γ_ϕ is the coefficient of diffusion transport, and the source term S_ϕ contains all the remaining components of the differential.

In order to calculate turbulence k- ϵ model was used with assumption that the flow was fully turbulent, and the effects of molecular viscosity were negligible (Kuan et al., 2007). The turbulence kinetic energy, k, and its rate of dissipation ϵ , are obtained from the following transport equations:

$$\frac{\partial}{\partial t}(\rho k) + \frac{\partial}{\partial x_i}(\rho k u_i) = \frac{\partial}{\partial x_j} \left[\left(\mu + \frac{\mu_t}{\sigma_k} \right) \frac{\partial k}{\partial x_j} \right] + G_k + G_b - \rho \epsilon - Y_M + S_k \quad (2)$$

$$\frac{\partial}{\partial t}(\rho \epsilon) + \frac{\partial}{\partial x_i}(\rho \epsilon u_i) = \frac{\partial}{\partial x_j} \left[\left(\mu + \frac{\mu_t}{\sigma_\epsilon} \right) \frac{\partial \epsilon}{\partial x_j} \right] + C_{1\epsilon} \frac{\epsilon}{k} (G_k + C_{3\epsilon} G_b) - C_{2\epsilon} \rho \frac{\epsilon^2}{k} + S_\epsilon \quad (3)$$

The particle trajectory is calculated according to its motion equation. If the phase density difference is very large, the equation of particle motion can be written as (Lain et al., 2012):

$$m_p \frac{du_p}{dt} = \frac{3}{4} C_D \frac{\rho m_p}{\rho_p d_k} u |u - u_p| (u - u_p) + g \quad (4)$$

where m_p is mass of the particle and C_D is the aerodynamic drag coefficient.

In the case of simulation of multiphase gas-solid flows, while processes similar to fluidization, the heterogeneous Euler-Euler model (the Euler model) is applied. In the case of the Euler model, the equations of mass and momentum conservation are similar to the equations for the one phase model (Doods et al. 2011). If there is no mass exchange between the considered phases, the equation of motion and continuity for phase “k” have a form:

$$\frac{\partial(\alpha_k \rho_k u_k)}{\partial t} + \nabla \cdot (\alpha_k \rho_k u_k u_k) = -\alpha_k \nabla p + \nabla \cdot (\alpha_k T_k) + \alpha_k \rho_k g + \alpha_k \rho_k (F_k + F_s) \quad (5)$$

$$\frac{\partial(\alpha_k \rho_k)}{\partial t} + \nabla \cdot (\alpha_k \rho_k u_k) = 0 \quad (6)$$

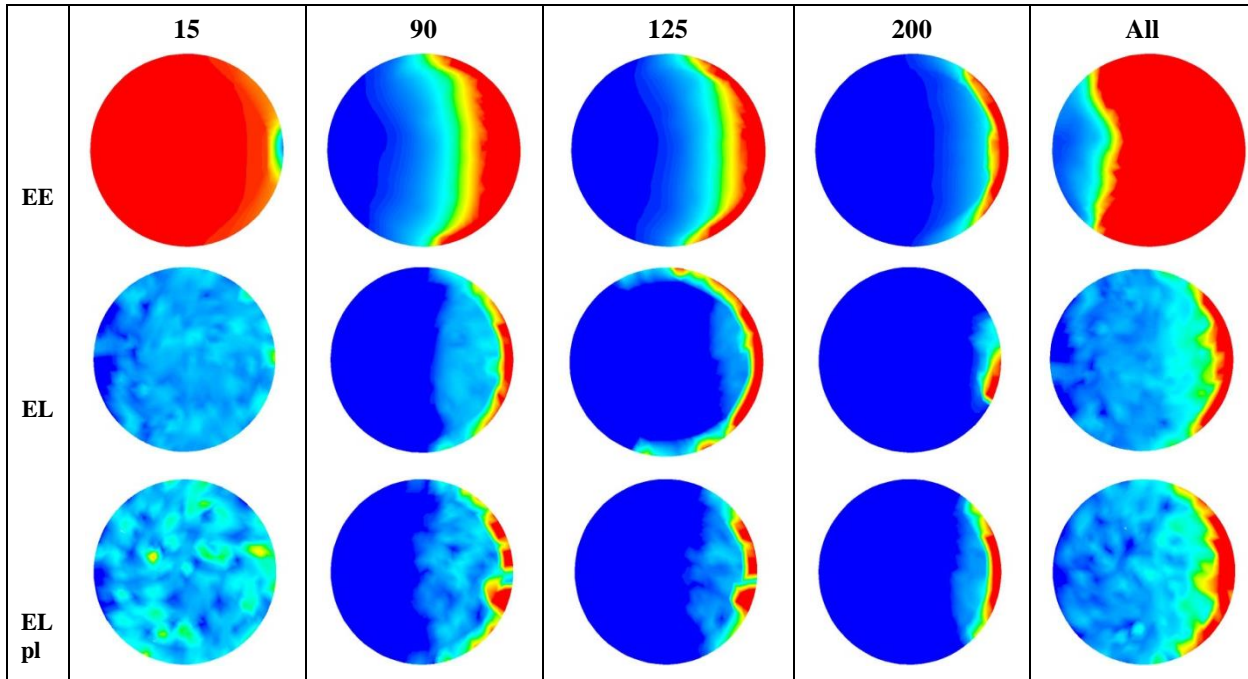
The FLUENT program was applied for numerical calculations. It allows to solve the systems of equations of mass, gas momentum and the solid phase transport completed with the turbulence model equations. Calculations were made according to the Euler-Lagrange method (the **EL** method) and the Euler-Euler method (the **EE** method). Moreover calculations were made also with use Euler-Lagrange method completed by particle turbulence effect and particle shape effect (the **ELpl** method).

3. Results and Discussion

In order to make calculations, the continuous flow systems with elbow were replaced by the calculation areas including non-structural calculation meshes. Disintegrated coal particles for diameters d_k : 15, 90, 125, 200 μm were tested. The inlet velocity was at level 30 m/s and diameter of the pipe was 1,2 m. In the case of the Euler-Lagrange model, when convergence of the velocity field solution is obtained and presence of solid particles and coupling between the phases are taken to calculations, trajectories of motion of the coal dust particles of density 1300 kg/m^3 was calculated. From analysis of the trajectories it appears that the particles with small diameters move along the paths corresponding to streamlines of the gaseous phase. The particles with larger diameters move along to the paths often forming a “cord”. This is a reason of local increase of concentration (Borsuk et al., 2006, Fokeer et al., 2004, Wydrych, 2010). This effect can cause increase of non-uniformity of the solid phase concentration right after the elbow. The centrifugal force causes that bigger solid particle fractions are rejected to the external surfaces of the arcs, and next they move as “the cords” of particles. This effect is undesirable because particles segregation

causes excessive wear of surfaces of the installation elements in some areas. From comparison of the results obtained with different methods it appears that the EL and ELpl models show greater particle concentration at the lesser area than the EE model. This difference is a result of including collisions between the particles of all the phases into the EE model. In the EL and ELpl models it is neglected.

Tab. 1: Distributions of concentration for particles 15, 90, 125, 200 μm in diameters and for all types of particle obtained with the EE, EL and ELpl methods.



The calculations performed with the Euler-Lagrange (EL, ELpl) and Euler-Euler (EE) methods allowed to determine distributions of the disintegrated phase in the outlet section after the tested elbow. In both methods, the uniform distribution of velocity was assumed at the inlet section. In the EE method, an uniform distribution of particle volume fraction at the level 0.9654 % was assumed at the inlet section. Tab. 1 contains distributions of dust particles 15, 90, 125 and 200 μm in diameters at the outlet after the elbow obtained with the EE, EL and ELpl methods. Maximum results in the table was truncated to 0.3% for EE method and to 1 $\text{g}/(\text{cm}^2 \cdot \text{s})$ for EL and ELpl methods. In the presented pictures inner part of elbow is located on left side of circles.

Measurements of the velocity distributions and concentration of dust in the measuring section after the elbow were performed in order to determine the real flow conditions. The measurements were performed in the working conditions (Dobrowolski et al., 2004). The coal-particle samples in the section before the

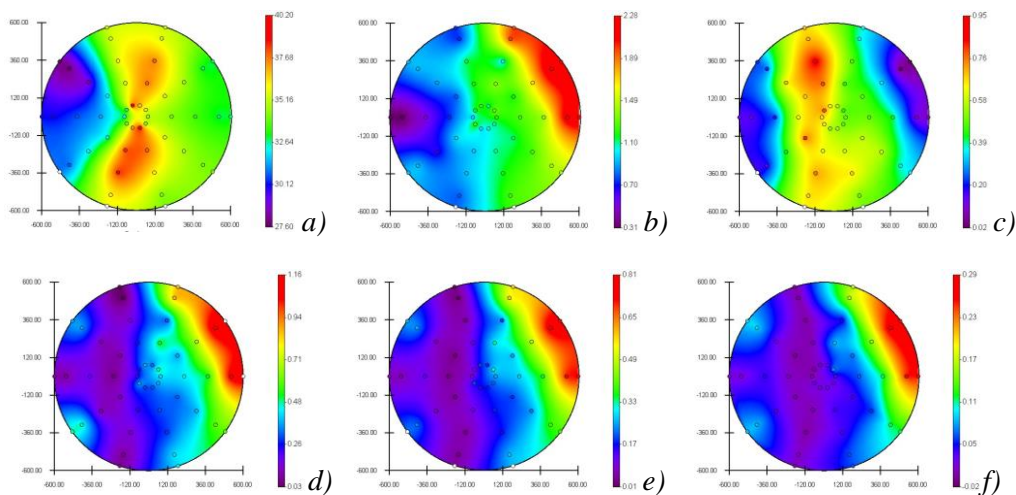


Fig. 1: Distributions of: a) Velocity in $[\text{m}/\text{s}]$ and concentration in $[\text{g}/\text{s}]$ for the particles; b) All diameters; c) 15, d) 90, e) 125 and f) 200 μm obtained with experiment.

separator were drawn with the device for isokinetic suction. Velocity and concentration distributions are similarly to obtained by other researchers. After comparison particle concentration distribution obtained with experiment and calculations, it appears that particles form “rope” after the elbows. It is especially evident for large diameter particles.

4. Conclusions

Comparison results let conclude that Euler-Euler is the best method to calculation of gas-particle flow in set with elbow. Differences between EE and EL methods are result of interparticle collisions included only in Euler-Euler method. Adding this mechanism to Euler-Lagrange method may improve efficiency of particles concentration distribution estimation. The EE method gives more uniform results of concentration calculations for all the tested particle fractions. Comparison reciprocal correlation for distribution of particle's concentration from experiment with EE, EL and ELpl methods shows that for particles 15 μm from experiment occurrence negative correlation for bigger particles from calculations. This phenomenon is a result of filling volumes by large particles, which cause crowding-out effect for smaller particles. Authors suggest to introduce a new definition “**anti-cord**”.

The observed quantitative differences between theory and experiment can result from the assumed simplifications and three-dimensionality of the flow in the tested system. It limits the applicability range of the methods used for the measurements of solid particles velocity and concentration. In such situations, the results obtained according to the Euler-Lagrange model are incorrect, and the error is a result of application of an incorrect method of calculations. In the case of volume fractions of solid particles in gas exceeding 12%, the Euler-Euler method (so-called Euler methods) seems to be more useful, and this method is recommended to the further investigations.

References

- Borsuk, G., Dobrowolski, B., Wydrych, J. (2006) Gas - solids mixture flow through a two-bend system, *Chemical and Process Engineering*, Vol. 27, No. 3/1, pp. 645-656.
- Dobrowolski, B., Pospolita, J., Wydrych, J. (2004) An attempt to improve the flow before the four-way divider system pulverized coal boiler BP-1150, *Inżynieria chemiczna i procesowa*, Vol. 25, No. 4, pp. 2105-2112 (in Polish).
- Dobrowolski, B., Wydrych, J. (2007) Computational and experimental analysis of gas-particle flow in furnace power boiler instalations with respect to erosion phenomena, *J. of theoretical and applied mechanics*, Vol. 45, No. 3, pp. 513-538.
- Wydrych, J. (2010) Comparative analysis of the methods of simulation of flow in boiler dust systems, *Chemical and Process Engineering*, Vol. 31, No. 4, pp. 603-623.
- Dodds, D., Naser, J., Staples, J., Black, C., Marshall, L., Nightingale, V. (2011) Experimental and numerical study of the pulverised-fuel distribution in the mill-duct system of the Loy Yang B lignite fuelled power station, *Powder Technology* 207, pp. 257-269.
- El-Behery, S. M., Hamed, M. H., El-Kadi, M. A., Ibrahim, K. A. (2009) CFD prediction of air–solid flow in 180° curved duct, *Powder Technology*, 191, pp. 130-142.
- Fokeer, S., Kingmana, S., Lowndes, I., Reynolds, A. (2004) Characterisation of the cross sectional particle concentration distribution in horizontal dilute flow conveying—a review, *Chemical Engineering and Processing*, 43, pp. 677-691.
- Jaworski, A. J., Dyakowski, T. (2002) Investigations of flow instabilities within the dense pneumatic conveying system, *Powder Technology*, 125, pp. 279-291.
- Kuan, B., Yang, W., Schwarz, M. P. (2007) Dilute gas–solid two-phase flows in a curved 90° duct bend: CFD simulation with experimental validation, *Chemical Engineering Science*, 62, pp. 2068-2088.
- Lain, S., Sommerfeld, M. (2012) Numerical calculation of pneumatic conveying in horizontal channels and pipes: Detailed analysis of conveying behavior, *International Journal of Multiphase Flow* 39, pp. 105-120.
- Miller, R. M., Singh, J. P., Morris, J. F. (2009) Suspension flow modeling for general geometries, *Chemical Engineering Science* 64, pp. 4597- 4610.
- Rajniak, P., Dhanasekharan, K., Sinka, C., MacPhail, N., Chern, R. (2008) Modeling and measurement of granule attrition during pneumatic conveying in a laboratory scale system, *Powder Technology*, 185, pp. 202-210.
- Spedding, P. L., Benard, E. (2007) Gas–liquid two phase flow through a vertical 90° elbow bend, *Experimental Thermal and Fluid Science*, 31, pp. 761-769.
- Woods, J. A., Thorpe, R. B., Johnson, S. E. (2008) Horizontal pneumatic conveying from a fluidized bed, *Chemical Engineering Science*, 63, pp. 1741-1760.

DYNAMIC FIELD BALANCING OF SENSITIVE ROTOR

J. Zachwieja *

Abstract: *The paper demonstrates problems arising during the field balancing of sensitive rotor. This term is referred to as rotors of which the response to excitation, expressed as a change of amplitude of vibration parameters, is significant after adding to it even small tested or correction masses.*

Keywords: Dynamic balancing, Resonance vibration, Matrix of influence coefficients, Amplitude-frequency characteristics, Fourier transform.

1. Introduction

A sensitive rotor is referred to as rotor of which response to excitation, expressed as a change of amplitude of vibration parameters, is disproportionately high compared to quantity of excitation. This occurs usually when rotary frequency of rotor is close to critical frequency. Width of interval in which rotor vibrations are approximately resonant, is largely dependent on external anisotropic, i.e. difference in stiffness of the foundation in the vertical and horizontal direction.

Dynamics of asymmetrical rotor with anisotropic bearing was investigated by Black and McTerman (Black and McTerman, 1968). Parkinson (Parkinson, 1968) proved that near the resonant frequency phase angle as well as vibrations amplitude are dependent on localisation of imbalance. Another particularity associated with the stiffness asymmetry of rotor foundation, noticed by Iwatsubo and Nakamura (Iwatsubo and Nakamura, 1968), is a domination in amplitude vibration spectrum for doubled synchronic frequency when its angular speed is equal to a half of critical speed. Gunter and Trumpler (Gunter and Trumpler, 1969) as well as Ehrich (Ehrich, 1992) have done research on the determination of the influence of stiffness anisotropy of foundation on the stability of rotor-bearing system. Black (Black, 1969) and Iwatsubo (Iwatsubo, Tomita, Kawai, 1973) have demonstrated that established vibrations of asymmetric rotor under the conditions of resonance can be unstable.

During analysing the motion of anisotropic rotor Ganesan (Ganesan, 1996; Ganesan, 2000) has stated that asymmetric of bearing stiffness leads to vibration instability if the rotational frequency of rotor is higher than frequency of its proper vibrations respectively in directions: horizontal (x) and vertical (y). Stable vibrations of rotor in x direction prevail in the range of the resonant frequency. At the rotor speed close to the critical speed, vibrations in x direction are more stable through effects of imbalance as well as asymmetric of systems which at the same time cause motion destabilisation in y direction. The effect of non-monotonic trend of increase or decrease in the vibration amplitude, inducted by imbalance, is strongly dependent on scale of foundation stiffness anisotropy.

2. Analysis of the Resonant Vibration of Radial Fan

Susceptibility of foundation and foundation of the body mainly determine natural vibrations of rotating machines because the body and rotor of the machine are usually rigid bodies. Derogation from this rule may occur for small fans which housings, in the form of box, are made of thin sheet.

Such fan was tested because during a test of balancing its rotor, there has been reported very high sensitivity to the test mass which has been attached to the disk. The orientation of fan body on the platform using rubber mat as a vibration isolator may suggest anisotropic stiffness of foundation, the

* Assoc. Prof. Janusz Zachwieja, PhD.: Department of Applied Mechanics, University of Technology and Life Sciences in Bydgoszcz, Kaliskiego 7, Bydgoszcz; Poland, janusz.zachwieja@utp.edu.pl

consequence of which should be rotor vibrations with greater amplitudes in vertical and horizontal direction.



Fig. 1: View of the fan and its model.

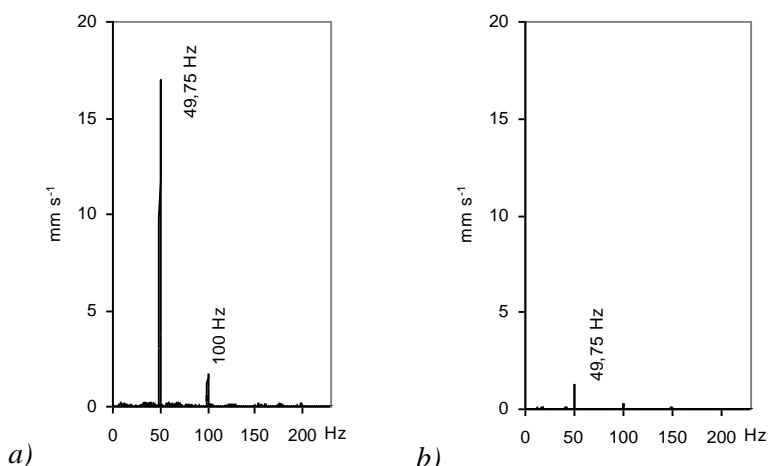


Fig. 2: Amplitude-frequency characteristics of rotor vibration velocity in direction: a) horizontal, b) vertical.

The rotor disk, with a mass of ~ 30 kg, is located on the motor shaft. Rotating speed of rotor is $2950 \text{ r}\cdot\text{min}^{-1}$. Ultra-harmonic rotational frequency of the motor on the vibration spectrum suggests that the system vibrations are non-linear. Similar situation occurs in the case of clearance in the foundation system of the rotor or the near resonant frequency.

Both cases represent a significant impediment to the process of the rotor balancing by using coefficient matrix of influence method (Zachwieja, 2011, 2012). Testing the characteristic of rotor vibrations allows choosing the most effective way of balancing. Removing the rotor from the resonant vibrations can be done by changing the rotational velocity of the rotor, which is the simplest and the most effective procedure, or by changing the stiffness of system. Changing mass is the most rarely used.

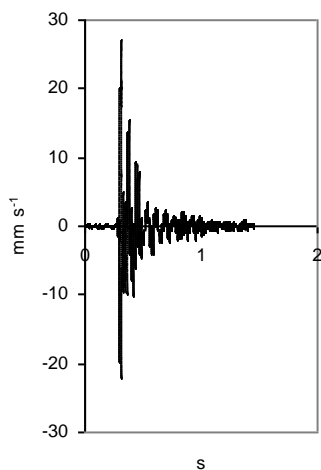


Fig. 3: Time course of system response to the impulse excitation.

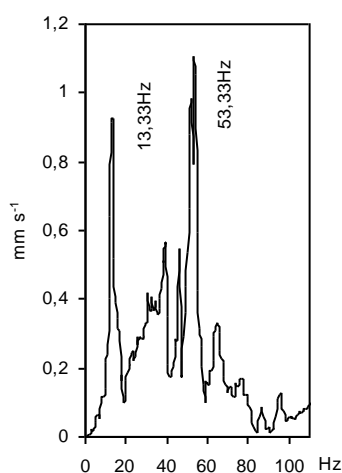


Fig. 4: Characteristic of resonant vibrations of rotor.

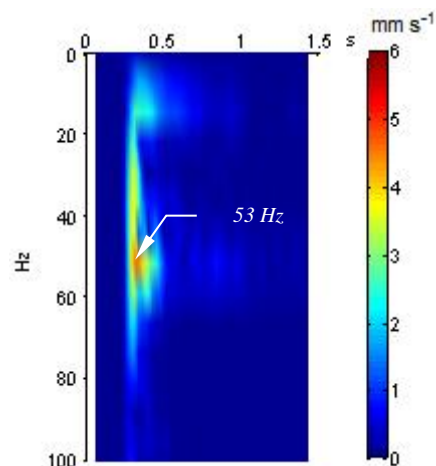


Fig. 5: Image of short-time Fourier transform of rotor vibration velocity.

Testing the characteristic of rotor vibrations was brought to the designation of its resonant characteristic by impulse excitation. Based on the time course of system response to the impulse excitation (Fig. 3) it can be concluded that there is a damping with a relatively high value. It means that stiffness of the rotor foundation is specific.

Amplitude-frequency characteristic of the response indicates the possibility of appearance of a number of critical frequencies, of which 13.3 Hz and 53 Hz have the main influence on rotor vibrations (Fig. 4). 53 Hz frequency is close to rotational frequency of the rotor (Fig. 5).

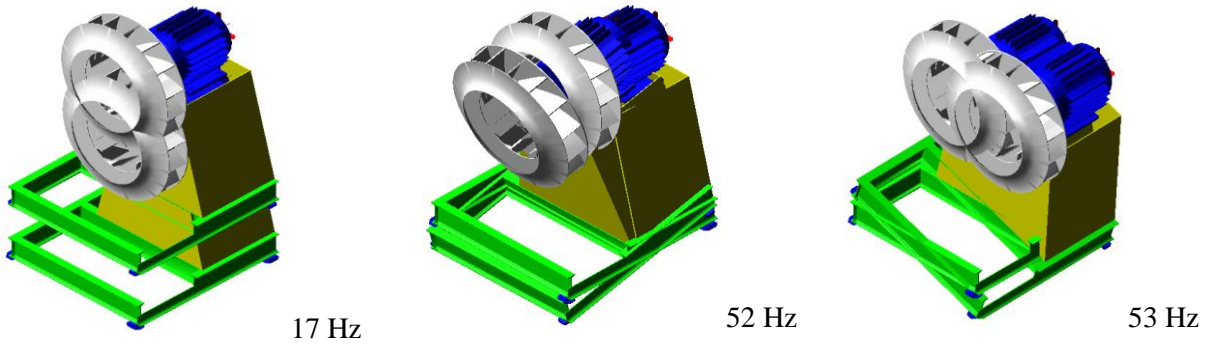


Fig. 6: The time course of system response to the impulse excitation.

Numerical analysis confirmed that the free vibration frequency of the rotor with parameters such as those of tested object, may correspond to the measured values (Fig. 6). Simultaneous input vibrations with the frequency of 52 Hz and 53 Hz cause that the vibrations with the highest amplitudes will be measured on a motor bearing on the side of winding cooling disk. Rotor balancing requires two corrections. One of them should be rotor disk, the second one should be cooling disk of rotor. However, the second one cannot be used for this purpose because of low stiffness and diameter.

3. Fan Rotor Balancing by Using the Optimisation Amplitudes of Vibration Method in the Directions of Measurement

According to coefficients matrix of influence method, it is assumed that there is a relation between force of rotor imbalance and vector of selected vibration parameter:

$$\mathbf{N}_n = \mathbf{A}\mathbf{F}_n \quad (1)$$

where: \mathbf{F}_n – imbalance force, \mathbf{N}_n – vector of selected vibration parameter for rotational frequency of rotor, \mathbf{A} - coefficients matrix of influence.

For rotor with an external anisotropic, the proper way of solving the balancing problem is a technique used by the author. It consists in optimising distribution of vibration amplitudes in a way that it will be the lowest for the selected directions of measurements. At a specific correction planes and unlimited number of measurement planes, coefficients matrix of influence is not a square matrix which means that inverse matrix to \mathbf{A} matrix does not exist. However, there is a possibility of obtaining a solution to the equation (1) in the terms of optimisation. One way is to define Moore-Penrose pseudoinverse of matrix which can be used as \mathbf{A}^{-1} inverse matrix if the inverse matrix does not exist. $\mathbf{A}^* \in \mathbf{R}^{n \times m}$ matrix is going to be pseudoinverse matrix for \mathbf{A} matrix if the condition $\mathbf{A}\mathbf{A}^*\mathbf{A}=\mathbf{A}$ is satisfied. Pseudoinverse matrix application causes that vector:

$$\mathbf{F}_n^* = \mathbf{A}^*\mathbf{N}_n \quad (2)$$

minimises the norm $\|\mathbf{A}\mathbf{F}_n - \mathbf{N}_n\|^2$. Therefore, instead of the equation (1) we will use the formulation:

$$\mathbf{F}_n = \mathbf{A}^*\mathbf{N}_n \quad (3)$$

which allows determining imbalance vector.

Disk rotor balancing shows its high sensitivity to the change in value of correction masses which is characteristic for the near resonant frequency. Location of correction mass was not stable which is also symptomatic for resonant frequency. However, the use of optimising method resulted in a decrease of the vibration amplitude of cooling disk of rotor bearing which demonstrates its high value with slight increase of vibration amplitudes in the rotor disk bearing.

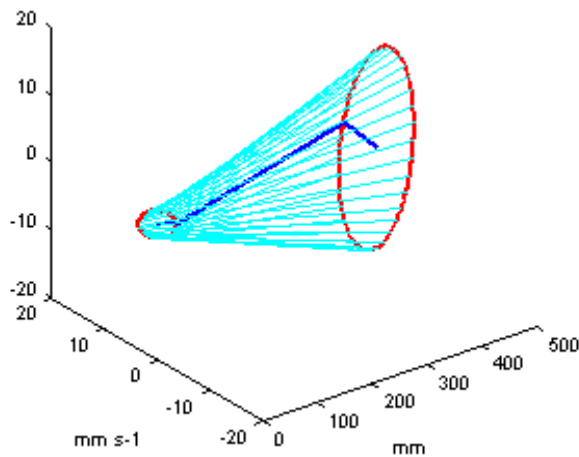


Fig. 7: 3D-holospectrum of rotor vibration velocity before balancing.

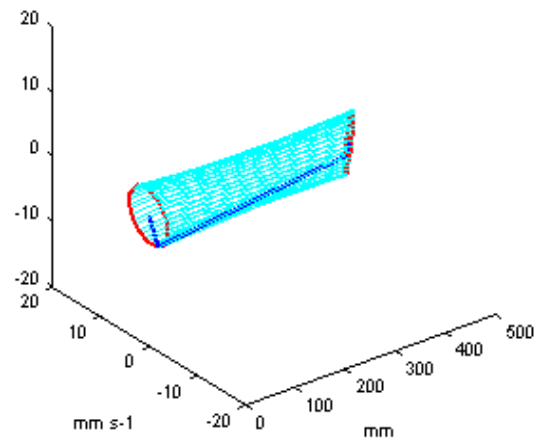


Fig. 8: 3D-holospectrum of rotor vibration velocity after balancing with correction mass 7.5 g.

4. Conclusions

Coaxial rotor with a high static imbalance compared to its mass can be balanced to some extent even in the resonant area. Achieved balance efficiency under the resonance conditions is usually worse than balancing outside those areas.

Coefficients matrix method is sensitive to the proximity of the resonance area of rotor. Correction masses calculated in resonant vibration areas, based on the classic coefficient matrix of influence method, can cause increase in rotor imbalance. Discussed case proves that using a proper optimisation allows an improvement of the dynamic rotor even under resonant vibrations.

References

- Black, H. F. (1969) Parametrically excited lateral vibrations of an asymmetrically slender shaft in asymmetrically flexible bearings. *Journal of Mechanical Engineering Science*, 11, pp. 57-67.
- Black, H. F., McTernan, A. J. (1968) Vibration of a rotating asymmetric shaft supported in asymmetric bearings. *Journal Mechanical Engineering Sciences*, 10(3), pp. 252-261.
- Ehrich, F. F. (1992) Observations of subcritical superharmonic and chaotic response in rotor dynamics, *ASME Journal of Vibration and Acoustics*, 114, pp. 93-100.
- Ganesan, R. (1996) Dynamic response and stability of a rotor-support system with non-symmetric bearing clearances. *Mechanism and Machine Theory*, 6(31), pp. 781-798.
- Ganesan, R. (2000) Effects of bearing and shaft asymmetries on the instability of rotors operating at near-critical speeds. *Mechanism and Machine Theory*, 35, pp. 737-752.
- Gunter, E. J., Trumpler, P. R. (1969) The influence of internal friction on the stability of high speed rotors with anisotropic supports. *ASME Journal of Engineering for Industry*, 91, pp. 1105-1113.
- Iwatsubo, T., Nakamura, M. (1968) Balancing of flexible rotors with asymmetric shaft stiffness. *Memoirs of the Faculty of Engineering Kobe University* No. 15.
- Iwatsubo, T., Tomita, A., Kawai, R. (1973) Vibrations of asymmetric rotors supported by asymmetric bearings. *Ingenieur Archive*, 42, pp. 416-432.
- Parkinson, A. G. (1965) On the balancing of shafts with axial asymmetry. *Proceedings Royal Society of London, Series A* 259, pp. 1095-1098.
- Zachwieja, J. (2011) The Influence of Rotor Foundation Stiffness on operating and Balancing Efficiency with Near Resonant Velocity. *Studia i Materiały Polskiego Towarzystwa Zarządzania Wiedzą*, 48, pp. 148-161 (in Polish).
- Zachwieja, J. (2012) Rotor Balancing of the Radial Fan under Different Dynamic States. Habilitation thesis No. 153, Wydawnictwo UTP (in Polish).

MECHANICAL BEHAVIOR OF THE LAMELLAE ANNULUS FIBROSUS IN FINITE ELEMENT MODEL

M. Żak^{*}, J. Słowiński^{**}, C. Pezowicz^{***}

Abstract: *The composite construction of annulus fibrosus stems from the specific arrangement of collagen fibers in the individual lamellar. Structural differences in collagen fiber connections within a single lamellar of annulus fibrosus determine the nonlinear mechanical properties of the intervertebral disc. This structure of annulus fibrosus facilitates the transfer of loads acting on the spine while ensuring stiffness and strength in intervertebral disc. The aim of this study was to build numerical model of single lamellar annulus fibrosus on the basis of experimental research. In next stages, the information about the directional mechanical properties obtained from numerical simulations would allow explain the mechanism of damage in the intervertebral disc.*

Keywords: Intervertebral disc, Annulus fibrosus, Mechanical properties, Numerical simulations.

1. Introduction

Annulus fibrosus consists of a hierarchically organized tissue structure, which is characterized by high deformability while transferring loads by the spine. Simultaneously forming part of annulus fibrosus collagen fiber network, determines the anisotropic mechanical properties in the entire structure (Pezowicz et al., 2005, Pezowicz et al., 2006, Fujita et al., 2000). Based on the above, the aim of this work was to develop a numerical model of single lamellar intervertebral disc according to the directional mechanical properties. The study included the impact of collagen fibers orientation, as the factor determining the functioning of the intervertebral disc.

2. Material and Methods

The numerical model of a single lamellar annulus fibrosus was developed on the basis of experimental study in animal models. 6 anterior parts of nondegenerate intervertebral disc taken from lumbar spine of pigs at 9 months of age were used in the experimental study. Blocks of annulus fibrosus were cut in the plane of outer lamellar sections in nominal thickness 40–50 μm . An uniaxial tensile test at a constant speed of 0.06 mm/s, until rupture, was carried out on the special microtensile device. Specimens were kept in NaCl medium in order to preserve comparable conditions tests (Żak et al., 2013).

Numerical model was generated in several steps. In the first step a rectangular area measuring 2.63 mm long and 1.76 mm wide was created. These values are averaging real sample dimensions. Then the area was cut into tens of areas by making a series of cuts parallel to the short edge of the area. Distance between each cuts was varied randomly within a certain range. Number of cuts was selected experimentally and was a result of a compromise between accuracy and the time necessary to carry out a simulation using the developed model. A component of vertical lines obtained as a result of first cutting operation simulate the main fibers system (Ir) in a single lamellar of annulus fibrosus. In the second cutting every area was cut into tens of subareas by making a series of cuts routed at an angle in the range

* M.Sc. Eng. Małgorzata Żak: Department of Biomedical Engineering, Mechatronics and Theory of Mechanisms, Wrocław University of Technology, ul. Łukasiewicza 7/9, 50-371 Wrocław, Poland, malgorzata.a.zak@pwr.wroc.pl

** Jakub J. Słowiński, PhD.: Department of Mechanics and Materials Science, Wrocław University of Technology, ul. Smoluchowskiego 25, 50-370, Wrocław, Poland, jakub.slowinski@pwr.wroc.pl

*** Prof. Celina Pezowicz: Department of Biomedical Engineering, Mechatronics and Theory of Mechanisms, Wrocław University of Technology, ul. Łukasiewicza 7/9, 50-371 Wrocław, Poland, celina.pezowicz@pwr.wroc.pl

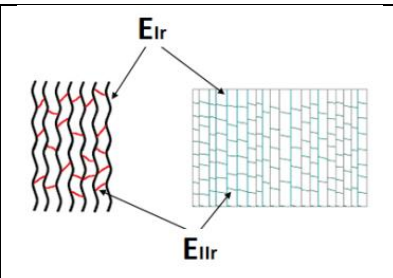
of 95 to 105 degrees relative to the main fibers. A component of lines from second cutting operation simulate short fibers system (IIr).

Arrangement of the main fibers (Ir) in the sample were defined as a random variable in the range $\pm 30\%$ of the distance between the fibers, assuming that all the fibers are evenly distributed. In IIr fibers oriented transversely to the main fiber and includes the random distribution and angle. A random arrangement of fibers Ir and IIr in numerical model gives larger regularity of the fibers as opposed to the actual model of the lamellar annulus fibrosus.

All lines from both components were discretized using 2-nodes link element. This type of element is used in the case of uniaxial tension test, no bending of the element is considered. A component of areas obtained during both, first and second, cutting operation simulate an annulus ground substance in which the fibers are immersed. Discretization of the areas was carried out using 4-nodes shell element.

The material properties (Young's modulus and Poisson's ratio) of the fibers and annulus ground substance were determined from experimental study and literature (Tab. 1). Two types of fibers were adopted: the main long fibers (Ir) and smaller short fibers (IIr) contained between the main fibers. The value of Young's modulus of the Ir fiber (E_{Ir}) was adopted on the basis of the average values obtained during the tensile test in parallel direction to orientation of collagen fibers. On the other hand the Young's modulus of the IIr fiber (E_{IIr}) was determined on the basis of the uniaxial stretching in perpendicular direction to orientation of collagen fibers

Tab. 1: The material properties of the fibers and annulus ground substance in a single lamellar of annulus fibrosus model.

			ν [-]	
	Collagen fibers ⁽¹⁾	E_{Ir} [MPa]	54.37	0.45
		E_{IIr} [MPa]	0.32	
Annulus ground substance ⁽²⁾	E_0 [MPa]	0.10	0.45	

⁽¹⁾ based on their own experimental data

⁽²⁾ Schmidt et al., 2010

In the numerical simulation, the sample was fixed by taking all the degrees of freedom of the nodes situated on the edge of the model. The nodes located on the opposite shore were loaded by a displacement acting in along or across to long fibers. The procedure of uniaxial tension was carried out iteratively. At each step the displacement of the fibers was increasing. Rupture of the fiber elements occurred when a certain strain exceeded an experimentally determined value (in parallel direction 60% and in perpendicular direction 80%).

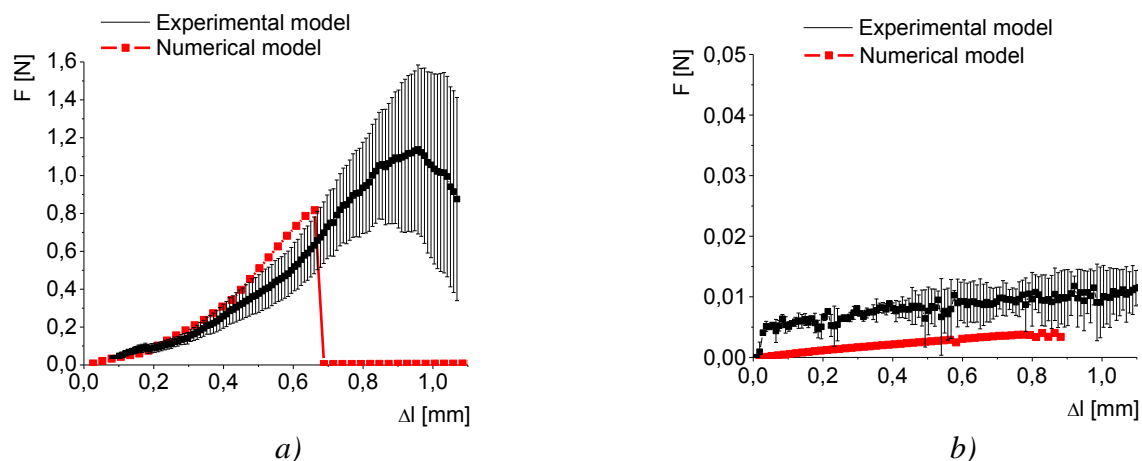


Fig. 1: Comparison of the example $F(p)$ characteristics of a single lamellar annulus fibrosus stretched in: a) parallel direction, b) perpendicular direction to orientation of collagen fibers.

3. Results

Results obtained from numerical simulations of the force - displacement characteristics were similar to the results obtained experimentally, but were varied in terms of these values (Fig. 1).

The mechanical characteristics of physiological single lamellar annulus fibrosus showed significant differences due to the orientation of collagen fibers. Characteristic stages of change in the structure of lamellar annulus fibrosus: straightening, tension, loss of cohesion and rupture of collagen fibers (Fig. 2.a) could be identified during stretching in parallel direction of the fibers. Contrary to parallel direction of stretching in a perpendicular direction structure of annulus fibrosus had a tendency to further reorganization and isolating the short fibers with collagen bundles (Fig. 2.b).

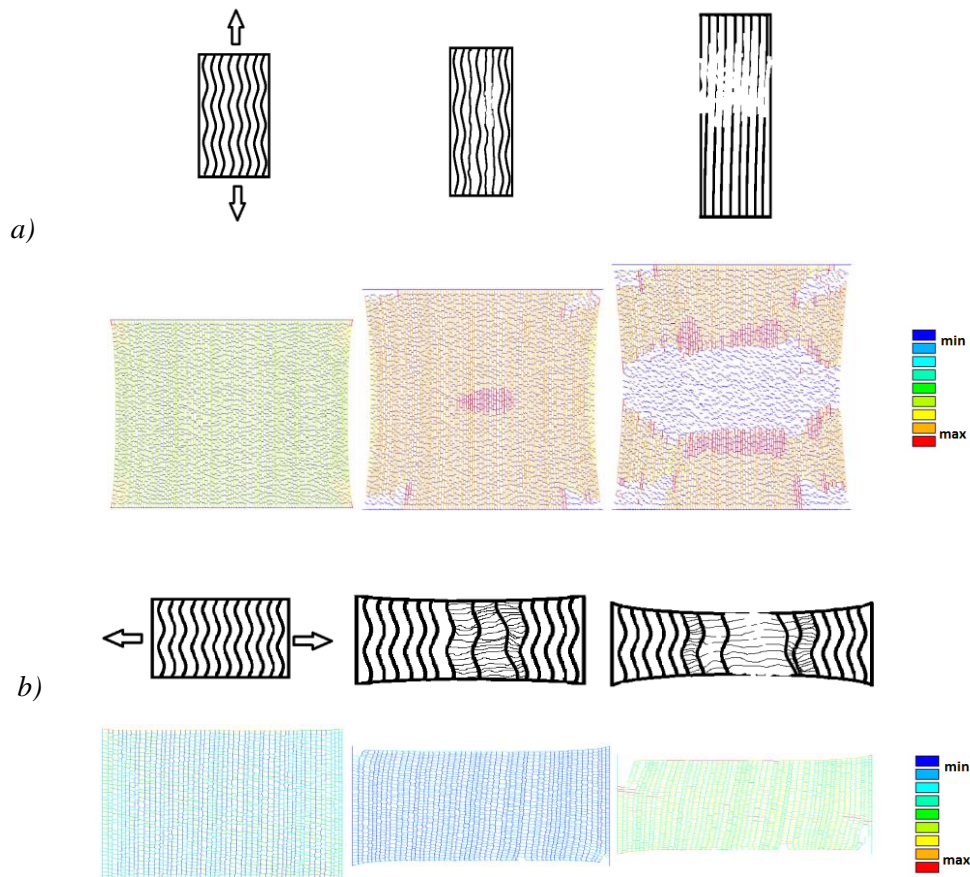


Fig. 2: Stages of structural changes in experimental and numerical model of a single lamellar annulus fibrosus stretched in: a) parallel direction, b) perpendicular direction to orientation of collagen fibers.

On the basis of the force and displacement of the sample in the numerical model the value of the ultimate force (F_{UTS}) was obtained. A stiffness coefficient (k) were determined based on the slope of the curve $F(\Delta l)$. Then, the obtained parameters were compared with experimental values which are presented in the form of a box-plot graphs and the estimated value of the numerical simulations are marked in blue line (Fig. 3).

The model of sample stretched in parallel direction to the collagen fibers obtained high compliance value of the analyzed mechanical parameters (Fig.3.a). The value of the ultimate force (F_{UTS}) in the numerical model was 13% smaller than the value in real sample (0.95 ± 0.40 N). The stiffness coefficient in numerical model was differed by 12% from the experimental value (1.87 ± 0.73 N/mm).

The value of ultimate force for the perpendicular direction tensile obtained from experiment (14.02 ± 8.26 mN) was 70% higher than from numerical model. In the case of the numerical model stiffness coefficient were 7% smaller than the average of experimental value (4.95 N \pm 2.68 mN/mm).

The discrepancy between the experimental and numerical model can be attributed to inhomogeneity of the biological material, as the strong scattering of the results obtained in experimental study.

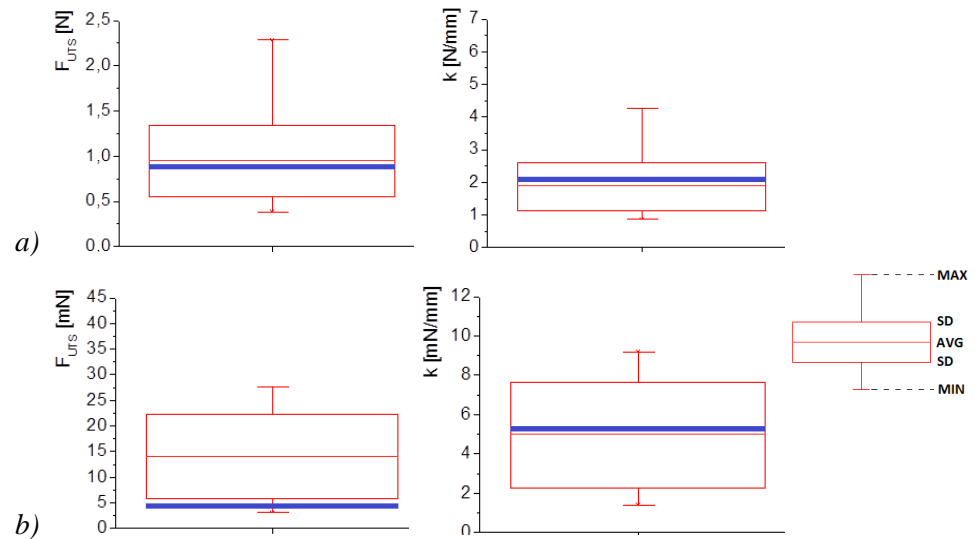


Fig. 3: Comparison of mechanical parameters (stiffness coefficient - k , ultimate force - F_{UTS}) in experimental and numerical model of a single lamellar annulus fibrosus stretched in: a) parallel direction, b) perpendicular direction to orientation of collagen fibers.

4. Conclusions

The knowledge gained from research, have confirmed the anisotropy of annulus fibrosus in animal model and indicated that fiber orientation has influence on the mechanical properties. Detailed characterization of single lamellar annulus fibrosus allows for the preparation numerical model of the multi lamellar fiber structure. In the next stage of the study, presented numerical model will be essential to understand the mechanism of damage in intervertebral disc.

Acknowledgement

This work is supported by Polish Ministry of Science and Education grant No. NN518501139.

References

- Fujita, Y., Wagner, D., Biviji, A., Duncan, N., Lotz, J. (2000) Anisotropic shear behavior of the annulus fibrosus: effect of harvest site and tissue prestrain. *Medical engineering & physics*, 22(5), pp. 349-57.
- Pezowicz, C. A., Robertson, P. A., Broom, N. D. (2006) The structural basis of interlamellar cohesion in the intervertebral disc wall. *Journal of Anatomy*, 208, pp. 317-330.
- Pezowicz, C. A., Robertson, P. A., Broom, N. D. (2005) Intralamellar relationships within the collagenous architecture of the annulus fibrosus imaged in its fully hydrated state. *Journal of Anatomy*, 207(4), pp. 299-312.
- Schmidt, H., Shirazi-Adl, A., Galbusera, F., Wilke, H. J. (2010) Response analysis of the lumbar spine during regular daily activities—a finite element analysis. *Journal of Biomechanics*, 43, pp. 1849-1856.
- Żak, M., Pezowicz, C. (2013) Spinal segments and regional variations in the mechanical properties of the annulus fibrosus subjected to tensile loading. *Acta of Bioengineering and Biomechanics* 15(1), pp. 51-59.

COMPARATIVE SIMULATIONS OF GUIDING BEHAVIOUR OF AN ELECTRIC LOCOMOTIVE

J. Zelenka^{*}, T. Michálek^{**}, M. Kohout^{***}

Abstract: *Computer simulations of vehicle running performance create an integral part of research and development of new rail vehicles. The simulations allow e.g. optimization of dynamic behaviour of the vehicle and it may be possible to use them in the certification process instead of results of some track tests in the future. Nowadays, many commercial as well as non-commercial simulation tools are commonly used for these purposes. However, verification of the computational model and validation of its results represent the most significant problems which must be solved to gain relevant data from the simulations. In the framework of solving the R&D project “Competence Centre of Rail Vehicles” of the Technology Agency of the Czech Republic, the attention of the work package WP5 is paid to this problem of model validation among others. This paper deals with results of simulations of an electric locomotive through curves of various radii which were performed by means of four simulation tools (SJKV-L3A, SIMPACK in versions 8900 and 9.4-build65 and ADAMS/VI-Rail) at three different workplaces (Jan Perner Transport Faculty of the University of Pardubice, VÚKV a.s. and ŠKODA Transportation a.s.). The simulation results allow comparison of these different models as well as revelation and clarification of problematic aspects of the individual models.*

Keywords: Rail vehicle dynamics, Comparative simulations, Guiding behaviour, Model validation.

1. Introduction

Nowadays, computer simulations are commonly used for the assessment of rail vehicle dynamics in the design stage of new vehicles and allow investigation of influence of many parameters on the dynamic behaviour of the vehicles (as it is shown e.g. in the paper by Michálek and Zelenka (2013)). It is possible to optimize e.g. characteristics of joints (springs, dampers, wheelset guiding etc.) and improve the running and guiding behaviour of the vehicle in this way. In the future, the next field of using the computer simulations could be the replacement of a certain part of track tests realized in the framework of certification process by the simulation results because new drafts of relevant standards (especially a new version of the EN 14363) permit such approach which could make the certification process shorter and less expensive. During the process of investigation of rail vehicle dynamics by means of computer simulations, the question of model validation is very important. Only if a validated computational model is used, the simulation results can reliably prove about the dynamic properties of a real vehicle. And in case of using the simulation results as a proof of the safety in the certification process, this question becomes more important than ever before.

The model validation is a very demanding process (see e.g. the paper by Polách et al. (2013)) at which it is necessary to know how the computational model works. However, a detailed knowledge of algorithms, on which the model is based, could be a problem, especially in case of commercial simulation tools. This is also the reason why an important part of solving the R&D project “Competence Centre of Rail Vehicles” in the work package WP5 is focused on the comparative simulations of rail vehicle running performance. More detailed knowledge of different simulation tools, which are being used by the project partners, together with clarification of problematic aspects, which occur during the realization of computer simulations, should enable easier validation of the models.

^{*} Assoc. Prof. Ing. Jaromír Zelenka, CSc.: University of Pardubice, Jan Perner Transport Faculty, Department of Transport Means and Diagnostics, Section of Rail Vehicles; Slovanská 452; 560 02, Česká Třebová; CZ, jaromir.zelenka@upce.cz

^{**} Ing. Tomáš Michálek: University of Pardubice, Jan Perner Transport Faculty, Department of Transport Means and Diagnostics, Section of Rail Vehicles; Slovanská 452; 560 02, Česká Třebová; CZ, tomas.michalek@upce.cz

^{***} Ing. Martin Kohout, PhD.: University of Pardubice, Jan Perner Transport Faculty, Department of Transport Means and Diagnostics, Section of Rail Vehicles; Slovanská 452; 560 02, Česká Třebová; CZ, martin.kohout@upce.cz

2. Computational Models

For purposes of the comparative simulations of vehicle running performance, results of four different simulation tools, which are being used by three project partners nowadays, were taken into account:

- SJKV-L3A, i.e. a version of the original multi-body simulation software SJKV, which has been developed at the Detached Branch of the Jan Perner Transport Faculty of the University of Pardubice in Česká Třebová, which is intended for simulations of a four-axle electric locomotive (more detailed information about this software can be found e.g. in the paper by Michálek and Zelenka (2011)).
- SIMPACK 8900, i.e. an older version of the commercial simulation tool by SIMPACK AG which is also being used at the Jan Perner Transport Faculty of the University of Pardubice.
- SIMPACK 9.4-build65 64 bit, i.e. a newer version of the commercial simulation tool by SIMPACK AG which is being used by the company VÚKV a.s.
- ADAMS/VI-Rail, i.e. the commercial simulation tool by VI-Grade built upon the MSC Software product MSC ADAMS which is being used by the company ŠKODA Transportation a.s.

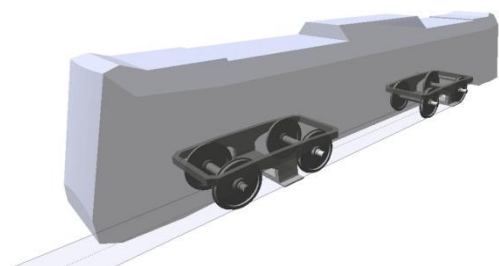


Fig. 1: Model of the locomotive in SJKV-L3A by the Jan Perner Transport Faculty.

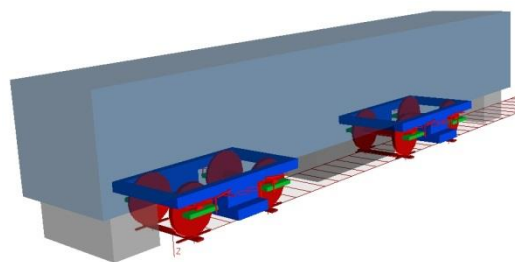


Fig. 2: Model of the locomotive in SIMPACK 8900 by the Jan Perner Transport Faculty.

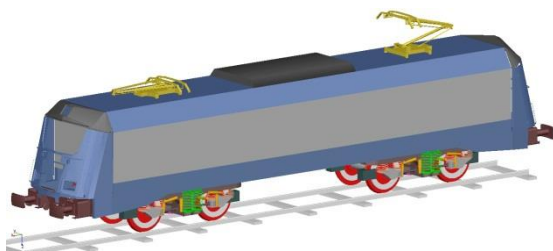


Fig. 3: Model of the locomotive in ADAMS/VI-Rail by ŠKODA Transportation.

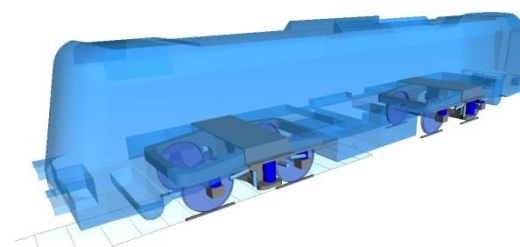


Fig. 4: Model of the locomotive in SIMPACK 9.4-build65 64 bit by VÚKV.

A model of a modern four-axle electric locomotive was chosen as a reference vehicle. All the project partners had the same input data (parameters of the locomotive, i.e. masses and inertia moments of individual constructional parts, characteristics of joints etc.) at their disposal to apply them into their models. All the computational models, which were used for the comparative simulations, are depicted in Fig. 1 up to Fig. 4.

In the first stage of realization of comparative simulations, the attention was paid to the guiding behaviour of the locomotive. The term “guiding behaviour of a rail vehicle” covers dynamic properties of the vehicle during its run through a curve (see the paper Michálek and Zelenka (2011), for example). Parameters of the track as well as parameters of the wheel/rail contact and vehicle speed were defined uniformly again. Specifically, following parameters of simulations were taken into account:

- Track with curves with 5 different radii from a range of 250 m up to 1500 m.
- Ideal track without irregularities.
- Friction coefficient in wheel/rail contact 0.4.
- Vehicle speed corresponding to cant deficiency of 130 mm and 165 mm.
- Wheel/rail contact geometry corresponding to wheelsets with theoretical wheel profiles ORE S1002 and track with theoretical rail profiles 60E1 with rail inclination 1:20 and 1:40.

3. Simulation Results

The complete simulation results including their assessment are presented in the report by Zelenka et al. (2013). In this stage, only the stable (quasistatic) values of chosen quantities observed during the run of the vehicle in full curve were compared. The following quantities were observed:

- Quasistatic guiding forces acting on each of wheels.
- Quasistatic wheel forces (wheel loads) acting on each of wheels.
- Angles of attack of each of wheelsets.
- Angles of bogie rotation to the vehicle body about the vertical axis.
- Lateral acceleration on the vehicle body (in its centre of mass).
- Roll angle of the vehicle body (about its longitudinal axis).

In Fig. 5, there is shown an example of results of the comparative simulations. There are presented the quasistatic values of guiding forces, angles of attack and angles of bogie rotation to the vehicle body about the vertical axis in the graphs. These results correspond to the simulations of run through a right hand curve with radius of 300 m at cant deficiency of 165 mm (i.e. at speed of ca. 90 km/h); wheel/rail contact geometry is determined with the rails 60E1 with inclination of 1:40. It is evident that the computational models of all involved project partners provide relatively close results of all the depicted quantities in this case.

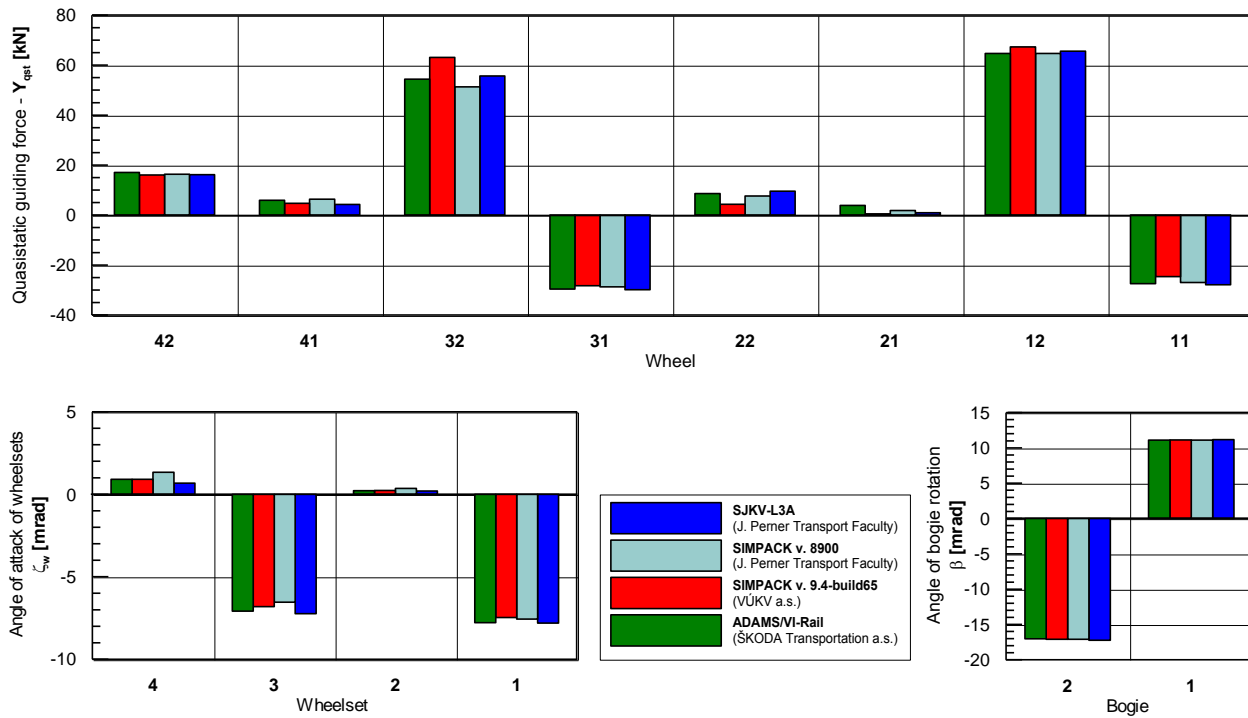


Fig. 5: Example of results of comparative simulations – quasistatic guiding forces, angles of attack and angles of bogie rotation to the vehicle body about the vertical axis during the run through a 300 m curve (cant deficiency: $I = 165$ mm; wheel/rail contact: ORE S1002 – 60E1/1:40).

On basis of the realized comparative simulations of guiding behaviour of the investigated electric locomotive, following observations can be stated:

- From the point of view of dependency of the observed quantities on the curve radius, all used computational models provide similar trends in dynamic behaviour of the locomotive.
- On the “structural level” (i.e. the behaviour of the vehicle body, whole wheelsets and bogies assessed by means of angles of attack and angles of bogie rotation to the vehicle body about the vertical axis), all computational models show good agreement in all investigated cases.
- Generally, the agreement of results of the used computational models is better in case of smaller curve radii and the wheel/rail contact geometry corresponding to the rails with inclination of 1:20.

4. Conclusions

This work is focused on results of the comparative simulations of dynamic behaviour of an electric locomotive which were performed by means of four different multi-body simulation tools at three workplaces in Czech Republic. In the described stage, the attention was paid only to the simulations of vehicle running performance in curves on ideal track without irregularities. Regardless, the gained data represent a large set of simulation results and show that all the used computational models provide similar results which can prove about the dynamic behaviour of a real vehicle.

However, some differences between the simulation results also occurred, especially in the values of quasistatic guiding forces in curves with larger radius. Because all the models show similar dynamic properties on the “structural level”, the reason of the different results can rather lie in the mode of wheel/rail contact modelling (i.e. processing of the wheel/rail contact geometry, consideration of one-point vs. multi-point contact, used theory of tangential forces etc.) than e.g. in the modelling of individual bodies or joints (springs, dampers etc.). Clarification of these problematic points should create the next part of the verification process of the computational models.

Besides to that, the next work will be focused on comparative simulations of vehicle running performance on a real track, i.e. on a track with irregularities. In this way, the rail vehicle dynamics (or more precisely: the dynamic behaviour of the computational models) can be assessed more complexly than in case of evaluation of the steady (quasistatic) values of observed quantities in curves as it was performed in this first stage. Then, the next target will be an investigation of the dynamic behaviour of the computational models at higher speeds, i.e. the question of stability of run.

The general aim of this work is a validation of the computational multi-body models of rail vehicles. The last draft of the European standard EN 14363 as well as the UIC Code No. 518:2009 and also e.g. the Technical Specification for Interoperability (TSI) of freight wagons (i.e. the Commission Regulation (EU) No. 321/2013) permit a substitution of a certain part of the track tests, which have to be performed in the framework of the certification process of new or modernized vehicles nowadays, by the computer simulations under certain conditions. This so-called “virtual certification” could have a potential to make the railway vehicles less expensive and more competitive. However, the model validation, which is based on comparison of results of track tests and simulation results, creates an essential condition for the use of simulation results in the certification process. Besides to that, all the problems of the model validation have not been fully solved yet. Therefore, the comparative simulations realized in the framework of activities of the WP5 of the “Competence Centre of Rail Vehicles” and their results should help with the model validation by means of clarification of functioning of different computational models at a wide range of various conditions.

Acknowledgement

This work was supported by the project No. TE01020038 “Competence Centre of Rail Vehicles” of the Technology Agency of the Czech Republic and the internal grant project No. 51030/20/SG540001 of the University of Pardubice.

References

- prEN 14363:2013. Railway applications – Testing and Simulation for the acceptance of running characteristics of railway vehicles – Running behaviour and stationary tests. CEN, Brussels.
- Michálek, T., Zelenka, J. (2011) Reduction of lateral forces between the railway vehicle and the track in small-radius curves by means of active elements. *Applied and Computational Mechanics*, 5, 2, pp. 187-196.
- Michálek, T., Zelenka, J. (2013) Sensitivity analysis of running gear parameters on dynamic behaviour of an electric locomotive, In: Proc. 21st Conf. with Int. Participation Current Problems in Rail Vehicles (M. Lata ed), University of Pardubice, Pardubice, pp. 85-92.
- Polách, O., Böttcher, A., Vannucci, D., Sima, J., Schelle, H., Chollet, H., Götz, G., Garcia Prada, M., Nicklisch, D., Mazzola, L., Berg, M., Osman, M. (2013) Validation of multi-body models for simulations in authorisation of rail vehicles, In: Ext. Abstracts 9th Int. Conf. on Railway Bogies and Running Gears (I. Zobory ed), BME, Budapest, pp. 67-69.
- Zelenka, J., Michálek, T., Krulich, P., Hora, M. (2013) Comparative Simulations of the passage of locomotives arc. Overall research report No. CKDV/WP5-2013-TM-02, University of Pardubice, Detached Branch of the Jan Perner Transport Faculty, Česká Třebová, (in Czech).

SEISMIC RESPONSE OF NUCLEAR FUEL ASSEMBLY COMPONENTS

V. Zeman^{*}, Z. Hlaváč^{**}

Abstract: *The paper deals with mathematical modelling and computer simulation of the seismic deformation and dynamic load of nuclear fuel assembly components. The seismic excitation is given by two horizontal and one vertical synthetic accelerogram at the level of the reactor pressure vessel suspension in the reactor hall. The seismic vibration is investigated by numerical integration method in time domain in two phases – at the global reactor level and at the fuel assembly level. Seismic vibration of the nuclear fuel assembly is caused by spatial motion of the fuel assembly lower and head pieces fixed in the support plates of the reactor core. The modal synthesis method with DOF reduction is used for calculation of the fuel assembly component deformations and dynamic load on the level of the spacer grid cells. The presented method is applied for the Russian TVSA-T fuel assembly in the WWER 1000/320 type reactor core in NPP Temelín.*

Keywords: Seismic response, Reactor, Fuel assembly, Condensation.

1. Introduction

One of the basic operation conditions of the nuclear reactor and its components is the guarantee of the feasible seismic response. The seismic action is most represented by the acceleration response spectra or by the synthetic accelerograms corresponding to given response spectra generally for damping value 2% - 10% (Betbeder-Matibet, 2008). An assessment of nuclear fuel assemblies (FA) behaviour at standard and extreme operating conditions belongs to important safety and reliability audit. A significant part of FA assessment plays dynamic deformation and load of FA components especial of fuel rods (FR). The beam type FA model used in seismic analyses of WWER type reactors (Hlaváč and Zeman, 2010) do not enable investigation of seismic deformations and load of FA components. The goal of this contribution, in direct sequence at an interpretation of FA modelling, modal analysis and calculation of dynamic response caused by pressure pulsation (Hlaváč and Zeman, 2013), is a presentation of the newly developed method for seismic analysis of FA components.

2. Condensed Mathematical Model of the Fuel Assembly

In order to model, the hexagonal type FA (Fig. 1 and Fig. 2) is divided into subsystems – six identical rod segments $s = 1, 2, \dots, 6$, centre tube (CT) and load-bearing skeleton (LS). Each rod segment of the TVSA-T FA (on Fig. 2 drawn in lateral FA cross section and circumscribed by triangles) is composed of 52 fuel rods with fixed bottom ends in lower piece (LP) and 3 guide thimbles (GT) fully restrained in lower and head pieces (HP). The fuel rods and guide thimbles are linked by transverse spacer grids $g = 1, 2, \dots, 8$ of three types (SG1-SG3) inside the segments. All FA components are modelled as one dimensional continuum of beam type with nodal points in the gravity centres of their cross-sections on the level of the spacer grids.

The mathematical model of the rod segment s was derived in the coordinate system (Hlaváč and Zeman, 2013)

$$\mathbf{q}_s = [\mathbf{q}_{1,s}^T, \dots, \mathbf{q}_{r,s}^T, \dots, \mathbf{q}_{55,s}^T], \quad r = 1, \dots, 55, \quad s = 1, \dots, 6, \quad (1)$$

^{*} Prof. Ing. Vladimír Zeman, DSc.: Department of Mechanics, University of West Bohemia, Univerzitní 8, 306 14 Pilsen; CZ, zemanv@kme.zcu.cz

^{**} Assoc. Prof. RNDr. Zdeněk Hlaváč, CSc.: Department of Mechanics, University of West Bohemia, Univerzitní 8, 306 14 Pilsen; CZ, hlavac@kme.zcu.cz

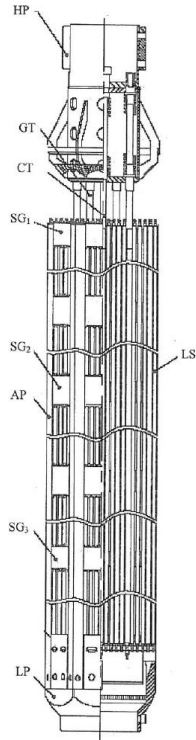


Fig. 1: Fuel assembly.

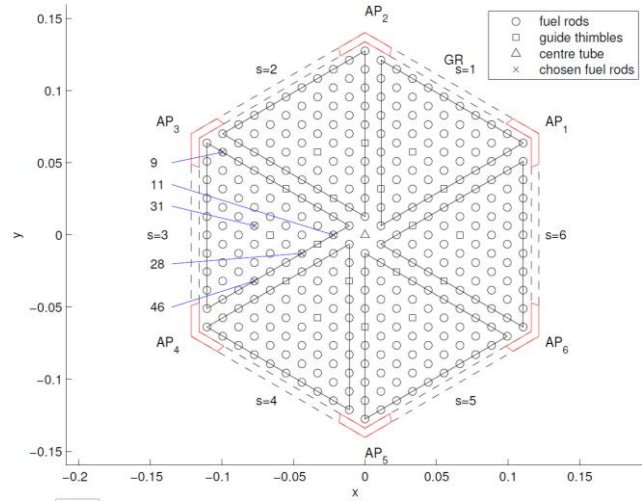


Fig. 2: Fuel assembly cross-section.

where $\mathbf{q}_{r,s}$ is vector of absolute lateral and bending displacements in nodal points of one rod r (fuel rod or guide thimble) in segment s on the level of all spacer grids $g = 1, \dots, 8$. The other subsystems – centre tube (CT) and load-bearing skeleton (LS) assembled from six angle pieces (AP) coupled by grid rims (GR) – are modelled similarly as one dimensional continua. The vectors \mathbf{q}_s of generalized coordinates of the subsystems loosed in kinematical excited nodes fixed by means of LP and HP into lower (L) and upper (U) support plates, can be partitioned in the form

$$\mathbf{q}_s = \left[\left(\mathbf{q}_L^{(s)} \right)^T, \left(\mathbf{q}_F^{(s)} \right)^T, \left(\mathbf{q}_U^{(s)} \right)^T \right]^T, \quad s = 1, 2, \dots, 6, CT, LS. \quad (2)$$

The displacements of free subsystem nodes (uncoupled with support plates) are integrated in vectors $\mathbf{q}_F^{(s)} \in \mathbb{R}^{n_s}$. The transformation between displacements of the all kinematical excited nodes of the subsystems and support plates in their gravity centres can be expressed in the global matrix form

$$\mathbf{q}_X^{(s)} = \mathbf{T}_X^{(s)} \mathbf{q}_X, \quad s = 1, 2, \dots, 6, CT, LS, \quad X = L, U. \quad (3)$$

The vectors \mathbf{q}_X of support plates $X = L, U$ absolute displacements result from seismic response of the reactor global model (Hlaváč and Zeman, 2010), where the fuel assemblies are replaced by beams.

The conservative mathematical models of the loosed subsystems in the decomposed block form corresponding to partitioned vectors according to (2) can be written as

$$\begin{bmatrix} \mathbf{M}_L^{(s)} & \mathbf{M}_{L,F}^{(s)} & \mathbf{0} \\ \mathbf{M}_{F,L}^{(s)} & \mathbf{M}_F^{(s)} & \mathbf{M}_{F,U}^{(s)} \\ \mathbf{0} & \mathbf{M}_{U,F}^{(s)} & \mathbf{M}_U^{(s)} \end{bmatrix} \begin{bmatrix} \ddot{\mathbf{q}}_L^{(s)} \\ \ddot{\mathbf{q}}_F^{(s)} \\ \ddot{\mathbf{q}}_U^{(s)} \end{bmatrix} + \begin{bmatrix} \mathbf{K}_L^{(s)} & \mathbf{K}_{L,F}^{(s)} & \mathbf{0} \\ \mathbf{K}_{F,L}^{(s)} & \mathbf{K}_F^{(s)} & \mathbf{K}_{F,U}^{(s)} \\ \mathbf{0} & \mathbf{K}_{U,F}^{(s)} & \mathbf{K}_U^{(s)} \end{bmatrix} \begin{bmatrix} \mathbf{q}_L^{(s)} \\ \mathbf{q}_F^{(s)} \\ \mathbf{q}_U^{(s)} \end{bmatrix} = \begin{bmatrix} \mathbf{f}_L^{(s)} \\ \mathbf{f}_C^{(s)} \\ \mathbf{f}_U^{(s)} \end{bmatrix}, \quad (4)$$

where letters \mathbf{M} (\mathbf{K}) correspond to mass (stiffness) submatrices of the subsystems. The force subvector $\mathbf{f}_C^{(s)}$ expresses the coupling forces between subsystem s and adjacent subsystems transmitted by spacer grids. The force subvectors $\mathbf{f}_L^{(s)}$ and $\mathbf{f}_U^{(s)}$ express the forces acting in kinematical excited nodes.

The detailed model of FA has to large DOF number for calculation of seismic response excited by FA support plate seismic motion. Therefore we assemble the FA condensed model with reduced DOF number. The vectors $\mathbf{q}_F^{(s)}$ of dimension n_s , corresponding to free nodes of subsystems, can be approximately transformed in the form

$$\mathbf{q}_F^{(s)} = {}^m \mathbf{V}_s \mathbf{x}_s, \mathbf{x}_s \in R^{m_s} \quad s = 1, 2, \dots, 6, CT, LS, \quad (5)$$

where ${}^m \mathbf{V}_s \in R^{n_s \times m_s}$ are modal submatrices compound out of chosen m_s master eigenvectors of subsystems fixed in kinematical excited nodes. The second set of equations extracted from (4) for each subsystem can be rewritten using (5) and orthonormality conditions

$${}^m \mathbf{V}_s^T \mathbf{M}_F^{(s)} {}^m \mathbf{V}_s = \mathbf{E}, \quad {}^m \mathbf{V}_s^T \mathbf{K}_F^{(s)} {}^m \mathbf{V}_s = {}^m \mathbf{\Lambda}_s, \quad s = 1, 2, \dots, 6, CT, LS \quad (6)$$

in the form

$$\ddot{\mathbf{x}}_s(t) + {}^m \mathbf{\Lambda}_s \mathbf{x}_s(t) = -{}^m \mathbf{V}_s^T \sum_{X=L,U} [\mathbf{M}_{F,X}^{(s)} \mathbf{T}_X^{(s)} \ddot{\mathbf{q}}_X + \mathbf{K}_{F,X}^{(s)} \mathbf{T}_X^{(s)} \mathbf{q}_X] + {}^m \mathbf{V}_s^T \mathbf{f}_C^{(s)}, \quad (7)$$

where spectral submatrices ${}^m \mathbf{\Lambda}_s \in R^{m_s \times m_s}$ correspond to chosen master eigenvectors in ${}^m \mathbf{V}_s$. The model (7) of all subsystems can be written in the configuration space $\mathbf{x} = [\mathbf{x}_s]$ of dimension $m = \sum m_s$ as

$$\ddot{\mathbf{x}}(t) + (\mathbf{\Lambda} + \mathbf{V}^T \mathbf{K}_C \mathbf{V}) \mathbf{x}(t) = -\mathbf{V}^T \sum_{X=L,U} [\mathbf{M}_X \ddot{\mathbf{Q}}_X(t) + \mathbf{K}_X \mathbf{Q}_X(t)], \quad (8)$$

where global vector of coupling forces between subsystems is $\mathbf{f}_C = [\mathbf{f}_C^{(s)}] = -\mathbf{K}_C \mathbf{q}_F$. Matrix \mathbf{K}_C is stiffness matrix of all couplings between subsystems derived in monograph Hlaváč and Zeman (2013) for Russian TVSA-T fuel assembly and $\mathbf{q}_F = [\mathbf{q}_F^{(s)}] = \mathbf{V} \mathbf{x}(t)$. Matrices $\mathbf{\Lambda} = \text{diag} [{}^m \mathbf{\Lambda}_s] \in R^{n,m}$, $\mathbf{V} = \text{diag} [{}^m \mathbf{V}_s] \in R^{n,m}$, $\mathbf{M}_X = \text{diag} [\mathbf{M}_{F,X}^{(s)} \mathbf{T}_X^{(s)}]$, $\mathbf{K}_X = \text{diag} [\mathbf{K}_{F,X}^{(s)} \mathbf{T}_X^{(s)}] \in R^{n,48}$, $n = \sum n_s$, $X = L, U$ are block diagonal, composed from corresponding matrices of subsystems. Vectors $\mathbf{Q}_X = [\mathbf{q}_X^T, \dots, \mathbf{q}_X^T]^T \in R^{48}$, $X = L, U$ are assembled for eight times repeating support plate displacement vectors.

In consequence of slightly damped FA components we consider modal damping of the subsystems characterized in the space of modal coordinates \mathbf{x}_s by diagonal matrices $\mathbf{D}_s = \text{diag} [2D_v^{(s)} \Omega_v^{(s)}]$, where $D_v^{(s)}$ are damping factors of natural modes and $\Omega_v^{(s)}$ are eigenfrequencies of the mutually uncoupled subsystems. The damping of spacer grids can be approximately expressed by damping matrix $\mathbf{B}_C = \beta \mathbf{K}_C$ proportional to stiffness matrix \mathbf{K}_C . The conservative condensed model (8) can be completed in the form

$$\ddot{\mathbf{x}}(t) + (\mathbf{D} + \beta \mathbf{V}^T \mathbf{K}_C \mathbf{V}) \dot{\mathbf{x}}(t) + (\mathbf{\Lambda} + \mathbf{V}^T \mathbf{K}_C \mathbf{V}) \mathbf{x}(t) = -\mathbf{V}^T \sum_{X=L,U} [\mathbf{M}_X \ddot{\mathbf{Q}}_X(t) + \mathbf{K}_X \mathbf{Q}_X(t)], \quad (9)$$

where $\mathbf{D} = \text{diag} [\mathbf{D}_s]$ is block diagonal matrix composed from damping matrices of subsystems.

3. Seismic Response of the Fuel Assembly Components

The FA seismic response in coordinates $\mathbf{x}(t)$ can be investigated by integration of motion equations (9) transformed into $2m$ differential equations of the first order using standard software (for example ODE45 in MATLAB code). We obtain the numerical values of the vector $\mathbf{x}(t_k)$ components in time steps. According to (5) we get the vector $\mathbf{q}_F^{(s)}(t_k) = {}^m \mathbf{V}_s \mathbf{x}_s(t_k)$ for select FA subsystem.

As an illustration, the time behaviour of lateral deformation of the chosen FR $r = 31$ in segment $s = 3$ on the level of the spacer grid $g = 8$ in the Russian TVSA-T FA of the WWER 1000/320 type reactors in

NPP Temelín (Hlaváč and Zeman, 2010) is presented in Fig. 3. The condensed FA model (9) with 650 DOF ($m_S = 100, m_{CT} = 20, m_{LS} = 30$) place of original model with 10 832 DOF ($n_S = 1760, n_{CT} = 32, n_{LS} = 240$), was used for numerical integration.

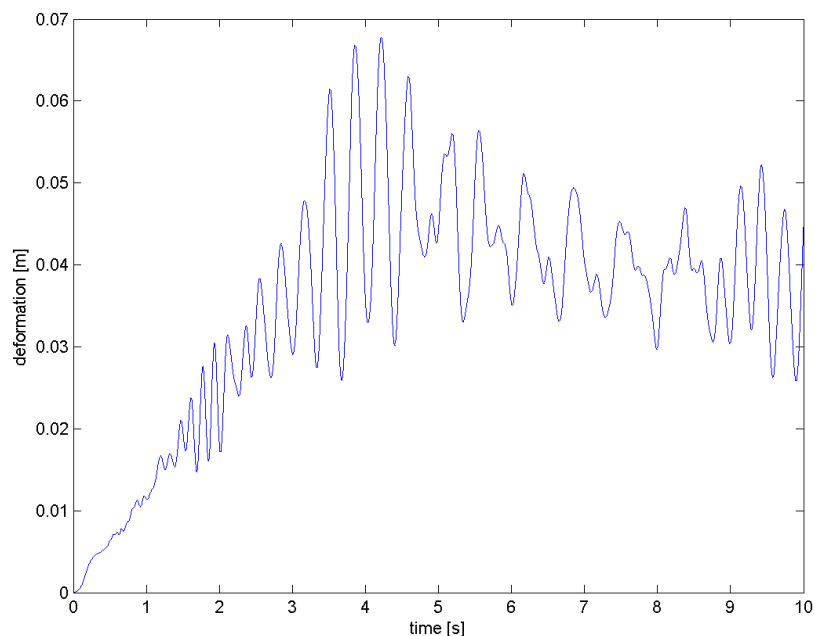


Fig. 3: Seismic deformation.

4. Conclusions

The described method, based on the FA decomposition and modal synthesis method with reduction of DOF number, enables to investigate effectively seismic response of the FA components. The FA seismic vibrations are caused by spatial motion of the supporting plates in the reactor core transformed into displacements of the kinematically excited nodes of the fuel assembly components – fuel rods, guide thimbles, centre tube and skeleton angle pieces – linked by spacer grids.

The developed methodology was used for seismic response of the Russian type nuclear fuel assembly. The developed software in MATLAB code is conceived in such a way that enables to calculation of the displacements and deformation of the arbitrary FA component on the arbitrary spacer grid level.

Acknowledgement

This work was supported by the European Regional Development Fund (ERDF), project “NTIS”, European Centre of Excellence, CZ.1.05/1.1.00/02.0090.

References

- Betbeder-Matibet, J. (2008) *Seismic Engineering*. J. Wiley&Sons, London.
- Hlaváč, Z., Zeman, V. (2010) The seismic response affection of the nuclear reactor WWER 1000 by nuclear fuel assemblies. *Engineering Mechanics*, 17, 3/4, pp. 147-160.
- Hlaváč, Z., Zeman, V. (2013) *Vibration of nuclear fuel assembly*. LAP Lambert Academic Publishing, Saarbrücken.

MODELLING OF THE VIBRATING DRYER DRIVE SYSTEM

D. Żórawski^{*}, W. Dzikowska^{**}, K. Peszyński^{***}

Abstract: *The paper presents an analysis of the drive system of the vibrating dryer. The source of the vibration exciting force is two electrovibrators fastened to the body of the dryer. It is possible to change the angle of their inclination and size of the unbalanced mass. The mathematical model of the vibrator was determined. Also components of excitation were analysed. The results were compared with values of force declared by the manufacturer of vibrators. The resulting mathematical model was implemented in the SCILAB environment. There were performed many simulations to determine the impact of parameters on the magnitude of the force.*

Keywords: Mathematical modelling, Vibrations, Dryer, Drive system, SCILAB.

1. Introduction

Drying is one of the basic technological operations applied before storage of seeds. The moist seeds tend to form lumps. As a result of this process a drying air flows through wide channels and does not flow precisely around drying seeds (Blechman, 1971; Luyben, 1996). To reduce this phenomenon the research on the use of vibrating dryers for drying seeds are carried out. It is hypothetically assumed that this type of dryer allows unifying the structure of drying deposit and thereby energy efficiency of the process will be improved.

Device used in the research is a vibrating dryer which is based on the previously made sifter (Korpál et al., 2005) with round sieves. The dryer is characterised by spatial motion caused by two identical electrovibrators fastened to the body of the dryer. Each vibrator consists of electric motor and unbalanced masses mounted on its shaft. Mathematical model of the process has to be designed to device the proper methodology of experimental research. In the initial phase the mechanical part of the device was designed.

2. Mathematical Model

The task of the vibrating dryer is to cause circumferential motion of seeds in the horizontal plane. Testing this trajectory is done by fluoridation of certain seeds and then their recording by motion-picture camera.

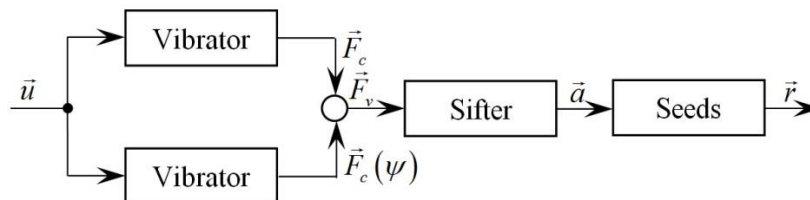


Fig. 1: Schematic diagram of mechanical system of vibrating dryer.

^{*} Damian Żórawski, MSc: PhD. student: Faculty of Chemical Technology and Engineering, University of Technology and Life Sciences; ul. Seminaryjna 3; 85-326 Bydgoszcz; Poland, damzor000@utp.edu.pl

^{**} Weronika Dzikowska, MSc: PhD. student: Faculty of Mechanical Engineering, University of Technology and Life Sciences; al. Prof. S. Kaliskiego 7; 85-789 Bydgoszcz; Poland, weronika.dzikowska@wp.pl

^{***} Assoc. Prof. Kazimierz Peszyński, CSc.: Mechanical Engineering Department, University of Technology and Life Sciences; al. Prof. S. Kaliskiego 7; 85-789 Bydgoszcz; Poland, peszyn@utp.edu.pl

Fig. 1 shows the schematic diagram of the process of forcing the seeds motion. The value of input is a vector of parameters $\vec{u} = u(n, \alpha, \beta, \psi)$, where n is a rotational speed set by the power inverter, α is an angle defining setting of the unbalanced masses in relation to a plane passing through the axis of the electric motor (Fig. 2), β is an angle of deviation of plane of centrifugal force rotation from vertical (Fig. 3) while ψ is a mutual phase shift of both vibrators.

The vibrations of vibrator are caused by 4 masses in the shape of semicircle (two masses on the one side of the motor) positioned relative to each other at an angle $\pi - 2\alpha$ (Fig. 2). Change in angle α allows to change the unbalance of the mass, i.e. a change of centrifugal force constituting the vibration extortion.

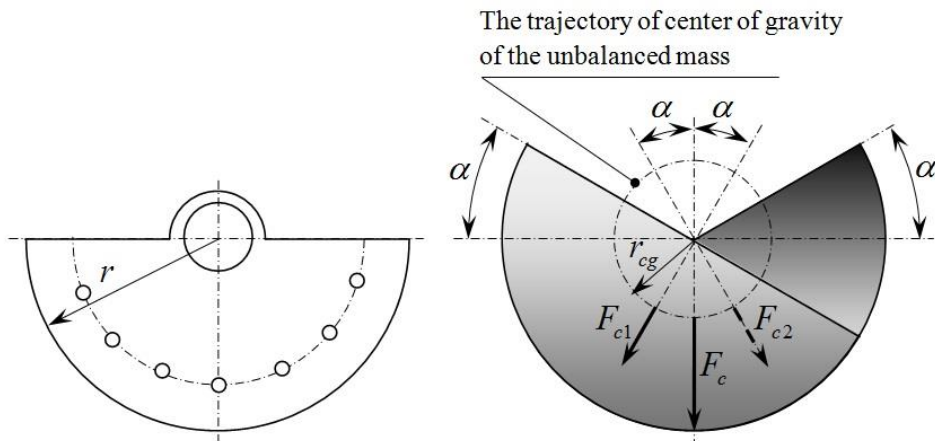


Fig. 2: Unbalanced masses: a) Real; b) Model system.

The real part for calculations, shown in Fig. 2a, was simplified to the form of full semicircle (Fig. 2b) hereinafter referred to as a disk. The ring of mounting was omitted as well as 7 boreholes used for positioning disks relative to each other. For the calculations, after precise weighting, the disk mass was $m_d = 0,9 \text{ kg}$. Radius of centre of gravity trajectory of unbalanced mass r_{cg} was determined from formula

$$r_{cg} = \frac{4r_d}{3\pi} \quad (1)$$

where r_d is a radius of the disk.

It is possible to define more precisely the radius of centre of gravity trajectory of unbalanced mass by taking into account the negative mass of 7 boreholes and the ring of mounting but it is not necessary. The difference was less than 1% in result.

The value of the centrifugal force acting on one disk, e.g. disk 1, was given by the formula

$$F_{c1} = m_d a_n = m_d r_{cg} \omega^2 \quad (2)$$

where: a_n - centrifugal acceleration, ω - angular speed of a disk. Angular speed is calculated from the rotational speed $\omega = 2\pi n$, where n is a value of rotational speed set by the power inverter.

Due to the symmetry the value of centrifugal force F_{c2} acting on the second disc is the same. The resultant centrifugal force that causes vibrations of the system is the vector sum of the centrifugal forces of both discs.

$$\vec{F}_c = \vec{F}_{c1} + \vec{F}_{c2} \Rightarrow F_c = 2m_d r_{cg} \omega^2 \cos \alpha \quad (3)$$

where: F_c is a value of resultant force.

The direction of the resultant force depends on the angles β and $\varphi = \omega t$. Fig. 3 shows established coordinate system $Oxyz$. Lined plane is perpendicular to the axis of the vibrator. In this plane the centrifugal force moves in a circular motion. In this arrangement, the values of centrifugal force components along the axis of the coordinate system were determined. They are necessary to determine the vibrations of vibrating dryer in the vertical and horizontal plane.

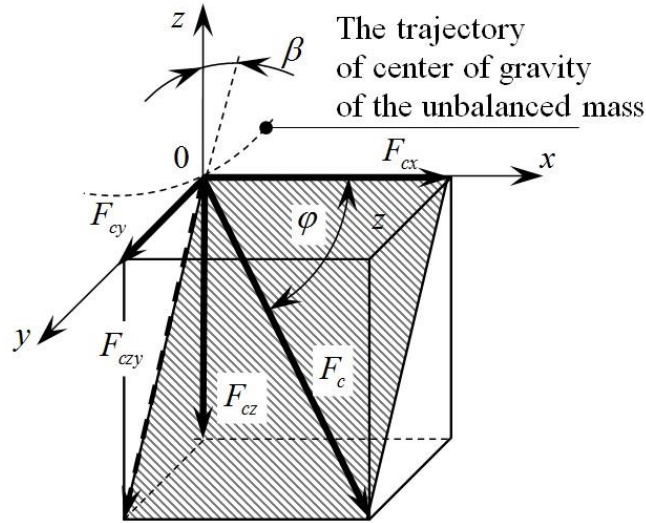


Fig. 3: Determination of the components of the centrifugal force.

$$F_{cx} = F_c \cos \varphi = 2m_d r_{cg} \omega^2 \cos \alpha \cos \varphi \quad (4)$$

$$F_{czy} = F_c \sin \varphi \quad (5)$$

$$F_{cz} = F_{czy} \cos \beta = F_c \sin \varphi \cos \beta = 2m_d r_{cg} \omega^2 \cos \alpha \sin \varphi \cos \beta \quad (6)$$

$$F_{cy} = F_{czy} \sin \beta = F_c \sin \varphi \sin \beta = 2m_d r_{cg} \omega^2 \cos \alpha \sin \varphi \sin \beta \quad (7)$$

Components calculated by equations (4), (6), and (7) determine vibrations which are motion excitation of vibrating dryer in specific planes for the system.

3. Numerical Model of the Vibrator

Numerical mathematical model of vibrator (equations (4), (6), and (7)) has been carried out in SCILAB environment, exactly in Xcos graphical editor.

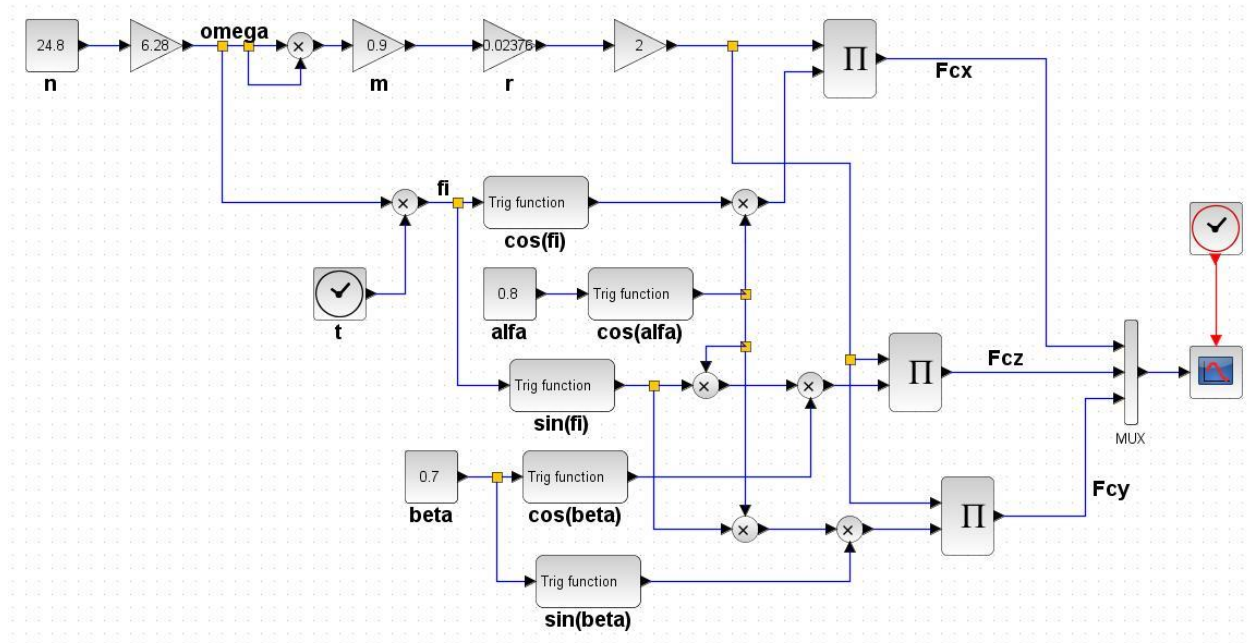


Fig. 4: Algorithm diagram for the mathematical model of the vibrator.

Variable parameters in the model are angles α and β . Several simulations were carried out for the vibrator with variable values of these parameters. Simulation results are presented in the form of diagrams for randomly chosen variables.

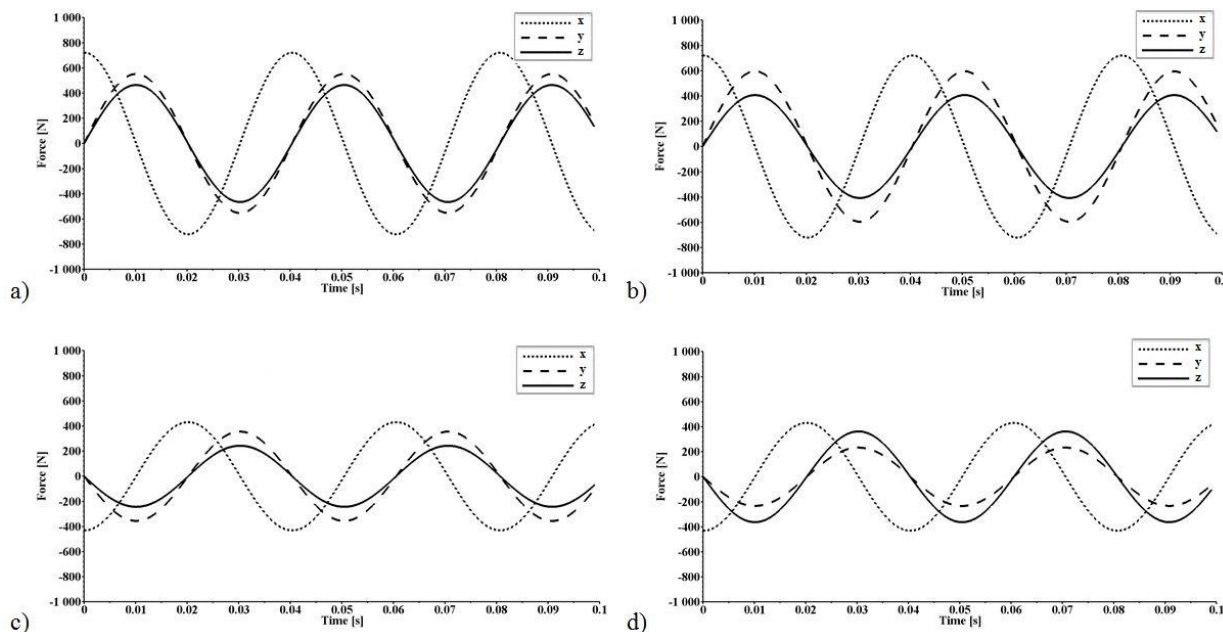


Fig. 5: Graphical simulation of excitation forces of drive system
 a) $\alpha = 0.8\text{rad}, \beta = 0.7\text{rad}$ b) $\alpha = 0.8\text{rad}, \beta = 0.6\text{rad}$
 c) $\alpha = 2.0\text{rad}, \beta = 0.6\text{rad}$ d) $\alpha = 2.0\text{rad}, \beta = 1.0\text{rad}$.

4. Conclusions

Values of forces determined from the mathematical model have been compared with the data obtained experimentally from the manufacturer. Despite the simplifying assumptions, there is a significant compatibility with data obtained from the manufacturer of electrically driven vibrators.

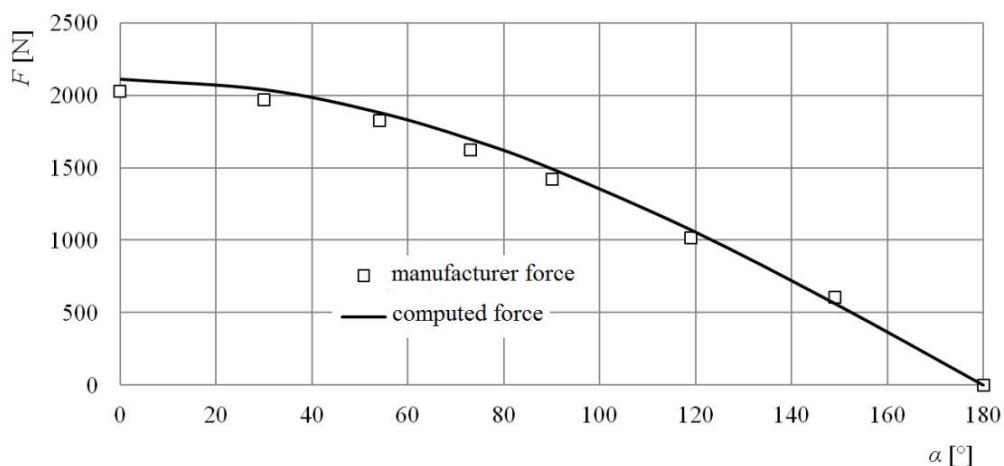


Fig. 6: Comparison of the calculated and the manufacturer data.

Obtained mathematical model will be very useful in subsequent steps of the mathematical modelling of the seeds motion during the drying process.

References

- Blechman, I. (1971) Synchronization of Dynamic Systems). Moskwa Nauka, (in Polish).
- Luyben, W. L. (1996) Process Modelling, Simulation, and Control for Chemical Engineers. WNT Warszawa (in Polish).
- Korpal, W., Weiner, W. (2005) Multilevel Vibration Sifter. University of Technology and Agriculture, University Press, Bydgoszcz.

PREDICTION OF ESHELBY'S INCLUSION PROBLEM SOLUTION USING ARTIFICIAL NEURAL NETWORK

L. Zrůbek^{*}, A. Kučerová^{**}, J. Novák^{***}

Abstract: *In this contribution we present our new approach to obtain or better estimate mechanical fields (strain, stress and displacement) inside isotropic infinite body with ellipsoidal-like inclusions. The precise solution has been given by J. D. Eshelby (1957) to internal and external points of inclusion domains and form the basis of our work. When the Eshelby's solution is extended to take into account perturbations due to the presence of numerous adjacent inclusions (Novák et al., 2012; Oberrecht et al., 2013) the solution given for dozens of points is very time demanding. Utilizing Artificial Neural Network (ANN) trained by exact Eshelby's solutions to predict mechanical fields can be achieved considerable speedup at the cost of approximate solution. At this state we only focus on prediction of one component of a perturbation strain tensor for single ellipsoidal inclusion.*

Keywords: Micromechanics, Isotropic Ellipsoidal Inclusions, Eshelby's Solution, Artificial Neural Network.

1. Introduction

In these days, composite materials form an integral part of the world around us. Whether it's a well-known material or material being just developed, we want to know the most about their properties and their behaviour at the macro or micro level. In this paper, we focus on the micro level behaviour of composite non-dilute material consisting of isotropic ellipsoidal-like inclusions and isotropic infinite matrix. Our main interest is the evaluation of micromechanical fields (strain, stress and displacement) on this type of material.

2. Eshelby's Solution

The analytical solution for elastic fields caused by inclusions has been given by J. D. Eshelby (1957). In his work Eshelby shows that this problem can be decomposed into exactly two tasks of a known solution

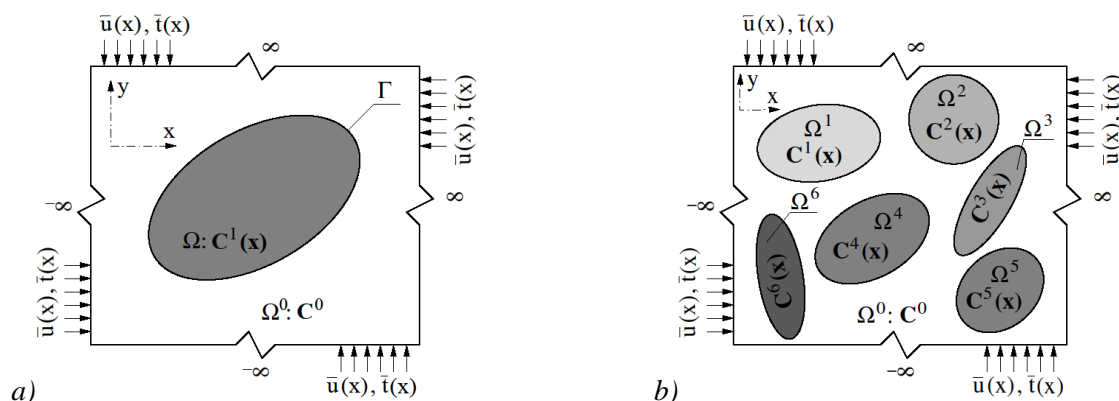


Fig. 1: a) Single inhomogeneity problem; b) Multiple inhomogeneity problem.

^{*} Ing. Lukáš Zrůbek: Czech Technical University in Prague, Faculty of Civil Engineering, Department of Mechanics; Thákurova 7, 166 29, Prague; CZ, lukas.zrubek@fsv.cvut.cz

^{**} Ing. Anna Kučerová, PhD.: Czech Technical University in Prague, Faculty of Civil Engineering, Department of Mechanics; Thákurova 7, 166 29, Prague; CZ, anicka@cml.fsv.cvut.cz

^{***} Ing. Jan Novák, PhD.: Czech Technical University in Prague, Faculty of Civil Engineering, Department of Mechanics; Thákurova 7, 166 29, Prague; CZ, novakj@cml.fsv.cvut.cz

and then assembled back by making use of the superposition principle. The solution of a single inhomogeneity problem, see Fig. 1a, is therefore given as the sum of homogeneous infinite body problem and homogeneous inclusion problem, so called perturbation part of mechanical fields (Eshelby, 1957; Mura, 1982). In case of multiple inhomogeneity (Fig. 1b), the solution of mechanical field within a body with N inclusions is obtained as the sum of N single inclusion tasks scaled by a multiplier associated with each inclusion so as to fulfil self-equilibrium as presented in paper by Novák (2008).

Using these solutions and computer programming the μ MECH library (Novák et al., 2012; Oberrecht et al., 2013) was created for solving micromechanical fields in materials with single or multiple inclusions. But, despite the performance of computers, the solution for thousands of points (no matter if internal or external) is very time demanding. Therefore, we came up with the idea of speeding up the process with predicting approximate solutions by an Artificial Neural Network (ANN).

3. Artificial Neural Network

Artificial Neural Networks (ANN) are computational models based on central nervous systems, especially on brain (Gurney, 2002; Haykin, 2009). These models are capable of machine learning and recognizing of patterns in given data. ANN consists of many simple processing nodes – so called neurons – interconnected into systems that can change their structure during the training (learning) phase. To each connection between two neurons is assigned an adaptive value representing synaptic weight of this connection. Based on given data and respective results used as an external information flowing through the system, these weights are balanced in a way that the output of ANN corresponds to the actual results.

There are numerous types of ANNs from single-directional systems to complicated multi-directional systems with many inputs and nested loops. One specific type of ANN is the feed-forward neural network. In this system, neurons are organized into layers where connections among neurons are placed only between adjacent layers, as shown in Fig. 2. There are no loops, cycles or feed-back connections.

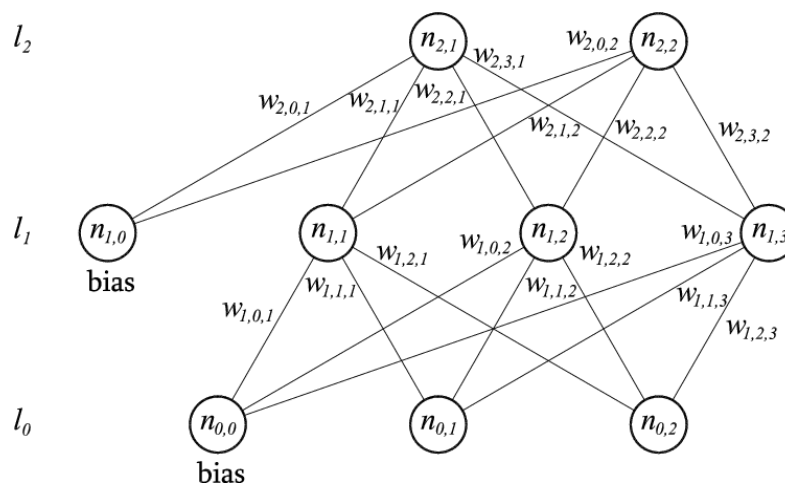


Fig. 2: Example of feed-forward Artificial Neural Network.

The most widely used example is the multi-layer perceptron (MLP) with the sigmoid transfer function and the gradient descent method of training – so called backpropagation learning algorithm. The power of MLPs lies in their ability to approximate nonlinear relations which corresponds to our problem, so when speaking about ANN in the following text, the MLP is considered.

4. Prediction of Eshelby's Solution

As described in section 2, the solution for materials with multiple inclusions is decomposed into separate solutions, each for every inclusion. Therefore, we assume here only single inclusion in the infinite isotropic body. But even so, the solution of mechanical fields depends on many input variables, such as load case, Young's modulus and Poisson's ratio of the inclusion and matrix, dimensions and rotations of the inclusion in space, coordinates of the inclusion centre and coordinates of a point where we want to evaluate mechanical fields.

4.1. ANN model and samples generation

For a sake of simplicity, we decided to start with the simplest model where the only variables are coordinates of a given point and all the inclusion and matrix parameters are fixed. In such a case, the coordinate system of the inclusion coincides with the coordinate system of the applied load case and we can limit the domain of point coordinates to only the first octant of the inclusion coordinate system. That is because the mechanical fields around inclusion are symmetrical to planes defined by semiaxes of inclusion. The centre of the inclusion matches the centre of a used coordinate system.

To generate uniformly distributed samples of point coordinates, we used software called SPERM 2.0 (Novák, 2011) based on method of Latin Hypercube Sampling (LHS). In total we generate 10 000 points with uniformly distributed coordinates x , y and z in range from 0.0 to 0.5. Other material properties and used constants are listed in table 1. As the load case is always the remote unit strain, particular units are irrelevant thus it is only a question of scaling.

Tab. 1: Material properties and used constants.

<i>Properties and constants</i>	<i>Infinite matrix</i>	<i>Inclusion</i>
<i>Young modulus</i>	5	50
<i>Poisson's ratio</i>	0.25	
<i>Load case</i>	<i>remote strain $\epsilon_{xx} = 1.0$ in inclusion centroid</i>	
<i>Semiaxes dimensions</i>	/	$a_1 = 0.15; a_2 = 0.1; a_3 = 0.05$
<i>Euler angles</i>	/	$\alpha = \beta = \gamma = 0.0$

4.2. Model training

For the ANN training phase the reference results are needed. We used the above-mentioned μ MECH library and for each point solve the perturbation fields. As another part of simplification we decide to predict only one element from the results, the perturbation strain ϵ_{xx} . From these results, we create a cumulative distribution function (CDF), as we want the results to be in uniform distribution.

To create and train the ANN we used software called RegNeN 2012 (Regression by Neural Network) (Mareš and Kučerová, 2012) which is a software package for computing a regression for given data using artificial neural network. During the training phase the neural system itself is created. It is composed from three input neurons in the first layer, n neurons in the second so called hidden layer and one output neuron in the third layer. Numbers of neurons in hidden layer depend on the self validating process for which the software uses so called cross-validation method.

In this method the samples are divided into m parts from which $m-1$ parts are used to calibrate the weights between neurons and the remaining part is used for validation. Then one neuron is added into hidden layer, the process of calibrating is repeated with different $m-1$ parts and for validation is used the current remaining part. This is repeated m -times and finally the ANN with smallest error is saved.

4.3. Results verification

In practical use, this is the place when the desired prediction of results takes a turn. Material for which we want to know the mechanical fields must be distributed in the same data format as was used in the training phase. These simple inputs are forwarded to already trained ANN which in a split of a second return predicted results based on previously calibrated synaptic weights.

But because of the development of this method we are more interested in the accuracy of predicted results than the results itself. So we take all of the 10 000 input samples that we used for the ANN training and perform the prediction of results. Since we used the CDF values for ANN training, the predicted results were also in a scale from 0 to 1. The difference between exact and predicted data in CDF values is shown on Fig. 3a. Data on Fig. 3b are the same values only converted back using the inverse CDF.

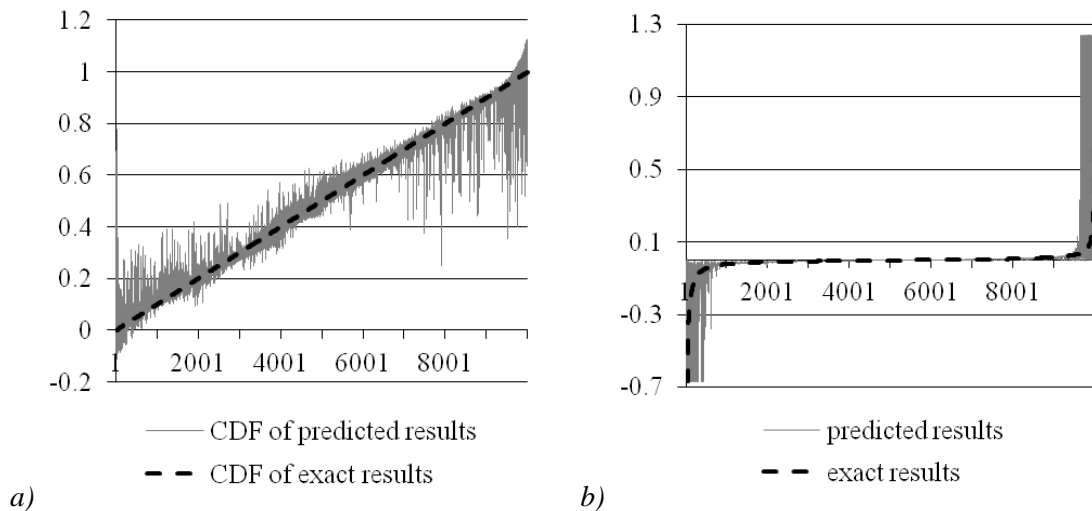


Fig. 3: Comparison of predicted results and exact results in: a) CDF values; b) Original values.

5. Brief Results

As can be seen from Fig. 3 the predicted results are distorted with an error which is most evident with the outlying data. In the case that the training data set will contain a sufficient representation of these outlying values the ANN should be able to better detect correlations for these values and predict better results. So we see a possible improvement in the use of a much larger set of training data.

Acknowledgement

This work was supported by the Czech Science Foundation, through projects No. P105/11/P370 (A. Kučerová), No. P105/12/0331 (J. Novák, L. Zrůbek) and by the Grant Agency of Czech Technical University in Prague through project No. SGS14/028/OHK1/1T/11 (L. Zrůbek, A. Kučerová).

References

- Eshelby, J. D. (1957) The determination of the elastic field of an ellipsoidal inclusion, and related problems, Proceedings of the Royal Society of London. Series A, Mathematical and Physical Sciences 241, no. 1226, pp. 376-396.
- Gurney, K. N. (2002) An introduction to neural networks. London: UCL Press.
- Haykin, S. S. (2009) Neural networks and learning machines (3rd ed.). New York: Prentice Hall/Pearson.
- Mareš, T., Kučerová, A. (2012) RegNeN 2012, Faculty of Civil Engineering, Czech Technical University in Prague, <http://klobouk.fsv.cvut.cz/~anicka/regnen/regnen.html>.
- Mura, T. (1982) Micromechanics of Defects in Solids., Martinus Nijhoff Publishers, P. O. Box 163, 3300 AD Dordrecht, The Netherlands, 1987. 587 p.
- Novák, J. (2008) Calculation of elastic stresses and strains inside a medium with multiple isolated inclusions, In: Proc. 6th International Conference on Engineering Computational Technology (Stirlingshire, UK) (M. Papadarakakis and B. H. V. Topping, eds.), Paper 127, 16 p.
- Novák, J. (2011) Generator of optimal LHS designs SPERM v. 2.0. Centre for Integrated Design of Advanced Structures (CIDEAS), Czech Technical University in Prague.
- Novák, J., Kaczmarczyk, L., Grassl, P., Zeman, J., Pearce, C. J. (2012) A micromechanics-enhanced finite element formulation for modelling heterogeneous materials. Computer Methods in Applied Mechanics and Engineering 201:53-64, 1103.5633.
- Oberrecht, S. P., Novák, J., Krysl, P. (2013) B-bar FEMs for anisotropic elasticity. International Journal for Numerical Methods in Engineering Published online in Wiley Online Library (wileyonlinelibrary.com), DOI: 10.1002/name.4621. [accepted, online appears soon]

Author Index

A

Andryszczyk M.	44, 724
Ansari R.I.	48
Aromiński A.	52
Astrouski I.	56, 236
Azzopardi J.P.	164

B

Bailly L.	72
Baláž I.	60, 304
Bansod Y.D.	30
Bednarik M.	64
Bednář L.	68
Belka M.	72
Benčat J.	76
Beňovský P.	80
Beroun S.	84, 88
Bertrand E.	72
Bittner T.	308
Blanchard R.	92, 552
Blasiak S.	96, 360, 644
Boiron O.	72
Borák L.	388
Borsuk G.	728
Boshoff W.P.	696
Bošanský M.	100
Brabec P.	84, 88
Brodňan M.	536
Březina L.	104
Březina T.	104
Bublík O.	108, 272
Buchar J.	544

Bula V.	224, 528
Bulejko P.	112
Burša J.	30
Byrtus M.	148

C

Cech V.	116
Čadek M.	120
Čečrdle J.	124
Čech J.	648
Čítek D.	536

D

Dittrich A.	84, 88
Dlouhý I.	596
Dlouhý T.	216
Dobrowolski B.	728
Dolanský J.	128
Doškář M.	132
Dowkontt S.	136
Drápal L.	444
Drdlová M.	544
Duda S.	140, 144
Dunčko M.	64
Dušková M.	224
Dyk Š.	148
Dzikowska W.	152, 748

E

Écsi L.	156
Élesztős P.	156
Eliáš J.	160, 352

F

Farrugia M.	164, 168
Fenech G.	168
Fernandéz-Canteli A.	220
Fíla T.	324
Filipský J.	172
Fischer C.	416
Fleckl T.	80
Florian Z.	424, 512
Foglar M.	176, 196, 208, 212
Fojtík F.	180
Friedel D.	600
Frydryšek K.	180
Fuis V.	184
Fürst J.	228

G

Gajewski M.	188
Gembalczyk G.	140, 144
Gołębiowska I.	192
Göringer J.	196
Grech N.	164

H

Hać M.	200
Hadas Z.	104, 204
Hadraba H.	596
Hagara M.	560
Hájek R.	208, 212
Hajžman M.	500
Halama J.	228
Hartl M.	34
Havlík J.	216
Hellmich Ch.	92, 552
Hlaváč Z.	744
Holický M.	624
Holub M.	296
Holušová T.	220
Holzer R.	64
Horáček J.	224, 528, 640, 680
Hoznedl M.	68
Hric V.	228
Hrstka M.	232
Hřibová V.	236
Huňady R.	256
Huňka P.	308, 536
Hutař P.	392, 396, 412, 496
Hyhlík T.	240
Hykl J.	656

CH

Chara Z.	684
Charvat M.	372
Chen K.	336
Chircop M.	164
Chládek Š.	244
Chleboun J.	248

Christé G.....476

I

Iván L.....252

Ivančo V.....256

Ivaničová L.....364

J

Jančo R.156

Janicek P.....260

Janouchová E.264

Janovcová M.....292

Jedelsky J.....72, 404

Jedlicka L.116

Jemiolo S.....188

Jevicky J.116

Jíra A.....324

Joch L.....268

Jonášová A.....108, 272

Jurík M.432

K

Kabeláč J.276

Kabele P.....516

Kaiser J.388

Kala Z.280

Kalina M.284

Kaňka S.....604

Kazakevičiūtė-Makovska R.288

Kiš R.....292

Klapka M.....468

Klusák J.232

Knobloch J.....296

Kočiš J.....424

Kohout M.....740

Kolařík F.....300

Kolber P.448, 452, 488

Koleková Y.60, 304

Kolísko J.308, 536, 648

Kolouch M.296

Komínek J.....236

Konfršt J.684

Kostecká M.308

Koteš P.312

Kotoul M.....232

Koudelka T.316

Kovář M.....176

Kovářová K.320

Kozánek J.688

Králík V.324

Krátký J.544

Kratochvíl O.328

Krauschneider R.....268

Krčmář M.....332

Krejsa J.....336

Křižan J.328

Kruis J.....316

Kruľáková M.364

Krúpa V.364

Krupička J.....684

Křupka I.34

Kubík M.....600

Kubík P.632

Kubíková T.....340

Kubín T.....180

Kučera P.344

Kučerová A.....264, 348, 752

Květoň J.352

Kyncl M.356

L

Laho M.	64
Laski P.A.	96, 360, 644
Laukkanen A.M.	528
Lawniczek R.	140, 144
Lazarová E.	364
Lengvarský P.	560
Lenner R.	624
Lepš M.	316, 408, 508
Liška V.	340
Lizal F.	72
Lo Monte F.	648
Lošák Pa.	428
Lošák Pe.	368, 460
Lukáč P.	428
Lukeš V.	532

M

Machacek J.	372
Majer Z.	376
Makovička D.	380
Makovička D. jr.	380
Malcho M.	292
Malíková L.	384
Malý M.	72
Manas P.	624
Mandlík T.	308
Marcján P.	388, 512
Marek J.	104
Maršálek O.	444
Martínek T.	640
Marvalová B.	120, 436
Máša B.	392
Matěcha J.	440

Materna A.	332
Miczan M.	68
Michálek T.	740
Mikeš K.	248
Míkula J.	396
Mikulanin L.	84
Milewski G.	400
Mlkvik M.	404
Morin C.	92
Myšáková E.	408

N

Náhlík L.	376, 392, 396, 412, 496
Náprstek J.	416, 420
Narra N.	388
Návrat T.	424
Nekvasil R.	428
Němec Z.	432, 468
Němeček J.	324
Nevrlý J.	432
Nguyen T.T.	88
Nhan P.T.	436
Nosek J.	316
Novák J.	132, 752
Novotný J.	440
Novotný P.	444
Novotný Z.	532
Nowicki K.	448, 452
Nowogońska B.	456

O

Omasta M.	34
Ondra V.	460

Orečný M.	256
Ostapski W.	136, 200
Ostaszewski M.	464

P

Panáček T.	468
Parham E.	472
Pásek M.	476
Patzák B.	100, 300
Pavlenko M.V.	480
Pečínka L.	484
Pelant J.	356
Perczyński D.	448, 452, 488
Peszyński K.	152, 452, 700, 748
Pešek L.	520
Petrikova I.	120, 436
Petruška J.	632
Pezowicz C.	736
Píštěk V.	344
Pleva L.	180
Podolka L.	492
Pohan P.	440
Pochylý F.	38
Pokorný P.	496
Polach P.	500
Polák M.	628
Pompach M.	180
Popov G.	504
Popovac M.	80
Popovič M.	252
Poruba Z.	180
Pospíšil S.	420
Pospíšilová A.	508
Prášilová E.	512
Profant T.	232
Přinosil M.	516

Půst L.	520
Pustulka A.	524

R

Radolf V.	224, 528
Raudensky M.	56, 236
Reichl Ch.	80
Ridzoň F.	80
Rohan E.	272, 532, 668
Rolc S.	544
Rossier S.	276
Roupec J.	600
Rudolf P.	38
Rusche H.	80
Řeháček S.	536
Řehák K.	540
Řídký R.	544
Řídký V.	548

S

Sahir M.H.	48
Sakiewicz W.	192
Samal S.M.	120, 436
Sant Z.	92, 552
Seitl S.	220
Sempruch J.	608, 664
Sergejev F.	636
Shirnesan A.	556
Schrötter M.	560
Siemieniako F.	464
Singule V.	660
Skalka P.	388, 564
Skallerud B.	540

Słowiński J.....	736
Sobieczky H.....	588
Sobotka J. Bc.....	564
Sobotka J. MSc.	568
Sokół K.	572
Sokolski P.	576
Solař J.....	580
Soltys R.....	584
Steen M.	692
Stodulka J.....	588
Stránský J.....	592
Stratil L.....	596
Strecker Z.....	600
Stryszewska T.	604
Strzelecki P.....	608
Stříž B.	612
Svěrák T.	112
Svojanovský T.....	616
Sýkora J.....	264, 348, 620
Sykora M.	624
Szabo I.	660
Šána V.....	628
Šebek F.	632
Šejnoha M.....	672
Ševčík M.	396
Ševčík R.	320
Ševeček O.	232
Šidlof P.....	548
Šimurda J.	476
Šín P.	636
Šiška F.....	596
Šperka P.	34
Štefan D.	38
Štegnarová K.....	412
Štorch V.....	172
Štubňa I.	636
Švancara P.....	640
Švec J.G.	640

Švrček M.....	484
---------------	-----

T

Tajč L.....	68
Takosoglu J.E.....	96, 360, 644
Tej P.	648
Tesár A.....	652
Tesař V.....	656
Theisz G.	180
Toman J.	660
Tomaszewski T.....	664
Tomko M.	584
Tonar Z.	340
Topoliński T.	44, 724
Trawinski T.....	140
Trtík L.....	616
Tseng A.A.	236
Tułodziecki M.....	136
Tummers M.J.....	692
Turjanicová J.	668

U

Učeň O.....	180
Urbanová S.....	672
Uzny S.	676

V

Vacek V.....	536, 648
Valeš J.	280
Vampola T.	224, 680
Vaysfeld N.....	504

Vechet S.	336
Vella A.	92, 552
Vetiska J.	104, 204
Vičan J.	312
Vimr J.	108, 272
Vlasak P.	684
Vlček V.	688
Vondál J.	692
Vorel J.	672, 696
Vosynek P.	424
Vyšanská M.	612

W

Wawrzyniak S.	448, 488, 700
Wieczorek B.	704, 708
Wieczorek M.	712, 716
Wigley G.	404
Winczek J.	720
Wirwicki M.	44, 724

Witter K.	340
Wolff J.	388
Wydrych J.	728

Z

Zachwieja J.	732
Žak M.	736
Zaremba M.	72, 404
Zelenka J.	740
Zeman J.	348
Zeman V.	148, 744
Ziobrowski P.	720
Zlámal P.	324
Zolotarev I.	244, 688
Žórawski D.	152, 748
Zozulevich B.	504
Zrůbek L.	752
Zubík M.	444
Žilka L.	180